Woodhead Publishing Series in Electronic and Optical Materials

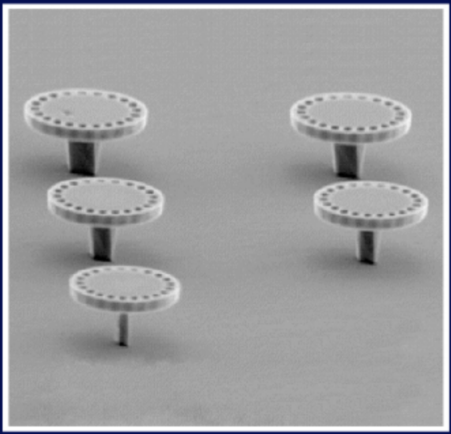

Semiconductor lasers

Fundamentals and applications

Edited by Alexei Baranov and Eric Tournié

WP
WOODHEAD
PUBLISHING

VISIT…

LANZAROTE Caliente.com

Semiconductor lasers

Related titles:

Handbook of solid-state lasers (ISBN 978-0-85709-272-4)

Lasers for medical applications (ISBN 978-0-85709-237-3)

Handbook of laser welding technologies (ISBN 978-0-85709-264-9)

Details of these books and a complete list of titles from Woodhead Publishing can be obtained by:

- visiting our web site at www.woodheadpublishing.com
- contacting Customer Services (e-mail: sales@woodheadpublishing.com; fax: +44 (0) 1223 832819; tel.: +44 (0) 1223 499140 ext. 130; address: Woodhead Publishing Limited, 80, High Street, Sawston, Cambridge CB22 3HJ, UK)
- in North America, contacting our US office (e-mail: usmarketing@woodheadpublishing.com; tel.: (215) 928 9112; address: Woodhead Publishing, 1518 Walnut Street, Suite 1100, Philadelphia, PA 19102-3406, USA)

If you would like e-versions of our content, please visit our online platform: www.woodheadpublishingonline.com. Please recommend it to your librarian so that everyone in your institution can benefit from the wealth of content on the site.

We are always happy to receive suggestions for new books from potential editors. To enquire about contributing to our Electronic and Optical Materials series, please send your name, contact address and details of the topic/s you are interested in to laura.pugh@woodheadpublishing.com. We look forward to hearing from you.

The Woodhead team responsible for publishing this book:

Commissioning Editor: Laura Pugh
Publications Coordinator: Anneka Hess
Project Editor: Cathryn Freear
Editorial and Production Manager: Mary Campbell
Production Editor: Mandy Kingsmill
Project Manager: Newgen Knowledge Works Pvt Ltd
Freelance Copyeditor: Newgen Knowledge Works Pvt Ltd
Proofreader: Newgen Knowledge Works Pvt Ltd
Cover Designer: Terry Callanan

Woodhead Publishing Series in Electronic and Optical Materials:
Number 33

Semiconductor lasers

Fundamentals and applications

Edited by
Alexei Baranov and
Eric Tournié

WOODHEAD
PUBLISHING

Oxford Cambridge Philadelphia New Delhi

Published by Woodhead Publishing Limited,
80 High Street, Sawston, Cambridge CB22 3HJ, UK
www.woodheadpublishing.com
www.woodheadpublishingonline.com

Woodhead Publishing, 1518 Walnut Street, Suite 1100, Philadelphia,
PA 19102–3406, USA

Woodhead Publishing India Private Limited, G-2, Vardaan House, 7/28 Ansari Road,
Daryaganj, New Delhi – 110002, India
www.woodheadpublishingindia.com

First published 2013, Woodhead Publishing Limited
© Woodhead Publishing Limited, 2013. Note: the publisher has made every effort to ensure that permission for copyright material has been obtained by authors wishing to use such material. The authors and the publisher will be glad to hear from any copyright holder it has not been possible to contact.
The authors have asserted their moral rights.

This book contains information obtained from authentic and highly regarded sources. Reprinted material is quoted with permission, and sources are indicated. Reasonable efforts have been made to publish reliable data and information, but the authors and the publisher cannot assume responsibility for the validity of all materials. Neither the authors nor the publisher, nor anyone else associated with this publication, shall be liable for any loss, damage or liability directly or indirectly caused or alleged to be caused by this book.

Neither this book nor any part may be reproduced or transmitted in any form or by any means, electronic or mechanical, including photocopying, microfilming and recording, or by any information storage or retrieval system, without permission in writing from Woodhead Publishing Limited.

The consent of Woodhead Publishing Limited does not extend to copying for general distribution, for promotion, for creating new works, or for resale. Specific permission must be obtained in writing from Woodhead Publishing Limited for such copying.

Trademark notice: Product or corporate names may be trademarks or registered trademarks, and are used only for identification and explanation, without intent to infringe.

British Library Cataloguing in Publication Data
A catalogue record for this book is available from the British Library.

Library of Congress Control Number: 2013931491

ISBN 978-0-85709-121-5 (print)
ISBN 978-0-85709-640-1 (online)
ISSN 2050-1501 Woodhead Publishing Series in Electronic and Optical Materials (print)
ISSN 2050-151X Woodhead Publishing Series in Electronic and Optical Materials (online)

The publisher's policy is to use permanent paper from mills that operate a sustainable forestry policy, and which has been manufactured from pulp which is processed using acid-free and elemental chlorine-free practices. Furthermore, the publisher ensures that the text paper and cover board used have met acceptable environmental accreditation standards.

Typeset by Newgen Knowledge Works Pvt Ltd, India
Printed by MPG Printgroup, UK

Contents

Contributor contact details *xi*
Woodhead Publishing Series in Electronic and Optical Materials *xv*
Preface *xix*

Part I Fundamentals of semiconductor lasers 1

1 Principles of semiconductor lasers 3
P. Blood, Cardiff University, UK

1.1 Introduction 3
1.2 The basic laser diode 7
1.3 Key physical concepts 16
1.4 Absorption and gain in low dimensional semiconductor structures 22
1.5 Recombination processes 32
1.6 Gain–current relations 34
1.7 Temperature dependence of threshold current 42
1.8 Rate equations 46
1.9 Future trends 49
1.10 Acknowledgements 50
1.11 References 50

2 Photonic crystal lasers 56
Y. Zhang and M. Lončar, Harvard University, USA

2.1 Introduction 56
2.2 Lasing threshold of photonic crystal lasers (PhCLs) 60
2.3 Photonic crystal nanobeam lasers 65
2.4 Photonic crystal disk lasers 72
2.5 Conclusion and future trends 74
2.6 Acknowledgements 76
2.7 References 76

3 High-power semiconductor lasers 81
M. Fallahi, University of Arizona, USA and
R. Bedford, Air Force Research Laboratory, USA

3.1 Introduction: theory and design concept 81
3.2 Single emitters 92
3.3 Array concept for power scaling 110
3.4 Conclusion and future trends 112
3.5 References 112

4 Semiconductor laser beam combining 121
B. Liu, Oak Ridge National Laboratory, USA, P. Colet, Instituto de Fisica Interdisciplinary Sistemas Complejos, IFISC (CSIC-UIB), Spain and Y. Braiman, Oak Ridge National Laboratory and University of Tennessee, USA

4.1 Introduction to laser beam combining 121
4.2 Experiments on external cavity broad-area laser diode arrays 125
4.3 Modeling the dynamics of a single-mode semiconductor laser array in an external cavity 138
4.4 Conclusion 144
4.5 Acknowledgments 145
4.6 References 145

5 Ultrafast pulse generation by semiconductor lasers 149
E. U. Rafailov, University of Dundee, UK and
E. Avrutin, University of York, UK

5.1 Introduction 149
5.2 Gain-switching 150
5.3 Important developments in gain-switched semiconductor lasers (SLs) 157
5.4 Q-switching 160
5.5 Mode-locking (ML) in semiconductor lasers: an overview 166
5.6 The main predictions of mode-locked laser theory 181
5.7 Important tendencies in optimising the ML laser performance 187
5.8 Novel mode-locking principles 196
5.9 Overview of applications of mode-locked diode lasers 206
5.10 Conclusion 207
5.11 Acknowledgements 208
5.12 References 208

Part II Visible and near-infrared lasers and their applications 219

6 Nonpolar and semipolar group III-nitride lasers 221
D. Feezell, University of New Mexico, USA and
S. Nakamura, University of California,
Santa Barbara, USA

6.1 Introduction 221
6.2 Applications of group III-nitride lasers 222
6.3 Introduction to properties of III-nitrides 223
6.4 Optical properties of nonpolar and semipolar III-nitrides 234
6.5 Substrates, crystal growth and materials issues 241
6.6 Optical waveguides and loss 246
6.7 Fabrication techniques 254
6.8 Nonpolar and semipolar laser history and performance 256
6.9 Future trends 260
6.10 Sources of further information and advice 261
6.11 References 262

7 Advanced self-assembled indium arsenide (InAs) quantum-dot lasers 272
M. Sugawara, QD Laser, Inc., Japan and The University of Tokyo, Japan and Y. Arakawa and K. Tanabe,
The University of Tokyo, Japan

7.1 Introduction 272
7.2 High-density and highly uniform InAs quantum dots 274
7.3 Quantum-dot Fabry–Pérot (FP) and distributed-feedback (DFB) lasers for optical communication 282
7.4 Quantum-dot FP and DFB lasers for high-temperature application 292
7.5 QD Laser, Inc. 299
7.6 Silicon hybrid quantum-dot lasers 303
7.7 Conclusion 309
7.8 Acknowledgements 309
7.9 References 310

8 Vertical cavity surface emitting lasers (VCSELs) 316
K. D. Choquette, University of Illinois, USA

8.1 Introduction 316
8.2 Device structure 319

8.3 Vertical cavity surface emitting laser (VCSEL) optical performance 329
8.4 Conclusion 336
8.5 Acknowledgements 337
8.6 References 337

9 Semiconductor disk lasers (VECSELs) 341
J. E. Hastie, S. Calvez and M. D. Dawson, University of Strathclyde, UK

9.1 Introduction 341
9.2 Principles of operation 342
9.3 Intracavity frequency control 352
9.4 Pulsed operation 367
9.5 Future trends and applications 376
9.6 Sources of further information and advice 378
9.7 References 378

10 Hybrid silicon lasers 394
D. Liang and J. E. Bowers, University of California, Santa Barbara, USA

10.1 Introduction 394
10.2 Fundamentals of Si lasers 395
10.3 Hybrid Si laser-based photonic integrated circuits 425
10.4 Conclusion 430
10.5 References 431

Part III Mid- and far-infrared lasers and their applications 439

11 Gallium antimonide (GaSb)-based type-I quantum well diode lasers: recent development and prospects 441
G. Belenky and L. Shterengas, State University of New York at Stony Brook, USA, M. V. Kisin, Ostendo Technologies, Inc., USA and T. Hosoda, State University of New York at Stony Brook, USA

11.1 Introduction 441
11.2 Diode lasers operating below 2.5 μm 448
11.3 Diode lasers for spectral range above 3 μm 465

11.4 Metamorphic GaSb-based diode lasers 477
11.5 Acknowledgements 481
11.6 References 481

12 Interband cascade (IC) lasers 487
R. Q. Yang, University of Oklahoma, USA

12.1 Introduction 487
12.2 Operating principle of interband cascade (IC) lasers 488
12.3 Early development and challenges 492
12.4 Recent progress and new developments 497
12.5 Future trends and conclusion 503
12.6 Acknowledgments 505
12.7 References 505

13 Terahertz (THz) quantum cascade lasers 514
S. Barbieri, University of Paris Diderot and CNRS, France and S. Kumar, Lehigh University, USA

13.1 Terahertz quantum cascade laser technology 514
13.2 Waveguides and photonic structures 516
13.3 Stabilisation, microwave modulation and active mode-locking of terahertz quantum cascade lasers 525
13.4 References 545

14 Whispering gallery mode lasers 551
A. Monakhov and N. Sablina, Ioffe Institute, Russia

14.1 Introduction to whispering gallery modes (WGM) 551
14.2 WGM in electrodynamics 555
14.3 Semiconductor WGM lasers 565
14.4 Light extraction from a WGM resonator 572
14.5 Conclusion 574
14.6 Acknowledgements 576
14.7 References 576

15 Tunable mid-infrared laser absorption spectroscopy 579
F. K. Tittel and R. Lewicki, Rice University, USA

15.1 Introduction 579
15.2 Laser absorption spectroscopic techniques 581
15.3 Quantum-cascade lasers (QCLs) for trace gas detection 595

15.4 Specific examples of QCL-based sensor systems 601
15.5 Conclusions and future trends 617
15.6 References 618

Index *631*

Contributor contact details

(* = main contact)

Editors

Alexei Baranov* and Eric Tournié
Institut d'Electronique du Sud
Université Montpellier 2/CNRS
France

E-mail: baranov@univ-montp2.fr; eric.tournie@univ-montp2.fr

Chapter 1

Peter Blood
School of Physics and Astronomy
Cardiff University
Queens Buildings
The Parade
Cardiff
CF24 3AA
UK

E-mail: bloodp@cf.ac.uk

Chapter 2

Yinan Zhang and Marko Lončar*
Harvard University
33 Oxford Street, Cambridge
MA 02188
USA

E-mail: loncar@seas.harvard.edu ; yinan@seas.harvard.edu

Chapter 3

Mahmoud Fallahi*
College of Optical Sciences
University of Arizona
Tucson, AZ 85721
USA

E-mail: fallahi@optics.arizona.edu

Robert Bedford
Air Force Research Laboratory
USA

E-mail: Robert.bedford@wpafb.af.mil

Chapter 4

Bo Liu
Center for Engineering Science Advanced Research
Computer Sciences & Mathematics Division
Oak Ridge National Laboratory
Oak Ridge
TN 37831
USA

E-mail: liub@ornl.gov

Pere Colet
Instituto de Fisica Interdisciplinary Sistemas Complejos (IFISC (CSIC-UIB))
Campus Universitat de les Illes Balears
E-07122
Palma de Mallorca
Spain

Yehuda Braiman*
Center for Engineering Science Advanced Research
Computer Sciences & Mathematics Division
Oak Ridge National Laboratory
Oak Ridge
TN 37831
USA

E-mail: braimany@ornl.gov

and

Department of Mechanical, Aerospace, and Biomedical Engineering
University of Tennessee
Knoxville
TN 37996
USA

Chapter 5

E. U. Rafailov*
School of Engineering, Physics and Mathematics
University of Dundee
Harris Building
Dundee
DD1 4HN
UK

E-mail: e.u.rafailov@dundee.ac.uk

Eugene Avrutin
Department of Electronics
University of York
Heslington
York
YO10 5DD
UK

E-mail: eugene.avrutin@york.ac.uk

Chapter 6

Daniel Feezell*
Assistant Professor of Electrical and Computer Engineering
Center for High Technology Materials
1313 Goddard St. SE (MSC04 2710)
University of New Mexico
Albuquerque
NM 87106-4343
USA

E-mail: dfeezell@unm.edu

Shuji Nakamura
University of California
Santa Barbara
USA

E-mail: shuji@engineering.ucsb.edu

Chapter 7

Mitsuru Sugawara*
QD Laser, Inc.
1–1 Minamiwataridacho
Kawasaki-ku
Kawasaki
Kanagawa 210-0855
Japan

E-mail: sugawara@qdlaser.com

and

Institute for Nano Quantum Information Electronics
The University of Tokyo
4–6–1 Komaba
Meguro-ku
Tokyo 153-8505
Japan

Y. Arakawa and K. Tanabe
Institute for Nano Quantum Information Electronics
The University of Tokyo
4-6-1 Komaba, Meguro-ku
Tokyo 153-8505
Japan

and

Institute of Industrial Science
The University of Tokyo
4-6-1 Komaba, Meguro-ku
Tokyo 153-8505
Japan

Chapter 8

Kent D. Choquette
Professor of Electrical and Computer Engineering
University of Illinois
208 North Wright Street
Urbana
IL 61801
USA

E-mail: choquett@illinois.edu

Chapter 9

Jennifer E. Hastie*, Stephane Calvez and Martin D. Dawson
Institute of Photonics
University of Strathclyde
Wolfson Centre
106 Rottenrow
Glasgow
G4 0NW
UK

E-mail: jennifer.hastie@strath.ac.uk; s.calvez@strath.ac.uk; m.dawson@strath.ac.uk

Chapter 10

Di Liang
Intelligent Infrastructure Laboratory
Hewlett Packard Laboratories
1501 Page Mill Road
Palo Alto
CA 94304
USA

and

Department of Electrical and Computer Engineering
University of California, Santa Barbara
CA 93106
USA

E-mail: dliang@ece.ucsb.edu

John E. Bowers*
Department of Electrical and Computer Engineering
University of California, Santa Barbara
CA 93106
USA

E-mail: bowers@ece.ucsb.edu

Chapter 11

Gregory Belenky*, Leon Shterengas and T. Hosoda
Department of Electrical and Computer Engineering
State University of New York at Stony Brook
Stony Brook
NY 11794
USA

E-mail: garik@ece.sunysb.edu

Mikhail V. Kisin
Ostendo Technologies, Inc.
6185 Paseo del Norte, Ste. 200
Carlsbad
CA 92011
USA

Chapter 12

Rui Q. Yang
School of Electrical and Computer Engineering
University of Oklahoma
110 W Boyd Street
Norman
OK 73019
USA

E-mail: Rui.Q.Yang@ou.edu

Chapter 13

Stefano Barbieri*
University of Paris Diderot and CNRS
Bâtiment Condorcet
10 rue A. Domont et L. Duquet
75205 Paris Cedex 13
France

E-mail: stefano.barbieri@univ-paris-diderot.fr

Sushil Kumar
Department of Electrical and Computer Engineering
Lehigh University
7 Asa Drive, Room 226,
Bethlehem
PA 18015
USA

E-mail: sushil@lehigh.edu

Chapter 14

A. M. Monakhov* and N. I. Sablina
Ioffe PhysicalTechnical Institute
Politekhnicheskaya, 26
Russia

E-mail: amon@les.ioffe.ru

Chapter 15

Frank K. Tittel* and Rafał Lewicki
Electrical and Computer Engineering Department
Rice University
6100 Main Street
Houston
TX 77005
USA

E-mail: fkt@rice.edu; Rafal.Lewicki@rice.edu

Woodhead Publishing Series in Electronic and Optical Materials

1 **Circuit analysis**
J. E. Whitehouse
2 **Signal processing in electronic communications: For engineers and mathematicians**
M. J. Chapman, D. P. Goodall and N. C. Steele
3 **Pattern recognition and image processing**
D. Luo
4 **Digital filters and signal processing in electronic engineering: Theory, applications, architecture, code**
S. M. Bozic and R. J. Chance
5 **Cable engineering for local area networks**
B. J. Elliott
6 **Designing a structured cabling system to ISO 11801: Cross-referenced to European CENELEC and American Standards**
Second edition
B. J. Elliott
7 **Microscopy techniques for materials science**
A. Clarke and C. Eberhardt
8 **Materials for energy conversion devices**
Edited by C. C. Sorrell, J. Nowotny and S. Sugihara
9 **Digital image processing: Mathematical and computational methods**
Second edition
J. M. Blackledge
10 **Nanolithography and patterning techniques in microelectronics**
Edited by D. Bucknall
11 **Digital signal processing: Mathematical and computational methods, software development and applications**
Second edition
J. M. Blackledge

12 **Handbook of advanced dielectric, piezoelectric and ferroelectric materials: Synthesis, properties and applications**
Edited by Z.-G. Ye
13 **Materials for fuel cells**
Edited by M. Gasik
14 **Solid-state hydrogen storage: Materials and chemistry**
Edited by G. Walker
15 **Laser cooling of solids**
S. V. Petrushkin and V. V. Samartsev
16 **Polymer electrolytes: Fundamentals and applications**
Edited by C. A. C. Sequeira and D. A. F. Santos
17 **Advanced piezoelectric materials: Science and technology**
Edited by K. Uchino
18 **Optical switches: Materials and design**
Edited by S. J. Chua and B. Li
19 **Advanced adhesives in electronics: Materials, properties and applications**
Edited by M. O. Alam and C. Bailey
20 **Thin film growth: Physics, materials science and applications**
Edited by Z. Cao
21 **Electromigration in thin films and electronic devices: Materials and reliability**
Edited by C.-U. Kim
22 ***In situ* characterization of thin film growth**
Edited by G. Koster and G. Rijnders
23 **Silicon-germanium (SiGe) nanostructures: Production, properties and applications in electronics**
Edited by Y. Shiraki and N. Usami
24 **High-temperature superconductors**
Edited by X. G. Qiu
25 **Introduction to the physics of nanoelectronics**
S. G. Tan and M. B. A. Jalil
26 **Printed films: Materials science and applications in sensors, electronics and photonics**
Edited by M. Prudenziati and J. Hormadaly
27 **Laser growth and processing of photonic devices**
Edited by N. A. Vainos
28 **Quantum optics with semiconductor nanostructures**
Edited by F. Jahnke
29 **Ultrasonic transducers: Materials and design for sensors, actuators and medical applications**
Edited by K. Nakamura

30 **Waste electrical and electronic equipment (WEEE) handbook**
Edited by V. Goodship and A. Stevels
31 **Applications of ATILA FEM software to smart materials: Case studies in designing devices**
Edited by K. Uchino and J.-C. Debus
32 **MEMS for automotive and aerospace applications**
Edited by M. Kraft and N. M. White
33 **Semiconductor lasers: Fundamentals and applications**
Edited by A. Baranov and E. Tournié
34 **Handbook of terahertz technology for imaging, sensing and communications**
Edited by D. Saeedkia
35 **Handbook of solid-state lasers: Materials, systems and applications**
Edited by B. Denker and E. Shklovsky
36 **Organic light-emitting diodes: Materials, devices and applications**
Edited by A. Buckley
37 **Lasers for medical applications: Diagnostics, therapy and surgery**
Edited by H. Jelínková
38 **Semiconductor gas sensors**
Edited by R. Jaaniso and O. K. Tan
39 **Handbook of organic materials for optical and optoelectronic devices: Properties and applications**
Edited by O. Ostroverkhova
40 **Metallic films for electronic, optical and magnetic applications: Structure, processing and properties**
Edited by K. Barmak and K. Coffey
41 **Handbook of laser welding technologies**
Edited by S. Katayama
42 **Nanolithography: The art of fabricating nanoelectronics, nanophotonics and nanobiology devices and systems**
Edited by M. Feldman
43 **Laser spectroscopy for sensing: Fundamentals, techniques and applications**
Edited by M. Baudelet
44 **Chalcogenide glasses: Preparation, properties and applications**
Edited by J.-L. Adam and X. Zhang
45 **Handbook of MEMS for wireless and mobile applications**
Edited by D. Uttamchandani
46 **Subsea optics and imaging**
Edited by J. Watson and O. Zielinski
47 **Carbon nanotubes and graphene for photonic applications**
Edited by S. Yamashita, Y. Saito and J. H. Choi

48 **Optical biomimetics: Materials and applications**
Edited by M. Large
49 **Optical thin films and coatings**
Edited by Angela Piegari and François Flory
50 **Computer design of diffractive optics**
Edited by V. A. Soifer
51 **Smart sensors and MEMS: Intelligent devices and microsystems for industrial applications**
Edited by S. Nihtianov and A. L. Estepa
52 **Fundamentals of femtosecond optics**
Edited by S. A. Kozlov and V. V. Samartsev

Preface

In 2012 the semiconductor laser celebrated its 50th anniversary. The first laser emission from a semiconductor was obtained almost simultaneously by several research teams in 1962. These early near infrared lasers made of GaAs p-n structures fabricated by liquid phase epitaxy could only operate at cryogenic temperatures and their poor performance made it difficult to imagine a brilliant future for such devices. The achievement of continuous wave operation at room temperature was a revolutionary step in the development of semiconductor lasers. This milestone was reached thanks to the use of the double heterostructure design providing more efficient optical and electronic confinement in the device. Further progress in semiconductor lasers, which made them actually a part of everyday life, was enabled by the development of novel physical concepts, as well as new materials and new growth techniques for their realization. This resulted in significant improvement of laser performances and expanded the accessible spectral range. Modern semiconductor lasers are based on sophisticated layered structures of multicomponent alloys grown by molecular beam epitaxy or by chemical vapor deposition. With III-nitride compounds the emission wavelength range of semiconductor lasers has been extended to the blue and ultraviolet domains. Quantum well and quantum dot concepts allowed an enormous reduction of the threshold current in lasers operating in visible and near infrared. The performances of the lasers employing interband radiative transitions across the band gap of a semiconductor however degrade at wavelengths above 3 μm because of the strong nonradiative Auger recombination in narrow gap materials. This problem has been overcome in quantum cascade lasers based on transitions between electron subbands in the conduction band where the Auger effect is weak. This technology allowed extending the wavelength range accessible to semiconductor lasers up to the THz region of the electromagnetic spectrum corresponding to wavelengths in the 40–300 μm range.

Semiconductor lasers have found many applications in different fields of science and industry. Mass scale production of semiconductor lasers for use as light sources for optical communications, barcode scanners and compact disc players, drastically reduced the prices and accelerated their penetration into everyday life. More sophisticated lasers such as high power devices for use in medicine or for efficient pumping of solid state lasers have been developed. Vertical cavity surface emitting lasers (VCSELs) made possible mass scale wafer level production of single mode coherent sources providing high coupling efficiency with optical fibers. VCSELs, as well as edge emitting single mode distributed feedback or photonic crystal lasers, are widely used nowadays in molecular spectroscopy for the selective detection of gases and vapors in trace concentrations. The development of new cavity configurations has yielded widely tunable spectroscopic sources and powerful lasers with excellent beam quality and extremely narrow linewidth. An accurate gain control in mode-locked devices can transform these lasers to generators of stable trains of ultra-short light pulses with a high repetition rate. A very important task in rapid development is the integration of III-V lasers and photonics in general with Silicon based electronics.

Despite the now long history of the semiconductor laser, it remains a subject of active research. New scientific tasks require better performance and novel functionalities of light sources, while new achievements in semiconductor lasers expand the area of their possible applications. For these reasons an up-to-date summary of their science and technology is highly desirable, which is the purpose of this book.

The fundamentals of semiconductor lasers are discussed in Part I of the volume. In order to prepare a reader not familiar with semiconductor lasers it starts with a chapter presenting general principles of semiconductor lasers. The latest achievements in the development of semiconductor laser cavities are then presented in the chapter on photonic crystal lasers. Issues related to the development of high power lasers and laser arrays are discussed in the following two chapters. The generation of ultrafast light pulses by semiconductor lasers is treated in the last chapter of Part I.

Part II of the book is devoted to semiconductor lasers that are especially well suited for operation in the visible and near infrared spectral regions. The first chapter of Part II summarizes the latest achievements in the field of short wavelength semiconductor lasers based on nonpolar and semipolar GaN and its alloys. The state of the art in quantum dot lasers is discussed in the next chapter. Electrically and optically pumped vertical cavity surface emitting lasers are then analyzed in Part II which is finished by a chapter on hybrid integration of III-V lasers on silicon.

Part III describes several other types of semiconductor lasers operating in the mid- and far-infrared. GaSb and related compounds were the first materials used to fabricate high performance mid-infrared quantum well lasers. The first chapter presents recent development and prospects of such lasers operating in the spectral range 2–3.5 μm. Interband cascade lasers which cover longer wavelengths starting from 3 μm are treated in the next chapter. Intersubband quantum cascade lasers operating at extremely long wavelengths in the THz region of the electromagnetic spectrum are then presented. The next chapter treats whispering gallery mode lasers employing disk or ring resonators which exhibit some unique properties due to the specific shape of the laser cavity. Applications of semiconductor lasers in absorption spectroscopy are analyzed in detail in the last chapter of the volume.

While it is difficult to review all aspects of the modern science and technology of semiconductor lasers, we attempted to include in this book contributions which cover most important fields of this large area. We hope that the reader will find useful information in this volume.

We sincerely thank all the authors of the book for their valuable contributions to this project.

Alexei Baranov and Eric Tournié

1

Principles of semiconductor lasers

P. BLOOD, Cardiff University, UK

DOI: 10.1533/9780857096401.1.3

Abstract: The purpose of this chapter is to provide an overview of the principles of quantum confined semiconductor lasers relevant to devices utilising conduction to valence band transitions. It begins with a short historical survey, and then provides a summary of the principles of laser action, optical processes in semiconductors, and quantum confinement. This leads to a detailed account of gain and recombination, culminating in discussion of the gain–current characteristics. Temperature dependence of threshold and the use of rate equations to describe behaviour above threshold and frequency response are covered in the final sections.

Key words: quantum wells, quantum dots, optical gain, recombination, threshold current.

1.1 Introduction

The purpose of this chapter is to provide an overview of the principles of quantum confined semiconductor lasers relevant to most devices utilising conduction to valence band transitions. It assumes a basic knowledge of stimulated emission, laser action and semiconductor physics and begins with a short historical survey.

1.1.1 Historical background

'Light amplification claimed by scientist'. So ran the headline of the *New York Times* on Friday, 8 July 1960 announcing that Theodore Maiman had realised an 'optical maser' using ruby and based on the Fabry-Perot cavity proposed by Schalow and Townes (1958). Semiconductors were also considered as a possible gain medium (Bertolotti, 1983, section 6.9; Bernard and Duraffourg, 1961) and four reports of laser action in semiconductors appeared in the autumn of 1962. Hall *et al*. (1962), Nathan *et al*. (1962) and Quist *et al*. (1962) used GaAs, while Holonyak and Bevacqua (1962) used GaAsP (see Casey and Panish, 1978, section 1.2; Bertolotti, 2005, pp. 254–9, and Hilsum, 1967, for an account contemporary with the events).

The threshold current densities of these devices were very high and the next crucial step was due to Kroemer (2000) who proposed the use of wider gap material to prevent carrier diffusion, enabling inversion to be achieved at lower current. A similar suggestion was made by Alferov and Kazarinov (see Alferov, 2000, ref, 4; Alferov *et al.*, 1969) and the Nobel Prize in Physics was awarded half jointly to Alferov and Kroemer. Single heterostructure lasers were made by Hayashi, Panish and Foy (1969) (see Hayashi and Panish, 1970) and by Kressel and Nelson (1969), and a double heterostructure laser, the model upon which the majority of present-day laser diodes are based, was reported by Alferov *et al.* (1970).

The double heterostructure paved the way for engineering the electronic properties of semiconductor structures. Henry recognised the analogy between confinement of light by a slab waveguide and confinement of electrons by the potential well formed by a heterostructure (Henry, 1993). Observation of confined states in quantum wells was reported by Dingle *et al*. (1974) and their potential for laser diodes prompted a patent filed in 1975 by Dingle and Henry. Photo-pumped laser operation was reported by van der Ziel *et al.* (1975) and Dupuis and co-workers (1978) achieved laser action by electrical injection. The use of quantum confinement in three dimensions was considered by Arakawa and Sakaki (1982), then by Asada *et al.* (1986), although quantum dots did not attract widespread attention for lasers until the Stranski–Krastanow growth mode was used to make dots by self-assembly by Kirstaedter *et al.* (1994).

A further heterostructure variant is the use of periodic superlattices for quantum cascade lasers which utilise transitions between states in the same sub-band, particularly to achieve laser action in the mid IR and THz wavebands (Faist *et al.* 1994). These devices are described elsewhere in this volume.

1.1.2 Principles of operation

A generic laser diode chip is shown in Fig. 1.1. It comprises an active region of two double heterostructures which separately confine the carriers in a well and the light in a waveguide, hence the term Separate Confinement Heterostructure (SCH). Light is amplified along the axis of the SCH (*y*-direction) by stimulated emission by recombination of electrons and holes injected into the active region by the *p-n* junction. The current is confined laterally (*x*-direction) by a narrow contact stripe (typically 10–50 μm wide) formed using a dielectric layer, or by a ridge (a few microns wide) which may also guide the light in the *x*-direction. Optical feedback is provided by partial reflection at the cleaved facets to sustain coherent oscillation. Alternatively, feedback may be provided by a grating (distributed Bragg reflector (DBR)) or by a periodic structure in the gain region

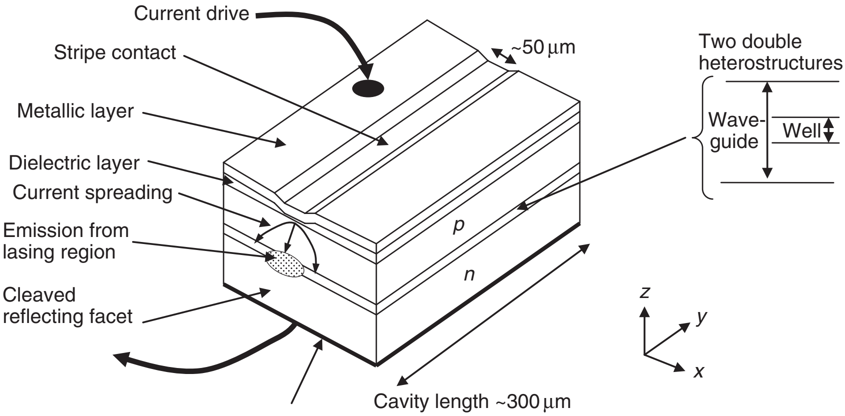
Current drive
Stripe contact
Metallic layer
Dielectric layer
Current spreading
Emission from lasing region
Cleaved reflecting facet
~50 µm
Two double heterostructures
Wave-guide
Well
p
n
z
y
x
Cavity length ~300 µm

1.1 Illustration of a generic diode laser chip, with active region comprising two double heterostructures forming the waveguide and well. The width of the contact between the metal and *p*-type semiconductor is restricted by a stripe in the dielectric layer. The active region is pumped by a *p-n* junction in the region below the contact stripe with some current spreading.

producing distributed optical feedback (DFB). Laser action occurs when the intensity gain experienced by the optical mode matches the loss of light through the end mirrors (power reflectivity R_1 and R_2) and by scattering as it propagates along the waveguide, represented by a loss coefficient α_i (typically 2–10 cm^{-1}). The modal gain required to achieve this laser threshold is given by (Coldren and Corzine, 1995, section 2.5):

$$G_{\text{th}} = \alpha + \frac{1}{2L_c}\ln(R_1R_2)^{-1} \qquad [1.1]$$

For a cavity length of 300 µm the modal gain required is about 50 cm^{-1}.

Although there are variations on this theme, the devices considered in this book contain means to guide and couple light to the gain medium, means to control the region over which the current is injected, means to provide optical feedback and a *p-n* junction to inject carriers to achieve population inversion.

The energy band diagram of the active region in the *z*-direction is shown in Fig. 1.2 under forward bias. The outer double heterostructure forms the slab waveguide and provides a diffusion barrier for injected electrons and holes; the thickness of the core is of the order of the wavelength of light in the semiconductor (a few 100 nm). The inner double heterostructure forms the quantum well, or may contain a layer of dots, typically a few nm thick, where the gain is generated. The success of the heterostructure rests on the ability to confine carriers and light to the same region and on the availability of alloy systems in which the band gap can be varied with very little change

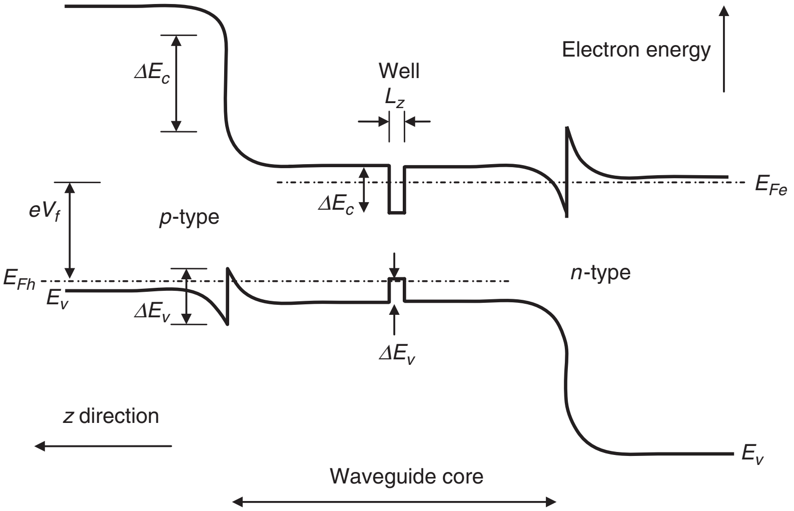

1.2 Energy band diagram of the conduction and valence band edges (E_c and E_v respectively) through the active region in the direction normal to the plane of the layers, drawn under forward bias, V_f, necessary for population inversion in the quantum well, width L_z. The structure comprises two double heterostructures forming the waveguide and the quantum well with band offsets ΔE_c and ΔE_v which may be different for the waveguide and well. The layer thicknesses are not drawn to scale; band-bending in the well and adjacent barrier material has been neglected.

in lattice parameter, so that the whole structure is lattice-matched, though modest amounts of strain can be used to good effect (Section 1.6.3 of this chapter; Chuang, 2009, section 4.5). The wide-gap nitride system used for blue emitters (Nakamura *et al.*, 1995) is exceptional in that growth techniques have been developed to produce active regions of sufficient quality for laser action to be achieved with a large mismatch to the substrate (see Chuang 2009, section 11.5).

1.1.3 Outline of chapter

The purpose of this chapter is to outline the physical principles of quantum well and dot lasers using transitions between the conduction and valence band, states based on the generic structure of Figs 1.1 and 1.2. Although reference is made to some specific types of laser, this is done simply to place them in the wider context of the 'generic' laser diode. Where these types are covered elsewhere in this book reference may be made to the relevant chapter for a complete account of their current development. The principles of laser action, optical processes in semiconductors and quantum confinement (Sections 1.2 and 1.3) lead to a detailed account of gain and recombination (Sections 1.4 and 1.5) culminating in the gain–current characteristics (Section 1.6). Temperature dependence of threshold and the use of rate equations to describe behaviour above threshold and frequency response are covered in Sections 1.7 and 1.8.

Some plots in the diagrams have been derived using ‘model’ calculations to provide realistic illustrations of general principles. These are simplified and do not correspond to specific materials, consequently published calculations may differ in the numerical values they produce for specific structures.

1.1.4 Further reading

Books by Bertolotti (1983, 2005; the former gives references to original sources), Henry’s 1993 foreword, and the first chapter of Casey and Panish (1976) provide reading on the historical background, and further articles can be found in the Millennium issue (2000) of the *Journal of Selected Topics in Quantum Electronics*.

Books by Casey and Panish (1978) and Thompson (1980) pre-date quantum structures yet provide valuable scientific background, while Agrawal and Dutta (1993) include quantum wells. The volume edited by Zory (1993) deals specifically with quantum well lasers and Bastard (1988) sets out the wave-mechanical background. Texts by Coldren and Corzine (1995) and Chuang (2009) are relevant to this chapter, as is Sands (2005). The physics of light-matter interactions is covered in chapter 2 of Loudon (2000); Chow and Koch (1999) give an advanced account of semiconductor gain media. Bimberg and co-workers (1999) have covered quantum dot lasers and recent review has been given by Mowbray and Skolnick (2005). References in this chapter to journal papers are representative examples.

1.2 The basic laser diode

The purpose of this section is to introduce the basic elements of a quantum confined laser diode: formation of quantum confinement and the waveguide by heterostructures, and injection of carriers by the *p-n* junction. Definitions are given for modal gain and the various efficiencies obtained from the light–current curve. This material provides the context for the physics which is described in the sections which follow.

1.2.1 Formation of quantum confined structures

The energy band diagram of a quantum well is shown in Fig. 1.3a, drawn assuming that the band-bending adjacent to the interfaces occurs over

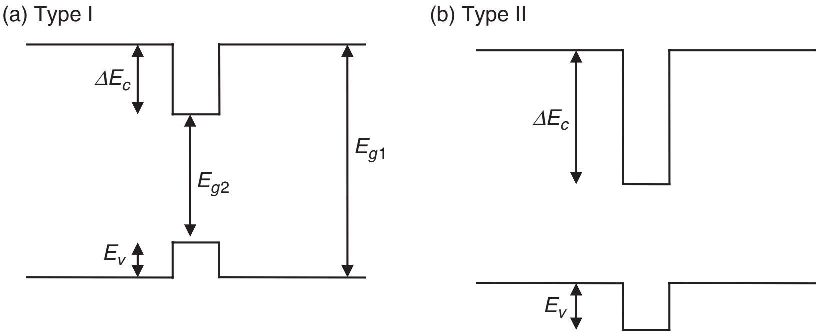

1.3 Energy band diagrams of (a) type I and (b) type II quantum wells formed of materials with band gaps E_{g1} and E_{g2}. The difference between the two structures is the magnitude and sense of the band offsets such that in the type I well electrons and holes have potential minima in the same spatial regions whereas in the type II well the potential minima for electrons and holes are in the narrow gap and wide gap material respectively.

distances much larger than the width of the well and barriers and can be ignored on this scale. The depths of the conduction and valence band wells are determined by the heterostructure band offsets ΔE_c, ΔE_v which sum to the band gap difference at the interface (Chuang, 2009, appendix A). For a conventional type I structure the band offsets confine electrons and holes to the same spatial region; these offsets are typically 200 meV and 100 meV respectively. In some systems carriers of opposite type are confined to adjacent regions (Fig. 1.3b) and these type II structures have found specialist application, particularly in mid infra-red laser diodes (Grein *et al.*, 1994) where they reduce the Auger recombination rate (Section 1.5.2).

Self-assembled dots are formed by deposition of material which has a large lattice mismatch (approaching 10%) with respect to the underlying layer. This strain is relieved by formation of islands of material and the resulting dots are flat pyramids with a base width larger than the height (Bimberg *et al.*, 1999). A thin continuous wetting layer remains, contiguous with the dots, which is regarded as a thin quantum well. Dots may be grown intentionally within a well: the dot-in-a-well (DWELL) structure (Lester *et al.*, 1999; Liu *et al.*, 2000). While it is possible to exercise a degree of control over the formation of dots by the growth conditions, there is an inevitable spread in size leading to inhomogeneous energy distribution of optical transitions.

1.2.2 Carrier injection

Carriers are injected by a forward biased *p-n* junction, and it is usually assumed that the electron and hole distributions in the well can each be

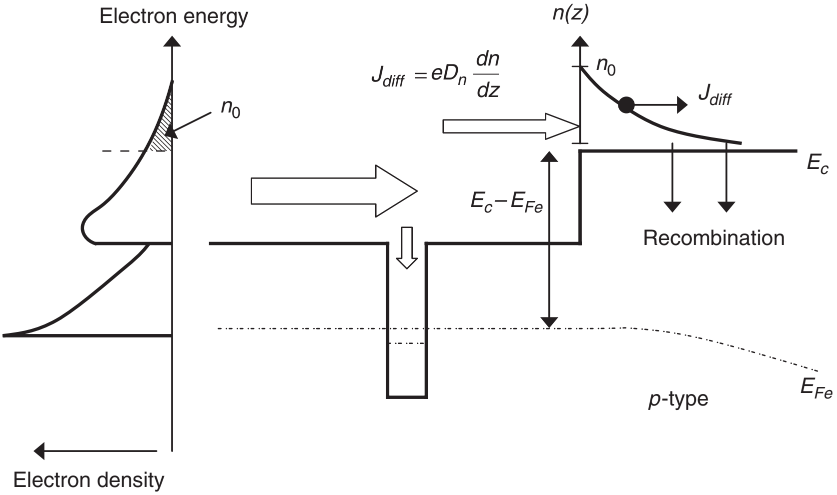

1.4 Schematic band diagram (without band-bending) illustrating loss of electrons over the heterobarrier by diffusion into the *p*-type cladding layer. The left hand side of the figure shows the electron distribution with increasing electron energy: n_0 electrons are above the heterobarrier at E_c and can diffuse into the *p*-type material with a profile $n(z)$ where they recombine with holes. The diffusion current across the interface is proportional to the electron concentration gradient and n_0 is determined by the energy difference ($E_c - E_{Fe}$).

described by a Fermi function specified by the lattice temperature and a quasi-Fermi level for each carrier type. In this chapter occupation probabilities always refer to electrons, whether in the conduction band or valence band. Most laser diode calculations use Fermi distributions and it is assumed that quasi-equilibrium within the carrier populations is brought about by internal scattering processes which are significantly faster than the rate of recombination.

The outer heterobarriers are not always fully effective in preventing carrier flow into the opposite material type. Figure 1.4 shows that electrons at energy above the heterobarrier diffuse down their concentration gradient into the *p*-type material, where they recombine with holes. Where the cladding layer resistance is significant, carriers appearing above the heterobarrier are extracted by the electric field (Fig. 1.5) produced by the flow of majority carrier holes through the resistive cladding layer. This drift can make a significant contribution to the temperature dependence of threshold current, particularly in materials where it is difficult to achieve high *p*-doping in the cladding layer to minimise its resistance. In practice, carrier loss occurs by a combination of drift and diffusion (Bour *et al.*, 1993) and is best treated using a self-consistent current continuity/Poisson simulation (e.g., Foulger *et al.*, 1997).

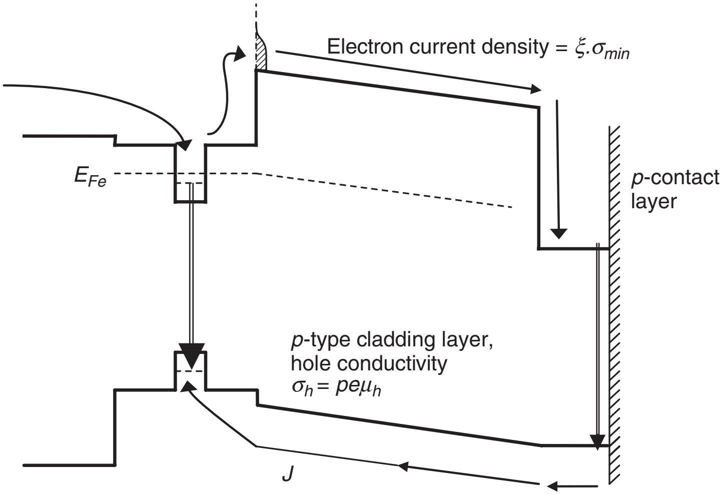
Electron current density = $\xi.\sigma_{min}$
E_{Fe}
p-contact layer
p-type cladding layer, hole conductivity $\sigma_h = pe\mu_h$
J

1.5 Band diagram illustrating the loss of electrons at the heterobarrier due to drift. The flow of majority carrier holes in the resistive *p*-cladding layer produces an electric field which extracts electrons which are above the heterobarrier from the active region. These electrons flow as a minority carrier current to the *p*-contact layer and recombine with holes at the contact. The diagram illustrates transport of electrons by drift only, so the separation of the conduction band edge and the electron quasi-Fermi level is constant because there is no electron concentration gradient in the cladding layer.

1.2.3 The waveguide and cavity

The output from the laser is in specific optical modes determined by solutions of Maxwell's equations for the waveguide and by the gain spectrum of the active medium, and is polarised usually with the electric field in the plane of the well (TE). Lateral guiding (x-direction, Fig. 1.1) may occur due to variation in the gain due to the current distribution (gain guiding) or in the refractive index (index guiding); the former is the case for a wide current-confining stripe, as in Fig. 1.1, whereas a narrow ridge provides strong index guiding. The transverse modes (z) are controlled by the refractive index profile of the slab waveguide (see Agrawal and Dutta, 1993, section 2.5).

The longitudinal modes are determined by constructive interference along the axis of the cavity (y), and in edge emitting devices where the cavity length is very large there are many such closely spaced modes within the gain spectrum of the material. In vertical cavity lasers there is only a small number of modes in the propagation direction within the gain spectrum, sometimes only one, due to the very short cavity length.

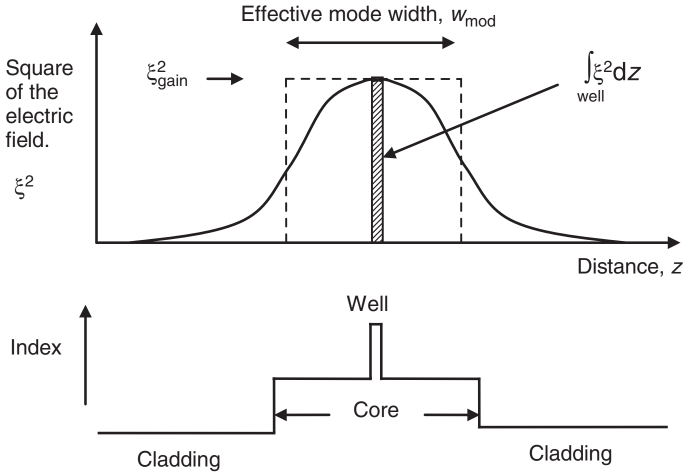
Effective mode width, w_{mod}
Square of the electric field.
ξ^2
ξ^2_{gain}
$\int_{\text{well}} \xi^2 dz$
Distance, z
Well
Index
Core
Cladding
Cladding

1.6 Transverse optical field profile due to waveguiding by the index profile of the SCH structure. In this diagram the gain region is a quantum well. The effective mode width as defined by Equation [1.4] is indicated, as is the integral of the squared field over the width of the well which is used to calculate the confinement factor (Equation [1.3]).

Figure 1.6 illustrates the transverse refractive index profile and the optical field of the first transverse mode. The gain experienced by this mode is defined as the fractional increase in energy in the mode ($\Delta U/U$) per unit distance (L) travelled along the y-direction:

$$G = \frac{\Delta U}{\Delta L}\frac{1}{U} \qquad [1.2]$$

The increase in energy is due to additional photons produced by the difference between rates of downward stimulated transitions and upward absorptive transitions (the net stimulated rate) in the well. Coupling of the optical field $\xi(z)$ of whole mode to the well is usually specified by the confinement factor, Γ:

$$\Gamma = \frac{\int_{\text{gain}} \xi^2 \mathrm{d}z}{\int_{\text{mod}} \xi^2 \mathrm{d}z} \qquad [1.3]$$

where the integrals are taken over the gain region (in this case the well) and the whole mode. This definition is appropriate when the width of the gain region can be specified (see Section 1.4.1). When the gain region is very thin, the optical field is constant over its 'width' (ξ_{gain}) and we show in

Section 1.4.1 that it is then convenient to define an effective mode width, w_{mod} as

$$w_{\mathrm{mod}} = \frac{\int_{\mathrm{mod}} \xi^2(z)\,\mathrm{d}z}{\xi_{\mathrm{gain}}^2} \quad [1.4]$$

This is the width of a fictitious rectangular mode having a constant field amplitude ξ_{gain} and the same total energy as the true optical mode, determined by the area under the field profile (Fig. 1.6).

1.2.4 Threshold and the light–current curve

Stimulated emission in the gain region supplies energy to the whole of the mode and when this makes up for that lost through the mirrors and by internal scattering, sustained coherent laser action is achieved (Equation [1.1]) and is usually identified by the abrupt increase in light output as a function of current as illustrated in Fig. 1.7. The threshold current is the current which flows at the quasi-Fermi level separation necessary to provide the threshold gain. Figure 1.8 is an energy band diagram of a quantum well at threshold: in the absence of lateral carrier leakage (x-direction) in the steady state the

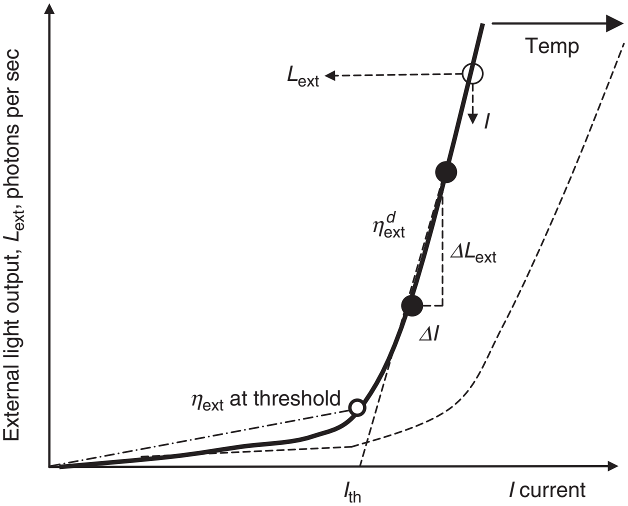

1.7 Schematic light–current curve illustrating identification of the threshold current, I_{th}. The overall external efficiency, η_{ext} at threshold is illustrated, as is the differential external efficiency above threshold. The effect of temperature on the light–current curve is also shown.

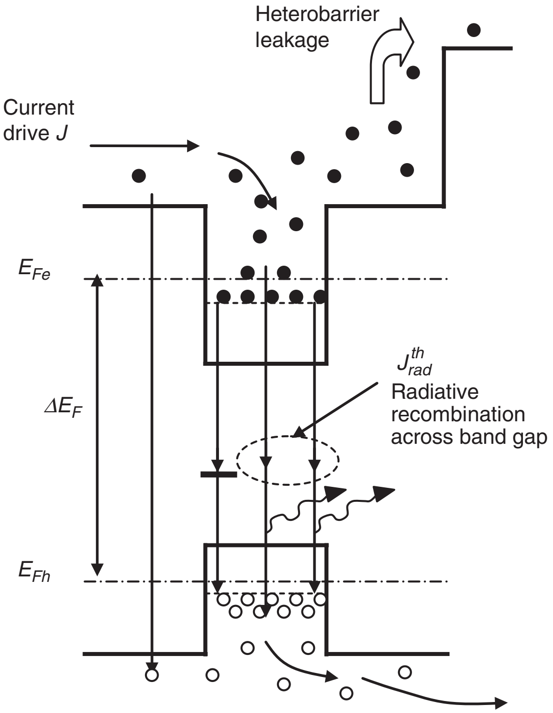

1.8 Band diagram of a quantum well with the quasi-Fermi level separation at threshold, ΔE_F. The current density, J, necessary to maintain the threshold gain must balance the loss of carriers by leakage over the heterobarrier, and radiative and non-radiative recombination in the barrier and well.

external rate of supply of electrons per unit area (J/e) balances the total recombination rate between conduction and valence bands in well and barrier, together with carrier loss over the heterobarrier (Figs 1.4 and 1.5). The contribution of stimulated emission *at threshold* is not significant because the photon density is very low.

Calculation of the threshold current due to all these contributions is difficult without detailed knowledge of the extrinsic properties of the structure. It is therefore usual to calculate the internal *radiative* threshold current density due to spontaneous recombination in the well alone, $J_{\mathrm{rad}}^{\mathrm{th}}$, by integrating the spontaneous emission spectrum, $R_{\mathrm{spon}}(\hbar\varpi)$,

$$J_{\mathrm{rad}}^{\mathrm{th}} = e\int R_{\mathrm{spon}}^{\mathrm{th}}(\hbar\varpi)\,\mathrm{d}\hbar\varpi \qquad [1.5]$$

To estimate the overall threshold current density (J_{th}), the carrier loss processes are lumped into a quantum efficiency (η) made up of the internal quantum efficiency η_{int} within the well and the fraction of total current which enters the well, the injection efficiency η_{inj}, which accounts for lateral current spreading, barrier recombination and leakage over the heterobarrier:

$$J_{\text{th}} = \frac{J_{\text{rad}}^{\text{th}}}{\eta} = \frac{J_{\text{rad}}^{\text{th}}}{\eta_{\text{inj}}\eta_{\text{int}}} \tag{1.6}$$

In the well alone

$$\eta_{\text{int}} = \frac{R_{\text{rad}}}{R_{\text{rad}} + R_{\text{nr}} + R_A} \tag{1.7}$$

where R_{nr} is due non-radiative deep state (Shockley–Read–Hall) recombination and R_A is the non-radiative Auger recombination rate.

Above threshold the photon density increases rapidly and every *extra* injected electron–hole pair recombines by photon-induced stimulated emission: the increase in current is due to shortening of the carrier lifetime by stimulated recombination. This coupling of the carrier and photon densities means that above threshold the carrier populations and quasi-Fermi level separations are pinned to fixed values (Section 1.8.2). This pinning should be established once recombination by stimulated emission dominates spontaneous emission, and it should be maintained so long as the carrier distributions are thermal.

1.2.5 Definitions of efficiency

The internal and injection efficiencies have been defined above. The power conversion efficiency is defined as the ratio of the optical power out (P_{Lout}) and the electrical power in (P_{Ein})

$$\eta_{\text{pow}} = \frac{P_{\text{Lout}}}{P_{\text{Ein}}} \tag{1.8}$$

This includes power loss due the difference between the external applied voltage and the energy of the emitted photons, which includes voltage drops across the internal resistance.

Quantum efficiency refers to generation and supply of *particles*: photons and electron–hole pairs. The overall external quantum efficiency is the ratio of the rate of external emission of photons (L_{ext}) to the rate of supply of electron–hole pairs (Fig. 1.7):

$$\eta_{\text{ext}} = \frac{L_{\text{ext}}}{I/e} \tag{1.9}$$

where I is the current. (η_{int} in Equation [1.6] refers to the *internal* generation of photons within the well due to spontaneous emission.)

If the Fermi levels pin at threshold, the rate of carrier loss over the heterobarrier, recombination in the well and barrier due to spontaneous emission and non-radiative processes also pin and do not increase further above threshold. In these circumstances every *extra* injected electron–hole pair produces an *extra* photon and the *internal differential quantum efficiency*, η_{int}^{d} above threshold should be unity:

$$\eta_{\text{int}}^{d}=\left[\frac{\Delta L_{\text{int}}}{\Delta I/e}\right]_{J>J_{\text{th}}}\approx 1 \tag{1.10}$$

However, we can only observe the external light output, L_{ext}, therefore the quantity measured is the *external differential quantum efficiency*, η_{ext}^{d}, above threshold (Fig. 1.7)

$$\eta_{\text{ext}}^{d}=\left[\frac{\Delta L_{\text{ext}}}{\Delta I/e}\right]_{J>J_{\text{th}}} \tag{1.11}$$

Light is retained within the cavity by reflection at the mirrors and η_{ext}^{d} is related to η_{int}^{d} by (Casey and Panish, 1978, equation 3.8–32)

$$\eta_{ext}^{d}=\left\{\frac{(1/L_c)\ell n(R^{-1})}{\alpha_i+(1/L_c)\ell n(R^{-1})}\right\}\eta_{\text{int}}^{d} \tag{1.12}$$

It is common to determine η_{int}^{d} and α_i by applying Equation [1.12] to measurements of η_{ext}^{d} as a function of cavity length (Coldren and Corzine, 1995, section 2.8.1) by plotting $1/\eta_{\text{ext}}^{d}$ *vs* L_c; however, this relies on quasi-equilibrium being maintained through the whole structure for all cavity lengths so that the efficiencies η_{inj} and η_{int} remain fixed and do not contribute to the external *differential* efficiency above threshold. This is not necessarily the case (Smowton and Blood, 1997a) due to current spreading for example. It is also necessary that the internal mode loss does not depend on the threshold carrier density, otherwise α_i will itself be dependent on cavity length. Analysis of data to determine α_i using Equation [1.12] should be scrutinised to ensure the necessary conditions have been met, for quantum wells (Blood and Smowton, 1997b) and dots (Asryan, 2006).

Values derived for the *differential* efficiency η_{int}^{d} are sometimes confused with η_{int} (Equation [1.7]) and used, erroneously, to estimate the *overall* efficiency (η Equation [1.6]) to obtain the radiative threshold current from the external drive current (Smowton and Blood, 1997b).

1.3 Key physical concepts

Having introduced the laser diode, the next task is to provide a survey of the physics of the light-matter interaction which produces the optical gain and recombination and the use of Schrödinger's equation to describe electron confinement in a potential well.

1.3.1 Interaction of light and matter

Quantum approach

There is a detailed balance relation between the rates of absorption, stimulated and spontaneous emission and it is usually assumed that spontaneous emission occurs into a free-space cavity much larger than the wavelength of light, such that the mode density is independent of cavity volume and the spectrum is described by the Planck law. When spontaneous emission is confined to a cavity with dimensions approaching the wavelength of light, these relations are substantially modified (Fox, 2006, chapter 10) and, while microcavity structures are of considerable interest, they will not be considered in this chapter.

In the presence of light, the states ψ_1 and ψ_2 of an atom are coupled coherently and the wavefunction is the linear combination

$$\psi(r,t) = c_1(t)\psi_1(r,t) + c_2(t)\psi_2(r,t) \tag{1.13}$$

with the initial condition that the electron is in state '1': $c_1(0) = 1$ and $c_2(0) = 0$. The probability of the electron being in the upper state ('2') after a time t due to transfer of energy from the light beam is $|c_2(t)|^2$, from which the optical absorption rate can be derived. If the coherent superposition of states in Equation [1.13] is maintained for a sufficiently long time the electron oscillates between the upper and lower levels (Rabi oscillations: see Fox, 2006, chapter 9; Loudon, 2000, chapter 2). Usually this does not occur, because collision processes destroy the phase coherence with the result that c_2 increases monotonically with time giving the absorption cross-section as:

$$\sigma(\hbar\varpi) = \frac{2\hbar}{n\varepsilon_0 c(\hbar\varpi)}\left(\frac{e}{2m_0}\right)^2 M_T^2 \frac{2\hbar\gamma}{(\hbar\varpi - E_i)^2 + (\hbar\gamma)^2} \tag{1.14}$$

where ϖ is the angular frequency of the light. Equation [1.14] shows that interaction is not restricted to photons which are precisely resonant with the energy separation of the atomic levels E_i. The cross-section spectrum is homogeneously broadened (Fig. 1.9) with a half-width in energy of $\Lambda\ (= \hbar\gamma)$ due to dephasing at a rate γ. M_T is the transition matrix element. In deriving Equation [1.14] the dephasing collisions are assumed to leave no 'memory'

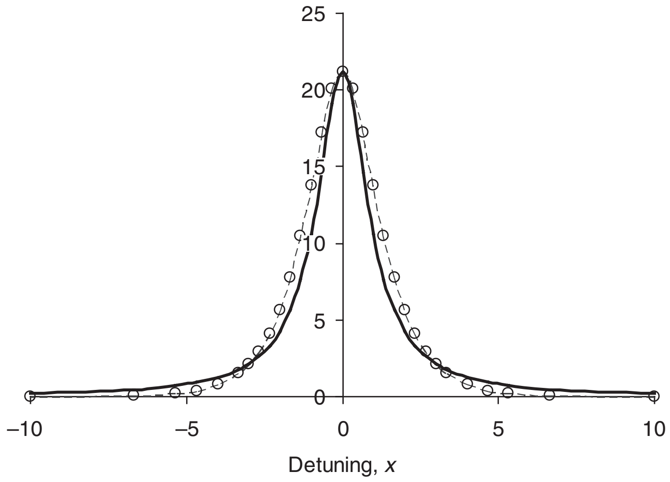

1.9 Normalised homogeneous broadening Lorentzian lineshape as a function of the relative detuning $x = \left(\hbar\varpi - E_i\right)/\Lambda$ (Equation [1.15]), shown as a continuous line. A sech function is plotted as open circles for comparison, illustrating the reduced tail at high energies.

of the previous state of the atom and the lineshape is a Lorentzian, which when normalised is

$$L\left(\hbar\varpi\right) = \frac{1}{\pi}\frac{\Lambda}{\left(\hbar\varpi - E_i\right)^2 + \Lambda^2} \qquad [1.15]$$

When the transitions take place to a continuum of final states, this treatment gives Fermi's Golden Rule (Coldren and Corzine, 1995, appendix 9) which removes explicit reference to homogeneous broadening. This is the usual starting point for calculation of absorption and gain by bands of states (Coldren and Corzine, 1995, p. 118).

Maxwell's equations

An alternative approach is to apply Maxwell's equations to an electromagnetic wave as it propagates through a dielectric (Chuang, 2009, chapter 5). This provides insights which are not easily gained from the quantum picture. It is based on calculation of the polarisation $P(\varpi)$ (dipole moment per unit volume) due to the displacement of the electrons and their nuclei, $x(t)$, by the oscillating electric field, and expressed as a complex susceptibility $\chi(\varpi)$. The amplitude gain is related to its imaginary part (Chow and Koch, 1999, section 1.8):

$$g_{\text{amp}} = -\frac{1}{2}k\chi'' \qquad [1.16]$$

where the wave vector in the medium of index n_b, is $k = \varpi n_b / c$. The intensity gain is twice the amplitude gain. The *macroscopic* polarisation in a small volume at **r** is the instantaneous vector addition of the *microscopic* dipole moments $\mu_i(t)$ of the individual atoms in this volume:

$$\mathrm{P}(\mathbf{r},t) = \frac{1}{\delta V} \sum_{t} \vec{\mu}_i(t) \qquad [1.17]$$

The oscillating dipoles are all initially in-phase and, while this is maintained, the decay rate of the macroscopic polarisation is the same as that of the individual atoms, and determined by their individual energy damping rate γ_d.

Dephasing collisions (at a rate $1/T_2$) destroy the in-phase motion of individual dipoles without dissipating energy and, although the microscopic polarisation is not changed by these events, destruction of the coherence between them reduces the macroscopic polarisation given by Equation [1.17] (Siegman 1986, chapter 2). Eventually the coherence is completely destroyed, resulting in zero macroscopic polarisation.

For frequencies of the external field which are close to the natural oscillator frequency, ϖ_o, the gain cross-section derived from the complex susceptibility is similar to [1.14] and is also homogeneously broadened by a Lorentzian of half-width in frequency of

$$\Delta\varpi = \left(\frac{\gamma_d}{2} + \frac{1}{T_2} \right) \qquad [1.18]$$

This makes the distinction between broadening due to damping of the individual oscillators (rate γ_d, sometimes designated by a time T_1) and elastic dephasing collisions (time T_2), sometimes called ‘pure dephasing’. In the quantum picture the line may also be broadened by decay of the population of electron–hole pairs by recombination.

Lineshape functions

The Lorentzian form of the lineshape follows from the assumption that the collisions are fully randomising, leading to an exponential decay with time of the in-phase population, but this is not always the case in quantum dot systems (Borri *et al.*, 2002; see also Borri *et al.*, 2001, fig. 1.4). In some gain calculations the homogeneous lineshape is represented by a *sech* function to avoid the artefact of absorption appearing below the band edge due to the long Lorentzian tail (Chow and Koch, 1999, section 2.3). Eliseev (1997) has proposed a family of functions, from Lorentzian to *sech,* to describe the dephasing process.

1.3.2 Confinement in a potential well

To calculate absorption, gain and emission it is necessary to determine the energies and wavefunctions of the states in the potential well (Fig. 1.10a). In crystalline materials the wavefunction is the product of an atomic-like part $u(\mathbf{r})$ which has the periodicity of the crystal and is specific to the valence and conduction bands (u_c, u_v), and a slowly varying envelope function $F(\mathbf{r})$ obtained by solving Schrodinger's equation for the macroscopic potential. When the sample dimension is large compared with the de Broglie wavelength the envelope functions are plane waves satisfying cyclic boundary conditions and the allowed states are very closely spaced in energy described by a density of states function.

When electrons are confined to a thin potential well the envelope function in the confinement direction $F(z)$ has the form of a standing wave within the well, $\exp\left(ik_z^{well}.z\right)$ and an exponential decay,

$$F^{barr}(z) = \exp\left(-k_z^{barr}\left(z - \frac{L_z}{2}\right)\right) \qquad [1.19]$$

due to tunelling into the barrier. There is a small number of solutions, localised to the vicinity of the well, which are widely spaced in energy compared with $k_B T$ (e.g., Fox, 2001, Section 6.3.3; Chuang, 2009, Section 3.2.2).

Many textbooks deal with a rectangular well; however, the potential may be of a different form due to intentional intermixing of the well and barrier material or unintentional inter-diffusion; it may be triangular due to electric fields, for example piezo-electric fields due to strain. Whatever the form of the potential (including type II systems) it is, in principle, possible to solve Schrodinger's equation to obtain the envelope function and the associated energy of the state.

Envelope function in quantum wells

In a quantum well confinement is imposed in only one direction (z) so the envelope function is a plane wave in the (x, y) plane, normalised to the area of the sample A, and a localised wavefunction in the z-direction, which includes a normalising constant (illustrated in Fig. 1.10b)

$$F(\mathbf{r}) = F(x,y)F(z) = \frac{1}{\sqrt{A}}\exp\left(ik_{xy}r_{xy}\right)F(z) \qquad [1.20]$$

The in-plane area is well-defined because tunnelling of the wavefunction into the 'barrier' at the periphery of the sample is negligible compared with its lateral dimensions. This is not the case in the z-direction and the normalising condition is $\int_{-\infty}^{\infty} F^2(z)\mathrm{d}z = 1$. The total energy of each state is given by

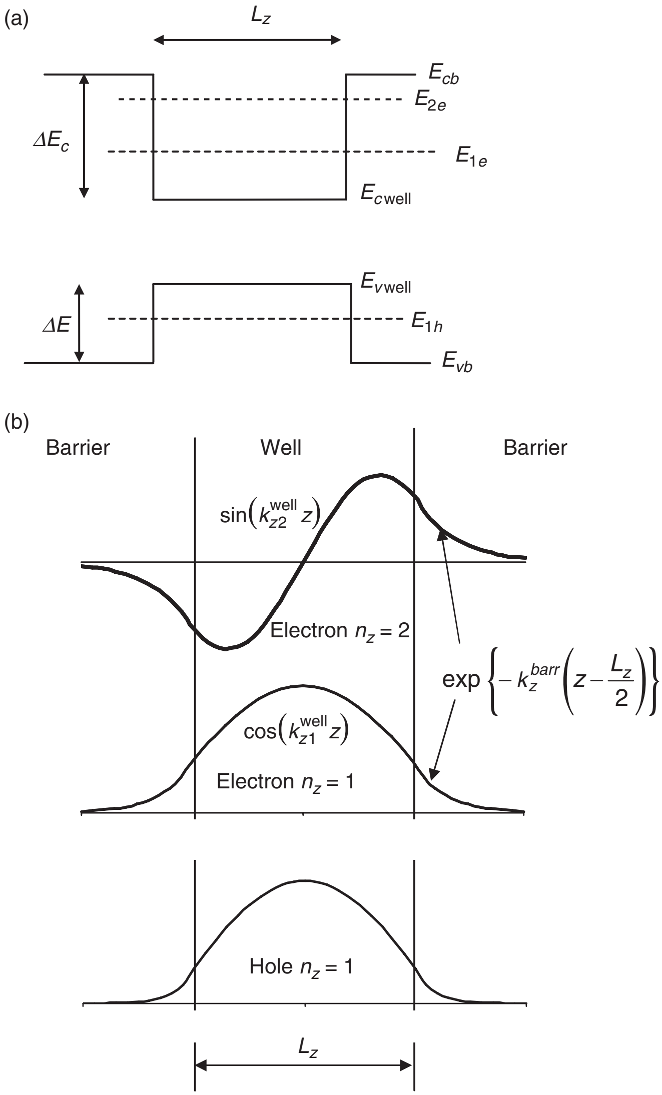
(a)
L_z
E_{cb}
E_{2e}
ΔE_c
E_{1e}
$E_{c\text{well}}$
$E_{v\text{well}}$
ΔE
E_{1h}
E_{vb}
(b)
Barrier
Well
Barrier
$\sin\left(k_{z2}^{\text{well}} z\right)$
Electron $n_z = 2$
$\exp\left\{-k_z^{barr}\left(z-\frac{L_z}{2}\right)\right\}$
$\cos\left(k_{z1}^{\text{well}} z\right)$
Electron $n_z = 1$
Hole $n_z = 1$
L_z

1.10 Illustration of solutions for Schrödinger's equation in the conduction and valence band potential wells. Diagram (a) shows the first and second electron states and the first hole state at energies E_{1e}, E_{2e} and E_{1h} and (b) shows the corresponding envelope functions $F(z)$ for a relatively wide well.

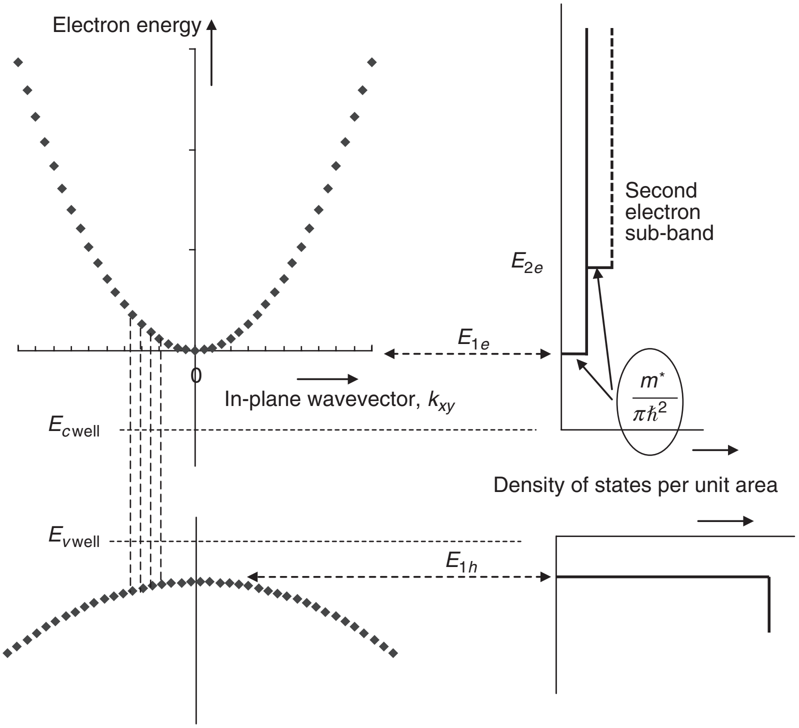
Electron energy
0
In-plane wavevector, k_{xy}
$E_{c\text{well}}$
$E_{v\text{well}}$
E_{1e}
E_{2e}
E_{1h}
Second electron sub-band
$\frac{m^*}{\pi\hbar^2}$
Density of states per unit area

1.11 Energy versus *k* curves for the in-plane (*x, y*) motion of the lowest electron and hole confined states in a quantum well (left hand diagram). At $k_{xy} = 0$ the energy is that of the $n_z = 1$ electron and hole confined states, E_{1e} and E_{1h}. The solid symbols are equally spaced in k_{xy} by the same increment for both bands as illustrated by the vertical dashed lines. The higher mass and lower curvature of the heavy-hole band compared with the electron band modifies the spacing of the states in energy resulting in a higher density of states in energy, shown on the right hand side of the diagram. The density of states for the $n_z = 2$ electron sub-band is shown as a dashed line.

$$E = \frac{\hbar^2}{2m}\left\{k_{xy}^2 + \left(k_z^{\text{well}}\right)^2\right\} \qquad [1.21]$$

For each confined solution (k_z^{well}) there is a continuum of extended states associated with the unconfined motion (k_{xy}) in the (x, y) plane (Fig. 1.11), and if the (x, y) and (z) solutions are independent this continuum is replicated for each confined solution leading to the states and density of states function illustrated in Fig. 1.11. The density of states for each sub-band is:

$$\rho_{xy} = \frac{m}{\pi\hbar^2} \text{ typically } 2.7 \times 10^{13}\,\text{cm}^2\text{eV}^{-1} \text{ for electrons} \qquad [1.22]$$

$$\text{(for two spin directions)}$$

Quantum dots

In quantum dots confinement occurs in all three directions so there are no extended states and the three dimensional envelope function is fully localised to the vicinity of each dot with a form similar to Fig. 1.10b in all directions. The function $F(\mathbf{r})$ extends into the barrier and the precise location of the electron is not known but is specified by the normalised probability function $F^2(\mathbf{r})$. The energies of the states are widely spaced and do not form a continuum and cannot be represented by a density of states distribution function. If the dots are widely spaced, electrons are unable to transfer directly between them by quantum mechanical tunnelling (see Bimberg *et al.*, 1999, for detailed accounts).

Key points

1. In the confinement direction(s) the envelope functions are not wholly contained in the well but decay exponentially in the barrier. The normalising constant in one dimension has dimensions $(\text{length})^{-1/2}$ but is not equal to $(\text{well width})^{-1/2}$; similarly the normalising constant for 3-D confinement in a dot is not necessarily $(\text{dot volume})^{-1/2}$.
2. Since the spatial extent of the electrons is not defined by the well dimensions a density of states per unit *volume* cannot be defined in a well or dot. Furthermore when the potential is not rectangular the extent of the well itself may not be defined.
3. In multiple well structures, if the barrier thickness is many multiples of $1/k_z^{\text{barr}}$ the wells are not quantum mechanically coupled, therefore there are no transitions between adjacent wells, and gain and recombination rates of individual wells should be added. When the barriers are thin, Schrödinger's equation must be solved for the multiple well system and the gain and emission rates computed for the whole system. Similarly, for strong 3-D confinement, electrons are fully localised to the vicinity of each dot.

1.4 Absorption and gain in low dimensional semiconductor structures

We next calculate the optical absorption and gain in the laser geometry in Fig. 1.12 where light propagates along a slab waveguide parallel to a thin gain region comprising one or more quantum wells or layers of quantum dots.

1.4.1 Quantum wells

Based on transition rates calculated from Fermi's Golden Rule (Coldren and Corzine, 1995, appendix 9) the general expression for modal gain for light of polarisation p is (Blood, 2000),

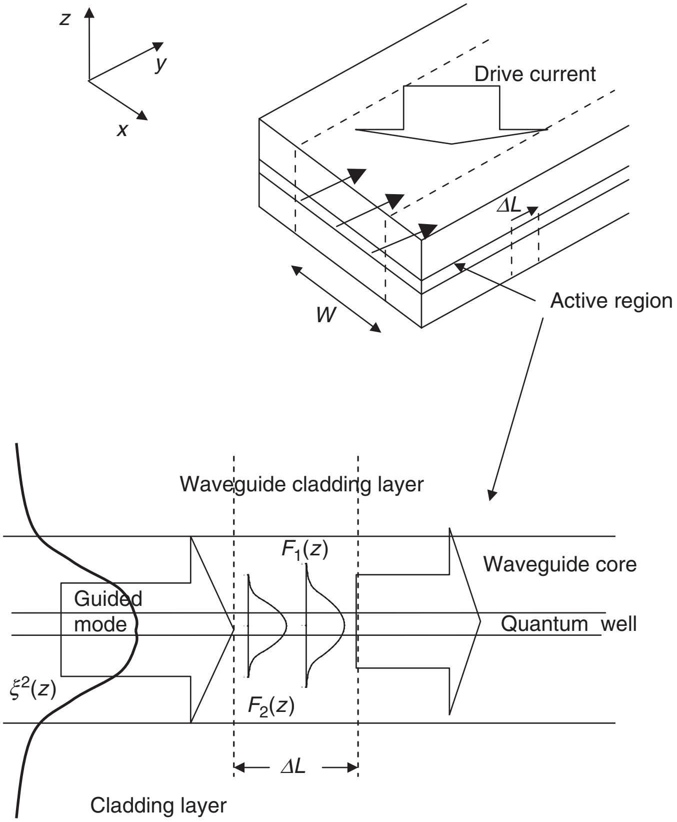
z
y
x
Drive current
ΔL
Active region
W
Waveguide cladding layer
F1(z)
Waveguide core
Guided mode
Quantum well
ξ2(z)
F2(z)
ΔL
Cladding layer

1.12 Illustration of the slab waveguide geometry for calculation of optical gain. The injected carriers invert the carrier population over a stripe of width *W* and gain is defined by Equation [1.2] for amplification of a guided mode over an element ΔL in the *y*-direction. The lower part of the diagram shows the detail of the overlap of the optical field of the guided mode $\xi^2(z)$, and the confined envelope functions of the electrons and holes in the *z*-direction $F_1(z)$ and $F_2(z)$ as expressed by Equation [1.23]. TE polarised light has its electric field vector in the (*x, y*) plane.

$$G_p\left(\hbar\varpi\right)=\frac{4\pi\hbar}{n\varepsilon_0 c\left(\hbar\varpi\right)}\left(\frac{e}{2m_0}\right)^2\gamma_p M^2\,\frac{\left\{\int F_2^*\left(z\right)\xi\left(z\right)F_1\left(z\right)\mathrm{d}z\right\}^2}{\left\{\int\limits_{\mathrm{mod}}\xi^2\left(z\right)\mathrm{d}z\right\}}\,\rho_{\mathrm{red}}\left(\hbar\varpi\right)\left(f_1-f_2\right) \qquad [1.23]$$

The terms originate as follows.

For transitions between states in the conduction (CB) and valence (VB) sub-bands u_c and u_v are orthogonal and the momentum matrix element is given by (Coldren and Corzine, 1995, appendices 8, 10)

$$\gamma_p M^2 = \gamma_p \left\{ \int_{\text{unitcell}} u_c^*(\mathbf{r})|\mathbf{e}.\mathbf{p}|u_v(\mathbf{r})\,\mathrm{d}\mathbf{r} \right\}^2 \qquad [1.24]$$

where **p** is the momentum operator, M is the matrix element of a 'bulk' unit cell and the factor γ_p takes account of angular dependence of the matrix elements for light of specific polarisation (defined by unit vector **e**) relative to the plane of the well and the different character of light and heavy valence bands. Equations [1.23] and [1.24] do not apply to transitions between different sub-bands within the same band, as in quantum cascade lasers for example, because the atomic wavefunctions of initial and final states both correspond to the CB (u_c) and they are not orthogonal (Chuang, 2009, Section 9.7). However, the envelope functions for the $n_z = 1, 2$ confined states are orthogonal.

The overlap integral of the CB (F_1) and VB (F_2) (x, y) plane wave envelope functions is zero except when the in-plane k-vectors of initial and final states are the same, when the integral is unity. Consequently it is necessary to sum only over transitions between pairs of states at the same value of $\mathbf{k}_{xy}$ (Fig. 1.13). The density of such transitions in energy is given by the reduced density of states (better termed the transition density) represented by $\rho_{\text{red}}(\hbar\varpi)$. Each of these transitions is homogeneously broadened (Section 1.3.1) and this may be included in Equation [1.23] (Coldren and Corzine 1995, equation 4.39). A normalised broadening function only changes the gain where the density of states changes over an energy interval comparable to or smaller than the linewidth.

The triple overlap integral in the z-direction of initial and final states and optical field enables Equation [1.23] to be applied to structures where the field varies over the gain region, for example multiple quantum well structures. For rectangular wells this overlap integral selects transitions only between sub-bands with the same n_z index.

The gain coefficient is the fractional change in energy in the mode, so an integral of $\xi^2(z)$ over the full width of the mode appears in the denominator. The magnitude of the gain is proportional to the difference between occupation probability of the upper and lower states participating in the transition at $\hbar\varpi$ (Fig. 1.13).

Equation [1.23] is very general, making no assumptions about the width of the gain region relative to the optical field. It can be applied to any structure and potential where the envelope function, confined energies, E-k curves and mode profile are known, such as a triangular potential due to a piezo-electric field or a parabolic potential due to intermixing of well and

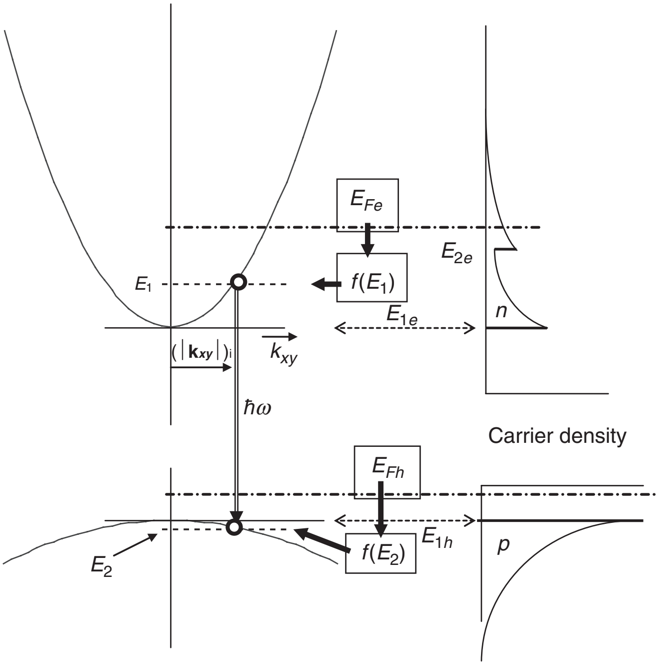

1.13 Illustration of an optical transition at photon energy $\hbar\omega$ between states at E_1 and E_2 at the same value of in-plane *k*-vector, $(|\mathbf{k}_{xy}|)_i$, such that $E_1 - E_2 = \hbar\omega$. The quasi-Fermi energies E_{Fe} and E_{Fh} determine the occupation probabilities, *f*, at E_1 and E_2 and are such that the numbers of electrons and holes are equal, $n = p$, given by the areas under the carrier density distributions.

barrier material. We next examine simplifications of Equation [1.23] in specific situations.

Thin gain region

When the gain region is thin such that the optical field is constant over the extent of the envelope functions with a value ξ_{well} the modal gain is

$$G(\hbar\varpi) = \frac{4\pi\hbar}{n\varepsilon_0 c(\hbar\varpi)}\left(\frac{e}{2m_0}\right)^2 M^2 \left\{\int F_2^*(z)F_1(z)\,\mathrm{d}z\right\}^2 \times \frac{\xi_{\mathrm{well}}^2}{\left\{\int\limits_{\mathrm{mod}} \xi^2(z)\,\mathrm{d}z\right\}} \rho_{\mathrm{red}}(\hbar\varpi)(f_1 - f_2) \qquad [1.25]$$

We define an effective mode width (Fig. 1.6) as in Equation [1.4] then

$$G(\hbar\varpi)=\frac{4\pi\hbar}{n\varepsilon_0 c(\hbar\varpi)}\left(\frac{e}{2m_0}\right)^2\gamma M^2\left\{\int F_2^*(z)F_1(z)\mathrm{d}z\right\}^2\frac{1}{w_{\mathrm{mod}}}\rho_{\mathrm{red}}(\hbar\varpi)(f_1-f_2)\tag{1.26}$$

The well itself usually has negligible effect on the index of the core of the waveguide so the effective mode width can be calculated independently of well itself.

Modal gain and local or material gain

A common form of the gain equation is obtained by multiplying numerator and denominator of Equation [1.25] by a factor X to give

$$G=\left[\frac{4\pi\hbar}{n\varepsilon_0 c(\hbar\varpi)}\left(\frac{e}{2m_0}\right)^2\gamma M^2\left\{\int F_2^*(z)F_1(z)\mathrm{d}z\right\}^2\frac{\rho_{\mathrm{red}}}{X}(f_1-f_2)\right]\frac{X\xi_{\mathrm{well}}^2}{\int\xi^2(z)\mathrm{d}z}\tag{1.27}$$

Mathematically, Equations [1.25] and [1.27] are equivalent, and consistently assigning any value to X in [1.27] recovers Equation [1.25]. Setting $X = L_z$ in [1.27] gives a term ρ_{red}/L_z which is interpreted as a reduced density of states per unit volume; the term in square brackets is called the material, or local gain (g). The final term then represents the optical confinement factor Γ (Equation [1.3], Fig. 1.6) so that

$$G = g\Gamma \tag{1.28}$$

The material gain and the confinement factor [1.3] can only be applied to a well with a defined width, though strictly the states are not wholly confined and a density of states per unit volume cannot be defined. However, if the same value is used for L_z in the local gain and the confinement factor, the result for G is correct, provided the field is uniform over the width used.

The well width determines the transition energy; however, Equation [1.26] shows that for a single pair of sub-bands in a rectangular well the modal gain has no *dimensional scaling* with well width (Blood 2000). Equation [1.27] indicates that the local gain increases with decreasing well width (putting $X = L_z$) but this is illusory as far as device operation is concerned because the confinement factor decreases, keeping the modal gain of a single sub-band pair constant.

Implementation of the gain equation

Starting with a chosen electron density or electron quasi-Fermi level, the hole density and quasi-Fermi level position is determined by charge neutrality. The energies and occupation probabilities of a pair of states of the same $\left|\mathbf{k}_{xy}\right|$ separated by photon energy $\hbar\varpi$ are calculated (Fig. 1.13) and the gain is calculated with knowledge of the overlap integrals. This is repeated for a range of photon energies to generate a gain spectrum for the chosen carrier density as shown in Fig. 1.14 for a model calculation for transitions between conduction and heavy-hole sub-bands, with and without homogeneous broadening of 5 meV. The influence of broadening at the band edge is clear. In real structures, inhomogeneous broadening due to variations in well width or composition also broadens the spectra at the band edges.

1.4.2 Quantum dots

The envelope functions and energy states for a specific dot can be calculated when the potential profile is known. This is not always the case, but some assumptions are often made. The height is usually smaller than the lateral dimensions, so this makes the major contribution to the confinement energy. The lateral x and y dimensions may be similar for a pyramidal structure, in which case the confinement energies associated with them are similar, leading to a doubly degenerate first excited state due to states with quantum numbers (2, 1, 1) and (1, 2, 1), consistent with measurements (Kim *et al.*, 2003; Osborne *et al.*, 2004). The potential is often assumed to be a parabola

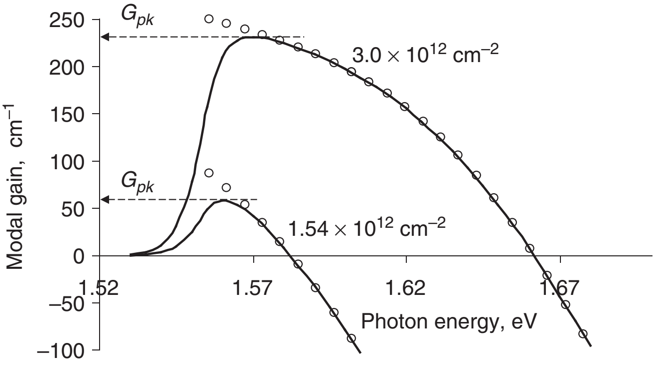

1.14 Quantum well gain spectra for transitions between a single pair of sub-bands based on typical III-V material parameters at 300 K for injected carrier densities of 1.54×10^{12} and 3.0×10^{12} cm^{-2} for charge neutrality in the well. The open circles are calculated without homogeneous broadening and therefore have a sharp cut-off at the sub-band edge. The solid lines are calculated with a sech homogeneous lineshape with linewidth $\Lambda = 5$ meV. The peak value of gain G_{pk} is indicated for each carrier density. For a Fabry-Perot laser the photon energy of the gain peak determines the laser wavelength.

of finite depth because successive transitions are equally spaced in energy, as are the states in an harmonic potential well (Deppe *et al.*, 1999; Park *et al.*, 2000).

Optical gain

Historically, the use of dots in laser diodes has emerged from traditional semiconductor physics so calculations of gain have often used Fermi's Golden Rule and the language associated with bands of states. While the results obtained are broadly correct, conceptually the starting point should be the homogeneously broadened optical cross-sections of the fully localised states Equation [1.14], widely separated in energy (Fig. 1.15). For a layer of N_{dots} *identical* dots per unit area in the waveguide structure of Fig. 1.12 the modal gain along the waveguide due to transitions between the upper (u) and lower (l) states, of separation E is:

$$G(\hbar\varpi) = N_{\text{dot}} \frac{\sigma(E,\hbar\varpi)}{w_{\text{mod}}}(f_u - f_l) \qquad [1.29]$$

where the optical cross-section (Equation [1.14]) is for the appropriate polarisation. This expression neglects effects due to injected carriers; the

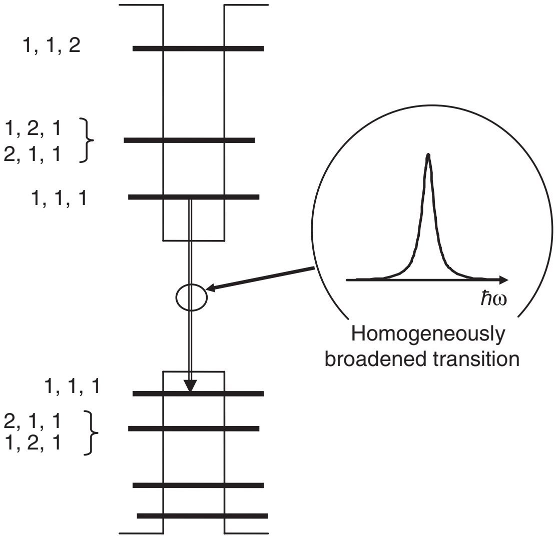

1.15 Localised states in an isolated quantum dot, with energy separations greater than k_BT. For this illustration it has been assumed that the x and y dimensions of the dot are the same so that the (2, 1, 1) and (1, 2, 1) states are degenerate. Homogeneously broadened optical transitions occur between states within individual dots.

major source of many body interactions is the large carrier population in the wetting layer (Schneider *et al.*, 2001), which causes both a shift in the transition energies and a reduction in gain at high injection due to the decrease in dephasing rate (Lorke *et al.*, 2006, 2007).

To calculate the gain spectrum of an inhomogeneous size distribution of dots it is usually assumed that the transition energies are represented by a Gaussian distribution, though it can be argued that it would be more appropriate to represent the *size* distribution by a Gaussian which then produces an asymmetrical distribution in transition energies. Figure 1.16 illustrates calculation of the gain spectrum of an inhomogeneous energy distribution given by a normalised Gaussian $P(E)$. The gain at any photon energy $\hbar\varpi$ is produced by all those dots of different size which contribute to the gain at this photon energy by virtue of their homogeneous broadening:

$$G(\hbar\varpi) = \frac{N_{\text{dot}}}{w_{\text{mod}}} \sum_i \sigma_0 (E_i) L(E_i, \hbar\varpi) P(E_i) (f_u - f_l)_i \qquad [1.30]$$

If the dots are not quantum mechanically coupled, stimulated recombination is localised within each dot therefore the gain in Equation [1.30] is obtained by summing over all contributing dots. Equation [1.14] shows that σ_0 is only weakly dependent on energy, E_i, so the gain spectrum is determined

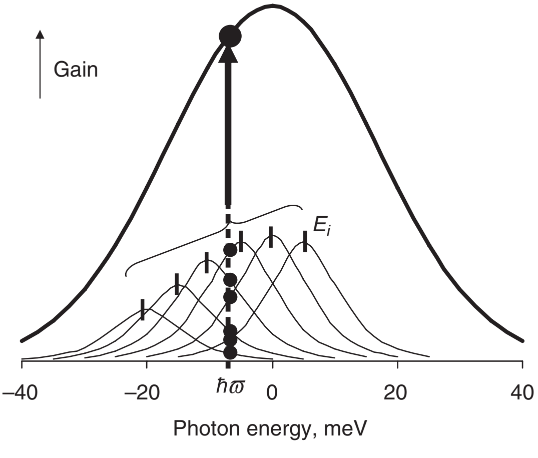

1.16 Homogeneously broadened transitions, of linewidth 5 meV, at a range of photon energies E_i, with strengths specified by a Gaussian inhomogeneous broadening as a function of E_i, with standard deviation 15 meV. The bold line is the spectrum which results by summing the individual homogeneously broadened transitions at each photon energy. The vertical dashed line illustrates this at the specific photon energy $\hbar\omega$; only those transitions contributing to absorption at the indicated photon energy $\hbar\omega$ are shown in the diagram.

primarily by the convolution of homogeneous and inhomogeneous broadening, together with the energy distribution of carriers across the inhomogeneous distribution.

Occupation of dot states

There are a number of views on the occupation of states. As illustrated in Fig. 1.17, electrons and holes are captured from, and thermally re-emitted to, the wetting layer. If these processes are rapid compared with the rate of recombination, the localised states in each dot come into equilibrium with each other by virtue of their interaction with the wetting layer. In this situation we can describe the average electron and hole populations of all the dots and the wetting layer by global quasi-Fermi levels, with the understanding that individual dot states are only occupied by an integer number of electrons.

The question also arises whether dots are populated independently by electrons and holes as implied by the use of separate quasi-Fermi levels, or whether the capture of an electron and a hole is correlated by virtue of their Coulomb attraction, occurring sequentially or by simultaneous capture of a bound electron–hole pair (an exciton).

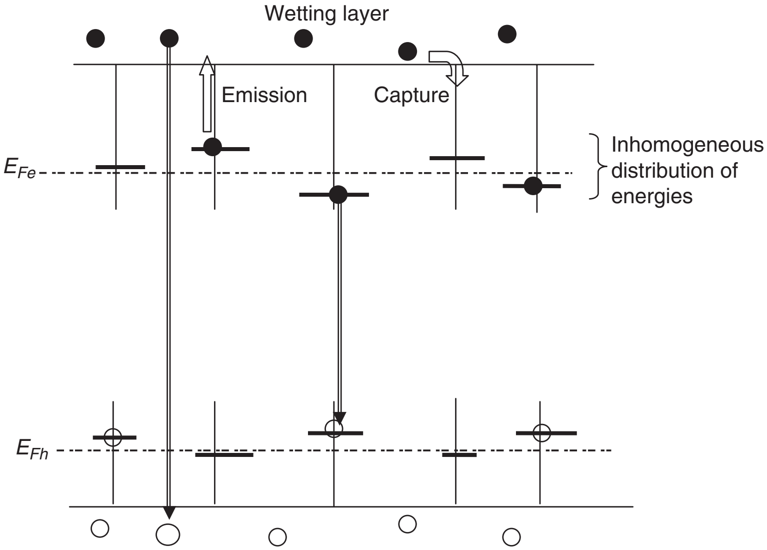

1.17 The occupation of dot states is determined by capture and emission of carriers from and to the wetting layer. When these processes are fast the occupation probabilities are described by global electron and hole quasi-Fermi levels, E_{Fe} and E_{Fh}. Recombination may occur between wetting layer states as well as within the dots.

Many calculations take the pragmatic approach and specify the occupation probabilities by global quasi-Fermi levels, and this has some validity at room temperature. At low temperature the interaction between dot and wetting layer is not sufficiently rapid to establish equilibrium and the dots are occupied 'randomly' by electron–hole pairs, that is, the occupation probability of each inhomogeneous group of dot states of the same index is the same, independent of its energy (Grundmann and Bimberg, 1997), so the occupation factors in Equation [1.30] are the same for all ground state energies.

The transition from random population at low temperature to thermal population at high temperature can be modelled using rate equations (Section 1.8.2) to describe coupling of the electron distribution with a Bose–Einstein phonon distribution (Huang and Deppe, 2001). Figure 1.18

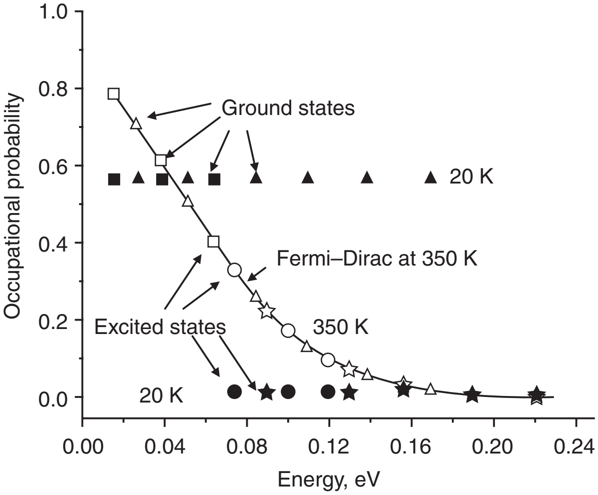

1.18 Rate equation calculations of the occupation probability of ground and first excited states. In the samples studied the dot distribution is bimodal so the calculations have been made for two inhomogeneous distributions each of which is coupled to the same wetting layer by interaction with a thermal distribution of phonons. The horizontal axis is the state energy relative to the energy at the bottom of the dot well. The two groups of ground states are indicated by squares and triangles, and the excited states by circles and stars. Closed symbols are at 20 K, open symbols at 350 K; the line is a Fermi–Dirac distribution at 350 K. At 20 K all ground states have the same occupation irrespective of their energy (0.57) and all excited states have the same occupation (0.01), lower because carriers relax from excited states to ground states. At 350 K the occupation of all states has the same energy dependence brought about by rapid thermal excitation to the wetting layer and this can be described by a global Fermi–Dirac distribution shown by the solid line. (O'Driscoll *et al.* (2010) *IEEE Journal Quantum Electronics*, **46**, 525–532; reproduced with permission, © 2010 IEEE.)

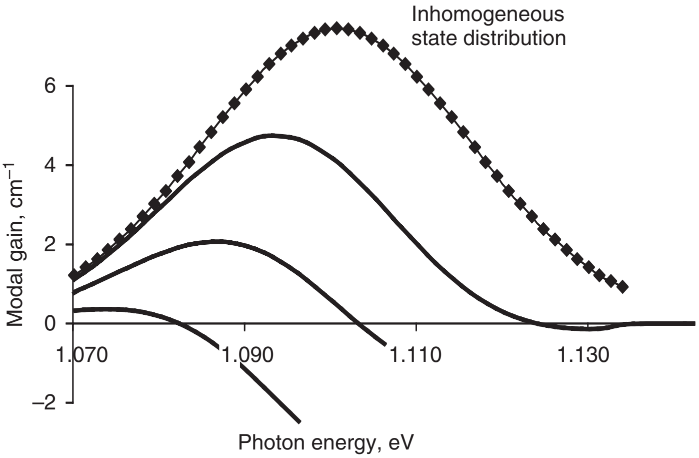

1.19 Calculated modal gain spectra (lines) at 300 K for three different levels of injection, for thermal occupation of the ground state of an inhomogeneous distribution of dots having a transition energy distribution shown by the diamonds. The dot density is 3×10^{10} cm^{-2} and the inhomogeneous and homogeneous linewidths are 15 meV and 10 meV respectively.

shows the electron occupation probability as a function of the energy of the state relative to the lowest ground state in the inhomogeneous distribution (O'Driscoll *et al.*, 2010). At low temperature (solid symbols) the occupations of ground and excited states are different but each is independent of energy, whereas at high temperature (open symbols) the occupation probabilities for all states lie on a single curve as a function of energy which corresponds to all states being occupied according to a Fermi–Dirac distribution (line). The model enables distributions between these limiting cases to be calculated.

Figure 1.19 shows illustrative modal gain spectra for thermal occupation of an inhomogeneous Gaussian ground state distribution at room temperature for three different levels of injection. The gain peak position shifts with temperature because the distribution is wider than k_BT whereas random population gives equal occupation of all states and the gain peak always coincides with the peak of the distribution.

1.5 Recombination processes

The intrinsic current which flows through the laser for a specific quasi-Fermi level separation and gain is due to carrier recombination in the active region. The principal radiative and non-radiative processes are reviewed in this section to enable the relation between peak gain and current to be derived in Section 1.6.

1.5.1 Spontaneous emission

The spontaneous emission spectrum for a single pair of sub-bands of a quantum well, based on the same principles as Equation [1.23] is

$$R_{\text{spon}}(\hbar\varpi) = \frac{16\pi n}{c^3 h^2 \varepsilon_0}(\hbar\varpi)\left(\frac{e}{2m_0}\right)^2 \overline{M}^2 \left\{\int F_v^*(z) F_c(z)\,\mathrm{d}z\right\}^2 \rho_{\text{red}}(\hbar\varpi)\left\{f_c\left(1-f_v\right)\right\} \quad [1.31]$$

where the matrix element $\overline{M}$ is averaged over all polarisations.

The spontaneous emission spectrum of an inhomogeneous ensemble of dots can be obtained by applying the Einstein relations to Equation [1.30]:

$$R_{\text{spon}}(\hbar\varpi) = N_{\text{dot}}\frac{8\pi n^2}{c^2 h^3}(\hbar\varpi)^2 \sum_i \sigma_0(E_i) L(E_i, \hbar\varpi) P(E_i)\left[f_u\left(1-f_l\right)\right]_i \quad [1.32]$$

In this expression the cross-section should also take account of the polarisation characteristics of the dots.

The radiative current in the gain medium for n injected carriers is given by:

$$J_{\text{rad}}(n) = e\int R_{\text{spon}}(\hbar\varpi, n)\,\mathrm{d}\hbar\varpi \quad [1.33]$$

and when calculated for the threshold condition [1.1] this gives the radiative threshold current density, Equation [1.5].

For a single quantum well at low injection when the occupation can be described by Boltzmann factors (Chow and Koch, 1999, equation 2.34):

$$R_{\text{rad}} = \int R_{\text{spon}}(\hbar\varpi)\,\mathrm{d}\hbar\varpi = Bnp \quad [1.34]$$

where B is the radiative recombination coefficient. This equation is widely used though the Boltzmann approximation restricts it to situations where each quasi-Fermi level is about 3 $k_B T$ within the band gap; therefore, it is not appropriate when the system is inverted because this requires the quasi-Fermi level separation to exceed the band gap.

Within a dot, radiative recombination requires the presence of an electron and a hole *in the same dot*, although when summed over all dots, populated by $n_{\text{dot}}, p_{\text{dot}}$ carriers per unit area, a simple dependence on the $(n_{\text{dot}}\, p_{\text{dot}})$ product may not always result (Blood, 2009).

1.5.2 Non-radiative processes and power laws

Non-radiative recombination may occur via deep states in the band gap (Shockley–Read–Hall recombination (SRH)) or by Auger recombination, and for quantum wells these processes have been described (Coldren and Corzine, 1995, section 4.5 and appendix 12). When the Boltzmann approximation is applicable and $n = p$, deep state (SRH), radiative and Auger recombination rates in wells are approximately proportional to n, n^2 and n^3 respectively (Chuang, 2009, section 10.1.1). In quantum dots, where electrons and holes are localised, it is not clear when these power laws can be applied to the dependence of ensemble recombination rates on the ensemble carrier density averaged over all the dots.

The power law approximations provide means of analysing and identifying the dominant non-radiative processes (originally by van Opdorp and ‘t Hooft, 1981; Olshansky *et al.*, 1984; Thompson, 1983). However, the carrier density cannot be measured directly, so following Equation [1.34] with $n = p$, it is taken as proportional to the square root of the external light output (e.g., Fehse *et al.*, 2002). The confidence which can be attached to these studies depends on the extent to which the assumptions underlying them are met in practice, particularly the absence of carrier leakage and current spreading which, over a limited range, masquerade as dependent upon some power of the carrier density.

The Auger coefficient increases with decreasing band gap, and this is thought to be the principal source of non-radiative current in long wavelength devices. Being intrinsic to the material, it is not easily eliminated other than by modification of the electronic band structure, and this has motivated interest in type II quantum well structures for mid-IR lasers (Grein *et al.*, 1994; Meyer *et al.*, 1998).

1.6 Gain–current relations

The relation between peak optical gain and the recombination current is the basis for the design and optimisation of Fabry-Perot lasers. This relation is calculated from the gain and spontaneous emission spectra described in earlier sections, and can be engineered by doping and by the use of strain.

1.6.1 Peak gain and radiative current

We can now calculate the relation between optical gain and current density using gain and emission spectra for a quantum well as an example; this is the basis for designing devices.

For a laser in which the loss is not strongly wavelength dependent and the laser modes are very closely spaced, the modal gain first matches the

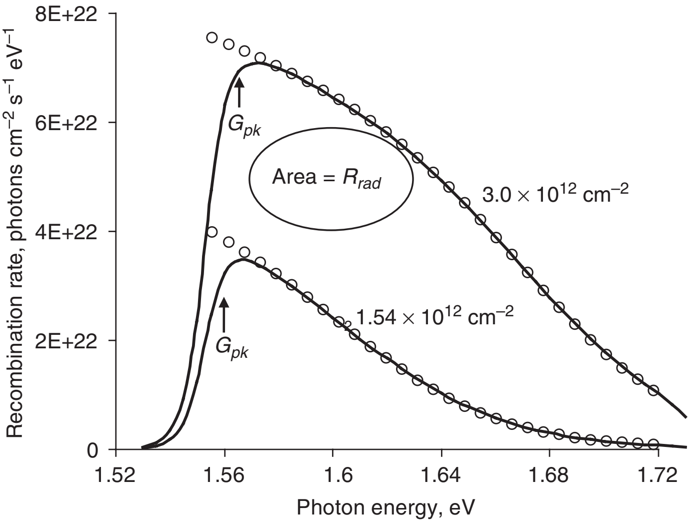

1.20 Calculated spontaneous emission spectra for transitions between the lowest pair of sub-bands in a quantum well based on typical III-V material parameters at 300 K for injected carrier densities of 1.54×10^{12} and 3.0×10^{12} cm^{-2} and for charge neutrality in the well. The open circles are calculated without homogeneous broadening and therefore have a sharp cut-off at the sub-band edge. The solid lines are calculated with a sech homogeneous lineshape with linewidth $\Lambda = 5$ meV. These spectra correspond to the gain spectra in Fig. 1.14. Laser emission occurs at the photon energy of the gain peak indicated (from Fig. 1.14) by the vertical arrows, G_{pk}.

losses at the peak of the gain spectrum. By repeating calculations of the gain (Fig. 1.14) and spontaneous emission spectra (Fig. 1.20) for different carrier densities it is possible to construct a plot of peak gain, G_{pk}, as a function of radiative current density J_{rad} by integrating the emission spectrum, for all polarisations (Equation [1.33]). The non-radiative recombination rate is not known, being dependent on the defect density of the sample, and an 'efficiency' is invoked to estimate the total current (Equation [1.6]). It is possible to calculate the Auger recombination rate, which is intrinsic (e.g. Wang *et al.*, 1995; Harder *et al.*, 2005), but this is rarely done.

A typical peak gain versus radiative current density curve is shown in Fig. 1.21 for a single pair of sub-bands in a quantum well (from Fig. 1.20) and this determines the intrinsic threshold current density for a specific optical loss (Equation [1.1]). In this example the transparency current density, where gain is first produced, is 250 A cm^{-2} and the threshold current density for an optical loss of 50 cm^{-1} is 356 A cm^{-2} which, for a cavity length of 300 μm and stripe width of 10 μm, translates to a current of about 10 mA. At high injection the gain–current curve flattens out due to the constant

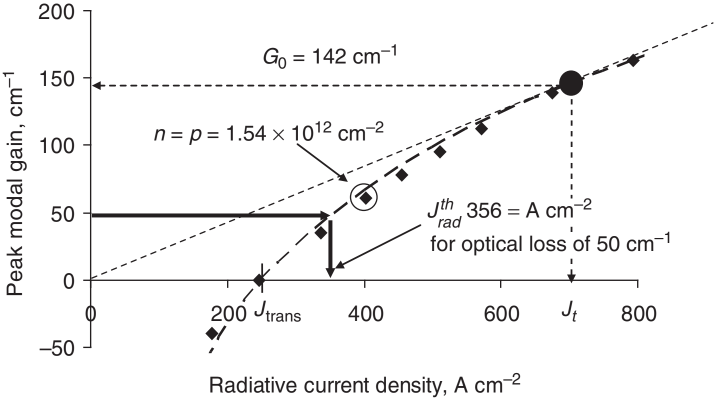

1.21 Illustrative calculated peak modal gain versus radiative current density (diamond points) for a single sub-band pair of a quantum well, obtained from plots such as Fig. 1.14 and by spectrally integrating the radiative recombination rate spectra (Fig. 1.20). The circled data point corresponds to the injected carrier density of 1.54 × 10^{12} cm^{-2} in Figs 1.14 and 1.20. The dashed line is a fit of Equation [1.35] with G_0 = 142 cm^{-1} (the point of contact with the tangent to the curve which passes through the origin) and J_{trans} = 250 A cm^{-2}. The threshold current for an optical loss of 50 cm^{-1} is indicated.

density of states of one sub-band, until the second sub-band contributes to the gain.

We have used a single particle picture and while this conveys the essential physics, the carrier density above inversion exceeds about 1×10^{12} cm^{-2} and 'many body effects' produced by their Coulomb interactions should also be considered. There are four principal effects:

1. At low carrier concentrations, mutual attraction between an electron and hole results in binding to form an exciton manifest as an excitonic absorption peak just below the band edge (Bastard, 1988). This has implications for the occupation of states in dots (Section 1.4.2).
2. Carrier–carrier scattering causes dephasing by homogeneous broadening (Section 1.3.1).
3. Screening of the interatomic potential by free charges causes a reduction in the effective band gap which produces a rigid narrowing of the band gap with increasing carrier density.
4. Coulomb interactions cause enhancement of the interaction probability leading to increased absorption and gain over that of a free-carrier model (Chow and Koch, 1999). Carrier scattering effects also maintain quasi-equilibrium energy distributions. These effects are part of full microscopic calculations (see Chow and Koch, 1999), giving good agreement with experiment (Chow *et al.*, 1997).

1.6.2 Parameterisation and optimisation

Gain–current parameters

The gain–current curves for a single pair of sub-bands of a quantum well can be represented by the functions (McIlroy *et al.*, 1985; Coldren and Corzine, 1995, p. 173)

$$G_{pk} = G_t \left\{ \ell n \frac{J}{J_t} + 1 \right\}$$

or

$$G_{pk} = G_t \ell n \frac{J}{J_{\text{trans}}} \qquad [1.35]$$

As illustrated in Fig. 1.21, G_t and J_t are the coordinates of the point of contact between the gain–current curve and a tangent to the curve through the origin; these simply serve as parameters which specify the curve. Alternatively, this equation can be written in terms of the transparency current density, J_{trans}. Using values of these parameters from the literature the gain–current curve can be reproduced. However, these equations are empirical and have no direct basis in the physics; indeed, for a flat density of states the gain from a single pair of sub-bands tends to an asymptotic value at high current whereas Equation [1.35] does not, so their use is limited to the lower gain region (see Ferguson *et al.*, 2011).

An alternative approximate expression has been proposed for quantum dots (Zhukov *et al.*, 1999):

$$G_{p_k} = G_0 \left\{ 1 - \exp\left[\frac{-\gamma\left(J - J_{\text{trans}}\right)}{J_{\text{trans}}} \right] \right\} \qquad [1.36]$$

where G_0 is the saturation peak gain, J_{trans} is the transparency current density and for an ideal system the parameter γ is unity. When values of γ less than unity are required to fit data it may indicate excited state or wetting layer recombination. This equation has the virtue that it tends to the asymptotic value of G_0 at high current. It gives a reasonable representation of model quantum dot data at low current but the value of G_0 from such a fit is not an accurate measure of the true saturation gain of the system.

Cavity length and multiple quantum wells

With Equation [1.35] it is possible to derive analytically the optimum threshold current and threshold current density with respect to cavity

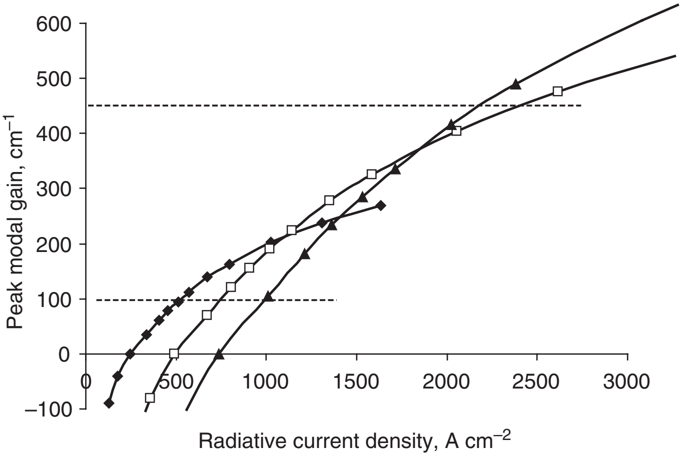

1.22 Modal gain versus radiative current density for 1, 2 and 3 identical quantum wells (solid diamonds, open squares and solid triangles respectively). For a structure with an optical loss of 100 cm^{-1} a single well gives the lowest radiative current density whereas at 450 cm^{-1} three quantum wells give the lowest value. This figure illustrates the importance of the transparency current density at low gain. The injected carrier density per well is 1.86 × 10^{12} cm^{-2} at G_{pk} = 112 cm^{-1} for a single well, whereas for three wells generating the same total modal gain the carrier density is reduced to 1.39 × 10^{12} cm^{-2} per well reducing the quasi-Fermi level separation by about 30 meV.

length and mirror reflectivity (McIlroy *et al.*, 1985; Coldren and Corzine, 1995, appendix 17). A distinctive feature of QW lasers is an optimum cavity length which minimises the threshold current for a given mirror reflectivity due to saturation of the gain–current curve (McIlroy *et al.*, 1985; Zory *et al.*, 1986).

Gain saturation at high current can be overcome using multiple wells, and Fig. 1.22 shows a family of curves for modal gain versus radiative current per unit area (assuming identical wells): at low gain a single well gives the lowest current density because transparency current has to be supplied to every well, irrespective of the gain produced; however, where the gain begins to saturate multiple wells give a lower threshold current density. There are other considerations in using multiple wells. The wells may not be equally pumped due to carrier transport within the SCH region and the confinement factor is reduced for wells where the optical field is lower than its peak in the centre of the waveguide. On the other hand multiple wells reduce the carrier density per well and lower the quasi-Fermi levels which reduces carrier leakage, which can be particularly beneficial in reducing the temperature dependence of threshold.

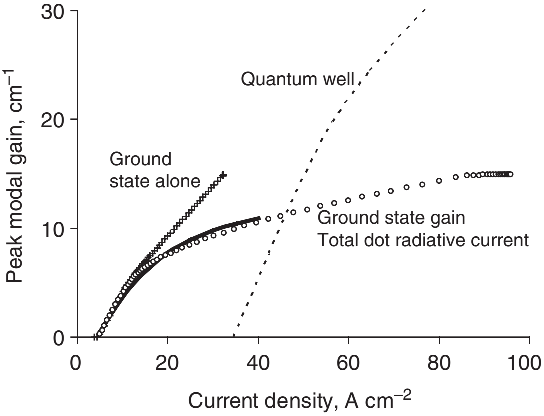

1.23 Peak modal gain as a function of radiative current density for thermal population at 300 K of an inhomogeneous distribution of 3×10^{10} dots cm^{-2}. The crosses are for gain from the ground state as a function of ground state radiative current density; the maximum peak gain available from the ground state is about 15 cm^{-1}. The circles are for ground state gain as a function of the total radiative current (ground and excited states), and the solid line is a fit of Equation [1.36]. The dashed line is for a single quantum well calculated using the same transition matrix element as for the dots. The diagram illustrates that a low threshold current density can be achieved using dots provided the gain requirement is not too large, below about 10 cm^{-1} in this example. (Derived from Blood, 2009.) (Calculation uses different parameters to Fig. 1.21.)

1.6.3 Engineering the gain–current curve

It is usually desirable to design a structure to give the maximum modal gain for a given current density. The waveguide design should maximise the overlap of the mode with the gain medium (this also affects the far field), and carrier leakage, non-radiative recombination and recombination from higher sub-bands or dot states and barriers should all be minimised. The gain is the key intrinsic characteristic determining the Fermi level positions and the threshold current. Quantum confinement is itself a means of engineering this characteristic.

Figure 1.23 shows calculations of the modal gain for dots and a well for the same material. The transparency current can be very small for dots because the number of states is small and proportional to the dot density. Figure 1.23 is calculated for 3×10^{10} dots cm^{-2} whereas the state density of a quantum well sub-band (Equation [1.22]) is $\approx \rho_{xy} \times (k_B T) \approx 6.7 \times 10^{11}$ cm^{-2}. However, in dots there is also a corresponding limit to the maximum peak gain. For a low optical loss the dot threshold *current density* is lower than the well; however, if it is necessary to increase the device length to access this low gain region the threshold *current* may be greater than that of a shorter well device.

Two factors in particular affect the gain–current curve of dots. The inhomogeneous broadening should be as small as possible, not only to minimise unproductive radiative transitions but also because the peak gain is inversely proportional to the linewidth (as can be shown from Equation [1.30]). Second, due to its high relative high density of states, the wetting layer makes a large contribution to the current (Matthews *et al.*, 2002) and it is difficult to achieve full inversion of the dots even at high current, restricting the maximum peak gain which can be obtained.

Beyond these considerations attention has turned to modifications of the electronic band structure. However, the Einstein relations show that, at any photon energy, stimulated and spontaneous emission are related so both gain and recombination rate are affected, furthermore it is important to treat gain and recombination consistently and not fall back on un-modified power law coefficients to calculate the current.

Figure 1.20 shows that many transitions contribute to the emission spectrum which do not contribute to the peak gain and eliminating these reduces the threshold current density without impairing the gain. This can be done directly by reducing the number of modes available for spontaneous emission by use of a photonic structure or microcavity. More common approaches to reducing the emission are strained quantum wells (Adams, 1986; Yablonovich and Kane, 1986) and p-doping.

Elastic strain

It is possible to deposit a material which has a relaxed lattice parameter different from that of the underlying layer without formation of defects provided the strain × thickness product does not exceed about 100% × Å. The deposited layer is elastically strained, taking up the lattice parameter of the underlying material in the plane of growth. This affects the light- and heavy-hole components of the valence band (LH and HH respectively) which are degenerate at $k = 0$ in bulk material. In a quantum well these states have a small energy separation as illustrated in the central part of Fig. 1.24. Laser action usually occurs in the TE_y mode due to transitions to the HH band and strain reduces other non-productive transitions and the carrier population at threshold by two effects: (i) the $E(k)$ curves are different in the growth plane and in the growth direction due to strain-induced tetragonal distortion of the unit cell, resulting in changes in the density of states, and (ii) the LH and HH bands are separated in energy, with consequences illustrated in Fig. 1.24. Under compressive strain the lowest gap is from conduction (C) to HH band, and the latter has a low in-plane mass and hence a low density of states. This lowers the quasi-Fermi levels, reducing the

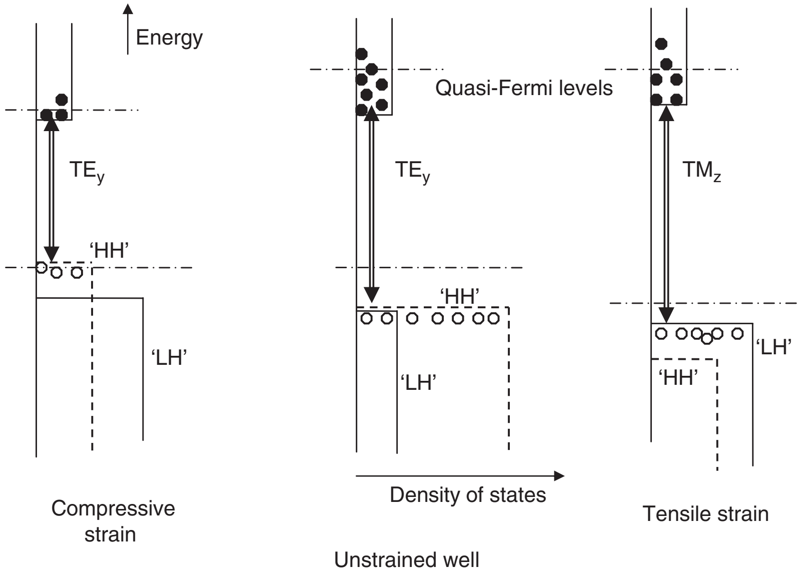

1.24 Diagrams showing the densities of states of the conduction, HH and LH sub-bands in a quantum well, showing the effects of compressive and tensile strain on the valence band edge energies and the densities of states.

carrier density and current to achieve inversion, and reducing unproductive transitions to the LH band. With tensile strain the former LH band is uppermost and while this does not bring about a significant reduction in carrier density, the matrix element for C-LH TM$_z$ transitions is large, representing about one half of the total transition strength which brings improvements in gain–current characteristics. Chuang (2009, pp. 141–2, 446) and O'Reilly and Ghiti (in Zory, 1993) give full accounts of strain effects.

Strain has been employed to good effect in short wavelength GaInP/GaAs lasers (for an analysis see Blood and Smowton, 1995) and in long wavelength devices (Thijs *et al.*, 1994). As well as giving improvements in performance, use of strained layers gives greater flexibility in selection of well and barrier materials, widening the range of wavelengths which can be achieved (see articles in Manasreh, 1997).

p-doping

In quantum wells the electron quasi-Fermi level is high in the band due to the high density of HH states, as illustrated in the central diagram in Fig. 1.24. By introducing holes into the VB by p-doping the adjacent barrier (modulation doping), the quasi-Fermi levels are lowered and the quasi-Fermi level separation necessary for a given inversion is reduced; this reduces the radiative current and electron leakage currents (Figs 1.4 and 1.5). In dots, p-doping fills the closely spaced hole states arising from the high effective mass, reducing the threshold current and its temperature dependence and improving the modulation performance (Shchekin and Deppe, 2002a, 2002b). An analysis has been given by Smowton *et al.* (2007). (Also see Crowley *et al.*, 2009; Ozgur, 2009).

1.7 Temperature dependence of threshold current

An important characteristic of a laser diode is the undesirable increase of threshold current with increasing temperature. This is modified by quantum confinement, but not eliminated. In grating feedback devices, particularly vertical cavity lasers, the temperature variation of threshold is determined by the relative shift of the gain and reflectivity spectra.

1.7.1 The T_0 parameter

The dependence of threshold current on temperature is a shortcoming of diode lasers and the quest for a temperature independent threshold was a major factor in the drive for quantum dot devices. It is usual to characterise the temperature dependence by a parameter T_0:

$$J_{\mathrm{th}}(T) = J_{\mathrm{th}0} \exp\left(\frac{T}{T_0}\right) \qquad [1.37]$$

and this parameter can be extracted for any $J_{\mathrm{th}}(T)$ data as:

$$\frac{1}{T_0} = \frac{\mathrm{d}(\ell n J_{\mathrm{th}})}{\mathrm{d}T} \qquad [1.38]$$

A low value of T_0 indicates a large fractional temperature dependence. Care is needed in the interpretation of T_0 values when the functional dependence of $J_{\mathrm{th}}(T)$ is not exponential. For example when $J_{\mathrm{th}} \propto T$ it can be shown, using Equation [1.38], that the value of T_0 obtained from measurements at two temperatures T_1 and T_2 is the mean temperature of measurement $\frac{1}{2}(T_1 + T_2)$ and the result therefore reflects the values chosen for T_1 and T_2. Results for T_0 should be accompanied by information about the method of determination and temperature range.

The temperature dependence of threshold arises from temperature dependence of the optical loss, which determines the gain required, and from the temperature dependence of the total current required to provide the required gain. In many devices the second effect is the major factor.

1.7.2 Quantum wells

When the injection efficiency is large the temperature sensitivity is determined by recombination processes in the well. The gain requirement determines the Fermi level positions and for a single sub-band the carrier density is:

$$n=\left[\frac{m^{*}k_{B}T}{\pi\hbar^{2}}\right]\ell n\left\{1+\exp\left(-\frac{E_{1e}-E_{\mathrm{Fe}}}{k_{B}T}\right)\right\} \qquad [1.39]$$

so there is an approximately linear increase in threshold carrier density with T for fixed Fermi level and the temperature sensitivity of the current is closely related to the dependence of the recombination rates on n (Section 1.5.2). The radiative recombination coefficient B varies as T^{-1} so for $n_{\mathrm{th}} \propto T$ (Equation [1.39]), from Equation [1.34] $R_{\mathrm{rad}}^{\mathrm{th}} \propto T$. Figure 1.25 shows experimental data for the temperature dependence of spontaneous emission from a quantum well laser at threshold, which confirms this behaviour (Blood *et al.*, 1989a) and shows that the temperature dependences of the current originate in thermal broadening of the carrier distribution. The Auger

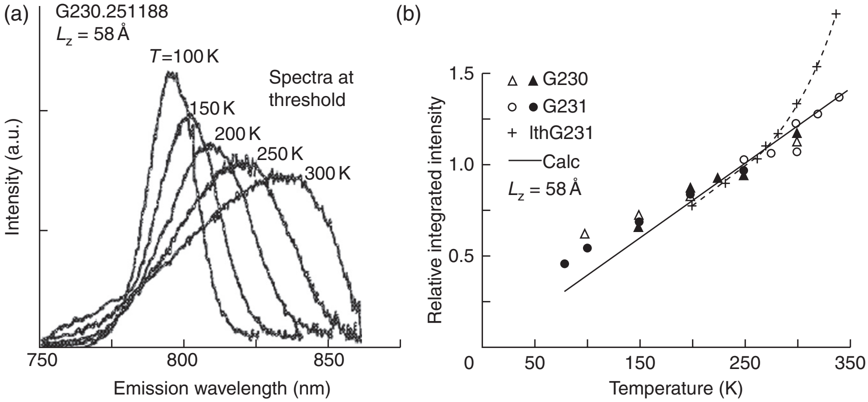

1.25 (a) Measurements of the true spontaneous emission spectrum from a GaAs quantum well laser recorded at threshold at each temperature between 100 K and 300 K. The peak shifts to longer wavelength due to the temperature dependence of the band gap and the spectrum broadens on the short wavelength side (higher energy) due to the increased thermal spread of carriers. The radiative threshold current is proportional to the area under each spectrum. Relative values of these areas are plotted as a function of temperature in panel (b) and exhibit dependence close to the predicted linear behaviour (line). The relative values of the measured threshold current (crosses) increase super-linearly above about 250 K due to thermally excited non-radiative recombination in the AlGaAs barrier. (Reprinted with permission from Blood *et al.*, *Applied Physics Letters* **55**, 1167–1169 (1989); Copyright 1989 American Institute of Physics.)

recombination rate varies as n^3 (Section 1.5.2) so the recombination current varies approximately as T^3, neglecting any temperature dependence of the Auger coefficient itself. The power law approach can be used to identify the dominant contribution to the device current as a function of temperature (Higashi *et al.*, 1999). Further temperature dependent contributions may arise from higher sub-bands in the well (Blood *et al.*, 1990).

When the well is not the dominant current path temperature sensitivity may also arise from recombination in adjacent barrier material (Blood *et al.*, 1989b), and from thermally activated leakage over the heterobarrier (Figs 1.4 and 1.5). If there is a contribution to the optical loss by free-carrier scattering of light then the increase in n with T will itself bring about an increase in optical loss.

For quantum well lasers measured around room temperature (T_1, T_2 ~ 300 K) values of T_0 should not exceed about 300 K (radiative recombination alone). In short wavelength lasers (e.g., 650 nm GaAlInP/GaAs), due to carrier leakage measured values of T_0 are smaller, in the range 190–270 K, depending on cavity length (Smowton and Blood, Chapter 9 in Manasreh, 1997). In long wavelength devices values of T_0 in the region of 100 K are common due to Auger recombination, and even smaller values may arise in the presence of carrier leakage.

1.7.3 Quantum dots

In a system of identical dots, if the spacing of the states exceeds many k_BT there are no spontaneous transitions other than those between states which provide gain and the threshold should be independent of T. Early papers on dots placed great emphasis on this property of an ideal dot system; however, this did not take account of the homogeneous linewidth (Λ) and its increase with temperature (Borri *et al.*, 2002, fig. 1.8). For a system of identical dots, the peak gain occurs when $\hbar\varpi = E_i$ in Equation [1.15] when Equation [1.29] gives the peak gain:

$$G_{pk}\left(\hbar\varpi = E_t\right) = N_{\text{dot}} \frac{\sigma_0}{\pi\Lambda w_{\text{mod}}} (f_u - f_l) \qquad [1.40]$$

and as T increases Λ increases it is necessary to increase $\left(f_u - f_l\right)$ to maintain the same peak gain, which results in an increase in recombination current. This introduces an intrinsic temperature dependence of threshold into a system of dots, even when they are all *identical* (Ozgur *et al.*, 2009).

There are other contributions to the temperature dependence in dot lasers, particularly recombination from non-inverted dots within the inhomogeneous distribution, higher lying dot states and thermal excitation of carriers to the wetting layer. This has led to investigation of tunnel injection

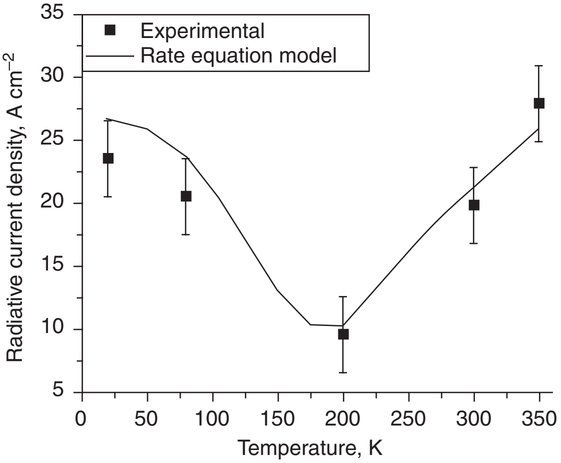

1.26 Experimental measurements (squares) of the temperature dependence of the radiative current density for a fixed modal gain of 4 cm^{-1} for a GaInAs quantum dot laser structure emitting at 0.98 eV, showing a minimum at about 200 K. The line is a calculation using a rate equation model for the dots in equilibrium with a Bose-Einstein distribution of phonons. The energy distributions of the occupation probabilities at 20 K and 350 K are shown in Fig 1.18, illustrating the transition from random population at 20 K to thermal at 350 K. (O'Driscoll *et al.* (2010) IEEE *Journal Quantum Electronics*, **46**, 525–532; reproduced with permission, © 2010 IEEE.)

directly into the dot states from a nearby quantum well (Asryan and Luryi, 2001; Chuang and Holonyak, 2002; Walter *et al.*, 2002; Bhattacharya *et al.*, 2003) though for such a scheme to be effective it is necessary that the carriers do not thermalise to higher lying states (George *et al.*, 2007).

Quantum dot lasers often show a minimum in the threshold current as a function of temperature in the region 200–300 K (Zhukov *et al.*, 1997); a typical example is shown by the data points in Fig. 1.26 (O'Driscoll *et al.*, 2010). This is due to the occupation of states across the inhomogeneous energy distribution becoming random at low temperatures (Section 1.4.2) so carriers are distributed over all states with equal probability (Fig. 1.18). This wider distribution increases the spontaneous recombination rate for a given gain, increasing the threshold over that of a thermal distribution.

Measured values of T_0 for quantum dot lasers range between 80 K and claims of ∞! Temperature dependent homogeneous broadening gives values as low as 157 K for the ground state alone (Ozgur *et al.*, 2009) and the large number of closely spaced hole levels and the wetting layer can reduce this to below 100 K. In some p-doped devices the minimum in the threshold current appears in the region of room temperature, and in some cases current components which are themselves temperature dependent combine to producing a threshold current which is constant over a limited region (e.g., Fathpour *et al.*, 2004). Again the results are very sensitive to the optical loss which controls the degree of inversion required.

1.7.4 Vertical cavity lasers

In vertical cavity lasers (see Chapter 8 of this volume) there is only one lasing mode within the gain spectrum so the laser wavelength is controlled by the cavity; as the band gap shifts with temperature the gain peak moves away from the cavity mode (due to increasing or decreasing temperature) and more current is required to produce the required gain giving a 'U' shaped temperature dependence of threshold current (see Chuang, 2009, section 11.2.4.

1.8 Rate equations

This section provides a short summary of the description of laser operation by coupled rate equations for the carrier and photon populations which are coupled through the stimulated emission process. These can be solved to obtain the light–current curve in the steady state, and the small signal modulation response.

1.8.1 Formulation of the rate equations

In this section we consider the coupled rate equations for carriers and photons necessary for an understanding of diode lasers above threshold.

The optical mode is coupled to a gain layer in the *x*-*y* plane and amplification is expressed as a modal gain. The carrier and photon populations are represented by averages which are uniform in the *x*-*y* plane, and are expressed as densities per unit area projected onto the *x*-*y* plane (n and N_{ph}, respectively). These populations are coupled by the net stimulated recombination rate per unit area:

$$R_{\text{stim}} = v_g G(n) N_{\text{ph}} \tag{1.41}$$

where v_g is the group velocity of the mode and the modal gain $G(n)$ takes account of the *z*-overlap of the mode with carriers, contained in Equation [1.25]. The rate of change of the electron population per unit area is given by:

$$\frac{\mathrm{d}n}{\mathrm{d}t} = \eta_{\text{inj}} \frac{J}{e} - R_{\text{rad}}(n,p) - R_{\text{nr}}(n) - R_{\text{stim}} \tag{1.42}$$

where η_{inj} is the injection efficiency, which for dots takes account of wetting layer recombination, and $R_{\text{nr}}(n)$ is the rate of all non-radiative processes in the active layer. The rate equation for the photon density is:

$$\frac{\mathrm{d}N_{\mathrm{ph}}}{\mathrm{d}t} = R_{\mathrm{stim}} - \frac{N_{\mathrm{ph}}}{\tau_{\mathrm{ph}}} + \beta_{\mathrm{spon}} R_{\mathrm{rad}}(n, p) \qquad [1.43]$$

where the photon lifetime characterises the rate at which photons are lost from the mode due to the waveguide and mirror losses:

$$\frac{1}{\tau_{\mathrm{ph}}} = v_g \{\alpha_i + \alpha_m\} = v_g \left\{\alpha_i + \frac{1}{L_c} \ell n (R)^{-1}\right\} \qquad [1.44]$$

and β_{spon} is the fraction of the total spontaneous emission which is coupled into the guided mode ($\approx 10^{-4}$). These equations can be solved if the functional dependences of gain, spontaneous and non-radiative recombination on n are known.

These expressions are cast in terms of the *modal* gain and current per *unit area*, which encompass differences in the 'thicknesses' of the optical mode and the gain region, and which can be computed from Equations [1.23] and [1.31] or [1.30] and [1.32] for any well or dot geometry. For dots, n is the average carrier density over the x-y area, which therefore depends on the areal dot density. Dot recombination only occurs within individual dots and this detailed physics is wrapped up in the functional relations for $G(n)$, $R_{\mathrm{spon}}(n)$ and $R_{\mathrm{nr}}(n)$ which cannot be assumed to be the same as for a quantum well.

1.8.2 Steady state solutions

The steady state solutions are obtained by setting Equations [1.42] and [1.43] to zero. Figure 1.27a shows the internal net photon generation rate (spontaneous emission +/– stimulated emission/absorption) as a function of the total recombination current, including non-radiative recombination. A large fraction of spontaneous emission coupled into the lasing mode softens the turn-on of the L-I characteristics as shown by the points for $\beta_{\mathrm{spon}} = 3 \times 10^{-3}$. The internal differential quantum efficiency (Equation [1.10]) (plot (b)) becomes one above threshold, whereas the overall ratio of the internal spontaneous recombination rate to the total current at threshold gives a quantum efficiency (Equation [1.7]) of 0.82, determined by the non-radiative lifetime of 3 ns. Part (c) is a logarithmic plot of the spontaneous rate and total emission rate into the mode as a function of current density showing pinning of the spontaneous emission and hence carrier density and gain, above threshold (see Section 1.2.5). Above threshold for the data point at 543 A cm^{-2}, the ratio of total emission rate into the mode divided by current density corresponds to a quantum efficiency of 0.17.

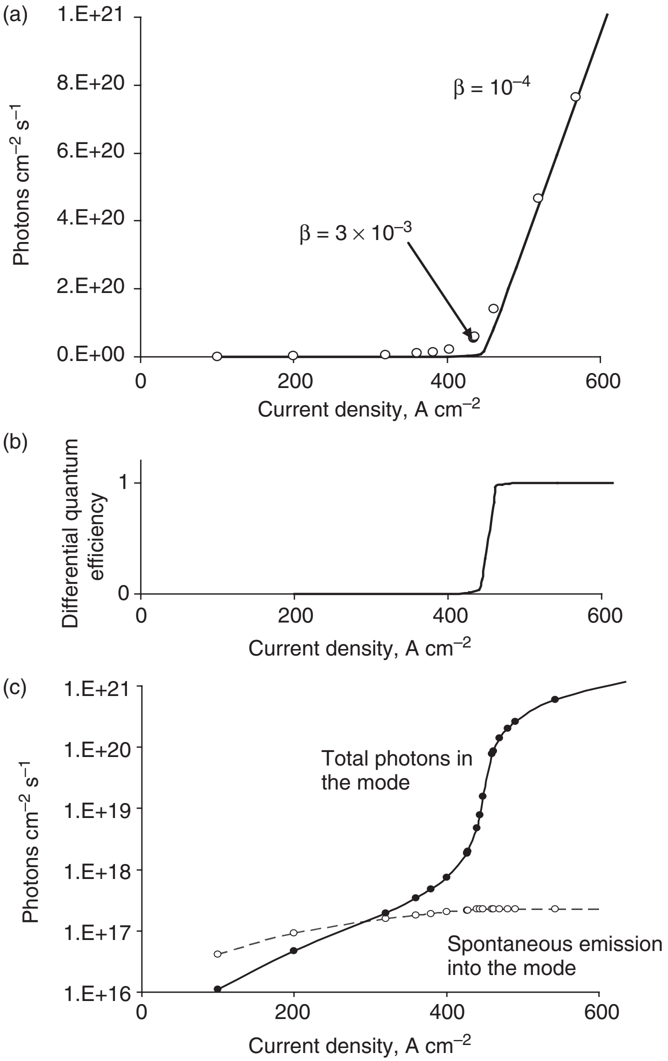

1.27 (a) Steady state rate equation calculations of the light–current characteristics of a quantum well laser diode for two values of the fraction of spontaneous emission coupled into the lasing mode (β). Panel (b) shows that the differential efficiency becomes unity above threshold and (c) shows the saturation of the spontaneous emission rate above threshold due to Fermi-level pinning. The cavity loss is 60 cm^{-1} and the non-radiative lifetime is 3 ns. The injection efficiency is taken to be 100%.

1.8.3 Small signal modulation response

The rate equations can be solved for the modulation in laser output in response to small signal modulation of the drive current by representing the current, carrier density and photon density as small oscillations about steady state values. The gain-carrier density relation $G(n)$ is calculated for a negligibly small photon density such that there is no current due to stimulated recombination. Above threshold, the carrier density at a given current is smaller than in the absence of photons due to additional recombination due to stimulated emission in Equation [1.42] and this suppresses the gain below that of the material in the absence of photons. Thus in calculations of modulation response above threshold the relation between gain and carrier density depends upon the photon density and this is incorporated by introducing a gain compression factor.

The general form of the modulation response is that of a forced, damped oscillator (Chuang, 2009, equation 12.1.23). The resonance frequency increases with drive current due to the increase in N_{ph}^{0}, and is proportional to the square root of the differential modal gain and of G_0 (through R_{stim}). For the model calculation of Fig. 1.27 the resonance frequency above threshold is about $3 \times 10^{10}\ \mathrm{s}^{-1}$. In quantum wells the modulation response is also affected by the time for carriers to be transported through the core of the SCH (about 100 ps; Nagarajan *et al.*, 1992) and explicit account should also be taken of the capture and emission of carriers between the reservoir in the barrier region and the well (Nagarajan *et al.*, 1991, 1992; McDonald and O'Dowd, 1995).

The excited states play an important role in the population of quantum dot states and multi-level rate equations, including capture and emission between dot states and the wetting layer, have been employed (Fiore and Markus, 2007), particularly to study switching of the laser wavelength from ground to excited states (Markus *et al.*, 2006; Grillot *et al.*, 2009).

Other phenomena can be determined from the rate equations including chirp (the variation of the lasing wavelength with current modulation brought about by carrier induced changes in the mode index), the linewidth enhancement factor (the ratio of the carrier density dependence of index and gain, the real and imaginary parts of the complex index) and the turn-on delay (the time required to build up the carrier density to achieve inversion and lasing).

1.9 Future trends

Topics of current research interest are well represented by the chapters in this book. The conventional view is that physical size of these devices is ultimately limited by the wavelength of the light generated within them, even though the electronic length scales of the gain regions are much smaller. This difference in optical and electronic length scales becomes an issue as efforts are made to incorporate optical devices in integrated electronic devices. There is therefore considerable interest in metal–cavity nano-lasers in which coherent light is produced in cavities with dimensions below the diffraction limit by use of plasmons at the dielectric–metal interface. This could be regarded as the extension of the semiconductor heterostructure to include different classes of materials. Fundamental aspects of the light-matter interaction lie at the heart of this topic and it therefore offers commercial and scientific opportunity as well as posing considerable technological challenges. Further reading can be found in the papers by Chang and Chuang (2009), Hill (2010) and Oulton *et al.* (2009).

1.10 Acknowledgements

The author thanks colleagues and students at Cardiff University for many discussions which have contributed to refinement of the ideas expressed in this chapter. The research activities which have stimulated interest in these topics have been funded by the Engineering and Physical Sciences Research Council and by Cardiff University.

1.11 References

Adams A R (1986) 'Band structure engineering for low threshold high efficiency semiconductor lasers', *Electr Lett,* **22**, 249–250.

Agrawal G P and Dutta N K (1993) *Semiconductor lasers*. New York, van Nostrand Reinhold.

Alferov Zh (2000) 'Double heterostructure lasers: early days and future perspectives', *IEEE J Sel Top Quantum Electron,* **6**, 832–840.

Alferov Zh I, Andreev V M, Korol'kov V I, Portnoi E L and Tret'yakov D N (1969) 'Injection properties of n-$Al_xGa_{1-x}As$ – p-GaAs heterojunctions', *Sov Phys Semic,* **2**, 843–844.

Alferov Zh I, Andreev V M, Portnoi E L and Trukan M K (1970) 'AlAs-GaAs heterojunction injection lasers with a low room-temperature threshold', *Sov Phys Semic*, **3**, 1107–1110.

Arakawa Y and Sakaki H (1982) 'Multidimensional quantum well laser and temperature dependence of its threshold current', *Appl Phys Lett*, **40**, 939–941.

Asada M, Miyamoto Y and Suematsu Y (1986) 'Gain and threshold of three-dimensional quantum box lasers', *IEEE J Quantum Electron,* **22**, 1915–1921.

Asryan L V and Luryi S (2001) 'Tunneling injection quantum dot laser: ultra high temperature stability', *IEEE J Quantum Elect,* **37**, 905–910.

Asryan L V (2006) 'Limitations on standard procedure of determining internal loss and efficiency in quantum dot lasers', *J Appl Phys,* **99**, 013102.

Bastard G (1988) *Wave mechanics applied to semiconductor heterostructures*. New York, Halstead Press.

Bertolotti M (1983) *Masers and lasers*. Bristol and Philadelphia, Adam Hilger.

Bertolotti M (2005) *The history of the laser*. Bristol and Philadelphia, IOP Publishing.

Bernard M G A and Duraffourg G (1961) 'Laser conditions in semiconductors', *Phys Stat Solid,* **1**, 669–703.

Bhattacharya P, Ghosh S, Pradhan S, Singh J, Wu Z-K, Urayama J, Kim K and Norris T B (2003) 'Carrier dynamics and high speed modulation properties of tunnel injection InGaAs-GaAs quantum dot lasers', *IEEE J Quantum Elect,* **39**, 952–962.

Bimberg D, Grundmann M and Ledentsov N N (1999) *Quantum dot heterostructures*. Chichester, John Wiley.

Blood P (2000) 'On the dimensionality of optical absorption, gain and recombination in quantum confined structures', *IEEE J Quantum Elect,* **36**, 354–362.

Blood P (2009) 'Gain and recombination in quantum dot lasers', *IEEE J Sel Topic Quantum Electron,* 1**5**, 808–818.

Blood P, Kucharska A I, Foxon C T and Griffiths K (1989a) 'Temperature dependence of spontaneous emission in GaAs-AlGaAs quantum well lasers', *Appl Phys Lett,* **55**, 1167–1169.

Blood P, Fletcher E D, Woodbridge K, Heasman K C and Adams A R (1989b) 'Influence of the barriers on the temperature dependence of threshold current in GaAs/AlGaAs quantum well lasers', *IEEE J Quantum Elect,* **25**, 1459–1468.

Blood P, Fletcher E D, Woodbridge K and Venning M (1990) 'Spontaneous recombination current in InGaAs/GaAs quantum well lasers', *Appl Phys Lett,* **57**, 1482–1484.

Blood P and Smowton P M (1995) 'Strain dependence of threshold current in fixed-wavelength GaInP laser diodes', *IEEE J Sel Topic Quantum Electron* **1**, 707–711.

Borri P, Langbein W, Schneider S, Woggon U, Sellin R L, Ouyang D and Bimberg D (2001) 'Ultra-long de-phasing time in InGaAs quantum dots', *Phys Rev Lett*, **87**, 15701-1-15407-4.

Borri P, Langbein W, Schneider S, Woggon U, Sellin R L, Ouyang D and Bimberg D (2002) 'Exciton relaxation and dephasing in quantum dot amplifiers from room to cryogenic temperature', *IEEE J Sel Topic Quantum Electron,* **8**, 984–991.

Bour D P, Treat D W, Thornton R L, Geels R S, and Welch D F, (1993) 'Drift leakage current in AlGaInP quantum well lasers', *IEEE J Quantum Elect,* **29**, 1337–1343.

Casey H C and Panish M (1978) *Heterostructure lasers*. San Diego, Academic Press.

Chang S-W and Chuang S L (2009) 'Fundamental formulation for plasmonic nanolasers', *IEEE J Quantum Elect*, **45**, 1014–1023.

Chow W W, and Koch S W, (1999) *Semiconductor-laser fundamentals*. Berlin, Springer-Verlag.

Chow W W, Smowton P M, Blood P, Girndt A, Jahnke F and Koch S W (1997), 'Comparison of experimental and theoretical GaInP quantum well gain spectra', *Appl Phys Lett,* **71**, 157–159.

Chuang S L (2009) *Physics of photonic devices*, 2nd ed. Hoboken NJ, Wiley.

Chuang S L and Holonyak N (2002), 'Efficient quantum well to quantum dot tunneling: analytic solutions', *Appl Phys Lett*, **80**, 1270–1272.

Coldren L A and Corzine S W (1995) *Diode lasers and photonic integrated circuits*. New York, Wiley.

Crowley M T, Pavlovich I, Masse N F, Andreev A D, Tomic S, Sweeney S J, O'Reilly E P and Adams A R (2009) 'The importance of recombination via excited states in InAs/GaAs 1.3 μm quantum dot lasers', *IEEE J Sel Topic Quantum Electron,* **15**, 799–807.

Deppe D G, Huffaker D L, Csutak S, Zou Z, Park G and Shchekin O B (1999) 'Spontaneous emission and threshold characteristics of 1.3-mu m InGaAs-GaAs quantum-dot GaAs-based lasers', *IEEE J Quantum Electron,* **35**, 1238–1246.

Dingle R, Weigmann W and Henry H C (1974) 'Quantised states of confined carriers in very thin AlGaAs-GaAs-AlGaAs heterostructures', *Phys Rev Lett,* **33**, 827–830.

Dupuis R D, Dapkus P D, Holonyak N, Jr, Rezekea and Chin R (1978) 'Room temperature operation of quantum well GaAlAs-GaAs laser diodes grown by metalorganic chemical vapour deposition', *Appl Phys Lett,* **33**, 73–75.

Eliseev P G (1997) 'Lineshape function for semiconductor laser modelling', *Electron Lett,* **33**, 2046–2048.

Faist J, Capasso F, Sivco D L, Sirtori C, Hutchingson A L and Cho A Y (1994) 'Quantum cascade laser', *Science,* **264**, 553–556.

Fathpour S, Mi Z, Bhattacharya P, Kovsh A R, Mikhrin S S, Krestnikov I L, Kozhukhov A V, and Ledentsov N N (2004) 'The role of Auger recombination in the temperature-dependent output characteristics ($T_0 = \infty$) of p-doped quantum dot lasers', *Appl Phys Lett*, **85**, 5164–5166.

Ferguson J W, Blood P, Smowton P M, Bae H, Sarmiento T, Harris Jr JS, Tansu N and Mawst L J (2011) 'Optical gain in GaInNAs and GaInNAsSb quantum wells', *IEEE J Quantum Elect,* **47**, 870–877.

Fehse R, Tomic S, Adams A R, Sweeney S J, O'Reilly E P, Andreev A and Riechert H, (2002) 'A quantitative study of radiative, Auger and defect related recombination processes in 1.3 μm GaInNAs-based quantum well lasers', *IEEE J Sel Top Quant,* **8**, 801–810.

Fiore A and Markus A (2007) 'Differential gain and gain compression in quantum dot lasers', *IEEE J Quantum Elect,* **43**, 287–294.

Foulger D L, Smowton P M, Blood P and Mawby P A (1997) 'Self-consistent simulation of AlGaInP/GaInP visible lasers', *IEEE Proc Optoelectronics*, **144**, 23–29.

Fox M (2001) *Optical properties of solids*. Oxford, Oxford University Press.

Fox M (2006) *Quantum optics*. Oxford, Oxford University Press.

George A A, Smowton P M, Mi Z and Bhattacharya P (2007) 'Long wavelength quantum dot lasers selectively populated using tunnel injection', *Semicond Sci Technol,* **22**, 557–560.

Grein C H, Young P M and Ehrenreich H (1994) 'Theoretical performance of InAs/InGaSb superlattice-based midwave infrared lasers', *J Appl Phys,* **76**, 1940–1942.

Grillot F, Vaselinov K, Gioannini M, Montrosset I, Even J, Piron R, Homeyer E and Loualiche S (2009) 'Spectral analysis of 1.55 μm InAs-InP (113)B quantum dot lasers based on a multipopulation rate equation model', *IEEE J Quantum Elect* **45**, 872–878.

Grundmann M and Bimberg D (1997) 'Theory of random population of quantum dots', *Phys Rev B,* **55**, 9740–9745.

Hall R N, Fenner G E, Kingsley J D, Soltys T J and Carlson R O (1962) 'Coherent light emission from GaAs junctions', *Phys Rev Lett*, **9**, 366–368.

Harder J, Moloney J V and Koch S W (2005) 'Microscopic evaluation of spontaneous emission and Auger processes in semiconductor lasers', *IEEE J Quantum Elect,* **41**, 1217–1226.

Hayashi I, Panish M B and Foy P W (1969) 'A low threshold room temperature injection laser', *IEEE J Quantum Elect,* **5**, 211–212.

Hayashi I and Panish M (1970) 'GaAs-$Ga_xAl_{1-x}As$ heterostructure injection lasers which exhibit low thresholds at room temperature', *J Appl Phys,* **41**, 150–163.

Henry C H (1993) 'The origin of quantum wells and the quantum well laser', in *Quantum well lasers*, ed P Zory, San Diego, Academic Press.

Higashi T, Sweeney S J, Phillips A F, Adams A R, O'Reilly E P, Uchida T and Fujii T (1999) 'Experimental analysis of temperature dependence in 1.3µm AlGaInAs-InP strained MQW lasers', *IEEE J Sel Top Quant Electr,* **5**, 413–419.

Hilsum C (1967) 'Semiconductor Lasers', in *A guide to the laser*, ed David Fishlock, p. 45, London, Macdonald and Co (publishers) Ltd.

Hill M T (2010) 'Status and prospects for metallic and plasmonic nano-lasers', *J Opt Soc Am B Opt Phys*, **27**, B26–B44.

Holonyak, Jr N and Bevacqua S F (1962) 'Coherent (visible) emission from $Ga(As_{1-x}P_x)$ junctions', *Appl Phys Lett*, **1**, 82–83.

Huang H and Deppe D (2001) 'Rate equation model for non-equilibrium operating conditions in a self-organised quantum dot laser', *IEEE J Quantum Elect*, **37**, 691–698.

Kim K, Norris T B, Ghosh S, Singh J and Bhattacharya P (2003) 'Level degeneracy and temperature-dependent carrier distributions in self-organized quantum dots', *Appl Phys Lett*, **82**, 1959–1961.

Kirstaedter N, Ledentsov N N, Grundmann M, Bimberg D, Ustinov V M, Ruvimov S S, Maximov M V, Kop'ev P S, Alferov Zh I, Richter U, Werner P, Gosele U and Heydenreich J. (1994) 'Low threshold, large T_O injection laser emission from In(Ga)As quantum dots', *Electron Lett*, **30**, 1416–1417.

Kressel H and Nelson H (1969) 'Close-confinement gallium arsenide pn junction lasers with reduced optical loss at room temperature', *RCA Rev,* **30**, 106–113.

Kroemer H (2000) Autobiography: The Nobel Prize in Physics 2000, http://nobelprize.org/nobel_prizes/physics/laureates/2000/kroemer-autobio.html.

Lester L F, Stintz A, Li H, Newell T C, Pease E A, Fuchs B A and Malloy K J (1999) 'Optical characteristics of 1.24µm InAs quantum dot laser diodes', *IEEE Photon Technol Lett,* **11**, 931–933.

Liu G T, Stintz S, Li H, Newell T C, Gray A L, Varangis P M, Malloy K J and Lester L F (2000) 'The influence of quantum-well composition on the performance of quantum dot lasers using InAs/InGaAs dots-in-a-well (DWELL) structures', *IEEE J Quantum Electron,* **36**, 1272–1279.

Loudon R (2000) *The quantum theory of light*, 3rd ed. Oxford, Oxford University Press.

Lorke M, Chow W W, Nielsen T R, Seebeck J, Gartner P and Jahnke F (2006) 'Anomaly in the excitation dependence of the optical gain of semiconductor quantum dots', *Phys Rev B*, **74**, 035334.

Lorke M, Jahnke F and Chow W W (2007) 'Excitation dependences of gain and carrier-induced refractive index change in quantum dot lasers', *Appl Phys Lett,* **90**, 051112.

Manasreh M O (1997) *Strained layer quantum wells and their applications*. Amsterdam, Gordon and Breach, Overseas Publishers Association.

Markus A, Rossetti M, Calligari V, Chek-Al-Kar D, Chen J X and Fiore A (2006) 'Two-state switching and dynamics in quantum dot two-section lasers', *J Appl Phys*, **100**, 113104.

Matthews D R, Summers H D, Smowton P M and Hopkinson M, (2002) 'Experimental investigation of the effect of the wetting layer states on the gain-current characteristics of quantum dot lasers', *Appl Phys Lett,* **81**, 4904–4906.

McDonald D and O'Dowd R F (1995) 'Comparison of two and three level rate equations in the modeling of quantum well lasers', *IEEE J Quantum Elect,* **31**, 1927–1934.

McIlroy PWA, Kurobe A and Uematsu Y (1985) 'Analysis and application of theoretical gain curves to the design of multiquantum well lasers', *IEEE J Quantum Elect*, **21**, 1958–1963.

Meyer J R, Felix C L, Bewley W W, Vurgaftman I, Aifer E H, Olafsen L J, Lindle J R, Hoffman C A, Yang M-J, Bennett B R and Shanabrook B V (1998) 'Auger coefficients in type II InAs/GaInSb quantum wells', *Appl Phys Lett,* **73**, 2857–2859.

Mowbray D J and Skolnick M S (2005) 'New physics and devices based on self-assembled semiconductor quantum dots', *J Phys D Appl Phys,* **58**, 2059–2076.

Nagarajan R, Fukushima T, Corzine S W and Bowers J E (1991) 'Effects of carrier transport on high-speed quantum well lasers', *Appl Phys Lett,* **59**, 1835–1837.

Nagarajan R, Ishikawa M K, Fujushima T, Geels R and Bowers J (1992) 'High speed quantum well lasers and carrier transport effects', *IEEE J Quantum Elect*, **28**, 1990–2008.

Nakamura S, Senoh M, Iwasa N and Nagahama S (1995) 'High-brightness InGaN Blue, Green and Yellow light-emitting diodes with quantum well structures', *Jap J Appl Phys,* **34**, L797–L799.

Nathan M I, Dumke W P and Burns G (1962) 'Stimulated emission of radiation from GaAs p-n junctions', *Appl Phys Letts,* **1**, 62–64.

O'Driscoll I, Blood P and Smowton P M, (2010) 'Random population of quantum dots in InAs-GaAs laser structures', *IEEE J Quantum Elect,* **46**, 525–532.

Olshansky R, Su C B, Manning J and Powazinik W (1984) 'Measurement of radiative and non-radiative recombination rates in InGaAsP and AlGaAs light sources', *IEEE J Quantum Elect,,* **20**, 838–854.

Osborne S W, Blood P, Smowton P M, Yin Y C, Stintz A, Huffaker D and Lester L F (2004) 'Optical absorption cross section of quantum dots', *J Phys C Condensed Matter,* **16**, S3749–S3756.

Oulton R F, Sorger V J, Zentgraf T, Ma R-M, Gladden C, Dai L, Bartal G and Zhang X (2009) 'Plasmon lasers at deep sub-wavelength scale', *Nature,* **461**, 629–632.

Ozgur G, Demir A and Deppe D G (2009) 'Threshold temperature dependence of a quantum dot laser diode with and without p-doping', *IEEE J Quantum Elect,* **45**, 1265–1272.

Park G, Shchekin O B and Deppe D (2000) 'Temperature dependence of gain saturation in multilevel quantum dot lasers', *IEEE J Quantum Electron,* **36**, 1065–1071.

Quist T M, Rediker R H, Keyes R J, Krag W E, Lax B, McWhorter A L and Zeigler H J (1962) 'Semiconductor maser of GaAs', *Appl Phys Lett,* **1**, 91–92.

Sands D (2005) *Diode lasers*. Bristol, Institute of Physics Publishing.

Schalow A L and Townes C H (1958) 'Infrared and optical masers', *Phys Rev*, **112**, 1940–1949.

Schneider H C, Chow W W and Koch S W (2001) 'Many body effects in the gain spectra of highly excited quantum dot systems', *Phys Rev B*, **64**, 115315-1–115315-7.

Shchekin O B and Deppe D G (2002a) 'The role of p-type doping and the density of states on the modulation response of quantum dot lasers', *Appl Phys Lett,* **80**, 2758–2760.

Shchekin O B and Deppe D G (2002b) ‘1.3 µm InAs quantum dot laser with T_0 = 161 K from 0 to 80 °C’, *Appl Phys Lett,* **80**, 3277–3279.

Siegman A E (1986) *Lasers*. Sausalatio, CA, University Science Books.

Smowton P M and Blood P (1997a) ‘The differential efficiency of quantum well lasers’, *IEEE J Sel Topic Quantum Electron*, **3**, 491–498.

Smowton P M and Blood P (1997b) ‘On the determination of internal optical mode loss of semiconductor lasers’, *Appl Phys Lett*, **70**, 2365–2367.

Smowton P M, Sandall I C, Liu H Y and Hopkinson M (2007) ‘Gain in p-doped quantum dot lasers’, *J Appl Phys,* **101**, 013107.

Thijs P J A, Tiemeijer L F, Binsma J J M and van Dongen T (1994) ‘Progress in long wavelength strained layer InGaAs(P) quantum well semiconductor laser and amplifiers’, *IEEE J Quantum Elect,* **30**, 477–499.

Thompson G H B (1980) *Physics of semiconductor laser devices*. Chichester, Wiley.

Thompson G H B (1983) ‘Analysis of radiative and nonradiative recombination law in lightly doped InGaAsP lasers’, *Elect Lett,* **19**, 154–155.

van der Ziel J P, Dingle R, Miller R C, Weigmann W and Nordland Jr W A, (1975) ‘Laser oscillation from quantum states in very thin GaAs-AlGaAs multilayer structures’, *Appl Phys Lett,* **26**, 463–465.

van Opdorp C and ‘t Hooft G W, (1981) ‘Method for determining effective non-radiative lifetime and leakage losses in double heterostructure lasers’, *J Appl Phys,* **52**, 3827–3839.

Wang J, von Allmen P, Leburton J-P and Linden K J (1995) ‘Auger recombination in long wavelength strained layer quantum well structures’, *IEEE J Quantum Elect,* **31**, 864–875.

Walter G, Chung T and Holonyak N (2002) ‘High-gain coupled InGaAs quantum well InAs quantum dot AlGaAs-GaAs-InGaAs-InAs heterostructure diode laser operation’, *Appl Phys Lett,* **80**, 1126–1128.

Yablonovich E and Kane E O (1986) ‘Reduction of lasing threshold current density by the lowering of valence band effective mass’, *IEEE J Lightwave Technol,* **4**, 504–506.

Zory P (1993) *Quantum well lasers*. San Diego, Academic Press.

Zory P S, Reisinger A R, Mawst L J, Costrini G, Zmudzinski C A, Emanuel M A, Givens M E and Coleman J J (1986) ‘Anomalous length dependence of threshold for thin quantum well AlGaAs diode lasers’, *Electron Lett,* **22**, 475–477.

Zhukov A E, Ustinov V M, Egorov A Y, Kovsh, A R, Tsatsulǹikov A F, Ledentsov N N, Zaitsev S V, Gordeev N Y, Kopèv P S and Alferov Z I (1997) ‘Negative characteristic temperature of InGsAs quantum dot injection lasers’, *Jap J Appl Phys*, **36**, 4216–4218.

Zhukov A E, Kovsh A R, Ustinov V M, Yu Egorov A, Ledentsov N N, Tsatsulǹikov A F, Maximov M V, Shernyakov Yu M, Kopchatov V I, Lunev A V, Kopèv P S, Bimberg D and Alferov Zh I (1999), ‘Gain characteristics of quantum dot lasers’, *Semicond Sci Technol,* **14**, 118–123.

2

Photonic crystal lasers

Y. ZHANG and M. LONČAR, Harvard University, USA

DOI: 10.1533/9780857096401.1.56

Abstract: Photonic crystal cavities with ultrahigh quality factors (*Q*) and small mode volumes enable realization of integrated lasers which feature small footprints, low lasing thresholds, high modulation speeds and high collection efficiencies of emitted light. In this chapter, we review the important characteristics of photonic crystal (PhC) lasers, including a theoretical discussion of lasing threshold, and illustrate them on two experimental examples: photonic crystal nanobeam lasers and photonic crystal disk lasers.

Keywords: photonic crystals, photonic crystal nanobeams, quality factor, mode volume, lasing threshold.

2.1 Introduction

Photonic crystal (PhC) (John, 1987; Yablonovitch, 1987), a material with a periodic variation of refractive index, is a versatile platform for manipulating the propagation, reflection and refraction of light. Specifically, light can be localized within the *photonic bandgap* (PBG), where the propagation of light is prohibited via *Bragg Scattering*. This is of great interest for the realization of functional optical devices including nano-cavities and waveguides. Empowered by numerical simulation methods, such as *finite-difference time-domain* (FDTD) and *finite element method* (FEM), and state-of-the-art nano-fabrication techniques (e-beam lithography, reactive-ion etching, scanning electron microscopy, etc.), PhC cavities can be designed and fabricated with ultrahigh quality factors, *Q*, of over a million and small *mode volume* (*V*) close to the diffraction limit [~$(\lambda/2n)^3$]. Current technologies enable the productions of one-dimensional (1D) (Velha *et al*., 2007; Zain *et al*., 2008; Deotare *et al*., 2009) and two-dimensional (2D) (Painter *et al*., 1999b; Yoshie *et al*., 2001; Akahane *et al*., 2003; Srinivasan *et al*., 2003; Song *et al*., 2005; Kuramochi *et al*., 2006; Notomi *et al*., 2008) PhC cavities with high integration capacity on a semiconductor chip. High quality three-dimensional (3D) PhC cavities have also been demonstrated (Aoki *et al*., 2008), yet scalable productions of 3D PhC devices still remain challenging.

Photonic crystal lasers (PhCL) are lasers that utilize PhC cavities to achieve the optical feedback. The history of developing lasers confined with photonic bandgap can be traced back to the *vertical-cavity surface-emitting lasers* (VCSEL) (Iga *et al.*, 1988), where distributed Bragg reflectors (DBR) were used to confine light in the vertical direction: in fact, the concept of Bragg reflector can be categorized as 1D PhC. On the other hand, typical VCSELs have device diameters orders of magnitude larger than the operating wavelengths, resulting in weak photon confinement in the lateral directions and correspondingly large mode volumes.

The first claimed PhC laser was demonstrated in Axel Scherer's group at Caltech in 1999 (Painter *et al.*, 1999a) using a 2D PhC slab cavity. In this work, a suspended InGaAsP membrane perforated with a 2D triangular lattice of holes was used to localize a cavity mode within a mode volume $V \sim 0.31(\lambda/n)^3$ using DBR in the lateral directions, and total internal reflection (TIR) in the vertical direction, as shown in Fig. 2.1a. The suspended slab contained four as-grown quantum wells (QW) that provided the optical gain at telecommunication wavelength (~1500 nm). The laser was pumped optically, using a pump laser operating at lower wavelength (830 nm). Furthermore, the pumped laser was pulsed with 4% duty cycle and the substrate was cooled to 143 K to avoid excessive heating of the device. Owing to their planar nature, large arrays of PhCLs can be easily fabricated and lithographically tuned to operate at different wavelengths. This is a clear advantage over VCSELs, for example, which require epitaxial growth of a large number of Bragg-mirror layers using *metal-organic chemical vapor deposition* (MOCVD) or *molecular beam epitaxy* (MBE).

Following this first demonstration, the PhCL operating at room temperature with continuous wave (CW) optical excitation was demonstrated by the Lee group at KAIST in year 2000 (Hwang *et al.*, 2000). In this work, a 2D-PhC slab containing semiconductor QWs was fabricated on a low-index Al_2O_3 substrate to facilitate heat dissipation. The same group at KAIST later demonstrated the first electrically driven PhCL in 2004 (Park *et al.*, 2004). The main difficulty associated with realization of electrically driven PhCL is the placement of electrodes close to the cavity to enable efficient carrier injection without inducing large optical losses due to metal absorption, which can significantly reduce the cavity Q and be detrimental for the laser performance. In their work, the KAIST group solved the problem by leaving a small post at the center of the cavity supporting the 2D-PhC slab, as shown in Fig. 2.1b and 2.1c. The post acted as an electronic wire that delivered the carriers directly into the center of the cavity without degrading the Q significantly.

Owing to their planar nature, PhCLs can easily be integrated with passive optical components. There are two main approaches demonstrated so far. The first is based on the so-called buried heterostructure (Matsuo *et al.*, 2010): the as-grown InGaAsP QWs were first patterned into a quantum box and

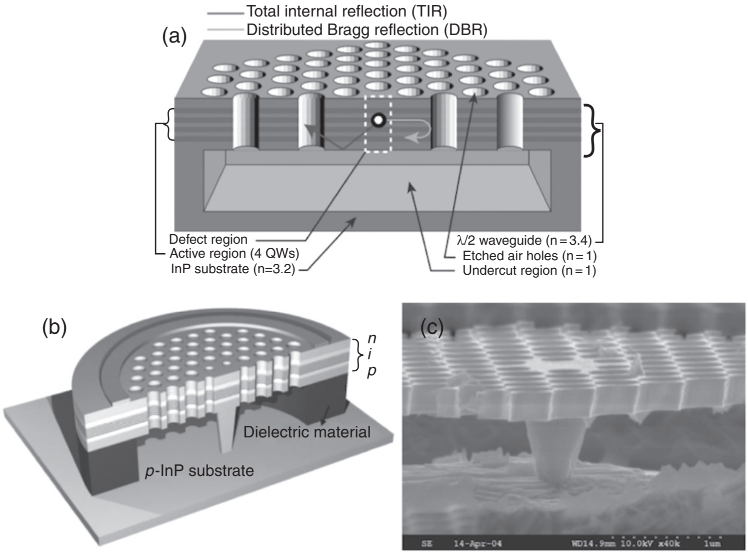
Total internal reflection (TIR)
Distributed Bragg reflection (DBR)
(a)
Defect region
Active region (4 QWs)
InP substrate (n=3.2)
λ/2 waveguide (n = 3.4)
Etched air holes (n = 1)
Undercut region (n = 1)
(b)
n
i
p
Dielectric material
p-InP substrate
(c)
SE 14-Apr-04 WD14.9mm 10.0kV x40k 1um

2.1 (a) Schematic diagram of the first reported PhC laser (Painter *et al.*, 1999b). It is based on a 2D PhC suspended membrane that contains four as-grown semiconductor QWs. (b) The electric field intensity profile of the defect mode in the 2D PhC cavity, calculated using FDTD simulations (Park *et al.*, 2004). (c, d) Schematic diagram and SEM of the first electrically injected PhC laser (Park *et al.*, 2004).

a passive InP layer was then regrown on top of them, with the sample planarized. The 2D PhC cavity was subsequently defined using e-beam lithography so that it spatially overlapped with the QWs. An optical waveguide was also realized in the same lithography step to enable efficient in-coupling of pump light and out-coupling of generated laser signal, as shown in Fig. 2.2a and 2.2b. This compact structure not only greatly improves pumping and collection efficiency through direct waveguide coupling, but also avoids excessive heating. The second example makes use of planarizing bisbenzocyclobutane (BCB) polymer to bond III-V active materials onto a silicon-on-insulator (SOI) wafer (Halioua *et al.*, 2009). The process started by defining an optical waveguide in the device layer of the SOI, followed with planarization of the SOI wafer and bonding with III-V material. After the bonding, the PhCL was fabricated in the active material, on top of the Si waveguide. In this way, the PhC cavity is evanescently coupled to the silicon waveguide, as shown in Fig. 2.2c and 2.2d, which facilitates in- and out-coupling of light. This approach has lower coupling efficiency than the first, direct waveguide coupling, method, but in turn enables PhCL integration with silicon photonics.

The advantages of PhCLs go well beyond their small footprints and integration capacity. The most prominent advantage of PhCLs is that they

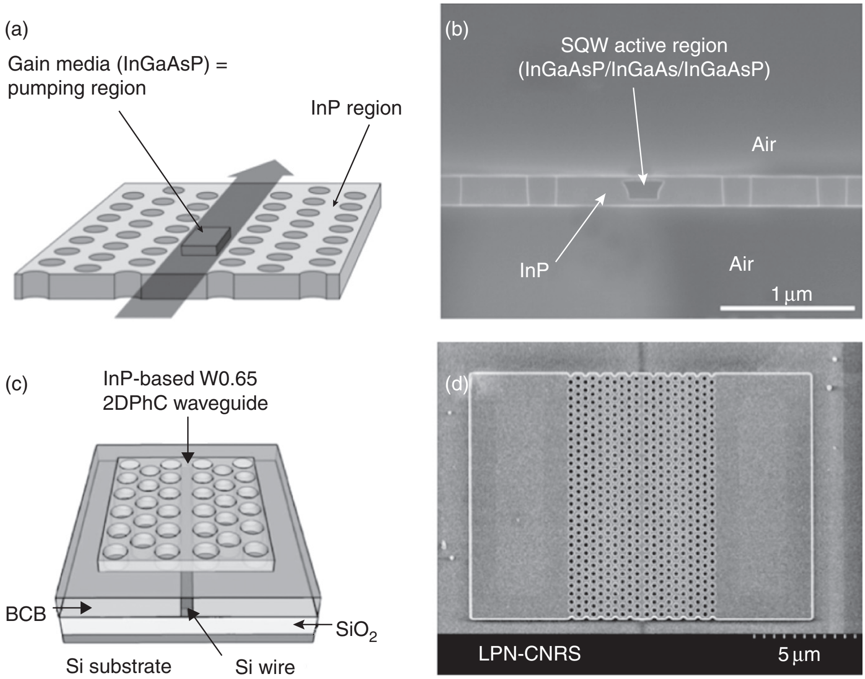
(a)
Gain media (InGaAsP) = pumping region
InP region
(b)
SQW active region (InGaAsP/InGaAs/InGaAsP)
Air
InP
Air
1 μm
(c)
InP-based W0.65 2DPhC waveguide
BCB
SiO2
Si substrate
Si wire
(d)
LPN-CNRS
5 μm

2.2 (a, b) Schematic diagram and SEM micrograph of the buried heterostructure PhCL. The active region is embedded in an InP layer (Matsuo *et al.*, 2010). (c, d) Schematic diagram and SEM of the PhCL bonded on SOI wafer (Halioua *et al.*, 2009). (LPN: Laboratoire de photonique et de nanostructures; CRNS: Centre national de la recherche scientifique.)

require low threshold powers, mostly attributed to their small mode volumes and high *Q*s. Optical pumping thresholds have been reported on the order of one microwatt for semiconductor quantum well lasers (Nozaki *et al.*, 2007; Matsuo *et al.*, 2010) and as low as tens of nanowatts for semiconductor quantum dot (QD) lasers (Nomura *et al.*, 2009, 2010b). In the case of electrical pumping, threshold currents as low as 181 nA have been reported, orders of magnitude less than other laser devices (Ellis *et al.*, 2011). In fact, theory predicts that threshold-less lasing is achievable in an ideal single-mode PhC cavity fabricated in perfect 3D PhC with omni-directional bandgap. In this case, radiative emission coupled to all non-lasing optical modes is prohibited (Yamamoto *et al.*, 1991; Yokoyama *et al.*, 1992). A detailed theoretical analysis of lasing thresholds of PhCLs is presented in Section 2.2.

In addition to low thresholds, PhCLs can also be driven with a high modulation speed: the high *Q*/*V* ratio of PhC cavities result in the cavity Purcell effect, which extensively reduces the radiative lifetime of carriers (Purcell, 1946). A modulation speed exceeding 100 GHz has been demonstrated based on a 2D-PhC laser (Altug *et al.*, 2006). This feature is especially important for information processing applications. Moreover, the design flexibility of PhC cavities allows tailoring the lasers' polarizations (Noda *et al.*, 2001) and far-field patterns (Kang *et al.*, 2009). Finally, the wavelength of PhCLs can be controllably tuned, by employing optomechanical effects (Perahia *et al.*, 2010) or liquid crystals (Maune *et al.*, 2004).

2.2 Lasing threshold of photonic crystal lasers (PhCLs)

It was first predicted by Yamamoto *et al.* that a high spontaneous emission factor (β), defined as the fraction of spontaneous emission that couples to the lasing mode, is responsible for decreasing the lasing threshold (Yamamoto *et al.*, 1991). In the ideal scenario where the emitter does not suffer from non-radiative decay, a system with a $\beta = 1$ can achieve a fascinating effect: threshold-less lasing. This limit, of β equals unity, can be achieved using two very different approaches (i) by increasing the rate of spontaneous emission into the lasing mode, or (ii) by suppressing the spontaneous emission into all other non-lasing modes. Both approaches will be discussed in this work.

In conventional semiconductor lasers based on Fabry–Perot cavities for example, $\beta < 0.001$ due to the large number of cavity modes that are supported by the large cavity (Petermann, 1979; Zhao *et al.*, 1995). Larger β factors can be achieved in microdisk lasers due to the larger free-spectral range (FSR) of this geometry. For instance, for a small 2 μm-diameter microdisk lasing at 1.55 μm wavelength, β factor as high as ~0.1 was measured (Fujita *et al.*, 2001). In contrast, as we will see, the PhC cavity can be designed to have very few (or only one) cavity modes localized within the photonic bandgap. This extensively decreases the number of non-lasing modes coupled to the gain medium and increases the β factor. Furthermore, the PhC bandgap can decrease the optical density of states within the gain spectrum, thereby reducing the coupling to other radiative modes.

2.2.1 Purcell effect and β factor

First consider a basic model: a quantum emitter coupled with a single optical mode through cavity-induced interaction. Predicted by Purcell (1946), the radiative lifetime of a quantum emitter located within a cavity can be altered. The dipole-cavity coupled system can be described using the Jaynes–Cummings Hamiltonian (Gerard, 2003):

$$\hat{H} = \mathrm{h}\omega\hat{\sigma}_z + \mathrm{h}\omega\left(\hat{a}^+\hat{a} + \frac{1}{2}\right) + i\mathrm{h}g\left(\hat{\sigma}_-\hat{a}^+ + \hat{\sigma}_+\hat{a}\right) \qquad [2.1]$$

where the first and second terms represent the dipole and photon energy respectively, and the third term represents the coupled energy between the dipole and the photon. The Rabi frequency is denoted by g. Two decay channels can induce decoherence to the system: emitter non-radiative decay (γ) and photon cavity loss (κ). The eigen-frequencies of the system can be derived as:

$$\omega_{\pm} = \frac{\omega_c + \omega_e}{2} \pm \sqrt{g^2 + \left(\frac{\delta\omega}{2} - i\frac{\kappa - \gamma}{4}\right)^2} - \frac{i}{4}(\kappa + \gamma) \qquad [2.2]$$

To simplify the analysis, one can make the assumption that there is no frequency detuning between the emitter and the cavity ($\delta\omega = 0$), and the loss rate induced by the cavity overtakes the loss of the emitter ($\gamma << \kappa$). Then, in the strong damping limit ($g << \kappa$), the emitter loss rate can be evaluated as:

$$\Gamma_{\mathrm{sp}} = 2\mathrm{Im}\{\omega_+\} = \frac{4g^2}{\kappa} \qquad [2.3]$$

where g^2 is inversely proportional to V, and κ is inversely proportional to Q.

Two more assumptions are made: (i) the emitter is located at the optical mode's field maximum and (ii) the dipole's oscillating direction is co-directional with the electric field. The Purcell factor can now be deduced by comparing Equation [2.3] to the spontaneous emission rate of an emitter in a homogeneous medium with refractive index n_{ref}.:

$$\mathrm{F} = \frac{\Gamma_{\mathrm{sp}}}{\Gamma_{\mathrm{sp,free}}} = \frac{3}{4\pi^2}\frac{Q}{V/(\lambda/n_{\mathrm{ref}})^3} \qquad [2.4]$$

Note that all the foregoing derivations are based on the assumption that $\gamma << \kappa$. However, for most solid-state emitters (bulk semiconductor, semiconductor QWs, etc.), non-radiative intraband transition is considerable at room temperature. For instance, the InGaAsP QWs have a homogeneous broadening of ~8.8 nm at room temperature (Nozaki *et al.*, 2007). Therefore, for high Q cavity with Q factor larger than 1000, the cavity mode linewidth is much narrower than the electronic transition spectrum. The Purcell factor should thus be modified to the more general expression:

$$F = \frac{\Gamma_{\mathrm{sp}}}{\Gamma_{\mathrm{sp,free}}} = \frac{3}{4\pi^2}\frac{\lambda}{\Delta\lambda_M}\frac{1}{V/(\lambda/n_{\mathrm{ref}})^3} \qquad [2.5]$$

where $\Delta\lambda_{\mathrm{M}} = \max\{\Delta\lambda_e, \Delta\lambda_c\}$.

Equation [2.5] applies to all models where the emitter is coupled to a single cavity mode. In reality, more than one optical mode can interact with the emitter. For instance, considering an ideal 3D photon gas model, where the photon is confined by metallic boundaries in all the three dimensions, the frequency spacing between two neighboring modes is calculated as:

$$\Delta\omega_{\mathrm{FSR}} = \frac{2\pi^2 c^3}{n_{\mathrm{ref}}^3 V \omega^2} \qquad [2.6]$$

Suppose the emitter spectrally overlaps with one of the cavity modes (mode 0 with double degeneracy) at ω, then Equation [2.5] is only valid under the single-mode condition when $\Delta\omega_{\mathrm{FSR}} >> \Delta\omega_M$. If V is large enough, the mode spacing allows the emitter to couple to multiple modes, and the alteration ratio of the total spontaneous emission rate (F') should include the sum of all these interactions, that is, $F' = \Gamma_{\mathrm{sp}}/\Gamma_{\mathrm{sp,free}} = \sum_{i=0}^{N-1} F_i$. As V approaches infinity, the number of modes within the broadening $\Delta\omega_M$ can be calculated as $N = \Delta\omega_M/\Delta\omega_{\mathrm{FSR}} = 4\pi(\Delta\lambda_M/\lambda)\left(V/(\lambda/n_{\mathrm{ref}})^3\right)$, and the total spontaneous emission ratio $F' \approx NF_0$ approaches unity, as expected (Baba, 1997).

For a dielectric cavity, in addition to the discrete cavity modes, the emitter also can couple to a continuum of radiative modes, which cannot be neglected. Thus, Equation [2.6] should be corrected:

$$F = \frac{\Gamma_{\mathrm{sp}}}{\Gamma_{\mathrm{sp,free}}} = \sum_{i=0}^{N-1} F_i + \varsigma \qquad [2.7]$$

where ζ denotes the ratio of the emitter's emission rate coupled to these radiative modes with respect to the emission rate in the homogeneous medium. If mode 0 denotes the lasing mode, the spontaneous emission factor β can be expressed as

$$\beta = \frac{\Gamma_{\mathrm{sp},0}}{\Gamma_{\mathrm{sp}}} = \frac{F_0}{\sum_{i=0}^{N-1} F_i + \varsigma} = \frac{F_0}{F_0 + \alpha} \qquad [2.8]$$

where α is defined as $\alpha = \sum_{i=0}^{N-1} F_i + \varsigma$, which represents the spontaneous emission coupled to all the non-lasing modes.

2.2.2 Rate equations and lasing threshold

In this subsection, the lasing threshold is analyzed from the laser rate equations (Yamamoto *et al.*, 1991):

$$\begin{cases} \dfrac{\mathrm{d}N}{\mathrm{d}t} = \dfrac{\gamma_{\mathrm{in}}\tilde{F}_{\mathrm{in}}}{V} - \Gamma G(N)P - \dfrac{N}{\tau_r} - \dfrac{N}{\tau_{\mathrm{nr}}} \\ \dfrac{\mathrm{d}P}{\mathrm{d}t} = \Gamma G(N)P - \dfrac{P}{\tau_c} + \beta\dfrac{N}{\tau_r} \end{cases} \tag{2.9}$$

where N and P are the carrier and photon density that are confined in the mode volume V; $\Gamma G(N)P$ represents the stimulated emission, where Γ is the confinement factor and $G(N)$ is the gain coefficient; τ_r and τ_{nr} are the carrier radiative and non-radiative lifetime respectively; τ_c is the photon's cavity lifetime; $\tilde{F}_{\mathrm{in}}$ is the pump flux (unit: s $^{-1}$) of either injected carriers or pumped photons; and $\tilde{F}_{\mathrm{out}} = P/\tau_{\mathrm{out}} \times V$ is the lasing output flux, where τ_{out} is the photon's out-coupling lifetime. Define γ_{in} as the pumping efficiency, and $\gamma_{\mathrm{out}} = \tau_c/\tau_{\mathrm{out}}$ as the output coupling efficiency. At steady state, Equation [2.9] can be written as:

$$\begin{cases} \dfrac{\gamma_{\mathrm{in}}\tilde{F}_{\mathrm{in}}}{V} = \Gamma G(N)P + (F_0 + \alpha)\dfrac{N}{\tau_{r,\mathrm{free}}} + \dfrac{N}{\tau_{\mathrm{nr}}} \\ \dfrac{\tilde{F}_{\mathrm{out}}}{\gamma_{\mathrm{out}}V} = \dfrac{P}{\tau_c} = \Gamma G(N)P + F_0\dfrac{N}{\tau_{r,\mathrm{free}}} \end{cases} \tag{2.10}$$

Solving Equation [2.10] leads to:

$$P = F_0\frac{N}{\tau_{r,\mathrm{free}}}\left[\frac{1}{\tau_c} - \Gamma G(N)\right] \tag{2.11}$$

It is evident from Equation [2.11] that, at steady state, the photon generation rate from the stimulated emission cannot exceed the photon cavity loss rate. Here define the *saturation carrier density* (N_s) that satisfies the following equation, $\Gamma G(N_s) = 1/\tau_c = \omega/Q$. As the carrier density approaches N_s, the photon gain rate approaches the cavity loss rate, and the stimulated emission term overtakes other contributions in the rate equations. In this saturation limit, all the pumped carriers predominantly recombine and emit to the lasing mode through stimulated emission, which results in a differential internal quantum efficiency of unity, or a linear light-in light-out (L-L) curve. In classical laser theory, this effect is also referred as 'gain clamping' or 'gain saturation' effect (Rigrod, 1963). The rate equations in the saturation limit can be modified to:

$$\begin{cases} \dfrac{\gamma_{\text{in}}\tilde{F}_{\text{in}}}{V} = \Gamma G(N_s)P + (F_0 + \alpha)\dfrac{N_s}{\tau_{r,\text{free}}} + \dfrac{N_s}{\tau_{\text{nr}}} \\ \dfrac{\tilde{F}_{\text{out}}}{\gamma_{\text{out}}V} = \dfrac{P}{\tau_c} = \Gamma G(N_s)P + F_0\dfrac{N_s}{\tau_{r,\text{free}}} \end{cases} \qquad [2.12]$$

The classical lasing threshold is defined as the pump level of the kink in *L-L* curve. From Equation [2.12], the classical lasing threshold can be derived:

$$\tilde{F}_{\text{th,classical}} = \frac{\left[\left(\sum_{i=1}^{N-1} F_i + \varsigma\right)\left(N_{\hat{s}}/\tau_{r,\text{free}}\right) + \left(N_{\hat{s}}/\tau_{\text{nr}}\right)\right]V}{\gamma_{\text{in}}} \qquad [2.13]$$

From Equation [2.13], it is evident that the lasing threshold is dependent on multiple factors: (1) mode volume: the threshold scales linearly with mode volume; (2) saturation carrier density: N_s is inversely proportional to the *Q* factor. A high *Q* cavity is desired to reduce N_s, though an ultrahigh *Q* (~10^6) is not necessary; (3) coupling to other cavity modes: this term can be eliminated by properly designing a single-mode PhC cavity; (4) coupling to radiative modes: ideally one needs an omni-directional PBG, that is a 3D PhC cavity, to eliminate this term (Tandaechanurat *et al.*, 2011). However, an incomplete PBG has also been shown to be able to greatly suppress this radiative coupling (Fujita *et al.*, 2005); (5) non-radiative recombination: most of the non-radiative recombination in a PhCL arises from surface recombination and Auger recombination. For QW-based PhCLs, surface recombination is especially prominent because of the many d holes perforating PhC structures; and (6) external pump efficiency. From Equation [2.13], it is interesting to note that the classical lasing threshold is independent of the cavity mode's Purcell factor F_0, though a high F_0 results in a large β factor.

It is also important to mention that there is another definition of the lasing threshold (Bjork *et al.*, 1994), which corresponds to the pump level at which the number of stimulated emitted photons starts to exceed the number of spontaneously emitted photons. In contrast to the classical threshold definition, this threshold is referred as 'quantum threshold'. From Equation [2.10], the quantum threshold can be derived,

$$\tilde{F}_{\text{th,quantum}} = \frac{\left[\left(2F_{\text{o}} + \sum_{i=1}^{N-1} F_i + \varsigma\right)\left(N_q/\tau_{r,\text{free}}\right) + \left(N_q/\tau_{\text{nr}}\right)\right]V}{\gamma_{\text{in}}} \qquad [2.14]$$

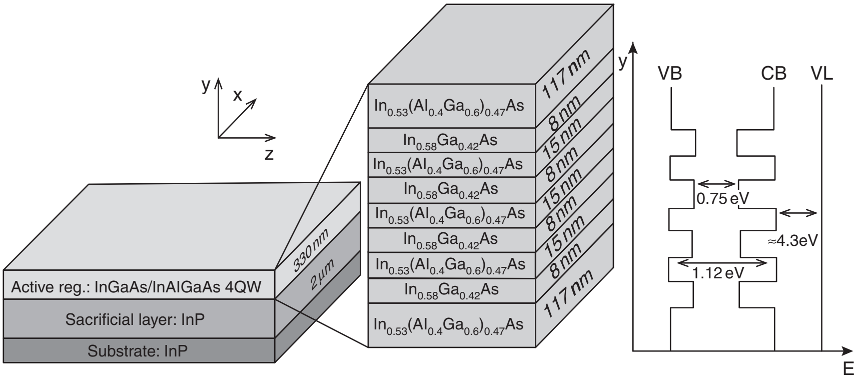
y
x
z
Active reg.: InGaAs/InAlGaAs 4QW
Sacrificial layer: InP
Substrate: InP
330 nm
2 μm
In0.53(Al0.4Ga0.6)0.47As
In0.58Ga0.42As
In0.53(Al0.4Ga0.6)0.47As
In0.58Ga0.42As
In0.53(Al0.4Ga0.6)0.47As
In0.58Ga0.42As
In0.53(Al0.4Ga0.6)0.47As
In0.58Ga0.42As
In0.53(Al0.4Ga0.6)0.47As
117 nm
8 nm
15 nm
8 nm
15 nm
8 nm
15 nm
8 nm
117 nm
y
VB
CB
VL
0.75 eV
≈4.3eV
1.12 eV
E

2.3 Layout of the material system of the semiconductor QW sample used to realize nanobeam lasers. The energy band of the semiconductor QWs are sketched on the right hand side. (VB: valence band; CB: conduction band; VL: vacuum level; E: energy.)

where N_q satisfies $\Gamma G(N_s) = 1/2\tau_c = \omega/2Q$. It has a similar form to Equation [2.13], with the exception that the quantum threshold increases as the Purcell factor increases. This counter-intuitive effect can be explained as follows: in the quantum threshold state, there are an equal number of photons emitted by spontaneous as by stimulated emission. The Purcell effect accelerates the spontaneous emission into the cavity mode. In order to reach the threshold condition for lasing in the presence of this effect, it is thus necessary to also increase the rate of stimulated emission.

To conclude, the ultimate low threshold laser requires a cavity with small mode volume, relatively high Q factor, single-mode operation, and high pumping efficiency. PhC cavities, with their flexibility in engineering the photonic band, offer the possibility to approach this ultimate goal.

2.3 Photonic crystal nanobeam lasers

The PhC nanobeam cavity is a type of 1D PhC cavity. It is based on a ridge dielectric waveguide, with an array of holes on top that form a PBG mirror (Foresi *et al.*, 1997). PhC nanobeam lasers (Ahn *et al.*, 2010; Gong *et al.*, 2010; Zhang *et al.*, 2010) have recently attracted much interest because they can achieve high Q/V factors while occupying smaller footprints than 2D PhC (Lee *et al.*, 1999; Loncar *et al.*, 2002) and 3D PhC lasers (Tandaechanurat *et al.*, 2011). Furthermore, nanobeam cavities can be designed to have no mode degeneracy, compared with other designs (Gerard *et al.*, 1998; Vuckovic *et al.*, 1999; Fujita *et al.*, 2001). This is crucial for nanolasers to operate in the single-mode regime, which is the key to achieving a large β factor and the reduction of lasing threshold (Fig. 2.3).

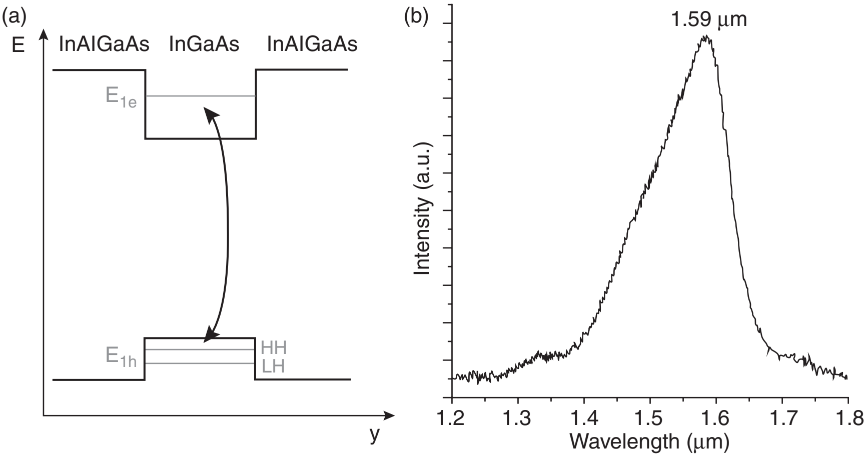

2.4 (a) Energy band diagram of electrons, LH and HH bands of the semiconductor QWs. (b) The PL emission spectrum of the quaternary QWs peaks at about 1.59 μm.

2.3.1 Material system

There are many promising ways to realize a nanobeam PhCL. The one described here features semiconductor QWs lattice-matched to an InP wafer. The QWs provide the optical gain. They contain four 8 nm thick compressively-strained $In_{0.58}Ga_{0.42}As$ layers, which are sandwiched in a 326 nm thick $In_{0.53}(Al_{0.4}Ga_{0.6})_{0.47}As$ slab. Below the semiconductor QW slab, there is a 2 μm thick InP sacrificial layer for selective wet etching. All the layers are grown with MOCVD technique to minimize crystalline defects (Huang *et al.*, 2011).

The ratio of III-V components in the semiconductor QWs results in a 0.32% in-plane compressive strain while satisfying the lattice-matching condition. This compressive strain shifts the heavy-hole (HH) state to lie on top of the light-hole (LH) state, which leads to a dominantly TE-polarized gain. The TE-polarized modes favor vertical light emission compared to the TM-polarized modes, and therefore are more suitable for surface-emitting lasers. Figure 2.4b shows the photoluminescence (PL) spectrum of the sample. The emission spectrum ranges from 1.40 to 1.65 μm, and peaks at 1.59 μm.

2.3.2 Cavity design

The PhC nanobeam design is based on a suspended ridge waveguide with an array of identical holes, forming a PBG mirror. The refractive index of the dielectric is 3.5 (the index of InAlGaAs/InGaAs QWs at 1.55 μm). The ridge

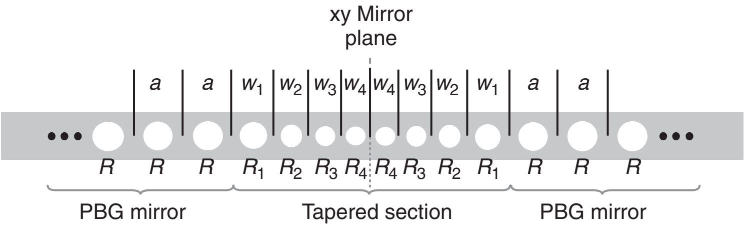

2.5 Layout of the photonic crystal nanobeam cavity design.

is 500 nm wide and 330 nm thick, the periodicity of the holes is $a = 400$ nm, and the hole radius is set to $r = 0.3a$ to optimize the bandgap.

Introducing a lattice grading to the periodic structure creates a localized potential for the fundamental TE-polarized mode. To optimize the mode's Q factor, the bandgap-tapering technique (Zhang and Loncar, 2008; Zhang *et al.*, 2009) is employed for suppressing the scattering losses that take place at the interface between the cavity section and the mirror section (Lalanne & Hugonin, 2003). This design contains a four-segment tapered section with holes R_1–R_4 and a 12-segment mirror section at each side of the cavity, as shown in Fig. 2.5. Two degrees of freedom are available to modify each tapered segment: the width w_k and the radius r_k. We keep the ratio r_k/w_k fixed at each segment and implement a linear interpolation of the grating constant π/w_k. When the central segment w_4 is set to $0.72a$, a cavity mode is obtained to resonate at 1.59 μm with an ultrahigh Q factor above 8 000 000, and a very small mode volume of $0.28(\lambda/n)^3$ (Fig. 2.6a). The ultrahigh Q factors can also be explained by looking at the momentum space of the cavity mode. Figure 2.6b and 2.6c demonstrate the spatial Fourier transformation (FT) of the electric field components E_x and E_z in the xz plane ($y = 0$), with the light cone indicated by the white circle. It can be seen that both modes' Fourier components are localized tightly at the band-edge of the Brillouin zone on the k_z axis: $k_z = \pi/a$. This minimizes the amount of mode energy within the light cone that is responsible for scattering losses (Srinivasan & Painter, 2002).

In addition to this fundamental mode, the cavity supports another mode at a longer wavelength of 1.72 μm with a larger mode volume of $0.67(\lambda/n)^3$. This is an extended mode with a node at the center of the cavity, as shown in Fig. 2.6d. This mode resonates at a wavelength outside the gain spectrum of the QWs, and therefore does not affect the single-mode operation of our laser.

2.3.3 Fabrication

The nanobeam pattern is defined using a negative e-beam lithography resist [hydrogen silsesquioxane (HSQ)]. The e-beam resist is spun on

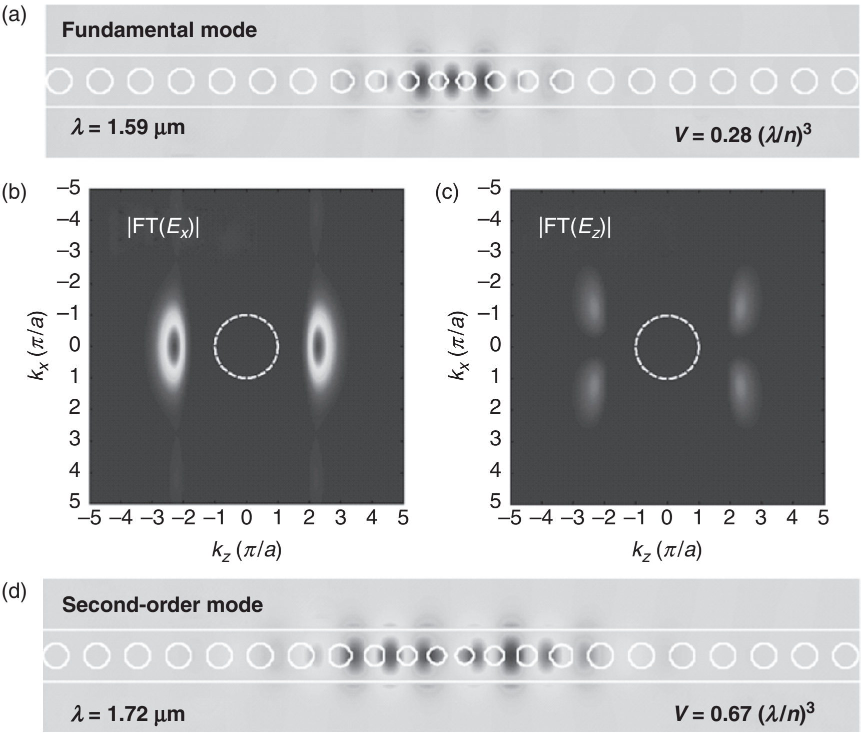

2.6 (a) Mode profile of the fundamental cavity mode of the nanobeam laser. (b, c) Spatial Fourier transform of the electric field component E_x and E_z at $y = 0$ plane. (d) Mode profile of the second-order mode, resonating at a higher wavelength outside the gain spectrum.

the surface with a spinning speed of 3000 rpm resulting in a thickness of ~100–150 nm. The resist is subsequently cross-linked using an STS Elionix ELS-7000 e-beam writer at an acceleration voltage of 100 kV and a beam current of 100 pA.

Next, the pattern is transferred to the substrate with inductively coupled plasma reactive-ion etching (ICP-RIE) using $BCl_3/CH_4/Ar/HBr$ chemistry at 180°C. This anisotropic etching creates a mesa extended to the sacrificial layer. Hydrofluoric acid (HF) is then used to dissolve the e-beam resist. Finally the InP sacrificial layer is selectively wet-etched by $HCl:H_2O$ 3:1 solution. The crystal orientation dependent etch rate is about 100–120 nm/s at 8°C, which leads to an etch time of 40 s for a completely suspended nanobeam structure. Figure 2.7 shows the scanning electron micrographs (SEMs) of an array of fabricated nanobeam lasers. The two pads are designed to support the suspended PhC structures.

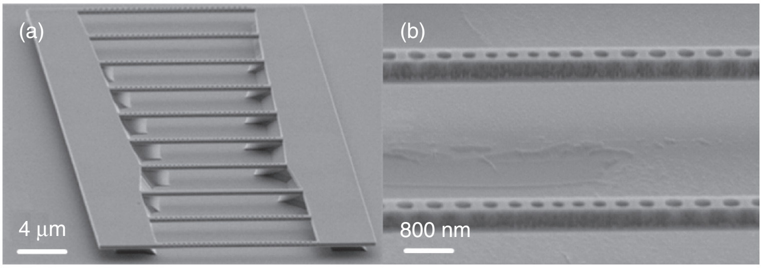
(a)
(b)
4 µm
800 nm

2.7 (a, b) SEMs of the fabricated photonic crystal nanobeam lasers.

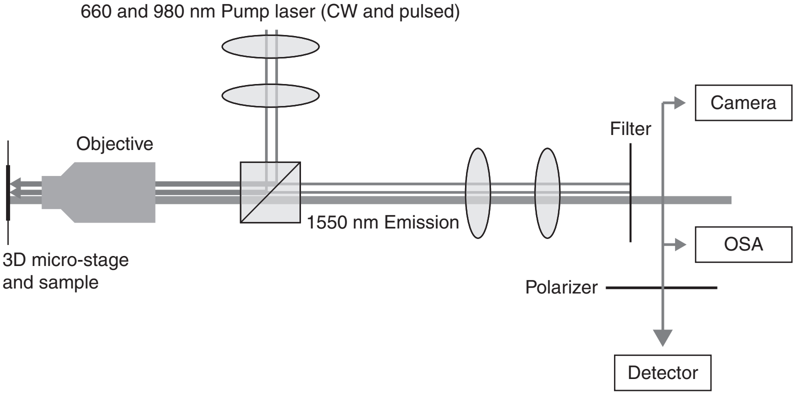
660 and 980 nm Pump laser (CW and pulsed)
Camera
Filter
Objective
1550 nm Emission
OSA
3D micro-stage
and sample
Polarizer
Detector

2.8 Illustration of the measurement setup. CW, continous wave.

2.3.4 Characterization

The devices are optically pumped at room temperature using a 660 nm pulsed laser diode. The pulse width is 9 ns at a 300 kHz repetition rate, which corresponds to a duty cycle of 0.27%. The pump beam is focused on the sample surface via a 100 × objective lens, and the emitted light is collected via the same objective lens and analyzed using an optical spectrum analyzer (OSA), near-infrared (NIR) camera, and an InGaAs detector (Fig. 2.8).

In Fig. 2.9a we show the *L-L* curve for one of the measured devices. It can be seen that there is no pronounced kink near the threshold. This soft turn-on of the laser indicates a large β factor. The lasing images taken at different pump levels, using the NIR camera, show that the emission spot is well confined to the center of the nanobeam, which unambiguously proves that the lasing is from the localized defect mode. Figure 2.9b shows the lasing spectrum near the threshold. The spectrum is fitted with a Lorentzian function with a full-width half-maximum (FWHM) of 0.11 nm, which

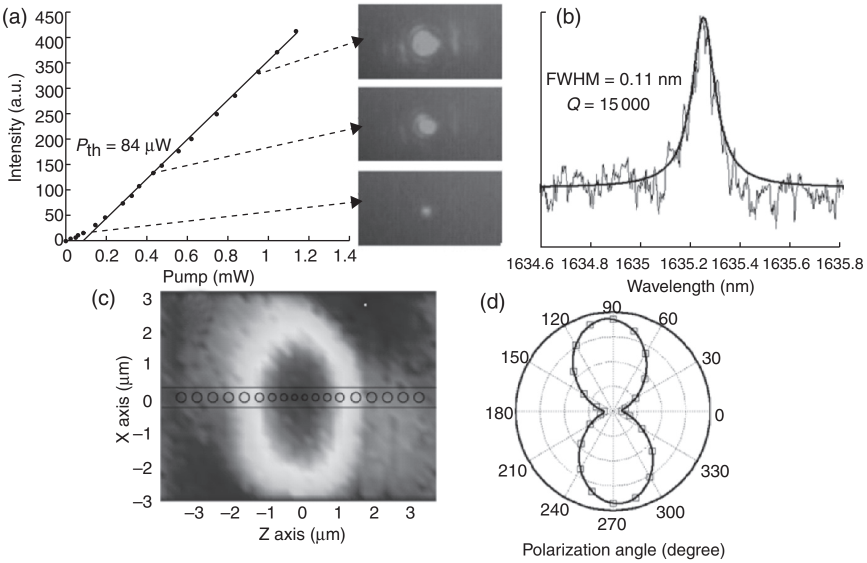

2.9 (a) Laser emitted power as a function of the incident power. The emission profiles obtained from the camera at different pump levels are shown on the right. (b) The spectrum of the emitted light near the threshold. (c) Output lasing power as a function of the pump beam position. The pattern of the nanobeam is superimposed as the background of the image. (d) Polarization dependence of the lasing mode.

corresponds to a *Q* factor of 15000. The *Q* factor is likely limited by the resolution of the OSA used.

In addition, Fig. 2.9c shows the dependence of the output power on the pump beam position by scanning the sample in x-z plane using a piezo-actuated stage with a spatial resolution of 6 nm. As the pump beam is moved away from the center of the cavity, the beam intensity decreases rapidly and finally vanishes. This is a further confirmation of emission from the localized mode of the cavity instead of extended band-edge emission. Here the pump spot is much bigger than the cavity mode, so the cavity mode samples the pump beam. Therefore, Fig. 2.9c shows the shape of the pump spot as opposed to the profile of the lasing mode. This also allows us to evaluate the effective pump power, that is, the overlap of the pump beam with the nanobeam, which is reported in Fig. 2.9a. An effective threshold of 84 µW is evaluated for this nanobeam laser, whereas the total power threshold measured behind the objective lens is 812 µW. The threshold power is even smaller, considering that not all the pump power incident onto the nanobeam is absorbed by the cavity. Finally, Fig. 2.9d shows the polarization dependence of the laser emission. The emission is

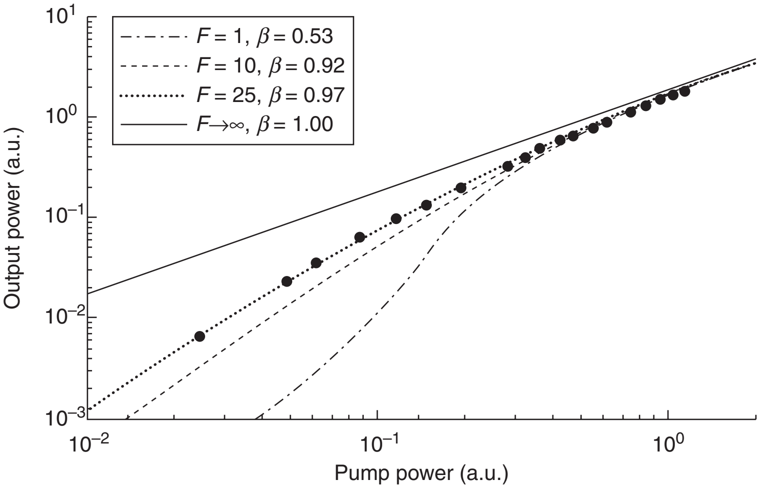

2.10 Log–log plot of the *L*–*L* curve, with predictions from the rate equations using different *β* factors (solid lines).

polarized along *x*-axis as expected, and exhibits a large polarization ratio of ~10.

Next, the behavior of this PhC nanobeam laser is analyzed by fitting to the rate equation that is similar to Equation [2.10]:

$$\begin{cases} \dfrac{\mathrm{d}N}{\mathrm{d}t} = \dfrac{\gamma_{\text{in}}\tilde{F}_{\text{in}}}{V} - \Gamma G(N)P - AN - (F_0 + \varsigma)BN^2 - CN^3 \\ \dfrac{\mathrm{d}P}{\mathrm{d}t} = \Gamma G(N)P - \dfrac{P}{\tau_c} + F_0 BN^2 \end{cases} \qquad [2.15]$$

where AN, $(F_0 + \alpha)BN^2$ and CN^3 represent the carrier loss rate through surface recombination, radiative recombination and Auger recombination, respectively. For this nanobeam cavity, ς is evaluated as 0.91 through FDTD simulation. The lasing mode's Purcell factor is estimated to be ~26, taking into account the QW's homogeneous broadening at room temperature and the spatial overlap between the active medium and the optical mode. For other parameters, typical values for InP-based QWs at room temperature are applied (Park *et al.*, 2002).

Figure 2.10 shows the measured *L-L* in log–log scale along with curves obtained from rate equations for different Purcell factors and spontaneous emission factors (β). It can be seen that the experimental data are in excellent agreement with the theoretical prediction of $F_0 \sim 25$ and $\beta = 0.97$. This is in good agreement with the theoretical estimation of Purcell factor.

2.4 Photonic crystal disk lasers

PhCLs based on 1D PhC nanobeams and 2D PhC slabs have proved to make good surface-emitter nanolasers with low threshold and high modulation speeds (Loncar *et al*., 2002; Altug *et al*., 2006; Zhang *et al*., 2010), but they have a few drawbacks. First, the multiple periodic Bragg layers used to confine the cavity mode limit the device footprint. Second, most PhC cavities depend upon the suspended membranes for a large index contrast. For electrically-injected lasers, the top contact has to be placed far from the cavity mode to avoid metal absorption losses, and this suspended membrane geometry makes efficient electrical injection of carriers into the cavity mode difficult. For this reason, very few demonstrations of electrically driven lasers have been reported so far (Park *et al*., 2004; Ellis *et al*., 2011). On the other hand, microdisk lasers, based on whispering gallery mode (McCall *et al*., 1992), offer a platform for developing compact electrically driven lasers, with device footprint on the order of one optical wavelength (Levi *et al*., 1992; Fujita *et al*., 1999; Liu *et al*., 2010). The disadvantage of microdisk lasers is that the whispering gallery mode only emits in in-plane directions, which makes the collection of photons difficult (Lee *et al*., 1998). Evanescent coupling via a tapered fiber is thus normally used to collect the emitted photons efficiently (Fujita *et al*., 1999). In addition, the whispering gallery mode spans over the whole circular edge of the microdisk causing a relatively large mode volume (Fig. 2.11c).

A new type of nanolaser, PhC disk lasers, has been recently demonstrated. This design combines the properties of microdisk and PhC nanobeam lasers.

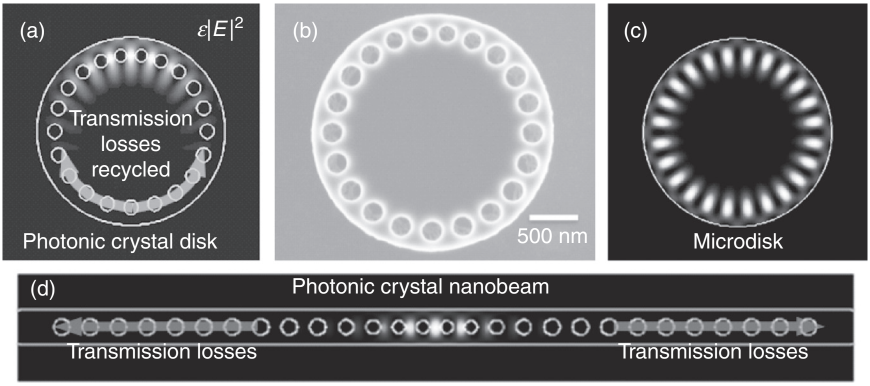

2.11 (a) Schematic of photonic crystal disk lasers and (b) scanning electron micrograph of a fabricated photonic crystal disk laser. The device can be viewed as a hybrid between (c) microdisk laser and (d) photonic crystal nanobeam laser with photonic crystal folded back to minimize the transmission losses.

It contains an array of holes at the perimeter of the microdisk to localize the whispering gallery mode within a limited angular range on the microdisk. The design can be seen, from another perspective, as bending a PhC nanobeam cavity (Fig. 2.11d) into a disk (Fig. 2.11a), so the two Bragg mirrors at the ends of the nanobeam are combined into one. In this way, the number of holes can be decreased because the transmission losses in nanobeam cavities are cycled through the disk, and hence, the device footprint can be smaller than PhC nanobeams.

The structure shown in Fig. 2.11b is based on a 2.56 μm diameter disk with 21 perforated holes. The positions and sizes of the top ten holes near the defect mode are slightly tuned to obtain a large *Q* factor, similar to the design in PhC nanobeam cavities (Zhang *et al*., 2009). The cavity mode resonates at 1546 nm with a *Q* factor of 1.0×10^5 and a modal volume of $0.52(\lambda/n)^3$. The structures were fabricated in the same material system using the same fabrication procedures as those described in Section 2.3. Microdisk lasers with the same diameter are also fabricated to compare the results (Fig. 2.12b). The two laser arrays shown in Fig. 2.12a and 2.12b are scaled linearly in size to vary the cavities' resonant wavelengths. The devices are optically pumped at

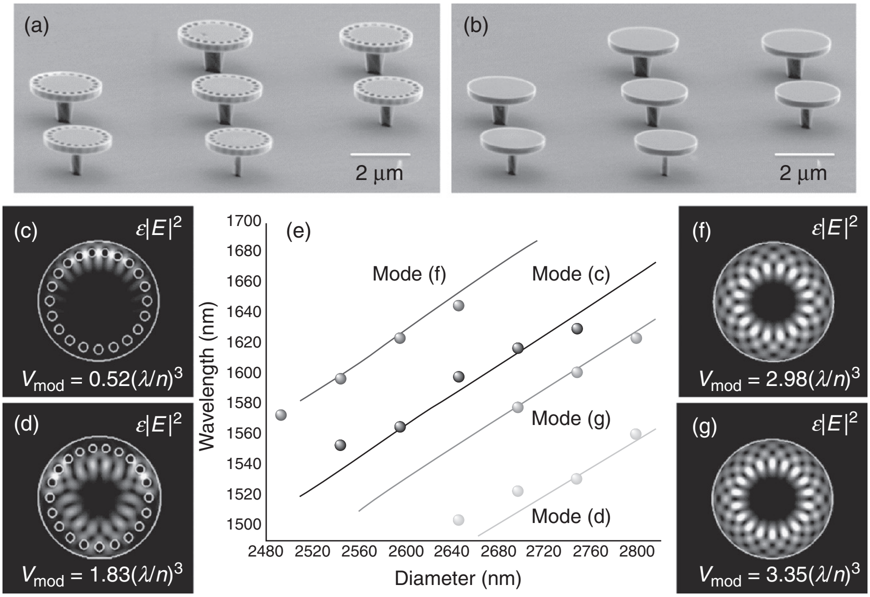

2.12 (a, b) Images of photonic crystal disk and microdisk lasers with different scaling factors. (c, d) Electric field density profiles of photonic crystal disk modes. (e) Experimental results of lasing wavelength dependence on diameter of photonic crystal disks and microdisks. The solid curves show the mode wavelength dependence obtained using simulations. (f, g) Electric field density profiles of microdisk modes.

room temperature using a 980 nm semiconductor laser, with 10 ns pulses and 400 kHz repetition rate. The effective pump power is estimated with power measurement behind the 100× optical objective, while taking in account the spatial overlap between the pump beam and the lasing mode. The emission beam is analyzed with an InGaAs detector filtered by a monochromator.

Figure 2.12e plots the measured lasing wavelength as a function of the diameter of the disk for the PhC disk and microdisk lasers. It shows a good agreement with the simulation results plotted in solid lines, which verifies that the lasing mode (c) is of the designed defect mode. Note that by controlling the position of the pump spot, lasing from two different PhC disk modes could be obtained in some structures (Fig. 2.12e). The nanolaser, however, does operate in single-mode regime in both cases (only one mode lases at a time). The two microdisk lasing modes are not the fundamental $TE_{1,m}$ modes, but the higher-order $TE_{2,8}$, and $TE_{2,9}$ modes. These modes have a node of electric field in the radial direction. The fundamental modes cannot be collected from top, because it emits in in-plane directions.

Next, Fig. 2.13b shows the lasing power as a function of the effective pump power (also known as *L-L* curve) from the PhC disk mode in one of the devices (Fig. 2.13a), in comparison with a microdisk laser emitting at the same wavelength. The injection efficiencies are estimated to be 1.74% and 4.36% for PhC disk mode and microdisk mode, respectively. From Fig. 2.13b, the PhC disk lasers have much better extraction efficiencies than microdisk lasers. This efficiency can be further boosted with subtle far-field engineering of PhCs (Kang *et al.*, 2009). Inset plots the spectrum at 3.2 times the threshold power of PhC disk mode, which shows clear single-mode lasing emission. Figure 2.13c plots the *L-L* curve for the PhC disk laser in log–log scale (black dots), along with the *L-L* curves obtained from rate equations for different spontaneous emission factors (β). The experimental data show good agreement with a β factor of 0.087. More than ten-fold reduction in β-factor of this laser compared to nanobeam laser can be attributed to the existence of higher-order modes. Figure 2.13d shows the lasing spectrum of the PhC disk lasers slightly above the lasing threshold. It has a FWHM of 0.26 nm, which corresponds to a Q factor of ~6000. Q is limited by the resolution of the monochromator. Free-carrier absorption is also known to decrease the Q factor extensively below its passive value. The lasing emission profile of the PhC disk laser is also shown in the inset of Fig. 2.13d, which is taken from a near-infrared camera.

2.5 Conclusion and future trends

In this chapter, we have introduced the basic concepts for the development of PhCLs. As illustrated by the rate equation analysis, PhC cavities are an ideal platform for the realization of ultimate low threshold nanolasers, since they can support a single-mode operation with a high Q and a small

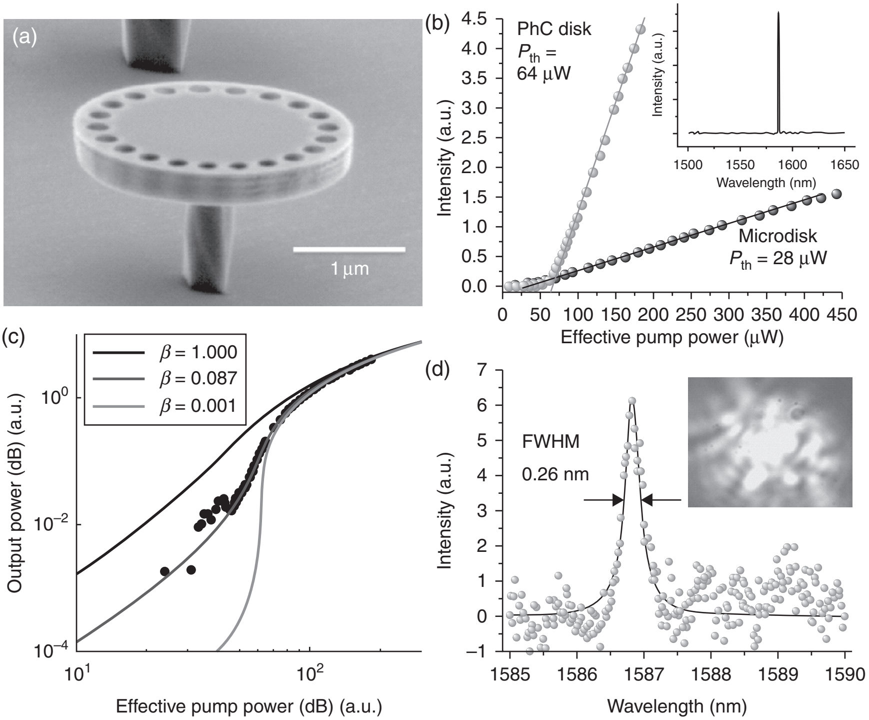

2.13 (a) Images of fabricated photonic crystal disk from SEM. (b) *L-L* curve for photonic crystal disk laser and microdisk laser, respectively. Inset shows the spectrum of photonic crystal disk lasers at 3.2 × lasing threshold. (c) Log–log plot of the photonic crystal disk laser's *L-L* curve (black dots). The solid curves show *L-L* curves deduced from rate equations with different *β* factors. (d) Lineshape of the lasing mode above threshold, fitted with a Lorentzian line function. Inset shows the emission profile taken from an infrared camera.

mode volume across the gain spectrum. Furthermore, the high *Q*/*V* factor leads to strong cavity Purcell effect, which enables high-speed operation of directly modulated lasers. Two examples of PhCL, which operate with pulsed optical pumping at room temperature, are then demonstrated. The PhC nanobeam laser shows a high spontaneous emission factor of 0.97 due to its single-mode nature; the PhC disk laser has a small device footprint, and a higher collection efficiency than microdisk lasers.

During the last decade we have witnessed rapid progress in the development of PhCLs: the reduced lasing threshold attributed to its PhC cavity's small mode volume and high *Q* factor (Nozaki *et al.*, 2007; Nomura *et al.*, 2010b), the nanoscale footprint, the boosted modulation speed resulting from Purcell effect (Altug *et al.*, 2006; Matsuo *et al.*, 2011), the controllable laser polarizations (Noda *et al*., 2001), the wavelength tunability integrated with optomechanics (Perahia *et al*., 2010), and so forth. Extensive research has revealed interesting underlying physics, including the strong coupling limit of cavity QED (Nomura *et al*., 2010a), and has also inspired applications such as those in biochemical sensing (Loncar *et al*., 2003; Kita *et al*., 2008).

Nevertheless, several challenges still remain to be solved. First, the current state-of-the-art technologies cannot produce PhCLs that operate at the designed wavelength, due to fabrication imperfections. This is especially important when the gain medium consists of quantum emitters with a very narrow gain spectrum (semiconductor QD, for instance). Second, while a couple of electrically driven PhCLs have been reported so far (Park *et al*., 2004; Ellis *et al*., 2011), the reliable production of the large-scale electrically pumped PhCL array calls for more research efforts. Finally, PhCLs need to find a niche in the commercial market for applications ranging from biochemical sensors to on-chip interconnects.

2.6 Acknowledgements

The authors would like to thank the following people for their help: Parag Deotare, Jennifer Choy, Raji Shankar, Anna Shneidman, Christoph Hamsen, Murray McCutcheon, Mughees Khan, Yong Huang, Jae-Hyun Ryou and Russell Dupuis. Part of this work was supported in part by NSF Grant No. ECCS-1028519, 'Collaborative Research: Nanobeam Lasers'. The authors acknowledge the support provided by CNS at Harvard University. Y. Zhang would like to dedicate this chapter to Uncle Peter.

2.7 References

Ahn, B. H., Kang, J. H., Kim, M. K., Song, J. H., Min, B., Kim, K. S. and Lee, Y. H. (2010) One-dimensional parabolic-beam photonic crystal laser. *Optics Express,* **18**, 5654–5660.

Akahane, Y., Asano, T., Song, B. S. and Noda, S. (2003) High-Q photonic nanocavity in a two-dimensional photonic crystal. *Nature,* **425**, 944–947.

Altug, H., Englund, D. and Vuckovic, J. (2006) Ultrafast photonic crystal nanocavity laser. *Nature Physics,* **2**, 484–488.

Aoki, K., Guimard, D., Nishioka, M., Nomura, M., Iwamoto, S. and Arakawa, Y. (2008) Coupling of quantum-dot light emission with a three-dimensional photonic-crystal nanocavity. *Nature Photonics,* **2**, 688–692.

Baba, T. (1997) Photonic crystals and microdisk cavities based on GaInAsP-InP system. *Ieee Journal of Selected Topics in Quantum Electronics,* **3**, 808–830.

Bjork, G., Karlsson, A. and Yamamoto, Y. (1994) Definition of a laser threshold. *Physical Review A,* **50**, 1675–1680.

Deotare, P. B., McCutcheon, M. W., Frank, I. W., Khan, M. and Loncar, M. (2009) High quality factor photonic crystal nanobeam cavities. *Applied Physics Letters,* **94**, 121106.

Ellis, B., Mayer, M. A., Shambat, G., Sarmiento, T., Harris, J., Haller, E. E. and Vuckovic, J. (2011) Ultralow-threshold electrically pumped quantum-dot photonic-crystal nanocavity laser. *Nature Photonics,* **5**, 297–300.

Foresi, J. S., Villeneuve, P. R., Ferrera, J., Thoen, E. R., Steinmeyer, G., Fan, S., Joannopoulos, J. D., Kimerling, L. C., Smith, H. I. and Ippen, E. P. (1997) Photonic-bandgap microcavities in optical waveguides. *Nature,* **390**, 143–145.

Fujita, M., Sakai, A. & Baba, T. (1999) Ultrasmall and ultralow threshold GaInAsP-InP microdisk injection lasers: Design, fabrication, lasing characteristics, and spontaneous emission factor. *IEEE Journal of Selected Topics in Quantum Electronics,* **5**, 673–681.

Fujita, M., Takahashi, S., Tanaka, Y., Asano, T. and Noda, S. (2005) Simultaneous inhibition and redistribution of spontaneous light emission in photonic crystals. *Science,* **308**, 1296–1298.

Fujita, M., Ushigome, R. and Baba, T. (2001) Large spontaneous emission factor of 0.1 in a microdisk injection laser. *Ieee Photonics Technology Letters,* **13**, 403–405.

Gerard, J. M. (2003) Solid-state cavity-quantum electrodynamics with self-assembled quantum dots. *Single Quantum Dots: Fundamentals, Applications and New Concepts,* **90**, 269–314.

Gerard, J. M., Sermage, B., Gayral, B., Legrand, B., Costard, E. and Thierry-Mieg, V. (1998) Enhanced spontaneous emission by quantum boxes in a monolithic optical microcavity. *Physical Review Letters,* **81**, 1110–1113.

Gong, Y. Y., Ellis, B., Shambat, G., Sarmiento, T., Harris, J. S. and Vuckovic, J. (2010) Nanobeam photonic crystal cavity quantum dot laser. *Optics Express,* **18**, 8781–8789.

Halioua, Y., Karle, T. J., Raineri, F., Monnier, P., Sagnes, I., Roelkens, G., Van Thourhout, D. and Raj, R. (2009) Hybrid InP-based photonic crystal lasers on silicon on insulator wires. *Applied Physics Letters,* **95**, 201119.

Huang, Y., Ryou, J. H., Dupuis, R. D., Pflugl, C., Capasso, F., Sun, K. W., Fischer, A. M. and Ponce, F. A. (2011) Optimization of growth conditions for InGaAs/InAlAs/InP quantum cascade lasers by metalorganic chemical vapor deposition. *Journal of Crystal Growth,* **316**, 75–80.

Hwang, J. K., Ryu, H. Y., Song, D. S., Han, I. Y., Park, H. K., Jang, D. H. and Lee, Y. H. (2000) Continuous room-temperature operation of optically pumped two-dimensional photonic crystal lasers at 1.6 μm. *IEEE Photonics Technology Letters,* **12**, 1295–1297.

Iga, K., Koyama, F. and Kinoshita, S. (1988) Surface emitting semiconductor-lasers. *IEEE Journal of Quantum Electronics,* **24**, 1845–1855.

John, S. (1987) Strong localization of photons in certain disordered dielectric superlattices. *Physical Review Letters,* **58**, 2486–2489.

Kang, J. H., Seo, M. K., Kim, S. K., Kim, S. H., Kim, M. K., Park, H. G., Kim, K. S. and Lee, Y. H. (2009) Polarized vertical beaming of an engineered hexapole mode laser. *Optics Express,* **17**, 6074–6081.

Kita, S., Nozaki, K. and Baba, T. (2008) Refractive index sensing utilizing a cw photonic crystal nanolaser and its array configuration. *Optics Express,* **16**, 8174–8180.

Kuramochi, E., Notomi, M., Mitsugi, S., Shinya, A., Tanabe, T. and Watanabe, T. (2006) Ultrahigh-Q photonic crystal nanocavities realized by the local width modulation of a line defect. *Applied Physics Letters,* **88**, 041112.

Lalanne, P. and Hugonin, J. P. (2003) Bloch-wave engineering for high-Q, small-V microcavities. *IEEE Journal of Quantum Electronics,* **39**, 1430–1438.

Lee, R. K., Painter, O. J., Kitzke, B., Scherer, A. and Yariv, A. (1999) Photonic band-gap disk laser. *Electronics Letters,* **35**, 569–570.

Lee, T. D., Cheng, P. H., Pan, J. S., Tsai, R. S., Lai, Y. and Tai, K. (1998) Far-field emission narrowing effect of microdisk lasers. *Applied Physics Letters,* **72**, 2223–2225.

Levi, A. F. J., Slusher, R. E., McCall, S. L., Tanbunek, T., Coblentz, D. L. and Pearton, S. J. (1992) Room-temperature operation of microdisk lasers with submilliamp threshold current. *Electronics Letters,* **28**, 1010–1012.

Liu, Z. J., Shainline, J. M., Fernandes, G. E., Xu, J., Chen, J. X. and Gmachl, C. F. (2010) Continuous-wave subwavelength microdisk lasers at lambda=1.53 mu m. *Optics Express,* **18**, 19242–19248.

Loncar, M., Scherer, A. and Qiu, Y. M. (2003) Photonic crystal laser sources for chemical detection. *Applied Physics Letters,* **82**, 4648–4650.

Loncar, M., Yoshie, T., Scherer, A., Gogna, P. and Qiu, Y. M. (2002) Low-threshold photonic crystal laser. *Applied Physics Letters,* **81**, 2680–2682.

Matsuo, S., Shinya, A., Chen, C. H., Nozaki, K., Sato, T., Kawaguchi, Y., Taniyama, H. and Notomi, M. (2011) 20-Gbit/s directly modulated photonic crystal nanocavity laser with ultra-low power consumption. *Optics Express,* **19**, 2242–2250.

Matsuo, S., Shinya, A., Kakitsuka, T., Nozaki, K., Segawa, T., Sato, T., Kawaguchi, Y. and Notomi, M. (2010) High-speed ultracompact buried heterostructure photonic-crystal laser with 13 fJ of energy consumed per bit transmitted. *Nature Photonics,* **4**, 648–654.

Maune, B., Loncar, M., Witzens, J., Hochberg, M., Baehr-Jones, T., Psaltis, D., Scherer, A. and Qiu, Y. M. (2004) Liquid-crystal electric tuning of a photonic crystal laser. *Applied Physics Letters,* **85**, 360–362.

McCall, S. L., Levi, A. F. J., Slusher, R. E., Pearton, S. J. and Logan, R. A. (1992) Whispering-gallery mode microdisk lasers. *Applied Physics Letters,* **60**, 289–291.

Noda, S., Yokoyama, M., Imada, M., Chutinan, A. and Mochizuki, M. (2001) Polarization mode control of two-dimensional photonic crystal laser by unit cell structure design. *Science,* **293**, 1123–1125.

Nomura, M., Kumagai, N., Iwamoto, S., Ota, Y. and Arakawa, Y. (2009) Photonic crystal nanocavity laser with a single quantum dot gain. *Optics Express,* **17**, 15975–15982.

Nomura, M., Kumagai, N., Iwamoto, S., Ota, Y. and Arakawa, Y. (2010a) Laser oscillation in a strongly coupled single-quantum-dot-nanocavity system. *Nature Physics,* **6**, 279–283.

Nomura, M., Ota, Y., Kumagai, N., Iwamoto, S. and Arakawa, Y. (2010b) Zero-cell photonic crystal nanocavity laser with quantum dot gain. *Applied Physics Letters,* **97**, 191108.

Notomi, M., Kuramochi, E. and Tanabe, T. (2008) Large-scale arrays of ultrahigh-Q coupled nanocavities. *Nature Photonics,* **2**, 741–747.

Nozaki, K., Kita, S. and Baba, T. (2007) Room temperature continuous wave operation and controlled spontaneous emission in ultrasmall photonic crystal nanolaser. *Optics Express,* **15**, 7506–7514.

Painter, O., Lee, R. K., Scherer, A., Yariv, A., O'Brien, J. D., Dapkus, P. D. and Kim, I. (1999a) Two-dimensional photonic band-gap defect mode laser. *Science,* **284**, 1819–1821.

Painter, O., Vuckovic, J. and Scherer, A. (1999b) Defect modes of a two-dimensional photonic crystal in an optically thin dielectric slab. *Journal of the Optical Society of America B-Optical Physics,* **16**, 275–285.

Park, H. G., Hwang, J. K., Huh, J., Ryu, H. Y., Kim, S. H., Kim, J. S. and Lee, Y. H. (2002) Characteristics of modified single-defect two-dimensional photonic crystal lasers. *IEEE Journal of Quantum Electronics,* **38**, 1353–1365.

Park, H. G., Kim, S. H., Kwon, S. H., Ju, Y. G., Yang, J. K., Baek, J. H., Kim, S. B. and Lee, Y. H. (2004) Electrically driven single-cell photonic crystal laser. *Science,* **305**, 1444–1447.

Perahia, R., Cohen, J. D., Meenehan, S., Alegre, T. P. M. and Painter, O. (2010) Electrostatically tunable optomechanical 'zipper' cavity laser. *Applied Physics Letters,* **97**, 191112.

Petermann, K. (1979) Calculated spontaneous emission factor for double-heterostructure injection-lasers with gain-induced waveguiding. *IEEE Journal of Quantum Electronics,* **15**, 566–570.

Purcell, E. M. (1946) Spontaneous emission probabilities at radio frequencies. *Physical Review,* **69**, 681–681.

Rigrod, W. W. (1963) Gain saturation and output power of optical masers. *Journal of Applied Physics,* **34**, 2602.

Song, B. S., Noda, S., Asano, T. and Akahane, Y. (2005) Ultra-high-Q photonic double-heterostructure nanocavity. *Nature Materials,* **4**, 207–210.

Srinivasan, K., Barclay, P. E., Painter, O., Chen, J. X., Cho, A. Y. and Gmachl, C. (2003) Experimental demonstration of a high quality factor photonic crystal micro-cavity. *Applied Physics Letters,* **83**, 1915–1917.

Srinivasan, K. and Painter, O. (2002) Momentum space design of high-Q photonic crystal optical cavities. *Optics Express,* **10**, 670–684.

Tandaechanurat, A., Ishida, S., Guimard, D., Nomura, M., Iwamoto, S. and Arakawa, Y. (2011) Lasing oscillation in a three-dimensional photonic crystal nanocavity with a complete bandgap. *Nature Photonics,* **5**, 91–94.

Velha, P., Picard, E., Charvolin, T., Hadji, E., Rodier, J. C., Lalanne, P. and Peyrade, D. (2007) Ultra-high Q/V Fabry-Perot microcavity on SOI substrate. *Optics Express,* **15**, 16090–16096.

Vuckovic, J., Painter, O., Xu, Y., Yariv, A. and Scherer, A. (1999) Finite-difference time-domain calculation of the spontaneous emission coupling factor in optical microcavities. *IEEE Journal of Quantum Electronics,* **35**, 1168–1175.

Yablonovitch, E. (1987) Inhibited spontaneous emission in solid-state physics and electronics. *Physical Review Letters,* **58**, 2059–2062.

Yamamoto, Y., Machida, S. and Bjork, G. (1991) Microcavity semiconductor-laser with enhanced spontaneous emission. *Physical Review A,* **44**, 657–668.

Yokoyama, H., Nishi, K., Anan, T., Nambu, Y., Brorson, S. D., Ippen, E. P. and Suzuki, M. (1992) Controlling spontaneous emission and threshold-less laser oscillation with optical microcavities. *Optical and Quantum Electronics,* **24**, S245–S272.

Yoshie, T., Vuckovic, J., Scherer, A., Chen, H. and Deppe, D. (2001) High quality two-dimensional photonic crystal slab cavities. *Applied Physics Letters,* **79**, 4289–4291.

Zain, A. R. M., Johnson, N. P., Sorel, M. and De la Rue, R. M. (2008) Ultra high quality factor one dimensional photonic crystal/photonic wire micro-cavities in silicon-on-insulator (SOI). *Optics Express,* **16**, 12084–12089.

Zhang, Y., Khan, M., Huang, Y., Ryou, J., Deotare, P., Dupuis, R. and Loncar, M. (2010) Photonic crystal nanobeam lasers. *Applied Physics Letters,* **97**, 051104.

Zhang, Y. and Loncar, M. (2008) Ultra-high quality factor optical resonators based on semiconductor nanowires. *Optics Express,* **16**, 17400–17409.

Zhang, Y., McCutcheon, M. W., Burgess, I. B. and Loncar, M. (2009) Ultra-high-Q TE/TM dual-polarized photonic crystal nanocavities. *Optics Letters,* **34**, 2694–2696.

Zhao, Y. G., McInerney, J. G. and Morgan, R. A. (1995) Measurement of spontaneous emission factor for vertical-cavity surface-emitting semiconductor-lasers. *IEEE Photonics Technology Letters,* **7**, 1231–1233.

3

High-power semiconductor lasers

M. FALLAHI, University of Arizona, USA and
R. BEDFORD, Air Force Research Laboratory, USA

DOI: 10.1533/9780857096401.1.81

Abstract: Over the last decades, high-power and high-brightness semiconductor lasers have transformed the solid-state laser, telecommunication, medical and military markets. This chapter covers concepts, characteristics and challenges of high-power semiconductor lasers. We begin by describing general considerations including epitaxial design, laser cavity designs and packaging specific to high-power lasers. We introduce several common high-power and high-brightness semiconductor lasers such as Fabry–Pérot lasers, grating-based lasers, large mode-area lasers, and optically pumped lasers, as well as concepts for long-wavelength operation. Arrays of devices for ultra-high-power are introduced, and device reliability challenges are addressed.

Key words: semiconductor lasers, high power, brightness, figures-of-merits, catastrophic optical mirror damage, passivation, broad-area lasers, tapered cavity, distributed feedback (DFB), distributed Bragg reflector (DBR), vertical-external-cavity suface-emitting laser (VECSEL), long wavelength, laser array.

3.1 Introduction: theory and design concept

This section deals with theory and design in relation to high-power semiconductor lasers, key device characteristics, and failure mechanisms.

3.1.1 General high-power quantum well design concepts

The quest for higher power, lower cost compact laser sources with desired characteristics continues to grow and remains an active field of research and development. High-power broad-area semiconductor laser systems based on diode laser bars are well established for a variety of applications including materials processing and solid-state laser pumping. These lasers can provide high optical power, high wall-plug efficiency and long lifetime, at a relatively low investment cost while maintaining a small footprint. In the past decade the output power from single emitter diode lasers have reached new levels,[1–5] today generating greater than 20 W of output power. These improvements have been made possible by optimal design, improved epitaxial growth, and mature fabrication techniques. The maximum achievable output power of the first generation semiconductor lasers was mainly limited by thermal rollover, due to high internal loss and poor efficiency. With the availability of high quality n-type substrates and state-of-the-art crystal growth, the performance of diode lasers has significantly improved to the point that the thermal rollover is not the limiting factor. The active layers of high-power diode lasers are generally strained or unstrained single quantum well (QW) structures for optimum optical and thermal performance. High quality, defect-free QWs are required. Precise epitaxial growth with accurate compositions, layer thickness, and doping profile are achieved by molecular beam epitaxy (MBE) and metal–organic chemical vapor deposition (MOCVD), additionally improving device reliability. By overcoming previous limitations, the main power limiting mechanism became the catastrophic optical mirror damage (COMD) of the diode facets, caused by temperatures exceeding the melting point of the laser crystal (1500 K for GaAs). This significant temperature increase is due to the high concentration of non-radiative centers localized at the mirrors. In this section we highlight the critical parameters and key design features relevant to high-power edge-emitting lasers. Figure 3.1 shows the schematic of a typical broad-area high-power Fabry–Pérot (FP) laser.

In Fig. 3.1, the epitaxial growth direction (direction of *t*) is often considered the 'transverse' dimension. Likewise, the direction of *w*, which is typically defined through processing, is known as the 'lateral' dimension, while the light propagates along the length *L* of the cavity, which is the 'longitudinal' dimension. While this last dimension is standard for most lasers, the first two (transverse and lateral) are defined differently out of necessity, as the semiconductor is most often not cylindrically symmetric. A notable difference is in vertical-cavity structures (e.g. in Section 3.2.4).

In comparison to the conventional edge-emitting lasers, the design and fabrication of high-power edge-emitting lasers requires specific attention.

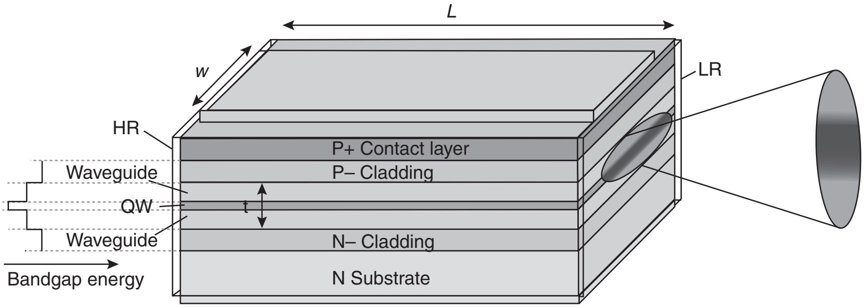

3.1 A schematic of a high-power FP laser. HR, high reflectivity; LR , low reflectivity; QW, quantum well.

For high-power diode lasers, in addition to optimum optical and electrical performance, significant effort must be given to their thermal behavior. An optimized high-power diode laser should meet the following requirements:

- low optical loss,
- high internal and external efficiency,
- optimum facet coating,
- low operating voltage,
- efficient heat dissipation and
- high temperature performance.

In the next sections, the key requirements and figure-of-merits critical to high-power diode lasers will be discussed. In addition, the laser beam quality, which can be very critical for numerous applications, will be discussed.

3.1.2 Key device characteristics

Significant insight into the design optimization of diode lasers can be obtained from their simple characteristics. For high-power semiconductor lasers, the output power is one of the most important parameters to be maximized. The optical power (P_{opt}) of a diode laser is simply related to the injection current by the relation:

$$P_{\text{opt}} = \frac{h\nu}{e} . \eta_d . \left(I - I_{\text{th}}\right) \qquad [3.1]$$

in which $h\nu$ is the photon energy, e is the electronic charge, I_{th} is the threshold current and I the injection current. A critical parameter in maximizing the output power is the differential quantum efficiency (η_d). Differential quantum efficiency is obtained from:

$$\eta_d = \eta_i \cdot \frac{\alpha_m}{\langle \alpha_i \rangle + \alpha_m} \qquad [3.2]$$

η_i is the internal quantum efficiency. $<\alpha_i>$ and α_m are the modal internal loss and the mirror loss, respectively. Minimizing modal internal loss is clearly one of the key design parameters in high-power lasers. The mirror loss is related to the mirror reflectivity (R_1 and R_2) and cavity length (L) through:

$$\alpha_m = \frac{1}{2L} \cdot \ln\left(\frac{1}{R_1 \cdot R_2}\right) \qquad [3.3]$$

High-power FP lasers are cleaved into bars with a cavity length in the range of 1–3 mm. The mirror reflectivity is then controlled by applying dielectric coatings to the front and rear facets. Typical values of mirror reflectivity are $R_1 < 10\%$ for the front (output) facet and $R_2 > 90\%$ for the rear facet.

One key figure-of-merits for high-power diode lasers is their power-conversion efficiency. Power-conversion efficiencies (PCE) of diode lasers, also known as wall-plug efficiency (η_{wp}), is the highest of all types of light sources. It is defined as the ratio of the emitted optical power (P_{opt}) to the injected electrical power (P_{elec}). Considering Equation [3.1], it is obtained from:

$$\eta_{\text{wp}} = \frac{P_{\text{opt}}}{P_{\text{elec}}} = \frac{(h\nu/e) \cdot \eta_d \cdot (I - I_{\text{th}})}{I \cdot V}, \qquad [3.4]$$

in which V is the applied voltage. In order to maximize the conversion efficiency the internal voltage drop should also be minimized. This is typically attained by minimizing the number of QWs and optimizing the transverse waveguide structure. The use of a strained QW helps in reducing the hole effective mass and thus improving differential gain. Concurrently, significant efforts have focused on maximizing the differential quantum efficiency by improving substrate quality and eliminating wafer growth imperfections. These not only improve the integrity of the epitaxial structure, but also reduce the total voltage drop across the device, especially when injecting through the substrate – a common geometry for broad-area, high-power diodes.

Recent advances in epitaxial designs and thermal management have resulted in a significant improvement in conversion efficiency. Diode lasers with conversion efficiency in excess of 65% operating in the 780–980 nm wavelength range are commercially available. Examples include individual 940 nm bars operating in CW mode at >1 kW and 808 nm bars operating at >60 W with 65% PCE The new-generation of 9xx nm epitaxial structures have values of $\eta_i > 98\%$ and internal loss $<\alpha_i>$ below 0.6 cm^{-1}. CW PCE as high as 72.2% are obtained in 9xx nm strained QW single emitters.[5,6]

Temperature characteristics

A fraction of the injected electrical power P_{elec} will be dissipated in the form of heat, which in turn causes a rise in the active region temperature. As the laser operates at higher electrical power, the temperature of the active region rises and causes degradation of the threshold current and conversion efficiency. The rise in the active region temperature is given by:

$$\Delta T = Z_T \cdot (P_{\text{elec}} - P_{\text{opt}}) = Z_T \cdot P_{\text{elec}} (1 - \eta_{\text{wp}}), \qquad [3.5]$$

where Z_T is the thermal impedance of the laser. In order to minimize the temperature rise one has to efficiently extract the generated heat by using highly efficient heatsink and laser mounting techniques to reduce Z_T. The thermal impedance for a 1-D heat flow can be obtained from:

$$Z_T = \frac{h}{\xi \cdot A}, \tag{3.6}$$

where h is the distance between the active region and the heat sink, A is the area of the heat source and ξ is the thermal conductivity of the semiconductor material. For reference, GaAs has a thermal conductivity of about 0.45 $\mathrm{W{\cdot}cm^{-1}\,K^{-1}}$. For high-power operation the thermal impedance of the laser should be minimized. This is achieved by bringing the active region very close to the heatsink through p-side down-mounting of the laser. The thermal resistance of the solder layer and heatsink must be taken into account. Moreover, thermally-induced stress upon the active material through differences in coefficients of thermal expansion must be considered when packaging high-power laser devices.

Threshold current and PCE of diode lasers are strongly affected by temperature rise. Threshold current increases and slope efficiency decreases with increasing the temperature. The dependence of threshold and slope efficiency on temperature can be estimated from:

$$I_{\text{th}}(T) = I_{\text{th}}(T_{\text{ref}})\, e^{(T - T_{\text{ref}})/T_0} \tag{3.7}$$

$$\eta_d(T) = \eta_d(T_{\text{ref}})\, e^{-(T - T_{\text{ref}})/T_1} \tag{3.8}$$

Similarly, the above-threshold current necessary to obtain a targeted output power at a given temperature T can be obtained from:

$$I(T) = I_{\text{th}}(T_{\text{ref}})\, e^{(T - T_{\text{ref}})/T_0} + I_{\text{p}}(T_{\text{ref}})\, e^{(T - T_{\text{ref}})/T_1}, \tag{3.9}$$

where T_{ref} is a reference temperature with known threshold, $I_{\text{th}}(T_{\text{ref}})$, and current, $I_p(T_{\text{ref}})$, to reach the desired output power. The constants, T_0 and T_1 are characteristic temperatures of the diode lasers at threshold and above threshold, respectively. Clearly, characteristic temperatures T_0 and T_1 should be maximized for high-current and high-temperature CW operation. They depend on the laser material and structure. GaAs-based lasers have significantly higher T_0 and T_1 values than InP-based lasers.

The use of QW and strained QW structures has been shown to improve the temperature characteristics of the lasers. For instance, characteristic temperatures of $T_0 \sim 200$ K and $T_1 \sim 700$ K are reported in 9xx nm InGaAs/GaAs strained QW laser structures under CW operation.[2]

Brightness and beam quality factor

High-power diode laser systems based on broad-area FP lasers and bars have several advantages, such as high optical power, and efficiency, in addition to low cost and a small footprint. For many applications high-power CW output is the main requirement, although many applications necessitate additional features such as good beam quality, narrow spectral linewidth, and wavelength stability over a wide range of temperature. A major drawback of broad-area FP lasers and laser bars is their poor beam quality. The beam quality of a laser is characterized by its brightness B. The brightness of a diode laser beam is calculated from:

$$B = \frac{P_{\text{opt}}}{\pi^2 \cdot \text{BPP}^2}, \tag{3.10}$$

where BPP is the beam parameter product obtained from:

$$\text{BPP} = \frac{w_0}{2} \cdot \frac{\theta}{2} \tag{3.11}$$

w_0 is the emission width (or beam diameter at the waist) and θ is full-angle beam divergence measured at the far field. BPP is related to the beam étendue.

Another important parameter used in evaluating the beam quality of a laser is its M^2 factor, which compares an arbitrary beam to a Gaussian beam of similar proportions. The M^2 factor, also called *beam quality factor*, is a common measure of the beam quality and is related to the beam parameter product as follows:

$$M^2 = \frac{\text{BPP} \cdot \pi}{\lambda} \tag{3.12}$$

For a diffraction-limited Gaussian beam the beam parameter product is $\text{BPP} = \lambda/\pi$, which gives an M^2 factor of 1. A laser beam is said to be 'M^2 times' diffraction limited. Clearly the M^2 factor of a laser beam limits the degree to which the beam can be focused for a given beam divergence angle. For asymmetric beams, the M^2 factor can be significantly different in the two orthogonal directions (M_T^2 for the transverse-dimension and M_L^2 for the lateral dimension). This is particularly the case for broad-area FP lasers. In fact in edge-emitting semiconductor lasers the waveguide in the transverse direction (normal to the growth plane) is single-mode, resulting in a very low M^2 factor with a typical value of 1.2–1.5. This direction is known as the 'fast axis', as the beam diverges very rapidly due to the small waveguide aperture. Meanwhile, the waveguide in the lateral direction (known as the 'slow axis') is large, and highly multimode. In the case of broad-area lasers the lateral emitting region is around 100 microns wide, resulting in a much larger M^2 factor. M^2 in the lateral direction of 30–50 has been observed. The brightness of the laser is then obtained by using the product of the beam quality factor in the two orthogonal directions:

$$B = \frac{P_{\text{opt}}}{\lambda^2 \cdot M_T^2 \cdot M_L^2} \qquad [3.13]$$

For a non-diffraction-limited beam, the brightness is reduced by the product of the M^2 for the transverse $\left(M_T^2\right)$ and lateral $\left(M_L^2\right)$ directions. The brightness (B) of diode lasers can be enhanced by increasing optical output power (P) and decreasing M^2 factor. The latter can be achieved by decreasing the far-field divergence and small emitter width. In order to achieve low M^2 factor the laser should mainly support single spatial mode in the transverse and lateral directions. In high-power broad-area diode lasers single transverse mode is usually achieved; however, the lateral direction is multimode with a high value of M_L^2.

In broad-area devices, beam filamentation is the main effect that limits the device brightness. While higher output power can be achieved by increasing the lateral dimension, this also results in significant degradation of the beam quality factor due to self-focusing nonlinearities and filamentation. With increasing power level, spatial hole burning occurs, due to the interaction between the amplified optical field and the carrier density in the active region. Therefore, the complex index of refraction becomes inhomogeneous, leads to self-focusing of the optical wave, and results in filament formation that severely deteriorates the beam quality.[7]

Spectral linewidth and stability

The need for narrow spectral linewidth and stable wavelength emission is growing. Narrow linewidth and stable wavelength emission under different operating and temperature conditions is critical for diode lasers used in solid-state laser and fiber laser pumping. In edge-emitting diode lasers, as the injection current increases more longitudinal modes can reach threshold, resulting in broad spectral linewidth emission. This results in multi-longitudinal modes emission of 2–4 nm. In addition, the gain shifts to longer wavelength as the temperature of the active region increases, causing a temperature-dependent lasing wavelength shift of about 0.3–0.5 nm/K. This can become a major bottleneck for a variety of applications. In order to narrow the spectral linewidth, wavelength-selective mirrors (such as gratings) are typically used. Distributed feedback (DFB) and distributed Bragg reflector (DBR) lasers are routinely used to generate spectrally narrow linewidth emission with less temperature sensitivity. This is covered more thoroughly in Section 3.2.2.

Maximum output power

The most important parameter in qualifying the performance of high-power diode lasers is the maximum achievable output power. While Equation [3.1] provides a linear relation governing the output power for low injection current, it cannot accurately describe the limit of the achievable power for a given laser. Two main factors limit the output power of edge-emitting FP lasers: thermal rollover and COMD. We will explore each of these in the following text.

High-power diode lasers are extremely efficient in converting electrical energy into light, with conversion efficiency better than 70%. However, the excess power not converted into light can be converted into heat causing material heating and performance degradation. As the laser is driven at higher current for higher output power, the active region starts heating up significantly. At higher injection current, when the dissipation of the generated heat becomes challenging, the temperature of the active region becomes overly hot, causing a reduction of the output power. Excessive heat generation by ohmic heating leads to a significant temperature rise in the active layer. This results in carrier spreading, significant gain reduction, and an increase in non-radiative recombination. Because laser diode characteristics are very sensitive with respect to the increase of temperature, for high-power operation they have to be mounted with great care in the p-down configuration, that is, epitaxial side on the heat sink.

Three key steps in eliminating thermal rollover are:

1. Minimizing internal loss and threshold current.
2. Minimizing thermal resistance between the active layer and the heat sink. A very low thermal resistance helps in efficient heat dissipation from the active region through the heat sink.
3. Maximizing conversion efficiency of the laser by reducing internal loss and carrier leakage and minimize non-radiative recombination.

The latest improvements in high-power diode lasers have resulted in an internal quantum efficiency η_i of over 98% and the internal loss (α_i) of less than 0.6 cm^{-1}.[6,8] These lasers can produce record high-power output by eliminating thermal rollover.

While progress in the design and growth has helped to practically eliminate thermal rollover, another power limiting process known as COMD has become the main limiting cause of achievable output power of diode lasers. COMD degradation of the diode facets is caused by facet heating and subsequently the rise in temperature exceeding the melting point of the laser crystal. The details about the cause of COMD and recent progress will be presented in Section 3.1.3. The maximum CW output power achievable in the diode lasers is directly proportional to the COMD power density limit. The maximum output power can be obtained from:[9]

$$P_{\max} = W \cdot \left(\frac{d}{\Gamma}\right) \cdot \left(\frac{1-R_1}{1+R_1}\right) \cdot P_{\mathrm{COMD}} \qquad [3.14]$$

Table 3.1 Approximate power densities necessary to cause COMD in different QW materials

Active-region material	P_{COMD} (MW/cm^2)
InGaAs (0.92–0.98 μm)	18–19
InGaAsP (0.81 μm)	18–19
InAlGaAs (0.81 μm)	13–14
GaAs (0.81–0.87 μm)	10–12
$Al_{0.07}GaAs$ (0.81 μm)	8–9
$Al_{0.13}GaAs$ (0.78 μm)	5

where d is the thickness of the active QW layer, Γ is the transverse confinement factor, and P_{COMD} is the internal optical power density at COMD, which is a function of the active-layer material. The COMD optical power density of major active-layer materials is summarized in Table 3.1.[10] While the latest advancement in material growth, processing, and passivation has results in higher P_{COMD} of these active regions, the trend presented in Table 3.1 can be very informative. The P_{COMD} decreases as the aluminum concentration in the active region increases. This is due to increased sensitivity of the aluminum-containing active regions to oxidation. COMD performance intensity as high as 30 MW/cm^2 has been demonstrated on devices with improved passivation.[11]

For a given material family the cavity parameters should be optimized for maximum output power. These include:

- minimizing $R_{1,}$
- increasing w,
- maximizing d/Γ.

A broad transverse waveguide design can provide a significant improvement in output power. It provides a large transverse effective spot size, d/Γ, resulting in lower optical density at the facet below P_{COMD}. At the same time, most of the optical field remains confined in the low-doped waveguide layer resulting in low internal modal loss, (α_i) required for differential quantum efficiency. High-power diode lasers in the 9xx nm range can now reach >20 W per emitter. This has a large impact on the cost/watt figure of merit, which now enables the diode power to be beam-shaped and engineered for direct materials processing applications.

3.1.3 Failure mechanisms

For most applications, semiconductor lasers are attractive, in part, due to their high reliability and long operating lifetime. It is therefore important to understand when lasers operate near a boundary which may threaten their lifetime. There are various effects which may damage high-power semiconductor lasers. These include thermally driven effects, including poor soldering layers. Another effect is optical feedback from an external reflection, causing instability and potentially laser damage. However, for high power edge-emitting lasers, one of the most detrimental effects attributing to laser failure is catastrophic facet damage.

Catastrophic facet failure and passivation techniques in high-power diode lasers

As discussed in the previous section COMD is the ultimate limit in achieving higher output power from diode lasers. Numerous studies have been made to understand and control the occurrence of COMD.[12–17] The cause of COMD is understood to be the formation of defect and excess non-radiative recombination at high operating current. Non-radiative recombination on surface defects leads to slow mirror overheating proportional to laser operating current. As the output power increases the optical absorption at the output mirror facet increases significantly. Such increase in optical absorption in the active-layer region of the mirror causes localized material heating. Mirror degradation is caused by facet heating due to non-radiative surface recombination of carriers. Facet heating results in a reduced bandgap energy of the material which consequently increases the absorption coefficient at the lasing wavelength leading to further heating. Such chain reaction results in thermal run-away and a rapid increase in facet temperature causing its ultimate catastrophic failure. The absorption coefficient increases to over of 100 cm^{-1} due to heating and the temperature rise corresponding to the melting point of the crystal can occur within 100 ns.[15] Figure 3.2b–3.2d shows the emission result of COMD on

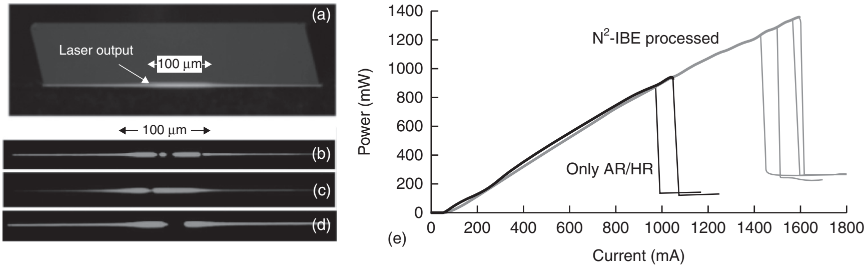

3.2 Electroluminescence from the output facet of an AlGaInP broad-area laser (a) before, and (b), (c), (d) after a COMD event. Source: Reprinted with permission from SPIE.[14] (e) COMD data for 806-nm laser diodes before operation. N^2-IBE is native-nitride ion-beam epitaxy. Source: Reprinted from the November 2003 edition of *Laser Focus World*, Copyright 2003 by PennWell.[21]

the electroluminescence of a broad-area laser, in comparison to the same laser facet prior to COMD (Fig. 3.2a). The catastrophic effects are very evident in device output power as well, as indicated by Fig. 3.2e, where several different coating types are compared, demonstrating improvements due to facet passivation.

A reliable facet passivation is then required to push the COMD to higher power densities, which reduces R_1 in Equation [3.14]. Since facet degradation is enhanced by the carrier density in the facet region, the first step is to ensure that current is not injected near the facet. Also, since the main contribution to facet degradation above threshold is due to non-radiative recombination of photon generated electron–hole pairs, reduction of the optical absorption coefficient in the facet region is essential. Creation of non-absorbing mirrors is a critical step in increasing the power capability of diode lasers. Increasing the bandgap energy of the mirror regions relative to the active layer reduces the absorption coefficient results in further increase of the COMD power density.

Key objectives of facet passivation are:[18,19]

(a) Removal of surface states resulting from dangling bond imperfections.
(b) Removal of surface oxides.
(c) Minimize optical absorption at the facet by formation of large bandgap interface.
(d) Creation of a diffusion barrier against oxygen incorporation from the atmosphere.

Several passivation techniques have been developed. Some of the most widely used techniques are:

- Ultrahigh-vacuum (UHV) cleaving followed by *in situ* passivation.[16]
- Selective area growth for producing non-absorbing mirror lasers.[17]
- Quantum well intermixing (QWI).[20]
- Air-cleaving followed by ablation under unreactive ions (e.g. argon or nitrogen).[21]
- Nitridization to reduce surface-state carrier recombination, prevent surface contamination and provide a higher bandgap surface layer.[22]
- Sulphation[23] followed by a dielectric layer deposition.
- Hydrogenation and silicon hydride barrier layers.[24]

In addition to reducing the absorption coefficient, the creation of higher bandgap energy of the non-absorbing mirror region helps prevent current diffusion into this region. The dielectric overcoat is applied directly following the passivation processes where providing specific facet reflectivity is required.

3.2 Single emitters

This section deals with recent developments and trends in single emitter semiconductor lasers. It covers several high power sources such as broad-area Fabry–Pérot lasers, high-power DFB and DBR lasers, large mode-area lasers, vertical-external-cavity surface-emitting lasers (VECSELs), and long-wavelength sources.

3.2.1 Broad-area Fabry–Pérot lasers

As reported earlier a primary issue limiting the maximum power of diode lasers is the heating of the active layer and COMD at high drive currents. To minimize heating in the active regions, optimization in every aspect of laser development including growth, processing, passivation, and packaging have been made. Today, laser structures with very low defect density are grown by low-pressure metal–organic chemical vapor deposition (LP-MOCVD) in multi-wafer reactors. III-V laser structures grown on GaAs have demonstrated significant maturity to allow the development of lasers in the 7xx–11xx nm range. The design and growth of new class of materials with low sensitivity to degradation have proven to be very successful. The growth of aluminum-free structures has pushed the COMD threshold to higher powers. One of the most challenging steps in FP laser development is facet passivation combined with low reflectivity coating (less than 10%) of the front and high-reflectivity coating (greater than 95%) of the rear facets. Efficient heat dissipation from the active region is achieved by bringing the active layer close to a heatsink. The chips are mounted p-side down on cooled heatsinks (such as copper or CuW). The use of expansion matched copper-diamond (CuD) composite carriers (allowing the use of hard solder) are also used as a heat spreader between the diode and the copper heat sink.[1] High-temperature solders such as AuSn provide relatively high thermal conductivity while vastly increasing long-term reliability. Laser chips with increased cavity length (2–5 mm) are then used to improve heat spreading and maximize the output power. Low propagation losses allow long optical cavities, which combined with wide-emitting apertures result in the low current density operation and improving the thermal behavior of lasers.

Among various semiconductor materials, GaAs-based lasers have proven to have highest power and performance. Strained QW active regions are used in order to remove the degeneracy between the heavy holes and light holes, providing higher differential gain and improved temperature characteristics (T_0 and T_1). A compressive strain QW gives TE polarization, while a tensile strain QW laser has a TM polarization. Based on the selection of the active layer, these lasers can cover a wide wavelength range of 7xx–1000 nm and above. Two families of active cladding layers are developed:

Al-containing compounds, and Al-free compounds. The main reservation in the use of Al-containing structures is defect formation and facet degradation at high-power operation. As a result, major challenges in Al-containing structures are mirror passivation and P_{COMD} improvement, as mentioned in Section 3.1.3. UHV cleaving and *in situ* passivation, known as E2 passivation, have been proved to provide excellent reliability. For other standard passivation techniques where air-cleaving is performed, Al-free structures seem more suitable and reliable.

The highest performances have been reported for ~9xx nm InGaAs/GaAs compressive strained QW. Single emitter InGaAs/GaAs/AlGaAs or InGaAs/GaAs/InGaP lasers with CW output power in excess of 20 W have been reported for a ~100 μm emitting aperture.[1,6] Commercially available fiber-coupled single emitter ~980 nm lasers can provide over 10 W power.

In contrast with 9xx nm devices, the semiconductor material of 8xx nm, especially 808-nm, is more challenging to produce with the highest performance. There are three main material choices for 808 nm devices: tensile strained GaAsP, compressively strained InGaAsP or compressively strained AlInGaAs. Single emitter output power in excess of 10 W is achieved at 808 nm.[25,26] Commercial 808 nm single emitter lasers can provide 5 W.

There are two active-layer designs, AlGa(In)As and Ga(In)AsP, used for 7xx nm lasers. The Al-free P-based Ga(In)AsP material system intrinsically offers the possibility of higher reliable power with standard passivation. However, with advanced passivation techniques, the As-based AlGa(In)As material system has also demonstrated leading performance. Broad-area lasers with an output power in the range of 4–7 W have been reported with Al-free structures.[27]

3.2.2 High-power distributed feedback and distributed Bragg reflector lasers

The high-power semiconductor laser industry is dominated by solid-state pumping, and therefore wavelength control within the absorption band of the solid-state gain medium is required. While the manufacturing epitaxial growth continues to result in high gain, high quality waveguides, and uniform growth across 4-inch wafers, wafer-to-wafer wavelength variability during epitaxy can significantly reduce yields, thus driving up ultimate device costs. In the 1990s, typical manufacturing required wavelength tolerances of <5 nm, which corresponds well with the (3–5 nm) absorption band at 940 nm for Yb:YAG lasers. As high-power lasers progressed toward being commodities, improvements in yield tightened tolerances on growth variation, and final devices required wavelengths variance to <2 nm. As an example, when pumping the same Yb:YAG solid-state crystal mentioned previously

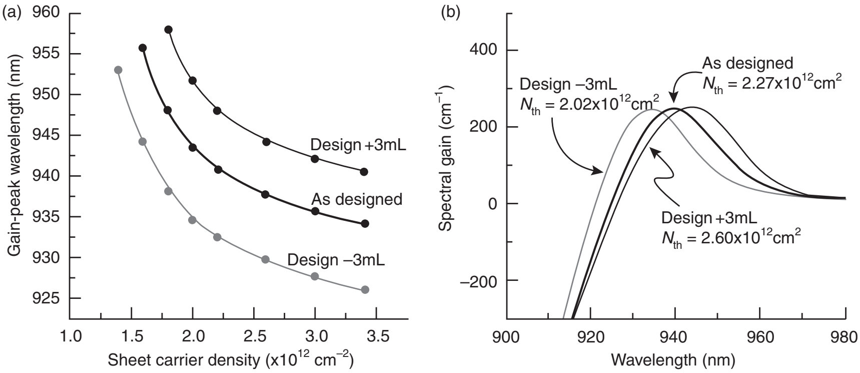

3.3 (a) Wavelength of peak gain as a function of sheet carrier density for different thicknesses of wells (varied by ±3 Å). (After Reference 81.) (b) Spectrally resolved gain assuming a g^{th} of 250 cm^{-1}. In these calculations, there is no consideration for a spectrally dependent loss mechanism.

at 980 nm (reducing the quantum defect and therefore creating a more efficient laser), the absorption linewidth is only on the order of 1–2 nm. While epitaxial growth remains precise, the thin QWs are very sensitive to wavelength variability. As an example, Fig. 3.3a shows the computed gain peak of a laser designed for 940 nm, operating at a QW temperature of 320 K.[28] Also plotted are the wavelengths of peak gain for an otherwise identical structure with QW thicknesses that deviate by three atomic layers (~2 Å) from the intended thickness. Such small variation, which nominally reflects in 1 s error in the QW growth, moves the peak gain by about ±7 nm, significantly outside typical tolerances of most manufacturing systems. Figure 3.3b shows the computed spectral gain, assuming a threshold-gain (gain at the peak) of approximately 250 cm^{-1}.

Although the center of a typical gain curve can vary from growth to growth, the gain is quite broad (over 50 nm) and therefore the introduction of a wavelength-selective element into the laser cavity can improve the device yields, with a modest increase of complexity in post-growth processing.

One method to accomplish this is to include an external grating. This method is not dissimilar to fiber-coupled single emitters, wherein a Bragg grating is integrated into the fiber, providing wavelength-selective feedback used to stabilize the wavelength.[29] Due to the nature of typical high-power semiconductors, it is difficult and inefficient to couple the high-power laser into a single-mode fiber typically used for Bragg grating stabilized fiber. In recent years, the proliferation of high quality photo-refractive materials, in which a volume Bragg grating (VBG) can be written into a piece of glass, bulk glass VBGs are easily used after fast-axis collimation to

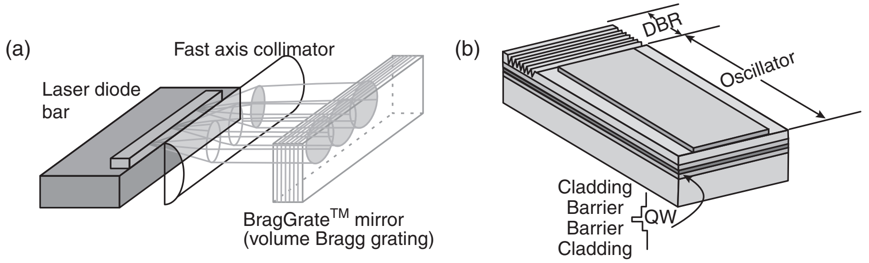

3.4 (a) Wavelength stabilization of a linear array of broad-area lasers through use of an external VBG. Image courtesy of OptiGrate Corp. (b) Wavelength stabilization through use of an internal DBR surface-relief grating.

wavelength-stabilize high-power semiconductor lasers. Schematically, this is pictured in Fig. 3.4a. The bulk VBG alleviates the issue of coupling a high-power laser into a small mode-area structure such as a single-mode fiber. Moreover, because the mode is distributed over a larger volume, one may achieve very high efficiency (>99%), a variety of center wavelengths, and reflection bandwidths in the picometer range.[30] The feedback is distributed over a volume of nominally 1 cm^3, so these structures may be used to stabilize very high-power lasers and arrays, and are able to withstand large optical fluences. Because the VBG has achieved such high efficiencies in practice, they are able to be spectrally tailored, and are transparent to wavelengths that are not within the stop-band of the Bragg mirror. As such their use has proliferated to other high-power schemes such as spectral beam combining,[31] and coherent phase locking.[32]

However, these are still devices that are assembled within the laser package. Packaging remains a significant portion of the assembly cost, primarily because it is accomplished through manual manipulation, and is done serially. This does not take advantage of the efficiency of parallel production leveraged by most of the semiconductor industry. An alternative approach is to actually integrate the external VBG into the chip. This is most economically done using post-growth first- or second-order gratings on the high-reflectivity side of the laser.[33] Surface-relief gratings are high contrast (n_{semi}–n_{air}), but they interact with the evanescent tail of the mode, therefore the coupling remains small. A schematic of the broad-area DBR laser in depicted in Fig. 3.4b. While this method requires higher resolution lithography than typical broad-area lasers use, manufacturing processes such as i-line projection lithography stepper systems are generally available and have proven reliable manufacturing implements. A DBR can also take the place of a high-reflectance facet coating, which may be difficult to achieve in practice, requiring three or more layers to reach the required back-facet high-reflectivities. The grating remains volumetric in nature because the growth axis remains guided.

Logically extending the single passive DBR, and the potential losses incurred in a passive region, DFB lasers can also be made high-power, making the mirror active. DFB ridge waveguides have been a mainstay of the laser diode industry, although to scale the power, it becomes necessary to laterally increase the size of the laser. DFB may be used in broad-area lasers for stabilization as well. Transverse waveguides for high-power lasers are often designed to be multimode, and the gain is positioned such that only the fundamental mode has sufficient gain to overcome losses and reach lasing. However, with the inclusion of a perturbation like surface-relief grating, these modes are no longer orthogonal and the different transverse modes beat against each other. This effect can be made negligible again if the refractive index perturbation is small, necessitating locating the grating much closer to the mode center in a region of large mode overlap. This is most often done with epitaxial regrowth after patterning the grating region.[34]

Finally, a unique DFB cavity known as the α-DFB achieves spatial and spectral mode selection through a Bragg grating at a modest (5°–20°) angle with respect to the cavity axis. The cavity facets and the grating are used to provide feedback because the light propagates through a 'zigzag' pattern, which creates an angular selectivity much greater than that of a Fabry–Pérot device. Such cavities have demonstrated watt-level output with $M^2 \sim 1.1$, and powers above 5 W.[35] The α-DFB is also ultimately limited by antiguiding, breaking up the lateral coherence.

3.2.3 Large mode-area lasers

A very powerful method to increase the power is that known as 'geometric power scaling'. For example, if the current injection density is held constant, and thermal abatement is maintained (e.g. one-dimensional heat flow), the CW power produced by a laser is linearly proportional to the gain volume. While this is true for all lasers, it can be a particularly powerful improvement to semiconductor lasers, due to their typical quantum confinement in one direction.

Generally, the main limitation to laser brightness in large mode-area lasers is the linewidth enhancement factor (so-called 'α-factor', and denoted as 'α_b' in this text). For most simple lasers (excluding DBR or DFB lasers), a transverse guided-laser mode propagating through material obeys the following partial differential equation:

$$\frac{\partial}{\partial z}E(x,z)=-\frac{i}{2\beta}\frac{\partial^2}{\partial x^2}E(x,z)-ik_o\left(\Delta\tilde{n}_{\text{eff}}(x,z)-\frac{\Delta\tilde{n}_{\text{eff}}^2(x,z)}{n_{\text{eff}}}\right)E(x,z), \quad [3.15]$$

where β is the transverse propagation factor, k_o is the vacuum wavenumber, n_{eff} is background the effective index $\left(\beta \equiv k_o n_{\text{eff}}\right)$, and the complex refractive index is composed of a background and a spatially varying term $\left(\tilde{n}_{\text{eff}}\left(x,z\right) \equiv n_{\text{eff}} + \Delta\tilde{n}_{\text{eff}}\left(x,z\right)\right)$. The 'interesting' physics, including gain and loss may be isolated in the spatially varying term, which includes several terms:

$$\Delta\tilde{n}_{\text{eff}}\left(x,z\right) = \Delta n_{\text{eff}}\left(x,z\right) + \alpha_T \Delta T\left(x,z\right) + i\frac{\alpha_{\text{effy}}\left(x,z\right)}{2k_o} - i\frac{\Gamma_y}{2k_o}\left(1 - i\alpha_b\right) g_a\left(x,z\right) \qquad [3.16]$$

The first term in Equation [3.16] is the intentional index guiding (such as a ridge waveguide), the second term is temperature-induced refractive index changes, the third term represents the modal loss, and the fourth term represents the modal gain, with an additional real term due to the linewidth enhancement factor. This term causes the effect of 'antiguiding'.[36] The antiguiding effect is a carrier-induced refractive index shift, causing the refractive index to drop with an increase in carrier density. This effect is primarily the result of band-to-band interactions, and lesser contributions from plasma interactions.[37] For our purposes, we call this proportionality 'α_b', and it is explicitly the dependence of the real part of the refractive index on carrier density in relation to the imaginary part of the refractive index in relation to the carrier density. The laser linewidth is increased by a factor of $1 + \alpha_b^2$, the result of phase ambiguities caused by recombination carrier density changes. This term is of the utmost importance in single-mode, large mode-volume lasers, and is one of the primary foes of wide-aperture lasers, as will be described in the following.

In wide-aperture (broad-area) lasers, the field may have some 'structure' within a region of uniform carriers, and spatially much wider than the ripples of the optical field. The optical field will cause stimulated emission, decreasing the carrier density in the regions of local maxima of irradiance distribution of the field. The reduction of carriers will cause an increase in the refractive index and further focus the local maxima, similar to a waveguide. This effect will break up the field, causing potential spatial incoherence between each of these 'filaments.' As carriers are locally depleted, there will be carrier build-up in regions that are not causing guiding. Subsequent build-ups will amplify the field in another region, and the field will not be amplified in guiding regions where the carriers have been depleted, thus the filaments are dynamic in nature. Many of the following types of lasers implement ways to counter this nonlinearity to maintain spatial coherence.

Master-oscillator power amplifiers

As mentioned above, the single-mode operation is most problematic at high currents and powers. One solution is to make a good low-power source, and amplify the output. This configuration utilizes what is known as a 'master-oscillator power amplifier' (MOPA) configuration.[38] In the early 1990s, an integrated MOPA design was proposed by Spectra Diode Labs. Such a device is typically composed of a single-mode DFB or DBR ridge laser acting as the low-power 'master-oscillator.' This high quality single-mode laser output is coupled from one of the ends of the laser to a gain-guided power amplifier, which is tapered to match the natural lateral diffraction of the mode. The adiabatic taper is designed to (i) distribute the current only in the region where the unidirectional mode has significant field and (ii) slowly change the mode and not excite higher-order lateral modes within the waveguide. A schematic of such a laser can be seen in Fig. 3.5a.

The oscillator is typically composed of a highly index-guided structure (e.g. an index-guided ridge laser, or a buried heterojunction laser, requiring regrowth). This laser is typically of low power, but of high spectral and spatial quality. The amplifier (especially in the tapered structures depicted in Fig. 3.5) is typically a gain-guided structure. Because the guiding is quite weak in a gain-guided waveguide, it becomes more difficult to excite higher-order modes. As such, the mode exciting in the emission aperture, while of similar lateral dimensions (~200 μm) as that of typical broad-area lasers, has a much better beam quality than multimode broad-area lasers mentioned in Section 3.2.1. In fact, this laser continues to operate in single lateral mode, and 'diffraction limited' for many times threshold, although it should be noted that the mode shape is not Gaussian, and therefore the M^2 is somewhat larger than unity.

While this configuration is useful and quite straight forward, the amplifier introduces engineering problems. Namely, an amplifier requires a high single-pass gain while not supporting self-oscillation. This involves reducing the facet reflectivity to very low levels ($R \sim 1 \times 10^{-4}$ or lower), which is difficult to achieve in a manufacturing environment.

Tapered unstable resonator lasers

An alternative is pictured in Fig. 3.5b, where there is no separation between the oscillator and the amplifier. This laser, known as a tapered unstable resonator laser (TURL), where the single-mode ridge waveguide remains, but is coupled directly to a tapered gain region. The mode behaves in this region much like its amplifier counterpart in the MOPA. However, when the mode impinges on the emitting aperture facet, a small fraction of the light is reflected (generally < 2%) and continues to expand in the taper, however propagating backward within the cavity. A small fraction of this mode is re-coupled to the ridge waveguide, and reflected off the back facet to seed lasing.

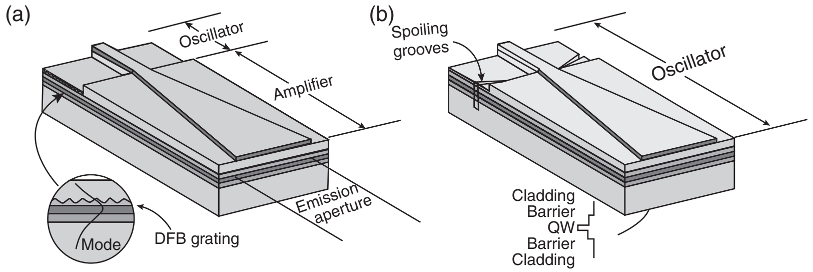

3.5 Integrated high-brightness laser examples. (a) Integrated MOPA configuration, composed of DFB oscillator with a tapered amplifier section. (b) Unstable resonator laser with tapered gain section.

This class of cavity is known as an 'unstable resonator,' and imparts a strong mode selectivity. This more complicated cavity design can avoid exciting higher-order modes, thus maintaining the single-mode nature of the laser. Unstable resonators are known for having this strong mode selectivity.[39] Typified by a large mode-dependent loss through some sort of aperture within the cavity, along with large mode sizes, they are only considered 'unstable' in the ray-sense; that is to say, rays are not bound to near on-axis propagation.

The ridge cannot easily be made long enough to impart the required mode-dependent loss. To solve this, the introduction of spoiling grooves becomes necessary to aid in maintaining a single mode. These spoiling grooves are troughs etched through the active region (seen in Fig. 3.5b), and are a means for scattering light out of the cavity, acting as a hard aperture. Numerical investigations have shown the most effective location for a hard aperture is at the ridge/taper junction. The mode coupled from the taper to the ridge is quite large after propagating from the ridge to the taper mirror and back. Such a wide mode (relative to the ridge width) means many modes of the ridge are excited, and only a small fraction of the power is in the fundamental guided mode. The spoiling grooves narrow the lateral dimensions of the field by acting as a spatial filter. The narrow field is centered about the ridge, similar to the guided mode. A larger percentage of the light that is transmitted through the spoiling grooves is coupled into the fundamental mode of the index-guided ridge.

For a generic paraxial laser cavity defined by: (i) a geometric ABCD matrix and (ii) a single aperture $\rho(x)$ within the cavity to laterally confine the mode, one can derive the following eigenmode equation for the scalar lateral field ($E(y)$) from the generalized Huygens's integral:

$$\gamma E(y) = e^{ikB}\sqrt{\frac{1}{i\lambda B}}\int_{-\infty}^{\infty}\rho(x)E(x)e^{i\frac{k}{2B}\left(Ax^2+Dy^2-2yx\right)}\mathrm{d}x, \qquad [3.17]$$

where γ is the eigenmode (the round-trip power loss is $1 - \gamma^2$). For each eigenmode $E^{(n)}$, there is an equivalent round-trip loss $1-\left|\gamma^{(n)}\right|^2$. For stable resonators, the loss is simply the mirror reflectivity, not considered in the equation above, and the aperture is essentially the gain diameter. As such, the gain width is quite large compared to the mode size (encompassing > 90% of the mode). This geometry results in modal losses which are nearly degenerate. Often at higher powers, small nonlinear effects such as thermal lensing will allow unwanted higher-order modes to also lase. Conversely, for unstable resonators, $\rho(x)$ is typically on the order of or smaller than the lateral extent of $E(x)$. As a result $\gamma^{(n)}$ can vary wildly for different modes. A recent calculation for finite-aperture tapered unstable resonators[40] (FATURL, a subset of TURLs) showed the modal discrimination $\left(\left|\gamma^{(1)}\right|/\gamma^{(2)}\right)$ to be well above 10 for most cases, and approaching 30 for some specific designs.[41] As such, these types of cavities (both TURLs and FATURLs) have achieved multi-watt-level operation while maintaining good mode quality.[42,43]

Beam brightness from these lasers is ultimately limited by heat extraction, antiguiding, and facet damage. Heat extraction and COMD can be made less significant by increasing the amplifier length, reducing thermal densities and laterally spreading the mode at the facet. Unfortunately, antiguiding will make a longer cavity more susceptible to filamentation. These are three design parameters to balance effects in practical laser cavities.

Slab-coupled optical waveguide lasers and other large mode-volume lasers

As previously mentioned, a design consideration for high power lasers is to increase the transverse size of the mode to increase the COMD threshold. As this epitaxial waveguide grows, it will also begin to support multiple modes. Most high-power laser epitaxial structures support multiple transverse modes, although the gain is positioned to allow only one mode to oscillate. As the size is increased, however, this selection becomes more difficult.

The slab-coupled optical waveguide laser (SCOWL) is a unique design which drastically increases the size of the transverse mode up to many wavelengths while maintaining a strong mode selectivity. This structure, seen schematically in Fig. 3.6a, consists of a narrow ridge ‘gain’ section with a weak, large area waveguide beneath it. The 2-D transverse modes that are defined by the weak waveguide all have very low mode overlap with the gain region. Higher-order lateral modes, some of which have gain overlaps comparable to those of the fundamental mode, leak to the slab waveguide, and therefore remain relatively unconfined and are not effectively supported by the waveguide.[44] If one considers the slab as a waveguide coupled to the ridge, the

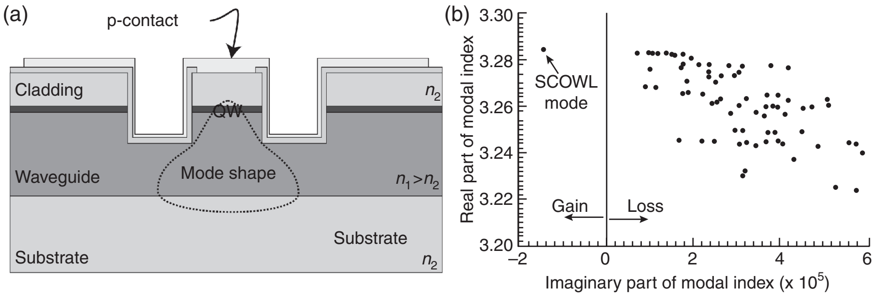

3.6 (a) Schematic cross-section of SCOWL device, with approximate mode shape defined. (b) Example of modal index (real) *vs* modal loss for many laser modes. Source: reprinted with permission from IEEE.[44]

filtering is accomplished by mode-coupling to the higher-order continuum of modes in the slab. Due to these large leaky modes, waveguide designs require very careful choices for boundary conditions, to avoid reflections from the edge of the computation window.

Figure 3.6b shows the computed modal refractive index on a rotated polar plot. The computed real part of the modal refractive index is shown along the ordinate axis. As is typical, the fundamental mode (labeled 'SCOWL Mode') has the largest refractive index, although there are many modes that have large refractive indices, commensurate with the fundamental. Along the x-axis, the modal loss is indicated for each waveguide mode. Because the higher-order modes are leaky, their leaking modal loss is large, and therefore only the fundamental mode achieves negative loss (gain).

The mode overlap remains very small (less than a percent), even for the lowest mode. As such, a longer cavity must be used to overcome other losses (e.g. mirror loss) to achieve threshold. The mode can be made almost circular, and makes packaging slightly easier because light coming from the laser facet has significantly lower divergence. Moreover, the transverse dimension of the mode can be designed to be nearly as large as the lateral mode dimension supported by a fiber, alleviating the necessity for cylindrical or aspheric optics. This last feature is extremely attractive for coupling the power to a single-mode fiber.

SCOWLs are typically many millimeters long (as much as a centimeter, or more), and lasers have achieved more than 1 W operating in CW[45] from a single device, and wavelength beam combination has allowed 30 W with an $M^2 < 2$ in both dimensions. Finally, their larger mode size reduces the significance of COMD as the facet power density is greatly reduced.

These low mode overlap lasers also have an interesting feature, a function of the small modal overlap with the gain. SCOWLs are able to create relatively high pulse-energies due to the lower gain confinement, as compared with edge-emitting lasers. The gain saturation limit is radically increased, and therefore SCOWLs can attain tens of picojoules pulses before gain saturation.[46]

Surface-emitting distributed Bragg feedback lasers

Utilizing the combination of unstable resonators to achieve large mode volumes with transverse mode selectivity, along with second-order gratings which provide surface emission and reflection simultaneously, the surface-emitting DFB (SE-DFB) has proven to be an ideal candidate for high-brightness semiconductor lasers.[47–49] This scheme has the advantage of spreading the output mode over a large area, thus avoiding the high-power densities, which can cause catastrophic optical damage often affecting high-power edge-emitting lasers. Because this area can be increased from the typical ~3 × 200 μm to ~2000 × 200 μm, the power density decreases by about 1000×, allowing for efficient, reliable power extraction.

When high-brightness output is desired, laterally increasing the extent of the device becomes necessary. The extended mode requires adjusting the local phase of the grating to tailor behavior of the laser. While any arbitrary shape may be considered, it is instructive to consider circular gratings where the radius of curvature ($R(z)$) is chosen such that each grating tooth images a point-source wavefront to another.[47,48] The radius of curvatures of these circular gratings are only a function of z, and vary according to:

$$\frac{2}{R(z)} = \frac{1}{D+z} - \frac{1}{D-z}, \tag{3.18}$$

where D is the distance from the $z = 0$ coordinate to the point sources (located symmetrically about z), and is graphically depicted in Fig. 3.7a. If the crating curves toward the center of the laser ($D < 0$), the cavity is likely to maintain geometric stability, and will allow multiple transverse modes to operate. A linear grating $(D = \pm\infty)$ will be quasi-stable and will become stable upon inclusion of thermal lensing. This type of cavity would be analogous to a cleaved-facet broad-area laser.

However, when the grating is convex toward the center ($D > 0$), the laser operates in the unstable resonator regime described earlier. Figure 3.7b represents a schematic of typical electrically-injected surface-emitting DFB laser. In this case, a patterned diffusion region is defined for current injection. A larger second-order curved-grating structure is patterned through interference lithography, and the entire device has a p-contact deposited over the surface. The device is soldered p-side down to a heat sink and the first diffraction order is collected through the substrate.

Such a laser has very strong mode discrimination, and has proven to be a very effective single-mode emitter. Single emitters have achieved powers as

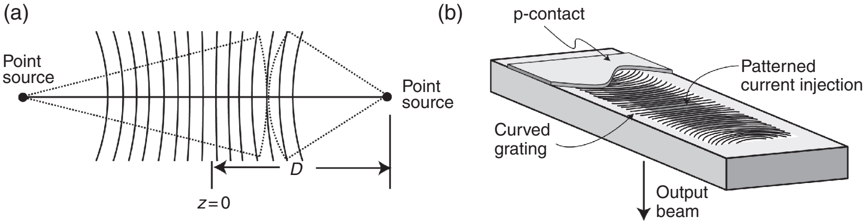

3.7 (a) Plan-view of curved grating showing curvature dependence upon position. (b) Schematic of an electrically injected surface-emitting DFB laser.

large as 73 W CW.[49] Corrections to the simplistic Equation [3.18] may be made to counteract aberrations such as thermally-induced lensing and antiguiding.

3.2.4 Vertical external-cavity surface-emitting laser

As discussed earlier in the chapter, one major drawback of high power broad-area diode lasers is their poor beam quality. Section 3.2.3 introduced several alternatives which are able to provide very good beam quality and high brightness. However, they all tend suffer from higher cavity loss and lower efficiency. Their output can be highly elliptical and the long gain regions are often sensitive to filamentation. VECSELs have been investigated as alternatives to high-power edge-emitting lasers. Essentially, VECSELs are a vertical-cavity surface-emitting laser (VCSEL) with the top DBR removed and replaced with an external curved mirror. The external-cavity optic forms a stable resonator geometry, and allows the gain extent (and hence the output power) to grow laterally in area to very large transverse sizes. The external output coupler (mirror) controls TEM_{00} operation with circular optical beam. VECSELs with good output power were first developed in the mid 1990s.[50,51] Since then major achievements have been reported on various types of materials and cavity configurations for VECSELs. Figure 3.8 shows the schematic of an OP-VECSEL cavity. The epitaxially grown VECSEL chip consists of a DBR stack and a resonant periodic gain (RPG) multi-QW structure where each semiconductor QW is placed at the antinodes of the cavity longitudinal standing wave to achieve the maximum modal gain. In order to reach multi-watt output power the active area should be several hundred microns in diameter. As a result, optical pumping is the most straightforward way to achieve uniform carrier distribution over the large pump area. Efficient heat dissipation is very critical for high-power operation. The energy difference between the pump and the lasing emission is a significant source of heat. VECSEL chips are commonly mounted on high thermal conductivity heat spreaders such as CVD diamond. Single chip VECSELs with output powers in excess of 100 W have been achieved at

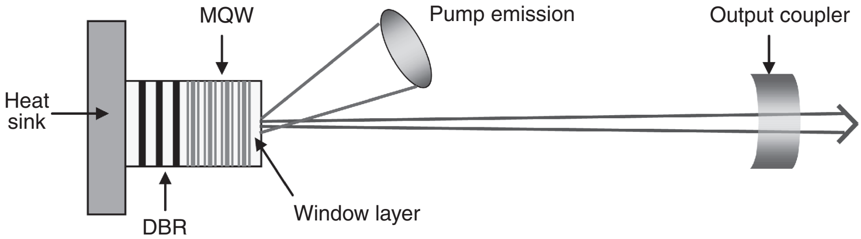

3.8 Schematic of a canonical OP-VECSEL cavity, composed of the semiconductor chip (DBR + MQW + window layer), the heat sink, the pump, and the output coupler. MQW, multi-quantum wells.

near room temperature.[52] A key property of VECSELs is their high output power with excellent beam quality, circular TEM_{00} emission. Highly efficient 20 W CW output power with an $M^2 \sim 1.3$ has been reported from a single chip VECSEL cavity.[53]

Power scaling VECSELs

As stated, increasing the VECSEL power is as easy as laterally increasing the modal size, provided the heat flow remains one-dimensional. Unfortunately, there are limitations to this growth.[54] The output power of a single chip VECSEL is limited by thermal rollover and undesired lateral lasing; these effects limit practical mode diameters to the order of 1-mm. As a coherent power scaling scheme, the multi-chip VECSEL was investigated,[55,56] and is schematically depicted in Fig. 3.9a. Compared to the single chip VECSEL, this multi-chip VECSEL has several advantages. First, the heating is distributed on various VECSEL chips instead of a single chip. The thermal rollover is delayed since less pump power on each chip is needed for achieving high-power VECSEL output, thus more pump power can be launched to the laser to achieve higher power scaling than that of the single chip VECSEL. Secondly, the multi-chip VECSEL has a much higher round-trip small signal gain than a single chip VECSEL. As a result, output couplers with lower reflectance can be used in order to increase slope efficiency or broaden the tuning range. Finally, the output of a multi-chip VECSEL remains a stable coherent beam with good beam quality, avoiding problems such as lateral lasing at each chip.

A two-chip VECSEL cavity provided over 19 W output power, doubling the maximum output power of each single chip VECSEL (see Fig. 3.9b).[56] High-brightness linearly polarized output with a tuning range of 33 nm is demonstrated in a two-chip VECSEL. A three-chip VECSEL experiment with intracavity nonlinear crystal achieved an impressive 50 W of *frequency-doubled* emission with $M^2 \sim 1.3$.[55,57]

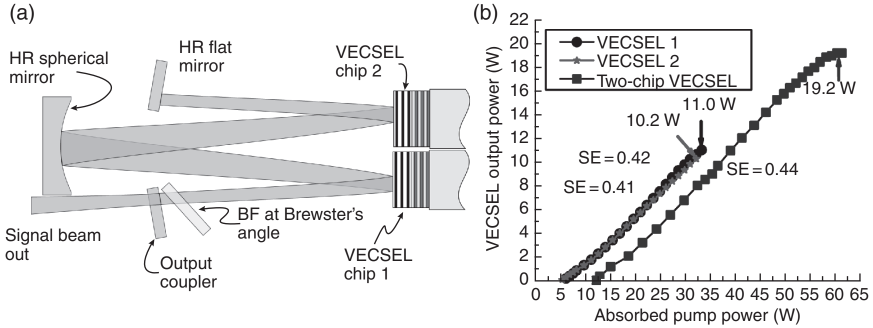

3.9 (a) Schematic setup of two-chip VECSEL (BF stands for birefringent filter and SE for slope efficiency), (b) comparison of the performance of single-chip and two-chip VECSELs.

Intracavity functionality enabling

Relatively long cavity lengths of a few centimeters in VECSELs combined with inhomogeneously broadened gain due to the width- and composition-fluctuation in multi-QWs, as well as material defects result in spectrally broad (a few nanometers) lasing emission. Having access to the laser intracavity mode allows the insertion of nonlinear elements in order to expand the high-power laser's functionality. For example, significant attention has been paid to saturable absorbing elements such as SESAMs inserted into the cavity to achieve passive mode locking. Mode-locked VECSELs with sub-picosecond pulse and high repetition rates of 50 GHz have been demonstrated.[58,59]

High-intensity lasers with high spectral purity may also be a key requirement in a variety of applications. The insertion of intracavity spectral filters, such as birefringent filters,[60] Fabry–Pérot etalons[61] or volume gratings[62] allows longitudinal-mode selection and single mode emission. Wavelength tuning can similarly be achieved by the rotation of the birefringent filter. Large wavelength tuning of over 25 nm was demonstrated utilizing a single gain element.

A unique benefit of the VECSEL is the access to the laser intracavity allowing nonlinear wavelength conversion. This has allowed the development of semiconductor VECSELs covering a very wide wavelength range from deep ultraviolet (DUV), through the visible, near-IR, mid-IR and up to terahertz regimes.[63–69] Numerous demonstrations of multi-watt blue-green lasers have been reported by frequency doubling of InGaAs/GaAs structures.[70] The use of intracavity frequency doubling in a highly-strained InGaAs/GaAs VECSEL structure resulted in 5 W yellow–orange power in the 585–589 nm bands[64] (schematic shown in Fig. 3.10a, and tuning shown in Fig. 3.10b). Intracavity nonlinear crystals allow for both up- and down-conversion, thereby spreading the wavelengths achievable with the VECSEL

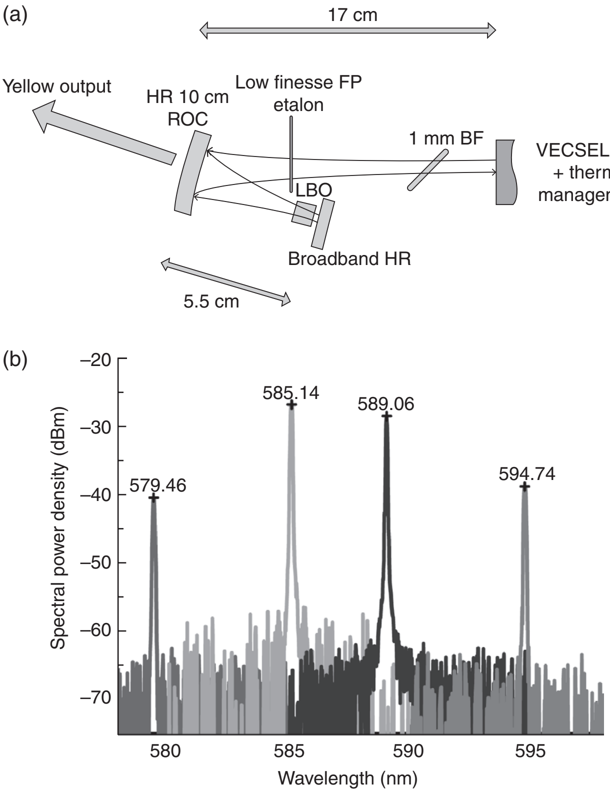

3.10 (a) Frequency-doubled, single longitudinal-mode cavity schematic (LBO is lithium triborate, ROC is radius of curvature), (b) spectra of several yellow lines selected with the intracavity birefringent filter.

from the UV through to THz frequencies. Figure 3.10b also shows the tuning capability through use of a birefringent filter, previously mentioned within this section.

3.2.5 Long-wavelength approaches (quantum cascade and type-II quantum well lasers)

Type-I[71–73] QWs are by far the most common semiconductor laser, due to their simplicity, high efficiency, and large wavelength range available, based on material systems. InGaAs/AlGaAs/GaAs-based lasers have shown excellent results in the near-infrared regime due to their ability to achieve large carrier and hole confinement structures. To achieve longer wavelengths than about 1.3 μm, one must change material systems. To reach the 1.3–1.6 μm region, the most mature material system is InGaAsP/InP,[74] which has been developed as the workhorse for telecommunications applications.

At longer wavelengths, one must utilize a smaller bandgap semiconductors, typically based on InGaSb/GaSb materials,[75–80] as thoroughly addressed in Chapter 13. This material system has produced results up to about 3.1 μm, with output power of ~80 mW at room temperature.[75] At wavelengths above 2.8 μm, degraded performance is primarily attributed to valence-band leakage and most importantly, Auger recombination, ultimately limiting laser operation.

At threshold, the current is proportional to the composite of the loss mechanisms:

$$j_{\mathrm{th}} = d_w \frac{q}{\eta_i} N_{\mathrm{th}} \left(\frac{1}{\tau_a} + \frac{1}{\tau_b} + \frac{1}{\tau_c} \right) \equiv d_w \frac{q}{\eta_i} \left(A N_{\mathrm{th}} + B N_{\mathrm{th}}^2 + C N_{\mathrm{th}}^3 \right) \equiv j_a + j_b + j_c, \quad [3.19]$$

where τ_a is the parasitic carrier lifetime due to Schockley–Read–Hall (SRH) recombination, τ_b is the result of spontaneous emission, and τ_c is due to Auger recombination. While it is an approximation, the current loss of each of these respective terms is proportional to AN_{th}, BN_{th}^2 and CN_{th}^3. The last term in Equation [3.19] becomes the dominant term at longer wavelengths (lower bandgap energies). This dependence results primarily from the approximate analytic form of bulk effective mass, where the recombination depends exponentially on the bandgap energy:

$$\frac{1}{\tau_c} \propto e^{-A \frac{E_g}{k_B T}}, \quad [3.20]$$

where A is between 0 and 0.5, depending on the exact nature of the Auger recombination process. It can be seen that the probability increases precipitously at longer wavelengths, and is nominally the shape of the measured Auger coefficients presented in Figure 3.11. Figure 3.11 shows the trend of the Auger coefficient C, as provided by US Naval Research Laboratory, where the current loss is proportional to the cube of the threshold current density. As the wavelength increases, there are a greater number of energy subbands between which transitions are probable. When comparing to 1.5 μm, the Auger coefficient increases approximately two orders of magnitude (100×) as the wavelength is doubled (by use of InAs QWs). If all else is held equal, this represents a carrier loss of 100×, which thus results in unwanted device heating.

To counter the Auger problem and extend to longer wavelengths, it becomes advantageous to look to a multi-layer QW structure. The type-II 'interband' cascade laser achieves this by confining the holes in a center 'well' while confining the electrons in layers immediately adjacent. If the

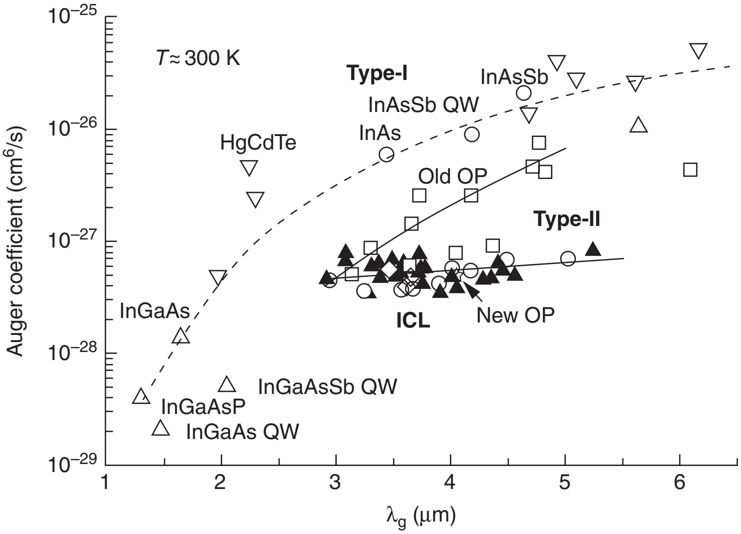

3.11 Auger recombination coefficient. Source: reported from Meyer *et al.* from several references 98–101, after reference 81.

layers are sufficiently thin, the wavefunction overlap can be considerable, with as much as 70% that of a type-I QW. This type of gain is described in greater detail in Chapter 14.

Carriers may be optically excited, and this optically pumped semiconductor laser (OPSL)[82] has demonstrated outstanding results and have been demonstrated between 2.2 and 9 μm[83] at cryogenic temperatures. At low temperatures, these devices exhibit multi-watt performance (primarily in the 3.5–5 μm band), but the output power drops off dramatically at higher temperatures. Optical pumping allows carrier 'injection' to each stage independently through strategically placed absorbing regions. One may also electrically pump the type-II laser, 'interband cascade lasers' (ICL), as carriers must be recycled from the valence band to the conduction band between stages. This carrier 'recycling' from one well to the next increases the differential quantum efficiency of these lasers. Devices based upon type-II QWs have significantly improved in recent years and are now showing promising results for high-temperature operation up to 340 K,[84] opening up the door to watt-level devices at room temperature.

For this type of active region, as one approaches room temperature, device performance can suffer dramatically if careful design is not considered. Excessive threshold power/current density is thought to be the cause in internal heating thus limiting the amount of power out prior to thermal rollover. Figure 3.12 indicates a recent critical improvement to this effect by altering not the QW but rather the cascade recycling mechanism. With

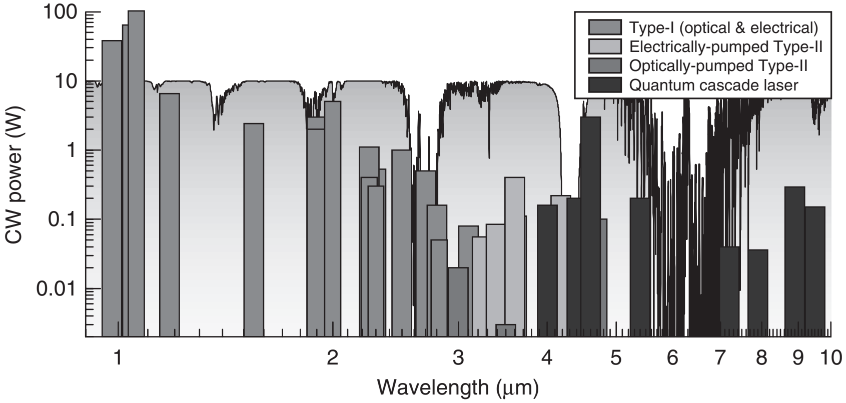

3.12 Exemplary demonstrated room-temperature continuous wave (CW) semiconductor laser operation published within the last 20 years in the near infrared (NIR), SWIR, MWIR, and LWIR.[75–93] Devices broken into type-I interband lasers, type-II optically pumped interband lasers, type-II electrically pumped interband lasers, and intersubband lasers (QCLs). Atmospheric transmission spectra (log-scale) are also shown with arbitrary units (maximum ~1).

this improvement, type-II ICLs hold a great deal of promise for filling in the region between 2.5 and 4 μm. Their operation is bound on the long-wavelength side by band-filling and blue-shifting the band-edges. On the short wavelength side, the limit is from control over the narrow center ‘well’ thickness of about four monolayers of InAs, with the unbiased bandgap of about 4 μm thick, even at low temperatures. ICLs are able to achieve modestly shorter wavelengths presumably, due to the additional energy resulting from externally applied bias. Difficulty in controlling features on this order limits the ability to achieve shorter wavelengths.

Rather than rely on conduction-to-valence-band transitions, quantum cascade lasers (QCL) are a unipolar device where energy differences between properly aligned conduction subbands result in lasing. In recent years, the QCL has made great strides in the MWIR and LWIR wavelength regimes,[85–94] increasing the room-temperature operation of single spatial mode lasers up to over 4 W, and wall-plug efficiencies up to about 20%. For shorter wavelengths, electron confinement, ‘intervalley leakage,’ surface plasmon loss, high power density, and non-uniform gain in the waveguide all diminish device performance.[95] While cryogenic temperatures have realized 3.5 μm operation, shorter wavelengths require larger ΔE_c values than are available in the commonly used InGaAs/AlInAs system.[96] An alternative of InGaAs/AlAsSb lattice matched to InP provides wells as deep as 1.6 eV,[97] and might extend QCLs to higher energies. Many state-of-the-art room-temperature CW results are reported in Fig. 3.12.

3.3 Array concept for power scaling

Single emitter maximum achievable power is limited in part by COMD and is capped by its P_{COMD}. In a single emitter laser with P_{COMD} of ~20 MW/cm^2 and an emitting aperture of 100 μm the maximum achievable power before catastrophic degradation can reach just over 20 W. In this case, a practical output power with high reliability would be significantly less than 20 W. Meanwhile power scaling by increasing the emitting aperture of a single emitter toward the millimeter regime causes unwanted amplified spontaneous emission and parasitic lasing in the lateral direction, drastically degrading the performance of the laser. In order to achieve usable outputs in the hundreds of watts and kilowatts laser bars and stacks are developed.

In a laser bar, N broad-area single emitters (N = 7–30 of them) each with an emitting aperture of approximately 100 μm are placed in a one-dimensional array providing a power scaling of almost N-times the number of a single laser. An important characteristic of a diode bar is the fill factor (FF), defined as the ratio of the pumped area to the total area of the bar. As the FF is increased the heat dissipation becomes even more critical. The thermal resistance depends on the bar geometry, including the FF and the cavity length. In general, in order to increase the maximum power high fill-factor bars with long cavities and high PCE are needed. However as the FF increases heat dissipation become even more important, which limits the increase of the FF. Also long cavities usually lead to lower slope efficiency and PCE. As a result thermal rollover is presently the main limitation in maximum achievable power in diode bars. For high-power efficient heat sinking, laser bars are mounted junction down using AuSn solder. While other solders such as indium have higher thermal conductivity, they have negative attributes such as 'solder creep', which adversely affect the package reliability. Two types of heatsink packages are widely used in commercial packages: micro channel cooled packages (MCCP) actively cooling and conductively cooled packages (CCP) passive cooling (also known as CS-Mounts). Expansion matched copper-diamond (CuD) composite carriers are widely used between the diode and the copper heat sink to both spread the heat (for improved thermal resistance) and for thermal expansion matching (allows the use of hard solder).

While diode laser bars are highly efficient devices, their beam quality is not as good as competing laser sources. To achieve the highest brightness, beam-conditioning techniques can be used in a single package. The most common form of beam conditioning is to collimate the fast axis with a single cylindrical lens. The light from individual emitter of a bar is then coupled into a separate fiber and all the fibers are bundled in a close-packed configuration.[102,103] Polarization-coupling and wavelength-multiplexing schemes are also used. For spectral linewidth stabilization VBGs can be deployed.[104]

An undesirable property of diode bars is slight bending of the emitted beam in the horizontal direction known as 'smile.' This is largely caused by the coefficient of thermal expansion (CTE) mismatch between laser bar, bonding solder and the package, casing a concave or convex near-field emission from the array. Smile error can degrade beam focusing, beam shaping and beam coupling efficiency into fiber. Optimized packaging process is critical in minimizing smile.[105] Commercial high-power laser bars have a typical smile of less than 1 μm.

In the past few years significant progress has been reported in the maximum achievable power. Minimizing operating voltage and internal loss in combination with high efficiency, long cavities lasers have been critical in higher power achievement.[6] Peak optical power in the range of 400–500 W from high FF, 1-cm wide laser bars have been demonstrated.[106–108] On a path to kW laser bars, highly efficient, two-sides cooling of the bars with 5-mm cavity length have provided impressive maximum power of over 800 W from a 77% fill factor at 25°C.[1]

Laser bars with a CW output power of 80–100 W in the 8xx–9xx nm are commercial available from several diode manufacturers. These bars have a typical fill factor of 20–50% and PCE better than 60%. Each bar is about 1 cm wide with several single emitters each with an emitting aperture of 100–150 μm. For kW output powers, laser bars are stacked together (known as 'stacks'). Commercially available stacks can deliver output powers in excess of 4 kW.

Although VCSELs have historically been restricted to low-power applications, the niche applications of large area (poor beam quality) devices which can operate with output powers approaching 100 mW. As individual lasers, they will ultimately not provide suitable output for most high-power applications. However, because the cavity is normal to the surface, their geometry is well suited to 2-D arrays. Relatively small lateral diameters (~100 μm × 100 μm) mean one may pack them very closely together. As such, arrays of thousands are not unusual, and CW powers in the hundreds of watts is readily achievable.[109]

Moreover, much as discussed in Section 3.2.2, the wavelength of the VCSEL array is significantly influenced by the Fabry–Pérot control of the short cavity between the DBR mirrors. The resulting array wavelength is narrower than typical bars of fewer broad-area lasers, and spectrally shifts less at higher powers and temperatures. In the case of VCSEL arrays, however, the limiting phenomenon is heat removal. Thermal power densities are on in the range of KW/cm^2, which are difficult to efficiently remove through most conventional means. Moreover, just as in VECSELs (Section 3.2.4), the additional heat not only reduces the peak gain, but also detunes the gain from the Fabry–Pérot cavity modes. Therefore at thermal rollover, COMD is not a particular issue because the mirrors are non-absorbing. Detuning will cause a completely reversible and non-destructive shut-off.

An alternative surface-emitting laser may be composed of surface-emitting DFB lasers, as introduced in Section 3.2.3. These cavities, while in-plane, maintain surface emission. Individual lasers are several orders of magnitude larger than VCSELs mentioned previously, although each laser provides greater power. While in principal, an entire wafer can be fabricated and assembled as a 2-D package where all devices are run in parallel, in practice, they are more often packaged as individual lasers and assembled into a two-dimensional array, to be run in series. This geometry has the advantage of reducing thermal crosstalk, making the entire array more reliable. Though it consumes approximately the same amount of electrical power, the laser array may be run in low current, high voltage mode.[104] These performance improvements, however, come at the detriment to more costly packaging.

SE-DFB arrays have low fill factor, which also provides a convenient method for beam combination by interleaving and offsetting multiple arrays. This method has resulted in 1 kW of optical power coupled into a 600 μm fiber.[49]

3.4 Conclusion and future trends

High-power semiconductor lasers have witnessed tremendous improvement in the past decade, making them the source of choice for many applications and commercial products. Recent progress in semiconductor growth, processing, passivation and packaging have resulted in efficiency, performance, reliability and cost unmatched by other laser sources. Lasers with a wide range of materials and cavity designs and a broad range of wavelengths and power are commercially available in small size for low cost. This chapter briefly outlined some of the fundamentals, design requirements and key characteristics of high-power semiconductor lasers. The key figures-of-merits are presented. Several common laser cavities including broad-area, tapered cavity, grating-based DFB or DBR lasers, optically pumped VECSEL, as well as concepts for long-wavelength operation are covered and their designs are highlighted. Their advantages and limitations are addressed and the current trends are discussed. Power scaling to kilowatts using array concept is introduced, and challenges are addressed.

3.5 References

1. Crump P., Wenzel H., Erbert G. and Tränkle G. (2009), "Advances in spatial and spectral brightness in 800–1100 nm GaAs-based high power broad area lasers," *Proc. SPIE,* **7483**, 74830B1–10.
2. Li H., Chyr I., Brown D., Reinhardt F., Romero O., Chen C.H., Miller R., Kuppuswamy K., Xu Jin, Touyen Nguyen, Towe T., Crum T., Mitchell C., Truchan T., Bullock R., Wolak E., Mott J. and Harrison J. (2007), "Next-generation

high-power, high-efficiency diode lasers at spectra-physics," *Proc. SPIE,* **6824**, 68240S.

3. Peters M., Rossin V., Everett M. and Zucker E. (2007), "High power, high efficiency laser diodes at JDSU," *Proc. SPIE*, **6456**, 64560G, 1–11.
4. Auerbach M., Weiss E. and Winhold H. (2009), "Recent developments of high-power and high brightness diodes at coherent," IEEE Conference, October 2009, 1–2.
5. Ma X. and Zhong L. (2007), "Advances in high power semiconductor diode lasers," *Proc. SPIE,* **6824**, 682402.
6. Li H., Reinhardt F., Chyr I., Jin X., Kuppuswamy K., Towe T., Brown D., Romero O., Liu D., Miller R., Nguyen T., Crum T., Truchan T., Wolak E., Mott J. and Harrison J. (2008), "High-efficiency, high-power diode laser chips, bars, and stacks", *Proc. SPIE,* **6876**, 68760G.
7. Marsh J.H. (2010), "Emerging technologies for high power diode lasers," *IEEE Photonic Society Newsletter*, PP-**47**.
8. Kanskar M., Dai Z., Earles T, Forbes D., Goodnough T., Nesnidal M, Stiers E., Botez D., Kim N., Kuech T. and Mawst L.J. (2004), "High power conversion efficiency 970 nm Aluminum-free diode lasers," LEOS 2004, Paper WC4, pp. 475–476.
9. Botez D. (1999), "Design considerations and analytical approximations for high continuous wave power, broad-waveguide diode lasers", *Appl. Phys. Lett.*, **74**(21), 3102–3104.
10. Botez D. (1999), "High-power Al-free coherent and incoherent diode lasers", *Proc. SPIE*, **3628**, 2–10.
11. Livshits D.A., Kochnev I.V., Lantratov V.M., Ledentsov N.N., Nalyot T.A., Tarasov I.S. and Alferov Zh. (2000), "Improved catastrophic optical mirror damage level in InGaAs/AlGaAs laser diodes," *Electron. Lett.*, **36**, 1848–1849.
12. Henry C.H., Petroff P.M., Logan R.A. and Merritt F.R. (1979), "Catastrophic damage of $Al_xGa_{1-x}As$ double-heterostructure laser material," *J. Appl. Phys.,* **50**(5), 3721–3732.
13. Ziegler M., Talalaev V., Tomm J.W., Elsaesser T., Ressel P., Sumpf B. and Erbert G. (2008), "Surface recombination and facet heating in high-power diode lasers," *Appl. Phys. Lett.*, **92**, 203506.
14. Bou Sanayeh M., Brick P., Schmid W., Mayer B., Müller M., Reufer M., Streubel K., Ziegler M., Tomm J.W. and Bacher G. (2008), "The physics of catastrophic optical damage in high-power AlGaInP laser diodes," *Proc. SPIE*, **6997**, 699703–1,12.
15. Hempel M., La Mattina F., Tomm J.W., Zeimer U., Broennimann R., and Elsaesser T. (2011), "Defect evolution during catastrophic optical damage of diode lasers," *Semicond. Sci. Technol.*, **26**, 075020, 1–10.
16. Tu L.W., Schubert E.F., Hong M. and Zydzik G.J. (1996), "In-vacuum cleaving and coating of semiconductor laser facets using thin silicon and a dielectric," *J. Appl. Phys*., **80**(11), 6448–6451.
17. Lammert R.M., Oh S.W., Osowski M.L., Panja C., Rudy P.T, Stakelon T.S. and Ungar J.E. (2006), "Advances in high brightness semiconductor lasers," *Proc. SPIE* **6104**, 62040I.
18. Ressel P., Erbert G., Zeimer U., Häusler K., Beister G., Sumpf B., Klehr A. and Tränkle G. (2005), "Novel passivation process for the mirror facets of Al-free

active-region high-power semiconductor diode lasers," *IEEE Photon. Techn. Lett.*, **17**, 962–964.

19. Lambert R.W., Ayling T., Hendry A.F., Carson J.M., Barrow D.A., McHendry S., Scott C.J., McKee A. and Meredith W. (2006), "Facet-passivation processes for the improvement of Al-containing semiconductor laser diodes," *J. Lightwave Technol.*, **24**, 956–961.
20. Walker C.L., Bryce A.C. and Marsh J.H. (2002), "Improved catastrophic optical damage level from laser with nonabsorbing mirrors," *IEEE Photon. Tech. Lett.*, **14**, 1394–1396.
21. Silfvenius C., Blixt P., Lindstrom C. and Feitisch A. (2003), "Native-nitride passivation eliminates facet failure," *Laser Focus World*, **39**, 69–73.
22. Yasui K., Tsukada Y., Arayama T., Okutani S. and Akahane T. (2001), "Characterization of the surface layer of GaAs nitride by high-density plasma," *Appl. Surf. Sci.*, **175–176**, 585–590.
23. Bessolov V.N., Lebedev M.V., Shernyakov Y.M. and Tsarenkov B.V. (1997), "Sulfur passivation of InGaAs/AlGaAs SQW laser (977 nm) facets in alcohol-based solutions," *Mater. Sci. Eng.*, **B44**, 380–382.
24. Hu M., Kinney L.D., Emmanuel E.C., Ouyang M.X. and Zah C. (2003), "Passivation of semiconductor laser facet," US patent 6618409.
25. Lammert R.M., Osowski M.L., Oh S.W., Panja C. and Ungar J.E. (2006), "High power (>10 W from 100 μm aperture) high reliability 808nm InAlGaAs broad area laser diodes," *Electron Lett.*, **42**, 535.
26. Hülsewede R., Schulze H., Sebastian J., Schröder D., Meusel J. and Hennig P. (2007), "Highly reliable, high-power AlGaAs/GaAs 808 nm diode laser bars," *Proc. SPIE*, **6456**, 645607–1-8.
27. Bao L., Wang J., Devito M., Xu D., Grimshaw M., Dong W., Guan X., Huang H., Leisher P., Zhang S., Wise D., Martinsen R. and Haden J. (2011), "Performance and reliability of high power 7xx nm laser diodes," *Proc. SPIE*, **7953**, 79531B-1–12.
28. Welch D.F., Cardinal M., Streifer B. and Scifres D. (1990), "High-power single mode InGaAs/AlGaAs laser diodes at 910nm," *Electron. Lett.*, **26**, 233.
29. Ventrudo B.F. and Rogers G. (1996), "Fibre-grating stabilized diode laser," USPTO 5485481.
30. Venus G.B., Sevian A., Smirnov V.I. and Glebov L.B. (2005), "High-brightness narrow-line laser diode source with volume Bragg-grating feedback," *P. Soc. Photo-Opt. Ins.*, SPIE Vol. **5711**, 166–176.
31. Kaneda Y., Fan L., Hsu T.C., Peyghambarian N., Fallahi M., Zakharian A.R., Hader J., Moloney J.V., Stoltz W., Koch S., Bedford R., Sevian R.A. and Glebov L. (2006), "High brightness spectral beam combination of high-power vertical-external-cavity surface-emitting lasers," *IEEE Photon. Tech. Lett.*, **18**(17), 1795–1797.
32. Andrusyak O., Smirnov V., Venus G., Rotar V. and Glebov L. (2009), "Spectral combining and coherent coupling of lasers by volume Bragg gratings," *IEEE J. Sel. Top. Quant. Elect.*, **15**(2), 344–353.
33. Fricke J., Bugge F., Ginolas A., John W., Klehr A., Matalla M., Ressel P., Wenzel H. and Erbert G. (2010), "High-power 980-nm broad-area lasers spectrally stabilized by surface Bragg gratings," *IEEE Photon. Tech. Lasers*, **22**, 5.
34. Kanskar M., Cai J., Galstad C., He Y., Macomber S.H., Stiers E. and Tatavarti-Bharatam S.R. (2006), "High power conversion efficiency and wavelength

stabilized, narrow bandwidth 975nm diode laser pumps," *Proc. SPIE*, **6216**, 621609.

35. Paschke K., Guther K.R., Fricke J., Sebastian J., Knauer A., Wenzel H., Erbert G., Trankle G., Bogatov A.P., Drakin A.E. and Stratonnikov A.A. (2002), "Design, fabrication and characterization of high-power angled-grating distributed-feedback lasers," *IEEE Semiconductor Laser Conference*.
36. Henry C.H. (1982), "Theory of the linewidth of semiconductor lasers," *IEEE J. Quant. Electron.*, **QE-18**(2), 259–264.
37. Van der Ziel J. P. (1979), "Spectral broadening of pulsating $Al_xGa_{1-x}As$ double heterostructure lasers," *IEEE J. Quant. Electron.*, **QE-15**(11), 1277–1281.
38. Andrews J.R. (1986), "Traveling-wave amplifier made from a laser diode array," *Appl. Phys. Lett.*, **48**(20), 1331–1333.
39. Siegman A.E. (1986), *Lasers*, University Sciences Books, California.
40. Bedford R. and Fallahi M. (2002), "Semiconductor unstable resonators with laterally finite mirrors," *IEEE J. Quantum. Electron.*, **38**(7), 716–723.
41. Spreemann M., Wenzel H., Eppich B., Lichtner M. and Erbert G. (2011), "Novel approach to finite-aperture tapered unstable resonator lasers," *IEEE J. Quant. Electron.*, **47**(1), 117–125.
42. O'Brien S., Mehuys D., Lang R.J. and Welch D.F. (1995), "1 W CW single frequency, diffraction-limited unstable resonator semiconductor laser with distributed Bragg reflector mirrors," *Electron. Lett.*, **31**(3), 203–205.
43. Kelemen M.T., Weber J., Rinner F., Rogg J., Mikulla M. and Weimann G. (2003), "High-brightness 1040-nm tapered diode lasers," *Proc. SPIE*, **4947**, 252.
44. Walpole J.N., Donnelly J.P, Taylor P.J., Missaggia L.J., Harris C.T., Bailey R.J., Napoleone A., Groves S.H., Chinn S.R., Huang R. and Plant J. (2002), "Slab-coupled 1.3-μm semiconductor laser with single-spatial large-diameter mode," *IEEE Photon. Tech. Lett.*, **14**(6), 756–758.
45. Huang R.K., Donnelly J.P., Missaggia L.J., Harris C.T., Plant J., Mull D.E. and Goodhue W.D. (2003), "High-power nearly diffraction-limited AlGaAs-InGaAs semiconductor slab-coupled optical waveguide laser," *IEEE Photon. Tech. Lett.*, **15**(7), 900–902.
46. Ahmad F.R. and Rana F. (2008), "Passively mode-locked high-power (210 mW) semiconductor lasers at 1.55-μm wavelength," *IEEE Photon. Tech. Lett.*, **20**(3), 190–192.
47. Macomber S.H., Mott J.S., Schwartz B.D., Setzko R.S., Powers J.J., Lee P.A., Kwo D.P., Dixon R.M. and Logue J.E. (1997), "Curved-grating, surface-emitting DFB lasers and arrays," *Proc. SPIE*, **3001**, 0277.
48. Noll J. Macomber S.H. (1990), "Analysis of grating surface emitting lasers," *IEEE J. Quant. Electron.*, **26**(3), 456–466.
49. Kanskar M., Cai J., Kedlaya D., Olson D., Xiao Y., Klos T., Martin M. and Galstad C. (2010), "High brightness 975 nm surface-emitting distributed feedback laser & arrays," *Proc. SPIE*, **7686**, 76860J.
50. Kuznetsov M., Hakimi F., Sprague R. and Mooradian A. (1997), "High-power (>0.5-W CW) diode-pumped verticalexternal-cavity surface-emitting semiconductor lasers with circular TEM00 beams," *IEEE Photon. Technol. Lett.*, **9**, 1063–1065.
51. Kuznetsov M., Hakimi F., Sprague R. and Mooradian A. (1999), "Design and characteristics of high-power (>0.5-W CW) diode-pumped vertical external-cavity

surface-emitting semiconductor lasers with circular TEM00 beams," *IEEE J. Sel. Top. Quantum Electron.*, **5**, 561–573.

52. Heinen B., Wang T.-L., Sparenberg M., Weber A., Kunert B., Hader J., Koch S.W., Moloney J.V., Koch M. and Stolz W. (2012), "106 W continuous-wave output power from vertical-external-cavity surface-emitting laser," *Electron. Lett.*, **48**, 516–517.
53. Rudin B., Rutz A., Hoffmann M., Maas D.J.H.C., Bellancourt A.R., Gini E., Sudmeyer T. and Keller U. (2008), "Highly efficient optically pumped vertical-emitting semiconductor laser with more than 20 W average output power in a fundamental transverse mode," *Opt. Lett.*, **33**, 2719–2721.
54. Bedford R., Kolesik M., Chilla J.L.A., Reed M., Nelson T. and Moloney J. (2005), "Power-limiting mechanisms in VECSELs," *Proc. SPIE*, **5814**, 199.
55. Hunziker L.E., Shu Q.Z., Bauer D., Ihli C., Mahnke G.J., Rebut M., Chilla J.R., Caprara A.L., Zhou H., Weiss E.S. and Reed M.K. (2007), "Power scaling of optically pumped semiconductor lasers," *Proc. SPIE*, **6451**(1), 64510A.
56. Fan L., Fallahi M., Hader J., Zakharian A.R., Moloney J.V., Murray J.T., Bedford R., Stolz W. and Koch S.W. (2006), "Multichip vertical-external-cavity surface emitting lasers: a coherent power scaling scheme," *Opt. Lett.*, **31**, 3612–3614.
57. Chilla J., Shu Q.Z., Zhou H., Weiss E., Reed M. and Spinelli L. (2007), "Recent advances in optically pumped semiconductor lasers," *Proc. SPIE*, **6451**, 645109.
58. Aschwanden A., Lorenser D., Unold H.J., Paschotta R., Gini E. and Keller U. (2005), "2.1-W picosecond passively modelocked external-cavity semiconductor laser," *Opt. Lett.*, **30**, 272–274.
59. Lorenser D., Maas D., Unold H.J., Bellancourt A.R., Rudin B., Gini E., Ebling D. and Keller U. (2006), "50-GHz passively mode-locked surface-emitting semiconductor laser with 100-mW average output power," *IEEE J. Quantum Electron.*, **42**, 838–847.
60. Fan L., Fallahi M., Murray J.T., Bedford R., Kaneda Y., Zakharian A.R., Hader J., Moloney J.V., Stolz W. and Koch S.W. (2006), "Tunable high-power high-brightness linearly polarized vertical-external-cavity surface-emitting lasers," *Appl. Phys. Lett.*, **88**, 021105-1-021105-3.
61. Baili G., Alouini M., Dolfi D., Bretenaker F., Sagnes I. and Garnach A. (2007), "Shot-noise-limited operation of a monomode high-cavity-finesse semiconductor laser for microwave photonics applications," *Opt. Lett.*, **32**, 650–652.
62. Giet S., Sun H.D., Calvez S., Dawson M.D., Suomalainen S., Harkonen A., Guina M., Okhotnikov O. and Pesa M. (2006), "Spectral narrowing and locking of a vertical-external-cavity surface-emitting laser using an intracavity volume Bragg grating," *IEEE Photon. Technol. Lett.*, **18**, 1786–1788.
63. Kaneda Y., Yarborough J.M., Li L., Peyghambarian N., Fan L., Hessenius C., Fallahi M., Hader J., Moloney J.V., Honda Y., Nishioka M., Shimizu Y., Miyazono K., Shimatani H., Yoshimura M., Mori Y., Kitaoka Y. and Sasaki T. (2008), "Continuous-wave all-solid-state 244nm deep-ultraviolet laser source by fourth-harmonic generation of an optically pumped semiconductor laser using CsLiB6O10 in an external resonator," *Opt. Lett.*, **33**, 1705–1707.
64. Fallahi M., Fan L., Kaneda Y., Hessenius C., Hader J., Li H., Moloney J.V., Kunert B., Stolz W., Koch S.W., Murray J. and Bedford R. (2008), "5-W yellow laser by intracavity frequency doubling of high-power vertical-external cavity surface-emitting laser," *IEEE Photon. Technol. Lett.*, **20**, 1700–1702.

65. Hastie J., Calvez S., Dawson M., Leinonen T., Laakso A., Lyytikainen J. and Pessa M. (2005), "High power CW red VECSEL with linearly polarized TEM00 output beam," *Opt. Express*, **13**, 77–81.
66. Lindberg H., Strassner M., Gerster E., Bengtsson J. and Larsson A. (2005), "Thermal management of optically pumped long-wavelength InP-based semiconductor disk lasers," *IEEE J. Sel. Top. Quantum Electron.*, **11**, 1126–1134.
67. Hopkins J.M., Maclean A.J., Burns D., Riis E., Schulz N., Rattunde M., Manz C., Kohler K. and Wagner J. (2007), "Tunable, single-frequency, diode pumped 2.3 mm VECSEL," *Opt. Express*, **15**, 8212–8217.
68. Rahim M., Khiar A., Felder F., Fill M. and Zogg H. (2009), "4.5 µm wavelength vertical external cavity surface emitting laser operating above room temperature," *Appl. Phys. Lett.*, **94**, 201112.
69. Scheller M., Yarborough J.M., Moloney J.V., Fallahi M., Koch M. and Koch S.W. (2010), "Room temperature continuous wave milliwatt terahertz source," *Opt. Express*, **18**, 27112–27117.
70. Calvez S., Hastie J.E., Guina M., Okhotnikov O.G. and Dawson M.D. (2009), "Semiconductor disk lasers for the generation of visible and ultraviolet radiation," *Laser Photon. Rev.*, **3**(5), 407–434.
71. Chilla J., Butterworth S., Zeitschel A., Charles J., Caprara A., Reed M. and Spinelli L. (2003), "High power optically pumped semiconductor lasers," *SPIE Photonics West*, **5332**, 143–150.
72. Hader J., Hardesty G., Wang T.L., Yarborough M.J., Kaneda Y., Moloney J.V., Kunert B., Stolz W. and Koch S.W. (2010), "Predictive microscopic modeling of VECSELs," *IEEE J. Quantum Electron.*, **46**(5), 810–817.
73. Moloney J.V., Hader J., Wang, T.-L., Ying, Y., Kaneda, Y., Yarborough, J.M., Rotter T. J., Balakrishnan G., Hains C., Koch S.W., Stolz W., Kunert B. and Bedford R. (2009), "Power scaling of cw and pulsed IR and mid-IR OPSLs", *Proc. SPIE*, **7991**(1), 79190S.
74. Heo D.C., Han I.K., Lee J.I. and Jeong J.C. (2003), "Maximum power CW 2.45-W 1.55-µm InGaAsP laterally tapered laser diodes," *J. Korean Phys. Soc.*, **43**, 352–356.
75. Shterengas L., Belenky G., Kipshidze G. and Hosoda T. (2008), "Room temperature operated 3.1µm type-I GaSb-based diode lasers with 80mW continuous wave output power," *Appl. Phys. Lett.*, **92**, 171111.
76. Shterengas L., Belenky G.L., Kim J.G. and Martinelli R.U. (2004), "Design of high-power room-temperature continuous-wave GaSb-based type-I quantum-well lasers with λ > 2.5 µm," *Semicond. Sci. Tech.*, **19**, 655.
77. Guina M., Härkönen A., Suomalinen S., Paajaste J., Koskinen R., Pessa M. and Okhotnikov O. (2009), "GaSb based compounds tailored for MID-IR disk lasers," *SPIE*, **7193**, 71931F.
78. Hempler N., Hopkins J.M., Rattunde M., Rosener B., Moser R., Manz C., Kohler K., Wagner J. and Burns D. (2009), "Tuning and brightness optimization of high-performance GaSb-based semiconductor disk lasers from 1.86 to 2.80 µm," European Conference on Lasers and Electro-Optics 2009 and the European Quantum Electronics Conference. CLEO Europe-EQEC 2009.
79. Wagner J., Hugger S., Rösener B., Fuchs F., Rattunde M., Yang Q., Bronner W., Aidam R., Köhler K., Raab M., Romasew E. and Tholl H.D. (2009), "Infrared semiconductor laser modules for DIRCM applications," *SPIE*, **7483**, 74830F.

80. Belenky G.L., Kim J.G., Shterengas L., Gourevitch A. and Martinelli R.U. (2004), "High-power 2.3 μm laser arrays emitting 10 W CW at room temperature," *Electron. Lett.*, **40**(12), 737–738.
81. Meyer J.R., Felix C.L., Bewley W.W., Vurgaftman I., Aifer E.H., Olafsen L.J., Lindle J.R., Hoffman C.A., Yang M.J., Bennett B.R., Shanabrook B.V., Lee H., Lin C.H., Pei S.S. and Miles R.H. (1998), "Auger coefficients in type-II InAs/$Ga_{1-x}In_xSb$ quantum wells," *Appl. Phys. Lett.*, **73**(20), 2857–2859.
82. Bewley W.W., Felix C.L., Vurgaftman I., Stokes D.W., Olafsen L.J., Aifer E.H., Meyer J.R., Yang M.J., Shanabrook B.V., Lee H., Martinelli R.U., Connolly J.C. and Sugg A.R. (1999), "High-temperature continuous-wave operation of optically-pumped type-II W lasers from 3–6.3 μm," summaries of papers presented at the Conference on Lasers and Electro-Optics. (CLEO'99), 366.
83. Dente G.C., Tilton M.L., Ongstad A.P. and Kaspi R. (2008), "Wavelength tuning predictions and experiments for type II antimonide lasers," *J. Appl. Phys.*, **103**(2), 023106–1.
84. Lindle J.R., Kim C.S., Kim M., Bewley W.W., Canedy C.L., Vurgaftman I. and Meyer J.R. (2009), "High-performance interband cascade lasers emitting in the 2.9–4.2 μm wavelength range," *SPIE*, **7230**, 72300R.
85. Blaser S., Yarekha D.A., Hvozdara L., Bonetti Y., Muller A., Giovannini M. and Faist J. (2005), "Room-temperature, continuous-wave, single-mode quantum-cascade lasers at λ:5.4 μm," *Appl. Phys. Lett.*, **86**(4), 041109.
86. Troccoli M., Corzine S., Bour D., Zhu J., Assayag O., Diehl L., Lee B.G., Hofler G. and Capasso F. (2005), "Room temperature continuous-wave operation of quantum-cascade lasers grown by metalorganic vapour phase epitaxy," *Electron. Lett.*, **41**, 1059–1060.
87. Muller A., Blaser S., Hvozdara L. and Page H. (2006), "Single mode room-temperature CW operation and high power pulsed operation of quantum cascade lasers," *Laser Applications to Chemical, Security and Environmental Analysis*, page MD3. Optical Society of America.
88. Yu J.S., Slivken S., Evans A., Darvish S.R., Nguyen J. and Razeghi M. (2006), "High-power λ ~ 9.5 μm quantum-cascade lasers operating above room temperature in continuous-wave mode," *Appl. Phys. Lett.*, **88**(9), 091113.
89. Yu J.S., Darvish S.R., Evans A., Nguyen J., Slivken S. and Razeghi M. (2006), "Room-temperature continuous wave operation of quantum-cascade lasers at λ~4μm," *Appl. Phys. Lett.*, **88**(4), 041111.
90. Fujita K., Furuta S., Sugiyama A., Ochiai T., Edamura T., Akikusa N., Yamanishi M. and Kan H. (2007), "Room temperature, continuous-wave operation of quantum cascade lasers with single phonon resonance-continuum depopulation structures," *Appl. Phys. Lett.*, **14**, 141121-1–141121-3.
91. Fujita K., Furuta S., Sugiyama A., Ochiai T., Ito A., Edamura T., Akikusa N., Yamanishi M. and Kan H. (2008), "Room temperature, CW operation of 5.2 μm quantum cascade lasers with simple ridge structures, grown by MOVPE," *Conference on Lasers and Electro-Optics/Quantum Electronics and Laser Science Conference and Photonic Applications Systems Technologies*, p. CTuF1. Optical Society of America.
92. Yu J.S., Slivken S., Evans A. and Razeghi M. (2008), "High-performance, continuous-wave quantum-cascade lasers operating up to 85C at 8.8 μm," *Appl. Phys. A Mater.*, **93**(2), 405–408.

93. Bai Y., Darvish S.R., Slivken S., Zhang W., Evans A., Nguyen J. and Razeghi M. (2008), "Room temperature continuous wave operation of quantum cascade lasers with watt-level optical power," *Appl. Phys. Lett.*, **92**(10), 101105.
94. Tsekoun A., Lyakh A., Maulini R., Lane M., Macdonald T., Go R. and Patel C. (2009), "High power and efficiency quantum cascade laser systems for defense and security applications," *Society of Photo-Optical Instrumentation Engineers (SPIE) Conference Series*, **7325**, 73250L-1–73250L-7.
95. Razeghi M., Evans A., Slivken S. and Yu J.-S. (2005) "High-power CW quantum cascade lasers: how short can we go?" *Proc. SPIE*, **5738**, 1–12.
96. Revin D.M., Cockburn J.W., Steer M.J., Zhang S., Wilson L.R., Hopkinson M. and Airey R.J. (2007), "Short wavelength InGaAs-AlAsSb-InP quantum cascade lasers," *Lasers and Electro-Optics Society, 2007. LEOS 2007. The 20th Annual Meeting of the IEEE*, Piscataway, NJ, USA, 705–706.
97. Revin D.G., Zhang S., Steer M.J., Airey R.J., Krysa A.B., Hopkinson M., Wilson L.R., Menzel S. and Cockburn J.W. (2008), "Short-wavelength quantum cascade lasers," *SPIE*, **6909**, 69090V.
98. Flatte M.E., Hasenberg T.C., Olesberg J.T., Anson, S.A., Boggess T.F., Yan C. and McDaniel F.L. Jr. (1997), "III-V interband 5.2 μm laser operating at 185 K," *Appl. Phys. Lett.*, **71**, 3764.
99. Flatté M.E., Grein C.H., Hasenberg T.C., Anson S.A., Jang D.J., Olesberg J.T. and Boggess T.F. (1999), "Carrier recombination in narrow-gap semiconductor superlattices," *Phys. Rev. B*, **59**, 5745–5750.
100. Lindle J.R., Meyer J.R., Hoffman C.A., Bartoli F.J., Turner G.W. and Choi H.K. (1995), "Auger lifetime in InAs, InAsSb, and InAsSb-InAlAsSb quantum wells," *Appl. Phys. Lett.*, **67**, 3153.
101. McCahon S.W., Anson S.A., Jang D.J., Flatte M.E., Boggess T.F., Chow D.H., Hasenberg T.H. and Grein C.H. (1996), "Carrier recombination dynamics in a (GaInSb/InAs)/AlGaSb superlattice multiple quantum," *Appl. Phys. Lett.*, **68**, 2135.
102. Apter M.M. and Leibreich F. (2006), "High-power diode-laser bars come of age," *Laser Focus World*, **42**, 91–94.
103. Fan T.Y. (2005), "Laser beam combining for high-power, high-radiance sources," *IEEE J. SEL. Top. Quant. Electron.*, **11**, 567–577.
104. Karlsen S.R., Price R.K., Reynolds M., Brown A., Mehl R., Patterson S. and Martinsen R.J. (2009), "100-W, 105-, 0.15NA fiber coupled laser diode module," *Proc. SPIE*, **7198–29**, 71980-1-71980-8.
105. Wang J., Yuan Z., Kang L., Yang K., Zhang Y. and Liu X. (2009), "Study of the mechanism of "smile" in high power diode laser arrays and strategies in improving near-field linearity," 59th Electronic Components and Technology Conference, 837–842.
106. Sebastian J., Schulze H., Hülsewede R., Hennig P., Meusel J., Schröder M., Schröder D. and Lorenzen D. (2007), "High brightness high power 9xx nm diode laser bars: Developments at JENOPTIK diode lab," *Proc. SPIE*, **6456**, 64560F, 1–11.
107. Li H., Towe T., Chyr I., Brown D., Nguyen T., Reinhardt F., Jin X., Srinivasan R., Berube M., Truchan T., Bullock R. and Harrison J. (2007), "Near 1 kW of continuous-wave power from a single high-efficiency diode-laser bar," *IEEE Photon. Techn. Lett.*, **19**, 960–962.

108. Crump P., Patterson S., Wang J., Dong W., Grimshaw M., Zhang S., Elim S., Bougher M., Patterson J., Das S., Wise D., DeFranza M., Bell J., Farmer J., DeVito M. and Martinsen R. (2006), "Diode laser bars deliver > 400-W peak CW power from 800-nm to 980-nm, enabling wide range of applications," *Proc. SPIE*, **6397**, 639706.
109. Seurin J.F., Ghosh C.L., Khalfin V., Miglo A., Xu G., Wynn J.D., Pradhan P. and D'Asaro L.A. (2008), "High-power high-efficiency 2D VCSEL arrays," *Proc. SPIE*, **6908**, 690808.

4

Semiconductor laser beam combining

B. LIU, Oak Ridge National Laboratory, USA,
P. COLET, Instituto de Fisica Interdisciplinary
Sistemas Complejos, IFISC (CSIC-UIB), Spain and
Y. BRAIMAN, Oak Ridge National Laboratory
and University of Tennessee, USA

DOI: 10.1533/9780857096401.1.121

Abstract: In this chapter, we will review recent advances and trends in phase locking of broad-area laser diode arrays. In particular, we will concentrate on coherent phase locking of high-power, broad-area diode arrays in a passive external cavity. We will present a newly designed external cavity called the V-shape external Talbot cavity. The V-shape external cavity is capable of selecting single transverse mode operation of individual laser diodes on an array and providing optical coupling among laser diodes. The high visibility far-field interference pattern confirms that phase locking is achieved among laser diodes on an array. Two experimental schematic designs of the V-shape external Talbot cavity are explored. One is the V-shape external Talbot cavity, and the other is the closed V-shape external Talbot cavity. The differences in external cavity design and performance will be discussed.

Key words: semiconductor, laser beam combining, Talbot external cavity, Lang–Kobayashi model.

4.1 Introduction to laser beam combining

Laser beam combining provides the means to achieve high power emission with excellent beam quality and reduced thermal management requirements. Several types of laser beam combining technologies have been explored in the past. Two types have been most extensively studied: (a) wavelength (spectral) beam combining and (b) coherent beam combining.[1]

Wavelength (spectral) beam combining technology provides perfect spatial overlapping of laser beams.[2–7] The beam quality of combined lasers is limited by the beam quality of single lasers. The near diffraction-limited beam is achieved by using a 100-element, 100-micron pitch array of slab-coupled optical waveguide lasers (single transverse mode lasers).[3,4] Wavelength beam combining technology is also applicable for beam combining in fiber lasers.[5] However, the wavelength beam combining trades high spatial brightness for relatively large spectral bandwidth.

For high-efficiency non-linear optic processes, such as second harmonic and terahertz generation, both a high quality laser beam and narrow spectral line-width are required. Coherent beam combining provides a very promising methodology to simultaneously achieve excellent beam quality (near diffraction-limited beam) and narrow spectral line-width.[8–27] Potential application fields for high power coherent beam include directed energy, space and underwater communication.

Coherent beam combining achieves increased brightness by maintaining a narrow spectral bandwidth. In order to achieve coherent beam combining, the crucial step is locking the phase of the combined lasers. In general, there are two ways to achieve phase locking among lasers. The first is active control. A typical example of active control is the master oscillator power amplifier (MOPA) architecture, accompanied by the active phase control loop. In the MOPA design, a stable master laser is used to injection-lock the slave laser frequency, while the fast electronic phase control loop is used to compensate the phase difference among lasers. The MOPA design requires a fast response phase control loop over all the lasers, which introduces a significant challenge, in particular when very large laser arrays are being considered.[9–11]

Compared with active phase locking, passive phase locking schemes require optical coupling among lasers instead of external electrical control.[8,15–18,20–27] Such designs are relatively simple and have been extensively studied. Evanescent wave coupling[12–14] and the external Talbot cavity are two prevalent approaches to achieving passive phase locking. The external Talbot cavity technology has been successfully used for single-mode laser diode array phase locking. The optical coupler provides the diffraction feedback which is normal to the front facet of the laser diode. This configuration has been successfully applied to an array of single-mode laser diodes. In order to increase the output power of the array and maintain the single transverse mode, the tapered laser diode was designed.[19] The tapered laser diode can provide near-diffraction-limited, high power coherent emission by means of a combination of a single-mode ridge structure and a tapered amplifier structure. Coherent beam combining of a tapered laser diode array has been investigated by a number of groups.[20–21] Phase locking of a tapered laser diode array with an external Talbot cavity was demonstrated with coherent emission power close to 1.7 W.[21] Recently, an important effort to develop high-brightness slab-coupled optical waveguide laser (SCOWL) arrays was demonstrated. The SCOWL coherent beam combining with 7.2 W output power was achieved using an external Talbot cavity.[23]

Broad-area laser diode technology with a large optical cavity (LOC) structure is well developed. It provides high electro-optic conversion efficiency of around 50%. Specially designed efficient broad-area lasers could reach 70% electro-optic conversion efficiency. Broad-area lasers emit high output power and have long life times. The fabrication process of broad-area laser diode is relatively simple. Consequently, high power broad-area laser diodes (BA-LD) are widely used in a wide variety of applications, such as material processing, illumination, spin-exchange optical pumping (SEOP), alkali laser, solid state and fiber laser pumping.

In order to increase the total output power, multiple BA-LDs are fabricated in a linear array on a monolithic chip. Each laser emitter has multi-transverse and multi-longitudinal modes, since the emitter size is around 100 μm or even wider. For the broad-area laser diode array (BA-LDA), the free-running spectrum bandwidth (FWHM) is 2 ~ 3 nm, and the beam divergence is around 120 mrad along the slow-axis. Poor beam quality and broad spectrum impose a significant limitation on applications of high power BA-LDAs. To improve beam quality and narrow spectral bandwidth of BA-LDA, a variety of external cavities have been considered and we will discuss this topic in the following sections.

Applications of the external cavity BA-LDA are mainly classified into three categories: (1) applications that require a narrow spectral line-width laser source with minimal requirement on the beam quality; (2) applications that require a laser source with excellent spatial beam quality and minimal requirements on the spectral line-width; and (3) applications that require a coherent laser source with narrow spectral line-width and excellent spatial beam quality.

Applications such as SEOP and the diode-pumped alkali laser (DPAL) fall into the first category. Spectral line-width narrowing is important in increasing optical pumping efficiency.[28–35] There are two different external cavity approaches to narrowing the spectral line-width. One approach is of using external cavity with a plane diffraction grating.[28–32] The other is of using an external cavity comprising a volume Bragg grating (VBG) and beam-transform optics.[33–35] Normally, the plane diffraction grating external cavity provides a wider wavelength tunable range, while the VGB external cavity generates a narrower spectral line-width.

On the other hand, for applications such as material processing, illumination, and solid state and fiber laser pumping, beam quality is the key factor for effective energy delivery. Wavelength (spectral) beam combining meets the need for second category. Indeed the BA-LDA was used in the first wavelength beam combining experiment.[2] The beam quality of wavelength beam combining is limited by the beam quality of a single BA-LD. In order to achieve the diffraction limit beam quality, the single transverse mode laser diode is highly desirable. Recently, a diffraction-limited combined beam was demonstrated by using an array of single-mode laser diodes (SCOWL array).[3–4]

Coherent beam combining belongs to the third category. Coherent beam combining was successfully demonstrated using an array of single-mode laser diodes.[15–18] However, the multi-transverse mode emission of a broad-area laser diode will destroy coherent interference at the far-field.

A well-designed amplitude mask can be placed into an external BA-LDA Talbot cavity to limit the transverse mode excitation. The single-lobe coherent addition was demonstrated at relatively low power level.[25] Achieving phase locking by regular external Talbot cavity seems very challenging.

In the past two decades, single transverse mode operation has been demonstrated for both single BA-LD and multi-stripe laser diode array based on off-axis external cavity feedback.[36–42] The off-axis feedback generated by a stripe mirror (aperture-limited mirror) provides the angle-selective feedback which allows only specific angle radiation. A plane diffraction grating replaces the stripe mirror and provides both angle and spectrum-selective feedback to a BA-LD. The BA-LD generates single transverse mode, narrow spectral line-width coherent radiation by the grating feedback. Recently, the above off-axis feedback scheme was studied in BA-LDA.[43–44] The stripe mirror array provided each BA-LD off-axis feedback. Therefore, the entire array beam divergence angle was reduced to 26 mrad at high power level without controlling the laser spectral line-width. For a more advanced design, the VBG or aperture-limited mirror can be used to provide angle-selective off-axis feedback. The beam quality of the entire array was improved and spectral line-width was reduced to 0.3 nm by VBG feedback. But in those systems there was no interference pattern to indicate that phase locking was achieved. Achieving high power and narrow spectral line-width coherent beam combining from BA-LDA still remains a significant challenge.

In our work we proposed and implemented an external cavity design which combines the advantages of single transverse mode control from the single BA-LD off-axis external cavity and phase locking from an array of single-mode laser diodes external Talbot cavity. The newly designed external cavity forces each BA-LD to oscillate at single transverse mode and provides optical coupling among BA-LDs. The twin off-axis beam from a single high-order BA-LD mode is spatially separated by two prism mirrors and each beam is bent 90 degrees by a prism mirror.

Therefore, there is sufficient space to build up the external Talbot cavity. The two prism mirrors, laser diode array, transform optics and diffraction grating form an external cavity. We call such an external cavity scheme a V-shape external cavity, since the reflecting surfaces of the two prism mirrors form a V-shape. Our experiment demonstrates coherent addition from a high power BA-LDA based on both the V-shape external cavity and the closed V-shape external cavity.

Both the V-shape external and the closed-V-shape external cavities provide single transverse mode selection for each individual BA-LD on an array and optical coupling among BA-LDs. When shifting the grating to the Talbot cavity position from the image plane, we observed the far-field pattern transition from one broad profile into discrete peaks, indicating the addition of far-field is in transition from incoherent to coherent. The external

Talbot cavity provides optical coupling among BA-LDs with strong mode discrimination. As a result, one super-mode was selected. The stable and high visibility interference pattern indicated that stable phase locking was achieved. The angle of the center lobe of the array far-field profile was around 1.0 mrad with 0.1 nm spectral line-width (V-shape cavity), or that the angle of the center lobe of the array far-field profile was 1.5 mrad with 0.07 nm spectral line-width (closed-V-shape cavity). The output power reached 9.0 W (for V-shape cavity) and 12.8 W (for a closed-V-shape cavity) with high current injection while the coherent addition far-field profile maintains the high visibility. The interference profile generated by a phase-locked array coherent addition was confirmed by numerical calculation.

4.2 Experiments on external cavity broad-area laser diode arrays

Our experimental scheme is shown in Fig. 4.1. The laser diode array was manufactured by Lasertel. It comprises 49 emitters with 100 μm of size, and 200 μm array pitch. The center wavelength of the laser diode array is around 770 nm. The front facet of the array is anti-reflection (AR) coated with reflectivity $R \approx 1\%$, and the rear facet is high-reflection coated.

A pair of prism mirrors separates the high-order BA-LD modes emission into two paths. One is the feedback path (right half of Fig. 4.1). The other one is the output path (left half of Fig. 4.1). Each prism mirror is mounted on a precision rotation stage. The angle ($\theta = 92.86°$) between the two reflection planes is carefully set in order to select one higher-order BA-LD mode. The two prism mirrors steer two separated laser beams parallel to the laser diode facet along the slow-axis direction.

In the feedback path, a telescope comprising a fast-axis collimation (FAC) lens ($f_g = 1.3$ mm, NA = 0.5) and a cylindrical lens CL2 ($f_2 = 200$ mm) collimate the laser beam along the fast-axis. The vertical position of the laser diodes on the linear array has a curved distribution due to non-perfect manufacturing process. As a result, the image of laser diodes shows a 'smile' pattern. With external grating feedback, the vertical position 'smile' distribution of laser diodes generates a lasing wavelength 'smile' distribution, and is called the 'smile' effect. By using a telescope in the external cavity, the 'smile' effect can be reduced. Our feedback branch telescope comprised cylindrical lenses. This design is slightly different from the round lens telescope in Reference 29. Following the ray-tracking calculation procedure in Reference 32, the 'smile' effect of the laser array in our configuration was reduced by $f_2/(d_2 - f_2 - f_g)$, where d_2 is the distance between CL2 and the laser diode array (d_2 is not shown in Fig. 4.1). The 'smile' effect was reduced by a factor of eight. A confocal cylindrical lens pair CL1 and CL3 ($f_1 = f_3 = 200$ mm) transfer laser diodes image to the surface of the diffraction grating

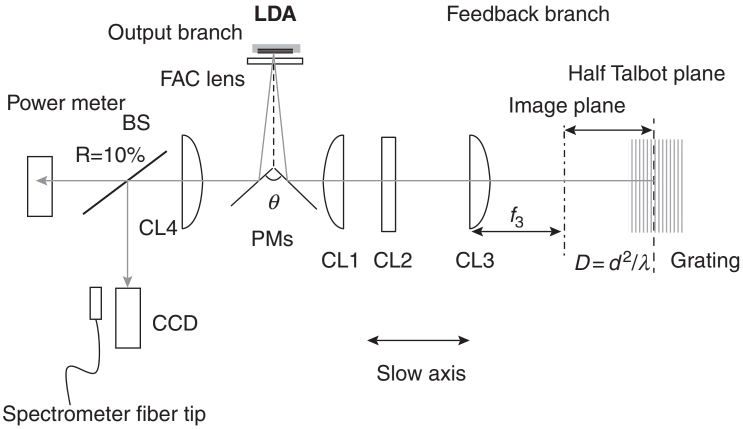

4.1 Schematic design of the V-shape external cavity. The V-shape external cavity is shown in top view (slow-axis). LDA is laser diode array, CL1–CL4 are cylindrical lenses. FAC lens and CL2 collimate the laser beam along the fast-axis and the confocal lens pair CL1, CL3 image laser diodes on the CL3 focal plane. There is an angle θ between the two reflecting surfaces of the prism mirrors. The two prism mirrors separate the laser beam into two paths: one for feedback and the other for output. The feedback path consists of CL1–CL3, and the grating. *D* is the distance between the grating and the focal plane of CL3. In the output path, cylindrical lens CL4 projects the laser diode array far-field profile on its focal plane. A CCD camera images the far-field profile and a spectrometer measures the spectrum while a power-meter monitors the output power (after Reference 26, © 2008 OSA).

(830-line/mm, gold-coating) which is arranged in a Littrow configuration. The grating blaze angle is about 18 degrees and the first-order diffraction efficiency was more than 85%. The locked center wavelength is determined by the grating title angle. The grating is mounted on a linear stage and its position is continuously tunable between the image plane (CL3 focal plane) and the half-Talbot plane at D = $Z_t/2$ where $Z_t = 2d^2/\lambda$ is the Talbot distance, λ is the laser wavelength, and d is the array pitch. Since cylindrical lenses transfer the laser diode image on the CL3 focal plane, the cavity round trip is calculated by the formula L = 2D. In the output path, the laser diode far-field profile is imaged on the focal plane of the cylindrical lens CL4 (f_4 = 300 mm) and is recorded by a CCD camera. A spectrometer with a fiber-collection tip is used to measure the spectrum, while the power-meter behind the beam-splitter monitors the output power.

Figure 4.2 shows the external cavity for one BA-LD. A single high-order BA-LD mode is selected by the external cavity which is composed of transformation optics and a diffractive grating. Figure 4.2 also shows that the feedback beam from the V-shape external cavity enters the laser cavity at

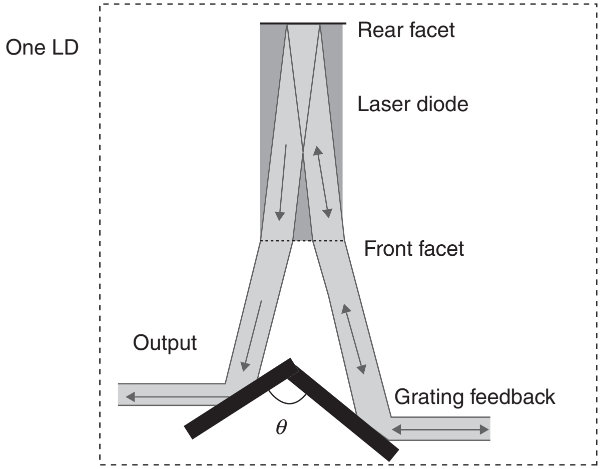

4.2 V-shape external cavity for individual broad-area laser diode (LD). The two branches of one high-order broad-area laser diode mode are spatially separated by the two prism mirrors. The right branch is sent to the diffraction grating. The diffraction grating provides the spectrum-selective feedback and coupling among the broad-area laser diodes (after Reference 26, © 2008 OSA).

a certain incidence angle. Such off-axis feedback will change the effective emission mode size of each laser emitter (see Fig. 4.2). The diffractive grating provides the spectrum selected optical coupling among the BA-LDs, (see Fig. 4.3). Once the grating is placed at the Talbot plane (external cavity round trip equals Talbot distance), the self-image optical feedback provides the strong mode discrimination diffraction optical coupling among BA-LDs.

Figure 4.4a shows the far-field profile generated from the phase-locked laser diode array when the grating is positioned around the half-Talbot plane (the round trip of the external cavity is the Talbot distance). The profile clearly demonstrates a coherent addition and the visibility of the profile is larger than 80%. The full width at half maximum (FWHM) of the center lobe far-field angle is about 1.0 mrad. The angle between two adjacent peaks is 3.85 mrad, which is consistent with the theoretical angle spacing between the different diffraction orders of a 200 μm-periodic source (λ/D = 0.77 μm/200 μm = 3.85 mrad). The spectral line-width (FWHM) is about 0.1 nm. The output power is 5.3 W at 30 A. We find that the energy ratio (center lobe/total) in the far-field profile does not match the calculation with the filling factor 0.5 of the laser diode array (100 μm emitter mode size and 200 μm emitter separation). This is because the off-axis feedback in our V-shape external cavity changes the effective emission mode size as observed in the single broad-area laser diode external cavity. In our cavity,

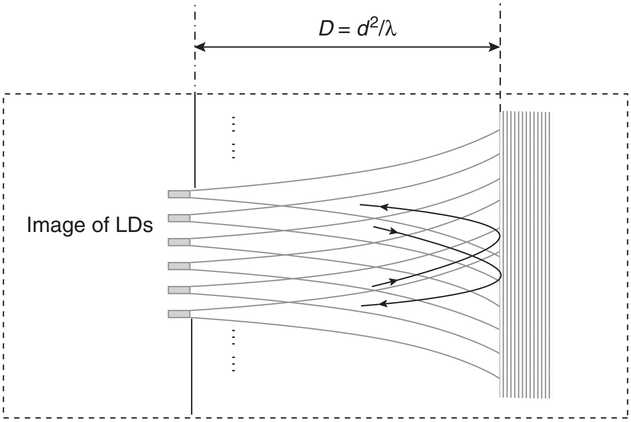

4.3 Effective external Talbot cavity. The effective cavity length is the distance between the image plane of the laser diodes (CL3 focal plane) and the grating (after Reference 26, © 2008 OSA).

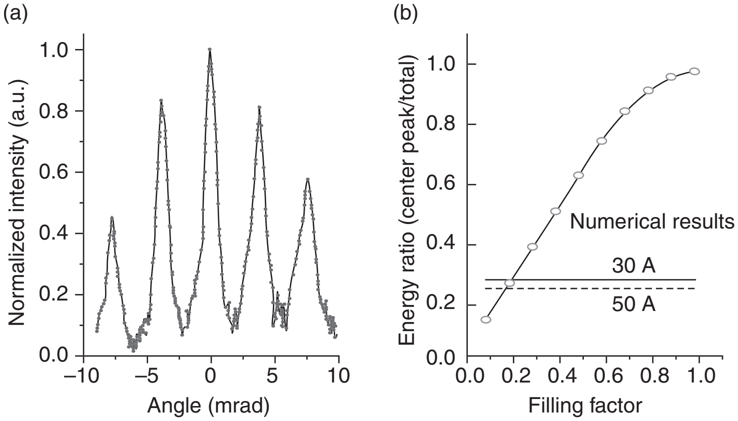

4.4 (a) Experimental results of the far-field profile of the phase-locked laser array at 30 A current injection, and (b) center energy ratio (center lobe energy/total energy) of the far-field profile versus the phase-locked laser diode array filling factor. In (b) the open-circles line is the numerical simulation of the far-field energy ratio for different filling-factor phase-locked laser diode arrays while the solid line and dashed line are the experimental measurements at 30 A (corresponding to Fig. 4.4a) and 50 A (corresponding to Fig. 4.6a), respectively (after Reference 26, © 2008 OSA).

each broad-area laser emitter in the array is forced to the single transverse mode operation. The actual emission mode size was estimated to be around 40 μm. To further verify the effective emission mode size, we have numerically calculated the center energy ratio as a function of the filling factor for the phase-locked array and results are plotted in Fig. 4.2b. The experimental measurements of the center energy ratio in both the 30 A and 50 A cases are shown in solid and dashed lines, respectively. This result confirms that the observed far-field coherent interference pattern is generated by a phase-locked laser diode array with a filling factor ~0.2, that is, 40 μm mode size with a 200 μm emitter separation. Due to the inhomogeneous AR-coating, intensity fluctuations of individual laser diodes in the array are of the order of 20%. Such intensity fluctuation broadens the far-field angle of each lobe and reduces the interference pattern visibility. It is important to note that no spatial filter is needed in our V-shape external cavity, since the V-shape external cavity provides sufficient mode discrimination.

In order to elucidate the effect of laser coupling on coherent addition, we studied the far-field patterns as the grating position was shifted. Figure 4.4 shows two far-field profiles corresponding to different cavity round-trip lengths. According to our V-shape external cavity configuration, the confocal cylindrical lens pair (CL1 and CL3) image the laser diode array on CL3 focal plane. The effective external cavity of feedback branch is shown in Fig. 4.3, which is similar to Fig. 4.3 in Reference 17. The effective external cavity consisted of the image of the laser diodes and the grating. The effective cavity round trip is 2D. When grating is shifted close to the image plane (D $\approx$ 0), the effective cavity round trip is close zero ($L \approx 0$). The emission of each laser diode is directly fed back to the laser diode itself. Such an image does not contain sufficient diffraction coupling among lasers and therefore is not able to lock the phase of the entire laser array. Accordingly, the far-field profile shows a single broad peak generated by the incoherent addition of individual laser beams. When grating is shifted close to the second plane (D $\approx Z_t/2$, $L \approx Z_t$), the self-image formed by the Talbot cavity creates a strong diffraction coupling among laser diodes and the entire array is phase-locked, as shown in Fig. 4.5b. The transition between incoherent addition and coherent addition shown in Fig. 4.5 is similar to the result of a single-mode laser diode array in a Talbot cavity.[21]

To examine our V-shape external Talbot cavity design at high power levels, the driving current of the array was increased to 50 A and the output power of the array was 9 W. At high power high-order modes are usually excited, and consequently the coherence of the LDA is deteriorated. Therefore, high power operation is usually challenging for LDA coherent addition external cavity designs. Nevertheless, in our experiment we observed the high visibility interference far-field profile shown in Fig. 4.6a. A narrow spectral line-width (FWHM = 0.1 nm) is demonstrated in Fig. 4.6b. The multi-lobe

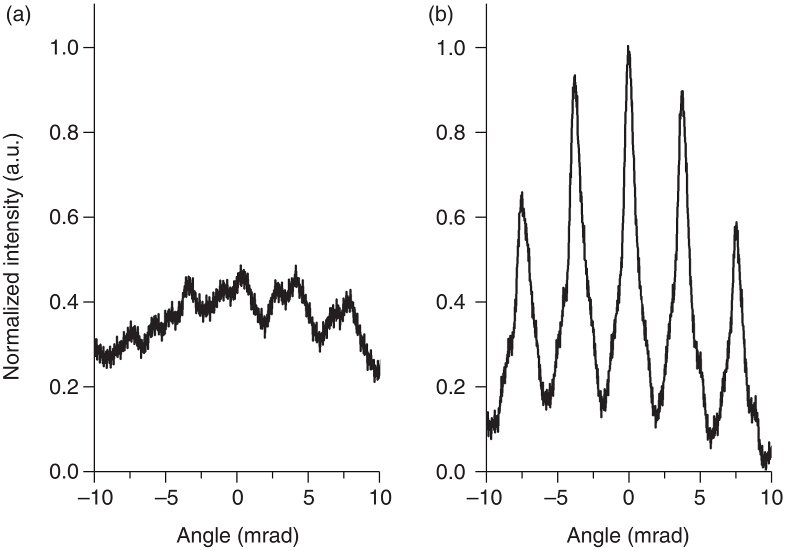

4.5 Transition between incoherent addition and coherent addition. (a) The grating position is around the image plane ($D = 0$) and the far-field profile shows a single broad peak. (b) The grating position is shifted to the half-Talbot plane ($D = d^2/\lambda$) and the far-field profile shows a multi-lobe interference pattern. Both intensities are normalized by the highest peak intensity in Fig. 4.5b (after Reference 26, © 2008 OSA).

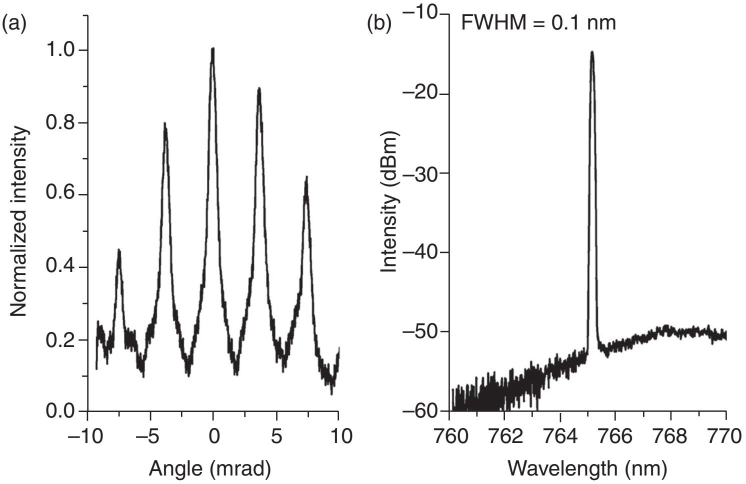

4.6 Experimental results of (a) the far-field profile, and (b) the spectrum of a phase-locked laser array at 50 A with a V-shape external Talbot cavity (after Reference 26, © 2008 OSA).

far-field profile indicates that our V-shape external Talbot cavity provides robust mode discrimination and strong coupling for coherent beam addition at high power levels.

The robust mode discrimination is primarily based on off-axis external cavity design. Previously, off-axis external feedback has been proved to increase the mode selection capability of single broad-area emitter as well as broad-area laser diode arrays. The V-shape Talbot external cavity described in this work provides spectrum-resolved, diffraction-coupled, off-axis external feedback. It also reduces the effective emission mode size, which helps to further increase the mode discrimination.

In our original V-shape cavity we only had one feedback source to laser cavities from the external cavity (the grating). To improve our design, we would like to first reiterate the differences between a single-mode laser diode and a broad-area laser diode. A single-mode laser diode has strong transverse mode confinement; the laser cavity is formed by two facets (front facet and end facet). A broad-area laser diode has weak transverse mode confinement, therefore multiple transverse modes exist in the broad-area laser diode cavity. The high-order mode emits twin beam along the off-axis direction. Once we feedback one branch of the twin beam in the broad-area laser cavity, the other branch of the twin beam is well controlled. This is the reason why we achieved the coherent addition, even though only controlling one of branch of the high-order mode. We designed a new experiment, and the schematic design of the setup is shown in Fig. 4.7. We added a second, grating to the cavity and called the cavity a closed V-shape cavity. For that experiment, our laser diode array was manufactured by Jenoptics. It comprised 47 emitters with emitter size 100 µm, and 200 µm spacing. The front facet of laser diodes is AR-coated with 0.5% residual reflectivity and the rear facet is high-reflection (HR) coated. The center wavelength is around 808 nm.

A pair of prism mirrors separates the laser beam into two different feedback paths. The right-side feedback path consists of cylindrical lenses CL1–CL3 and grating G1, while the left-side path consists of cylindrical lenses CL4–CL6 and grating G2. The optical axis of the feedback optics and the slow-axis of the laser array form a small angle $\theta = 2.38°$. This angle is equal to half the angle separating the two laser beams (see Fig. 4.7).

In the right-side feedback path, a telescope comprising a FAC lens (f_g = 1.3 mm, NA = 0.5) and a cylindrical lens CL2 collimates the laser beam along the fast-axis. The 'smile' effect due to a non-perfect manufacturing process could be reduced eight-fold by the fast-axis telescope in our external cavity configuration, according to the ray-tracking calculation. The laser diodes are imaged on the focal plane of CL3 through the transform optics comprising a pair of confocal cylindrical lenses CL1 and CL3. The laser beam is reflected by diffraction grating G1, which is arranged in the Littrow configuration.

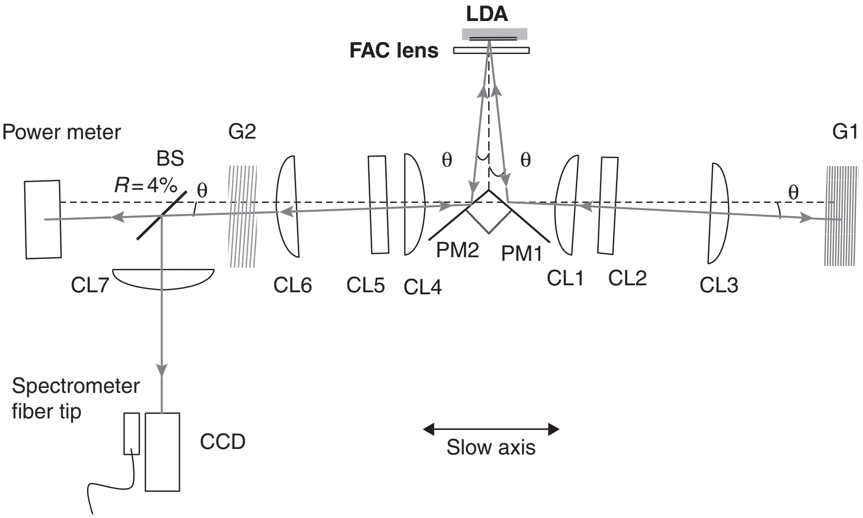

4.7 A schematic diagram of a closed-V-shape external cavity (top view). LDA is broad-area laser diode array, CL1–CL6 are cylindrical lenses with the focal length 200 mm. G1 and G2 are diffraction gratings. PM1, PM2 are prism mirrors. Two prism mirrors form a right angle to separate the laser beams into two paths. One feedback path consists of cylindrical lenses CL1–CL3, and G1. FAC lens and CL2 collimate the laser beam along the fast-axis, and the confocal lens pair CL1, CL3 image laser diodes on the CL3 focal plane. The second feedback path consists of CL4–CL6, and G2. The FAC lens and CL5 collimate the laser beam along the fast-axis, and the confocal lens pair CL4, CL6 image laser diodes on the CL6 focal plane. Grating G2 feeds back the first-order diffraction beam and couples the zero-order diffraction beam out. The far-field profile of the laser diode array is projected on CL7 ($f_7 = 300$ mm) focal plane. A CCD camera records the far-field profile and an optical spectrum analyzer measures the spectrum while a power-meter monitors the output power (after Reference 27, © 2010 OSA).

The blaze angle of G1 is about 18° and the first-order diffraction efficiency is more than 85%. The locked center wavelength of the laser array is determined by the grating tilting angle with respect to the laser diodes front facet. In the left-side feedback path, a telescope comprising the FAC lens and CL5 collimates the laser beam along the fast-axis. Another confocal cylindrical lens pair, CL4 and CL6, images the laser diodes onto the surface of the grating G2 (2000-line/mm, gold-coating) which is also mounted in the Littrow configuration. G2 reflects the first-order diffraction into the laser diodes while coupling the zero-order out. The grating G2 reflects 20% of the incident light back to the laser array and couples the rest out of the cavity. G2 serves as an optical coupler for the entire array. The far-field profile is projected to the focal plane of cylindrical lens CL7 and recorded by a CCD

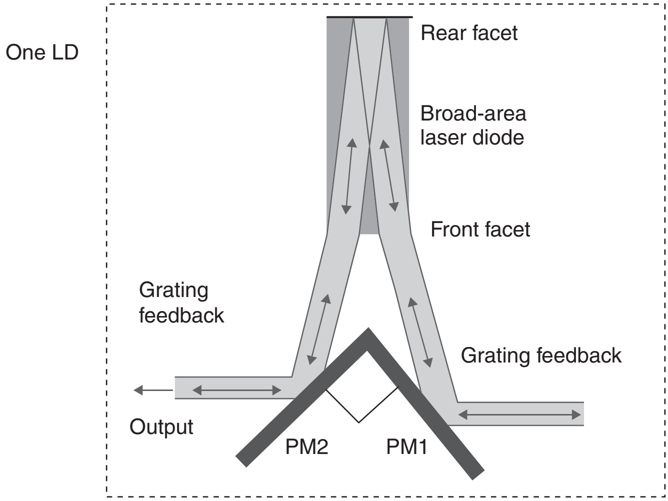

4.8 Closed-V-shape external cavity for an individual broad-area laser diode (after Reference 27, © 2010 OSA).

camera. An optical spectrum analyzer with a sensitivity of 70 pm is used to measure the spectrum, while a power-meter behind the beam-sampler monitors the output power.

Figure 4.8 shows the external cavity for an individual broad-area laser diode. The effective external cavity is composed of gratings G1 and G2 (the AR-coated front-facet reflectivity of the laser diode is much lower than the reflectivity of the gratings). G1 serves as an end mirror and as a spectral selector, while the HR coating rear facet serves as a beam folding mirror. G2 serves as both a spectral selector and as an output coupler. The unfolded external cavity for the entire array is shown in Fig. 4.9. The near-field distribution of laser diode emission toward the right feedback path or toward the left feedback path is imaged on the CL3 and CL6 focal planes, respectively. The distance between the grating G1 and the CL3 focal plane equals the half-Talbot distance $D = Z_t/2$, where $Z_t = 2d^2/\lambda$ is the Talbot distance, λ is the laser wavelength, and d is the array pitch. The diffractive coupling is achieved through the Talbot self-image effect. G2 is located at the CL6 focal plane and provides non-coupled feedback as well as an output. The effective cavity round trip is calculated using the expression $L = 2(D) = Z_t$.

Figure 4.10 shows the two different symmetric far-field profiles generated from the phase-locked laser diode array when G1 is positioned around the half-Talbot plane from the CL3 focal plane and G2 is positioned at CL6 focal plane (effective round trip of the external cavity equals Talbot distance). To characterize the degree of coherence in our laser system,

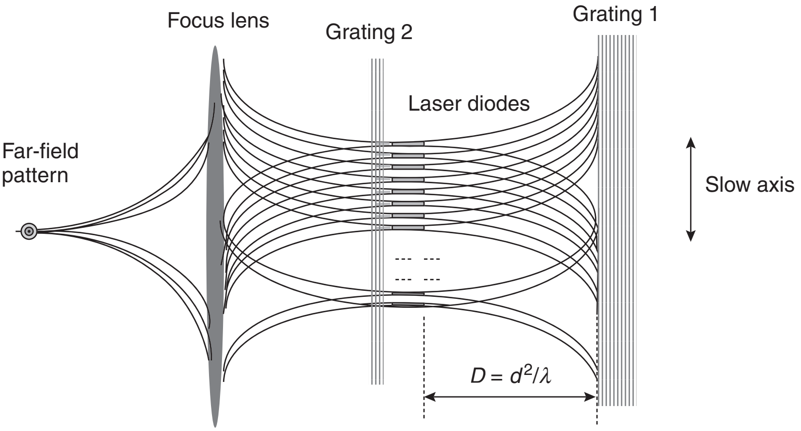

4.9 Unfolded closed-V-shape external cavity. The unfolded laser diode array is in an external cavity formed by gratings G1 and G2. G1 is located at the half-Talbot plane and provides a self-imaged diffractive-coupling feedback. G2 is located at the image plane and feeds back the first-order diffraction and couples the zero-order out. G2 serves as an optical coupler for the entire laser system. CL7 projects the laser output and shows the far-field profile on its focal plane (after Reference 27, © 2010 OSA).

we calculated the visibility of the far-field profile using the following expression: $V = (I_{\max}-I_{\min})/(I_{\max} + I_{\min})$. The far-field profile clearly demonstrates coherent addition, and the visibility of the profile is higher than 97%, which significantly exceeds the 80% visibility obtained in our earlier work.[26] The FWHM of the center lobe far-field angle is about 1.2 mrad. The angle between two adjacent peaks is 4.4 mrad and is consistent with the theoretical angle spacing expected from a 200 μm-periodic coherent light source (λ/D = 0.808 μm/200 μm = 4.04 mrad). The FWHM of spectral line-width is measured at 0.07 nm, which is the resolution limit of our spectrum analyzer. The output power was approximately 1.5 W at the injection current of 34 A. The out-of-phase super-mode far-field profile is shown in Fig. 4.10a. One can observe a symmetric structure with the two highest symmetric peaks in the far-field profile equally spaced around the center. This indicates that out-of-phase super-mode was selected. When we tuned the tilting angle of G2 (rotated in the optical table plane) by 2.2 mrad, the far-field profile showed a symmetric structure with the highest peak positioned at the center (see Fig. 4.10b), which indicates that the in-phase super-mode was selected. The change of the grating tilting angle 2.2 mrad is close to $\alpha = \lambda / 2d = 2.02$ mrad.[8,20,21]

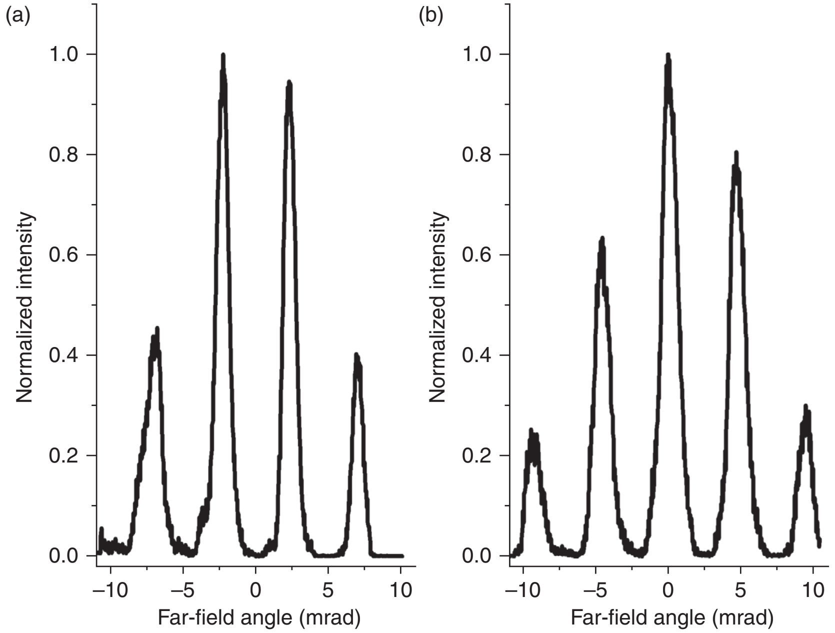

4.10 Two different symmetric far-field profiles of a laser diode array at injection current 34 A corresponding to different phase locking states: (a) out-of-phase super-mode, and (b) in-phase super-mode (after Reference 27, © 2010 OSA).

The emission power of a laser diode array with out-of-phase super-mode far-field profile is slightly higher than emission power of a laser array with in-phase super-mode far-field profile. We measured laser output power as a function of the injection current with the in-phase super-mode far-field profile. The measured L–I characteristic curves are shown in Fig. 4.11. The squares-curve shows the L–I dependence for an array placed in the external closed V-shape cavity while the circles-curve shows the L–I dependence for a free-running array. We measured different values of the threshold currents and slopes for the laser diode array with or without the external cavity. For the closed V-shape cavity, the threshold current is 32 A and the output slope efficiency is 0.41 W/A. For the AR-coated broad-area laser array, the threshold current is approximately 40 A and output slope efficiency is 0.98 W/A. There is a cross-over of the two curves at the value of 56 A. Different threshold currents and different L–I slopes can be explained by analyzing the laser system configurations. The closed-V-shape external cavity only enhances a certain off-axis broad-area laser diode mode, which is shown in Fig. 4.12. The enhanced off-axis lasing broad-area laser diode mode suppresses other broad-area laser diode modes. Consequently, the beam

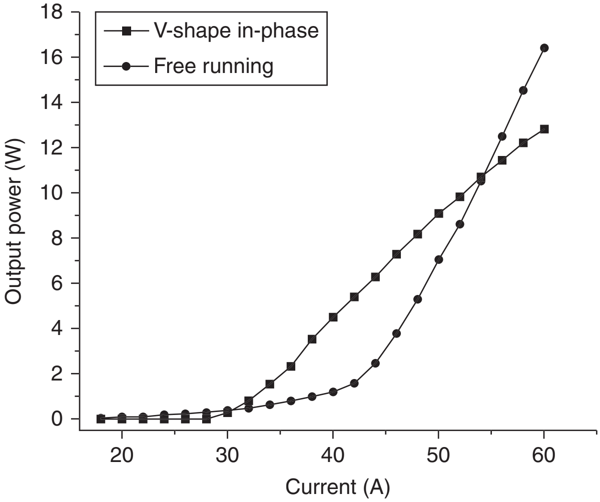

4.11 CW L–I characteristic of the AR-coated broad-area laser diode array with and without external cavity. Solid-squares show the output from the closed-V-shape external cavity with in-phase super-mode far-field profile. Solid-circles show the output from free-running broad-area laser diode array (after Reference 27, © 2010 OSA).

quality of an individual broad-area laser diode has been greatly improved. as shown in References 36–42. The gratings G1 and G2 serve as cavity mirrors, which provide more feedback than the AR-coated front facet. As a result, the closed-V-shape external cavity reduces the laser threshold from 40 to 32 A. The slope efficiency is reduced due to the coupling out efficiency reduction. A similar behavior of the L–I curves for the laser diode array with and without an external cavity was demonstrated in References 45, 46. By carefully designing the external cavity (optimizing the reflectivity of the gratings and the gain medium length), we can increase the slope efficiency and, accordingly, the coherent emission power. It is important to emphasize that, although the slope efficiency of the AR-coated laser diode array without external cavity is higher, it only generates a broad-spectrum (2 ~ 3 nm), poor beam quality non-coherent emission.

Our closed V-shape cavity generates a high contrast coherent pattern from an AR-coated broad-area laser diode array. A high visibility (>97%) coherent far-field pattern at low power (0.8 W, I = 32 A) is shown in Fig. 4.12a, and the narrow spectral line-width (0.07 nm FWHM) with 50 dB side-mode suppression spectrum is shown in the Fig. 4.12b. The increased visibility indicates that a better spatial coherence is achieved. By comparing configurations of the closed-V-shape external cavity with our earlier experimental design, we found that the closed-V-shape external cavity provided

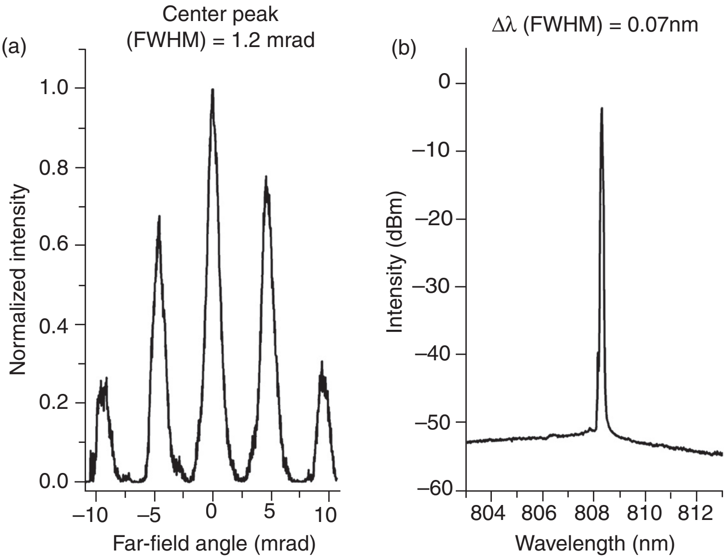

4.12 Experimental measurements for far-field profile and spectrum at injection current 32 A: (a) far-field profile and (b) spectrum of the laser diode array (after Reference 27, © 2010 OSA).

more feedback and increased cavity quality factor. The feedback of two gratings provides more spectral control to the laser diode array and, as a result, the spatial coherence is enhanced and spectral line-width of laser diode array is further narrowed down from 0.1 to 0.07 nm.

Figure 4.13 shows the far-field pattern and the spectrum of a closed-V-shape external cavity laser diode array at high injection current ($I = 60$ A). The corresponding output power was 12.8 W. The visibility of the far-field profile was 84% while the spectral line-width showed the same value as for low current operation (0.07 nm). Compared with the low injection current ($I = 32$ A), the visibility of the far-field profile was reduced from 97% to 84%, and the far-field angle (FWHM) of the center lobe was increased from 1.2 to 1.5 mrad. Far-field profile visibility decreased with the increase of injection current. Coherence deterioration may occur because of mode competition between intrinsic broad-area laser diode modes and external cavity modes. Further reduction of the front facet AR-coating reflectivity will increase the threshold of the free-running broad-area laser diode array and will shift the cross-over point of the two L–I curves (see Fig. 4.11) toward the higher value of the driving current. Consequently mode competition will be reduced and high spatial coherence will be maintained at higher injection current.

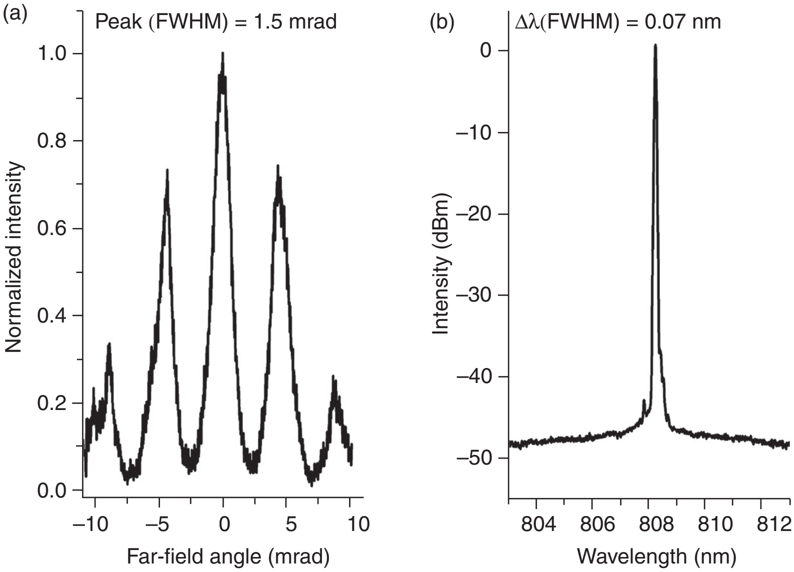

4.13 Experimental results of (a) far-field profile and (b) spectrum of a phase-locked laser array at 60 A with a closed V-shape external cavity (after Reference 27, © 2010 OSA).

4.3 Modeling the dynamics of a single-mode semiconductor laser array in an external cavity

In this section we will discuss how to model the dynamics of a single-mode semiconductor laser array in an external cavity. Modeling arrays of broad-area lasers is a much more challenging task and will not be discussed in this chapter. We believe, though, that modeling single-mode semiconductor laser arrays can provide some insight into the dynamics of broad-area lasers subject to the closed V-shape cavity, since only one transverse mode will be present due to grating filtering and cavity design.

The dynamics of a single-mode semiconductor laser array with external cavity feedback can by described as a set of coupled laser diodes rate equations. In this section we will first recall the Lang–Kobayashi model for a single semiconductor laser subject to external feedback, and then we will extend this to describe the laser array.

4.3.1 Lang–Kobayashi model

Lang and Kobayashi introduced a relatively simple model based on the laser rate equations to describe the dynamics of a single-mode semiconductor laser subject to feedback from an external mirror:[49]

$$\dot{E}(t) = \frac{1+i\alpha}{2}[G(N(t)) - \gamma]E(t) + kE(t-\tau)e^{i\theta} \qquad [4.1]$$

$$\dot{N}(t) = J - \gamma_n N(t) - G(N(t), E(t)) \mid E(t) \mid^2. \qquad [4.2]$$

$E(t)$ is the slowly varying complex amplitude of the electrical field with respect to the laser emitting frequency and $N(t)$ is the carrier number. The dot stands for time derivatives, $\alpha = 5$ is the line-width enhancement factor, $\gamma = 0.5$ ps^{-1} is the photon decay rate, $\gamma_N = 0.5$ ns^{-1} is the decay time for the carriers, J is the injected electrical current (pump), τ is the feedback delay time, κ is the feedback strength and θ is the optical feedback phase. The Lang and Kobayashi model assumes that multiples reflections on the external cavity can be disregarded which is valid for moderate feedback strength. The feedback strength κ is given by:

$$\kappa = \frac{c}{2nl_d}\frac{1-R_2}{\sqrt{R_3 / R_2}} \qquad [4.3]$$

where l_d is the laser diode cavity length, n is the refractive index of semiconductor material, c the speed of the light in vacuum, R_2 is the intensity reflection coefficient at the semiconductor facet and R_3 is the external mirror reflectivity.

Originally Lang and Kobayashi considered the gain $G(N(t), E(t))$ to be just linear with N. However when the intensity of the emission becomes large there is saturation of the gain. This effect can be taken into account by using:

$$G(N(t), E(t)) = g\frac{N(t) - N_0}{1 + s \mid E(t) \mid^2} \qquad [4.4]$$

where $g = 1.5 \times 10^{-8}$ ps^{-1} is the differential gain coefficient, $N_0 = 1.5 \times 10^8$ is the carrier number at transparency and $s = 2 \times 10^{-7}$ is the gain saturation coefficient.

The steady state solutions without feedback ($\kappa = 0$) are obtained setting $E(t) = 0$ and $N(t) = 0$. From Equation [4.1] one has $(G(N_{st},E_{st}) - \gamma)E_{st} = 0$, which leads to two solutions. The non-lasing state, $E_{st} = 0$, $N_{st} = J/\gamma_N$ and the on-state for which $G(N_{st},E_{st}) = \gamma$, so that,

$$\mathrm{I}_{st} = \frac{1}{\gamma}\frac{gJ - g\gamma_N N_0 - \gamma\gamma_N}{\gamma_N s + g} \qquad [4.5]$$

$$N_{st} = N_0 + \frac{1 + sI_{st}}{g}, \qquad [4.6]$$

where $I_{st} = |E_{st}|^2$ is the stationary intensity while the stationary phase is arbitrary. This solution exists only for an injection current larger than the threshold given by:

$$J_{th} = \gamma_N \left(N_0 - \frac{\gamma}{g} \right) \quad [4.7]$$

The presence of the feedback term can effectively decrease the threshold. Close to threshold, a laser diode can possess chaotic behavior. Chaotic laser synchronization was proposed[50] and demonstrated[51–53] for two semiconductor lasers with external feedback coupled unidirectional, a configuration that draws attention since it can be used for secure chaotic communication. Anticipated synchronization has also been found in this configuration.[54] In the case of bidirectional coupling of two identical semiconductor lasers with optical feedback, one encounters a spontaneous symmetry breaking leading to lead–lag synchronization.[55] Zero lag synchronization of two chaotic semiconductor lasers with bidirectional coupling can be achieved by using a third system that acts as relay.[56]

If we consider that the external reflection takes place in a frequency selective grating rather than in a mirror, the field is spectrally filtered before being feed back to the laser. The dynamics of the field feed back to the laser $F(t)$ can be modeled as:[57,58]

$$F(t) = \Lambda E(t-\tau) + (i\Omega - \Lambda)F(t), \quad [4.8]$$

where Ω and Γ are the grating central frequency and bandwidth respectively.

4.3.2 Semiconductor laser array model

Now we consider several systems described earlier as coupled together. In practice, we should consider that, due to irregularities in the fabrication process, the elements of the array will be slightly different. The most important difference to be considered is that on the lasing frequency. Therefore, it is necessary to include a term of the form $i\,\omega E(t)$ in the field equation, where ω is the frequency detuning of the laser natural frequency with respect to a common reference frequency. Besides the natural lasing frequencies, for simplicity we will take the other laser parameters to be identical for all the elements of the array. It is also necessary to establish how the lasers are coupled. In this case the natural assumption is that a fraction of the field from laser k after reflection in the grating is fed back into laser j. This can be taken into account by a complex coupling constant C_{jk} including the strength of the coupling and the feedback phase. In general, the value of time-delay τ not only depends on the distance between LD and grating, but also depends on the distance between the laser diodes on the chip. Since the distance between LDs on the chip is much less than the distance between LDs and a grating, in order to simplify the numerical simulation, we assume that the time-delay τ is only dependent on the distance between the array and the grating and assumes the same value for all the lasers. Then we have

$$\dot{E}(t) = \frac{1+i\alpha}{2}\left[G(N_j(t), E_j(t)) - \gamma\right]E(t) + i\omega_j E_j(t) + k\sum_{k} {}^{C} jk^{F} k(t) \qquad [4.9]$$

$$\dot{N}_j(t) = J_j - \gamma_n N_j(t) - G(N_j(t), E_j(t)) \mid E_j(t) \mid^2 \qquad [4.10]$$

$$\dot{F}_j(t) = \Lambda E_j(t-\tau) + (i\Omega - \Lambda)F_j(t), \qquad [4.11]$$

where

$$G_j(N_j(t), E_j(t)) = g\frac{N_j(t) - N_0}{1 + s \mid E_j(t) \mid^2} \qquad [4.12]$$

In the following, for simplicity, we will consider a 1D array in which the coupling between the lasers j and k decays with the distance between them as $d^{|j-k|}$ where $d < 1$ can be estimated based on the laser diode array geometry configuration (emitter size and pitch of laser diode array). We will also assume that the phase of the feedback is the same for all the laser elements. Therefore, we will take $C_{jk} = d^{|j-k|}$. The characteristic values of the laser array parameters are presented in the Table 4.1 below.

The total electric field emitted by the array is given by:

$$E_{\text{Total}}(t) = \sum_{j=1}^{N} E_j(t), \qquad [4.13]$$

where N is the number of array elements. The total output intensity is given by $I_{\text{Total}}(t) = |E_{\text{Total}}(t)|^2$. Since the calculation of $I_{\text{Total}}(t)$ is based on the field addition, it contains information about the degree of coherence of the laser diodes. The average output power density of the individual elements of the array is given by:

$$I_{\text{Ave}}(t) = \frac{1}{N}\sum_{j=1}^{N} I_j(t) = \frac{1}{N}\sum_{j=1}^{N} \mid E_j(t) \mid^2 \qquad [4.14]$$

The ratio between the total and the average intensities $R_I(t) = I_{\text{Total}}(t)/I_{\text{Ave}}(t)$ is a measure of the degree of coherence of the array, that is a measure of the degree of synchronization between the array elements. If the dynamics

Table 4.1 Parameter values for the laser diode used in the numerical simulation

Symbol	Parameter	Value
G	The differential gain coefficient	1.5×10^{-5} ns^{-1}
s	Gain saturation coefficient	2.0×10^{-7}
N_0	The number of carriers at transparency	1.5×10^{8}
λ	Laser wavelength	770 nm
α	Line-width enhancement factor	5.0
γ	The photon decay rate	500.0 ns^{-1}
γ_n	The carrier decay rate	0.5 ns^{-1}
τ_{in}	Internal cavity round-trip time	11.67 ps
T	External cavity round-trip time	3.0 ns
Ω	Center frequency of grating	20.0 GHz
Λ	Bandwidth of grating	16.0 GHz
R_3	Power reflection from grating	0.83%
κ	Feedback coefficient	10 ns^{-1}

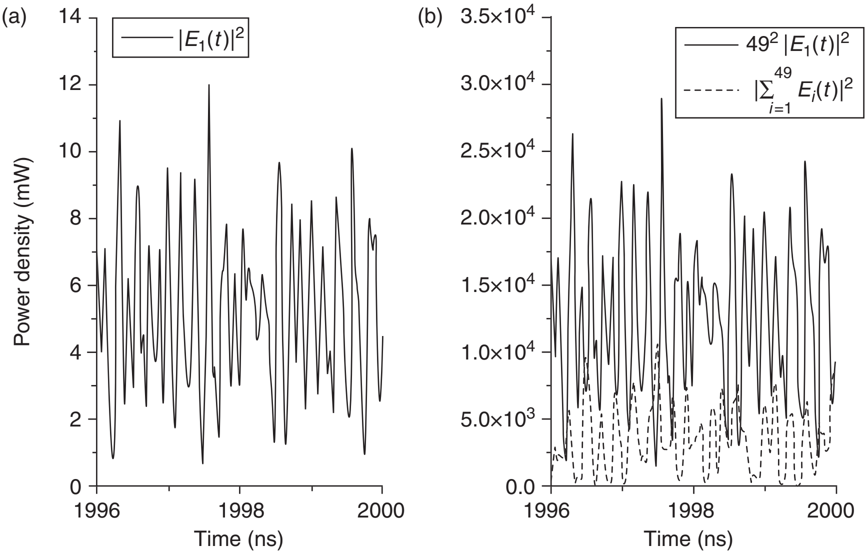

4.14 Time series of chaotic output intensity of laser diode array with external cavity feedback (with global coupling $d = 1.0$) at driven current $I = 1.1\ I_{th}$. (a) Output of one of the array elements and (b) total output of the array (lower, dashed line) compared with 49^2 times the output of one element (upper line).

of the elements is in-phase synchronized the electrical fields add coherently. Assuming each laser diode has a similar emission power $E_j(t) = E_0(t)$ for $j = 1,\ldots, N$, $R_I(t) = |NE_0(t)|^2 / |E_0(t)|^2 = N^2$.

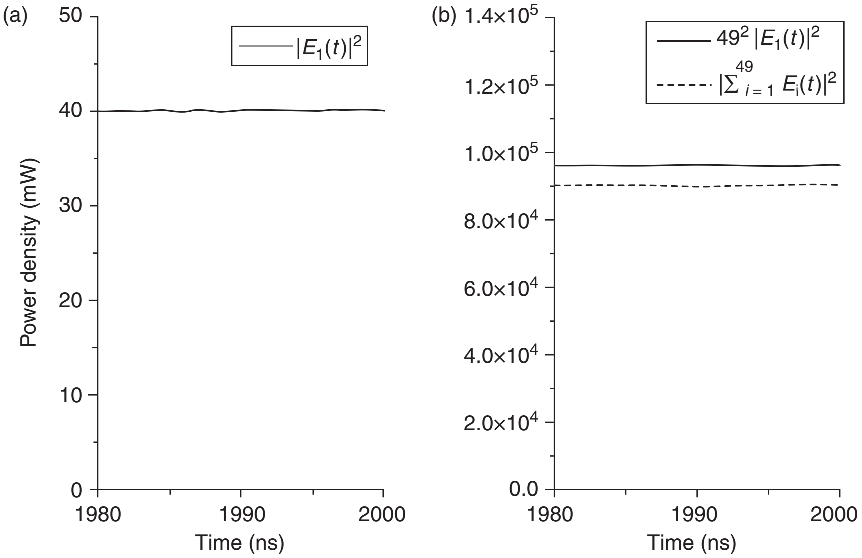

4.15 Time series of the output intensity from array element 1 (a) and total intensity of the laser array (panel b, dashed line) with pump current $I_j = 4.0\ I_{\text{th}}$ and $d = 1.0$. For comparison the upper line in panel (b) shows 49^2 times the output of array element 1.

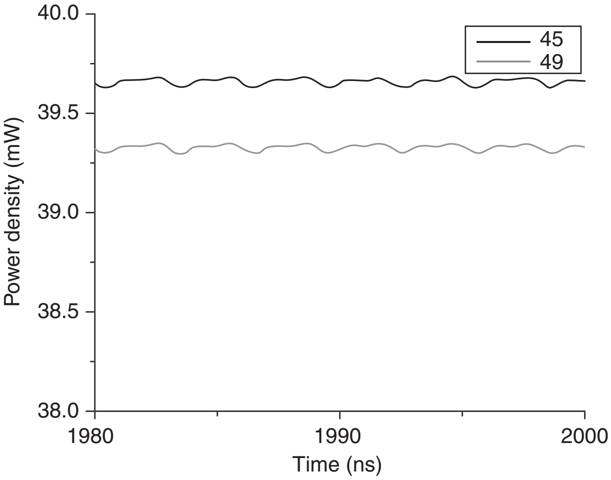

4.16 Time series of the output intensity from elements 45 (upper line) and 49 (lower line). Parameters chosen as in Fig. 4.15.

Thus, in the ideal case that all the elements are perfectly synchronized the total intensity is N^2 times the intensity of a single element. If the array is emitting incoherently then $R_I(t) \sim N$.

4.3.3 Numerical simulation of semiconductor laser arrays

In this section we provide some numerical results for an array with 49 semiconductor lasers obtained from the integration of Equations [4.9–4.11] with the parameters given in Table 4.1. Close to the threshold, the laser diode output is very sensitive to the external feedback. The output of each element shows chaotic behavior. Figure 4.14 shows the output intensity of element 1 (panel a) as well as the total intensity (panel b). For comparison, the output intensity of an element 1 multiplied by 49^2 times is also shown in Fig. 4.14b. In this case $R_I(t) \sim 800$ which is only around one third of the maximum possible value 49^2. Still, it is quite larger than 49 thus some degree of phase synchronization is achieved but only partially when injection current of the semiconductor lasers is close to threshold.

Increasing the injection current to 4.0 times the solitary laser threshold current, the semiconductor laser shows a practically stable output, as shown in Fig. 4.15. In this case $R_I(t) = 2257$, which is very close to $49^2 = 2401$. This is a clear indication of the good degree of synchronization of the array elements. Figure 4.16 shows the output power of the elements 45 and 49. The two time series show that almost perfect synchronization is achieved between two laser diodes, despite the fact that they have a different natural oscillation frequencies (we took $\omega_{45} = 1.66$ GHz and $\omega_{49} = 0.07$ GHz) and despite the fact that the initial condition for both elements was taken differently.

4.4 Conclusion

In conclusion, we have implemented high power coherent addition of LDA with a narrow line-width by using a novel V-shape external cavity design. The off-axis optical feedback induced in the V-shape external cavity forces each broad-area laser diode to operate at single transverse mode and the Talbot configuration external cavity results in coherent addition of laser beams. The far-field profile of phase-locked laser diode array is consistent with our numerical simulation. The V-shape external cavity design is robust and provides the high power operation capability.

We demonstrated high power, coherent beam combing of a broad-area laser diode array with narrow spectral line-width by using a closed-V-shape external Talbot cavity. The off-axis optical feedback from the two gratings enhanced the feedback into the external cavity, increasing the cavity quality factor and spectrum selection capability. The visibility of the far-field profile using a closed-V-shape external Talbot cavity was higher than that obtained in the V-shape external Talbot cavity. We observed the far-field profile transition between the out-of-phase and in-phase super-modes by tuning the tilting angle of one of the gratings. The closed V-shape external cavity design is robust and offers the capability of high power operation. By further optimizing our closed-V-shape-cavity, it will be possible to further increase the output power and maintain high visibility of the far-field profile.

The multi-lobe far-field profile is generated by the low-filling factor of the phase-locked array. There are two possible solutions to increase the beam combining efficiency. One is to increase the filling factor by customizing higher-filling-factor laser diode arrays. The other is to use two phase masks to compensate the non-uniform phase distribution along array due to the low-filling factor and therefore to concentrate the energy in the center lobe.[59–60]

4.5 Acknowledgments

The authors are grateful to Dr Yun Liu for providing valuable comments. This research was supported by the Office of Naval Research (ONR), National Science Foundation under grant EFRI#1024660, and the Laboratory Directed Research and Development Program of Oak Ridge National Laboratory. Oak Ridge National Laboratory is managed by UT-Battelle, LLC for the U.S. Department of Energy (DoE) under contract DEAC05–00OR22725. PC acknowledges financial support from MINECO, Spain, and Feder under projects FIS2007–60327 (FISICOS) and TEC2009–14101 (DeCoDicA).

4.6 References

1. T. Y. Fan, 'Laser beam combining for high-power, high-radiance sources', *IEEE J. Sel. Top. Quantum Electron.*, **11**, 567–577 (2005).
2. V. Daneu, A. Sanchez, T. Y. Fan, H. K. Choi, G. W. Turner and C. C. Cook, 'Spectral beam combining of a broad-strip diode laser array in an external cavity', *Opt. Lett.*, **25**, 405–407 (2000).
3. B. Chann, R. K. Huang, L. J. Missaggia, C. T. Harris, Z. L. Liau, A. K. Goyal, J. P. Donnelly, T. Y. Fan, A. Sanchez-Rubio and G. W. Turner, 'Near-diffraction-limited diode laser arrays by wavelength beam combining', *Opt. Lett.*, **30**, 2104–2106 (2005).
4. R. K. Huang, B. Chann, L. J. Missaggia, J. P. Donnelly, C. T. Harris, G. W. Turner, A. K. Goyal, T. Y. Fan and A. Sanchez-Rubio, 'High-brightness wavelength beam combined semiconductor laser diode arrays', *IEEE Photon. Technol. Lett.*, **19**, 209–211 (2007).
5. E. J. Bochove, 'Theory of spectral beam combining of fiber lasers', *IEEE, J. Quantum Electron.*, **38**, 432–445 (2002).
6. A. Jechow, V. Raab and R. Menzel, 'High cw power using an external cavity for spectral beam combining of diode laser-bar emission', *Appl. Opt.*, **45**, 3545 (2006).

7. D. Vijayakumar, O. B. Jensen and B. Thestrup, ‘980 nm high brightness external cavity broad area diode laser bar’, *Opt. Express*, **17**, 5684 (2009).
8. A. F. Glova, ‘Phase locking of optically coupled lasers’, *Quantum Electron.*, **33**, 283–306 (2003).
9. L. Bartelt-Berger, U. Brauch, A. Giesen, H. Huegel and H. Opower, ‘Power-scalable system of phase-locked single-mode diode lasers’, *Appl. Opt.*, **38**, 5752–5760 (1999).
10. W. Liang, A. Yariv, A. Kewitsch and G. Rakuljic, ‘Coherent combining of the output of two semiconductor lasers using optical phase-lock loops’, *Opt. Lett.*, **32**, 370–372 (2007).
11. T. M. Shay, V. Benham, J. T. Baker, C. B. Ward, A. D. Sanchez, M. A. Culpepper, S. D. Pilkington, L. J. Spring, L. D. J. Nelson and L. C. A. Lu, ‘First experimental demonstration of self-synchronous phase locking of an optical array’, *Opt. Express* **14**, 12015–12021 (2006).
12. D. Botez, L. J. Mawst, G. Peterson and T. J. Roth, ‘Resonant optical transmission and coupling in phase-locked diode laser arrays of antiguides: the resonant optical waveguide array’, *Appl. Phys. Lett.*, **54**, 2183–2185 (1989).
13. D. Botez, L. J. Mawst, G. L. Peterson and T. J. Roth, ‘Phase-locked arrays of antiguides: modal content and discrimination,’ *IEEE J. Quantum Electron.*, **26**, 482–495 (1990).
14. D. Botez, M. Jansen, L. J. Mawst, G. Peterson and T. J. Roth, ‘Watt-range, coherent, uniphase powers from phase-locked arrays of antiguided diode lasers’, *Appl. Phys. Lett.*, **58**, 2070–2072 (1991).
15. J. R. Leger, M. L. Scott and W. B. Veldkamp, ‘Coherent addition of AlGaAs lasers using microlenses and diffractive coupling’, *Appl. Phys. Lett.*, **52**, 1771–1773 (1988).
16. D. Mehuys, K. Mitsunaga, L. Eng, W. K. Marshall and A. Yariv, ‘Supermode control in diffraction-coupled semiconductor laser arrays’, *Appl. Phys. Lett.*, **53**, 1165–1167 (1988).
17. F. X. D’Amato, E. T. Siebert and C. Roychoudhuri, ‘Coherent operation of an array of diode lasers using a spatial filter in a Talbot cavity’, *Appl. Phys. Lett.*, **55**, 816–818 (1989).
18. R. Waarts, D. Mehuys, D. Nam, D. Welch, W. Streifer and D. Scifres, ‘High-power, cw, diffraction-limited, GaAlAs laser diode array in an external Talbot cavity’, *Appl. Phys. Lett.*, **58**, 2586–2588 (1991).
19. J. N. Walpole, ‘Semiconductor amplifiers with tapered gain regions’, *Opt. Quantum Electron.*, **28**, 623–645 (1996).
20. I. Hassiaoui, N. Michel, G. Bourdet, R. McBride, M. Lecomte, O. Parillaud, M. Calligaro, M. Krakowski and J. P. Huignard, ‘Very compact external cavity diffraction-coupled tapered laser diodes’, *Appl. Opt.*, **47**, 746–750 (2008).
21. D. Paboeuf, G. Lucas-Leclin, P. Georges, N. Michel, M. Krakowski, J. Lim, S. Sujecki and E. Larkins, ‘Narrow-line coherently combined tapered laser diodes in a Talbot external cavity with a volume Bragg grating’, *Appl. Phys. Lett.*, **93**, 211102 (2008).
22. R. K. Huang, L. J. Missaggia, J. P. Donnelly, C. T. Harris and G. W. Turner, ‘High-brightness slab-coupled optical waveguide laser arrays’, *IEEE Photon. Tech. Lett.*, **17**, 959–961 (2005).
23. R. K. Huang, B. Chann, L. J. Missagia, S. J. Augst, R. B. Swint, J. P. Donnelly, A. Sanchez-Rubio and G. W. Turner, ‘High-power coherent beam combination of semiconductor laser arrays’, CLEO 2008, paper CMN1.

24. J. R. Leger, 'Lateral mode control of an AlGaAs laser array in a Talbot cavity', *Appl. Phys. Lett.*, **55**, 334–336 (1989).
25. Q. Li, P. Zhao and W. Guo, 'Amplitude compensation of a diode laser array phase locked with a Talbot cavity', *Appl. Phys. Lett.*, **89**, 231120 (2006).
26. B. Liu, Y. Liu and Y. Braiman, 'Coherent addition of high power laser diode array with a V-shape external Talbot cavity', *Opt. Express*, **16**, 20935–20942 (2008).
27. B. Liu, Y. Liu and Y. Braiman, 'Coherent beam combining of high power broad-area laser diode array with a closed-V-shape external Talbot cavity', *Opt. Express*, **18**, 7361–7368 (2010).
28. T. G. Walker and W. Happer, 'Spin-exchange optical pumping of noble-gas nuclei', *Rev. Mod. Phys*., **69**, 629–642 (1997).
29. B. Chann, I. Nelson and T. G. Walker, 'Frequency-narrowed external-cavity diode-laser-array bar', *Opt. Lett.*, **25**, 1352–1354 (2000).
30. E. Babcock, B. Chann, I. A. Nelson and T. G. Walker, 'Frequency-narrowed diode array bar', *Appl. Opt.*, **44**, 3098–3104 (2005).
31. C. L. Talbot, M. E. J. Frese, D. Eang, I. Brereton, N. R. Heckenberg and H. Rubinsztein-Dunlop, 'Linewidth reduction in a large-smile laser diode array', *Appl. Opt.*, **44**, 6264–6268 (2005).
32. B. Liu, Y. Liu and Y. Braiman, 'Linewidth reduction of a broad-area laser diode array in a compound external cavity', *Appl. Opt.*, **46**, 365–370 (2009).
33. G. J. Steckman, W. Liu, R. Platz, D. Schroeder, C. Moser and F. Havermeyer, 'Volume holographic grating wavelength stabilized laser diodes', *IEEE J. Sel. Top. Quantum Electron*. **13**, 672–678 (2007).
34. L. S. Meng, B. Nizamov, P. Madasamy, J. K. Brasseur, T. Henshaw and D. K. Neuman, 'High power 7-GHz bandwidth external-cavity diode laser array and its use in optically pumping singlet delta oxygen', *Opt. Express,* **14**, 10469–10474 (2006).
35. A. Gourevitch, G. Venus, V. Smirnov, D. A. Hostutler and L. Glebov, 'Continuous wave, 30W laser-diode bandwidth 10 GHz linewidth for Rb laser pumping', *Opt. Lett.*, **33**, 702–704 (2008).
36. C. J. Chang-Hasnain, J. Berger, D. R. Scifres, W. Streifer, J. R. Whinnery and A. Dienes, 'High power with high efficiency in a narrow single-lobed beam from a diode laser array in an external cavity', *Appl. Phys. Lett.*, **50**, 1465–1467 (1987).
37. L. Goldberg and J. F. Weller, 'Narrow lobe emission of high power broad strip laser in external resonator cavity', *Electron. Lett.*, **25**, 112–114 (1989).
38. R. M. R. Pillai and E. M. Garmire, 'Paraxial-misalignment insensitive external-cavity semiconductor-laser array emitting near-diffraction limited single-lobed beam", *IEEE J Quantum Electron*., **32**, 996–1008 (1996).
39. V. Raab and R. Menzel, 'External resonator design for high-power laser diodes that yields 400mW of TEM00 power', *Opt. Lett.*, **27**, 167–169 (2002).
40. V. Raab, D. Skoczowsky and R. Menzel, 'Tuning high-power laser diodes with as much as 0.38W of power and $M^2 = 1.2$ over a range of 32nm with 3-GHz bandwidth', *Opt. Lett.*, **27**, 1995–1997 (2002).
41. J. Chen, X. D. Wu, J. H. Ge, A. Hermerschmidt and H. J. Eichler, 'Broad-area laser diode with 0.02nm bandwidth and diffraction limited output due to double external cavity feedback', *Appl. Phys. Lett.*, **85**, 525–527 (2004).
42. A. Jechow, V. Raab, R. Menzel, M. Cenkier, S. Stry and J. Sacher, '1 W tunable near diffraction limited light from a broad area laser diode in an external cavity with a line width of 1.7MHz', *Opt. Comm*., **277**, 161–165 (2007).

43. X. Gao, Y. Zheng, H. Kan and K. Shinoda, 'Effective suppression of beam divergence for a high-power laser diode bar by an external-cavity technique', *Opt. Lett.*, **29**, 361–363 (2004).
44. Y. Zheng and H. Kan, 'Effective bandwidth reduction for a high-power laser-diode array by an external-cavity technique', *Opt. Lett.*, **30**, 2424–2426 (2005).
45. L. Hildebrandt, R. Knispel, S. Stry, J. R. Sacher and F. Schael, 'Antireflection-coated blue GaN laser diodes in an external cavity and Doppler-free indium absorption spectroscopy', *Appl. Opt.*, **42**, 2110–2118 (2003).
46. M. W. Pan, D. J. Evans, G. R. Gray, L. M. Smith, R. E. Benner, C. W. Johnson and D. D. Knowlton, 'Spatial and temporal coherence of broad-area lasers with grating feedback', *J. Opt. Soc. Am. B,* **15**, 2531–2536 (1998).
47. Y. Zheng and H. Kan, 'Narrow-bandwidth high-brightness external-cavity laser diode bar', *Jpn. J. Appl. Phys.*, **46**, L218–L220 (2007).
48. Z. Su, Q. Lou, J. Dong, J. Zhou and R. Wei, 'Beam quality improvement of laser diode array by using off-axis external cavity', *Opt. Express,* **15**, 11776–11780 (2007).
49. R. Lang and K. Kobayashi, 'External optical feedback effects on semiconductor injection laser properties', *IEEE J. Quantum Electron.*, **16**, 347–355 (1980).
50. C.R. Mirasso, P. Colet and P. García-Fernández, 'Synchronization of chaotic semiconductor lasers: application to encoded communication', *IEEE Photonics Tech. Lett.*, **8**, 299–301 (1996).
51. S. Sivaprakasam and K.A. Shore, 'Demonstration of optical synchronization of chaotic external-cavity laser diodes', *Opt. Lett.* **24**, 466–468 (1999).
52. H. Fujino and J. Ohtsubo, 'Experimental synchronization of chaotic oscillations in external-cavity semiconductor lasers', *Opt. Lett.* **25**, 625–627 (2000).
53. I. Fischer, Y. Liu and P. Davis, 'Synchronization of chaotic semiconductor laser dynamics on sub-ns timescales and its potential for chaos communication', *Phys. Rev. A,* **62**, 11801(R)–11804(R) (2000).
54. C. Massoler, 'Anticipation in the synchronization of chaotic semiconductor lasers with optical feedback', *Phys. Rev. Lett.,* **86**, 2782–2785 (2001).
55. T. Heil, I. Fischer, W. Elsasser, J. Mulet and C.R. Mirasso, 'Chaos synchronization and spontaneous symmetry breaking in symmetrically delay coupled semiconductor lasers', *Phys. Rev. Lett.*, **86**, 795–798 (2001).
56. I. Fisher, R. Vicente, J. Buldu, M. Peil, C.R. Mirasso, M. C. Torres and J. Garcia-Ojalvo, 'Zero-lag long-range synchronization via dynamical relaying', *Phys. Rev. Lett.* **97**, 123902(1)–123902(4) (2006).
57. M. Yousefi and D. Lenstra, 'Dynamical Behavior of a Semiconductor Laser with Filtered External Optical Feedback', *IEEE J. Quantum Electron.*, **35**, 970–976 (1999).
58. A. P. A. Fischer, O. K. Andersen, M. Yousefi, S. Stolte and D. Lenstra, 'Experimental and theoretical study of filtered optical feedback in a semiconductor laser', *IEEE J. Quantum Electron.*, **36**, 375–384 (2000).
59. J. R. Leger, G. J. Swanson, and M. Holz, 'Efficient side lobe suppression of laser diode arrays', *Appl. Phys. Lett.*, **50**, 1044–1046 (1987).
60. G. J. Swanson, J. R. Leger and M. Holz, 'Aperture filling of phase-locked laser arrays', *Opt. Lett.*, **12**, 245–247 (1987).

5

Ultrafast pulse generation by semiconductor lasers

E. U. RAFAILOV, University of Dundee, UK and
E. AVRUTIN, University of York, UK

DOI: 10.1533/9780857096401.1.149

Abstract: The chapter reviews the physical foundations, the theoretical analysis, the experimental implementation, and possible applications of the three main regimes of ultrafast pulse generation by semiconductor lasers (SLs): gain-switching, passive Q-switching (QS) or self-sustained pulsation (SSP), and mode-locking. Key parameters governing the laser performance, and advantages and limitations of these three methods of pulse generation are discussed. Emphasis is given to the recent progress in theory and experiment, harnessing new materials and physical principles, and current application trends.

Key words: semiconductor lasers, ultrashort pulses, gain-switching, passive Q-switching, mode-locking.

5.1 Introduction

The numerous advantages of semiconductor lasers (SLs), such as high efficiency, compactness, straightforward (injection) pumping mechanism, and integrability, have long since established their unique place in applications including, but not restricted to, tele- and data-communications, information storage and retrieval, measurement and sensing, medicine and biosciences. For some of these applications, generation of (sub) picosecond pulses is important (information storage, measurements, imaging) or may become important (future high-bit-rate communications). Thus, ultrafast SLs have attracted considerable research effort over at least two decades. A number of literature sources, of which the monograph by P. Vasil'ev[1] is the most comprehensive, have presented an excellent overview of the principles, physics, and applications of ultrafast pulse generation by lasers. In the years since that book was published, further progress has been achieved in both the understanding of the physics of the ultrafast operation of SLs, and in using this understanding for improving their performance. The purpose of this chapter is to present both an up-to-date view of the physical foundations of ultrafast pulse generation by SLs (with emphasis, as much as possible, on analytical methods illustrating physical tendencies) and an overview of the recent practical achievements. Reviewing the entire body of the literature on the subject, particularly the earlier papers covered by earlier reviews, is not attempted; apologies are extended to authors whose work will have to be left out. Instead, we shall try to highlight those tendencies and achievements of the recent years which we believe to be significant and promising.

The organisation of the chapter is straightforward. To generate short (a few tens of picoseconds, or comparable to the round-trip of the laser cavity) or ultrashort pulses (~1 ps, or smaller than round-trip time) optical pulses from SLs, three *main* techniques can be used: gain-switching, Q-switching (QS) and mode-locking.[1] These methods will be considered in turn in Sections 5.2, 5.3, and 5.4, with a brief summary to follow.

5.2 Gain-switching

This section reviews gain-switching in terms of its basic features and theoretical foundations.

5.2.1 The basic features

The term 'gain-switching' (GSw) refers to the regime of laser operation whereby the pumping, and thus the gain, in the laser is modulated by a short intense pulse, as a result of which the laser emits a short optical pulse, commensurate in duration with the photon lifetime and thus with the round-trip of the laser cavity, and typically about an order of magnitude shorter than the pumping pulse that caused it.

In the context of *semiconductor* lasers, the pumping is usually by injection current, so GSw involves a short (~ 1 ns) current pulse (though GSw in *optically* pumped SLs has also been studied[2]). The pumping can be either in the form of a single intense pulse, or a regular trail of such pulses, typically at a repetition frequency of ~ 0.1–1 GHz; the latter case is known as *repetitive QS*. A frequently used practical means of realising this is *large-signal harmonic modulation* of the laser: with an SL being electrically a diode, a large-signal sinusoidal voltage modulation is translated into a repetitive pulsed current modulation.

The advantages of gain-switching over the other methods of short pulse generation are, firstly, that standard commercially available laser constructions can be used in this method (if not necessarily with the best results, as discussed below), so long as the electrical properties of the laser circuit allow for fast modulation. Secondly, the method does not rely on introducing any losses into the cavity, and so provides the highest electrical to optical conversion *efficiency* of the main three methods; it also allows for the highest optical *pulse energy*. Thirdly, the repetition frequency in the case of repetitive

QS is determined entirely by the modulating source and can thus be varied through a fairly wide range subject to the possibilities of the electronics.

The same considerations, on the other hand, determine also the limitations of the method. Firstly, the regime relies by its very essence on large-signal, fast electric modulation being available. Secondly, the pulse duration in this method is commensurate with the photon lifetime in the laser and thus typically does not fall below a few tens of picoseconds (at least without sacrificing a significant amount of energy). Thirdly, in the case of repetitive GSw by large-signal modulation, the modulation frequency is restricted to values below the small-signal 3 dB modulation frequency of the laser, typically of the order of 0.1–1 GHz. These considerations determine the main applications of the method. Due to repetition rate and pulsewidth limitations, it is of little use for applications such as communications, either current or future, but is indispensable in a broad variety of applications where high pulse energy is of the essence, such as automobile safety devices, 3D imaging, laser tomography and time imaging spectroscopy. The requirements on the optical pulses for most of those applications are, firstly, the high optical pulse energy, and secondly, a moderately short pulsewidth (tens of ps is usually sufficient); the latter also implies the absence of any trailing pulses following the QS pulse. Efficiency, or the ability to extract high optical energy out of pumping pulses with a moderate (~ 10 A) amplitude, is also important for a number of applications.

Being thus the most mature and established of all the methods of short pulse generation, GSw has been studied for almost as long as lasers themselves; therefore, a very large amount of literature exists on the subject, with earlier books[1,3] providing some references. In the following, without attempting to review the entire literature on the subject, we shall first present the foundations of the theory and then show how the tendencies that can be deduced from the theory have influenced some important recent progress in the area.

5.2.2 The theoretical foundations

As GSw operates with optical pulses longer than, or at least commensurate with, the round-trip, a simple rate equation model is adequate for its theoretical description. The equations are written for the averaged electron density N and photon density S in the laser, in the form:

$$\frac{\mathrm{d}N}{\mathrm{d}t} = \frac{i(t)}{eV} - \frac{N}{\tau_n} - v_g g(N,S)S \qquad [5.1]$$

$$\frac{\mathrm{d}S}{\mathrm{d}t} = v_g(\Gamma_a g(N,S) - \alpha_t)S + \frac{\Gamma_a \beta N}{\tau_n}, \qquad [5.2]$$

where i is the pump current, e the electron charge, V is the active layer volume (for definiteness, we shall consider the case of an edge-emitting laser, with $V = d_a Lw$ where L is the cavity length, w the stripe width, d_a the active layer thickness), $\tau_n(N)$ the carrier lifetime, v_g the group velocity of light, Γ_a is the mode overlap (confinement) factor of the active layer, and $\alpha_t = \alpha_{\text{out}} + \alpha_{\text{int}}$ is the total (outcoupling and internal parasitic) cavity loss, and β is the spontaneous emission factor. Assuming that the front facet is anti-reflection coated and the rear one, high-reflected coated, with their respective reflectances satisfying $R_f << R_r$, the output power P out of the front facet is calculated from S using the usual formula:

$$P(t) = \hbar\omega v_g \alpha_{\text{out}} \frac{d_a wL}{\Gamma_a} S(t), \qquad [5.3]$$

where $\hbar\omega$ is the photon energy, and, as usual, $\alpha_{\text{out}} = (1/2L)\,\text{In}\left(1/R_f R_r\right)$. The dependence of gain on the photon density is usually introduced through the phenomenological gain compression coefficient:

$$g = \frac{g(N)}{1 + \varepsilon S}, \qquad [5.4]$$

and the dependences $g(N)$ usually taken as linear form for bulk active layers or logarithmic in single or multiple quantum wells (QW):

$$g^{(\text{bulk})} \approx \sigma_g (N - N_{\text{tr}}); \quad g^{(\text{QW})} \approx \sigma_g N_{\text{tr}}\, \text{In}\frac{N}{N_{\text{tr}}}, \qquad [5.5]$$

with N_{tr} the transparency carrier density and σ_g the gain cross-section (at transparency, in the case of QWs). Some authors[4] use a logarithmic approximation for bulk materials as well. A numerical solution of the equation system [5.1]–[5.2], with a pumping pulse $\tau_p = 3$ ns in duration, is shown in Fig. 5.1. It is seen that the carrier density at the front of the pumping pulse passes the threshold value at a certain time t_0, at which point the net gain in the laser becomes positive and the photon density starts growing from a small seed provided by the spontaneous emission. However, with S still too small to cause any significant stimulated recombination, N continues to grow as well for a certain time interval t_2 until the optical pulse emerges. During the pulse, the carrier density N is depleted by stimulated recombination; after the pulse, the pumping fully or partially replenishes it again. If the optical pulse is intense enough for the depletion of N to be strong, and occurs near enough to the trailing edge of the pumping pulse, then the recovering N does not re-cross the threshold value, and the pulse remains single. This is 'proper' GSw, the intended regime of operation. Figure 5.1 shows the dynamics for the pumping pulse amplitude and duration close to the highest possible values (for the construction analysed) for which this regime is possible – note that the carrier

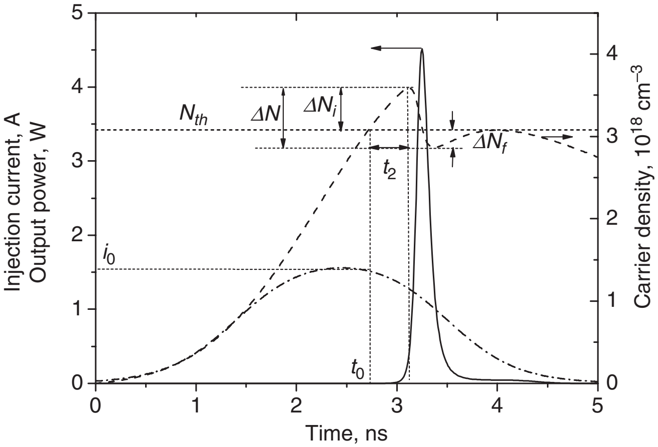

5.1 Illustration of the gain-switching process.

density after the pulse *touches* the threshold value but does not exceed it. Higher pumping pulse amplitudes, or longer durations at the same amplitude, would result in trailing pulses emerging and eventually, for sufficiently long and/or intense pumping pulses, the light dynamics would take the form not of gain-switching but of the standard modulation pattern: a decaying relaxation oscillation sequence followed by a long trail reproducing the pumping pulse in a quasi-stationary manner. The object of designing a laser and pumping source for GSw is to maximise the single-pulse energy while avoiding trailing pulses.

To appreciate the tendencies predicted by the theory, it is instructive to obtain some *analytical* rather than numerical results. To achieve such analytical progress, one separates the dynamics of GSw into distinct stages: the fast stage (commensurate with the photon lifetime) during the pulse, and the slower stages preceding and following it. During the fast stage, the analysis follows[1] in neglecting all terms except stimulated recombination in the carrier dynamics and, as usual, neglecting the spontaneous emission; this results in a reduced system:

$$\frac{\mathrm{d}N}{\mathrm{d}t} \approx -v_g g(N,S)S; \qquad \frac{\mathrm{d}S}{\mathrm{d}t} v_g(\Gamma_a g(N,S) - \alpha)S; \qquad [5.6a,b]$$

which applies during the pulse emission only. Integrating this over the entire pulse gives an estimate for the total pulse energy in the form:

$$E_{\mathrm{opt}} = \hbar\omega v_g \frac{wLd_a}{\Gamma_a} \alpha_{\mathrm{out}} \int S\mathrm{d}t = \hbar\omega V \frac{\alpha_{\mathrm{out}}}{\alpha_t} \Delta N \qquad [5.7]$$

where ΔN is the absolute value of the variation of the carrier density during the entire pulse. The maximisation of energy then requires maximising the quantity ΔN.

This parameter can be subdivided into two contributions: $\Delta N = \Delta N_i + \Delta N_f = (N_i - N_{\text{th}}) + (N_{\text{th}} - N_f)$. The first term, $\Delta N_i = \Delta N_i - N_{\text{th}}$, is the excess carrier density above the threshold value N_{th} stored in the active layer before the pulse is emitted, and the second, $\Delta N_f = N_{\text{th}} - N_f$, describes the dip in the carrier density below N_{th} due to carrier depletion by the pulse.

The evaluation of the initially stored excess carrier density ΔN_i is relatively straightforward.[3] To obtain it, we turn to the slow phase of dynamics that precedes the pulse and observe, slightly generalising the treatment presented in References 3 and 5, that the interval t_2 (Fig. 5.1) finishes when S, growing from a small spontaneous seed S_{sp}, reaches a high enough value, say S_1, at the leading front of the optical pulse. Assuming that the interval t_2 is short enough to neglect the current variation during this interval and the carrier density variation is weak to moderate $(\Delta N_i < N_{\text{th}})$, we obtain for the stored excess carrier density a very simple estimate $\Delta N_i \approx \left(i_0 - i_{\text{th}}/eV\right)t_2$, where i_0 is the instantaneous current value at the time t_0 and i_{th} the continuous wave (CW) threshold current. Since $\Delta N_i < N_{\text{th}}$, we can linearise the dependence $g(N)$ in Equation [5.2] (if it is not taken to be linear from the start) during the interval t_2 and thus obtain an estimate for the duration of this interval in the form:

$$t_2 \approx \sqrt{\frac{2eV}{i_0 - i_{\text{th}}}\left(\Gamma_a v_g \frac{\partial g}{\partial N}\bigg| N_{\text{th}}\right)^{-1} \text{In}\frac{S_1}{S_{\text{sp}}}} \qquad [5.8]$$

Hence, ΔN_i is given by:

$$\Delta N_i \approx \sqrt{\frac{2(i_0 - i_{\text{th}})}{eV}\left(\Gamma_a v_g \frac{\partial g}{\partial N}\bigg|_{N_{\text{th}}}\right)^{-1} \text{In}\frac{S_1}{S_{\text{sp}}}} \qquad [5.9]$$

where both the spontaneous seed S_{sp} and the characteristic photon density S_1 at the start of the pulse are yet to be determined; however, since the function $f(x) = \sqrt{\ln x}$ is extremely slow, only crude estimates are required for these values. For S_{sp}, such an estimate is obtained, following Reference 5, in the form:

$$S_{\text{sp}} \approx \Gamma_a \beta N_{\text{th}} \sqrt{\frac{2}{\pi}\frac{1}{v_g \alpha_t \tau_n(N_{\text{th}})}\frac{i_{\text{th}}}{i_{\max}}} \qquad [5.10]$$

As for S_1, it can be naturally assumed[5] to correspond to the photon density at which the pumping term in Equation [5.1] is compensated by the spontaneous and stimulated terms; then:

$$S_1 \approx \left(\Gamma_a \frac{i_0 - i_{\text{th}}}{eV}\frac{1}{v_g \alpha_t}\right) \qquad [5.11]$$

Equations [5.9] with [5.10] and [5.11] give a fully analytical (except for the need to evaluate the current i_0 at the point of crossing the threshold, which is a function of the current pulse profile) result for the excess carrier density ΔN_i stored before the pulse. The result of Equation [5.9] agrees well with numerical simulations and can be relatively easily refined further by a more accurate account of spontaneous recombination and current profile during the interval t_2. Next, to calculate the post-pulse dip ΔN_f, one returns to the fast stage of GSw dynamics, during the pulse. By dividing one of the Equations [5.6a,b] by the other, the time t can be eliminated; a transcendental equation for ΔN_f is then obtained by integrating the resulting single equation to obtain $S(N)$ and recalling that $S = 0$ both before and after the GSw pulse. In the simplest case, when gain compression can be neglected and the dependence $g = g(N)$ linearised as in deriving Equation [5.9], this procedure results in a relatively simple transcendental equation.[3] In our notations, it has the form:

$$\Delta N_i + \Delta N_f = N_0' \ln \frac{N_0' + \Delta N_i}{N_0' - \Delta N_f}, \qquad [5.12]$$

where

$$N_0' = \left(\frac{\Gamma a}{\alpha_t} \frac{\partial g}{\partial N} |_{N_a} \right)^{-1} \qquad [5.13]$$

The result Equation [5.12] can be simplified further by using the first order Padé approximation, which is in excellent agreement with the exact solution of Equation [5.12] for $\Delta N_i < \Delta 2 N_0'$:

$$\Delta N_f \approx \Delta N_i \left(1 + \frac{2}{3} \frac{\Delta N_i}{N_0'} \right)^{-1} \qquad [5.14]$$

This gives a *fully analytical estimate* for $\Delta N = \Delta N_i + \Delta N_f$, and hence for the GSw pulse energy:

$$E_{\text{opt}} \approx 2\hbar\omega \frac{\alpha_{\text{out}}}{\alpha_t} V \Delta N_i \frac{3N_0' + \Delta N_i}{N_0' + 2\Delta N_i} \qquad [5.15]$$

where ΔN_i and N_0' are given by Equations [5.9] and [5.13], respectively.

If Equation [5.15] is complemented by an estimate for the pulse duration, the peak pulse power can also be estimated. The duration of a gain-switched pulse was shown by theoretical[2] and numerical[1] analysis, as well as experimentally, to be of the order of the photon lifetime $\tau_{\text{phot}} \approx 1/v_g \alpha_t$ in the laser and to vary not too strongly with the bias current. An analytical estimate has been obtained[2] for the pulse duration; in our notations:

$$\tau_{\mathrm{FWHM}} \approx \frac{\mathrm{In}2}{\Gamma_a v_g \left(\partial g/\partial N\right)|_{N_{\mathrm{th}}}}\left[\frac{1}{\Delta N_i}+\frac{1}{\Delta N_f}\right], \qquad [5.16]$$

but it relies on stronger assumptions than Equation [5.15] and is therefore less accurate.

Equation [5.12] can be generalised[5] for the case of a non-zero gain compression coefficient in Equation [5.4], though for the time being only as a fairly cumbersome transcendental equation. However, to identify the most important qualitative trends, Equations [5.15] and [5.9] are sufficient.

First of all, it is seen from Equation [5.15] that intense pumping pulses (high $(i_0 - i_{th})$ in Equation [5.9]) are desirable for high output pulse energy. However, this needs to be contrasted with the requirement for single-pulse emission. The analysis presented above and leading to Equation [5.15] does not address the issue of single-pulse regime directly, though the carrier density depletion ΔN_f combined with the carrier dynamics after the pulse can be used to find the condition for the recovering carrier density to stay below the threshold value, thus ensuring that the pulse remains single. A simplified approximate form for this criterion for single-pulse emission is:

$$\int_{t_{0+t_2}}^{+\infty} \frac{i(t)-i_{\mathrm{th}}}{eV}\,\mathrm{d}t < \Delta N_f \qquad [5.17]$$

where the integral is from the time the optical pulse is emitted till the end of the pumping pulse, and ΔN_f is given by Equation [5.12] or [5.14]. Since ΔN_f is a monotonically growing function of ΔN_i and thus of the pulse energy, higher pulse energy simultaneously helps single-pulse generation – however, to ensure that the tendency continues, the pumping pulse durations should be shorter than the repetition frequency of the electron–photon oscillations in the current range studied, which realistically means $\tau_p < 1$ ns. This tends to require custom-built III-V semiconductor-based electrical pulse generators (see e.g., Reference 6).

It is clear, therefore, that high pumping pulse amplitudes need to be complemented by suitable laser design to achieve an optical pulse that is both high-energy and free from trailing pulses, particularly with the moderate pumping pulse durations (>1–1.5 ns) more readily obtainable with silicon electronics. Some clues for such laser design can also be taken from Equations [5.15] and [5.9]. Indeed, it follows from Equations [5.15] and [5.9] that the pulse energy, for a given peak pump current/duration, has a tendency to increase roughly as a square route of the *modal volume* V/Γ_a. This is mainly because an increase in V/Γ_a increases the time t_2 Equation [5.8] during which the carrier density builds up before the pulse; this in turn increases the stored carrier density ΔN_i given by Equation [5.9] and thus the pulse energy estimated via Equation [5.15]. In the case of a sublinear g(N) as in QW materials, the high threshold densities and thus the decreased dg/dN (which features the denominator in Equation [5.9]) contributes to an increased ΔN_i in structures with a decreased Γ_a. One notes, however, that the dependence of the output pulse energy on V/Γ_a for a given pulse amplitude is not monotonic: if the modal volume is made too large, the CW threshold current i_{th} increases too much, and the factor $i_0 - i_{\text{th}}$ in Equation [5.9] brings the output pulse energy down; thus for a given pumping pulse amplitude there is an optimal modal volume that maximises the pulse energy. However, the higher the modal volume, the higher is the single-pulse energy that can be obtained from the laser given a sufficiently intense optical pulse.

In the case of an edge-emitting laser, the stripe width w is limited to about 100 μm by beam shape considerations, and increasing the length L tends to increase the photon lifetime and hence the GSw pulsewidth; besides, a longer laser has a lower threshold carrier density than a shorter laser which decreases the relative excess current at which the secondary pulses appear and thus partly counters any improvement to single-pulse generation. Thus, increasing $V/\Gamma_a = d_a wL/\Gamma_a$ usually involves increasing the ratio of the active layer thickness to the confinement factor d_a/Γ_a (sometimes referred to as the effective transverse mode size, though technically this term is only meaningful for symmetric waveguides with the active layer in the middle).

5.3 Important developments in gain-switched semiconductor lasers (SLs)

The main achievements in increasing the energy of gain-switched pulse duration from a single laser in the last decade or so have indeed been mainly associated with the use of specialised laser constructions.

5.3.1 Single-heterostructure lasers

One construction successfully used for GS by a number of teams has been the *single-heterostructure* (SH) laser, in which the active layer is effectively a thick (several micrometres) weakly doped p-layer in an N_+-p-p_+ single heterostructure.[7,8] It has to be noted that the theoretical analysis of Section 5.2.2 does not apply to such laser structures directly – firstly, because the pumping term for the very thick active layer cannot be written in the simple form used in Equation [5.1] and secondly, because the refractive index step at the p-p_+ homojunction is so weak (~ 10^{-3}) that the optical confinement used in Equation [5.2] is not constant in SH lasers but depends noticeably on the carrier density (therefore it can be said that the dynamics of the laser combines features of GS and active QS, see Section 5.3); in fact, the waveguiding for some wavelengths can be destroyed during pulse emission. Accurate analysis of such structures involves solving the drift–diffusion equation for carriers and the analysis of N resolved along the vertical direction as well as dynamic waveguiding analysis.[8] However, such lasers still *combine a wide effective active layer and hence the large active area volume with relatively low optical confinement*, that is, conform to the qualitative optimisation route suggested by the relatively simple analysis presented in Section 5.2.2. Gain-switched pulses with pulse powers up to 400 W, with a duration of just 32 ps full width at half maximum (FWHM), corresponding to a pulse energy of more than 12 nJ, have been reported from such lasers at $\lambda = 0.89$ μm,[7,8] when pumped by electric pulses ~4 ns long at half maximum and 40 A in amplitude. The optical pulses had a small (suppressed by about 20 dB) quasi-stationary trail, but this did not prevent their intended use in laser radars.

A modification of the structure in the form of an AlGaAs heterostructure in which an extra barrier layer serves to separate the thick, strongly p-doped (10^{19} cm^{-3}) active layer from the p_+-n_+ junction and to control the accumulation of electrons before the pulse, leading to sharper pulses, has also been proposed. Pulses of a duration of 20–30 ps have been registered from this structure, but the powers obtained appear to be more modest than those of the single-heterostructure lasers.[9]

5.3.2 Narrow asymmetric waveguide lasers and related structures

Recently,[10] a team including one of the current authors proposed a structure for high power laser operation involving strongly asymmetric, non-broadened double heterostructure lasers, in which the combination of a relatively thick (d_a ~ 0.1 μm) active layer with a very low confinement factor (Γ_a ~ 0.01) is explicitly designed to provide a large V/Γ_a. Theoretical analysis[10] predicted that lasers of this type should be capable of producing pulses with energies of 1–5 nJ, with a duration around 100 ps, when pumped by current pulses of a nanosecond duration, with an amplitude of ~ 10 A, that is, within the reach of standard silicon electronics.

Experimental results obtained with a laser structure based on this design have indeed demonstrated successful operation, with pumping pulses 10 A in amplitude and about 1 ns long, generated by an Si avalanche diode source.[11] The pulse durations were around 100 ps as predicted; the peak powers obtained so far have not exceeded 10 W (corresponding to a total energy of ~ 1 nJ);[12] higher amplitudes are expected with further structure optimisation. The structures employed so far have used bulk active layers; theoretical predicions[13] show that operating with multiple quantum well active layers may be beneficial (the sublinear $g(N)$ dependence helps carrier accumulation before the pulse, in agreement with estimates [5.9, 5.10].

Essentially a modification of this design is the waveguide with a vertical 1-dimensional photonic crystal (periodic modulation of composition and hence refractive index) in the waveguide structure.[14] As the crystal in the structure used in this work operated in the *index-guiding* rather than *photonic bandgap* mode, the shape of the modal distribution is virtually identical to that in an asymmetric waveguide (apart from very small periodic perturbations by the crystal layers). Gain-switched lasers of this type have been recently used to achieve pulses about 100 ns in duration, with an energy of about 11 nJ (though some of the energy was contained in a low-power tail of the pulse).[14]

5.3.3 Gain-switching structures with saturable absorbers (SAs)

SAs in the form of unpumped sections of the laser cavity are typically introduced in the laser structure for the purposes of passive QS or mode-locking (see Sections 5.3 and 5.4). However, an SA can also be introduced to aid the performance of a laser intended for GS. In this case, the associated high threshold ensures that a large carrier density is accumulated before the pulse, while the saturation of the SA during the pulse helps increase the peak power and reduce duration in a regime that combines features of true GS and passive QS; the fast SA recovery can also prevent trailing pulses. Since concentrating the SA in a single area of the laser was shown to lead to strong spatial hole burning reducing the pulse power,[15] a geometry whereby the SA was distributed in short sections along the length can be used instead. Ion implantation was used[15] to create such an SA. A simple double heterostructure laser with $d_a = 0.25$ μm and 20 short SA sections occupying one-fifth of the length produced pulses with a relatively modest energy of 50 pJ. In a single-heterostructure laser similar to that used in the experiments of References 7 and 8, the introduction of an SA at the laser facets helped to achieve shorter, more intense pulses than a similar laser without the SA, with peak powers up to 380 W and a FWHM duration of 40–45 ps, implying energies as high as ~ 15 nJ.[16]

5.3.4 Spectral properties and control of gain-switching

By default, Fabry–Perot GS lasers have a broad lasing spectrum; therefore, considerable effort has been dedicated to the control of their spectral properties and achieving narrowband emission, desirable for a number of applications. Most straightforwardly, this is achieved by using specialised constructions such as distributed Bragg reflector (DBR)/DFB lasers or external cavity grating coupled[17] constructions. These can generate single-frequency pulses (tuneable in the case of the construction of Reference 17) in either repetitive or single-pulse GS. In simpler constructions not involving integrated gratings, spectral narrowing in repetitive GS (large-signal modulation) can be achieved by a method known as *self-(injection)seeding*,[18,19] whereby a small fraction of the laser emission is spectrally filtered (*resonant* self-seeding) and fed back to the laser with a time delay slightly smaller than an integer number of modulation periods. This seeds the GS pulses and leads to GS in a narrow line (down to a single longitudinal mode), with little loss in pulse energy/power. In the case of the external reflector being a diffraction grating, which is easily spectrally tuneable, tuning of the gain-switching pulses over a range of > 40 nm is possible. Interestingly, even *non-resonant* self-seeding,[20] whereby the pulse is fed back from a simple, spectrally *non-selective* external reflector, can lead to a considerable spectral narrowing (from 11 to 0.05 nm), though slightly less pronounced than with a spectrally selective feedback.[21]

5.4 Q-switching

This section covers QS in terms of its main features, its theoretic foundations, and the applications of passive QS.

5.4.1 The main features

In general, the term 'QS' can refer to any regime whereby short pulse generation is achieved by modulating, not the optical gain as in the case of GS, but the optical loss in the cavity (internal or outcoupling) and hence the quality factor 'Q' of the cavity – hence the term QS. QS can be active, with a modulator inserted in the laser cavity, or passive, usually achieved either with an SA or a saturable *reflector*. Thus, QS is different from GS in the sense that it requires a specially designed laser construction, often involving a separate electrical contact for the SA/reflector or modulator, whereas GS can be achieved in standard lasers not intended specifically for short pulse generation, as discussed in Section 5.2.

Active QS is, from the physical point of view, fundamentally not too dissimilar from GS: modulating either gain (in GS) or loss (in active QS) essentially represents modulating the *net gain* in the cavity. Like GS, active QS can be single-pulse or repetitive. The difference is mainly quantitative: in most practical GS schemes it is not the gain directly that is modulated but the current applied to the laser, as discussed in Section 5.2; therefore, the effect on the gain is moderated by the dynamics of carrier density, which limits the sharpness of the net gain modulation. In active QS, on the other hand, the modulation of loss (e.g., with an intracavity electro-absorption modulator) can be more direct, leading to a possibility of shorter net gain pulses and hence shorter, intense single output optical pulses – at the expense of, firstly, a more complex laser construction, as mentioned above, and, secondly, a reduced efficiency because a realistic modulator always introduces some extra loss into the cavity. An example of the potential of active QS has been shown by recent experiments on a DBR laser with a tapered gain section, which have demonstrated optical pulses ≈75 ps wide with a pulse power of 6.3 W at a repetition frequency of 1 GHz, corresponding to a pulse energy of 0.47 nJ at $\lambda = 1064$ nm.[22] Since the structure was a DBR one, the laser operated in a dynamically single-mode regime, with a spectral width of only < 0.05 nm.

Passive QS, on the other hand, is fundamentally different from GS since it does not require pulsed, nor high-frequency modulated, pumping; the laser operates in a self-pulsating mode under a *CW* pumping regime. In fact, self-sustained pulsation (SSP) is a frequently used alternative term for passive QS. The term SSP is more often used when the effect is unwanted (e.g., as an envelope modulation in ML lasers, see Section 5.4), whereas the term 'passive QS' is more often reserved for constructions where essentially the same regime is the desired and intended mode of operation. Below, we shall concentrate on passive QS. This can be achieved by including a saturable element (absorber or reflector) in the laser cavity, with a recovery time of the same order as, or shorter than, the gain recovery (carrier recombination) time. An SA can be realised either by designing the laser waveguide and contact stripe so as to have an unpumped area (which then acts as the SA) alongside the centre of the stripe (which in this case is the gain area) or by introducing an absorbing layer in the laser structure, or finally as a special reverse-biased segment in tandem with the gain segment as in Fig. 5.2 (the latter is known as the two-section, or tandem, laser geometry, which is also the standard geometry for mode-locking, see Section 5.4).

5.4.2 Foundations of theory

Passive QS, like GS, operates with pulses at least of the same order as the cavity round-trip. Therefore, passive QS with SAs, too, can usually be described using a rate equation model, with an extra equation of the type of Equation [5.1] for the carrier density in the SA:

$$\frac{\mathrm{d}N_g}{\mathrm{d}t} = \frac{i(t)}{eV} - \frac{N_g}{\tau_n} - v_g g(N_g, S)S \qquad [5.18]$$

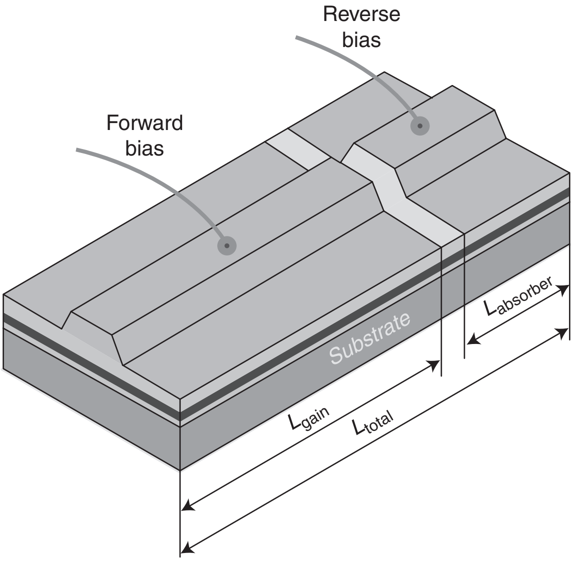

5.2 A schematic diagram of a monolithic two-section laser.

$$\frac{dN_a}{dt} = -\frac{N_a}{\tau_a} + v_g \alpha(N_a, S)S \qquad [5.19]$$

$$\frac{dS}{dt} = v_g (f_g g - f_\alpha \alpha - \alpha_t)S + \frac{f_g \beta N_g}{\tau_n} \qquad [5.20]$$

Here, f_g and f_α are the overlaps of the laser mode with the gain and SA areas that supersede the confinement factor in Equation [5.2]; in the case of a tandem geometry with two contacts, $f_g + f_\alpha = \Gamma_\alpha$; α is the saturable absorption coefficient, the carrier densities N_g and N_α relate to the corresponding sections, the rest of notations are as in Equations [5.1] and [5.2]. As in the case of GS, gain and saturable absorption can be calculated microscopically; in the simplest version of the model, for gain one can use the expressions [5.4] and [5.5], and for the SA, a similar linear approximation:

$$\alpha \approx \alpha_0 - \sigma_\alpha N, \qquad [5.21]$$

can be adopted.

The system [5.18]–[5.20] has a formal steady-state solution; however, within a certain range of parameters this solution is unstable due to the presence of the SA; within this range of parameters, what is normally decaying relaxation oscillations turns into SSP, or passive QS. The range of parameters for QS for a typical tandem laser is illustrated in Fig. 5.3; note

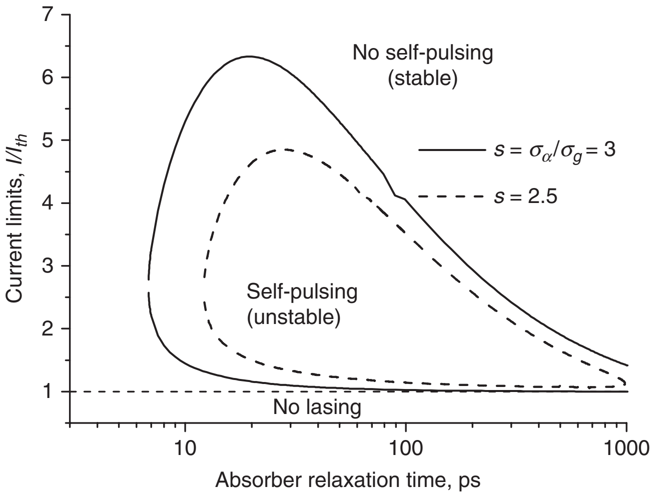

5.3 Stability limits of Q-switched SL operation. The effect of the *s*-parameter is illustrated.

that the SSP range increases with a decrease in the SA lifetime. Another important parameter whose increase increases the range of QS, at all values of the SA recovery time, and also leads to shorter, more intense pulses, is the SA to gain cross-section ratio $s = \sigma_\alpha / \sigma_g$ [1,23] (a condition $s>1$ is necessary for successful passive QS;[1,23] as will be shown in Section 5.4, this parameter is also very important for the other important dynamic regime of two-section lasers, mode-locking; note that the parameter range in Fig. 5.3 has been calculated without regard to the possibility of the ML regime, which considerably alters the operating regimes map observed experimentally).

Within the current range for passive QS, the pulse amplitude (defined as the difference between the maximum and minimum power) shows a non-monotonic behaviour on current, with a broad maximum towards the higher side of the current range. At the high-current side of this maximum, the pulses have an extinction ratio significantly below 100%, with a large SW background, before dying out completely with an increase in current. An approximate analytical theory of QS predicts that the repetition frequency F of QS shows, within the first approximation, a linear dependence on current: $F \propto i - i_{\text{th}}$.[23] From more accurate numerical solution of Reference 24, the dependence $F(i)$ at low currents is somewhat superlinear, turning sublinear at high currents when the QS pulses gradually approach normal decaying relaxation oscillations, whose frequency is known to vary with current roughly proportionally to $F \propto \sqrt{i - i_{\text{th}}}$. Near the peak pulse amplitude range, the approximation $F \propto i - i_{\text{th}}$ still holds as a good approximation.

Instead of the SA, QS can also be achieved with a saturable *reflector*, in particular with a double-contact[25] or triple-contact[26] distributed feedback (DFB) lasers, in which one of the sections is biased at lower (but positive) current to act as the reflector, while the other, more strongly pumped, section(s) act(s) as the gain section(s). The carrier dynamics in the amplifier and reflector section, combined with the strong carrier dependence of the refractive index, lead to the dynamic detuning between the lasing wavelength and the reflector peak; due to the strong dispersion of reflectance this can lead to the reflectance increasing with an increase in light power, which is equivalent to SA operation. The regime is therefore known as dispersive self-QS. It has produced pulsations at repetition rates up to 12 GHz in a double-section construction,[25] dependent (somewhat more weakly than the SA-induced QS) on the operating currents of the gain and reflector sections. In triple-section constructions,[26] frequencies of up to 28 GHz have been attributed to this phenomenon. Reliable theoretical analysis of such constructions is not possible with a simple rate equation model; it can be performed using either dynamic analysis of laser cavity eigenvalues or a travelling-wave model similar to those used for ML lasers discussed below. The advantage of those constructions, over those incorporating an SA, is single-frequency generation, typical in DFB lasers. However, they are more complex construction, and the parameter (current) range for pulse generation tends to be relatively narrow.

5.4.3 Applications of passive Q-switching

By far the most widespread application of passively Q-switched SLs is related to the fact that, unlike CW operated lasers, these self-pulsating devices are virtually immune to optical feedback. This is very important in information storage and retrieval systems such as CD players and have led to mass production of self-pulsating red ($\lambda = 650$ nm) lasers, in which saturable absorption is provided by unpumped areas in the laser stripe, thus enabling a cheap, single-contact construction. The exact pulse properties are not very important in such lasers, only the actual fact that self-pulsation takes place.

Early work on more sophisticated Q-switched SLs with an electrically isolated reverse-biased SA section concentrated on their possible applications in communications, including all-optical clock generation and clock recovery, which was indeed demonstrated;[27,28] some later work followed this trend.[29] The fact that the repetition frequency in Q-switched lasers is not a function of the construction, but varies with current, makes for a relatively broad (several per cent of the free-running frequency, depending on the signal amplitude) locking range of clock recovery.

However, the bit rates accessible with passively Q-switched lasers with SAs are most often restricted to a few GHz, so all-optical clock extraction using passively Q-switched lasers was only possible at limited bit rates of up to about 10 GBit/s per channel (bit rates of 2.5 and 5 GBit/s per channel with a SA-induced QS were reported in References 27 and 28, and clock recovery with DQS lasers was shown at 10 GBit/s[29]), for which more traditional electronic means of clock recovery are now available at reasonable cost. Besides, since each Q-switched pulse emerges independently from spontaneous noise, these lasers are known to suffer from considerable jitter (though no degradation in bit error rate was reported by the authors of References 27 and 28).

Probably for these reasons, after considerable interest in the (mainly early) 1990s, research in Q-switched SLs and their applications has seen somewhat less attention in the subsequent decade; however, new applications have emerged over the recent years.

In Reference 30, the broad injection-locking property of self-pulsating lasers has been exploited for optically assisted radio communications. The self-pulsating laser was locked onto a 1.393-GHz carrier amplitude shift key modulated with 155-MB/s pseudo-random data. Tuneable selection of carriers at 1.409 and 1.630 GHz have been demonstrated, with the resultant injection-locked signals being amplified by ≈20 dB.

Another application[31,32] makes use of the properties of passively Q-switched lasers operated near the peak QS power, namely, the fact that this regime shows a roughly linear dependence of the pulse repetition frequency on current, combined with a roughly constant pulse amplitude, as discussed in the previous section. This makes such lasers attractive sources for *stroboscopic measurements* of fluorescence lifetimes, for example in biological tissues. The stroboscopic technique does not require costly and bulky time-domain measurement techniques; instead, the material under investigation is excited by a stream of short (much shorter than the repetition period) optical pulses with a roughly constant energy and variable repetition rate (which in a Q-switched laser near peak pulse power is easily varied by current variation). The *average* luminescence intensity is then measured as a function of the repetition rate, and the lifetime is extracted from this measured dependence. The authors used simple, cheap, single-contact Q-switched lasers intended for use in CD players to successfully demonstrate the technique for measuring lifetimes in a dye, which are in the nanosecond range.[31,32] The technique was then used and extended for demonstrating wide-field, real-time, lifetime imaging of cancer cells.[32]

5.5 Mode-locking (ML) in semiconductor lasers: an overview

This section provides an overview of ML in SLs, focusing on the principles and positioning of SLs among ML sources, ML techniques in SLs, and progress in the modelling of ML lasers.

5.5.1 General principles and the place of SLs among ML laser sources

ML is a regime whereby the laser emits light in several modes with constant and precisely equidistant frequencies. Usually, the term is used more specifically in referring to *amplitude modulation* (AM) ML, meaning that the phases of the (longitudinal) modes may be considered approximately equal. In time domain, this corresponds to the laser's emitting a train of ultrashort (shorter than the round-trip) optical pulses, at a repetition frequency F near the cavity round-trip frequency or its harmonic:

$$F \approx \frac{M_h v_g}{2L} \tag{5.22}$$

(v_g being the group velocity of light in the laser, L the cavity length and M_h the harmonic number, or the number of pulses coexisting in the cavity; in the simplest and most usual case, $M_h = 1$).

In most cases (some important exceptions will be mentioned in Section 5.8.3), ML does not occur spontaneously and requires a special laser construction and/or operating conditions. Namely, it is usually achieved either by modulation of the laser net gain at a frequency F or its (sub)harmonic (*active* ML) or by exploiting non-linear properties of the medium to shorten the propagating pulse, countering the broadening effects of gain saturation and dispersion (*passive* ML). Passive ML, in turn, is usually achieved by introducing an SA into the laser cavity, as in passive QS. The SA both facilitates a self-starting mechanism for ML and, more importantly, plays a crucial role in shortening the pulse duration. More recently, saturable *refractive index non-linearities* approximately equivalent in their action to SA have been intensely studied; salient examples are *additive pulse ML* and *Kerr lens ML* in solid-state lasers. A combination of active and passive methods of ML is known as *hybrid* ML; if the external modulation is in the form of short pulses, the corresponding regime is known as *synchronous* ML.

SLs (at least in a monolithic configuration) cannot yet directly generate the sub-100 fs pulses routinely available from diode-pumped crystal-based lasers,[33–35] but they represent the most compact and efficient sources of (sub-)picosecond pulses. They are directly electrically pumped, and the bias can be easily adjusted to determine the pulse duration and the optical power, thus offering some electrical control of the output pulse parameters. They also offer the best option for the generation of high repetition rate trains of pulses, owing to the small L in Equation [5.22] and hence the large values of F. Ultrafast SLs have thus been favoured over other laser sources for high-frequency applications such as optical data/telecoms. Being much cheaper to fabricate and operate, ultrafast SLs also offer the potential for dramatic cost savings in a number of applications that traditionally use solid-state lasers. The deployment of high-performance ultrafast SLs could therefore have a significant economic impact, by enabling ultrafast applications to become more profitable, and even facilitate the emergence of new applications.

The basic physical mechanisms underlying the generation of short pulses from SLs are fundamentally similar to those of other types of lasers, but a number of features are very different. Semiconductors have both a higher gain per unit length and a higher non-linear refractive index than other gain media. The interaction of the pulse with the gain and the resulting large changes in the non-linear refractive index lead to significant self-phase modulation, imparting a noticeable *chirp* to the ML pulses, usually up-chirp in the case of passive ML lasers, which combined with the positive dispersion of the gain material leads to substantial pulse broadening. This mechanism has been among the limitations in obtaining pulse durations of the order of 100 fs *directly* from the SLs, with picosecond pulses being the norm. Furthermore, a strong saturation of the gain also results in stabilisation of the pulse energy, which limits the average and peak power to much lower levels than in vibronic lasers. Output average power levels for ML SLs are usually between 0.1 and 100 mW, while peak power levels remain between 10 mW and 1 W. Only with additional amplification/compression setups can the peak power reach the kW level.[36] In addition, the typical scale of carrier relaxation times in semiconductor materials is of the order of hundreds of picoseconds, comparable to the ML repetition time, leading to a rich variety of dynamic instabilities in the laser behaviour. This combination of practical promise and scientific challenge has made ML SLs an important topic of research for more than two decades; they have arguably attracted considerably more attention than all other methods of ultrashort pulse generation taken together. Early work concentrated on external cavity structures; later, monolithic and multi-gigahertz constructions, reviewed in an earlier paper,[37] became a research priority. The most recent years have seen considerable progress in both improving the theoretical understanding of ML in SLs, and using this understanding to improve their performance in terms of power, pulse duration/chirp, stability, accessible repetition rates, and integrability issues. To this end, new constructions as well as new materials have been proposed. Here, as with the other laser types, we attempt to summarise both the current theoretical understanding of ML laser performance, including the recent theoretical progress (Sections 5.5 and 5.6), and the use of this understanding for improving ML laser performance (Sections 5.7 and 5.8). The use of more radical novel ML principles is also briefly discussed (Sections 5.8.2 and 5.8.3).

5.5.2 Mode-locking techniques in SLs: the main features

The main advantages of ML over other methods of generating ultrafast pulses by SLs are the higher repetition rate pulses and shorter pulse durations. To realise these advantages to the full, a variety of ML techniques and device structures have been investigated and optimised.[1] All three main forms of ML – active, passive and hybrid – have been extensively studied for SLs.

Purely *active* ML in a SL can be achieved by direct modulation of the gain section current with a frequency very close to the pulse repetition frequency in the cavity, or to a subharmonic of this frequency. Alternatively, an electro-absorption segment of a multi-element device can be modulated to produce the same effect, or a separate modulation section introduced. The main advantages of active ML techniques are the resultant low jitter and the ability to synchronise the laser output with the modulating electrical signal, which is a fundamental attribute for optical transmission and signal processing applications. However, high repetition frequencies are not readily obtained through directly driven modulation of lasers because fast RF modulation, particularly of current, becomes progressively more difficult with increase in frequency.

Passive ML of SLs typically utilises an SA region in the SL. Upon start-up of laser emission, the laser modes initially oscillate with relative phases that are random; in other words, the radiation pattern consists of irregular bursts. If one of these bursts is energetic enough to provide a fluence of the order of the saturation fluence of the absorber, it will partly bleach the absorption. This means that around the peak of the burst where the intensity is higher, the loss will be smaller, while the low-intensity wings become more attenuated. The pulse generation process is thus initiated by this family of intensity spikes that experience lower losses within the absorber carrier lifetime. The dynamics of absorption and gain play a crucial role in pulse shaping. In steady state, the unsaturated losses are higher than the gain. When the leading edge of the pulse reaches the absorber, the loss saturates more quickly than the gain, which results in a net gain window, as depicted in Fig. 5.4. The absorber then recovers from this state of

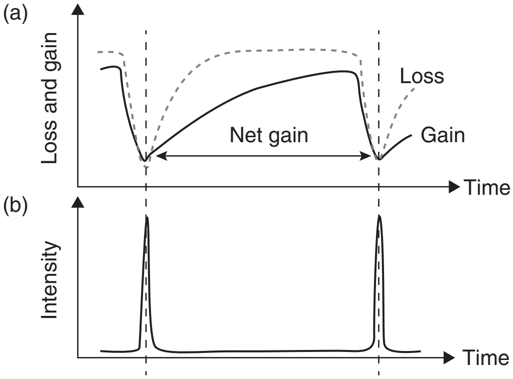

5.4 The mechanism of passive ML: (a) the loss and gain dynamics that lead to (b) pulse generation.

saturation to the initial state of high loss, thus attenuating the trailing edge of the pulse. It is thus easy to understand why the saturation fluence and the recovery time of the absorber are of primary importance in the formation of ML pulses.

In practical terms, the SA can be monolithically integrated into an SL by electrically isolating one section of the device (as in the Q-switched laser, Fig. 5.2). By applying a reverse bias to this section, the carriers photogenerated by the pulses can be more efficiently swept out of the absorber, thus enabling the SA to recover more quickly to its initial state of high loss. An increase in the reverse bias serves to decrease the absorber recovery time, which will have the effect of further shortening the pulses. Alternatively, an SA can also be implemented through ion implantation on one of the facets of the laser, thus increasing the non-radiative recombination.[38]

Passive ML provides the shortest pulses achievable by all three techniques and the absence of an RF source simplifies the fabrication and operation considerably (albeit at the expense of somewhat larger pulse jitter and RF linewidth than in active or hybrid ML). It also allows for higher pulse repetition rates than those determined solely by the cavity length, by means of harmonic ML ($M_h > 1$ in Equation [5.22]; the means of achieving this will be reviewed in more detail in Section 5.7.4).

Hybrid ML is usually achieved by applying RF modulation to the SA section, which in this case doubles as an electro-absorption modulator (RF modulation of the gain section current is also possible but has been proven to be less efficient). In this case the pulse generation may be seen as initiated by a modulation provided by the RF signal, while further shaping and shortening is assisted by the SA. This process results in high quality pulses, synchronised with an external source.

5.5.3 Progress in modelling of ML lasers

Until recently, there were three main types of ML laser models; more recently one of them got significantly developed, to become effectively the new, fourth type of a model. These four approaches are explained below, with the most recent one explained in most detail.

1. Conceptually the simplest, and historically the oldest, models of ML lasers are **time-domain lumped models**, based on the approximation that the pulsewidth is much smaller than the repetition period, and treating a hypothetic ring laser geometry with unidirectional propagation. The amplification and gain/group velocity dispersion, which in reality are experienced by the pulse simultaneously, may then be approximately treated in two independent stages. This allows the representation of the distributed amplifier in the model by a lumped *gain element* performing the functions of amplification and self-phase-modulation. Mathematically, this element can be described by a non-linear integral or integro-differential operator $\hat{G}$ acting on the complex pulse shape function (complex slow amplitude) $Y(t)$, t being the *local* time of the pulse. Separate time scales are introduced explicitly for the pulse (the short time scale) and relaxation period between pulses (the long time scale). A similar element, described by a non-linear operator $\hat{Q}$, is introduced to describe the saturable absorption, and the dispersion (gain/absorption and group velocity) is introduced as a separate, linear dispersion operator $\hat{D}$. With the approximation of small gain and saturable absorption per pass (inherited from the non-semiconductor laser theory, for which the model was originally developed), neglecting dispersion, and assuming emission of pulses of equal energy, the model yields transcendental equations that allow for quasi-analytical calculation of ML boundaries, and also of the pulse energy (but not duration and peak power, which cannot be calculated without accounting for dispersion). This is known as New's model of ML (though G. New's original paper[39] related to non-semiconductor lasers). If, on the other hand, dispersion is taken into account, but, in addition to the approximation of the small gain and absorption per pass, also the gain and absorption *saturation* are taken as small, expanding the integral and differential operators $\hat{\mathrm{G}}$, $\hat{Q}$, and $\hat{\mathrm{D}}$ in series and requiring that both the amplitude and the *shape* of the pulse is conserved from one repetition period to the next allows for a single integro-differential equation for the pulse profile $Y(t)$ on the short time scale to be obtained. The equation, known as the master equation of ML, admits an analytical solution of the form:

$$Y(t) = Y_0 \exp(i\Delta\omega t)\left(\cosh\frac{t}{\tau_p}\right)^{-1+i\beta} \qquad [5.23]$$

known as the *self-consistent profile* (SCP). The corresponding theoretical approach is known as the SCP, or Haus's, ML theory; it is based on H Haus's work on ML in lasers of an arbitrary type[40] and was later extended to account for large self-phase modulation in SLs.[41,42] Substituting the SCP in the ML equation, one obtains three complex, or six real, transcendental algebraic equations[41,42] for six real variables: pulse amplitude $|Y_0|$, duration measure τ_p, chirp parameter β, optical frequency shift $\Delta\omega = \omega - \omega_0$, repetition period detuning δT, and phase shift $\arg(Y_0)$ (which is not a measurable parameter, so in reality there are five meaningful equations). These equations, being nonlinear and transcendental, generally speaking, cannot be solved analytically, but still allow for some insight into the interrelation of pulse parameters. The Haus model also allows the conditions for stable ML to be determined, which are different from those obtained using New's model.

Thus lumped models, particularly the SCP model, allow for considerable analytical progress in treating ML, but quantitatively are very far from describing monolithic ML SLs accurately, and are not even capable of simulating the variety of dynamic regimes observed experimentally (see analysis below).

2. At the other end of the spectrum of theoretical approaches to the ML laser properties are **distributed time-domain**, or **travelling-wave**, models, which treat the propagation of an optical pulse through a waveguide medium with space as well as time resolution. The model starts with decomposing the optical field in the laser into components propagating forward and reverse in the longitudinal direction (say, z):

$$Y(r,t) = \Phi(x,y)\Big(Y_f \exp(i\beta_{\text{ref}} z) + Y_b \exp(-i\beta_{\text{ref}} z)\Big)\exp(-i\omega_{\text{ref}} t) \qquad [5.24]$$

with Φ being the transverse/lateral waveguide mode profile and ω_{ref} and $\beta_{\text{ref}} = n(\omega_{\text{ref}})k_{\text{ref}} = n(\omega_{\text{ref}})\omega_{\text{ref}}/c$ being the reference optical frequency and the corresponding wave vector respectively. This results in equations for slowly varying amplitudes $Y_{f,b}$:

$$\begin{aligned} \pm\frac{Y_{f,b}}{\partial z} + \frac{1}{v_g}\frac{Y_{f,b}}{\partial t} = & \left(\frac{1}{2}\left(\hat{g}_{\text{mod}} - \alpha_{\text{int}}\right) + ik_{\text{ref}}\hat{\Delta} n_{\text{mod}}\right) \\ & \times\ Y_{f,b} + ik_{bf,fb}Y_{b,f} + F_{\text{spont}}(z,t), \end{aligned} \qquad [5.25]$$

where $\hat{g}_{\text{mod}}$ is the modal gain, which in general is implemented as an operator to represent gain dispersion (at z values within SA sections, the gain value g is naturally changed to $-\alpha$, α being the saturable absorption coefficient), α_{int}, the internal parasitic loss, $\hat{\Delta} n_{\text{mod}}$ dynamic correction to the modal refractive index, including the group velocity dispersion operator if needed. The coupling coefficients $k_{bf,fb}$ allow for introduction of built-in distributed reflectors or dynamic gratings introduced by standing wave profiles, and the last term is the Langevin noise source that drives the model.

The equations are directly solved numerically, in a system with spatially resolved rate equations for the carrier populations in the gain and SA sections, which are used to calculate the gain and absorption dynamics. This is usually done using phenomenological relations, though an interesting recent development has been an introduction of an efficient, if somewhat simplified, miscroscopically-based model of spectral-temporal dynamics of gain and absorption into a travelling-wave simulator.[43]

Travelling-wave models are very powerful and general; they combine large-signal approach with accurate account for spectral features. They have been extensively and successfully used by a number of research groups to analyse and design many edge-emitting laser constructions including ML lasers; they also form the core of several commercial simulators, some of which have been applied to ML laser design – see Reference 44 for an overview. The main limitations of travelling-wave models are, firstly, the absence of any analytically solvable cases – the approach is essentially numerical which limits the physical insight gained from the models – and, secondly, the relatively high requirements such models pose on the computing time and memory.[44]

3. An approach totally alternative (or complementary) to the time-domain analysis of ML is offered by the technique of **modal analysis, static or dynamic** (as in Reference 45 and references therein, and also in References 46 and 47). In this approach, instead of analysing the pulse shape dynamics, a modal decomposition is used and the dynamics of mode amplitudes and phases followed, with the dynamics of gain and absorption providing the non-linear coupling terms that ensure ML is given the right parameter values. The advantage of the modal expansion is that the time steps can be much longer (and the number of variables can be smaller) than in the travelling-wave model, which makes the modal approach particularly efficient in analysing, say, long scale dynamics of external locking of DBR hybridly mode-locked lasers. It also has the logical advantage of describing steady-state ML as a steady-state solution of the model. Unfortunately, this is contrasted by the limitations, chief of which is the inherent assumption of weak to modest non-linearity (the model is not large-signal, which can be a significant limitation in edge-emitting ML SLs), which causes time-domain approaches to be more widely used.

4. Arguably the most significant development in the ML theory during the recent years has been the development of a model intermediate between the traditional lumped models of ML and the travelling-wave models.[48,49] This approach, known as the **delay-differential equation (DDE) model or theory**, contains a rigorous extension of Haus's and New's theories for the case of strong gain and absorption per pass, which is usually realised in SLs. Like those traditional ML models, it can provide significant analytical insight, with parameter values more relevant to SLs, but unlike those models, it allows also for detailed, self-starting, and computationally efficient, large-signal numerical analysis. This combination of analytical insight and numerical potential, small- and large-signal possibilities, within a single framework – which is unique among time-domain ML models – makes the DDE model very attractive for analysis of performance trends (if not necessarily numerical parameters) in real lasers. Extensions of the model to specialised constructions such as quantum dot (QD) lasers have also been developed and used successfully,[50] though not addressed here; the reader is referred to a recent monograph[51] for details of QD ML laser theory.

As the traditional ML theory, the DDE uses a model of unidirectional ring propagation, giving a gain operator in the form:

$$\hat{G}Y(t) = \exp\left(\frac{1}{2}(1-i\alpha_{\mathrm{Hg}})G(t)\right)Y(t) \qquad [5.26]$$

with α_{Hg} the Henry linewidth enhancement factor in the amplifier and $G(t) = \Gamma\int g(z,t)\mathrm{d}z$ the total gain integrated over the length of the amplifying region.

The SA element is described by a similar element:

$$\hat{Q}sY(t) = \exp\left(-\frac{1}{2}(1-\alpha_{H\alpha})Qs(t)\right)Y(t), \qquad [5.27]$$

with Q_s the saturated absorber, and $\alpha_{H\alpha}$, the absorber linewidth enhancement factor. There are, however, significant differences from the traditional models. Firstly, the DDE model dispenses with the assumption of $G, Q_s << 1$ necessary in traditional ML models, and also does not, in its general form, introduce the two separate time scales, neglecting non-stimulated recombination between the pulses. Instead, ordinary differential equations are written for G, Q_s, based on the spatially integrated carrier rate equations. Assuming that the pulse in the unidirectional cavity treated by the model passes the absorber before the amplifier, the equations take the form:

$$\frac{\mathrm{d}G(t)}{\mathrm{d}t} = -\left[\exp(G(t))-1\right]\exp\left(-Q(t)\right)\frac{P(t)}{U_g}+\frac{g_0-G(t)}{\tau_g} \qquad [5.28]$$

$$\frac{\mathrm{d}Q(t)}{\mathrm{d}t} = -\left(1-\exp\left(-Q\right)\right)\frac{P(t)}{U_\alpha}-\frac{q_0-Q}{\tau_\alpha}; \qquad [5.29]$$

Here, g_0 (or $G_0 = \tau_g g_0/\tau_\alpha$) characterises the unsaturated gain determined by the pumping conditions, q_0 is the unsaturated absorption, $P(t) = v_g\hbar\omega A_X\,|Y(t)|^2$ is the optical power, τ_g and τ_α are the gain and SA recovery times, and:

$$U_g = \frac{\hbar\omega A_{Xg}}{\sigma_g},\quad U_\alpha = \frac{\hbar\omega A_{X\alpha}}{\sigma_\alpha} \qquad [5.30]$$

are the saturation energies of the amplifier and the SA, with $\sigma_g = \mathrm{d}g/\mathrm{d}N$; $\sigma_\alpha = \mathrm{d}\alpha/\mathrm{d}N$ being the gain cross-sections (the derivative of the gain on the carrier density N) and A_{xg} and $A_{x\alpha}$ the cross-sections of the optical beam (mode) in the gain and SA sections.

The second difference of DDE from traditional ML theories is in the treatment of the dynamics of ML. As in previous theories, it describes pulse propagation by cascading the operators. However, in previous theories the dynamics are essentially described by an iterative procedure, setting $Y_{i+1}(t) = (\sqrt{\kappa}\hat{\mathrm{G}}\,\hat{\mathrm{Q}}\,\hat{\mathrm{D}})\,Y_i(t)$, where i is the number of the pulse round-trip (determining the 'slow' evolution of the ML pulse), the time t is on the fast time scale commensurate with the pulse duration, and the dimensionless parameter $\kappa < 1$ introduces the total (integrated) unsaturable intensity losses in the cavity, both dissipative and outcoupling. The *stationary* ML equation can then be obtained by writing out the condition that the broadening and narrowing cancel each other, and the shape of the pulse is conserved from one repetition period to the next: $\left(\sqrt{\kappa}\hat{\mathrm{G}}\,\hat{\mathrm{Q}}\,\hat{\mathrm{D}}\right) Y(t) = e^{i\delta\psi} Y(t+\delta T)$, where δT is the shift of the pulse or detuning between the repetition period and the round-trip of the 'cold' cavity (or its fraction in case of locking at harmonics of the fundamental frequency), and $\delta\psi$ is the optical phase shift induced by the round-trip. In between the pulses, on the slow time scale commensurate with the round-trip time, gain and SA are allowed to recover with their characteristic relaxation times, according to the rate equation for carrier density with $S = 0$. This allows one to calculate the values of gain and saturable absorption at the onset of the pulse, given the pulse energy and repetition period. In DDE, with the two different scales for pulse analysis, in general, abandoned, the iteration procedure is substituted by a *delay* one. In its most general form, this procedure may be written as $Y(t) = \left(\sqrt{\kappa}\hat{\mathrm{G}}\,\hat{\mathrm{Q}}\,\hat{\mathrm{D}}\right) Y(t - T_{\mathrm{RT}})$, where T_{RT} is again the round-trip of the cold cavity, and t is still the local time of the pulse. A particularly useful form of this model, however, is obtained if the dispersion operator $\hat{\mathrm{D}}$ is expanded as a differential one The authors of References 48 and 49 showed that for a bandwidth limiting element with a Lorentzian spectrum $\hat{\mathrm{D}}\,Y^T(\omega) = \left[1\big/\left(1 - i(\omega - \omega_p)\right)\big/\gamma\right] Y^T$ (i.e., neglecting group velocity dispersion), assuming without much loss of generality that the peak gain frequency ω_p coincides with one of the laser resonator modes, and taking it as the reference optical frequency, we can re-write the equation for Y as:

$$Y(t) = -\gamma^{-1}\frac{\partial Y(t)}{\partial t} + \left(\sqrt{\kappa}\hat{\mathrm{G}}\,\hat{\mathrm{Q}}\right) Y(t - T_{\mathrm{RT}}) \qquad [5.31]$$

Equation [5.31], which is a delay-differential one, gives the DDE model its name; note that the original papers[48,49] use a slightly more general form of it, without assumptions on the peak and reference frequencies.

Equations [5.28]–[5.29] and [5.31] are a closed system suitable for a detailed numerical simulation of both stationary and dynamic behaviour of passive ML. They can also be fairly easily adapted to allow numerical analysis of *hybrid* ML behaviour. As shown in Reference 49, the DDE model also allows for significant *analytical* progress, similar to one achieved with classical New's and Haus's models, but for large single-pass gain and absorption, more relevant for most SL constructions than the classical SCP. In the analytical procedure, the slow absorption and gain approximation (neglect of non-stimulated recombination and absorption recovery during the pulse) has to be reintroduced, and the slow (relaxation of gain and absorption between pulses) and fast (evolution during the pulse) stages of laser dynamics are, as in the traditional ML models, treated separately.

In particular, it is possible to analyse the stability of the solutions by requiring that net gain both immediately before the pulse and immediately after the pulse are smaller than one:

$$\begin{aligned} G_- - Q_- - \mathrm{In}\,\kappa < 0 \\ G_+ - Q_+ - \mathrm{In}\,\kappa < 0 \end{aligned} \qquad [5.32]$$

Here G_-, Q_- are the total (integrated) gain and absorption immediately before the pulse, G_+, Q_+ are the values immediately after the pulse. This is a generalisation of the condition proposed in traditional ML theory[39] for the case $\ln\ (1/\kappa) << 1$, to the case of an arbitrary κ.

Further analytical progress is possible in two limiting cases. The first is the case of a model without spectral filtering ($\gamma \to \infty$), which the authors of Reference 49 identified as the *generalised New's model* for the arbitrarily large gain and absorption per pass. This theory, as the traditional New's one, cannot predict the pulse shape or duration, leading to pulses collapsing to a delta-function shape. The total pulse *energy* U_p, however, can be estimated approximately from a closed system of five (non-linear and transcendental) equations for the five unknowns: $G\pm$, $Q\pm$ and U_p. The solution gives the dependence of pulse energy (though not duration or peak power) on pulse parameters, represented by the unsaturated gain (which is related to pumping current) and absorption (which is related to the reverse bias applied to the absorber). The other fundamental absorber parameter also dependent on the reverse bias, the absorber lifetime, only enters the calculations through the relaxation equation for the absorption between pulses, obtained from and does not influence the results from this model at all if $\tau_\alpha << T_{\mathrm{RT}}$ (in which case, obviously, $Q_- \approx q_0$). The solution to this non-linear algebraic equation system can then be substituted into the inequalities [5.32] to analyse the stability boundaries of the ML operating range with respect to the leading-edge and trailing-edge instability. The curves, in general, can only be calculated numerically, though some special points can be determined analytically.[49] In particular, the model confirms the conclusions from the traditional ML analysis on the importance of *the gain-to-absorber saturation energy ratio* $s = U_g / U_\alpha = \sigma_\alpha A_{Xg} / \sigma_g A_{X_\alpha}$. Namely, it shows that the condition $s > 1$ for any range of successful ML to be present, derived in the traditional SCP approach for the case of small gain and loss per period (and thus small dissipative loss), needs to be generalised in the case of arbitrary losses in the cavity as,

$$s\kappa > 1 \tag{5.33}$$

(in a more realistic construction, an extra geometric factor could also be required).

The second case when full (semi-) analytical solution of the DDE model (with relaxation terms during the pulse neglected) is possible is when the dispersion is taken into account, but the saturation of gain and absorption during the pulse is assumed to be small, as in the Haus model of ML (though the gain and absorption themselves are not necessarily small, unlike the case of the traditional Haus model). The authors of Reference 49 called this the generalised Haus's model. In this case, a steady-state solution is sought, as in the standard Haus's model; in our notations, $Y(t + T_{\mathrm{RT}}) = e^{-i\delta\Psi} Y(t - \delta T)$. Then, from Equation [5.31], a generalised form of the master equation of ML in Haus's theory can be derived,[49] which admits solutions of the same Equation [5.23] as the original master equation. Six equations are then obtained for six real parameters: peak pulse power, duration, time shift δT, optical frequency shift $\Delta\omega$, phase shift per round-trip $\delta\Psi$, and the chirp parameter β.

By substituting the solutions into the conditions [5.32], stability limits in the generalised Haus's form can be obtained. In general, they depend on the linewidth enhancement factors; however, for direct comparison with other models, the case of $\alpha_{\mathrm{Hg}} = \alpha_{H\alpha} = 0$ is useful. Results of such analysis, reproduced from Reference 49, are plotted in Fig. 5.5. In the plot, the subscript *N* refers to results from New's model, generalised (solid lines) or standard (dashed lines); and the subscript *H*, to those from Haus's model (calculated with zero linewidth enhancement factors). The filled/empty dots are the leading/trailing instability boundary calculated by numerical integration of the model. In this numerical integration, the gain and absorber operators are treated on a continuous time scale, without the need to introduce separate time scales for pulse and the free relaxation period as in the iterative procedure. As seen in the figure, standard Haus's and New's models are extremely inaccurate in predicting the instability boundaries of ML in a typical SL (with the range predicted by New's model being too wide, and that from Haus's model, too narrow, as noted also in Reference 52). The generalised Haus's model gives good agreement within its validity limits at low currents/unsaturated gain values, while the generalised New's model gives

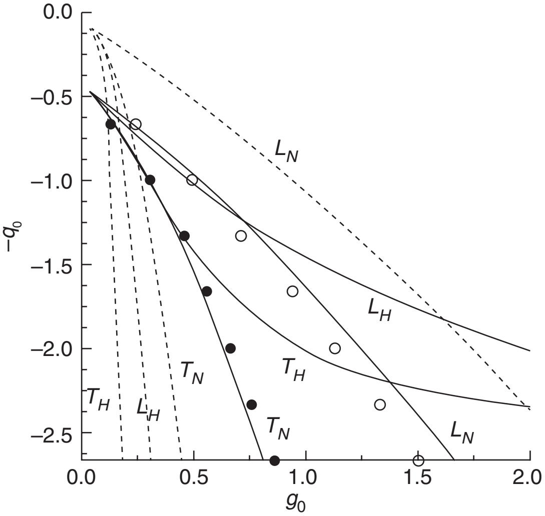

5.5 Stability boundaries of ML with respect to leading (L) and trailing (T) edge instabilities, calculated semi-analytically in traditional and generalised New's (N) and Haus's (H) models. In the calculations, $s = 25$, $T_{RT}/\tau_\alpha = 1.875$, $\tau_\alpha/\tau_g = 0.0133$, $\kappa = 0.1$, $g_0 = (\tau_\alpha/\tau_g)G_0$, $q_0 = Q_0$. Source: After Reference 49, reproduced with permission.

very good agreement with numerical simulations at all parameter values (there are some modest deviations, which will be discussed in more detail below). Thus, the large-signal nature of the DDE model is proven to be a very important advantage over the classical ML theories.

Apart from allowing some analytical progress in the limiting cases, the DDE model also allows the use of numerical techniques that have been developed for the analysis of delay-differential equations, in particular of numerical packages that allow a full bifurcation analysis of delay-differential equations. Such a study was indeed performed in Reference 49, comprising the full (in)stability analysis of the stationary solution of the DDE. The stationary solution (the steady-state light-current characteristic of the laser) itself is found by seeking the steady-state light output in the form of $Y(t)=Y_{0s}\exp(i\Delta\omega_s t)$, which gives an equation for the steady state in a parametric form. The equation is a transcendental trigonometric one and thus has an infinite set of formal solutions, corresponding to the cavity modes. The steady-state solution, as usual in laser theory, is the one with the lowest value of the threshold gain $G_s(Y = 0)$, in other words, the closest to the peak of the gain spectrum. Figure 5.6, after Reference 49, shows the results of a numerical bifurcation analysis of this solution. The line H_1 indicates the *Andronov-Hopf bifurcation* (transition from a steady state to a periodically oscillating solution with an amplitude smoothly

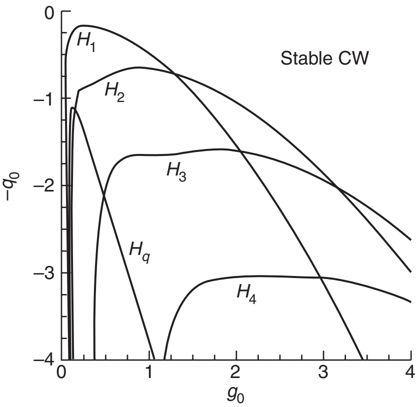

5.6 Bifurcation analysis of the steady-state solutions of the DDE model. Parameters used: $\gamma\tau_\alpha = 33.3$; $\alpha_{\mathrm{Hg},\alpha} = 0$, the rest as in Fig. 5.5. Source: After Reference 49, reproduced with permission.

increasing from zero as the controlling parameter, the unsaturated gain in this case, increases beyond a critical value), corresponding to oscillations at the fundamental ML frequency. ML is predicted at a certain range of conditions (unsaturated gain and absorption) above threshold, whereas at high enough unsaturated gain (or current) and low enough absorption, CW lasing is expected to be stable. The line H_q indicates the Andronov-Hopf bifurcation corresponding to passive QS, or SSP, instability, of the type discussed in Section 5.3. The frequency of these oscillations is about an order of magnitude below the ML frequency, so that at low current and with a sufficiently high saturable absorption in the cavity, the ML pulse train is expected to be modulated by the SSP envelope. The lines H_m. $m > 1$, show the bifurcations corresponding to a solution oscillating at the m^{th} *harmonic* of the fundamental ML frequency. At high enough values of unsaturated absorption, there are ranges of G_0 (or current) in which ML at higher harmonics is predicted to be stable, but ML at fundamental harmonic is not.

These predictions are confirmed by a full numerical integration of the DDE model (Fig. 5.7), showing the extrema of the laser intensity time dependence calculated for different values of the pumping parameter $g_0 = (\tau_\alpha/\tau_g)G_0$. At low values of g_0 (and thus current), the laser exhibits a regime when the ML pulse power is modulated by passive QS envelope, originally with nearly 100% modulation depth (Fig. 5.8a). As the pumping parameter increases, the QS modulation gradually decreases in amplitude, and eventually the modulation regime undergoes backward bifurcation, moving to a stable ML regime (this corresponds to the border of the trailing-edge instability in Fig. 5.5). Within the area of stable ML fundamental round-trip frequency, a train

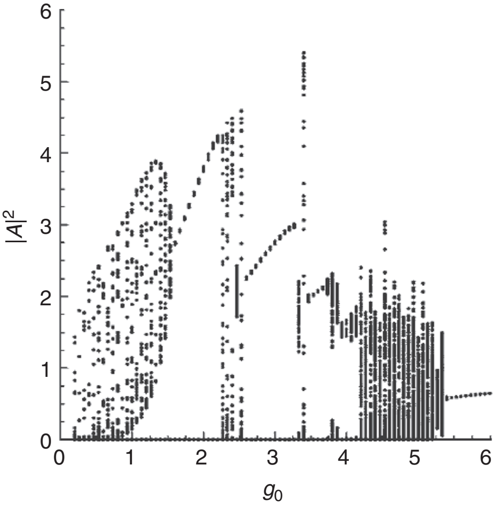

5.7 Bifurcation diagram obtained by direct numerical implementation of a DDE model. $q_0 = 4$, the other parameters as in Fig. 5.5. Source: After Reference 49, reproduced with permission.

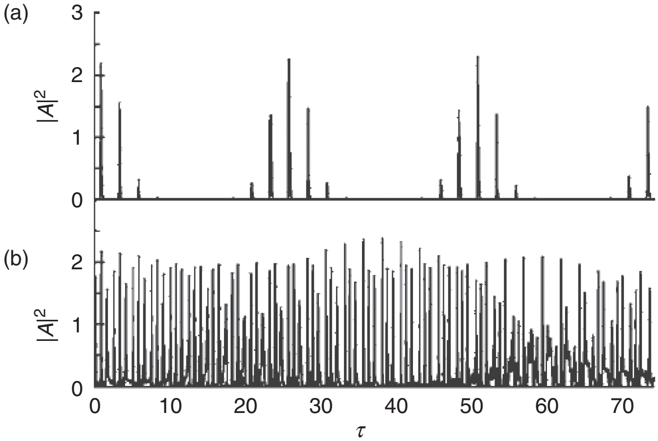

5.8 Illustration of the aperiodic regimes in Fig. 5.7: combined ML/QS regime at $G_0 = 50$ (a) and chaotic pulse competition regime at $G_0 = 350$ (b) $\tau = t/\tau_\alpha$. Source: After Reference 49, reproduced with permission.

of short pulses is observed as in Fig. 5.9a, with amplitudes increasing with G_0. At higher still pumping, the laser dynamics sees areas of harmonic ML at the second and third harmonic of the fundamental ML frequency Fig. 5.9b and 5.9c, separated by narrow areas of unstable operation. Finally, the ML breaks up completely with the onset of chaotic modulation of the pulse power, with

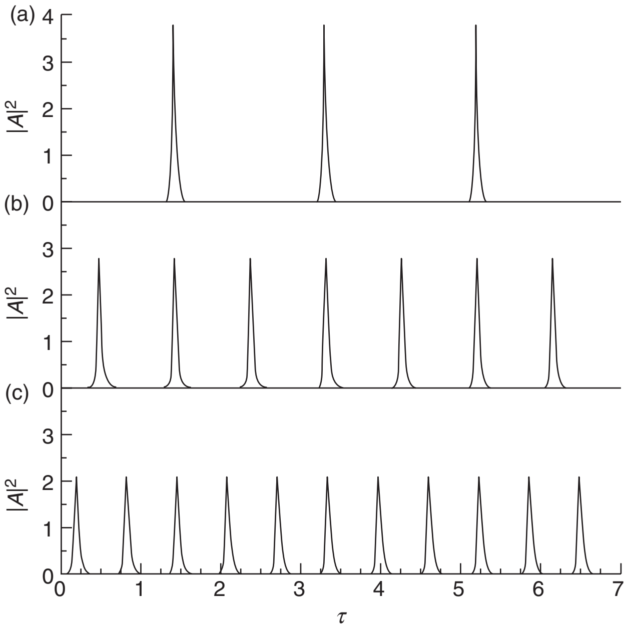

5.9 Illustration of the periodic regimes in Fig. 5.7: fundamental frequency mode-locking at $G_0 = 150$ (a) and second and third harmonic ML $G_0 = 225$ (b) and 270 (c) $\tau = t/\tau_\alpha$. Source: After Reference 49, reproduced with permission.

multiple pulse trains competing in the cavity, as in Fig. 5.8b (the regimes separating fundamental frequency ML and harmonic ML areas are similar). Eventually, the system undergoes a transition to CW single-frequency operation in agreement with the bifurcation diagrams of Fig. 5.5.

An interesting result obtained in Reference 49 is that, while the conditions [5.32] of negative net gain before and after the pulse are useful indications of the stability ranges of ML operation, the onset of instabilities in numerical simulations does not coincide with those limits *exactly*. One of the consequences of this effect is that the onset of instabilities may be expected to be sensitive to perturbations such as spontaneous noise. The effect of spontaneous emission was indeed studied analytically and numerically in Reference 49, with the noise introduced as a delta-correlated random term in the right-hand-side of Equation [5.31]. It was concluded that, while the onset of QS oscillations (trailing pulse edge instability) is a dynamic process independent of noise, the onset of the chaotic envelope instability (leading-edge instability) is strongly affected by the noise, with an increase in the noise narrowing the window of stable ML. This is confirmed by the more complex travelling-wave models.

The DDE model when used as a numerical tool is not only fully large-signal, but also self-starting: it does not, unlike previous lumped time-domain theories, require a trial pulse to start with and can reproduce the emergence of ML pulse train from randomly pulsing light output that is seen as the laser crosses the threshold condition.

There remain however some limitations to linking the DDE approach directly to the performance of a specific practical laser construction. Firstly, the model as studied in Reference 49 does not account for fast absorber saturation and fast gain non-linearity (though it could be possible to include them, at least in some approximation, and in the QD case, the explicit introduction of fast non-linearities may not be necessary – instead, separate rate equations for dot and reservoir populations are used). Next, the spatial integration of gain and absorption in DDE is mathematically justified only if both g and α have a simple linear dependence on the carrier densities in the corresponding elements, which is in itself an approximation, or alternatively if $G,Q << 1$. Finally, like traditional ML theories, the DDE model studies an artificial unidirectional ring geometry. The latter two assumptions are relatively easily addressed in the case of ML *vertical external cavity surface-emitting* lasers (VECSEL, see Section 5.7.3), which consist of an amplifying (gain) chip and a semiconductor SA mirror (SESAM) chip, separated by an unguided propagation path (possibly with collimating optics). As both the gain chip and SESAM are very short asymmetric resonators, the lumped-element formalism is a very natural one for their description. A special version of DDE, derived independently and presented in a somewhat different form than one of Reference 49, was indeed used to analyse the dynamics of external cavity VECSELs, with reasonable quantitative agreement with experiments.[53] More advanced constructions known as MIXCELs (see Section 5.7.3), with the QW gain and QD absorber layers located in one chip, could be described by a similar, possibly even somewhat simpler, model, with the single chip reflectance operator containing the effects of both the gain and the absorption. In the case of edge-emitting lasers, the accuracy of a DDE model is more suspect, and travelling-wave analysis looks more suitable for quantitative analysis of specific laser structures.

5.6 The main predictions of mode-locked laser theory

This section considers the main predictions of ML laser theory, taking into account the dependence of operating regime on operating point, and the primary parameters affecting ML laser behaviour.

5.6.1 Operating regime depending on the operating point

The most basic result of all the modern ML theories, confirmed by the experiments, is that the dynamics of notionally ML SLs are quite rich and can show, apart from stable ML, a number of other dynamic regimes. Here, we shall briefly discuss the general trends in their dependence on the laser parameters.

One of the most important features in the dynamic map of operating regimes of an ML laser is the SSPs, or passive QS, instability at low currents. As shown in Fig. 5.7, produced by the DDE model, the range of currents, or unsaturated gain, values in which this regime is observed increases with the amount of saturable absorption in the laser (which, in a given laser construction, either QW or QD, may be varied to some extent with reverse bias, due to electro-absorption). The other model parameter affected by the reverse bias is the *absorber lifetime* τ_α, which is known to decrease approximately exponentially with the reverse bias in QW materials (see Reference 54 and references therein) and to some extent in QDs too[55]). The dependence of the QS range on τ_α is not straightforward; the *QS* range tends to be broadest at a certain absorber recovery time, of the order of the round-trip time though somewhat longer. At longer τ_α, the SP range slowly decreases; however, it also decreases as τ_α is decreased and at τ_α of fraction of the round-trip, QS instability can be expected to disappear, leaving a broad area of stable ML. This is illustrated by Fig. 5.10, produced using a travelling-wave model and showing approximate borders of different dynamic regimes for a representative Fabry–Perot laser operating at 40 GHz.

This means, firstly, that care needs to be taken when interpreting the bias voltage effects on the performance of either QW or QD ML laser, as both the unsaturated absorption, the SA cross-section, and the SA recovery time τ_α are likely to be affected. The effect on the latter is probably the most significant though, as the dependence of τ_α on voltage is quite strong (exponential), while the effect on the unsaturated absorption appears, from measured threshold currents, to be more modest. Secondly, it means that for the same SA parameters, longer lasers with longer repetition periods are less likely to suffer from the QS instability, which needs to be borne in mind when analysing the dynamics of QD lasers (due to the relatively low gain, these often have to be quite long if operation at the ground state band is desired).

The lower current (or unsaturated gain) limit of the self-pulsing instability may be positioned either below or above the low boundary of ML itself, depending on the gain and absorber saturation energies (*s*-parameter) and the absorber recovery time. If the boundary for ML is below that

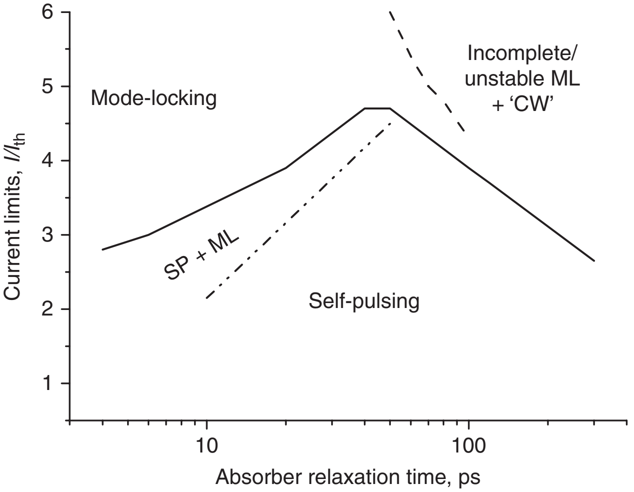

5.10 Schematic diagram of regimes in a generic QW mode-locked laser operating at the repetition rate of 40 GHz.

for self-pulsing (which tends to happen in long lasers, when τ_α is significantly smaller than T_{RT} but not small enough to completely eliminate self-pulsing), then the stable ML range is split in two by the self-pulsing area, with an area of stable ML seen below the QS limit at currents just above threshold. The area is narrow however, and the pulse powers generated in this regime are typically rather low. If, on the other hand, the boundary for ML is above that for self-pulsing (which tends to be the case for shorter lasers or longer absorber relaxation time, when $T_{\mathrm{RT}} > \tau_\alpha$, then an area of pure self-pulsing, with noisy/chaotic filling of pulses, is seen at small to modest excess currents above threshold, as in Fig. 5.7; as the current is increased, the pulses acquire a regular structure and the combined ML/SP regime develops.

Figure 5.10 also shows the other main instability of ML, the leading-edge, or chaotic, instability. As was shown by the DDE model, the border of this instability is pushed towards higher currents by the increased amount of absorption in the laser. Shortening τ_α also decreases the risk of this instability.

At long τ_α and high currents, the laser operates in a chaotic regime, which gradually evolves into some type of CW or quasi-CW operation. Whether or not true single-frequency CW operation predicted by the DDE is achieved depends on the length of the laser and the gain bandwidth; longer lasers (with a repetition frequency ~ 10 GHz) with broader gain tend to not reach true CW, instead operating in a chaotic quasi-CW regime with a narrow spectrum including only a few modes.

5.6.2 The main parameters that affect ML laser behaviour

To understand the rationale behind the recent advances in ML laser science and technology, it is instructive to briefly overview the effects of the main laser parameters affecting ML in SLs in general, as predicted by the models discussed above and confirmed by experiments.

The effects of the operating point (gain section bias and SA voltage, determining the unsaturated gain and absorption and the SA time) on the operating *regime* of the laser have been discussed in the previous section. Furthermore, within the stable ML range, the effect of the operating point on the pulse parameters is as follows.

The pulse *amplitude* grows with pumping current, as illustrated in Fig. 5.11, calculated by a travelling-wave simulation. Notice that qualitatively, the figure is quite close to the bifurcation behaviour seen from Fig. 5.7, except that in the numerical model, and with the different set of parameters, only the second rather than third harmonic operation is predicted. As regards the pulse *duration*, it has been predicted by early frequency-domain theories[56] to reach a minimum near the area of QS instability; this has been later confirmed by both experiments and time-domain simulations. The pulse duration thus tends to grow with current within the stable ML range *above* the upper boundary of QS. On the other hand, if an area of stable ML below the QS range is observed (which is sometimes the case in longer resonators), then a *decrease* of pulse duration with current can be expected within this area.

The dependence of the pulse duration on τ_α (and this on the absorber bias) within the stability range is shown in Fig. 5.12. As seen in the figure, to achieve stable ML, the absorber relaxation time needs to be below a certain critical value; longer τ_α produces instabilities. Within the stable ML range, a decrease in τ_α tends to shorten the pulses, due to both the effects of partial absorber relaxation during the pulse and, probably more significantly, to the fact that the slow relaxation of the absorber leads to the absorber being always partially saturated, thus reducing the initial absorption Q_-.

Among the other important parameters that affect the ML properties are:

The s-factor, or the absorber to gain saturation energy ratio

While it is well known that the increase in s facilitates ML, it is not immediately intuitively clear whether an increased s helps ML stability, as it is known[23] that the passive QS regime, which is one of the instabilities affecting ML, is also facilitated by an increase in s. However, the results from both DDE and travelling-wave simulations[57] show that in fact it is the stable ML range that is increased with s at the expense of the QS (or self-pulsing) range.

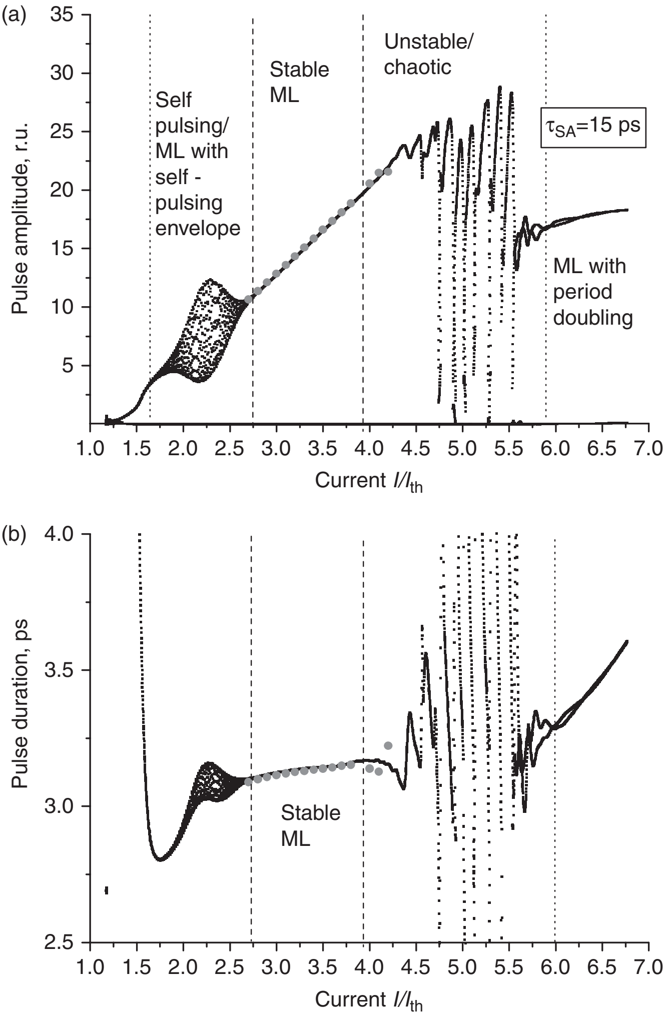

5.11 Simulated dependence of the pulse amplitude (a) and duration (b) on the pumping current – simulations using a travelling-wave model with typical values for a QW laser. Solid line: obtained by slowly ramping the current; filled circles: time-averaged steady-state results for a fixed current.

Gain and group velocity dispersion parameters

Most models of ML laser operation predict that without *gain* dispersion, stable ML with a finite pulse duration is impossible, and so the gain dispersion, or width of gain curve, represented by the parameter γ in the DDE or ω_L in the travelling-wave model, should play an important role in determining

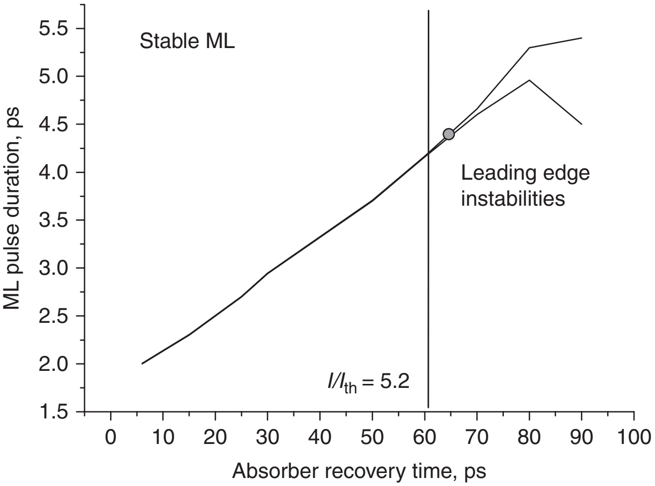

5.12 Typical simulated dependence of pulse duration on the absorber recovery time – simulations using a travelling-wave model.

the pulse width and stability. Within the range of gain dispersion typical in ML SLs, which usually corresponds to $\hbar\omega_L$ of the order of tens of meV (or the wavelength range of tens of nm) and does not change too much with operating conditions or construction, gain dispersion is not the most drastic factor limiting the pulse width. However, achieving a broad gain spectrum is still desirable. This may be one of the advantages of QD active media, as discussed below.

Group velocity dispersion (GVD), like gain dispersion, acts to broaden the pulses in the case of normal dispersion (which is usual in SLs). As discussed above, the effect of this parameter is modest in most SLs since the pulse durations at which it would become important (~100 fs) are never achieved; however, with stronger GVD possible in QD lasers, some account for this effect may be necessary.

The gain suppression and absorber compression coefficients

Pulses generated by ML lasers tend to be of picosecond duration. This is below the critical pulsewidth at which the fast gain saturation, rather than the average carrier density dynamics, begins to dominate the pulse amplification and shaping, at least in the gain section; this critical pulse duration has been estimated[58,59] to be of the order of $\varepsilon_g / v_g (\mathrm{d}g/\mathrm{d}N)$. With typical semiconductor parameters, this estimate gives values of the order of 10 ps. Thus, the gain compression (and, similarly, absorber compression) effects and the coefficients that describe them (if introduced) may be expected to play a significant part in ML properties.

In practice, the effect of non-linearities is twofold. Firstly, gain compression tends to broaden ML pulses, with absorption compression having the opposite effect. Secondly, and in some regards more importantly, an increase in gain compression *stabilises ML operation*, suppressing the *QS* instability (the latter can be easily shown by rate equation analysis of Q-switched lasers[60]). Again, fast absorber saturation has the opposite effect.

The gain and absorber linewidth enhancement factors

The linewidth enhancement factors have a very modest effect on pulse *energy* for a given current and absorption, but a more noticeable one on amplitude and duration. They do not significantly affect the onset of the *QS* instability (the lower current or unsaturated gain limit of ML stability), but have a stronger effect on the upper limit of ML stability associated with the irregular envelope and pulse competition. ML behaviour is most stable when the gain and absorber linewidth enhancement factors are not too different from each other. According to the DDE model predictions, the most stable operating point (which also corresponds to the highest pulse amplitude and lowest duration) is for $\alpha_{Hg} = \alpha_{H\alpha}$; however, travelling-wave and modal analysis predict that the best quality ML is achieved with $\alpha_{Hg} > \alpha_{H\alpha}$; the discrepancy is likely to be caused by the different geometry of the long amplifier and the shorter absorber. The main parameter determined by the linewidth enhancement factors is the *chirp* (dynamic shift of the instantaneous frequency) of the pulse. Passively ML pulses tend to be up-chirped (with the instantaneous optical frequency increasing towards the end of the pulse) when the absorber saturation factor $\alpha_{H\alpha}$ is small and the chirp is mainly caused by α_{Hg}. With a certain combination of α_{Hg} and $\alpha_{H\alpha}$ (typically $\alpha_{Hg} > \alpha_{H\alpha}$), an almost complete compensation of chirp is possible; with $\alpha_{H\alpha} > \alpha_{Hg}$, the pulse is typically down-chirped.[61] As up-chirp is observed more frequently than down-chirp in experiments, one may conclude that typical values of $\alpha_{H\alpha}$ are smaller than α_{Hg}. In active ML, *down-chirp* is typically observed, while hybrid ML allows the chirp to be tuned to some extent, and there is typically a combination of bias and current or voltage modulation amplitude for which the chirp is minimised and close to zero, if only in a very narrow range of operating parameters.

5.7 Important tendencies in optimising the ML laser performance

This section reviews ML laser optimisation in the light of gain-to-absorber saturation energy, reducing SA recovery time, increasing the optical power, and engineering the bit rate.

5.7.1 Achieving a high gain-to-absorber saturation energy ratio

The importance of a high gain-to-absorber saturation energy ratio *s* for short pulse generation has been semi-empirically understood for some time, and the recent analysis with the DDE model reconfirmed its importance also for maximising the stable ML range.[48,49] Since, by definition, $s = U_g / U_\alpha = \sigma_\alpha A_{Xg} / \sigma_g A_{X\alpha}$ there are at least two ways of increasing *s*:

(i) In most non-SLs, where the absorber and gain regions are discrete elements, the most straightforward way of increasing the *s*-parameter is to ensure that the light is focused more tightly in the SA than in the gain section so that $A_{X_\alpha} < A_{Xg}$. The same is usually done in non-monolithic semiconductor constructions such as vertical external cavity lasers (VCSEL). In *monolithic* SLs, a similar strategy can be pursued to some degree by *tapering* the laser waveguide so that the absorber region is narrower than the gain region. Used originally for QS QW lasers in a 'bow-tie' construction with the narrow SA in the middle of the cavity and the two amplifier sections tapering outwards,[62] this strategy has later been realised most convincingly in QD ML lasers. In 2006, Thompson *et al.* demonstrated the generation of pulses as short as 780 fs, by using a tapered waveguide configuration in a two-section InGaAs QD laser.[63] Further optimisation of the SA length later resulted in the demonstration of transform-limited ultrashort pulses with pulse duration of 360 fs, average power of 15.6 mW and peak power of 2.25W (at 12°C).[64] Nikitichev *et al.* have recently demonstrated operation of a tapered monolithic passively ML QD laser in a very broad range of absorber reverse bias (3–6 V) and gain section current (700–1500 A). This structure had a peak power of 3.6 W, with a corresponding pulse duration of 3.2 ps at a repetition rate of 14.6 GHz.[65] In the later work by the same team, the pulse power was brought up to the value as high as 17 W[66] (see Section 5.7.3 for more detail).

(ii) In many cases, however, fabrication ease and fibre coupling considerations suggest the same waveguide structure in the gain and absorber sections, and so $A_{X_\alpha} < A_{Xg}$. The parameter *s* is then equal to the *absorber to gain cross-section ratio* $s = \sigma_\alpha / \sigma_g$. QWs, with their sublinear (approximately logarithmic) dependence of gain on carrier density (population inversion) have long been seen as superior to bulk material for ML performance, since the sublinear $g(N)$ helps achieve $\sigma_\alpha / \sigma_g > 1$. The authors of References 48 and 49 used their analysis to conclude further that when designing a QW laser for ML purposes, a structure with a *smaller number* of QWs was preferable to one with a larger number – indeed, the smaller number of QWs means a smaller confinement factor, hence a higher threshold carrier density, hence a smaller dg/dN at threshold due to the sublinear $g(N)$, which in turn gives a higher value of the ratio s. These considerations influenced the choice of structures with just 2–3 QWs for realising DBR ML lasers capable of generating very stable pulses about 2 ps long at 40 GBit/s.[57] It may be argued that the same logic also in part accounts for the success of QD ML lasers, in which the dependence of gain on the (total) carrier density in the active layer is even more sublinear than in QWs; however, it has to be borne in mind that the concept of total carrier density is somewhat misleading in QDs – a more accurate picture is given by more complex analysis, considering separately the population of the dots themselves and of the reservoir that supplies them with carriers.

5.7.2 Improving stability and pulse duration by reducing the saturable absorber recovery time

As described above (Section 5.6), decreasing the SA recovery time leads to both shorter and more stable ML pulses. Therefore, a number of teams have suggested alternative routes for reducing the time τ_{α}:

(i) In earlier experiments, **heavy ion implantation** of the laser facet was used to produce SAs with a recovery time $\tau_{\alpha} \sim 10$ ps, governed by non-radiative recombination. This enabled some of the first results on ML monolithic SLs, with picosecond pulses at both 0.87 and 1.55 µm wavelength band.[67,68]

(ii) In more modern QW laser constructions with a reverse-biased SA, the most fundamental of the processes governing τ_{α} is the sweep-out of photocarriers from the absorber QWs into the waveguide layer by the bias field. In InGaAsP materials most frequently used in lasers operating at 1.55 µm, the potential well for heavier holes is deeper than that for lighter electrons, making hole sweep-out a bottleneck for achieving small τ_{α} at sensible values of the SA reverse bias (of the order of a few volts). On the other hand, **AlGaInAs quaternaries** have a shallower potential well for holes, making for much more efficient sweep-out. Absorber recovery times as low as 2.5–3 ps at a bias of –4 V, several times shorter than in InGaAsP quaternaries at the same bias voltage, have been measured in such QW heterostructures.[69,70] Lasers with AlGaInAs quaternaries have been successfully used for ML operation in both a relatively traditional 40 GHz constructions[71] and in more advanced harmonic ML lasers operating at 160+ GHz,[70,72,73] as will be discussed in Section 5.7.4. The pulse durations obtained were in the sub-picosecond range for harmonic operation at 160 GHz.

(iii) Thirdly, it has been pointed out that faster sweep-out may be achieved by **engineering the quantum well profile** to include steps or oblique rather than vertical walls.[74] At the time of writing, such structures do not appear to have been realised experimentally, but theoretical predictions are encouraging.

(iv) It is also important to note that, even after carriers have been swept out of the *absorbing (active) layer*, they need to be efficiently removed from the *waveguide layer*, to prevent both their diffusion back to the SA and the carrier screening of the electric field applied to the well. In a standard structure, this happens through drift in the electric bias field, with the transport of heavy holes limiting the process speed.[44,75] To avoid this, lasers with **unitravelling carrier absorbers** have been proposed and realised.[76,77] In these devices, the SA is not a reverse-biased section of the same *p-i-n* heterostructure as the gain section, as is the case in more usual constructions. Instead, the laser heterostructure is etched away in the SA section and a separate structure is grown for the SA, in which light is absorbed in a special *p*+-layer. Then, the holes are majority carriers so they are removed from the structure via collective relaxation (a faster process than drift), and it is only the electron drift (faster than hole drift) that limits the absorber recovery speed. The limitation of such structures is the need for a regrowth procedure, which increases the complexity and potentially the cost of the structure. Besides, even very small ($< 10^{-4}$) residual reflectances between the laser and absorber waveguides can lead to formation of satellite pulses (as in compound cavity lasers discussed in Section 5.7.4), which was indeed encountered in practice. Satellite-free pulses 0.9 ps long at the repetition rate of 40 GHz have been achieved in UTC structures, or 0.6-ps pulses with some satellite pulses.[76,77]

(v) Finally, absorber recovery speed is one of the advantages of **QD** materials (Section 5.8.1), which have shallower potential wells for both electrons and holes than QWs, hence faster sweep-out. The relatively small total numbers of photogenerated carriers compared to QWs can also partly alleviate any potential problems with carrier screening of the bias field.

5.7.3 Increasing the optical power – broadening the effective modal cross-section

While optimising the absorber parameters can help reduce the pulse duration, and increasing the stability range helps somewhat extend the achievable power range too, non-linear processes, such as the onset of high-current instabilities, by necessity limit the total average power in standard ML lasers to a few units to tens of milliwatts, depending on the construction and repetition rate. A route to a considerable increase in the output power is suggested by observing that in the theoretical analysis in Section 5.6. The non-linearities that limit the achievable power (including irregular non-linearities) respond, not to the absolute power, but to the *photon densities* $S_{g,\alpha} = \left|Y_{g,\alpha}\right|^2 = P/v_g\hbar\omega A_{X(g,\alpha)}$ in the gain and absorption sections of the laser. With an increase in the modal cross-section A_{Xg}, the entire map of the dynamic regimes of the laser, including the onset of chaotic instabilities, is scaled towards higher power while keeping the photon density constant. Therefore increasing the modal cross-section A_{xg} is a robust way of achieving stable high power output. As with ordinary CW operating lasers, arguably the main challenge is to achieve this while keeping the laser operating in a single transverse-lateral mode. The logic here is similar to the expansion of mode volume in gain-switched lasers, discussed in Section 5.3.

(i) One laser construction that realises this principle, whether operated CW or ML, is a *slab-coupled* laser waveguide, in which the active layer is positioned at the edge (rather than in the centre, as is the case usually) of a waveguide (slab) layer, which is as thick as 3–4 μm in the transverse direction and unbounded laterally. Lateral waveguiding is by means of a relatively shallow ridge, with the width also of a few microns. The combination of the waveguide structure and active layer position ensures laser operation in a single longitudinal-lateral mode which is broad (e.g., in Reference 78, the effective cross-section was $A_{xg} = A_{x\alpha} \approx 14\ \mu\text{m}^2$, about an order higher than in ordinary stripe lasers) and fairly isotropic.

By introducing the SA section in the usual way of electrically isolating a section of the cavity, passive ML of a structure of this type was realised.[78–82] Average power value achieved at $\lambda = 1.55$ μm was as high as 210 mW with $F \approx 4.6$ GHz ($L = 9$ mm).[78] The pulses corresponding to the highest average power were not the shortest (~ 25 ps in Reference 78), though at different operating condition, pulses < 6 ps long were realised. At $\lambda = 890$ nm, ML with an even higher average power of 489 mW at 7.92 GHz from a 5-mm device with a 300-μm long SA was demonstrated.[80] By applying fundamental and harmonic voltage modulation to a modulator section fabricated next to the SA section, the same team that produced some of the passive ML results[78] reported *hybrid* ML operation of a similar, slightly shorter ($F \approx 5.2$ GHz) structure, with the average power of 220 mW and the pulse duration reduced by about 20% (from 14.5 to 11.7 ps in an example quoted) compared to the passive ML case.[81] Colliding-pulse ML has also been realised in slab-coupled lasers, yielding an average power of up to 240 mW per (uncoated) facet (480 mW in total) at 8.6 GHz, with pulse durations of 8–14 ps (11 ps at the highest power), at $\lambda = 1.55$ μm.[82]

The limitation of slab-coupled structures is that the very low confinement factor limits the minimum resonator length needed to achieve lasing and is thus likely to pose an upper limit of at most 10–20 GHz on the repetition frequency, unless some form of a harmonic ML construction (Section 5.7.4) were to be implemented.

Theoretical predictions imply that asymmetric waveguide lasers such as those used for gain-switching (Section 5.3), which share the feature of large modal cross-section can deliver similar powers when operated in a ML regime, though so far there has been no experimental confirmation of this.

(ii) As mentioned in Section 5.7.1, **tapered ML lasers** also achieve high power by expanding the mode, in this case in the lateral rather than transverse direction, and, importantly, in the gain section only. The added advantage of the simultaneously increased *s*-parameter (Section 5.7.1) helps further improving the achievable power by increasing the stable operation range. In the λ = 1300 nm QD structure analysed in Reference 65, besides the high peak power of 3.6 W, the high average power of about 210 mW was also achieved; again, as in slab-coupled lasers, this was at somewhat different bias conditions from those for those for shortest and most intense pulses (corresponding to pulses ≈6 ps long at 14.6 GHz). Most recently, the laser design was improved further, on the basis of numerical simulations of the dynamic ML regimes and their dependence on the structural parameters. Two designs with different gain and absorber section lengths were proposed. One device design demonstrated the record–high peak power of 17.7 W with 1.26 ps pulse width (Fig. 5.13) and a second design enabled the generation of a Fourier-limited 672 fs pulse width with a peak power of 3.8 W. A maximum output average power of 288 mW with 28.7 pJ pulse energy was

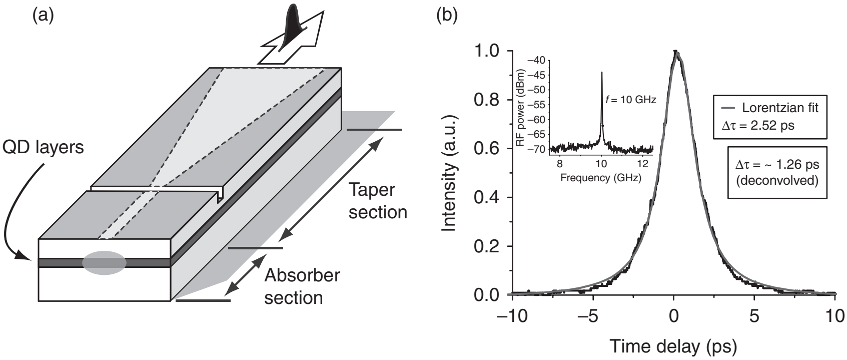

5.13 (a) Schematic of a tapered QD laser for ultrahigh power pulse generation; (b) the pulse achieved.

also attained. QD tapered gain-guided lasers have therefore shown promising results as high power ultrafast and ultracompact semiconductor-based laser sources.

(iii) Finally, in ML VECSELs, the power can be increased by increasing the lateral dimensions of the active area. The highest average output power achieved so far in such structures (and thus in any single ML SL) has been 6.4 W, in pulses 28 ps long at $F = 2.5$ GHz.[83] For the time being, this high power is achieved at the expense of sacrificing some of the usual advantages of SL sources. VECSELs are external cavity structures and thus need some optical alignment and have a footprint somewhat larger than monolithic ones (although still smaller than the vast majority of non-semiconductor ML sources), and mostly use optical rather than injection pumping, which is less efficient (the optical to optical efficiency in Reference 83 was 17%). However, considerable progress has been achieved towards overcoming these limitations. In particular, the first generation of VECSELs used separate gain chips and SESAMs; the latter could be based on QWs or dots. Such structures were used for generating average powers as high as 2.1 W, with pulse duration down to 4.7 ps at 4 repetition rate at $\lambda \approx 960$ nm.[84] These lasers required a 'folded cavity' with a need for non-trivial optical alignment. The more recent mode-locked integrated external cavity surface-emitting laser (MIXCEL) structures, of which the construction of Reference 83 has been the most successful so far, combine a QW active region and a QD SA layer within the same wafer structure, and thus reduce the number of components in the cavity to just two – the MIXCEL chip and the output coupler doubling as the external mirror; this also allows for a straight external cavity, simplifying the optical alignment. The curvature of the output coupler, the cavity length, and the size of the pumping spot allow the size of the waveguide mode to be tuned (in Reference 83, the pumping spot and the mode had the radii of 215 and 223 μm respectively, corresponding to a mode cross-section three orders of magnitude greater than in monolithic in-plane structures).

A fully vertically, monolithically or hybridly, integrated MICXEL type laser looks foreseeable in future. Current MIXCEL constructions are specifically designed for optical pumping. They contain an intracavity multistack 'pump DBR' structure which reflects light at the pump wavelength (808 nm in Reference 83), but not the signal wavelength (960 nm in Reference 83), thus blocking the penetration of pumping light into the SA but not affecting the cavity structure for the signal light. In principle, electrical isolation of the SA and the active section (e.g., by intracavity electric contacts) could also be possible in vertical cavity structures so in principle electrically pumped MIXCEL type should be possible too. However, due to thermal budget considerations it is not clear how powerful these can be made.

5.7.4 Engineering the bit rate: high power and high-bit-rate operation and harmonic ML

Depending on the potential application, a very wide range of repetition rates may be required from an ML laser. A number of applications in manufacturing, sensing and non-linear imaging involve high output power at moderate (<~ 1 GHz) repetition rates, whereas potential applications such as high-bit-communications may benefit from a ML laser with a multi-gigahertz (80, 100, 160 or 640 GHz) repetition rate.[37]

As mentioned in the previous section, low bit rates with a high power in a ML SL are achieved by increasing the cavity length (L in Equation [5.22]), which necessitates using an external cavity construction, whether edge-emitting or VECSEL. This is not a trivial task since, as follows from the theoretical analysis of Sections 5.5.3–5.6, at low bit rates ML lasers are particularly prone to switching to harmonic ML as the current (and hence power) is increased. Still, ML at repetition rate as low as 0.19 GHz has been recently realised with a QD edge-emitting laser[85] in an external cavity configuration (Fig. 5.14). In addition to high pulse energy, external cavity constructions also have the advantage of low jitter and RF linewidth (down to 30 Hz at some operating conditions in Reference 85).

At the other end of the repetition rate scale, multi-gigahertz repetition rates can be achieved by straightforwardly decreasing L. However, this makes for high fabrication tolerance, and obtaining substantial ML powers from short resonators may need working high above threshold, making them prone to instabilities and limiting the power. Hence, harmonic ML techniques that use $M_h > 1$ L in Equation [5.22] have attracted attention. Second harmonic operation at 80 GHz ($M = 2$) has been experimentally observed in standard notionally 40-GHz lasers at some operating conditions (involving high current) in agreement with both DDE (see Section 5.5.3) and travelling-wave theoretical simulations.[57] However, stable multi-gigahertz generation by operation at higher harmonics requires specialist constructions. These fall into two categories.

The first is colliding-pulse ML (CPM), including *multiple* (MCPM)[86,87] *and asymmetric* (ACPM)[88,89] colliding-pulse ML constructions. These achieve ML at the M_hth harmonic by positioning one SA (in CPM or ACPM) or several SAs (in MCPM) at fraction(s) M_h'/M_h of the laser cavity length, where $M_h'<M_h$ is an integer, and M' (or at least some of the values of M_h' in case of MCPM) and M are mutually prime. The standard CPM corresponds to $M_h = 2$ (and obviously $M_h' = 1$) with the SA in the centre of the cavity. Constructions of this type have produced ML operation at rates of up to 860 GHz[89] – in that particular case, the $\lambda = 1.55$ μm ACPM construction used $M_h' = 5$, $M_h = 12$. A more detailed review is given in Reference 37.

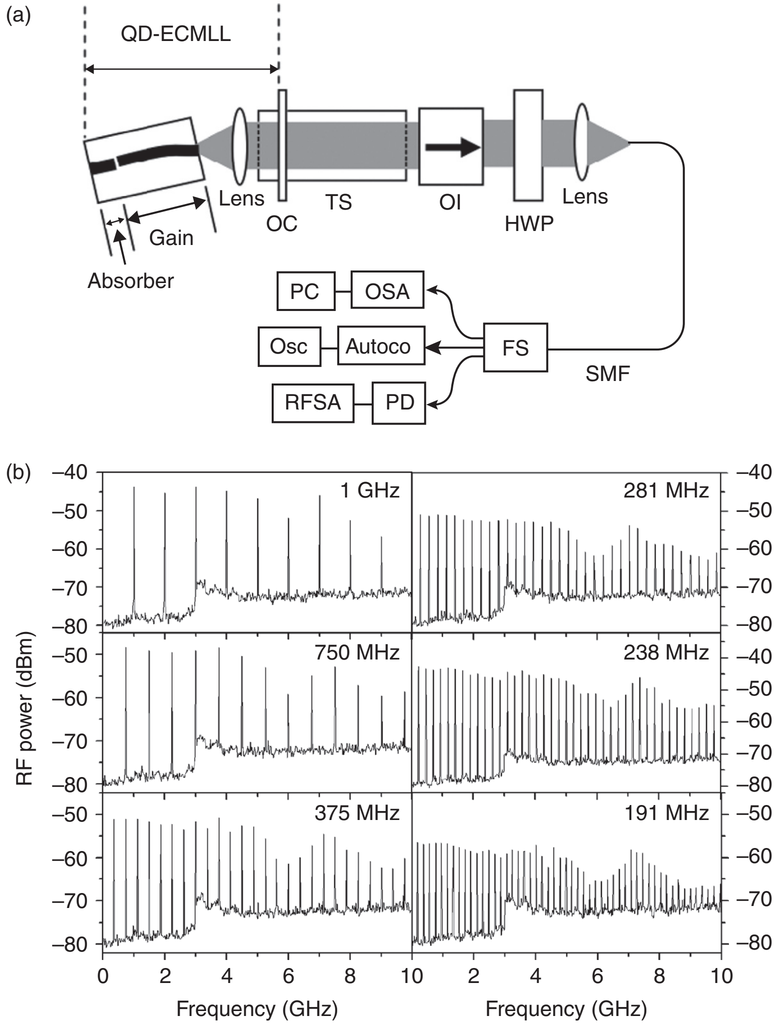

5.14 (a) Schematic of a QD external cavity mode-blocked laser (QD-ECMLL); (b) RF spectra for the variable repetition rate from 1 GHz to 191 MHz from this construction.

The alternative harmonic ML technique is the use of a *spectrally selective laser cavity*. This may be in the form of a *compound cavity*, which has one or several *intracavity reflectors* (ICR) positioned at fractions M_h'/M_h of the laser cavity length, rather like the SAs in the MCPM or ACPM technique. The highest ML repetition rates reported to date have been achieved by GaAs/AlGaAs ($\lambda \approx 0.89$ μm) lasers with the ICRs in the shape of deeply etched slots, either single or multiple in a 1-D photonic bandgap (PBG) mirror arrangement.[90] A 608 μm long cavity used ICRs at 1/33 of the cavity lengths, giving $F = 2.1$ THz (similar structures with lower M_h values produced ML at bit rates of the order of hundreds of GHz depending on M_h and L).

Later,[73,91] the technique was extended to $\lambda = 1.55$ μm by using AlGaInAs quaternary materials, whose short absorber recovery time (see Section 5.7.2) proved indispensable for high-bit-rate ML. The ICR slots in these structures were filled with dielectric (rather than air as in Reference 90) improving the reliability of the structure. Pulses as short as 0.8–0.9 ps at repetition rates of 160–640 GHz have been achieved,[73,91] with the time-bandwidth product of ~0.8 indicating moderate chirp. Theoretical predictions[91] show that the scheme is relatively tolerant to the precision of the ICR position, with harmonic operation (with a somewhat increased pulse duration) maintained for imperfections of the ICR position of up to 10 μm.

Theoretical analysis conducted in Reference 90 implied also that the stability of harmonic ML operation at high M_h numbers would be higher with several weak reflectors than with one strong ICR, which was supported by experimental results.[90] This idea has seen its ultimate realisation in the so-called *discrete mode* laser structures. Such structures contain multiple ICRs, but in the form, not of deep etched structures, but of simple step discontinuities in the laser waveguide thickness. Taken individually, these steps have weaker reflectances than deeply etched structures; however, they are more production friendly (a single step, unlike an etched slot, does not require high resolution ion beam etching). Tailoring the number of steps and the distances between them presents a very powerful tool for engineering the cavity to select either a single mode or a set of a predetermined number of equidistant modes.[92,93] Originally designed for single-mode operation, such lasers have recently been adapted for harmonic ML.[92,93] Lasers 875 μm long have been reported to provide nearly transform-limited pulses about 2 ps long, at $F = 100$ GHz ($M_h = 2$);[92] higher harmonic numbers should be possible as well.

In principle, ACPM (or MCPM) and compound cavity techniques can be combined in one structure. Other cavity structures that have been proposed for high-frequency ML not restricted by the cavity length are resonators with sample grating reflectors[94] and possibly coupled-ring resonators[95,96] discussed in Section 5.8.4.

5.8 Novel mode-locking principles

This section considers novel ML principles in the light of QD materials, femtosecond pulse generation, spontaneous ML, miniaturisation and integration.

5.8.1 Quantum dot materials

As seen from Section 4.5, much of the progress in ML laser technology achieved in the last decade has been associated with the use of QD ML lasers, which is largely to do with the novel physical properties of these materials.[97,98]

Ultrafast QD lasers have been considered in detail in a separate monograph;[98] here, we shall reiterate only the main points relevant for ML.

QDs are essentially clusters of semiconductor material having all three dimensions of a few nanometres. QDs used in monolithic ML laser structures belong to the category of self-assembled QDs; they have the geometry of a pyramid or a truncated pyramid with a base of 5–10 nm and are arranged in layers (typically 1–10) within the structure, with a density of 10^{10}–10^{11} cm^{-2} per layer. In each dot, electrons and holes see full three-dimensional localization and are thus occupying discrete energy levels rather than continuous bands as in bulk or QW semiconductors; in lasers, the most significant are transitions involving the lowest electron energy state (the ground state) and the next one (ES, the first excited-state, sometimes referred to simply as the excited-state, which is a few tens of meV higher). There is no direct interaction between carriers in different dots; the (imperfect) thermodynamic equilibrium between them is achieved through the processes of capture of carriers from the *reservoir* formed by nearby QW and bulk layers into the dots, their possible thermal escape and recapture into different dots. Due to the dispersion of dot size and composition, there is considerable *inhomogeneous broadening* of optical emission and absorption in dots (about 50–100 meV), which largely determines their emission and absorption spectra. These features translate into a number of advantages, of which the following are relevant to ML.

Firstly, ML QD lasers share with other QD lasers the advantages of a possible low threshold, reduced amount of amplified spontaneous emission (hence narrow linewidth/low noise), and in particular lower temperature sensitivity . If their high-speed performance is also proven to be resilient to temperature, QD lasers can become the next generation of sources for ultrafast optical telecoms and datacoms, because the constraint of using thermo–electric coolers can be avoided, thus decreasing cost and complexity. In this context, we have demonstrated stable passive ML operation of a two–section QD laser over an extended temperature range, at relatively high output average powers.[99] We observed very stable ML operation from 20°C to 70°C, with the corresponding RF spectra exhibiting signal-to-noise ratios well over 20 dB and a –3 dB-linewidth smaller than 80 kHz. The ML regime became less stable only at 80°C, where the –3 dB-linewidth was 700 kHz and the signal-to-noise ratio was 15 dB. No self–pulsations were observed for all temperature ranges. It has been also shown that, perhaps counter-intuitively, both the pulse duration and the spectral width decrease significantly as the temperature is increased up to 70°C.[100] The combination of all these effects resulted in a 7-fold decrease of the time-bandwidth product (the pulses were still highly chirped due to the strong self-phase modulation and dispersion effects in the semiconductor material).

The discrete nature of QDs also helps reduce the effects of surface recombination, allowing for higher pulse energies and extending the possibilities of etching in the laser technology (in the context of ML lasers, this helps precise cavity definition and possibly harmonic cavity techniques).

Secondly, the *very broad gain spectrum*, and stronger spectral hole burning than in other type of lasers (due to inhomogeneous broadening exceeding the homogeneous one) tend to lead to very broad emission spectrum, which potentially opens a possibility of direct femtosecond pulse generation by ML in monolithic structures. In 2004, we demonstrated for the first time the generation of sub-picosecond pulses directly from a QD laser, the shortest pulse durations being 390 fs, without any form of pulse compression[103] from a two-section passively ML QD laser (Fig. 5.15). Owing to the excellent electrical characteristics of the device, it was possible to apply very high values of current and reverse bias (up to 10V), which provided some latitude for exploring a wider range of these parameters. ML operation was observed over a broad range of injection currents from above laser threshold (~30 mA) up to 360 mA and over a relatively wide latitude of reverse bias levels on the absorber section (from 4.5V to 10V). The broad spectrum (14 nm) and the ultrashort pulse durations measured suggest that the generation of pulses in the sub-100 fs domain may yet be possible from relatively simple QD laser

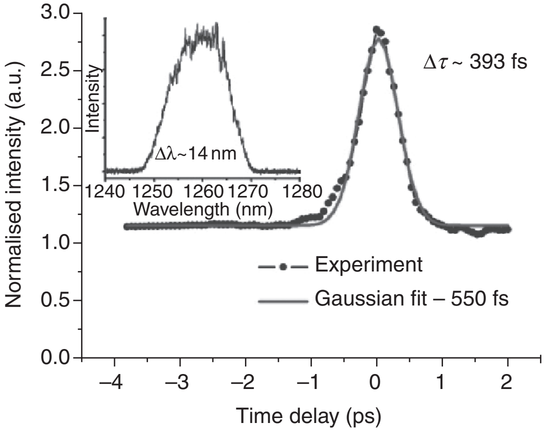

5.15 Optical spectrum and sub-picosecond pulse from a 2-section QD laser.

configurations. Since then, sub-picosecond pulse durations have been also demonstrated in single-section QD lasers (see Section 5.8.3).

Thirdly, as mentioned above, the role of ultrafast (characteristic time of 50–100 fs) carrier collisions that normally establish the quasi-equilibrium energy distribution of carriers in a SL is taken in QD lasers by the processes of carrier capture and escape, which are 1–2 orders of magnitude slower. This means the corresponding increase in the *gain compression* in QD lasers by about the same order of magnitude; as discussed in Section 5.6.2, this suppresses the QS instability and leads to a broader range of ML; indeed, experimentally, the SSP instability range in QD lasers tends to be considerably narrower than in QW ones with comparable performance and is often completely absent.

Fourthly, a number of advantages are associated with the properties of the QD *SAs*, chief of which is the *short recovery time* due to fast carrier sweep-out out of QDs (Sections 5.6.2 and 5.7.2). SA recovery in QDs has been shown experimentally[55,101] and theoretically[50,101] to be a complex process, with at least two time constants involved, and both intra-level transitions (capture and escape of carriers) and field-induced sweep-out playing a part (Fig. 5.16a). The capture and escape rates in the SA (which have an activation dependence of temperature) have been shown theoretically[50,102] to be responsible for a decrease of the SA recovery time with increasing temperature, leading to a decrease in the pulse durations. This fact was verified using ultrafast spectroscopy to probe the absorber recovery time as a function of temperature.[100,101,103–105,107–109] Furthermore, *p*-doping has the potential of enabling an accelerated gain recovery, through a pre-filling of the hole states, as previously demonstrated in high-speed laser modulation experiments.[105] With the intracavity dynamics sped up by temperature, the slowest time constant in the absorber response, associated in this case with the field sweep-out, can be brought down to 1–2 ps with realistic values of reverse bias[55] (Fig. 5.16b).

This ultrafast SA recovery dynamics helped the generation of sub-picosecond pulses from QD lasers reported by several groups.[63,106] Furthermore, it was confirmed that the pulse duration decreases exponentially with increasing reverse bias (up to 8V) on the SA.[63] This decrease was attributed mainly to the corresponding exponential decrease of the SA recovery time as the reverse bias is increased[55] (it has to be noted that there are some limits within which this is beneficial; at very high bias, the laser behaviour degrades[107] possibly due to strong unsaturable absorption introduced, or to an increased spectral misalignment between gain and absorption bands).

The possibilities demonstrated so far open the way for the ultimate deployment of ultra-stable, uncooled ML SLs incorporating QD materials.

Another advantage of QD SAs is the low saturation fluence (effectively, a high absorber cross-section at a given wavelength) due to the inhomogeneous nature of absorption saturation.

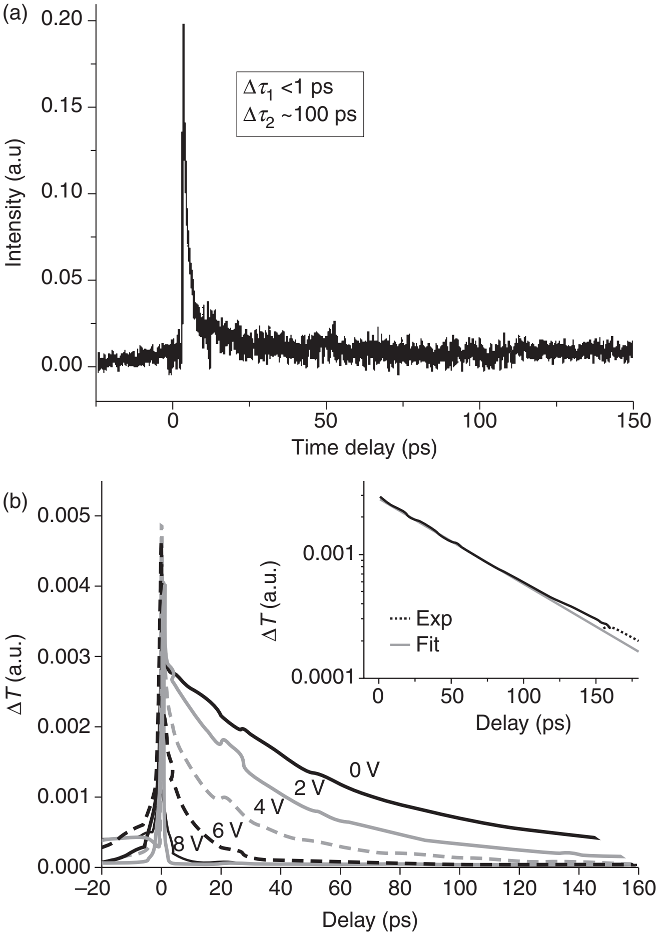

5.16 Pump-probe measurements of QD SA: (a) passive and (b) with reverse bias. Note the multiple scales and the reduction of the recovery time with reverse bias.

Fifthly, QD lasers open a unique opportunity of achieving dual-wavelength lasers, including dual-wavelength ML. It has been observed that laser emission in QD lasers can access the transitions in ground state (GS), excited state (ES) or both.[108] Sub-picosecond gain recovery has been demonstrated for both GS and ES transitions in electrically pumped QD amplifiers.[109] It has also demonstrated an optically gain-switched QD laser, where pulses were generated from both GS and ES, and where the ES pulses were shorter than those generated by GS alone.[110] Passive ML via GS (1260 nm) or ES (1190 nm) in a QD laser demonstrated at repetition frequencies of 21 and 20.5 GHz, respectively.[111] The switch between these two states in the

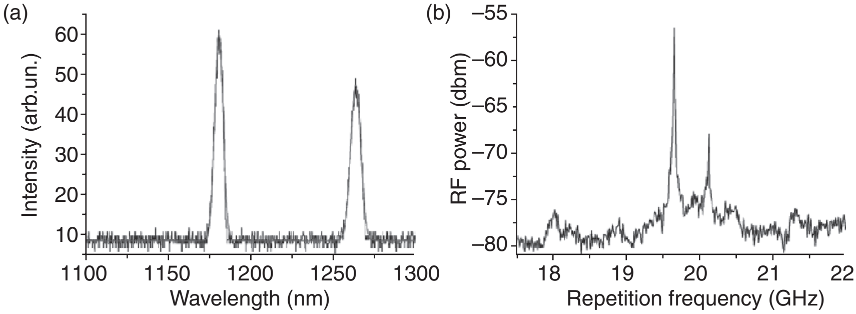

5.17 (a) Optical spectrum and (b) RF spectrum characteristic of the dual-wavelength mode-locked regime in a mode-locked QD laser.

ML regime was easily achieved by changing the electrical biasing conditions, thus providing full control of the operating spectral band. It is important to stress that the average power in both operating modes was relatively high and exceeded 25 mW. In the range of bias conditions explored in this study, the shortest pulse duration measured for ES transitions was ~7 ps, where the spectral bandwidth was 5.5 nm, at an output power of 23 mW.[100] These pulse durations are similar to those generated by GS ML at the same power level. Although the pulses generated from both GS and ES ML are still far from the transform limit (with a time-bandwidth product exceeding 7), they could be reduced by using external compression techniques.

More recently, a dual-wavelength passive ML regime where pulses are generated simultaneously from both ES (λ = 1180 nm) and GS (λ = 1263 nm), in a two-section GaAs-based QD laser.[112] This is the widest spectral separation (83 nm) ever observed in a dual-wavelength ML non-vibronic laser (Fig. 5.17). The dual-wavelength ML regime was achieved in a range of bias conditions, which simultaneously satisfied the conditions for achieving ML via GS and ES – for current levels in the gain section between 330 and 430 mA, and values of reverse bias between 6 and 10 V in the SA region. The ES levels have higher degeneracy, and consequently higher saturated gain than the GS. This means that a transition from the GS to the ES can be achieved by increasing loss, which in this case can be manipulated through the increase in reverse bias applied to the SA. The spectral separation between the two modes results in different repetition rates, due to the dispersive nature of the laser semiconductor material, which induces different cavity round-trip times for the propagation of the two modes. As such, the repetition rates of the generated pulses were 19.7 and 20 GHz for the ES (λ = 1180 nm) and GS (λ = 1263 nm), respectively. The development of dual- and multiple-wavelength ultrafast lasers is a research area that aims to address a number of important applications such as time-domain spectroscopy, wavelength division multiplexing and non-linear optical frequency conversion. In this context, the compactness, lower cost and direct electrical pumping associated with SLs form a set of attractive features for reducing the footprint and complexity of these applications, with the potential to also open up new avenues in ultrafast optical processing and optical interconnects.

Finally, under certain conditions, QD lasers can show *weak self-phase modulation* and consequently can be expected to produce nearly transformed limited pulses. Unfortunately, this occurs within a relatively narrow current range at low currents;[113] in general, self-phase modulation of QD lasers has a very complex nature due to a large number of different carrier populations each with its own dynamics, and can be stronger than in other types of lasers.[114–117]

It has to be noted that most of the QD laser progress, including the ultrashort pulses and high power operation from ML lasers, has been achieved with InGaAsP/InP QD structures emitting at λ = 1.1–1.25 µm. For many prospective applications, particularly those in communications, λ = 1.5 µm is required. QD and Quantum Dash (QDh) lasers operating at λ = 1.5 µm have been intensely researched, and single-section QD and QDh lasers have shown extremely promising performance (Section 5.8.3). QD λ = 1.5 µm lasers with SA-induced ML, on the other hand, do show successful ML operation, but the emission observed tends to show extreme chirp to the extent that in some experiments no pulses can be discerned in the unfiltered broadband emission; pulsed structure is only visible after spectral filtering which then limits the pulse duration. Further work on these lasers will be necessary to optimise their behaviour and establish the possible range of their applications.

5.8.2 Femtosecond pulse generation by mode-locked vertical cavity lasers: coherent population effects as possible saturable absorption mechanism

One of the most important developments in ML SL technology in the recent years has been direct generation of ultrashort (tens to ~200 fs) pulses that until recently have been the domain of solid-state lasers only. Only one type of SL has been reported to produce such pulses, namely vertical external cavity disk lasers, consisting of separate gain and SESAM chips in a folded (V-shaped) external cavity arrangement.[118–121] Single pulses 260 fs long[118] and 190 fs long at λ = 1040 nm[121] were obtained from such lasers, followed later[120] by 'pulse molecules' consisting of several 60-fs long pulses separated by intervals of about 1 ps, with an envelope about 2 ps at half maximum; this was the first demonstration of sub-100 fs pulses, if not single, from a SL. In Reference 119, pulses about 110 fs long were reported at a repetition rate of 92 GHz, the 18th harmonic of the 29-mm long cavity.

A significant difference between lasers of this type and other SLs is the very small length of the optical path in both the gain and SA sections and correspondingly the low gain and absorption per pass, combined with the relatively broad cross-section, which makes it easier to keep the gain and absorption saturation per pulse weak. These features have very probably contributed to the uniquely short pulses generated by lasers of this type (about an order of magnitude shorter than the best values obtained from monolithic constructions at comparable bit rates). However, the qualitatively different pulse parameters and different regimes obtained suggest that different physical mechanisms may be responsible for this femtosecond ML regime as compared to the picosecond one more usual in SLs. Indeed, such short pulse durations are difficult to reproduce theoretically in the model of slow SA which usually applies in SLs (Sections 5.4.2 and 5.5.3). One of the teams that produced the femtosecond ML pulses attributed their results to coherent effects in the SESAM elements, namely the optical (ac) Stark effect. This effect, similar in nature to self-induced transparency, has the relaxation rate equal to the inverse of the dephasing (coherence decay) time. In semiconductors, this time is determined by carrier–carrier (and carrier–phonon) collisions and is of the order of 50–100 fs. This belongs to the *fast*, rather than slow, absorber regime, when the SA recovery time is shorter than the pulse duration. Indeed, theoretical analysis[118,122] showed that the pulse duration possible with this mechanism is about twice the dephasing time, which agrees well with the experiments. Further developments in this work, including further improvement and optimisation of pulse parameters, moving towards simpler structures, and improving the understanding of the underlying physics, can be expected in the near future.

5.8.3 Spontaneous mode-locking in single-section lasers

Most of the tendencies in improving ML pulse properties covered in Section 5.7, have dealt with evolutionary improvements in the passive ML constructions including a SA. However, in recent years, a truly revolutionary development in ML laser technology occurred, when several teams have observed – and utilised – ML in *single-section lasers without SA sections and without any external modulation either.*

QDh lasers operating at $\lambda = 1.56$ µm, with dash or dash-in-a-well structures, were seen to generate sub-picosecond optical pulses at cavity length corresponding to repetition frequencies ranging from about 10 to about 350 GHz.[123–125] In a broad range of repetition frequencies, transform-limited operation was obtained, with pulses from about 2 ps short at 42 GHz to 0.56 ps at 346 GHz.

The use of single-section QDh lasers for a wide range of practical applications was successfully demonstrated, showing the maturity of this technology.[124,126] All-optical clock recovery at 40 GBit/s was achieved, with jitter removal demonstrated, and subharmonic clock recovery at 40 GBit/s from 80 and 160 GBit/s streams achieved, opening the way for the use of such lasers for optical time-division multiplexing (OTDM) demultiplexing systems. By beating the modes of QDh lasers, microwave electrical signal was generated, with a RF linewidth in the range of 20–50 kHz, depending on the number of dash layers in the structure. Generation of an optical frequency comb at 100 GHz, of use for wavelength division multiplexing (WDM) communications, was also successfully shown.

ML in *QD* single-section lasers has also been reported, in an even wider range of repetition frequencies (from 10 to 400 GHz), and pulse durations down to 0.3 ps under some conditions.[127,128]

Single-section ML has been also reported in QWs[129,130] and even bulk materials[130] showing that the effect is fairly generic.

Single-section ML lasers have two considerable advantages over ML lasers with a SA. Firstly, the single-contact simplifies the laser operation, and secondly, the absence of the SA eliminates the risk of the QS instability, which has indeed not been observed in single-section ML. Some of the techniques (harmonic ML, Section 5.7.4) that are used with SA ML may also be opened to single-section ones. Further optimisation of these lasers may partly depend on the establishment of full understanding of their behaviour.

At the time of writing, a universally agreed theoretical explanation for ML in single-section lasers is still pending, and it is not impossible that different effects can play the main part in different constructions. In the past, some authors[131,132] used frequency-domain models with postulated non-linearity coefficients to show that non-linearities in single-section SLs could lead to a steady-state regime with fixed phases; however, this was predicted to produce, not the amplitude modulation (AM) ML which corresponds to short pulse emission, but the so-called frequency fodulation ML, in which the phases of adjacent modes differ approximately by π, and the outcome is a regime with periodic carrier frequency oscillation. More recent work,[46,47] also using frequency-domain analysis with microscopically calculated[46] or phenomenological[47] description of linear and non-linear gain, predicted a possibility of ML type signal generation, including AM ML for certain cavity lengths and active layer parameters, in a single-section laser with three modes involved in lasing, due to mode coupling by population pulsations/four-wave mixing effects. This appears to agree in principle with travelling-wave modelling for the case of a DBR laser without a SA;[133] the authors of Reference 133 also identified the role of four-wave mixing in their construction. A full analysis for truly multimode Fabry–Perot construction, either in time or frequency domain, which would be the final proof of the validity of this explanation, has not however been reported yet, to the best of our knowledge. Yang and co-authors[130,134] put forward a theory which attributes the (AM) ML in single-section lasers with deeply etched waveguide structures to carrier redistribution in the lateral direction and the associated variations of the lateral mode profile. Given significant scattering losses at the lateral waveguide walls, this redistribution can reduce the losses for high-energy light, producing effective SA action. Stability analysis using a generalisation of Haus's ML theory to the case of multiple spatial modes of an unperturbed waveguide supported this explanation, but qualitative analysis of fully developed ML is not yet available. Double lateral modes have been seen operating phase-locked also in a different single-section construction, producing a ML type regime at a frequency different from the round-trip.[135]

5.8.4 Miniaturisation and integration: ring and microring resonator cavities

One important potential application of ML lasers would be as clock generators in future optoelectronic integrated circuits (OEIC). The majority of ML lasers studied so far, however, have been Fabry–Perot constructions with at least one reflector formed by the chip facet, which makes them poorly suitable for integration. Fabry–Perot lasers with etched reflectors such as those discussed in Section 5.7.4, Bragg lasers with DBR reflectors either side, and ring resonators can all be seen as potential candidates for monolithically integrable ML laser constructions. Ring lasers, in particular, have been attracting attention for a number of years, with the improvement of fabrication technology gradually removing the high scattering losses, which reduced the efficiency of early structures (see review in Reference 37) to 15–20% at most. In the last decade, the technology has been transferred from GaAs/AlGaAs structures to InGaAsP quaternaries,[136] and hybrid integration with silicon passive Si waveguides also realised,[137,138] with avoiding internal reflectances at butt joints between different waveguide sections identified as the necessary condition for such integration. The formula [5.22] in a standard ring construction is modified as $F \approx M_h v_g / L_{\text{ring}}$, where L_{ring} is the ring circumference and normally $M_h = 1$. Moreover, the ring laser is by default a colliding-pulse structure, with clockwise and counter-clockwise propagating pulses colliding in the SA(s). The amplitudes of the two pulses are by default the same, though in an integrated structure are influenced by the relative positions of the SA, amplifier, and output couplers.[138]

The ring structure is more amenable to integration than a linear one; however, the length of the ring still remains the necessary limitation to the footprint of the device. The next step towards miniaturised, integrable constructions of ML lasers could be the recently proposed use of coupled microring resonators, possibly embedded in a two-dimensional photonic crystal, for creating utlra-compact lasers for active ML.[95,96] Coupled-ring resonators can be viewed as slow-light structures, so could allow for ML at not-too-high (tens of GHz) repetition rates for very small physical footprints of the device. Theoretical analysis using the coupled-mode frequency-domain formalism suggests that such structures may be realisable in practice, though achieving stable ML poses stringent requirements on the fabrication accuracy.[96] Passive sub-picosecond pulse generation in microring devices has also been predicted theoretically, using a frequency-domain approach.[139]

5.9 Overview of applications of mode-locked diode lasers

ML SLs are well-suited for a wide range of applications, including optical fibre communications, optical clock distribution, clock recovery, radio over fibre signal generation, optical sampling of high-speed signals and metrology.[140–143]

In *optical communications*, ML lasers (particularly QD and QDh ones) are poised to make a large impact on the next generation of optical networks and communication systems. The current InAs QD technology is well-suited for optical communications using the O-band (1260–1360 nm) as defined by the International Telecommunication Union (ITU-T). The O-band coincides with the spectral window of lowest dispersion in optical fibres, and is of particular interest for metropolitan networks. The telecom optical C-band of 1530—1565 nm ('erbium window') has also been addressed,[144] particularly with InP- based QDh materials as mentioned above (Section 5.8.3).

For OTDM, the possibility to generate pulses at very high repetition rate and with record-low jitter is highly desirable; here, an ML QD laser can be used either as a pulse source or in a clock recovery circuit. Very recently, the enormous potential of QD ML lasers for OTDM up to 160 Gb/s was demonstrated by temporally interleaving the split output of a 40GHz hybridly ML QD laser.[145] Return-to-zero eye diagrams for transmission rates of 40 and 80 Gb/s presented in this paper show clear open-eye.

On the other hand, the broad spectral bandwidth offered by QD structures can be deployed in WDMs,[146] potentially involving multi-wavelength ML.

Finally, very recent results have been reported showing the promise of QD ML lasers for the generation of microwave signals, directly from the intra-waveguide SA.[147] In this paper, the authors demonstrate a differential efficiency of 33% in optical-to-RF power conversion, while the best extraction efficiency of the SA is shown to be about 86% (for a 10 GHz signal).

These results could pave the way for a new range of applications where monolithic QD passively ML lasers could be used as compact RF sources for wireless communications.[148]

Telecoms and datacoms are two particular niche applications that semiconductor ultrafast SLs have been traditionally designed to address.[37] The ultimate goal is to access applications that have been mainly in the domain of solid-state lasers. Such is the case *of biophotonics and medical applications* in particular, where compact, rugged and turnkey sources are crucial for the deployment of sophisticated and non-invasive optical diagnostics and therapeutics. In this respect, compact and simple semiconductor ultrafast sources based on QD materials can offer a number of advantages.

Optical Coherence Tomography (OCT) – a technique that enables imaging with resolutions up to the micrometre level – is one of the medical diagnostics that may benefit in the near future from developments in QD ultrafast lasers. The resolution achieved by this technique is determined by the wavelength and spectral bandwidth of the optical source and it is desirable to achieve as high a bandwidth as possible. The optical source used in OCT should also have a short coherence length. All these requirements can be satisfied by ML lasers, which have been the best performing sources deployed for OCT, in particular Ti:Sapphire lasers (800 nm) and Cr:Forsterite and fibre lasers (1300 nm). However, in order to turn OCT an interesting and practical tool, it is crucial to decrease the footprint and complexity of the laser system. Superluminescent diodes have been used to this end, but power levels can be very low.

An alternative could be to use QD-based ML lasers. The spectral range that is most routinely accessed with QD lasers (around 1.3 μm) can penetrate deeper into biological tissue[148–151] as it suffers less scattering and absorption than at 800 nm. In fact, the use of this longer wavelength has allowed imaging depths of 3 mm in non-transparent tissues.[151]

It can be concluded from the content of this chapter that there is an ongoing evolution in the development of ultrafast optoelectronic devices, particularly QD ones, from laboratory configurations to an increasingly practical and potentially deployable system status. Further progress will rely both on new insights from the fundamental science as well as technical innovations, and so we can predict that research and development activities in this field are set to remain at the forefront of international endeavour for the foreseeable future.

5.10 Conclusion

We have attempted to review the most important developments in ultrashort pulse generation by SLs. Due to the practical limitations and the increasingly broad nature of the field, the choice of emphasis may have been by necessity subjective; apologies are extended to those authors whose work may not have been given due prominence. The overall conclusion is that the SL technology is now successfully challenging lasers of other type in a wide variety of existing applications. In many cases, particularly with mode-locked lasers, it can be confidently expected that new applications will emerge stimulated by the high performance available.

5.11 Acknowledgements

The authors are extremely grateful to Boris Ryvkin who has read the section on gain-switching and made some very constructive suggestions.

5.12 References

1. P. Vasil'ev, *Ultrafast Diode Lasers: Fundamentals and Applications*. Boston: Artech House, 1995.
2. L. G. Melcer, J. R. Karin, R. Nagarajan and J. E. Bowers, "Picosecond dynamics of optical gain switching in vertical cavity surface emitting lasers," *IEEE Journal of Quantum Electronics*, vol. **27**, pp. 1417–1425, Jun 1991.
3. A. E. Siegman, *Lasers*. Oxford: Oxford University Press, 1986.
4. L. A. Coldren and S. W. Corzine, *Diode Lasers and Photonic Integrated Circuits*. New York: Wiley, 1995.
5. K. Y. Lau, "Gain switching of semiconductor injection-lasers," *Applied Physics Letters*, vol. **52**, pp. 257–259, Jan 1988.
6. B. Lanz, S Vainshtein and J. T. Kostamovaara, "High power gain-switched laser diode using a superfast GaAs avalanche transistor for pumping," *Applied Physics Letters*, vol. **89**, Aug 2006.
7. A. Biernat and G. Kompa, "Powerful picosecond laser pulses enabling high-resolution pulsed laser radar," *Journal of Optics-Nouvelle Revue D Optique*, vol. **29**, pp. 225–228, Jun 1998.
8. A. Biernat and G. Kompa, "Numerical simulation of the generation of gain switched laser pulses," *Optical and Quantum Electronics,* vol. **31**, pp. 981–995, Oct 1999.
9. S. Vainshtein, *et al.*, "Laser diode structure for the generation of high-power picosecond optical pulses," *Applied Physics Letters*, vol. **80**, pp. 4483–4485, Jun 2002.
10. B. Ryvkin, *et al.*, "Asymmetric-waveguide laser diode for high-power optical pulse generation by gain switching," *Journal of Lightwave Technology*, vol. **27**, pp. 2125–2131, Jun 2009.
11. L. W. Hallman, B. Ryvkin, K. Haring, S. Ranta, T. Leinonen and J. T. Kostamovaara, "Asymmetric waveguide laser diode operated in gain switching mode with high-power optical pulse generation," *Electronics Letters,* vol. **46**, pp. 65–U93, Jan 2010.
12. E. A. Avrutin, B. S. Ryvkin, J. Kostamovaara, and E.L. Portnoi, "Analysis of symmetric and asymmetric broadened-mode laser structures for short and ultrashort optical pulse generation," in *12th International Conference on Transparent Optical Networks*, Munich, 2010, p. Tu.B2.2.

13. B. S. Ryvkin, E. A. Avrutin and J. T. Kostamovaara, “Quantum well laser with an extremely large active layer width to optical confinement factor ratio for high-energy single picosecond pulse generation by gain switching,” *Semiconductor Science and Technology*, vol. **26**, Apr 2011, article 045010.
14. S. Riecke, *et al.*, “10.7W peak power picosecond pulses from high-brightness photonic band crystal laser diode,” *Electronics Letters,* vol. **46**, pp. 1393–1394, Sep 2010.
15. G. Venus, *et al.*, *Multi-section Ion-implantation-induced Saturable Absorbers for High-power 1.5-mu m Picosecond Laser Diodes*. New York: IEEE, 2000.
16. E. L. Portnoi, *et al.*, “Superhigh-po ner picosecond optical pulses from Q-switched diode laser,” *IEEE Journal of Selected Topics in Quantum Electronics*, vol. **3**, pp. 256–260, Apr 1997.
17. Y. Hu, *et al.*, “Gain switching of an external cavity grating-coupled surface emitting laser with wide tunability,” *Applied Physics Letters*, vol. **82**, pp. 4236–4237, Jun 2003.
18. D. Huhse, *et al.*, “Generation of electrically wavelength tunable (delta-lambda = 40 nm) singlemode laser-pulses from a 1.3 mu-m Fabry-Perot laser by self-seeding in a fiberoptic configuration,” *Electronics Letters,* vol. **30**, pp. 157–158, Jan 1994.
19. M. Schell, *et al.*, “jitter and dynamics of self-seeded Fabry-Perot laser-diodes,” *IEEE Journal of Selected Topics in Quantum Electronics*, vol. **1**, pp. 528–534, Jun 1995.
20. E. U. Rafailov, *et al.*, “Nonresonant self-injection seeding of a gain-switched diode laser,” *IEEE Journal of Selected Topics in Quantum Electronics*, vol. **7**, pp. 287–292, Mar–Apr 2001.
21. D. J. L. Birkin, *et al.*, “Tunable operation of a gain-switched diode laser by non-resonant self-injection seeding,” *IEEE Photonics Technology Letters*, vol. **13**, pp. 1158–1160, Nov 2001.
22. A. Klehr, *et al.*, “High peak power pulse generation with GHz repetition rate using a Q-switched 1060nm DBR tapered laser,” in *Novel in-Plane Semiconductor Lasers Ix*. vol. 7616, A. A. Belyanin and P. M. Smowton, Eds., Bellingham: Spie-Int Soc Optical Engineering, 2010.
23. M. Kuznetsov, “Pulsations of semiconductor-lasers with a proton bombarded segment – well-developed pulsations,” *IEEE Journal of Quantum Electronics*, vol. **21**, pp. 587–592, 1985.
24. E. A. Avrutin, “Analysis of spontaneous emission and noise in self-pulsing laser-diodes,” *IEE Proceedings-J Optoelectronics*, vol. **140**, pp. 16–20, Feb 1993.
25. B. Sartorius, *et al.*, “Dispersive self-Q-switching in self-pulsating DFB laser,” *IEEE Journal of Quantum Electronics*, vol. **33**, pp. 211–218, Feb 1997.
26 P. P. Vasilev and I. H. White, “Ultrafast single-mode self-pulsations in InGaAsP/InP lambda/4-phase-shifted distributed feedback multi-quantum-well triplet-contact diode lasers,” *Kvantovaya Elektronika*, vol. **22**, pp. 1176–1178, Dec 1995.
27. P. Barnsley, “All-optical clock extraction using 2-contact devices,” *IEE Proceedings-J Optoelectronics*, vol. **140**, pp. 325–336, Oct 1993.
28. P. E. Barnsley and H. J. Wickes, “All-optical clock recovery from 2.5gbit/s NRZ data using selfpulsating 1.58 mu-m laser diode,” *Electronics Letters*, vol. **28**, pp. 4–6, Jan 1992.
29. S. Nishikawa, *et al.*, “All-optical clock recovery and wavelength conversion by combination of self-pulsation laser and semiconductor-optical-amplifier-based

Mach-Zehnder interferometer," *Japanese Journal of Applied Physics Part 1-Regular Papers Brief Communications & Review Papers,* vol. **45**, pp. 3457–3461, Apr 2006.

30. S. E. M. Dudley, *et al.*, "Direct off-air detection, transmission, and tunable band-pass filtering using self-pulsating lasers and substrate antennae," *Journal of Lightwave Technology*, vol. **23**, pp. 809–817, Feb 2005.
31. D. R. Matthews, *et al.*, "Technique for measurement of fluorescence lifetime by use of stroboscopic excitation and continuous-wave detection," *Applied Optics,* vol. **45**, pp. 2115–2123, Mar 2006.
32. M. D. Holton, *et al.*, "Stroboscopic fluorescence lifetime imaging," *Optics Express*, vol. **17**, pp. 5205–5216, Mar 2009.
33 C. T. A. Brown, *et al.*, "Compact laser-diode-based femtosecond sources," *New Journal of Physics*, vol. **6**, p. 175, Nov 2004.
34 R. Ell, *et al.*, "Generation of 5-fs pulses and octave-spanning spectra directly from a Ti: sapphire laser," *Optics Letters*, vol. **26**, pp. 373–375, Mar 2001.
35. E. Innerhofer, *et al.*, "60-W average power in 810-fs pulses from a thin-disk Yb: YAG laser," *Optics Letters*, vol. **28**, pp. 367–369, Mar 2003.
36. K. Kim, *et al.*, "1.4 kW high peak power generation from an all semiconductor mode-locked master oscillator power amplifier system based on eXtreme Chirped Pulse Amplification(X-CPA)," *Optics Express,* vol. **13**, pp. 4600–4606, Jun 2005.
37. E. A. Avrutin, *et al.*, "Monolithic and multi-GigaHertz mode-locked semiconductor lasers: Constructions, experiments, models and applications," *IEE Proceedings-J Optoelectronics*, vol. **147**, pp. 251–278, Aug 2000.
38. E. L. Delpon, *et al.*, "Ultrafast excitonic saturable absorption in ion-implanted InGaAs/InAlAs multiple quantum wells," *Applied Physics Letters*, vol. **72**, pp. 759–761, 1998.
39. G. H. C. New, "Pulse evolution in mode-locked quasicontinuous lasers," *IEEE Journal of Quantum Electronics*, vol. **QE10**, pp. 115–124, 1974.
40. H. A. Haus, "Theory of mode-locking with a slow saturable absorber," *IEEE Journal of Quantum Electronics*, vol. **11**, pp. 736–746, 1975.
41. J. A. Leegwater, "Theory of mode-locked semiconductor lasers," *IEEE Journal of Quantum Electronics*, vol. **32**, pp. 1782–1790, Oct 1996.
42. R. Koumans and R. vanRoijen, "Theory for passive mode-locking in semiconductor laser structures including the effects of self-phase modulation, dispersion, and pulse collisions," *IEEE Journal of Quantum Electronics*, vol. **32**, pp. 478–492, Mar 1996.
43. J. Javaloyes and S. Balle, "Mode-locking in semiconductor Fabry-Perot lasers," *IEEE Journal of Quantum Electronics*, vol. **46**, pp. 1023–1030, Jul 2010.
44. V. V. N. E. A. Avrutin, and D. Gallagher, "Monolithic mode-locked semiconductor lasers," in *Optoelectronic Devices – Advanced Simulation and Analysis,*, J. Piprek, Ed., New York: Springer, 2005, pp. 185–215.
45. E. A. Avrutin, *et al.*, "Dynamic modal analysis of monolithic mode-locked semiconductor lasers," *IEEE Journal of Selected Topics in Quantum Electronics,* vol. **9**, pp. 844–856, May–Jun 2003.
46. Y. Nomura, *et al.*, "Mode locking in Fabry-Perot semiconductor lasers," *Physical Review A*, vol. **65**, Apr 2002.
47. J. Renaudier, *et al.*, "Phase correlation and linewidth reduction of 40 GHz self-pulsation in distributed Bragg reflector semiconductor lasers," *IEEE Journal of Quantum Electronics*, vol. **43**, pp. 147–156, Jan–Feb 2007.

48. A. G. Vladimirov, *et al.*, "Delay differential equations for mode-locked semiconductor lasers," *Optics Letters*, vol. **29**, pp. 1221–1223, Jun 2004.
49. A. G. Vladimirov and D. Turaev, "Model for passive mode locking in semiconductor lasers," *Physical Review A*, vol. **72**, Sep 2005.
50. E. A. Viktorov, *et al.*, "Model for mode locking in quantum dot lasers," *Applied Physics Letters*, vol. **88**, pp. 201102–3, 2006.
51. E. U. Rafailov, M. A. Cataluna, and E. A. Avrutin, *Ultrafast Lasers Based on Quantum Dot Structures*. New York/Berlin: Wiley, 2011.
52. J. L. A. Dubbeldam, *et al.*, "Theory of mode-locked semiconductor lasers with finite absorber relaxation times," *Applied Physics Letters*, vol. **70**, pp. 1938–1940, Apr 1997.
53. J. Mulet and S. Balle, "Mode-locking dynamics in electrically driven vertical-external-cavity surface-emitting lasers," *IEEE Journal of Quantum Electronics,* vol. **41**, pp. 1148–1156, Sep 2005.
54. V. V. Nikolaev and E. A. Avrutin, "Photocarrier escape time in quantum-well light-absorbing devices: Effects of electric field and well parameters," *IEEE Journal of Quantum Electronics*, vol. **39**, pp. 1653–1660, Dec 2003.
55. D. B. Malins, *et al.*, "Ultrafast electroabsorption dynamics in an InAs quantum dot saturable absorber at 1.3 μm," *Applied Physics Letters*, vol. **89**, pp. 171111–3, 2006.
56. K. Y. Lau and J. Paslaski, "Condition for short pulse generation in ultrahigh frequency mode-locking of semiconductor-lasers," *IEEE Photonics Technology Letters*, vol. **3**, pp. 974–976, Nov 1991.
57. U. Bandelow, *et al.*, "40 GHz mode-locked semiconductor lasers: Theory, simulations and experiment," *Optical and Quantum Electronics*, vol. **38**, pp. 495–512, Mar 2006.
58. J. Mork and A. Mecozzi, "Theory of nondegenerate four-wave mixing between pulses in a semiconductor waveguide," *IEEE Journal of Quantum Electronics*, vol. **33**, pp. 545–555, Apr 1997.
59. A. Mecozzi and J. Mork, "Saturation effects in nondegenerate four-wave mixing between short optical pulses in semiconductor laser amplifiers," *IEEE Journal of Selected Topics in Quantum Electronics*, vol. **3**, pp. 1190–1207, Oct 1997.
60. E. A. Avrutin, *et al.*, "Effect of nonlinear amplification on characteristics of quality modulation regime in semiconducting laser with fast saturated absorbers," *Pisma V Zhurnal Tekhnicheskoi Fiziki,* vol. **17**, pp. 49–54, Jun 1991.
61. R. A. Salvatore, *et al.*, "Supermodes of high-repetition-rate passively mode-locked semiconductor lasers," *IEEE Journal of Quantum Electronics*, vol. **32**, pp. 941–952, 1996.
62. K. A. Williams, *et al.*, "Q-switched bow-tie lasers for high-energy picosecond pulse generation," *Electronics Letters*, vol. **30**, pp. 320–321, Feb 1994.
63. M. G. Thompson, *et al.*, "Subpicosecond high-power mode locking using flared waveguide monolithic quantum-dot lasers," *Applied Physics Letters*, vol. **88**, pp. 133119–3, 2006.
64. M. G. Thompson, *et al.*, "InGaAs quantum-dot mode-locked laser diodes," *IEEE Journal of Selected Topics in Quantum Electronics,* vol. **15**, pp. 661–672, May–Jun 2009.
65. D. I. Nikitichev, *et al.*, "High-power passively mode-locked tapered InAs/GaAs quantum-dot lasers," *Applied Physics B-Lasers and Optics*, vol. **103**, pp. 609–613, Jun 2011.

66. D. I. Nikitichev, *et al*., "15W peak power sub-picosecond pulse generation directly from a passively mode-locked quantum-dot two-section gain-guided tapered laser," presented at the CLEO Europe, Munich, 2011.
67. J. H. Zarrabi, *et al.*, "Passive-mode locking of a multistripe single quantum-well GAAS-laser diode with an intracavity saturable absorber," *Applied Physics Letters*, vol. **59**, pp. 1526–1528, Sep 1991.
68. A. G. Deryagin, *et al*., "Generation of high repetition frequency subpicosecond pulses at 1.535 mu-m by passive mode-locking of InGaAsP/InP laser diode with saturable absorber regions created by ion implantation," *Proceedings of 14th IEEE Semiconductor Laser Conference*, New York: IEEE, pp. 107–108, 1994.
69. R. P. Green, *et al.*, "Fast saturable absorption and 10 GHz wavelength conversion in Al-quaternary multiple quantum wells," *Optics Express,* vol. **19**, pp. 9737–9743, May 2011.
70. M. H. Lianping Hou, Bocang Qiu, Eugene A. Avrutin, A. Catrina Bryce, "Ultrashort pulse generation using fast saturable absorbers in AlGaInAs/InP 1.55 μm mode-locked lasers," in *13th International Conference on Transparent Optical Networks*, Stockholm, 2011.
71. L. P. Hou, *et al.*, "Subpicosecond pulse generation at quasi-40-GHz using a passively mode-locked AlGaInAs-InP 1.55-mu m strained quantum-well laser," *IEEE Photonics Technology Letters*, vol. **21**, pp. 1731–1733, Dec 2009.
72. L. P. Hou, *et al.*, "160-GHz passively mode-locked AlGaInAs 1.55-mu m strained quantum-well compound cavity laser," *IEEE Photonics Technology Letters*, vol. **22**, pp. 727–729, May 2010.
73. L. P. Hou, *et al.*, "160 GHz harmonic mode-locked AlGaInAs 1.55 mu m strained quantum-well compound-cavity laser," *Optics Letters*, vol. **35**, pp. 3991–3993, Dec 2010.
74. V. V. Nikolaev and E. A. Avrutin, "Quantum-well design for monolithic optical devices with gain and saturable absorber sections," *IEEE Photonics Technology Letters,* vol. **16**, pp. 24–26, Jan 2004.
75. V. V. Nikolaev and E. A. Avrutin, "Quantum well saturable absorber dynamics: Physical processes and modelling," in *Nusod '05: Proceedings of the 5th International Conference on Numerical Simulations of Optoelectronic Devices*, 2004, pp. 111–112.
76. R. Scollo, *et al.*, "Mode-locked laser diode with an ultrafast integrated uni-traveling carrier saturable absorber," *Optics Letters*, vol. **30**, pp. 2808–2810, Oct 2005.
77. R. Scollo, *et al.*, "Mode-locked InP-based laser diode with a monolithic integrated UTC absorber for subpicosecond pulse generation," *IEEE Journal of Quantum Electronics*, vol. **45**, pp. 322–335, Apr 2009.
78. F. R. Ahmad and F. Rana, "Passively mode-locked high-power (210 mW) semiconductor lasers at 1.55-mu m wavelength," *IEEE Photonics Technology Letters*, vol. **20**, pp. 190–192, Jan–Feb 2008.
79. J. J. Plant, *et al.*, "250 mW, 1.5 mu m monolithic passively mode-locked slab-coupled optical waveguide laser," *Optics Letters*, vol. **31**, pp. 223–225, Jan 2006.
80. J. T. Gopinath, *et al.*, "980-nm monolithic passively mode-locked diode lasers with 62 pJ of pulse energy," *IEEE Photonics Technology Letters,* vol. **19**, pp. 937–939, May–Jun 2007.

81. F. R. Ahmad and F. Rana, "Fundamental and subharmonic hybrid mode-locking of a high-power (220 mW) monolithic semiconductor laser," *IEEE Photonics Technology Letters*, vol. **20**, pp. 1308–1310, Jul–Aug 2008.
82. P. W. Juodawlkis, *et al.*, "High-power, low-noise 1.5-mu m slab-coupled optical waveguide (SCOW) emitters: Physics, devices, and applications," *IEEE Journal of Quantum Electronics*, vol. **47**, 1698–1714, 2011.
83. B. Rudin, *et al.*, "High-power MIXSEL: An integrated ultrafast semiconductor laser with 6.4 W average power," *Optics Express*, vol. **18**, pp. 27582–27588, Dec 2010.
84. A. Aschwanden, *et al.*, "2.1-W picosecond passively mode-locked external-cavity semiconductor laser," *Optics Letters*, vol. **30**, pp. 272–274, Feb 2005.
85. Y. Ding, M. A. Cataluna, D. Nikitichev, I. Krestnikov, D. Livshits, and E. Rafailov, "Broad repetition-rate tunable quantum-dot external-cavity passively mode-locked laser with extremely narrow radio frequency linewidth," *Applied Physics Express*, vol. **4**, article 062703, 2011.
86. J. F. Martins, *et al.*, "Monolithic multiple colliding pulse mode-locked quantum-well lasers – experiment and theory," *IEEE Journal of Selected Topics in Quantum Electronics*, vol. **1**, pp. 539–551, Jun 1995.
87. S. D. McDougall, *et al.*, "The crucial role of doping for high repetition rate monolithic mode locking of multiple quantum well GaAs/AlGaAs lasers," *Applied Physics Letters*, vol. **71**, pp. 2910–2912, Nov 1997.
88. T. Shimizu, *et al.*, "Asymmetric colliding-pulse mode-locking in InGaAsP semiconductor lasers," *Optical Review,* vol. **2**, pp. 401–403, Nov–Dec 1995.
89. T. Shimizu, *et al.*, "860 GHz rate asymmetric colliding pulse modelocked diode lasers," *Electronics Letters*, vol. **33**, pp. 1868–1869, Oct 1997.
90. D. A. Yanson, *et al.*, "Ultrafast harmonic mode-locking of monolithic compound-cavity laser diodes incorporating photonic-bandgap reflectors," *IEEE Journal of Quantum Electronics*, vol. **38**, pp. 1–11, Jan 2002.
91. L. Hou, R. Dylewicz, M. Haji, B. Qiu, and A. Catrina Bryce, "AlGaInAs mode-locked lasers for ultrashort pulse harmonic ML," in *13th International Conference on Transparent Optical Networks*, Stockholm, 2011.
92. S. O'Brien, *et al.*, "Design and applications of discrete mode Fabry-Perot diode lasers," *Photonics and Nanostructures-Fundamentals and Applications*, vol. **8**, pp. 218–227, Sep 2010.
93. S. O'Brien, *et al.*, "Optical synthesis of terahertz and millimeter-wave frequencies with discrete mode diode lasers," *IEEE Transactions on Microwave Theory and Techniques*, vol. **58**, pp. 3083–3087, Nov 2010.
94. B. S. Kim, *et al.*, "Dynamic analysis of mode-locked sampled-grating distributed Bragg reflector laser diodes," *IEEE Journal of Quantum Electronics*, vol. **35**, pp. 1623–1629, Nov 1999.
95. Y. Liu, *et al.*, "Mode-locking of monolithic laser diodes incorporating coupled-resonator optical waveguides," *Optics Express*, vol. **13**, pp. 4539–4553, Jun 2005.
96. C. Agger, *et al.*, "Modeling of mode-locked coupled-resonator optical waveguide lasers," *IEEE Journal of Quantum Electronics*, vol. **46**, pp. 1804–1812, Dec 2010.
97. E. U. Rafailov, *et al.*, "Mode-locked quantum-dot lasers," *Nature Photonics,* vol. **1**, pp. 395–401, 2007.

98. E. U. Rafailov, *et al.*, Ultrafast Lasers Based on Quantum Dot Structures, Berlin: Wiley-VCH, 2011.
99. M. A. Cataluna, *et al.*, "Stable mode-locked operation up to 80°C from an InGaAs quantum-dot laser," *IEEE Photonics Technology Letters*, vol. **18**, pp. 1500–1502, 2006.
100. M. A. Cataluna, *et al.*, "Stable mode locking via ground- or excited-state transitions in a two-section quantum-dot laser," *Applied Physics Letters*, vol. **89**, pp. 81124–3, 2006.
101. E. A. Viktorov, *et al.*, "Recovery time scales in a reversed-biased quantum dot absorber," *Applied Physics Letters,* vol. **94**, article 263502, Jun 2009.
102. M. A. Cataluna, *et al.*, "Temperature dependence of pulse duration in a mode-locked quantum-dot laser," *Applied Physics Letters*, vol. **90**, pp. 101102–3, 2007.
103. D. B. Malins, *et al.*, "Temperature dependence of electroabsorption dynamics in an InAs quantum dot saturable absorber at 1.3μm.," in *European Conference on Lasers and Electro-Optics*, Munich, Germany, 2007.
104. M. A. Cataluna, *et al.*, "Temperature dependence of electroabsorption dynamics in an InAs quantum-dot saturable absorber at 1.3 mu m and its impact on mode-locked quantum-dot lasers," *Applied Physics Letters*, vol. **97**, article 121110, Sep 2010.
105. S. Fathpour, *et al.*, "High-speed quantum dot lasers," *Journal of Physics D-Applied Physics*, vol. **38**, pp. 2103–2111, Jul 2005.
106. M. Laemmlin, *et al.*, "Distortion-free optical amplification of 20–80 GHz modelocked laser pulses at 1.3 μm using quantum dots," *Electronics Letters*, vol. **42**, pp. 697–699, 2006.
107. G. Fiol, *et al.*, "Quantum-dot semiconductor mode-locked lasers and amplifiers at 40 GHz," *IEEE Journal of Quantum Electronics*, vol. **45**, pp. 1429–1435, Nov 2009.
108. A. Markus, *et al.*, "Simultaneous two-state lasing in quantum-dot lasers," *Applied Physics Letters*, vol. **82**, pp. 1818–1820, 2003.
109. S. Schneider, *et al.*, "Excited-state gain dynamics in InGaAs quantum-dot amplifiers," *IEEE Photonics Technology Letters*, vol. **17**, pp. 2014–2016, 2005.
110. E. U. Rafailov, *et al.*, "Investigation of transition dynamics in a quantum-dot laser optically pumped by femtosecond pulses," *Applied Physics Letters*, vol. **88**, pp. 41101–3, 2006.
111. M. A. Cataluna, *et al.*, "Ground and excited-state modelocking in a two-section quantum-dot laser," in *18th Annual Meeting of the IEEE Lasers and Electro-Optics Society*, Sydney, Australia, 2005, pp. 870–871.
112. M. A. Cataluna, *et al.*, "Dual-wavelength mode-locked quantum-dot laser, via ground and excited state transitions: experimental and theoretical investigation," *Optics Express*, vol. **18**, pp. 12832–12838, Jun 7, 2010.
113. T. C. Newell, *et al.*, "Gain and linewidth enhancement factor in InAs quantum-dot laser diodes," *IEEE Photonics Technology Letters*, vol. **11**, pp. 1527–1529, Dec 1999.
114. A. Martinez, *et al.*, "Static and dynamic measurements of the alpha-factor of five-quantum-dot-layer single-mode lasers emitting at 1.3 μm on GaAs," *Applied Physics Letters*, vol. **86**, p. 211115, May 2005.

115. H. Su and L. F. Lester, “Dynamic properties of quantum dot distributed feedback lasers: high speed, linewidth and chirp,” *Journal of Physics D-Applied Physics*, vol. **38**, pp. 2112–2118, Jul 2005.
116. B. Dagens, *et al.*, “Giant linewidth enhancement factor and purely frequency modulated emission from quantum dot laser,” *Electronics Letters,* vol. **41**, pp. 323–324, Mar 2005.
117. J. Kim and P. J. Delfyett, “Above threshold spectral dependence of linewidth enhancement factor, optical duration and linear chirp of quantum dot lasers,” *Optics Express*, vol. **17**, pp. 22566–22570, Dec 2009.
118. K. G. Wilcox, *et al.*, “Ultrafast optical Stark mode-locked semiconductor laser,” *Optics Letters,* vol. **33**, pp. 2797–2799, Dec 2008.
119. P. Klopp, *et al.*, “Pulse repetition rate up to 92 GHz or pulse duration shorter than 110 fs from a mode-locked semiconductor disk laser,” *Applied Physics Letters*, vol. **98**, Feb 2011.
120. A. H. Quarterman, *et al.*, “A passively mode-locked external-cavity semiconductor laser emitting 60-fs pulses,” *Nature Photonics*, vol. **3**, pp. 729–731, Dec 2009.
121. P. Klopp, *et al.*, “Mode-locked InGaAs-AlGaAs disk laser generating sub-200-fs pulses, pulse picking and amplification by a tapered diode amplifier,” *Optics Express*, vol. **17**, pp. 10820–10834, Jun 2009.
122. Z. Mihoubi, *et al.*, Numerical Model of a Vertical-External-Cavity Surface-Emitting Semiconductor Lasers Mode-locked by the Optical Stark Effect. New York: IEEE, 2008.
123. C. Gosset, *et al.*, “Subpicosecond pulse generation at 134 GHz using a quantum-dash-based Fabry-Perot laser emitting at 1.56 mu m,” *Applied Physics Letters*, vol. **88**, Jun 2006.
124. G. H. Duan, *et al.*, “High performance InP-based quantum dash semiconductor mode-locked lasers for optical communications,” *Bell Labs Technical Journal*, vol. **14**, pp. 63–84, Fal 2009.
125. K. Merghem, *et al.*, “Pulse generation at 346 GHz using a passively mode locked quantum-dash-based laser at 1.55 mu m,” *Applied Physics Letters*, vol. **94**, article 021107, Jan 2009.
126. F. Lelarge, *et al.*, “Recent advances on InAs/InP quantum dash based, semiconductor lasers and optical amplifiers operating at 1.55 mu m,” *IEEE Journal of Selected Topics in Quantum Electronics*, vol. **13**, pp. 111–124, Jan–Feb 2007.
127. J. Renaudier, *et al.*, “45 GHz self-pulsation with narrow linewidth in quantum dot Fabry-Perot semiconductor lasers at 1.5 μm,” *Electronics Letters,* vol. **41**, pp. 1007–1008, 2005.
128. Z. G. Lu, *et al.*, “Ultra-high repetition rate InAs/InP quantum dot mode-locked lasers,” *Optics Communications,* vol. **284**, pp. 2323–2326, May 2011.
129. K. Sato, “Optical pulse generation using Fabry-Perot lasers under continuous-wave operation,” *IEEE Journal of Selected Topics in Quantum Electronics*, vol. **9**, pp. 1288–1293, Sep–Oct 2003.
130. W. G. Yang, “Single-section Fabry-Perot mode-locked semiconductor lasers,” *Advances in OptoElectronics*, vol. **2011**, p. 780373, 2011.
131. K. A. Shore and W. M. Yee, “Theory of self-locking fm operation in semiconductor-lasers,” *IEE Proceedings-J Optoelectronics*, vol. **138**, pp. 91–96, Apr 1991.

132. W. M. Yee and K. A. Shore, "Multimode analysis of self locked FM operation in laser-diodes," *IEE Proceedings-J Optoelectronics*, vol. **140**, pp. 21–25, Feb 1993.
133. P. Bardella and I. Montrosset, "Analysis of self-pulsating three-section DBR lasers," *IEEE Journal of Selected Topics in Quantum Electronics*, vol. **11**, pp. 361–366, Mar–Apr 2005.
134. W. G. Yang, "Picosecond dynamics of semiconductor Fabry-Perrot lasers: A simplified model," *IEEE Journal of Selected Topics in Quantum Electronics*, vol. **13**, pp. 1235–1241, Sep–Oct 2007.
135. A. Enard, *et al.*, *Mode Locking and Bandwidth Enhancement in Single Section Ridge Laser with Two Spatial Modes*. New York: IEEE, 2010.
136. Y. Barbarin, *et al.*, "Characterization of a 15 GHz integrated bulk InGaAsP passively modelocked ring laser at 1.53 mu m," *Optics Express*, vol. **14**, pp. 9716–9727, Oct 2006.
137. Y. Barbarin, *et al.*, "Realization and modeling of a 27-GHz integrated passively mode-locked ring laser," *IEEE Photonics Technology Letters*, vol. **17**, pp. 2277–2279, Nov 2005.
138. M. S. Tahvili, *et al.*, "Directional control of optical power in integrated InP/InGaAsP extended cavity mode-locked ring lasers," *Optics Letters*, vol. **36**, pp. 2462–2464, Jul 2011.
139. L. Gil and L. Columbo, "Theoretical description of spontaneous pulse formation in a semiconductor microring laser," *Physical Review A*, vol. **83**, article 013822, Jan 2011.
140. T. Ohno, *et al.*, "Recovery of 160 GHz optical clock from 160 Gbit/s data stream using modelocked laser diode," *Electronics Letters,* vol. **40**, pp. 265–267, Feb 19, 2004.
141. P. J. Delfyett, *et al.*, "Optical clock distribution using a mode-locked semiconductor-laser diode system," *Journal of Lightwave Technology,* vol. **9**, pp. 1646–1649, Dec 1991.
142. A. J. C. Vieira, *et al.*, "A mode-locked microchip laser optical transmitter for fiber radio," *IEEE Transactions on Microwave Theory and Techniques*, vol. **49**, pp. 1882–1887, Oct 2001.
143. H. Takara, "High-speed optical time-division-multiplexed signal generation," *Optical and Quantum Electronics*, vol. **33**, pp. 795–810, Jul 2001.
144. J. P. Reithmaier, *et al.*, "InP based lasers and optical amplifiers with wire-/dot-like active regions," *Journal of Physics D-Applied Physics*, vol. **38**, pp. 2088–2102, Jul 2005.
145. H. Schmeckebier, *et al.*, "Complete pulse characterization of quantum-dot mode-locked lasers suitable for optical communication up to 160 Gbit/s," *Optics Express*, vol. **18**, pp. 3415–3425, Feb 15, 2010.
146. J. Liu, *et al.*, "Uniform 90-channel multiwavelength InAs/InGaAsP quantum dot laser," *Electronics Letters,* vol. **43**, pp. 458–460, Apr 2007.
147. C. Y. Lin, *et al.*, "Compact optical generation of microwave signals using a monolithic quantum dot passively mode-locked laser," *Photonics Journal, IEEE*, vol. **1**, pp. 236–244, 2009.
148. J. Kim, *et al.*, "Hybrid integration of a bowtie slot antenna and a quantum dot mode-locked laser," *IEEE Antennas and Wireless Propagation Letters*, vol. **8**, pp. 1337–1340, 2009.

149. M. E. Brezinski and J. G. Fujimoto, “Optical coherence tomography: High-resolution imaging in nontransparent tissue,” *IEEE Journal of Selected Topics in Quantum Electronics*, vol. **5**, pp. 1185–1192, Jul–Aug 1999.
150. P. Fischer, *et al.*, “Deep tissue penetration of radiation: 3D modelling and experiments,” in *European Conference on Lasers and Electro-Optics*, Munich, Germany, 2005, pp. 641–641.
151. M. E. Brezinski, *et al.*, “Optical coherence tomography for optical biopsy – Properties and demonstration of vascular pathology,” *Circulation*, vol. **93**, pp. 1206–1213, Mar 1996.

6

Nonpolar and semipolar group III-nitride lasers

D. FEEZELL, University of New Mexico, USA and
S. NAKAMURA, University of California, Santa Barbara, USA

DOI: 10.1533/9780857096401.2.221

Abstract: Visible III-nitride laser diodes (LDs) are key components for a variety of applications, including high-definition data storage systems, projectors, and displays. Device performance has been accelerated by the recent development of III-nitride LDs on nonpolar and semipolar crystal orientations, which provide a variety of beneficial characteristics. In this chapter we first introduce the fundamentals of III-nitride materials, including polarization effects and nonpolar and semipolar orientations. We then discuss optical properties, materials issues, and waveguide design for nonpolar and semipolar LDs. A brief description of applications for III-nitride LDs is also included, followed by a discussion of fabrication techniques. We then present a history of results and show LDs with state-of-the-art performance on nonpolar and semipolar orientations. Finally, future directions and information on additional reference materials are provided.

Keywords: gallium nitride, laser diode, nonpolar, semipolar.

6.1 Introduction

Group III-nitrides, including AlN, GaN, and InN, represent a remarkable materials system with direct bandgaps spanning the entire visible spectrum. Prior to the development of these materials, there existed no efficient violet or blue optical devices, and green emitters based on II–VI materials characteristically suffered from poor lifetimes (Kasai *et al.*, 2010). Over the past 15 years, progress in materials synthesis, fabrication techniques, and device design has enabled high-performance III-nitride LDs operating in the violet, blue, and green regions of the optical spectrum. These devices are now key components in an expanding cross-section of commercial products, including high-definition digital versatile disc (DVD) systems, stand-alone projectors, pico-projectors, televisions, and displays.

Optically-pumped stimulated emission was first observed from GaN crystals in 1971 at Bell Laboratories (Dingle *et al.*, 1971). The authors measured relatively high material gains (~10^4–10^5 cm^{-1}) and thus speculated about the strong potential of GaN-based materials for LDs. While this prediction has indeed come to fruition, significant challenges necessitated an additional 25 years of development before the first demonstration of an electrically injected III-nitride laser diode (Nakamura *et al.*, 1996a). Key breakthroughs were required in epitaxial growth technology, including modification of the traditional metal–organic chemical vapor deposition (MOCVD) reactor and the development of high-temperature buffer layers. To further complicate the situation, the large activation energy of Mg acceptors initially prevented any significant p-type conduction. Amano *et al.* (1989) first demonstrated p-type conduction in Mg-doped GaN using low energy electron beam irradiation (LEEBI). Nakamura *et al.* (1992a) also realized p-type conduction using thermal annealing and later clarified that the mechanism is related to passivation of Mg dopants by H radicals (Nakamura *et al.*, 1992b).

While issues related to epitaxy and doping have seen substantial progress, conventional *c*-plane III-nitrides also contend with large internal polarization-related electric fields, which limit the efficiency of optical processes and present significant restrictions on device design. Alternatively, growth of devices on nonpolar and semipolar III-nitrides circumvents the issues associated with polarization-related electric fields and offers additional advantages for the development of higher-performance III-nitride LDs. Devices on these novel orientations have experienced rapid progress over the last several years and are quickly becoming viable alternatives to LDs on conventional *c*-plane GaN, particularly for the realization of higher efficiency green-emitting LDs.

6.2 Applications of group III-nitride lasers

III-nitride lasers initially entered the market as sources for high-density optical data storage. Devices with an emission wavelength in the violet region (405 nm) have enabled high-density optical disc systems with approximately five times the storage capacity of traditional DVD systems, which utilize 650 nm red lasers. Sony's Blu-Ray technology is an example of a high-density optical disc system. Since storage capacity is inversely proportional to $(\lambda/\mathrm{NA})^2$, where λ is the laser wavelength and NA is the numerical aperture of the scanning objective, by decreasing the laser wavelength from 650 to 405 nm and by increasing the NA of the scanning objective from 0.6 to 0.85, the tracking pitch in the system can be reduced from 0.74 to 0.32 μm. With these modifications, the data density can be significantly increased. For example, the single layer storage capacity is 4.7 Gb/layer for traditional DVDs and approximately 25 Gb/layer for Blu-Ray Discs. For optical data storage, single-lateral and transverse mode lasers are desirable due to their Gaussian output beam profiles. As a result, careful design of the waveguide structure is necessitated. For read-only applications, low-power lasers emitting around 20 mW are sufficient, while for read/write applications, output powers exceeding 100 mW are required. Higher output powers translate into increased writing speeds and allow for multi-layer 3-D storage. As a result, significant research into developing higher-power violet emitters continues (Koda *et al.*, 2011).

Due to their spectral purity, potential for high wall-plug efficiency (WPE), and focus-free operation, lasers are also attractive components for a variety of projection and display systems such as televisions, full-color pico-projectors, and head-up and head-mounted displays. Current televisions are capable of displaying only a fraction of the color gamut the human eye can perceive, while laser-based TVs would provide the widest possible color gamut with highly saturated colors. Laser-based HDTVs with screen sizes up to 75″ have been commercialized by Mitsubishi Electric, and stand-alone laser-based projectors are commercially available from several manufacturers. Pico-projectors would integrate red, green, and blue lasers in a small-form-factor projection system that could be housed in mobile phones. These next-generation systems represent the largest emerging market for green lasers. The pico-projector market is expected to hit $1.1 billion by 2014 (Semiconductor Today, 2009) and the green laser market is expected to reach $500 million by 2016, representing more than 45 million devices (Semiconductor Today, 2010). For applications such as this where device form-factor is critical, direct emission diode lasers are more attractive than devices based on second harmonic generation (SHG). III-nitride LDs are the most likely candidates to address the need for blue and green direct emission diodes in next-generation projection systems. In Section 6.8, recent progress on III-nitride green LDs is discussed.

6.3 Introduction to properties of III-nitrides

III-nitrides most commonly form in the wurtzite crystal structure, which is depicted in Fig. 6.1 for the specific case of GaN. The Bravais lattice of the wurtzite structure is hexagonal and the axis perpendicular to the hexagonal layers is typically labeled the *c*-axis ([0001] direction). The structure for GaN, for example, can be envisioned as two interlaced hexagonal-close-packed (HCP) lattices, one consisting of Ga atoms and one consisting of N atoms, offset along the c-axis by the parameter u. The result is a sequence of alternating hexagonal layers consisting entirely of one type of atom. The space group for the wurtzite structure is $C_{\mathbf{6}v}^{\mathbf{4}}\left(P\mathbf{6}_{\mathbf{2}}mc\right)$ and bonding to nearest neighbors is tetrahedral and mixed covalent/ionic in nature. The vectors $\vec{a}_{\mathbf{1}}$, $\vec{a}_{\mathbf{2}}$, and $\vec{c}$ define the primitive cell, which contains Ga atoms at (0,0,0) and (2/3, 1/3, 1/2) and N atoms at (0,0,u) and (2/3, 1/3, 1/2 + u). The values

Table 6.1 Values for the lattice constants, *a* and *c*, and the offset parameter, *u*, for AlN, GaN, and InN

	AlN	GaN	InN
a	3.111 Å	3.189 Å	3.544 Å
c	4.978 Å	5.185 Å	5.718 Å
u	0.382	0.377	0.379

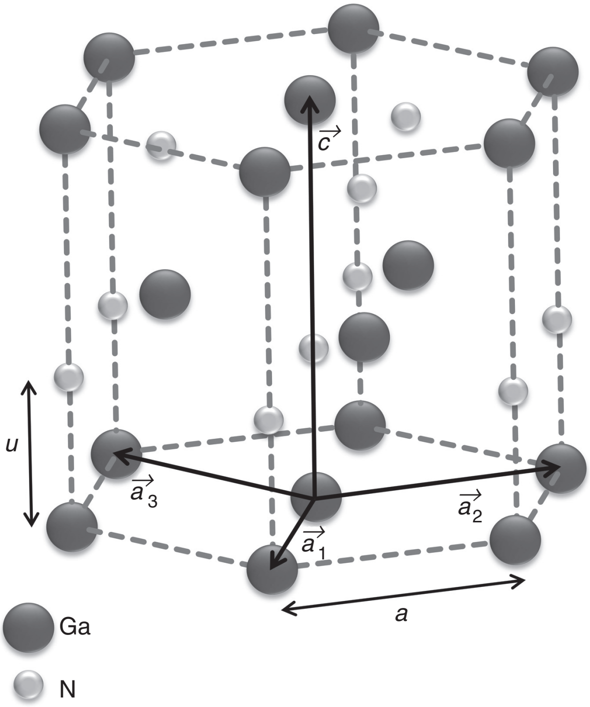

6.1 GaN crystal structure showing the primitive vectors $\vec{a}_1$, $\vec{a}_2$, $\vec{a}_3$, and $\vec{c}$, the offset parameter *u*, and the lattice constants *a* and *c*.

for the lattice constants, *a* and *c*, and the offset parameter, *u*, are provided in Table 6.1 for AlN, GaN, and InN.

6.3.1 Nonpolar and semipolar orientations

Traditionally, III-nitride heterostructures are grown on the basal *c*-plane (0001) of the wurtzite crystal, which is depicted in Fig. 6.2a. This convention

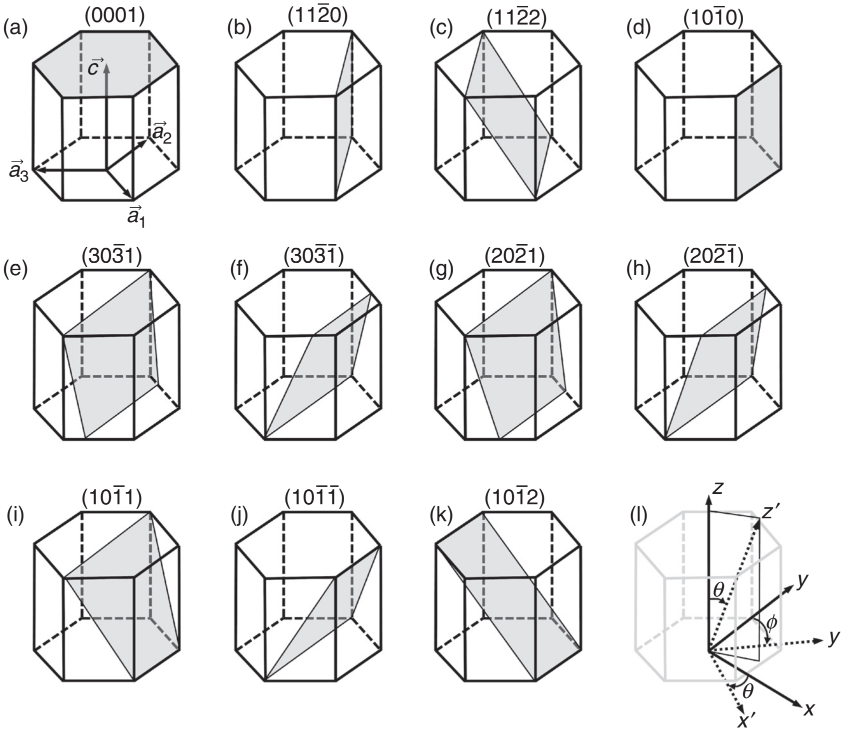
(a)
(0001)
$\vec{c}$
$\vec{a}_2$
$\vec{a}_3$
$\vec{a}_1$
(b)
(11$\bar{2}$0)
(c)
(11$\bar{2}$2)
(d)
(10$\bar{1}$0)
(e)
(30$\bar{3}$1)
(f)
(30$\bar{3}\bar{1}$)
(g)
(20$\bar{2}$1)
(h)
(20$\bar{2}\bar{1}$)
(i)
(10$\bar{1}$1)
(j)
(10$\bar{1}\bar{1}$)
(k)
(10$\bar{1}$2)
(l)
z
z'
y
θ
ϕ
y'
θ
x
x'

6.2 Various polar, nonpolar, and semipolar orientations, along with the coordinate systems used throughout this chapter.

is mainly due to the wide availability of *c*-plane sapphire substrates and the development of low-temperature buffer layers that provide relatively high-quality GaN templates. Consequently, the earliest high-brightness III-nitride light-emitting diodes (LED) and LDs were demonstrated on *c*-plane sapphire substrates (Amano *et al.*, 1989; Nakamura *et al.*, 1995, 1996b). However, by 2000 there was a growing realization that the elimination of internal electric fields associated with polarization discontinuities on the polar *c*-plane could yield devices with higher optical efficiencies (Waltereit *et al.*, 2000). As a result, significant attention turned toward the so-called *nonpolar* and *semipolar* orientations (see, e.g., Speck and Chichibu (2009) and related articles). Figure 6.2b through 6.2k illustrate various nonpolar and semipolar orientations, along with their (*hkil*) Miller indices. Planes perpendicular to the *c*-plane, such as the *a*-plane and *m*-plane, shown in Fig. 6.2b and 6.2d, respectively, intersect an equal number of Ga and N atoms and are nonpolar planes. The remaining planes in Fig. 6.2 that are inclined between the *c*-plane and a nonpolar plane are semipolar planes. Semipolar planes are characterized by nonzero *i* and *l* indices.

Table 6.2 Various crystal planes and the associated values of ϕ and θ

Orientation	ϕ (°)	θ (°)
(0001)	0	0
$(11\bar{2}0)$	–30	90
$(11\bar{2}2)$	–30	58
$(10\bar{1}0)$	0	90
$(30\bar{3}1)$	0	80
$(30\bar{3}\bar{1})$	0	100
$(20\bar{2}1)$	0	75
$(20\bar{2}\bar{1})$	0	105
$(10\bar{1}1)$	0	62
$(10\bar{1}\bar{1})$	0	118
$(10\bar{1}2)$	0	43

The coordinate systems used throughout this chapter are illustrated in Fig. 6.2l. The directions x, y, and z correspond to the $[10\bar{1}0]$, $[\bar{1}2\bar{1}0]$, and [0001] directions, respectively. Note that x points along the *m*-direction and y points along $\vec{a}_{\mathbf{2}}$. Therefore, rotation around the y-axis ($\phi = 0°$) by the angle θ produces the family of planes that includes nonpolar $(10\bar{1}0)$ (*m*-plane), semipolar $(10\bar{1}1)$, and semipolar $(20\bar{2}1)$, while rotation by the angle θ with $\phi = 30°$ produces the family of planes that includes nonpolar $(11\bar{2}0)$ (*a*-plane) and semipolar $(11\bar{2}2)$. Primed coordinates x′, y′, and z′ are used to describe nonpolar and semipolar planes in the rotated system, where x′ and y′ lie within the plane of the quantum wells and z′ points along the growth direction. Table 6.2 lists various crystal planes and the associated values of ϕ and θ.

6.3.2 Band gaps and lattice constants

Figure 6.3 shows a plot of energy gap *vs* in-plane lattice constant for the wurtzite III-nitride materials system. The binary compounds have room-temperature band gaps ranging from 0.61 eV (InN) to 3.44 eV (GaN) to 6.00 eV (AlN). The binary band gaps and lattice constants, and the ternary bowing parameters are taken from Vurgaftman and Meyer (2007). The triangular area bounded by the binary compounds represents $Al_yIn_xGa_{1-x-y}N$ quaternary alloys and the vertical dashed line represents quaternary and ternary alloys that are lattice matched to GaN. In general, the workhorse alloys for

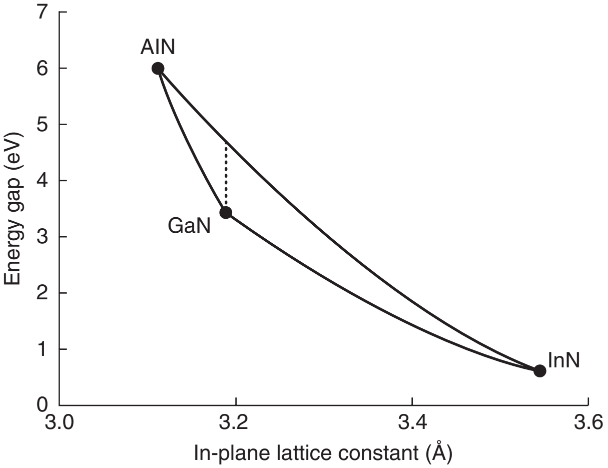

6.3 Energy gap *vs* in-plane lattice constant for the wurtzite III-nitride materials system. The triangular area bounded by the binary compounds represents $Al_yIn_xGa_{1-x-y}N$ quaternary alloys and the vertical dotted line represents quaternary and ternary alloys that are lattice matched to GaN.

optical devices, $In_xGa_{1-x}N$ and $Al_yGa_{1-y}N$, are not lattice matched to GaN. For example, an $In_xGa_{1-x}N$ film with $x = 0.25$ has a lattice mismatch with GaN of approximately 3%. The magnitude of the lattice mismatch also increases as the indium mole fraction increases, which complicates the growth of longer wavelength emitters.

LEDs constitute the majority of commercial III-nitride devices. They are typically grown on foreign substrates, such as sapphire (Al_2O_3) or SiC, because native GaN substrates are relatively expensive and less readily available. The lattice mismatches for GaN films grown on sapphire and SiC are approximately 16% and 4%, respectively. As a result, LEDs grown on sapphire or SiC typically contain a high density (10^8–10^9 cm^{-2}) of threading dislocations (TDs) (several orders of magnitude higher than that of AlInGaP or InGaAs devices). Despite this, compositional fluctuation issues associated with InGaN are postulated to be responsible for the relative insensitivity of III-nitride LEDs to dislocations (Chichibu *et al.*, 2009), and devices grown on sapphire have achieved remarkable wall-plug efficiencies (>80%) (Narukawa *et al.*, 2010) and operating lifetimes (~50 000 h). Nevertheless, III-nitride LDs operate at significantly higher current densities than LEDs, and epitaxial layers with substantially reduced dislocation densities are required to achieve long lifetimes and high yields. This restriction initially led to the development of epitaxial lateral overgrowth (ELO) techniques (Kapolnek *et al.*, 1997; Usui *et al.*, 1997; Zheleva *et al.*, 1997; Tomiya *et al.*,

2004) and provided motivation for the development of free-standing GaN substrates (Motoki *et al.*, 2001; Fujito *et al.*, 2008; Paskova and Evans, 2009; Dwilinski *et al.*, 2011).

6.3.3 Polarization and internal electric fields

Due to the polar nature of the Ga-N bond and the lack of inversion symmetry in the wurtzite crystal structure, III-nitrides are characterized by spontaneous and piezoelectric polarization (Bernardini *et al.*, 1997; Fiorentini *et al.*, 1999). These polarizations generate internal electric fields in III-nitride materials that significantly impact device performance. The majority of the discussion here will focus on polarization effects in $In_xGa_{1-x}N$ films since III-nitride LDs typically employ quantum wells composed of $In_xGa_{1-x}N$. For a further review of polarization effects in III-nitride heterostructures see Yu (2003). Spontaneous polarization is an intrinsic material property related to the nature of the bonds and is present in lattices under equilibrium. It arises primarily from bonding asymmetry and requires a deviation in the c/a ratio from that of an ideal HCP structure. On the other hand, piezoelectric polarization only exists in pseudomorphically-grown strained layers (e.g., InGaN grown on GaN) and is the result of mechanical stress. III-nitride films with higher alloy compositions experience increased strain and, as a result, increased piezoelectric polarization. This consequence plays an important role in the design and realization of green LDs, which require quantum wells with In mole fractions of approximately 30%. Figure 6.4a shows the directions of spontaneous and piezoelectric polarization for GaN, $In_xGa_{1-x}N$, and $Al_yGa_{1-y}N$ films on GaN substrates. For all configurations the spontaneous polarization always points from the cation (Ga) to the anion (N) parallel to the $[000\bar{1}]$ direction. On the other hand, the direction of the piezoelectric polarization depends upon the nature of the strain, pointing in opposite directions for compressive and tensile strained layers. The total polarization in a given layer is the sum of the spontaneous and piezoelectric polarizations. The spontaneous polarization as a function of In composition for a *c*-plane $In_xGa_{1-x}N$ film can be calculated using Vegard's Law (Fiorentini *et al.*, 1999):

$$P_{\text{sp}}\left(\text{In}_x\text{Ga}_{1-x}\text{N}\right) = xP_{\text{sp}}\left(\text{InN}\right) + \left(1-x\right)P_{\text{sp}}\left(\text{GaN}\right) \qquad [6.1]$$

where P_{sp} (InN) and P_{sp}(GaN) are the spontaneous polarizations for the constituent binary alloys, InN and GaN, respectively. These values have been theoretically calculated and are listed in Table 6.3. The piezoelectric polarization as a function of In composition for a *c*-plane $In_xGa_{1-x}N$ film

Table 6.3 Spontaneous polarizations (P_{sp}), piezoelectric coefficients (e_{31}, e_{33}), and elastic coefficients (C_{13}, C_{33}) for GaN, InN, and AlN

Material	P_{sp} (C/m^2)	E_{31} (C/m^2)	e_{33} (C/m^2)	C_{13} (GPa)	C_{33} (GPa)	$(e_{31} - e_{33}(C_{13}/C_{33}))$
GaN	–0.029	–0.49	0.73	103	405	–0.68
InN	–0.032	–0.49	0.73	92	224	–0.79
AlN	–0.081	–0.58	1.55	108	373	–1.03

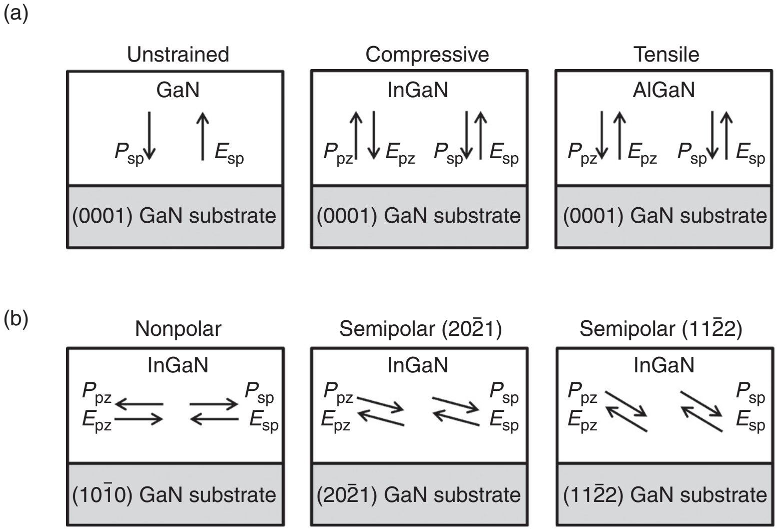
(a)
Unstrained
Compressive
Tensile
GaN
InGaN
AlGaN
P_{sp}
E_{sp}
P_{pz}
E_{pz}
(0001) GaN substrate
(b)
Nonpolar
Semipolar (20$\bar{2}$1)
Semipolar (11$\bar{2}$2)
(10$\bar{1}$0) GaN substrate
(20$\bar{2}$1) GaN substrate
(11$\bar{2}$2) GaN substrate

6.4 (a) Polarization and electric field directions for unstrained, compressively strained, and tensiley strained films on Ga-face *c*-plane GaN substrates. (b) Polarization and electric field directions for nonpolar $(10\bar{1}0)$, semipolar $(20\bar{2}1)$, and semipolar $(11\bar{2}2)$ InGaN films on GaN substrates. P_{sp} always points toward the $[000\bar{1}]$ direction.

pseudomorphically grown on a GaN substrate/template can be calculated by (Yu, 2003):

$$P_{pz}\left(\mathrm{In}_x\mathrm{Ga}_{1-x}\mathrm{N}\right) = 2\left(\frac{a_{\mathrm{GaN}} - a_{\mathrm{InGaN}}}{a_{\mathrm{InGaN}}}\right)\left(e_{31} - e_{33}\frac{C_{13}}{C_{33}}\right) \qquad [6.2]$$

where a_{GaN} and a_{InGaN} are the in-plane lattice constants of the GaN substrate/template and the $\mathrm{In}_x\mathrm{Ga}_{1-x}\mathrm{N}$ film, respectively, e_{31} and e_{33} are the piezoelectric coefficients for the $\mathrm{In}_x\mathrm{Ga}_{1-x}\mathrm{N}$ film, and C_{13} and C_{33} are the elastic coefficients for the $\mathrm{In}_x\mathrm{Ga}_{1-x}\mathrm{N}$ film, all of which can be calculated from the constituent binary values (see Table 6.3) using Vegard's Law. In III-nitride heterostructures, discontinuities between the total polarization in adjacent layers give rise to sheet charges at the heterojunction interfaces via the relation:

$$\nabla \cdot P = \nabla \cdot \left(P_{sp} + P_{pz}\right) = -\rho_{pol} \Rightarrow \left(P_{\mathrm{sp}} + P_{\mathrm{pz}}\right)_{\mathrm{layer\,1}} - \left(P_{\mathrm{sp}} + P_{\mathrm{pz}}\right)_{\mathrm{layer\,2}} = \sigma_{\mathrm{pol}} \qquad [6.3]$$

where P_{sp} and P_{pz} are the total spontaneous and piezoelectric polarizations in each layer, ρ_{pol} is the volume charge density, and σ_{pol} is the sheet charge density at the heterojunction interface. For nonpolar and semipolar orientations, Equations [6.1], [6.2], and consequently [6.3], must be modified by the appropriate coordinate transformation (Romanov *et al.*, 2006). Several groups have performed calculations of the total polarization discontinuity parallel to the growth direction between GaN and strained $\mathrm{In}_x\mathrm{Ga}_{1-x}\mathrm{N}$ layers of arbitrary crystal orientations (Takeuchi *et al.*, 2000; Romanov *et al.*, 2006; Wei *et al.*, 2010). Figure 6.5 shows the result of this calculation for various In compositions, where we have followed the approach used by Romanov *et al.* (2006). Also indicated on the plot are the locations of several common nonpolar and semipolar planes, and the conventional Ga-face and N-face *c*-planes. The total polarization discontinuity is maximum for *c*-plane (0001) films, crosses zero around 45°, switches polarity, and again becomes zero for the case of nonpolar $(10\bar{1}0)$. For angles beyond 90°, the total polarization discontinuity follows

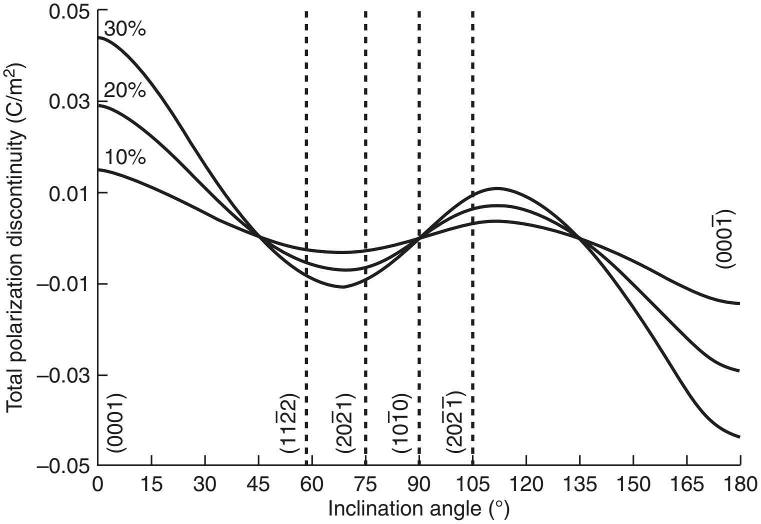

6.5 Total polarization discontinuity along the growth direction between GaN and strained $\mathrm{In}_x\mathrm{Ga}_{1-x}\mathrm{N}$ *vs* inclination angle for indium compositions of 10%, 20%, and 30%. Also indicated are the angle locations of several common polar, nonpolar, and semipolar orientations.

a similar trend with opposite sign and direction. Figure 6.5 demonstrates that specific orientations may be selected to reduce or eliminate polarization in these heterostructures. We note that there is some debate regarding the existence or exact location of the polarization cross-over in Fig. 6.5, which strongly depends on the sign of the piezoelectric tensor component e_{15} (Feneberg and Thonke, 2007; Feneberg *et al.*, 2010). However, more recent experiments using electro-reflectance on semipolar $\mathrm{In}_x\mathrm{Ga}_{1-x}\mathrm{N}$ quantum wells have confirmed the cross-over in polarization, determining that it occurs somewhere below an angle of 58° (Shen *et al.*, 2009; Funato *et al.*, 2010).

The interface sheet charges produced by the polarization discontinuities in III-nitride heterostructures (see Equation [6.3]) induce internal electric fields that are on the order of MV/cm. For *c*-plane (0001) films the internal electric fields are entirely parallel to the growth direction. Conversely, on nonpolar orientations the internal electric fields are entirely perpendicular to the growth direction. On semipolar orientations the electric fields are directed at an angle between 0° and 90° or 90° and 180° with respect to the growth direction. Figure 6.4a illustrates the internal electric field directions for *c*-plane GaN, $\mathrm{In}_x\mathrm{Ga}_{1-x}\mathrm{N}$, and $\mathrm{Al}_y\mathrm{Ga}_{1-y}\mathrm{N}$ films on GaN substrates, while Fig. 6.4b shows the directions for nonpolar $(10\bar{1}0)$, semipolar $(20\bar{2}1)$, and semipolar $(11\bar{2}2)$ $\mathrm{In}_x\mathrm{Ga}_{1-x}\mathrm{N}$ films. We note that due to the relatively small difference in spontaneous polarization between GaN and InN, polarization effects in $\mathrm{In}_x\mathrm{Ga}_{1-x}\mathrm{N}$ are dominated by the piezoelectric component. For $\mathrm{Al}_y\mathrm{Ga}_{1-y}\mathrm{N}$ films, both types of polarization must be accounted for to obtain a clear picture. For an $\mathrm{In}_x\mathrm{Ga}_{1-x}\mathrm{N}$ multiple quantum well active region with GaN barriers, the electric fields in the quantum wells and barriers along the growth direction can be estimated from the following expressions (Butte and Grandjean, 2008):

$$E_{\mathrm{QW}} = L_B \frac{\left(P_{\mathrm{sp},B} - P_{\mathrm{sp,QW}}\right)}{\left(L_B\varepsilon_{\mathrm{QW}} + L_{\mathrm{QW}}\varepsilon_B\right)} - L_B \frac{P_{\mathrm{pz,QW}}}{\left(L_B\varepsilon_{\mathrm{QW}} + L_{\mathrm{QW}}\varepsilon_B\right)} \qquad [6.4]$$

$$E_B = -E_{\mathrm{QW}} \frac{L_{\mathrm{QW}}}{L_B}$$

where the subscripts QW and *B* denote the quantum well and barrier, respectively, and *L* and *ε* are the layer thickness and static dielectric constant, respectively.

6.3.4 Energy band diagrams

The consequences of internal electric fields are easily illustrated by examining a simple heterostructure in the form of an InGaN quantum well. Figure 6.6a shows the band diagram and corresponding ground-state wavefunctions

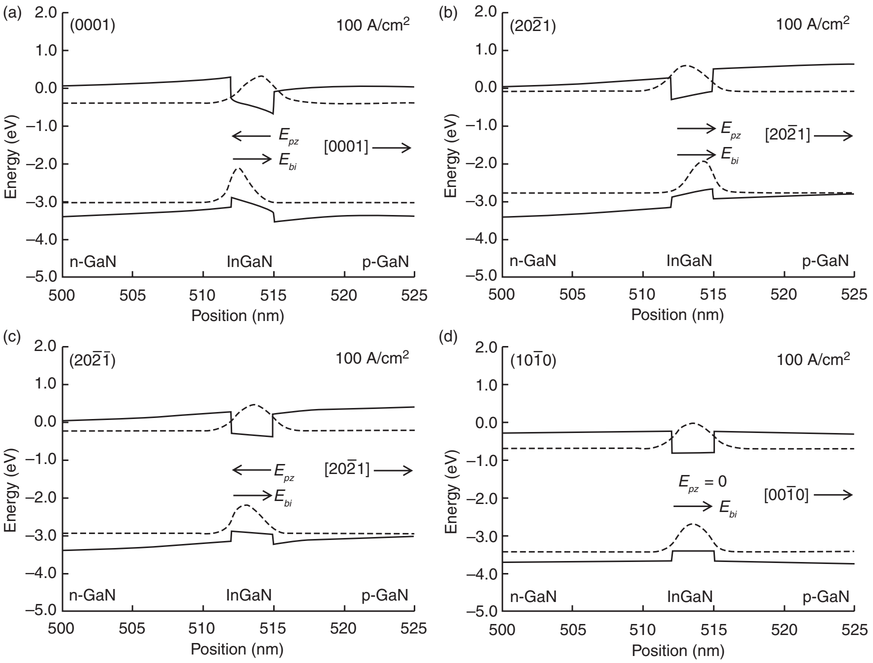

6.6 Energy band diagrams and corresponding ground-state wavefunctions for 3 nm thick $In_{0.23}Ga_{0.77}N$ quantum wells clad by GaN under low bias (100 A/cm²) on (a) (0001), (b) $(20\bar{2}1)$, (c) $(20\bar{2}\bar{1})$, and (d) $(10\bar{1}0)$ GaN. Also shown are the directions of the piezoelectric and built-in electric fields in the quantum wells.

for a 3 nm thick $In_{0.23}Ga_{0.77}N$ quantum well clad by GaN on *c*-plane GaN under low bias (100 A/cm²). The discontinuity in piezoelectric polarization between the $In_{0.23}Ga_{0.77}N$ quantum well and GaN cladding causes an electric field in the quantum well pointing in the $[000\bar{1}]$ direction, which is opposite to that of the built-in electric field. The energy bands are accordingly distorted and a spatial separation between the electron and hole wavefunctions results. This phenomenon is known as the quantum-confined Stark effect (QCSE) (Chichibu *et al.*, 1996; Takeuchi *et al.*, 1997). Although some Coulomb screening of the electric field occurs at typical LD injection levels (e.g., 5 kA/cm²), the electron-hole overlap integral on *c*-plane remains in the range of 0.3–0.5 for quantum well thicknesses between 2 and 4 nm (Strauss *et al.*, 2011). The relatively poor overlap integral reduces the strength of the transition matrix element, lowers the optical efficiency of the quantum well, and limits the available optical gain. Spatial separation of the wavefunctions increases with quantum well thickness and therefore *c*-plane quantum wells are typically only 2–3 nm thick. Additionally, due to the distortion of the energy bands from polarization-related sheet charges, the photoluminescence (PL) emission wavelength of a *c*-plane quantum well under zero bias is red-shifted compared to a quantum well with no polarization effects. This red shift increases with quantum well thickness and can be utilized to achieve a given emission wavelength (e.g., 520 nm) with a lower In content than a quantum well with no polarization effects (Strauss *et al.*, 2011). However, with increasing bias, the energy bands flatten somewhat and the emission wavelength of the quantum well blue shifts as the internal electric fields are screened by the injection of free carriers. For *c*-plane LDs with high In contents, the blue shift between spontaneous emission and lasing can be quite substantial (>30 nm) and potentially erases any benefits from the originally red-shifted emission. A design trade off emerges for *c*-plane quantum wells: thicker wells require less In to achieve a given emission wavelength but suffer from a lower electron-hole overlap integral, while thinner wells have an improved electron–hole overlap integral but require more In to achieve a given emission wavelength.

6.3.5 Motivation for nonpolar and semipolar orientations

An alternative that provides considerable design flexibility is to grow LDs on nonpolar or semipolar orientations. Nonpolar orientations are completely free from polarization-related electric fields, and semipolar orientations have significantly reduced fields. Figure 6.6b and 6.6c show the band diagrams and corresponding ground-state wavefunctions for a 3 nm thick $In_{0.23}Ga_{0.77}N$ quantum well clad by GaN on semipolar $(20\bar{2}1)$ GaN and semipolar $(20\bar{2}\bar{1})$ GaN, respectively. For these orientations the polarization-related electric field is reduced to approximately 20% of that in a *c*-plane quantum well. Additionally, the polarization-related electric fields in the $(20\bar{2}1)$ and $(20\bar{2}\bar{1})$ quantum wells are parallel and antiparallel to the built-in electric field, respectively. This suggests that, for a given indium content, a particular semipolar orientation may be chosen that results in the cancellation of the built-in electric field and the polarization-related electric field. Indeed, for blue emission wavelengths the $(20\bar{2}\bar{1})$ orientation results in such a condition and nearly flat-banded quantum wells at low biases. For the case of nonpolar $(10\bar{1}0)$ there is no polarization-related electric field component along the growth direction and the wavefunction overlap is close to unity. This situation is depicted in Fig. 6.6d.

With the constraints from polarization-related electric fields lifted, a relatively free choice of quantum well width is allowed on nonpolar and semipolar orientations. Early work demonstrated decreased radiative lifetimes from nonpolar $(10\bar{1}0)$ quantum wells compared to *c*-plane quantum wells and the difference was attributed to a higher electron–hole overlap integral in the nonpolar quantum wells (Waltereit *et al.*, 2000). Theoretical calculations have also predicted a significantly enhanced transition matrix element, largely due to the increased *e–h* overlap integral, for quantum wells on nonpolar and semipolar orientations (Park *et al.*, 2008). Consequently, quantum wells on these orientations should have higher radiative efficiencies than those on *c*-plane. Furthermore, a multitude of additional unique characteristics such as polarized emission, anisotropic gain, and reduced effective hole mass result. These differences from *c*-plane structures provide significant motivation to thoroughly explore optical devices on nonpolar and semipolar orientations.

6.4 Optical properties of nonpolar and semipolar III-nitrides

Compared to *c*-plane InGaN quantum wells, higher optical gain has been theoretically predicted for nonpolar and semipolar quantum wells. A complete treatment of optical gain in a quantum well requires knowledge of the band structure, the transition matrix elements, and the quasi-Fermi level positions for a given injection level. These parameters are typically determined using a 6 × 6 $k \cdot p$-model and by solving Schrodinger's equation and Poisson's equation self-consistently (Scheibenzuber *et al.*, 2009). However, to simply illustrate the dependence of the optical gain on crystal orientation in III-nitrides, it is instructive to examine the various terms in the expression for gain. The expression for gain for states separated by energy $E_{21} = E_2 - E_1$ is given by:

$$g \propto \left|M_T\right|^2 \cdot \rho_r\left(E_{21}\right) \cdot \left(f_c - f_v\right) \qquad [6.5]$$

where $\left|M_T\right|^2$ is the square of the transition matrix element, $\rho_r\left(E_{21}\right)$ is the reduced density of states for a transition between E_2 and E_1, and f_c and f_v are the Fermi occupation probabilities at energies E_2 and E_1, respectively (Coldren and Corzine, 1995). Each of the components in the gain expression is significantly modified for nonpolar and semipolar $In_xGa_{1-x}N$ quantum wells. In the following sections, we will examine the components of the gain expression in more detail and discuss their effects on the gain and threshold characteristics of nonpolar and semipolar LDs.

6.4.1 Transition matrix element, band structure, and polarized light emission

Nonpolar and semipolar quantum wells offer the potential to increase the magnitude of the transition matrix element, which enters directly into the expression for optical gain. The transition matrix element determines the strength of the optical transitions and introduces to the gain dependencies on wavefunction overlap and polarization. The transition matrix element is given by:

$$\left|M_T\right|^2 = |< u_c \,|\, \hat{e} \cdot p \,|\, u_v >|^2 |< F_2 \,|\, F_1 >|^2 \qquad [6.6]$$

where u_c and u_v are the basis states (Bloch functions) for the conduction and valence bands, respectively, $\hat{e}$ a unit polarization vector indicating the direction of the electric field, p is the momentum operator, and F_2 and F_1 are the wavefunction envelope functions for the conduction and valence bands, respectively (Coldren and Corzine, 1995). The square of the wavefunction overlap integral, $|< F_2 \,|\, F_1 >|^2$, is strongly influenced by the degree of the QCSE and depends upon the width and composition of the quantum well. Early theoretical work by Takeuchi *et al.* yielded the wavefunction overlap versus crystal orientation for a 3 nm $In_{0.10}Ga_{0.90}N$ quantum well (Takeuchi *et al.*, 2000). Figure 6.7 shows that the square of the wavefunction overlap integral more than doubles when going from the polar (0001) orientation to the nonpolar $(10\bar{1}0)$ orientation. This increases the overall transition matrix element for nonpolar and semipolar quantum wells, which leads to increased optical gain. The difference between polar and nonpolar is even more pronounced for thicker quantum wells and higher indium compositions due to the more pronounced QCSE. We note that the angle of maximum overlap for the semipolar planes in Fig. 6.7 depends upon the zero-crossing of the total polarization discontinuity in Fig. 6.5, which

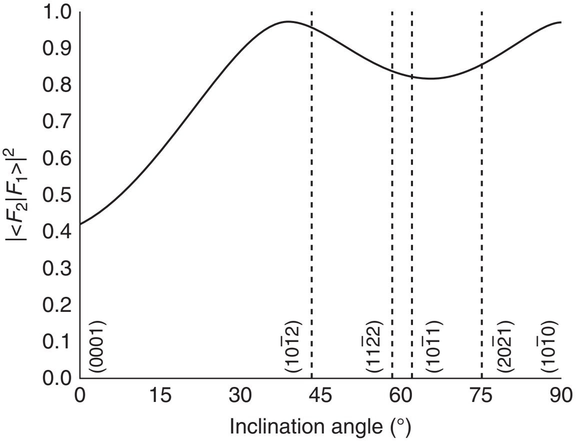

6.7 Square of the electron and hole wavefunction overlap *vs* inclination angle for a 3 nm $In_{0.10}Ga_{0.90}N$ quantum well. Also indicated are the angle locations of several common polar, nonpolar, and semipolar orientations. Source: After Takeuchi *et al.* (2000).

depends upon the values of the piezoelectric and elastic constants used in the calculations. Zero-crossings of 39° (Takeuchi *et al.*, 2000), 42° (Wei *et al.*, 2010), and 45° (Romanov *et al.*, 2006) have been reported.

The remaining term in the transition matrix element, $\left|\langle u_c | \hat{e} \cdot p | u_v \rangle\right|^2$, contains the polarization dependence of the optical transitions and depends upon the specific symmetries of the conduction and valence band basis states. For *c*-plane wurtzite GaN, the conduction band is primarily composed of s-like states, while the valence band has the character of p-orbitals and includes heavy-hole (HH), light-hole (LH), and split-off (CH) bands. Around the Γ-point, the top two valence bands (HH and LH) are composed of $|X \pm iY\rangle$ basis states and the split-off band is composed of $|Z\rangle$ basis states. Since the wurtzite crystal structure possesses sixfold azimuthal symmetry around the *c*-axis, biaxial compressive strain on *c*-plane films has little consequence on the character of the valence bands. Thus, even under compressive strain, the HH and LH bands remain composed of $|X \pm iY\rangle$ valence band basis states. The emission from a compressively strained InGaN quantum well on *c*-plane is therefore isotropic and unpolarized in the *x*-*y* plane. Figure 6.8a shows the valence band dispersion curves for a 3 nm $In_{0.20}Ga_{0.80}N$ quantum well on *c*-plane GaN in the *x*-*y* plane (Scheibenzuber *et al.*, 2009). The valence band subbands in the quantum well are labeled A1, B1, A2, and B2, and are the quantum-confined bands corresponding to the bulk valence bands A and B. Any inclination of the crystal with respect to the *c*-axis breaks the in-plane symmetry and results in an anisotropic strain tensor. InGaN quantum wells on nonpolar

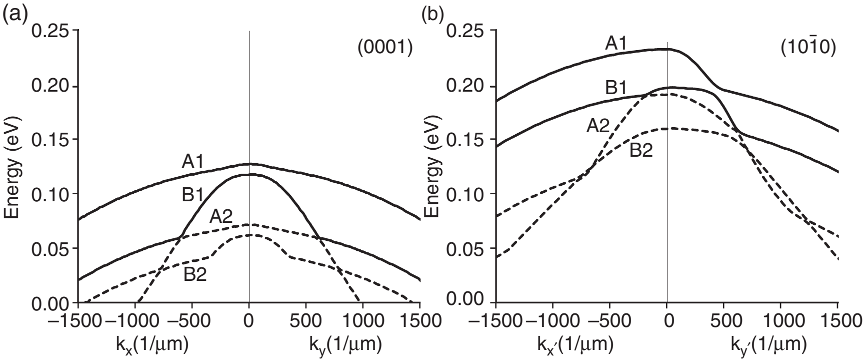

6.8 Valence band dispersion curves for a 3 nm $In_{0.20}Ga_{0.80}N$ quantum well on (a) (0001) (*c*-plane) GaN in the *x*-*y* plane and (b) (10$\bar{1}$0) (nonpolar) GaN in the *x*′-*y*′ plane. The valence band subbands in the quantum well are labeled A1, B1, A2, and B2, and are the quantum-confined bands corresponding to the bulk valence bands A and B. Source: Adapted with permission from Scheibenzuber *et al.* (2009). Copyrighted by the American Physical Society.

and semipolar orientations experience unbalanced in-plane biaxial strain, which significantly modifies the band structure compared to *c*-plane. Figure 6.8b shows the valence band dispersion curves for a 3 nm $In_{0.20}Ga_{0.80}N$ quantum well on nonpolar GaN in the *x*′-*y*′ plane. Several differences from the *c*-plane dispersion curves are evident. The top two valence bands for the nonpolar quantum well are further separated in energy compared to the *c*-plane quantum well, which emphasizes emission from the topmost band under typical injection levels. Additionally, nonpolar and semipolar planes experience valence band mixing, with the *c*-plane basis states combining to form new valence band states. For the nonpolar $(10\bar{1}0)$ case, the topmost valence band (A1) becomes entirely composed of $|Y\rangle = |Y'\rangle$ states and the next lower valence band (B1) becomes entirely composed of $|Z\rangle = |X'\rangle$ states near the Γ-point. This results in fully y′-polarized emission from the topmost valence band and fully x′-polarized emission from the next lower valence band. Since emission from the highest energy band is most probable (due to the Fermi occupation probability), nonpolar quantum wells emit light that is strongly y′ polarized. For semipolar quantum wells, the valence band states become a partial mix of the original $|X + iY\rangle$, $|X - iY\rangle$, and $|Z\rangle$ bases, giving rise to varying degrees of polarization (Schade *et al.*, 2011; Scheibenzuber *et al.*, 2011). The separation of the top two valence bands, along with band-mixing effects, forms the basic mechanism for polarized light emission from nonpolar and semipolar strained quantum wells. The degree of in-plane polarization (i.e., anisotropy) is described by the polarization ratio, which is given by:

$$\rho = \frac{I'_y - I'_x}{I'_y + I'_x} \qquad [6.7]$$

where I'_y is the intensity of light polarized along the y′-direction and I'_x is the intensity of light polarized along the x′-direction. This metric is also directly related to the difference between the squares of the transition matrix elements for the y′-direction and the x′-direction. The polarization ratio for various orientations has been extensively studied (Ueda *et al.*, 2008; Kyono *et al.*, 2010; Brinkley *et al.*, 2011; Schade *et al.*, 2011; Zhao *et al.*, 2011). For *c*-plane InGaN quantum wells, the polarization ratio is essentially zero. In contrast, values greater than 0.9 have been reported for nonpolar quantum wells (Brinkley *et al.*, 2011). An increase in polarization ratio with increasing indium content has been predicted and observed for several planes (Kojima *et al.*, 2008; Zhao *et al.*, 2011), while the semipolar $(11\bar{2}2)$ plane shows a characteristic switch in the dominant polarization direction at an indium content of approximately 25% (Ueda *et al.*, 2008; Huang *et al.*, 2010; Scheibenzuber *et al.*, 2011). As a result of the optical polarization properties of nonpolar and semipolar III-nitrides, the optical

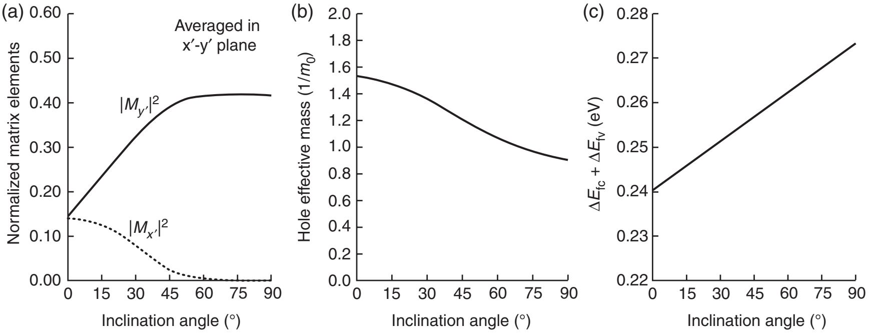

6.9 (a) Normalized matrix elements *vs* inclination angle for y'-polarized ($|M_{y'}|^2$) and x'-polarized ($|M_{x'}|^2$) light. (b) Average hole effective mass in the k_x'–k_y' plane *vs* inclination angle. (c) Separation of the quasi-Fermi levels from their equilibrium positions *vs* inclination angle. Data shown for a 3 nm $In_{0.15}Ga_{0.85}N$ quantum well with $N_{2D} = 20 \times 10^{12}$ cm^{-2}. Values are averaged over all states in the k_x'–k_y' plane. Source: After Park (2003) and Park *et al.* (2008).

gain is anisotropic within the plane of the quantum wells. Consequently, specific waveguide orientations will maximize the optical gain. For nonpolar and semipolar lasers, orientation of the ridge along the *c*-axis or the projection of the *c*-axis typically provides the highest gain.

The normalized matrix element describes the relative transition strengths for various polarizations and includes the effects of wavefunction overlap and polarization dependence. This parameter has been calculated for various crystal orientations for a 3 nm $In_{0.15}Ga_{0.85}N$ quantum well with a 2-D carrier density $N_{2D} = 20 \times 10^{12}$ cm^{-2} (Park, 2003; Park *et al.*, 2008). Figure 6.9a shows the dependence of transition strength on crystal angle for y′-polarized ($|M_{y'}|^2$) and x′-polarized ($|M_{x'}|^2$) light. A several-fold increase in the matrix element for y′-polarized light is observed as the crystal angle progresses from polar *c*-plane (0°) to nonpolar *m*-plane (90°). For x′-polarized light, a decrease is observed. The increase observed for y′-polarized light results from band-mixing effects (i.e., the topmost valence band becomes dominated by $|Y'\rangle$) and the increased wavefunction overlap. Note that the values shown in Fig. 6.9 for the normalized matrix element are averaged over all states in the $k_x' - k_y'$ plane due to the in-plane anisotropy for non-*c*-oriented crystals.

6.4.2 Density of states, gain and transparency

Further inspection of the nonpolar band structure in Fig. 6.8b reveals that the hole effective mass in the $k_x' - k_y'$ plane is anisotropic. In the k_y' direction, for the topmost (A1) subband, the effective mass is significantly reduced for a range of k_y' values. Semipolar orientations show similar modifications to the valence band structure and effective mass (Kojima *et al.*, 2010a). Figure 6.9b shows a calculation of the average hole effective mass in the $k_x' - k_y'$ plane versus crystal orientation for a 3 nm $In_{0.15}Ga_{0.85}N$ quantum well with $N_{2D} = 20 \times 10^{12}$ cm^{-2} (Park, 2003). Note that the average effective mass depends upon the carrier density due to the non-parabolic nature of the valence bands. For nonpolar and semipolar orientations, Fig. 6.9b reveals that the average effective mass is lower, mainly due to the lower effective mass in the k_y' direction. This translates to a smaller reduced density of states, which affects the quasi-Fermi level separation for a given carrier density. Figure 6.9c shows the separation of the quasi-Fermi levels versus crystal orientation for a 3 nm $In_{0.15}Ga_{0.85}N$ quantum well with $N_{2D} = 20 \times 10^{12}$ cm^{-2} (Park, 2003). The quasi-Fermi level separation $\Delta E_{fc} \left(\Delta E_{fv}\right)$ is defined as the energy difference between the quasi-Fermi level and the ground-state energy in the conduction (valence) band. The quasi-Fermi level separation increases as the angle of inclination increases. This allows for the transparency condition (i.e., $E_{fc} - E_{fv} = E_g$) to be more easily achieved on nonpolar and semipolar orientations. Recent experimental evidence suggests a lower transparency carrier density and current density for nonpolar *m*-plane lasers than polar *c*-plane lasers (Farrell *et al.*, 2011c; Melo *et al.*, 2012).

The cumulative result of the increased transition matrix element and larger quasi-Fermi level separation on nonpolar and semipolar orientations is increased optical gain. Figure 6.10 shows the *y*′-polarized peak optical gain versus crystal orientation for a 3 nm $In_{0.15}Ga_{0.85}N$ quantum well with $N_{2D} = 20 \times 10^{12}$ cm^{-2} (Park, 2003). In Fig. 6.10, the gain increases by a factor of more than two when rotating the crystal from *c*-plane to *m*-plane. Other groups have calculated an increase of up to a factor of ten (Scheibenzuber *et al.*, 2009). Note that due to the anisotropy in the transition matrix elements and band structure, the gain is also anisotropic within the quantum well plane (Kojima *et al.*, 2010b). For nonpolar *m*-plane, the optical gain for *x*′-polarized light is a factor of three to four lower than that for *y*′-polarized light.

Several groups have performed gain measurements on nonpolar and semipolar lasers (Sizov *et al.*, 2009; Rass *et al.*, 2011; Melo *et al.*, 2012). Sizov *et al.* (2009) employed the variable stripe length (VSL) method (Shaklee *et al.*, 1973) to verify the optical gain anisotropy on semipolar $(11\bar{2}2)$. The authors reported that the gain for light propagating along the $[1123]$ direction was approximately twice that of light propagating along the $[1\bar{1}00]$ direction. These measurements were extended by Rass *et al.* (2011) to include analysis of transverse electric (TE) and transverse magnetic (TM) modes and birefringence. Researchers at Kyoto University and Sumitomo Electric Industries (SEI) also measured the gain spectra of violet, blue, and blue-green *c*-plane LDs and green semipolar $(20\bar{2}1)$ LDs (Kim *et al.*, 2011)

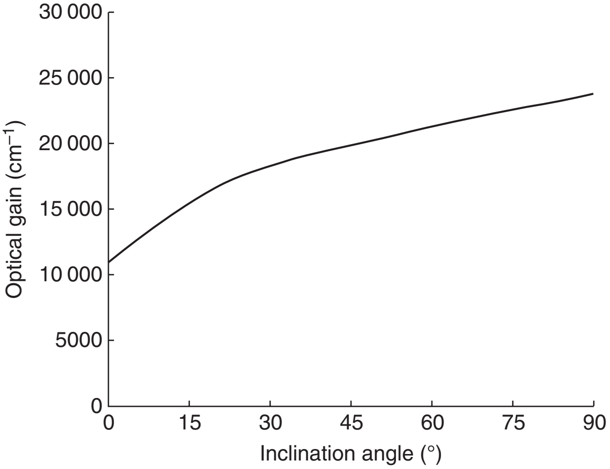

6.10 y'-polarized peak optical gain *vs* inclination angle for a 3 nm $In_{0.15}Ga_{0.85}N$ quantum well with $N_{2D} = 20 \times 10^{12}$ cm^{-2}. Source: After Park (2003).

using the Hakki-Paoli method (Hakki and Paoli, 1975). Gain saturation was observed for the *c*-plane devices emitting at 440 and 470 nm and for the semipolar $(20\bar{2}1)$ device emitting at 527 nm. Gain saturation was not observed for the *c*-plane device emitting at 404 nm. The degree of gain saturation observed for the true-green semipolar $(20\bar{2}1)$ device was similar to that of the blue–green *c*-plane device, suggesting that gain saturation effects may be reduced on some semipolar orientations. Gain saturation typically occurs for longer wavelength III-nitride LDs, suggesting the presence of gain suppression mechanisms such as potential fluctuations, Shockley-Read-Hall (SRH) recombination, Auger recombination, or current overflow. These mechanisms may not completely clamp at threshold and may reduce the injection efficiency. In contrast to *c*-plane LDs, SEI observed that inhomogeneous broadening is suppressed in $(20\bar{2}1)$ LDs, suggesting that it is not primarily responsible for gain saturation on this orientation.

While the reduced effective mass on nonpolar and semipolar orientations suggests that the transparency *carrier densities* should be lower on nonpolar and semipolar orientations, it is not *a priori* clear that lower transparency *current densities* will follow. To translate between transparency carrier density and transparency current density an empirical model of the following form is often employed:

$$\frac{J_{\text{tr}}}{qd} = \frac{N_{\text{tr}}}{\tau(N_{\text{tr}})} = \left(AN_{\text{tr}} + BN_{\text{tr}}^2 + CN_{\text{tr}}^3\right) \qquad [6.8]$$

where N_{tr} is the transparency carrier density, J_{tr} is the transparency current density, $\tau(N_{tr})$ is the transparency carrier lifetime, and A, B, and C are the SRH, bimolecular, and Auger recombination coefficients, respectively. Due to the higher wavefunction overlap in nonpolar and semipolar QWs, shorter carrier lifetimes have been experimentally observed (Waltereit *et al.*, 2000; Wunderer *et al.*, 2007; Funato and Kawakami, 2008) and a higher bimolecular recombination coefficient has been theoretically predicted (Park, 2003b) for nonpolar and semipolar orientations. Consequently, although N_{tr} is reduced due to band structure modifications, $\tau(N_{tr})$ is also reduced and the resulting direction of change in J_{tr} depends upon the ratio of the changes in N_{tr} and $\tau(N_{tr})$. A recent experimental comparison of J_{tr} for *c*-plane and *m*-plane violet and blue lasers using Hakki-Paoli gain measurements shows lower J_{tr} for the *m*-plane structures, suggesting that the reduced N_{tr} dominates over the reduced carrier lifetime (Melo *et al.*, 2012). The reduction in J_{tr} was more than a factor of two for the violet devices and approximately 20–40% for the blue devices. However, the carrier lifetime is a strong function of the carrier density and wavelength, and the band structure is a function of indium composition, suggesting that lower J_{tr} on nonpolar and semipolar orientations may not be universally true. If cavity losses are assumed to be equal between the various orientations, similar reasoning applies to the comparison of threshold current density.

An additional consequence of the smaller reduced density of states for nonpolar and semipolar quantum wells is that the differential gain $\mathrm{d}g/\mathrm{d}N$ should be increased. Although $\mathrm{d}g/\mathrm{d}N$ is not well documented for nonpolar or semipolar LDs, Melo *et al.* (2012) reported similar differential modal gains, $\mathrm{d}g/\mathrm{d}J$, for violet *c*-plane (13.5 cm/kA) and nonpolar (12.4 cm/kA) LDs. Although nonpolar LDs should have increased gain per carrier from the larger wavefunction overlap, the current density per carrier also increases by the same factor due to the reduced recombination lifetime, rendering the ratio $\mathrm{d}g/\mathrm{d}J$ unchanged to first order for nonpolar orientations. The authors reported slightly higher values of $\mathrm{d}g/\mathrm{d}J$ for blue nonpolar (8.1 cm/kA) than blue *c*-plane (6.9 cm/kA).

6.5 Substrates, crystal growth and materials issues

Early *c*-plane III-nitride lasers were fabricated on sapphire substrates using low-temperature buffer layers but suffered from poor operating lifetimes due to high TD densities (Nakamura *et al.*, 1996a, 1996b). ELO was subsequently utilized to reduce TD densities from 10^8–10^{10} cm^{-2} down to 10^6–10^7 cm^{-2}, and led to improved operating lifetimes (Usui *et al.*, 1997; Nakamura *et al.*, 1998; Tomiya *et al.*, 2004). Heteroepitaxy on foreign substrates was also initially utilized for growth of nonpolar and semipolar films (Craven *et al.*, 2002; Ng, 2002; Gardner *et al.*, 2005; Baker *et al.*, 2006). However, high densities of TDs and basal-plane stacking faults (BPSF) had a significant impact on device performance. Consequently, nonpolar and semipolar LEDs grown on foreign substrates typically exhibited output powers of less than 1 mW at 20 mA (Chakraborty *et al.*, 2004, 2005).

6.5.1 Free-standing GaN substrates

Current commercially available III-nitride LDs are grown on free-standing GaN substrates. Early free-standing *c*-plane substrates were grown on GaAs using an ELO technique (Motoki *et al.*, 2001). With this technique, after growth of a 500 μm thick GaN film by hydride vapor phase epitaxy (HVPE), the GaAs substrate is dissolved in aqua regia, leaving a free-standing GaN substrate with a TD density of approximately 10^5 cm^{-2}. This technique continues to be utilized to produce free-standing *c*-plane substrates. In 2006, research at Mitsubishi Chemical Corporation (MCC) and Furukawa Company Ltd (FCL) led to nonpolar and semipolar free-standing GaN substrates with low dislocation densities (~10^5–10^6 cm^{-2}). These substrates are produced by growing relatively thick (5–10 mm) layers of GaN via HVPE on 2-inch GaN substrates in the [0001] direction to create free-standing GaN pucks. By sawing vertically through the pucks, nonpolar *m*-plane and *a*-plane substrates can be produced, while sawing at an angle results in semipolar substrates (Fujito *et al.*, 2008, 2009). Figure 6.11 shows an illustration of the free-standing GaN puck and a sawed cross-section of a nonpolar *m*-plane substrate. The typical dimensions for substrates produced using this technique are approximately 5–10 mm × 20 mm. The performance of LEDs on free-standing nonpolar and semipolar GaN substrates was significantly enhanced compared to that on foreign substrates, with output powers of more than 20 mW achieved at 20 mA reported for nonpolar *m*-plane devices (Schmidt *et al.*, 2007a). The introduction of free-standing GaN substrates led to rapid device progress, and in February 2007

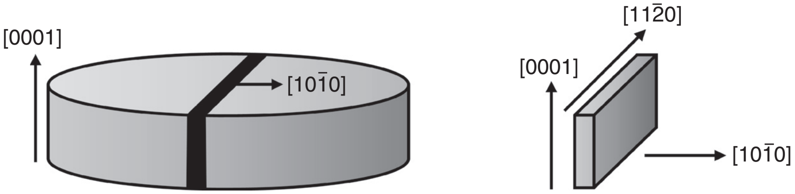

6.11 Illustration of a free-standing GaN puck (left) and a sawed cross-section of a nonpolar $(10\bar{1}0)$ *m*-plane substrate (right).

researchers from the University of California Santa Barbara (UCSB) and Rohm simultaneously demonstrated the first *m*-plane LDs (Okamoto *et al.*, 2007; Schmidt *et al.*, 2007b). Further development of both *c*-plane and nonpolar/semipolar free-standing GaN substrates continues and has intensified in recent years (Paskova and Evans, 2009; Dwilinski *et al.*, 2011). Ultimately, a bulk crystal growth technique (e.g., ammonothermal) is desired to achieve large-area, low-defect-density substrates (Avrutin *et al.*, 2010; Dwilinski *et al.*, 2011). In 2010, SEI announced the first large-scale production of 2″ nonpolar and semipolar GaN substrates (Semiconductor Today, 2010b). More recently, AMMONO from Poland has demonstrated 26 mm × 26 mm nonpolar GaN substrates grown by the ammonothermal method (Kucharski *et al.*, 2012).

6.5.2 Pyramidal hillocks and basal-plane stacking faults

Nonpolar and semipolar LDs are typically grown using MOCVD. While the growth conditions to achieve high-quality nonpolar and semipolar films on free-standing GaN substrates are remarkably similar to those required for *c*-plane, several issues arise that are unique to nonpolar and semipolar growth. For a comprehensive review of materials and crystal growth issues on nonpolar and semipolar orientations, see the article by Farrell *et al.* (2012). Initial nonpolar *m*-plane films on free-standing GaN were grown on nominally on-axis substrates and suffered from poor surface morphology that persisted over a wide range of growth conditions. These films were characterized by the presence of four-sided pyramidal hillocks, with faces inclined towards the $\pm[11\bar{2}0]$, [0001], and $[000\bar{1}]$ directions (Hirai *et al.*, 2007). Figure 6.12 illustrates the typical surface morphology of the four-sided pyramidal hillocks. The effect of substrate misorientation on surface morphology and LED performance was studied by Hirai *et al.* (2007) and Farrell *et al.* (2010a). Further studies on the effect of carrier gas were also performed (Farrell *et al.*, 2010c). The authors demonstrated that the formation of pyramidal hillocks can be suppressed by growing on substrates that are misoriented toward the $[000\bar{1}]$ direction by approximately 1°. Furthermore, growth of nonpolar *n*-GaN layers in N_2 carrier gas is preferable to growth in H_2 carrier gas (Farrell *et al.*, 2010c). The mechanism for the formation of pyramidal hillocks on nonpolar *m*-plane was later clarified, with spiral growth around screw-component TDs suggested as the cause (Farrell *et al.*, 2010a). The presence of pyramidal hillocks leads to variations in emission wavelength, impurity incorporation, and growth rate over the growth surface. Additionally, the rough surface morphology may introduce additional optical loss to the LD waveguide. It is therefore not surprising that pyramidal hillocks are expected to degrade LD performance. To clarify this, Lin

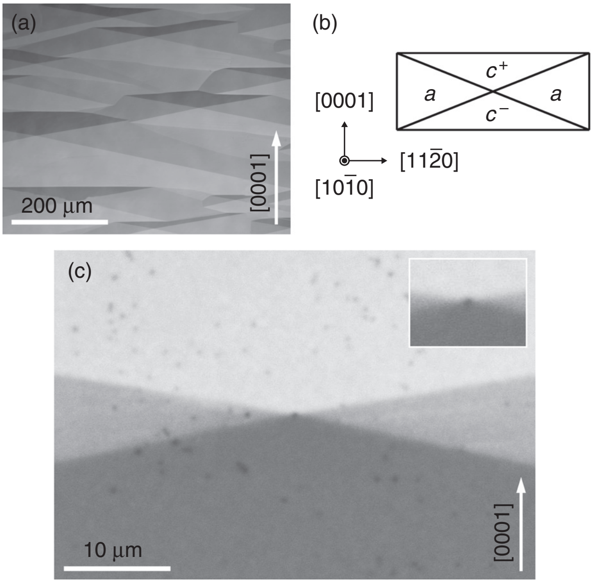

6.12 (a) Nomarski optical micrograph, (b) schematic, and (c) panchromatic cathodoluminescence image of the four-sided pyramidal hillocks that develop during on-axis *m*-plane GaN growth. Source: Reprinted with permission from Farrell *et al.* (2010a). Copyright 2010, American Institute of Physics.

et al. (2009b) performed a comparison of blue–green ridge LDs, with one set grown nominally on-axis and the other set grown with a misorientation of 1° toward the $[000\bar{1}]$ direction. The devices grown on the misoriented substrates showed smoother surface morphologies, lower threshold current densities, higher device-to-device uniformity, and increased yield.

BPSF formation has been observed for InGaN QWs on *m*-plane GaN (Wu *et al.*, 2010). The authors noted the formation of BPSFs with increasing indium content and QW thickness. They observed SFs for $In_{0.26}Ga_{0.74}N$ QWs with a thickness of 4 nm, but not for QWs with a thickness of 2.5 nm. SFs function as non-radiative carrier sinks and their presence is correlated with the degradation of *m*-plane emitters with increasing indium content and QW thickness (Lin *et al.*, 2009b). To date, BPSF formation has limited the operation of *m*-plane LDs to wavelengths below 500 nm.

6.5.3 Indium incorporation

An additional motivation for growing LDs on nonpolar and semipolar orientations is the potential to achieve longer wavelength emitters. The transition energy versus inclination angle for an InGaN QW depends upon the indium content, the band gap of InGaN, and the QCSE. Each of these properties is expected to vary with inclination angle. Due to the angular dependence of the strain energy in InGaN grown on GaN, differences in indium incorporation with inclination angle have been predicted and experimentally observed (Durnev *et al.*, 2010; Wernicke *et al.*, 2012; Zhao *et al.*, 2012). The differences in indium incorporation may result from the lower strain-induced repulsive interaction between indium atoms for specific orientations (Northrup, 2009). For example, semipolar $(11\bar{2}2)$ is predicted to have a higher indium incorporation rate than nonpolar $\left(10\bar{1}0\right)$. This is supported by the achievement of green and yellow emitters on semipolar $(11\bar{2}2)$ (Sato *et al.*, 2007, 2008), while nonpolar $(10\bar{1}0)$ is typically limited to wavelengths below 500 nm. The band gap of InGaN also varies with inclination angle due to strain effects, becoming larger for nonpolar and semipolar orientations (Durnev *et al.*, 2011). Finally, the energies of the quantum states in the QW depend upon the degree the QCSE, which is known to vary with inclination angle. The lower QCSE in nonpolar and semipolar orientations reduces the built-in red shift in emission typically observed in c-plane QWs. Consequently, InGaN QWs on these planes may not provide remarkably longer wavelength emission than those on *c*-plane despite their potential for higher indium incorporation. Growth kinetics and surface chemistry are also expected to affect indium incorporation, with surfaces with N-polar and Ga-polar character showing distinct differences in impurity incorporation (Cruz *et al.*, 2009). For example, higher indium incorporation has been reported for QWs grown on semipolar $(20\bar{2}\bar{1})$ than for QWs grown on semipolar $(20\bar{2}1)$ (Zhao *et al.*, 2012). Higher indium incorporation has also been reported for QWs grown on semipolar $(30\bar{3}\bar{1})$ than for QWs grown on semipolar $(30\bar{3}1)$ (Hsu *et al.*, 2011a; Zhao *et al.*, 2012).

6.5.4 Stress relaxation

As discussed above, strain effects can significantly influence the emission wavelengths of InGaN QWs. Moreover, managing strain in lattice-mismatched films is critical for proper structure design and required to achieve high-efficiency emitters. In conventional zincblende III-V materials, stress relaxation can occur in the two in-plane directions via misfit dislocation (MD) formation and glide on the energetically favorable (111) slip system. In wurtzite III-nitrides, the most energetically favorable slip system is the basal plane (*c*-plane). However, there is no resolved shear stress on the basal plane for *c*-plane, *m*-plane, or *a*-plane films, so MDs will typically not form on these orientations. Conversely, for strained layers grown on semipolar GaN, the basal plane is inclined with respect to the growth direction and stress relaxation can occur by MD glide on the (0001) plane (Tyagi *et al.*, 2009; Young *et al.*, 2010a; Hsu *et al.*, 2011b). One-dimensional

MD arrays form and stress relaxation occurs only along the direction of the projection of the *c*-axis. This typically occurs beyond some critical film thickness, which is often modeled by the Matthews-Blakeslee limit (Matthews and Blakeslee, 1974). For a complete discussion of stress relaxation on nonpolar and semipolar III-nitrides, see Farrell *et al.* (2012). The phenomenon of stress relaxation can be used to produce an intentionally relaxed InGaN template upon which QWs with reduced strain may be grown. This technique has been utilized to demonstrate the longest wavelength (444.9 nm) semipolar $(11\bar{2}2)$ LD to date (Hsu *et al.*, 2012). By using an intentionally stress relaxed structure, the flexibility of the design space for the LD waveguide is significantly increased. The device demonstrated by Hsu *et al.* also utilized AlGaN electron/hole blocking layers to isolate carriers from the MDs at the relaxed interfaces. This combination of techniques allowed the authors to increase the longest reported lasing wavelength on semipolar $(11\bar{2}2)$ by ~20 nm. Intentional stress relaxation may also offer advantages for shorter wavelength (i.e., ultra violet) emitters (Young *et al.*, 2010b). AlGaN buffer layers are currently being explored and have been utilized to demonstrate a 384 nm $(20\bar{2}1)$ near-ultra-violet LD (Haeger *et al.*, 2012). For further reference, Romanov *et al.* (2011) provide a thorough discussion of stress relaxation in semipolar III-nitrides.

6.6 Optical waveguides and loss

Optical waveguides for LDs are typically designed to maximize the overlap of the fundamental optical mode with the QW active region. This overlap is known as the confinement factor, Γ (Coldren and Corzine, 1995). Structures that confine photons in one dimension contain transverse waveguiding, while structures that confine photons in two dimensions contain both transverse and lateral waveguiding. III-nitride LDs for most applications utilize both transverse and lateral confinement. In this section, we discuss transverse waveguiding, lateral waveguiding, and optical loss, which are common to all orientations of III-nitride LDs. We also highlight AlGaN-cladding-free (ACF) waveguide designs and birefringence, which are unique to nonpolar and semipolar LDs.

6.6.1 Transverse waveguides

The majority of commercial III-nitride LDs employ a ridge structure to confine the optical mode (shown in Fig. 6.13). This structure provides both transverse and lateral mode confinement. Transverse confinement is achieved by situating layers of higher index of refraction within or near the active region and surrounding them by cladding layers of lower index of refraction. Due to the presence of the QCSE, *c*-plane LDs typically

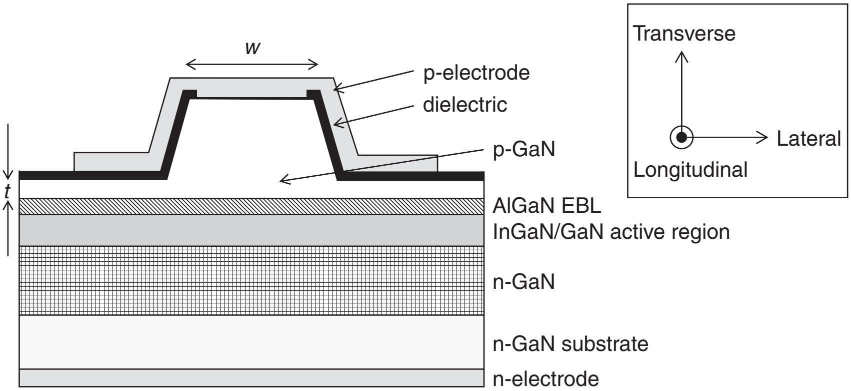

6.13 Cross-section of a typical ACF ridge laser.

utilize thin (<3 nm) InGaN QWs and therefore require thick Al-containing cladding layers, such as AlGaN/GaN superlattices or AlGaN, to achieve transverse mode confinement. These strained AlGaN layers introduce several significant problems, including increased cracking from tensile strain, higher voltage operation, shorter device lifetime, reduced yield, and MOCVD reactor instabilities. For examples of *c*-plane LD structures, see Fig. 6.14 and Ohta *et al.* (2007). In contrast to *c*-plane LDs, the absence of the QCSE in nonpolar and semipolar structures permits the implementation of thick (~8 nm) InGaN QWs, which can be used to produce effective guiding of the transverse mode (Feezell *et al.*, 2007). The addition of InGaN separate-confinement-heterostructure (SCH) waveguiding layers enables nonpolar and semipolar LDs that are completely free of AlGaN cladding layers (Kelchner *et al.*, 2009). These structures can be grown and fabricated in a manner analogous to InGaN/GaN LEDs, providing a highly manufacturable platform for GaN-based LDs. Figures 6.13 and 6.15 show examples of ACF designs. Demonstrations of violet, blue, and green LDs have been achieved utilizing ACF designs (Farrell *et al.*, 2007; Kelchner *et al.*, 2010; Lin *et al.*, 2010). Although nonpolar and semipolar orientations afford excellent design flexibility, practical QW thicknesses are ultimately limited by decreasing valence subband spacing, which results in thermal hole redistribution and lowers the optical gain (Kisin *et al.*, 2009). Consequently, an optimum QW width for each orientation and indium composition is expected.

Design of transverse waveguides for nonpolar and semipolar green LDs is complicated by stress relaxation and the decreased index contrasts between GaN and InGaN and GaN and AlGaN at longer wavelengths (Okamoto *et al.*, 2007b). Figure 6.14 shows a typical transverse waveguide design for a *c*-plane LD, while Fig. 6.15 show a typical design for a nonpolar

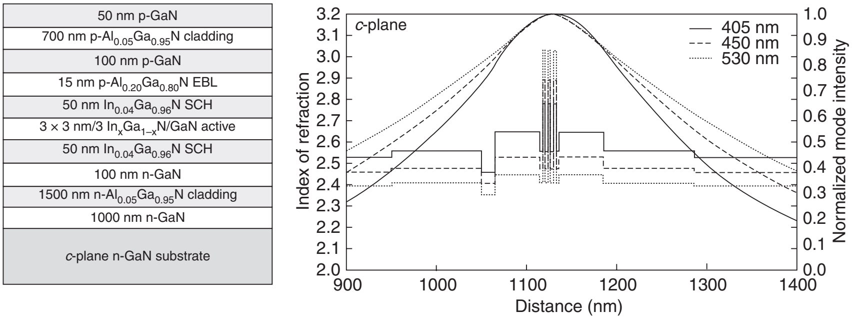

6.14 Typical transverse waveguide design for a *c*-plane LD. Layer designs and mode profiles are presented for three common wavelength targets (405 nm, 450 nm, 530 nm) using $In_{0.04}Ga_{0.96}N$ SCH layers and $Al_{0.05}Ga_{0.95}N$ cladding layers.

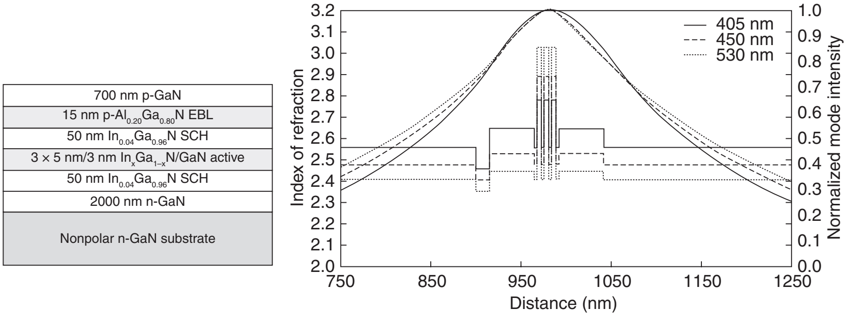

6.15 Typical transverse waveguide design for a nonpolar ACF LD. Layer designs and mode profiles are presented for three common wavelength targets (405 nm, 450 nm, 530 nm) using $In_{0.04}Ga_{0.96}N$ SCH layers.

ACF LD. Layer designs and mode profiles are presented for three common wavelength targets (405 nm, 450 nm, 530 nm) using typical compositions for InGaN SCH layers and AlGaN cladding layers. The index contrasts between GaN and $In_{0.04}Ga_{0.96}N$ and GaN and $Al_{0.05}Ga_{0.95}N$ are presented in Fig. 6.16, along with the calculated transverse confinement factors for the two designs. For a given SCH or cladding composition, the achievable index contrast (and confinement factor) is reduced at longer wavelengths. To overcome this issue, additional or thicker QWs must be added, or the compositions of the SCH or cladding regions must be increased, which often leads to issues with stress relaxation, as described above. We note that the indices used in generating Figs 6.14 and 6.15 do not include birefringence, so the results are only relevant for *c*-plane lasers, *m*-plane lasers oriented along the *c*-axis, and semipolar lasers oriented along the projection of the

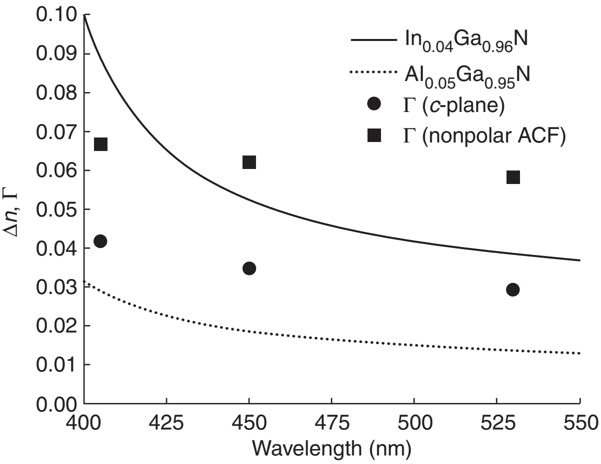

6.16 Index contrasts (Δn) between GaN and $In_{0.04}Ga_{0.96}N$ and GaN and $Al_{0.05}Ga_{0.95}N$, along with the calculated transverse confinement factors (Γ), for *c*-plane and nonpolar ACF designs *vs* wavelength.

c-axis. For a full discussion of optical waveguiding in III-nitride lasers see Huang *et al.* (2010).

6.6.2 Lateral waveguides

Lateral waveguiding is most easily accomplished by forming ridge structures. The cross-section of a typical ACF ridge laser is shown in Fig. 6.13. For devices operating with a single-lateral mode, the typical ridge width, *W*, ranges from 1.4 to 2.2 μm, depending upon the lasing wavelength. Typical cavity lengths range from 500 to 2000 μm, with the longer lengths preferred for high-power devices. Accurate control of the ridge width and depth are critical for stable, kink-free operation, control of the far-field pattern (FFP), and to optimize the threshold current density (Tojyo *et al.*, 2002). Schwarz *et al.* (2005) have studied in-depth the effects of ridge geometry on the performance of III-nitride lasers. The ridge width can be controlled by lithographic techniques, but control of the ridge depth is more difficult. If the ridge depth is too shallow, the index contrast between the core and cladding of the waveguide in the lateral direction will be insufficient to effectively guide the mode. Furthermore, shallow etches can result in undesirable current spreading underneath the ridge (Muller *et al.*, 2009). If the ridge depth is too deep, higher order lateral modes can develop and plasma-related damage to the QWs may occur (Coldren and Corzine, 1995). If the ridge depth proceeds through the QWs, surface recombination currents are enhanced and issues with device lifetime arise.

The distance between the bottom of the ridge etch and the top of the active region, *t*, is important for mode control and is typically around 150 nm for *c*-plane devices using AlGaN cladding. Frequently, this distance is controlled by timed-etches using known etch rates or by laser interferometry. Accurate control of this distance on nonpolar and semipolar LDs can be achieved using ACF designs and AlGaN etch-stop layers (ESLs). Farrell *et al.* (2011a) demonstrated control of this distance utilizing $Al_{0.09}Ga_{0.91}N$ ESLs embedded within the p-GaN of ACF LDs. The layer structure for their device with the embedded $Al_{0.09}Ga_{0.91}N$ ESL is shown in Fig. 6.17a. Plasma etching in a mixture of BCl_3 and SF_6 was used to realize an etch selectivity of 11:1 between the GaN and embedded $Al_{0.09}Ga_{0.91}N$ ESL, enabling simple and repeatable control of the etch depth. A plot of etch depth *vs* etch time is shown in Fig. 6.17b and illustrates the significantly reduced etch rate that was obtained within the ESL layer. The selectivity provided by this technique is unique to ACF designs, where GaN rather than AlGaN surrounds the $Al_{0.09}Ga_{0.91}N$ ESL. The high selectivity achieved renders the etch depth relatively insensitive to variations in etch rate or etch time and it becomes primarily determined by control of epitaxial growth rates.

6.6.3 Optical loss

Optical absorption losses in group III-nitride lasers are typically higher than those in conventional III-V lasers. The primary reason for this stems from the large acceptor activation energy (200 meV) for Mg, which ensures that p-type GaN contains a high fraction of non-ionized acceptors. The fraction of ionized acceptors at room temperature is only around one per cent.

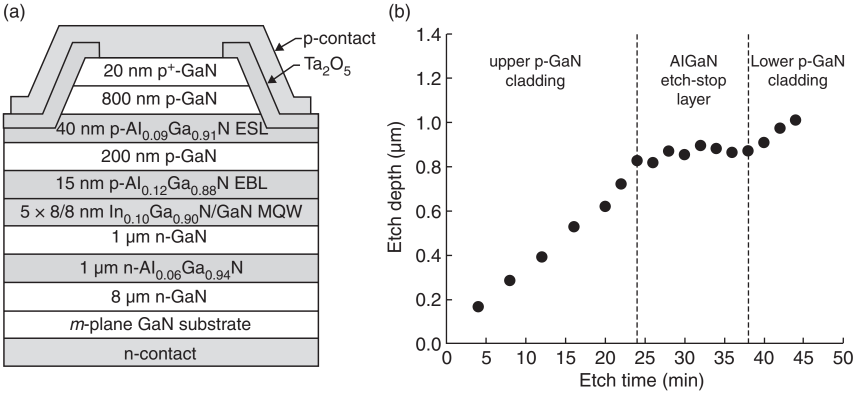

6.17 (a) Layer structure and (b) etch depth *vs* etch time for an LD with an $Al_{0.09}Ga_{0.91}N$ ESL embedded within the p-GaN. Source: Reproduced with permission from Farrell *et al.* (2011a).

Consequently, high doping concentrations are required to achieve useful free-carrier concentrations in p-type GaN. The large indirect phonon-assisted free-carrier absorption and acceptor-bound carrier absorption further contribute to the loss. The material loss associated with p-type GaN has been calculated from first principles to be in the range of 15–20 cm^{-1} per 1e19 cm^{-3} of Mg and experimentally determined to be around 25 cm^{-1} per 1e19 cm^{-3} (Kuramoto *et al.*, 2002; Huang *et al.*, 2010; Kioupakis *et al.*, 2010). Similarly, the material loss associated with Si-doped n-type GaN was in the range of 1–15 cm^{-1} per 1e18 cm^{-3} (Kuramoto *et al.*, 2002; Huang *et al.*, 2010; Kioupakis *et al.*, 2010). Although the material absorption coefficients for p-type and n-type GaN are of the same order, the activation energy for n-type material is only 15–25 meV. Consequently, lower Si concentrations are required to achieve useful free-carrier concentrations. For example, highly conductive n-type GaN may have a Si concentration of 1e18 cm^{-3}, while highly conductive p-type GaN usually requires a Mg concentration of 5e19 cm^{-3}. Several groups have extracted experimental modal internal loss estimates for III-nitride lasers. They are typically in the range of 15–35 cm^{-1} (Uchida *et al.*, 2003; Kojima *et al.*, 2006; Melo *et al.*, 2011).

Designs to mitigate optical losses in III-nitride lasers typically focus on reducing the overlap of the optical mode with the highly-doped p-type material. One approach is to step-down (or grade) the p-type doping scheme where the mode is strongest (i.e., near the active region). Farrell *et al.* (2011b) have demonstrated a high-power violet *m*-plane laser diode with this approach. A 1D transverse mode simulation was performed to examine a simple ACF structure, similar to that presented by Farrell (2011b). Figure 6.18 shows the mode profile and index of refraction for this structure. If the Mg doping concentration in this region is reduced

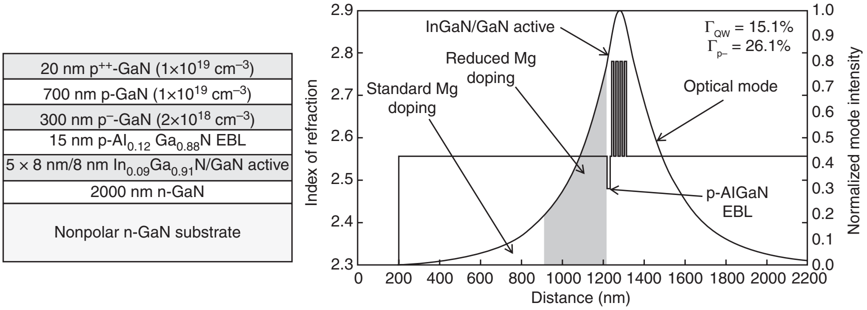

6.18 Layer structure, transverse optical mode profile, and index of refraction for a violet nonpolar ACF LD with a stepped Mg doping profile. The confinement factor for the 300 nm of p-GaN directly adjacent to the AlGaN EBL is Γ_{p-} = 0.261. Source: After Farrell *et al.* (2011b).

from 1e19 cm^{-3} to 2e18 cm^{-3} and a material loss of 25 cm^{-1} per 1e19 cm^{-3} is assumed, the internal modal loss associated with this portion of the p-GaN is reduced from 6.5 to 1.3 cm^{-1}.

6.6.4 Birefringence

GaN is a birefringent material with $n_e \approx 1.011\, n_o$, where n_e is the refractive index of the extraordinary direction and n_o is the refractive index of the ordinary direction. The extraordinary direction is oriented along the *c*-axis of the wurtzite crystal. For LDs on *c*-plane GaN, the waveguide ridges can be oriented along the *m*-direction or the *a*-direction, with the *m*-direction being preferable due to the ease of cleaving mirror facets on the *m*-plane. The extraordinary direction in these waveguides is perpendicular to the growth plane and the ordinary direction lies within the quantum well plane. For *c*-plane LDs, the mode always propagates along the ordinary direction and these devices show true TE and TM modes, with polarizations perpendicular to and parallel to the quantum well plane, respectively. In contrast, ridge waveguides formed on semipolar planes of GaN can be oriented along the projection of the *c*-axis (*c′*-axis) or along the direction perpendicular to the projection of the *c*-axis (i.e., *m*-direction or *a*-direction). For LDs oriented along the projection of the *c*-axis, the extraordinary and ordinary directions perpendicular to the propagation direction match the TE and TM polarizations, and stimulated emission is still linearly polarized as the TE mode. Conversely, for LDs oriented along one of the nonpolar directions perpendicular to the projection of the *c*-axis, the extraordinary and ordinary directions are no longer aligned with the TE or TM modes, but rather rotated within a plane perpendicular to the propagation direction. As a result, the polarization of the propagating optical mode is pulled toward the extraordinary direction, causing optical modes other than TE or TM to emerge. Figure 6.19a illustrates the modes for a semipolar $(11\bar{2}2)$ LD with the laser stripe oriented along the projection of the *c*-axis and Fig. 6.19b shows the modes for the laser stripe oriented along the *m*-axis. For orientation of the stripe along the *m*-axis, birefringence is observed (Rass *et al.*, 2010a; Scheibenzuber *et al.*, 2010).

Rass *et al.* (2010a) experimentally studied the polarization of stimulated emission for various ridge orientations on semipolar $(11\bar{2}2)$ and nonpolar $(1\bar{1}00)$. Ridges oriented along the $[1\bar{1}00]$ (*m*-direction) direction on the semipolar $(11\bar{2}2)$ plane showed stimulated emission into a mode that is rotated out of the plane of the quantum wells and linearly polarized in the extraordinary direction, nearly parallel to the *c*-axis. In contrast, ridges oriented in the $[\bar{1}\bar{1}23]$ direction on the semipolar $(11\bar{2}2)$ plane showed

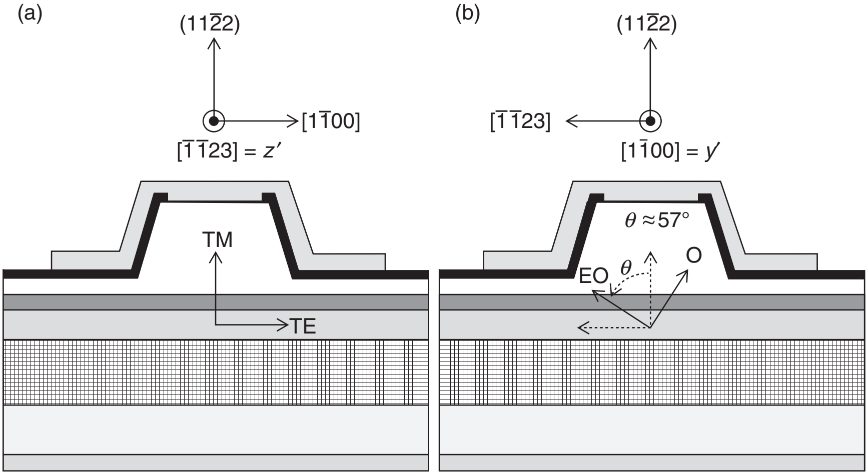

6.19 Mode orientations for (11$\bar{2}$2) LDs with (a) stripes orientated along the projection of the *c*-axis [$\bar{1}\bar{1}$23] where standard TE and TM modes are observed and (b) stripes oriented along the *m*-axis [1$\bar{1}$00] where the electric field is rotated out of the QW plane and extraordinary (EO) and ordinary (O) modes are observed.

stimulated emission into the normal TE mode within the quantum well plane. Nonpolar LDs were also measured and showed stimulated emission into the normal TE mode within the quantum well plane for ridge waveguides oriented along both the *c*-direction and *a*-direction. In summary, birefringence is only problematic on semipolar planes with ridges oriented along one of the nonpolar directions.

6.6.5 Laser stripe orientation

The birefringence observed in semipolar III-nitride optical waveguides presents trade-offs with respect to ridge orientation. For example, on semipolar (11$\bar{2}$2), ridges may be oriented parallel to the projection of the *c*-axis along the [$\bar{1}\bar{1}$23] direction or perpendicular to the projection of the *c*-axis along the [1$\bar{1}$00] direction. The former choice avoids issues with birefringence in the waveguide but necessitates mirror facets that are formed by etching, as the ($\bar{1}\bar{1}$23) plane is not an appropriate cleave plane. The latter option allows for convenient cleaving along the nonpolar *m*-plane but introduces birefringence that reduces the optical gain, which remains higher for LDs oriented along the [$\bar{1}\bar{1}$23] direction (Rass *et al.*, 2010b). For nonpolar *m*-plane devices, the preferred stripe orientation is parallel to the *c*-axis, where the optical gain is highest.

6.7 Fabrication techniques

Like conventional III-V lasers, the fabrication steps for III-nitride lasers include standard photolithography, wet and dry etching, and thin film deposition techniques. However, compared to traditional III-V lasers, some subtleties arise during the fabrication of III-nitride lasers and additional care is often required. The primary concern is passivation and/or damage to p-GaN layers. The presence of abundant H_2 in the MOCVD growth environment results in a high concentration of H_2 in the epitaxial layers. The H_2 binds to Mg acceptors and forms Mg–H complexes, which are electrically inactive and render the p-type material extremely resistive. As a result, p-GaN must be 'activated' (annealed) to remove the H_2 from the structure. This can be done *in situ* in the MOCVD reactor or in an annealing furnace. Since p-GaN is easily damaged or re-passivated, direct exposure of p-GaN to plasmas is typically avoided and the number of fabrication steps to which the p-GaN is exposed is minimized. Additionally, with the exception of photoelectrochemical (PEC) etching, traditional wet-etching techniques and stop-etch layers are non-existent in III-nitride materials. Despite these difficulties, fabricating a basic III-nitride laser structure is relatively straight forward.

Figure 6.20 illustrates the wafer-level fabrication steps for a basic self-aligned III-nitride ridge laser. Due to the narrow ridge widths required for single-lateral mode operation, a self-aligned process is preferred to a direct alignment process for the ridge etch and passivation steps. The first step in the process is to activate in an N_2/O_2 environment in the range of 600–900°C (Fig. 6.20a). This drives the H_2 out of the structure and results in decreased p-GaN resistivity. Typical p-GaN resistivities after activation range from 1 to 2 Ω-cm. Following activation, a surface clean and pre-treatment is performed. This typically consists of a solvent clean to remove organics and an acid dip to remove surface oxides. Since p-GaN is sensitive to re-passivation from H_2 and plasma damage, some surface treatments should be avoided. For the interested reader, there is an abundance of literature available on p-GaN surface treatments. See, for example, Chapter 1 of Morkoc (2008b). After the surface treatment, a two-layer mask consisting of a UV-sensitive polymer and a photoresist is spun, patterned with projection lithography, and undercut by approximately 0.2 μm (Fig. 6.20b). The ridge etch is then performed with Cl_2-based inductively coupled plasma etching (Fig. 6.20c). Next, a low-temperature chemical vapor deposition (CVD) process or sputtering is used to deposit a dielectric material such as SiO_2 on the ridge sidewalls and the two-layer mask (Fig. 6.20d). Lift-off of the two-layer undercut mask is then performed in a solvent, leaving a ridge with self-aligned dielectric on the sidewalls (Fig. 6.20e). A second photolithography step using a negative photoresist is then performed to define the p-electrode (Fig. 6.20f)

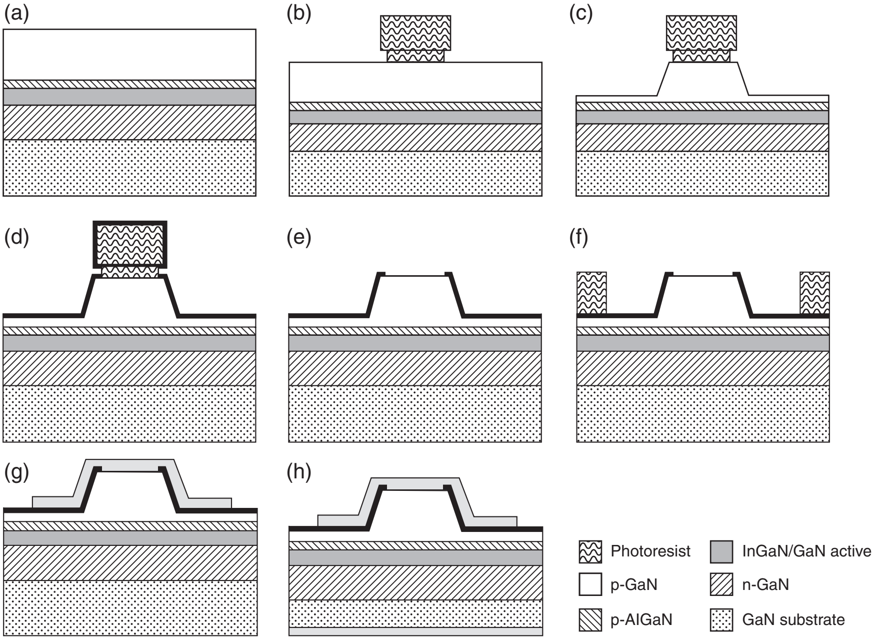

6.20 Wafer-level fabrication steps for a basic self-aligned III-nitride ridge laser. For explanation of panels see text.

and the p-electrode is deposited via remote-plasma sputtering or electron beam evaporation and lifted off in a solvent. Many configurations exist for p-electrodes but they typically consist of metals with high work functions such as Pd/Au, Pt/Au, or Ni/Au. After the p-electrode is deposited, the wafer is mounted on a carrier wafer, thinned by chemical–mechanical polishing (CMP) to a thickness of 60–80 μm, and the n-electrode is deposited via sputter or electron beam evaporation (Fig. 6.20g and 6.20h). Many configurations also exist for n-electrodes, with two common options being Al/Ni/Au and Ti/Al/Ni/Au. Although additional steps may be required to achieve long operating lifetime and high reliability, the basic device can be completed in only two photolithography steps. This is another advantage of the self-aligned process.

After wafer-level fabrication is complete, the wafer is scribed with a diamond-tip or laser-based scribing system and cleaved to form cavities. High-reflection (HR) and/or anti-reflection (AR) facet coating are then typically applied. HR coatings commonly consist of several periods of SiO_2/Ta_2O_5, while AR coatings often utilize a single layer of SiO_2 or Al_2O_3. Individual chips may then be mounted on an AlN sub-mount, wire bonded, and packaged in a TO can. A scanning electron microscope (SEM) image of the facet area of a completed III-nitride ridge laser is shown in Fig. 6.21. This laser

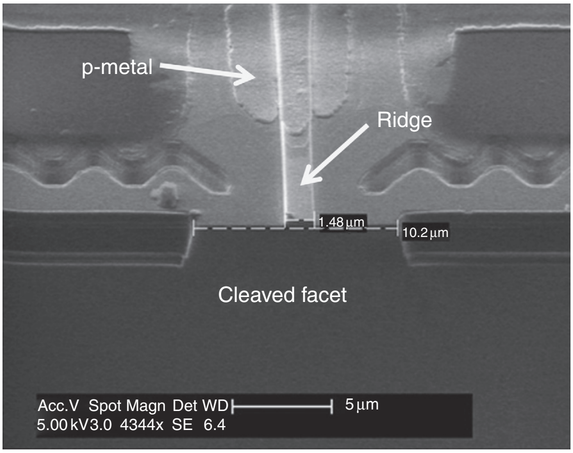

6.21 SEM image of the facet area of a commercial III-nitride ridge laser that was extracted from a Blu-ray Disc player.

was extracted from a Blu-ray Disc player and the manufacturer of the diode is unknown.

6.8 Nonpolar and semipolar laser history and performance

The first nonpolar LDs were simultaneously demonstrated by UCSB and Rohm (Okamoto *et al.*, 2007; Schmidt *et al.*, 2007). The devices emitted in the violet region and utilized free-standing m-plane $(10\bar{1}0)$ GaN substrates. Several months later, the first semipolar LD was demonstrated on free-standing $(10\bar{1}\bar{1})$ GaN, again emitting in the violet region (Tyagi *et al.*, 2007). Noting that thick InGaN QWs could be used to produce effective waveguiding of the transverse optical mode, researchers at UCSB then demonstrated pulsed and continuous wave (CW) m-plane $(10\bar{1}0)$ ACF violet LDs (Farrell *et al.*, 2007; Feezell *et al.*, 2007). These designs were later modified to create m-plane $(10\bar{1}0)$ ACF violet LDs with low-threshold current densities and high output powers (Farrell *et al.*, 2010b, 2011b). Internal cavity parameters were also extracted from violet m-plane LDs and verified predictions of lower transparency carrier density for the nonpolar m-plane orientation (Farrell *et al.*, 2011b).

The initial demonstrations of violet LDs soon gave way to the development of longer wavelength blue and green emitters for projection and display applications. Rohm and Sharp led the way with m-plane $(10\bar{1}0)$ LDs, demonstrating pulsed lasing at 452 nm (Okamoto *et al.*, 2007b), CW lasing at 460 nm (Kubota *et al.*, 2007), pulsed lasing at 463 nm (Tsuda *et al.*, 2008), and

CW lasing at 481 nm (Okamoto *et al.*, 2008). While work on *m*-plane continued, researchers at UCSB also explored semipolar $(11\bar{2}2)$, demonstrating CW lasing at 406 nm (Asamizu *et al.*, 2009) and observing stimulated emission at 514 nm from optically-pumped samples (Tyagi *et al.*, 2008). Hsu *et al.* (2010) also demonstrated LDs operating in the blue region on semipolar $(30\bar{3}1)$, which is angled 10° off of *m*-plane. In 2009, progress toward long wavelength LDs on *m*-plane stalled at 500 nm (Okamoto *et al.*, 2009) and no suitable semipolar plane could be found to produce longer wavelength LDs. In the same year, OSRAM and Nichia demonstrated pulsed and CW lasing, respectively, at 515 nm on *c*-plane (Avramescu *et al.*, 2009; Miyoshi *et al.*, 2009).

When it appeared that nonpolar and semipolar orientations were losing the race toward true-green emitters to conventional *c*-plane, SEI reported pulsed lasing at 531 nm on the previously-unexplored semipolar $(20\bar{2}1)$ plane (Enya *et al.*, 2009). SEI continued with reports of CW lasing at 520 nm (Yoshizumi *et al.*, 2009) and CW lasing between 520 and 530 nm with low-threshold current density (4.3 kA/cm^2) (Adachi *et al.*, 2010). SEI also examined the carrier localization effects on semipolar $(20\bar{2}1)$ (Funato *et al.*, 2010) and the optical polarization characteristics, verifying that the preferred orientation for laser stripes is along the projection of the *c*-axis (Kyono *et al.*, 2010). With the reports from SEI, it became clear that some semipolar orientations were very well-suited to producing green lasers. Meanwhile, OSRAM continued to extend the lasing wavelength of *c*-plane LDs to 524 nm (CW) and 531 nm (pulsed), and suggested that the main limiting factor for performance in the green spectral region is not polarization-related electric fields but QW crystal quality (Avramescu *et al.*, 2010). Other groups continued to report green lasers on non-*c*-plane orientations. UCSB demonstrated 516 nm pulsed ACF LDs on $(20\bar{2}1)$ using AlGaN barriers (Lin *et al.*, 2010). Corning demonstrated 519 nm semipolar LDs with 60 mW CW output power on an unspecified semipolar plane (Sizov *et al.*, 2011). The researchers at Corning examined a range of device designs with and without EBL and showed that the absence of an EBL had no effect on the characteristic temperature (T_0) for the examined plane. We note that this conclusion may not apply to all semipolar orientations due to the effect that the direction and magnitude of the polarization-related electric fields have on carrier transport.

High-performance violet, blue, and green nonpolar/semipolar LDs have been demonstrated by Soraa Inc. (formerly Kaai Inc.) (Raring *et al.*, 2010a, 2010b). Figure 6.22a and 6.22b show the CW light-current (LI) and WPE curves for Soraa's blue and green single-mode (SM) devices at 20°C. These LDs were fabricated on unspecified nonpolar/semipolar orientations and mounted in TO38 packages. Soraa has achieved ~515 nm LDs on nonpolar/semipolar substrates with >100 mW CW SM output power,

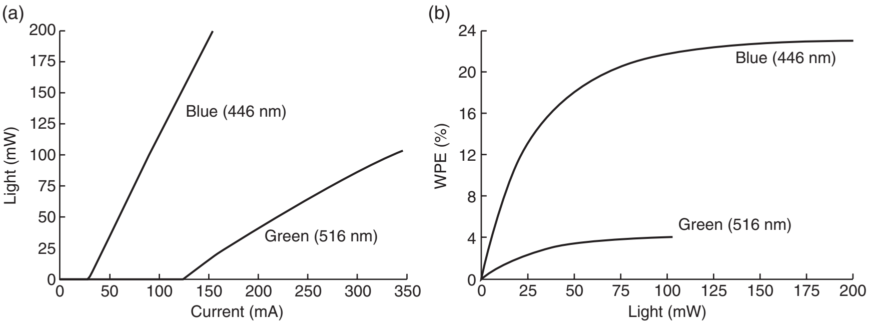

6.22 CW (a) light *vs* current and (b) WPE *vs* light for blue and green SM nonpolar/semipolar LDs at 20°C. Source: Data courtesy of Soraa Inc.

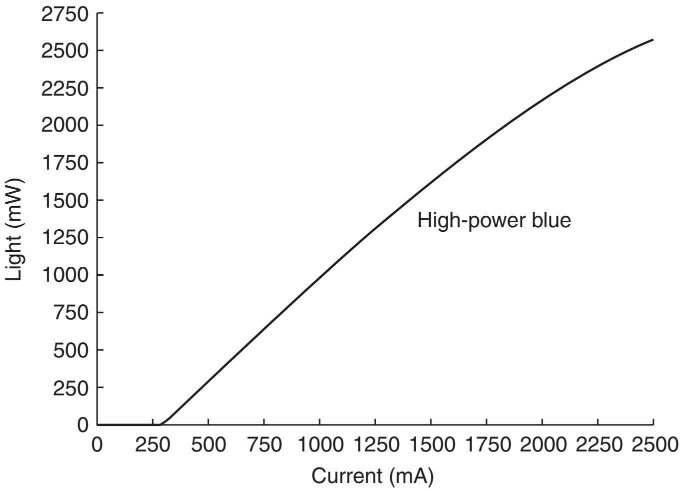

6.23 CW light *vs* current for a high-power blue MM single-emitter nonpolar/semipolar LD at 25°C. Source: Data courtesy of Soraa Inc.

>4% peak WPE, and characteristic temperatures (T_0) of 160–180 K. Soraa has also demonstrated ~445 nm LDs on nonpolar/semipolar substrates with >200 mW CW SM output power, >23% peak WPE, characteristic temperatures (T_0) of 125–140 K, and mean operating lifetimes of more than 10 000 h. Kink-free SM operation up to 750 mW was also realized for similar devices. High-power ~445 nm devices with >2.5 W CW multi-mode (MM) output power were also produced from a single-emitter can-type LD by implementing a longer cavity design and an improved packaging scheme (Raring *et al.*, 2011). An LI curve for Soraa's high-power MM blue device is shown in Fig. 6.23. The WPE of this high-power device was over 20% and is expected to increase with further optimization.

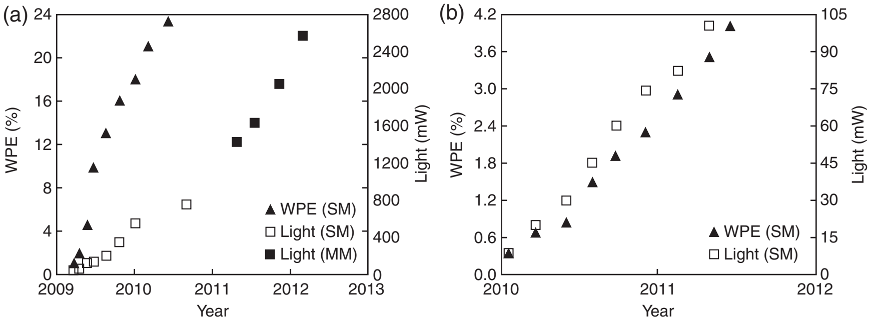

6.24 Progress in peak WPE and output power *vs* time for (a) blue and (b) green nonpoplar/semipolar LDs at 25°C (a) and 20°C (b). Source: Data courtesy of Soraa Inc.

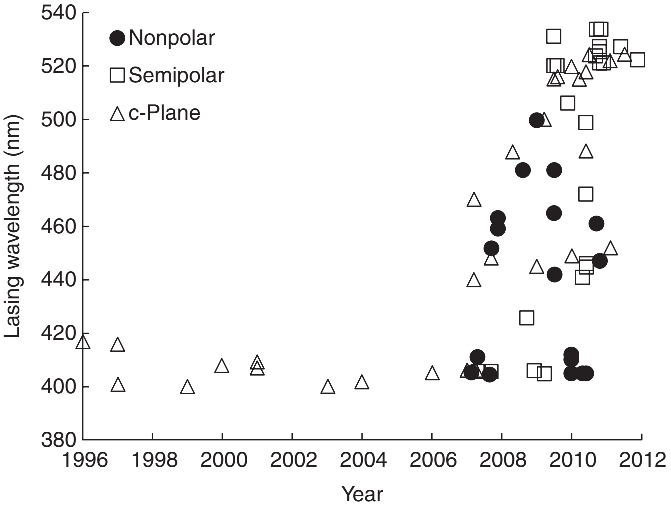

6.25 Progression of lasing wavelength *vs* time for nonpolar, semipolar, and *c*-plane LDs.

Although the development time for nonpolar and semipolar LDs has spanned less than five years, the current performance of these devices is already competitive with state-of-the-art *c*-plane LDs, which have undergone nearly 20 years of development. The progress in peak WPE and output power *vs* time for Soraa's blue and green LDs on nonpolar/semipolar orientations is illustrated in Fig. 6.24a and 6.24b, respectively. The peak WPEs and output powers have increased by a factor of more than ten within a 3-year time period for both blue and green devices. Figure 6.25 shows the progression of lasing wavelength *vs* time for nonpolar, semipolar,

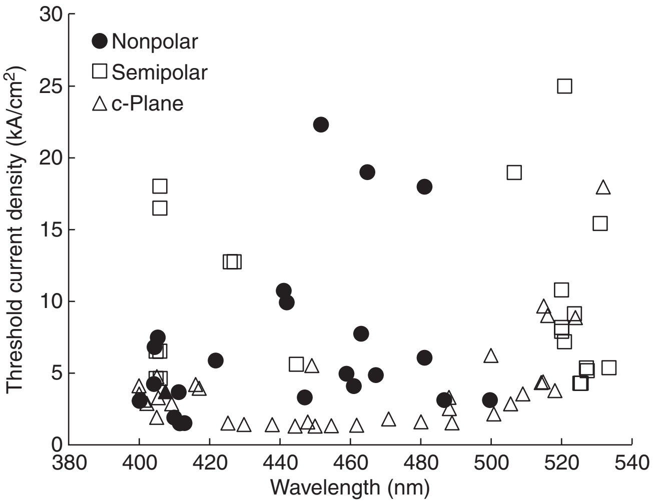

6.26 Threshold current density *vs* lasing wavelength for nonpolar, semipolar, and *c*-plane LDs.

and *c*-plane LDs (using values reported in the literature). Since 2007, the lasing wavelength on nonpolar and semipolar orientations has progressed rapidly to the green region. SEI has reported the longest wavelength high-performance LDs to date by utilizing the semipolar $(20\bar{2}1)$ plane to achieve an emission wavelength of 533.6 nm and a threshold current density of 5.4 kA/cm^2 (Adachi *et al.*, 2010). Figure 6.26 shows threshold current density *vs* lasing wavelength for nonpolar, semipolar, and *c*-plane LDs (using values reported in the literature). As seen in Fig. 6.26, threshold current densities for nonpolar LDs are competitive with *c*-plane in the violet and blue regions, while those for semipolar LDs are typically superior to *c*-plane in the green region.

6.9 Future trends

While high-performance LDs have been demonstrated on nonpolar and semipolar GaN substrates, the single biggest challenge facing these technologies is substrate availability. Currently available nonpolar and semipolar GaN substrates are significantly smaller and more costly than their *c*-plane counterparts, which presents significant issues with scale-up for mass production. To become competitive, performance levels of nonpolar and semipolar LDs must well surpass those of *c*-plane LDs or nonpolar and semipolar substrates must approach cost-parity with free-standing *c*-plane substrates. With the development of ammonothermal growth methods for GaN, large-scale nonpolar and semipolar substrates are ultimately expected. However, semipolar planes are not typically naturally occurring growth planes, so fabrication of semipolar substrates will still likely require slicing of *c*-plane boules at an angle. How rapidly these substrates become available will be a key factor in the commercialization timeline of nonpolar and semipolar technologies.

The violet market for high-density optical data storage will likely continue to be dominated by *c*-plane LDs due to their maturity and high-performance. The high-power blue market may be an attractive space for nonpolar and semipolar LDs. If gain saturation effects can be reduced on these orientations, LDs with intentionally larger mirror losses and higher differential efficiencies can be designed for high-power applications. To become attractive alternatives to green lasers based on SHG, direct-diode lasers operating at 515 nm will need to reach WPEs in excess of five per cent and provide more than 60 mW of output power. Ultimately these devices may be fabricated on *c*-plane, nonpolar, or semipolar substrates. Perhaps the greatest advantage provided by nonpolar and semipolar orientations is the design flexibility they afford. With reduced polarization-related electric fields restrictions on QW thicknesses are lifted, alternative waveguide structures may be employed, and novel device designs may be created to improve performance. The emergence of semipolar devices with intentional strain-relaxation also presents interesting opportunities for LDs with high indium or aluminum contents. This may play an important role in the future development of UV or green emitters.

6.10 Sources of further information and advice

For a complete development history of early *c*-plane violet and blue LDs, see *The Blue Laser Diode: The Complete Story* by Nakamura *et al.* (2000b) and Chapter Seven in *Introduction to Nitride Semiconductor Blue Lasers and Light Emitting Diodes* (Nakamura, 2000a). For comprehensive references on III-nitride materials, devices, and applications see the three volume set *Handbook of Nitride Semiconductors and Devices* (Morkoc, 2008a, 2008b, 2008c) and the multi-contributor book *Nitride Semiconductor Devices: Principles and Simulation* (Piprek, 2007). For references on nonpolar III-nitrides see the multi-contributor book *Nitrides with Nonpolar Surfaces* (Paskova, 2008) and the May 2009 issue of MRS Bulletin (MRS Bulletin, 2009). Further information on materials issues in III-nitrides can be found in Hardy *et al.* (2011) and Farrell *et al.* (2012).

A large number of university groups are heavily involved in nonpolar and semipolar LD research, including but not limited to the groups of Professors Nakamura, DenBaars, and Speck at the University of California Santa Barbara, the group of Professor Kneissl at the Technical University Berlin, the group of Professor Schwarz at the University of Regensburg, the groups of Professors Scholz and Thonke at the University of Ulm, and the groups of Professors Kawakami, Funato, and Kojima at Kyoto University. From the commercial sector, Kaai/Soraa Inc., SEI, Corning, and Rohm have all reported on the development of nonpolar and semipolar LDs.

6.11 References

Adachi M, Yoshizumi Y, Enya Y, Kyono T, Sumitomo T, Tokuyama S, Takagi S, Sumiyoshi K, Saga N, Ikegami T, Ueno M, Katayama K and Nakamura T (2010), 'Low threshold current density InGaN based 520–530 nm green laser diodes on semi-polar $(20\bar{2}1)$ free-standing GaN substrates', *Appl. Phys. Express*, **3**, 121001(1–3).

Amano H, Kito M, Hiramatsu K and Akasaki I (1989), 'P-type conduction in Mg-doped GaN treated with low-energy electron beam irradiation (LEEBI)', *Jpn. J. Appl. Phys.*, **28**, L2112–L2114.

Avramescu A, Lermer T, Muller J, Tautz S, Queren D, Lutgen S and Strauss U (2009), 'InGaN laser diodes with 50 mW output power emitting at 515 nm', *Appl. Phys. Lett.*, **95**, 071103(1–3).

Avramescu A, Lermer T, Muller J, Eichler C, Bruederl G, Sabathil M, Lutgen S and Strauss U (2010), 'True green laser diodes at 524 nm with 50 mW continuous wave output power on c-plane GaN', *Appl. Phys. Express*, **3**, 061003(1–3).

Avrutin V, Silversmith D, Mori Y, Kawamura F, Kitaoka Y and Morkoc H (2010), 'Growth of bulk GaN and AlN: Progress and challenges', *Proc. of the IEEE,* **98**, 1302–1315.

Baker T, Haskell B, Wu F, Speck J and Nakamura S (2006), 'Characterization of planar semipolar gallium nitride films on sapphire substrates', *Jpn. J. Appl. Phys.*, **45**, L154–L157.

Bernardini F, Fiorentini V and Vanderbilt D (1997), 'Spontaneous and piezoelectric constants of III-V nitrides', *Phys. Rev. B*, **56**, R10024–R10027.

Brinkley S, Lin Y, Chakraborty A, Pfaff N, Cohen D, Speck J, Nakamura S and DenBaars S (2011), 'Polarized spontaneous emission from blue-green m-plane GaN-based light emitting diodes', *Appl. Phys. Lett.*, **98**, 011110(1–3).

Butte R and Grandjean N (2008), 'Effects of polarization in optoelectronic quantum structures', in Wood J and Jena D, *Polarization Effects in Semiconductors,* New York, Springer, 467–511.

Chakraborty A, Baker T, Haskell B, Wu F, Speck J, DenBaars S, Nakamura S and Mishra U (2005), 'Milliwatt power blue InGaN/GaN light-emitting diodes on semipolar GaN templates', *Jpn. J. Appl. Phys.*, **44**, L945–L947.

Chakraborty A, Haskell B, Keller S, Speck J, DenBaars S, Nakamura S and Mishra U (2004), 'Nonpolar InGaN/GaN emitters on reduced-defect lateral epitaxially overgrown *a*- plane GaN with drive-current-independent electroluminescence emission peak', *Appl. Phys. Lett.*, **85**, 5143–5145.

Chichibu S, Azuhata T, Sota T and Nakamura S (1996), 'Spontaneous emission of localized excitons in InGaN single and multiquantum well structures', *Appl. Phys. Lett.*, **69**, 4188–4190.

Chichibu S, Uedono A, Onuma T, Haskell B, Chakraborty A, Koyama T, Fini P, Keller S, DenBaars S, Speck J, Mishra U, Nakamura S, Yamaguchi S, Kamiyama S, Amano H, Akasaki I, Han J and Sota T (2009), 'Origin of localized excitons in In-containing three dimensional bulk (Al,In,Ga)N alloy films probed by time-resolved photoluminescence and monoenergetic positron annihilation techniques', *Philos. Mag.*, **87**, 2019–2039.

Coldren L and Corzine S (1995), *Diode Lasers and Photonic Integrated Circuits*, New York, John Wiley and Sons, Inc.

Craven M, Lim S, Wu F, Speck J and DenBaars S (2002), 'Structural characterization of nonpolar $(11\bar{2}0)$ a-plane GaN thin films grown on $(1\bar{1}02)$ r-plane sapphire', *Appl. Phys. Lett.*, **81**, 469–471.

Cruz S, Keller S, Mates T, Mishra U and DenBaars S (2009), 'Crystallographic orientation dependence of dopant and impurity incorporation in GaN films grown by metalorganic chemical vapor deposition', *J. Cryst. Growth*, **311**, 3817–3823.

Dingle R, Shaklee K, Leheny R and Zetterstrom R (1971), 'Stimulated emission and laser action in gallium nitride', *Appl. Phys. Lett.*, **19**, 5–7.

Durnev M, Omelchenko A, Yakovlev E, Evstatov I and Karpov S (2010), 'Indium incorporation and optical transitions in InGaN bulk materials and quantum wells with arbitrary polarity', *Appl. Phys. Lett.*, **97**, 051904(1–3).

Durnev M, Omelchenko A, Yakovlev E, Evstatov I and Karpov S (2011), 'Strain effects on indium incorporation and optical transitions in green-light InGaN heterostructures of different orientations', *Phys. Stat. Sol. (a)*, **208**, 2671–2675.

Dwilinski R, Doradzinski R, Garczynski J, Sierzputowski L, Kucharski R, Zajac M, Rudzinski M, Kudrawiec R, Strupinski W and Misiewicz J (2011), 'Ammonothermal GaN substrates: growth accomplishments and applications', *Phys. Stat. Sol. (a)*, **208**, 1489–1493.

Enya Y, Yoshizumi Y, Kyono T, Akita K, Ueno M, Adachi M, Sumitomo T, Tokuyama S, Ikegami T, Katayama K and Nakamura T (2009), '531 nm green lasing of InGaN based laser diodes on semi-Polar $(20\bar{2}1)$ free-standing GaN substrates', *Appl. Phys. Express*, **2**, 082101(1–3).

Farrell R, Feezell D, Schmidt M, Haeger D, Kelchner K, Iso K, Yamada H, Saito M, Fujito K, Cohen D, Speck J, DenBaars S and Nakamura S (2007), 'Continuous-wave operation of AlGaN-cladding-free nonpolar m-plane InGaN/GaN laser diodes', *Jpn. J. Appl. Phys*., **46**, L761–L763.

Farrell R, Haeger D, Chen X, Gallinat C, Davis R, Cornish M, Fujito K, Keller S, DenBaars S, Nakamura S and Speck J (2010a), 'Origin of pyramidal hillocks on GaN thin films grown on free-standing *m*-plane GaN substrates', *Appl. Phys. Lett*., **96**, 231907(1–3).

Farrell R, Hsu P, Haeger D, Fujito K, DenBaars S, Speck J and Nakamura S (2010b), 'Low-threshold-current-density AlGaN-cladding-free m-plane InGaN/GaN laser diodes', *Appl. Phys. Lett.*, **96**, 231113(1–3).

Farrell R, Haeger D, Chen X, Iza M, Hirai A, Kelchner K, Fujito K, Chakraborty A, Keller S, DenBaars S, Speck J and Nakamura S (2010c), 'Effect of carrier gas and substrate misorientation on the structural and optical properties of m-plane InGaN/GaN light-emitting diodes', *J. Cryst. Growth*, **313**, 1–7.

Farrell R, Haeger D, Hsu P, Hardy M,, Kelchner K, Fujito K, Feezell D, Mishra U, DenBaars S, Speck J and Nakamura S (2011a), 'AlGaN-cladding-free m-plane InGaN/GaN laser diodes with p-type AlGaN etch stop layers', *Appl. Phys. Express*, **4**, 092105(1–3).

Farrell R, Haeger D, Hsu P, Schmidt M, Fujito K, Feezell D, DenBaars S, Speck J and Nakamura S (2011b), 'High-power blue-violet AlGaN-cladding-free m-plane InGaN/GaN laser diodes', *Appl. Phys. Lett*., **99**, 171113(1–3).

Farrell R, Haeger D, Hsu P, Fujito K, Feezell D, DenBaars S, Speck J and Nakamura S (2011c), 'Determination of internal parameters for AlGaN-cladding-free m-plane InGaN/GaN laser diodes', *Appl. Phys. Lett.*, **99**, 171115(1–3).

Farrell R, Young E, Wu F, DenBaars S and Speck J (2012), 'Materials and growth issues for high-performance nonpolar and semipolar light-emitting devices', *Semicond. Sci. Technol.*, **27**, 024001.

Feezell D, Schmidt M, Farrell R, Kim K, Saito M, Fujito K, Cohen D, Speck J, DenBaars S and Nakamura S (2007), 'AlGaN-cladding-free nonpolar InGaN/GaN laser diodes', *Jpn. J. Appl. Phys.*, **46**, L284–L286.

Feezell D, Schmidt M, DenBaars S and Nakamura S (2009), 'Development of nonpolar and semipolar InGaN/GaN visible light-emitting diodes', *MRS Bull.*, **34**, 318–323.

Feneberg M and Thonke K (2007), 'Polarization fields of III-nitrides grown in different crystal orientations', *J. Phys. Condens. Matter.*, **19**, 403201(1–26).

Feneberg M, Thonke K, Wunderer T, Lipski F and Scholz F (2010), 'Piezoelectric polarization of semipolar and polar GaInN quantum wells grown on strained GaN templates', *J. Appl. Phys.*, **107**, 103517(1–6).

Fiorentini V, Bernardini F, Della Sala F, Di Carlo A and Lugli P (1999), 'Effects of macroscopic polarization in III-V nitride multiple quantum wells', *Phys. Rev. B*, **60**, 8849–8858.

Fujito K, Kiyomi K, Mochizucki T, Oota H, Namita H, Nagao S and Fujimura I (2008), 'High-quality nonpolar m-plane GaN substrates grown by HVPE', *Phys. Stat. Sol. (a)*, **205**, 1056–1059.

Fujito K, Kubo S, Nagaoka H, Mochizuki T, Namita H and Nagao S (2009), 'Bulk GaN crystals grown by HVPE', *J. Cryst. Growth*, **311**, 3011–3014.

Funato M and Kawakami Y (2008), 'Excitonic properties of polar, semipolar, and nonpolar InGaN/GaN strained quantum wells with potential fluctuations', *J. Appl. Phys.*, **103**, 093501(1–7).

Funato M, Ueda M, Inoue D, Kawakami Y, Narukawa Y and Mukai T (2010), 'Experimental and theoretical considerations of polarization field direction in semipolar InGaN/GaN quantum wells', *Appl. Phys. Express*, **3**, 071001(1–3).

Hardy M, Feezell D, DenBaars S and Nakamura S (2011), 'Group III-nitride lasers: A materials perspective', *Mater. Today*, **14**, 408–415.

Gardner N, Kim J, Wierer J, Shen Y and Krames M (2005), 'Polarization anisotropy in the electroluminescence of m-plane InGaN-GaN multiple-quantum-well light emitting diodes', *Appl. Phys. Lett.*, **86**, 111101(1–3).

Haeger D, Chung R, Young E, Pfaff N, Tsai M, Fujito K, DenBaars S, Speck J, Nakamura S and Cohen D (2012), '384 nm near-uv laser diode grown on a $(20\bar{2}1)$ semipolar relaxed AlGaN buffer layer', *Appl. Phys. Lett.,* **100**, 161107(1–4).

Hakki B and Paoli T (1975), 'Gain spectra in GaAs double-heterostructure injection lasers', *J. Appl. Phys.*, **46**, 1299–1306.

Hirai A, Jia Z, Schmidt M, Farrell R, DenBaars S, Nakamura S and Speck J (2007), 'Formation and reduction of pyramidal hillocks on m-plane $\{1\bar{1}00\}$ GaN, *Appl. Phys. Lett.*, **91**, 191906(1–3).

Hsu P, Kelchner K, Tyagi A, Farrell R, Haeger D, Fujito K, Ohta H, DenBaars S, Speck J and Nakamura S (2010), 'InGaN/GaN blue laser diode grown on semipolar $(30\bar{3}1)$ free-standing GaN substrates', *Appl. Phys. Express*, **3**, 052702(1–3).

Hsu P, Sonoda J, Kelchner K, Tyagi A, Farrell R, Haeger D, Young E, Romanov A, Fujito K, Ohta H, DenBaars S, Speck J and Nakamura S (2011a), 'Blue InGaN/GaN laser diodes grown on $(3\mathbf{031})$ free-standing GaN substrates', *Phys. Stat. Sol. (c)*, **8**, 2390–2392.

Hsu P, Young E, Romanov A, Fujito K, DenBaars S, Nakamura S and Speck J (2011b), 'Misfit dislocation formation via pre-existing threading dislocation glide in $(1\mathbf{1\bar{2}2})$ semipolar heteroepitaxy', *Appl. Phys. Lett.*, **99**, 081912(1–3).

Hsu P, Hardy M, Wu F, Koslow I, Young E, Romanov A, Fujito K, Feezell D, DenBaars S, Speck J and Nakamura S (2012), '444.9 nm semipolar $(1\mathbf{1\bar{2}2})$ laser diode grown on an intentionally stress relaxed InGaN waveguiding layer', *Appl. Phys. Lett.*, **100**, 021104(1–3).

Huang C, Lin Y, Tyagi A, Chakraborty A, Ohta H, Speck J, DenBaars S and Nakamura S (2010), 'Optical waveguide simulations for the optimization of InGaN-based green laser diodes', *J. Appl. Phys.*, **107**, 023101(1–7).

Kapolnek D, Keller S, Vetury R, Underwood R, Kozodoy P, DenBaars S and Mishra U (1997), 'Anisotropic epitaxial lateral growth in GaN selective area epitaxy', *Appl. Phys. Lett.*, **71**, 1204–1206.

Kasai J, Akimoto R, Kuwatsuka H, Hasama H, Ishikawa H, Fujisaki S, Kikawa T, Tanaka S, Tsuji S, Nakajima H, Tasai K, Takiguchi Y, Asatsuma T and Tamamura K (2010), '545 nm room-temperature continuous-wave operation of BeZnCdSe quantum-well green laser diodes with low threshold current density', *Appl. Phys. Express*, **3**, 091201(1–3).

Kelchner K, Lin Y, Hardy M, Huang C, Hsu P, Farrell R, Haeger D, Kuo H, Wu F, Fujito K, Cohen D, Chakraborty A, Ohta H, Speck J, Nakamura S and DenBaars S (2009), 'Nonpolar AlGaN-cladding-free blue laser diodes with InGaN waveguiding', *Appl. Phys. Express*, **2**, 071003(1–3).

Kelchner K, Farrell R, Lin Y, Hsu P, Hardy M, Wu F, Cohen D, Ohta H, Speck J, Nakamura S and DenBaars S (2010), 'Continuous-wave operation of pure blue AlGaN-cladding-free Nonpolar InGaN/GaN laser diodes', *Appl. Phys. Express*, **3**, 092103(1–3).

Kim Y, Kaneta A, Funato M, Kawakami Y, Kyono T, Ueno M and Nakamura T (2011), 'Optical gain spectroscopy of a semipolar $(2\mathbf{0\bar{2}1})$ -oriented green InGaN laser diode', *Appl. Phys. Express*, **4**, 052103(1–3).

Kioupakis M, Rinke P and Van de Walle C (2010), 'Determination of internal loss in nitride lasers from first principles', *Appl. Phys. Express*, **3**, 082101(1–3).

Kisin M, Brown R and El-Ghoroury H (2009), 'Optimum quantum well width for III-nitride nonpolar and semipolar laser diodes', *Appl. Phys. Lett.*, **94**, 021108(1–3).

Koda R, Kuramoto M, Ikeda M, Oki T, Watanabe H, Miyajima T, Kono S and Yokoyama H (2011), 'High peak power picoseconds optical pulse generation from GaInN semiconductor diode lasers', *Proc. SPIE-Novel In-Plane Semiconductor Lasers X*, **7953**, 79530J(1–7).

Kojima K, Funato M, Kawakami Y, Nagahama S, Mukai T, Braun H and Schwarz U (2006), 'Gain suppression phenomena observed in InxGa1-xN quantum well laser diodes emitting at 470 nm', *Appl. Phys. Lett.*, **89**, 241127(1–3).

Kojima K, Kamon H, Funato M and Kawakami Y (2008), 'Theorectical investigations on anisotropic optical properties in semipolar and nonpolar InGaN quantum wells, *Phys. Stat. Sol. (c)*, **5**, 3038–3041.

Kojima K, Funato M, Kawakami Y and Noda S (2010a), 'Valence band effective mass of non-c-plane nitride heterostructures', *J. Appl. Phys.*, **107**, 123105(1–7).

Kojima K, Yamaguchi A, Funato M, Kawakami Y and Noda S (2010b), 'Gain anisotropy analysis in green semipolar InGaN quantum wells with inhomogeneous broadening', *Jpn. J. Appl. Phys.*, **49**, 081001(1–4).

Kubota M, Okamoto K, Tanaka T and Ohta H (2007), 'Continuous-wave operation of blue laser diodes based on nonpolar m-plane gallium nitride', *Appl. Phys. Express*, **1**, 011102(1–3).

Kucharski R, Zajac M, Doradzinski R, Rudzinski M, Kurdrawiec and Dwilinski R (2012), 'Non-polar and semi-polar ammonothermal GaN substrates', *Semicond. Sci. Technol.*, **27**, 024007(1–15).

Kuramoto M, Sasaoka C, Futagawa N, Nido M and Yamaguchi A (2002), 'Reduction of internal loss and threshold current in a laser diode with a ridge by selective re-growth (RiS-LD)', *Phys. Stat. Sol. (a)*, **192**, 329–334.

Kyono T, Yoshizumi Y, Enya Y, Adachi M, Tokuyama S, Ueno M, Katayama K and Nakamura T (2010), 'Optical polarization characteristics of InGaN quantum wells for green laser diodes on semi-polar $(2\mathbf{0}\bar{\mathbf{2}}\mathbf{1})$ GaN substrates', *Appl. Phys. Express*, **3**, 011003(1–3).

Lin Y, Chakraborty A, Brinkley S, Kuo H, Melo T, Fujito K, Speck J, DenBaars S and Nakamura S (2009a), 'Characterization of blue-green m-plane InGaN light emitting diodes', *Appl. Phys. Lett.*, **94**, 261108(1–3).

Lin Y, Hardy M, Hsu P, Kelchner K, Huang C, Haeger D, Farrell R, Fujito K, Chakraborty A, Ohta H, Speck J, DenBaars S and Nakamura S (2009b), 'Blue-green InGaN/GaN laser diodes on miscut m-plane GaN substrate', *Appl. Phys. Express*, **2**, 082102(1–3).

Lin Y, Yamamoto S, Huang C, Hsiung C, Wu F, Fujito K, Ohta H, Speck J, DenBaars S and Nakamura S (2010), 'High quality InGaN/AlGaN multiple quantum wells for semipolar InGaN green laser diodes', *Appl. Phys. Express*, **3**, 082001(1–3).

Matthews J and Blakeslee A (1974), 'Defects in epitaxial multilayers', *J. Cryst. Growth*, **27**, 118–125.

Melo T, Hu Y, Weisbuch C, Schmidt M, David A, Ellis B, Poblenz C, Lin Y, Krames M and Raring J (2012), 'Gain comparison in polar and nonpolar/semipolar gallium-nitride-based laser diodes', *Semicond. Sci. Technol.*, **27**, 024015(1–6).

Miyoshi T, Masui S, Okada T, Yanamoto T, Kozaki T, Nagahama S and Mukai T (2009), '510–515 nm InGaN-based green laser diodes on c-plane GaN substrates', *Appl. Phys. Express*, **2**, 062201.

Morkoc H (2008a), *Handbook of Nitride Semiconductors and Devices Volume 1: Materials Properties, Physics, and Growth*, Weinheim, Wiley-VCH.

Morkoc H (2008b), *Handbook of Nitride Semiconductors and Devices Volume 2: Electronic and Optical Processes in Nitrides*, Weinheim, Wiley-VCH.

Morkoc H (2008c), *Handbook of Nitride Semiconductors and Devices Volume 3: GaN-Based Optical and Electronic Devices*, Weinheim, Wiley-VCH.

Motoki K, Okahisa T, Matsumoto N, Matsushima M, Kimura H, Kasai H, Takemoto K, Uematsu K, Hirano T, Nakayama M, Nakahata S, Ueno M, Hara D, Kumagi Y, Koukitu A and Seki H (2001), 'Preparation of large freestanding GaN substrates by hydride vapor phase epitaxy using GaAs as a starting substrate', *Jpn. J. Appl. Phys.*, **40**, L140–L143.

Muller J, Bruderl G, Schillgalies M, Tautz S, Dini D, Breidenassel A, Galler B and Lutgen S (2009), ‘Burn-in mechanism of 450 nm InGaN ridge laser test structures’, *Appl. Phys. Lett.*, **95**, 051104(1–3).

MRS Bulletin (2009), *Nonpolar and Semipolar Group III Nitride-Based Materials*, Cambridge, Cambridge University Press. Available from: http://journals.cambridge.org/action/displayIssue?jid=MRS&volumeId=34&seriesId=0&issueId=05 [March 15, 2012].

Nakamura S, Mukai T, Senoh M and Iwasa N (1992a), ‘Thermal annealing effects on p-type Mg-doped GaN films’, *Jpn. J. Appl. Phys.*, **31**, L139–L142.

Nakamura S, Iwasa N, Senoh M and Mukai T (1992b), ‘Hole compensation mechanism of p-type GaN films’, *Jpn. J. Appl. Phys.*, **31**, 1258–1266.

Nakamura S, Senoh M, Iwasa N and Nagahama S (1995), ‘High-brightness InGaN Blue, green and yellow light-emitting diodes with quantum well structures’, *Jpn. J. Appl. Phys.*, **34**, L797–L799.

Nakamura S, Senoh M, Nagahama S, Iwasa N, Yamada T, Matsushita T, Kiyoku H and Sugimoto Y (1996a), ‘InGaN-based multi-quantum-well-structure laser diodes’, *Jpn. J. Appl. Phys.*, **35**, L74–L76.

Nakamura S, Senoh M, Nagahama S, Iwasa N, Yamada T, Matsushita T, Sugimoto Y and Kiyoku H (1996b), ‘Room-temperature continuous-wave operation of InGaN multi-quantum-well structure laser diodes’, *Appl. Phys. Lett.*, **72**, 211–213.

Nakamura S, Senoh M, Nagahama S, Iwasa N, Yamada T, Matsushita T, Kiyoku H, Sugimoto Y, Kozaki T, Umemoto H, Sano M and Chocho K (1998), ‘InGaN/GaN/AlGaN-based laser diodes with modulation-doped strained-layer superlattices grown on an epitaxially laterally overgrown GaN substrate’, *Appl. Phys. Lett.*, **69**, 4056–4058.

Nakamura S (2000), ‘Development and future prospects of InGaN-based LEDs and LDs’, in Nakamura S and Chichibu S, *Introduction to Nitride Semiconductor Blue Lasers and Light Emitting Diodes*, Boca Raton, CRC Press, 317–350.

Nakamura S, Pearton S and Fasol G (2000), *The Blue Laser Diode*, Berlin, Springer.

Narukawa Y, Ichikawa M, Sanga D, Sano M and Mukai T (2010), ‘White light emitting diodes with super-high luminous efficacy’, *J. Phys. D: Appl. Phys.*, **43**, 354002(1–6).

Ng H (2002), ‘Molecular-beam epitaxy of GaN/AlxGa1-xN multiple quantum wells on R-plane $(10\bar{1}2)$ sapphire substrates’, *Appl. Phys. Lett.*, **80**, 4369–4371.

Northrup J (2009), ‘GaN and InGaN $(11\bar{2}2)$ surfaces: Group-III adlayers and indium incorporation’, *Appl. Phys. Lett.*, **95**, 133107(1–3).

Ohta M, Ohizumi Y, Hoshina Y, Tanaka T, Yabuki Y, Funato K, Tomiya S, Goto S and Ikeda M (2007), ‘High-power pure blue laser diodes’, *Phys. Stat. Sol. (a)*, **204**, 2068–2072.

Okamoto K, Ohta H, Chichibu S, Ichihara J and Takasu H (2007), ‘Continuous-wave operation of m-plane InGaN multiple quantum well laser diodes’, *Jpn. J. Appl. Phys.*, **46**, L187–L189.

Okamoto K, Tanaka T, Kubota M and Ohta H (2007), ‘Pure blue laser diodes based on nonpolar m-plane gallium nitride with InGaN waveguiding layers’, *Jpn. J. Appl. Phys.*, **46**, L820–L822.

Okamoto K, Tanaka T and Kubota M (2008), ‘High-efficiency continuous-wave operation of blue-green laser diodes based on nonpolar m-plane gallium nitride’, *Appl. Phys. Express*, **1**, 072201(1–3).

Okamoto K, Kashiwagi J, Tanaka T and Kubota M (2009), 'Nonpolar m-plane InGaN multiple quantum well laser diodes with a lasing wavelength of 499.8 nm', *Appl. Phys. Lett.*, **94**, 071105(1–3).

Park S (2003), 'Crystal orientation effects on many-body optical gain of wurtzite InGaN/GaN quantum well lasers', *Jpn. J. Appl. Phys.*, **42**, L170–L172.

Park S (2003), 'Effect of $(10\bar{1}0)$ crystal orientation on many-body optical gain of wurtzite InGaN/GaN quantum well, *J. Appl. Phys.*, **93**, 9665–9668.

Park S, Ahn D and Oh J (2008), 'Optical anisotropy in ultraviolet InGaN/GaN quantum-well light-emitting diodes with a general crystal orientation', *Appl. Phys. Lett.*, **92**, 011130(1–3).

Paskova T (2008), *Nitrides with Nonpolar Surfaces*, Weinheim, Wiley-VCH.

Paskova T and Evans K (2009), 'GaN substrates – progress, status, and prospects', *J. Sel, Topics Quantum Elec.*, **15**, 1041–1052.

Raring J, Schmidt M, Poblenz C, Chang Y, Mondry M, Li B, Iveland J, Walters B, Krames M, Craig R, Rudy P, Speck J, DenBaars S and Nakamura S (2010), 'High-efficiency blue and true-green-emitting laser diodes based on non-c-plane oriented GaN substrates', *Appl. Phys. Express*, **3**, 112101(1–3).

Raring J, Hall E, Schmidt M, Poblenz C, Li B, Pfister N, Kebort D, Chang Y, Feezell D, Craig R, Speck J, DenBaars S and Nakamura S (2010), 'State-of-the-art continuous-wave InGaN laser diodes in the violet, blue, and green wavelength regimes', *Proc. SPIE Laser Technology for Defense and Security VI*, **7686**, 76860L(1–10).

Raring J, Schmidt M, Poblenz C, Lin Y, Bai C, Rudy P, Speck J, DenBaars S and Nakamura S (2011), 'Recent progress in InGaN-based laser diodes fabricated on nonpolar/semipolar substrates', *IEEE Photonics Conference*, Arlington, VA.

Rass J, Wernicke T, Scheibenzuber W, Schwarz U, Kupec J, Witzigmann B, Vogt P, Einfeldt S, Weyers M and Kneissl M (2010), 'Polarization of eigenmodes in laser diode waveguides on semipolar and nonpolar GaN', *Phys. Stat. Sol. (RRL)*, **4**, 1–3.

Rass J, Wernicke T, Kremzow R, John W, Einfeldt S, Vogt P, Weyers M and Kneissl M (2010), 'Facet formation for laser diodes on nonpolar and semipolar GaN', *Phys. Stat. Sol. (a)*, **207**, 1361–1364.

Rass J, Wernicke T, Ploch S, Brendel M, Kruse A, Hangleiter A, Scheibenzuber W, Schwarz U, Weyers M and Kneissl M (2011), 'Polarization dependent study of gain anisotropy in semipolar InGaN lasers', *Appl. Phys. Lett.*, **99**, 171105(1–3).

Romanov A, Baker T, Nakamura S and Speck J (2006), 'Strain-induced polarization in wurtzite III-nitride semipolar layers', *J. Appl. Phys.,* **100**, 023522(1–10).

Romanov A, Young E, Wu F, Tyagi A, Gallinat C, Nakamura S, DenBaars S and Speck J (2011), 'Basal plane misfit dislocations and stress relaxation in III-nitride semipolar heteroepitaxy', *J. Appl. Phys.*, **109**, 103522(1–12).

Sato H, Tyagi A, Zhong H, Fellows N, Chung R, Saito M, Fujito K, Speck J, DenBaars S and Nakamura S (2007), 'High power and high efficiency green light emitting diode on free-standing semipolar $(11\bar{2}2)$ bulk GaN substrate', *Phys. Stat. Sol. (RRL),* **1**, 162–164.

Sato H, Chung R, Hirasawa H, Fellows N, Masui H, Wu F, Saito M, Fujito K, Speck J, DenBaars S and Nakamura S (2008), 'Optical properties of yellow light-emitting diodes grown on semipolar $(11\bar{2}2)$ bulk GaN substrates', *Appl. Phys. Lett.*, **92**, 221110(1–3).

Schade L, Schwarz U, Wernicke T, Weyers M and Kneissl M (2011), 'Impact of band structure and transition matrix elements on polarization properties of the photoluminescence of semipolar and nonpolar InGaN quantum wells', *Phys. Stat. Sol. B*, **248**, 638–646.

Scheibenzuber W, Schwarz U, Veprek R, Witzigmann B and Hangleiter A (2009), 'Calculation of optical eigenmodes and gain in semipolar and nonpolar InGaN/GaN laser diodes', *Phys. Rev. B*, **80**, 115320(1–16).

Scheibenzuber W, Schwarz U, Veprek R, Witzigmann B and Hangleiter A (2010), 'Optical anisotropy in semipolar (Al,In)GaN laser waveguides', *Phys. Stat. Sol. C*, **7**, 1925–1927.

Scheibenzuber W and Schwarz U (2011), 'Polarization switching of the optical gain in semipolar InGaN quantum wells', *Phys. Stat. Sol. B*, **248**, 647–651.

Schmidt M, Kim K, Sato H, Fellows N, Masui H, Nakamura S, DenBaars S and Speck J (2007), 'High power and high external efficiency m-plane InGaN light emitting diodes', *Jpn. J. Appl. Phys.*, **46**, L126–L128.

Schmidt M, Kim K, Farrell R, Feezell D, Cohen D, Saito M, Fujito K, Speck J, DenBaars S and Nakamura S (2007), 'Demonstration of nonpolar m-Plane InGaN/GaN laser diodes', *Jpn. J. Appl. Phys.*, **46**, L190–L191.

Schwarz U, Pindl M, Sturm E, Furitsch M, Leber A, Miller S, Lell A and Harle V (2005), 'Influence of ridge geometry on lateral mode stability of (Al,In)GaN laser diodes', *Phys. Stat. Sol. A*, **202**, 261–270.

Semiconductor Today (2009). Market for embedded pico-projector modules to exceed $1bn. Cheltenham: Juno Publishing and Media Solutions Ltd. Available from: http://www.semiconductor-today.com/news_items/2009/APRIL/INSTAT_080409.htm [March 8, 2012].

Semiconductor Today (2010). Green laser diode market $500m by 2016 as pico-projector market drives growth. Cheltenham: Juno Publishing and Media Solutions Ltd. Available from: http://www.semiconductor-today.com/news_items/2010/APRIL/YOLE_140410.htm [March 8, 2012].

Semiconductor Today (2010). SEI Announces first semipolar/ nonpolar GaN for green lasers. Cheltenham: Juno Publishing and Media Solutions Ltd. Available from: http://www.semiconductor-today.com/news_items/2010/NOV/SEI_241110.htm [March 19, 2012].

Shaklee K, Nahory R and Leheny R (1973), 'Optical gain in semiconductors', *J. Lumin.*, **7**, 284–309.

Shen H, Wraback M, Zhong H, Tyagi A, DenBaars S, Nakamura S and Speck J (2009), 'Determination of polarization field in a semipolar $(11\bar{2}2)$ InGaN/GaN single quantum well using Franz-Keldysh oscillations in electroreflectance', *Appl. Phys. Lett.*, **94**, 241906(1–3).

Sizov D, Bhat R, Napierala J, Gallinat C, Song K and Zah C (2009), '500-nm optical gain anisotropy of semipolar $(11\bar{2}2)$ InGaN quantum wells', *Appl. Phys. Express*, **2**, 071101(1–3).

Sizov D, Bhat R, Song K, Allen D, Paddock B, Coleman S, Hughes L and Zah C (2011), '60 mW pulsed and continuous wave operation of GaN-based semipolar green laser with characteristic temperature of 190 K', *Appl. Phys. Express*, **4**, 1021034(1–3).

Speck J and Chichibu S (2009), 'Nonpolar and semipolar group III nitride-based materials', *MRS Bull.,* **34**, 304–312.

Strauss U, Avramescu A, Lermer T, Queren D, Gomez- Iglesias A, Eichler C, Muller J, Bruderl G and Lutgen S (2011), 'Pros and cons of green InGaN laser on c-plane GaN', *Phys. Stat. Sol. (b)*, **248**, 652–657.

Takeuchi T, Sota S, Katsuragawa M, Komori M, Takeuchi H, Amano H and Akasaki I (1997), 'Quantum-confined stark effect due to piezoelectric fields in GaInN strained quantum wells', *Jpn. J. Appl. Phys.*, **36**, L382–L385.

Takeuchi T, Amano H and Akasaki I (2000), 'Theoretical study of orientation dependence of piezoelectric effects in wurtzite strained GaInN/GaN heterostructures and quantum wells', *Jpn. J. Appl. Phys.*, **39**, 413–416.

Tojyo T, Uchida S, Mizuno T, Asano T, Takeya M, Hino T, Kijima S, Goto S, Yabuki Y and Ikeda M (2002), 'High-power AlGaInN laser diodes with high kink level and low relative intensity noise', *Jpn. J. Appl. Phys.*, **41**, 1829–1833.

Tomiya T, Hino T, Goto S, Takeya M and Ikeda M (2004), 'Dislocation related issues in the degredation of GaN-based laser diodes', *J. Sel, Topics Quantum Elec.*, **10**, 1277–1286.

Tsuda Y, Ohta M, Vaccaro P, Ito S, Hirukawa S, Kawaguchi Y, Fujishiro Y, Takahira Y, Ueta Y, Takakura T and Yuasa T (2008), 'Blue laser diodes fabricated on m-plane GaN substrates', *Appl. Phys. Express*, **1**, 011104(1–3).

Tyagi A, Zhong H, Chung R, Feezell D, Saito M, Fujito K, Speck J, DenBaars S and Nakamura S (2007), 'Semipolar $(10\bar{1}\bar{1})$ InGaN/GaN laser diodes on bulk GaN substrates', *Jpn. J. Appl. Phys.*, **46**, L444–L445.

Tyagi A, Lin Y, Cohen D, Saito M, Fujito K, Speck J, DenBaars S and Nakamura S (2008), 'Stimulated emission at blue-green (480 nm) and green (514 nm) wavelengths from nonpolar (m-plane) and semipolar $(11\bar{2}2)$ InGaN multiple quantum well laser diode structures', *Appl. Phys. Express*, **1**, 091103(1–3).

Tyagi A, Wu F, Young E, Chakraborty A, Ohta H, Bhat R, Fujito K, DenBaars S, Nakamura S and Speck J (2009), 'Partial strain relaxation via misfit dislocation generation at heterointerfaces in (Al,In)GaN epitaxial layers grown on semipolar $(11\bar{2}2)$ GaN free standing substrates ', *Appl. Phys. Lett.*, **95**, 251905(1–3).

Uchida S, Takeya M, Ikeda S, Mizuno T, Fujimoto T, Matsumoto O, Goto S, Tojyo T and Ikeda M (2003), 'Recent progress in high-power blue-violet lasers', *IEEE J. Sel. Topics Quantum Elec.*, **9**, 1252–1259.

Ueda M, Funato M, Kawakami Y, Narukawa Y and Mukai T (2008), 'Polarization switching phenomena in semipolar $In_xGa_{1-x}N$/GaN quantum well active layers', *Phys. Rev. B*, **78**, 233303(1–4).

Usui A, Sunakawa H, Sakai A and Yamaguchi A (1997), 'Thick GaN epitaxial growth with low dislocation density by hydride vapor phase epitaxy', *Jpn. J. Appl. Phys.*, **36**, L899–L902.

Vurgaftman I and Meyer J (2007), ' Electron Bandstructure Calculations', in Piprek J, *Nitride Semiconductor Devices: Principles and Simulations*, Berlin, Wiley-VCH, 13–48.

Waltereit P, Brandt O, Trampert A, Grahn H, Menniger J, Ramsteiner M, Reiche M and Ploog K (2000), 'Nitride semiconductors free of electrostatic fields for efficient white light-emitting diodes', *Nature*, **406**, 865–867.

Wei Q, Li T, Wu Z and Ponce F (2010), 'In-plane polarization of GaN-based heterostructures with arbitrary crystal orientation', *Phys. Stat. Sol. (a)*, **207**, 2226–2232.

Wernicke T, Schade L, Netzel C, Rass J, Hoffmann V, Ploch S, Knauer A, Weyers M, Schwarz U and Kneissl M (2012), 'Indium incorporation and emission wavelength of polar, nonpolar and semipolar InGaN quantum wells', *Semicond. Sci. Technol.*, **27**, 024014(1–7).

Wu F, Lin Y, Chakraborty A, Ohta H, DenBaars S, Nakamura S and Speck J (2010), 'Stacking fault formation in the long wavelength InGaN/GaN multiple quantum wells grown on m-plane GaN', *Appl. Phys. Lett.*, **96**, 231912(1–3).

Wunderer T, Bruckner P, Hertkom J, Scholz F, Beirne G, Jetter M, Michler P, Feneberg M and Thonke K (2007), 'Time- and locally resolved photoluminescence of semipolar GaInN/GaN facet light emitting diodes', *Appl. Phys. Lett.*, **90**, 171123(1–3).

Yoshizumi Y, Adachi M, Enya Y, Kyono T, Tokuyama S, Sumitomo T, Akita K, Ikegami T, Ueno M, Katayama K and Nakamura T (2009), 'Continuous-wave operation of 520 nm green InGaN based laser diodes on semi-polar $(20\bar{2}1)$ GaN substrates', *Appl. Phys. Express*, **2**, 092101(1–3).

Young E, Wu F, Romanov A, Tyagi A, Gallinat C, DenBaars S, Nakamura S and Speck J (2010), 'Lattice tilt and misfit dislocations in $(11\bar{2}2)$ semipolar GaN heteroepitaxy', *Appl. Phys. Express*, **3**, 011004(1–3).

Young E, Romanov A, Gallinat C, Hirai A, Beltz G and Speck J (2010), 'Anisotropy of tensile stresses and cracking in nonbasal plane AlxGa1-xN/GaN heterostructures', *Appl. Phys. Lett.*, **96**, 041913(1–3).

Yu E (2003), 'Spontaneous and piezoelectric polarization in nitride heterostructures', in Yu E and Manasreh M, *III-V Nitride Semiconductors: Applications and Devices,* London, Taylor & Francis, 161–192.

Zhao Y, Tanaka S, Yan Q, Huang C, Chung R, Pan C, Fujito K, Feezell D, Van de Walle C, Speck J, DenBaars S and Nakamura S (2011), 'High optical polarization ratio from semipolar $(20\bar{2}\bar{1})$ blue-green InGaN/GaN light-emitting diodes', *Appl. Phys. Lett.*, **99**, 051109(1–3).

Zhao Y, Yan Q, Huang C, Huang S, Hsu P, Tanaka S, Pan C, Kawaguchi Y, Fujito K, Van de Walle C, Speck J, DenBaars S, Nakamura S and Feezell D (2012), 'Indium incorporation and emission properties of nonpolar and semipolar InGaN quantum wells', *Appl. Phys. Lett.*, **100**, 201108–201108-4.

Zheleva T, Nam O, Bremser M and Davis R (1997), 'Dislocation density reduction via lateral epitaxy in selectively grown GaN structures', *Appl. Phys. Lett.*, **71**, 2472–2474.

7

Advanced self-assembled indium arsenide (InAs) quantum-dot lasers

M. SUGAWARA, QD Laser Inc., Japan and The University
of Tokyo, Japan and Y. ARAKAWA and K. TANABE,
The University of Tokyo, Japan

DOI: 10.1533/9780857096401.2.272

Abstract: This chapter provides an account of the performance of advanced self-assembled InAs quantum-dot (QD) lasers, achieved through five years of collaborative research and development between QD Laser, Inc., Fujitsu Laboratories Ltd, and The University of Tokyo. The chapter first reviews state-of-the-art self-assembling growth methods for high-density and highly uniform InAs QDs, and the use of Fabry–Pérot (FP) and distributed-feedback (DFB) lasers for optical communications and for extremely-high-temperature environments. The chapter then introduces the activities and products of QD Laser, Inc., a start-up company based on GaAs-based semiconductor quantum-dot, quantum-well and DFB technologies, and silicon hybrid quantum-dot lasers for future optical interconnections.

Key words: quantum dot, self-assembled InAs quantum dot, quantum-dot laser, Fabry–Pérot (FP) laser, distributed-feedback (DFB) laser.

7.1 Introduction

Over the past five years, remarkable progress has been made in the area of self-assembled InAs quantum-dot lasers through industrial–academic collaboration between the start-up company QD Laser, Inc., Fujitsu Laboratories Ltd, and the University of Tokyo in Japan. Following the book entitled *Self-assembled InGaAs/GaAs Quantum Dots* (Sugawara, 1999) describing technology achievements in 1990s, this chapter reviews the state-of the-art for quantum-dot crystal growth technology and quantum-dot lasers, including mass production for the optical communication market.

Three-dimensional quantum confinement of electrons and holes in a quantum dot of size ranging up to ten nanometers causes the atom-like, or a series of a delta-function, density of states, which is believed to be essential to improved semiconductor laser performance. This was first proposed by Arakawa and Sakaki (1982). Semiconductor lasers with QDs

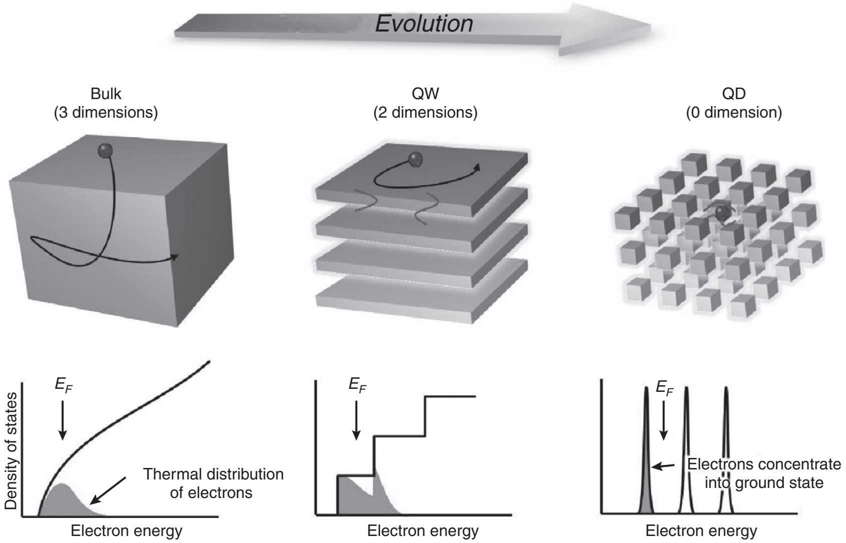
Evolution
Bulk
(3 dimensions)
QW
(2 dimensions)
QD
(0 dimension)
E_F
Density of states
Thermal distribution
of electrons
Electron energy
E_F
Electron energy
E_F
Electrons concentrate
into ground state
Electron energy

7.1 Active regions in semiconductor lasers and the electron density of states with the dimension of quantum confinement. QW, quantum well. E_F, Fermi level.

as the active region were expected to exhibit ultralow threshold current, temperature-insensitive operation, narrow spectrum line width, and large modulation bandwidth (Arakawa *et al.*, 1983; Asada *et al.*, 1986). Figure 7.1 shows how active regions in semiconductor lasers and the electron density of states vary with the dimensionality of quantum confinement. By the use of quantum-confined structures, freedom of carrier motion is reduced to limited directions, leading to complete carrier confinement in the quantum dot. The peculiar electronic structure of QDs prevents carrier distribution from thermal broadening, resulting in a narrow and discrete optical gain spectrum whose width is ideally limited to homogeneous broadening of 5–20 meV due to intraband scattering (Sugawara *et al.*, 2005). This gain property is the basis that gives quantum-dot lasers their advantage over conventional lasers.

A key challenge has been in the development of fabrication technology of highly uniform and high-density QDs to realize narrow optical gain spectrum with sufficient magnitude. Numerous efforts have been made, based primarily on microscopic lateral patterning and regrowth of epitaxial layers (Petroff *et al.*, 1984; Chang *et al.*, 1985; Fukui and Saito, 1987; Miyamoto *et al.*, 1987; Kapon *et al.*, 1989; Kash *et al.*, 1991; Nakamura *et al.*, 1991). However, these artificial structures did not take full advantage of engineered energy states, with drawbacks such as larger size, low density, and size irregularity, resulting in insufficient optical properties.

The advent of self-assembled QDs opened the way for quantum-dot lasers, owing to their uniformity, high-density, and dislocation-free crystal quality. The real breakthrough was that self-assembled QDs emit light of 1.3 μm (Mukai *et al*., 1995), which is the zero-dispersive wavelength of 1.3 silica optical fiber used in optical transmission. This was followed by the quantum-dot lasers at 1.3 μm (Huffaker *et al*., 1998; Mukai *et al*., 1999) in the late 1990s, and intensive R&D for their practical application. One of the most exciting milestones of the R&D was the temperature-insensitive 1.3 μm FP quantum-dot lasers operating at 10 Gbits/s (Otsubo *et al*., 2004), which were realized by the high gain of ten quantum-dot layers in the active region to extend the modulation bandwidth (Ishida *et al*., 2004), and *p*-type doping to make the lasers immune to temperature (Shchekin and Deppe, 2002).

This book describes the remarkable progress of self-assembled InAs quantum-dot lasers over the past five years following the above-mentioned R&D milestones. Section 7.2 provides the state-of-the-art growth technology of high-density and highly uniform InAs QDs. Section 7.3 reviews quantum-dot FP and DFB lasers for optical communication. Section 7.4 focuses on extremely-high-temperature operation of quantum-dot FP and DFB lasers for high–harsh temperature environments. These lasers are based on the quantum-dot wafer technology of Section 7.2. Section 7.5 introduces the activities and products of QD Laser, Inc., a start-up company based on GaAs-based semiconductor quantum-dot, quantum-well, and DFB technologies. Section 7.6 presents silicon hybrid quantum-dot lasers for future optical interconnections. Section 7.7 summarizes this chapter and describes the challenges for further development of self-assembled quantum-dot lasers.

7.2 High-density and highly uniform InAs quantum dots

This section reviews high-density, highly uniform InAs QDs in the light of their self-assembly for optical devices, the roadmap for their properties (in terms of increasing optical gain) and the use of high-density QDs. It then considers highly uniform QD structures for sharpening optical gain, the future direction for QD-based optical devices, and finally provides a summary.

7.2.1 Self-assembled quantum dots for optical devices

For realizing superior optical devices, such as laser diodes with semiconductor nanostructures, it is important to form high-density and highly

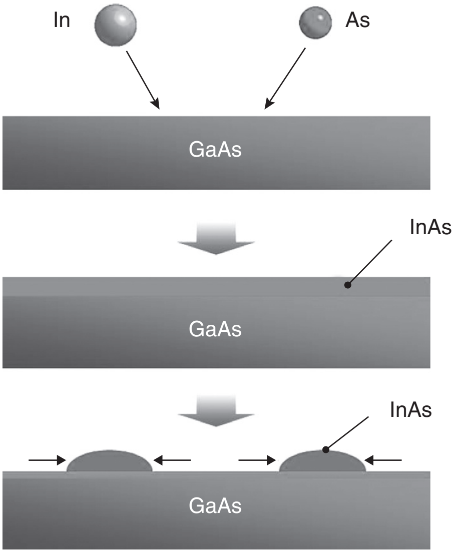

7.2 A schematic illustration of InAs QD formation on GaAs surface.

uniform structures with sufficient optical quality. In the very early stages of forming two- or three-dimensional quantum nanostructures (so-called quantum wires or QDs, many techniques were proposed and experimentally carried out, as cited in Section 7.1. Now it is almost conclusive that the self-assembling technique is the most suitable way to realize high-density and high-optical quality QDs for optical devices (Sugawara, 1999). By combining carrier-conducting layers, electron/hole injection as well as current generation can be realized with those QDs, which means that the QDs can emit light as well as detect photons.

In the self-assembling formation method, strain-driven formation of nanostructures is utilized. It is known as Stranski–Krastanow growth mode of semiconductor growth, such as InAs growth on GaAs, as shown in Fig. 7.2 (Stranski and Krastanow, 1939). In the case of molecular beam epitaxy (MBE), an indium molecular beam is supplied on a GaAs surface with an arsenic molecular beam. After forming about one monolayer of InAs on GaAs at the first stage to reduce the surface energy (InAs has lower surface energy compared to GaAs), InAs island-like structures start to form after a certain supply of In. This phenomenon was first seen as a way to realize small InAs islands (Goldstein *et al.*, 1985). Those InAs islands behave as QDs, and they have been used for active layers of semiconductor lasers (Shoji *et al.*, 1996). Because of their small size, the carrier confinement energy is almost comparable to room-temperature thermal energy

Table 7.1 Roadmap to show how the quantum-dot formation methods improve to increase peak optical gain in laser diodes

	Recently reported uniform QD structure	First step to increase gain	Second step to increase gain
QD density	Low	High	High
Inhomogeneous broadening	Narrow (around 25 meV or less)	Mid (around 35 meV)	Narrow (around 25 meV)
Schematic gain curve	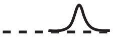	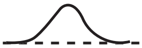	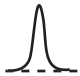
Peak gain	Low	Mid	High
	Conventional reports with uniform QDs	Apply growth sequence for high-density	Improved growth sequence for better uniformity

and the device characteristics are expected to be improved as predicted by Arakawa and Sakaki (1982) even at or above room temperature.

7.2.2 Roadmap of quantum-dot properties in view of increasing optical gain

Table 7.1 shows how the quantum-dot formation methods improve to increase peak optical gain in laser diodes. Some reports showed that significantly narrow photoluminescence (PL) full-width at half-maximum (FWHM) (or 'linewidth') can be realized in self-assembly grown QDs. For example, 21 meV linewidth at room temperature (Nishi *et al.*, 1999) and a linewidth of 18.6 meV at 14 K (Yamaguchi *et al.*, 2000) have been reported. From this, it can be seen that QD uniformity is drastically improved compared to the QDs reported in early 1990s where a low temperature PL linewidth was about 60 meV (Leonard *et al.*, 1993, 1994). However, increasing QD density is typically difficult while maintaining size uniformity. Then the real peak optical gain was not so different compared to conventional QDs with less-uniformity but rather higher density, which is shown to the right of the column in the table. So, the objective was to increase QD density (lateral density as well as layer numbers) even though the size uniformity may not be ideal. It is shown as the first step in the table. Moderate optical gain is expected to be realized by this high-density but a rather broadened size distribution (in Table 7.1, typical PL linewidth of 35 meV is shown as an example).

The next step was to reduce the size distribution for narrow PL linewidth, keeping almost the same QD density and layer numbers. This

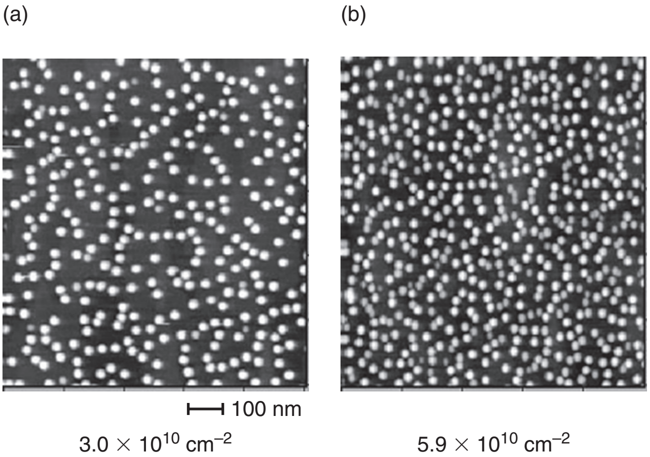
(a)
(b)
100 nm
3.0×10^{10} cm^{-2}
5.9×10^{10} cm^{-2}

7.3 Atomic force microscope images of 1 × 1 micrometer scale InAs QDs on GaAs. After growth sequence improvements, the dot density is almost doubled (from (a) before optimization to (b) optimized for high-density).

advanced QD formation method was studied and experimentally confirmed where high-optical gain was realized for high-temperature laser operation (Kageyama *et al.*, 2011). In the far right side of the table, this second step to increase gain is summarized, with the desirable linewidth of about 25 meV with high quantum-dot density.

7.2.3 High-density quantum dots for increased optical gain

As the first step to increase optical gain, as shown in Table 7.1, growth conditions for obtaining InAs QDs were improved. The structural properties of InAs QDs grown on GaAs (100) surface by MBE are characterized by atomic force microscope (AFM). Figure 7.3 shows typical AFM images of the grown structures. The AFM image shown in Fig. 7.3a corresponds to the InAs QD structures formed by a conventional growth sequence. The density was about 3×10^{10} cm^{-2}. Judging from the individual QD image, the typical in-plane size (diameter) is about 20 nm and the typical height is about 7 nm. Those values are close to the parameters listed in literatures (Nakata *et al.*, 2000; Kaizu *et al.*, 2007). In order to increase the QD density, the growth parameters were intensively optimized. Although it was known that high-density QDs can be formed by alternate beam supply in MBE growth (Saito *et al.*, 1999), the usual growth sequence of simultaneous beam

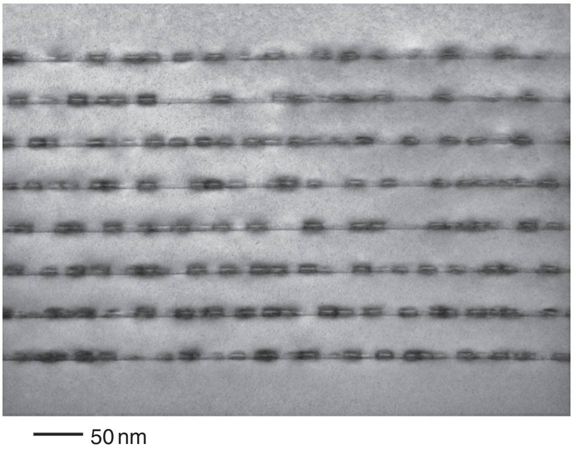

7.4 TEM image of eight QD layers. No misfit dislocation was observed within this observation area.

supply was used and the growth temperatures, supplied In and As beam flux intensities, and many other parameters were varied over a wide range and precisely optimized for higher density. As a result, the QD density was increased up to 5.9×10^{10} cm^{-2} with almost identical QD dimensions to using standard MBE growth procedures (Tanaka *et al.*, 2009, 2010; Takada *et al.*, 2010). This high-density QD structure is shown in Fig. 7.3b. In the usual InAs QD formation, some giant dot structure also grows, which means some incoherent giant island is generated with probably misfit dislocations. Such giant dots may act as non-radiative recombination centers. In our observation, even though the InAs QD density is doubled, increase of the giant dot formation was suppressed and the giant dots were not observed in the scale of the AFM image (Fig. 7.3b) because of about two orders of magnitude lower density of the giant dots compared to usual QDs through optimized growth conditions. By using those high-density QDs, the optical gain was increased from that of conventional QDs.

In order to increase the total QD number, multi-stacking is also very important. In the previous report of the high-density QDs with alternate beam supply (Saito *et al.*, 1999), the total layer number was three. Here the total layer number was increased up to eight with the high-density InAs QDs. In Fig. 7.4, the transmission electron microscope (TEM) image of eight QD layers is depicted. Even though the total InAs QD number was increased, no misfit dislocation was observed within this observation area. Also, it should be noted that the morphology of QDs in the upper most layer is similar to the QD structure at the bottom layer. So the growth sequence of InAs QD formation was optimized not only in the QD formation but also during the intermediate layer growth.

7.2.4 Highly uniform quantum-dot structure for sharpening the optical gain

After realizing the high-density QDs with multi-stacked layers, it became rather difficult to further increase total optical gain, as it relates directly to the total number of QDs. So as shown in the second step in Table 7.1, the next challenge was to increase peak optical gain. It was carried out by improving growth sequence for better uniformity.

As described above, growth sequence and condition during InAs growth was first optimized. This resulted in high-density QDs with small size as shown in Fig. 7.3b. There were several reports of obtaining uniform QDs possessing very narrow PL linewidth. By increasing surface adatom mobility with smaller growth rate (Yamaguchi *et al*., 2000), the QD size was usually found to have enough uniformity to realize less than 25-meV PL linewidth. In our experiments, growth conditions and procedures were optimized so as to realize this growth condition with high-surface adatom mobility even though the growth rate was not much changed, resulting in highly uniform, high-density QDs on a GaAs surface with intense PL intensity at room temperature.

Despite the uniform InAs QDs on GaAs observed by AFM measurements, the PL linewidth was not so much changed. Then it was suspected that during the dot overgrowth, the uniformity of QD size and shape were deteriorated. Such degradation was known to be suppressed by introducing an InGaAs cover layer on InAs (Nishi *et al*., 1999), which could also relieve the strain of InAs islands and make the emission of longer wavelength. So, this InGaAs layer was denoted the strain reducing layer (SRL). In our recent growths, even without InGaAs SRL and just covering by GaAs, the original uniformity of InAs QDs was maintained by optimizing the covering layer growth condition so as not to enhance the In out-diffusion. Then, it is believed, the original InAs QD uniformity observed by AFM was kept unchanged even after being buried by GaAs or InGaAs. This situation holds even after growing several layers. Such a situation can be proved through PL observations, which drastically reflects the effect of size uniformity. Figure 7.5 shows the typical PL spectra from high-density QDs before and after our modifications for better uniformity. The linewidth was about 38 meV before the modification but it was reduced to about 24 meV. Note that this reduction was achieved without changing the QD density and the layer numbers. Thus it was found that QDs could both have sufficient size and shape uniformity even after covering to obtain narrow PL linewidth, as well as high-density to realize high-optical gain. So, as can be seen in Fig. 7.5, the peak optical gain can be increased by sharpening the PL linewidth. This situation is ideal for achieving the predicted improvements in QD lasers, as the InAs QDs are high-density and highly uniform with high-optical quality.

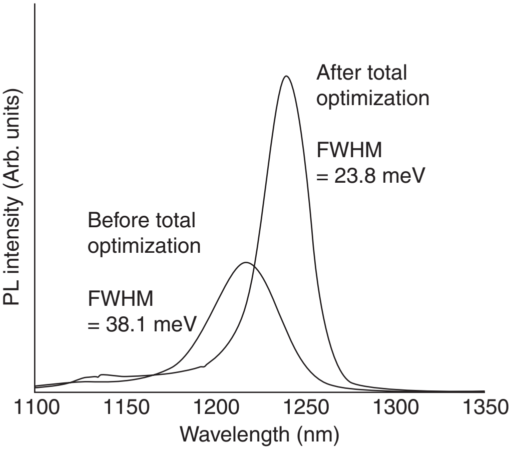

7.5 Photoluminescence characterization of high-density QDs. 'After total optimization' corresponds to the situation with improved uniformity by optimized QD and barrier growth sequence.

From the view point of laser application, the lasing wavelengths should be controlled according to the laser applications. PL emission wavelengths can be controlled by several methods, and among them, controlling with SRL was known to be very simple as the QDs should not be changed. Actually, the PL peak of InAs QDs was far from the original, unstrained InAs bulk band gap energy. The strain that originates from lattice mismatch between InAs and GaAs increases InAs QDs band gap energy, and causes the emission of a much shorter wavelength. By adopting InGaAs SRL on InAs, the compressive strain of InAs QDs can be partly relieved and the band gap of InAs QDs can become smaller. Then the emission wavelength can be tuned by controlling the SRL thickness and compositions. Such experiments were performed with rather small-density QDs (Nishi *et al.*, 1999). So, it was not obvious whether such control by SRL could be adopted in the recent high-density, highly uniform QDs. The experimental results are shown in Fig. 7.6. $In_{0.13}Ga_{0.87}As$ SRLs were grown on InAs QDs of differing thickness. As can be seen, the PL shapes are almost the same, but peak positions change according to the SRL thickness. It changed from about 1240 nm to 1290 nm (SRL: 0 to 3.5 nm). Thus, laser applications of around 1.3 μm wavelength can be covered by QDs with different SRL thicknesses.

7.2.5 Future directions for achieving novel optical devices with quantum dots

For future improvements of laser characteristics, the basic properties of InAs QDs should be improved. One direction is to improve uniformity to reduce PL linewidth. This would be necessary to further increase the peak gain. After

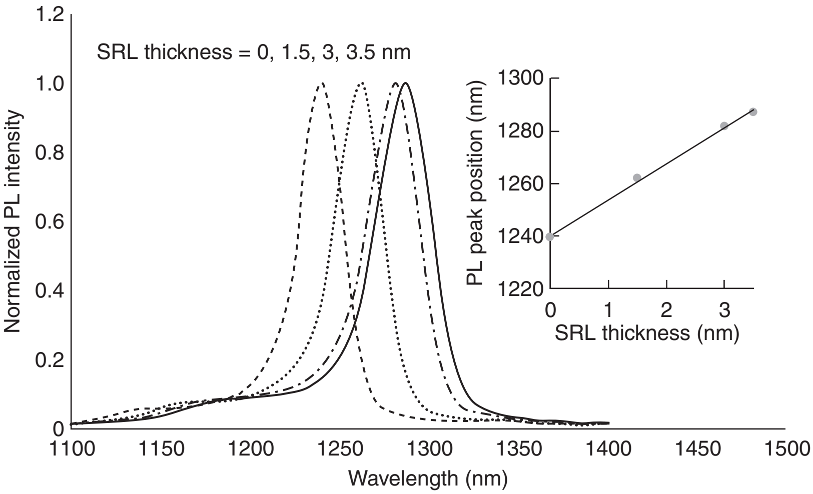

7.6 Normalized photoluminescence spectra measured under different $In_{0.13}Ga_{0.87}As$ SRL thicknesses (nm) with identical InAs quantum dots. Peak position changes according to SRL thickness as shown in the inset.

achieving ultimate uniformity of the QDs, the peak optical gain becomes maximum at a certain QD density, resulting in the theoretically predicted ideal laser characteristics of the lowest threshold and highest efficiency.

Another direction is to increase total optical gain while keeping a certain gain width. This is effective for realizing DFB lasers with a QD active layer. The lasing wavelength of a DFB laser is determined by the refractive index profile of the periodical grating structure. As the temperature dependence of the reflective index is much smaller compared to the gain peak change, the optical gain should have a certain broadening in order to cover the whole DFB wavelength under wide temperature range. Then the QD active layer should have enough peak gain as well as certain gain width, corresponding to a certain distribution of QD sizes. There, the total QD number should be increased by increasing QD density and layer numbers. By applying this direction, QD DFB lasers should be realizable with high-efficiency.

7.2.6 Summary

Advanced QDs are realized with high-density and high-uniformity. Those QDs can be adopted as laser active materials because of their good optical properties. The areal density had been doubled by improving the QD formation conditions, and uniformity was further improved by optimizing whole growth sequences, such as state-of-the-art MBE technology. As a result, uniform InAs QDs whose PL linewidth is less than 25 meV were realized with high-density of up to 5.9×10^{10} cm^{-2} on GaAs. Those improved

QDs have been used for novel QD lasers and approved laser characteristics improvement. Also, future directions of QD formation way are discussed to realize ultimate improvements in usual FP and DFB lasers.

7.3 Quantum-dot Fabry–Pérot (FP) and distributed-feedback (DFB) lasers for optical communication

Optical communication, which started its commercial use over telephone networks in the 1980s, has reached to individual users in terms of fiber to the home (FTTH) and optical local area networks (LANs). While FTTH has been introduced in many countries as access systems to households or buildings, optical LANs connect personal computers in offices. Quantum dot lasers are best suited to these environments with compactness, low-power consumption, and low cost. This is due to their excellent temperature stability of laser output characteristics and high temperature durability, which enables simplified laser control circuits as well as easy evaluation and adjustment of laser modules.

Optical interconnections between integrated circuits in the computers, that is, CPUs and memories, are expected to break the limit of electrical interconnections in data rate and capacity. This notion has driven many research institutes into study of a future data bus architecture. Temperature-stable and low-power-consumption QD lasers are promising light sources for this optical interconnection with inevitable high-temperature environments due to the heat of integrated circuits.

This section introduces state-of-the-art QD FP and DFB lasers for optical communication and interconnections, based on the advanced self-assembled QDs shown in Section 7.2. Before moving on to QD lasers, the current state of semiconductor lasers for optical communication is briefly reviewed.

7.3.1 Current trends in semiconductor lasers for optical communication

In the optical communication markets, the last few years have marked rapid growth of FTTH in China with the Gigabit Ethernet Passive Optical Network (GEPON) and Gigabit Passive Optical Network (GPON) for broadband services. The mainland of China has already become the center of production, sales, and procurement in this industry. Other major trends are optical data transmission among wireless base stations of LTE (Long Term Evolution)-based services in China, and fiber channels in data centers of North America.

Semiconductor lasers at a wavelength of 1.3 μm play a major role in FTTH and LANs in terms of volume as the best wavelength choice for short-distance signal transmission. An optical communication industry report (Fuji Chimera Research Institute, 2010) shows the shipment of FP lasers at 155/622 Mb/s at 6.5 million units, FP lasers over 1.25 Gb/s at 24.5 million, DFB lasers less than 2.5 Gb/s at 10.0 million, and DFB lasers over 10 Gb/s 1.9 million worldwide in 2010. All these lasers, 42.9 million in total, were InP-based quantum-well lasers.

7.3.2 Quantum-dot FP lasers

Quantum dots, utilized as the active medium in semiconductor lasers, are expected to improve lasing characteristics, compared with bulk or quantum-well (QW) devices, resulting from three-dimensional carrier confinement (Arakawa and Sakaki, 1982). In recent years, low threshold current density, excellent temperature stability, and low chirp have been reported, as predicted a couple of decades ago. As opposed to the theory, however, a high-modulation bandwidth has been difficult to attain in QD lasers, which is attributed to their finite intraband relaxation time and the difficulty in reducing photon lifetime due to insufficient optical gain: these bandwidth limiting effects are characterized in the K-factor (Ishida *et al.*, 2004).

Here, we describe a design principle to realize high-speed modulation in QD lasers. Based on the design as well as the high-density dot technology, we demonstrate modulation bandwidth up to 11 GHz, and show 25 Gb/s direct modulation in 1.3 μm InAs/GaAs QD lasers (Tanaka *et al.*, 2010).

Laser design for high-speed modulation

The response function of the small-signal modulation of semiconductor lasers is given by the following simple equation of Chuang (1995):

$$M(\omega) \propto \frac{\omega_r^4}{\left(\omega^2 - \omega_r^2\right)^2 + \omega^2 \gamma^2} \tag{7.1}$$

where $\omega_r = 2\pi f_r$ is the relaxation oscillation frequency, and γ is the damping factor given by:

$$\gamma = K f_r^2 + \tau^{-1} \tag{7.2}$$

with the K-factor and the carrier recombination lifetime of τ.

As the optical power inside the cavity increases the relaxation oscillation frequency increases, resulting in the extension of the modulation bandwidth according to Equation [7.1]. However, there is a maximum 3-dB bandwidth due to damping determined by the K-factor as (Ishida *et al.*, 2007):

$$f_{3\mathrm{dB}} = \frac{1}{2\pi}\sqrt{\frac{(1-T/\tau)+\sqrt{(1-T/\tau)^2+T^2/\tau^2}}{T^2}} \tag{7.3}$$

with

$$T = K / 4\pi^2 \tag{7.4}$$

Here, $f_{3\text{dB}} = \omega_{3\text{dB}} / 2\pi$, and $\omega_{3\text{dB}}$ gives the 3-dB reduction of Equation [7.1] as ω increases. In the limit of $\tau^{-1} \to 0$, Equation [7.3] reduces to the well-known equation of Chuang (1995):

$$f_{3\text{dB}} = 2^{3/2}\,\pi / K. \tag{7.5}$$

Based on a set of simple rate equations for the QD laser active region, taking into account the time dependence of carrier density in the wetting layer and in the ground state as well as that of the photon density in the cavity, we derived an expression of Ishida *et al.* (2004):

$$K = 4\pi^2 \left(\tau_p + \tau_{\text{cap}}\right), \tag{7.6}$$

where τ_p is the cavity photon lifetime,

$$\tau_{\text{cap}} = \frac{\tau_0}{1 - p} \tag{7.7}$$

τ_{cap} is the carrier capture time from the wetting layer to the ground state, and τ_0 is the carrier capture time when $P = 0$. Equations [7.5] and [7.6] tell us that the 3-dB bandwidth of the laser is determined by the sum of the photon lifetime and the carrier capture time. The *K*-factor of Equation [7.5] is a function of the photon lifetime and has its minimum at an optimum photon lifetime, giving the maximum modulation bandwidth. This is because, as the photon lifetime decreases, the threshold modal gain given by:

$$\Gamma g_{\text{th}} = \frac{n_g}{c\tau_p} \tag{7.8}$$

increases, resulting in the increase of the threshold occupation probability of:

$$P = P_{\text{th}} = \left[g_{\text{th}} / g_{\max} + 1\right] / 2 \tag{7.9}$$

as derived from a simple gain equation of $g = g_{\max}(2P-1)$, and thus, the capture time of τ_{cap} given by Equation [7.7]. In Equation [7.8], Γ is the optical confinement factor and n_g is the group-velocity refractive index. From Equations [7.6–7.9], the *K*-factor takes its minimum as:

$$\begin{aligned} T_{\min} &= K_{\min} / 4\pi^2 \\ &= 2\tau_0 + \frac{1}{\upsilon_g \Gamma g_{\max}} + 2\sqrt{\frac{2\tau_0}{\upsilon_g \Gamma g_{\max}}} \end{aligned} \tag{7.10}$$

at the photon lifetime of:

$$\tau_p = \frac{1}{\upsilon_g \Gamma g_{\max}} + \sqrt{\frac{2\tau_0}{\upsilon_g \Gamma g_{\max}}} \qquad [7.11]$$

where $\upsilon_g = c/n_g$ is the group velocity. The *K*-factor limited maximum bandwidth is given by Equations [7.3] and [7.10], or, given in the limit of $\tau^{-1} \to 0$ by:

$$f_{3\mathrm{dB}}^{\max} = \left[\sqrt{2}\pi \left(2\tau_0 + \frac{1}{\upsilon_g \Gamma g_{\max}} + 2\sqrt{\frac{2\tau_0}{\upsilon_g \Gamma g_{\max}}} \right) \right]^{-1}. \qquad [7.12]$$

Note that the maximum modulation bandwidth of QW lasers is usually limited by relaxation oscillation frequency, except for RC time constant. On the other hand, the maximum modulation bandwidth of QD lasers is limited by the strong damping determined by the *K*-factor. Equation [7.12] tells us that the way to extend the modulation bandwidth is two-fold: one is to increase the gain maximum, and the other is to reduce the carrier relaxation time.

Lasing spectrum

FP lasers show a multimode broad longitudinal lasing spectrum because its cavity has no mode-selective feedback mechanism such as DFB grating and DBR. In spite of this multimode spectrum, the wavelength of 1.3 μm allows the FP lasers to work in the optical fiber communication due to zero wavelength dispersion as long as the spectrum width is less than a few nm.

The lasing spectrum of QD FP lasers and its physics have been intensively studied by Sugawara *et al.* (1999, 2000, 2005). In continuous-wave lasing experiments, while lasing occurred with a narrow-line, including a few longitudinal modes around the top of the ground state at room temperature, spectra at 80 K showed broadband lasing emission over a range of 50–60 nm. This is in contrast to QW lasers, where the lasing spectrum broadens as the temperature increases, primarily due to thermal broadening of optical gain.

A theoretical model based on a coupled set of rate equations taking into account the spatial localization and resonant energy distribution of QDs and a series of longitudinal cavity modes clearly explained the measured temperature dependence of lasing spectra in terms of homogeneous broadening of optical gain of a single QD (Sugawara, 2000). The agreement between the experiments and the theory was excellent. Dots with different energies start lasing independently at 80 K due to their spatial localization as well as a δ-function-like gain, leading to broadband lasing emission. At room temperature, the dot ensemble in the cavity contributes to narrow-line lasing

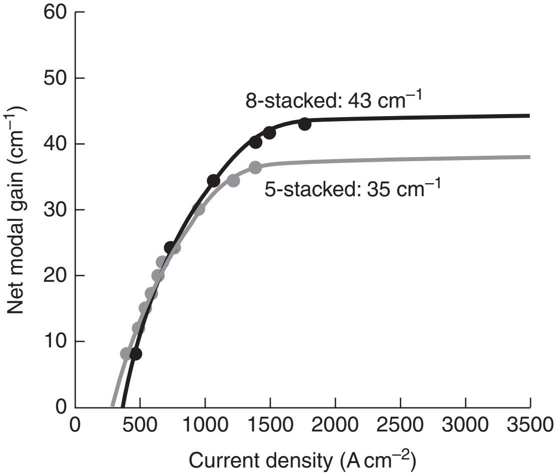

7.7 Net modal gain curves as a function of the current density for five-stacked QD layers and eight-stacked QD layers evaluated by broad-area laser measurements. Solid circles are measured gain and solid lines are guides.

collectively via the homogeneous broadening of optical gain: the side modes are suppressed because carriers are extracted to the central lasing modes by the stimulated emission, leading to a narrow lasing line. It can be said that spatially isolated dots with different resonant energies interact each other through stimulated emission process. The magnitude of the homogeneous broadening was found to reach about 20 meV at room temperature (Sugawara, 2001, 2005), which is comparable to inhomogeneous broadening due to size distribution.

This collective lasing mechanism not only clarifies the lasing process of the QD laser but also plays a major role in its application to fiber communication. Mass produced QD lasers by QD Laser, Inc. (see Section 7.5) have a lasing spectrum width of less than 3 nm above room temperature, which meets the optical communication standard.

Optical gain

Based on the high-density technology described in Section 7.2 for high-density with mid inhomogeneous broadening, we grew the active layers of eight-stacked QD layers with areal density of 5.9×10^{10} cm^{-2}. The GaAs barrier layers were partially *p*-type doped. The active layers were sandwiched between the *n*-type $Al_{0.4}Ga_{0.6}As$ lower cladding layer and the *p*-type $Al_{0.4}Ga_{0.6}As$ upper cladding layer. Figure 7.7 compares net modal gain, that is, gain minus internal loss, curves as a function of the current density for five-stacked QD layers and eight-stacked QD layers evaluated

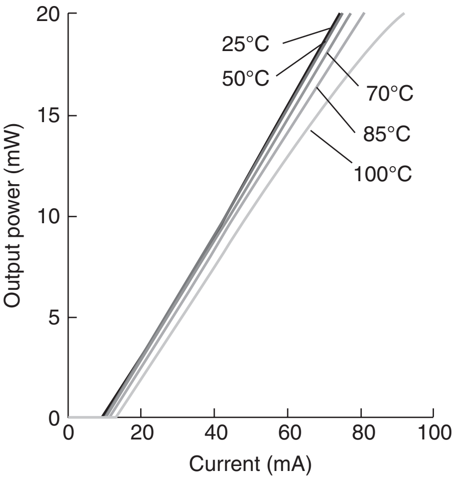

7.8 Light-current characteristics of the high-mesa waveguide FP laser in the continuous-wave condition. The temperature ranged from 25°C to 100°C.

by broad-area laser measurements. The net maximum modal gain of the eight-stacked QD lasers reached to 43 cm^{-1}.

Light-current and modulation characteristics

Using the eight-stacked high-density QD layers, we fabricated high-mesa waveguide FP lasers with the mesa-width of 3 μm. With the mirror-loss of 16 cm^{-1} to minimize the K-factor of Equation [7.6], we designed the laser to have a cavity length of 400 μm and mirror reflectivity of 30% and 95%. The light-current characteristics of the fabricated device in the continuous-wave condition are shown in Fig. 7.8. The temperature ranged from 25 to 100ºC. Threshold current was approximately 10 mA at room temperature and remained unchanged at temperatures up to 85ºC, followed by a slight increase at 100ºC. The characteristic temperature of the threshold current was 625 K. Note that we achieved sufficient output power of more than 20 mW even at 100ºC. The slope efficiency at room temperature was 0.3 W/A, with a degradation of –0.4 dB at 85ºC.

Figure 7.9 gives the small-signal modulation characteristics for the fabricated laser. It is seen that the modulation bandwidth is extended with an increase in injection currents. At 109 mA, the 3dB-down modulation bandwidth reached 11 GHz. We fitted the measurement results with theoretical curves, achieving the relaxation oscillation frequency of 9.8 GHz, and the K-factor of 0.63 ns. We attribute these improved modulation bandwidth to the increased modal gain by stacking high-density QD layers.

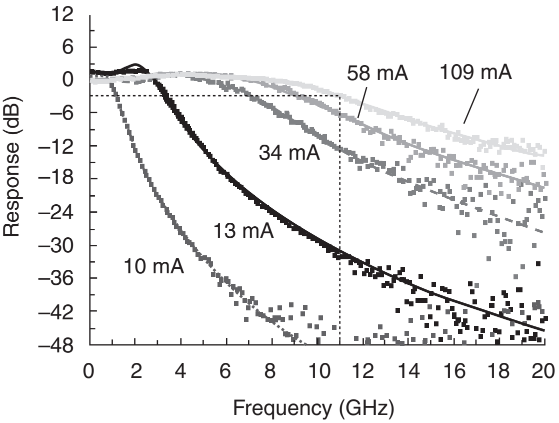

7.9 Small-signal modulation characteristics.

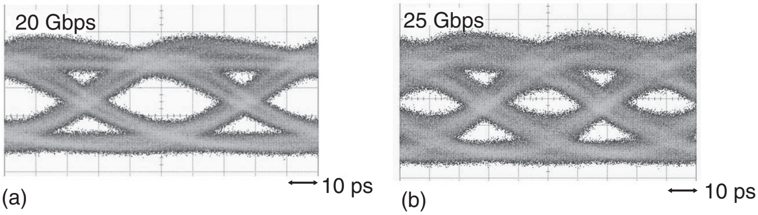

7.10 Room-temperature eye diagrams at 20 and 25 Gbps modulations.

We next confirmed the room-temperature eye diagrams at 20 and 25 Gb/s modulations using a non-return-to-zero2^{31}–1 pseudo-random binary sequence pattern. For both modulation speeds, the bias currents were set at 100 mA. The modulation voltages were 4 Vp-p. We obtained clear eye-openings having a dynamic extinction ratio (ER) of 3.8 dB at 20 Gb/sand 3.5 dB at 25 Gb/s, as shown in Fig. 7.10.

The bandwidth of 11 GHz and 25-Gb/s direct modulation are the fastest lasing modulation in 1.3 μm QD lasers, to our knowledge. Further improvements will be made possible not only by the increase in the optical gain but also by the reduction of the carrier relaxation time, now estimated to be about 3 ps.

7.3.3 Quantum-dot DFB lasers

DFB lasers for 10G-EPON (Ethernet passive optical network)

To cope with the explosive increase of data traffic in access networks, in 2009 10G-EPON was standardized by IEEE 802.3 av, which supports

10.3-Gb/s transmission in both upstream and downstream directions using EPON systems. In 10G-EPON, the wavelength of the directly-modulated DFB lasers in the optical network units (ONU) for the upstream signal is allocated between 1260 and 1280 nm. An important requirement for the 1.27-μm DFB lasers, due to stringent power budgets, is the relatively high output power of +4 to +9 dBm. Therefore, to spread 10G-EPON systems, low-power-consuming and low-cost 1.27-μm DFB lasers with high output power are strongly required.

For power and cost savings in transmitter modules, QD lasers in the 1.3-μm wavelength range have exhibited remarkable progress owing to the realization of high-density self-assembled InAs quantum dots on GaAs substrates (Tanaka *et al.*, 2010). QD FP lasers with temperature-insensitive lasing characteristics, which cannot be achieved in the conventional QW lasers, are already commercially available for optical communications in the access and LANs (http://qdlaser.com). Furthermore, we have also reported the 1.3-μm QD DFB lasers employing InGaP/GaAs gratings, showing stable single-longitudinal-mode oscillation (Takada *et al.*, 2010).

We have developed 1.27-μm QD DFB lasers for 10G-EPON ONUs. In order to improve output power, especially at high temperatures, we adjusted the stacking number and the gain wavelength of the active layers with high-density QDs as well as the cavity designs such as the cavity length and the coupling coefficient of the gratings (κ). The fabricated 1.27-μm QD DFB lasers demonstrated temperature-stable light-current characteristics with low threshold currents of less than 11 mA and a high output power of over 15 mW, even at 85°C. We also demonstrated 10.3-Gb/s operation with an averaged output power of +4.5 dBm over a wide temperature range from −10°C to 85°C.

Device structure, fabrication, and gain characteristics of high-density QDs

We applied the active layers with high-density QDs to the ridge-waveguide lasers having InGaP/GaAs index-coupled gratings located just above the active layers as shown in Fig. 7.11 (Takada *et al.*, 2010). In the inset of Fig. 7.12, we show the AFM image of the InAs/GaAs QDs with extremely-high density of 5.9×10^{10} cm^{-2}. We set the grating pitch so that the lasing wavelength was 1270 nm at 25°C, while we tuned the gain peak wavelength of the QDs' active layers to 1255 nm. This detuning compensated for the deterioration of the lasing characteristics at high temperatures because the gain peak moved close to the lasing wavelength with increasing temperature. In addition, we designed the cavity length of 500 μm to improve the saturation of output power at high temperatures and κ of 30 cm^{-1} to obtain sufficient single-longitudinal-mode yields.

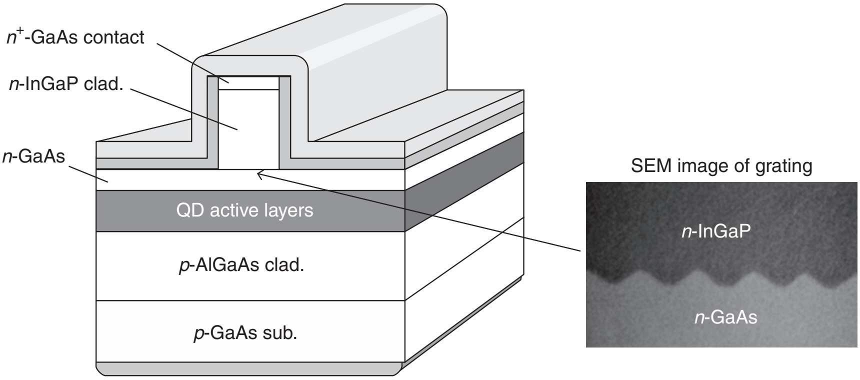
n^+-GaAs contact
n-InGaP clad.
n-GaAs
QD active layers
p-AlGaAs clad.
p-GaAs sub.
SEM image of grating
n-InGaP
n-GaAs

7.11 Schematic structure of a DFB laser on a GaAs substrate.

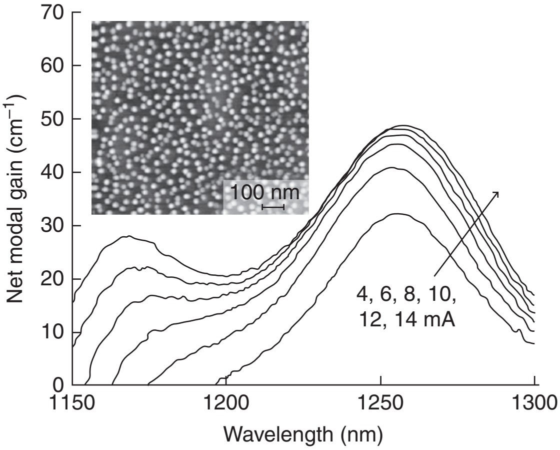

7.12 AFM image of the high-density QDs and gain characteristics at 25°C.

A *p*-type AlGaAs lower cladding layers and QD active layers on a *p*-type GaAs substrate were grown by MBE. To increase the optical gain of the active layers, we applied 10-stacked QD layers where GaAs barriers were partly *p*-type doped. On the *n*-type GaAs layer just above the active layers, we formed corrugated structures by means of electron beam lithography and wet etching, and overgrew *n*-type InGaP upper cladding layers by metal–organic vapor phase epitaxy to form the InGaP/GaAs index-coupled gratings. After forming the ridge-waveguide structure and the electrodes on both *p*- and *n*-sides, we applied anti-reflective (AR) and high-reflectivity (HR) coatings to front and rear facets, respectively.

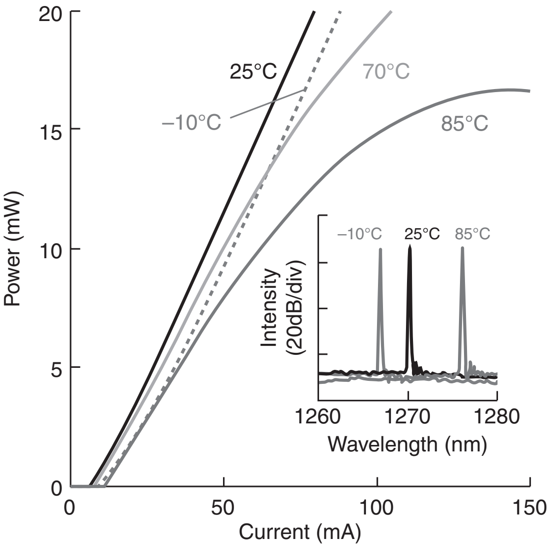

7.13 L–I characteristics and lasing spectra at 5 mW.

Figure 7.12 shows the gain characteristics of 10-stacked high-density QDs evaluated by the Hakki–Paoli method at 25ºC using a 200-μm-long FP laser, which was simultaneously fabricated with DFB lasers. We confirmed that the maximum net modal gain increased up to 49 cm^{-1}.

Light-current and modulation characteristics

Figure 7.13 shows the light–current (L–I) characteristics and the lasing spectra of the fabricated QD DFB laser. We confirmed that the lasing wavelength met the specifications for the 10G-EPON ONUs with the side-mode suppression ratios (SMSR) of more than 45dB. The threshold currents were below 11 mA in the temperature range from −10ºC to 85ºC. Owing to the high modal gain and the fine-tuning of the cavity design, L–I characteristics were improved, especially at high temperatures, compared to the previous results (Takada *et al*., 2010). In this study, we obtained an output power of over 15 mW even at 85ºC. In comparison with the L–I characteristics of conventional QW DFB lasers emitting in the 1.3 or 1.55 μm wavelength range, temperature stability is drastically improved in QD DFB lasers.

Figure 7.14 shows the 10.3 Gb/s filtered eye diagrams at (a) −10ºC, (b) 25ºC and (c) 85ºC. The pseudo-random binary sequence was set at 2^{31}–1. In this experiment, the fiber-coupled averaged output power (Pf) was adjusted at +4.5 dBm, which was within the specifications for the 10G-EPON PR30. In the temperature range from −10ºC to 85ºC, we obtained clearly-opened eye diagrams with an ER of 6 dB and the mask margin of more than 30%.

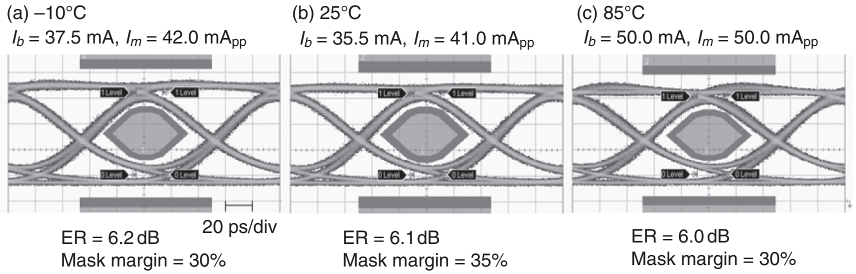

7.14 10.3-Gb/s eye diagram. I_b is the bias current, and I_m is the modulation current. mA$_{pp}$ is the peak-to-peak current in mA.

We have developed 1.27-μm QD DFB lasers for 10G-EPON ONUs. Owing to the high modal gain of 49 cm^{-1} at 25ºC and the 500-μm-long cavity, we achieved temperature-stable L–I characteristics and demonstrated 10.3-Gb/s operation with a high averaged output power of +4.5 dBm in the temperature range from −10ºC to 85ºC. The temperature-stable lasing characteristics of the QD DFB lasers, which are superior to those of conventional QW DFB lasers, would contribute to realizing low-cost light sources for 10G-EPON ONUs.

7.4 Quantum-dot FP and DFB lasers for high-temperature application

High-temperature-resistant semiconductor lasers are attractive to light sources for data transmission, optical sensing, and fiber gyros in a variety of harsh scenarios, such as automobile engine rooms, densely-packed interconnections, plants on deserts, and underground exploration of natural resources. While conventional semiconductor lasers for telecom and data storage operate below 80°C, these novel applications require lasing operation at least up to 150°C, and, in some cases, over 200°C. Reported that the highest lasing temperature of 225°C under CW conditions (Vail *et al.*, 1998) was at around 1000 nm wavelength range. On the other hand, the highest lasing temperature for the optical fiber window range of 1300 nm has been limited below 200°C (Wada *et al.*, 1999), primarily due to its material property such as insufficient conduction band offset between the QWs and barrier layers, which prevent lasing due to heated carrier overflow. Temperature-insensitive operation of semiconductor lasers with QD active layers was theoretically predicted (Arakawa and Sakaki, 1982). Recent progress of epitaxial growth technology enhances QD laser characteristics, such as very low FP laser threshold current density operation (Liu *et al.*, 1999), very low VCSEL threshold current operation (Huffaker *et al.*, 1998), high temperature T_0 of

600 K (Tanaka *et al.*, 2010), 25 Gb/s characteristic of the FP laser (Tanaka *et al.*, 2010), and 10 Gb/s of the DFB laser (Takada *et al.*, 2009, 2010, 2011). However, no lasing operation of the QD laser over 200°C has been reported. In this paper, we report extremely-high-temperature CW operation up to 220°C emitted at 1300 nm range for the first time by improving the size and compositional uniformity of QDs with high QD density in the active region (Kageyama *et al.*, 2011). In addition, this QD active medium was also incorporated into a DFB laser in which detuning was designed to lase up over 100°C, exhibiting CW lasing operation up to 150°C.

7.4.1 Epitaxy and wafer characterization

Epitaxial wafers were grown by commercially available solid source MBE with elemental Ga, In and Al as group-III sources, and elemental As as group-V source. An *n*-type GaAs buffer layer, *n*-AlGaAs cladding layer, 8-stacked QD active layer separated by partially *p*-doped 40 nm-thick GaAs barriers, *p*-AlGaAs cladding layer and *p*+-GaAs contact layer were successively grown for the laser wafer. The test wafer with the same active layer structure without doping sandwiched by 100 nm AlGaAs was also grown for epitaxial layer evaluation, such as photoluminescence (PL). The test wafer included a surface QD to evaluate QD density. A sheet density of the each QD layer for both test and laser wafer were fixed at 5.9×10^{10} cm^{-2}.

Nd:YAG laser (1064 nm) was used for PL excitation source. AFM was used to measure dot density for surface dot structure on PL wafers. Broad-area lasers were also fabricated to characterize the gain with varying mirror-loss.

7.4.2 Device fabrication and characterization

Ridge lasers with an FP cavity were fabricated with a mesa-width of 2 μm using conventional dry-etching (Fig. 7.15). Conventional photolithography and metal evaporation technique were used to form the laser structure. Cavity length was 1200 μm to form the FP laser. High-reflectivity (HR) coatings were employed on both sides of the facets as the reflectivity of 77/97%.

In addition, DFB lasers were also fabricated (Takada *et al.*, 2010, 2011) using same active layer as FP lasers. We grew *p*-type AlGaAs lower cladding layers, 8-stacked QD active layers as same as FP laser as shown above, and *n*-type GaAs layers on a p-type GaAs substrate by using MBE. Next, on the *n*-type GaAs layer just above the active layers, we formed the corrugated structures by means of electron beam lithography and wet etching. Then

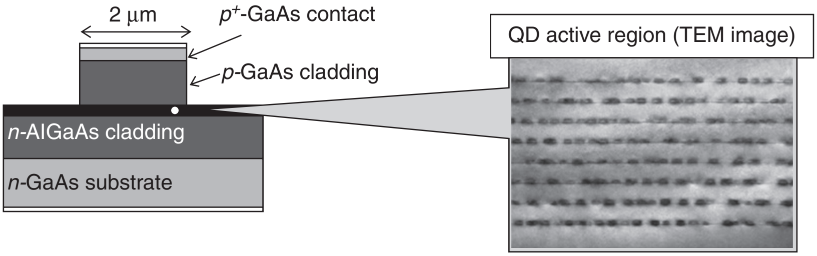

7.15 Schematic structure of fabricated ridge FP laser. Inset shows TEM image of QD active region.

we overgrew *n*-type InGaP upper cladding layers by metal-organic vapor phase epitaxy to form the InGaP/GaAs gratings. Owing to both enough overlap of the optical field in the grating and the high refractive index contrast between GaAs and InGaP, we can easily realize sufficient coupling coefficient (k) values even with the shallow gratings (Takada *et al.*, 2009). In this study, we designed a coupling coefficient (k) of 30 cm^{-1} with the grating depth of 15 nm and a cavity length of 500 μm. Lasing wavelength and detuning procedure will be discussed later. After forming the ridge-waveguide structure and electrodes, we applied AR and highly reflective coatings to front and rear facets, respectively.

Fabricated chips were mounted on TO-CAN using AuSn solder. FP and DFB lasers were characterized by a TO-CAN tester which was designed to measure laser characteristics at high temperatures over 200°C.

7.4.3 Design direction for high-temperature operation

Modal gain in semiconductor laser diodes tends to decrease with increasing temperature. In general, the maximum operating temperature of a diode laser is decided by the crossing point between decreasing maximum modal gain and total loss g_{th} of laser cavity, which is the amount of mirror-loss and internal loss, as shown in Fig. 7.16. Two approaches are considered to increase maximum operating temperature namely (a) increasing maximum gain, and (b) decreasing temperature dependence on maximum gain. Here we took approach (a). Some approaches can be considered for increasing maximum gain, such as (i) enhancing material gain on the active layer by modifying epitaxial growth procedure, (ii) increasing the number of the QD layers, (iii) increasing the QD density, and (iv) increasing the optical confinement factor by modifying the index profile. Here we took the approach (i), to increase gain in order to increase maximum operation temperature, and other factors were fixed to show potential of the QD on high-temperature

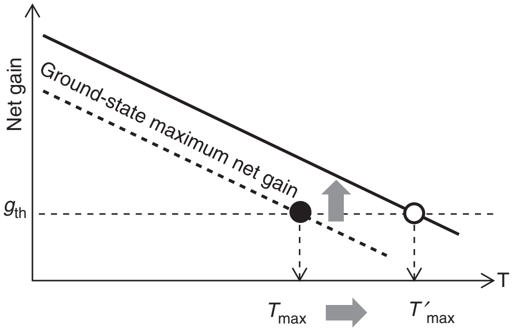

7.16 Design direction to enhance maximum operation temperature.

laser operation. The approach to increasing gain will contribute to realizing high-temperature operation not only FP lasers but also DFB lasers. The detailed approach will be discussed later in Section 7.2.

We have also developed DFB lasers having a grating above the QD active layers. Fabricated QD DFB lasers emitting at 1.3 μm wavelength have successfully exhibited temperature-stable operations over a wide temperature range from −40°C to 80°C (Takada *et al.*, 2010, 2011). In order to develop DFB lasers operating under high-temperature environments over 125°C, the design of the so-called detuning between the lasing wavelength and the gain peak wavelength needs to be adjusted at a different value from that applied in the QD DFB lasers for optical communications. At the 1.3 μm wavelength range, the lasing wavelength and the gain peak wavelength shift longer at the rates of about 0.1 and 0.5 nm/K, respectively, with increasing temperature. Therefore, we set the lasing wavelength at 50 nm longer than the gain peak wavelength at 25°C, so that they would accord at around 150°C.

7.4.4 Device characteristics

FP lasers

The L–I characteristics of the fabricated laser and its temperature dependence are shown in Fig. 7.17. The lasing wavelengths at 30 and 220°C were 1268 nm and 1359 nm, respectively, as shown in Fig. 7.18. Temperature dependence of lasing wavelength, $d\lambda/dT$, remained constant at 0.489 nm/K, which means the ground-state lasing operation was maintained up to the maximum lasing temperature. The maximum lasing temperature of 220°C is believed to be the highest lasing temperature for the optical fiber window range of 1300 nm, and a level comparable to the formerly-reported highest lasing temperature of all semiconductor lasers

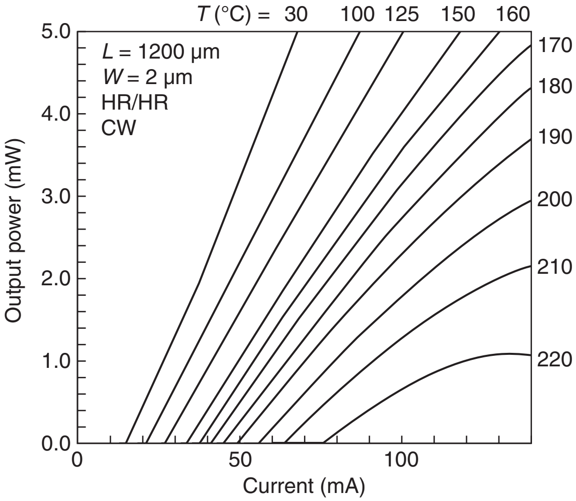

7.17 CW L–I curves of QD FP laser from 30 to 220°C.

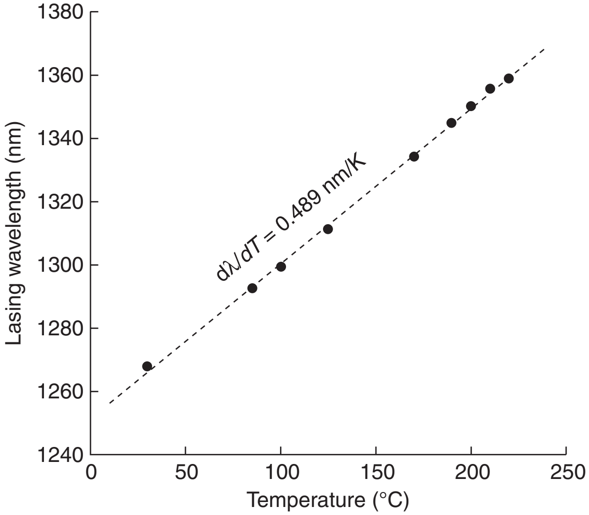

7.18 Temperature dependence of center lasing wavelength for QD FP laser from 30°C to 220°C.

(Vail *et al.*, 1998). Quantized-energy difference between the ground state and the first exited-state is about 80 meV in our highly uniform QDs. This large level separation and narrow photoluminescence FWHM are believed to effectively enhance gain, and suppress the carrier overflow and noticeable Auger-recombination even at elevated temperatures. The

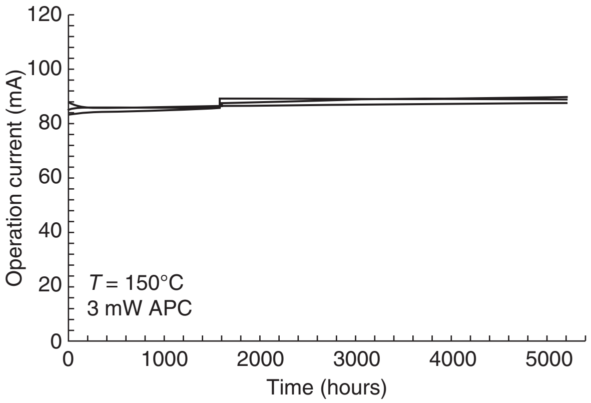

7.19 Preliminary aging test result with $N = 3$ (pcs) under 150°C, 3 mW-APC condition.

threshold currents kept as low as 21 mA up to 100°C and 75.5 mA up to 220°C, respectively, in this laser. As a result, a high characteristic temperature T_0 of 117 K was obtained between 30°C and 220°C. Output power exceeded 1 mW, even at 220°C, with an injection current of only 125 mA. Operation currents were lower than 100 mA up to 210°C with output power of 1 mW, which means that a standard laser driver for telecom can be applied if the driver can work at around 200°C.

A preliminary reliability test was performed with three chips under auto-power-control (APC) mode with constant output power of 3 mW at 150°C, as shown in Fig. 7.19. There is no significant increase in driving current up to 5200 h. These preliminary data show the potential of the QD laser in a high-temperature environment.

DFB lasers

Figure 7.20 shows the CW light–current characteristics for the fabricated QD DFB laser. Although the threshold currents were relatively high at lower temperatures, due to the large detuning between the lasing wavelength and the gain peak wavelength, they decreased to 20 mA at 125°C. As shown in this figure, the fabricated device successfully exhibited lasing operations up to 150°C. The maximum output power was 14 mW and 4 mW at 125°C and 150°C, respectively. The operating voltages at 50 mA were sufficiently small, below 1.5 V at all temperatures. Figure 7.21 shows the lasing spectra at 100, 125 and 150°C. We obtained stable single-mode oscillations with the SMSRs of more than 40 dB at all temperatures. The lasing wavelength was about 1306 nm at 25°C (not shown), which was 46-nm longer than the gain peak. We confirmed that this QD DFB laser provides single-mode oscillation with more than 10 mW output power at 125°C.

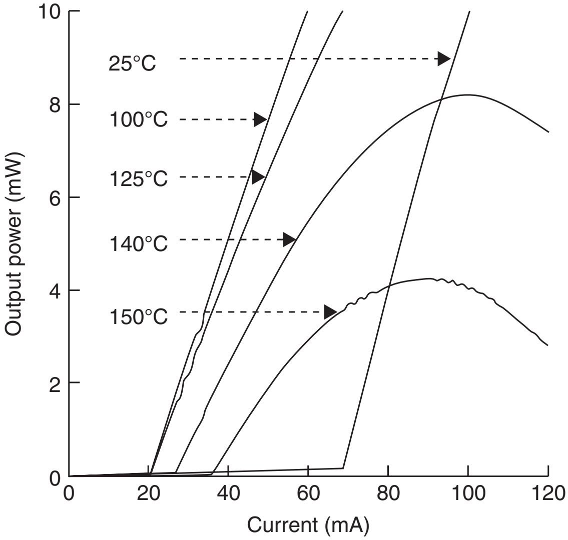

7.20 CW L–I curves of QD DFB laser from 25°C to 150°C.

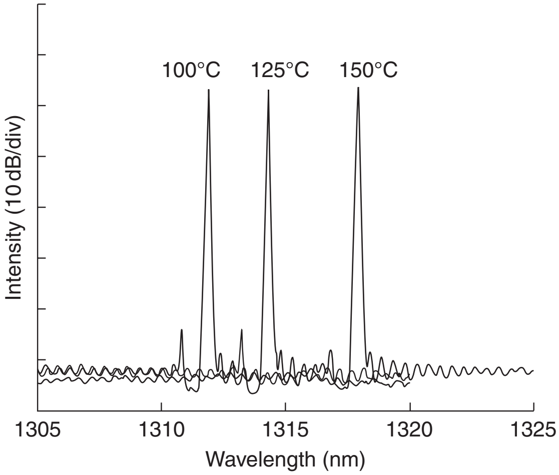

7.21 Lasing spectra of QD DFB laser with the output power of 4 mW at 100, 125 and 150°C.

Owing to the excellent temperature tolerance of the QD active region, and the state-of-the-art DFB laser technology originally developed towards telecom and datacom applications, QDL's QD DFB lasers are considered to be quite promising light sources for high-temperature sensing applications.

7.4.5 Summary

We realized extremely-high-temperature CW operation of the 1300 nm range QD FP laser utilizing highly uniform and high-density InAs/GaAs QD active region up to 220°C, which is believed to be the highest CW lasing temperature for the long-wavelength laser and a comparable level to the highest temperature for all semiconductor lasers. We also realized high-temperature operation of QD DFB laser up to 150°C maintaining single-mode operation with SMSR of more than 40dB throughout the measured temperature range. The QD laser including FP and DFB can be applied to high-temperature-resistant applications with silica-based optical fibers.

7.5 QD Laser, Inc.

7.5.1 About QD Laser, Inc.

QD Laser, Inc. (QDL) was launched in April 2006 in order to commercialize QD lasers for optical communication, with investment from Fujitsu Ltd and Mitsui & Co. Global Investment Ltd. Its business area and product portfolio have expanded to make it a leading provider of highly efficient semiconductor laser solutions, not only for telecom/Datacom but also for consumer electronics and industrial use. QDL distinguishes itself in the marketplace by its product values of finely tuned wavelengths from 532, 1064 to 1310 nm, high-temperature operation and stability, and mass-production capability on the GaAs platform. Its products reliably help customers create new laser light markets in a variety of applications such as LAN/FTTH, optical interconnection, material processing, sensing, laser projection, etc.

The technological core of QDL is cutting-edge GaAs-based semiconductor wafer technologies including crystal growth of quantum dots and wells and grating formation both on GaAs substrates. The laser chips, packages, and modules are all produced through horizontal processing and assembling lines, making it possible to access not only niche markets but also mass-production markets through supply chain management. Here, the main technologies and products of QD Laser, Inc. are briefly introduced.

7.5.2 MBE crystal growth

QDL owns the MBE crystal growth systems of Fig. 7.22a, which can precisely control grown layer thicknesses by less than one atomic layer. By using these systems, epitaxial layers made of semiconductor active layers and cladding layers can be fabricated, where compound materials such as InAs, GaAs, AlGaAs, and InGaAs can be grown on GaAs substrates. QDL has realized

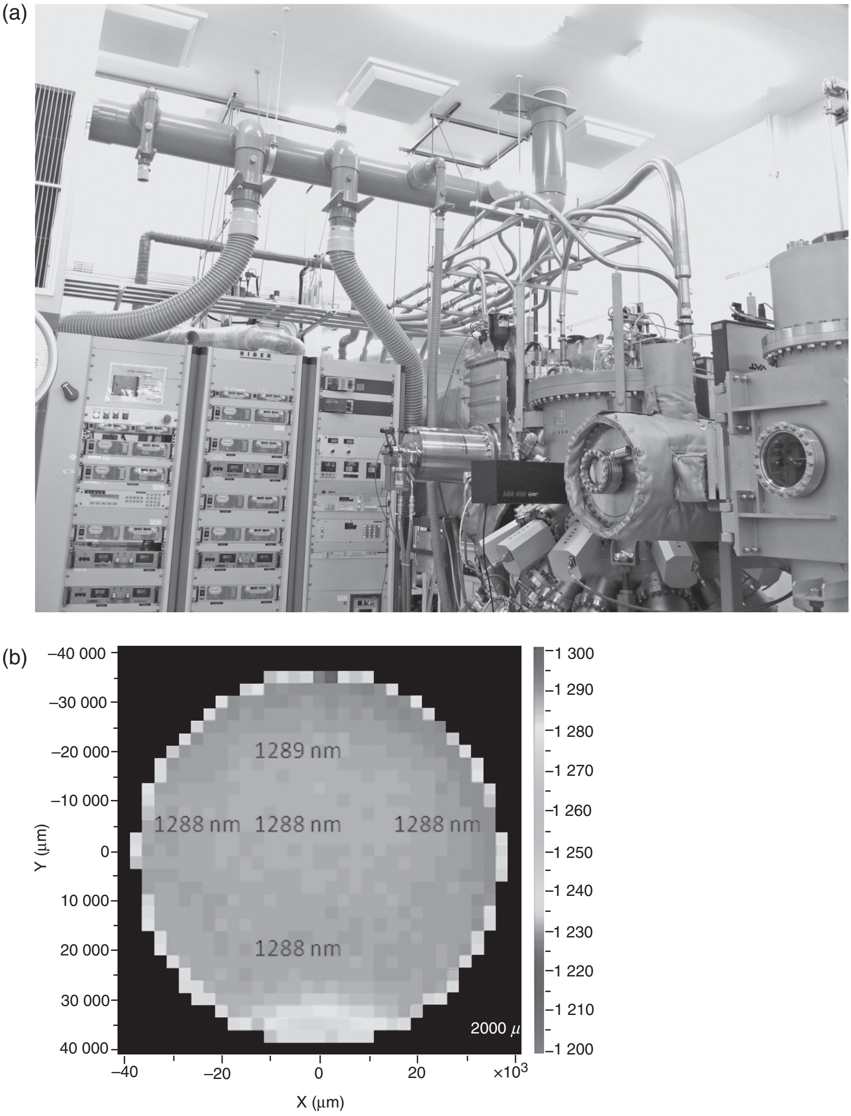

7.22 (a) MBE crystal growth system, (b) photoluminescence peak wavelength mapping of QD wafer on 3-inch GaAs substrate.

cutting-edge MBE technology, making it possible to form highly uniform epitaxial layers on 3-inch substrates. With this technology, the accuracy of thickness distribution is confined to ±1% and the photoluminescence peak wavelength distribution is less than ±0.5% on a 3-inch substrate (Fig. 7.22b).

The MBE system can perform crystal growth of QDs on five 3-inch GaAs substrates simultaneously, thus having sufficient productivity.

7.5.3 DFB lasers on GaAs substrates

In a DFB laser, only a specific wavelength of light, determined by the grating structure, is selectively reflected and amplified, hence the oscillation wavelength can be precisely controlled. DFB lasers have been used mainly for optical communications, and they are usually fabricated on InP substrates. Among several experimental approaches to fabricating DFB lasers on GaAs substrates, QD Laser, Inc. utilizes index-coupled grating – the same structure as for optical communications. QD Laser, Inc. has developed technologies of grating formation above the active layer and regrowth of the upper cladding layer on the grating, allowing extremely stable single-mode oscillation characteristics in DFB lasers under various conditions, such as driving current, temperature, and pulsed operation. This wavelength stability is also effective in industrial applications, such as material processing or sensing.

7.5.4 Mass production of quantum-dot FP lasers for optical communication

QDL started mass production of quantum-dot FP lasers through its horizontal laser processing line in 2010. The QLF1335 product – a temperature-resistant 1300 nm wavelength FP laser – was shipped to the Chinese market in 900 kpcs TO-CAN packages (Fig. 7.23a) for use in 155 M 1 × 9 optical transceivers. The temperature stability of Fig. 7.8 enables operation without a monitor photo-detector, and allows customers much easier handling in evaluations and adjustments than conventional QW lasers, realizing the cost effectiveness.

QDL is now developing QD lasers for FTTH, including FP lasers for 1.25 Gb/s GEPON as well as DFB lasers for 2.5 to 10 Gb/s GPON and 10G-EPON. A key to this application is high-density and highly uniform InAs QDs as described in Section 7.2. These products are planned to be introduced into the optical communication markets in 2013–14.

7.5.5 Other products

Semiconductor lasers are now being used in a variety of areas, such as factory automation, material processing, life science, spectroscopy, sensing, measurements, and laser display, etc. A laser with an appropriate wavelength is selected for each application from the broad wavelength range

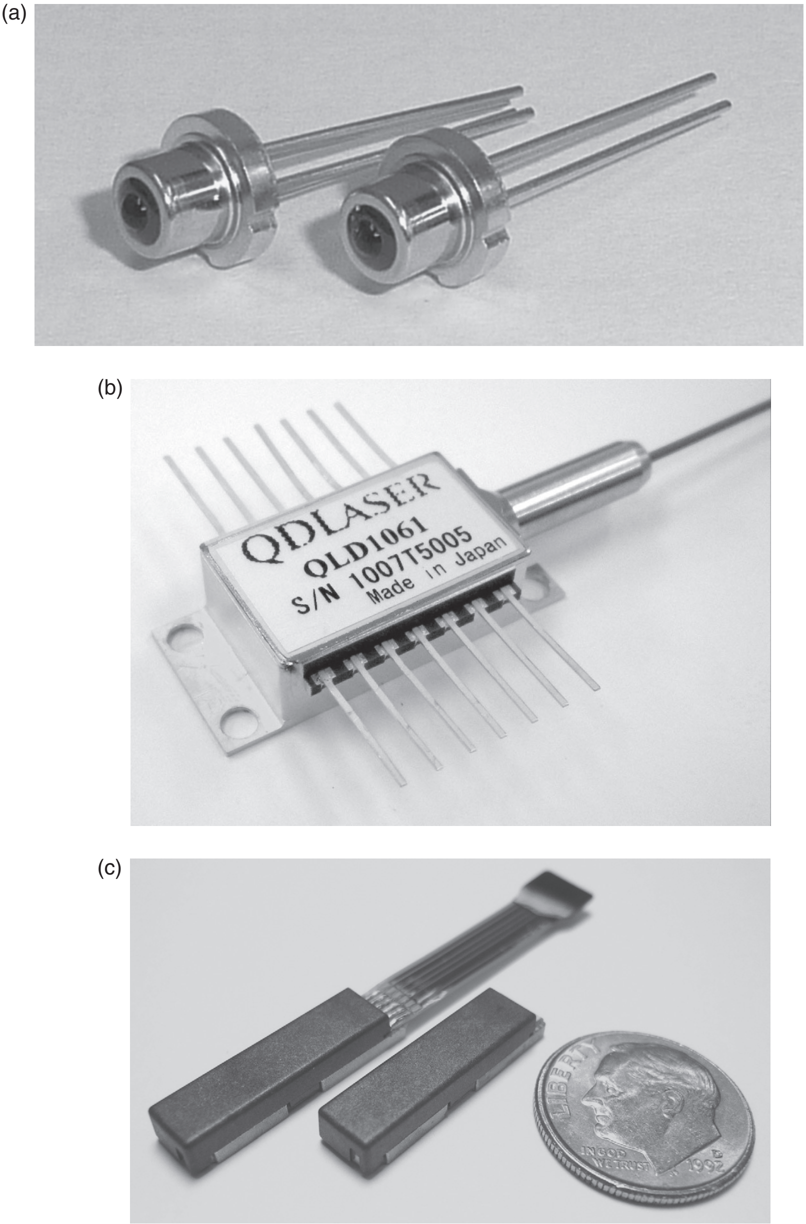
(a)
(b)
QDLASER
QLD1061
S/N 1007T5005
Made in Japan
(c)
LIBERTY
IN GOD WE TRUST
D
1992

7.23 Products of QD Laser, Inc. (a) 1310 nm quantum-dot FP laser up to 2.5 Gbps, (b) 1000–1120 nm DFB lasers for material processing and sensing, and (c) pure green laser module in compact package.

of 532–1310 nm on the GaAs platform, with the help of second harmonic generation (SHG) devices to compensate the 'Green Gap' including green, yellow, and orange.

1000–1120 nm DFB lasers for material processing and sensing

There is an increasing trend for fiber lasers to be employed in material processing, due to easy maintenance, compact size and low cost, when compared to conventional laser processing systems. The 1064 nm DFB laser of Fig. 7.23b is suitable for the seed light of the fiber lasers because of its excellent single-mode stability, tunable wavelength, and sub-nanosecond short pulse operation at high repetition rate. Its standard 14-pin butterfly package is pigtailed by a polarization-maintaining optical fiber. The choice of wavelength is from 1000 nm to 1180 nm, depending on customers' needs. These features enable unheated precise cutting of thin films of solar cells, display panels, LEDs, etc.

Green, yellow, and orange lasers

Microscopes in life science tend to employ visible light of green, yellow, and orange, which the combination of 10xx nm wavelength lasers with SHG devices can provide. QDL provides compact green (532 nm), yellow (561 nm), and orange (590 nm) laser modules (Fig. 7.24c), which integrate 1064 nm, 1122 nm, and 1180 nm lasers with SHG devices of PPLN (periodic-poled $LiNbO_3$), respectively. Unlike the diode-pumped solid-state laser (DPSS), this laser utilizes DFB laser technology, which provides video rate amplitude modulation capability and power stability.

The pico projector is an emerging technology consisting of an image projector in a handheld device. There is an increasing demand to make the projector more convenient and comfortable, where the laser projection is a solution to provide bright images at low-power-consumption and focus-free operation, that is, the image is always in focus. A key to laser projectors is high-performance green lasers. The module of Fig. 7.23c provides superior performance to GaN-based direct green lasers in its pure green color of 532 nm, higher power up to 80 mW or more, better wall plug efficiency, and higher operation temperature.

7.6 Silicon hybrid quantum-dot lasers

7.6.1 Introduction

Silicon optoelectronic integrated circuits (OEIC) are a key technological component for next-generation ultrahigh speed computation and telecommunication. In the absence of a practical silicon laser, III–V semiconductor compound light sources monolithically integrated onto Si chips or waveguides are highly sought after for the realization of OEICs utilizing well-established CMOS fabrication technologies (Miller, 2000; Fang *et al.*, 2006). Semiconductor QD lasers are particularly promising for use in high-density OEICs for their low lasing threshold current density and high-temperature stability (Arakawa and Sakaki, 1982), which can minimize and address thermal accumulation in dense circuits. In this section, we give an overview of III–V semiconductor compound quantum-dot lasers integrated onto Si substrates.

7.6.2 III–V quantum-dot lasers on Si substrates by heteroepitaxial growth

For III–V/Si hybrid integration, direct epitaxial growth of III–V compounds on Si substrates would be the most desirable approach. Mi *et al.* (2005, 2006) demonstrated an InGaAs/GaAs QD laser grown directly on a Si substrate for the first time as a semiconductor quantum-dot laser on silicon by MBE yielding ground-state lasing at 1.0 μm at room temperature with a threshold current density of 900 A/cm^2. In this study, they incorporated a GaAs buffer layer between the AlGaAs lower cladding layer and the Si substrate including InAs QDs as a dislocation filter to stop threading dislocation propagation stemming from the lattice-mismatched GaAs/Si heterointerface. Using the on-Si QD laser and selective-area growth, they also demonstrated a laser-waveguide coupling through a vertical groove etched by focused-ion-beam milling between the III–V QD laser layers and an amorphous Si waveguide integrated onto an identical Si substrate (Yang and Bhattacharya, 2008) (Fig. 7.24).

For optical communication and interconnections, it is of first importance to achieve ground-state lasing at the telecommunication band of 1.3 μm or longer. As a series of effort towards the realization of optical communication applicable III–V quantum-dot lasers on Si substrates, we ourselves have been growing 1.3 μm InAs QDs embedded in GaAs layers (InAs/GaAs QDs) on Si substrates and Si-based alternative substrates by metal-organic chemical vapor deposition (MOCVD) incorporating antimony surfactant. We grew InAs/GaAs QDs on Si substrates and observed their photoluminescence at 1.3 μm at room temperature (Li *et al.*, 2008). We also obtained 1.3 μm InAs/GaAs QDs grown on germanium-on-silicon (Ge/Si) (Rajesh *et al.*, 2011a) and germanium-on-insulator-on-silicon (GeOI) substrates (Bordel *et al.*, 2010; Rajesh *et al.*, 2011b) with high intensity photoluminescence comparable to reference InAs/GaAs QDs grown on GaAs substrates (Fig. 7.25).

In 2011, Wang *et al.* (2011) grew a 1.3 μm room-temperature InAs/GaAs quantum-dot laser on a Si substrate by MBE with a threshold current density

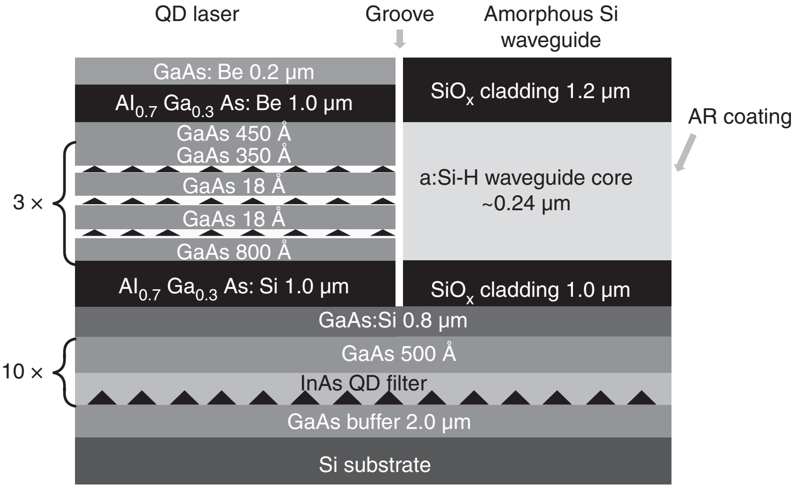
QD laser
Groove
Amorphous Si waveguide
GaAs: Be 0.2 μm
$Al_{0.7}Ga_{0.3}As$: Be 1.0 μm
GaAs 450 Å
GaAs 350 Å
GaAs 18 Å
GaAs 18 Å
GaAs 800 Å
$Al_{0.7}Ga_{0.3}As$: Si 1.0 μm
SiO_x cladding 1.2 μm
a:Si-H waveguide core ~0.24 μm
SiO_x cladding 1.0 μm
AR coating
3 ×
GaAs:Si 0.8 μm
10 ×
GaAs 500 Å
InAs QD filter
GaAs buffer 2.0 μm
Si substrate

7.24 Cross-sectional schematic of the $In_{0.5}Ga_{0.5}As$ QD laser heterostructure grown on a Si substrate with incorporation of InAs QDs as dislocation filters and coupled to an a:Si (amorphous silicon) waveguide (reprinted with permission from Yang and Bhattacharya (2008); © 2008, Optical Society of America).

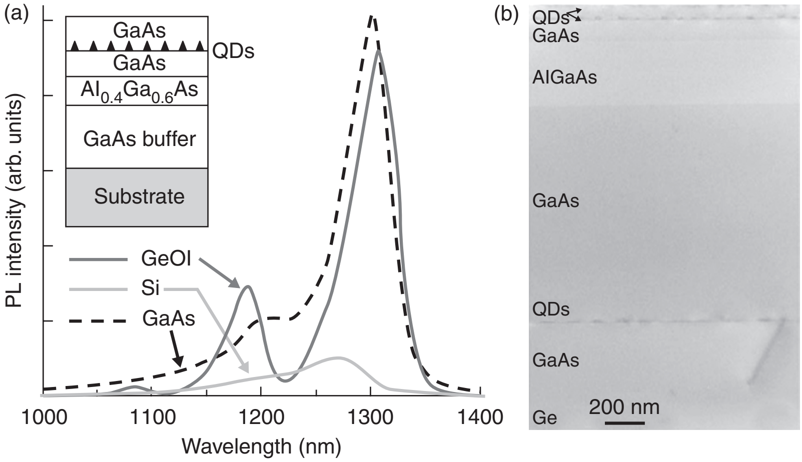

7.25 (a) Room temperature photoluminescence spectra of the InAs QDs grown on silicon (light (green) solid curve), GaAs (dashed curve), and GeOI with QD dislocation filter (dark (blue) solid curve). The inset shows the schematic diagram of the sample structure used for photoluminescence evaluation. (b) Bright-field cross-sectional TEM image of the QD sample grown on GeOI with QD dislocation filter. (reprinted with permission from Bordel *et al.* (2010); © 2010, American Institute of Physics).

of 725 A/cm^2. They adopted InAs/In$_{0.15}$Ga$_{0.85}$As dot-in-a-well structure as the core gain layer and dislocation-filtering In$_{0.15}$Ga$_{0.85}$As/GaAs superlattices in the buffer layer in this work.

7.6.3 III–V quantum-dot lasers on Si substrates by wafer bonding

Although direct heteroepitaxial growth would be the most desirable approach for III–V/Si hybrid integration, heteroepitaxy typically introduces a substantial crystalline defect density, due to the large lattice mismatch and the polar-nonpolar nature of the III–V/IV semiconductor system that can adversely affect device performance (Kroemer *et al.*, 1989; Sugo *et al.*, 1990). Wafer bonding (Shimbo *et al.*, 1986; Tong and Gosele, 1998) on the other hand is not subject to the lattice matching limitations associated with epitaxial growth, and has been used to fabricate materials that consist of crystalline semiconductors on amorphous materials and also to integrate crystalline materials of different lattice constants. For the integration of both crystalline–amorphous and crystalline–crystalline pairs, defects caused by the lack of crystallographic registry are isolated to the wafer-bonded interface. Thus, heterostructure devices fabricated via wafer bonding can, in principle, have a performance close to that obtained by homoepitaxy by confining the defect network needed for lattice mismatch accommodation to the bonded interfaces.

By using the wafer bonding technique, we fabricated an electrically pumped 1.3 μm room-temperature InAs/GaAs quantum-dot laser on a Si substrate with a threshold current density of 360 A/cm^2. The double-hetero laser structure was grown on a GaAs substrate by MOCVD and layer-transferred onto a Si substrate by GaAs/Si wafer bonding mediated by a 380-nm-thick Au-Ge-Ni alloy layer (Tanabe *et al.*, 2010a). We demonstrated that insertion of a metal thin film in a wafer-bonded GaAs/Si interface enhances interfacial electrical conductivity and suppresses optical leakage from the laser cavity into the substrate (Tanabe *et al.*, 2011a) and therefore is suitable for III-V-on-Si hybrid laser applications.

We fabricated QD lasers on a Si substrate with a single wafer bonding step, demonstrating the advantage of this approach for high volume, low-cost integration over the conventional pick-and-place scheme (Friedrich *et al.*, 1992; Kato and Tohmori, 2000). InAs/GaAs QD growth on GaAs substrates by MOCVD we adopted in this study gives further merits for large-scale, low-cost, high-throughput fabrication over those using InP substrates or MBE growth. Evanescent optical coupling to waveguides underneath (Fang *et al.*, 2006; Van Campenhout *et al.*, 2007) would be realized by opening patterned arrays of optical windows in the metal bonding layer (Tanabe *et al.*, 2011b). In contrast to oxide-mediated bonding used for evanescent hybrid laser fabrication to date, conductive wafer-bonded heterointerfaces enable vertical carrier injection that prevents current spreading towards cavity stripe edges. Therefore, metal-mediated- or direct-semiconductor-bonded evanescent III–V/Si hybrid lasers would have the advantages of higher quantum efficiencies and simpler fabrication without mesa etching or ion implantation for carrier confinement that was required in the fabrication of earlier lateral-current-injection evanescent hybrid lasers (Tanabe *et al.*, 2011b). The wafer bonding and layer transfer approach to fabricate metal/semiconductor/metal thin film structure demonstrated in this work is also applicable for development of subwavelength-scale plasmonic lasers (Dionne *et al.*, 2006; Hill *et al.*, 2009).

We also fabricated 1.3 μm room-temperature InAs/GaAs QD lasers on Si substrates by means of direct GaAs/Si wafer bonding with no mediating agent, using a MBE-grown QD laser structure (Tanabe *et al.*, 2012) (Fig. 7.26). Our on-chip QD laser achieved a threshold current density of 205 A/cm^2, the lowest of any kind of semiconductor laser on silicon reported to date.

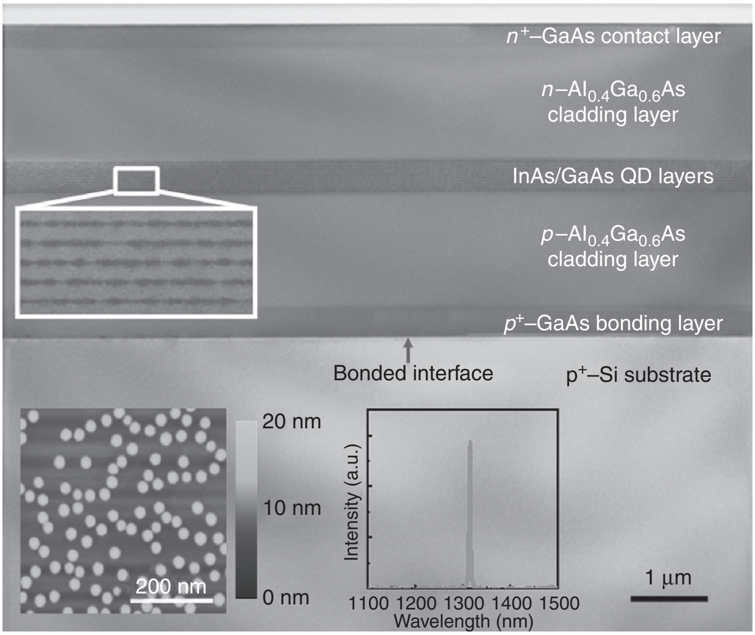
n^+–GaAs contact layer
n–Al$_{0.4}$Ga$_{0.6}$As cladding layer
InAs/GaAs QD layers
p–Al$_{0.4}$Ga$_{0.6}$As cladding layer
p^+–GaAs bonding layer
Bonded interface
p$^+$–Si substrate
200 nm
20 nm
10 nm
0 nm
Intensity (a.u.)
1100 1200 1300 1400 1500
Wavelength (nm)
1 μm

7.26 Cross-sectional TEM image of the fabricated InAs/GaAs QD laser on a Si substrate. The upper inset shows a detailed image of the InAs/GaAs QD layers. The lower left inset shows an atomic force microscope image of the as-grown InAs/GaAs quantum dots. The lower right inset shows the lasing spectrum at room temperature.

7.6.4 III–V quantum-dot–photonic crystal nanocavity lasers on Si substrates

Photonic crystal (PhC) structures can provide wavelength-scale laser cavities with high quality factors (*Q*-factors), representing an extremely long photon lifetime. The spontaneous emission rate to the cavity modes of materials inside small high-*Q* cavities can be potentially enhanced due to Purcell effect. This enhancement enables low threshold operation of PhC cavity lasers (Painter *et al.*, 1999). Monat *et al.* (2001) reported the first demonstration of PhC lasers on Si substrates. A couple of groups have subsequently presented PhC band-edge (Monat *et al.*, 2002; Mouette *et al.*, 2003; Vecchi *et al.*, 2007) and nanocavity (Monat *et al.*, 2003; Shih *et al.*, 2007) lasers on Si substrates or coupled to Si waveguides underneath (Halioua *et al.*, 2009, 2011) with gain media of In-Ga-As-P system compound multiple quantum-wells (MQW) grown on InP substrates and layer-transferred onto Si substrates using wafer bonding.

The superior characteristics in semiconductor QD lasers represented by low lasing threshold current/power and high-temperature stability for are promising for future nanoscale, ultrahigh density circuitries. Thanks to these advantages, Yoshie *et al.* (2002) demonstrated QD-PhC lasers operating for the first time at room temperature with pulsed optical pumping. We reported the first demonstration of room-temperature continuous-wave lasing in a QD-PhC nanocavity (Nomura *et al.*, 2006) followed by lasing gained by a single quantum dot as an extreme class of light source (Nomura *et al.*, 2009b, 2010), both with InAs/GaAs QDs grown on GaAs substrates.

Ben Bakir *et al.* (2006) demonstrated an InAs/InP QD-PhC band-edge laser transferred onto a Si substrate with a SiO_2/Si multilayer Bragg reflector inside operating with pulsed pumping at room temperature, as the first QD-PhC laser on silicon. A merit of photonic band-edge or Bloch-mode lasers is potentially higher output power than for PhC cavity-mode or defect-mode lasers (Letartre *et al.*, 2005). PhC cavity lasers, however, generally have a lower lasing threshold than photonic band-edge lasers, due to the higher in-plane optical confinement and with smaller mode volume of cavities (Monat *et al.*, 2003; Nomura *et al.*, 2009a). Other advantages of PhC cavity lasers are represented by the controllability of the *Q*-factor and the mode volumes with the cavity geometry and size to maximize the Purcell factor and thus spontaneous emission rate.

We ourselves fabricated InAs/GaAs QD-PhC nanocavity lasers on Si substrates through wafer bonding and layer transfer techniques and observed their continuous-wave lasing at room temperature by optical pumping (Tanabe *et al.*, 2009, 2010b). This work is the first demonstration of room-temperature continuous-wave lasing in a PhC nanocavity on silicon. This surface-emitting laser exhibited emission at 1.3 μm with a threshold absorbed power of 2 μW, the lowest of any type of semiconductor laser on silicon. Generally lasers with QD gain have significantly lower lasing threshold than QW lasers due to the higher spatial carrier confinement and discrete energy levels in QDs as long as the Q-factors are large enough to compensate QDs' smaller modal gain than QWs' (Arakawa and Sakaki, 1982). As an example, we observed a difference of three orders of magnitude between the threshold powers of QD- and QW-PhC band-edge lasers with similar PhC structures (Nomura *et al.*, 2009a).

7.7 Conclusion

This chapter has reviewed the marked progress of self-assembled InAs QD lasers over the past five years. Since the first proposal of QD lasers in 1982 (Arakawa and Sakaki, 1982), the technology reached real-world application, as seen in the mass production of optical communication lasers by QD Laser, Inc. This owes to the growth technology of high-density and highly uniform InAs QDs (described in Section 7.2), and the device technology of quantum-dot FP and DFB lasers (described in Sections 7.3 and 7.4). The business area and product portfolio of QD Laser, Inc. (QDL) has expanded to make it a leading provider of highly efficient semiconductor laser solutions for not only telecom/Datacom but also consumer electronics and industrial use. QDL is now opening a way to new laser application worlds by its product values of finely tuned wavelengths from 532, 1064 to 1310 nm, high-temperature operation and stability, and mass-production capability on GaAs platform including quantum dots.

The next five years will see mass production of high-speed FP and DFB quantum-dot lasers in the FTTH area prevailing in the optical communication market, a wide variety of emerging applications for industrial, medical, and consumer use by GaAs-based wide-wavelength-range lasers, and QD lasers working in various extremely-high-temperature harsh environments. The silicon hybrid QD lasers discussed in Section 7.6 will be a key technology of optical interconnects on silicon LSIs to overcome the bottleneck of the speed and power consumption as a goal of this nanotechnology in late 2010s.

7.8 Acknowledgements

The authors would like to thank Dr T. Kageyama of QD Laser Inc., Dr K. Nishi of QD Laser Inc. and the University of Tokyo, Mr K. Takemasa of QD Laser Inc., Mr T. Yamamoto of QD Laser Inc. and Fujitsu Laboratories Ltd, Mr K. Takada of QD Laser Inc. and Fujitsu Laboratories Ltd, Dr Y. Tanaka of Fujitsu Laboratories Ltd, and Dr M. Ishida of Fujitsu Laboratories Ltd, for their valuable contributions to this book chapter.

This work was partly supported by the Project for Developing Innovation Systems of the Ministry of Education, Culture, Sports, Science and Technology (MEXT), Japan, and by the New Energy and Industrial Technology Development Organization (NEDO).

Part of this work belongs to the 'Next-generation High-efficiency Network Device Project', which the Photonics Electronics Technology Research Association (PETRA) contracted with NEDO.

This work was also partly supported by the Japan Society for the Promotion of Science (JSPS) through the 'Funding Program for World-Leading Innovative R&D on Science and Technology (FIRST Program)', initiated by the Council for Science and Technology Policy (CSTP).

This work was also partly supported by Intel Corporation.

7.9 References

Arakawa, Y. and Sakaki, H. (1982) 'Multidimensional quantum well lasers and temperature dependence of its threshold current', *Appl Phys Lett*, **40**, 939–941.

Arakawa, Y., Sakaki, H., Nishioka, M., and Miura, N. (1983) 'Two-dimensional quantum-mechanical confinement of electrons in DH laser by strong magnetic fields', *IEEE J Quantum Electron*, QE-**19**, 1255–1257.

Asada, M., Miyamoto, Y., and Suematsu, Y. (1986) 'Gain and the threshold of three-dimensional quantum-box lasers', *IEEE J Quantum Electron*, QE-**22**, 1915–1921.

BenBakir, B., Seassal, C., Letartre, X., Regreny, P., Gendry, M., Viktorovitch, P., Zussy, M., Di Cioccio, L., and Fedeli, J. M. (2006) 'Room-temperature InAs/InP quantum dots laser operation based on heterogeneous "2.5 D" Photonic Crystal', *Opt Express*, **14**, 9269–9276.

Bordel, D., Guimard, D., Rajesh, M., Nishioka, M., Augendre, E., Clavelier, L., and Arakawa, Y. (2010) 'Growth of InAs/GaAs quantum dots on germanium-on-insulator-on-silicon (GeOI) substrate with high optical quality at room temperature in the 1.3 μm band', *Appl Phys Lett*, **96**, 043101.

Chang, Y.-C., Chang, L. L., and Esaki, L. (1985) 'A new one-dimensional quantum well structure', *Appl Phys Lett,* **47**, 1324–1326.

Chuang, S. L. (1995) *Physics of Optoelectronics Devices.* New York, Wiley.

Dionne, J. A., Sweatlock, L. A., Atwater, H. A., and Polman, A. (2006) 'Plasmon slot waveguides: towards chip-scale propagation with subwavelength-scale localization', *Phys Rev B*, **73**, 035407.

Fang, A. W., Park, H., Cohen, O., Jones, R., Paniccia, M. J., and Bowers, J. E. (2006) 'Electrically pumped hybrid AlGaInAs-silicon evanescent laser', *Opt Express*, **14**, 9203–9210.

Friedrich, E. E. L., Oberg, M. G., Broberg, B., Nilsson, S., and Valette, S. (1992) 'Hybrid integration of semiconductor lasers with Si-based single-mode ridge waveguides', *J Lightwave Tech*, **10**, 336–340.

Fuji Chimera Research Institute, Inc. (2010) 'Comprehensive Survey of Optical Telecommunication Devices Market 2010'.

Fukui, T. and Saito, H. (1987) '(AlAs)0.5(GaAs)0.5 fractional-layer superlattices grown on (001) vicinal surfaces by metalorganic chemical vapor deposition', *Appl Phys Lett*, **50**, 824–826.

Goldstein, L., Glas, F., Marzin, J. Y., Charasse, M.N., and LeRoux, G. (1985) 'Growth by molecular beam epitaxy and characterization of InAs/GaAs strained-layer superlattices', *Appl Phys Lett*, **47**, 1099.

Halioua, Y., Karle, T. J., Raineri, F., Monnier, P., Sagnes, I., Roelkens, G., Van Thourhout, D., and Raj, R. (2009) 'Hybrid InP-based photonic crystal lasers on silicon on insulator wires', *Appl Phys Lett*, **95**, 201119.

Halioua, Y., Basin, A., Monnier, P., Karle, T. J., Roelkens, G., Sagnes, I., Raj, R., and Raineri, F. (2011) 'Hybrid III-V semiconductor/silicon nanolaser', *Opt Express*, **19**, 9221–9231.

Hill, M. T., Marell, M., Leong, E. S. P., Smalbrugge, B., Zhu, Y., Sun, M., van Veldhoven, P. J., Geluk, E. J., Karouta, F., Oei, Y., Notzel, R., Ning, C., and Smit, M. K. (2009) 'Lasing in metal-insulator-metal sub-wavelength plasmonic waveguides', *Opt Express*, **17**, 11107–11112.

Huffaker, D. L., Park, G., Zou, Z., Shchekin, O. B., and Deppe, D. G. (1998) '1.3 μm room-temperature GaAs-based quantum-dot laser', *Appl Phys Lett,* **73**, 2564–2566.

Huffaker, D. L., Deng, H., and Deppe, D. G. (1998) '1.15-μm wavelength oxide-confined quantum-dot vertical-cavity surface-emitting laser', *Photon Technol Lett*, **10**, 185–187.

Ishida, M., Hatori, N., Akiyama, T., Otsubo, K., Nakata, Y., Ebe, H., Sugawara, M., and Arakawa, Y. (2004) 'Photon lifetime dependence of modulation efficiency and K factor in 1.3 μm self-assembled InAs/GaAs quantum-dot lasers: impact of capture time and maximum modal gain on modulation bandwidth', *Appl Phys Lett*, **85**, 4145–4147.

Ishida, M., Sugawara, M., Yamamoto, T., Hatori, N., Ebe, H., Nakata, Y., and Arakawa, Y. (2007) 'Theoretical study on high-speed modulation of Fabry-Pérot and distributed-feedback quantum-dot lasers: K-factor-limited bandwidth and 10 Gbit/s eye diagrams', *J Appl Phys*, **101**, 13108–13114.

Kageyama, T., Nishi, K., Yamaguchi, M., Mochida, R., Maeda, Y., Takemasa, K., Tanaka, Y., Yamamoto, T., Sugawara, M., and Arakawa, Y. (2011) 'Extremely high temperature (220°C) continuous-wave operation of 1300-nm-range quantum-dot lasers', CLEO/Europe-EQEC 2011, PDA.1.

Kaizu, T., Takahasi, M., Yamaguchi, K., and Mizuki, J. (2007) 'Modification of InAs quantum dot structure during annealing', *J Crystal Growth* **301–**302, 248–251.

Kapon, E., Simhony, S., Bhat, R., and Hwang, D. M. (1989) 'Single quantum wire semiconductor lasers', *Appl Phys Lett,* **55**, 2715–2717.

Kash, K., Van der Gaag, B. P., Mahoney, D. D., Gozdz, A. C., Florez, L. T., Harbison J. P., and Sturge, M. D. (1991) 'Observation of quantum confinement by strain gradients', *Phys Rev Lett*, **67**, 1326–1329.

Kato, K. and Tohmori, Y. (2000) 'PLC hybrid integration technology and its application to photonic components', *IEEE J Select Top Quant Electron*, **6**, 4–13.

Kroemer, H., Liu, T-Y., and Petroff, P. M. (1989) 'GaAs on Si and related systems: problems and prospects', *J Cryst Growth*, **95**, 96–102.

Leonard, D., Krishnamurthy, M., Reaves, C. M., DenBaars, S. P., and Petroff, P. M. (1993) 'Direct formation of quantum sized dots from uniform coherent islands of InGaAs on GaAs surfaces', *Appl Phys Lett,* **63**, 3203–3205.

Leonard, D., Fafard, S., Pond, K., Zhang, Y. H., Merz, J. L., and Petroff, P. M. (1994) ‘Structural and optical properties of self-assembled InGaAs quantum dots’, *J Vac Sci Technol B,* **12**, 2516–2520.

Letartre, X., Monat, C., Seassal, C., and Viktorovitch, P. (2005) ‘Analytical modeling and an experimental investigation of two-dimensional photonic crystal microlasers: defect state (microcavity) versus band-edge state (distributed feedback) structures’, *J Opt Soc Am B*, **22**, 2581–2595.

Li, L., Guimard, D., Rajesh, M., and Arakawa, Y. (2008) ‘Growth of InAs/Sb:GaAs quantum dots on silicon substrate with high density and efficient light emission in the 1.3 μm band’, *Appl Phys Lett*, **92**, 263105.

Liu, G. T., Stintz, A., Li, H., Malloy, K. J., and Lester, L. F. (1999) ‘Extremely low room-temperature threshold current density diode lasers using InAs dots in In0.15Ga0.85As quantum well’, *Electron Lett*, **35**, 1163–1165.

Mi, Z., Bhattacharya, P., Yang, J., and Pipe, K. P. (2005) ‘Room-temperature self-organised In0.5Ga0.5As quantum dot laser on silicon’, *Electron Lett*, **41**, 742–743.

Mi, Z., Yang, J., Bhattacharya, P., and Huffaker, D. L. (2006) ‘Self-organised quantum dots as dislocation filters: The case of GaAs-based lasers on silicon’, *Electron Lett*, **42**, 121–122.

Miller, D. A. B. (2000) ‘Rationale and challenges for optical interconnects to electric chips’, *Proc IEEE*, **88**, 728–749.

Miyamoto, Y., Cao, M., Shingai, Y., Furuya, K., Suematsu, Y., Ravikumar, K. G., and Arai, S. (1987) ‘Light emission from quantum-box structure by current injection”, *Jpn J App Phys*, **26**, L225–L227.

Monat, C., Seassal, C., Letartre, X., Viktorovitch, P., Regreny, R., Gendry, M., Rojo-Romeo, P., Hollinger, G., Jalaguier, E., Pocas, S., and Aspar, B. (2001) ‘InP 2D photonic crystal microlasers on silicon wafer: Room temperature operation at 1.55 μm’, *Electron Lett*, **37**, 764–766.

Monat, C., Seassal, C., Letartre, X., Regreny, R., Rojo-Romeo, P., Viktorovitch, P., d’Yerville, M. L., Cassagne, D., Albert, J. P., Jalaguier, E., Pocas, S., and Aspar, B. (2002) ‘InP-based two-dimensional photonic crystal on silicon: In-plane Bloch mode laser’, *Appl Phys Lett*, **81**, 5102–5104.

Monat, C., Seassal, C., Letartre, X., Regreny, P., Rojo-Romeo, P., Viktorovitch, P., LeVassor d’ Yerville, M., Cassagne, D., Albert, J. P., Jalaguier, E., Pocas, S., and Aspar, B. (2003) ‘Modal analysis and engineering on InP-based two-dimensional photonic-crystal microlasers on a Si wafer’, *IEEE J Quantum Electron*, **39**, 419–425.

Mouette, J., Seassal, C., Letartre, X., Rojo-Romeo, P., Leclereq, J., Regreny, P., Viktorovitch, P., Jalaguier, E., Perreau, P., and Moriceau, H. (2003) ‘Very low threshold vertical emitting laser operation in InP graphite photonic crystal slab on silicon’, *Electron Lett*, **39**, 526–528.

Mukai, K., Ohtsuka, N., Sugawara, M., and Yamazaki, S. (1994) ‘Self-formed In0.5Ga0.5As quantum dots on GaAs substrates emitting at 1.3 μm’, *Jpn J Appl Phys*, **33**, L1710–L1712.

Mukai, K., Nakata, Y., Otsubo, K., Sugawara, M., Yokoyama, N., and Ishikawa, H. (1999) ‘1.3-μm CW lasing of InGaAs-GaAs quantum dots at room temperature with a threshold current of 8 mA’, *IEEE Photon Tech Lett*, **11**, 1205–1207.

Nakamura, Y., Koshiba, S., Tsuchiya, T., Kano, H., and Sakaki, H. (1991) ‘Enhanced crystallographic selectivity in molecular beam epitaxial growth of GaAs on mesas and formation of (001)-(111)B facet structures for edge quantum wires', *Appl Phys Lett*, **59**, 700–702.

Nakata, Y., Mukai, K., Sugawara, M., Ohtsubo, K., Ishikawa, H., and Yokoyama, N. (2000) 'Molecular beam epitaxial growth of InAs self-assembled quantum dots with light-emission at 1.3 μm', *J Crystal Growth,* 2**08**, 93–99.

Nishi, K., Saito, H., Sugou, S., and Lee, J.-S. (1999) 'A narrow photoluminescence linewidth of 21 meV at 1.35 μm from strain reduced InAs quantum dots covered by In0.2Ga0.8As grown on GaAs substrates', *Appl Phys Lett*, **74**, 1111–1113.

Nomura, M., Iwamoto, S., Watanabe, K., Kumagai, N., Nakata, Y., Ishida, S., and Arakawa, Y. (2006) 'Room temperature continuous-wave lasing in photonic crystal nanocavity', *Opt Express*, **14**, 6308–6315.

Nomura, M., Iwamoto, S., Tandaechanurat, A., Ota, Y., Kumagai, N., and Arakawa, Y. (2009a) 'Photonic band-edge micro lasers with quantum dot gain', *Opt Express*, **17**, 640–648.

Nomura, M., Kumagai, N., Iwamoto, S., Ota, Y., and Arakawa, Y. (2009b) 'Photonic crystal nanocavity laser with a single quantum dot gain', *Opt Express*, **17**, 15975–15982.

Nomura, M., Kumagai, N., Iwamoto, S., Ota, Y., and Arakawa, Y. (2010) 'Laser oscillation in a strongly coupled single-quantum-dot-nanocavity system', *Nature Phys*, **6**, 279–283.

Otsubo, K., Hatori, N., Ishida, M., Okumura, S., Akiyama, T., Nakata, Y., Ebe, H., Sugawara, M., and Arakawa, Y. (2004) 'Temperature-insensitive eye-opening under 10-Gb/s modulation of 1.3-μm P-doped quantum-dot lasers without current adjustments', *Jpn J Appl Phys Part 2*, **43**, L1124–1126.

Petroff, P. M., Gossard, A. C., and Wiegmann, W. W. (1984) 'Structure of AlAs-GaAs interfaces grown on (100) vicinal surfaces by molecular beam epitaxy', *Appl Phys Lett,* **45**, 620–622.

Painter, O., Lee, R. K., Scherer, A., Yariv, A., O'Brien, J. D., Dapkus, P. D. , and Kim, I. (1999) 'Two-dimensional photonic band-gap defect mode laser', *Science*, **284**, 1819–1821.

Rajesh, M., Bordel, D., Kawaguchi, K., Faure, S., Nishioka, M., Augendre, E., Clavelier, L., Guimard, D., and Arakawa, Y. (2011a) 'Growth of InAs/GaAs quantum dots on Si, Ge/Si and germanium-on-insulator-on-silicon (GeOI) substrates emitting at 1.3 μm band for silicon photonics', *J Cryst Growth*, **315**, 114–118.

Rajesh, M., Faure, S., Nishioka, M., Augendre, E., Clavelier, L., Guimard, D., and Arakawa, Y. (2011b) 'Effect of antimony on the photoluminescence intensity of InAs quantum dots grown on germanium-on-insulator-on-silicon substrate', *Appl Phys Express*, **4**, 045201.

Saito, H., Nishi, K., Sugimoto, Y., and Sugou, S. (1999) 'Low-threshold lasing from high-density InAs quantum dots of uniform size', *Electron Lett,* **35**, 1561–1562.

Shchekin, O. B. and Deppe, D. G. (2002) '1.3 μm InAs quantum dot laser with To = 161 K from 0 to 80 °C', *Appl Phys Lett* **80**, 3277–3279.

Shih, M. H., Mock, A., Bagheri, M., Suh, N., Farrell, S., Choi, S., O'Brien, J. D., and Dapkus, P. D. (2007) 'Photonic crystal lasers in InGaAsP on a SiO2/Si substrate and its thermal impedance', *Opt Express*, **15**, 227–232.

Shimbo, M., Furukawa, K., Fukuda, K., and Tanzawa, K. (1986) 'Silicon-to-silicon direct bonding method', *J Appl Phys*, **60**, 2987–2989.

Shoji, H., Nakata, Y., Mukai, K., Sugiyama, Y., Sugawara, M., Yokoyama, N., and Ishikawa, H. (1996) 'Room temperature CW operation at the ground state of self-formed quantum dot lasers with multi-stacked dot layer', *Electron. Lett.*, **32**, 2023–2024.

Stranski, I. N. and Von Krastanow, L. (1939) 'Abhandlungen der mathematisch-naturwissenschaftlichen klasse', *Akademie der Wissenschaften und der Literatur in Mainz,* 1**46**, 797–810.

Sugawara, M. (1999) *Self-Assembled InGaAs/GaAs Quantum Dots*. San Diego, Academic Press.

Sugawara, M., Mukai, K., and Nakata, Y. (1999) 'Light emission spectra of columnar-shaped self-assembled InGaAs/GaAs quantum-dot lasers: Effect of homogeneous broadening of the optical gain on lasing characteristics', *Appl Phys Lett*, **74**, 1561–1563.

Sugawara, M., Mukai, K., Nakata, Y., Ishikawa, H., and Sakamoto, A. (2000) 'Effect of homogeneous broadening of optical gain on lasing spectra in self-assembled InxGa1−xAs/GaAs quantum dot lasers', *Phys Rev B*, **61**, 7595–7603.

Sugawara, M., Hatori, N., Ebe, H., Ishida, M., Arakawa, Y., Akiyama, T., Otsubo, K., and Nakata, Y. (2005) 'Modeling room-temperature lasing spectra of 1.3-μm self-assembled InAs/GaAs quantum-dot lasers: Homogeneous broadening of optical gain under current injection', *J Appl Phys*, **97**, 43523–43530.

Sugo, M., Takanashi, Y., Aljassim, M. M., and Yamaguchi, M. (1990) 'Heteroepitaxial growth and characterization of InP on Si substrates', *J Appl Phys*, **68**, 540–547.

Takada, K., Tanaka, Y., Matsumoto, T., Ekawa, M., Nakata, Y., Yamamoto, T., Sugawara, M., and Arakawa, Y. (2009) 'Temperature-stable 10.3 Gb/s operation of 1.3 μm quantum-dot DFB lasers with GaInP/GaAs gratings', *OFC'***09**, JWA28.

Tanaka, Y., Ishida, M., Takada, K., Yamamoto, T., Song, H. Z., Nakata, Y., Yamaguchi, M., Nishi, K., Sugawara, M., and Arakawa, Y. (2010) '25 Gbps direct modulation in 1.3-μm InAs/GaAs high-density quantum dot lasers', CLEO2010, CTuZ1.

Takada, K., Tanaka, Y., Matsumoto, T., Ekawa, M., Song, H. Z., Nakata, Y., Yamaguchi, M., Nishi, K., Yamamoto, T., Sugawara M., and Arakawa, Y. (2010) '10.3-Gb/s operation over a wide temperature range in 1.3-μm quantum-dot DFB lasers with high modal gain', *Optical Fiber Communication Conference (OFC) 2010*, OThK2.

Takada, K., Tanaka, Y., Matsumoto, T., Ekawa, M., Song, H. Z., Nakata, Y., Yamaguchi, M., Nishi, K., Yamamoto, T., Sugawara, M., and Arakawa, Y. (2011) 'Wide-temperature-range 10.3-Gb/s operations of 1.3-μm high-density quantum-dot DFB lasers', *Electron Lett*, **47**, 206–208.

Tanabe, K., Nomura, M., Guimard, D., Iwamoto, S., and Arakawa, Y. (2009) 'Room temperature continuous wave operation of InAs/GaAs quantum dot photonic crystal nanocavity laser on silicon substrate', *Opt Express*, **17**, 7036–7042.

Tanabe, K., Guimard, D., Bordel, D., Iwamoto, S., and Arakawa, Y. (2010a) 'Electrically pumped 1.3 μm room-temperature InAs/GaAs quantum dot lasers on Si substrates by metal-mediated wafer bonding and layer transfer', *Opt Express*, **18**, 10604–10608.

Tanabe, K., Nomura, M., Guimard, D., Iwamoto, S., and Arakawa, Y. (2010b) 'Design, fabrication and optical characterization of GaAs photonic crystal nanocavity lasers with InAs quantum dots gain wafer-bonded onto Si substrates', *Physica E*, **42**, 2560–2562.

Tanabe, K., Guimard, D., Bordel, D., Iwamoto, S., and Arakawa, Y. (2011a) ‘Fabrication of electrically pumped InAs/GaAs quantum dot lasers on Si substrates by Au-mediated wafer bonding’, *Phys Stat Sol C*, **8**, 319–321.

Tanabe, K., Iwamoto, S., and Arakawa, Y. (2011b) ‘Novel III-V/Si hybrid laser structures with current injection across conductive wafer-bonded heterointerfaces: a proposal and analysis’, *IEICE Electron Express*, **8**, 596–603.

Tanabe, K., Watanabe, K., and Arakawa, Y. (2012) ‘III-V/Si hybrid photonic devices by direct fusion bonding’, *Sci. Rep.*, **2**, 349.

Tanaka, Y., Ishida, M., Maeda, Y., Akiyama, T., Yamamoto, T., Song, H. Z., Yamaguchi, M., Nakata, Y., Nishi, K., Sugawara, M., and Arakawa, Y (2009) ‘High-speed and temperature-insensitive operation in 1.3-μm InAs/GaAs high-density quantum dot lasers’, *Optical Fiber Communication Conference (OFC) 2009*, OWJ1.

Tanaka, Y., Ishida, M., Takada, K., Yamamoto, T., Song, H. Z., Nakata, Y., Yamaguchi, M., Nishi, K., Sugawara, M., and Arakawa, Y (2010) ‘25 Gbps direct modulation in 1.3-μm InAs/GaAs high-density quantum dot lasers’, *Conference on Lasers and Electro-Optics (CLEO) 2010*, CTuZ1, San Jose, USA.

Tong, Q.-Y. and Gosele, U. (1998) *Semiconductor wafer bonding: Science and technology*. New Jersey, Wiley.

Vail, E. C., O’Brien, S., Ziari, M., and Lang, R. (1998) ‘Semiconductor lasers with 2.5 Gb/s operation at 200°C’, *Proc. 16th IEEE Int. Semiconductor Laser Conf.*, TuD 1.

Van Campenhout, J., Rojo-Romeo, P., Regreny, P., Seassal, C., Van Thourhout, D., Verstuyft, S., Di Cioccio, L., Fedeli, J. -M., Lagahe, C., and Baets, R. (2007) ‘Electrically pumped InP-based microdisk lasers integrated with a nanophotonic silicon-on-insulator waveguide circuit’, *Opt Express*, **15**, 6744–6749.

Vecchi, G., Raineri, F., Sagnes, I., Yacomotti, A., Monnier, P., Karle, T. J., Lee, K., Bravive, R., Gratiet, L. L., Guilet, S., Beaudoin, G., Talneau, A., Bouchoule, S., Levenson, A., and Raj, R. (2007) ‘Continuous-wave operation of photonic band-edge laser near 1.55 μm on silicon wafer’, *Opt Express*, **15**, 7551–7556.

Wada, H., Takemasa, K., Munakata, T., Kobayashi, M., and Kamijoh, T. (1999) ‘Effects of well number on temperature characteristics in 1.3μm AlGaInAs-InP quantum well lasers’, *IEEE J Select Topics Quantum Electron*, **5**, 420–427.

Wang, T., Liu, H., Lee, A., Pozzi, F., and Seeds, A. (2011) ‘1.3-μm InAs/GaAs quantum-dot lasers monolithically grown on Si substrates’, *Opt Express*, **19**, 11381–11386.

Yamaguchi, K., Yujobo, K., and Kaizu, T. (2000) ‘Stranski-Krastanov growth of InAs quantum dots with narrow size distribution’, *Jpn J Appl Phys,* **39**, L1245–L1248.

Yang, J. and Bhattacharya, P. (2008) ‘Integration of epitaxially-grown InGaAs/GaAs quantum dot lasers with hydrogenated amorphous silicon waveguides on silicon’, *Opt Express*, **16**, 5136–5140.

Yoshie, T., Shchekin, O. B., Chen, H., Deppe, D. G., and Scherer, A. (2002) ‘Quantum dot photonic crystal lasers’, *Electron Lett*, **38**, 967–968.

8

Vertical cavity surface emitting lasers (VCSELs)

K. D. CHOQUETTE, University of Illinois, USA

DOI: 10.1533/9780857096401.2.316

Abstract: The semiconductor vertical cavity surface emitting laser (VCSEL) diode is introduced and the dominant applications that use the nearly one billion VCSELs that have been deployed world-wide are reviewed. The chapter focusses on fundamental aspects such as the VCSEL device structure, including the distributed Bragg reflector mirrors, the optical cavity and various emission wavelengths, and the means for creating electrical and optical transverse confinement in the laser diode. The critical interplay of the spectral alignment of the Fabry–Pérot cavity resonance, which selects the lasing wavelength, and the laser gain bandwidth, which influences the threshold of the VCSEL, is shown to dominate nearly every aspect of VCSEL performance. Finally, the performance of 850 nm VCSELs is presented and the influence of various VCSEL parameters on the laser efficiency, threshold, transverse mode characteristics, and polarization are described.

Keywords: vertical cavity surface emitting laser, distributed Bragg reflector, single transverse mode, laser applications, two-dimensional arrays.

8.1 Introduction

The vertical cavity surface emitting laser (VCSEL) is a semiconductor microcavity laser that has found deployment in numerous applications around the world and can be considered a critical technology for the information age infrastructure. After reviewing the historical development of VCSELs over the past 30 years, the commercial applications that are driving the development of this optoelectronic technology are introduced. The epitaxial device structure of the VCSEL is described, including the requirements of the distributed Bragg reflector mirrors, the active region which produces the various laser emission wavelengths, and the lateral device structure arising from the fabrication processes. The spectral alignment between the laser gain and the cavity resonance is shown to be an important phenomenon for understanding VCSEL performance. The VCSEL optical properties are reviewed. The device parameters that affect the laser efficiency are discussed, as well as the transverse mode and polarization properties of VCSELs. Finally, two-dimensional VCSEL arrays are introduced, and the different array geometries are briefly reviewed. The conclusion of the chapter includes a discussion of the future trends in VCSEL development and performance.

8.1.1 History

The semiconductor laser was discovered and invented in 1962, which launched 50 years and counting of continued laser diode development and introduction of new applications. In 1978 Professor Kenicha Iga at the Tokyo Institute of Technology had the idea of causing the light emission to be perpendicular, rather than horizontal, to the semiconductor wafer from which the laser is made (Iga, 2000). The first report of a VCSEL followed in 1979 (Soda *et al*., 1979) and by the mid 1980s VCSEL research had significantly increased, fueled by the development of semiconductor distributor Bragg reflector (DBR) mirrors (Gourley and Drummond, 1986). Compared to their edge-emitting laser counterparts, the primary VCSEL advantages include their circularly symmetric high-quality optical beam, ultralow power operation, ease of integration in dense two-dimensional (2D) arrays, and the potential of low cost and high volume manufacture. With the advent of the Internet, low cost laser sources which could be easily coupled to optical fiber were in great demand, which stimulated further research toward continuously improved VCSEL performance. By the mid 1990s, an industry was established by numerous companies manufacturing VCSEL driven by the continued deployment VCSEL applications. Since the year 2000, VCSEL production has grown to more than 50 million manufactured annually, and nearly a billion have been deployed around the world. Compared to the past, there are now fewer companies, manufacturing greater and increasing numbers of VCSELs. Without a doubt, VCSELs can be considered the laser source for the information age.

8.1.2 Applications

For what applications can you use a VCSEL? In Table 8.1 we list their general application areas. The division of the application areas is according to whether the light emission is in multiple transverse optical modes or in the single fundamental Gaussian mode (Section 8.3.2), and whether an individual laser or an array of lasers is used (Section 8.3.3). If we consider an individual VCSEL operating in multiple modes, the overwhelmingly dominant application is in optical data links for local area and storage area networks. These optical links are composed of a laser, an optical fiber, and a photodetector, and are used to send high speed digital data from centimeters to 300 m or more in length. These optical data links are also used to connect routers

Table 8.1 VCSEL applications

	Multi-mode operation	Single-mode operation
Individual VCSEL	• Local and storage area network • Server/router interconnect • Active cable • Plastic fiber links (automotive)	• Position sensing (laser mice) • Chemical sensing • Encoder • Metro access networks
2D VCSEL array	• Solid state pumps • Laser Imaging Detection and Ranging (LIDAR) • Medical therapy • Tailored heating	• Laser printing • Parallel channel high speed links • Coherent arrays (high brightness) • Chip optical interconnects

and servers in data centers and mobile telephone switching offices, as well as interconnects between central processing units and memory within high performance computing applications. The biggest advantages that VCSELs hold for these applications are their excellent coupling to optical fiber, low operation power, and low cost/high volume manufacture.

Why is data communication such an important application? Since the mid 1990s there has been an explosion of optical data network deployment, driven by Internet and mobile telephone applications. Hence increasing data bandwidth demand, combined with a greater number of Internet and mobile phone users, has created an ever-increasing need for higher performance optical data links. Whereas optical telecommunication networks deployed across the Pacific and Atlantic oceans in the 1970s had exploited the low attenuation of optical signals in fiber, data communication requirements in the 2010s are driven more and more by increasing the data communication bandwidth. While ever-higher direct modulation rates continue to drive the research and development of VCSELs, achieving these rates at lower power will become increasingly important.

Another application, that uses many millions of VCSELs, is position sensing. The most common example is the computer 'mouse'. Note that this application requires single mode emission for accurate position tracking. The principle advantage of a VCSEL in this application is its ultralow power and excellent beam quality. For both optical data links and optical mice, the lasers typically emit at 850 nm, which is the most mature VCSEL technology.

There are other applications for VCSELs that continue to develop. For single mode VCSELs emitting at longer wavelengths (such as 1300 and 1550 nm), optical communication over longer length spans (> 1 km), such as in metro access networks, become of interest. For VCSELs that emit at mid infrared wavelengths (> 2000 nm), gas sensing applications are numerous because of the many molecular vibration modes that can be excited. VCSELs emitting at 650 nm continue to be attractive for ultralow cost plastic optical fiber systems of potential use in automotive applications. The ability to fabricate dense two-dimensional (2D) arrays is a unique VCSEL advantage

(Section 8.3.4), which has high power application for optical pumping, heating, and medical therapy. Finally, dense arrays of single mode VCSELs are currently deployed in laser printer applications, and will open up coherent array applications for high brightness laser sources, as well as very high-density optical interconnects at the board-level or even chip-level.

What makes the VCSEL attractive for these applications? Perhaps the biggest advantage of the VCSEL is its excellent lifetime characteristics. VCSEL reliability is considered superior to all other types of lasers. The reason for this excellent reliability lies with the VCSEL's monolithic epitaxial structure and relatively simple manufacturing steps. The rapid acceptance of VCSELs in the optoelectronic industry arises because of the many manufacturing advantages they possess. In particular, VCSELs can be tested at the wafer level at every step during their fabrication. This is significantly different for an edge-emitting semiconductor laser, since cleaving its laser facets is usually the last step of manufacturing. In addition the generic VCSEL has monolithic semiconductor DBR mirrors, which are fashioned during the growth of the epitaxial wafer, making it very amenable to high volume manufacture.

8.2 Device structure

We next discuss the VCSEL structure (Jewell *et al.*, 1991; Chow *et al.*, 1997). We first consider the epitaxial semiconductor layers of a VCSEL, which include the DBR mirrors which provide the longitudinal optical confinement. We next consider the semiconductors used for various emission wavelengths, and discuss the spectral overlap between laser gain and cavity resonance and the critical role this has on VCSEL performance. Finally, we describe the transverse confinement of a VCSEL, which is related to, and created by, the manufacturing process used to fabricate the laser.

There are three components needed for a laser. First, we need an optical medium to generate photons to generate light. We use direct bandgap semiconductors (GaAs is the most commonly used), or more specifically semiconductor quantum wells, to generate the necessary photons. In addition we need an excitation source, which will be electrical current injected into a p-n junction. Semiconductor laser diodes have been shown to be the most efficient means to generate stimulated emission. Finally, the third component needed for a laser is the optical resonator, which is the optical cavity needed to build up the photon density required to achieve stimulated emission.

8.2.1 Longitudinal confinement

The VCSEL utilizes a Fabry–Pérot optical cavity, which is composed of two parallel mirrors separated by a distance of $\lambda/2$, where λ is the desired laser emission wavelength. To have emission from the top surface of a semiconductor wafer, the mirrors that form the cavity must have reflectivities that are nearly unity. Such a mirror can be made from a sequence of two layers with varying refractive index which are called distributed Bragg reflector (DBR) mirrors. The top and bottom DBR mirrors, the active region containing the quantum wells inside of the optical cavity, and the electrical contacts needed for injection of current, are all sketched in the lower part of Fig. 8.1. The reflectivity of the top mirror is slightly lower as compared to the bottom mirror, and thus the light is emitted from the top in Fig. 8.1.

In Fig. 8.2 is a transmission electron micrograph showing a portion of the DBR mirrors on either side of the optical cavity of a VCSEL, alongside a sketch of the refractive index of the semiconductor layers and the intensity profile of the longitudinal mode. Note the optical cavity contains five gallium arsenide quantum wells (darkest lines in micrograph) which will emit light at approximately 850 nm. On the top and bottom of the optical cavity are the DBR mirrors composed of low (light layers) and high (dark layers) refractive index semiconductors. As you can see in the Fig. 8.2 sketch, the longitudinal optical mode of a VCSEL is defined by the DBR mirrors.

The refractive index variation of the DBR mirror creates the required reflectance of the mirror. Notice the overlap between the longitudinal mode standing wave that 'sets up' in the optical cavity in Fig. 8.2. Clearly the mode overlaps the quantum wells, which is good since they provide the generated photons for the lasing emission. Further, notice that when there is an interface between a high index and low index semiconductor layer, the mode intensity (and thus electric field) is a relative maximum. This indicates the reflectance from this interface is relatively high; to achieve a mirror with high overall reflectivity, we position a multiple number of these interfaces to be one half a wavelength apart, so that the reflectivity from each interface will add constructively. The simplest manner to achieve this condition is to make each high and low refractive index layer thickness equal to $\lambda/4$; thus DBR mirrors are sometimes called 'quarterwave stacks'. The DBR mirrors of an 850 nm VCSEL can use low (high) Al-containing $Al_xGa_{1-x}As$ layers for the high (low) index layers, and can achieve a reflectivity as high as 99.9% by using 30 periods or greater. The calculated reflectance spectrum measured from the top surface of a 850 nm VCSEL wafer is shown in Fig. 8.3. Note that this mirror exhibits a reflectance value near unity over a wavelength span, which is called the mirror stop band, of nearly 100 nm.

Figures 8.2 and 8.3 demonstrate that correct growth of the semiconductor layers in the epitaxial structure is very important: there are three aspects that must be achieved to high precision. Firstly, the semiconductor composition dictates the refractive index and we need to get the correct refractive indices; secondly, we require the correct layer thickness to define a proper DBR mirror and optical cavity. So to have the proper longitudinal mode in

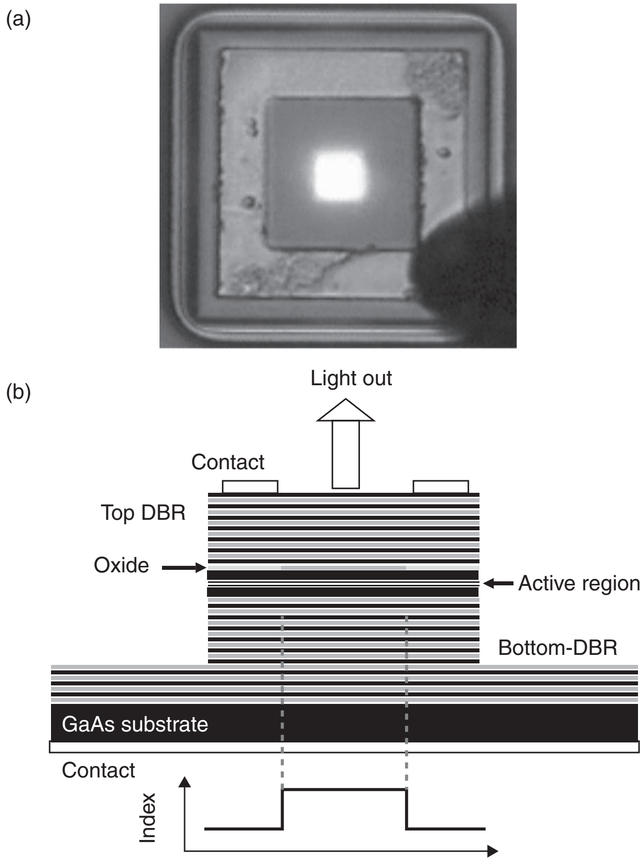

8.1 Side view sketch (b) of an oxide-confined VCSEL; the lower inset shows the refractive index profile across the cavity, while panel (a) shows a lasing mode confined by an oxide aperture inside a top electrical contact.

the VCSEL structure we need both the composition and thickness of each DBR layer to be correct.

The third important epitaxial issue is the introduction of electrical impurities (doping) into the semiconductor layers (Chow *et al.*, 1997; Choquette and Geib, 1999). Since we need to have an electrical p-n junction within the optical cavity (not shown in Figs 8.1 or 8.2), typically one DBR is doped p-type and the other DBR is doped n-type. Figure 8.4 shows the impurity depth profiles in the top (carbon doped), and bottom (silicon doped) DBR, and the varying Al content of an 850 nm VCSEL composed of $Al_xGa_{1-x}As$ layers (Kim *et al.*, 2004). The impurities and Al composition are measured by secondary ion mass spectroscopy. The active region can be identified as the region with the lowest Al content and dopant impurities (the quantum

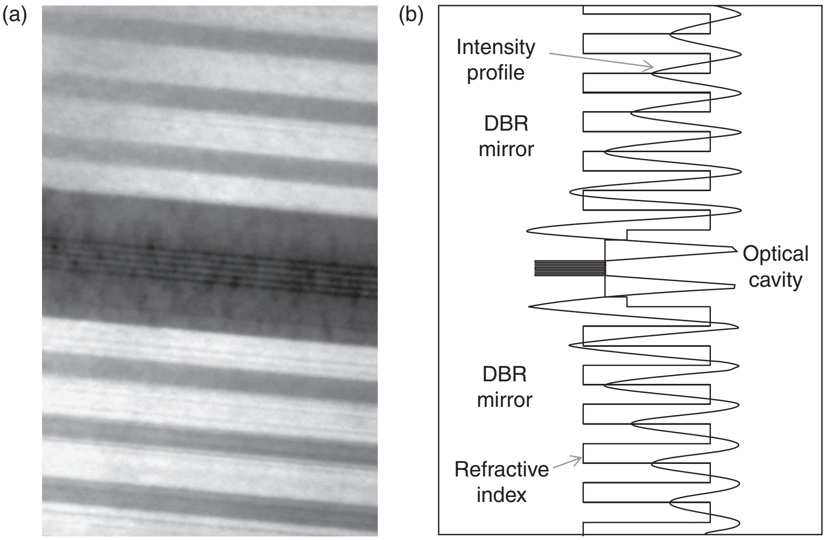

8.2 Transmission electron micrograph (a) and sketch (b) of the refractive index and optical intensity profiles in the optical cavity and surrounding regions of the top and bottom DBR mirror.

wells cannot be resolved), while the 23 period top mirror is p-type (using C) and the bottom mirror is n-type (using Si). To achieve low electrical resistance, the compositional grading between the high and low index layers, as well as the dopant impurity concentration profile is carefully controlled and tailored over every layer of the epitaxial material (Choquette and Geib, 1999).

So far we have discussed the optical reflectivity and electrical impurities of the DBR mirrors. However, to form a proper optical cavity as noted previously, the mirrors must be separated by a thickness equal to a multiple of a half-wavelength of the desired emission wavelength. For most VCSELs the optical cavity is made to be λ thick; this ensures that the peak of the longitudinal mode occurs in the center of the active region, which is where the quantum wells are positioned (see Fig. 8.2), and that the cavity resonance is at the peak of the DBR reflectivity. The latter condition is shown in Fig. 8.3 by the very sharp ‘dip’ in the reflectance spectrum (i.e. a transmission peak) at the center of the mirror stop band, which in Fig. 8.2 is 850 nm wavelength. This is the cavity resonance, which specifically defines the laser emission wavelength, as long as the quantum wells in the optical cavity emit appropriately. Thus the cavity resonance as determined by the Fabry–Pérot cavity dominates the optical performance of the VCSEL. The effects of the spectral alignment between the resonance and the optical gain will be discussed in greater detail in Section 8.2.3.

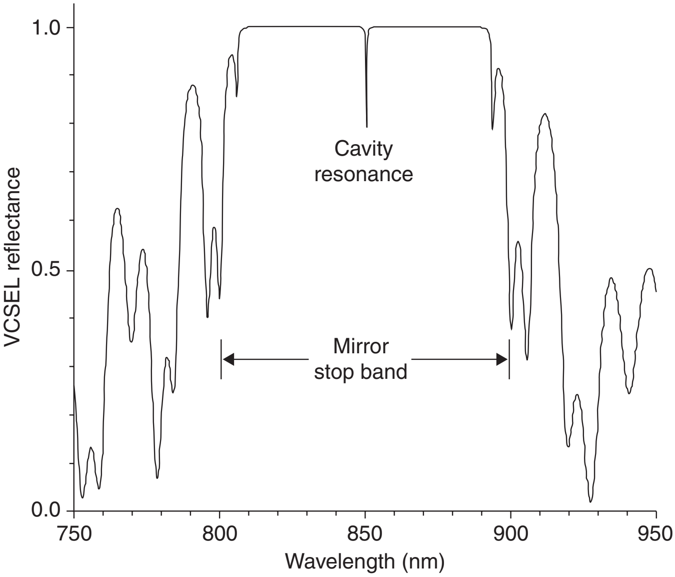

8.3 Calculated VCSEL reflectance spectrum showing the cavity resonance at 850 nm inside the DBR mirror stop band.

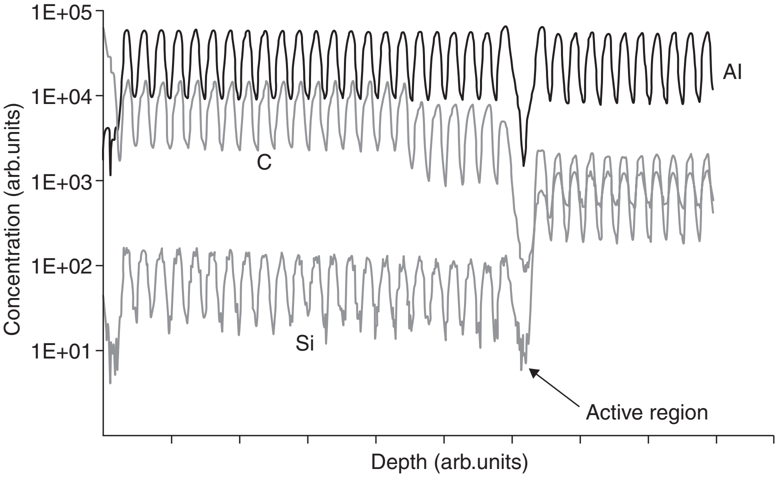

8.4 Al, C, and Si concentrations measured by secondary ion mass spectroscopy as a function of depth into a VCSEL.

8.2.2 Optical cavity

VCSELs are composed of approximately 100 different semiconductor layers; we have seen that the composition, thickness and doping concentrations

Table 8.2 VCSEL semiconductor materials

Wavelength (nm)	Quantum well	High index	Low index
450	$In_{0.2}Ga_{0.8}N$	GaN	AlN
650	InGaP	$Al_{0.5}Ga_{0.5}As$	$Al_{0.96}Ga_{0.04}As$
780	$Al_{0.12}Ga_{0.88}As$	$Al_{0.25}Ga_{0.75}As$	$Al_{0.92}Ga_{0.08}As$
850	GaAs	$Al_{0.16}Ga_{0.84}As$	$Al_{0.92}Ga_{0.08}As$
980	$In_{0.2}Ga_{0.8}As$	GaAs	$Al_{0.92}Ga_{0.08}As$
1300	$Al_{0.34}Ga_{0.46}AsN_{0.01}$ or GaAsSb	GaAs	$Al_{0.92}Ga_{0.08}As$
1300 and 1550	InGaAsP	GaAs (wafer bonded)	$Al_{0.92}Ga_{0.08}As$ (wafer bonded)
1300 and 1550	InGaAsP	InGaAsP	InP
1500	AlInGaAs	AlAsSb	AlGaAsSb
2300	GaInAsSb	AlAsSb	GaSb

are all important quantities that must be correct in order to define the longitudinal mode. Notice that the control of the epitaxial layers is on the same length scale as the wavelength of light in the material. Hence, VCSELs can be considered microcavity lasers, for which in one-dimension (the longitudinal direction) the cavity and optical mode are uniquely and specifically engineered. To accomplish this at different laser wavelengths will require different semiconductors (Choquette and Hou, 1997).

In Table 8.2 we show commonly employed semiconductor materials for the DBR mirrors and the quantum wells (i.e. active region) for VCSEL emission wavelength from 450 to 2300 nm. The layers of the DBR mirrors need to have a differing values of refractive index, but both must be transparent to the laser emission. In Table 8.2 we only show semiconductor materials for the DBR layers which can be grown epitaxially with a semiconductor quantum well active region. It is also possible to use dielectric materials to form the DBR mirrors (Baba *et al.*, 1993; Huffaker *et al.*, 1994; Lu *et al.*, 2008), but in these cases the electrical current does not flow through the DBR mirrors such as shown in Fig. 8.1.

For VCSEL wavelengths longer than 840 nm, GaAs can be used as a high index DBR layer and the low index layer can be high Al-containing $Al_xGa_{1-x}As$ (typically AlAs is not used in oxide-confined VCSELs as discussed in Section 8.2.4). Note that Table 8.2 indicates that quantum wells using the InGaP, AlGaInAs(N) and GaAsSb alloy systems that emit in the wavelength regime of 650–1300 nm and are lattice matched to GaAs substrates can all exploit AlGaAs layers for the DBR mirrors (Choquette and Hou, 1997). Example wavelengths of GaAs lattice-matched VCSELs include visible 650 nm (Choquette *et al.*, 1993; Schneider *et al.*, 1995), 850 nm (Lee *et al.*, 1990; Wang *et al.*, 1990), 980 nm (Geels *et al.*, 1993) and 1300 nm (Choquette *et al.*, 2000; Yamada *et al.*, 2000). Because of the relative maturity of device fabrication using GaAs substrates, as well as the large index contrast that is available in the AlGaAs alloy system (Gourley and Drummond, 1986), VCSELs which use GaAs quantum wells emitting at 850 nm are by far the most commonly manufactured commercially.

Wavelengths outside of the range 650–1300 nm have required other semiconductor materials for the epitaxial wafers. The dual challenges of VCSELs at these wavelengths is achieving sufficiently high reflectivity in the semiconductor DBR mirrors (due to the relatively small variation of the refractive index between the DBR layers which requires many periods) and achieving sufficiently high electrical impurity concentration (usually the p-type dopant) in the semiconductor DBR layers for efficient diode operation. Table 8.2 shows examples for shorter wavelength and longer wavelength VCSELs that do not use $Al_xGa_{1-x}As$-based DBR mirrors. Blue VCSELs have been demonstrated utilizing the InGaN alloy system grown on sapphire substrate (Higuchi *et al.*, 2008; Lu *et al.*, 2008). These lasers are of interest for imaging and display applications, but commercial production is not yet available.

VCSELs appropriate for telecommunication wavelengths are desirable for optical interconnect applications. The wavelength regimes of interest are 1300 nm, which corresponds to the dispersion minimum of silica optical fiber, and 1550 nm, which is the optical attenuation minimum of optical fiber. Usually semiconductor lasers emitting at these wavelengths rely upon quantum wells that are lattice matched to InP substrates. The challenge of obtaining sufficient DBR reflectivity from semiconductor mirrors grown on InP is particularly prominent, so various VCSEL device structures have been considered. As noted above, suitable quantum wells combined with dielectric DBRs can be used (Baba *et al.*, 1993). Table 8.2 shows the two other dominant approaches: (i) using semiconductor DBR layers lattice matched to InP (Tadokoro *et al.*, 1992; Salet *et al.*, 1997; Hall *et al.*, 2000); or (ii) using wafer-bonded GaAs/AlGaAs DBRs to a InP-lattice-matched quantum wells (Dudley *et al.*, 1994; Dubravko, 1995). Various combinations of dielectric, wafer-bonded or epitaxially grown DBRs have also been demonstrated for 1300 and 1550 nm VCSELs.

For wavelengths of 2.3 μm and longer, InGaSb quantum wells with DBR mirrors lattice matched to GaSb substrates have been pursued (Bachmann *et al.*, 2008; Ducanchez *et al.*, 2009). These long wavelength VCSELs have been used for gas sensing applications. To date commercial manufacture of 1300, 1550 or 2300 nm VCSELs is very limited because of the challenging fabrication required, in spite of the promising applications that are enabled.

8.2.3 Gain bandwidth and cavity resonance spectral alignment

Because of the microcavity effect, that is, how the optical cavity determined by the epitaxial layers dictates the longitudinal mode, virtually every

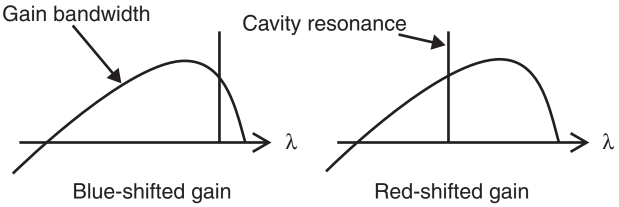

8.5 Sketch of the spectral alignment between the cavity resonance and VCSEL gain bandwidth for blue- and red-shifted conditions.

optical (and some electrical) property of the VCSEL can be understood by considering how this mode spectrally and spatially overlaps the laser gain bandwidth (Hasnain *et al.*, 1991). A schematic showing the gain profile as a function of wavelength is shown in Fig. 8.5. The long wavelength spectral endpoint of the VCSEL gain bandwidth is determined roughly by the bandgap energy (or more precisely the ground state electron quantum well confinement energy) of the active region material. The high energy side of the gain is roughly the difference in energy of the quasi-Fermi levels on the electron and hole side of the p-n junction. Between these energies the semiconductor will emit photons from recombination of electron/hole pairs creating optical gain.

The vertical lines in Fig. 8.5 represent the cavity resonance that is allowed to oscillate in the cavity (see also the sharp dip in the reflectance in Fig. 8.3). Because of the short VCSEL cavity (typically one λ in length) there is only one cavity resonance that overlaps the laser gain of a VCSEL. Notice that the resonance could be at longer or shorter wavelength than the wavelength of maximum gain, as illustrated in Fig. 8.5. Hence, the threshold gain (and threshold current) for stimulated emission will be influenced by the spectral alignment between the laser gain and cavity resonance. Therefore the *cavity resonance* (and not the peak gain) dictates the lasing wavelength of a VCSEL, and anything that influences the alignment between the resonance and the gain bandwidth will change the laser threshold.

As an aside, this is a very different situation from an edge-emitting semiconductor laser, which usually has a much longer cavity (roughly hundreds of λ in length). Now the spectral splits between the longitudinal modes, which are inversely proportional to the cavity length, are spectrally quite close together. Because of this, there is always a cavity mode that will overlap the peak of the gain bandwidth. Hence the *peak gain* determines the lasing wavelength of an edge-emitting laser.

In Fig. 8.5 we show two conditions for a VCSEL: blue- and red-shifted gain where the resonance is at longer and shorter wavelength than the peak gain, respectively. Recall that the long wavelength side of the gain is determined roughly by the bandgap wavelength; hence, as temperature increases, the gain bandwidth will shift to a longer wavelength. However, the resonance wavelength will also shift to longer wavelengths, due to the increase of the refractive index of the cavity materials with increasing temperature. Unfortunately, the gain shifts much faster with temperature (for GaAs roughly six times faster) than the resonance wavelength. As a result, a VCSEL can be designed to have blue-shifted gain at room temperature, and with increasing temperature the threshold for lasing will decrease as the resonance becomes aligned with the peak gain. For increasing temperature the gain will continue to shift to longer wavelengths, producing the red-shifted gain condition shown in Fig. 8.5, and increasing threshold will be observed. So the spectral overlap between the resonance and the gain will dictate the wavelength that the laser will emit and will also influence its performance. (Note that an edge-emitter will exhibit monotonically increasing threshold current with increasing temperature, due to the decrease of the peak gain.)

The variation of threshold current with temperature can thus be engineered through proper design of the VCSEL cavity. Hence, VCSELs can be optimized for high temperature (Young *et al.*, 1993) or cryogenic applications (Goncher *et al.*, 1996), an attribute that is absent for edge-emitting lasers. The uniformity of the epitaxial layer thickness and composition in a wafer will also influence the uniformity of VCSEL threshold current found at difference regions of a wafer. Finally, in Section 8.3.1 we will see that the maximum output power of a VCSEL is related to the spectral alignment between the cavity resonance and gain.

8.2.4 Lateral confinement

As shown in Section 8.2.2, the longitudinal mode is engineered by the layer thicknesses and composition of the DBR mirrors and cavity, and this is determined during the epitaxial growth of the VCSEL wafer. In contrast, the transverse confinement of the laser emission is determined by the device structure, which is affected by how the VCSEL is fabricated (Choquette and Geib, 1999). We next compare the two most common VCSEL device structures: the ion-implanted and selectively oxidized VCSEL.

The electrical current injected between a ring contact on the top DBR (see Fig. 8.1a) and a broad area contact on the bottom DBR (or backside of the wafer) must be laterally constrained to flow into the region of the optical cavity. The simplest method to constrain the current is to etch a pillar through the top and bottom DBR mirrors. This turns out to create inefficient lasers, since the exposed sidewalls will experience nonradiative recombination and the removed semiconductor around the cavity reduces the heat sinking, exacerbating thermal effects (Choquette *et al.*, 1991).

A surprisingly effective means to control the current path is to use ion implantation into the top DBR mirror (Tai *et al.*, 1989; Lee *et al.*, 1990). Typically proton implantation is used to bombard the top semiconductor mirror to render the material nonconductive. By masking the center of the top ring contact to block the ion implantation, the injected current will avoid the damaged perimeter and will funnel into the central region to produce gain in the active region, thus defining the laser cavity. Hence the ion-implanted VCSEL is described to be 'gain-guided'. The advantages of this structure are (i) the resulting device is planar, and (ii) the reliability of implanted VCSELs is extremely good. This latter point may be surprising, but remember the ion-damage surrounds the laser cavity and only determines the current path. Therein also lies the primary disadvantage of implanted VCSELs: there is no transverse refractive index variation created by the ion implantation to transversely guide the laser emission. In fact the transverse cavity of an implanted VCSEL is usually defined by thermal effects, which limits the maximum modulation to less than a few gigabits/sec (Hasnain *et al.*, 1991; Lear *et al.*, 1996).

In order to introduce a transverse index profile and simultaneously create a current path, a buried oxide layer as sketched in Fig. 8.1b is introduced (Choquette *et al.*, 1994; Choquette 2000b). These lasers are called 'oxide-confined' VCSELs and have enabled significant laser performance enhancements (Choquette *et al.*, 1995; Lear *et al.*, 1995). As shown in Fig. 8.1, the highest Al-containing layers of the DBR mirror is oxidized and converted to Al_2O_3, which is electrically insulating. Obviously this will funnel the current into the center of the cavity. But as importantly, this oxide layer has a significantly lower refractive index. Hence, the step index profile sketched in Fig. 8.1b can be produced, which will transversely confine the photons in the laser cavity. This significantly reduces the diffraction loss of oxide-confined VCSELs, leading to very low values of threshold current (Huffaker *et al.*, 1994).

An example of an oxide aperture is apparent in Fig. 8.1a, where the laser emission is contained with an oxide aperture (inside the ring electrical contact) located within the top DBR near the optical cavity. This can be seen in more detail in cross-section in the transmission electron micrograph depicted in Fig. 8.6. Here five layers of the DBR mirror have been selectively oxidized, where the lowest layer immediately adjacent to the optical cavity has a greater extent. This layer thus defines the cavity diameter, since the injected current and photons are confined. It should be apparent from Fig. 8.6 that the transverse index profile can be tailored by controlling the relative oxidation rates of individual DBR layers, which has been used to modify the VCSEL modal properties (Choquette, 2000b). Because of the excellent confinement of both electrons and photons inside the cavity of oxide-confined VCSELs, which will be shown in Section 8.3.1,

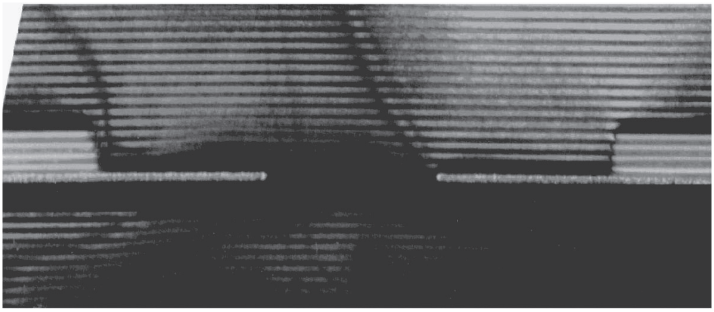

8.6 Transmission electron micrograph of an oxide-confined VCSEL aperture showing five oxide layers, with one layer defining a 1 μm aperture.

these lasers exhibit the best levels of performance in nearly every laser property.

8.3 Vertical cavity surface emitting laser (VCSEL) optical performance

The continuous wave optical properties (i.e. DC injection current) will be discussed in this section. The device parameters that influence the output power and efficiency will be described and the transverse and polarization properties of VCSELs will be introduced.

8.3.1 Output and efficiency

Figure 8.7 shows the light and voltage curves as a function of injection current for an oxide-confined 850 nm VCSEL with square aperture with size 5 × 5 μm^2. This VCSEL epitaxy is a generic commercial wafer with three GaAs quantum wells in the active region and 21 top (35 bottom) DBR periods using the layer compositions noted in Table 8.2. As the injection current increases from zero, the applied voltage increases to approximately 1.3 V (diode turn-on) and subsequently shows an approximately constant series resistance. The laser output of the VCSEL shows a threshold current of 220 μA and threshold voltage of 1.54 V. The light increases approximately linearly until a maximum power of 3.5 mW at 11 mA is obtained; this point is commonly called 'rollover'. Further increase of the injection current leads to decreased laser output. As discussed in Section 8.2.2, when the laser gain becomes 'red-shifted' relative to the cavity resonance, the available laser gain decreases, which implies reduced laser output. The laser gain shifts to a longer wavelength due to the increased temperature at the p-n junction

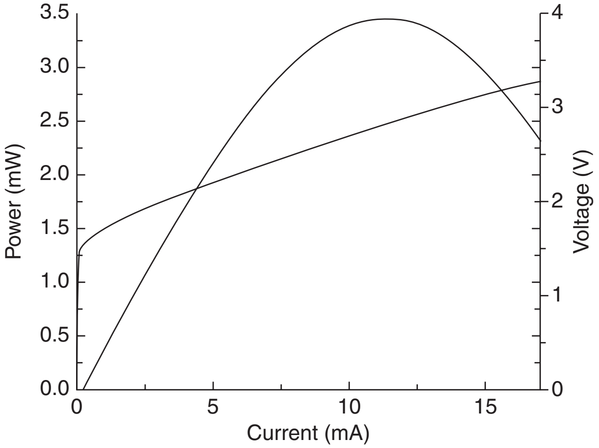

8.7 Light and voltage curves versus injection current for an 850 nm VCSEL.

arising from the series resistance parasitic heating. To increase the VCSEL maximum power level, reduction of the series resistance and better heat sinking is required.

Figure 8.8a shows the light versus current characteristics of VCSELs with varying sized oxide apertures. Note that for larger laser cross-section, the roll over maximum power and injection current increases. This is due to the improved heat sinking for the larger diameters. In Fig. 8.8b the threshold current is plotted as a function of the aperture size. Note that for cross-section area varying 1–100 μm^2, the threshold current is less than 1 mA for this VCSEL wafer design. For aperture sizes 4 μm and greater, the threshold current density is constant. However, for smaller aperture sizes, the threshold current density and eventually the threshold current increases. This deviation from the expected scalability arises because the VCSEL transverse optical mode begins to interact with the oxide aperture creating additional optical loss (Choquette *et al*., 1997).

Another means to control the output power of a laser is to design the output mirror reflectivity. By changing the number of periods of the top DBR mirror, the reflectivity can be varied. In Fig. 8.9 we show the threshold current and the differential slope efficiency (ratio of photons emitted/electrons injected) for VCSEL wafers with differing numbers of periods and reflectivity in the top DBR mirror. (These nominally 850 nm VCSELs have five GaAs quantum wells and have 5 × 5 μm^2 oxide apertures). For a decreasing number of periods (decreasing reflectivity) we see a monotonically increasing threshold current and differential slope efficiency. As the mirror loss of the VCSEL increases, more light is emitted but a higher threshold to achieve stimulated emission is also required. Note that viable VCSELs can

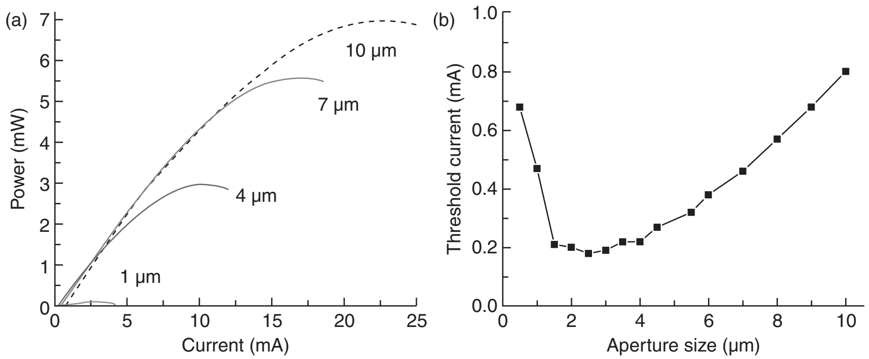

8.8 (a) Light versus injection current for VCSELs with square oxide apertures with side length of 1, 4, 7 and 10 µm; and (b) threshold current versus aperture size.

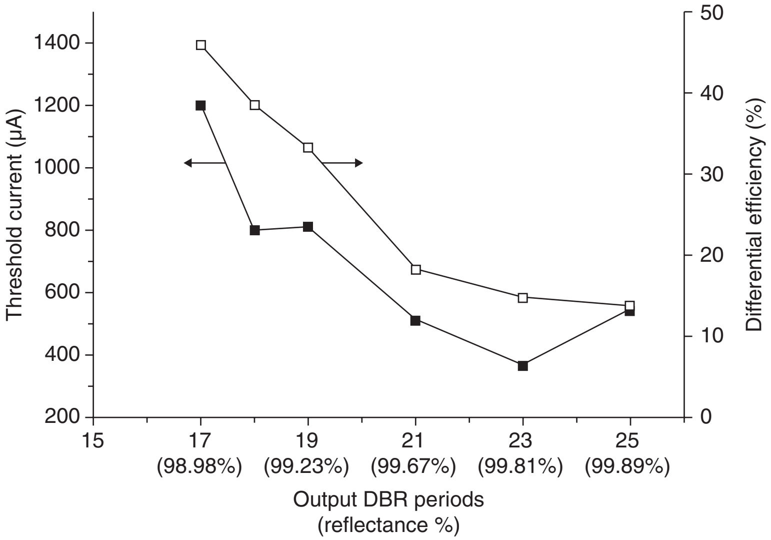

8.9 Threshold current and differential slope efficiency for VCSELs with 5x5 µm^2 apertures and varying top output DBR periods and reflectivity.

be obtained with an output reflectivity less than 99%, but this comes at the expense of higher threshold. The lowest threshold occurs for high reflectivity, but with a low slope efficiency.

For data communication applications, often the light emission must remain low (for eye safety reasons), and it is desirable to have a low threshold current. For direct modulation of VCSELs, to increase the modulation rate requires increasing the photon cavity density. This implies operating the VCSEL at high current levels above threshold; the limit will be the roll over current, since greater injection actually leads to lower light output. Therefore for high speed VCSEL modulation, often VCSELs are designed with increased output mirror reflectivity and a correspondingly modest differential slope efficiency.

8.3.2 Transverse optical modes

Lasers operate in both longitudinal and transverse optical modes (edge-emitting lasers also have lateral modes, but in a VCSEL transverse and lateral modes are the same). What are transverse modes? Figure 8.2 illustrates the longitudinal intensity standing wave that sets up in the DBR mirrors and cavity of a VCSEL. We called this an optical microcavity, since the epitaxial periodicity precisely matches the emission wavelength (i.e. on the order of several hundreds of nm). However in the transverse dimension, VCSELs tend to be fairly broad, on the order of 5–20 microns in diameter. Hence there can be many allowable transverse modes in a VCSEL, where each mode has a unique intensity (electric field) profile, with a slightly different wavelength. In Section 8.1.2, we divided VCSEL applications according to whether the VCSEL operated in multiple transverse modes or a single mode.

The lasing emission spectra for a 10 μm diameter oxide-confined VCSEL at different ambient temperature (and 2 × threshold) are plotted in Fig. 8.10a. The approximately four different peaks that are apparent at each temperature correspond to the multiple transverse optical modes that are lasing in the VCSEL. Notice that the modes all shift to longer wavelength with increasing temperature, as expected. In Fig. 8.10b we plot the spectral

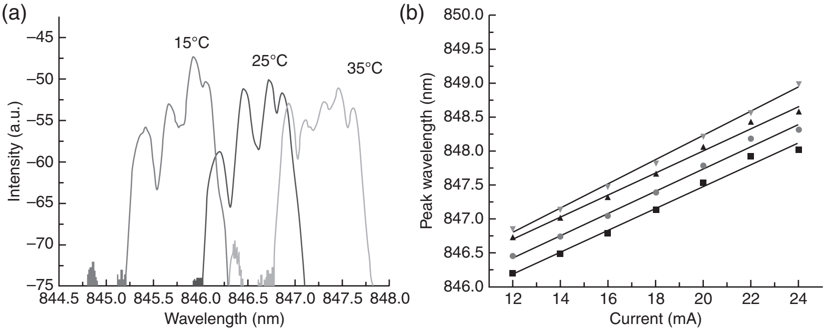

8.10 Multi-mode VCSEL emission as a function of ambient temperature for 10 μm diameter oxide-confined VCSEL: (a) spectrum at 15°C, 25°C and 35°C and (b) peak wavelengths of the transverse modes versus injection current where each line corresponds to a different transverse mode peak maximum for each transverse mode of a VCSEL as a function of injection current. The transverse modes are separated by approximately 0.2 nm, which is expected for 10 μm diameter oxide-confined VCSELs.

If we were to isolate and image any given transverse mode, we would find it would have a unique transverse intensity profile. The longest wavelength (lowest energy) transverse mode is called the fundamental mode, and it has a Gaussian intensity profile: the maximum intensity is found in the center and it decreases radially. Higher order modes will tend to have an intensity null on the axis and intensity maxima at off-axis locations, and they will all have shorter wavelength as compared to the fundamental mode. A single mode VCSEL is presented in Fig. 8.11; the spectra shown in Fig. 8.11b depicts a single emission peak that is more than 40 dB (1000 times) greater in power as compared to the next higher order mode (Danner *et al*., 2006).

For multi-mode applications, such as shown in Table 8.1, the laser spot size is usually not relevant, but rather the light output power is important. Multi-mode VCSELs tend to have the highest efficiency, since the various transverse modes can spatially overlap the quantum well gain in the optimal manner. For optical data links that use multi-mode optical fiber, a laser operating in multiple transverse modes can be tolerated. Dispersion effects in the fiber (that is different fiber modes traveling at different speeds) can limit the bandwidth × length product of the optical link. However, VCSELs with relatively large diameter that operate multi-mode, also tend to have the lowest operation current density and correspondingly best reliability.

For other applications single fundamental mode operation is preferred. Utilizing a VCSEL in a position sensing, printing, or scanning application, often a small beam spot size is required; the fundamental Gaussian mode has the smallest beam waist of all the higher order modes. For high modulation

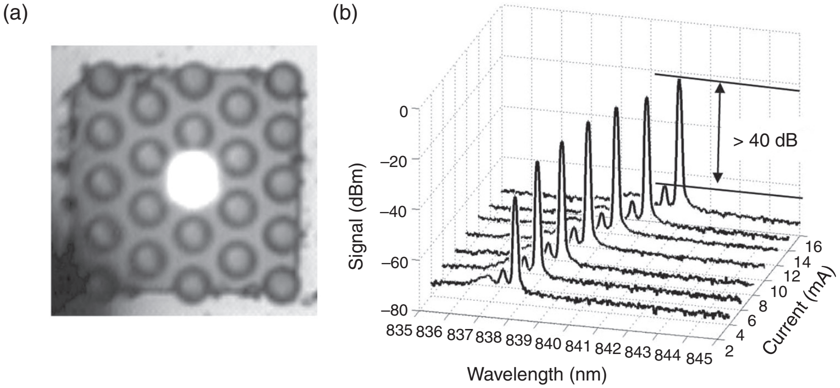

8.11 (a) Top facet image and (b) lasing spectra for single mode photonic crystal VCSEL.

optical data links, fiber dispersion limits the performance in either data rate or link length. Hence using a single mode VCSEL will eliminate dispersion effects, although alignment between the laser and fiber is more challenging.

Numerous efforts have been made to obtain stable fundamental mode lasing in VCSELs. The approaches to promote single mode lasing include: (i) creating a small diameter waveguide that only supports the fundamental mode; (ii) preferentially pumping the fundamental mode by creating a gain area smaller than the optical aperture (Young *et al.*, 2001) and (iii) introducing greater losses such as diffraction (Unold *et al.*, 2000), scattering (Nishiyama *et al.*, 2000), free carrier absorption (Floyd *et al.*, 1995), antiguiding (Wu *et al.*, 1995; Zhou and Mawst, 2002), and/or mirror loss (Morgan *et al.*, 1993; Martinsson, 1999; Lehman *et al.*, 2007) to the higher order modes. Whereas these methods create single mode VCSELs, they often require complex fabrication steps, highly specialized epitaxial structure, and/or fabrication of features with specific dimensions that must match the desired wavelength, all of which hinder manufacturability. Using small diameter VCSELs will also create single mode lasers, but as discussed in Section 8.3.1 this will also produce higher series resistance, leading to undesirable device heating and degraded laser reliability.

The single mode VCSEL in Fig. 8.11a employs an etched photonic crystal pattern to control the laser modal properties (Choquette *et al.*, 2012). The periodic pattern of etched holes creates a waveguide that can only support propagation of the Gaussian mode. The use of a photonic crystal has the advantage that the dimensions of the photonic crystal pattern can be independent of the laser wavelength and larger diameters will still support single mode emission, enabling improved reliability.

The last optical VCSEL characteristic that we will mention is polarization. Electromagnetic radiation can have two polarization states, depending on the orientation of the electric field perpendicular to the direction of propagation. In the case of the VCSEL emission, the light is linearly polarized and emitted perpendicular to the surface of the wafer; in this case we define the polarization to be in the transverse electric (TE) state. However, there will be two possible orthogonal directions for the TE polarization. Hence every transverse optical mode actually has two independent states, corresponding to the two different polarizations. Often these polarization states are nondegenerate, that is, there is a slight birefringence (wavelength difference) between the polarizations. Therefore for an application that has sensitivity to polarization, the polarization state of the VCSEL should be controlled.

8.3.3 Two-dimensional VCSEL arrays

A unique advantage of VCSELs over any other type of laser is the ability to fabricate 2D laser arrays (Iga, 2000). Various applications of 2D VCSEL

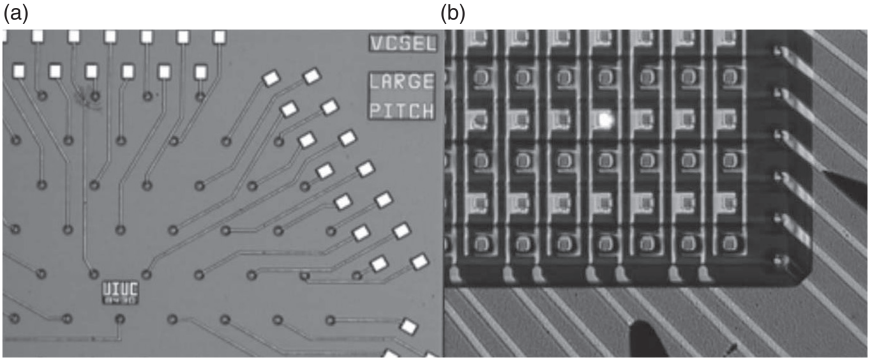

8.12 (a) Hexagonal individually addressable VCSEL array and (b) square matrix addressable VCSEL array with a lasing element in the fourth column from the right and the fourth row from the bottom.

arrays are suggested in Table 8.1. In some applications all of the VCSELs in an array are operated simultaneously, and thus thermal management is the challenge. For other applications it is necessary to electrically contact each individual array element. For example, massively parallel optical interconnects and optical imaging are applications that would benefit from high-density two-dimensional arrays of lasers. The principal challenge, especially for closely spaced arrays, is achieving electrical contact to both the anode and cathode of the diode. As the array element count increases, this challenge can become severe.

There are two approaches contacting the elements of 2D VCSEL arrays: individually addressing (Fig. 8.12a) and matrix addressing (Fig. 8.12b). Individually addressing each VCSEL element necessarily requires long metal contacts linking the top electrical contact to a wire bonding pad located at the periphery of the array. As apparent in the partial image of a hexagonal VCSEL array in Fig. 8.12a, the array elements must be separated by sufficient space to allow access of the metal runners. Another challenge is that the number of bonding pads to address each array element eventually limits the array size. This can be somewhat alleviated by using matrix address, as shown in Fig. 8.12b (Geib *et al.*, 2002). By connected in series the VCSELs in N rows and N columns, the number of bonding pads is $2N$ rather than N^2. The matrix addressable architecture is less flexible than that of an independently addressable array, since an arbitrary set of VCSELs cannot be operated simultaneously. Minimizing the number of electrical connections between the VCSEL array and the electronic circuitry will become very important for high-count arrays, even using advanced packaging techniques such as flip-chip bonding. Another important issue for matrix addressable VCSEL arrays is the larger effective series resistance and capacitance of each row or column lead.

8.4 Conclusion

In this chapter, the vertical cavity surface emitting laser has been introduced and the dominant applications that use the nearly one billion VCSELs that have been deployed world-wide have been reviewed. We have necessarily focused on the fundamentals of VCSELs, such as their device structure, including the DBR mirrors, the optical cavity, and the means for creating electrical and optical transverse confinement in the laser diode. The critical interplay of the spectral alignment of the Fabry–Pérot cavity resonance, which selects the lasing wavelength, and the laser gain bandwidth, which influences the threshold of the VCSEL, is shown to dominate nearly every aspect of VCSEL performance. The wavelength regimes of VCSELs have been discussed, including visible blue and red wavelength (450–650 nm) and infrared wavelength (780–2300 nm) which includes the most common 850 nm VCSEL. Finally, the performance of generic 850 nm VCSELs is presented to illustrate the influence of various VCSEL parameters on the laser efficiency, threshold, transverse mode characteristics, and polarization.

New applications for VCSELs continue to be explored, which in turn drives the device research and development. GaAs-based VCSELs emitting around 850 nm have the most mature technology and manufacturing; these devices can be found in many millions of optical data links and laser mice. VCSELs at shorter wavelengths, such as blue or ultraviolent, are promising for imaging, lighting, biological sensing and medical treatment. VCSELs emitting at 1300–1550 nm have potential application in longer length ($\geq$ 1 km) optical fiber based interconnects, and wavelengths greater than 2 μm have potential for low cost/low power chemical and environmental sensing systems.

High power VCSEL applications should continue to expand, since the form factor and geometry of VCSEL arrays can be custom tailored. One area that is particularly suitable for VCSEL arrays is high brightness laser sources. By creating coherently coupled 2D VCSEL arrays, a single array mode can be achieved (Siriani and Choquette, 2010). The inherent two-dimensional scalability could potentially be a unique advantage creating a revolutionary change for high brightness pump sources.

At the other extreme, ultralow power VCSELs for on-chip or chip-to-chip communication are presently under development to determine their suitability to satisfy short distance but high bandwidth interconnects. The first 'killer application' of VCSELs in the short-reach optical interconnect area has had perhaps the most dominant influence on VCSEL development. The increasing numbers of VCSELs used in optical interconnects, as well as the always increasing performance demands continues to drive VCSEL research. The digital modulation rate achieved with a VCSEL has increased several hundredfold during the years of 1990–2010. The next decade will demand what is now considered outrageous bandwidth increases, to answer the insatiable demands of the Internet and high performance computing. Perhaps even more importantly, the bandwidth enhancement must be accompanied with much lower power requirements, to maintain sustainability of optical communication networks. VCSELs should continue to evolve to address the future needs of the information age.

8.5 Acknowledgements

The collaborations of many former colleagues at Sandia National Laboratories, including W. Chow, K. Geib, A. Allerman, H. Hou, and D. Serkland; colleagues at the University of Illinois including J. Coleman and P. S. Carney, as well as the present and past members of the Photonic Device Research Group are gratefully acknowledged. Special thanks to L. Choquette for preparation of the manuscript.

8.6 References

Baba T., Yogo Y., Suzuki K., Koyama F. and Iga K. (1993), "Near room temperature continuous wave lasing characteristics of GaInAsP/InP surface emitting laser," *Electron. Lett.* **29**, 913–914.

Bachmann A., Lim T., Kashani-Shirazi K., Dier O., Lauer C. and Amann M. C. (2008), "Continuous wave operation of electrically pumped GaSb-based vertical cavity surface emitting laser at 2.3 μm," *Electron. Lett.* **44**, No. 3, 202–203.

Choquette K. D., Hasnain G., Wang Y., Wynn J., Freund R. S. and Cho A. Y. (1991), "GaAs vertical cavity surface emitting lasers fabricated by reactive ion etching," *IEEE Photon. Technol. Lett.* **3**, 859–862.

Choquette K. D., Schneider R. P., Choquette K. D., Kilcoyne S. P. and Figiel J. J. (1993), "Room temperature continuous wave operation of red vertical cavity surface emitting laser diodes", *Electron. Lett.* **29,** 1693–1694.

Choquette K. D., Schneider R. P., Jr., Lear K. L. and Geib K. M. (1994), "Low threshold voltage vertical-cavity lasers fabricated by selective oxidation," *Electron. Lett.* **30**, 2043–2044.

Choquette K. D., Lear K. L., Schneider R. P., Jr., Geib K. M., Figiel J. J. and Hull R. (1995), "Fabrication and performance of selectively oxidized vertical-cavity lasers," *IEEE Photon. Technol. Lett.* **7**, 1237–1239.

Choquette K. D. and Hou H. Q. (1997), "Vertical cavity surface emitting lasers: moving from research to manufacturing," *(invited) Proceedings of the IEEE* **85**, 1730–1739.

Choquette K. D., Chow W. W., Hadley G. R., Hou H. Q. and Geib K. M. (1997), "Scalability of small-aperture selectively oxidized vertical-cavity lasers," *Appl. Phys. Lett.* **70**, 823–825.

Choquette K. D. and Geib K. M. (1999), "Fabrication and Performance of Vertical Cavity Surface Emitting Lasers," in *Vertical Cavity Surface Emitting Lasers,* Eds. C. Wilmsen, H. Temkin and L. Coldren, Cambridge: Cambridge University Press, 192–232.

Choquette K. D., Klem J. F., Fischer A. J., Blum O., Allerman A. A., Fritz I. J., Kurtz S. R., Breland W. G., Sieg R., Geib K. M., Scott J. W. and Naone R. L. (2000), "Room temperature continuous wave InGaAsN quantum well vertical cavity lasers emitting at 1.3 μm," *Electron. Lett.* **36**, 1388–1389.

Choquette K. D. (2000b), "The Technology of Selectively Oxidized Vertical Cavity Lasers" Chapter 2 in *Vertical Cavity Surface Emitting Laser: Technologies and Applications*, Eds. J. Cheng and N. Dutta, Gordon and Breach Science Publishers, The Netherlands.

Choquette K. D., Siriani D. S., Kasten A. M., Tan M. P., Sulkin J. D., Leisher P. O., Raftery J. J., Jr. and Danner A. J. (2012), "Single mode photonic crystal vertical cavity surface emitting lasers," *Adv. Opt. Technol.* **2012**, D280920.

Chow W. W., Choquette K. D., Crawford M. H., Lear K. L. and Hadley G. R. (1997), "Design, fabrication, and performance of infrared and visible vertical-cavity surface emitting lasers," *IEEE J. Quantum. Electron*. **33**, 1810–1824.

Danner A. J., Raftery J. J., Jr., Leisher P. O. and Choquette K. D. (2006), "Single mode photonic crystal vertical cavity lasers," *Appl. Phys. Lett*. **88**, 091114.

Dubravko, B. I., Dudley, J. J., Steubel, K., Mirin, R. P., Bowers, J. E. and Hu, E. L. (1995) "Double-fused 1.52μm vertical cavity lasers," *Appl. Phys. Lett*. **66**, 1030.

Ducanchez A., Cerutti L., Grech P., Genty F. and Tournie E. (2009), "Mid infrared GaSb-based EP-VCSEL emitting at 2.63 μm," *Electron. Lett*. **45**, No. 5, 265–267.

Dudley J. J., Babic D. I., Mirin R., Yang L., Miller B. I., Ram R. J., Reynolds T., Hu E. L. and Bowers J. E. (1994), "Low threshold wafer fused long wavelength vertical cavity lasers," *Appl. Phys. Lett.* **64**, 1463–1465.

Floyd P. D., Peters M. G., Coldren L. A. and Merz J. L. (1995), "Suppression of higher-order transverse modes in vertical-cavity lasers by impurity-induced disordering," *IEEE Photon. Technol. Lett.* **7**, 1388–1390.

Geels R. S., Thibeault B. J., Corzine S. W., Scott J. W. and Coldren L. A. (1993), "Design and characterization of In0.2Ga0.8As MQW vertical cavity surface emitting lasers," *IEEE J. Quantum Electron.* **29**, 2977–2987.

Geib K. M., Choquette K. D., Serkland D. K., Allerman A. A. and Hargett T. W. (2002), "Fabrication and performance of 2-dimensional matrix addressable arrays of integrated vertical cavity lasers and resonant cavity photodetectors," *J. Sel. Topics Quantum Electron*. **8**, 943–947.

Goncher G., Bo L., Wen-Lin L., Cheng J., Hersee S., Sun S. Z., Schneider R. P. and Zolper J. C. (1996), "Cryogenic operation of AlGaAs-GaAs vertical-cavity surface-emitting lasers at temperatures from 200 K to 6 K," *IEEE Photon. Technol. Lett.* **8**, 316–318.

Gourley P. L. and Drummond T. J. (1986), "Single crystal, epitaxial multilayers of AlAs, GaAs, and AlxGa1-xAs for use as optical interferometric elements," *Appl. Phys. Lett*. **49**, 489–491.

Hall E., Nakagawa S., Almuneau G., Kim J. K. and Coldren L. A. (2000), "Room temperature CW operation of lattice matched long wavelength VCSELs," *Electron. Lett.* **36**, 1465–1467.

Hasnain G., Tai K., Yang L., Wang Y. H., Fischer R. J., Wynn J. D., Weir B., Dutta N. K. and Cho A. Y. (1991), "Performance of gain-guided surface emitting lasers with semiconductor distributed Bragg reflectors," *IEEE J. Quantum Electron*. **27**, 1377–1385.

Higuchi Y., Omae K., Matsumura H. and Mukai T. (2008), "Room temperature CW lasing of a GaN-based vertical cavity surface emitting laser by current injection," *Appl. Phys. Exp.* **1**, 121102.

Huffaker D. L., Deppe D. G., Kumar K. and Rogers T. J. (1994), "Native-oxide defined ring contact for low threshold vertical-cavity lasers," *Appl. Phys. Lett.* **65**, 97–99.

Iga K. (2000), "Surface emitting laser–its birth and generation of new optoelectronics field," *IEEE J. Sel. Topics Quantum Electron*. **6**, 1201–1215.

Jewell J. L., Harbison J. P., Scherer A., Lee Y. H. and Florez L. T. (1991), "Vertical-cavity surface-emitting lasers: design, growth, fabrication, characterization," *IEEE Journal of Quantum. Electron.* **27**, 1332–1346.

Kim Y. K., Choquette K. D., Baker J. and Allerman A. A. (2004), "Secondary ion mass spectroscopy analysis of vertical-cavity surface emitting lasers," *J. Vac. Sci. Tech*. **B22**, 949.

Lear K. L., Choquette K. D., Schneider R. P., Jr., Kilcoyne S. P. and Geib K. M. (1995), "Selectively oxidized vertical cavity surface emitting lasers with 50% power conversion efficiency," *Electron. Lett.* **31**, 208–209.

Lear K. L., Schneider R. P., Jr., Choquette K. D. and Kilcoyne S. P. (1996), "Index guiding dependent effects in implant and oxide confined vertical-cavity lasers," *IEEE Photon. Technol. Lett.* **8**, 740–742.

Lee Y. H., Tell B., Brown-Goebeler K. F. and Jewell J. L (1990), "Top-surface-emitting GaAs four-quantum-well lasers emitting at 0.85mm," *Electron. Lett.* **26**, 710–711.

Lehman A. C., Yamaoka E. A., Willis C. W., Choquette K. D., Geib K. M and Allerman A. A. (2007), "Variable reflectance vertical cavity surface emitting lasers," *Electron. Lett.* **43**, 460–461.

Lu T. C., Kao C. C., Juo H. C., Huang G. S. and Wang S. C. (2008), "CW lasing of current injection blue GaN-based vertical cavity surface emitting laser," *Appl. Phys. Lett.* **92**, 141102.

Martinsson H., Vukušić J. A., Grabherr M., Michalzik R., Jäger R., Ebeling K. J. and Larsson A. (1999), "Transverse mode selection in large-Area oxide-confined vertical-cavity surface-emitting lasers using a shallow surface relief," *IEEE Photon. Technol. Lett.* **11**, 1536–1538.

Morgan R. A., Guth G. D., Focht M. W., Asom M. T., Kojima K., Rogers L. E. and Callis S. E. (1993), "Transverse mode control of vertical-cavity top-surface-emitting lasers," *IEEE Photon. Technol. Lett.* **4**, 374–377.

Nishiyama N., Arai M., Shinada S., Suzuki K., Koyama F. and Iga K. (2000), "Multi-oxide layer structure for single-mode operation in vertical-cavity surface-emitting lasers," *IEEE Photon. Technol. Lett.* **12**, 606–608.

Salet P. Gaborit F., Panod- Rossiaux P., Plais A., Derouin E., Pasquier J. and Jacquet J. (1997), "Room temperature pulsed operation of 1.3μm vertical cavity lasers including bottom InGaAsP/InP multilayer Bragg mirrors," *Electron. Lett.* **33**, 2048–2049.

Schneider R. P., Hagerott Crawford M., Choquette K. D., Lear K. L., Kilcoyne S. P. and Figiel J. J. (1995), "Improved AlGaInP-based red (670–690nm) surface emitting lasers with novel C-doped short cavity epitaxial design," *Appl. Phys. Lett.* **67**, 329–331.

Soda H., Iga K., Kitahara C. and Suematsu Y. (1979), "GaInAsP/InP surface emitting injection lasers," *Jpn. J. Appl. Phys*. **18**, 2329–2330.

Siriani D. F. and Choquette K. D. (2010), "In-phase coherent photonic crystal vertical cavity surface emitting laser arrays with low divergence," *Electron. Lett.* **46**, 712–714.

Tadokoro T., Okamoto H., Kohama Y., Kawakami T. and Kurokawa T. (1992), "Room temperature pulsed operation of 1.5 μm GaInAsP/InP vertical cavity surface emitting laser," *IEEE Photon. Tech. Lett.*, **4**, 409–411.

Tai K., Fischer R. J., Wang K. W., Chu S. N. G. and Cho A. Y. (1989), "Use of implant isolation for fabrication of vertical-cavity surface-emitting laser diodes," *Electron. Lett.* **25**, 1644–1645.

Unold H. J., Mahmoud S. W. Z., Jäger R., Kicherer M., Riedl M. C. and Ebeling K. J. (2000), "Improving single-mode VCSEL performance by introducing a long monolithic cavity," *IEEE Photon. Technol. Lett.* **12**, 939–941.

Wang Y. H., Tai K., Wynn J. D., Hong M. Fischer R. J., Mannaerts J. P. and Cho A. Y. (1990), "GaAs/AlGaAs multiple quantum well GRIN-SCH vertical cavity surface emitting laser diodes," *IEEE Photon. Tech. Lett.* **2**, 456–458.

Wu Y. A., Li G. S., Nabiev R. F., Choquette K. D., Caneau C. and Chang Hasnain C. J. (1995), "Single-mode, passive antiguide vertical cavity surface emitting laser," *IEEE J. Sel. Topics Quantum Electron.* **1**, 629–637.

Yamada M., Anan T., Kurihara K., Nishi K., Tokutome K., Kamei A. and Sugou S. (2000), "Room temperature low threshold CW operation of 1.23um GaAsSb VCSELs on GaAs substrates," *Electron. Lett.* **36**, 637–638.

Young D. B., Scott J. W., Peters F. H., Thibeault B. J., Corzine S. W., Peters M. G., Lee S. L. and Coldren L. A. (1993), "High-power temperature-insensitive gain-offset InGaAs/GaAs vertical-cavity surface-emitting lasers," *IEEE Photon. Technol. Lett.* **5**, 129–132.

Young E. W., Choquette K. D., Chuang S. L., Geib K. M., Fischer A. J. and Allerman A. A. (2001), "Single-transverse-mode vertical-cavity lasers under continuous and pulsed operation," *IEEE Photon. Technol. Lett.* **13**, 927–929.

Zhou D. and Mawst L. (2002), "High-power single-mode antiresonant reflecting optical waveguide-type vertical-cavity surface-emitting lasers," *IEEE J. Quantum. Electron.* **38**, 1599–1606.

9

Semiconductor disk lasers (VECSELs)

J. E. HASTIE, S. CALVEZ and M. D. DAWSON,
University of Strathclyde, UK

DOI: 10.1533/9780857096401.2.341

Abstract: Semiconductor disk lasers (SDLs), also known as vertical-external-cavity surface-emitting lasers (VECSELs) are optically-pumped semiconductor lasers (OPSLs), with oscillation perpendicular to the epitaxial gain structure with an external macroscopic laser resonator. SDLs have outstanding wavelength flexibility combined with excellent beam quality, and their fundamental spectral coverage is further extended by efficient, intracavity non-linear frequency conversion. This chapter gives a broad overview of the SDL field: design, principles of operation, and typical performance. We review various techniques used for intracavity frequency filtering and conversion, pulsed operation and mode-locking. The trends and applications foreseen as the future drivers of SDL research are discussed.

Key words: vertical-external-cavity surface-emitting lasers (VECSELs), optically-pumped semiconductor lasers (OPSLs), intracavity non-linear frequency conversion, mode-locked semiconductor lasers, tunable lasers.

9.1 Introduction

The subject of this chapter is semiconductor disk lasers (SDLs), also commonly known as vertical-external-cavity surface-emitting lasers (VECSELs). These are usually optically-pumped semiconductor lasers (hence the further acronym OPSL in occasional use) with oscillation perpendicular to the plane of the epitaxial gain structure and with an external macroscopic laser resonator, typically millimetres up to tens of centimetres in length. They are thus quite different in form and operation from the vertical-cavity surface-emitting lasers (VCSELs) described in Chapter 8 and are in many ways more akin to conventional doped-dielectric solid-state lasers, albeit with intermediate output powers (typically <10 W) and unsuitability for high-energy pulsed operation. The primary distinctiveness of SDLs lies in outstanding wavelength flexibility combined with excellent beam quality, where their wavelength versatility stems from semiconductor bandgap and quantum well engineering and the fact that their fundamental spectral coverage can be greatly extended by their eminent suitability for efficient, intracavity non-linear frequency conversion.

In the following sections, we will give a broad but concise overview of the SDL field, which has expanded rapidly over the past decade. In Section 9.2 we will set out the basics of SDL design, their principles of operation, and typical performance characteristics. Section 9.3 will summarise the various techniques used for continuous-wave operation, intracavity frequency filtering and conversion, with particular emphasis on the broad spectral coverage achieved and the prospects for further development. Pulsed operation of SDLs will be reviewed in Section 9.4, including a brief overview of the extensive work on mode-locking. The trends and applications that we foresee as being the future drivers of SDL research and technology will be discussed in Section 9.5, and we conclude with a list of references for further and more detailed information.

9.2 Principles of operation

SDLs have now been demonstrated with fundamental emission wavelengths ranging from 390 nm to 6.5 μm (see Table 9.1) with the general design of the gain structure almost independent of the semiconductor material used. This consists of a distributed Bragg reflector (DBR) mirror, on top of which is grown a multi-quantum well gain region with the quantum wells (QWs) positioned to coincide with the antinodes of the cavity standing wave for resonant periodic gain (see Fig. 9.1). SDLs are sometimes referred to as ‘a 1/2 VCSEL’ as they resemble a VCSEL without the top DBR (Chapter 8), although in general the active region of an SDL is several times longer and contains more quantum wells. The SDL gain structure is usually optically-pumped and aligned as the end mirror of a high-finesse, bulk-optics laser cavity. Due to this external air-spaced laser cavity, SDLs are often referred to as ‘hybrid’ lasers: combining conventional solid-state laser engineering (e.g., power scaling, intracavity techniques and excellent beam quality) with a semiconductor gain region and therefore the flexibility of bandgap engineering. This most commonly recognised format of SDL and the modelling of its basic characteristics was set down by Kuznetsov and co-workers in 1999,[1] following their initial report of the laser performance two years earlier.[2] Further development of these lasers was pursued by a number of groups using an expanding range of semiconductor material systems, and in 2006 Tropper *et al*. published a review of the field as it then was, including a thorough description of the principles of operation.[3] We refer the reader to these previous works for in-depth design criteria and macroscopic modelling of the performance, together with Reference 4 for a study of the effects of tailoring the gain structure resonances. The group of Moloney at the University of

Table 9.1 Demonstrated wavelength range of SDLs for all-semiconductor material systems used to date

Wavelength range	Material system (QW/barrier)	Substrate	Selected references
390 nm, 410 nm	InGaN (microchip with dielectric DBR)	Sapphire	8, 9, 46
640–690 nm	InGaP/AlGaInP	GaAs	21, 47–49
700–750 nm	InP QDs/AlGaInP	GaAs	50
850–870 nm	GaAs/AlGaAs	GaAs	25, 51–53
850 nm	InAlGaAs/GaAs	GaAs	54
0.9–1.18 μm	InGaAs/GaAs	GaAs	1, 41, 55–57
1–1.3 μm	InAs QDs/GaAs	GaAs	17, 58–60
1.16–1.32 μm	GaInNAs/GaAs	GaAs	61–64
1.2–1.57 μm	AlGaInAs (fused to AlGaAs DBR)	InP	12, 65
1.55 μm	InGaAsP	InP	66–69
2–2.8 μm	GaInAsSb/AlGaAsSb	GaSb	70–72
4–5 μm	PbTe or PbSe/PbSrSe (IV–VI)	BaF_2	73, 74
3.3–6.5 μm	PbTe or PbSe/PbSrSe (IV–VI)	Si	75–77

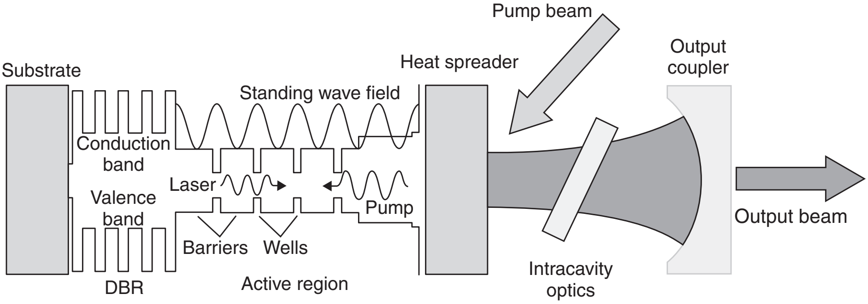

9.1 Schematic of a typical SDL, incorporating a simplified diagram of the gain structure semiconductor bandgap profile and the optical field in the active region, showing the principle of operation. DBR: distributed Bragg reflector.

Arizona with main collaborator Koch at the University of Marburg have published extensively on the *microscopic* modelling of SDLs (e.g., review in Reference 5), and are able to accurately compute the performance of SDLs demonstrating excellent agreement with experimental data;[6] however, in the more typical case where the material parameters are less well known and such precise control over the semiconductor growth is not available, good laser performance is generally achieved via the basic design that we will set out in the following section, together with empirical optimisation. Best performance is subject to the constraints of the particular material system required for emission within the spectral region of interest, and we will give an overview of SDL materials in Section 9.2.2.

9.2.1 Design features and performance characteristics

In order to understand the expected laser performance when using a vertically-emitting architecture and what this means for the design parameters of SDLs, we will first look at the laser threshold condition which is given by:

$$R_1 R_2 T \exp\left(2\Gamma g_{\mathrm{th}} L\right) = 1 \qquad [9.1]$$

where R_1 and R_2 are the reflectivities of the DBR and the output coupler respectively (or in the case of a VCSEL, R_2 is the reflectivity of the top DBR), T is the round-trip loss transmission factor, Γ is the longitudinal confinement factor which describes the optical field overlap with the gain (up to 2 for perfect resonant periodic gain), g_{th} is the material threshold gain and L is the length of gain material. For a vertically-emitting structure, where the gain is provided by a few quantum wells, L may be on the order of ~50 nm. Therefore, while the semiconductor material gain may be very high, the *gain length* is extremely short, so that these are low-gain lasers. From the above condition, and assuming a reasonable threshold gain of ~2000 cm^{-1}, we require very high mirror reflectivity of >99%, and low loss. This stringent requirement on the DBR reflectivity has impaired the development of vertical emitters using GaN materials for blue/violet emission for example, as the materials necessary for the large refractive index contrast required for high reflectivity introduce significant strain and therefore crack-free structures are difficult to grow. Considerable progress has been made in the development of GaN-based VCSELs;[7] however, the only GaN-based SDLs demonstrated to date used dielectric mirrors deposited directly on the epilayer and transmission through the buffer layer and transparent sapphire substrate.[8,9]

SDLs are usually[*] optically-pumped and therefore power scaling may be simply achieved by uniformly pumping a large area[10] and using the external cavity to efficiently extract the power in a single transverse mode. SDLs have a longer active region (~1–2 μm) than VCSELs, generally determined by the pump absorption length. Thus more quantum wells may be incorporated, even allowing tailoring of the carrier confinement in distinct gain regions with different quantum wells for dual-wavelength operation.[11] Further details on all the design features labelled in Fig. 9.1 are given in the following:

Substrate

- The SDL structure is usually grown monolithically, lattice-matched to the substrate.

---

[*] For the special case of electrical pumping of SDLs, see the end of Section 9.4.3.

- The substrate may be removed via etching in order to decrease the thermal impedance of the structure for a so-called 'thin device'.[10]
- Recently, in order to access spectral regions where lattice-matching is difficult, wafer fusion techniques have been used to allow gain structure components based on different material systems, grown on different substrates, to be assembled.[12,13]

Distributed Bragg reflector (DBR)

The DBR consists of alternating $\lambda/4$ layers of transparent, lattice-matched material with high and low refractive index, n, with N repeats. Reflectivity is given by:[14]

$$R_{\text{DBR}} = \left(\frac{1 - P^{2N}}{1 + P^{2N}} \right)^2, \quad P = \frac{n_{\text{low}}}{n_{\text{high}}}$$

- It is desirable to minimise P (within the constraints of transparency at the laser wavelength), so that fewer layers are required, thus reducing growth time and minimising the thermal impedance. For AlAs/GaAs DBRs, N is typically ~25–30.
- The DBR may be designed for dual band reflectivity in order to reflect residual pump light.[10,15]

Active region

- The gain is provided by multiple quantum wells with composition, thickness, and strain tailored for high gain at the design wavelength (see Section 9.2.2).
- If compressively-strained quantum wells are used, tensile-strained compensation layers may be incorporated to balance the strain of the active region (see e.g., Reference 16).
- Gain may also be provided by multiple layers of quantum dots (e.g., Reference 17, see Section 9.2.2).
- Quantum wells are positioned at the antinodes of the optical field in order to maximise the efficiency of gain extraction, a technique known as resonant periodic gain (RPG).[18] This has the additional effect of suppressing spatial hole burning for single-frequency operation (e.g., Reference 19, see Section 9.3.1).
- The length of the active region is limited by the pump absorption length to ensure all quantum wells are pumped, and is typically 1–2 μm. The composition of the quantum well barriers is normally chosen to maximise carrier confinement.
- Groups of more than one quantum well per antinode may be used to 'stack' the gain towards the top of the device to account for the

exponential profile of the pump absorption;[3,20] or as a means to fit more gain within the absorption length.[21]

- Fine tuning of the active region length is used to control the effect of sub-cavity resonances. A sub-cavity resonant at the design wavelength maximises the optical field at the quantum wells and minimises the laser threshold; however, an anti-resonant sub-cavity is less temperature sensitive and has spectrally broader *effective* gain.[4]

Heat spreader

- High thermal conductivity, transparent crystalline intracavity heatspreaders may be used for thermal management.[22,23] This method of thermal management, where the main route for heat extraction is via the top of the device, is particularly effective for SDLs with large, thermally resistive DBRs.[24]
- Sapphire,[22] silicon carbide,[25] silicon,[26] and diamond,[27] have all been used as intracavity heatspreaders.
- Optical contact to the intracavity surface is achieved via liquid capillary bonding.[28]

Pump beam

- Pump light is absorbed in the semiconductor within ~1–2 μm, therefore low brightness sources, such as diode lasers, may be used – SDLs are efficient 'brightness converters'.
- For more compact set-ups, it may be convenient to pump through the DBR after removal of the substrate.[29] The close proximity achieved in this case has enabled efficient optical pumping even without pump-coupling optics.[30]
- Due to the broad absorption spectra of the semiconductor materials the exact pump wavelength is not critical, although longer wavelengths are desirable to reduce the quantum defect. Shorter pump wavelengths will, in general, have a shorter absorption length.[21]
- In the special case of in-well pumping, used to minimise the quantum defect, the pump light absorption per pass of the active region is very low and therefore multiple passes are required for efficient operation.[31]

Output coupler

- Generally an external dielectric mirror on a bulk optic is used, although in the case of microchip SDLs the output coupler is a dielectric mirror coating directly on the surface of the crystalline heatspreader.[32,33]
- SDLs are low-gain lasers with typical optimum output coupling of a few per cent.
- Non-linear output coupling may be used (see Section 9.3.2).

Output beam

- Circularly-symmetric, diffraction-limited output beams are achieved with mode-matching, that is, optimum overlap of the intracavity mode beam with the pumped area of the SDL gain structure.[24,34] Up to 20 W output power has been demonstrated in a single transverse mode with $M^2 < 1.1$.[35]

Intracavity optics

- Intracavity optics are conveniently accommodated for frequency control and non-linear conversion (see Section 9.3), cavity-dumping and mode-locking (see Section 9.4).
- A common intracavity element, used to tune the oscillation wavelength of an SDL, is a birefringent filter (BRF). A BRF is an off-axis birefringent plate, inserted in the cavity at Brewster's angle and rotated in order to tune the wavelength at which the phase delay results in zero net change of polarisation angle, hence varying the wavelength that experiences zero reflection losses.[36]

The performance of an SDL will of course depend on the optical gain of the quantum wells, the quality of the DBR, material losses, and the efficiency of the optical pumping.[1] All of these can vary depending on the material system and experimental configuration used, leading to variation in the power and efficiency that has been achieved across the spectral range of SDL emission. What all SDLs have in common, however, is their temperature sensitivity, intrinsic to the design: the semiconductor quantum well gain and the overlap of this gain with the RPG wavelength and sub-cavity resonances are both sensitive to the *absolute* temperature of the gain region. With respect to the latter, each SDL gain structure has an optimum temperature at which the gain and the resonances overlap such that the *effective* gain is optimised, beyond which thermal rollover will eventually shut off the laser. However, while this overlap can be partly accounted for by designing in an appropriate offset for the cold laser,[37] for example, the room temperature RPG wavelength may be fixed at a longer wavelength than the peak of the quantum well gain (which has higher $d\lambda/dT$), thermal escape of the carriers from the quantum wells limits high temperature operation. The pump induced temperature increase, therefore, ultimately limits the maximum output power of an SDL. There are two main methods used for thermal management: removal of the substrate for a so-called thin device which is then soldered to an efficient (extra-cavity) heatsink; and high thermal conductivity crystalline heatspreaders, bonded directly to the intracavity surface of the unprocessed gain structure. Kemp *et al.* have carried out in-depth thermal modelling of the heatspreader approach (e.g. References 23, 38), and have compared the two techniques for a broad range of SDL materials.[24] They find that for SDLs emitting around 1 μm, the relatively high thermal conductivity of the materials used means that both techniques are effective at reducing the maximum temperature rise in the active region; however, away from 1 μm, the thermally resistive DBRs required reduce the efficacy of substrate removal. Heatspreaders, especially diamond heatspreaders, have been instrumental in the demonstration of Watt level output power from SDLs operating in almost all other spectral regions. Both methods are a step towards the ideal of one-dimensional heat flow from the gain region which would allow power scaling by indefinitely increasing the pumped area; however, in practise, modelling has shown that radial heat flow continues to set an upper limit for power scaling of SDLs.[24] Alternative thermal management methods for power scaling are pulsed or quasi-continuous-wave pumping[39] (see Section 9.4.1 and Fig. 9.15), or dividing the pump power between more than one gain structure within one laser cavity.[34,40]

9.2.2 Materials

The materials used for SDL development to date are listed in Table 9.1, the large range testament to the 'design freedom' afforded by optical pumping. The most successful SDL material system to date, in terms of laser performance, is undoubtedly InGaAs/GaAs quantum wells with AlGaAs DBRs (see Fig. 9.4), now the basis for the commercially available range of SDLs and a 'workhorse' for the development of any new laser architectures and studies of fundamental operating characteristics and dynamics. InGaAs quantum wells have high gain, and in this spectral region (~1 μm) the AlGaAs DBR can use maximum refractive index contrast for very high reflectivity with relatively low thermal impedance. This material system also has the distinct advantage of being efficiently pumped with low quantum defect by the high-power 808 nm laser diodes that have been extensively developed for pumping solid-state lasers. Ignoring spectral coverage, most SDL performance records are held by InGaAs-based devices, from maximum continuous-wave output power (>100 W, 3-chip SDL[40]) and diode-pumped slope efficiency (60%[41,42]), to the highest spectral brightness (Reference 43, see Section 9.3.1), the shortest mode-locked pulses (~60 fs,[44] see Section 9.4.3) and the highest repetition rates (50 GHz[45]). Most of the techniques developed with InGaAs-based SDLs are being applied to a broader range of material systems, to fully exploit the wavelength flexibility of the SDL format. For each material system, the reader should refer to the selected references in Table 9.1 for details of particular SDL designs, including any peculiarities of bandgap engineering, growth or fabrication, although in general these do not deviate significantly from the schematic shown in Fig. 9.1. Below we will highlight some recent examples.

While the vast majority of SDLs use quantum wells, much of the recent materials development has focussed on the incorporation of multiple layers of quantum dots. The quantum dots are 'self-assembled' during epitaxial growth and the specific challenge for a quantum-dot-based SDL is to grow a relatively large number of repeatable highly strained quantum dot layers within an RPG structure. The incentive for the development of edge-emitting quantum dot lasers was to take advantage of the increased quantum confinement for low-threshold operation and reduced temperature sensitivity.[78] Reduced temperature sensitivity is certainly attractive for SDLs, given the temperature dependence of the gain and resonance overlap discussed above; however, the reduced *modal* gain of quantum dot layers, compared with quantum wells, in the vertically-emitting format means that their incorporation into SDLs[*] is motivated primarily by the opportunity to extend the spectral coverage of a particular material system. Quantum dots allow longer wavelength emission than quantum wells since they enable the use of lower bandgap alloys with higher lattice mismatch, that is, higher strain. The feasibility of quantum dot SDLs was first demonstrated by Lott *et al.* using InAs quantum dots to achieve 120 mW output power at 1.3 μm,[58] and later by Germann and co-workers at the Technical University Berlin for emission around 1.2 μm.[17] This group was able to demonstrate temperature independent operation over the pump excitation range 0–70 kW/cm^2 with stable efficiency and output spectrum, although the slope efficiency was only ~2%.[79] Since this initial work, power scaling has been shown by a number of groups, for example, >4 W at 1032 nm reported by Butkus *et al.*,[60] and recently Hoffmann *et al.* demonstrated 5.2 W at 960 nm with ~24% slope efficiency.[80] However, of greater interest for extending spectral coverage, Albrecht and co-workers at the universities of New Mexico and Arizona recently reported multi-Watt operation at an emission wavelength of 1.25 μm, beyond that which may be achieved using InGaAs quantum wells.[59]

In general, the spectral range of efficient performance for each material system used for SDLs is limited at the short-wavelength end by reduced carrier confinement, and at the long-wavelength end by unmanageable strain. Taking the material used for visible red emission as an example, $(Al_yGa_{1-y})_xIn_{1-x}P$ is lattice-matched to GaAs for an indium fraction of ~0.5.[81] For aluminium fraction less than ~0.6, the bandgap is direct and ranges from 1.9 to 2.3 eV.[81,82] Above the band crossover the conduction band offset decreases,

---

[*] Quantum dots are also used in saturable absorber layers for low saturation fluence in mode-locked SDLs and mode-locked integrated external-cavity surface-emitting lasers (MIXSELs) – see Section 9.4.3.

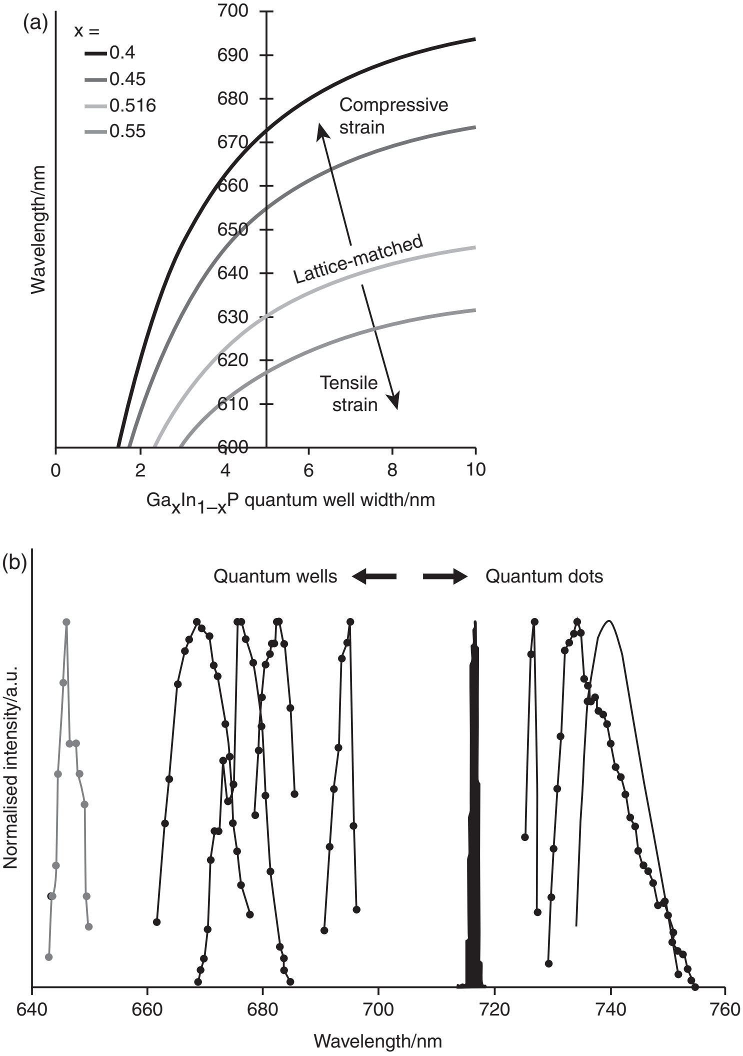

9.2 (a) Calculated room temperature emission wavelength of $Ga_xIn_{1-x}P$ quantum wells as a function of well width for four different alloy fractions of gallium. (b) Normalised tuning curves of several AlGaInP-based SDLs using GaInP quantum wells and InP quantum dots.

and the maximum conduction band offset achievable is ~270 meV (compared with 350 meV for AlGaAs heterostructures), limiting the electron confining potential and leading to electron barrier leakage, especially in short-wavelength devices. Using $(Al_{0.6}Ga_{0.4})_{0.5}In_{0.5}P$ barriers for maximum confinement, the wavelength range available from strained GaInP quantum wells spans ~600 nm to >700 nm. In Fig. 9.2a we have plotted the calculated emission wavelength with quantum well thickness for different gallium alloy fractions. For III-V semiconductor quantum wells, a small amount of strain is desirable to remove the degeneracy of the heavy hole and light hole valence bands.[83] For vertically-emitting structures which require transverse electric (TE) polarisation, *compressive* strain is used so that the heavy hole band is the ground state and is more easily inverted.[81] With compressively-strained GaInP, increased confinement cannot provide enough blue-shift at a reasonable quantum well thickness to obtain efficient emission for wavelengths below about 630 nm. The first high-power, continuous-wave, red SDL reported by Hastie *et al.* used 6 nm thick quantum wells with gallium fraction of 0.45 for room temperature emission at ~660 nm.[48] Up to 1.1 W output power was demonstrated with 20% slope efficiency.[84]

The wavelength coverage of the AlGaInP material system can be extended further into the red via the use of InP quantum dots. Schlosser *et al.*, in collaboration with the University of Sheffield who had previously reported edge-emitting lasers based on InP quantum dots,[85] demonstrated continuous-wave emission from SDLs over the range 716–755 nm, with up to 26 nm tuning from a single device.[50] In Fig. 9.2b we have plotted the *normalised* tuning curves of various AlGaInP-based SDLs using compressively-strained GaInP quantum wells and InP quantum dots, as demonstrated by our group.[21,48–50]

As previously explained, the suitability of a particular material system for SDL development is determined to a large extent by the quality of DBR that may be lattice-matched to the active region. While III–V materials lattice-matched to InP provide broad spectral coverage from 1.2 μm to 2.0 μm, the small refractive index contrast available with this material system has limited the performance of SDL gain structures. Lindberg *et al.* were able to demonstrate up to 0.8 W output power at 1550 nm by using an intracavity diamond heatspreader to bypass the 48-period InP/InGaAsP DBR, pumping at 1250 nm and cooling to −30°C.[67] Recently, however, wafer fusion techniques (previously developed for VCSELs at communications wavelengths) have allowed the fabrication of SDLs consisting of AlGaInAs active regions grown on InP substrates, subsequently bonded to high quality AlGaAs DBRs. Rautiainen *et al.* demonstrated 2.6 W at 1.57 μm from a wafer-fused SDL, in this case pumping at 980 nm with heatsink temperature of 10°C (also using an intracavity diamond heatspreader).[12] This group later demonstrated 2.7 W at 1.3 μm,[86] with further power scaling to 6.6 W,[65] attractive for frequency doubling to red wavelengths (see Section 9.3.2). While ‘dilute nitride’ material (GaInNAs) and InAs quantum dots have been used to extend SDL spectral coverage beyond 1.2 μm, the complex and problematic growth of both and the low-gain of the latter mean that wafer-fused phosphide-based structures now look like the most promising route to practical and commercially viable high-power SDLs in this wavelength range.

Finally, of particular interest for spectroscopic applications, researchers at the Thin Film Physics Group, ETH Zurich have developed broadly tuneable (although highly temperature sensitive) SDLs emitting at wavelengths >3 μm by using lead chalcogenide (IV–VI) narrow gap semiconductors. The SDL gain structures are grown via MBE and pumped with 1.5 μm laser diodes. Pulsed and continuous-wave emission at wavelengths up to 6.5 μm have been demonstrated to date using PbTe, PbSe or PbSnSe active layers,[73,74,77] and latterly multiple PbSe/PbSrSe quantum wells positioned for RPG.[13] Initial structures were grown on transparent BaF_2 substrates with the first report of peak powers >50 mW at 5 μm at 100 K;[73] however, much improved performance was achieved by growing on silicon substrates for better thermal management so that as much as 1 W output power was demonstrated in pulsed mode at –172°C.[76] The large refractive index contrast achievable with these materials (Δn up to ~4) means that high quality DBRs are possible with only two layer pairs, for example, BaF_2/PbEuTe[73] or PbEuTe/EuTe.[13] Due to the high-sensitivity of the narrow bandgap to temperature, in the region of 0.5 meV/K, extremely broad tuning may be achieved by varying the heatsink temperature. In recent work, Fill *et al.* reported an emission wavelength range of 3.6–5.1 μm from a single device by varying the heatsink temperature from –173°C to 52°C (see Fig. 9.3).

To summarise, the spectral coverage of continuous-wave SDLs is illustrated in Fig. 9.4. This shows selected results reported over almost a decade of development. It is particularly informative to plot SDL performance linearly with photon energy, as the fundamental wavelength range achieved results directly from semiconductor bandgap engineering.

9.3 Intracavity frequency control

In the previous section we have given an overview of the performance of SDLs emitting at wavelengths from the visible to the mid infrared. In all cases, the same general design principles and laser architecture allow relatively easy access to the intense intracavity beam, which may be exploited in a number of ways for sophisticated frequency control in each spectral region, as summarised in this section.

While SDLs are proving increasingly desirable as cheap and compact alternatives to gas and solid-state lasers at many common wavelengths, it is perhaps their combination of high-finesse external cavities and short carrier lifetime that will prove their most interesting attribute in the longer term. The photon lifetime in an SDL is much longer than the ‘upper state’ lifetime, leading to some important advantages for low-noise, narrow-linewidth operation and intracavity non-linear conversion.

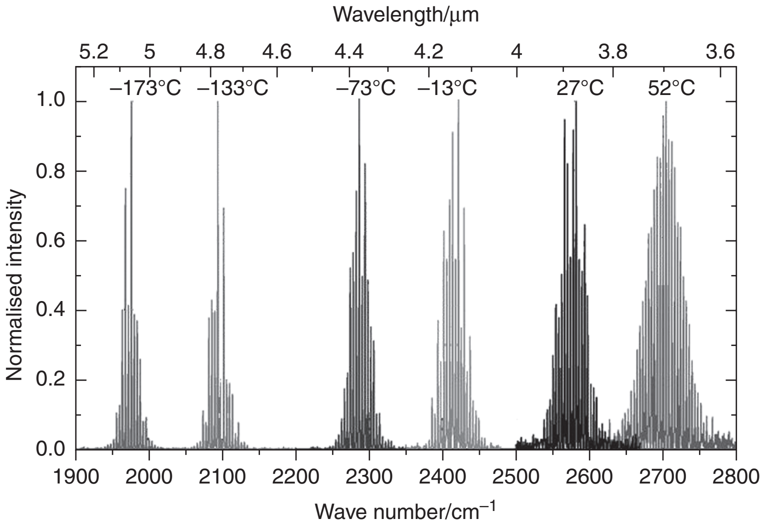

9.3 Normalised laser emission spectra of a PbSe/PbSrSe multi-quantum-well SDL for varying heat sink temperature.[13]

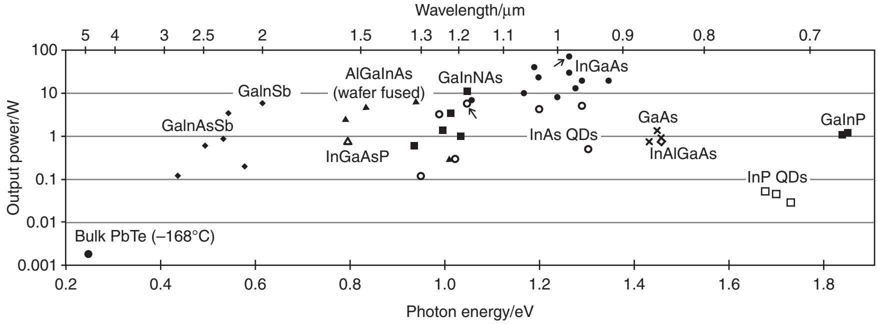

9.4 Fundamental spectral coverage of SDLs. Selected results are plotted to illustrate the maximum continuous-wave output power and spectral range of all materials used and refer to quantum wells unless otherwise indicated. Arrows indicate dual-chip SDLs. GaInP;[84,87] InP QDs;[50] GaAs;[53,88] InAlGaAs;[54] InGaAs;[35,41,42,55,57,89–91] InAs QDs;[17,58–60,80,92] GaInNAs;[61,62,64,93,94] InGaAsP;[67] AlGaInAs (wafer-fused);[12,65,95,96] GaInSb;[97] GaInAsSb;[70,72,97–99] bulk PbTe.[77]

9.3.1 Single-frequency operation

It was recognised early in SDL development that these lasers should be very attractive for single-frequency operation.[19] The fundamental limit for the minimum frequency bandwidth, or linewidth, Δ_L, of a laser, as calculated by Schawlow and Townes,[100] is given by:[101]

$$\Delta_L = \Delta_C{}^2 \xi \left(1+\alpha^2\right) \frac{2\pi hc}{P\lambda} \qquad [9.2]$$

where Δ_C is the laser cavity mode linewidth, h is Planck's constant, c is the speed of light, P is the emitted power, λ is the laser wavelength, ξ is the ratio of spontaneous emission rate to stimulated emission rate, and α is the linewidth enhancement factor. SDLs have very high-finesse cavities (small Δ_C), but relatively high output power, so that the fundamental limit for a typical SDL turns out to be a few Hz, compared to MHz for an edge-emitting semiconductor laser. In practice, even with a carefully designed stable cavity this is usually broadened by shot noise, and up to ~100 kHz by normal laboratory acoustic noise and noise from the pump laser, so that narrower linewidths must be achieved through vibration isolation and stabilisation of the laser frequency against an external reference. With the use of RPG, the quantum wells are positioned with nanometre-scale accuracy to coincide with the electric field maxima of a single frequency only, effectively eliminating spatial hole burning. Thus, single-frequency operation may be achieved with a simple, compact, standing wave cavity geometry that is easier to isolate from acoustic noise than, say, a dye laser.

Tuneable single-frequency operation of SDLs is usually achieved using one of two techniques: for long external cavities (more than a few centimetres) an intracavity BRF is typically used; for short cavities with only one longitudinal mode within the gain bandwidth, tuning is achieved by mounting the output coupler on a piezoelectric transducer (PZT) and varying the total cavity length, and hence the free spectral range (FSR). Single-frequency operation with limited tuning may also be achieved with the use of a volume Bragg grating (VBG),[102] or a high-reflectivity grating (HRG) as a cavity mirror;[103] however, kHz level linewidth has yet to be demonstrated with such techniques.

To date, the minimum linewidth demonstrated from an SDL is 3 kHz, as demonstrated by Holm *et al.* in early work with infrared GaAs-based SDLs.[19] Single frequency selection was achieved by insertion of an intracavity Lyot filter (three-plate BRF[110]) and an etalon. Narrow-linewidth operation was attained via active stabilisation, by locking the laser frequency to a reference cavity via an electronic feedback loop as shown in Fig. 9.5. The output of the reference cavity is monitored using a fast photodiode, used to produce an error signal that is sent to the PZT on which the SDL output coupler is mounted. This method was also used by Abram *et al.* to demonstrate an InGaAs-based SDL emitting up to 400 mW at 970 nm with linewidth of only 5 kHz.[43] Other reported narrow-linewidth SDLs are summarised in Table 9.2. Of particular note is the frequency quadrupled InGaAs SDL recently reported by Paul and co-workers, for Doppler-free spectroscopy of mercury in the deep ultraviolet.[104] Active stabilisation was used to

Table 9.2 Selection of narrow-linewidth single-frequency SDLs

λ (nm)	Linewidth (kHz)	Power (mW)	Tuning (GHz)	Intracavity filters	Active stabilisation	Reference
253.7 (λ/4)	60 (λ)	125 (λ/4)	6	Etalon and BRF	Reference cavity	104
488 (λ/2)	1500†	100	—	*	*	105
501 (λ/2)	*	62	—	Etalon and Lyot filter	—	106
532 (λ/2)	1500†	150	—	*	*	105
674	145	52	—	Etalon and BRF	Reference cavity	107
852	500	17	14	Etalon	Caesium transition	52
870	3	42	0.25	Etalon and Lyot filter	Reference cavity	19
970	5	400	—	Birefringent etalon[108]	Reference cavity	43
1014	60	1500	—	Etalon and BRF	Reference cavity	104
1020	37	2100	840	5 mm cavity length	—	109
2320	20	5	50	15 mm cavity length	—	101

* Not reported.
† Commercial device.

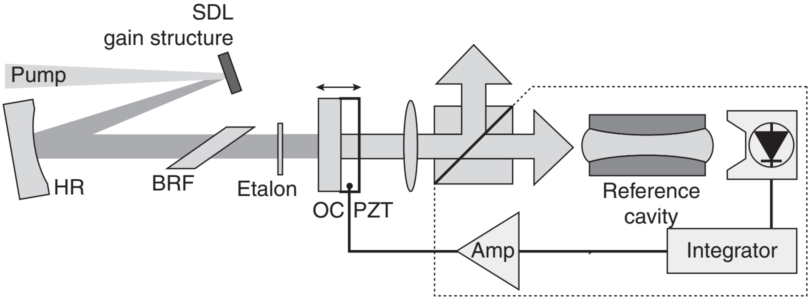

9.5 Schematic of an actively stabilised SDL. HR: high reflector; OC: output coupler; BRF: birefringent filter; PZT: piezoelectric transducer.

achieve <60 kHz linewidth for 1.5 W output power at 1014 nm, which was subsequently injected into successive stabilised frequency doubling resonators to generate up to 125 mW at 253.7 nm.

CNRS researchers at laboratories including the Institut d'Electronique du Sud, the Laboratoire Charles Fabry de l'Institut d'Optique, and the Laboratoire de Photonique et Nanostructures, and researchers at Thales

Research and Technology France have, via various collaborations, reported extensively on the design, modelling and characterisation of low-noise, single-frequency SDLs (e.g., References 52, 106, 109, 111–114). Garnache *et al.* have shown theoretically and experimentally that SDLs, with their high-finesse external cavities, can exhibit ideal homogeneous gain behaviour, with very low intensity and frequency noise in free-running operation.[114] As SDLs have external-cavity lengths longer than a few millimetres, the cavity photon lifetime exceeds the carrier lifetime (~3 ns), leading to so-called class-A dynamical behaviour, free from relaxation oscillations – the laser relative intensity noise (RIN), in Reference 111, reached the shot noise limit of –155 dB/Hz for frequencies above 50 MHz, limited by the pump RIN below. This work has recently culminated in the impressive performance demonstrated by the SDL shown in Fig. 9.6. By using a 5-mm-long cavity – long enough for class-A dynamical behaviour, but short enough to select a single longitudinal mode without additional intracavity filtering – Laurain *et al.* demonstrated multi-Watt low-noise single-frequency operation from a 1 μm SDL with linewidth of only 37 kHz.[109] Figure 9.6 also shows the laser power spectral density. A similar configuration was used to demonstrate 20 kHz linewidth at 2.32 μm from an antimonide-based SDL, of interest for spectroscopic applications.[101]

As narrow-linewidth operation and low-noise characteristics are intrinsic to SDL gain and design, kHz linewidth operation should be possible from SDLs at any wavelength. Indeed, linewidths on the order of Hz may be achieved by locking to an ultra-stable reference cavity for metrology applications. For example, 0.5 Hz linewidth has been demonstrated with an external-cavity diode laser (ECDL), by stabilisation to a well-isolated cavity made of ultralow-expansion glass;[115] however, in contrast to SDLs, ECDLs have low output power and beam quality, and therefore require intermediate beam shaping and amplification stages. In addition, frequency

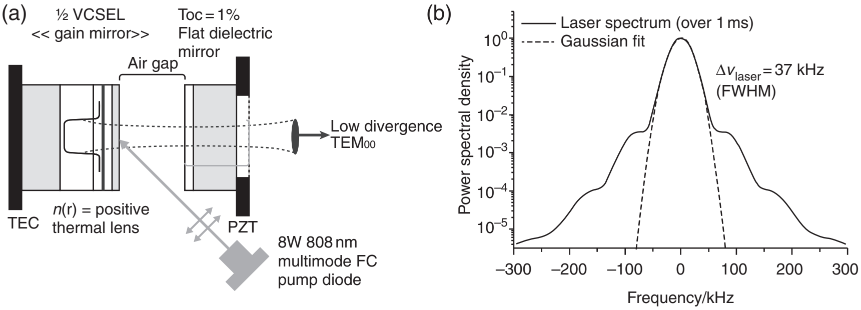
(a)
½ VCSEL
<< gain mirror>>
Toc = 1%
Flat dielectric mirror
Air gap
Low divergence TEM00
TEC
n(r) = positive thermal lens
PZT
8W 808 nm multimode FC pump diode
(b)
Laser spectrum (over 1 ms)
Gaussian fit
$\Delta\nu_{laser}$ = 37 kHz (FWHM)
Power spectral density
10^0
10^{-1}
10^{-2}
10^{-3}
10^{-4}
10^{-5}
–300
–200
–100
0
100
200
300
Frequency/kHz

9.6 Single-frequency SDL (referred to here as a 1/2 VCSEL) as reported by Laurain *et al.*[109] (a) Experimental set-up; (b) laser power spectral density.

conversion to target the wavelength of interest must be carried out separately, thus further reducing power and efficiency. Frequency conversion of SDLs on the other hand can be very efficient, as we shall see in the following section.

9.3.2 Non-linear conversion

Non-linear frequency conversion of SDLs, or indeed continuous-wave lasers in general, is most efficiently and conveniently achieved within the laser cavity. The non-linear medium, usually a crystal, is placed within the high-finesse resonator with cavity mirrors designed for high reflectivity at the fundamental wavelength and high transmission at the converted wavelength, such that power may be coupled out of the laser cavity via non-linear conversion only. Being low-gain lasers, the optimum output coupling of SDLs is usually on the order of a few per cent, and therefore relatively low single-pass non-linear conversion efficiency is required to obtain the maximum available output power at the converted wavelength. In addition, the gain properties of the SDL that favour low-noise operation, as discussed in the previous section, also have the consequence that so-called ‘green noise’[116] is minimised (for lasers operating on multiple longitudinal modes, mode coupling through cross saturation of the gain and sum-frequency mixing leads to strong intensity noise, historically called green noise due to the association with the frequency-doubled green lasers in which the phenomenon was first studied). For conventional solid-state lasers, green noise is avoided by operating the laser on a single frequency, using filtering or unidirectional oscillation, or lengthening the laser cavity to increase the number of longitudinal modes, hence averaging the effect. SDLs, on the other hand, with their characteristic short carrier lifetime, do not store gain and therefore avoid these dynamic fluctuations.[117]

An increasing variety of intracavity non-linear techniques, previously exploited in solid-state and dye lasers for both up- and down-conversion of the laser frequency, are now being utilised to further extend the spectral coverage of SDLs. Perhaps the simplest, and by far the most widely applied technique to date, is that of intracavity second harmonic generation (SHG) – also referred to as frequency doubling. As explained in Section 9.2.2, the spectral region around 1 μm is where SDLs have the best performance in terms of both power and wall-plug efficiency, by utilising superior AlGaAs-based DBRs, high gain InGaAs QWs and cheap and efficient 808 nm pump diodes. The use of SHG, therefore, enables these high performance SDLs to provide broad coverage of the visible region, from blue to yellow, thus providing an attractive all-semiconductor alternative to gas and solid-state lasers without compromising coherence or beam quality. This has proved a powerful commercial driver for these lasers, with extensive development carried out by Coherent Inc., who now supply a range of frequency-doubled

SDLs (which they refer to as OPSLs) at common visible wavelengths, historically determined by the previously available gas and solid-state lasers, for example, 488 nm, 514 nm (argon ion) and 532 nm (neodymium-doped glass/crystal), the so-called 'legacy wavelengths'. From the point of view of SDL design these wavelengths are almost arbitrary; the availability of new wavelengths outside of the laboratory is currently still market-driven.

In this section we will briefly describe the basic concepts and relevant types of non-linear frequency conversion, and review their application in SDLs. The non-linear polarisation, $\mathscr{P}(\mathrm{t})$, induced in a dielectric medium by an incident optical field with strength $E(t)$, is described by:[118]

$$\mathscr{P}\left(t\right) = \epsilon_0\,\chi^{(1)}E\left(t\right) + \epsilon_0\,\chi^{(2)}E^2\left(t\right) + \epsilon_0\,\chi^{(3)}E^3\left(t\right) + \cdots \qquad [9.3]$$

where ϵ_0 is the permittivity of free space, $\chi^{(1)}$ is the linear optical susceptibility, and $\chi^{(2)}$ and $\chi^{(3)}$ are the second- and third-order non-linear optical susceptibilities respectively. If the incident optical field has two frequency components, ω_1 and ω_2 with corresponding amplitudes E_1 and E_2, the second order term may be expanded thus:

$$\begin{aligned}\mathscr{P}^{(2)}\left(t\right) = \epsilon_0\,\chi^{(2)}&\left[E_1^2e^{-2i\omega_1 t} + E_2^2e^{-2i\omega_2 t} + 2E_1E_2e^{-i(\omega_1+\omega_2)t} + 2E_1E_2^*e^{-1(\omega_1-\omega_2)t} + \text{c.c.}\right]\\ &+ 2\,\epsilon_0\,\chi^{(2)}\left[E_1E_1^* + E_2E_2^*\right]\end{aligned} \qquad [9.4]$$

where c.c. stands for complex conjugate terms. According to Maxwell's equations, this non-linear polarisation leads to the generation of electromagnetic waves with frequencies $2\omega_1, 2\omega_2$ (SHG), $\omega_1 + \omega_2$ (sum-frequency generation – SFG), and $\omega_1 - \omega_2$ (difference frequency generation – DFG), illustrated schematically in Fig. 9.7. The efficiency with which these different frequency components are generated, however, strongly depends on meeting specific phase-matching conditions, typically only satisfied for one frequency component in a given system. These second order non-linear optical responses do not occur in crystals that display inversion symmetry, that is, $\chi^{(2)}$ is only non-zero for non-centrosymmetric crystals. Third-order non-linear interactions, such as stimulated Raman scattering (described at the end of this section), however can occur in both centrosymmetric and non-centrosymmetric media for sufficiently intense optical fields.

For the case of sum-frequency mixing, it can be shown that for incident intensities, $I_{1,2}$, at the fundamental frequencies, the intensity generated at the sum frequency ω_3, is given by:

$$I_3 = \frac{2d_{\text{eff}}^2\,\omega_3^2 L_m^2}{\epsilon_0\, c^3 n_1 n_2 n_3}\sin c^2\left(\frac{\Delta k L_m}{2}\right)I_1 I_2 \qquad [9.5]$$

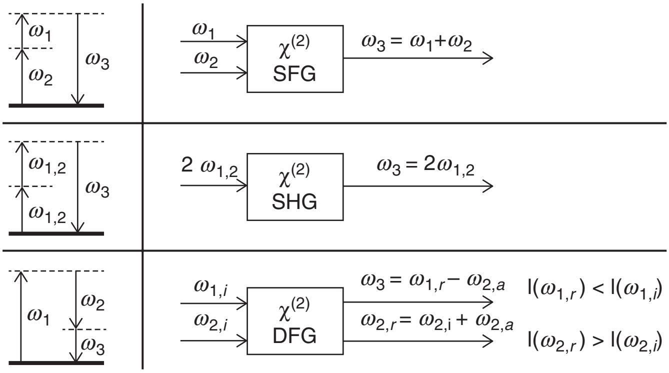

9.7 Energy level diagrams and corresponding schematics representing the processes of sum-frequency generation (SFG), second harmonic generation (SHG) and difference frequency generation (DFG).

where d_{eff} is the effective non-linear coefficient of the material, L_{m} is the length of material, $n_{1,2,3}$ are the refractive indices for the fundamental and sum frequencies, and Δk is the wavevector (or momentum) mismatch:

$$\Delta k + k_1 + k_2 - k_3 = \frac{n_1 \omega_1}{c} + \frac{n_2 \omega_2}{c} - \frac{n_3 \omega_3}{c} \tag{9.6}$$

where $\omega_1 + \omega_2 = \omega_3$. Phase-matching requires $\Delta k = 0$, which is generally achieved by selecting a birefringent non-linear crystal which allows control of the refractive indices at the different frequencies via angle or temperature tuning. Δk, and therefore the non-linear conversion efficiency, is strongly dependent on wavelength, temperature and incident angle. Alternatively, where it is desirable to use a non-birefringent crystal, for example, to access larger d_{eff}, quasi-phase-matching may be achieved via a technique called periodic poling. Periodically-poled crystals are fabricated in such a way that the orientation of the domain is reversed every $2/\Delta k$ (coherent build-up length) leading to alternation of the sign of d_{eff} to compensate for wavevector mismatch. Both birefringent and quasi-phase-matching have been used with a wide range of non-linear crystals for non-linear conversion of SDLs (see Table 9.3, where pp denotes periodically-poled material).

SHG, or frequency doubling, is the special case of $\omega_1 + \omega_2 = \omega$ in Equation 9.5; thus the second harmonic intensity depends on the square of the fundamental intensity. In terms of power, and assuming perfect phase-matching ($\Delta k = 0$):

$$P_{2\omega} = \frac{2 d_{\text{eff}}^2 \omega^2 L_m^2}{\epsilon_0\, c^3 n_\omega^2 n_{2\omega} \pi w_0^2} P_\omega^2 = \frac{\eta_{\text{NL}}}{\pi w_0^2} P_\omega^2 \tag{9.7}$$

where w_0 is the collimated beam radius and we have introduced η_{NL} as the non-linear coupling coefficient.

Table 9.3 Crystals used for second order (parametric) non-linear frequency conversion of SDLs

Non-linear crystal	Transparency (nm)	SDL conversion examples
LBO	160–2600	SHG[55,119,120] SFG[121] SFG (third harmonic)[122]
CLBO	180–2750	SHG (extra-cavity UV)[123]
BBO	190–3500	SHG (UV)[84] SHG[65,93,124]
BiBO	286–2500	SHG[125,126]
KTA	500–3500	DFG (OPO)[127]
KTP	350–4500	SHG[126]
ppKTP	350–4500	SFG[128]
MgO:ppLN	420–5200	SHG[129,130] DFG (THz)[131] DFG (OPO)[132,133]
MgO:ppSLT	270–4500	SHG[134]

A typical cavity configuration for intracavity frequency doubling in an SDL is shown in Fig. 9.10. As noted above, the cavity mirrors are highly reflective for the fundamental wavelength, but highly transmissive at the second harmonic; output coupling is achieved via non-linear conversion only. The gain bandwidth of a typical SDL is generally broader than the phase-matching bandwidth of most non-linear crystals. To prevent the SDL from operating at a wavelength outside the phase-matching condition, and thus avoiding conversion loss, a BRF, inserted in the cavity at Brewster's angle, is typically used to fix the wavelength. The BRF has the additional function of fixing the polarisation of the SDL, required for type-I phase-matching.

Kim *et al.* derived an analytical model to describe the power that may be extracted at the second harmonic by adding the photon reduction rate due to the non-linear conversion process to the SDL photon rate equation and solving for the fundamental intensity, S, in the non-linear crystal:[135]

$$S = \frac{1}{2\eta_{\mathrm{NL}}}\left(-1+\sqrt{1+4\eta_{\mathrm{NL}}\frac{\Gamma\eta_{\mathrm{abs}}\left(P_p-P_{\mathrm{th}}\right)}{\pi w_0^2 L_a \alpha_L}\frac{\lambda_p}{\lambda_f}}\right) \quad [9.8]$$

where Γ is the optical confinement factor, η_{abs} is the pump absorption efficiency, P_p is the pump power, P_{th} is the pump power at SDL threshold, α_L is the total round-trip loss, and λ_P and λ_f are the pump and fundamental wavelengths. The second harmonic power is then given by $\eta_{\mathrm{NL}} S^2 \pi w_0^2$.[135] Figure 9.8 shows the second harmonic output power of a frequency-doubled InGaAs-based SDL for different lengths of intracavity non-linear crystal.[117]

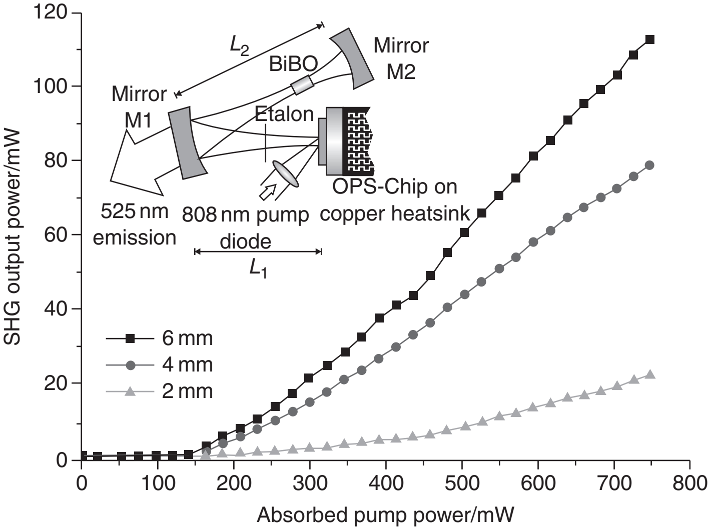

9.8 Output power at the second harmonic for an InGaAs-based semiconductor disk laser, frequency-doubled using different lengths of intracavity BiB_3O_6 (BiBO), as reported by Hartke *et al.*[117] Inset: experimental set-up.

Frequency doubling of quantum well SDLs was extensively reviewed by us in Reference 49, where it was shown that InGaAs-based SDLs, using a variety of common non-linear crystals, have been used to cover the range from ~460 to 589 nm (e.g., 10 s of watts demonstrated at various wavelengths by researchers at Coherent Inc.[55,120,136,137]), with GaInNAs-based SDLs extending this up to 610 nm.[93] Frequency doubling directly to the ultraviolet was also made possible with the development of high-power AlGaInP-based visible red SDLs.[84] Recently, more effort has been dedicated to the further development and power scaling of materials to push high performance SDLs to $\lambda > 1.18$ μm, and hence to realise high-power orange and red SDLs via frequency doubling. As described in Section 9.2.2, achieving fundamental emission at wavelengths >1.18 μm, beyond the range of InGaAs-based gain regions, has been tackled via three material routes: incorporation of small amounts of nitrogen in InGaAs to lower the bandgap – so-called dilute nitrides;[63] accommodating high strain by using quantum dots;[17] and wafer fusion techniques in order to use InP-based active regions bonded to AlGaAs-based DBRs.[86] Much of the work on frequency doubling of SDLs based on these materials has been reported by Rautiainen and co-workers using intracavity beta barium borate (BBO) non-linear crystals, notably achieving 2.7 W output power at 610 nm from a frequency-doubled GaInNAs SDL,[93] and later the first demonstration of frequency doubling of an InAs quantum-dot-based SDL.[92] In the latter case, in order to generate sufficient gain to compensate for the non-linear output coupling, it was necessary to incorporate two gain structures into the same cavity which were pumped with a total of 60 W to achieve 6 W output power at 1180 nm. This was subsequently frequency-doubled to achieve 2.5 W of orange emission. Perhaps more promising for this application are the wafer-fused SDLs with higher gain, a recent example of which was frequency-doubled to give as much as 3 W at 650 nm for half the pump power of the quantum-dot-based laser.[65] Orange and red SDLs have recently become commercially available from Coherent Inc. in multi-transverse mode operation with output power of 1.25 W at 607 nm and up to 2 W at 639 nm,[138] although the details of the gain structure composition have not been disclosed.

The shortest wavelengths are achieved by frequency doubling in an external resonant cavity the output of an already frequency-doubled SDL. In this way, continuous-wave emission at the fourth-harmonic of a 976 nm SDL has been generated by intracavity doubling using LBO, and extra-cavity doubling in $CsLiB_6O_{10}$ (CLBO).[123,139] More than 1 W continuous-wave output power was thus demonstrated at 244 nm by Bell and co-workers.[139]

While the common 4-mirror cavity example shown in Fig. 9.10, and the 3-mirror cavity shown in the inset of Fig. 9.8 are convenient for positioning the non-linear crystal at an intracavity focus and are simple to implement in the laboratory, more compact configurations have also been engineered (see e.g., Reference 34). OSRAM Opto Semiconductors are pursuing miniaturised versions for mobile laser projection applications (see Fig. 9.9) and were able to show wall-plug efficiencies > 7%.[130] Recently, steps towards a quasi-monolithic frequency-doubled SDL have been made by bonding the non-linear crystal directly to the diamond heatspreader which was already bonded to the SDL gain structure.[140]

Frequency *tripling* may be achieved within an SDL cavity by the use of two different non-linear crystals at separate cavity mode foci; one cut for frequency doubling of the fundamental beam, and the other cut for sum-frequency mixing of the resulting second harmonic with the fundamental beam to generate the third harmonic (see Fig. 9.10). This technique was used

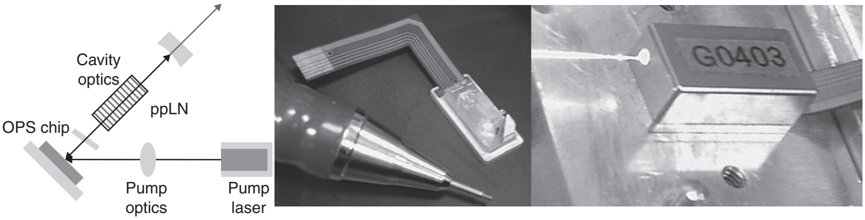

9.9 Ultra-compact, frequency-doubled SDL developed by OSRAM Opto Semiconductors GmbH.[130]

by Chilla *et al.* to demonstrate up to 1.1 W at 355 nm from a 1064 nm SDL.[122] In another configuration for sum-frequency mixing, Andersen *et al.* generated 593 nm emission by focussing the output beam of a 1342 nm Nd:YVO_4 disk laser into periodically poled potassium titanyl phosphate (ppKTP) situated within the cavity of an 1064 nm SDL.[128] Up to 20% of the 1342 nm beam was converted to the sum frequency on a single pass.

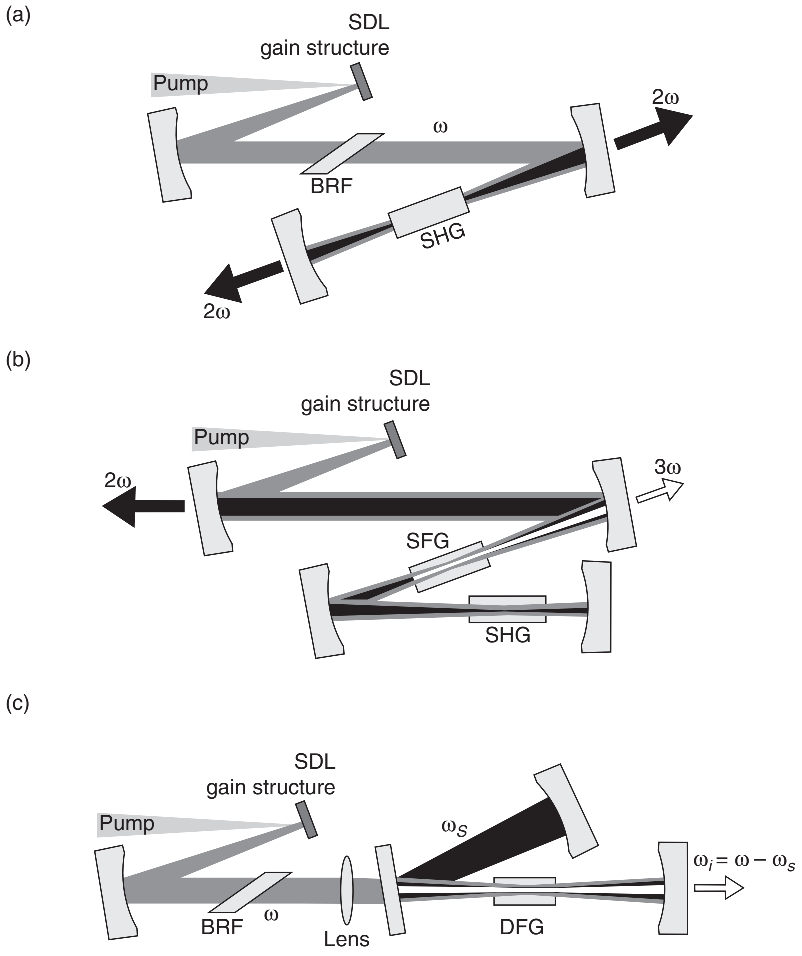
(a)
SDL
gain structure
Pump
2ω
ω
BRF
SHG
2ω
(b)
SDL
gain structure
Pump
2ω
3ω
SFG
SHG
(c)
SDL
gain structure
Pump
ω_S
ω_i = ω − ω_s
BRF
ω
Lens
DFG

9.10 Examples of SDL cavity configurations used for intracavity parametric non-linear conversion. (a) Frequency doubling; (b) frequency tripling and (c) optical parameter oscillator. SHG, SFG and DFG: second harmonic, sum and difference frequency generation in a non-linear crystal either cut for phase-matching, or poled for quasi-phase-matching; BRF: birefringent filter; ω, ω_s and ω_i: fundamental, signal and idler frequencies respectively. All cavity mirrors are highly reflective for the fundamental frequency.

The first demonstration of sum-frequency mixing in an SDL cavity was reported by Härkönen and co-workers using an InGaAs-based SDL gain structure designed for simultaneous oscillation at two wavelengths – 986 and 1043 nm.[121] With the use of an intracavity lithium triborate (LBO) crystal, cut for type-I phase matching at 213°C, 130 mW output power was achieved at the sum frequency of 507 nm. While this wavelength could just as easily be generated via frequency doubling of a single wavelength InGaAs SDL, this result proved the principle that a dual-wavelength SDL could be used for non-linear frequency conversion, with the authors suggesting the interesting prospect for such a device to be used for DFG to target mid-infrared emission. Indeed a continuous-wave *terahertz* source has since been demonstrated by Scheller *et al.* via DFG in a dual-wavelength SDL, in this case the more closely spaced dual-wavelength operation (~5 nm) achieved by insertion of an intracavity etalon rather than gain structure design.[131] The high intracavity power of the InGaAs SDL, ~500 W, enabled the generation of 2 mW at 1.9 THz in periodically-poled MgO-doped lithium niobate (MgO:ppLN). *Tuneable* dual frequency operation of an SDL has also been reported by Baili *et al.* who inserted a birefringent plate to achieve a small spatial separation of two cavity polarisation eigenstates at the SDL gain structure and therefore simultaneous oscillation of two optical frequencies.[141] By thermally varying the birefringence, the frequency separation could be tuned as demonstrated by the continuous tuning of the beat-note frequency from a few MHz up to 3.66 GHz. This SDL architecture should also be suitable for terahertz generation,[142] although, to our knowledge, this has not yet been demonstrated.

In DFG, as illustrated in the energy level diagram in Fig. 9.7, for every photon generated with frequency $\omega_{2,}$ a ω_1, photon is destroyed and a ω_2 photon is created. DFG is therefore commonly referred to as optical parametric amplification. Further, if the lower frequency fields are generated within an optical cavity that resonates these frequencies, oscillation can occur. This is the basis of an optical parametric oscillator (OPO).[143] Stothard *et al.* recognised that a continuous-wave OPO could be efficiently pumped within the cavity of an SDL and were the first to report such a device,[132] using intracavity MgO:ppLN to generate up to 205 mW at 3.05 μm in the configuration shown in Fig. 9.10 (ω was 1.05 μm; ω_s 1.6 μm). While intracavity pumping of OPOs had previously been investigated for efficient continuous-wave operation within conventional solid-state lasers (e.g., those based on neodymium-doped crystals), the authors demonstrated here that the short carrier lifetime of the SDL eliminated the problem of relaxation oscillations that had severely limited the practicality of these systems. Subsequently, two industrial labs have reported continuous-wave OPOs pumped within 1.06 μm InGaAs SDLs: Caprara *et al.* at the Coherent Laser Group demonstrated 2 W at 3.5 μm using non-critical phase matching in KTA, and achieved an idler tuning range of ~12 nm at lower powers by tuning the SDL oscillation wavelength via rotation of an intracavity BRF;[127] and Hempler *et al.* of M Squared Lasers Ltd. demonstrated single-frequency operation with narrow-linewidth (<0.2 nm) and output power of 250 mW at 3.3 μm using MgO:ppLN in a compact system.[133]

The final non-linear frequency conversion technique that we will discuss here, used for down-conversion, is intracavity Raman conversion. This is a χ^3 non-linear process, and as such was, until relatively recently, mainly associated with high-power Q-switched lasers. Following the development of diode-pumped continuous-wave solid-state Raman lasers,[144,145] and notably the broad investigation carried out by Pask and co-workers at Macquarie University,[146] Raman conversion has recently been applied to SDLs with competitive efficiency.[147,148] In contrast to the χ^2 parametric processes described earlier, we will see that intracavity Raman conversion, as it has been applied in continuous-wave lasers, is more akin to intracavity pumping of a laser rather than non-linear output coupling.

The technique is based on the inelastic Raman scattering process. This provides a non-linear means to red-shift the pump wavelength by transfer of some of the photon energy to vibration of a molecule or crystal lattice via a virtual intermediate state, resulting in a characteristic, fixed Stokes shift (see Fig. 9.11). The typical Stokes shift imparted by crystalline Raman media is on the order of 1000 cm^{-1}; thus for near infrared pump lasers this is equivalent to a red-shift of approximately 100 nm.

Stimulated Raman scattering (SRS), can occur when a spontaneously scattered Stokes photon stimulates the emission of a second Stokes photon, and therefore, for sufficiently intense pump excitation, laser oscillation at the Stokes wavelength can occur. For an input pump beam with intensity I_P, the intensity of the generated Stokes radiation after a distance z through a medium is given by:[149]

$$I_S(z) = I_S(0)e^{g_R I_P z} \qquad [9.9]$$

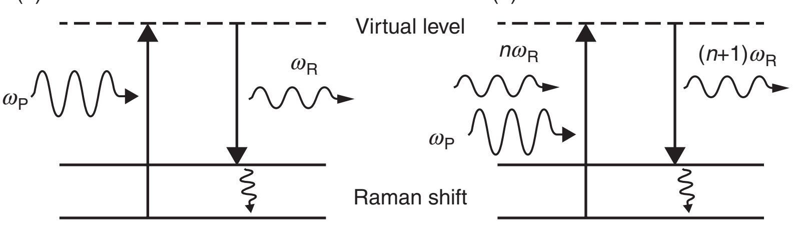

9.11 Raman Stokes scattering via a virtual energy level. (a) Spontaneous Raman scattering; (b) stimulated Raman scattering (SRS).

where g_R is the Raman gain coefficient of the medium, and the initial Stokes intensity, $I_s(0)$, builds from spontaneously scattered Stokes photons. Given that a typical Raman gain coefficient might be ~6 cm/GW, Raman conversion on a single pass with any sort of useful efficiency is generally in the realm of very high-power Q-switched lasers. However, analogous to a conventional laser, the Stokes field may be resonated in a high-Q cavity with the threshold condition that the Raman gain balances the resonator losses:

$$R_1 R_2 \left(1-L\right) e^{2 g_R I_P Z} = 1 \qquad [9.10]$$

$R_{1,2}$ is the reflectivity of the resonator mirrors, L is the round-trip loss, and z is the length of the Raman medium. Assuming total round-trip losses of 1%, the typical threshold intensity for a 3-cm-long Raman crystal is thus on the order of ~280 kW/cm^2. With a reasonable pump beam radius of 50 μm, the threshold becomes ~22W – well within the reach of the high intracavity powers that may be accessed inside an SDL. The set-up of a crystalline Raman laser, intracavity-pumped within an SDL, as reported by Parrotta *et al.,* is shown in Fig. 9.12.[147] In contrast to the previously used χ^2 techniques, such as the OPO, phase-matching is not required. The optical frequency shift induced by SRS is fixed by the properties of the Raman crystal; therefore the broad tunability of an SDL (typically tuned with an intracavity BRF) may be directly transferred to broad tuning of the Raman laser, ~100 nm deeper in the red.

The SDL-pumped Raman lasers demonstrated to date utilise KGW[147] and diamond[148] to reach wavelengths around 1150 and 1230 nm respectively (see Table 9.4 and Fig. 9.13). Although SDLs can and have been designed

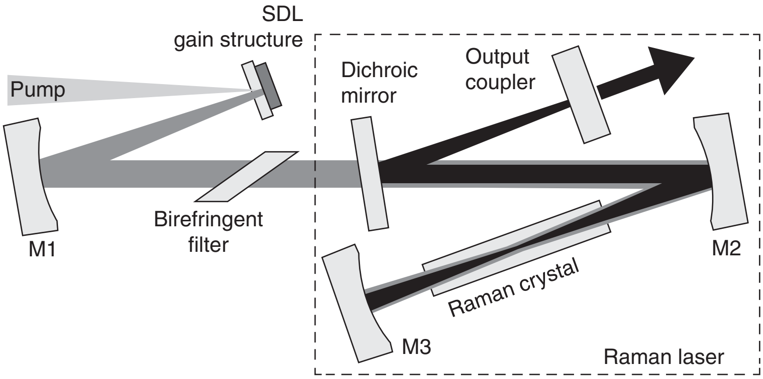

9.12 Schematic of a crystalline Raman laser, intracavity-pumped within an SDL. Mirrors M1–3 are high reflectors for both the SDL and Stokes wavelengths. The birefringent filter allows frequency selection and tuning of the SDL.

Table 9.4 Summary of Raman gain crystal properties intracavity-pumped in an InGaAs SDL

	KGW	Diamond
Raman gain (cm/GW)	~6	~15
Raman shift (cm^{-1})	767 or 901	1332
Thermal conductivity (W/m K)	3	3000
Available length (mm)	~30	~6
References	150	151
Demonstrated performance within a 1 μm InGaAs SDL		
Maximum output power (W)	0.8	1.3
Tuning range (nm)	1133–1157	1209–1245
Slope/optical efficiency (%)	22/7.5	36/14.4
References	147	148

to operate around these wavelengths without non-linear conversion (see Section 9.2.2), this method provides an alternative to the highly strained gain structures or less robust materials required to directly generate these wavelengths and makes use of the superior InGaAs-based SDLs around their peak performance wavelength (~1 μm).

9.4 Pulsed operation

Up to this point, this review has concentrated on the versatility of SDLs to generate *continuous-wave* high-brightness beams with an emission wavelength ranging from the ultraviolet to the mid-infrared. In the next sections, we will turn our attention to the behaviour of these sources in the pulsed regime, presenting the techniques used to obtain increasingly short pulses, namely gain-switching and cavity-dumping for the generation of nanosecond pulses and mode-locking for pico- and even femto-second pulsed emission.

9.4.1 Pulsed-pumped SDLs

The most straightforward method to generate a pulsed output from a laser is by turning its pump on and off. Should the pump remain turned on for a substantial fraction of the overall on/off cycle, the laser is said to be operating in a quasi-continuous-wave regime. The primary objective of such a technique is to mitigate the thermal build-up and its associated detrimental effects (such as the reduction of internal efficiency, thermal lensing, stress and damage) that is, to operate the laser in a 'cold' state.

To evaluate when this technique offers its best benefits, the experimentally verified results of a finite-element thermal analysis of a set of 2.3 μm SDLs under 905 nm diode pumping are presented in Fig. 9.14 (see Reference 39

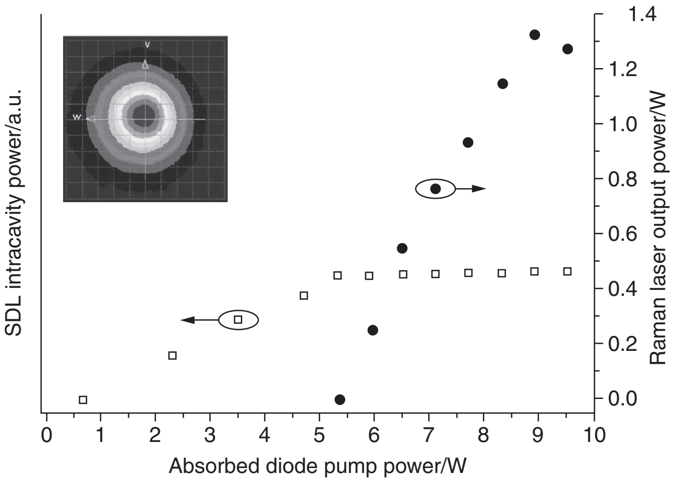

9.13 Power transfer characteristics of the continuous-wave diamond Raman laser, including the SDL intracavity power measured via signal leakage through a cavity folding mirror. Inset: far-field profile of the Raman laser output beam with beam propagation ratio (M^2) ~ 1.1.

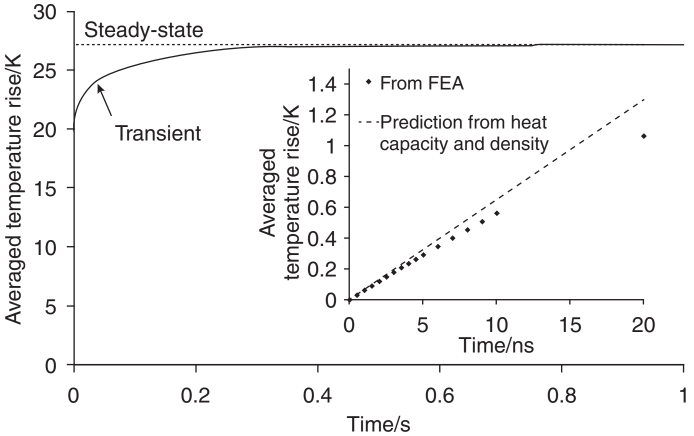

9.14 Evolution of the average temperature of the active region of 2.3 µm SDLs under 905 nm diode pumping for 10 W of absorbed power (200-µm-diameter pump spot). Inset: close-up of the average temperature rise over the first 20 ns.

for details). As expected, they reveal that after typically >0.5 s, the sample temperature saturates to its continuous-wave value and that, as long as the heat diffusion process can be neglected (i.e., in the first ~20 ns), the evolution of sample temperature rise, ΔT, with the pump pulse on-time, Δt, is independent of the sample mounting and can be approximated by the following expression:

$$\Delta T = \frac{P_{\text{abs}}\Delta t}{C_p \rho V_{\text{abs}}} \tag{9.11}$$

where C_p and ρ are the specific heat capacity and density of the active layer respectively, and $P_{\text{abs}}/V_{\text{abs}}$ is the volume density of absorbed pump power inside the active region. Since the emission wavelength of a free-running SDL is linearly dependent on the chip temperature, the pulses are inherently spectrally chirped as illustrated in Reference 39.

As indicated above and clearly illustrated in Fig. 9.15, the prime benefit of quasi-continuous-wave operation is to reach higher on-time powers than would be achievable under continuous-wave operation. The associated pulse profile follows the square pump profile but with a short (few ns) turn-on time lag and exponential rise and fall times controlled by the pumping rate and the cavity lifetime.

To generate more energetic pulses, a standard technique is to opt for 'gain-switched' operation of the laser, that is, setting the pump pulse duration to be only a few times (say <20x) the cavity photon lifetime. In this scenario, the rapid pump turn-on allows the gain to reach a very high level (ultimately full saturation) before the cavity photons start to deplete the established population-inversion. The pump pulse duration and trailing edge are then used to permit an effective build-up of the laser output pulse and some tailoring of its trailing edge, thereby maximising its energy. We note that this

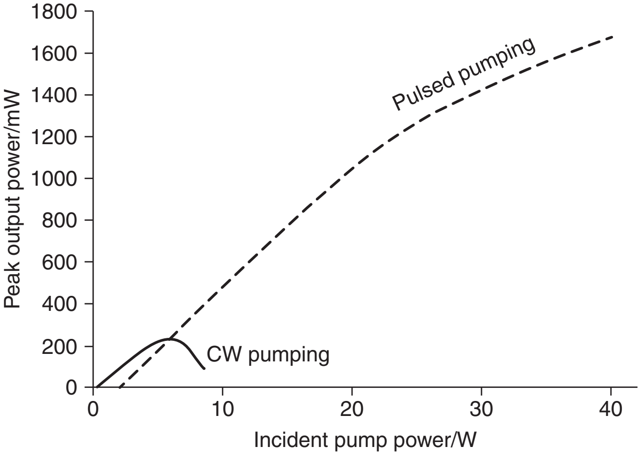

9.15 Comparison of the achievable performance with a 2.3 μm SDL under continuous-wave and quasi-continuous-wave pumping highlighting the benefits of the latter for high on-time powers.[39]

Table 9.5 Reported gain-switched SDLs

λ (nm)	Pulse duration (ns)	Peak power (W)	Energy (μJ)	Rep. rate (kHz)	Pump laser	Reference
1360	25	500	14	10	1064 nm Q-switched Nd:YAG	152
1570	20	290	5.8	20	1064 nm Q-switched Nd:GdVO$_4$	153
1550	~60	520*	31.2	20	1342 nm Q-switched Nd:YVO$_4$	154
2000	200	70	14	1	1064 nm Q-switched Nd:YAG	155
2000	143	342	48.9	1	1064 nm Q-switched Nd:YAG	156

* This peak power value was calculated based on the data provided in Reference 154 and differs from the 1.5 kW claimed by the authors of the original paper.

particular mode of operation also benefits from the 'cold' state of the laser gain media as described above.

As shown in Table 9.5, using this technique with nanosecond-pulsed (Q-switched) doped-dielectric pump sources,[152–156] the most energetic pulses obtained to date are from a 2-μm-emitting SDL pumped over a ~3.6-mm diameter spot delivering ~50-μJ and 140-ns pulses at 1 kHz[156] while the highest peak powers >500 W were achieved with a 1360-nm SDL.[152] This pulsed mode of operation was also instrumental in the demonstration of a recently introduced variety of SDLs, which make use of organic active regions rather than epitaxial semiconductors.[157]

9.4.2 Cavity-dumped SDLs

As mentioned previously, one of the key characteristics of SDLs is that they are low-gain lasers with high intracavity intensities. As a result, an alternative way to produce high-energy pulses is to abruptly and repetitively release the power stored in the cavity to the outside, a technique referred to as cavity-dumping and more commonly used in dye or solid-state lasers that can also be mode-locked.[158]

To embody this technique in practice, as shown in Fig. 9.16, the SDL semiconductor chip is included in a cavity constructed with all high-reflectivity mirrors inside which an acousto-optic (or an electro-optic) beam deflector is incorporated.[159] Figure 9.17 shows the typical response of a cavity-dumped 1055 nm SDL as a function of pulse repetition rate, demonstrating that

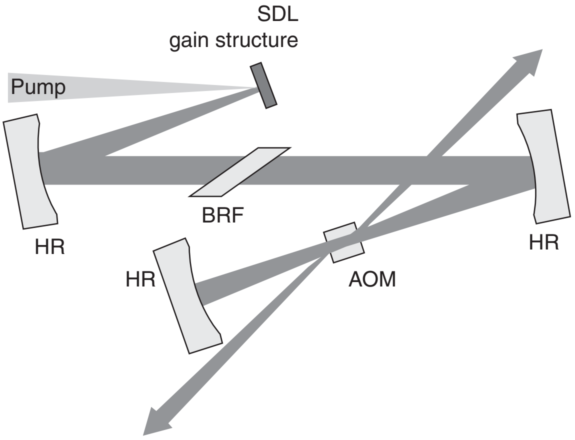

9.16 Schematic of a cavity-dumped SDL. HR: high reflector; BRF: birefringent filter; AOM: acousto-optic modulator.

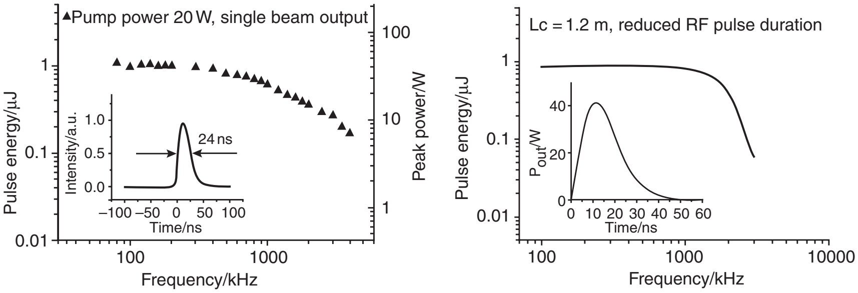

9.17 Performance of the reported cavity-dumped 1055 nm SDL and associated modelled characteristics.

the produced pulse energy remains nearly constant as long as the internal field has sufficient time to be restored to its continuous-wave regime level. Moreover, it can easily be understood that the associated pulse duration is controlled by the cavity-dumping element opening time and the cavity lifetime for its leading and falling edges respectively. Experimental data and modelling results, obtained by adding a time-dependent loss to the laser rate equations that takes into account the deflector rising time and efficiency,[159] show that the pulse energy scales linearly with cavity length due to an approximately square root increase in peak power and in pulse duration. The reported demonstration of such a cavity-dumped SDL led to the generation of wavelength-tuneable ~24 ns pulses with up to ~1 µJ of output at a central wavelength of ~1055 nm.[159]

9.4.3 Mode-locked SDLs

The generation of even shorter pulses, entering the domain of ultrafast (<250 ps) pulse generation, requires the use of so-called mode-locking techniques, which consist in introducing a gain or loss modulation at a frequency corresponding to the SDL round-trip cavity length or one of its harmonics to synchronise as many of the supported longitudinal modes as possible.

Synchronously-pumped systems where the modulation originates from the gain variation introduced by ultrashort pump pulses were the first to be reported.[160] The technique has been shown to allow the generation of highly-chirped 1–250 ps pulses[160–165] directly from the laser, and 200–400 fs after external compression.[162–165] However, the power transfer characteristics are critically dependent on the accurate and stringent match of the pump and SDL cavity lengths and mainframe pump lasers are typically used.[163,165] Additionally, large variations in the pulse characteristics, duration and chirp in particular, are observed since these result from a complex interplay between the cavity detuning, pump-pulse-induced self-phase modulation, gain dynamics and saturation.[163–165] The second option for achieving mode-locking is of actively imposing a loss modulation. Using a fast acousto-optic prism modulator placed inside an 850 nm SDL cavity, a 26-mW-average-power 336 MHz train of ~100 ps pulses was generated in this manner in an early demonstration.[166]

To get away from the requirement for fast (opto)-electronics or complex synchronisation, the latest and more versatile approach to SDL mode-locking relies on passive loss modulation. This specific strand of work has been the subject of comprehensive reviews and the interested reader is invited to refer to References 167, 168 for more in-depth discussion as the following section is only intended to provide basic information and a brief overview of the topic. As indicated above, passive mode-locking is achieved by introducing inside the SDL cavity another semiconductor component, a semiconductor saturable absorber mirror (SESAM), whose absorption varies because of saturation effects induced by the laser intracavity field. Practically, the absorber is incorporated on a semiconductor mirror and attenuates low-power noise and leaves nearly-unaffected high-power spikes thereby initiating and maintaining short pulse formation. As shown in Fig. 9.18, its four key parameters are:

- the saturation fluence, which corresponds to the power density at which the absorption is mid-way between its unsaturated and saturated levels;
- the modulation depth, which is the change in absorption between unsaturated and saturated levels;
- the non-saturable loss, which is the minimum inherent loss introduced in the laser cavity (with the absorber fully saturated); and
- the recovery time, which represents the time needed to return to full absorption after a saturation event.

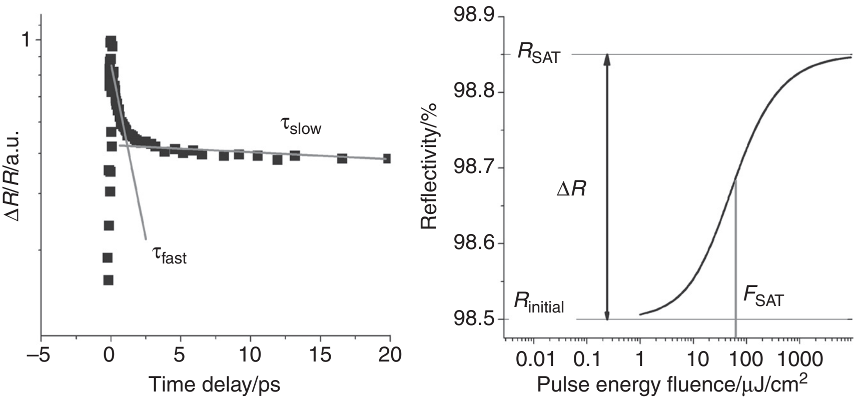

9.18 SESAM characteristics.

Key to successful operation of such ultrafast sources is the requirement for the absorber to saturate earlier than the gain element, a condition usually met by setting up a V- or Z-type laser cavity as shown in Fig. 9.19 such that the power density on the SESAM is higher than on the gain chip. To ensure effective operation, the SESAM should also present low non-saturable losses and a recovery time chosen to be fast (<50 ps) by exploiting fast-transient non-linear effects such as the quantum-confined Stark effect[169] and/or providing effective non-radiative recombination routes to the photo-excited carriers by controlled incorporation of (mid-bandgap) defects (typically achieved by low-temperature growth,[170] ion-implantation[167] or doping of impurities,[167] coupling to surface states,[169] or even reverse-bias-induced carrier sweep-out[171]). Furthermore, to generate the shortest pulses possible, the gain and saturable absorber semiconductor chips should offer wide spectral bandwidths that is, the considered structures should be designed and operated at or near anti-resonance and all spurious filters removed with a particular attention to the etalon effects resulting from the reflections originating from the (polished) semiconductor substrate back-surfaces.

Taking the above into account, and the fact that the gain elements typically possess nanosecond lifetimes, passively mode-locked SDLs have been successfully developed to emit (multi-)GHz repetition-rate trains of pico- and even femto-second pulses. Figure 9.20 illustrates from selected references[44,169,170,172–178] the progress made towards short pulse generation from the original demonstration of passive mode-locking[168] to the most recent generation of a burst of ~60 fs pulses[44] in 2009 or of a stable train of 107 fs pulses.[178] This graph highlights a rapid evolution in the first few years up to the introduction of quantum-confined Stark effect SESAMs and associated first generation of sub-picosecond pulses. Since then, the steady reduction in pulse length has mainly come from optimising and matching the gain chips and

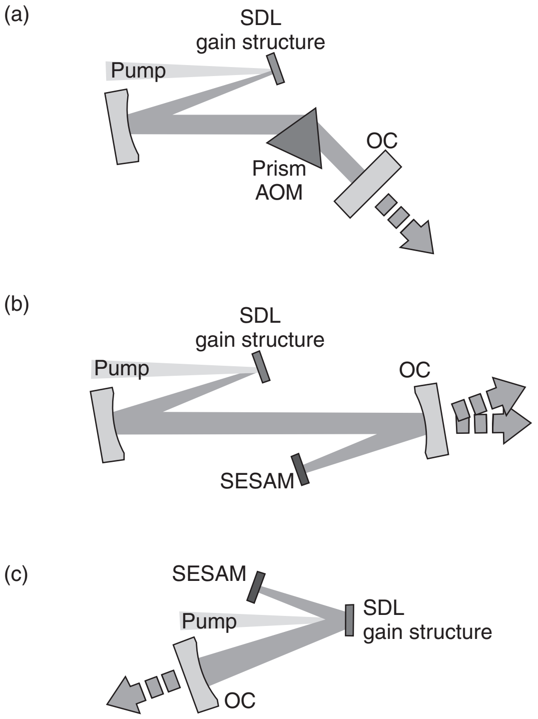
(a)
SDL gain structure
Pump
OC
Prism
AOM
(b)
SDL gain structure
Pump
OC
SESAM
(c)
SESAM
Pump
SDL gain structure
OC

9.19 Mode-locked SDL configurations. (a) Active mode-locking; (b) and (c) passive mode-locking: AOM: acousto-optic modulator, OC: output coupler, SESAM: semiconductor saturable absorber mirror.

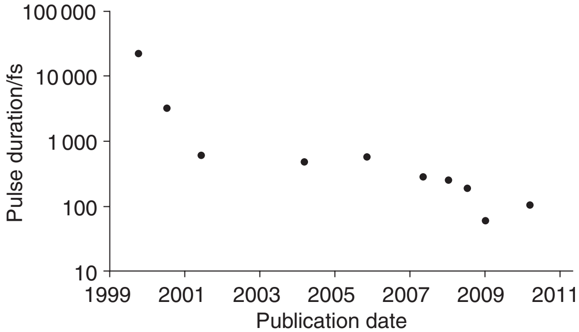

9.20 Progress in ultrashort pulse generation with SDLs emitting at ~1 μm.

SESAMs to offer appropriate gain, gain saturation, and modulation depth. It is worth noting that the fastest pulse durations that have been obtained are on a par with the absorber dephasing time that is controlled by carrier scattering processes and might limit the ability to produce shorter pulses.[44]

Table 9.6 Wavelength diversification of mode-locked SDLs outside 0.9–1.1 μm

λ (nm)	Pulse duration (ps)	Rep. rate (GHz)	Average power (mW)	Gain QW/ substrate	SESAM QW/ substrate	Reference
1518	6.5	1.34	14	InGaAsP/InP	InGaAs/InP	183
1554	3.2	2.97	120	InGaAsP/InP	GaInNAs/GaAs	184
1570	13	1.29	600	AlInGaAs/InP	GaInNAs/GaAs	185
1560	1.7	2.02	15	AlInGaAs/InP	GaInNAs/GaAs	186
1308	18.7	6.1	57	GaInNAs/GaAs	GaInNAs/GaAs	187
1300	6.4	0.91	100	AlInGaAs/InP	GaInNAs/GaAs	188
1220	5	0.84	275	GaInNAs/GaAs	GaInNAs/GaAs	189
832	15.2	1.9	5	GaAs/GaAs	GaAs/GaAs	190
1950	1.1	0.88	25	InGaSb/GaSb	InGaSb/GaSb	191
1950	0.384	0.89	25	InGaSb/GaSb	InGaSb/GaSb	192

Another strand of investigation in passively mode-locked SDLs has been dedicated to exploiting the short carrier lifetime in semiconductors (as compared to doped-dielectric media) and associated resilience to Q-switching to generate ultrashort pulses at high repetition rates. The most impressive result in this area is the demonstration of 3.3 ps pulses from a laser with a 3-mm-long V-type cavity, that is, a fundamental repetition frequency of 50 GHz.[45] Looking at the reported performance from a pulse energy point of view, the recorded results demonstrated emission of 0.5 nJ pulses from a system with separate gain and absorber,[179] and up to 2.5 nJ from an integrated version,[180] somewhat compromised by the propensity to observe multi-pulse or harmonic mode-locked behaviour when over-saturating the SESAM.[44,178,181,182]

Most of these developments to date have been made at a wavelength of operation of ~1 μm since, as explained in Section 9.2.2, this corresponds to a 'sweet spot' in terms of semiconductor growth and laser performance. However, as shown in Table 9.6,[183–192] strides at longer wavelengths are being made, afforded by recent material developments and efficient thermal management.

Additionally, an emerging research strand in this field aims at achieving integrated versions of mode-locked SDLs, also referred to as mode-locked integrated external-cavity surface-emitting lasers (MIXSEL), where the gain and saturable absorber elements are combined in one structure. Key steps have already been made in that direction with the demonstrations that (i) a quantum-dot-based SESAM can saturate before a quantum well gain section even when the laser mode size on both devices is identical thanks to saturation fluence engineering,[193] and that (ii) an integrated SESAM/gain structure can be successfully made and operated in the mode-locked regime[194] even with truly remarkable performance (6.4 W average power, 28 ps, 2.5 GHz).[180] A natural evolution for this work, as suggested in

Reference 168 is to achieve (quasi-) monolithic wafer-based versions of the MIXSEL exploiting hybrid integration of the plano-concave external cavity in similar ways as those experimentally validated for continuous-wave 'microchip' SDLs.[33,195,196] Furthermore, in the context of miniaturisation, it would be attractive to replace the prevailing optical pumping arrangement with a direct[197] or indirect[198] electrically-injected configuration. To date, all the demonstrated directly electrically-pumped SDLs make use of compound cavities (i.e., including an intracavity partial reflector) which restrict the optical bandwidth and add large dispersion, therefore limiting the achievable minimum pulse duration to the picosecond regime.[171,199,200] A variety of experimental and numerical assessments are under way with the explicit objective of obtaining devices which overcome these limitations while maintaining or even improving beam quality.[201,202]

9.5 Future trends and applications

As highlighted throughout this review, SDLs are low-noise, high-beam-quality sources of intermediate power whose emission wavelength can be designed to suit a particular application through material engineering or intracavity non-linear conversion. As such, they have been proposed and made commercially available to replace bulky and inefficient sources such as argon-ion lasers.[203,204] They have also been introduced as compact and more cost-effective solutions to frequency-doubled doped-dielectric lasers for forensic applications.[205] Frequency down-conversion of SDLs via intracavity-pumped OPOs and Raman lasers are more recent developments, but with significant commercial potential especially when targeting the generation of mid-infrared frequencies.[127,133] Similarly, the proof-of-concept generation of milliwatt-level continuous-wave terahertz radiation by frequency mixing of dual-wavelength SDLs[131] is expected to become an avenue for further research with great industrial potential.

The above-mentioned features also make SDLs particularly attractive for pumping laser systems which require high-brightness pumps. More specifically, SDLs have been successfully used in bulk solid-state lasers with low population-inversion efficiency (low sigma-tau product) such as transition-metal-based systems (Ti:sapphire;[206] Cr:ZnSe[207] lasers) or up-conversion sources.[208] They have also been deployed to power core-pumped fibre amplifiers and lasers exploiting rare-earth[209–211] or Raman gain.[140,212,213]

Furthermore, the amenability of these SDLs to generate tuneable single-frequency radiation with sub-kHz linewidth (see Section 9.3.1) further expands their potential applications to gas spectroscopy and sensing, or in the metrology sector where they can be effectively used as sources for atom cooling and trapping[214] as required in atomic clock referencing/control, or as gyroscopes.[112]

Table 9.7 Further reading list

Title	Lead author	Year	Description	Reference
Design and characteristics of high-power (> 0.5-W CW) diode-pumped vertical-external-cavity surface-emitting semiconductor lasers with circular TEM_{00} beams	Kuznetsov	1999	The first paper to introduce SDL design in the currently recognised format	1
Extended cavity surface-emitting semiconductor lasers	Tropper	2006	Review of SDL design	3
Passively mode-locked surface-emitting semiconductor lasers	Keller	2006	Review of passive mode-locking of SDLs	167
Quantum design of semiconductor active materials: laser and amplifier applications	Moloney	2007	Review of microscopic modelling of SDLs	5
High-brightness long-wavelength semiconductor disk lasers	Schulz	2008	Review of the design and performance of midinfrared SDLs	71
Semiconductor disk lasers for the generation of visible and ultraviolet radiation	Calvez	2009	Review of the design and performance of visible and ultraviolet SDLs via frequency-doubling from the infrared	49
Semiconductor Disk Lasers: Physics and Technology	Okhotnikov (Editor)	2010	SDL textbook	222
Vertical External Cavity Surface Emitting Lasers (VECSELs)	Keller (Editor)	2011	Overview of the field as presented at SPIE Photonics West 2011	221

When operated in pulsed regime, SDLs are bright sources with direct modulation capabilities up to ~100 MHz at fundamental or nonlinearly converted frequencies, which makes them useful for projection/display[122] or sensing applications. Furthermore, and contrary to their doped-dielectric counterparts, these devices are inherently suited to the generation of (multi)-GHz trains of pico-or femto-second pulses which, in turn, could open new fields of application such as excitation sources for multi-photon biomedical imaging,[215] or for time-domain terahertz radiation spectroscopy when used as a trigger for photoconductive emitters/receivers.[216–218] Their intrinsically-limited capability to generate high-energy pulses can be somewhat compensated by special pulsing schemes including cavity-dumping or by using them as seed lasers for (fibre) master-oscillator power amplifier systems[219] for wavelengths where such amplification technology exists.

SDLs have essentially emerged over the past decade as diode-pumped solid-state lasers with epitaxially-grown semiconductor gain elements – in effect a 'solid-state dye laser' technology. Interestingly, the drive for high-power and tuneable operation has meant that the development of electrical-injected devices as traditionally associated with semiconductor lasers has not received as much attention as other aspects. Nevertheless, as explained in Section 9.4.3, interest in directly electrically-driven devices has recently re-emerged, since they are perceived to offer a more practical avenue for high repetition-rate (10 s GHz) pulsed SDLs or as alternative green sources for mobile projection/display should GaN-based green laser diodes not be mature enough at the time of general release. Another interesting development is the substitution of the semiconductor element by an organic-based gain section, providing a more direct route for visible and ultraviolet emission with lower manufacturing costs, albeit with compromises in performance.[157,220]

9.6 Sources of further information and advice

This chapter serves as a broad overview of the semiconductor disk laser field; however, readers who wish to study the design, performance, and application of these lasers in greater depth should consult Table 9.7 for further reading. The field is expanding rapidly with an increasing number of contributing research groups, as evidenced by the introduction, in January 2011, of an annual conference dedicated to these lasers at the international meeting SPIE Photonics West.[221]

9.7 References

1. M. Kuznetsov, F. Hakimi, R. Sprague, and A. Mooradian, 'Design and characteristics of high-power (> 0.5-W CW) diode- pumped vertical-external-cavity surface-emitting semiconductor lasers with circular TEM_{00} beams', *IEEE J. Sel. Top. Quantum Electron.* **5**, 561–573 (1999).
2. M. Kuznetsov, F. Hakimi, R. Sprague, and A. Mooradian, 'High-power (>0.5-W CW) diode-pumped vertical-external-cavity surface-emitting semiconductor lasers with circular TEM_{00} beams', *IEEE Photon. Tech. Lett.* **9**, 1063–1065 (1997).

3. A. C. Tropper and S. Hoogland, 'Extended cavity surface-emitting semiconductor lasers', *Prog. Quantum Electron.* **30**, 1–43 (2006).
4. A. Garnache, A. A. Kachanov, F. Stoeckel, and R. Houdré, 'Diode-pumped broadband vertical-external-cavity surface-emitting semiconductor laser applied to high-sensitivity intracavity absorption spectroscopy', *J. Opt. Soc. Am. B* **17**, 1589–1598 (2000).
5. J. V. Moloney, J. Hader, and S. W. Koch, 'Quantum design of semiconductor active materials: laser and amplifier applications', *Laser Photonics Rev.* **1**, 24–43 (2007).
6. J. Hader, G. Hardesty, T.-L. Wang, J. M. Yarborough, Y. Kaneda, J. V. Moloney, B. Kunert, W. Stolz, and S. W. Koch, 'Predictive microscopic modeling of VECSELs', *IEEE J. Quantum Electron.* **46**, 810–817 (2010).
7. T.-C. Lu, J.-R. Chen, S.-W. Chen, H.-C. Kuo, C.-C. Kuo, C.-C. Lee, and S.-C. Wang, 'Development of GaN-based vertical-cavity surface-emitting lasers', *IEEE J. Sel. Top. Quantum Electron.* **15**, 850–860 (2009).
8. S.-H. Park, J. Kim, H. Jeon, T. Sakong, S.-N. Lee, S. Chae, Y. Park, C.-H. Jeong, G.-Y. Yeom, and Y.-H. Cho, 'Room-temperature GaN vertical-cavity surface-emitting laser operation in an extended cavity scheme', *Appl. Phys. Lett.* **83**, 2121–2123 (2003).
9. R. Debusmann, N. Dhidah, V. Hoffmann, L. Weixelbaum, U. Brauch, T. Graf, M. Weyers, and M. Kneissl, 'InGaN-GaN disk laser for blue-violet emission wavelengths', *IEEE Photon. Tech. Lett.* **22**, 652–654 (2010).
10. R. Häring, R. Paschotta, A. Aschwanden, E. Gini, F. Morier-Genoud, and U. Keller, 'High-power passively mode-locked semiconductor lasers', *IEEE J. Quantum Electron.* **38**, 1268–1275 (2002).
11. T. Leinonen, Y. A. Morozov, A. Härkönen, and M. Pessa, 'Vertical external-cavity surface-emitting laser for dual-wavelength generation', *IEEE Photon. Tech. Lett.* **17**, 2508–2510 (2005).
12. J. Rautiainen, J. Lyytikäinen, A. Sirbu, A. Mereuta, A. Caliman, E. Kapon, and O. Okhotnikov, '2.6 W optically-pumped semiconductor disk laser operating at 1.57-mm using wafer fusion', *Opt. Express* **16**, 21881–21886 (2008).
13. M. Fill, A. Khiar, M. Rahim, F. Felder, and H. Zogg, 'PbSe quantum well mid-infrared vertical external cavity surface emitting laser on Si-substrates', *J. Appl. Phys.* **109**, 093101 (2011).
14. D. I. Babic and S. W. Corzine, 'Analytic expressions for the reflection delay, penetration depth, and absorptance of quarter-wave dielectric mirrors', *IEEE J. Quantum Electron.* **28**, 514–524 (1992).
15. S. Calvez, D. Burns, and M. D. Dawson, 'Optimization of an optically pumped 1.3-mm GaInNAs vertical-cavity surface-emitting laser', *IEEE Photon. Tech. Lett.* **14**, 131–133 (2002).
16. K. S. Kim, J. R. Yoo, S. M. Lee, S. J. Lim, J. Y. Kim, J. H. Lee, S. H. Cho, T. Kim, and Y. J. Park, 'Highly efficient InGaAs QW vertical external cavity surface emitting lasers emitting at 1060 nm', *J. Cryst. Growth* **287**, 629–632 (2006).
17. T. D. Germann, A. Strittmatter, J. Pohl, U. W. Pohl, D. Bimberg, J. Rautiainen, M. Guina, and O. Okhotnikov, 'Quantum-dot semiconductor disk lasers', *J. Cryst. Growth* **310**, 5182–5186 (2008).
18. M. Y. A. Raja, S. R. J. Brueck, M. Osinski, C. F. Schaus, J. G. McInerney, T. M. Brennan, and B. E. Hammons, 'Resonant periodic gain surface-emitting semiconductor-lasers', *IEEE J. Quantum Electron.* **25**, 1500–1512 (1989).

19. M. A. Holm, A. I. Ferguson, D. Burns, and M. D. Dawson, 'Actively stabilized single-frequency vertical-external-cavity AlGaAs laser', *IEEE Photon. Tech. Lett.* **11**, 1551–1553 (1999).
20. J. Geske, K. G. Gan, Y. L. Okuno, J. Piprek, and J. E. Bowers, 'Vertical-cavity surface-emitting laser active regions for enhanced performance with optical pumping', *IEEE J. Quantum Electron.* **40**, 1155–1162 (2004).
21. A. Smith, J. E. Hastie, H. D. Foreman, T. Leinonen, M. Guina, and M. D. Dawson, 'GaN diode-pumping of a red semiconductor disk laser', *Electron. Lett.* **44**, 1195–1196 (2008).
22. W. J. Alford, T. D. Raymond, and A. A. Allerman, 'High power and good beam quality at 980nm from a vertical external-cavity surface-emitting laser', *J. Opt. Soc. Am. B* **19**, 663–666 (2002).
23. A. J. Kemp, G. J. Valentine, J. M. Hopkins, J. E. Hastie, S. A. Smith, S. Calvez, M. D. Dawson, and D. Burns, 'Thermal management in vertical-external-cavity surface-emitting lasers: finite-element analysis of a heatspreader approach', *IEEE J. Quantum Electron.* **41**, 148–155 (2005).
24. A. J. Maclean, R. B. Birch, P. W. Roth, A. J. Kemp, and D. Burns, 'Limits on efficiency and power scaling in semiconductor disk lasers with diamond heatspreaders', *J. Opt. Soc. Am. B* **26**, 2228–2236 (2009).
25. J. E. Hastie, J. M. Hopkins, S. Calvez, C. W. Jeon, D. Burns, R. Abram, E. Riis, A. I. Ferguson, and M. D. Dawson, '0.5-W single transverse-mode operation of an 850-nm diode-pumped surface-emitting semiconductor laser', *IEEE Photon. Tech. Lett.* **15**, 894–896 (2003).
26. H. Lindberg, M. Strassner, J. Bengtsson, and A. Larsson, 'High-power optically pumped 1550-nm VECSEL with a bonded silicon heat spreader', *IEEE Photon. Tech. Lett.* **16**, 1233–1235 (2004).
27. S. A. Smith, J. M. Hopkins, J. E. Hastie, S. Calvez, A. J. Kemp, D. Burns, and M. D. Dawson, 'A diamond-microchip GaInNAs VECSEL operating at 1315nm', *2004 IEEE LEOS Annual Meeting Conference Proceedings* **1–2**, 330–331 (2004).
28. Z. L. Liau, 'Semiconductor wafer bonding via liquid capillarity', *Appl. Phys. Lett.* **77**, 651–653 (2000).
29. J. H. Lee, J. Y. Kim, S. M. Lee, J. R. Yoo, K. S. Kim, S. H. Cho, S. J. Lim, G. B. Kim, S. M. Hwang, T. Kim, and Y. J. Park, '9.1-W high-efficient continuous-wave end-pumped vertical-external-cavity surface-emitting semiconductor laser', *IEEE Photon. Tech. Lett.* **18**, 2117–2119 (2006).
30. S. Cho, G. B. Kim, J. Y. Kim, K. S. Kim, S. M. Lee, J. Yoo, T. Kim, and Y. Park, 'Compact and efficient green VECSEL based on novel optical end-pumping scheme', *IEEE Photon. Tech. Lett.* **19**, 1325–1327 (2007).
31. S. S. Beyertt, M. Zorn, T. Kubler, H. Wenzel, M. Weyers, A. Giesen, G. Trankle, and U. Brauch, 'Optical in-well pumping of a semiconductor disk laser with high optical efficiency', *IEEE J. Quantum Electron.* **41**, 1439–1449 (2005).
32. J. E. Hastie, J. M. Hopkins, C. W. Jeon, S. Calvez, D. Burns, M. D. Dawson, R. Abram, E. Riis, A. I. Ferguson, W. J. Alford, T. D. Raymond, and A. A. Allerman, 'Microchip vertical external cavity surface emitting lasers', *Electron. Lett.* **39**, 1324–1326 (2003).
33. N. Laurand, C. L. Lee, E. Gu, J. E. Hastie, S. Calvez, and M. D. Dawson, 'Microlensed microchip VECSEL', *Opt. Express* **15**, 9341–9346 (2007).

34. L. E. Hunziker, C. Ihli, and D. S. Steingrube, 'Miniaturization and power scaling of fundamental mode optically pumped semiconductor lasers', *IEEE J. Sel. Top. Quantum Electron.* **13**, 610–618 (2007).
35. B. Rudin, A. Rutz, M. Hoffmann, D. J. H. C. Maas, A.-R. Bellancourt, E. Gini, T. Südmeyer, and U. Keller, 'Highly efficient optically pumped vertical-emitting semiconductor laser with more than 20W average output power in a fundamental transverse mode', *Opt. Lett.* **33**, 2719–2721 (2008).
36. A. L. Bloom, 'Modes of a laser resonator containing tilted birefringent plates', *J. Opt. Soc. Am.* **64**, 447–452 (1974).
37. N. Schulz, M. Rattunde, C. Ritzenthaler, B. Rösener, C. Manz, K. Köhler, and J. Wagner, 'Effect of the cavity resonance-gain offset on the output power characteristics of GaSb-based VECSELs', *IEEE Photon. Tech. Lett.* **19**, 1741–1743 (2007).
38. A. J. Kemp, A. J. Maclean, J. E. Hastie, J. M. Hopkins, S. Calvez, G. J. Valentine, M. D. Dawson, and D. Burns, 'Thermal lensing, thermal management and transverse mode control in microchip VECSELs', *Appl. Phys. B* **83**, 189–194 (2006).
39. N. Hempler, J. M. Hopkins, A. J. Kemp, N. Schulz, M. Rattunde, J. Wagner, M. D. Dawson, and D. Burns, 'Pulsed pumping of semiconductor disk lasers', *Opt. Express* **15**, 3247–3256 (2007).
40. L. E. Hunziker, Q.-Z. Shu, D. Bauer, C. Ilhi, G. J. Mahnke, M. Rebut, J. Chilla, A. L. Caprara, H. Zhou, E. S. Weiss, and M. K. Reed, 'Power-scaling of optically-pumped semiconductor lasers', *Proc. SPIE* **6451**, 64510A (2007).
41. S. Lutgen, T. Albrecht, P. Brick, W. Reill, J. Luft, and W. Späth, '8-W high-efficiency continuous-wave semiconductor disk laser at 1000nm', *Appl. Phys. Lett.* **82**, 3620–3622 (2003).
42. F. Demaria, S. Lorch, S. Menzel, M. Riedl, F. Rinaldi, R. Rösch, and P. Unger, 'Design of highly efficient high-power optically pumped semiconductor disk lasers', *IEEE J. Sel. Top. Quantum Electron.* **15**, 973–977 (2009).
43. R. H. Abram, K. S. Gardner, E. Riis, and A. I. Ferguson, 'Narrow linewidth operation of a tunable optically pumped semiconductor laser', *Opt. Express* **12**, 5434–5439 (2004).
44. A. H. Quarterman, K. G. Wilcox, V. Apostolopoulos, Z. Mihoubi, S. P. Elsmere, I. Farrer, D. A. Ritchie, and A. C. Tropper, 'A passively mode-locked external-cavity semiconductor laser emitting 60-fs pulses', *Nat. Photonics* **3**, 729–731 (2009).
45. D. Lorenser, D. J. H. C. Maas, H. J. Unold, A.-R. Bellancourt, B. Rudin, E. Gini, D. Ebling, and U. Keller, '50-GHz passively mode-locked surface-emitting semiconductor laser with 100-mW average output power', *IEEE J. Quantum Electron.* **42**, 838–847 (2006).
46. S.-H. Park and H. Jeon, 'Microchip-type InGaN vertical external-cavity surface-emitting laser', *Opt. Rev.* **13**, 20–23 (2006).
47. M. I. Müller, C. Karnutsch, J. Luft, W. Schmid, K. Streubel, N. Linder, S. S. Beyertt, U. Brauch, A. Giesen, and G. H. Döhler, 'Optically pumped vertical external cavity semiconductor thin-disk laser with CW operation at 660nm', *Inst. Phys. Conf. Ser. No* **174**, 427–430 (2002).
48. J. E. Hastie, S. Calvez, M. D. Dawson, T. Leinonen, A. Laakso, J. Lyytikäinen, and M. Pessa, 'High power CW red VECSEL with linearly polarized TEM_{00} output beam', *Opt. Express* **13**, 77–81 (2005).

49. S. Calvez, J. E. Hastie, M. Guina, O. Okhotnikov, and M. D. Dawson, ‘Semiconductor disk lasers for the generation of visible and ultraviolet radiation’, *Laser Photonics Rev*. **3**, 407–434 (2009).
50. P. J. Schlosser, J. E. Hastie, S. Calvez, A. B. Krysa, and M. D. Dawson, ‘InP/AlGaInP quantum dot semiconductor disk lasers for CW TEM00 emission at 716–755 nm’, *Opt. Express* **17**, 21782–21787 (2009).
51. M. A. Holm, D. Burns, P. Cusumano, A. I. Ferguson, and M. D. Dawson, ‘High-power diode-pumped AlGaAs surface-emitting laser’, *Appl. Opt*. **38**, 5781–5784 (1999).
52. B. Cocquelin, D. Holleville, G. Lucas-Leclin, I. Sagnes, A. Garnache, M. Myara, and P. Georges, ‘Tunable single-frequency operation of a diode-pumped vertical external-cavity laser at the cesium D2 line’, *Appl. Phys. B* **95**, 315–321 (2009).
53. S. S. Beyertt, U. Brauch, F. Demaria, N. Dhidah, A. Giesen, T. Kübler, S. Lorch, F. Rinaldi, and P. Unger, ‘Efficient gallium-arsenide disk laser’, *IEEE J. Quantum Electron*. **43**, 869–875 (2007).
54. S. McGinily, R. Abram, K. S. Gardner, E. Riis, A. I. Ferguson, and J. S. Roberts, ‘Novel gain medium design for short-wavelength vertical-external-cavity surface-emitting laser’, *IEEE J. Quantum Electron*. **43**, 445–450 (2007).
55. J. L. Chilla, S. D. Butterworth, A. Zeitschel, J. P. Charles, A. L. Caprara, M. K. Reed, and L. Spinelli, ‘High power optically pumped semiconductor lasers’, *Proc. SPIE* **5332**, 143–150 (2004).
56. K. S. Kim, J. Yoo, G. Kim, S. Lee, S. Cho, J. Kim, T. Kim, and Y. Park, ‘920-nm vertical-external-cavity surface-emitting lasers with a slope efficiency of 58% at room temperature’, *IEEE Photon. Tech. Lett*. **19**, 1655–1657 (2007).
57. L. Fan, C. Hessenius, M. Fallahi, J. Hader, H. Li, J. V. Moloney, W. Stolz, S. W. Koch, J. T. Murray, and R. Bedford, ‘Highly strained InGaAs/GaAs multiwatt vertical-external-cavity surface-emitting laser emitting around 1170 nm’, *Appl. Phys. Lett*. **91**, 131114 (2007).
58. J. A. Lott, A. R. Kovsh, N. N. Ledentsov, and D. Bimberg, ‘GaAs-based InAs/InGaAs quantum dot vertical cavity and vertical external cavity surface emitting lasers emitting near 1300 nm’, *Conference on Lasers and Electro-Optics 2006*, CTuJ2–2 (2006).
59. A. R. Albrecht, T. J. Rotter, C. P. Hains, A. Stintz, J. V. Moloney, K. J. Malloy, and G. Balakrishnan, ‘Multi-Watt 1.25 mm quantum dot VECSEL’, *Electron. Lett*. **46** (2010).
60. M. Butkus, K. G. Wilcox, J. Rautiainen, O. Okhotnikov, S. S. Mikhrin, I. L. Krestnikov, A. R. Kovsh, M. Hoffmann, T. Südmeyer, U. Keller, and E. U. Rafailov, ‘High-power quantum-dot-based semiconductor disk laser’, *Opt. Lett*. **34**, 1672–1674 (2009).
61. J. M. Hopkins, S. A. Smith, C. W. Jeon, D. Burns, S. Calvez, M. D. Dawson, T. Jouhti, and M. Pessa, ‘A 0.6W CW GaInNAs vertical external-cavity surface-emitting laser operating at 1.32mm’, *Electron. Lett*. **40**, 30–31 (2004).
62. S. L. Vetter, J. E. Hastie, V.-M. Korpijarvi, J. Puustinen, M. Guina, O. Okhotnikov, S. Calvez, and M. D. Dawson, ‘Short-wavelength GaInNAs/GaAs semiconductor disk lasers’, *Electron. Lett*. **44**, 1069–1070 (2008).
63. V.-M. Korpijärvi, M. Guina, J. Puustinen, P. Tuomisto, J. Rautiainen, A. Härkönen, A. Tukiainen, O. Okhotnikov, and M. Pessa, ‘MBE grown GaInNAs-based multi-Watt disk lasers’, *J. Cryst. Growth* **311**, 1868–1871 (2009).

64. V.-M. Korpijärvi, T. Leinonen, J. Puustinen, A. Härkönen, and M. Guina, '11 W single gain-chip dilute nitride disk laser emitting around 1180 nm', *Opt. Express* **18**, 25633–25641 (2010).
65. A. Rantamäki, A. Sirbu, A. Mereuta, E. Kapon, and O. G. Okhotnikov, '3 W of 650 nm red emission by frequency doubling of wafer-fused semiconductor disk laser', *Opt. Express* **18**, 21645–21650 (2010).
66. C. Symonds, I. Sagnes, A. Garnache, S. Hoogland, G. Saint-Girons, A. C. Tropper, and J.-L. Oudar, 'Continuous-wave operation of monolithically grown 1.5-mm optically pumped vertical-external-cavity surface-emitting lasers', *Appl. Opt.* **42**, 6678–6681 (2003).
67. H. Lindberg, M. Strassner, E. Gerster, and A. Larsson, '0.8 W optically pumped vertical external cavity surface emitting laser operating CW at 1550 nm', *Electron. Lett.* **40**, 601–602 (2004).
68. H. Lindberg, M. Strassner, E. Gerster, J. Bengtsson, and A. Larsson, 'Thermal management of optically pumped long-wavelength InP-based semiconductor disk lasers', *IEEE J. Sel. Top. Quantum Electron.* **11**, 1126–1 (2005).
69. H. Lindberg, A. Larsson, and M. Strassner, 'Single-frequency operation of a high-power, long-wavelength semiconductor disk laser', *Opt. Lett.* **30**, 2260–2262 (2005).
70. J. M. Hopkins, A. J. Maclean, D. Burns, E. Riis, N. Schulz, M. Rattunde, C. Manz, K. Köhler, and J. Wagner, 'Tunable, single-frequency, diode-pumped 2.3mm VECSEL', *Opt. Express* **15**, 8212–8217 (2007).
71. N. Schulz, J.-M. Hopkins, M. Rattunde, D. Burns, and J. Wagner, 'High-brightness long-wavelength semiconductor disk lasers', *Laser Photon. Rev.* **2**, 160–181 (2008).
72. B. Rösener, M. Rattunde, M. Moser, S. Kaspar, T. Töpper, C. Manz, K. Köhler, and J. Wagner, 'Continuous-wave room-temperature operation of a 2.8 mm GaSb-based semiconductor disk laser', *Opt. Lett.* **36**, 319–321 (2011).
73. M. Rahim, M. Arnold, F. Felder, K. Behfar, and H. Zogg, 'Midinfrared lead-chalcogenide vertical external cavity surface emitting laser with 5mm wavelength', *Appl. Phys. Lett.* **91**, 151102 (2007).
74. M. Rahim, A. Khiar, F. Felder, M. Fill, and H. Zogg, '4.5 mm wavelength vertical external cavity surface emitting laser operating above room temperature', *Appl. Phys. Lett.* **94**, 201112 (2009).
75. A. Khiar, M. Rahim, M. Fill, F. Felder, F. Hobrecker, and H. Zogg, 'Continuously tunable monomode mid-infrared vertical external cavity surface emitting laser on Si', *Appl. Phys. Lett.* **97**, 151104 (2010).
76. M. Rahim, M. Fill, F. Felder, D. Chappuis, M. Corda, and H. Zogg, 'Mid-infrared PbTe vertical external cavity surface emitting laser on Si-substrate with above 1 W output power', *Appl. Phys. Lett.* **95**, 241107 (2009).
77. M. Rahim, A. Khiar, F. Felder, M. Fill, H. Zogg, and M. W. Sigrist, '5-mm vertical external-cavity surface-emitting laser (VECSEL) for spectroscopic applications', *Appl. Phys. B* **100**, 261–264 (2010).
78. D. Bimberg, N. Kirstaedter, N. N. Ledentsov, Zh. I. Alferov, P. S. Kop'ev, and V. M. Ustinov, 'InGaAs-GaAs quantum-dot lasers', *IEEE J. Sel. Top. Quantum Electron.* **3**, 196–205 (1997).
79. T. D. Germann, A. Strittmatter, J. Pohl, U. W. Pohl, D. Bimberg, J. Rautiainen, M. Guina, and O. Okhotnikov, 'Temperature-stable operation of a quantum dot semiconductor disk laser', *Appl. Phys. Lett.* **93**, 051104 (2008).

80. M. Hoffmann, O. D. Sieber, W. P. Pallmann, V. J. Wittwer, I. L. Krestnikov, S. S. Mikhrin, D. A. Livshits, G. Malcolm, C. Hamilton, Y. Barbarin, T. Südmeyer, and U. Keller, ‘All quantum-dot based femtosecond VECSEL’, *Proc. SPIE* **7919**, 79190X (2011).
81. D. P. Bour, R. S. Geels, D. W. Treat, T. L. Paoli, F. Ponce, R. L. Thornton, B. S. Krusor, R. D. Bringans, and D. F. Welch, ‘Strained $Ga_xIn_{1-x}P/(AlGa)_{0.5}In_{0.5}P$ heterostructure and quantum-well laser diodes’, *IEEE J. Quantum Electron*. **30**, 593–607 (1994).
82. M. D. Dawson and G. Duggan, ‘Band-offset determination for GaInP-AlGaInP structures with compressively strained quantum well active layers’, *Appl. Phys. Lett*. **64**, 892–894 (1994).
83. E. Yablonovitch and E. O. Kane, ‘Reduction of lasing threshold current density by the lowering of valence band effective mass’, *J. Lightwave Technol*. **LT-4**, 504–506 (1986).
84. J. E. Hastie, L. G. Morton, A. J. Kemp, M. D. Dawson, A. B. Krysa, and J. S. Roberts, “Tunable ultraviolet output from an intra-cavity frequency-doubled red vertical-external-cavity surface-emitting laser,” *Appl. Phys. Lett*. **89**, 061114 (2006).
85. A. B. Krysa, S. L. Liew, J. C. Lin, J. S. Roberts, J. Lutti, G. M. Lewis, and P. M. Smowton, ‘Low threshold InP/AlGaInP on GaAs QD laser emitting at ~740 nm’, *J. Cryst. Growth* **298**, 663–666 (2007).
86. J. Lyytikäinen, J. Rautiainen, L. Toikkanen, A. Sirbu, A. Mereuta, A. Caliman, E. Kapon, and O. G. Okhotnikov, ‘1.3-mm optically-pumped semiconductor disk laser by wafer fusion’, *Opt. Express* **17**, 9047–9052 (2009).
87. T. Schwarzbäck, M. Eichfelder, W.-M. Schulz, R. Roßbach, M. Jetter, and P. Michler, ‘Short wavelength red-emitting AlGaInP-VECSEL exceeds 1.2 W continuous-wave output power’, *Appl. Phys. B* **102**, 789–794 (2011).
88. J. E. Hastie, ‘High power surface emitting semiconductor lasers’, *PhD Thesis, University of Strathclyde* (2004).
89. C. Seaton, Coherent Inc., *Personal communication* (2005).
90. T.-L. Wang, Y. Kaneda, J. M. Yarborough, J. Hader, J. V. Moloney, A. Chernikov, S. Chatterjee, S. W. Koch, B. Kunert, and W. Stolz, ‘High-power optically pumped semiconductor laser at 1040 nm’, *IEEE Photon. Tech. Lett*. **22**, 661–663 (2010).
91. K. S. Kim, J. R. Yoo, S. H. Cho, S. M. Lee, S. J. Lim, J. Y. Kim, and J. H. Lee, ‘1060nm vertical-external-cavity surface-emitting lasers with an optical-to-optical efficiency of 44% at room temperature’, *Appl. Phys. Lett*. **88**, 091107–1–091107–3 (2006).
92. J. Rautiainen, I. L. Krestnikov, J. Nikkinen, and O. G. Okhotnikov, ‘2.5W orange power by frequency conversion from a dual-gain quantum-dot disk laser’, *Opt. Lett*. **35**, 1935–1937 (2010).
93. J. Rautiainen, A. Härkönen, V.-M. Korpijärvi, F. Tuomisto, M. Guina, and O. Okhotnikov, ‘2.7W tunable orange-red GaInNAs semiconductor disk laser’, *Opt. Express* **15**, 18345–18350 (2007).
94. J. Konttinen, A. Härkönen, F. Tuomisto, M. Guina, J. Rautiainen, M. Pessa, and O. Okhotnikov, ‘High-power (>1W) dilute nitride semiconductor disk laser emitting at 1240nm’, *New J. Phys*. **9** 140 (2007).
95. J. Lyytikäinen, J. Rautiainen, A. Sirbu, V. Iakovlev, A. Laakso, S. Ranta, M. Tavast, E. Kapon, and O. G. Okhotnikov, ‘High-power 1.48-mm wafer-fused

optically pumped semiconductor disk laser', *IEEE Photon. Tech. Lett.* **23**, 917–919 (2011).

96. J. Rautiainen, L. Toikkanen, J. Lyytikäinen, A. Sirbu, A. Mereuta, A. Caliman, E. Kapon, and O. G. Okhotnikov, 'Wafer fused optically-pumped semiconductor disk laser operating at 1220- nm', *European Conference on Lasers and Electro-Optics 2009* (2009).
97. D. Burns, J.-M. Hopkins, A. J. Kemp, B. Rösener, N. Schulz, C. Manz, K. Köhler, M. Rattunde, and J. Wagner, 'Recent developments in high-power, short-wave mid-infrared semiconductor disk lasers', *Proc. SPIE* **7193**, 719311 (2009).
98. J. M. Hopkins, R. D. Preston, A. J. Maclean, S. Calvez, H. Sun, J. Ng, M. Steer, M. Hopkinson, and D. Burns, 'High performance 2.2mm optically-pumped vertical external-cavity surface emitting laser', *J. Mod. Opt.* **54**, 1677–1683 (2007).
99. J. Nikkinen, J. Paajaste, R. Koskinen, S. Suomalainen, and O. G. Okhotnikov, "GaSb-based semiconductor disk laser with 130-nm tuning range at 2.5 mm," *IEEE Photon. Tech. Lett.* **23**, 777–779 (2011).
100. A. L. Schawlow and C. H. Townes, 'Infrared and optical masers', *Phys. Rev*. **112**, 1940–1949 (1958).
101. A. Ouvrard, A. Garnache, L. Cerutti, F. Genty, and D. Romanini, 'Single-frequency tunable Sb-based VCSELs emitting at 2.3 mm', *IEEE Photon. Tech. Lett.* **17**, 2020–2022 (2005).
102. S. Giet, H. D. Sun, S. Calvez, M. D. Dawson, S. Suomalainen, A. Härkönen, M. Guina, O. Okhotnikov, and M. Pessa, 'Spectral narrowing and locking of a vertical-external-cavity surface-emitting laser using an intracavity volume Bragg grating', *IEEE Photon. Tech. Lett.* **18**, 1786–1788 (2006).
103. S. Giet, C.-L. Lee, S. Calvez, M. D. Dawson, N. Destouches, J. C. Pommier, and O. Parriaux, 'Stabilization of a semiconductor disk laser using an intra-cavity high reflectivity grating', *Opt. Express* **15**, 16520–16526 (2007).
104. J. Paul, Y. Kaneda, T.-L. Wang, C. Lytle, J. V. Moloney, and R. J. Jones, 'Doppler-free spectroscopy of mercury at 253.7 nm using a high-power, frequency-quadrupled, optically pumped external-cavity semiconductor laser', *Opt. Lett.* **36**, 61–63 (2011).
105. 'Coherent launches Sapphire SF', *Coherent Ltd. Press Release* **20th April** (2011).
106. M. Jacquemet, M. Domenech, G. Lucas-Leclin, P. Georges, J. Dion, M. Strassner, I. Sagnes, and A. Garnache, 'Single-frequency cw vertical external cavity surface emitting semiconductor laser at 1003nm and 501nm by intracavity frequency doubling', *Appl. Phys. B* **86**, 510 (2007).
107. L. G. Morton, H. D. Foreman, J. E. Hastie, M. D. Dawson, and E. Riis, 'Actively stabilised single-frequency red VECSEL', *Advanced Solid State Photonics Conference 2007*, Paper WB7 (2006).
108. K. S. Gardner, R. H. Abram, and E. Riis, 'A birefringent etalon as single-mode selector in a laser cavity', *Opt. Express* **12**, 2365–2370 (2004).
109. A. Laurain, M. Myara, G. Beaudoin, I. Sagnes, and A. Garnache, 'Multiwatt-power highly-coherent compact single-frequency tunable Vertical-External-Cavity-Surface-Emitting-Semiconductor-Laser', *Opt. Express* **18**, 14627–14636 (2010).
110. D. R. Preuss and J. L. Gole, 'Three-stage birefringent filter tuning smoothly over the visible region: theoretical treatment and experimental design', *Appl. Opt.* **19**, 702–710 (1980).

111. G. Baili, F. Bretenaker, M. Alouini, L. Morvan, D. Dolfi, and I. Sagnes, ‘Experimental investigation and analytical modeling of excess intensity noise in semiconductor class-A lasers’, *J. Lightwave Technol.* **26**, 952–961 (2008).
112. A. Mignot, G. Feugnet, S. Schwartz, I. Sagnes, A. Garnache, C. Fabre, and J.-P. Pocholle, ‘Single-frequency external-cavity semiconductor ring-laser gyroscope’, *Opt. Lett.* **34**, 97–99 (2009).
113. G. Baili, M. Alouini, T. Malherbe, D. Dolfi, I. Sagnes, and F. Bretenaker, ‘Direct observation of the class-B to class-A transition in the dynamical behavior of a semiconductor laser’, *Europhys. Letters* **87**, 44005 (2009).
114. A. Garnache, A. Ouvrard, and D. Romanini, ‘Single-frequency operation of external-cavity VCSELs: non-linear multimode temporal dynamics and quantum limit’, *Opt. Express* **15**, 9403–9417 (2007).
115. J. Alnis, A. Matveev, N. Kolachevsky, Th. Udem, and T. W. Hänsch, ‘Subhertz linewidth diode lasers by stabilization to vibrationally and thermally compensated ultralow-expansion glass Fabry-Pérot cavities’, *Phys. Rev. A* **77**, 053809 (2008).
116. T. Baer, ‘Large-amplitude fluctuations due to longitudinal mode coupling in diode-pumped intracavty-doubled Nd:YAG lasers’, *J. Opt. Soc. Am. B* **3**, 1175–1180 (1986).
117. R. Hartke, V. Baev, K. Seger, O. Back, E. Heumann, G. Huber, M. Kuhnelt, and U. Steegmuller, ‘Experimental study of the output dynamics of intracavity frequency doubled optically pumped semiconductor disk lasers’, *Appl. Phys. Lett.* **92**, 101107 (2008).
118. R. W. Boyd, *Nonlinear Optics*, 3rd ed. Burlington: Elsevier Inc., 2008.
119. M. Fallahi, L. Fan, Y. Kaneda, C. Hessenius, J. Hader, H. Li, J. V. Moloney, B. Kunert, W. Stolz, S. W. Koch, J. T. Murray, and R. Bedford, ‘5-W yellow laser by intracavity frequency doubling of high-power vertical-external-cavity surface-emitting laser’, *IEEE Photon. Tech. Lett.* **20**, 1700–1702 (2008).
120. J. Chilla, Q.-Z. Shu, H. Zhou, E. Weiss, M. Reed, and L. Spinelli, ‘Recent advances in optically pumped semiconductor lasers’, *Proc. SPIE* **6451**, 645109 (2007).
121. A. Härkönen, J. Rautiainen, T. Leinonen, Yu. A. Morozov, L. Orsila, M. Guina, M. Pessa, and O. Okhotnikov, ‘Intracavity sum-frequency generation in dual-wavelength semiconductor disk laser’, *IEEE Photon. Tech. Lett.* **19**, 1550–1552 (2007).
122. J. Chilla, ‘Recent advances in optically pumped semiconductor lasers,” *Conference on Photonic Applications Systems Technologies*, Paper PTuD3 (2008).
123. Y. Kaneda, J. M. Yarborough, L. Li, N. Peyghambarian, L. Fan, C. Hessenius, M. Fallahi, J. Hader, J. V. Moloney, Y. Honda, M. Nishioka, Y. Shimizu, K. Miyazono, H. Shimatani, M. Yoshimura, Y. Mori, Y. Kitaoka, and T. Sasaki, ‘Continuous-wave all-solid-state 244nm deep-ultraviolet laser source by fourth-harmonic generation of an optically pumped semiconductor laser using $CsLiB_6O_{10}$ in an external resonator’, *Opt. Lett.* **33**, 1705–1707 (2008).
124. J. Lee, S. Lee, T. Kim, and Y. Park, ‘7 W high-efficiency continuous-wave green light generation by intracavity frequency doubling of an end-pumped vertical external-cavity surface emitting semiconductor laser’, *Appl. Phys. Lett.* **89**, 241107 (2006).
125. S. Lutgen, M. Kuehnelt, U. Steegmüller, P. Brick, T. Albrecht, W. Reill, J. Luft, B. Kunert, S. Reinhard, K. Volz, and W. Stolz, ‘Green semiconductor disk laser with 0.7W cw output power’, *Proc. SPIE* **5737**, 109–112 (2005).

126. R. Hartke, E. Heumann, G. Huber, M. Kühnelt, and U. Steegmüller, ‘Efficient green generation by intracavity frequency doubling of an optically pumped semiconductor disk laser’, *Appl. Phys. B* **87**, 95–99 (2007).
127. A. Caprara, ‘2 W cw OPO in mid-IR pumped by OPSL laser intra-cavity radiation’, *Proc. SPIE* **7919**, 79190A (2011).
128. M. T. Andersen, P. Schlosser, J. E. Hastie, P. Tidemand-Lichtenberg, M. D. Dawson, and C. Pedersen, ‘Singly-resonant sum-frequency generation of visible light in a semiconductor disk laser’, *Opt. Express* **17**, 6010–6017 (2009).
129. R. Hartke, E. Heumann, and G. Huber, ‘Magnesium-oxide doped PPLN for intracavity frequency doubling of semiconductor disk lasers’, *Advanced Solid State Photonics Conference, Vancouver*, Paper TuB14 (2007).
130. U. Steegmüller, M. Kühnelt, H. Unold, T. Schwarz, R. Schulz, S. Illek, I. Pietzonka, H. Lindberg, M. Schmitt, and U. Strauss, ‘Green laser modules to fit laser projection out of your pocket’, *Proc. SPIE* **6871** (2008).
131. M. Scheller, J. M. Yarborough, J. V. Moloney, M. Fallahi, M. Koch, and S. W. Koch, ‘Room temperature continuous wave milliwatt terahertz source’, *Opt. Express* **18**, 27112–27117 (2010).
132. D. J. M. Stothard, J.-M. Hopkins, D. Burns, and M. H. Dunn, ‘Stable, continuous-wave, intracavity, optical parametric oscillator pumped by a semiconductor disk laser (VECSEL)’, *Opt. Express* **17**, 10648–10658 (2009).
133. N. Hempler, G. Robertson, L. Bromley, C. Hamilton, and G. Malcolm, ‘Compact, narrow linewidth, continuous-wave, intracavity optical parametric oscillator pumped by a semiconductor disk laser’, *Conference on Lasers and Electro-Optics 2011*, Paper CTuK2 (2011).
134. J. Rautiainen, K. A. Fedorova, J. Nikkinen, D. Eger, V.-M. Korpijärvi, E. U. Rafailov, and O. G. Okhotnikov, ‘1.2-mm semiconductor disk laser frequency doubled with periodically poled lithium tantalate crystal’, *IEEE Photon. Tech. Lett.* **22**, 453–455 (2010).
135. J.-Y. Kim and J. Shim, ‘An analytical model of the intracavity optical second harmonic generation in a vertical-external-cavity surface-emitting laser’, *IEEE J. Quantum Electron.* **44**, 755–762 (2008).
136. J. L. A. Chilla, H. Zhou, E. Weiss, A. L. Caprara, Q. Shou, S. V. Gorvokov, M. K. Reed, and L. Spinelli, ‘Blue and green optically-pumped semiconductor lasers for display’, *Proc. SPIE* **5740**, 41 (2005).
137. S. Hilbich, W. Seelert, V. Ostroumov, C. Kannengiesser, R. v.Elm, J. Mueller, E. Weiss, H. Zhou, and J. Chilla, ‘New wavelengths in the yellow-orange range between 545nm and 580nm generated by an intracavity frequency-doubled optically pumped semiconductor laser’, *Proc. SPIE* **6451**, 64510C (2007).
138. S. B. Morioka, ‘High-power optically pumped semiconductor laser applications’, *Proc. SPIE* **7919**, 791913 (2011).
139. A. S. Bell, M. J. Snadden, D. A. Clubley, C. Ihli, and L. E. Hunziker, “>1W, 244-nm generation by resonant cavity, second-harmonic generation of an optically pumped semiconductor laser,” *Proc. SPIE* **7193**, 51 (2009).
140. S. Calvez, ‘GaInNAs(Sb) for solid-state laser engineering’, *Proceedings of the DILSEM-PHOTON workshop, ICTON, Stockholm, June 2011* (2011).
141. G. Baili, L. Morvan, M. Alouini, D. Dolfi, F. Bretenaker, I. Sagnes, and A. Garnache, ‘Experimental demonstration of a tunable dual-frequency semiconductor laser free of relaxation oscillations’, *Opt. Lett.* **34**, 3421–3423 (2009).

142. V. Pal, P. Trofimoff, B.-X. Miranda, G. Baili, M. Alouini, L. Morvan, D. Dolfi, F. Goldfarb, I. Sagnes, R. Ghosh, and F. Bretenaker, 'Measurement of the coupling constant in a two-frequency VECSEL', *Opt. Express* **18**, 5008–5014 (2010).
143. S. T. Yang, R. C. Eckardt, and R. L. Byer, 'Power and spectral characteristics of continuous-wave parametric oscillators: the doubly to singly resonant transition', *J. Opt. Soc. Am. B* **10**, 1684–1695 (1993).
144. A. A. Demidovich, A. S. Grabtchikov, V. A. Lisinetskii, V. N. Burakevich, V. A. Orlovich, and W. Kiefer, 'Continuous-wave Raman generation in a diode-pumped Nd^{3+}:$KGd(WO_4)_2$ laser', *Opt. Lett.* **30**, 1701–1703 (2005).
145. H. M. Pask, 'Continuous-wave, all-solid-state, intracavity Raman laser', *Opt. Lett.* **30**, 2454–2456 (2005).
146. H. M. Pask, P. Dekker, R. P. Mildren, D. J. Spence, and J. A. Piper, 'Wavelength-versatile visible and UV sources based on crystalline Raman lasers', *Prog. Quantum Electron.* **32**, 121–158 (2008).
147. D. C. Parrotta, W. Lubeigt, A. J. Kemp, D. Burns, M. D. Dawson, and J. E. Hastie, 'Continuous-wave Raman laser pumped within a semiconductor disk laser cavity', *Opt. Lett.* **36**, 1083–1085 (2011).
148. D. C. Parrotta, A. J. Kemp, M. D. Dawson, and J. E. Hastie, 'Tunable continuous-wave diamond Raman laser', *Opt. Express* **19**, 24165–24170 (2011).
149. H. M. Pask, 'The design and operation of solid-state Raman lasers', *Prog. Quantum Electron.* **27**, 3–56 (2003).
150. I. V. Mochalov, 'Laser and nonlinear properties of the potassium gadolinium tungstate laser crystal $KGd(WO_4)_2$:Nd^{3+} (KGW:Nd)', *Opt. Eng.* **36**, 1660–1669 (1997).
151. I. Friel, S. L. Geoghegan, D. J. Twitchen, and G. A. Scarsbrook, 'Development of high quality single crystal diamond for novel laser applications', *Proc. SPIE* **7838**, 783819 (2010).
152. K. W. Su, S. C. Huang, A. Li, S. C. Liu, Y. F. Chen, and K. F. Huang, 'High-peak-power AlGaInAs quantum-well 1.3-mm laser pumped by a diode-pumped actively Q-switched solid-state laser', *Opt. Lett.* **31**, 2009–2011 (2006).
153. S. C. Huang, H. L. Chang, K. W. Su, A. Li, S. C. Liu, Y. F. Chen, and K. F. Huang, 'AlGaInAs/InP eye-safe laser pumped by a Q-switched Nd:$GdVO_4$ laser', *Appl. Phys. B* **94**, 483–487 (2009).
154. H. L. Chang, S. C. Huang, Y.-F. Chen, K. W. Su, Y. F. Chen, and K. F. Huang, 'Efficient high-peak-power AlGaInAs eye-safe wavelength disk laser with optical in-well pumping', *Opt. Express* **17**, 11409–11414 (2009).
155. J. M. Yarborough, Y.-Y. Lai, Y. Kaneda, J. Hader, J. V. Moloney, T. J. Rotter, G. Balakrishnan, C. Hains, D. L. Huffaker, S. W. Koch, and R. Bedford, 'Record pulsed power demonstration of a 2 mm GaSb-based optically pumped semiconductor laser grown lattice-mismatched on an AlAs/GaAs Bragg mirror and substrate', *Appl. Phys. Lett.* **95**, 081112 (2009).
156. Y.-Y. Lai, J. M. Yarborough, Y. Kaneda, J. Hader, J. V. Moloney, T. J. Rotter, G. Balakrishnan, C. Hains, and S. W. Koch, '340-W peak power from a GaSb 2-mm optically pumped semiconductor laser (OPSL) grown mismatched on GaAs', *IEEE Photon. Tech. Lett.* **22**, 1253–1255 (2010).
157. H. Rabbani-Haghighi, S. Forget, S. Chénais, and A. Siove, 'Highly efficient, diffraction-limited laser emission from a vertical external-cavity surface-emitting organic laser', *Opt. Lett.* **35**, 1968–1970 (2010).

158. O. Svelto, ‘Transient laser behaviour’, in D. C. Hanna, ed., *Principles of Lasers,* 5th ed. New York: Springer, 2010, 313–373.
159. V. G. Savitski, J. E. Hastie, S. Calvez, and M. D. Dawson, ‘Cavity-dumping of a semiconductor disk laser for the generation of wavelength-tunable micro-Joule nanosecond pulses’, *Opt. Express* **18**, 11933–11941 (2010).
160. R. S. Putnam, C. B. Roxlo, and M. M. Salour, ‘Optically pumped mode-locked InGaAsP lasers’, *Appl. Phys. Lett.* **40**, 660–662 (1982).
161. W. B. Jiang, S. R. Friberg, H. Iwamura, and Y. Yamamoto, ‘High powers and subpicosecond pulses from an external-cavity surface-emitting InGaAs/InP multiple quantum-well laser’, *Appl. Phys. Lett.* **58**, 807–809 (1991).
162. W. B. Jiang, R. Mirin, and J. E. Bowers, ‘Mode-locked GaAs vertical cavity surface emitting lasers’, *Appl. Phys. Lett.* **60**, 677–679 (1992).
163. W. B. Jiang, D. J. Derickson, and J. E. Bowers, ‘Analysis of laser-pulse chirping in mode-locked vertical-cavity surface-emitting lasers’, *IEEE J. Quantum Electron.* **29**, 1309–1318 (1993).
164. W. Zhang, T. Ackemann, M. Schmid, N. Langford, and A. I. Ferguson, ‘Femtosecond synchronously mode-locked vertical-external cavity surface-emitting laser’, *Opt. Express* **14**, 1810–1821 (2006).
165. W. Zhang, A. McDonald, T. Ackemann, E. Riis, and G. McConnell, ‘Femtosecond synchronously in-well pumped vertical-external-cavity surface-emitting laser’, *Opt. Express* **18**, 187–192 (2010).
166. M. A. Holm, P. Cusumano, D. Burns, A. I. Ferguson, and M. D. Dawson, ‘Mode-locked operation of a diode-pumped, external-cavity GaAs/AlGaAs surface emitting laser’, *Technical Digest of the Conference on Lasers and Electro-Optics* **1999**, 153–154 (1999).
167. U. Keller and A. C. Tropper, ‘Passively modelocked surface-emitting semiconductor lasers’, *Phys. Rep.* **429**, 67–120 (2006).
168. T. Südmeyer, D. J. H. C. Maas, and U. Keller, ‘Mode-locked semiconductor disk lasers’, in *Semiconductor Disk Lasers: Physics and Technology*. O. G. Okhotnikov, Ed. Weinheim: Wiley-VCH, 2010, 213–261.
169. A. Garnache, S. Hoogland, A. C. Tropper, I. Sagnes, G. Saint-Girons, and J. S. Roberts, ‘Sub-500-fs soliton-like pulse in a passively mode-locked broadband surface-emitting laser with 100mW average power’, *Appl. Phys. Lett.* **80**, 3892–3894 (2002).
170. S. Hoogland, S. Dhanjal, A. C. Tropper, J. S. Roberts, R. Häring, R. Paschotta, F. Morier-Genoud, and U. Keller, ‘Passively mode-locked diode-pumped surface-emitting semiconductor laser’, *IEEE Photon. Tech. Lett.* **12**, 1135–1137 (2000).
171. K. Jasim, Q. Zhang, A. V. Nurmikko, E. Ippen, A. Mooradian, G. Carey, and W. Ha, ‘Picosecond pulse generation from passively modelocked vertical cavity diode laser at up to 15 GHz pulse repetition rate’, *Electron. Lett.* **40**, 34–36 (2004).
172. R. Häring, R. Paschotta, E. Gini, F. Morier-Genoud, D. Martin, H. Melchior, and U. Keller, ‘Picosecond surface-emitting semiconductor laser with >200mW average power’, *Electron. Lett.* **37**, 766–767 (2001).
173. S. Hoogland, A. Garnache, I. Sagnes, J. S. Roberts, and A. C. Tropper, ‘10-GHz train of sub-500-fs optical soliton-like pulses from a surface-emitting semiconductor laser’, *IEEE Photon. Tech. Lett.* **17**, 267–269 (2005).
174. F. Saas, G. Steinmeyer, U. Griebner, M. Zorn, and M. Weyers, ‘Exciton resonance tuning for the generation of subpicosecond pulses from a mode-locked semiconductor disk laser’, *Appl. Phys. Lett.* **89**, 141107 (2006).

175. P. Klopp, F. Saas, M. Zorn, M. Weyers, and U. Griebner, '290-fs pulses from a semiconductor disk laser', *Opt. Express* **16**, 5770–5775 (2008).
176. K. G. Wilcox, Z. Mihoubi, G. J. Daniell, S. Elsmere, A. Quarterman, I. Farrer, D. A. Ritchie, and A. C. Tropper, 'Ultrafast optical Stark mode-locked semiconductor laser', *Opt. Lett.* **33**, 2797–2799 (2008).
177. P. Klopp, U. Griebner, M. Zorn, A. Klehr, A. Liero, M. Weyers, and G. Erbert, 'Mode-locked InGaAs-AlGaAs disk laser generating sub-200-fs pulses, pulse picking and amplification by a tapered diode amplifier', *Opt. Express* **17**, 10820–10834 (2009).
178. P. Klopp, U. Griebner, M. Zorn, and M. Weyers, 'Pulse repetition rate up to 92 GHz or pulse duration shorter than 110 fs from a mode-locked semiconductor disk laser', *Appl. Phys. Lett.* **98**, 071103 (2011).
179. A. Aschwanden, D. Lorenser, H. J. Unold, R. Paschotta, E. Gini, and U. Keller, '2.1-W picosecond passively mode-locked external-cavity semiconductor laser', *Opt. Lett.* **30**, 272–274 (2005).
180. B. Rudin, V. J. Wittwer, D. J. H. C. Maas, M. Hoffmann, O. D. Sieber, Y. Barbarin, M. Golling, T. Südmeyer, and U. Keller, 'High-power MIXSEL: an integrated ultrafast semiconductor laser with 6.4 W average power', *Opt. Express* **18**, 27582–27588 (2010).
181. E. J. Saarinen, A. Härkönen, R. Herda, S. Suomalainen, L. Orsila, T. Hakulinen, M. Guina, and O. G. Okhotnikov, 'Harmonically mode-locked VECSELs for multi-GHz pulse train generation', *Opt. Express* **15**, 955–964 (2007).
182. E. J. Saarinen, R. Herda, and O. G. Okhotnikov, 'Dynamics of pulse formation in mode-locked semiconductor disk lasers', *J. Opt. Soc. Am. B* **24**, 2784–2790 (2007).
183. S. Hoogland, A. Garnache, I. Sagnes, B. Paldus, K. J. Weingarten, R. Grange, M. Haiml, R. Paschotta, U. Keller, and A. C. Tropper, 'Picosecond pulse generation with 1.5mm passively modelocked surface-emitting semiconductor laser', *Electron. Lett.* **39**, 846–847 (2003).
184. H. Lindberg, M. Sadeghi, M. Westlund, S. Wang, A. Larsson, M. Strassner, and S. Marcinkevicius, 'Mode locking a 1550 nm semiconductor disk laser by using a GaInNAs saturable absorber', *Opt. Lett.* **30**, 2793–2795 (2005).
185. E. J. Saarinen, J. Puustinen, A. Sirbu, A. Mereuta, A. Caliman, E. Kapon, and O. G. Okhotnikov, 'Power-scalable 1.57 mm mode-locked semiconductor disk laser using wafer fusion', *Opt. Lett.* **34**, 3139–3141 (2009).
186. A. Khadour, S. Bouchoule, G. Aubin, J.-C. Harmand, J. Decobert, and J.-L. Oudar, 'Ultrashort pulse generation from 1.56 mm mode-locked VECSEL at room temperature', *Opt. Express* **18**, 19902–19913 (2010).
187. A. Rutz, V. Liverini, D. J. H. C. Maas, B. Rudin, A.-R. Bellancourt, S. Schön, and U. Keller, 'Passively modelocked GaInNAs VECSEL at centre wavelength around 1.3mm', *Electron. Lett.* **42** (2006).
188. J. Rautiainen, J. Lyytikäinen, L. Toikkanen, J. Nikkinen, A. Sirbu, A. Mereuta, A. Caliman, E. Kapon, and O. G. Okhotnikov, '1.3-mm mode-locked disk laser with wafer fused gain and SESAM structures', *IEEE Photon. Tech. Lett.* **22**, 748–750 (2010).
189. J. Rautiainen, V.-M. Korpijärvi, J. Puustinen, M. Guina, and O. G. Okhotnikov, 'Passively mode-locked GaInNAs disk laser operating at 1220 nm', *Opt. Express* **16**, 15964–15965 (2008).

190. K. G. Wilcox, Z. Mihoubi, S. Elsmere, A. Quarterman, H. D. Foreman, S. Hashimoto, T. Südmeyer, U. Keller, and A. C. Tropper, 'Passively modelocked 832 nm vertical-external-cavity surface-emitting semiconductor laser producing 15.3 ps pulses at 1.9 GHz repetition rate', *Electron. Lett.* **44**, 1469–1470 (2008).
191. A. Härkönen, J. Paajaste, S. Suomalainen, J.-P. Alanko, C. Grebing, R. Koskinen, G. Steinmeyer, and M. Guina, 'Picosecond passively mode-locked GaSb-based semiconductor disk laser operating at 2 mm', *Opt. Lett.* **35**, 4090–4092 (2010).
192. A. Härkönen, C. Grebing, J. Paajaste, R. Koskinen, J.-P. Alanko, S. Suomalainen, G. Steinmeyer, and M. Guina, 'Modelocked GaSb disk laser producing 384 fs pulses at 2 mm wavelength', *Electron. Lett.* **47**, 454–456 (2011).
193. D. Lorenser, H. J. Unold, D. J. H. C. Maas, A. Aschwanden, R. Grange, R. Paschotta, D. Ebling, E. Gini, and U. Keller, 'Towards wafer-scale integration of high repetition rate passively mode-locked surface-emitting semiconductor lasers', *Appl. Phys. B* **79**, 927–932 (2004).
194. D. J. H. C. Maas, A.-R. Bellancourt, B. Rudin, M. Golling, H. J. Unold, T. Südmeyer, and U. Keller, 'Vertical integration of ultrafast semiconductor lasers', *Appl. Phys. B* **88**, 493–497 (2007).
195. R. I. Aldaz, M. W. Wiemer, D. A. B. Miller, and J. S. Harris Jr, 'Monolithically-integrated long vertical cavity surface emitting laser incorporating a concave micromirror on a glass substrate', *Opt. Express* **12**, 3967–3971 (2004).
196. G. A. Keeler, D. K. Serkland, K. M. Geib, G. M. Peake, and A. Mar, 'Single transverse mode operation of electrically pumped vertical-external-cavity surface-emitting lasers with micromirrors', *IEEE Photon. Tech. Lett.* **17**, 522–524 (2005).
197. A. Mooradian, A. Shchegrov, A. Tandon, and G. Yoffe, 'External-cavity surface-emitting diode lasers', in *Semiconductor Disk Lasers: Physics and Technology*. O. G. Okhotnikov, Ed. Weinheim: Wiley-VCH, 2010, 263–304.
198. S. Illek, T. Albrecht, P. Brick, S. Lutgen, I. Pietzonka, M. Furitsch, W. Diehl, J. Luft, and K. Streubel, 'Vertical-external-cavity surface-emitting laser with monolithically integrated pump lasers', *IEEE Photon. Tech. Lett.* **19**, 1952–1954 (2007).
199. K. Jasim, Q. Zhang, A. V. Nurmikko, A. Mooradian, G. Carey, W. Ha, and E. Ippen, 'Passively modelocked vertical extended cavity surface emitting diode laser', *Electron. Lett.* **39**, 373–375 (2003).
200. Q. Zhang, K. Jasim, A. V. Nurmikko, A. Mooradian, G. Carey, W. Ha, and E. Ippen, 'Operation of a passively mode-locked extended-cavity surface-emitting diode laser in multi-GHz regime', *IEEE Photon. Tech. Lett.* **16**, 885–887 (2004).
201. P. Kreuter, B. Witzigmann, D. J. H. C. Maas, Y. Barbarin, T. Südmeyer, and U. Keller, 'On the design of electrically pumped vertical-external-cavity surface-emitting lasers', *Appl. Phys. B* **91**, 257–264 (2008).
202. D. T. D. Childs, J. R. Orchard, D. Williams, C.-C. Lin, B. J. Stevens, J. S. Roberts, and R. A. Hogg, 'Trade-offs in the realization of electrically pumped vertical external cavity surface emitting lasers', *22nd IEEE International Semiconductor Laser Conference* **Paper P12**, 88 (2010).
203. B. Hitz, 'Solid-state lasers are gunning for argon-ion's place', *Photonics Spectra* **37**, 54–58 (2003).

204. E. H. Wahl, B. A. Richman, C. W. Rella, G. M. H. Knippels, and B. A. Paldus, ‘Optical performance comparison of argon-ion and solid-state cyan lasers’, *Opt. Photonics News* **14**, 36–42 (2003).
205. R. Harris, ‘OPSL technology provides new wavelengths that benefit forensics’, *Photonik International* **March**, **2** (2009).
206. B. Resan, E. Coadou, S. Petersen, A. Thomas, P. Walther, R. Viselga, J.-M. Heritier, J. Chilla, W. Tulloch, and A. Fry, ‘Ultrashort pulse Ti:sapphire oscillators pumped by optically pumped semiconductor (OPS) pump lasers’, *Proc. SPIE* **6871**, 687116 (2008).
207. N. Hempler, J.-M. Hopkins, B. Rösener, M. Rattunde, J. Wagner, V. V. Fedorov, I. S. Moskalev, S. B. Mirov, and D. Burns, ‘Semiconductor disk laser pumped Cr^{2+}:ZnSe lasers’, *Opt. Express* **17**, 18136 (2009).
208. E. Heumann, S. Bär, K. Rademaker, G. Huber, S. Butterworth, A. Diening, and W. Seelert, ‘Semiconductor-laser-pumped high-power upconversion laser’, *Appl. Phys. Lett.* **88**, 061108 (2006).
209. G. E. Giudice, S. C. Guy, S. G. Crigler, L. A. Zenteno, and B. S. Hallock, ‘Effect of pump laser noise on an erbium-doped fiber-amplified signal’, *IEEE Photon. Tech. Lett.* **14**, 1403–1405 (2002).
210. L. Fan, M. Fallahi, J. Hader, A. R. Zakharian, M. Kolesik, J. V. Moloney, T. Qiu, A. Schülzgen, N. Peyghambarian, W. Stolz, S. W. Koch, and J. T. Murray, ‘Over 3 W high-efficiency vertical-external-cavity surface-emitting lasers and application as efficient fiber laser pump sources’, *Appl. Phys. Lett.* **86**, 211116 (2005).
211. S. L. Vetter, L. J. McKnight, S. Calvez, M. D. Dawson, F. Fusari, A. A. Lagatsky, W. Sibbett, C. T. A. Brown, V.-M. Korpijärvi, M. Guina, B. Richards, G. Jose, and A. Jha, ‘GaInNAs semiconductor disk lasers as pump sources for Tm^{3+}(,Ho^{3+})-doped glass, crystal and fibre lasers’, *Proc. SPIE* **7193**, 719317 (2009).
212. A. Chamorovskiy, A. Rantamäki, A. Sirbu, A. Mereuta, E. Kapon, and O. G. Okhotnikov, ‘1.38-mm mode-locked Raman fiber laser pumped by semiconductor disk laser’, *Opt. Express* **18**, 23872–23877 (2010).
213. A. Chamorovskiy, J. Rautiainen, A. Rantamäki, and O. G. Okhotnikov, ‘Low-noise Raman fiber amplifier pumped by semiconductor disk laser’, *Opt. Express* **19**, 6141–6146 (2011).
214. B. Cocquelin, G. Lucas-Leclin, P. Georges, I. Sagnes, and A. Garnache, ‘Design of a low-threshold VECSEL emitting at 852 nm for Cesium atomic clocks’, *Opt. Quantum Electron.* **40**, 167–173 (2008).
215. R. Aviles-Espinosa, G. Filippidis, C. Hamilton, G. Malcolm, K. J. Weingarten, T. Südmeyer, Y. Barbarin, U. Keller, S. I. C. O. Santos, D. Artigas, and P. Loza-Alvarez, “Compact ultrafast semiconductor disk laser: targeting GFP based nonlinear applications in living organisms,” *Biomedical Optics Express* **2**, 739–747 (2011).
216. K. G. Wilcox, F. Rutz, R. Wilk, H. D. Foreman, J. S. Roberts, J. Sigmund, H. L. Hartnagel, M. Koch, and A. C. Tropper, ‘Terahertz imaging system based on LT-GaAsSb antenna driven by all-semiconductor femtosecond source’, *Electron. Lett.* **42** (2006).
217. Z. Mihoubi, K. G. Wilcox, S. Elsmere, A. Quarterman, R. Rungsawang, I. Farrer, H. E. Beere, D. A. Ritchie, A. C. Tropper, and V. Apostolopoulos, ‘All-semiconductor room-temperature terahertz time domain spectrometer’, *Opt. Lett.* **33**, 2125–2127 (2008).

218. R. Gebs, P. Klopp, G. Klatt, T. Dekorsy, U. Griebner, and A. Bartels, 'Time-domain terahertz spectroscopy based on asynchronous optical sampling with femtosecond semiconductor disk laser', *Electron. Lett.* **46**, 75–77 (2010).
219. P. Dupriez, C. Finot, A. Malinowski, J. K. Sahu, J. Nilsson, D. J. Richardson, K. G. Wilcox, H. D. Foreman, and A. C. Tropper, 'High-power, high repetition rate picosecond and femtosecond sources based on Yb-doped fiber amplifications of VECSELs', *Opt. Express* **14**, 9611–9616 (2006).
220. S. Forget, H. Rabbani-Haghighi, N. Diffalah, A. Siove, and S. Chénais, 'Tunable ultraviolet vertically-emitting organic laser', *Appl. Phys. Lett.* **98**, 131102 (2011).
221. U. Keller, *Vertical External Cavity Surface Emitting Lasers (VECSELs).* January 2011, San Francisco, California, USA, Proceedings of SPIE Volume 7919, Bellingham, WA: SPIE, 2011.
222. O. Okhotnikov, *Semiconductor Disk Lasers: Physics and Technology.* Weinheim: Wiley-VCH, 2010.

10

Hybrid silicon lasers

D. LIANG and J. E. BOWERS,
University of California, Santa Barbara, USA

DOI: 10.1533/9780857096401.2.394

Abstract: Silicon (Si) lasers have long been a goal for semiconductor scientists. A number of important breakthroughs in the past decade have focused attention on Si as a photonic platform. We first briefly study the fundamentals of carrier transition physics in crystalline Si, followed by the most recent progress in the fields of achieving lasing in Si or materials monolithically grown on Si. The hybrid Si platform, a novel III-V-on-Si hybrid integration approach, and the basics of hybrid lasers are then discussed in detail. Advanced hybrid Si lasers based on grating components and ring resonators are reviewed. Several demonstrated photonic integrated circuits on this hybrid Si platform are discussed, showing future possibilities for hybrid Si lasers to be high-performance light sources for Si photonics.

Key words: Si lasers, diode lasers, photonic integrated circuits, hybrid integration

10.1 Introduction

The photonics market today is shared by several material systems, including compound semiconductors (i.e., indium phosphide (InP) and gallium arsenide (GaAs)), elementary semiconductors (i.e., Si and Ge), silica and rare earth-doped glasses (e.g., glass fiber), and polymers. They target discrete applications or individual components. Today, the volume of silicon photonics is dwarfed by electronics made from silicon or compound semiconductors. The small size of the silicon photonics market is largely due to the problems in making silicon a host material for efficient light emission, and subsequently realizing a laser. Fifty years ago, the birth of the laser started a scientific and technological revolution. Two years later, diode lasers were demonstrated in III-V compound semiconductors. Since then, many scientists and engineers have researched lasing on silicon substrates (Soref and Larenzo, 1986). In the past two decades, rapid advances in silicon photonics have been driven by the combination of a need for more complex, higher functionality and lower cost photonics integrated circuits, and also by pin count and power limits for communications, as summarized

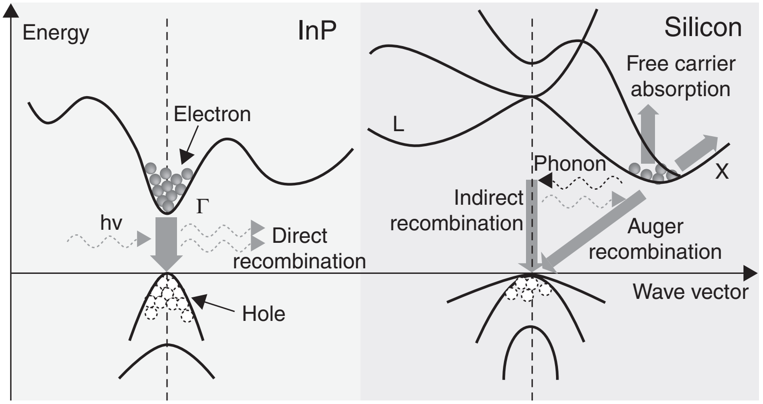

10.1 Energy band diagrams and major carrier transition processes in InP and silicon crystals. In a direct band structure (e.g., InP), it is easy for direct electron-hole recombination to take place for photon emission, while in an indirect band structure (e.g., Si), free carrier absorption (FCA), Augar recombination and indirect recombination exist simultaneously, resulting in little photon emission (Liang and Bowers, 2010).

in the International Technology Roadmap for Semiconductors (ITRS). Electronics giants, such as Intel, IBM, HP, ST Microelectronics, IMEC and Alcatel-Thales, have teamed up with research institutes around the world to drive progress in silicon photonics. The momentum to make a useful laser in or on silicon is significant.

10.2 Fundamentals of Si lasers

At the time of the demonstration of the first laser 50 years ago, the fundamental hurdle to realizing stimulated emission in silicon was understood. Optical transitions have to obey the laws of conservation of energy and momentum. In *direct* bandgap materials (e.g., GaAs and InP), radiative recombination occurs rapidly and efficiently via a simple two-particle process, as shown by the simplified band diagram in Fig. 10.1. Direct bandgap materials exhibit a structure where the lowest energy points of both conduction band and valence band line up vertically in wave vector axis, that is, they share the same crystal momentum. This is the biggest reason why GaAs-, InP- and GaN-based materials have been the dominant material systems for semiconductor diode lasers since their invention in 1962.

Silicon, like germanium, is an indirect bandgap material, and is not naturally capable of accomplishing efficient radiative recombination. Free electrons tend to reside in the *X* valley of the conduction band, which is not aligned with free holes in the valence band. Therefore, if a recombination is to result in the emission of a photon, a third particle must be involved to carry away the excess momentum, which leads to slow optical transition rates. A major non-radiative process is Auger recombination where an electron (or hole) is excited to a higher energy level by absorbing the released energy from an electron–hole recombination. The Auger recombination rate increases with injected free-carrier density and is inversely proportional to the bandgap. Free-carrier absorption (FCA) represents another major non-radiative process wherein the free electrons in the conduction band can jump to higher energy levels by absorbing photons. In high-level carrier injection devices (e.g., lasers and amplifiers) or heavily-doped layers, free-carrier loss in silicon is orders of magnitudes higher than the material gain (Soref and Larenzo, 1986). For both non-radiative processes, the electrons pumped to higher energy levels release their energy by heat rather than photons. They also have much shorter lifetimes τ_{nonrad} than radiative processes in Si, resulting in an extremely poor internal quantum efficiency η_i of light emission, which is of the order of 10^{-6} and is defined in Equation [10.1] (Pavesi, 2009):

$$\eta_i = \frac{\tau_{\mathrm{nonrad}}}{\tau_{\mathrm{nonrad}} + \tau_{\mathrm{rad}}} \tag{10.1}$$

Consequently, the focus of semiconductor laser research for the first 50 years has been on compound semiconductor substrates, but now there is intense interest in lasers on silicon.

Despite its fundamental limitations of indirect bandgap and low mobility, silicon exhibits a number of important properties that make it a good substrate, if not necessarily a good gain medium for diode lasers. From a materials perspective, silicon wafers are light-weight and robust, and have incredible purity and defect density. State-of-the-art 22 nm complementary metal–oxide semiconductor (CMOS) technology is sufficiently good to fabricate virtually all silicon photonic components, which are mostly still in the micrometer regime. Both factors allow for silicon waveguides with propagation loss that is typically one order of magnitude lower than that of compound semiconductor waveguides. Silicon has a high thermal conductivity, ~130 W/m-K, being one of the most thermally conductive semiconductors. Its high-quality native oxide, SiO_2, is one of its major advantages over Ge and other semiconductors for electronic integrated circuits due to easiness to form, stability and high interface quality between Si and SiO_2. The oxide also serves as a protective layer and a naturally good optical waveguide cladding due to its large refractive index difference from silicon ($\Delta n \sim 2.1$). Further loss reduction in silicon waveguides by oxidation (Lee *et al.*, 2000) and hosting rare earth doping in SiO_2 bring additional benefits to passive silicon lightwave circuits. Advantages in purity, waveguide loss, and thermal conductivity make Si ideal for wave-guiding media for high-Q resonator and high power lasers. From a mass production perspective, Si is the second most abundant element on earth. The solidification of silicon's role has resulted in rational technology development and deployment, drastically reducing the uncertainties in investments, critical research directions and resource allocations. The past half-century technology revolution in design tools, circuit architecture, substrate manufacturing and epitaxy, device processing, packaging, testing and quality control has led to the present Si IC industry with about 200 billion USD revenue per year. The annual research and development investment in electronic ICs, particularly in device innovation, is about 45 billion USD/year. Thus, leveraging CMOS superpower in IC design, fabrication, and testing gives Si photonics incredible potential (Liang and Bowers, 2009).

10.2.1 A brief history of Si light emitters

There have been increasing efforts to make Si an efficient light emitter in the past two decades. With the availability of nanotechnology, the traditional phonon-selection rule in indirect bandgap materials can be relaxed by breaking the crystal-symmetry or by phonon localization. The motivation is to achieve the quantum confinement of excitons in a nanometer-scale crystalline structure (Bisi *et al.*, 2000). A number of groups have reported enhanced light-emitting efficiency and optical gain in low-dimensional (i.e., on the order of the de Broglie wavelength) Si at low temperatures. They include porous Si (Canham, 1990; Cullis and Canham, 1991; Gösele and Lehmann, 1995; Hirschman *et al.*, 1996), Si nanocrystals (Wilson *et al.*, 1993; Minoru *et al.*, 1997; Pavesi *et al.*, 2000; Iacona *et al.*, 2006), Si-on-insulator (SOI) superlattices (Lu *et al.*, 1995) and photonic crystal-like nanopatterns (Cloutier *et al.*, 2005), and Si nano-pillars (Nassiopoulos *et al.*, 1996; Malinin *et al.*, 2000). However, achieving room-temperature continuous-wave (cw) lasing based on these temperature-dominated processes remains a challenge (Pavesi, 2005, 2008, 2009).

The first Si laser realized by amplification in Si itself is the Si Raman laser (Rong *et al.*, 2005). Though amplification is not based on conventional band-to-band radiative emission but through stimulating Stokes transition, that is, stimulated Raman scattering, low Si waveguide loss and high-Q resonator enhancement with proper design have enabled low pump power threshold and cw operation at room temperature. Unfortunately, the optical pump requirement is the biggest hurdle to extending its practical and commercial value.

In addition to the attempt of achieving lasing *in* Si, efforts to enable diode lasers *on* Si substrate possess even longer research history. Monolithic growth of direct bandgap materials on the Si substrate is usually preferred; however, large-area, low-defect density compound semiconductors are still difficult to achieve on Si. Compared to Si, GaAs and InP have a lattice mismatch of 4.1% and 8.1%, respectively and coefficient of thermal expansion (CTE) mismatches of 120.4% and 76.9%. These result in a 10^8–10^{10} cm^{-2} threading or misfit dislocation density when GaAs or InP is grown on Si substrates (Kawanami, 2001). Numerous approaches, including special surface treatment (Xie *et al.*, 1985), strained superlattices (Masafumi *et al.*, 1989; Samonji *et al.*, 1996), low-temperature buffers (Nozawa and Horikoshi, 1991) and growth on patterned substrates (Yamaichi *et al.*, 1994), have been employed to reduce the dislocation density to around 10^5–10^6 cm^{-2}, still two orders of magnitude higher than the typical number ($<10^4$ cm^{-2}) in InP- or GaAs-based epitaxial wafers for room-temperature cw lasers. Recent advanced epitaxial techniques with SiGe (Groenert *et al.*, 2003a, 2003b) and GaSb (Cerutti *et al.*, 2010) buffer layers have enabled GaAs-based cw diode lasers on Si substrate at room-temperature. Decent performance of InGaAs quantum dot lasers on Si has been demonstrated by utilizing GaAs buffer layer and quantum dot as dislocation filters (Mi *et al.*, 2006). Lasing in III-V nano-structure grown on Si in low temperature indicated a possible different growth mechanism to suppress dislocation formation (Chen *et al.*, 2010). An exciting path is epitaxial growth of novel compound semiconductors lattice-matched to Si, such as GaNAsP (Kunert *et al.*, 2006, 2008).

The room-temperature Ge-on-Si laser is another recent noticeable breakthrough in bandgap engineering (Liu *et al.*, 2010). While Ge has an indirect band structure, a moderate tensile strain of 0.2%–0.25% is able to reduce the energy difference between the Γ and the L valley to 115 meV (Liu *et al.*, 2007; Sun *et al.*, 2009). If the strain can be increased to 2%, Ge becomes a direct bandgap material, but there are issues with incorporating that much strain. Achieving high electron concentrations via heavy n-doping results in free electrons filling up the L valley to a level equal to that of the Γ valley, creating a much larger probability that those free carriers will begin to occupy the Γ valley for radiative recombination. These techniques have enabled room-temperature direct bandgap electroluminescence (Cheng *et al.*, 2009; Sun *et al.*, 2009), and cw room-temperature optically pumped operation of Ge-on-Si lasers (Liu *et al.*, 2010). If electrically-pumped Ge lasers can be realized, Ge light source with SiGe PIN and avalanche photodetectors (Kang *et al.*, 2008, 2009), and modulators (Kuo *et al.*, 2005; Roth *et al.*, 2007) will make Ge-on-Si photonic integrated circuits (PIC) attractive.

10.2.2 Basics of hybrid Si lasers

Apart from monolithic integration of gain materials on Si, conventional hybrid integration shows better overall system performance and practical manufacturability. The traditional approach to hybrid integration is to take prefabricated III-V lasers and amplifiers and die bond (i.e., flip chip bond) these elements onto a passive planar lightwave circuit (PLC). But serious optical loss at active/passive component joints due to misalignment and mode mismatch is inevitable. The production efficiency and chip yield also result in expensive integration cost, preventing it from being adopted by the industry widely so far.

Very recently two novel and similar hybrid techniques show promise to maximize material advantages of both Si and III-V gain medium, and simultaneously minimize or even avoid pitfalls that conventional hybrid approaches possess. The first one, named *hybrid Si (evanescent) platform*, was initially developed by a joint effort between Professor John Bowers' group at University of California-Santa Barbara and Intel corporation (Park *et al.*, 2005), and the other one, *heterogeneous integration technology*, was initially developed through a collaboration between Prof. Roel Baets' group at Ghent University and IMEC (Roelkens *et al.*, 2006). Both techniques are based on epitaxially transfer thin (few μm thick) III-V active layers onto pre-patterned Si passive waveguide layer in the SOI substrate, and fabricate active photonic devices afterwards. In this chapter we focus on the principle to achieve lasing on the hybrid Si platform, and discuss a variety of lasers demonstrated so far.

Figure 10.2 highlights the critical steps to form a hybrid Si platform, starting from transferring a III-V epitaxial layer to a Si waveguide layer through a low-temperature (300°C), O_2 plasma-assisted wafer bonding process (Fig. 10.2a) (Pasquariello and Hjort, 2002; Liang and Bowers, 2008). This wafer bonding technique results in extremely strong bonding surface energy, void-free and low-strain bonding interface. Improved III-V active region quality is also observed after epitaxial transfer by photoluminescence measurement (Liang *et al.*, 2011a). Upon removing the thick InP substrate selectively, the mesa structure to enable a carrier injection scheme similar to vertical-cavity surface-emitting laser (VCSEL) is then formed on the III-V region by standard photolithography and etching

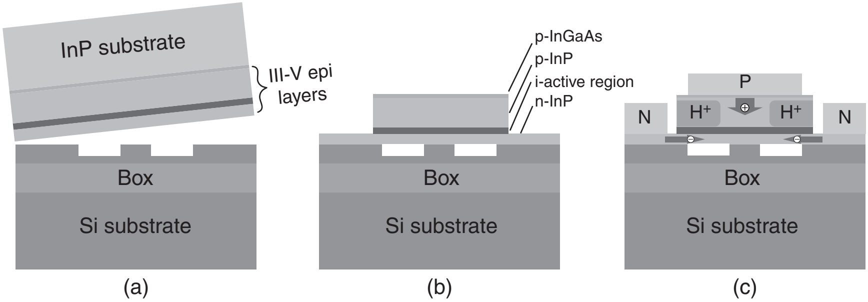

(a) (b) (c)

10.2 A simplified fabrication process to form a hybrid Si device platform starting from (a) transferring III-V epilayers to patterned Si substrate, (b) forming III-V mesa and (c) forming current injection path and metallization.

Table 10.1 The III-V epitaxial layer structure (Fang *et al.*, 2006)

Name	Composition	Doping concentration	Thickness
P contact layer	p-type $In_{0.53}Ga_{0.47}As$	1×10^{19} cm^{-3}	0.1 μm
Cladding	p-type InP	1×10^{18} cm^{-3}	1.5 μm
SCH	p-type $Al_{0.131}Ga_{0.34}In_{0.653}As$	1×10^{17} cm^{-3}	0.25 μm
Quantum wells	$Al_{0.089}Ga_{0.461}In_{0.45}As$ (9×)	Undoped	10 nm
	$Al_{0.055}Ga_{0.292}In_{0.653}As$ (8×)	Undoped	7 nm
N layer	n-type InP	1×10^{18} cm^{-3}	110 nm
Superlattice	n-type $In_{0.85}Ga_{0.15}As_{0.327}P_{0.673}$ (2×)	1×10^{18} cm^{-3}	7.5 nm
	n-type InP (2×)		7.5 nm
N bonding layer	n-type InP	1×10^{18} cm^{-3}	10 nm

(Fig. 10.2b). Typically, the III-V mesa width (>10 μm) is much larger than Si waveguide (1–2 μm), which results in essentially zero alignment challenge. Amplifiers and lasers have a wide III-V mesa (12–14 μm) for better heat conduction and mechanical strength while a narrow III-V mesa (2–4 μm) is chosen for detectors and modulators for high-speed operation with a reduced capacitance. H^+ proton implantation is used if carrier confinement or electrical isolation between integrated devices is necessary (Fig. 10.2c). Detailed fabrication steps can be found in Park *et al.* (2005) and Fang *et al.* (2006).

The general structure of III-V layers consists of a p-type InGaAs contact layer, a p-type InP cladding, an optional p-type separated confinement heterostructure (SCH) layer, an undoped multiple quantum well (MQW) active region, an optional n-type SCH layer, a thin n-type InP contact layer, a set of n-type superlattice bonding layers, and a think InP bonding layer. An example of an epitaxial structure for electrically-pump lasers (Fang *et al.*, 2006) is shown in Table 10.1.

Owing to similar refractive index of Si and III-V materials, the optical mode in this hybrid waveguide lies both in the Si layer and III-V layer, and position is determined by the Si waveguide section. This is the most significant difference from *heterogeneous integration technology* where optical mode is mostly confined in the III-V layers. A unique figure of merit associated with this platform is the flexibility to adjust optical confinement factors in Si and III-V by designing the Si waveguide dimension and III-V layer thickness and composition (i.e., refractive index). As shown in Fig. 10.3 using the beam propagation method (BPM) simulation and corresponding measured near-field optical mode images, the manipulation of confinement factors in III-V and Si regions of the hybrid waveguide is realized by changing the Si waveguide dimensions. The III-V layers in Fig. 10.3 are listed in Table 10.1. The MQW confinement factor is a critical design parameter in order to achieve enough optical gain (absorption) for

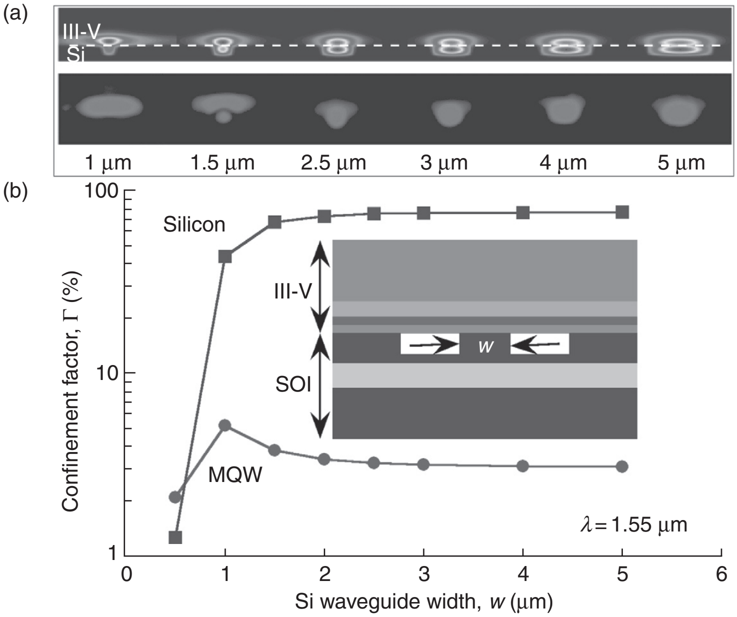

10.3 (a) Simulated and measured fundamental TE mode profiles with different waveguide widths. (b) Optical confinement factor of Si and MQW as a function of Si waveguide width. The III-V layer structure is given in Table 10.1 and height of the Si waveguide is fixed at 0.7 μm.

lasers (detectors) while the Si confinement factor is an important parameter determining coupling efficiency when the device is integrated with Si passive devices. Fundamental TE mode profiles from different waveguide widths (W = 1 to 5 μm) in Fig. 10.3 indicate that a narrow Si waveguide pushes the mode up to III-V, resulting in a large III-V confinement factor, while a wide Si waveguide accommodates a larger portion of optical mode. Though a large MQW confinement factor is desired for laser design, the Si waveguide cannot be too small. Otherwise (e.g., W = 0.5 μm in Fig. 10.2), the mode center is squeezed into the p-InP cladding, so MQW confinement is reduced and optical loss in highly-doped InGaAs contact layer increases quickly. A taller Si waveguide also leads to a larger Si confinement factor, while thicker active region and SCH layer pull the mode up towards III-V layers. This unique characteristic therefore allows different confinement factors at different regions of the hybrid waveguide for the same III-V epitaxial structure, catering to the requirements of different components on the same chip.

Typically, the waveguide layers in a III-V diode laser are symmetric in the epitaxial direction, leading to QW layers located at the optical mode center. It results in a maximum QW confinement factor. However, offset QW design is sometimes preferred, for example, the hybrid Si lasers discussed here, or employed for certain purpose, for example, increasing gain saturation point, as long as the modal gain is sufficient to overcome the total cavity loss to reach lasing threshold in Equation [10.2] (Coldren and Corzine, 1995):

$$< g >_{\mathrm{th}} = \Gamma g_{\mathrm{th}} =< a_i > +a_m \qquad [10.2]$$

$$a_m = \frac{1}{2L} \ln\left(\frac{1}{R_1 R_2}\right) \qquad [10.3]$$

where $<g>_{\mathrm{th}}$, Γg_{th}, $<a_i>$ and $<a_m>$ are threshold modal gain, QW the confinement factor, QW the material gain at threshold carrier density, average internal cavity (modal) loss and mirror loss, respectively. Mirror loss can be expressed as a function of cavity length L and front and back mirror reflectances R_1, R_2 in Equation [10.3] (Coldren and Corzine, 1995). For a 1 mm long hybrid Si Fabry–Pérot (FP) cavity laser with identical coating-free front and back mirrors (i.e., $R_1 = R_2 \sim 0.3$), and with the typical internal loss of 15 cm^{-1} and QW material gain 1000 cm^{-1}, 3% QW confinement factor is sufficient.

Figure 10.4a and 10.4b demonstrates the cw light-current (LI) characteristic of InAlGaAs-MQW, hybrid Si FP lasers with emission wavelength around 1550 nm (Park *et al.*, 2008a) and 1310 nm (Chang *et al.*, 2007), respectively. For 1550 nm devices, it can be seen that the maximum laser output power, threshold, and differential efficiency at 15°C are 32.8 mW, 70 mA, and 26% (before thermal roll-over), respectively. For 1310 nm devices, the corresponding numbers are 31.6 mW (after taking fiber coupling loss into account and doubling the output), 30 mA and 46%. The better performance of 1310 nm devices is due to higher order TE mode lasing and different active region design. The higher order mode in 1310 nm lasers shows a 10.5% (Fig. 10.4b inset) confinement factor, while 1510 nm devices lasing in fundamental TE mode only have 4% MQW confinement factor. Lasing is also observed up to a stage temperature of 105°C for 1310 nm, in contrast to 45°C for 1550 nm devices. The higher temperature performance is due to a higher confinement factor and a larger conduction band offset than the 1550 nm epitaxial design, as well as the reduced intravalence band absorption and Auger scattering (Chang *et al.*, 2007) at 1310 nm.

The fabricated hybrid lasers are usually tested with the III-V junction side up on a copper stage actively controlled by a thermal electric controller (TEC). The temperature cited here is the stage temperature, rather than chip surface or junction temperature. As mentioned previously, Si is one of the most thermally conductive semiconductor materials, which is a big advantage for dissipating device joule heating. However, fast thermal roll-over (Fig. 10.4a) is obvious and typical in most demonstrated hybrid

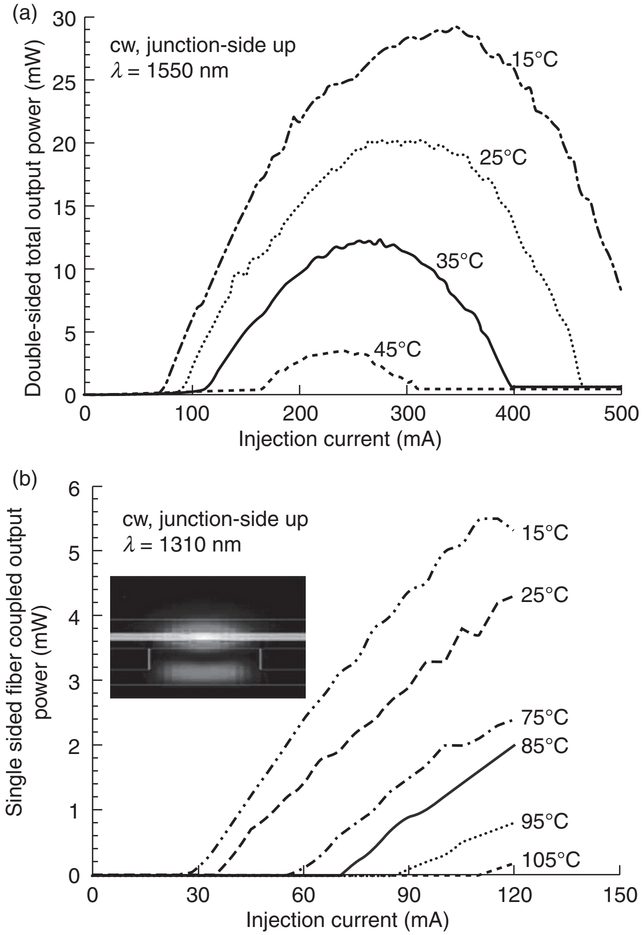

10.4 (a) LI curves for a 1550 nm hybrid Si FP laser. (b) LI curves for a 1310 nm hybrid Si FP laser. Inset: simulated higher order TE mode (Chang *et al.*, 2007; Fang *et al.*, 2007b).

devices. The primary cause of serious device heating and inefficient heat dissipation is because of the thick buried oxide layer (BOX), typically 1–3 μm, with a low thermal conductivity around 1.3 W/m-K, 100 times worse than Si, and the carrier injection scheme of hybrid Si lasers (Liang *et al.*, 2011b; Sysak *et al.*, 2007, 2011).

A circuit model, shown in Fig. 10.5a, has been used to study device heating in hybrid Si lasers with a typical schematic cross-section shown in Fig. 10.5b (Sysak *et al.*, 2007, 2011). For joule heating, the heat is generated in the current path, including the p-InP cladding, n-InP contact layer, SCH layers and active region, and p- and n-metal contacts, along with heat generated

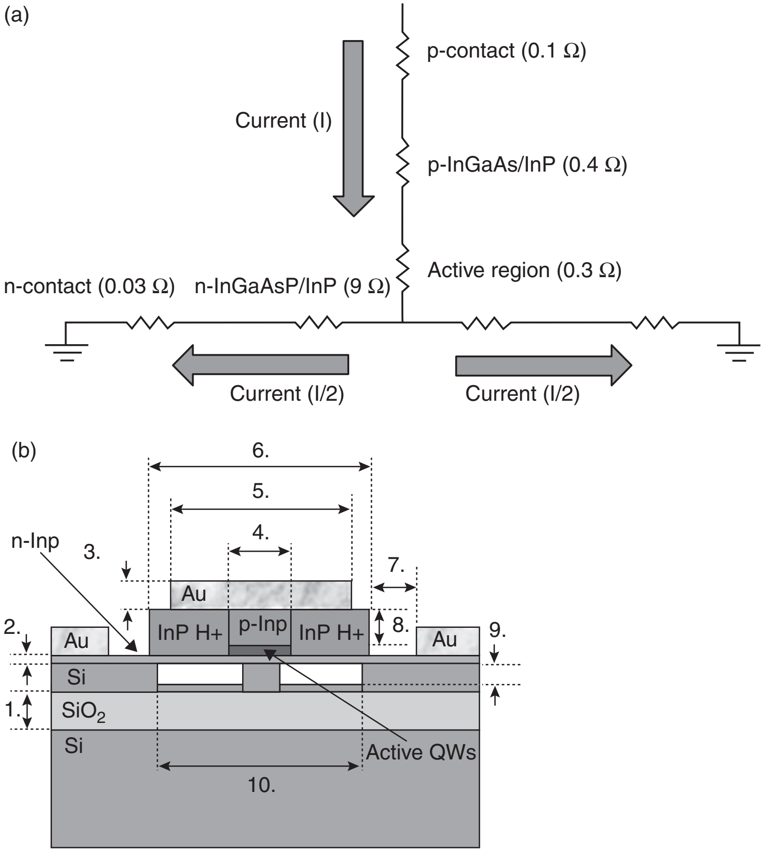
(a)
p-contact (0.1 Ω)
Current (I)
p-InGaAs/InP (0.4 Ω)
Active region (0.3 Ω)
n-contact (0.03 Ω)
n-InGaAsP/InP (9 Ω)
Current (I/2)
Current (I/2)
(b)
6.
5.
4.
n-Inp
3.
7.
Au
2.
Au
InP H+
p-Inp
InP H+
8.
Au
9.
Si
1.
SiO2
Si
Active QWs
10.

10.5 (a) Outline of current flow and equivalent circuit in the hybrid laser. Measured and calculated values for each of the resistances are indicated. (b) Description of hybrid laser structures used for thermal modeling. Specific dimensional parameters are listed in Table 10.2 (Sysak *et al.*, 2011).

by the diode drop associated with the active region (Sysak *et al.*, 2011). It is noted that the overall effect of the n-InP contact and superlattice layers needs to be halved due to the current flowing out through both sides of the III-V mesa (Sysak *et al.*, 2011). The dissipated electrical power P_d associated with resistive heating is expressed in Equation [10.4]:

$$P_d = I^2 \sum R_i + IV_d - P_o \qquad [10.4]$$

where I is injected current, R_i is resistance of a specific layer, V_d is turn-on voltage drop at MQW, and P_o is optical output power.

A detailed description of the dimensions based on Fig. 10.5b, as well as the thermal conductivity of the various layers, is shown in Table 10.2. The

Table 10.2 Dimensions for finite element hybrid laser structure, including thermal conductivity of layers (Sysak *et al.*, 2011)

Marker	Description	Dimension	Thermal conductivity (W/m-K)
1	SiO_2	1.0 μm	1.3
2	n-InP/InGaAsP	100 nm	68
3	P/N metal	1.5 μm	300
4	p-InP (no implant)	4 μm	68
5	p-metal width	8 μm	N/A
6	III-V mesa	12 μm	N/A
7	Metal separation	4 μm	N/A
8	p-InP cladding	2 μm	N/A
9	Rib etch depth (Si)	0.5 μm	156
10	Rib width	8 μm	N/A
N/A	Active MQWs	N/A	5

calculated resistance components are used in a 2D finite element method (FEM) model to simulate the temperature profile. Figure 10.6a shows the simulated temperature profile under 500 mA injection, corresponding to 1.54 W dissipated electrical power. It illustrates the hot spot around the active region, current channel in p-InP cladding, Si waveguide, and n-InP layer under III-V mesa. An obvious temperature gradient from the Si waveguide layer to the Si substrate indicates extremely inefficient heat dissipation through the BOX layer.

The predicted temperature rise in the laser active region, as a function of applied current, is shown in Fig. 10.6b. Results show that the largest source of power dissipation in the laser is the diode drop, followed by the n-InP contact layer, and the p-InP cladding/InGaAs layers. If the n-type metal contact area is limited by the device architecture, as in hybrid Si microring lasers, its resistance contribution increases drastically and becomes another major heat source with decrease of device dimension (Liang *et al.*, 2011b). For conventional III-V edge emitters, the n-type metal contact is usually distributed to the entire chip back-side, minimizing the resistance (i.e., heat generation) of the n-type metal contact and III-V layers from the n-metal contact to the active region. The large area of back-side contact without a thermal barrier also helps heat dissipation to the TEC. For hybrid Si lasers, the n-InP contact layer resistance can be reduced by increasing the n-type doping, its thickness, and distance from the active region. Unfortunately, this leads to higher FCA loss in n-InP contact layer, reduced MQW confinement factor, narrow III-V mesa, and processing challenges.

Using the simulated temperature rise and dissipated electrical power, the thermal impedance of the laser is 43.5°C/W compared with 18.3°C/W if the 1 μm-thick BOX layer could be replaced by Si (Sysak *et al.*, 2011). However, a BOX layer of 1 μm thickness is already close to the borderline

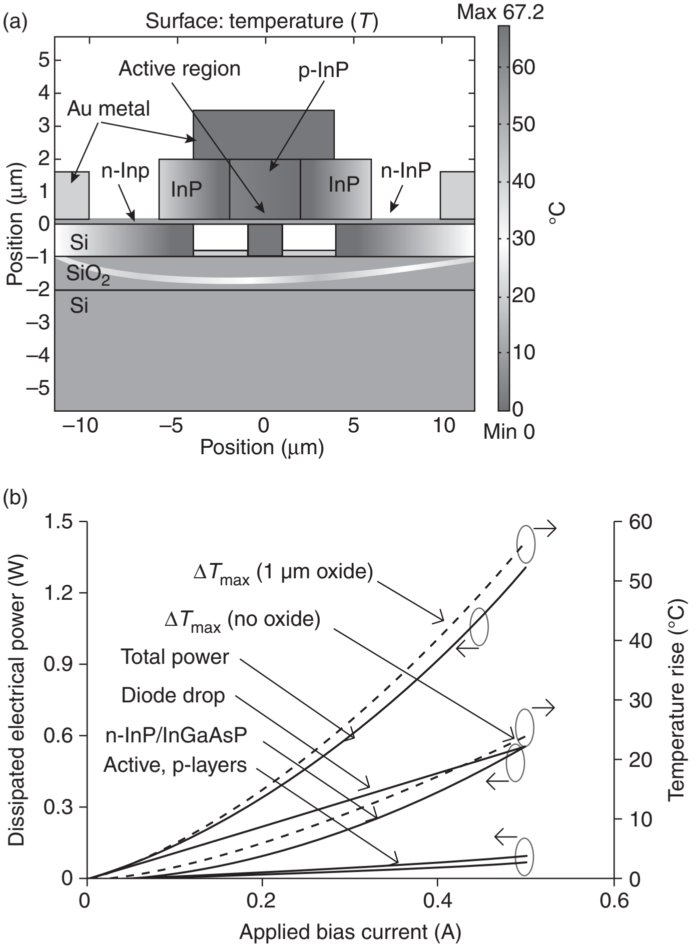

10.6 (a) 2D profile of the temperature in the hybrid laser under 1.54 W of electrical power. (b) Temperature rise (dashed lines) and electrical power dissipation (solid lines) in the various hybrid laser regions (Sysak *et al.*, 2011).

to keep the optical mode from leaking into the Si substrate with the present design.

The thermal impedance Z_T in Equation [10.5] can be experimentally determined by measuring lasing wavelength shift as a function of active region (stage) temperature ($d\lambda/dT$) and then as a function of dissipated electrical power. The former measurement is performed under pulsed injection mode to minimize device heating other than what is provided by the temperature controlled stage, while the latter is conducted under cw operation with a fixed active region (stage) temperature (Sysak *et al.*, 2007). Lasing wavelength shifts of 0.067 nm/°C and 2.8 nm/W have been determined in 800 µm-long hybrid Si FP lasers discussed in Figs 10.5 and 10.6. It results in a measured thermal impedance of 41.8°C/W, which agrees with FEM simulation well (Sysak *et al.*, 2007):

$$Z_T = \frac{\mathrm{d}T}{\mathrm{d}P_d} = \left(\frac{\mathrm{d}\lambda}{\mathrm{d}P_d}\right)\left(\frac{\mathrm{d}\lambda}{\mathrm{d}T}\right)^{-1} \qquad [10.5]$$

Device thermal performance is also measured by an overall characteristic temperature (T_0) and an above threshold characteristic temperature (T_1) (Coldren and Corzine, 1995). T_0 indicates threshold dependence on temperature, while T_1 characterizes the differential quantum efficiency dependence on temperature after lasing. Due to the exponential temperature dependence of transparent carrier density, material gain, internal modal loss, carrier leakage and non-radiative recombination such as Auger recombination, temperature-induced threshold increase and power decrease at a fixed injection level above threshold also obey an exponential relationship expressed in Equations [10.6] and [10.7], where T is junction temperature, I is injection current above threshold I_{th} in order to reach a certain output power level. I_0 and I_{P_0} are fitting parameters (Coldren and Corzine, 1995):

$$I_{\mathrm{th}} = I_0 e^{T/T_0} \qquad [10.6]$$

$$I - I_{\mathrm{th}} = I_{P_0} e^{T/T_1} \qquad [10.7]$$

T_0 can be extracted by fitting measured I_{th} at different stage temperatures using Equation [10.6]. Pulsed current injection is required to minimize device heating, so that stage temperature can be treated as junction temperature. A similar process can be done for T_1. Measured T_0 and T_1 are 51 K and 100 K, respectively for devices in Fig. 10.6 (Sysak *et al.*, 2007).

Upon determining Z_T, T_0 and T_1, a temperature-dependent output power *vs* injected current relationship can be expressed in Equations [10.8] and [10.9] (Sysak *et al.*, 2007; Srinivasan *et al.*, 2011):

$$I_{\mathrm{th}} = I_0 e^{(Z_T P_d + T)/T_0} \qquad [10.8]$$

$$P_o = \eta_i \left(\frac{a_m}{\langle a_i \rangle + a_m}\right)\left(\frac{h\upsilon}{q}\right) e^{-(Z_T P_d + T)/T_1}\left(I - I_{\mathrm{th}}\right) \qquad [10.9]$$

where η_i, h, v are internal quantum efficiency, Planck's constant, and lasing frequency at vacuum, respectively. Given a typical injection efficiency of 70%, a modal loss of 10 cm^{-1}, and an estimated mirror loss of 11.4 cm^{-1} (facet reflectance R ~ 38%), Fig. 10.7 shows the predicted and experimental single sided laser output power at various stage temperatures (Sysak

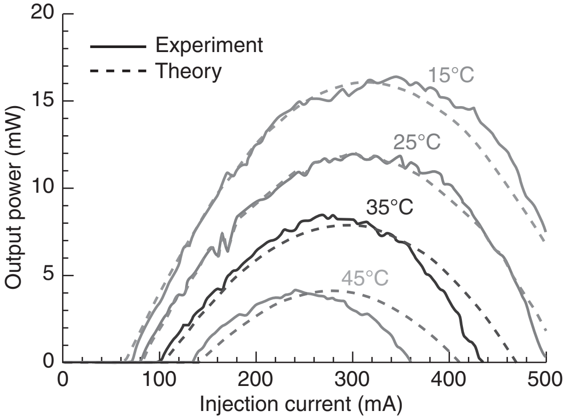

10.7 CW LI experimental results (solid lines) and theoretical predictions (dashed lines) for the FP hybrid laser at stage temperatures between 15°C and 45°C (Sysak *et al.*, 2007).

et al., 2007). A good agreement between experiment and theory indicates that hybrid lasers, small dimension designs in particular (Liang *et al.*, 2010), are subject to device joule heating, which needs to be taken into account in advanced hybrid Si laser design.

Solutions to minimize or totally eliminate the negative impact from the BOX layers have been proposed and demonstrated and will be employed to more advanced devices (Liang *et al.*, 2011c; Sysak *et al.*, 2011).

10.2.3 Advanced hybrid Si lasers

Both optically pumped (Park *et al.*, 2005) and electrically driven hybrid Si lasers (Fang *et al.*, 2006; Chang *et al.*, 2007) based on an FP cavity enable us to study the general optical, electrical and material properties of the hybrid Si platform, paving the way for advanced device design. To make hybrid Si lasers attractive candidates as on-chip light sources of optical interconnect systems or other Si PICs, the requirements of a polished (cleaved) facet-free resonator, and single longitudinal mode operation need to be met at the first place. It motivates the demonstration of grating-based devices and ring resonator devices on the hybrid Si platform.

Grating-based diode lasers, for example, distributed feedback (DFB) and distributed Bragg reflector (DBR) lasers, are the most popular single-wavelength on-chip light sources in conventional III-V PICs. The hybrid Si platform provides several design freedom and fabrication advantages over III-V counterparts. As shown in Fig. 10.8, passive gratings (Fig. 10.8a) can be fabricated by etching a surface corrugation on the top

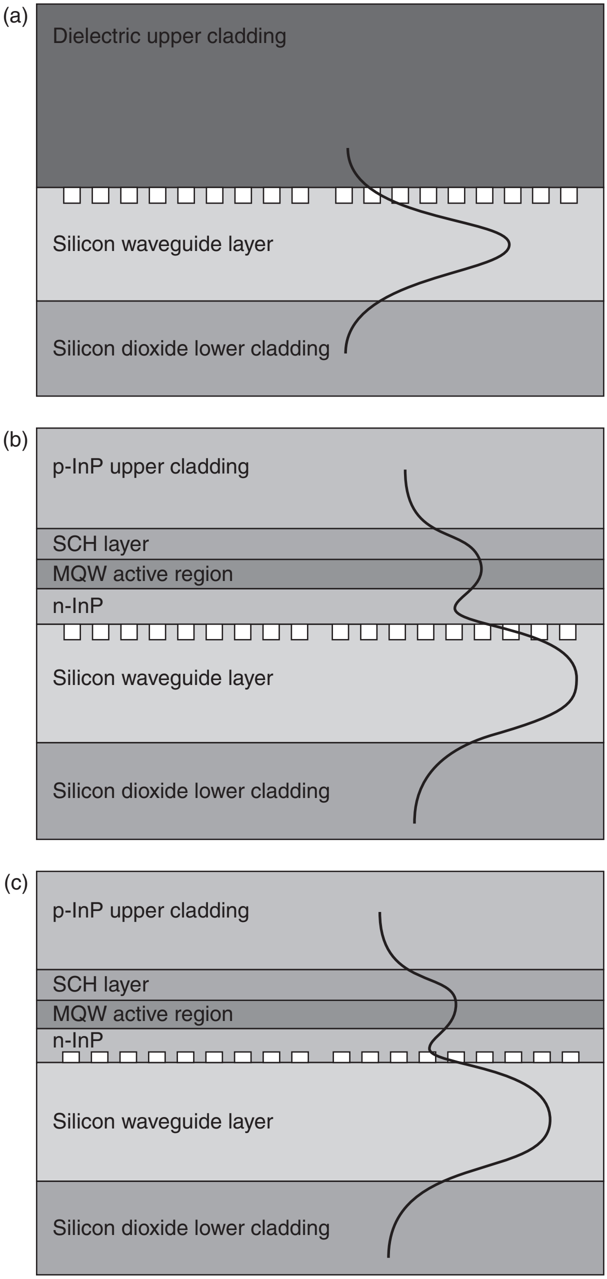
(a)
Dielectric upper cladding
Silicon waveguide layer
Silicon dioxide lower cladding
(b)
p-InP upper cladding
SCH layer
MQW active region
n-InP
Silicon waveguide layer
Silicon dioxide lower cladding
(c)
p-InP upper cladding
SCH layer
MQW active region
n-InP
Silicon waveguide layer
Silicon dioxide lower cladding

10.8 Longitudinal cross structure and mode intensity profile of (a) a passive Si grating; (b) a Si hybrid grating and (c) a III-V hybrid grating (Fang *et al*., 2009; Jones *et al*., 2009).

surface of the Si waveguide. Hybrid gratings can be formed by patterning a surface corrugation at the bonding interface between the III-V regions and the Si on either the Si surface (Fig. 10.8b), or III-V surface (Fig. 10.8c) (Fang *et al.*, 2009; Jones *et al.*, 2009). Gratings etched in Si can use advanced high-resolution CMOS lithography, leading to lithographically defined first order gratings that are spectrally aligned to other Si photonic components on the chip (Fang *et al.*, 2009; Jones *et al.*, 2009). Gratings patterned on III-V may have increased etch control through the use of specially designed epitaxial layer structures for etch stop (Park *et al.*, 2011). Similar to III-V DFB/DBR lasers with re-grown upper cladding, a surface corrugation close to the optical mode center naturally results in hybrid grating (Fig. 10.8b and 10.8c). But wafer bonding can be simpler and more straightforward than epitaxial regrowth, and hybrid grating formation does not require additional processing since wafer bonding is an inevitable core step to this platform.

The airgap in the etched grating segments, plus the strong electrical field at the bonding interface, enable stronger grating reflection per unit length, κ, in hybrid gratings than do passive Si grating or re-grown III-V grating with equal grating dimensions. Figure 10.9 is a comparison of calculated square wave-shape, 50% duty cycle grating strength for the three structures in Fig. 10.8 based on Equations [10.10]–[10.13] (Coldren and Corzine, 1995):

$$\kappa = \frac{\Delta\bar{n}}{\bar{n}\Lambda} \qquad [10.10]$$

$$\Delta n_{\text{eff}} = \left| n_{\text{eff}1} - n_{\text{eff}2} \right| \qquad [10.11]$$

$$n_{\text{eff}} = \frac{\left(n_{\text{eff}1} + n_{\text{eff}2}\right)}{2} \qquad [10.12]$$

$$\Lambda = \frac{\lambda_0}{4}\left(\frac{1}{n_{\text{eff}1}} + \frac{1}{n_{\text{eff}2}}\right) \qquad [10.13]$$

where $n_{\text{eff}1}$($n_{\text{eff}2}$) is modal index of etched (unetched) grating segment at Bragg wavelength λ_0, and Λ is grating period. Si rib waveguide in the calculation is 0.7 μm thick, 1.5 μm wide with 0.5 μm etch depth. The III-V structure is shown in Table 10.1. If the grating duty cycle is not 50%, a correction factor $sin(m\pi D)$ is required in Equation [10.10], where m is grating order and D is duty cycle (Fang, 2008).

The grating strength is important as it determines both the bandwidth of the grating, and hence its ability to select a single laser mode, and in DFB lasers the effective laser cavity length, which impacts on its high temperature performance (Fang *et al.*, 2009; Jones *et al.*, 2009).

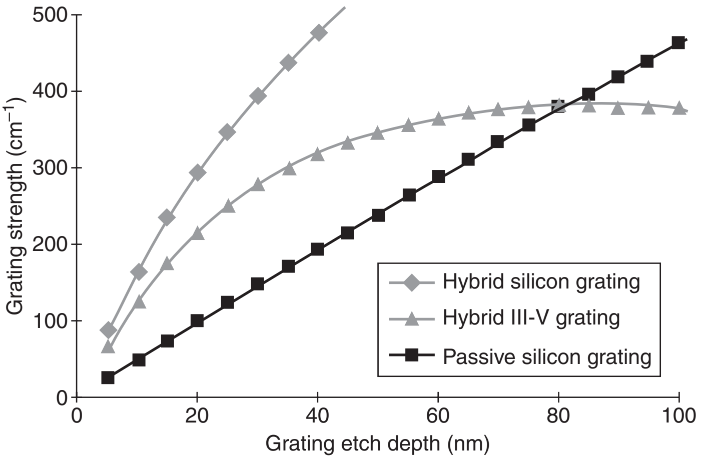

10.9 Grating strength as a function of etch depth for the three grating architectures in Fig. 10.8 (Fang *et al.*, 2009; Jones *et al.*, 2009).

As shown in Fig. 10.10, hybrid Si DFB lasers with a ~25 nm surface corrugated grating pattern with a 238 nm grating period and 71% duty cycle (κ = 247 cm^{-1}) were formed on Si (Fig. 10.10a) for a grating stop-band designed at around 1600 nm (Fang *et al.*, 2008, 2009). The device consisted of a 14 μm-wide and 200 μm-long gain region and two 80-μm long III-V tapers with a quarter wavelength shifted region centered at gain section. 50 dB side-mode suppression ratio (SMSR), over 100 nm single-mode operation span, and 3.5 MHz linewidth, were comparable to III-V DFBs (Fang *et al.*, 2008). Figure 10.10b shows the cw LI curves of the device, showing lasing up to a stage temperature of 80°C. The output power is measured by the integrated hybrid Si photodetectors with a responsivity ~1 A/W (Park *et al.*, 2007a). More than 10 mW output power was obtained at 15°C (Park *et al.*, 2011).

The hybrid DBR counterpart includes two passive (i.e., Si) Bragg reflector mirrors (Fig. 10.8a) placed 600 μm apart to form an optical cavity, and two 80 μm long tapers sandwich the 440 μm long hybrid gain region as shown schematically in Fig. 10.11 (Fang *et al.*, 2008). The back and front mirror lengths are 300 and 100 μm, respectively. The power reflectivities of the back and front mirrors are calculated to be 97% and 44%, respectively. The surface corrugated gratings have an etch depth and duty cycle of 25 nm and 75%, respectively, with an upper cladding of SU-8, leading to a grating strength, κ of 80 cm^{-1}.

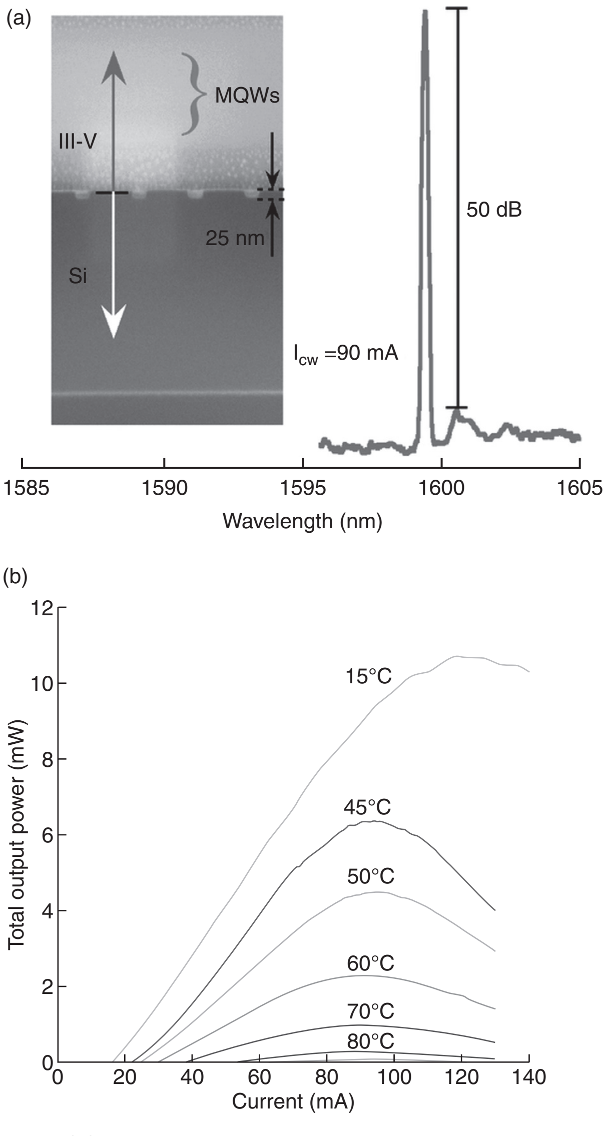

10.10 (a) Experimental spectrum of a Si DFB laser at 90 mA cw injection current. Inset: SEM image of longitudinal hybrid grating cross-section. (b) LI curves for stage temperatures of 15–80°C (Park *et al.*, 2011).

The front mirror L-I characteristic is shown in Fig. 10.12. The device has a lasing threshold of 65 mA and a maximum front mirror output power of 11 mW, leading to a differential efficiency of 15%. The laser operates up to a stage temperature of 45°C. The kinks in the LI are because of longitudinal mode hop caused by the laser wavelength red-shifting due to self-heating.

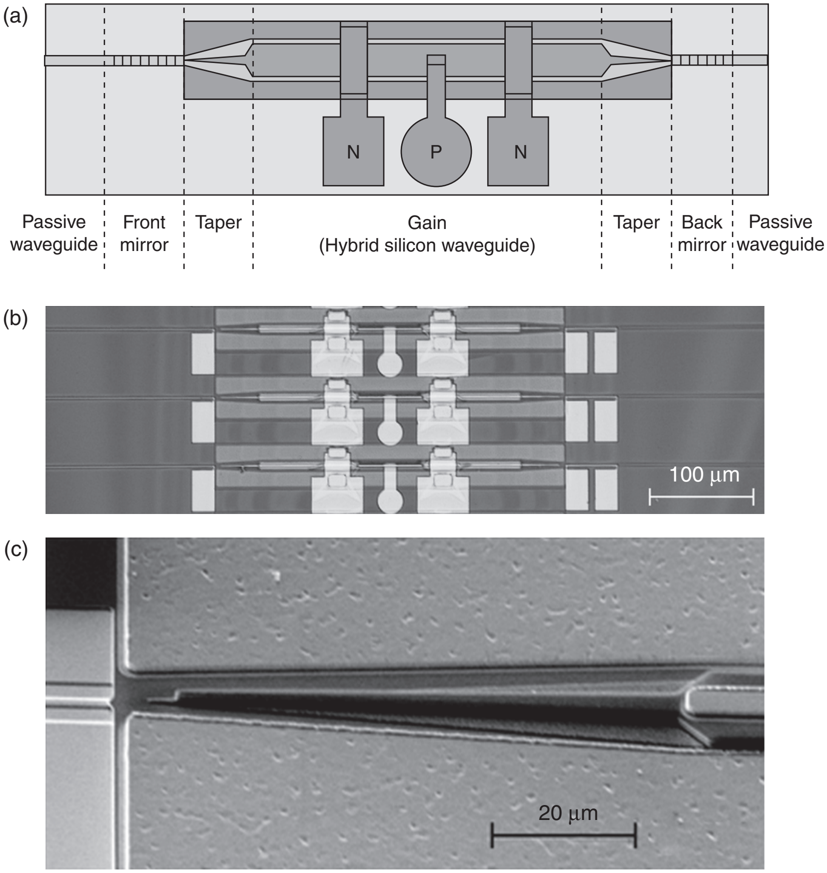
(a)
N
P
N
Passive waveguide
Front mirror
Taper
Gain (Hybrid silicon waveguide)
Taper
Back mirror
Passive waveguide
(b)
100 μm
(c)
20 μm

10.11 (a) Hybrid DBR laser schematic topographical structure, (b) top-view microscope image of fabricated devices, (c) SEM image of a hybrid taper for optical mode conversion (Fang *et al.*, 2008; Park *et al.*, 2011).

The lasing spectrum is shown in Fig. 10.12 inset, with a lasing peak at 1597.5 nm and 50 dB SMSR when driven at 200 mA (Fang *et al.*, 2008).

Compared to hybrid DFB devices, DBR lasers need to overcome the additional taper transmission loss, which partially contributes to a higher threshold. The mode conversion in hybrid DBR lasers is done by laterally tapering the III-V mesa to a narrow point above the Si waveguide, as shown by the SEM image in Fig. 10.11c. This tapering adiabatically transforms the mode from the hybrid waveguide to the passive Si waveguide. For typical 70 μm-long tapers, the measured single taper loss is in the range 0.6–1.2 dB with reflectivity around 6×10^{-4} (Jones *et al.*, 2009). Enhanced device performance is expected with reduced taper transmission loss.

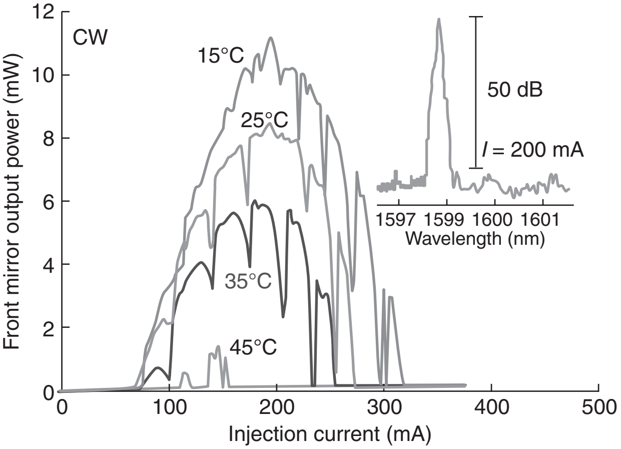

10.12 DBR laser LI curve for various temperatures measured out of the front mirror. Inset: The lasing spectrum at 200 mA injection current, showing a single-mode operation with 50 dB SMSR (Fang *et al.*, 2008).

Another attractive on-chip wavelength selection component is a ring resonator. In contrast to FP laser resonators where only a standing wave can exist under steady state between front and back mirrors, a ring resonator does not have mirrors and supports traveling waves at specific resonance frequencies. Optical modes at resonance frequencies travel either in clockwise or counter-clockwise direction along a closed loop representing a round trip and retrace themselves without reversing direction. The resonance condition of a traveling-wave resonator is the same as that of standing wave resonator, and can be expressed in Equation [10.14]:

$$v_0 = m\frac{c_0}{nL} \text{ or } L = m\frac{\lambda_0}{n} \quad m = 1, 2, \ldots \qquad [10.14]$$

where $v_0(\lambda_0)$ is resonance frequency(wavelength) in vacuum, n is modal index, and L is round-trip distance. Substituting 2π into Equation [10.14], it is easy to have Equation [10.15] to explain how optical modes reproduce themselves after exactly one round trip, which is also a condition for simulated amplification under steady state.

$$\frac{2\pi n}{\lambda_0}L = \beta L = 2m\pi \qquad [10.15]$$

Unlike FP or DFB/DBR lasers, where lasing emission is achieved through partial transmission of the front or back mirror, typical ring resonator lasers couple out power using a directional coupler to couple to a bus waveguide, close to the resonator, for evanescent power extraction. The power outcoupling ratio is critical to determining threshold and output power, and can be treated as mirror loss using Equation [10.3].

For a high-index-contrast (HIC) platform, for example, SOI, optical mode is usually tightly confined in the waveguide core. The coupling gap between resonator and bus waveguide, therefore, can be very small, in the order of 100 nm or so, in order to have sufficient electrical field overlap with the bus waveguide. This increases the fabrication challenge to achieve controllable and repeatable coupling. Incorporating a straight section in the ring loop results in a straight directional coupler with a longer interaction length, subsequently leading to enhanced coupling controllability. It also makes a strong coupling to the bus waveguide attainable at the situation of relatively wide coupling. The interaction length is easier to accurately determine through photolithography than through a narrow gap. This type of traveling-wave resonator is called a racetrack ring resonator (R3).

For a straight directional coupler with symmetric waveguide structure, due to structure symmetry, every two eigenmodes exist as a pair of supermodes, one even and one odd, with similar intensity profile but different phase velocity. An example of the fundamental TE supermode set (mode 1: even, mode 2: odd) of an Si directional coupler is shown in Fig. 10.13. Light coupling between two waveguides as it propagates along the coupler is the consequence of superposition of even and odd modes, and follows a sinusoidal relationship. The 100% power coupling from the first waveguide to the second occurs when the phase shift of even and odd modes is an odd number of π, and back to the first one when the phase shift is an even multiple of π. The waveguide length to realize energy complete coupling back and forth to one waveguide is the beat length L_{beat}, which can be calculated as Equation [10.16] (Fang, 2008):

$$L_{\text{beat}} = \frac{2\pi}{|\beta_1 - \beta_2|} = \frac{\lambda_0}{|n_2 - n_1|} \qquad [10.16]$$

where $\beta_1(n_1)$ and $\beta_2(n_2)$ are the propagation constant (modal index) of odd and even supermodes, respectively. The amplitude coupling ratio k is expressed as Equation [10.17]:

$$k = \sin\left(\pi \frac{L_{\text{coupler}}}{L_{\text{beat}}}\right) \qquad [10.17]$$

where L_{coupler} is the coupler length. The power coupling ratio K is the square of the amplitude coupling ratio.

Obviously, the larger the phase shift (i.e., modal index difference) between odd and even supermodes, the shorter the beat length will be, which is desired for compact device design. If the electrical field of one mode that is launched into one waveguide has large penetration into the

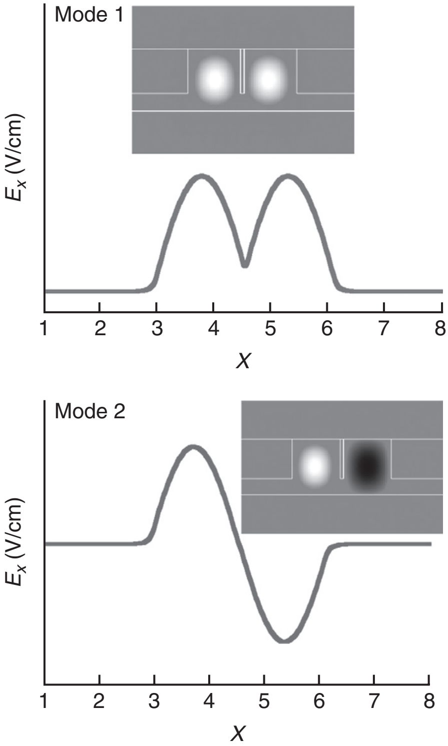

10.13 Electrical field in x direction of the even (mode 1) and odd (mode 2) supermodes. Insets: 2D (x–y direction) electrical field of even and odd supermodes.

other waveguide, a large phase shift between even and odd supermodes is resulted. It is usually accomplished by reducing the coupling gap width or effective index discontinuity between waveguide core and gap region. Compared with a Si directional coupler, a hybrid III-V-on-Si directional coupler consists of a III-V layer stack covering the entire Si directional coupler. The continuity of III-V stack reduces effective index discontinuity between the hybrid waveguide core and the coupling region, leading to a larger phase shift between odd and even hybrid supermodes. Thus, a shorter beat length is intrinsic for a hybrid directional coupler with the same symmetric Si waveguide (e.g., Fig. 10.13) dimension and coupling gap, as per the example shown in Fig. 10.14.

R3 lasers with two on-chip photodetectors fabricated on the hybrid Si platform are shown in Fig. 10.15a schematically. The device has a bending radius of 200 μm, and 700 μm long straight section, resulting in ~2.66 μm-long cavity. A 12.6% power outcoupling (L_{coupler} = 400 μm, 600 nm coupling gap) is expected based on simulations, and Fig. 10.15b shows cw lasing up to 60°C

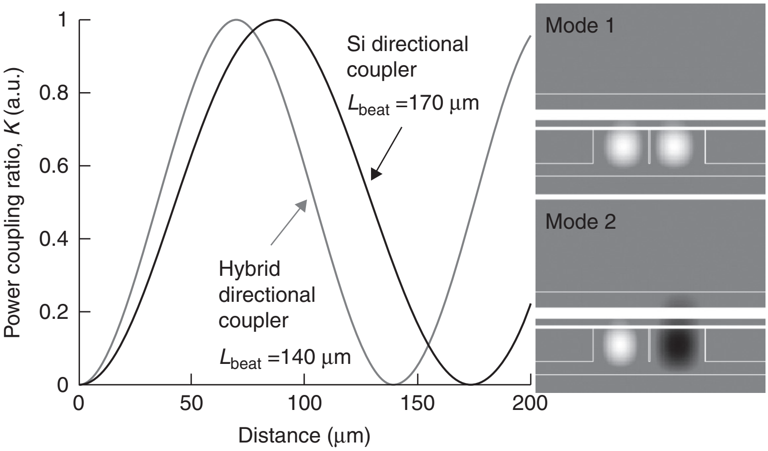

10.14 Calculated power coupling ratio of Si directional coupler and hybrid directional coupler. Insets: 2D (*x–y* direction) electrical field of even and odd hybrid supermodes. For both couplers, Si thickness is 0.7 μm; etch depth is 0.5 μm; coupling gap is 50 nm and III-V epitaxial structure is in Table 10.1.

with a minimum threshold of 175 mA and a maximum power of 29 mW at 15°C for a hybrid R3 laser (Fang *et al.*, 2007a).

The relatively high threshold is primarily due to long cavity length. Other than a straight section for hybrid directional coupler, a large bending radius is required in order to minimize additional bending loss contribution to the total internal cavity loss. As indicated in the hybrid directional coupler, III-V layers on top of a HIC Si rib waveguide immediately reduce the index contrast of core and cladding laterally (*x* direction). Figure 10.16 inset compares the effective refractive indices of core and cladding of hybrid waveguide (red) and Si rib waveguide (gray) with dimensions in Fig. 10.15. Lateral effective index contrast in the hybrid structure is 0.086, much less than Δn_{eff} = 0.59 in the Si counterpart. The simulated bending losses in Fig. 10.16 (Fang *et al.*, 2007a) show drastic loss increase in the hybrid waveguide as the bending radius becomes less than 150 μm, while no noticeable bending loss is found in the Si waveguide until the radius is less than 10 μm.

A modified hybrid Si structure in Fig. 10.17a is then created to realize a HIC microring resonator with lateral effective index contrast $\Delta n_{\mathrm{eff}} = 1.57$, allowing a much smaller bending radius with negligible bending loss (Liang *et al.*, 2009b). Rather than a typical process to pattern Si waveguide prior to III-V epitaxial transfer shown in Fig. 10.2, the hybrid Si microring resonator mesa is patterned and formed from III-V to Si through a self-aligned process (Liang *et al.*, 2009b). As shown in Fig. 10.17a, an anisotropic dry etch is employed to etch through the p-contact metal, entire III-V epi-layers and

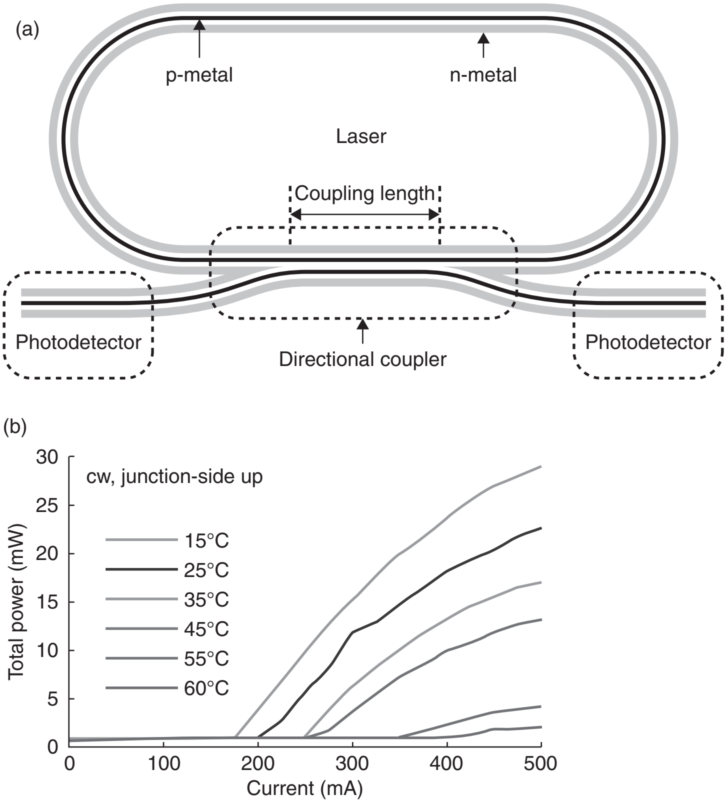

10.15 (a) The layout of the racetrack resonator and the photodetectors; (b) cw light-current characteristic of the hybrid racetrack ring laser from 15 to 60 °C.

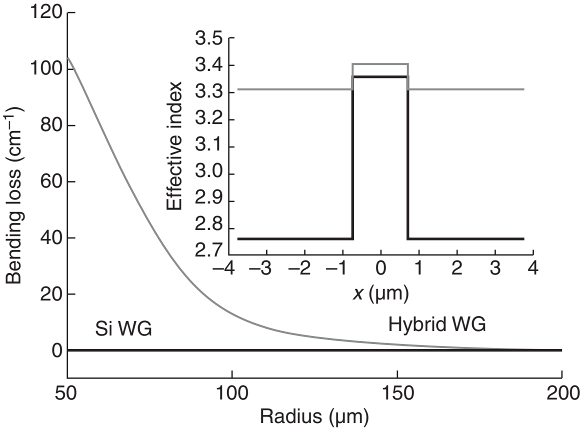

10.16 The simulated bending loss as a function of radius for the hybrid waveguide and Si waveguide structure.

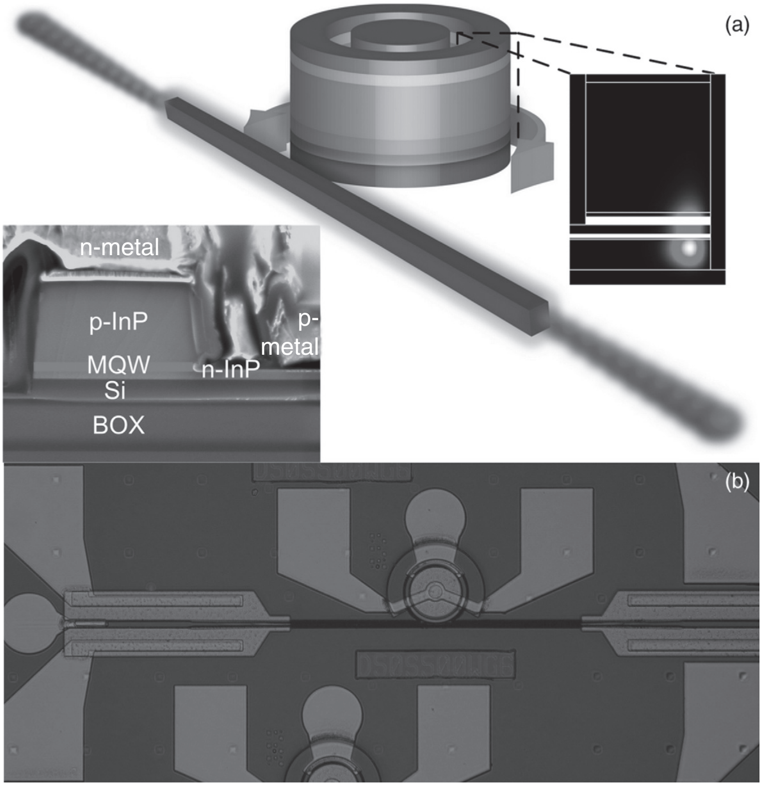

10.17 (a) Schematic of hybrid microring laser. Inset: cross-sectional SEM image of a microring waveguide with metal contacts (left). Simulated fundamental TE mode shifting towards waveguide edge (right). (b) Top view of a $D = 50$ μm hybrid microring laser with two integrated hybrid photodetectors (Liang *et al.*, 2009a, 2011b).

Si, and then a circular opening is created inside where the etch stops at the n-InP contact layer of the III-V stack, followed by placing the n-contact metal. It results in a III-V ring resonator sitting on top of an Si disk resonator perfectly aligned with the same dimensions. The outer edge of the hybrid microring resonator is passivated by SiO_2, allowing the optical mode to be squeezed and shifted towards the semiconductor/SiO_2 interface but still well confined inside resonator at the sharp bend (Fig. 10.17a inset) (Liang *et al.*, 2009a, 2011b). An Si bus waveguide distances a small gap from the hybrid microring resonator laterally to extract a fraction of power. Hybrid Si photodetectors are also integrated at the ends of the bus waveguide as a fabricated diameter $D = 50$ μm hybrid microring laser chip shown in Fig. 10.17b.

The typical cw LI characteristic of $D = 50$ μm devices is shown in Fig. 10.18 (Liang *et al.*, 2009b). The power outcoupling ratio of this microring resonator

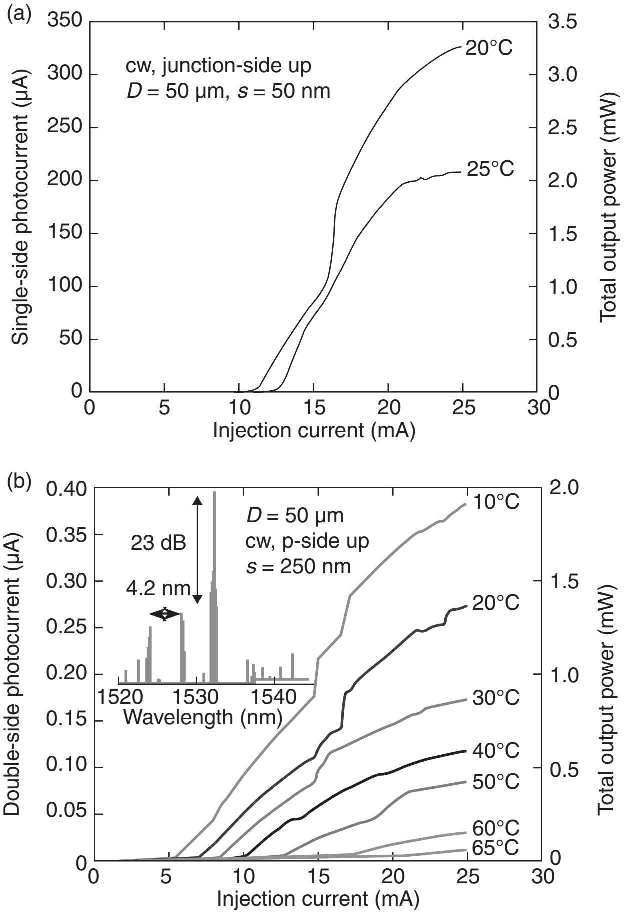

10.18 LI characteristic of $D = 50$ μm hybrid microring lasers with coupling gap (a) $s = 50$ nm and (b) $s = 250$ nm at various stage temperatures. Inset: typical spectrum showing 4.2 nm FSR and 23 dB SMSR (Liang *et al.*, 2009b).

mainly depends on the coupling gap width s. The smaller the coupling gap is, the higher the outcoupling ratio, and the higher is the mirror loss. Therefore, higher (lower) threshold and differential quantum efficiency result from narrower (wider) coupling gap in Fig. 10.18a and 10.18b). Maximum output power of over 3 mW is obtained in an $s = 50$ nm device at a stage temperature of 20°C, while the minimum threshold is 5 mA in an $s = 250$ nm device at a stage temperature of 10°C (Liang *et al.*, 2009b). Improved device performance after increasing carrier injection efficiency from 59% to 78% is achieved by selectively reducing the active region volume (Liang *et al.*, 2011b). In Fig. 10.18b inset, devices demonstrate around 4.2 nm free spectra range (FSR), which agrees with calculation based on Equation [10.18] (Liang *et al.*, 2009b):

$$\mathrm{FSR} = \frac{\lambda_0^2}{n_g \pi D} \qquad [10.18]$$

where λ_0 and n_g are laser vacuum wavelength and group index, respectively. πD is the round-trip modal length. Owing to the gain profile of active region, laser peaks one FSR apart from the primary laser peak show over 20 dBm less power (Liang *et al.*, 2009b).

As indicated in Fig. 10.19a, in addition to a smaller outcoupling ratio ($R = 1 - k^2$), further scaling down of the laser diameter (i.e., cavity length) results in a drastic threshold reduction. The calculation in Fig. 10.19a shows how the threshold can decrease from the previously demonstrated large hybrid Si R3 lasers (blue dot) (Fang *et al.*, 2007a) to recently fabricated microring lasers (inset SEM image) (Liang *et al.*, 2009b) and eventually to the ultra-compact 4.5 μm in diameter device with ~400 μA threshold. A sub-mA threshold has been achieved in hybrid micro-disk lasers fabricated with heterogeneous integration technology (Van Campenhout *et al.*, 2007; Spuesens *et al.*, 2009).

The biggest obstacle for compact devices, particularly on the SOI substrate, however, is immediately increased thermal impedance (i.e., device heating) in Fig. 10.19b. Buried oxide has been identified as the primary reason in the previous section, and shown by a FEM simulated D = 15 μm hybrid microring laser cross-section in Fig. 10.19b inset. Several approaches are being investigated to minimize or eliminate the thermal barrier of the BOX layer (Liang *et al.*, 2011d; Sysak *et al.*, 2011).

One unique characteristic of a traveling-wave resonator is the possible co-existence of two counter-propagating modes. Bi-directional lasing in a standard traveling-wave resonator is typical in low injection level, while uni-directional lasing occurs under high carrier injection (Sorel *et al.*, 2002). Lasing direction switch alternatively can be useful for optical memory application (Hill *et al.*, 2004) but is undesirable for on-chip light source application. Since these clockwise and counter-clockwise modes have spatially separated outputs, mode competition can be observed as the kinks (i.e., power sudden drop or jump) at the LI curves of the individual modes (e.g., Fig. 10.20 top) although the combined LIs (Figs 10.15 and 10.18) are no different from other lasers. Uni-directional lasing can be achieved by seeding one mode over the other with an external light source (Dragic, 2004; Fang *et al.*, 2007a). In this way, the photon density of the propagating mode with external light injection is greater than the photon density of the other mode, creating a differential in the amount of stimulated emission occurring in these two modes. This ultimately leads to controlled uni-directional lasing (Dragic, 2004; Fang *et al.*, 2007a).

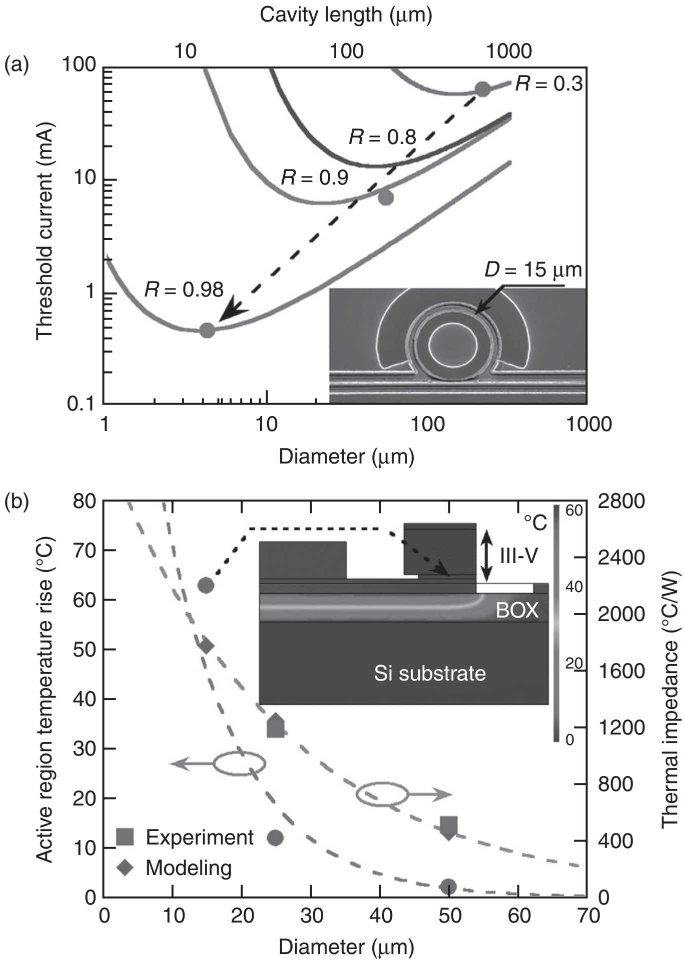

10.19 (a) Calculated threshold current as a function of device cavity length. Inset: top-view SEM image of a 15 μm in diameter device. (b) Calculated active region temperature rise at threshold, and experimental and modeling thermal impedance as a function of device dimension. Inset: FEM modeling of a *D* = 15 μm device temperature profile at threshold 9.4 mA (Liang and Bowers, 2010; Liang *et al.*, 2010).

For hybrid Si ring lasers with integrated hybrid Si photodetectors, one photodetector can function as an amplified spontaneous emission (ASE) light source with forward biasing. As light is generated from the ASE source on the left hand side of a hybrid R3 laser, for example, the photon density of the counter-clockwise propagating mode starts to become greater than the photon density of the clockwise propagating mode. At low ASE bias level (Fig. 10.20 top), the external power coupled into the R3 laser is not

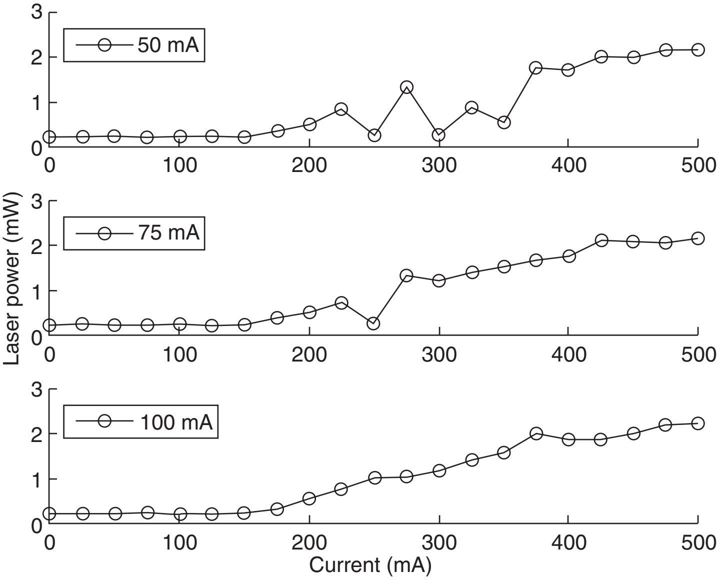

10.20 The LI curve for the clockwise lasing mode for three forward bias currents for the photodiode on the left of a hybrid R3 laser (Fang *et al.*, 2007a).

sufficient to break the balance. At 75 mA bias, some kinks disappear until stable uni-directional lasing is achieved under 100 mA bias at the left photodetector (Fang *et al.*, 2007a).

One advantage of microring lasers is the capability to cascade many of them, each with slightly different perimeter and coupling signal, out to the same bus waveguide, to realize a multiwavelength light (MWL) source (Van Campenhout *et al.*, 2008). For a linear-cavity device, for example, DFB/DBR devices, an MWL source can be realized by multiplexing several of them with a star coupler, an arrayed waveguide grating (AWG), or other wavelength combiners. One intrinsic drawback of such a configuration is that they are complex to operate, as each channel has to be aligned to an AWG passband. Another approach is to make an AWG laser (Poguntke *et al.*, 1993; Staring *et al.*, 1996; Kurczveil *et al.*, 2011). Here, the AWG is used not only as a multiplexer but also as an intracavity grating to select the lasing wavelength. These devices are easier to operate, as the lasing wavelength is determined by the bandpass characteristics of the AWG, so no external tuning is required (Kurczveil *et al.*, 2011).

Such a device on the hybrid Si platform has also been demonstrated recently (Kurczveil *et al.*, 2011). Compared with its III-V counterparts, the AWG section in hybrid AWG lasers can be much more compact and low loss when fabricated with advanced CMOS tools. The schematic diagram, mask layout, and fabricated device of a hybrid Si AWG laser are shown in

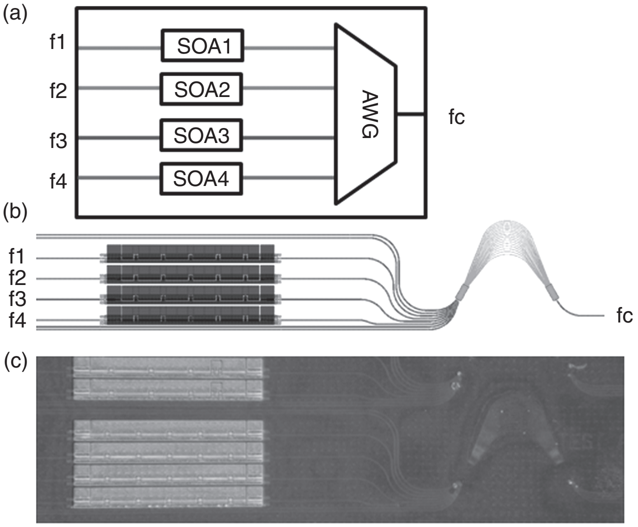

10.21 (a) Schematic diagram of an AWG laser with four channels. (b) Schematic diagram of the fabricated chip. The AWG has eight channels. Four of the eight channels have hybrid silicon SOAs. (c) Optical photograph of the fabricated chip. The sample is covered with thick SU8 polymer which decreases the contrast of the image (Kurczveil *et al.*, 2011).

Fig. 10.21a–10.21c, respectively. The device is 5 mm in length and consists of an FP cavity with an AWG. The AWG has eight channels with channel spacing of 360 GHz and footprint of 900 μm × 700 μm. A III-V die was bonded to the SOI die and 1 mm long hybrid silicon semiconductor optical amplifiers (SOAs) on four of the eight channels were defined by a typical process in Fig. 10.2. Adiabatic tapers on three etch levels are used to transition the mode from hybrid to passive regions (Kurczveil *et al.*, 2011).

The transmission characteristics of a reference AWG with randomly polarized light input is shown in Fig. 10.22a. The crosstalk and insertion loss were measured to be 9 and 3.5 dB, respectively, in good agreement with simulations. The crosstalk can be improved by increasing the number of arms, but as a laser filter 9 dB of cross talk is sufficient to prevent one channel from lasing in another channel, as the material gain does not vary by more than 9 dB from one channel to another (Kurczveil *et al.*, 2011).

A peak gain of ~19 dB/mm in hybrid gain SOA section is seen around 1560 nm at an injection current density of 5 kA/cm^2. Cw lasing is observed in all four channels with threshold between 110 and 150 mA at a stage temperature of 17°C. Around 0.3 mW power emits from a single, uncoated, polished facet (Kurczveil *et al.*, 2011). The optical spectrum of all four channels is shown in Fig. 10.22b. The currents in the SOAs were tuned to maximize the SMSR up to 35 dB. Better device performance of lower threshold,

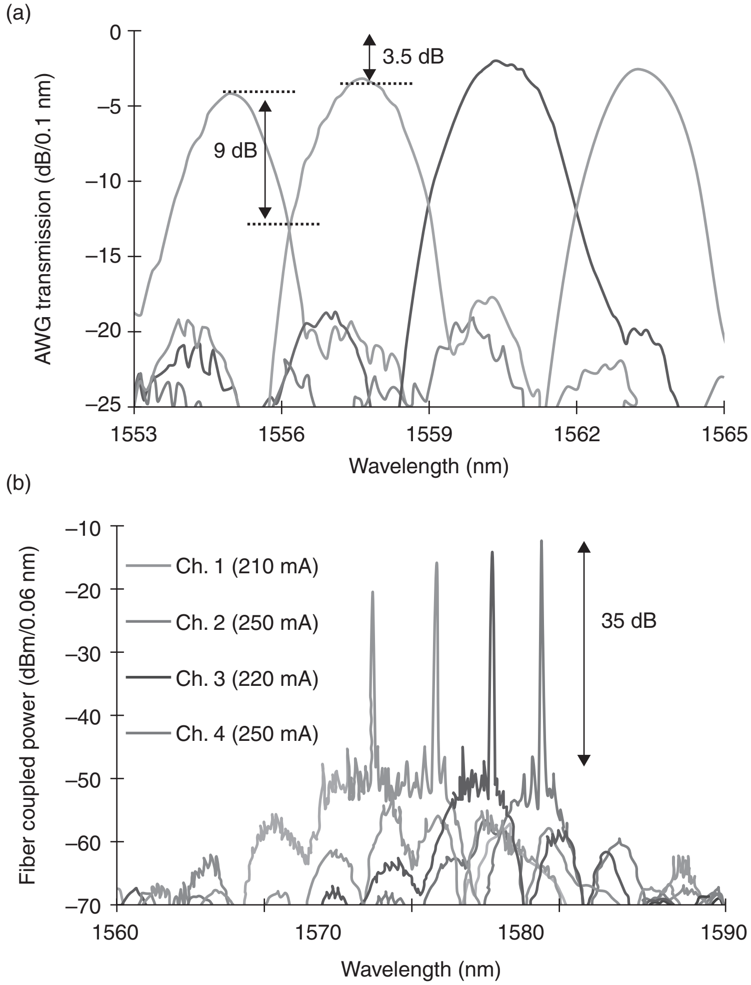

10.22 (a) AWG transmission for randomly polarized light. The average insertion loss and cross talk are 3.5 and 9 dB, respectively. (b) 4-channel lasing spectrum with injection current between 210 and 250 mA (Kurczveil *et al.*, 2011).

higher differential efficiency and higher SMSR is expected in future chips if passive AWG section can be better protected during III-V SOA fabrication processing (Kurczveil *et al.*, 2011).

10.3 Hybrid Si laser-based photonic integrated circuits

Having demonstrated a number of hybrid Si lasers, Si PICs are the next to demonstrate their potential. It means that more devices are fabricated and their individual functionality is linked on the same chip. Single crystalline Si has shown decent versatility to manipulate and absorb light. High-speed Si modulators (Liu *et al.*, 2004; Xu *et al.*, 2005; Liao *et al.*, 2007), optical buffers (Xia *et al.*, 2007), and photodetectors (Geis *et al.*, 2009) have been demonstrated recently. Most of them are not intrinsically optical bandwidth limited, which means the same material and device design (or with a small dimensional tweak) can be duplicated on each signal channel for on-chip wavelength division multiplexing (WDM) application. The only optical bandwidth limited component is the diode lasers, including hybrid Si lasers here, because of limited material gain bandwidth per active region design, typically around 60 nm. It restricts how many channels can be integrated together from a single III-V epitaxial transfer (Park *et al.*, 2011), particularly for coarse WDM with channel spacing > 200 GHz.

The first and most straightforward solution to break gain bandwidth and bandgap limits is simultaneously bonding different epi-layer structures to the selective area in the same Si chip. Then III-V back-end processing is identical for the entire chip. Figure 10.23a shows the photo of the laser array chip after two different III-V epi-layers are transferred to the Si (Park *et al.*, 2011). The chip consists of four DBR lasers with target wavelengths from 1290 to 1350 nm, with a wavelength spacing of 20 nm and a 4:1 Si multiplexer. Figure 10.23b shows the representative lasing spectrum taken at the output of the multiplexer with all four channels operating simultaneously. The lasing wavelengths from the four channels are measured to be 1289.8, 1309.5, 1329.7 and 1348.2 nm, respectively. The thresholds are 180 and 125 mA from epi-structure1, and 165 and 115 mA from epi-structure2, respectively. The ratio of the threshold is 44% between two channels on the same III-V die, due to detuning of one channel from gain peak. The total threshold difference is 56%, over 7× less than that of the same four hybrid DBR lasers fabricated on one epi-structure (Park *et al.*, 2011). The improved overall performance of the four-channel hybrid DBR Si laser array eventually enables the demonstration of a 50 Gb/s transmitter when four Si Mach–Zehnder interferometer (MZI) modulators with 12.5 Gb/s modulator rate are integrated on the same chip (Andrew *et al.*, 2010).

Meanwhile, key components with comparable or even better performance over Si counterparts have also been fabricated on this hybrid Si platform (Park *et al.*, 2007a, 2007b, 2008b; Chen *et al.*, 2008, 2011; Kuo *et al.*, 2008; Tang *et al.*, 2011). But they all rely on III-V bandgap engineering, which either makes integration impossible or has to compromise device performance if only one type of III-V epi-layer structure is used.

Another demonstrated hybrid Si PIC by multiple III-V die selective-area bonding is the hybrid Si integrated triplexer (Chang *et al.*, 2010). As shown in Fig. 10.24, it contains a 1310 nm R3 laser for upstream data transmission as well as 1310/1500 and 1490/1550 nm wavelength selective splitters and

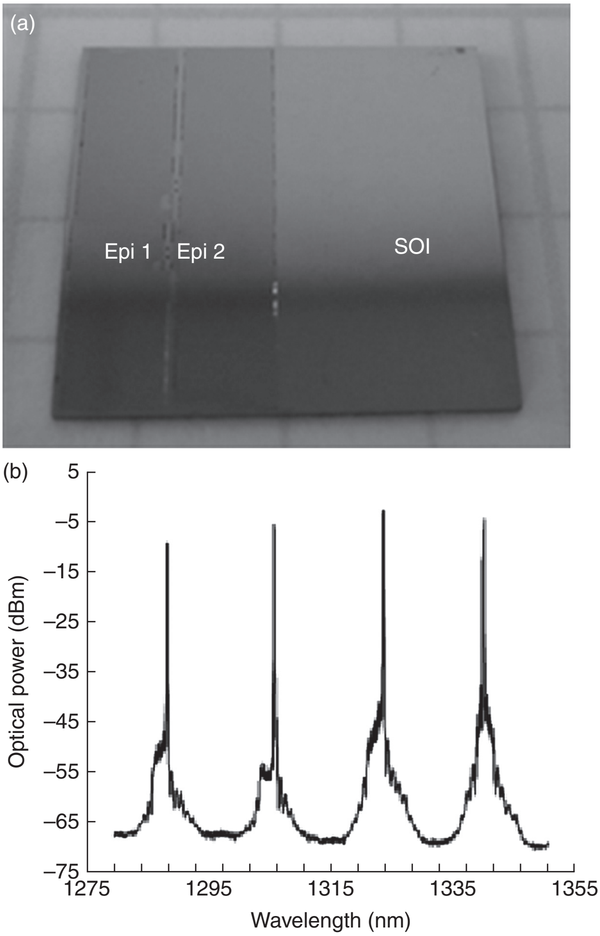

10.23 (a) Photograph of the laser array chip after bonding two types of III-V epi-layers. (b) Representative lasing spectrum of four-channel DBR laser array measured from the integrated silicon multiplexer (Park *et al.*, 2011).

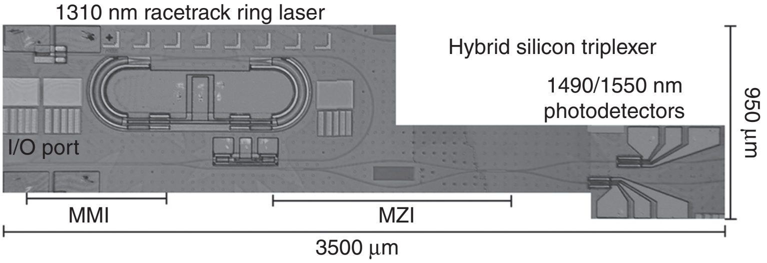
1310 nm racetrack ring laser
Hybrid silicon triplexer
1490/1550 nm
photodetectors
I/O port
MMI
MZI
3500 μm
950 μm

10.24 Photo of a hybrid silicon integrated triplexer chip (Chang *et al.*, 2010).

photodetectors for downstream digital and video reception (Chang *et al.*, 2010). The 1310 nm R3 laser is based on the same III-V epi-structure used in Fig. 10.4b (Chang *et al.*, 2007), while the other is a InGaAs PIN structure designed for high-speed photodetectors to detect 1490 and 1550 nm signals. The device has a compact size of 1 mm × 3.5 mm. The measured upstream channel 3 dB bandwidth of the integrated triplexer is ~2.7 GHz. Eye diagrams of the upstream channel are also measured at 1 and 1.25 GHz PRBS inputs, respectively, which satisfy the data rate requirement of 1.25 GHz for the upstream channel of a triplexer under ITU standards (Chang *et al.*, 2010).

Multiple III-V die selective-area bonding has its own limitations as well. Close integration of two III-V structures is usually very difficult, due to finite size and proximity of bonding two (or more) III-V dies in reality. Hybrid tapers are also required at hybrid/pure Si sections, contributing to insertion loss and design complexity. One solution to this problem involves using a quantum well intermixing technology (QWI) to shift the as-grown QW bandgap across the III-V wafer before bonding.

The QWI technique used in this work combines the selective removal of an InP buffer with implant enhanced intermixing (Skogen, 2003). An outline of the as-grown III-V QWI base structure, along with details of the intermixing process, is shown in Fig. 10.25 (Sysak *et al.*, 2008). The QWI process begins with a blanket phosphorous implant into the patterned III-V base structure as shown in Fig. 10.25a. The implant is used to generate vacancies, which act as a catalyst in the QWI process. The as-grown material bandgap is preserved in the region with SiN_x dielectric protection. Following the implant, the vacancies generated in the InP buffer layer are diffused through the quantum wells and barriers via a rapid thermal anneal (RTA) (Fig. 10.25b). The vacancy diffusion causes atomic interdiffusion between the wells and barriers, modifying their composition, and hence bandgap. Once a desired bandgap has been reached, the InP buffer layer can be selectively etched to remove the vacancies from the intermixing process (Fig. 10.25c). Additional RTA steps are then used to continue shifting the bandgap in regions where the InP buffer remains (Fig. 10.25d). In the end, the InP buffer layer is removed to leave a mirror-like planar III-V surface for epitaxial transfer. It is noted that rough alignment is required here in order to position the right bandgap to the corresponding Si waveguide section.

QWI first largely extends the effective gain bandwidth to make hybrid Si laser array with large lasing wavelength spacing possible. Figure 10.26a shows spectra from the hybrid Si FP lasers that utilize four intermixed bandgaps across the chip. Their lasing peak wavelengths align well with material photoluminescence (PL) peaks at 1540, 1495, 1465, and 1425 nm (Park *et al.*, 2011), respectively. Figure 10.26b shows the pulsed threshold currents and slope efficiencies determined from LI curves as a function of

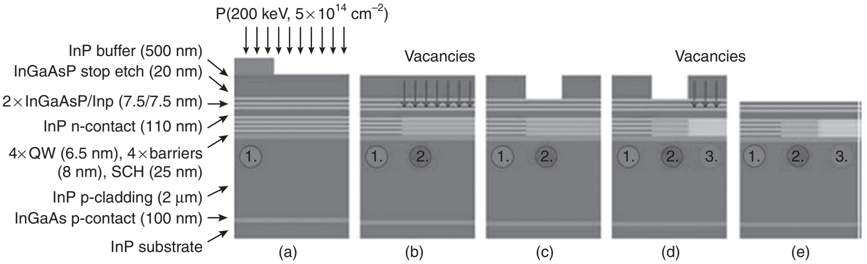
P(200 keV, 5×10^14 cm^−2)
InP buffer (500 nm)
InGaAsP stop etch (20 nm)
2×InGaAsP/Inp (7.5/7.5 nm)
InP n-contact (110 nm)
4×QW (6.5 nm), 4×barriers (8 nm), SCH (25 nm)
InP p-cladding (2 μm)
InGaAs p-contact (100 nm)
InP substrate
Vacancies
Vacancies
1.
2.
3.
(a)
(b)
(c)
(d)
(e)

10.25 Overview of the hybrid laser QWI process. The three bandgaps realized are numbered 1, 2, and 3. (a) Implantation of P into InP buffer with SiNx mask to preserve the as-grown bandgap. (b) Diffusion of vacancies through QWs and barriers for bandgap 2. (c) Removal of InP buffer layer to halt intermixing. (d) Diffusion of vacancies via RTA for bandgap 3. (e) Removal of InP buffer layer and InGaAsP stop etch layer before bonding (Sysak *et al.*, 2008).

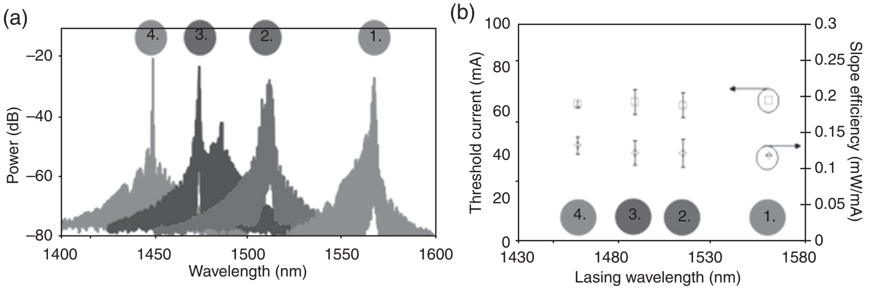

10.26 (a) Lasing spectra from four lasers that utilize the four intermixed bandgaps across the hybrid FP laser chip, (b) threshold current and single sided slope efficiency for an array of 580 μm lasers with different wavelengths (Sysak *et al.*, 2008).

the lasing wavelength for a set of 585 μm long lasers. Threshold currents are 65 ± 5 mA and single side output slope efficiencies are 12% ± 2%, indicating consistent material quality after QWI process (Nie *et al.*, 2005; Park *et al.*, 2011). Recently, 13 CW operational lasers with threshold currents between 40 and 70 mA and maximum power of 4 mW at 20°C have also been realized on a QWI-resultant gain bandwidth from 1255 to 1345 nm (Jain *et al.*, 2010).

Multiple bandgap without material structural discontinuity also allows compact integration with small optical loss at bandgap junctions. A sample-grating (SG) DBR laser integrated with an electroabsorption modulator (EAM) has been successfully fabricated using this technique (Sysak *et al.*, 2008). Figure 10.27 schematically shows the integrated SGDBR-EAM, where the gain region bandgap is at 1520 nm; the mirror

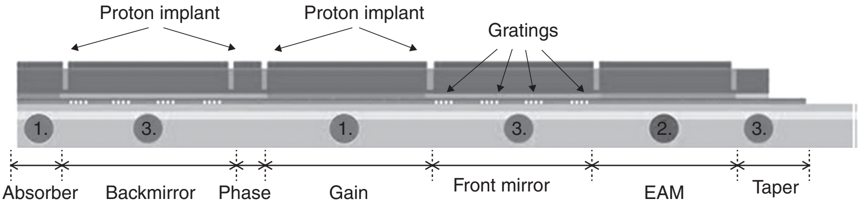

10.27 Schematic cross-section of a hybrid Si SGDBR-EAM shown with four front mirror and back mirror grating bursts (Sysak *et al.*, 2008).

bandgap is at 1440 nm; and the EAM bandgap is at 1480 nm (Sysak *et al.*, 2008). SG-DBR laser operation with around 45 mA threshold, 0.5 mW output and up to 45°C cw lasing has been demonstrated, and integrated EAM shows 2 GHz bandwidth with >5 dB extinction ratio at 6 V reverse bias (Sysak *et al.*, 2008).

More recent progress has been to fabricate hybrid Si DFB lasers externally modulated by on-chip EAMs whose bandgap is shifted 30 nm towards shorter wavelength (Jain *et al.*, 2010). Laser CW operation up to 60°C has been achieved with 4 mW single sided output power at 20°C and a threshold current of 30 mA. The integrated EAMs in this work showed DC extinction of 17 dB at –5V bias and a modulation bandwidth of 2 GHz (Jain *et al.*, 2010). High-speed EAMs with bandwidths of 42 GHz and 2 V drive have been demonstrated (Tang *et al.*, 2011)and can be integrated with hybrid silicon lasers.

10.4 Conclusion

Silicon photonics is a rapidly evolving research field with a tremendous potential. The term, 'semiconductor lasers', now includes a broad spectrum of approaches to lasers on Si. While exciting advances to convert Si to an efficient light-emitting material and monolithic integrated gain medium on the Si substrate continue, lasers realized on the *hybrid Si platform* have rapidly evolved to include ring, DFB, DBR, and SGDBR lasers, as well as PICs based on these laser elements. A vision for terabit transmitters using 25 hybrid DFB Si lasers modulated by 40 Gb/s Si modulators and combined by a passive multiplexer to achieve 1 Tb/s data transmission (Fig. 10.28) is at hand (Fang *et al.*, 2008). The challenge is to combine this technology with CMOS processing on a 200 or 300 mm wafer scale.

Lasers on Si are a reality. The recent progress to make lasers on Si, regardless of the lasing mechanism, is exciting. New opportunities continue to appear. The pin count needed for advanced electronic chips is rapidly approaching a practical limit of 2000 balls. Further, the power required to drive these interconnects is typically 40% or more of the total power and is

10.28 Schematic of a Si terabit transmitter with 25 single-wavelength hybrid Si lasers externally modulated at 40 Gb/s (Fang *et al.*, 2008).

a major contributor to the power density problem limiting advanced electronics. Silicon photonics is on the verge of being able to compete for lower power off-chip and on-chip interconnects (Miller, 2009) and thus solve the power and pin problems of electronics, provided we can reduce the laser size, cost and power, and increase the yield of lasers on Si.

The authors thank Scott Rodgers, Ron Esman, Mike Haney and Jag Shah of DARPA/MTO, the Kavli Foundation, Intel and Hewlett Packard for funding this research. Many others contributed to the hybrid silicon research described here, including Alexander Fang, Hyundai Park, Daniel Blumenthal, Hsu-Hao Chang, Hui-Wen Chen, Martijn Heck, Geza Kurczveil, Siddharth Jain, Sudha Srinivasan, Daoxin Dai, Richard Jones, Matthew Sysak, Brian Koch, Mario Paniccia, Omri Raday, Hanan Bar, Marco Fiorentino and Raymond Beausoleil.

10.5 References

Andrew, A., Ling, L., Richard, J., Michael, M., Brian, K., Wei-Zen, L., Juthika, B., Brian, K., Hai-Feng, L., Haisheng, R., Matthew, S., Christine, K., Rushdy, S., Dror, L., Lior, H., Roi, B., Stas, L., Ansheng, L., Kevin, S., Olufemi, D., Neil, N., Tao, Y., Frederick, H., Hsieh, I. W., John, H., Robert, B., Hyundai, P., Jock, B., Simon, L., Hat, N., Hinmeng, A., Katie, N., Priya, M., Mahtab, H. and Mario, P. (2010) Demonstration of a High Speed 4-Channel Integrated Silicon Photonics WDM Link with Hybrid Silicon Lasers. *Integrated Photonics Research, Silicon and Nanophotonics*. Optical Society of America.

Bisi, O., Ossicini, S. and Pavesi, L. (2000) Porous silicon: A quantum sponge structure for silicon based optoelectronics. *Surface Science Reports,* **38**, 1–126.

Canham, L. T. (1990) Silicon quantum wire array fabrication by electrochemical and chemical dissolution of wafers. *Applied Physics Letters,* **57**, 1046–1048.

Cerutti, L., Rodriguez, J. B. and Tournie, E. (2010) GaSb-based laser, monolithically grown on silicon substrate, emitting at 1.55 um at room temperature. *IEEE Photonics Technology Letters,* **22**, 553–555.

Chang, H.-H., Fang, A. W., Sysak, M. N., Park, H., Jones, R., Cohen, O., Raday, O., Paniccia, M. J. and Bowers, J. E. (2007) 1310 nm silicon evanescent laser. *Optics Express,* **15**, 11466–11471.

Chang, H.-H., Kuo, Y.-H., Chen, H.-W., Jones, R., Barkai, A., Paniccia, M. J. and Bowers, J. E. (2010) Integrated Triplexer on Hybrid Silicon Platform. *OFC/NFOEC*. San Diego, CA, USA.

Chen, H.-W., Kuo, Y.-H. and Bowers, J. E. (2008) A hybrid silicon AlGaInAs phase modulator. *Photonics Technology Letters, IEEE,* **20**, 1920–1922.

Chen, H.-W., Peters, J. D. and Bowers, J. E. (2011) Forty Gb/s hybrid silicon Mach-Zehnder modulator with low chirp. *Optics Express***, 19**, 1455–1460.

Chen, R., Tran, T.-T. D., Ng, K. W., Ko, W. S., Chuang, L. C., Sedgwick, F. G. and Chang-Hasnain, C. (2010) As-grown InGaAs nanolasers for integrated silicon photonics. *Integrated Photonics Research, Silicon and Nanophotonics (IPRSN*). Monterey, CA, USA.

Cheng, S.-L., Lu, J., Shambat, G., Yu, H.-Y., Saraswat, K., Vuckovic, J. and Nishi, Y. (2009) Room temperature 1.6 um electroluminescence from Ge light emitting diode on Si substrate. *Optics Express,* **17**, 10019–10024.

Cloutier, S. G., Kossyrev, P. A. and Xu, J. (2005) Optical gain and stimulated emission in periodic nanopatterned crystalline silicon. *Nature Materials,* **4**, 887–891.

Coldren, L. A. and Corzine, S. W. (1995) *Diode Lasers and Photonic Integrated Circuits*, New York, USA, Wiley-Interscience.

Cullis, A. G. and Canham, L. T. (1991) Visible light emission due to quantum size effects in highly porous crystalline silicon. *Nature,* **353**, 335–338.

Dragic, P. D. (2004) Injection-seeded Q-switched fiber ring laser. *IEEE Photonics Technology Letters,* **16**, 1822–1824.

Fang, A. W. (2008) Silicon evanescent lasers. *Department of Electrical and Computer Engineering*. Santa Barbara, University of California.

Fang, A. W., Jones, R., Park, H., Cohen, O., Raday, O., Paniccia, M. J. and Bowers, J. E. (2007a) Integrated AlGaInAs-silicon evanescent race track laser and photodetector. *Optics Express,* **15**, 2315–2322.

Fang, A. W., Koch, B. R., Jones, R., Lively, E., Di, L., Ying-Hao, K. and Bowers, J. E. (2008) A distributed Bragg reflector silicon evanescent laser. *IEEE Photonics Technology Letters,* **20**, 1667–1669.

Fang, A. W., Lively, E., Kuo, Y.-H., Liang, D. and Bowers, J. E. (2008) A distributed feedback silicon evanescent laser. *Optics Express,* **16**, 4413–4419.

Fang, A. W., Park, H., Cohen, O., Jones, R., Paniccia, M. J. and Bowers, J. E. (2006) Electrically pumped hybrid AlGaInAs-silicon evanescent laser. *Optics Express,* **14**, 9203–9210.

Fang, A. W., Park, H., Kuo, Y.-H., Jones, R., Cohen, O., Liang, D., Raday, O., Sysak, M. N., Paniccia, M. J. and Bowers, J. E. (2007b) Hybrid silicon evanescent devices. *Materials Today,* **10**, 28–35.

Fang, A. W., Sysak, M. N., Koch, B. R., Jones, R., Lively, E., Liang, D., Raday, O. and Bowers, J. E. (2009) Single wavelength silicon evanescent lasers. *IEEE Journal of Selected Topics in Quantum Electronics,* **15**, 535–544.

Geis, M. W., Spector, S. J., Grein, M. E., Yoon, J. U., Lennon, D. M. and Lyszczarz, T. M. (2009) Silicon waveguide infrared photodiodes with >35 GHz bandwidth and phototransistors with 50 AW-1 response. *Optics Express,* **17**, 5193–5204.

Gösele, U. and Lehmann, V. (1995) Light-emitting porous silicon. *Materials Chemistry and Physics,* **40**, 253–259.

Groenert, M. E., Leitz, C. W., Pitera, A. J., Yang, V., Lee, H., Ram, R. J. and Fitzgerald, E. A. (2003a) Monolithic integration of room-temperature cw GaAs/AlGaAs lasers on Si substrates via relaxed graded GeSi buffer layers. *Journal of Applied Physics,* **93**, 362–367.

Groenert, M. E., Pitera, A. J., Ram, R. J. and Fitzgerald, E. A. (2003b) Improved room-temperature continuous wave GaAs/AlGaAs and InGaAs/GaAs/AlGaAs lasers fabricated on Si substrates via relaxed graded Ge_xSi_{1-x} buffer layers. *Journal of Vacuum Science & Technology B: Microelectronics and Nanometer Structures,* **21**, 1064–1069.

Hill, M. T., Dorren, H. J. S., De Vries, T., Leijtens, X. J. M., Den Besten, J. H., Smalbrugge, B., Oei, Y.-S., Binsma, H., Khoe, G.-D. and Smit, M. K. (2004) A fast low-power optical memory based on coupled micro-ring lasers. *Nature,* **432**, 206–209.

Hirschman, K. D., Tsybeskov, L., Duttagupta, S. P. and Fauchet, P. M. (1996) Silicon-based visible light-emitting devices integrated into microelectronic circuits. *Nature,* **384**, 338–341.

Iacona, F., Irrera, A., Franz, G., Pacifici, D., Crupi, I., Miritello, M. P., Presti, C. D. and Priolo, F. (2006) Silicon-based light-emitting devices: Properties and applications of crystalline, amorphous and Er-doped nanoclusters. *IEEE Journal of Selected Topics in Quantum Electronics,* **12**, 1596–1606.

Jain, S. R., Sysak, M. N., Kurczveil, G. and Bowers, J. E. (2010) Integrated broadband hybrid silicon DFB laser array using quantum well intermixing. *European Conference on Optical Communication*. Torino, Italy.

Jones, R., Koch, B., Sysak, M., Fang, A., Lively, E., Liang, D., Kuo, Y. H. and Bowers, J. E. (2009) Grating based hybrid silicon lasers. *Proceeding of SPIE*. San Jose, CA, USA.

Kang, Y., Liu, H.-D., Morse, M., Paniccia, M. J., Zadka, M., Litski, S., Sarid, G., Pauchard, A., Kuo, Y.-H., Chen, H.-W., Zaoui, W. S., Bowers, J. E., Beling, A., Mcintosh, D. C., Zheng, X. and Campbell, J. C. (2008) Monolithic germanium/silicon avalanche photodiodes with 340 GHz gain-bandwidth product. *Nature Photonics,* **3**, 59–63.

Kang, Y., Morse, M. and Paniccia, M. J. (2009) Monolithic Ge/Si Avalanche photodiodes. *The 6th IEEE international conference on Group IV Photonics*. San Francisco, CA, USA.

Kawanami, H. (2001) Heteroepitaxial technologies of III-V on Si. *Solar Energy Materials and Solar Cells,* **66**, 479–486.

Kunert, B., Volz, K., Koch, J. and Stolz, W. (2006) Direct-band-gap Ga(NAsP)-material system pseudomorphically grown on GaP substrate. *Applied Physics Letters,* **88**, 182108.

Kunert, B., Zinnkann, S., Volz, K. and Stolz, W. (2008) Monolithic integration of Ga(NAsP)/(BGa)P multi-quantum well structures on (001) silicon substrate by MOVPE. *Journal of Crystal Growth,* **310**, 4776–4779.

Kuo, Y.-H., Chen, H.-W. and Bowers, J. E. (2008) High speed hybrid silicon evanescent electroabsorption modulator. *Optics Express,* **16**, 9936–9941.

Kuo, Y.-H., Lee, Y. K., Ge, Y., Ren, S., Roth, J. E., Kamins, T. I., Miller, D. A. B. and Harris, J. S. (2005) Strong quantum-confined Stark effect in germanium quantum-well structures on silicon. *Nature,* **437**, 1334–1336.

Kurczveil, G., Heck, M. J. R., Peters, J. D., Garcia, J. M., Spencer, D. and Bowers, J. E. (2011) An integrated hybrid silicon multiwavelength AWG laser. *IEEE Journal of Selected Topics in Quantum Electronics*, online article.

Lee, K. K., Lim, D. R., Luan, H.-C., Agarwal, A., Foresi, J. and Kimerling, L. C. (2000) Effect of size and roughness on light transmission in a Si/SiO$_2$ waveguide: Experiments and model. *Applied Physics Letters,* **77**, 1617–1619.

Liang, D. and Bowers, J. E. (2008) Highly efficient vertical outgassing channels for low-temperature InP-to-silicon direct wafer bonding on the silicon-on-insulator (SOI) substrate. *Journal of Vacuum Science & Technology B,* **26**, 1560–1568.

Liang, D. and Bowers, J. E. (2009) Photonic integration: Si or InP substrates? *Electronics Letters* (invited insight letter) **45**, 578–581.

Liang, D. and Bowers, J. E. (2010) Recent progress in lasers on silicon. *Nature Photonics,* **4**, 511–517.

Liang, D., Bowers, J. E., Oakley, D. C., Napoleone, A., Chapman, D. C., Chen, C.-L., Juodawlkis, P. W. and Raday, O. (2009a) High-quality 150 mm InP-to-silicon epitaxial transfer for silicon photonic integrated circuits. *Electrochemical Solid-State Letters,* **12**, H101–H104.

Liang, D., Chapman, D., Li, Y., Oakley, D. C., Napoleone, T., Juodawlkis, P. W., Brubaker, C., Mann, C., Bar, H., Raday, O. and Bowers, J. E. (2011a) Uniformity study of wafer-scale InP-to-silicon hybrid integration. *Applied Physics A: Materials Science & Processing,* **103**, 213–218.

Liang, D., Fiorentino, M., Beausoleil, R. G. and Bowers, J. E. (2010) Compact low-threshold hybrid silicon microring resonator lasers. *IEEE Winter Topicals.* Marjoca, Spain.

Liang, D., Fiorentino, M., Okumura, T., Chang, H.-H., Spencer, D., Kuo, Y.-H., Fang, A. W., Dai, D., Beausoleil, R. G. and Bowers, J. E. (2009b) Hybrid silicon ($\lambda = 1.5$ μm) microring lasers and integrated photodetectors. *Optics Express,* **17**, 20355–20364.

Liang, D., Fiorentino, M., Srinivasan, S., Todd, S. T., Kurczveil, G., Bowers, J. E. and Beausoleil, R. G. (2011b) Optimization of hybrid silicon microring lasers. *IEEE Photonics Journal*, **3**, 580–587.

Liang, D., Fiorentino, M., Todd, S. T., Kurczveil, G., Beausoleil, R. G. and Bowers, J. E. (2011c) Fabrication of silicon-on-diamond substrate and low-loss optical waveguides. *IEEE Photonics Technology Letters,* **23**, 657–659.

Liang, D., Fiorentino, M., Todd, S. T., Kurczveil, G., Beausoleil, R. G. and Bowers, J. E. (2011d) Low-loss silicon-on-diamond optical waveguides. *CLEO*. Baltimore, MD, USA.

Liao, L., Liu, A., Basak, J., Nguyen, H., Paniccia, M., Rubin, D., Chetrit, Y., Cohen, R. and Izhaky, N. (2007) 40 Gbit/s silicon optical modulator for highspeed applications. *Electronics Letters,* **43**, 1196–1197.

Liu, A., Jones, R., Liao, L., Samara-Rubio, D., Rubin, D., Cohen, O., Nicolaescu, R. and Paniccia, M. (2004) A high-speed silicon optical modulator based on a metal-oxide-semiconductor capacitor. *Nature,* **427**, 615–618.

Liu, J., Sun, X., Camacho-Aguilera, R., Kimerling, L. C. and Michel, J. (2010) Ge-on-Si laser operating at room temperature. *Optics Letters,* **35**, 679–681.

Liu, J., Sun, X., Pan, D., Wang, X., Kimerling, L. C., Koch, T. L. and Michel, J. (2007) Tensile-strained, n-type Ge as a gain medium formonolithic laser integration on Si. *Optics Express,* **15**, 11272–11277.

Lu, Z. H., Lockwood, D. J. and Baribeau, J. M. (1995) Quantum confinement and light emission in SiO_2/Si superlattices. *Nature,* **378**, 258–260.

Malinin, A., Ovchinnikov, V., Novikov, S., Tuovinen, C. and Hovinen, A. (2000) Fabrication of a silicon based electroluminescent device *Materials Science and Engineering B,* **74**, 32–35.

Masafumi, Y., Mitsuru, S. and Yoshio, I. (1989) Misfit stress dependence of dislocation density reduction in GaAs films on Si substrates grown by strained-layer superlattices. *Applied Physics Letters,* **54**, 2568–2570.

Mi, Z., Yang, J., Bhattacharya, P., Chan, P. K. L. and Pipe, K. P. (2006) High performance self-organized InGaAs quantum dot lasers on silicon. *Journal of Vacuum Science and Technology B*, **24**, 1519–1522.

Miller, D. A. B. (2009) Device requirements for optical interconnects to silicon chips. *Proceedings of IEEE,* 9**7**, 1166–1185.

Minoru, F., Masato, Y., Yoshihiko, K., Shinji, H. and Keiichi, Y. (1997) 1.54 μm photoluminescence of Er3+ doped into SiO2 films containing Si nanocrystals: Evidence for energy transfer from Si nanocrystals to Er3+. *Applied Physics Letters,* **71**, 1198–1200.

Nassiopoulos, A. G., Grigoropoulos, S. and Papadimitriou, D. (1996) Electroluminescent device based on silicon nanopillars. *Applied Physics Letters,* **69**, 2267–2269.

Nie, D., Mei, T., Djie, H. S., Chin, M. K., Tang, X. H. and Wang, Y. X. (2005) Implementing multiple bandgaps using inductively coupled argon plasma enhanced quantum well intermixing. *Journal of Vacuum Science and Technology B,* **23**, 1050–1053.

Nozawa, K. and Horikoshi, Y. (1991) Low threading dislocation density GaAs on Si(100) with InGaAs/GaAs strained-layer superlattice grown by migration-enhanced epitaxy. *Japanese Journal of Applied Physics,* **30**, L668–L671.

Park, H., Fang, A. W., Jones, R., Cohen, O., Raday, O., Sysak, M. N., Paniccia, M. J. and Bowers, J. E. (2007a) A hybrid AlGaInAs-silicon evanescent waveguide photodetector. *Optics Express,* **15**, 6044–6052.

Park, H., Fang, A. W., Kodama, S. and Bowers, J. E. (2005) Hybrid silicon evanescent laser fabricated with a silicon waveguide and III-V offset quantum wells. *Optics Express,* **13**, 9460–9464.

Park, H., Fang, A. W., Liang, D., Kuo, Y.-H., Chang, H.-H., Koch, B. R., Chen, H.-W., Sysak, M. N., Jones, R. and Bowers, J. E. (2008a) Photonic integration on the hybrid silicon evanescent device platform. *Advances in Optical Technologies,* **2008**, Article ID 682978.

Park, H., Kuo, Y.-H., Fang, A. W., Jones, R., Cohen, O., Paniccia, M. J. and Bowers, J. E. (2007b) A hybrid AlGaInAs-silicon evanescent preamplifier and photodetector. *Optics Express,* **15**, 13539–13546.

Park, H., Mack, J. P., Bluementhal, D. J. and Bowers, J. E. (2008b) An integrated recirculating optical buffer. *Optics Express,* **16**, 11124–11131.

Park, H., Sysak, M. N., Chen, H.-W., Fang, A. W., Liang, D., Liao, L., Koch, B. R., Bovington, J., Tang, Y., Wong, K., Jacob-Mitos, M., Jones, R. and Bowers, J. E.

(2011) Device and integration technology for silicon photonic transmitters. *IEEE Journal of Selected Topics in Quantum Electronics*, online article.

Pasquariello, D. and Hjort, K. (2002) Plasma-assisted InP-to-Si low temperature wafer bonding. *IEEE Journal of Selected Topics in Quantum Electronics,* **8**, 118–131.

Pavesi, L. (2005) Routes toward silicon-based lasers. *Materials Today,* **8**, 18–25.

Pavesi, L. (2008) Silicon-based light sources for silicon integrated circuits. *Advances in Optical Technologies,* **2008**, Article ID 416926.

Pavesi, L. (2009) Optical gain and lasing in low dimensional silicon: The quest for an injection laser. In Koshida, N. (Ed.) *Device Applications of Silicon Nanocrystals and Nanostructures.* New York, Springer US, 103.

Pavesi, L., Dal Negro, L., Mazzoleni, C., Franzo, G. and Priolo, F. (2000) Optical gain in silicon nanocrystals. *Nature,* **408**, 440–444.

Poguntke, K. R., Soole, J. B. D., Scherer, A., Leblanc, H. P., Caneau, C., Bhat, R. and Koza, M. A. (1993) Simultaneous multiple wavelength operation of a multistripe array grating integrated cavity laser. *Applied Physics Letters,* **62**, 2004–2006.

Roelkens, G., Van Thourhout, D., Baets, R., Notzel, R. and Smit, M. (2006) Laser emission and photodetection in an InP/InGaAsP layer integrated on and coupled to a Silicon-on-Insulator waveguide circuit. *Optics Express,* **14**, 8154–8159.

Rong, H., Jones, R., Liu, A., Cohen, O., Hak, D., Fang, A. and Paniccia, M. (2005) A continuous-wave Raman silicon laser. *Nature,* **433**, 725–728.

Roth, J. E., Fidaner, O., Schaevitz, R. K., Kuo, Y.-H., Kamins, T. I., Harris, J. S. and Miller, D. A. B. (2007) Optical modulator on silicon employing germanium quantum wells. *Optics Express,* **15**, 5851–5859.

Samonji, K., Yonezu, H., Takagi, Y., Iwaki, K., Ohshima, N., Shin, J. K. and Pak, K. (1996) Reduction of threading dislocation density in InP-on-Si heteroepitaxy with strained short-period superlattices. *Applied Physics Letters,* **69**, 100–102.

Skogen, E. (2003) *Quantum Well Intermixing for Wavelength Agile Photonic Integrated Circuits*. University of California, Santa Barbara.

Soref, R. and Larenzo, J. (1986) All-silicon active and passive guided-wave components for λ = 1.3 and 1.6 μm. *IEEE Journal of Quantum Electronics,* **22**, 873–879.

Sorel, M., Laybourn, P. J. R., Giuliani, G. and Donati, S. (2002) Unidirectional bistability in semiconductor waveguide ring lasers. *Applied Physics Letters,* **80**, 3051–3053.

Spuesens, T., Liu, L., Vries, T. D., Romeo, P. R., Regreny, P. and Thourhout, D. V. (2009) Improved design of an InP-based microdisk laser heterogeneously integrated with SOI. *The 6th IEEE International Conference on Group IV Photonics.* San Francisco, CA, USA.

Srinivasan, S., Fang, A. W., Liang, D., Peters, J., Kaye, B. and Bowers, J. E. (2011) Design of phase-shifted hybrid silicon distributed feedback lasers. *Optics Express,* **19**, 9255–9261.

Staring, A. A. M., Spiekman, L. H., Binsma, J. J. M., Jansen, E. J., Dongen, T. V., Thijs, P. J. A., Smit, M. K. and Verbeek, B. H. (1996) A compact nine-channel multiwavelength laser. *IEEE Photonics Technology Letters,* **8**, 1139–1141.

Sun, X., Liu, J., Kimerling, L. C. and Michel, J. (2009) Room-temperature direct bandgap electroluminesence from Ge-on-Si light-emitting diodes. *Optics Letters,* **34**, 1198–1200.

Sysak, M. N., Anthes, J. O., Bowers, J. E., Raday, O. and Jones, R. (2008) Integration of hybrid silicon lasers and electroabsorption modulators. *Optics Express,* **16**, 12478–12486.

Sysak, M. N., Liang, D., Fiorentino, M., Beausoleil, R. G., Kurceival, G., Piels, M., Jones, R. and Bowers, J. E. (2011) Hybrid silicon evanescent laser technology: A thermal perspective. *IEEE Journal of Selected Topics in Quantum Electronics*, **17**, 1490–1498.

Sysak, M. N., Park, H., Fang, A. W., Bowers, J. E., Jones, R., Cohen, O., Raday, O. and Paniccia, M. J. (2007) Experimental and theoretical thermal analysis of a hybrid silicon evanescent laser. *Optics Express,* **15**, 15041–15046.

Tang, Y., Chen, H.-W., Jain, S., Peters, J. D., Westergren, U. and Bowers, J. E. (2011) 50 Gb/s hybrid silicon traveling-wave electroabsorption modulator *Optics Express,* **19**, 5811–5816.

Van Campenhout, J., Liu, L., Romeo, P. R., Van Thourhout, D., Seassal, C., Regreny, P., Di Cioccio, L., Fedeli, J. M. and Baets, R. (2008) A compact SOI-integrated multiwavelength laser source based on cascaded InP microdisks. *IEEE Photonics Technology Letters,* **20**, 1345–1347.

Van Campenhout, J., Rojo Romeo, P., Regreny, P., Seassal, C., Van Thourhout, D., Verstuyft, S., Di Cioccio, L., Fedeli, J. M., Lagahe, C. and Baets, R. (2007) Electrically pumped InP-based microdisk lasers integrated with a nanophotonic silicon-on-insulator waveguide circuit. *Optics Express,* **15**, 6744–6749.

Wilson, W. L., Szajowski, P. F. and Brus, L. E. (1993) Quantum confinement in size-selected, surface-oxidized silicon nanocrystals. *Science,* **262**, 1242–1244.

Xia, F., Sekaric, L. and Vlasov, Y. (2007) Ultracompact optical buffers on a silicon chip. *Nature Photon,* **1**, 65–71.

Xie, Y. H., Wang, K. L. and Kao, Y. C. (1985) An investigation on surface conditions for Si molecular beam epitaxial (MBE) growth. *Journal of Vacuum Science & Technology A: Vacuum, Surfaces, and Films,* **3**, 1035–1039.

Xu, Q., Schmidt, B., Pradhan, S. and Lipson, M. (2005) Micrometre-scale silicon electro-optic modulator. *Nature,* **435**, 325–327.

Yamaichi, E., Ueda, T., Gao, Q., Yamagishi, C. and Akiyama, M. (1994) Method to obtain low-dislocation-density regions by patterning with SiO2 on GaAs/Si followed by annealing. *Japanese Journal of Applied Physics,* **33**, L1442–L1444.

11

Gallium antimonide (GaSb)-based type-I quantum well diode lasers: recent development and prospects

G. BELENKY and L. SHTERENGAS, State University
of New York at Stony Brook, USA, M. V. KISIN, Ostendo
Technologies, Inc., USA and T. HOSODA, State University of
New York at Stony Brook, USA

DOI: 10.1533/9780857096401.3.441

Abstract: Type-I quantum well gallium antimonide (GaSb)-based diode lasers are the most suitable for operating within the spectral region of 2 to 3.5 µm. This chapter reviews the general milestones in the development of this technology. Specific features of the laser heterostructures, current device performance parameters, and prospects for further development are discussed.

Key words: diode laser, infrared, quantum well, waveguide, optical mode, optical loss, threshold current.

11.1 Introduction

Binary, ternary, quaternary and, recently, quinary alloys with lattice constants matching or close to the lattice constant of GaSb have become increasingly important materials for mid infrared optoelectronics. Fundamental band gaps and band alignment of binary arsenides and antimonides define an extraordinarily wide range of energies available for bandgap engineering (Fig. 11.1) (Vurgaftman *et al.,* 2001). Large conduction band discontinuity between AlSb and InAs can be utilized for the development of intersubband and quantum cascade lasers for mid infrared applications (Devenson *et al.,* 2007a, 2007b; Cathabard *et al*., 2010). Staggered band alignment between InAs and GaSb can span the spectral range from mid infrared to far infrared, and corresponding optically pumped lasers have been reported (Kaspi and Ongstad, 2006). Interband cascade lasers have been developed using type-II W quantum wells (QW) in the active region (Kim *et al*., 2008; Vurgaftman *et al*., 2009; Caffey *et al*., 2010). In this chapter we discuss the peculiarities of the design of diode lasers with type-I QWs in the active region. Active type-I QW compositions acceptable for pseudomorphic

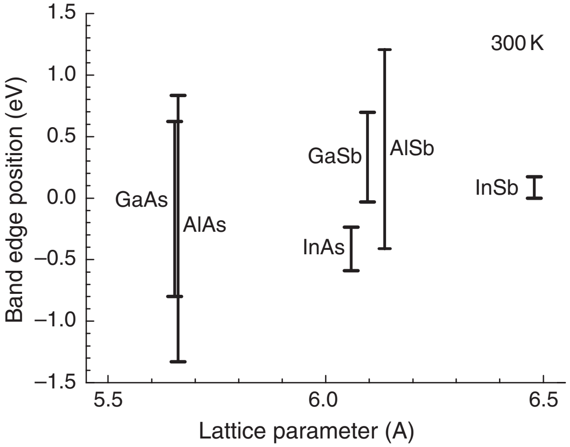

11.1 Band gap positions of selected binary alloys. Energy is referenced to InSb valence band top.

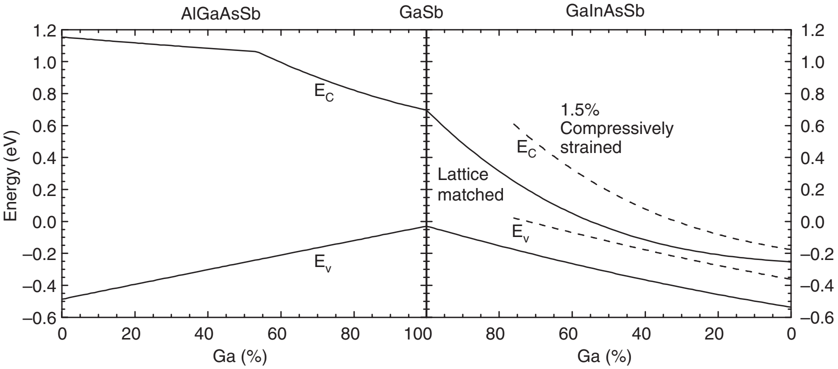

11.2 Band-edge positions for AlGaAsSb and GaInAsSb alloys lattice matched to GaSb (solid lines) and 1.5% compressively strained (dashed lines). Data according to Vurgaftman *et al.* (2001); valence band bowing is neglected.

growth on GaSb substrates restrict the optical range for the corresponding antimonide structures to below 4 μm. Figure 11.2 plots the band-edge positions of the AlGaAsSb and GaInAsSb quaternary alloys with variable Ga composition. The requirement for pseudomorphic growth enforces increased As content in alloys where Ga is replaced by Al or In. Compressive strain can be introduced into GaInAsSb QWs with AlGaAsSb barriers to improve hole confinement. Adding In into AlGaAsSb would require the inclusion of more As, in order to match the lattice of the GaSb substrate, thus improving hole confinement in GaInAsSb QWs even further. The use of quinary alloys and the beneficial role of compressive strain above 1% in active GaInAsSb QWs are discussed in detail.

Diode lasers with type-I QW active regions grown by solid-source molecular beam epitaxy on GaSb substrates currently operate at room temperature in the spectral region from below 2 μm and up to 3.5 μm. The typical laser heterostructure utilizes direct-bandgap GaInAsSb alloys for QWs and AlGaInAsSb alloys (with either direct or indirect bandgap) for barriers, waveguide cores and cladding layers. The laser active region contains several compressively strained GaInAsSb QWs where the width of the QW layers range from 7 to 16 nm. It has already become typical in modern laser designs to have QW compressive strains in excess of 1%. The total thickness of the laser heterostructure, including all auxiliary layers, is about 6 μm. Devices operate under a forward bias voltage of 1.5–2 V. The heterostructures are typically grown onto 2–inches-GaSb substrates doped with tellurium up to 10^{17}–10^{18} cm^{-3}. Epi-ready GaSb substrates of 3 inches diameter have recently become commercially available.

The feasibility of room temperature (RT) continuous wave (CW) high power operation of diode lasers with emission wavelengths above 2 μm was for a long time subject to debate, due to the common belief that the Auger recombination in combination with free carrier absorption could lead to excessive threshold current density for lasing. As of the year 2011, however, the RT CW operation of GaSb-based diode lasers was achieved at emission wavelengths as high as 3.44 μm. The success of the development of long-wavelength antimonide-based diode lasers is mainly attributable to a well-established fact: the narrowing of the active QW bandgap leads to a reduction of the density of states (DOS). The electron band-edge effective mass scales down with the material bandgap, while the in-plane effective mass in the upper hole subband decreases with the compressive strain. The lower DOS of electrons and holes in lasing states implies that a lower level of carrier injection would be required to achieve QW population inversion. Since the optical matrix element does not show pronounced energy dependence in the 1–4 μm spectral range, the transparency and threshold carrier concentrations can be expected to scale down with the increasing wavelength.

Mid infrared diode lasers are expected to have much lower transparency and, possibly, lower threshold carrier concentrations in comparison to their near infrared counterparts. Auger recombination is a three-particle process and its net rate is superlinear in carrier concentration. The threshold current density of mid infrared diode lasers can therefore be rather low, despite the increased probability of an individual Auger event in narrow-bandgap QWs.

Detailed calculations of QW optical characteristics show that an increase in the emission wavelength from 2 to 3.5 μm can be accompanied by a nearly two-fold reduction of the QW transparency carrier concentration,

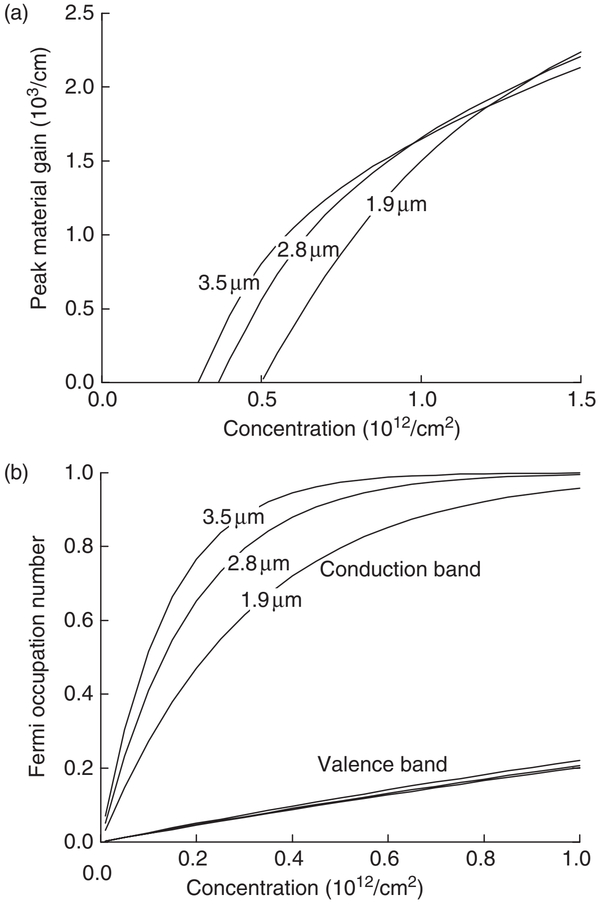

11.3 QW characteristics *vs* 2D carrier concentration level in three QWs with different emission wavelengths: (a) peak material gain; (b) Fermi occupation numbers for QW lasing states.

which has a favorable effect on laser performance. Figure 11.3a illustrates this trend by showing the concentration dependence of the peak QW material gain (maximum gain of QW-confined carriers divided by the QW width) for a set of three 10 nm wide QWs with progressively longer band-edge emission wavelengths. All three modeled QW compositions, $Ga_{0.75}In_{0.25}Sb$, $Ga_{0.55}In_{0.45}As_{0.19}Sb_{0.81}$ and $Ga_{0.40}In_{0.60}As_{0.32}Sb_{0.68}$, have the same compressive strain of 1.5% and emit near 1.9, 2.8 and 3.5 μm, respectively. The wide-gap $AlAs_{0.08}Sb_{0.92}$ barriers were chosen for clarity of presentation. They provide ample confinement for both electrons (from above 600 meV for 1.9 μm to above 1100 meV for 3.5 μm emitting QW) and holes (from above 500 meV for 1.9 μm to above 300 meV for 3.5 μm emitting QW), so that the resulting reduction in QW transparency concentration could be attributed solely to the decrease in confined carrier DOS. To achieve consistency in the calculations, all the material parameters for binaries were taken from a single source (Vurgaftman *et al.*, 2001). An interpolation scheme for alloy materials was adopted from Donati *et al.* (2003); however, the valence band-edge bowing was ignored due to a lack of reliable experimental information. Calculations were performed using COMSOL-based simulation software developed at Ostendo Technologies for the design of III–V semiconductor optoelectronic components (Kisin and El-Ghoroury, 2010). Special attention was paid to creating a detailed microscopic description of carrier confinement in active QWs. Confined states were calculated using a multi-band matrix Hamiltonian with strain-induced deformation potentials and valence band mixing terms (Bir and Pikus, 1974). QW optical characteristics were derived from the calculated complex susceptibility of injected carriers, taking into account thermal carrier redistribution between QW subbands. The calculations proved that transparency concentration improvement in longer-wavelength QWs is predominantly related to the conduction band DOS decrease. Figure 11.3b shows the Fermi occupation numbers for zone-centered states of the lowest (lasing) QW subbands. The hole state occupations can be seen to be lagging behind even at injection levels well beyond the QW transparency level. This is an obvious result of the close proximity of the next hole subbands in 10 nm wide QWs, which tends to obscure the DOS improvement in the uppermost valence band subband, and prevents overall DOS balancing in strained QWs. Further QW optimization might be necessary to improve the differential gain, which remains practically unaffected at transparency level in all three QWs. The QW radiative current at a given concentration decreases with the reduction of the confined carrier DOS, thus enhancing the differential gain characteristics with respect to injection current. This effect, however, is more relevant to the performance of shorter wavelength emitters, where the radiative current constitutes a large part of the threshold (Kisin *et al.*, 2009a, 2009b). In long-wavelength MIR lasers, the radiative component of the threshold becomes less important, since the radiative recombination rate scales down as a square of the optical transition energy.

In order to take full advantage of the lower carrier DOS in narrow-gap active QWs, an adequate carrier confinement should be provided in the laser active region. In GaSb-based laser heterostructures, the net band offsets between GaInAsSb QWs and Al-containing barriers tend to be distributed unequally between conduction and valence bands. Small valence band discontinuity results in insufficient hole confinement and leads to excessive thermal population of the hole states in the adjacent barriers. This keeps the quasi-Fermi level away from the QW valence band-edge and increases the threshold carrier concentration.

As of the year 2011, GaSb-based type-I QW diode lasers demonstrate CW output optical power above 1 W in spectral range 1.9–2.5 μm. Corresponding linear laser arrays produce more than 10 W of CW or 25 W of quasi-CW optical power. These laser diodes demonstrate threshold current densities below 100 A/cm^2; the same if not better than those typical for state-of-the-art GaAs-based diode lasers operating below 1 μm, that is, with active QW bandgap above 1.24 eV (Fekete *et al.*, 2008). More than 350 mW of CW output power at a RT has been reported at 3 μm. These achievements are the result of almost two decades of effort aimed at technological development and design refinement.

The double heterostructure (DH) GaSb-based lasers with bulk GaInAsSb active regions were developed in 1985. The devices operated at RT under a pulsed regime at a wavelength of 2.2 μm, with a threshold current density of 6 kA/cm^2 (Bochkarev *et al.*, 1985) and at 2.3 μm with 20 kA/cm^2 (Caneau *et al.*, 1985). The modified confinement layers reduced the hetero-barrier leakage, which in turn led to a lower threshold current density. The RT CW operation of DH structures utilizing GaInAsSb/AlGaAsSb active regions has been reported in the spectral range of 2.2–2.4 μm (Bochkarev *et al.*, 1988; Choi and Eglash, 1991; Baranov *et al.*, 1994). Using the QW active regions led to improved output in devices operating near 2 μm (Choi and Eglash, 1992; Choi *et al.*, 1994). The use of broadened waveguide separate confinement heterostructures (Botez, 1999) allowed minimization of internal optical losses and prompted the next significant improvement in the performance of GaSb-based type-I QW lasers. Lasers emitting at 2 μm with RT CW output power about 1.9 W (Garbuzov *et al.*, 1997) and RT CW threshold current density of 50 A/cm^2 (Turner *et al.*, 1998) have been fabricated. Further improvement of the hole confinement in the device active region produced lasers operating at 2 μm with differential quantum efficiency of 74% and T_0 of 140 K (Newell *et al.*, 1999). Utilization of heavily strained GaInAsSb QWs with improved hole confinement produced diode lasers operating above 2 μm (Choi *et al.*, 1998; Garbuzov *et al.*, 1999; Walpole *et al.*, 1999; Mermelstein *et al.*, 2000; Rouillard *et al.*, 2001; Kim *et al.*, 2002, 2003; Garcia *et al.*, 2004; Rattunde *et al.*, 2006; Donetsky *et al.*, 2007). High power CW RT operation was demonstrated with nearly 2 W at 2 μm (Rattunde *et al.*, 2006), and with more than 1 W within a spectral region of 2.3 to 2.5 μm (Kim *et al.*, 2002; Donetsky *et al.*, 2007). Improved beam quality was achieved in diode lasers utilizing a flared gain section (Choi *et al.*, 1998; Walpole *et al.*, 1999).

Single-frequency lasers are in high demand for spectroscopic applications. Narrow ridge structures can be used to fabricate single spatial mode lasers emitting at 2.1 μm (Choi *et al.*, 1993) and at 2.3 μm (Yarekha *et al.*, 2000; Wang *et al.*, 2000). Under certain operating conditions these devices demonstrate single spectral mode operation. Distributed feedback (DFB) lasers with stable single spectral mode operation were developed in the last decade for a range of emission wavelengths: 2.3 μm (Salhi *et al.*, 2006), 2.4 μm (Hümmer *et al.*, 2004; Gupta *et al.*, 2009a), 2.6 μm (Rößner *et al.*, 2005), 2.84 μm (Hümmer *et al.*, 2006) and 3 μm (Lehnhardt *et al.*, 2008).

Electrically pumped vertical cavity surface emitting lasers (VCSEL) are especially suitable for a variety of spectroscopy applications, and were successfully demonstrated (Baranov *et al.*, 1998; Cerutti *et al.*, 2008; Ducanchez *et al.*, 2008; Bachmann *et al.*, 2008, 2009). These single mode devices, which emit within a spectral region between 2 and 2.5 μm, are characterized by a circular output beam and low energy consumption. The first GaSb-based electrically pumped VCSELs operating near 2.2 μm at 296 K in pulsed mode were reported by Baranov *et al.* (1998). CW RT operations have only been reported since the year 2008 (Cerutti *et al.*, 2008; Ducanchez *et al.*, 2008; Bachmann *et al.*, 2008, 2009). Low threshold currents to the order of several mA were achieved for VCSELs, with the current and optical confinement obtained through the use of buried tunnel junction (Bachmann *et al.*, 2008, 2009). Optically pumped vertical-external-cavity surface emitting lasers have also been reported, which emit in a spectral range of 2 μm to 2.8 μm with a nearly diffraction limited output beam and CW power in excess of 1 W (Roesener *et al.*, 2008, 2009, 2011; Paajaste *et al.*, 2009).

Extensive efforts have been dedicated to developing type-I QW GaSb-based diode lasers that are able to operate at wavelengths near and above 3 μm. AlGaAsSb/GaInAsSb heterostructures have been used in devices operating in CW at RT (2.72 μm (Grau *et al.*, 2002), 2.82 μm (Shterengas *et al.*, 2004), 2.96 μm (Grau *et al.*, 2003), 3.04 μm (Lin *et al.*, 2004) and 3.1 μm (Shterengas *et al.*, 2008)). The lack of valence band offset between the narrow-bandgap GaInAsSb QWs and AlGaAsSb barriers was identified as the deficiency of the laser heterostructure (Shterengas *et al.*, 2004; Raino *et al.*, 2008; Motyka *et al.*, 2009; Sek *et al.*, 2010) that limited the available output power of these devices.

An important step in the development of long-wavelength type-I QW GaSb-based diode lasers was the introduction of quinternary AlGaInAsSb barriers (Grau *et al.*, 2005; Shterengas *et al.*, 2009; Gupta *et al.*, 2009b, 2010; Hosoda *et al.*, 2010a, 2010b). The use of AlGaInAsSb/GaInAsSb heterostructure in the device active region led to an improvement in hole confinement in the GaInAsSb QWs. Under a pulsed regime, laser operation at temperatures of up to 50°C was demonstrated at emission wavelengths above 3.3 μm (Grau *et al.*, 2005). High power 3 μm lasers based on an AlGaInAsSb/GaInAsSb heterostructure demonstrate 360 mW of CW output power at RT (Belenky *et al.*, 2011). CW RT operation was achieved above 3.4 μm, which is the longest wavelength ever reported for diode lasers (Hosoda *et al.*, 2010b).

This chapter illustrates the design and development of GaSb-based type-I QW laser heterostructures for operation under a CW regime at RT in spectral regions from 1.9 to 3.5 μm.

11.2 Diode lasers operating below 2.5 μm

High power diodes emitting in spectral regions between 1.9 and 2.5 μm are used for a variety of medical, industrial and military applications. Medical applications include surgery, particularly aesthetic surgery, and infrared nerve stimulation. Industrial applications include material processing, including transparent plastic welding, as well as optical pumping of various laser hosts and nonlinear wavelength converters. Resonant or nearly resonant optical pumping of chromium doped II–VI semiconductors, novel type-II QW Sb-based semiconductors, and holmium doped crystals, glasses and fibers can be achieved. High power narrow spectrum lasers are required to seed the cavity of high energy lasers for laser detection and ranging. Tunable devices find applications for absorption spectroscopy of CO_2, CO, etc.

In order to obtain emissions in the 1.8–2.5 μm spectral region, the composition of GaInAsSb QWs ranges from 20% to 40% In and from 0% to 15% As. Ternary GaInSb QWs with 20–25% of In are used to fabricate devices that emit near 2 μm. Operation at near 2.5 μm requires QWs containing 35–40% In and about 15% As to maintain compressive strain below 1.5%. The broadened waveguide approach is often used to improve laser efficiency (Garbuzov *et al.*, 1996). In laser heterostructures with broadened waveguides, the QW optical confinement is traded for reduced overlap of the optical field with the doped cladding region, in order to reduce internal optical loss.

Figure 11.4 shows the flat band diagram of the central part of a broadened waveguide heterostructure of 2.2 μm emitting high power diode lasers (Liang *et al.*, 2011). The laser heterostructure was grown by solid-source molecular beam epitaxy (MBE) on Te-doped GaSb substrates in a Veeco GEN-930 modular system equipped with valved cracker cells for As and Sb. All layers except for the QWs were lattice matched to the substrate.

Heavily doped graded bandgap layers were introduced between the n(p)-GaSb buffer(cap) layers and the n(p)-$Al_{0.85}Ga_{0.15}As_{0.07}Sb_{0.93}$ cladding layers. The claddings were 1.5 μm thick and were doped with Te (nominal $n = 10^{18}$ cm^{-3}) and Be (nominal $p = 10^{17}$ cm^{-3} for the first 500 nm adjacent to the waveguide core and 10^{18} cm^{-3} for the remaining 1 μm). Lower than nominal n-doping levels are expected in quaternary aluminum-containing alloys. The waveguide core was composed of a dual-QW active region centered between 400 nm thick nominally undoped $Al_{0.3}Ga_{0.7}As_{0.03}Sb_{0.97}$ layers. The QWs were 11 nm thick $Ga_{0.72}In_{0.28}As_{0.03}Sb_{0.97}$ with a compressive strain of 1.5% separated by a 20 nm thick $Al_{0.3}Ga_{0.7}As_{0.02}Sb_{0.98}$ barrier. The

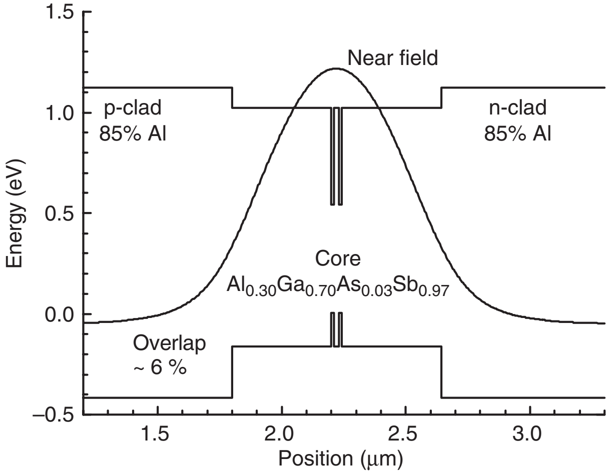

11.4 Calculated band diagram of the laser heterostructure overlaid with the near field optical mode distribution (Liang *et al.*, 2011).

valence band offset between the QW and barrier materials was estimated to be adequate at about 150 meV, while the band offset in the conduction band is ample and in excess of 500 meV. Optical field calculations predicted the overlap of the laser mode with the p-cladding to be about 6%, resulting in low optical losses in these broadened waveguide lasers.

The laser wafer was processed into an index-guided ridge waveguide structure by wet etching the p-cladding layer outside the 100 μm wide current stripes. For CW characterization, the bars were cleaved and immediately loaded to vacuum reactor to be coated to reflect 3% (AR) at the front mirror and 95% (HR) at the back mirror. The anti-reflection (AR) coating was single quarter wave layer of Al_2O_3 while the high-reflection (HR) coating was two periods of a Si/Al_2O_3 Bragg reflector. Both the individual devices and the linear laser arrays were In–soldered epi-side-down with flux onto gold-coated copper blocks. Top contacts were wire-bonded. CW characterization was performed with mounted devices bolted to a Peltier-cooled copper plate. The hot side of the Peltier was water-cooled. The cooling system was capable of removing about 100 W of heat. Laser output power was measured using a calibrated thermopile sensor with a 2 cm diameter aperture. The sensor was placed about 1 cm away from the laser output mirror and no collecting optics were used. Figure 11.5 shows the measured CW output powers and power-conversion efficiencies of individual lasers at a heat sink temperature of 17°C.

A CW output power of 1.5 W was reached at 6 A for the 2 mm long 100 μm wide devices. Lasers with 3 mm long cavities, and hence increased thermal footprints, generate 1.6 W at 7A despite reduced overall device

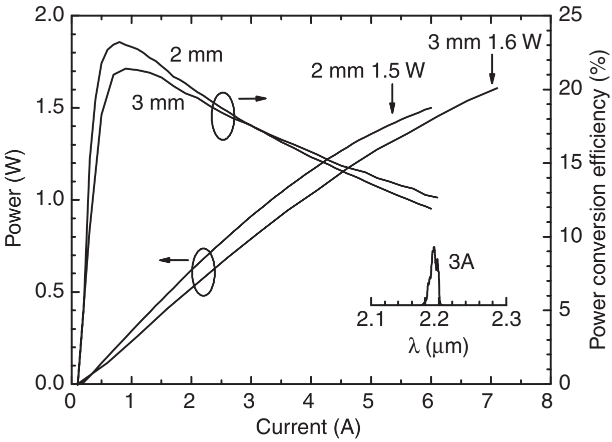

11.5 CW power and power conversion characteristics of single emitter 2.2 μm lasers with 2 and 3 mm long cavities (AR/HR, 17°C). Inset shows laser spectrum (Liang *et al.*, 2011).

efficiency. High power lasers demonstrate CW threshold current densities below 100 A/cm^2, that is, less than 50 A/cm^2 per QW. The threshold current density demonstrates excellent temperature stability as indicated by a T_0 parameter above 90 K, as measured in a short pulse regime over a temperature range from 15°C to 60°C for 1 mm long uncoated devices. Device power-conversion efficiency peaked at more than 20% and remained above 10% at the maximum output power level. CW external efficiency near the threshold was above 50%. The temperature stability of the efficiency is characterized by a parameter T_1 of about 290 K. The laser spectrum was centered near 2.19 μm at a current of 3 A, with a full-width at half-maximum (FWHM) of 12 nm.

Optical gain spectra for several under-threshold currents were measured using the Hakki–Paoli method (Hakki and Paoli, 1975) with a Fourier transform spectrometer and external InSb detector (Fig. 11.6). Amplified spontaneous emission collection and beam focusing on the photodetector were performed using reflective optics. A mechanical slit (about 1 mm) in front of the reflective objective (NA = 0.5) was used to filter out the higher order lateral modes of the laser cavity.

A total optical loss of 15–16 cm^{-1} can be estimated from the long- wavelength part of the gain spectrum, resulting in an internal optical loss of about 4 cm^{-1} (mirror loss of about 12 cm^{-1} can be calculated for uncoated 1 mm long lasers). This relatively low internal optical loss was achieved through waveguide broadening in combination with reduced doping of the p-cladding section adjacent to the waveguide core. Transparency current density is only about 20 A/cm^2 per QW. The net modal differential

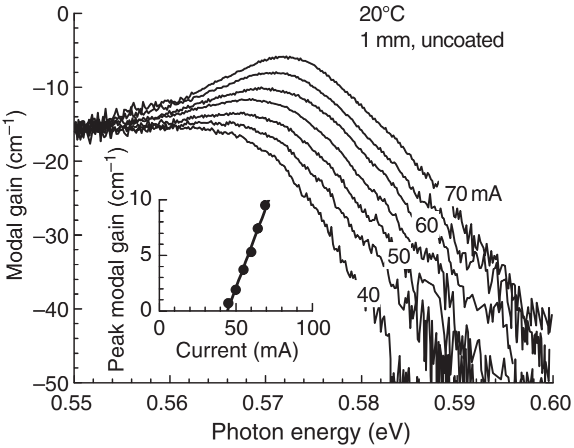

11.6 Current dependences of the modal gain spectra measured at 17°C for 1 mm long uncoated devices. The inset shows the corresponding dependence of the peak modal gain on current (Liang *et al.*, 2011).

gain is above 350 cm^{-1}/A. Threshold is achieved when quasi-Fermi levels are separated by about 35 meV above bandgap (see gain width at threshold as measured at total loss level). The threshold is achieved at a current density that is only about twice that at transparency.

The far field distributions were measured by scanning a single 500 μm diameter photodetector at a distance of about 30 cm from the laser front mirror (Fig. 11.7a). Divergence in the fast axis direction was typical for diffraction limited broadened waveguide lasers with a FWHM of about 63 degrees that is independent of current. The calculated fast axis far field distribution (from near field in Fig. 11.4) had a beam divergence of about 62 degrees, corresponding closely to the experimental value. The multimode beam in the slow axis direction shows a far field divergence of about 10 degrees that tends to increase somewhat with current. The corresponding near field pattern clearly shows filamentation with an average filament spacing of about 12 μm (Fig. 11.7b).

11.2.1 2 μm diode lasers with asymmetric waveguide and improved beam properties

Beam divergence in excess of 60 degrees FWHM complicates fiber coupling and requires expensive optics with numerical apertures above 0.5. In order to improve device brightness, the broadened waveguide design approach was abandoned. GaSb-based diode lasers with narrow symmetric waveguides and increased spot size in the near field have since been developed.

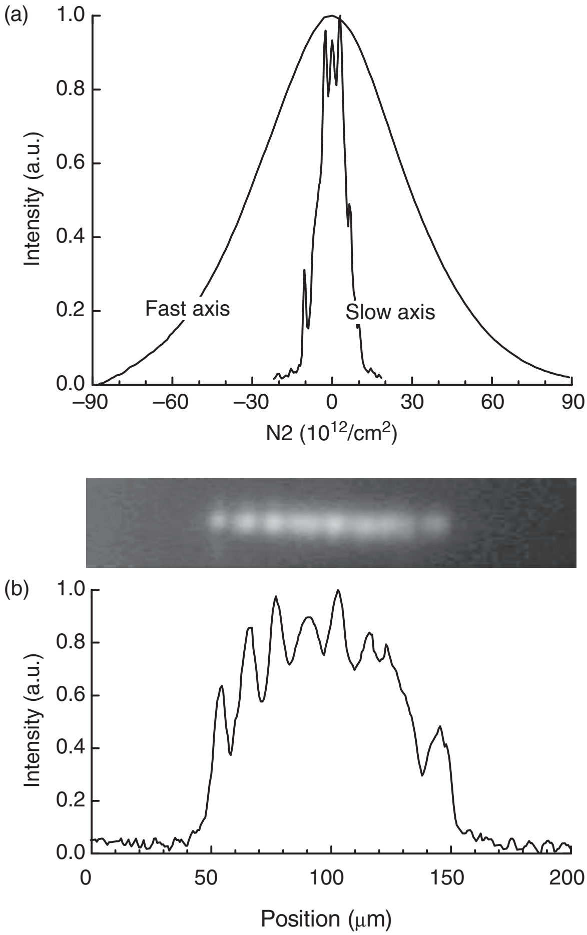

11.7 (a) Fast and slow axis far field distributions measured for 2 mm long, AR/HR coated single emitter lasers; (b) near field distribution measured for 1 mm long, AR/HR coated lasers (Liang *et al*., 2011).

High power CW operation with 1.96 W at 17°C from a 150 μm wide aperture (which corresponds to about 1.3 W from a 100 μm wide aperture) and fast axis beam divergence of 44 degrees FWHM was reported by Rattunde *et al*. (2006). Reduction of the beam divergence below 44 degrees can be achieved by further decreasing the waveguide core. However, it leads to enhanced interaction of the optical field with p-cladding and possibly even p-contact layers. The necessary modifications of the laser heterostructure are likely to increase the electrical and thermal resistance of the device.

Asymmetric waveguide design can be utilized to reduce the fast axis beam divergence below 40 degrees FWHM. In laser heterostructures with asymmetric waveguides, the beam quality can be improved by spreading the optical mode selectively into n-cladding but not into p-cladding (Ryvkin and Avrutin, 2005).

In this design concept, the p-cladding thickness does not need to be increased to accommodate the mode interaction with heavily doped p-contact layers, since penetration of the optical field into p-cladding is restricted. This is expected to benefit thermal transport in p-down mounted lasers. In our experience, an increased overlap with n-cladding should not lead to a substantial internal loss increase in contrast to increased overlap with p-cladding, presumably due to the dominant role of inter valence band absorption (Chandola *et al.*, 2005). Details of the conduction band structure of the particular cladding material should be taken into account to accurately predict the contribution of the free electron absorption to total loss. In the specific structures used here, the n-cladding composition resulted in material with three valleys in the conduction band that had almost the same energy minimum, so no inter valley resonances were expected. Hence, no substantial increase in internal loss could be expected in structures where the optical field extends selectively into n-cladding of the particular composition.

Diode lasers with very low output power (below 50 mW) and fast axis beam divergence (30 degrees FWHM) were obtained by developing a laser heterostructure with an asymmetric waveguide core (Li *et al.*, 2009). Asymmetric penetration of the modal field into p- and n-cladding can be achieved using cladding materials with different compositions. The beam properties of the high power 2 μm emitting GaSb-based diode lasers were improved by utilization of the waveguide structure with asymmetric claddings. The AlGaAsSb p-cladding contained about 85–90% of Al while n-cladding aluminum content was reduced to 45–50%. A corresponding increase in refractive index led to modal spreading to the n-cladding layer, resulting in reduced fast axis beam divergence. The refractive index step between $Al_{0.9}Ga_{0.1}As_{0.07}Sb_{0.93}$ claddings and $Al_{0.25}Ga_{0.75}As_{0.02}Sb_{0.98}$ core in symmetric broadened waveguide laser structure 1 can be estimated as 0.45 for 2 μm light (Alibert *et al.*, 1991). Devices with asymmetric claddings and variable waveguide core thicknesses ranging from above 800 down to below 300 nm were designed, fabricated and characterized (Table 11.1).

Figure 11.8a plots schematically the calculated band alignment and near field distribution in a typical reference symmetric broadened waveguide laser heterostructure (Chen *et al.*, 2010a). Changing the composition of the n-cladding from $Al_{0.9}Ga_{0.1}As_{0.07}Sb_{0.93}$ to $Al_{0.5}Ga_{0.5}As_{0.03}Sb_{0.97}$, reduces the refractive index step between n-cladding and waveguide core down to about 0.2. The resulting waveguide asymmetry leads to spreading of the laser mode into the n-cladding, but keeps overlap with p-cladding low (Fig. 11.8b).

Table 11.1 Composition and width of the claddings and core layers of the 2 μm emitting laser heterostructures studied

	p-clad		core		n-clad	
	% Al	nm	% Al	nm	% Al	nm
1	90	1500	25	859	90	1500
2	90	1500	25	850	50	2000
3	90	1500	25	550	50	2000
4	90	1500	25	350	50	2000
5	90	1500	25	250	50	2500

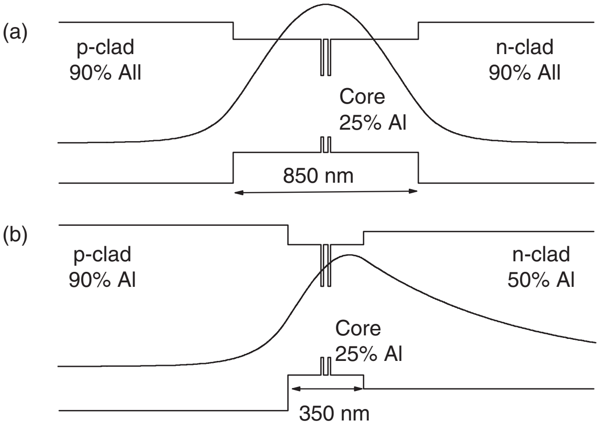

11.8 Calculated band alignment diagram and transverse near field distribution of (a) symmetric broadened waveguide laser structure 1 and (b) asymmetric narrow waveguide laser structure 4 (Chen *et al.*, 2010a).

Reducing the waveguide core width in a laser structure with asymmetric claddings from 850 nm to 550 (structure 3), then to 350 (structure 4), and finally down to 250 nm (structure 5), was accompanied by gradual improvement in beam quality. Figure 11.9a shows that the FWHM maximum of the far field reduces to below 40 degrees, thanks to progressive expansion of the modal field in the n-cladding direction.

Favorable reduction of the beam divergence eventually brings unfavorable degradation of the laser parameters for structure 5. The threshold current increases to 300 mA and T_0 decreases to 50 K. Lasers with structures 3 and 4 demonstrate fast axis beam divergences below 50 and 45 degrees, respectively, and do not experience other parameter degradation. A two-fold increase in threshold current density in lasers with waveguide core widths of 250 nm can be explained by: (a) reduction of the coupling between the

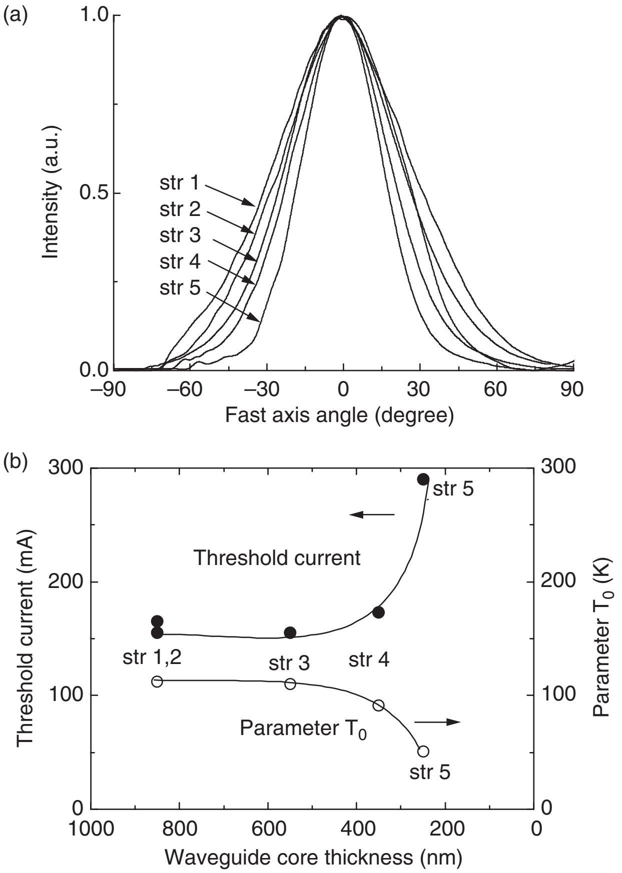

11.9 (a) Measured fast axis far field distributions of 2 μm emitting laser diodes with 1 mm long, 100 μm wide uncoated cavities. Structure (str) numbers correspond to Table 11.1; (b) dependences of the threshold current density at 20°C and parameter T_0 on waveguide core thickness. Measurements were performed under pulsed excitation (200 ns/100 kHz) for 1 mm long, 100 μm wide uncoated lasers mounted epi-side up onto gold-coated copper blocks (Chen *et al*. 2010a).

double-QW active region and laser mode; and (b) modal leakage into the high-index GaSb substrate. Both (a) and (b) are caused by spreading of the optical field in the direction of the n-cladding. The double-QW optical confinement factor decreases gradually, since mode occupies a bigger volume and its maximum shifts from the waveguide core center. Eventually, the waveguide core width can be reduced below the cut-off value (estimated to be about 150 nm), below which no mode could be supported. A progressive increase in field amplitude in the n-cladding would necessitate an increase in n-cladding thickness when decreasing core width, in order to prevent modal

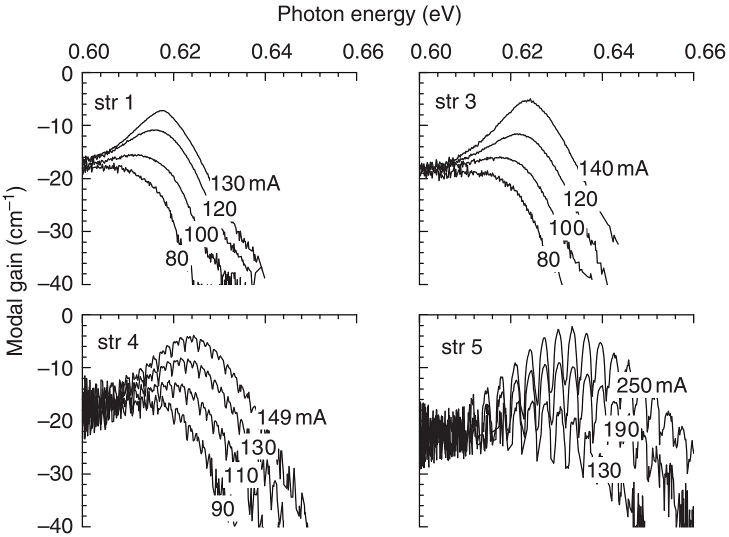

11.10 Modal gain spectra measured at several different currents below thresholds for 1 mm long, 100 μm wide uncoated lasers. Structure numbers (str) correspond to Table 11.1 (Chen *et al.* 2010a).

leakage into the substrate. Reduction of the optical confinement, increase of the internal optical loss, and modal leakage into the substrate, were identified from modal gain spectral measurements.

Modal gain spectra were measured for multimode diode lasers using the Hakki–Paoli method supplemented by spatial filtering optics. Figure 11.10 plots selected spectra obtained at several different currents below the thresholds for diode lasers with structures 1, 3, 4 and 5.

Values for the internal optical losses can be estimated as 5–6 cm^{-1} for structures with 850, 550 and 350 nm wide waveguide cores. Indeed, the internal optical loss is not expected to increase if the overlap of the optical field with p-cladding does not increase in asymmetric narrow waveguide laser heterostructures. However, the internal optical loss in structure 5 does increase up to 8–10 cm^{-1}. The loss increase is also accompanied by pronounced periodic modulation of the modal gain spectra. The modulation is indicative of high modal leakage into the substrate, despite the increase in n-cladding thickness up to 2500 nm. A slight hint of modulation can be seen in gain spectra for structure 4, implying that the cladding thickness should have been increased in lasers with 350 nm cores.

Figure 11.11 plots current dependencies of the peak modal gain for structures 1, 3, 4 and 5. Transparency current is 90–100 mA regardless of laser waveguide heterostructure geometry. Indeed, the devices with identical double-QW active regions are expected to have very similar transparency

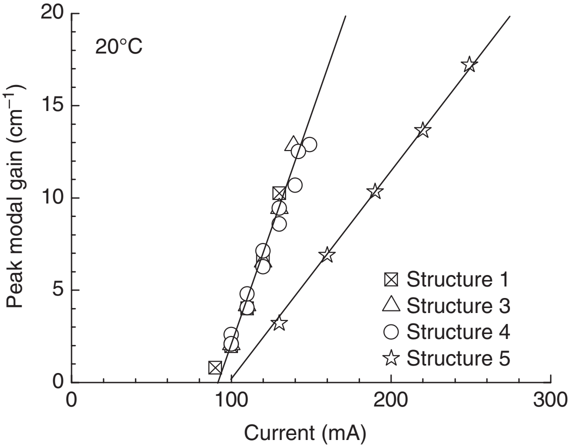

11.11 Current dependences of the peak modal gain of laser with structures 1, 3, 4 and 5 (Chen *et al.*, 2010a).

currents unless injection efficiency changes with waveguide core width. Differential gain with respect to current is directly proportional to the optical confinement factor and thus is expected to decrease together with waveguide core width. Marginal (if any) decrease in differential gain is observed when the waveguide width is reduced from 850 nm down to 350 nm. Two-fold reduction of the differential gain is observed in structure 5 with core width of 250 nm. A sharp drop in the optical confinement factor with reduction of the waveguide width in the range of narrow waveguides can account for this observation. The estimated ratio of the confinement factors of structures 1 and 5 is indeed 2.

Figure 11.12a shows the calculated band alignment and near field distribution for 1.95 μm high power diode lasers with asymmetric waveguides and optimized laser heterostructures (Chen *et al.*, 2010b). The active region contained three 7 nm wide compressively strained $In_{0.25}Ga_{0.75}Sb$ QWs separated by 20 nm thick $Al_{0.3}Ga_{0.7}As_{0.03}Sb_{0.97}$ barriers. The active region was placed into the maximum of the near field distribution. The 360 and 170 nm thick $Al_{0.3}Ga_{0.7}As_{0.03}Sb_{0.97}$ layers separated the active region from p- and n-claddings. A 1 μm thick $Al_{0.85}Ga_{0.15}As_{0.06}Sb_{0.94}$ p-cladding layer was Be-doped to 10^{17} cm^{-3} over the 400 nm adjacent to the waveguide core and to 10^{18} cm^{-3} over the remaining 600 nm. 2500 nm thick $Al_{0.45}Ga_{0.55}As_{0.04}Sb_{0.96}$ n-cladding layer was Te-doped to a nominal 10^{18} cm^{-3}. 20 nm thick AlSb and 5 nm thick $AlAs_{0.1}Sb_{0.9}$ layers were inserted between the waveguide core and n- and p-cladding layers, respectively.

Current independent far field patterns with beam divergences of 42 and 15 degrees FWHM were measured in fast and slow axes, respectively

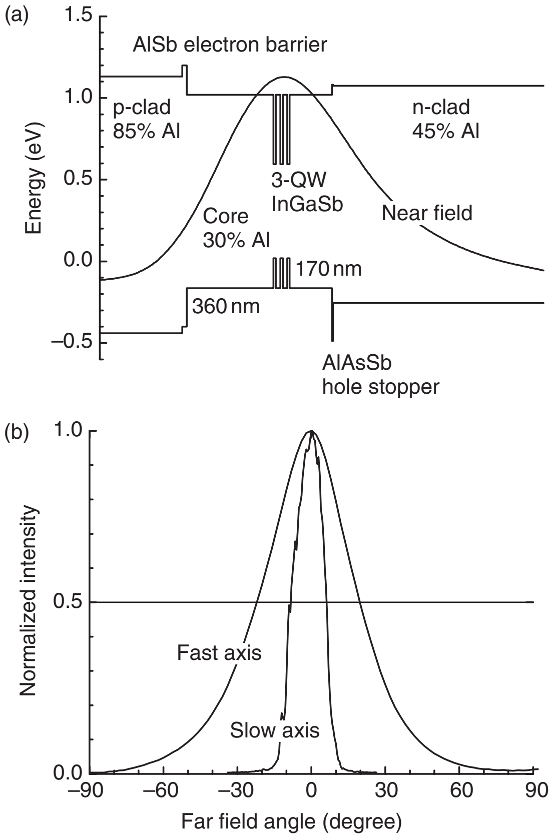

11.12 (a) Calculated band diagram of the laser heterostructure overlapped with near field distribution; (b) corresponding far field patterns measured in slow and fast axis directions (Chen *et al.* 2010b).

(Fig. 11.12b). The stable multimode slow axis far field pattern can be ascribed to strong index guiding achieved in the lateral deeply etched ridge waveguide. Low divergence of only 42 degrees was observed in the diffraction limited fast axis direction due to enhanced spot size in the corresponding near field. The estimated refractive index step between waveguide core and p-cladding is about 0.4, while that between core and n-cladding is only 0.1. Reduction of the aluminum content in n-cladding from 85% to 45% was accompanied by undesired reduction of the corresponding valence band offset with core alloy by about 200 meV. The hole stopper layer was introduced in order to balance the reduced valance band offset. The electron stopper layer was added on the p-side to further reinforce carrier confinement in the waveguide core.

Figure 11.13 plots the corresponding device power and power-conversion characteristics. A maximum CW output power of about 1.45 W was measured

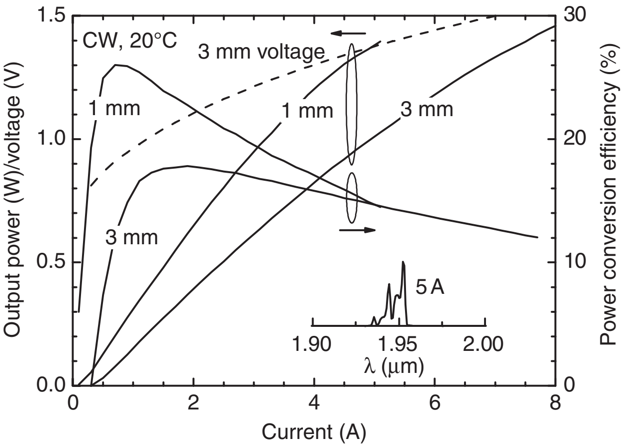

11.13 CW power and power conversion characteristics of 100 μm wide, 1 and 3 mm long AR/HR coated devices measured at 20°C. Inset shows spectrum of 3 mm long laser at 5 A (Chen *et al.* 2010b).

for 100 μm wide, 3 mm long coated lasers at 20°C. Power-conversion efficiency remained above 11% at the maximum output power level.

The devices operated at voltages below 1.5 V. Parameters $T_0 \approx 80$ K and $T_1 \approx 250$ K characterized exponential temperature dependence of the threshold current and slope efficiency of 1 mm long uncoated devices in the temperature range from 15°C to 50°C. Power scaling to above 10 W CW level was demonstrated by fabricating 1.9–2.2 μm linear laser arrays and fiber bundles (Chen *et al.*, 2010a).

11.2.2 Role of compressive strain above 1%

GaInAsSb/AlGaAsSb heterostructures are characterized by a strong imbalance between conduction and valence band offsets, with the conduction band offset usually exceeding the valence band offset. Despite the large difference in band gaps between AlGaAsSb and GaInAsSb alloys, which are used as barrier and QW materials, hole confinement in QWs might be poor while electron confinement is more than adequate. As a result type-I GaSb-based QW laser heterostructures suffer from insufficient hole confinement. Hole confinement can be improved by using GaInAsSb QWs with lower arsenic content, i.e. using heavily compressively strained QWs. Introducing compressive strain to active QWs can also improve the laser differential gain by reducing the hole DOS, that is, through balancing the carrier DOS in the lasing electron and hole subbands (Yablonovitch and Kane, 1986).

Detailed experimental and theoretical analysis of the laser threshold in type-I mid infrared lasers with compressively strained QWs has been carried out, in order to quantify the importance of hole confinement for laser performance. Two laser heterostructures were designed and fabricated for this purpose. Both structures included strained QW layers of different compositions, which were presumably characterized by different hole confinements. Both structures were emitting at 2.3 μm at RT and had the same waveguide and contact layer designs. The nominally undoped $Al_{0.25}Ga_{0.75}As_{0.02}Sb_{0.98}$ waveguide layer with a total thickness of about 800 nm contained two $Ga_{0.65}In_{0.35}As_xSb_{1-x}$ QWs centered in the waveguide and spaced 20 nm apart. The structure referred to as 'moderately strained' contained two 10 nm QWs with a compressive strain of 1%. The second, heavily strained structure contained two 12 nm QWs with a compressive strain of 1.5%. The difference in strain was achieved by changing the QW arsenic content from about 9% (heavily strained) to about 17% (moderately strained). In the moderately strained structure, the QW width was reduced from 12 nm to 10 nm, causing both lasers to operate at the same wavelength (near 2.3 μm) at RT. Both wafers were processed into 100 μm wide oxide confined gain guided lasers. Figure 11.14a shows the light–current characteristics measured at RT (20°C) for moderately strained and heavily strained diode lasers (Chen *et al.*, 2008). A threshold current density of about 230 A/cm^2 was measured for moderately strained lasers, but only 120 A/cm^2 for heavily strained devices. Five devices from each group were characterized at 20°C and threshold currents in the ranges 120–140 mA and 230–260 mA were measured respectively for heavily strained and moderately strained lasers. Heavily strained devices also tended to have higher slope efficiency (0.16 W/A per facet) than low strain ones (0.14 W/A per facet). At low temperatures (Fig. 11.14b) the threshold currents for both structures become nearly identical and equal to 40 mA (20 A/cm^2 per QW) at 150 K. At 200 K the threshold current of heavily strained lasers is already slightly larger than that of moderately strained ones, and the difference tends to increase with temperature. At RT, the moderately strained lasers demonstrate nearly twice the threshold currents of heavily strained devices.

Hakki–Paoli gain measurements confirmed that the internal optical loss value ~4 cm^{-1} was independent of the active region strain, meaning that the nearly two-fold difference in threshold currents between moderately and heavily strained lasers could not be attributed to either difference in optical losses or internal efficiencies. Figure 11.15 plots the current dependences of the peak modal gain measured at 200 K and 293 K.

RT data (293 K) showed that the differential gain and transparency current were highly dependent on the laser active region strain. Heavily strained devices demonstrated an increase in differential gain from 120 cm^{-1}/A up to 250 cm^{-1}/A, and a reduction in transparency current from 120 mA down to 60 mA, as compared to moderately strained lasers. A two-fold difference in the differential gain and transparency current accounts for the two-fold

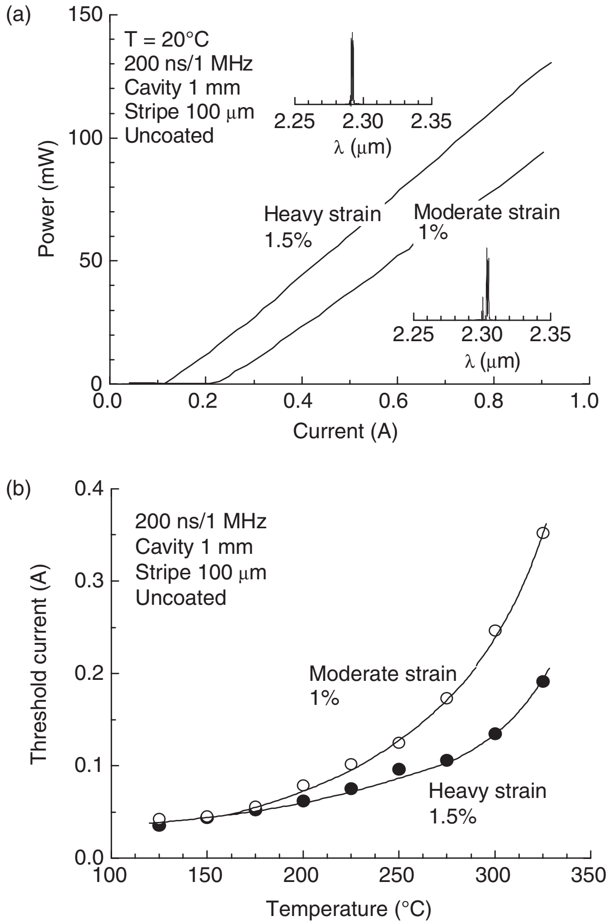

11.14 (a) Pulsed (200 ns/1 MHz) light–current characteristics of 1 mm long uncoated lasers with 1% and 1.5% of compressive strain in InGaAsSb QWs. Inset shows RT laser spectra near threshold; (b) temperature dependences of the laser threshold current for moderately and heavily strained lasers (Chen *et al.*, 2008).

reduction in RT threshold current of the heavily strained devices. At low temperatures, the differences in both the differential gain and transparency current between moderately and heavily strained lasers tended to decrease. At 200 K, the transparency current values for both types of the devices were about 30 mA, while the differential gain increased up to 730 cm^{-1}/A for heavily strained lasers and up to 390 cm^{-1}/A for moderately strained ones. The similar values of the transparency currents and high values of the differential gains lead to a small relative difference in threshold currents, namely 60 mA for heavily strained and about 80 mA for moderately strain

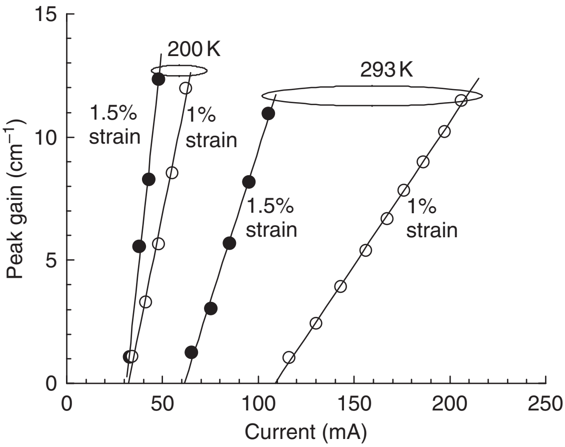

11.15 Current dependences of the peak modal gain measured for moderately and heavily strained devices at 200 K and 293 K (Chen *et al.* 2008).

devices. When the temperature decreased below 200 K the difference in threshold currents between moderately and heavily strained lasers tended to disappear.

The effect of strain on laser performance can be illustrated by calculating the modal optical gain in structures with moderate (1%) and high (1.5%) level of compressive strain in the active QWs. According to our estimation, the hole confinement in the first structure was insufficient, with valence band QW depth for heavy holes of only 35 meV. In the second structure, which was designed for the same lasing wavelength, the arsenic concentration in QW was lowered, thus increasing the QW compressive strain. Due to combined effect of reduced arsenic concentration and increased QW strain, the confining barriers for the heavy holes in the highly compressed QW increased up to 105 meV. Calculations prove that this improvement in hole confinement was primarily responsible for the enhancing the optical gain, while the additional strain-induced subband DOS balancing was only of secondary importance. The Schrödinger equation system was solved self-consistently with the Poisson equation iteratively. During each iteration, the hole populations and Fermi distribution functions were recalculated, taking into account the thermal redistribution of holes between QW and barrier states. In all the modeled structures, electrons were strongly localized in conduction band QWs, predominantly occupying states in the lowest electronic subband.

Figure 11.16 illustrates the electron and hole DOS distribution in GaSb-based QW heterostructures. Figure 11.16a shows energy subbands (left panel) and subband DOS (right panel) in a reference lattice matched

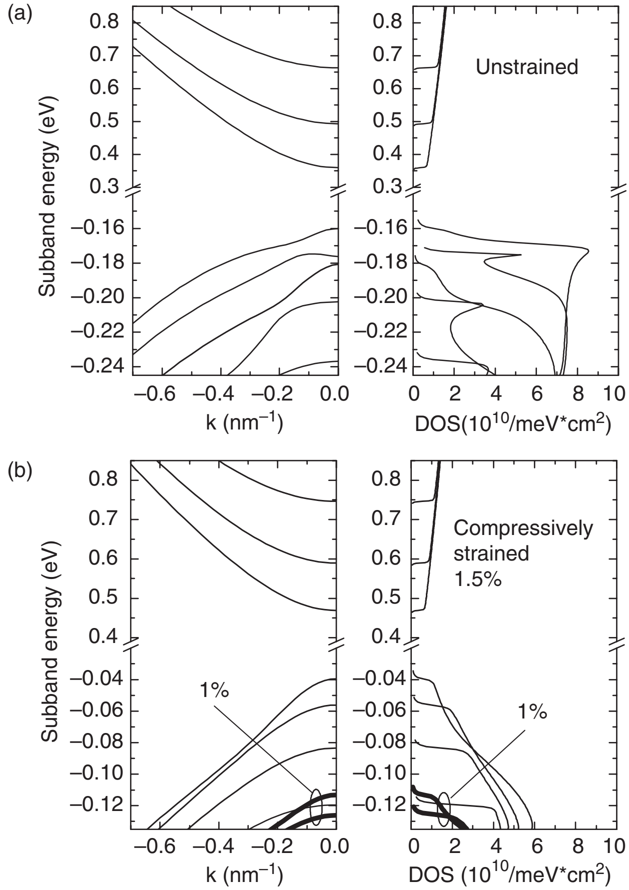

11.16 Left panel of each plot shows the subband dispersion, i.e. the subband energy *vs* the electron/hole wave vector k; right panel shows the subband DOS for: (a) $Ga_{0.8}In_{0.2}As_{0.2}Sb_{0.8}$ QW lattice matched to GaSb and (b) 1.5% compressively strained $Ga_{0.65}In_{0.35}As_{0.09}Sb_{0.91}$ QW. Bold lines indicate valence subbands and DOS for 1% strained $Ga_{0.65}In_{0.35}As_{0.17}Sb_{0.83}$ QW (Chen *et al.* 2008).

(unstrained) $Al_{0.50}Ga_{0.50}As_{0.04}Sb_{0.96}/Ga_{0.80}In_{0.20}As_{0.20}Sb_{0.80}$ QW heterostructure. Electron and hole subbands have noticeably different DOS in unstrained QW due to the anticrossing between second (heavy-hole) and third (light-hole) valence subbands, which induces strong subband nonparabolicity. Figure 11.16b demonstrates a much better balance between lower electron and upper hole subband DOS in the $Al_{0.25}Ga_{0.75}As_{0.02}Sb_{0.98}/Ga_{0.65}In_{0.35}As_{0.09}Sb_{0.91}$ heterostructure (heavily strained laser in section III), with highly compressively strained QW (strain 1.5%). All three upper hole subbands in this heterostructure are of the heavy-hole type in the Brillouin zone center, and no anticrossing effects are visible in the subband DOS structure.

Bold lines in the lower part of Figure 11.16b represent the valence subbands (left panel) and the subband DOS (right panel) for QW with a higher arsenic concentration (17%) and lower strain (1%). This structure is characterized by a heavy-hole QW depth of only 35 meV. It is readily seen, however, that the DOS at the upper subband edge in this shallow QW does not differ noticeably from the DOS of the uppermost states in the deeper QW. The main difference between the two structures is the hole confinement, which is significantly lower in structure with lower strain and higher arsenic contents.

The QW depth for electrons is more than adequate in both structures, so that the electrons predominantly occupy the lowest electronic subband with negligible thermal redistribution into the higher subbands, even at RT. A deficit in hole confinement in the moderately strained structure (Figure 11.17a), combined with high valence band DOS in bulk waveguide layers, leads to strong thermal hole redistribution and reduces the population of the hole lasing states. Since the electrons are strongly localized in deep conduction band QWs, the thermal redistribution of holes between the shallow valence band QWs and the optical waveguide layers creates Coulomb barriers, which can improve hole confinement to some extent. Even in this case, however, the bulk heavy-hole states of the waveguide material with high DOS remain energetically close to the lasing states in the uppermost hole subband and, therefore, unfavorably affect the population of the lasing states.

In compressively strained GaInAsSb QWs with low arsenic content, the heavy-hole states move upwards, thus making the heavy-hole QW deeper. Improved hole confinement, in turn, reduces the thermally activated hole redistribution between the QW subbands and the adjoining bulk barrier states and, therefore, increases the occupation of the uppermost hole subband states participating in the lasing transition. Improved hole confinement ultimately enhances the laser differential gain and reduces the threshold current density. Figure 11.17b shows peak modal gain calculated at 100, 200 and 300 K as a function of the injected carrier concentration for structures with moderate strain (dashed lines) and heavy strain (solid lines). Structures with heavily strained QWs, and hence better hole confinement, demonstrate higher differential gain and lower transparency concentration compared to moderately strained structures. Reducing the laser threshold concentration in structures with heavily strained QWs also minimizes the contribution of the Auger processes, though it cannot eliminate them completely. The carrier concentration required to reach the lasing threshold increases with temperature. In moderately strained structures with inadequate valence band offset, an extra carrier injection is required a set of closely separated hole

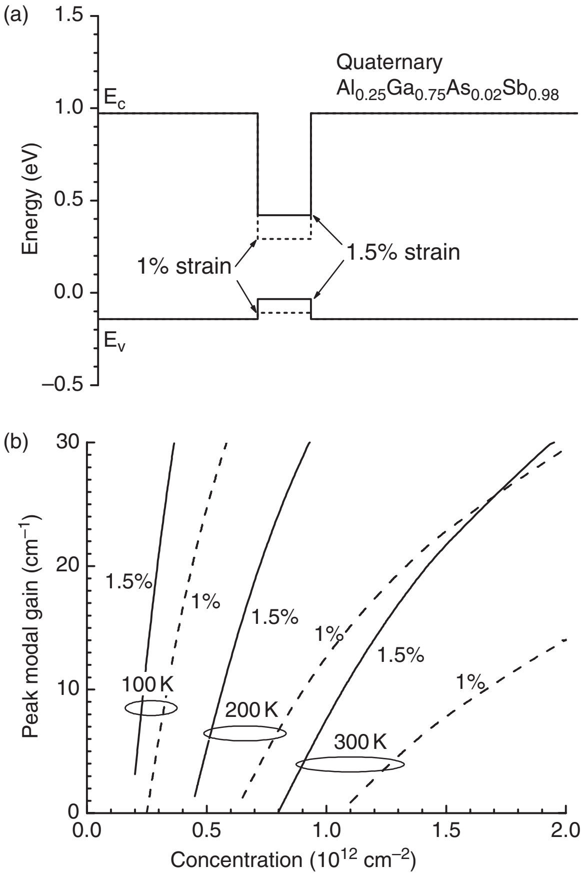

11.17 Peak modal gain as a function of the injected carrier concentration in QW for different temperatures. Dashed lines indicate structure with 1% compressive strain (moderate strain), solid lines indicate structure with 1.5% strain (heavy strain) (Chen *et al.* 2008).

subbands with inherently large DOS. A corresponding increase in threshold carrier concentration triggers Auger processes, which in turn increases the laser threshold current density, and worsens the temperature stability of the device.

11.3 Diode lasers for spectral range above 3 μm

Diode lasers operating in the spectral region above 3 μm are used for a variety of applications. Many important gases and other chemical agents can be remotely detected by tunable laser spectroscopy in this spectral region. For instance, methane, ethane, acetylene, methanethiol, dimethyl sulfide, hydrogen cyanide, etc. absorb strongly between 3 and 4 μm. Analysis of concentrations and isotopic composition of these gases provides key information on geochemical processes, atmospheric photochemistry, and hydrothermal and biological activity. High power $\lambda \geq 3$ μm beams are required for medical therapy, laser surgery, infrared illumination, countermeasures, etc. Compact, efficient and low cost diode lasers are often desirable components for system realization. High power diode lasers can be used either directly or as pumps for solid state/fiber/nonlinear hosts. In many cases, CW operation of diode lasers is either necessary or at least preferred. Laser operation at or near RT dramatically simplifies system design. The voltage drop across the diode laser heterostructure is about 1.5 V, and is used to achieve population inversion in the active region and to send current through auxiliary layers.

The GaInAsSb QWs composition in GaSb-based diode lasers emitting above 3 μm ranges from 50 to 60% In and from 20 to 30% As. Mid infrared diode lasers at wavelengths above 3 μm suffer from temperature sensitivity of both threshold current and external efficiency. Several factors contribute to undesirable temperature sensitivity, including free carrier absorption and Auger recombination. Besides these fundamental factors, there may also be heterostructure deficiencies. These can cause hetero-barrier carrier leakage into the cladding, carrier accumulation in the waveguide core, and thermal population of useless energy states inside and close to the active QWs. Such deficiencies can be eliminated by improving material quality and by designing laser heterostructures with strong carrier confinement.

It is easy to arrange for a conduction band offset above 300 meV in GaInAsSb QWs with AlGaInAsSb barriers. In 300 meV deep and 10–15 nm wide QWs, with the second subband quantized away by more than 100 meV, only one electron subband is populated at RT. At the same time, the valence band offset can easily become inadequate in a GaSb-based material system. The heavy-hole subband separation is also low; about 15 meV between the two topmost subbands. Valence band states in the barriers and higher order hole subbands can unfavorably increase the number of states available for population in the valence band. One critical design task is to minimize the number of states in the valence band that are available for population.

The in-plane effective mass in the fundamental heavy-hole subband can be reduced almost to the level of electron effective mass by compressive strain of about 1%. The strain values beyond that range have little effect on the band-edge heavy-hole DOS, since at such high strain the heavy-hole and light-hole subbands are already well separated in energy. The population of the second heavy-hole subband is minimized by use of relatively narrow QWs. The barrier state population should be minimized by constructing QWs with adequate hole confinement energies.

Performance of the GaSb-based type-I QW diode laser with wavelengths above 2.5 μm was improved when the quinternary AlGaInAsSb alloy replaced quaternary AlGaAsSb as a barrier material. An increase in the As composition in any Sb-based alloy tends to lower the position of the valence band on the absolute energy scale. The requirement for strong hole confinement can thus be realized by minimizing As composition in GaInAsSb QW and maximizing As composition in AlGaInAsSb barrier materials. This can be achieved by maximizing the compressive strain in quaternary QW and by maximizing In and Al compositions in the quinternary barrier materials. QWs under compressive strain require less As and benefit from heavy–light hole splitting. Quinternary AlGaInAsSb alloys with increased In and Al compositions require more As to maintain lattice matching to the GaSb substrate.

Figure 11.18 illustrates the benefits of using quinternary AlGaInAsSb barriers in 3.1 μm lasers. Replacement of the quaternary $Al_{0.35}Ga_{0.65}As_{0.03}Sb_{0.97}$ with quinternary $Al_{0.2}Ga_{0.55}In_{0.25}As_{0.24}Sb_{0.76}$ barrier alloy improves the hole confinement by about 100 meV (Fig. 11.18a) and leads to a two-fold reduction in RT threshold current density (Fig. 11.18b). Again, at low temperatures, the difference tends to disappear since the hole confinement offered by both types of barriers becomes equally adequate.

It should be noted that neither detailed studies of the optical properties nor detailed development of the growth procedure of the quinternary AlGaInAsSb material have yet been performed. Carrier transport issues were identified in the course of optimization of the laser waveguide heterostructure with the aforementioned quinternary alloy as a waveguide core. Three laser heterostructures were grown with $Al_{0.2}Ga_{0.55}In_{0.25}As_{0.24}Sb_{0.76}$ waveguide core widths of 470 nm, 1070 nm and 1470 nm. The lasers emit near 3 μm at RT. Laser heterostructure parameters, other than the waveguide core widths, were nominally kept the same for all three lasers. Figure 11.19a shows pulsed (200 ns, 10 kHz) light–current characteristics measured at RT for 1 mm long uncoated devices (Hosoda *et al.*, 2009). The light–current characteristics demonstrate the roll-over for all three structures that becomes more severe as the waveguide width increases. Figure 11.19b shows the threshold current densities measured in a wide temperature range for three structures. At 150 K all three devices have very low threshold current densities of about 25 A/cm^2, which increases with temperature at rates dependent on waveguide width. At 300 K the threshold current density is more than twice as high for devices with the widest waveguide than for lasers with the narrowest one.

Roll-over of the light–current characteristics in devices with broadened waveguides can be accounted for by the carrier transport constraints in the waveguide region. Accumulation of the free carriers in waveguide regions between claddings and two-QW active can lead to reduction of the slope efficiency due to both free carrier absorption and recombination.

Analysis of the effect of waveguide width on the threshold current density on should take into account the distribution of the optical field in the

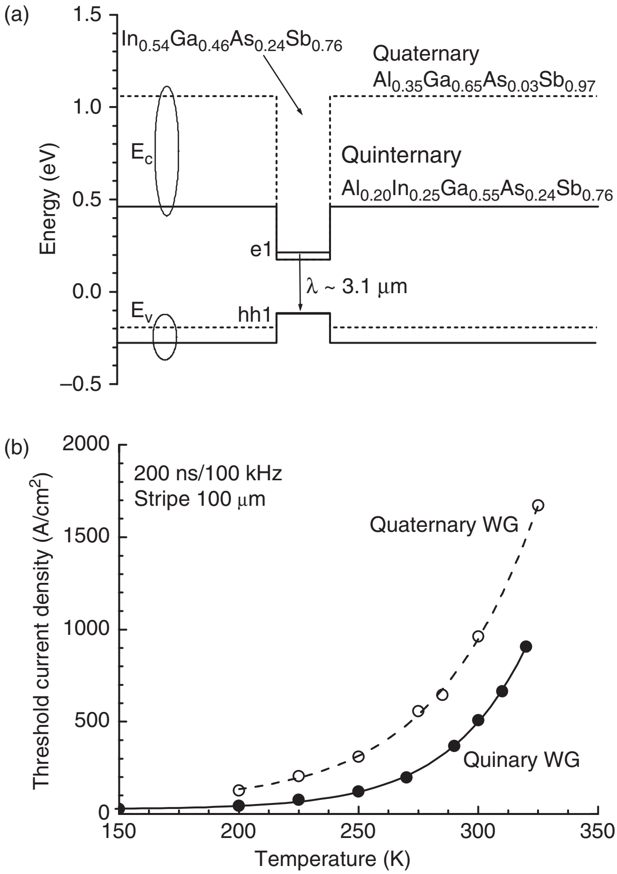

11.18 (a) Calculated band alignment for 3.1 μm emitting lasers. Solid line shows the band edges for QW materials and for quinternary AlInGaAsSb barriers. The dashed line shows the band-edge position for quaternary AlGaAsSb alloys. (b) Temperature dependences of the threshold current density for 3.1 μm emitting lasers with AlGaAsSb quaternary and AlGaInAsSb quinternary barriers.

laser heterostructure. Changing the optical field distribution leads to a 1.7 times higher optical confinement factor in lasers with 470 nm wide waveguides compared to devices with 1470 nm wide ones. Enhancing the optical confinement factor should improve differential gain in narrow waveguide lasers.

Figure 11.20a shows the experimental dependences of the peak modal gain on current for all types of lasers measured by the Hakki–Paoli method. In devices with very narrow waveguides, the differential gain is about 2.5 times higher than in those with the widest waveguide, that is, the experimental rate of the differential gain increase exceeds the growth of the optical

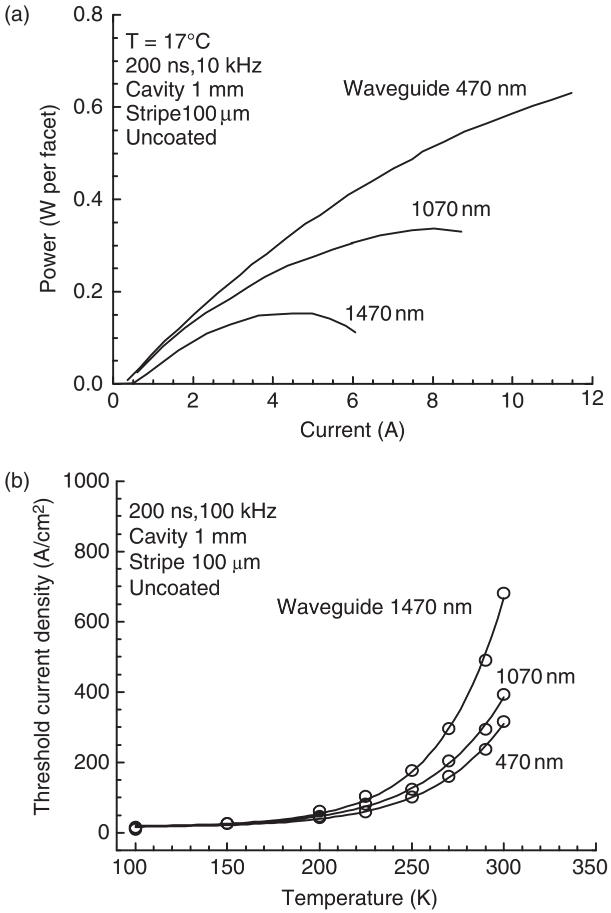

11.19 (a) Pulsed (200 ns, 10 kHz) light–current characteristics and (b) temperature dependence of the threshold current density for 1 mm long, 100 µm wide, uncoated 3 µm lasers having different waveguide widths (Hosoda *et al.*, 2009).

confinement factor. The enhancement in differential gain is facilitated by improved device injection efficiency (Fig. 11.20b). Since the diffusion current through a narrowed waveguide can be supported by lower carrier concentration, the waveguide recombination current is smaller in devices with 470 nm wide waveguides than in lasers with 1070 and 1470 nm wide waveguides. Figure 11.20b shows that, as expected, the broadening of the waveguide reduced internal loss. However, the combined effects of carrier transport through the waveguide and reduction of the multiple quantum well (MQW) optical confinement factor did not allow the 3 µm lasers to benefit from associated internal optical loss reduction. This indicates the

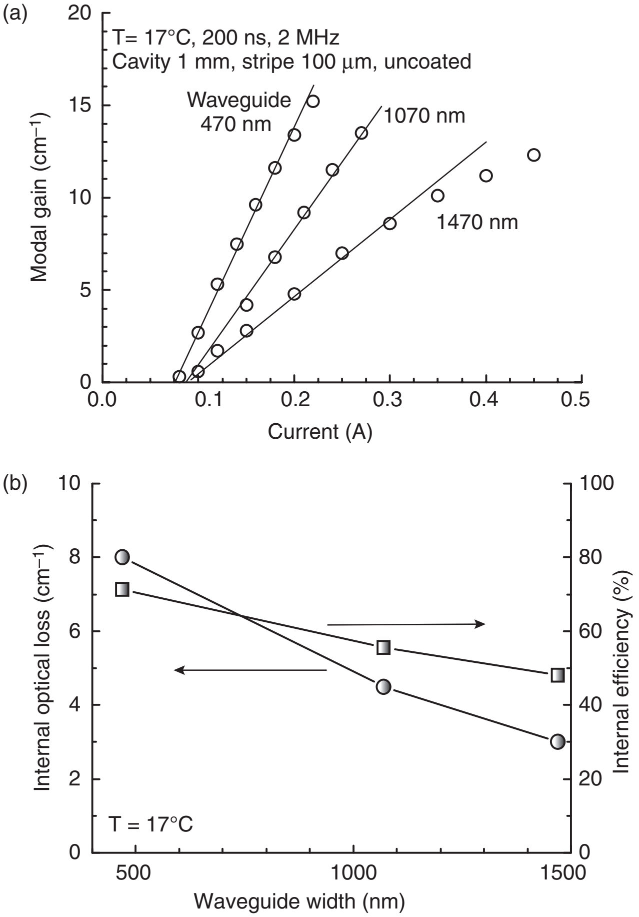

11.20 (a) Current dependences of the peak modal gain for 3 μm lasers with different waveguide widths, and (b) dependence of the internal optical loss (circles) and internal efficiency (squares) on waveguide width (Hosoda *et al.*, 2009).

possibility of further device performance enhancement after detailed material development studies are completed, and perhaps the carrier mobility in quinternary materials might improve.

11.3.1 CW RT operation of 3–3.4 μm multimode diode lasers

Laser heterostructures with heavily compressively strained QWs with quinternary barriers were developed to produce diode lasers operating at RT in a CW regime in spectral regions from 3 to 3.4 μm. The heterostructures were grown by solid-source MBE on tellurium-doped GaSb substrates. The claddings were $Al_{0.85}Ga_{0.15}As_{0.07}Sb_{0.93}$ doped with tellurium and beryllium for n– (2.5 μm thick) and p-cladding (1.5 μm thick), respectively. The doping level of the part of the p-cladding layer adjacent to the waveguide was kept to around 10^{17} cm^{-3} to reduce internal losses associated with free hole absorption. Wafers were processed into 100 μm wide index-guided ridge lasers by wet etching the top-cladding layer outside the current stripe. The values of the empirical parameters T_0 and $T_{1,}$ which characterize the exponential dependences of the laser threshold current and slope efficiency on temperature, were measured in a pulsed regime near 300 K for 1 mm long uncoated lasers. For CW characterization, the coated lasers were indium-soldered epi-side down.

Figure 11.21a shows the CW RT light–current and power-conversion characteristics of 3 μm emitting lasers. The laser active region comprised two 11 nm wide, 50 nm spaced GaInAsSb QWs with a nominal indium composition of 50% and a compressive strain of 1.7%. The barrier and waveguide material was $Al_{0.20}Ga_{0.55}In_{0.25}As_{0.24}Sb_{0.76}$ quinternary.

The total width of the waveguide region (from n-cladding to p-cladding) including double-QW active was about 570 nm. Laser mirrors were cleaved and coated to obtain mirror reflectivity of below 5% for AR and above 90% for high reflection (HR). The maximum power of 360 mW was achieved at the current of 4.6 A at coolant (water) temperature of 17°C. The power-conversion efficiency was better than 4% for the whole range of operation, with the maximum value approaching 9% at an output power level of about 120 mW. The CW threshold current density was 200 A/cm^2 (100 A/cm^2 per QW). The voltage drop across the laser heterostructure was below 1.4 V at the maximum output power level. Parameters T_0 and T_1 are 50 K and 200 K, respectively. The current dependence of the modal gain spectra is shown in Figure 11.21b. The internal optical loss of 4–5 cm^{-1} was estimated from the long-wavelength part of the gain spectrum, assuming mirror losses of about 12 cm^{-1}. The transparency current density was below 100 A/cm^2.

Figure 11.22a shows the CW RT light–current and power-conversion characteristics of 3.1 μm emitting lasers. The laser active region comprised three 13 nm wide 1.6% compressively strained InGaAsSb QWs separated by 50 nm wide barriers. Quinternary $Al_{0.20}Ga_{0.55}In_{0.25}As_{0.24}Sb_{0.76}$ was used in both the barriers and waveguide. The nominal indium composition of QWs was more than 50%. The total undoped waveguide core width was about 650 nm from p-cladding to n-cladding.

A maximum CW output power of 190 mW was achieved using a 3.8 A current at a coolant (water) temperature of 17°C. The power-conversion efficiency was better than 2% for the whole range of operation, with a maximum value of more than 4% at an output power level of about 100 mW. The

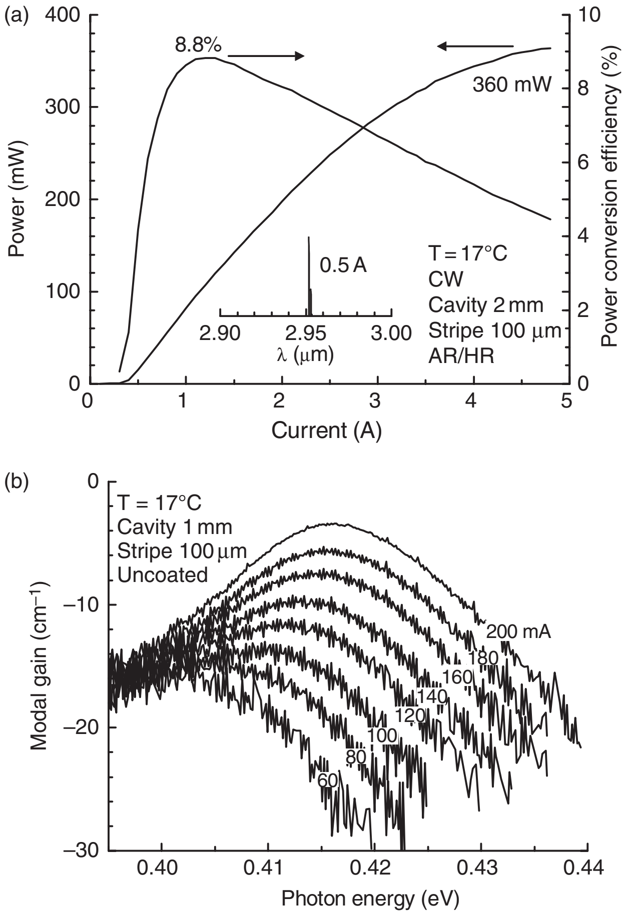

11.21 (a) Light–current characteristics measured in CW regime at 17°C for 2 mm long, 100 μm wide, AR/HR coated diode lasers with optimized design and emitting near 3 μm; (b) current dependence of the modal gain spectra for corresponding 1 mm long, 100 μm wide, uncoated lasers measured in pulsed regime (200 ns/2 MHz) (Shterengas *et al.*, 2009).

CW threshold current density was 350 A/cm^2 (about 120 A/cm^2 per QW). The internal loss is estimated to be about 8 cm^{-1} (Fig. 11.22b). The values of the parameters T_0 and T_1 are 34 K and 74 K, respectively.

Figure 11.23a shows the CW RT light–current and power-conversion characteristics of 3.2 μm emitting lasers. The active layer consists of three 13 nm wide InGaAsSb compressively strained QWs (1.6%) separated by 50 nm wide barriers. The nominal indium composition of QWs was near 55%. The total undoped waveguide core width was about 650 nm from

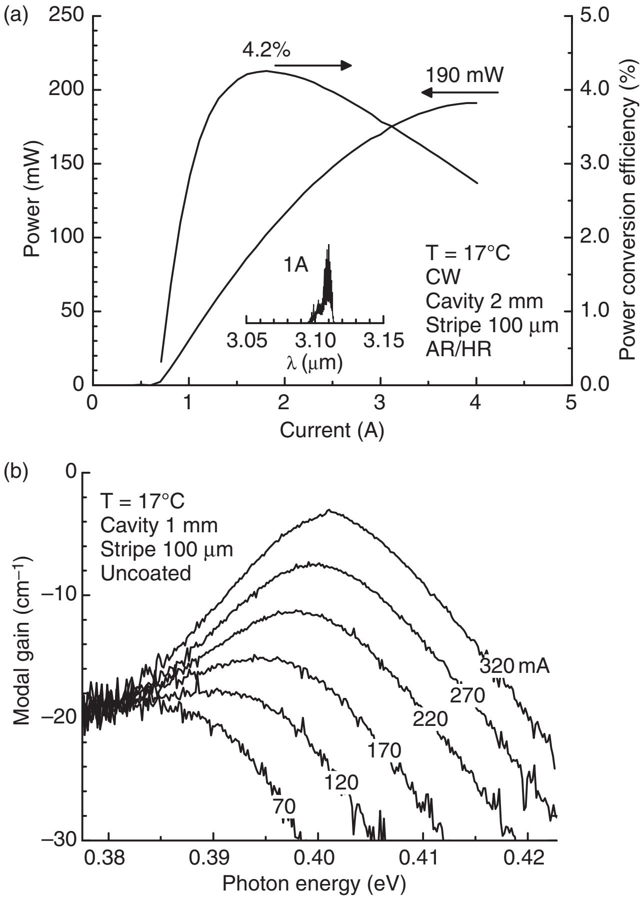

11.22 (a) Light–current characteristics measured in CW regime at 17°C for 2 mm long, 100 μm wide, AR/HR coated diode lasers emitting near 3.1 μm; (b) current dependence of the modal gain spectra for corresponding 1 mm long, 100 μm wide, uncoated lasers measured in pulsed regime (200 ns/2 MHz) (Hosoda *et al.*, 2010a).

p-cladding to n-cladding. A maximum power of 165 mW was achieved with a 4.2 A current at a coolant (water) temperature of 17°C. The CW threshold current density was less than 400 A/cm^2 (about 130 A/cm^2 per QW). The voltage drop across the laser heterostructure was below 1.5 V at the maximum output power level. The internal loss is estimated to be about 9 cm^{-1} from Fig. 11.23b.

Quinternary $Al_{0.22}Ga_{0.46}In_{0.32}As_{0.30}Sb_{0.70}$ was used in the barriers and waveguide. The increase in indium content in the barriers from 25% to 32% raised the valence band offset between QWs and the barriers. The experiment showed that using 32% indium in the AlGaInAsSb barrier improves

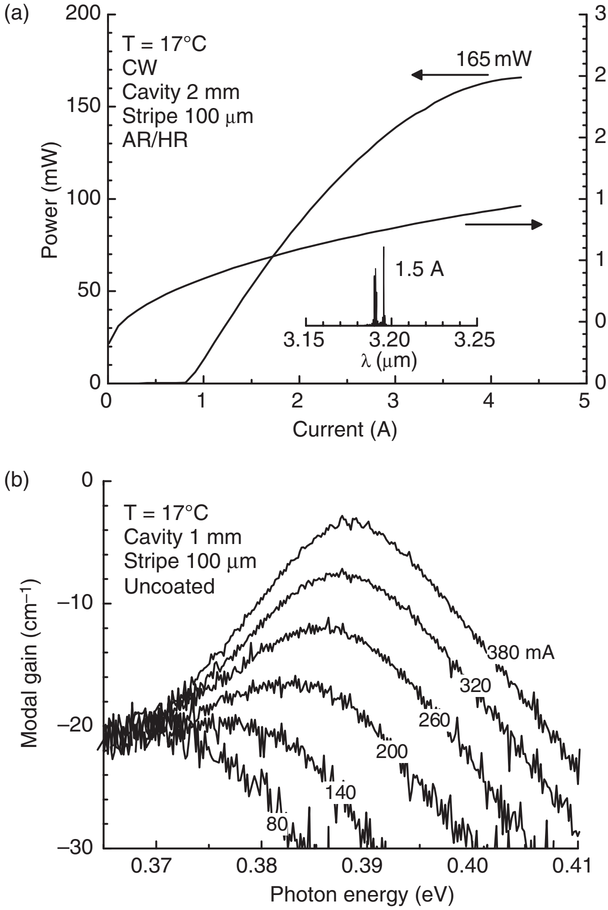

11.23 (a) Light–current and voltage–current characteristics measured in CW regime at 17°C for 2 mm long, 100 μm wide, AR/HR coated diode lasers emitting near 3.2 μm; (b) current dependence of the modal gain spectra for corresponding 1 mm long, 100 μm wide, uncoated lasers measured in pulsed regime (200 ns/2 MHz) (Hosoda *et al.*, 2010a).

the characteristics of 3.2 μm emitting lasers. Figure 11.24 plots the current dependences of the peak modal gain measured for 3.1 μm emitting laser heterostructures (Fig. 11.22) and 3.2 μm emitting lasers heterostructures with different barrier compositions, that is, the same as in typical 3.1 μm emitters but with increased In and As content. Clearly, an increase in In and As improved differential gain and decreased threshold current densities.

Diode lasers, emitting in the spectral region between 3.1 and 3.3 μm and with adequate hole confinement, operated in CW up to above 40°C (Fig. 11.25). Figure 11.26a shows the CW RT light–current and power-conversion characteristics of 3.4 μm emitting lasers. The active region consisted of three

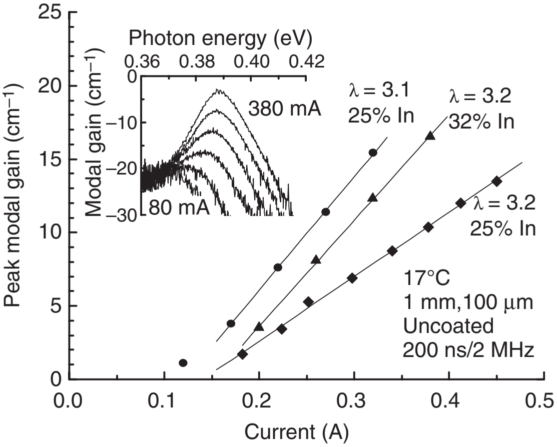

11.24 Dependences of the peak modal gain on current of four 1 mm long, 100 µm wide, uncoated lasers emitting in spectral region from 3.1 to 3.3 µm at 17°C. Inset shows the gain spectra of 3.2 µm laser with improved hole confinement (current increments are 60 mA) (Hosoda *et al.*, 2010a).

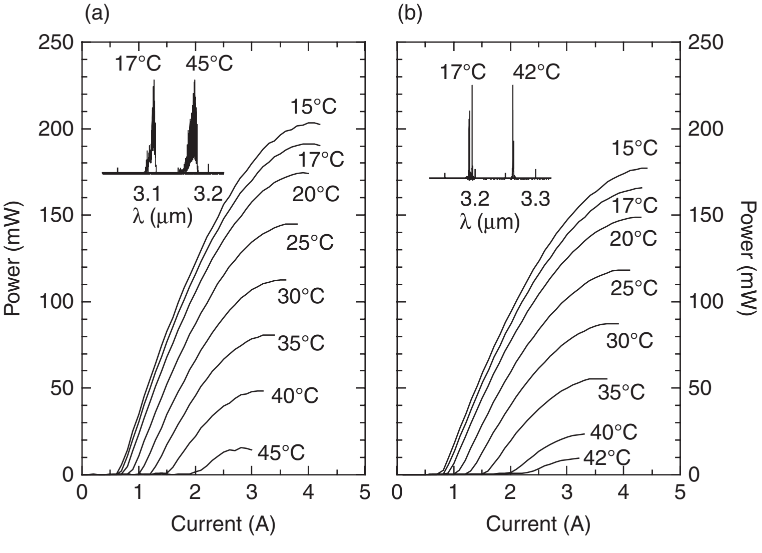

11.25 CW output power and spectral characteristics measured above RT for mm long, AR/HR coated, 100 µm wide lasers emitting at (a) 3.1 µm and (b) 3.2 µm (Hosoda *et al.*, 2010a)).

13 nm wide, 1.5% compressively strained $In_{0.57}Ga_{0.43}As_{0.29}Sb_{0.71}$ QWs separated by 50 nm wide $Al_{0.22}In_{0.32}Ga_{0.46}As_{0.30}Sb_{0.70}$ barrier layers. The waveguide core was formed by a 250 nm wide barrier alloy on both sides of active region. More than 40 mW of CW output power was obtained at 12°C.

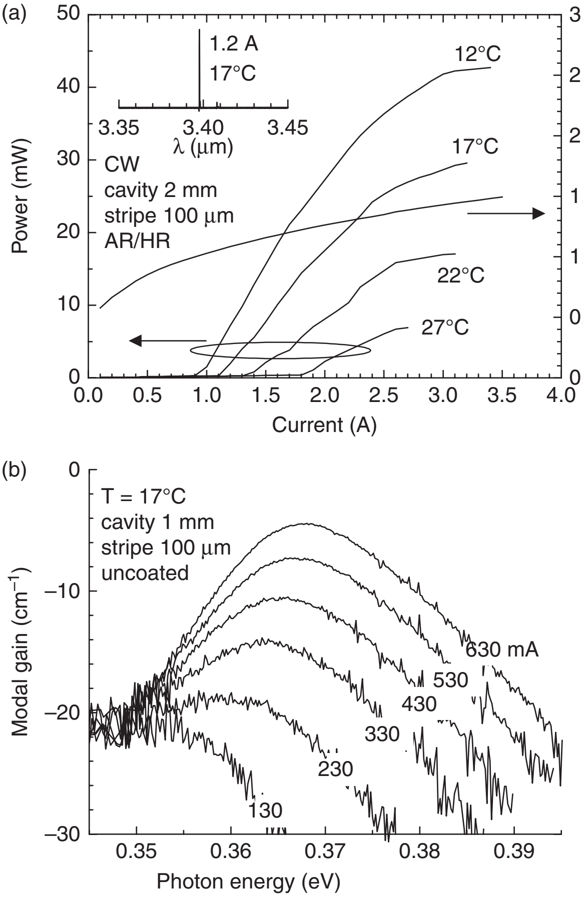

11.26 (a) Temperature dependence of light–current characteristics and voltage–current characteristics (17°C) measured in CW regime for 2 mm long, 100 μm wide, AR/HR coated diode lasers emitting near 3.4 μm; (b) current dependence of the modal gain spectra for corresponding 1 mm long, 100 μm wide, uncoated lasers measured in pulsed regime (200 ns/2 MHz) (Hosoda *et al.*, 2010b).

Increasing the heatsink temperature to 27°C led to a two-fold increase in threshold current. Voltage drop across the laser heterostructure was below 1.5 V at the maximum output power level. More than 5 mW of CW output power was available at 27°C with a wavelength near 3.44 μm. The internal loss is estimated to be about 9 cm^{-1} (Fig. 11.26b).

The increase in laser wavelength from 3 to 3.4 μm was accompanied by a three-fold rise in threshold current density and a corresponding reduction of the device efficiency. Increasing individual Auger recombination events three-fold is hardly feasible when the bandgap is reduced by only about 10%.

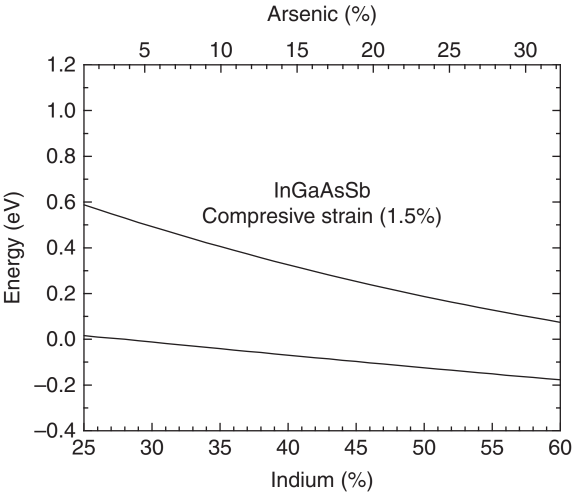

11.27 Calculated positions of the band edges on absolute energy scale for GaInAsSb QW alloy with 1.5% compressive strain with respect to GaSb substrate (Belenky *et al.*, 2011).

However, to reduce the active region bandgap by 10% the GaInAsSb QWs of 3.4 μm lasers were made wider and incorporated more indium than QWs of 3 μm lasers. Extra indium requires extra arsenic to maintain pseudomorphic growth. Increased As concentration moves the QW valence band edge down on the absolute energy scale, thus degrading the hole confinement. Figure 11.27 illustrates this trend by plotting the compositional dependence of the band-edge positions of the GaInAsSb alloy with 1.5% compressive strain.

Increasing the QW indium contents from about 25% (2.2 μm RT emission wavelength in 10–15 nm wide QWs) to about 60% (3.5–4 μm RT emission wavelength) lowers the QW valence band edge by about 200 meV. Unless the barrier material is correspondingly adjusted, the hole confinement will degrade and can even completely disappear. Poor hole confinement increases the number of states in the valence band available for thermal population, thus increasing threshold carrier concentration and triggering the Auger, as well as other temperature-activated processes that are detrimental to high power RT operation of diode lasers.

11.4 Metamorphic GaSb-based diode lasers

The poor hole confinement in QWs made of In-rich GaInAsSb alloys can be somewhat improved if QWs are grown on substrates with lattice constants greater than those of GaSb. Figure 11.28a illustrates this concept by plotting

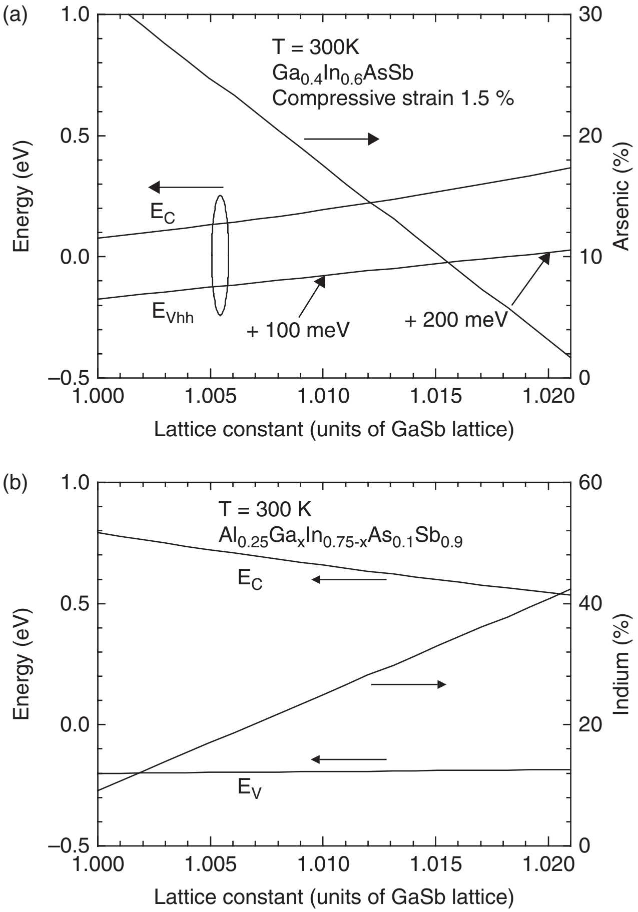

11.28 Calculated positions of the band edges on absolute energy scale for: (a) $Ga_{0.4}In_{0.6}As_ySb_{1-y}$ QW alloy with y adjusted to have 1.5% of strain on the virtual substrate; (b) $Al_{0.25}Ga_xIn_{0.75-x}As_{0.1}Sb_{0.9}$ barrier alloy with x adjusted to lattice match to the virtual substrate (Belenky *et al.*, 2011).

the band edges for 1.5% strained QW containing 60% indium. Calculations predict an increase in the absolute position of the valence band edge in about 100 and 200 meV when the reference lattice constant is increased, correspondingly, by 1% and 2% from that of GaSb. Figure 11.28b plots band edges of the quinary AlGaInAsSb barrier material lattice matched to this new lattice. Increase of the lattice constant of AlGaInAsSb quinary alloy can be achieved by replacing Ga with In while keeping the As composition unchanged. Thus, if the reference lattice constant is increased from that of GaSb, the QW As composition can be reduced while that of the barrier remains unchanged.

The availability of high-quality virtual substrates with lattice constants larger than those of GaSb would allow for the development of mid infrared laser heterostructures with improved carrier confinement in the active region, which would extend operating wavelengths and enhance output power levels for the GaSb-based type-I QW diode lasers. One possible way of increasing the reference lattice constant from that of GaSb is to use GaInSb or AlGaInSb alloys as substrates (Pease *et al.*, 2003). The corresponding bulk substrates are not currently available. Metamorphic MBE can be used to grow GaInSb or AlGaInSb virtual substrates with designed lattice constants on top of GaSb substrates. The lattice constant can be adjusted by varying In content. Graded buffers can be used to accommodate lattice mismatch between parent and virtual substrates and confine the corresponding misfit dislocation network (Tersoff, 1993).

Linearly graded GaInSb buffers have been developed and $Ga_{0.84}In_{0.16}Sb$ virtual substrates with lattice constants ~0.8% bigger than that of GaSb realized. The virtual substrates were grown on top of 2 μm thick GaInSb buffer layers. The buffer layers had linearly graded native lattice constants. Figure 11.29a shows the (004) $\theta/2-\theta$ scan measured for the epi structure containing a 500 nm thick $Ga_{0.84}In_{0.16}Sb$ virtual substrate with a lattice constant 0.8% larger than that of GaSb (Kipshidze *et al.*, 2011).

The rightmost intensive peak corresponds to the GaSb substrate. The flat shoulder to the left of the substrate peak corresponds to the graded buffer. The reflex from the $Ga_{0.84}In_{0.16}Sb$ virtual substrate layer can be clearly seen. Intensive photoluminescence was observed at RT from the test structure grown directly on top of the virtual substrate (Fig. 11.29b). The test structure consisted of two 10 nm wide compressively strained $Ga_{0.65}In_{0.35}Sb$ QWs separated by 50 nm of $Al_{0.25}Ga_{0.64}In_{0.11}Sb$ alloy. Figure 11.29c shows a cross sectional transmission electron microscopy micrograph of the test structure grown on the virtual substrate. The misfit dislocation network is fully confined to the bottom 1500 nm of the graded buffer layer.

A virtual substrate with an 0.8% bigger lattice constant than that of GaSb was used to demonstrate the compatibility of metamorphic growth with high power diode laser technology, particularly high power 2.2 μm lasers. The laser heterostructures, designed for operation at a wavelength of 2.2 μm, were grown on the $Ga_{0.84}In_{0.16}Sb$ virtual substrate. The laser active region and the waveguide core resembled the test structure described above. The n- and p-cladding layers were Te- and Be-doped $Al_{0.85}Ga_{0.07}In_{0.08}Sb$. To create the graded bandgap, heavily doped transition layers were introduced between the substrate and the n-cladding and between the p-cladding and the p-$Ga_{0.84}In_{0.16}Sb$ cap layers. Figure 11.30 plots the power and power-conversion characteristics measured for diode lasers with cavity lengths of 2 and 3 mm.

The devices demonstrate a CW threshold current density of below 150 A/cm^2 at 20°C. The maximum CW output power above 1.4 W was obtained

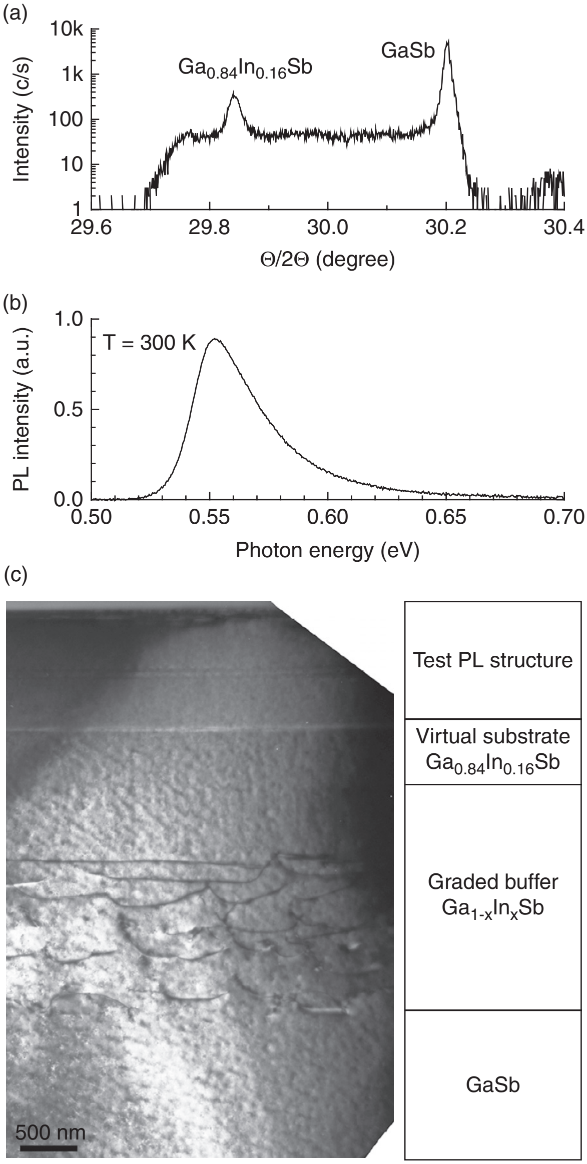

11.29 (a) High resolution x-ray diffraction (HRXRD) (004) $\theta/2-\theta$ scan of an unstrained $Ga_{0.84}In_{0.16}Sb$ virtual substrate grown on a GaInSb graded buffer layer; (b) RT PL spectrum of the test structure grown on the virtual substrate (PL – photoluminescence); (c) XTEM of the test structure grown on the virtual substrate (Kipshidze *et al.*, 2011).

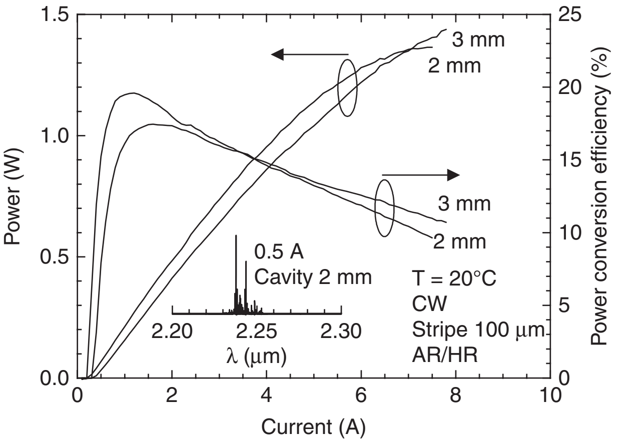

11.30 CW power and power-conversion characteristics of 100 μm-wide 2 and 3 mm long AR/HR coated devices measured at 20°C. Inset shows the laser spectrum at 5 A (Kipshidze *et al.*, 2011).

from 3 mm long lasers at 20°C. The power-conversion efficiency peaked at about 20% and remained above 10% at the maximum output power level. Parameters $T_0 \approx 70$ K and $T_1 \approx 230$ K were measured in the temperature range from 20 to 70°C for 1 mm long uncoated lasers under a pulsed regime. The voltage drop across the laser heterostructure remained below 2 V at the maximum output power level. It should be noted that devices were processed using a standard double-side contact diode laser technology, in which current flows through the virtual substrate and the graded buffer layer. Relatively low voltage drops measured across the metamorphic laser heterostructures indicate that the strain relaxed section of the graded GaInSb buffer does not obstruct the current flow.

11.5 Acknowledgements

The authors would like to acknowledge the long term support of the research efforts at Stony Brook University aimed at development of GaSb-based diode laser technology by US Air Force Office of Scientific Research, US Army Research Office and US National Science Foundation.

11.6 References

Alibert C, Skouri M, Joullie A, Benouna M and Sadiq S (1991), 'Refractive indices of AlSb and GaSb-lattice-matched AlXGa1-XAsYSb1-Y in the transparent wavelength region', *J Appl Phys*, **69**, 3208.

Bachmann A, Lim T, Kashani-Shirazi K, Dier O, Lauer C and Amann M C (2008), ‘Continuous-wave operation of electrically pumped GaSb-based vertical cavity surface emitting laser at 2.3 μm’, *Electron Lett*, **44**, 202.

Bachmann A, Arafin S and Kashani-Shirazi K (2009), ‘Single-mode electrically pumped GaSb-based VCSELs emitting continuous-wave at 2.4 and 2.6 μm’, *New J Phys*, **11**, 125014.

Baranov A N, Fouillant C, Grunberg P, Lazzari J L, Gaillard S and Joullié A (1994), ‘High temperature operation of GalnAsSb/AIGaAsSb double-heterostructure lasers emitting near 2.1 μm’, *Appl Phys Lett*, **65**, 616.

Baranov A N, Rouillard Y, Boissier G, Grech P, Gaillard S and Alibert C (1998), ‘Sb-based monolithic VCSEL operating near 2.2 μm at room temperature’, *Electron Lett*, **34**, 281.

Belenky G, Shterengas L, Kipshidze G and Hosoda T (2011), ‘Type-I diode lasers for spectral region above 3 μm’, *IEEE J Sel Topics Quantum Electron*, **17**, 1426.

Bir G L and Pikus G E (1974), *Symmetry and Strain-Induced Effects in Semiconductors*, New York, Wiley.

Bochkarev A E, Dolginov L M, Drakin A E, Druzhinina L V, Eliseev P G and Sverdlov B N (1985), ‘Injection InGaSbAs lasers emitting radiation of wavelengths 1.9–2.3 μm at room temperature’, *Sov J Quantum Electron*, **15**, 869.

Bochkarev A E, Dolginov L M, Drakin A E, Eliseev P G and Sverdlov B N (1988), ‘Continuous-wave lasing at room temperature in InGaSbAs/GaAlSbAs injection heterostructures emitting in the spectral range 2.2–2.4 μm’, *Sov J Quantum Electron*, **18**, 1362.

Botez D (1999), ‘Design considerations and analytical approximations for high continuous-wave power, broad-waveguide diode lasers’, *Appl Phys Lett*, **74**, 3102.

Caffey D, Day T, Kim C S, Kim M, Vurgaftman I, Bewley W W, Lindle J R, Canedy C L, Abell J and Meyer J R (2010), ‘Performance characteristics of a continuous-wave compact widely tunable external cavity interband cascade lasers’, *Opt Exp*, **18**, 15691.

Caneau C, Srivastava A K, Dentai A G, Zyskind J L and Pollack M A (1985), ‘Room-Temperature GalnAsSb/AIGaAsSb DH injection lasers at 2.2 μm’, *Electron Lett,* **21**, 815.

Cathabard O, Teissier R, Devenson J, Moreno J C and Baranov A N (2010), ‘Quantum cascade lasers emitting near 2.6 μm’, *Appl Phys Lett*, **96**, 141110.

Cerutti L, Ducanchez A, Grech P, Garnache A and Genty F (2008), ‘Continuous-wave operation of electrically pumped GaSb-based vertical cavity surface emitting laser at 2.3 μm’, *Electron Lett*, **44**, 203.

Chandola A, Pino R and Dutta P S (2005), ‘Below bandgap optical absorption in tellurium-doped GaSb’, *Semicond Sci Technol*, **20**, 886.

Chen J, Donetsky D, Shterengas L, Kisin M, Kipshidze G and Belenky G (2008), ‘Effect of quantum well compressive strain above 1% on differential gain and threshold current density in type-I GaSb-based diode lasers’, *IEEE J Quantum Electron*, **44**, 1204.

Chen J, Kipshidze G and Shterengas L (2010a), ‘High-power 2 μm diode lasers with asymmetric waveguide’, *IEEE J Quantum Electron*, **46**, 1464.

Chen J, Kipshidze G and Shterengas L (2010b), ‘Diode lasers with asymmetric waveguide and improved beam properties’, *Appl Phys Lett*, **96**, 241111.

Choi H K and Eglash S J (1991), ‘Room-temperature CW operation at 2.2 μm of GalnAsSb/AIGaAsSb diode lasers grown by molecular beam epitaxy’, *Appl Phys Lett*, **59**, 1165.

Choi H K and Eglash S J (1992), 'High-power multiple-quantum-well GalnAsSb/AIGaAsSb diode lasers emitting at 2.1 μm with low threshold current density', *Appl Phys Lett*, **61**, 1154.

Choi H K, Eglash S J and Connors M K (1993), 'Single-frequency GalnAsSWAGaAsSb quantum-well ridge-waveguide lasers emitting at 2.1 μm', *Appl Phys Lett*, **63**, 3271.

Choi H K, Turner G W and Eglash S J (1994), 'High-power GaInAsSb-AlGaAsSb multiple-quantum-well diode lasers emitting at 1.9 μm', *IEEE Photon Technol Lett*, **6**, 7.

Choi H K, Walpole J N, Turner G W, Connors M K, Missaggia L J and Manfra M J (1998), 'GaInAsSb–AlGaAsSb tapered lasers emitting at 2.05 μm with 0.6-W diffraction-limited power', *IEEE Photon Technol Lett*, **10**, 938.

Devenson J, Cathabard O, Teissier R and Baranov A N (2007a), 'High temperature operation of $\lambda\approx3.3$ μm quantum cascade lasers', *Appl Phys Lett*, **91**, 141106.

Devenson J, Cathabard O, Teissier R and Baranov A N (2007b), 'InAs/AlSb quantum cascade lasers emitting at 2.75–2.97 μm', *Appl Phys Lett*, **91**, 251102.

Donati G P, Kaspi R and Malloy K J (2003), 'Interpolating semiconductor alloy parameters: application to quaternary III-V band gaps', *J Appl Phys*, **94**, 5814.

Donetsky D, Kipshidze G, Shterengas L, Hosoda T and Belenky G (2007), '2.3-μm Type-I Quantum Well GaInAsSb/AlGaAsSb/GaSb laser diodes with a quasi-CW output power of 1.4 W', *Electron Lett*, **43**, 810.

Ducanchez A, Cerutti L, Grech P and Genty F (2008), 'Room-temperature continuous-wave operation of 2.3-μm Sb-based electrically pumped monolithic vertical-cavity lasers', *IEEE Photon Technol Lett*, **20**, 1745.

Fekete D, Yasin M, Rudra A and Kapon E (2008), 'Very low transparency currents in double quantum well InGaAs semiconductor lasers with delta-doped resonant tunneling', *Appl Phys Lett*, **92**, 021109.

Garbuzov D Z, Martinelli R U, Lee H, York P K, Menna R J, Connolly J C and Narayan S Y (1996), 'Ultralow-loss broadened-waveguide high-power 2 μm AlGaAsSb/InGaAsSb/GaSb separate-confinement quantum-well lasers', *Appl Phys Lett*, **69**, 2006.

Garbuzov D Z, Martinelli R U, Lee H, Menna R J, York P K, DiMarco L A, Harvey M G, Matarese R J, Narayan S Y and Connolly J C (1997), '4 W quasi-continuous-wave output power from 2 μm AlGaAsSb/InGaAsSb single-quantum-well broadened waveguide laser diodes', *Appl Phys Lett*, **70**, 2931.

Garbuzov D Z, Lee H, Khalfin V, Martinelli R, Connoly J C and Belenky G L (1999), '2.3–2.7 μm room temperature CW operation of InGaAsSb/AlGaAsSb broad waveguide SCH-QW diode lasers', *IEEE Photon Technol Lett*, **11**, 794.

Garcia M, Salhi A, Pérona A, Rouillard Y, Sirtori C, Marcadet X and Alibert C (2004), 'Low threshold high-power room-temperature continuous-wave operation diode laser emitting at 2.26 μm', *IEEE Photon Technol Lett*, **16**, 1253.

Grau M, Lin C and Amann M C (2002), 'Low threshold 2.72 μm GalnAsSb/AlGaAsSb multiple-quantum-well laser', *Electron Lett*, **38**, 1678.

Grau M, Lin C, Dier O and Amann M C (2003), 'Continuous-wave GaInAsSb/AlGaAsSb type-I double quantum well lasers for 2.96 μm wavelength', *Electron Lett*, **39**, 1816.

Grau M, Lin C, Dier O, Lauer C and Amann M C (2005), 'Room-temperature operation of 3.26 μm GaSb-based type-I lasers with quinternary AlGaInAsSb barriers', *Appl Phys Lett*, **87**, 241104.

Gupta J A, Barrios P J, Lapointe J, Aers G C and Storey C (2009a), 'Single-mode 2.4 μm InGaAsSb/AlGaAsSb distributed feedback lasers for gas sensing', *Appl Phys Lett*, **95**, 041104.

Gupta J A, Barrios P J, Aers G C, Waldron P and Storey C (2009b), 'Room-temperature continuous-wave operation of type-I GaSb-based lasers at 3.1 μm', *Electron Lett*, **45**, 835.

Gupta J A, Ventrudo B F, Waldron P and Barrios P J (2010), 'External cavity tunable type-I diode laser with continuous-wave singlemode operation at 3.24 μm', *Electron Lett*, **46**, 1218.

Hakki B W and Paoli T L (1975), 'Gain spectra in GaAs double-heterojunction injection lasers', *J Appl Phys*, **46**, 1299.

Hosoda T, Kipshidze G, Shterengas L and Belenky G (2009), '200 mW type-I GaSb-based laser diodes operating at 3 μm. Role of waveguide width', *Appl Phys Lett*, **94**, 261104.

Hosoda T, Kipshidze G, Tsvid G, Shterengas L and Belenky G (2010a), 'Type-I GaSb-Based Laser Diodes Operating in 3.1- to 3.3-μm Wavelength Range', *IEEE Photon Technol Lett*, **22**, 718.

Hosoda T, Kipshidze G, Shterengas L and Belenky G (2010b), 'Diode lasers emitting near 3.44 μm in continuous-wave regime at 300K', *Electron Lett*, **46**, 1455.

Hümmer M, Rößner K, Benkert A and Forchel A (2004), 'GaInAsSb–AlGaAsSb distributed feedback lasers emitting near 2.4 μm', *Photon Technol Lett*, **16**, 380.

Hümmer M, Röβner K, Lehnhardt T, Müller M, Forchel A, Werner R, Fischer M and Koeth J (2006), 'Long wavelength GaInAsSb-AlGaAsSb distributed-feedback lasers emitting at 2.84 μm', *Electron Lett*, **42**, 583.

Kaspi R and Ongstad A P (2006), 'High performance optically pumped antimonide lasers operating in the 2.4–9.3 μm wavelength range', *Appl Phys Lett*, **88**, 041122.

Kim J G, Shterengas L, Martinelli R U, Belenky G L, Garbuzov D Z and Chan W K (2002), 'Room-Temperature 2.5 μm InGaAsSb/AlGaAsSb Diode Lasers Emitting 1 W Continuous-Wave', *Appl Phys Lett*, **81**, 3146.

Kim J G, Shterengas L, Martinelli R U and Belenky G L (2003), 'High-Power Room-Temperature Continuous Wave Operation of 2.7- and 2.8 μm In(Al)GaAsSb/GaSb Diode Lasers', *Appl Phys Lett*, **83**, 1926.

Kim M, Canedy C L, Bewley W W, Kim C S, Lindle J R, Abell J, Vurgaftman I and Meyer J R (2008), 'Interband cascade laser emitting at λ=3.75 μm in continuous wave above room temperature', *Appl Phys Lett*, **92**, 191110.

Kipshidze G, Hosoda T, Sarney W L, Shterengas L and Belenky G (2011), 'High-Power 2.2-μm diode lasers with metamorphic arsenic-free heterostructures', *IEEE Photon Technol Lett*, **23**, 317.

Kisin M V, Brown R G W and El-Ghoroury H S (2009a), 'Optimum quantum well width for III-nitride nonpolar and semipolar laser diodes', *Appl Phys Lett*, **94**, 021108.

Kisin M V, Brown R G W and El-Ghoroury H S (2009b), 'Optical characteristics of III-nitride quantum wells with different crystallographic orientations', *J Appl Phys*, **105**, 013112.

Kisin M V and El- Ghoroury H S (2010), 'Modeling of injection characteristics of polar and nonpolar III-nitride multiple quantum well structures', *J Appl Phys*, **107**, 103106.

Lehnhardt T, Hümmer M, Rößner K, Müller M, Höfling S and Forchel A (2008), 'Continuous wave single mode operation of GaInAsSb/GaSb quantum well lasers emitting beyond 3 μm', *Appl Phys Lett*, **92**, 183508.

Li Z G, Liu G J, You M H, Li L, Li M, Wang Y, Zhang B S and Wang X H (2009), '2.0 μm room temperature CW operation of InGaAsSb/AlGaAsSb laser with asymmetric waveguide structure', *Laser Phys*, **19**, 1230.

Liang R, Chen J, Kipshidze G, Westerfeld D, Shterengas L and Belenky G (2011), 'High-power 2.2-μm diode lasers with heavily strained active region', *IEEE Photon Technol Lett*, **23**, 603.

Lin C, Grau M, Dier O and Amann M C (2004), 'Low threshold room-temperature continuous-wave operation of 2.24–3.04 μm GaInAsSb/AlGaAsSb quantum-well lasers', *Appl Phys Lett*, **84**, 5088.

Mermelstein C, Simanowski S, Mayer M, Kiefer R, Schmitz J, Walther M and Wagner J (2000), 'Room-temperature low-threshold low-loss continuous-wave operation of 2.26 μm GaInAsSb/AlGaAsSb quantum-well laser diodes', *Appl Phys Lett*, **77**, 1581.

Motyka M, Sek G, Ryczko K, Misiewicz J, Belahsene S, Boissier G and Rouillard Y (2009), 'Optical transitions and band gap discontinuities of GaInAsSb/AlGaAsSb quantum wells emitting in the 3 μm range determined by modulation spectroscopy', *J Appl Phys*, **106**, 066104.

Newell T, Wu X, Gray A L, Dorato S, Lee H and Lester L F (1999), 'The Effect of Increased Valence Band Offset on the Operation of 2 μm GaInAsSb-AlGaAsSb Lasers', *IEEE Photon Technol Lett*, **11**, 30.

Paajaste J, Suomalainen S, Koskinen R, Harkonen A, Guina M and Pessa M (2009), 'High-power and broadly tunable GaSb-based optically pumped VECSELs emitting near 2 μm', *J Crystal Growth*, **311**, 1917.

Pease E A, Dawson L R, Vaughn L G, Rotella P and Lester L F (2003), '2.5–3.5 μm optically pumped GaInSb/AlGaInSb multiple quantum well lasers grown on AlInSb metamorphic buffer layers', *J Appl Phys*, **93**, 3177.

Raino G, Salhi A, Tasco V, Intartaglia R, Cingolani R, Rouillard Y, Tournie E and DeGiorgi M (2008), 'Subpicosecond timescale carrier dynamics in GaInAsSb/AlGaAsSb double quantum wells emitting at 2.3 μm', *Appl Phys Lett*, **92**, 101931.

Rattunde M, Schmitz J, Kiefer R and Wagner J (2006), 'GaSb-based 2.X μm quantum-well diode lasers with low beam divergence and high output power', *Appl Phys Lett*, **88**, 081115.

Roesener B, Schulz N, Rattunde M, Manz C, Koehler K and Wagner J (2008), 'High-power high-brightness operation of a 2.25-μm (AlGaIn)(AsSb)-based barrier-pumped vertical-external-cavity surface-emitting laser', *IEEE Photon Technol Lett*, **20**, 502.

Roesener B, Rattunde M, Moser R, Manz C, Koehler K and Wagner J (2009), 'GaSb-based optically pumped semiconductor disk laser using multiple gain elements', *IEEE Photon Technol Lett*, **21**, 848.

Roesener B, Rattunde M, Moser R, Kaspar S, Toepper T, Manz C, Koehler K and Wagner J (2011), 'Continuous-wave room-temperature operation of a 2.8 μm GaSb-based semiconductor disk laser', *Opt Lett*, **36**, 319.

Rouillard Y, Genty F, Perona A, Vicet A, Yarekha D A, Boissier G, Grech P, Baranov A N and Alibert C (2001), 'Edge and vertical surface emitting lasers around 2.0–2.5 μm and their applications', *Phil Trans R Soc London A*, **359**, 581.

Rößner K, Hümmer M, Benkert A and Forchel A (2005), 'Long-wavelength GaInAsSb/AlGaAsSb DFB lasers emitting near 2.6 μm', *Physica E*, **30**, 159.

Ryvkin B S and Avrutin E A (2005), 'Nonbroadened asymmetric waveguide diode lasers promise much narrower far fields than broadened symmetric waveguide ones', *J Appl Phys*, **98**, 026107.

Salhi A, Barat D, Romanini D, Rouillard Y, Ouvrard A, Werner R, Seufert J, Koeth J, Vicet A and Garnache A (2006), 'Single-frequency Sb-based distributed-feedback lasers emitting at 2.3 μm above room temperature for application in tunable diode laser absorption spectroscopy', *Appl Opt*, **45**, 4957.

Sek G, Motyka M, Ryczko K, Janiak F, Misiewicz J, Belahsene S, Boissier G and Rouillard Y (2010), 'Band offsets and photoluminescence thermal quenching in mid-infrared emitting GaInAsSb quantum wells with quinary AlGaInAsSb barriers', *Jpn J Appl Phys*, **49**, 031202.

Shterengas L, Belenky G L, Kim J G and Martinelli R U (2004), 'Design of high-power room-temperature continuous-wave GaSb-based type-I quantum-well lasers with λ > 2.5 μm', *Semicond Sci Technol*, **19**, 655.

Shterengas L, Belenky G, Kipshidze G and Hosoda T (2008), 'Room temperature operated 3.1 μm type-I GaSb-based diode lasers with 80 mW continuous-wave output power', *Appl Phys Lett*, **92**, 171111.

Shterengas L, Kipshidze G, Hosoda T, Chen J and Belenky G (2009), 'Diode lasers emitting at 3 μm with 300 mW of continuous-wave output power', *Electron Lett*, **45**, 942.

Tersoff J (1993), 'Dislocation and strain relief in compositionally graded layers', *Appl Phys Lett*, **62**, 693.

Turner G W, Choi H K and Manfra M J (1998), 'Ultralow-threshold 50 A/cm^2 strained single-quantum-well GaInAsSb/AlGaAsSb lasers emitting at 2.05 μm', *Appl Phys Lett*, **72**, 876.

Vurgaftman I, Meyer J R and Ram-Mohan L R (2001), 'Band parameters for III-V compound semiconductors and their alloys', *J Appl Phys*, **89**, 5815.

Vurgaftman I, Canedy C L, Kim C S, Kim M, Bewley W W, Lindle J R, Abell J and Meyer J R (2009), 'Mid-infrared interband cascade lasers operating at ambient temperatures', *New J Phys*, **11**, 125015.

Walpole J N, Choi H K, Missaggia L J, Liau Z L, Connors M K, Turner G W, Manfra M J and Cook C C (1999), 'High-power high-brightness GaInAsSb-AlGaAsSb tapered laser arrays with anamorphic collimating lenses emitting at 2.05 μm', *IEEE Photon Technol Lett*, **11**, 1223.

Wang J, Maiorov M, Baer D S, Garbuzov D Z, Connolly J C and Hanson R K (2000), 'In situ combustion measurements of CO with diode-laser absorption near 2.3 μm', *Appl Opt*, **39**, 5579.

Yablonovitch E and Kane E (1986), 'Reduction of lasing threshold current density by the lowering of valence band effective mass', *IEEE J Lightwave Technol*, **4**, 504.

Yarekha D A, Glastre G, Perona A, Rouillard Y, Genty F, Skouri E M, Boissier G, Grech P, Joullie A, Alibert C and Baranov A N (2000), 'High temperature GalnSbAs/GaAlSbAs quantum well singlemode continuous wave lasers emitting near 2.3 μm', *Electron Lett*, **36**, 537.

12

Interband cascade (IC) lasers

R. Q. YANG, University of Oklahoma, USA

DOI: 10.1533/9780857096401.3.487

Abstract: This chapter discusses relevant concepts, material systems, quantum well structures, and physical processes involved in interband cascade (IC) lasers, reviewing their development from original concept to practical devices. Recent progress and new developments are presented. Future prospects for IC lasers are also discussed.

Key words: mid infrared, quantum wells, diode lasers, antimonide, type-II heterostructure.

12.1 Introduction

At a conference in 1994, the same year when the intersubband quantum cascade (QC) laser[1] was first reported, the concept of the interband cascade (IC) laser was initially proposed[2] for realizing an efficient mid infrared (IR) semiconductor laser source. Since then, the development of IC lasers has been pursued by a number of groups, and significant progress in device performance has been made, particularly in recent years.[3–50] The achievements include the development of thermoelectrically-cooled single-mode distributed feedback (DFB) continuous wave (cw) IC lasers[28,29] in hermetically sealed packages, and the demonstration of cw IC lasers above room temperature (up to 380 K) with low power consumption (e.g., <0.1 W at room temperature).[37–44,50] DFB IC lasers have been used in laboratories and in the field for detection of important gas molecules such as CH_4, HCl, H_2CO, and C_2H_6.[24,51–55] This chapter will discuss relevant concepts, material system, quantum well structures, and physical processes involved in IC lasers. In Section 12.2, we describe the general operating principle of IC lasers. In Section 12.3, we review their early development and challenges, from original concept to practical devices. In Section 12.4, we present some recent progress and new developments. Future prospects for IC lasers and concluding remarks are given in Section 12.5.

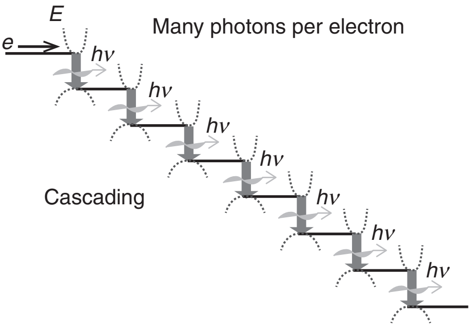

12.1 Illustration of the IC laser under a forward bias.

12.2 Operating principle of interband cascade (IC) lasers

In contrast to conventional diode lasers, where multiple active quantum wells (QW) are connected in parallel for carrier injection, IC lasers have their multiple active regions connected in series such that the entire IC laser structure, under a forward bias, forms an energy staircase as shown in Fig. 12.1. Hence, every injected electron is able to emit an additional photon when it cascades down each stage, leading to high quantum efficiencies (>1, defined by the number of photons generated per electron) similar to intersubband QC lasers.[1] The idea of utilizing a cascade structure to achieve a quantum efficiency greater than unity is not original in IC (or QC) lasers. Rather, it was explicitly pointed out in 1982 by van der Ziel and Tsang[56] when they studied monolithic integrated GaAs diode lasers with tunnel junctions. However, in the configuration that van der Ziel and Tsang studied, the diode lasers were separated in different optical waveguides, while in IC (and QC) lasers all the active regions are in the same waveguide, and the differential gain increases with the number of cascade stages (N_c).

In contrast to the conventional parallel configuration, the threshold voltage (V_{th}) of IC lasers is proportional to the number of cascade stages. The required forward bias is no less than $N_c h\nu/e$, where $h\nu$ is the photon energy and e is the electron charge. Ideally, if the transparency current could be ignored, the operating current of an IC laser would be N_c times less than that in an equivalent parallel diode laser. Hence, IC lasers essentially trade higher threshold voltage for lower threshold current. This trade yields an electric power consumption from parasitic resistance (e.g., from contact and cladding regions) that is N_c^2 times less compared to the parallel diode laser structure,[3,44] suggesting more efficient operation of cascade lasers compared to conventional parallel diode lasers. In practical circumstances, a cascade laser may not follow such an exact trade-off between the current and voltage, due to the finite transparency current and other factors. Nevertheless, the cascade structure preserves advantages over the conventional parallel configuration, especially for longer wavelength lasers, where the photon energy $h\nu$ is smaller, and both suitable optical confinement and sufficient gain require larger N_c. The voltage drop across the parasitic resistance and, therefore, the electrical power wasted on the parasitic resistance of a conventional parallel diode laser becomes a larger percentage of the applied voltage and total power dissipation. With the cascade configuration, the entire structure is effectively equivalent to a semiconductor with a bandgap that is approximately equal to $N_c h\nu$ in terms of the voltage usage. As such, the percentage of applied voltage across the parasitic resistance from the contact and cladding regions is reduced significantly, leading to a high voltage efficiency ($\eta_v = N_c h\nu/(eV_{\text{th}})$) in a cascade laser. Also, with more active QWs, the injected carriers cannot be uniformly distributed to all photon-emission regions in a conventional parallel laser and the band-filling effect may be substantial at high current injection. These factors will significantly lower the performance of conventional parallel lasers in the longer wavelengths. However, identical injection of carriers to each active region can be ensured by the series connection in the cascade laser structure and the carrier concentration required for threshold is lower than in conventional parallel diode lasers. Consequently, the band-filling effect and losses are reduced in cascade laser configurations.

Although IC and QC lasers both have the advantage of reusing electrons to generate multiple photons with high quantum efficiencies, there are important differences in the nature of the optical transition. In contrast to QC lasers, where fast phonon scattering is inherent to intersubband transitions, IC lasers emit photons based on transitions between conduction and valence bands with opposite dispersion curvatures, as shown in Fig. 12.1. As such, IC lasers circumvent the fast phonon scattering, but, like other interband diode lasers, they may encounter significant Auger recombination. Nevertheless, Auger recombination is usually slower than the optical phonon scattering in the mid IR spectrum (e.g., 3–5 μm). Consequently, population inversion can be well established between two interband transition states in IC lasers[3] without using the fast phonon-mediated depletion as in QC lasers.[1] Therefore, excess voltage, threshold current density and power consumption can be significantly lowered in IC lasers.

IC lasers can be constructed from the nearly lattice-matched InAs/GaSb/AlSb III-V material system. In this material system, the conduction band-edge of InAs is lower in energy than the valence band-edge of GaSb and they form a semimetal-like hetero-interface – a unique feature in type-II broken-gap heterostructure, QWs, and superlattices (SLs).[57–59] Such a characteristic band-edge alignment leads to some properties and applications that are distinctive from type-I QWs and SLs. An excellent

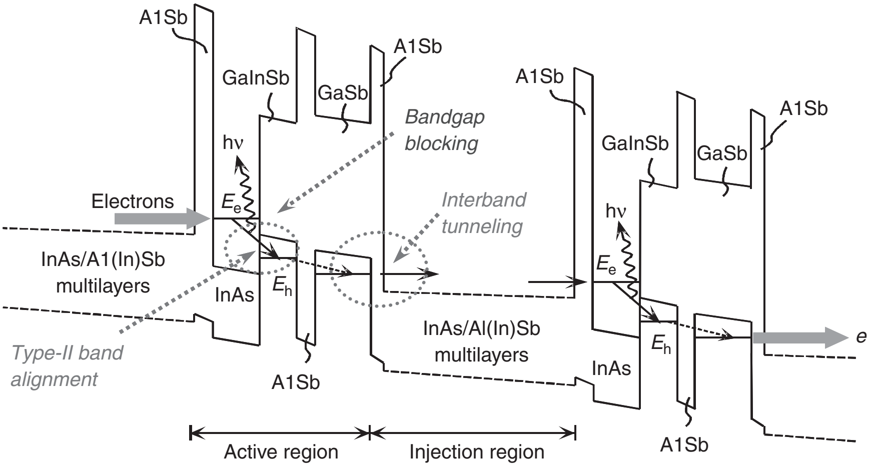
A1Sb
GaInSb
GaSb
A1Sb
Bandgap blocking
hν
Electrons
E_e
Interband tunneling
InAs/A1(In)Sb multilayers
InAs
E_h
Type-II band alignment
A1Sb
A1Sb
GaInSb
GaSb
A1Sb
hν
E_e
InAs/Al(In)Sb multilayers
E_h
InAs
e
A1Sb
Active region
Injection region

12.2 Schematic energy band-edge diagram for an IC laser.

review on the development of type-II InAs/GaSb SLs from historic perspectives and their applications in detectors is given by Ting *et al.*[60] As pointed out below, this broken-gap alignment facilitates the efficient interband tunneling needed for reusing injected electrons in IC lasers.[2,3] The schematic energy band-edge diagram of a typical type-II IC laser structure under a forward bias is shown in Fig. 12.2, where repeated active regions are separated by *n*-type injection regions consisting of digitally graded InAs/Al(In)Sb multilayers. Each active region comprises InAs/GaInSb type-II QWs, where optical transitions occur between the conduction states E_e and the valence state E_h with their wave-functions residing mainly in InAs and GaInSb layers, respectively. The InAs QW layer is designed to have the ground electron level E_e positioned within the bandgap of GaInSb as shown in Fig. 12.2. As such, the electrons injected from an injection region in the left hand side to the level E_e are essentially blocked from directly tunneling out by the GaInSb, AlSb and GaSb layers, which effectively suppresses the current leakage from the upper energy state to the injector of the next stage. Thus, the only likely way for electrons to reach the next stage is to make interband transitions to the valence state E_h that is above the conduction band-edge of InAs. Following the transition, electrons go through the valence band GaSb QW and then, through interband tunneling, arrive in the conduction band of the injection region in the next cascade stage, ready to be reused for additional photon emissions. In this electron transport recycling process, the type-II band alignment between InAs and GaSb plays an important role in facilitating the interband tunneling from one stage to the next. One can view the type-II hetero-interface as a semimetal source of injecting electrons

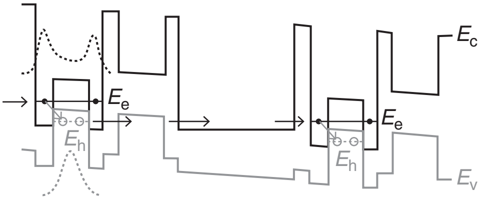

12.3 A schematic IC laser with W-shape QW active regions.

and holes[61,62] and consider the GaSb QW (adjacent to the electron injection region) as the hole injector.[3,44]

Owing to the type-II broken-gap band alignment in the InAs/GaSb material system, the energy separation between states E_e and E_h can be changed from a few meV to 700 meV by manipulating the InAs and GaInSb QW layer thickness. Hence, excellent carrier confinement can be obtained in this III-V compound material system and the lasing wavelength of IC lasers can be tailored by merely adjusting QW thickness, enabling a wide range of spectral coverage that includes the important 3–12 μm region.

One possible drawback of using type-II QWs as the active region is the reduced wave-function overlap between two interband transition states, leading to a smaller gain compared to that in type-I QW lasers where the electron and hole wave-functions are localized in the same layer. Nevertheless, due to the broken-gap band alignment (as circled out in Fig. 12.2) and the small electron effective mass of InAs, the electron wave-function penetration into the GaInSb layer is sufficient for obtaining gain for lasing. To enhance the wave-function overlap, a 'W' shape type-II QW,[63] that is, inserting an extra InAs layer adjacent to the right hand side of GaInSb as shown in Fig. 12.3, can be introduced to increase the gain in IC lasers.[7–9] An example of such a W-QW IC laser was given in Reference 9 with detailed layer sequence (thickness in Å) as:

$\mathbf{18}/19/\underline{32}/13/\mathbf{10}/\mathit{60}/\mathbf{15}/\underline{40}/\mathbf{15}/40/\mathbf{15}/70/\mathbf{14}/51/\mathbf{12}/43/\mathbf{12}/35/\mathbf{13}/30/\mathbf{13}/26/\mathbf{14}/23/\mathbf{14}/21$

for one cascade period, where bold numbers represent the thickness of AlSb layers, underlined numbers are for $Ga_{0.7}In_{0.3}As$ layers, one italic number is for the GaSb layer, and the other numbers denote the thickness of InAs layers. Both conventional type-II SL and W-shape QW active regions have been explored in optically-pumped and electrically-pumped non-cascade diode lasers in mid IR spectrum with impressive device performance.[64–85] It should be noted that the type-I QW active regions can also be incorporated into IC laser configurations[3,10,61,62] although they are less explored in the mid IR wavelength spectrum. Here, we focus our discussion on IC lasers with type-II QW active regions, which are capable of being tailored to cover a wide wavelength range from mid IR to far IR spectrum.

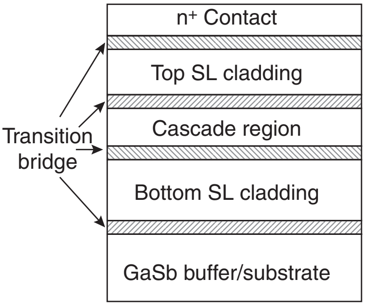

12.4 Schematic layer structure of an IC laser on a GaSb substrate.

12.3 Early development and challenges

Following the proposal of IC lasers and being stimulated by the demonstration of QC lasers, experimental efforts in developing type-II IC lasers started in early 1995 at the University of Houston, where a Riber-32 molecular beam epitaxy (MBE) system was available for the growth of Sb-containing compound semiconductor QWs. These early IC lasers, grown on unintentionally doped *p*-type GaSb (001) substrates, were typically composed of many (>15) cascade stages sandwiched between the bottom and top optical waveguide cladding layers as shown in Fig. 12.4. The cascade regions are composed of multi-QW layers made from the semiconductor materials InAs, Ga(In)Sb, and Al(In)Sb with the overall periodicity of roughly 680–860 Å depending on the desired lasing wavelength. The cladding layers are made of short-period (~5 nm) InAs/AlSb SLs with typical thickness of 1.5–3 μm. Digitally graded multi-QW regions are inserted as transitional/connecting bridges for smoothing carrier transport between the cascade stages and the cladding layers, and between the cladding and the contact (or the buffer) layers. In these IC laser structures on GaSb substrates, the InAs layer is slightly tensile strained (~0.6%), while the GaInSb and Al(In)Sb layers are compressive strained. Every region is designed to be strain-balanced as accurately as possible with minimal residual strain. The entire IC laser structure consists of thousands of thin layers with a total thickness that could be as high as 5 μm (or thicker depending on the wavelength), which presents challenges for the MBE growth.

In early 1997, the University of Houston and Sandia National Laboratories jointly demonstrated pulsed lasing near 3.8 μm from a 20-stage IC laser at temperatures up to 170 K.[4] Although this first IC laser burned out shortly after lasing with high threshold current densities (4.17 kA/cm^2 at 80 K) and did not exhibit the features expected from the cascade process, it established the feasibility of growing complicated IC laser structures by MBE on a GaSb substrate. Shortly thereafter, direct evidence of the cascade process, that is, a differential quantum efficiency exceeding the conventional limit of unity, was obtained from IC lasers emitting at wavelengths of ~4 μm (with simple type-II QW active regions)[5,6] and ~3 μm (with W-QW active regions).[7,8] These IC lasers had relatively low threshold current densities (100–200 A/cm^2 at 80 K) and were operated in pulsed mode at temperatures up to 225 K. Later, an IC laser near 3.6 μm could be operated with short current pulses at temperatures up to 286 K[9] despite the fact that its threshold current density at low temperatures (<180 K) was even higher than the earlier W-QW IC lasers.[7–9] In this pioneering development period, IC laser performance was far below the theoretical projections[10–12] and cw operation was not achieved. More details were discussed in an early review article.[13]

In this period, an IC light emitting diode (LED) was developed for electroluminescence at wavelengths as long as 15 μm at room temperature,[86] demonstrating the unique capability of these Sb-family type-II QW structures to be tailored over a wide spectral range. Also, some issues were encountered during the investigations. These include (1) substantial variations in crystal growth conditions and thus poor reproducibility, (2) inadequately-controlled material quality with various defects and interface roughness due to the intermixing of atoms such as Sb and As, leading to large leakage currents, (3) and long growth times (>15 h) with high shutter moving frequencies, resulting in high rates of failure. There were other problems related to device fabrication and operation. In contrast to a conventional ridge waveguide diode laser, where the ridge is formed by etching from the top to a position above the active region, an IC laser should be etched from the top through the entire active region of cascade stages to ensure identical carrier injection over every stage. This is because current spreading along the transverse plane is very significant in such a cascade structure with thousands of thin layers (that magnify resistance anisotropy) if there is no means (e.g., etching) to confine the current along the vertical injection. These early IC lasers with deep etched mesa structures tended to become damaged at high injection levels before saturation, which limited the output power and operating temperature. W-active-region IC lasers, although lasing at higher temperatures, could be operated only with short pulses (~100 ns) at low repetition rates (5–200 Hz).

In early 1999, IC laser development began at Army Research Laboratory (ARL) where a Varian Gen-II MBE system was available. With improved understanding and material quality, significant progress was quickly achieved at ARL in terms of cw operation, higher quantum efficiency (>600%), peak power (~6 W/facet), power conversion efficiency (>14%) and reproducibility.[14–19] Room temperature pulsed operation was achieved in 2001 from an IC laser near 3.5 μm with reduced threshold current density (13 A/cm^2 at 80 K).[19] Subsequent progress was made at ARL facilities by Maxion Technologies in terms of higher cw operation temperature (214 K) and power efficiency (23%).[20] In this period, it was recognized that the strain balance in IC lasers needed to be designed more appropriately by considering variations of the elastic stiffness constants for different semiconductor materials (e.g., InAs, GaInSb, AlSb). The commonly used average lattice (matched to the substrate) method may not always be adequate for designing device structures such as IC lasers with many different strained layers and with the total thickness of ~5 μm or more. This is because even the slightest strain could be accumulated to become significant in the MBE growth of a thick structure. This consideration has been discussed with examples and calculations for other device structures.[87,88]

In 2002, a new Gen-III MBE system was set up at the Jet Propulsion Laboratory (JPL). In the following years, fast progress was made there.[21–26] Some outstanding performance features included low threshold current densities (8 A/cm^2 at 80 K and 630 A/cm^2 at 300 K),[24,26] above room temperature pulsed operation (350 K limited by cryostat setup),[26] cw operation up to 237 K, and extension of lasing wavelength in the 5.1–5.6 μm region with cw operation up to 165 K.[25] The primary effort at JPL was focused on the spectral range from 3 to 4 μm where many molecules, particularly those with a C–H stretch such as methane and ethane, have strong absorptions. Cryogen-cooled single-mode cw distributed feedback (DFB) IC lasers were developed at JPL (and Maxion) in that spectral range and used to profile atmospheric methane and HCl from airborne platforms as well as to make laboratory measurements of ethane and formaldehyde.[24,51–54] In early 2006, an important milestone was reached at JPL – demonstration of cw operation of a mid IR IC laser at temperatures up to 264 K with power consumption <1.1 W.[27] This made it feasible to operate IC lasers in cw mode with a simple one-stage thermoelectric (TE) cooler at room temperature. In addition, no degradation was observed after continuous operation of nearly 2000 h, indicative of good reliability for practical applications. Subsequently, single-mode DFB IC lasers were developed with cw operating temperature up to 261 K and a tuning range to cover absorption lines of CH_4 near 3.27 μm.[28,29] These lasers were packaged with TE coolers and delivered in the 2007 NASA flight project for the Mars Science Laboratory (MSL) mission's Tunable Laser Spectrometer instrument for methane and methane isotope measurements.[89]

In the development of TE-cooled single-mode DFB IC lasers for the NASA MSL mission, a major technical challenge was to match the lasing wavelength with the desired absorption line of methane, with an adequate tuning range (a few wavenumbers, done by altering current) within the narrow operating temperature window (250–260 K) of IC lasers. This required very precise control of active QW layer thickness and DFB grating period,[28] as well as minimization of losses introduced by the DFB grating considering that the maximum cw operating temperature of

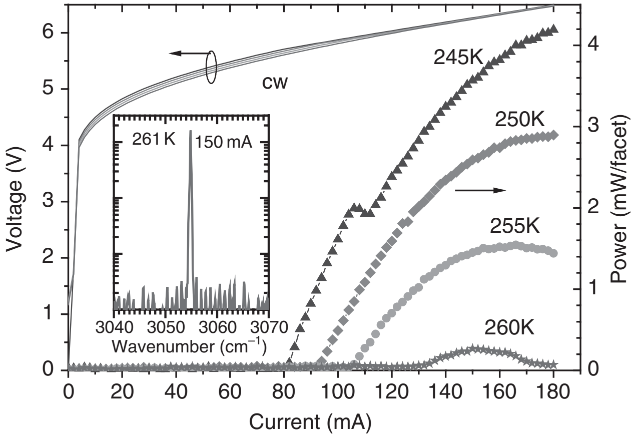

12.5 Current-voltage-light (*I*-V-*L*) characteristics for an IC laser and its lasing spectrum (inset) at 261 K.

Febry–Perot IC lasers had just been lifted to 264 K.[27] Intensive efforts in MBE growth, device fabrication and characterization, along with careful device design considerations and facility use priority, were devoted to accomplishing the then seemingly impossible task. The IC lasers ultimately produced were able to lase under cw operation in stable single-mode with high side-mode-suppression ratio (>20 dB) at temperatures up to 261 K, as shown in inset in Fig. 12.5. The output power of the laser in Fig. 12.5 was higher than 1 mW, sufficient for *in situ* gas sensing. The threshold current and voltage were lower than 140 mA and 6 V, respectively, through the entire operating temperature range. Hence, the total electric power consumption of the IC laser is less than 1.1 W over the entire operating range of this device, which enables cw operation at temperatures achievable with simple one-stage TE coolers. Furthermore, the wavelength of this DFB laser can be tuned with current at a rate of ~0.057 nm/mA over 3 nm and hit the targeted narrow wavelength band (at 3.27 μm) at both 250 and 255 K as shown in Fig. 12.6, which is critically important for sensitive detection of CH_4 and its isotopes. The laser has been under 24-hours burn-in at 140 mA at room temperature. Also shown in Fig. 12.6, the wavelengths measured after the burn-in nearly overlap with the initial measured data within the instrument precision and temperature uncertainty, indicative of reliable operation of the DFB IC laser. In these TE-cooled IC lasers, a fewer number of cascade stages (11 or 12) were used compared to earlier IC lasers and typical QC lasers, because of a high gain per unit current density in IC lasers as verified later by experimental investigations.[30,31] With fewer stages, the threshold voltage is lowered, resulting in reduced power consumption and thus benefiting portable instrument applications. A fully

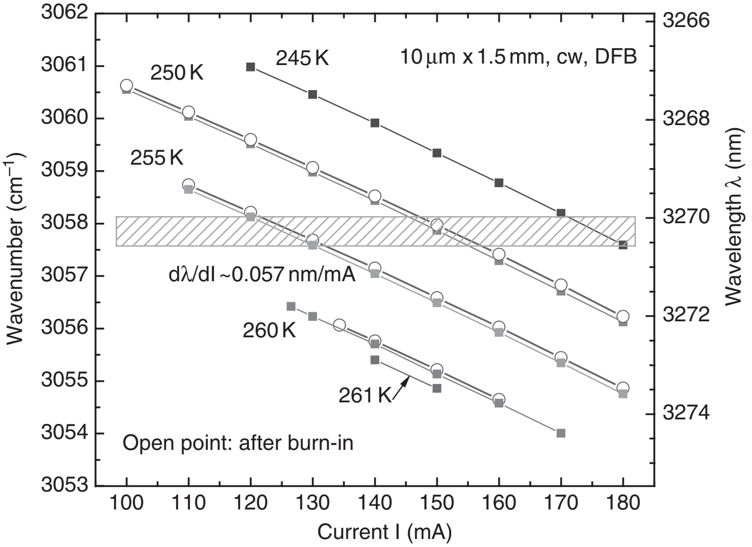

12.6 DFB laser wavelength tuning with current *I* at several temperatures. The open points are measured after 24-hours burn-in. The shaded area is the target wavelength for detection of CH_4 and its isotopes.

packaged single-mode DFB IC laser was later used successfully for field measurements of methane and water.[55]

Despite the similar cascade architecture, there are important differences between IC and QC lasers. For example, the non-radiative relaxation processes of the interband transitions are over an order of magnitude slower than the corresponding intersubband transitions. Additionally, electric current in IC lasers is carried by both conduction band and valence band states, making it a bipolar device. Thus, there can be significant variations in the design considerations for optimizing the carrier transport and population inversion to achieve lasing. Even so, the early device design and implementation of IC lasers were influenced by the parallel research into QC lasers, which progressed very rapidly and had many outstanding accomplishments. For example, to ensure a smooth and fast transport as required in QC lasers to establish population inversion, the AlSb layer at the type-II hetero-interface between the hole and electron injectors was kept very thin (10 or 12 Å) in typical IC lasers[13,19] as suggested by early theoretical work.[11] However, the AlSb barrier should also be kept thick enough to suppress optical interband absorption loss across the semimetal-like interface. This type of optical loss might be partially responsible for the significant internal loss (36–62 cm^{-1} at temperatures from 80 to 200 K[90]) that was observed from early IC lasers. Later at JPL, several design modifications were implemented, which included the use of thicker AlSb barrier layers (16–32 Å) at the type-II hetero-interfaces in the cascade stages and transitional/connecting bridges, and between the electron injector and the active region. The relatively thick AlSb barrier at the type-II hetero-interfaces reduces the optical interband absorption loss across the semimetal-like interface. While the thicker AlSb barrier between the other end of the electron injector and active region suppresses the wave-function extension of the conduction band transition state in the active region into the adjacent injection region. As such, the electron state for optical transition is more confined in the active region, which enhances the wave-function overlap between two interband transition states, and consequently increases the gain. Devices with these design changes were able to achieve higher operating temperatures (e.g., 350 K in pulsed mode) with fewer stages and lower optical internal losses (17 cm^{-1} at 80 K to 35 cm^{-1} at 270 K[30]) compared to earlier IC lasers. However, it should be noted that the design improvements did not always produce the expected advances in device performance. Due to the complexity of the IC laser and the wide variability of material quality and fabrication for devices based on Sb materials, it is difficult to predict what influence certain design modifications will have on device performance purely through theoretical modeling. Progress often must be made using a combination of suggestions from theory coupled with empirical trial and error.

The early IC lasers mentioned above employed the simple regular three-layer-waveguide structure, consisting of the bottom cladding region, cascade region, and the top cladding region. The cladding region is composed of short-period InAs/AlSb SL and has a refractive index (~3.37) that is slightly smaller than that (~3.43–3.47) of the cascade region, which leads to substantial optical wave penetration deep into cladding regions as shown in Fig. 12.7. If the bottom cladding layer is not thick enough, there is significant optical waveguide mode leakage into the high index (~3.8) GaSb substrate and interference with the substrate modes. This leads to gain/loss modulation at a period inversely proportional to the substrate thickness.[91–93] This was the reason for the observation of mode grouping with multiple peaks and inter-grouping hopping from early IC lasers,[19–23] which complicated the mode selection and wavelength tuning for DFB lasers.[23] This problem can be remedied by increasing the bottom SL cladding layer thickness at the cost of a longer growth time and poorer thermal conductivity. The more optimal solution is to incorporate separate confinement layers (SCL) with adequate cladding layers in IC lasers, which are discussed in the next section.

12.4 Recent progress and new developments

This section reviews recent progress and deveopments in IC lasers with GaSb separate confinement layers, and plasmon waveguide IC lasers on InAs substrates.

12.4.1 IC lasers with GaSb separate confinement layers

Although SCL laser structures were well known and established for diode lasers, SCLs were not implemented into early IC lasers with many stages. It was realized later that fewer cascade stages could be used in IC lasers because of their higher differential gain per unit current density. Reducing the number of stages resulted in a lowered operating voltage and possibly higher cw operating temperature with reduced power consumption. This consideration, combined with the insertion of two GaSb SCLs between the cascade and the cladding regions for IC lasers, would make better devices with other benefits as elaborated below. Because the two GaSb layers have a higher refractive index (~3.8) than the cascade stage active region, the average refractive index for the waveguide core region (cascade region plus SCLs) is raised, which increases the contrast of refractive index between the cladding and core regions. Consequently, the optical wave attenuates at a much faster rate into the cladding regions as shown in Fig. 12.7, and the SL cladding regions can be thinner with reduced thermal resistance. Furthermore, higher optical intensity and a more uniform optical field over the cascade stages can be achieved with SCLs as shown in Fig. 12.7. Therefore, IC lasers with SCLs were expected to have significantly improved cw performance over regular waveguide IC lasers. Some initial efforts (from 2005 to 2006 at JPL) on IC lasers with GaSb SCLs and few stages (6 – 10) did not produce devices with performance better than the regular three-layer waveguide IC lasers.[33] In those early IC lasers with SCLs, each GaSb layer (~100–200 nm thick) was either slightly

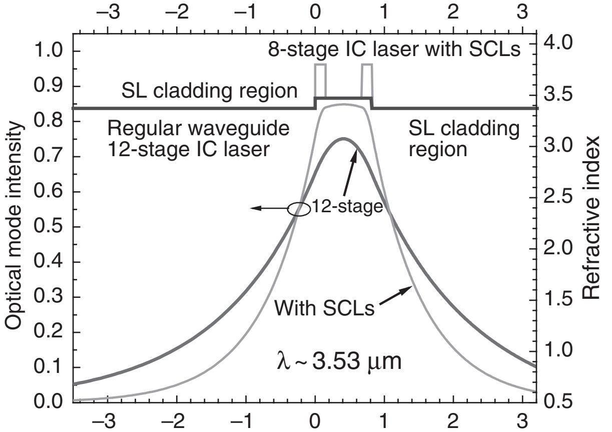

12.7 Optical mode (left axis) and refractive index (right axis) for regular waveguide 12-stage IC laser and 8-stage IC laser with SCLs.

p-type doped, for smooth transport with negligible resistance, or undoped. These lasers may have had significant free carrier absorption loss caused by the substantial hole concentrations (around 2×10^{17} cm^{-3} or somewhat higher) due to inherent p-type background on GaSb layers. The later IC lasers grown at JPL explored Te-doped n-type GaSb SCLs for reducing the optical loss. Nevertheless, due to variations of background doping and difficulties in precise control of Te doping concentration, as well as other factors, device performance from these IC laser wafers with Te-doped SCLs showed only slight improvements (e.g., somewhat above 31% power efficiency at 80 K and maximum cw operating temperature of 266 K) over regular waveguide IC lasers.[33]

In 2005, the Naval Research Laboratory (NRL) began the growth of IC laser structures using a Riber MBE system. With their expertise in Sb-based devices and previous extensive experience including work on optically-pumped and electrically-pumped type-II QW mid IR lasers,[76–78,84,85] NRL quickly made significant progress (e.g., cw output power exceeding 1 W,[34] cw operation at temperatures up to 269 K[35] and 288 K[36]). Finally in 2008, with the use of two n-type GaSb SCLs in the waveguide, the NRL group demonstrated cw operation of IC lasers up to 319 K near 3.7 μm[37] as shown in Fig. 12.8, exceeding the particularly important milestone of room temperature cw operation. This IC laser had an output power more than 10 mW at 300 K and exhibited a superior performance in terms of low power consumption at the threshold (<0.6 W at 300 K). Subsequently, the NRL group was able to extend the superior device performance of IC lasers to the wavelength range from 2.9 to 4.2 μm with higher cw operating temperature

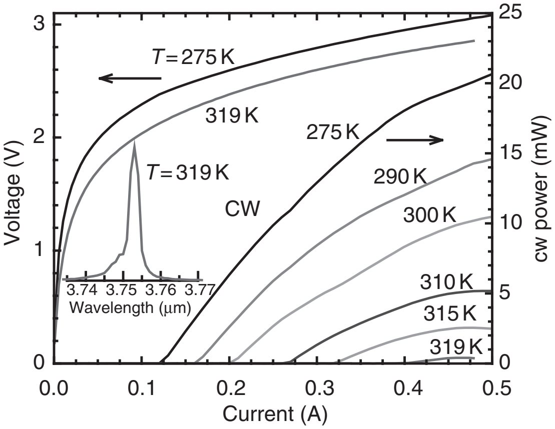

12.8 Current-voltage-light (*I*-V-*L*) characteristics for an IC laser and its lasing spectrum (inset) at 319 K (Courtesy of Jerry R. Meyer, Naval Research Laboratory).

(345 K), single-mode operation with DFB grating and external cavity configurations.[38–44] These high-performance IC lasers are typically composed of five (5) stages with low threshold voltages (2.1–2.5 V at 300 K) and showed very low threshold current densities (1.7 A/cm^2 at 78 K, 360 A/cm^2 at 300 K), resulting in reduced power consumption (0.9–2.5 kW/cm^2).[44] These IC lasers were based on the waveguide structures with *n*-type GaSb SCLs and were grew on Te-doped *n*-type GaSb substrates, in which the optical absorption loss is significantly reduced compared to *p*-type GaSb SCLs and substrates. Other IC laser design considerations such as the shortened electron injection region are discussed in detail in Reference 44.

The shortened injector IC lasers were discussed in a paper published in 2010 by a group at University of Wurzburg[49] in Germany. It was showed with calculations and experimental results that the optical mode intensity in the active region could be increased in the shortened injector IC laser to improve the device performance.[49] This group has worked on Sb-based type-I QW lasers for many years and recently began efforts in the development of IC lasers on *n*-type GaSb substrates using an Eiko EV100S solid source MBE chamber. The group reported their initial work in IC lasers in 2009.[48] Nevertheless, in about two years the group has developed IC lasers (near 3.5 μm) that are capable of operating in cw mode at temperatures up to 303 K.[94] The improved device performance with the shortened injector demonstrates a high-quality of material and device fabrication, and alleviates early concerns[13] about the possible dielectric breakdown of materials due to high electric field on the shortened injector.

More recently, the NRL group developed a new generation of IC lasers that are capable of cw operation at temperatures up to 109°C (382 K) at wavelengths near 3.9 μm.[50,95] In this new generation of IC lasers, high *n*-type doping (5×10^{18} cm^{-3}) is employed in the electron injector to rebalance excessive holes in the active region as revealed by theoretical calculations.[95] As such, the optical internal loss in IC lasers is reduced to values as low as 6.5 cm^{-1} at 300 K, leading to further lowered threshold current density (e.g., 170 A/cm^2 at 300 K). At 25°C, these newly developed narrow ridge IC lasers can deliver cw output power as high as 158 mW and have power efficiency up to 13.5%. Compared to early IC lasers and the best QC lasers, these new IC lasers consume significantly less power (<0.1 W) to operate. The lowest power required to operate an IC laser is about 30 mW at 25°C. The low power consumption feature of new IC lasers is important and desirable for many practical applications with portable and battery-powered instruments. These low power consumption IC lasers are being extended to the longer wavelength spectrum beyond 4.2 μm as the NRL group has just demonstrated cw operation of IC lasers at temperatures up to 60°C and 45°C at wavelengths of 4.9 μm and 5.7 μm, respectively.[96]

12.4.2 Plasmon waveguide IC lasers on InAs substrates

All the IC lasers mentioned above were grown on GaSb substrates with thick (several micron) InAs/AlSb SL cladding layers that typically have more than 2000 interfaces. Besides the challenges in the MBE growth to achieve high-quality strain-balanced material for such complicated IC laser structures with so many shutter movements, an outstanding issue is the low thermal conductivity (κ ~0.03 W/cm·K[97]) of the InAs/AlSb SL material. As with all lasers, thermal management is an important issue, and thick SL layers cause significant heating, which may lead to reliability concerns. This situation will become worse if SL cladding layers are still used in IC lasers for longer wavelengths because of the requirement of thicker cladding layers to compensate the longer optical wave decay length. The problem can be circumvented by using a plasmon waveguide, which was explored early in QC lasers,[98–102] but not in interband diode lasers until the recent demonstration of InAs-based 6 μm[45] and 7.4 μm[46] IC lasers by researchers at the University of Oklahoma (OU).

The plasmon waveguide IC laser approach is to employ relatively highly-doped n^+-type InAs cladding layers instead of thick InAs/AlSb SL layers, resulting in easier and less demanding MBE growth on InAs substrates with far fewer shutter movements and significantly reduced strain built-up in the structure. Because the thermal conductivity of InAs is approximately ten times larger than that of InAs/AlSb SL materials, replacing the SL cladding layer with an InAs plasmon layer significantly improves the thermal dissipation. The thermal modeling of plasmon- and SL-waveguide IC lasers (20 μm narrow ridge devices, with the same cladding layer thickness, and no thick gold layer on the top) suggested a ~42% reduction of the specific thermal resistance R_{sth} (from 12.5 Kcm^2/kW for the SL-waveguide IC lasers to 7.2 Kcm^2/kW for the plasmon waveguide IC lasers).[47] The actual reduction is expected to be even greater because for longer wavelengths the required SL cladding layer is considerably thicker than the plasmon cladding layer.

An important advantage of using the InAs plasmon waveguide structure is significant suppression of the wave penetration into the cladding region, thus potentially reducing optical waveguide loss primarily from the cladding region. The refractive index of a highly-doped n^+-InAs plasmon layer can be less than 3.0, which is substantially lower than that for the cascade core region in IC lasers. Hence, with the use of InAs plasmon layers in the cladding regions and InAs (refractive index near 3.5) SCLs, the light is more confined to the center of the waveguide and extends less into the cladding layers and substrate, as shown in Fig. 12.9 for an example of a 10-stage two-sided plasmon waveguide IC laser at 4.6 μm. Compared to the 20-stage regular (without SCLs) SL cladding waveguide (Fig. 12.9a) and the 10-stage SL cladding

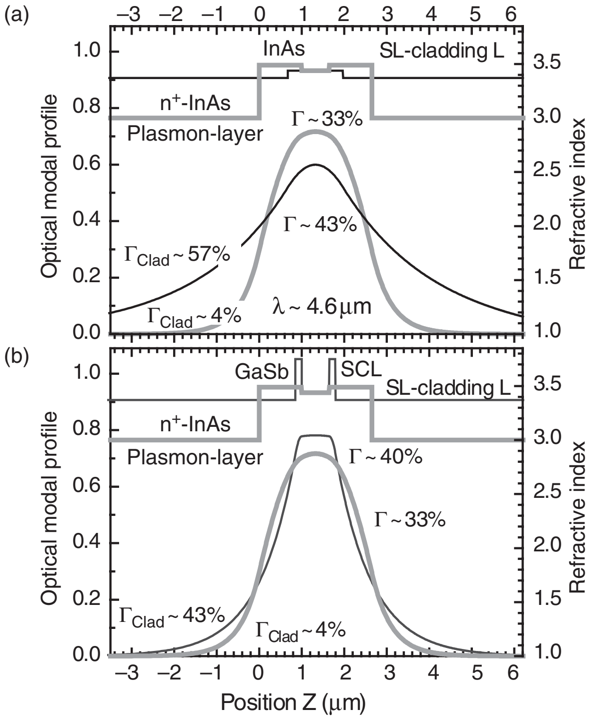

12.9 Optical modal and refractive index profiles for a 10-stage plasmon waveguide (thick line) vs. (a) 20-stage regular and (b) 10-stage SL-SCL IC laser structures. The confinement factor (Γ) in the cascade stage region (not including SCLs) and the portion (Γ_{clad}) into the cladding regions are given for three waveguide structures.

SCL (with two GaSb SCLs) waveguide (Fig. 12.9b), the optical mode penetration (Γ_{clad}) into the cladding regions is reduced for the plasmon waveguide where it is only about 4%. In this way, optical loss could be suppressed since only a very small portion of the optical wave is in the relatively highly-doped n^+-InAs cladding regions where the loss may be significantly higher. This is supported by observations of low optical losses (e.g., 6–8 cm^{-1}) in InAs-based QC lasers at 4.5 and 10 µm[101,102] with similar plasmon waveguide structures. Another benefit of using the InAs plasmon waveguide structure is the flexibility and freedom to manipulate the number of cascade stages for optimizing device performance without being concerned about wave penetration into the cladding and substrate regions.

Preliminary efforts on the two initial IC laser wafers grown on InAs substrates in a MBE system at OU have demonstrated the expected advantage of plasmon waveguide IC lasers in terms of reduced thermal resistance (~50%) compared to early SL-waveguide IC lasers.[45–47] Although the initial

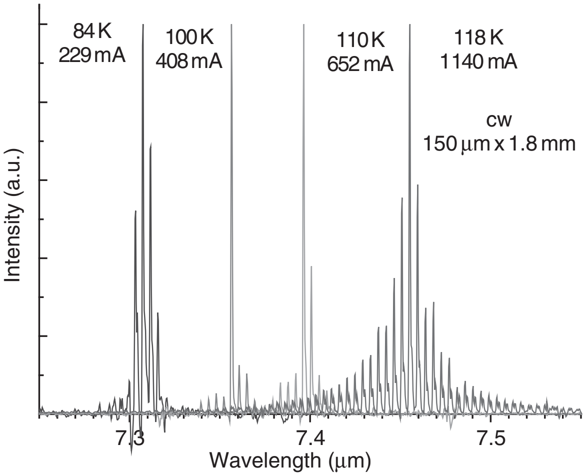

12.10 Lasing spectrum for a broad-area plasmon waveguide IC laser.

attempts are far from optimal in terms of material quality and device design, these plasmon waveguide IC lasers (without a thick gold layer on the top) could lase in cw mode up to 184 K near 6 μm and 141 K near 7.5 μm. Some of their lasing spectra are shown in Fig. 12.10, which holds the longest lasing wavelength achieved among all mid IR III-V interband diode lasers. With a thick gold layer, a plasmon waveguide IC laser lased in cw up to 152 K near 7 μm, which was mainly limited by the intrinsic device properties, rather than thermal dissipation, as evidenced by the fact that its pulse operation was only possible up to 168 K. Their threshold current densities (49 A/cm^2 for ~6-μm laser at 82 K and 72 A/cm^2 for 7-μm laser at 84 K) are low compared with all mid IR semiconductor lasers in the wavelength region beyond 5.5 μm. Also, high voltage efficiencies (e.g., 93%) were obtained in these initial plasmon waveguide IC lasers. The latest efforts at OU have reduced their threshold current densities (e.g., ≤10 A/cm^2 at 80 K) and pushed cw operating temperature of plasmon waveguide IC lasers up to 253 K near 5.3 μm, to 189 K at 7.4 μm, and to 166 K at 10.3 μm, although these devices were not capped with a thick gold layer on the top.[103–106] Significant improvements in these plasmon waveguide IC lasers are expected with further efforts and development, as well as the implementation of the recent carrier rebalance innovation.[95]

12.5 Future trends and conclusion

After about 16 years of exploration and development, IC lasers have now proven to be capable of cw operation at room temperature and above for

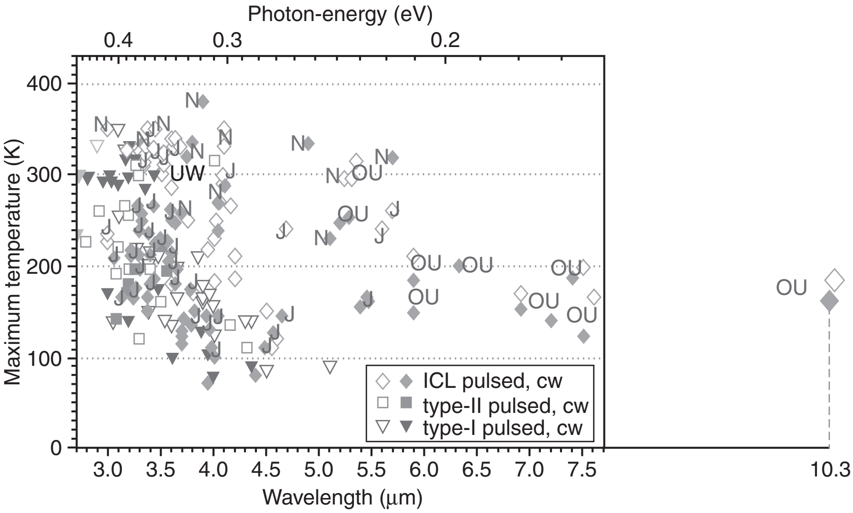

12.11 Reported maximum temperature vs. wavelength for mid IR Sb-based interband diode lasers. Letters J, N, OU and UW denote lasers grown at JPL, NRL, OU, and the University of Wurzburg, respectively.

wavelength range from 2.9 to 5.7 µm. A summary of these results is partially shown in Fig. 12.11, along with those from other types of III-V interband diode lasers reported in the literature. It is likely that cw operation of IC lasers at room temperature will be extended beyond 6 µm, considering there is significant room for further improvements. It is still unclear where the boundaries for cw operating temperatures and lasing wavelengths are for IC lasers, and it may depend on the extent to which Auger recombination can be suppressed. In type-II QWs, Auger recombination is decreased, due to the reduced wave-function overlap, and can be in principle suppressed further by quantum engineering.[107–109] Such quantum engineering is challenging in design and realistic implementation because it involves excited states and its effectiveness has not been proved with experimental evidence. Nevertheless, recent studies[110,111] found that Auger coefficients for type-II QWs in ICLs were much lower than had been anticipated and their dependence on wavelength is much weaker than was implied by earlier work. However, another recent study on IC lasers suggested that non-radiative current loss is still significant in threshold current and dominant at high temperatures (e.g., >90% at 300 K),[112] implying intimate involvement of Auger recombination. Although questions remain on what role Auger recombination and other non-radiative mechanisms play in IC laser performance and optimization, it is clear now that IC lasers have emerged as the only confirmed semiconductor interband diode laser technology covering a wide mid

IR wavelength spectrum with needed device performance in terms of output powers and operating temperatures. Compared to another semiconductor laser technology – QC lasers, that are also capable of covering wide mid IR spectrum – IC lasers have significantly lower threshold current density (e.g., 200 A/cm^2 at 300 K) and voltage (e.g., 2.3 V), which translates to much lower power consumption density (e.g., 460 W/cm^2). Another difference is in their polarizations of emitted photons. Like all interband diode lasers, IC lasers have the transverse electric polarization, in contrast to transverse magnetic (TM) polarization for QC lasers. Hence, electrically-pumped mid IR Vertical Cavity Surface Emitting Lasers (VCSELs) are feasible based on IC laser structures. Considering that optically-pumped mid IR VCSELs have been demonstrated based on Sb-based type-II QWs[113] and the remarkable progress made recently in edge-emitting IC lasers, mid IR IC VCSELs are expected to be developed in the future with more desirable beam quality and with versatile formats in two-dimensional arrays. Currently, edge-emitting IC lasers still need advancement to attain higher cw output powers (>1 W) at room temperature for certain applications such as remote sensing and IR countermeasures. This is possible with improvements in thermal management (e.g., epilayer side-down mounting) and device design combined with device fabrication and material quality.

12.6 Acknowledgments

The author would like to thank A. Bauer for updating his new results and J. R. Meyer for communicating his group's latest results and sending their papers prior to the publication. The author is also grateful to his colleagues, collaborators, and group members L. E. Christensen, M. E. Curtis, C. J. Hill, R. T. Hinkey, Y. Jiang, M. B. Johnson, J. C. Keay, J. F. Klem, L. Li, K. Mansour, T. D. Mishima, Y. Qiu, M. B. Santos, Z. Shi, J. Sluss, A. Soibel, Z. Tian, H. Ye, Z. Yin, M. Zaman, F. Zhao for their support, helps, and contributions to the development of IC lasers at OU. This work at OU was partially supported by NSF (ECCS-1002202), and by C-SPIN, the Oklahoma/Arkansas MRSEC (DMR-050550).

12.7 References

1. J. Faist, F. Capasso, D. L. Sivco, C. Sirtori, A. L. Hutchinson, and A. Y. Cho, 'Quantum cascade lasers', *Science* **264**, 553–556 (1994).
2. R. Q. Yang, 'Infrared laser based on intersubband transitions in quantum wells', at *7th Inter. Conf. on Superlattices, Microstructures and Microdevices*, Banff, Canada, Aug. 22–26, 1994; Superlattices and Microstructures **17**(1), 77–83 (1995).
3. R. Q. Yang, 'Novel concepts and structures for infrared lasers', chapter 2 in *Long Wavelength Infrared Emitters Based on Quantum Wells and Superlattices*, M. Helm, editor, pp. 13–64, Gordon and Breach, Singapore (2000); R. Q. Yang

and S. S. Pei, 'Novel type-II quantum cascade lasers', *J. Appl. Phys.* **79**, 8197–8203 (1996).

4. C.-H. Lin, R. Q. Yang, D. Zhang, S. J. Murry, S. S. Pei, A. A. Allerma, and S. R. Kurtz, 'Type-II interband quantum cascade laser at 3.8 μm', *Electron. Lett.*, **33**(7), 598–599 (1997).
5. R. Q. Yang, B. H. Yang, D. Zhang, C.-H. Lin, S. J. Murry, H. Wu, and S. S. Pei, 'High power mid-IR interband cascade lasers based on type-II quantum wells', *Appl. Phys. Lett.* **71**(17), 2409–2411 (1997).
6. B. H. Yang, D. Zhang, R. Q. Yang, C.-H. Lin, S. J. Murry, and S. S. Pei, 'Mid-infrared interband cascade lasers with quantum efficiencies > 200%', *Appl. Phys. Lett.* **72**(18), 2220–2222 (1998).
7. C. L. Felix, W. W. Bewley, I. Vurgaftman, J. R. Meyer, D. Zhang, C.-H. Lin, R. Q. Yang, and S. S. Pei, 'Interband cascade laser emitting > 1 photon per injected electron', *IEEE Photonics Technol. Lett.* **9**(11), 1433–1435 (1997).
8. C. L. Felix, W. W. Bewley, I E. H. Aifer, Vurgaftman, J. R. Meyer, C.-H. Lin, D. Zhang, S. J. Murry, R. Q. Yang, and S. S. Pei, 'Low threshold 3 μm Interband Cascade "W" Laser', *J. Electronic Materials* **27**(2), 77–80 (1998).
9. L. J. Olafsen, E. H. Aifer, I. Vurgaftman, W. W. Bewley, C. L. Felix, J. R. Meyer, D. Zhang, C.-H. Lin, and S. S. Pei, 'Near-room-temperature mid-infrared interband cascade laser', *Appl. Phys. Lett.* **72**, 2370 (1998).
10. J. R. Meyer, I. Vurgaftman, R. Q. Yang, and L. R. Ram-Mohan, 'Type-II and type-I interband cascade lasers', *Electron. Lett.*, **32**(1), 45–46 (1996).
11. I. Vurgaftman, J. R. Meyer, and L. R. Ram-Mohan, 'High-power/low-threshold type-II interband cascade mid-IR laser design and modeling', *IEEE Photo. Tech. Lett.* **9**, 170–172 (1997).
12. Y.-M. Mu and R. Q. Yang, 'Theoretical investigation of mid-IR interband cascade lasers based on type-II quantum wells', *J. App. Phys*. **84**(9), 5357–5359 (1998).
13. R. Q. Yang, 'Mid-infrared interband cascade lasers based on type-II heterostructures', *Microelectronics J*. **30**, 1043–1056 (1999); and references therein.
14. R. Q. Yang, J. D. Bruno, J. L. Bradshaw, J. T. Pham, and D. E. Wortman, "High-power interband cascade lasers with quantum efficiency > 450%', *Electron. Lett.,* **35**(15), 1254–1255 (1999).
15. J. L. Bradshaw, R. Q. Yang, J. D. Bruno, J. T. Pham, D. E. Wortman, 'High-efficiency interband cascade lasers with peak power exceeding 4W/facet', *Appl. Phys. Lett*. **75**(16), 2362–2364 (1999).
16. J. L. Bradshaw, J. D. Bruno, J. T. Pham, D. E. Wortman, and R. Q. Yang, 'Continuous wave operation of type-II interband cascade lasers', *IEE Proceedings- Optoelectronics* **147**(3), 177–180 (2000).
17. J. D. Bruno, J. L. Bradshaw, R. Q. Yang, J. T. Pham, and D. E. Wortman, 'Low-threshold interband cascade lasers with power efficiency exceeding 9%', *Appl. Phys. Lett.* **76**(22), 3167–3169 (2000).
18. J. L. Bradshaw, J. T. Pham, R. Q. Yang, J. D. Bruno, and D. E. Wortman, 'Enhanced CW performance of interband cascade laser using improved device fabrication', *IEEE J. Sel. Top. Quantum Electron*. **7**(2), 102–105 (2001).
19. R. Q. Yang, J. L. Bradshaw, J. D. Bruno, J. T. Pham, and D. E. Wortman, 'Mid-IR type-II interband cascade lasers', *IEEE J. Quantum Electron*. **38**(6), 559–568 (2002); and references therein.

20. J. L. Bradshaw, N. P. Breznay, J. D. Bruno, J. M. Gomes, J. T. Phama, F. J. Towner, D. E. Wortman, R. L. Tober, C. J. Monroy, and K. A. Olver, 'Recent progress in the development of type II interband cascade lasers', *Physica E* **20**, 479–485 (2004).
21. C. J. Hill, B. Yang, and R. Q. Yang, 'Low threshold interband cascade lasers operating above room temperature', *Physica E* **20**, 486–490 (2004).
22. R. Q. Yang, C. J. Hill, B. Yang, and J. K. Liu, 'Room-temperature type-II interband cascade lasers near 4.1 μm', *Appl. Phys. Lett.* **83**(11), 2109–2111 (2003).
23. R. Q. Yang, C. J. Hill, B. Yang, C. M. Wong, R. Muller and P. Echternach, 'Continuous-operation of distributed feedback interband cascade lasers', *Appl. Phys. Lett.* **84**(18), 3699–3701 (2004).
24. R. Q. Yang, C. J. Hill, L. E. Christensen, and C. R. Webster, 'Mid-IR type-II interband cascade lasers and their applications', *Proc. SPIE* **5624**, 413–422 (2005).
25. C. J. Hill and R. Q. Yang, 'MBE growth optimization of Sb-based interband cascade lasers', *J. Crystal Growth* **278**, 167–172 (2005).
26. R. Q. Yang, C. J. Hill, and B. Yang, 'High-temperature and low-threshold mid-infrared interband cascade lasers', *Appl. Phys. Lett.* **87**(15), 151109 (2005).
27. K. Mansour, Y. Qiu, C. J. Hill, A. Soibel, and R. Q. Yang, 'Mid-IR interband cascade lasers at thermoelectric cooler temperatures', *Electron. Lett.*, **42**(18), 1034–1035 (2006).
28. R. Q. Yang, C. J. Hill, K. Mansour, Y. Qiu, A. Soibel, R. E. Muller, P. M. Echternach, 'Distributed feedback mid-IR interband cascade lasers at thermoelectric cooler temperatures', *IEEE J. Sel. Top. Quantum Electron.,* **13**(5), 1074–1078 (2007).
29. R. Q. Yang, C. J. Hill, K. Mansour, Y. Qiu, A. Soibel, R. E. Muller, and P. M. Echternach, 'Development of thermoelectric cooled single-mode distributed feedback mid-IR interband cascade lasers for chemical sensing', paper 2007–01–3151 in the Proceedings of 37th International Conference on Environmental Systems (ICES), Chicago, IL, July 9–12 (2007).
30. A. Soibel, K. Mansour, Y. Qiu, C. J. Hill, and R. Q. Yang, 'Optical gain, loss and transparency current in high performance mid-IR interband cascade lasers', *J. Appl. Phys*. **101**(9), 093104 (2007).
31. W. W. Bewley, J. R. Lindle, C. L. Canedy, M. Kim, C. S. Kim, D. C. Larrabee, I. Vurgaftman, and J. R. Meyer, 'Gain, loss, and internal efficiency in interband cascade lasers emitting at $\lambda = 3.6$–4.1 μm', *J. Appl. Phys*, **103**(1), 013114 (2008).
32. K. Mansour, C. J. Hill, Y. Qiu, and R. Q. Yang, 'Dual-wavelength interband cascade lasers in mid-infrared spectral region', paper CTuZ4 at The Conference on Lasers and Electro-Optics (CLEO) and the Quantum Electronics and Laser Science Conference (QELS), San Jose, CA, May 4–9, 2008.
33. R. Q. Yang, Z. Tian, R. Hinkey, F. Zhao, K. Mansour, C. J. Hill, and Y. Qiu, 'Recent progress in interband cascade lasers with separate-confinement layers', *Proc. SPIE* **7230**, paper 72300S (2009).
34. C. L. Canedy, W. W. Bewley, J. R. Lindle, C. S. Kim, M. Kim, I. Vurgaftman, and J. R. Meyer, 'High-power and high-efficiency midwave-infrared interband cascade lasers', *Appl. Phys. Lett.* **88**, 161103 (2006).
35. W. W. Bewley, C.L. Canedy, M. Kim, C.S. Kim, J.A. Nolde, J.R. Linda, I. Vurgaftman, and J. R. Meyer, 'Interband cascade laser operating to 269 K at $\lambda = 4.05$ μm', *Electron. Lett.*, **43** (5), 283 (2007).

36. C. L. Canedy, C. S. Kim, M. Kim, D. C. Larrabee, J. A. Nolde, W. W. Bewley, I. Vurgaftman, and J. R. Meyer, 'High-power, narrow-ridge, mid-infrared interband cascade lasers', *J. Vac. Sci. Technol. B* **26**, 1160 (2008).
37. M. Kim, C. Canedy, W. Bewley, C. Kim, J. Lindle, J. Abell, I. Vurgaftman, and J. R. Meyer, 'Interband cascade laser emitting at $\lambda = 3.75$ μm in continuous wave above room temperature', *Appl. Phys. Lett.* **92**(19), 191110 (2008).
38. C. L. Canedy, W. W. Bewley, M. Kim, C. S. Kim, J. A. Nolde, D. C. Larrabee, J. R. Lindle, I. Vurgaftman, and J. R. Meyer, 'Interband cascade lasers with wavelengths spanning 3.2–4.2 μm', *J. Electron. Materials* **38**, 1948 (2009), where there was a typo in the label for the vertical axis j_{th} in Fig. 2, which should be A/cm^2 instead of kA/cm^2.
39. I. Vurgaftman, C. L. Canedy, C. S. Kim, M. Kim, W. W. Bewley, J. R. Lindle, J. Abell, and J. R. Meyer, 'Mid-infrared interband cascade lasers operating at ambient temperatures', *New J. Phys*. **11**(12), 125015 (2009).
40. C. S. Kim, M. Kim, W. W. Bewley, J. R. Lindle, C. L. Canedy, J. Abell, I. Vurgaftman, and J. R. Meyer, 'Corrugated-sidewall interband cascade lasers with single-mode midwave-infrared emission at room temperature', *Appl. Phys. Lett.* **95**, 231103 (2009).
41. C. L. Canedy, J. Abell, W. W. Bewley, E. H. Aifer, C. S. Kim, J. A. Nolde, M. Kim, J. G. Tischler, J. R. Lindle, E. M. Jackson, I. Vurgaftman, and J. R. Meyer, 'Molecular beam epitaxial growth effects on type-II antimonide lasers and photodiodes', *J. Vac. Sci. Technol*. B **28**, C3G8 (2010).
42. D. Caffey, T. Day, C. S. Kim, M. Kim, I. Vurgaftman, W. W. Bewley, J. R. Lindle, C. L. Canedy, J. Abell, and J. R. Meyer, 'Performance characteristics of a continuous wave compact widely tunable external cavity interband cascade lasers', *Opt. Exp.*, **18**, 15693 (2010).
43. W. W. Bewley, C. L. Canedy, C. S. Kim, M. Kim, J. R. Lindle, J. Abell, I. Vurgaftman, and J. R. Meyer, 'Ridge-width dependence of midinfrared interband cascade laser characteristics', *Opt. Eng.*, **49**(11), 111116, (2010).
44. I. Vurgaftman, W. W. Bewley, C. L. Canedy, C. S. Kim, M. Kim, J. R. Lindle, C. D. Merritt, J. Abell, and J. R. Meyer, 'Mid-IR type-II interband cascade lasers', *IEEE J. Sel. Top. Quantum Electron*. **17**(5), 1435 (2011).
45. Z. Tian, R. Q. Yang, T. D. Mishima, M. B. Santos, R. T. Hinkey, M. E. Curtis, and M. B. Johnson, 'InAs-based interband cascade lasers near 6 μm', *Electron. Lett.*, **45**(1), 48–49 (2009).
46. Z. Tian, R. Q. Yang, T. D. Mishima, M. B. Santos, and M. B. Johnson, 'Plasmon-waveguide interband cascade lasers near 7.5 μm', *Photon. Technol. Lett.* **21**(21), 1588–1590 (2009).
47. Z. Tian, C. Chen, R. Q. Yang, T. D. Mishima, M. B. Santos, J. C. Keay, M. B. Johnson, and J. F. Klem, 'InAs-based plasmon waveguide interband cascade lasers', *Proc. SPIE* **7616**, paper 7616–47 (2010); and at MIOMD-10, Shanghai, Sept. 6, 2010.
48. A. Bauer, F. Langer, M. Dallner, M. Kamp, M. Motyka, G. Sek, K. Ryczko, J. Misiewicz, S. Hofling, and A. Forchel, 'Emission wavelength tuning of interband cascade lasers in the 3–4 μm spectral range', *Appl. Phys. Lett.* **95**, 251103 (2009).
49. A. Bauer, M. Dallner, M. Kamp, S. Hofling, L. Worschech, and A. Forchel, 'Shortened injector interband cascade lasers for 3.3- to 3.6-μm emission', *Optic. Eng.*, **49**, 111117 (2010).

50. J. R. Meyer, private communications (2011); W. W. Bewley, C. S. Kim, M. Kim, C. D. Merritt, C. L. Canedy, I. Vurgaftman, J. Abell, and J. R. Meyer, ‘A new generation of interband cascade lasers’, *AIP Conf. Proc*. **1416**, 46 (2011).
51. M. Horstjann, Y. A. Bakhirkin, A. A. Kosterev, R. F. Curl, F. K. Tittel, C. M. Wong, C. J. Hill, and R. Q. Yang, ‘Formaldehyde sensor using interband cascade laser based quartz-enhanced photoacoustic spectroscopy’, *Appl. Phys. B* **79**, 799–803 (2004).
52. G. Wysocki, Y. Bakhirkin, S. So, F. K. Tittel, C. J. Hill, R. Q. Yang, and M. P. Fraser, ‘Dual interband cascade laser based trace-gas sensor for environmental monitoring’, *Appl. Opt*. **46**(33), 8202–8210 (2007).
53. L. E. Christensen, C. R. Webster, and R. Q. Yang, ‘Aircraft and balloon in situ measurements of methane and hydrochloric acid using interband cascade lasers’, *Appl. Opt*. **46**(7), 1132–1138 (2007).
54. K. R. Parameswaran, D. I. Rosen, M. G. Allen, A. M. Ganz, and T. H. Risby, ‘Off-axis integrated cavity output spectroscopy with a mid-infrared interband cascade laser for real-time breath-ethane measurements’, *Appl. Opt*. **48**(4), B73-B79 (2009).
55. L. E. Christensen, K. Mansour, and R. Q. Yang, ‘Thermoelectrically cooled interband cascade laser for field measurements’, *Optic. Eng.*, **49**, 111119 (2010).
56. J. P. van der Ziel and W. T. Tsang, ‘Integrated multilayer GaAs lasers separated by tunnel junctions’, *Appl. Phys. Lett*. **41**, 499 (1982).
57. G. A. Sai-Halasz, R. Tsu, and L. Esaki, ‘A new semiconductor superlattice’, *Appl. Phys. Lett*. **30** (12), 651–653 (1977).
58. W. R. Frensley and H. Kroemer, ‘Theory of the energy-hand lineup at an abrupt semiconductor heterojunction’, *Phys. Rev. B*. **16**, 2642 (1977).
59. G. A. Sai-Halasz, L. Esaki, and W. A. Harrison, ‘InAs-GaSb superlattice energy structure and its semiconductor-semimetal transition’, *Phys. Rev. B* **18**, 2812 (1978).
60. D. Z.-Y. Ting, A. Soibel, L. Hoglund, J. Nguyen, C. J. Hill, A. Khoshakhlagh, and S. D. Gunapala, ‘Type-II superlattice infrared detectors’, Chapter 1 in Semiconductors and Semimetals, vol. 84, Academic Press, 2011.
61. A. A. Allerman, R. M. Biefeld, and S. R. Kurtz, ‘InAsSb-based mid-infrared lasers (3.8–3.9 μm) and light-emitting diodes with AlAsSb claddings and semimetal electron injection, grown by metalorganic chemical vapor deposition’, *Appl. Phys. Lett*. **69**, 465 (1996).
62. S. R. Kurtz, A. A. Allerman, R. M. Biefeld, and K.C. Baucom, ‘High slope efficiency, “cascaded” midinfrared lasers with type I InAsSb quantum wells’, *Appl. Phys. Lett*. **72**, 2093 (1998).
63. J. R. Meyer, C. A. Hoffman, F. J. Bartoli, and L. R. Ram-Mohan, ‘Type-II quantum well lasers for the mid wavelength infrared’, *Appl. Phys. Lett.*, **67**(6), 757–759 (1995).
64. D. H. Chow, R. H. Miles, T. C. Hasenberg, A. R. Kost, Y. H. Zhang, H. L. Dunlap, and L. West, ‘Mid-wave infrared diode lasers based on GaInSb/InAs and InAs/AlSb superlattices’, *Appl. Phys. Lett*. **67**, 3700 (1995).
65. T. C. Hasenberg, R. H. Miles, A. R. Kost, and L. West, ‘Recent advances in Sb-based midwave-infrared lasers’, *IEEE J. Quantum Electron.* **33**, 1403 (1997).
66. A. N. Baranov, N. Bertru, Y. Cuminal, G. Boissier, C. Alibert, and A. Joullié, ‘Observation of room-temperature laser emission from type III InAs/GaSb multiple quantum well structures’, *Appl. Phys. Lett*. **71**, 735 (1997).

67. W. W. Bewley, E. H. Aifer, C. L. Felix, I. Vurgaftman, J. R. Meyer, C.-H. Lin, S. J. Murry, D. Zhang, and S. S. Pei, 'High-temperature type-II superlattice diode laser at $\lambda = 2.9$ µm', *Appl. Phys. Lett.* **71**, 3607 (1997).
68. A. Wilk, M. El Gazouli, M. El Skouri, P. Christol, P. Grech, A. N. Baranov, and A. Joullié, 'Type-II InAsSb/InAs strained quantum-well laser diodes emitting at 3.5 µm', *Appl. Phys. Lett.* **77**, 2298 (2000).
69. N. Deguffroy, V. Tasco, A. Gassenq, L. Cerutti, A. Trampert, A.N. Baranov, and E. Tournie, 'InAs/GaSb short-period superlattice injection lasers operating in the 2.5 µm to 3.5 µm mid-infrared wavelength range', *Electron. Lett.*, **43**, 1285 (2007).
70. A. Gassenq, G. Boissier, P. Grech, G. Narcy, A.N. Baranov, and E. Tournie, 'InAs/GaSb/InSb short-period super-lattice diode lasers emitting near 3.3 µm at room-temperature', *Electron. Lett.*, **45**, no. 3, 165–167 (2009).
71. J. I. Malin, J. R. Meyer, C. I. Felix, J. R. Lindle, L. Goldberg, C. A. Hoffman, F. J. Bartoli, C.-H. Lin, P. C. Chang, S. Murry, R. Q. Yang, and S. S. Pei, 'Type-II mid-IR quantum well lasers', *Appl. Phys. Lett.* **68**, 2976 (1996).
72. J. I. Malin, C. L. Felix, J. R. Meyer, C.A. Hoffman, J. F. Pinto, C.-H. Lin, P.C. Chang, S. J. Murry, and S.-S. Pei, 'Type II mid-IR lasers operating above room temperature', *Electron. Lett.* **32**, 1593 (1996).
73. C.-H. Lin, R. Q. Yang, S. J. Murry, S. S. Pei, C. Yan, D. L. McDaniel Jr., and M. Falcon, 'Room-temperature low-threshold type-II quantum well lasers at 4.5 µm', *IEEE Phot. Tech. Lett.* **9**, 1573 (1997).
74. W. W. Bewley, C. L. Felix, E. H. Aifer, I. Vurgaftman, L. J. Olafsen, J. R. Meyer, H. Lee, R. U. Martinelli, J. C. Connolly, A. R. Sugg, G. H. Olsen, M. J. Yang, B. R. Bennett, and B. V. Shanabrook, 'Above-room-temperature optically pumped midinfrared W lasers', *Appl. Phys. Lett.* **73**, 3833 (1998).
75. M. E. Flatté, T. C. Hasenberg, J.T. Olesberg, S. A. Anson, T. F. Boggess, C. Yan, and D. L. McDaniel Jr., 'III–V interband 5.2 µm laser operating at 185 K', *Appl. Phys. Lett.* **71**, 3764 (1997).
76. E. H. Aifer, W.W. Bewley, C. L. Felix, I. Vurgaftman, L. J. Olafsen, J. R. Meyer, H. Lee, R. U. Martinelli, and J. C. Connolly, 'Cw operation of 3.4 µm optically pumped type-II W laser to 220 K', *Electron. Lett.* **34**, 1587 (1998).
77. W. W. Bewley, C. L. Felix, I. Vurgaftman, D. W. Stokes, E. H. Aifer, L. J. Olafsen, J. R. Meyer, M. J. Yang, B. V. Shanabrook, H. Lee, R.U. Martinelli, and A. R. Sugg, 'High-temperature continuous-wave 3–6.1 µm 'W' lasers with diamond-pressure bond heat sinking', *Appl. Phys. Lett.* **74**, 1075 (1999).
78. C. L. Felix, W.W. Bewley, L. J. Olafsen, D.W. Stokes, E. H. Aifer, I. Vurgaftman, J. R. Meyer, and M. J. Yang, 'Continuous-wave type-II 'W' lasers emitting at $\lambda =$ 5.4–7.1 µm', *IEEE Photon. Technol. Lett.* **11**, 964 (1999).
79. R. Kaspi, A. P. Ongstad, G. C. Dente, J. R. Chavez, M. L. Tilton, and D. M. Gianardi, 'High performance optically pumped antimonide lasers operating in the 2.4–9.3 µm wavelength range', *Appl. Phys. Lett.*, **88**, 041122 (2006).
80. A. P. Ongstad, G. C. Dente, M. L. Tilton, J. R. Chavez, R. Kaspi, and D. M. Gianardi, 'High brightness from unstable resonator mid-IR semiconductor lasers', *J. Appl. Phys.* **107**, 123113 (2010).
81. H. Lee, L. J. Olafsen, R. J. Menna, W.W. Bewley, R. U. Martinelli, I. Vurgaftman, D. Z. Garbuzov, C. L. Felix, M. Maiorov, J. R. Meyer, J. C. Connolly, A. R. Sugg, and G. H. Olsen, 'Room-temperature type-II W quantum well diode laser

with broadened waveguide emitting at λ_I= 3.30 μm', *Electron. Lett.* **35**, 1743 (1999).

82. W. W. Bewley, H. Lee, I. Vurgaftman, R. J. Menna, C. L. Felix, R. U. Martinelli, D. W. Stokes, D. Z. Garbuzov, J. R. Meyer, M. Maiorov, J. C. Connolly, A. R. Sugg, G. H. Olsen, 'Continuous-wave operation of λ=3.25 μm broadened-waveguide W quantum well diode lasers up to T=195K', *Appl. Phys. Lett.* **76**, 256 (2000).
83. A. Joullié, E. M. Skouri, M. Garcia, P. Grech, A. Wilk, P. Christol, A. N. Baranov, A. Behres, J. Kluth, A. Stein, K. Heime, M. Heuken, S. Rushworth, E. Hulicius, and T. Simecek, 'InAs(PSb)-based 'W' quantum well laser diodes emitting near 3.3 μm', *Appl. Phys. Lett.* **76**, 2499 (2000).
84. C.L. Canedy, W.W. Bewley, J.R., Lindle, I. Vurgaftman, C.S. Kim, M. Kim, and J.R. Meyer, 'High-power continuous-wave mid-infrared type-II "W" diode lasers', *Appl. Phys. Lett.,* **86**, 211105 (2005).
85. C.L. Canedy, W.W. Bewley, C.S. Kim, M. Kim, J.R. Lindle, I. Vurgaftman, and J.R. Meyer, 'CW mid-infrared "W" diode and interband cascade lasers', *J. Vac. Sci. Technol. B*, **24**, 1613 (2006).
86. D Zhang, E. Dupont, R. Q. Yang, H. C. Liu, C.-H. Lin, M. Buchanan, and S. S. Pei, 'Long-wavelength infrared (~10–15 μm) electroluminescence from Sb-based interband cascade devices', *Opt. Exp.*, **1**, 97 (1997).
87. N. J. Ekins-Daukes, K. Kawaguchi, and J. Zhang, 'Strain-balanced criteria for multiple quantum well structures and its signature in X-ray rocking curves', *Cryst. Growth Des.*, **2** (4), 287–292 (2002).
88. V. D. Jovanovic, Chapter 7 in *Quantum Wells, Wires and Dots*, 2nd edition, P. Harrison, Wiley Interscience (2005).
89. C.R. Webster and P. R. Mahaffy, 'Determining the local abundance of martian methane and Its ^{13}C/^{12}C and D/H isotopic ratios for comparison with related gas and soil analysis on the 2011 Mars Science Laboratory (MSL) Mission', *Planet. Space Sci.*, **59**, 271 (2011).
90. S. Suchalkin, J. Bruno, R. Tober, D. Westerfeld, M. Kisin, and G. Belenky, 'Experimental study of the optical gain and loss in InAs/GaInSb interband cascade lasers', *Appl. Phys. Lett.* **83**, 1500 (2003).
91. E. V. Arzhanov, A. P. Bogatov, V. P. Konuaev, O. M. Nikitina, and V. I. Shveikin, 'Waveguiding properties of heterolasers based on InGaAs/GaAs strained quantum-well structures and characteristics of their gain spectra', *Quantum Electron.*, **24**, 581 (1994).
92. E. P. O'Reilly, A. I. Onischenko, E. A. Avrutin, D. Bhattacharyya, and J. H. Marsh, 'Longitudinal mode grouping in InGaAs/GaAs/AlGaAs quantum dot lasers: origin and means of control', *Electron. Lett.* **34**, 2035 (1998).
93. D. Westerfeld, S. Suchalkin, M. Kisin, G. Belenky, J. Bruno and R. Tober, 'Experimental study of optical gain and loss in 3.4–3.6 μm interband cascade lasers', *IEE Proc.-Optoelectron.*, **150**(4), 293 (2003).
94. A. Bauer, private communications (2011); S. Höfling, R. Weih, A. Bauer, M. Kamp and A. Forchel, 'Room temperature continuous wave interband cascade lasers for gas sensing', *Proc. SPIE* **8432**, paper 84320N, 2012.
95. I. Vurgaftman, W. W. Bewley, C. L. Canedy, C. S. Kim, M. Kim, C. D. Merritt, J. Abell, J. R. Lindle, and J. R. Meyer, 'Rebalancing of internally generated carriers for mid-infrared interband cascade lasers with very low power consumption', *Nature Communications*, **2**, 585 (2011).

96. W. W. Bewley, C. L. Canedy, C. S. Kim, M. Kim, C. D. Merritt, J. Abell, I. Vurgaftman, and J. R. Meyer, 'Continuous-wave interband cascade lasers operating above room temperature at $\lambda = 4.7–5.6$ μm', *Opt. Express* **20**, 3235 (2012).
97. T. Borca-Tasciuc, D. Achimov, W. L. Liu, G. Chen, H.-W. Ren, C.-H. Lin, and S. S. Pei, 'Thermal conductivity of InAs/AlSb superlattices', *Microscale Thermophys. Eng*. **5**, 225 (2001); T. Borca-Tasciuc, D. W. Song, J. R. Meyer, I. Vurgaftman, M.-J. Yang, B. Z. Nosho, L. J. Whitman, H. Lee, R. U. Martinelli, G. W. Turner, M. J. Manfra, and G. Chen, 'Thermal conductivity of $AlAs_{0.07}Sb_{0.93}$ and $Al_{0.9}Ga_{0.1}As_{0.07}Sb_{0.93}$ alloys and $(AlAs)_1/(AlSb)_{11}$ digital-alloy superlattices', *J. Appl. Phys.* **92**, 4994 (2002).
98. C. Sirtori, J. Faist, F. Capasso, D. L. Sivco, A. L. Hutchinson, and A. Y. Cho, 'Continuous wave operation of midinfrared (7.4–8.6 μm) quantum cascade lasers up to 110 K temperature', *Appl. Phys. Lett*. **68**, 1745 (1996).
99. K. Ohtani, and H. Ohno, 'An InAs-based intersubband quantum cascade laser', *Jpn. J. Appl. Phys*. **41**, L1279 (2002); 'InAs/AlSb quantum cascade lasers operating at 10 μm', *Appl. Phys. Lett.* **82**, 1003 (2003).
100. R. Teissier, D. Barate, A. Vicet, D. A. Yarekha, C. Alibert, A. N. Baranov, X. Marcadet, M. Garcia, and C. Sirtori, 'InAs/AISb quantum cascade lasers operating at 6.7 μm', *Electron. Lett*. **39**, 1252 (2003).
101. R. Teissier, D. Barate, A. Vicet, C. Alibert, A. N. Baranov, X. Marcadet, C. Renard, M. Garcia, C. Sirtori, D. Revin, and J. Cockburn, 'Room temperature operation of InAs/AlSb quantum cascade lasers', *Appl. Phys. Lett*. **85**, 167 (2004).
102. K. Ohtani, K. Fujita, and H. Ohno, 'Mid-infrared InAs/AlGaSb superlattice quantum-cascade lasers', *Appl. Phys. Lett*. **87**, 211113 (2005).
103. Z. Tian, L. Li, Y. Hao, R. Q. Yang, T. D. Mishima, M. B. Santos, and M. B. Johnson, 'InAs-based interband cascade lasers with emission wavelength at 10.4 μm', *Electronics Lett*. **48**, 113 (2012); and OU unpublished results (2011).
104. Z. Tian, Y. Jiang, L. Li, R. T. Hinkey, Z. Yin, R. Q. Yang, T. D. Mishima, M. B. Santos, and M. B. Johnson, 'InAs-based interband cascade lasers near 5.3 μm', *IEEE J. Quantum Electron.*, **48**, 915 (2012).
105. Y. Jiang, L. Li, Z. Tian, R. T. Hinkey, R. Q. Yang, T. D. Mishima, M. B. Santos, M. B. Johnson, and K. Mansour, 'Room-temperature InAs-based interband cascade lasers', paper CF3K.1 at The Conference on Lasers and Electro-Optics (CLEO) and the Quantum Electronics and Laser Science Conference (QELS), San Jose, CA, May 6–11, 2012.
106. L. Li, Z. Tian, Y. Jiang, H. Ye, R. Q. Yang, T. D. Mishima, M. B. Santos, and M. B. Johnson, 'Interband cascade lasers at long wavelengths', paper CF3K.2 at The Conference on Lasers and Electro-Optics (CLEO) and the Quantum Electronics and Laser Science Conference (QELS), San Jose, CA, May 6–11, 2012.
107. H. P. Hjalmarson and S. R. Kurtz, 'Electron Auger processes in mid-infrared InAsSb/InGaAs heterostructures', *Appl. Phys. Lett*., **69**, 949 (1996).
108. C. H. Grein, M. E. Flatte, J. T. Olesberg, S. A. Anson, L. Zhang, and T. F. Boggess, 'Auger recombination in narrow-gap semiconductor superlattices incorporating antimony', *J. Appl. Phys*., **92**, 7311 (2002).
109. M. E. Flatte, C. H. Grein, and H. Ehrenreich, 'Sensitivity of optimization of mid-infrared InAs/GaInSb laser active regions to temperature and composition variations', *Appl. Phys. Lett*. **72**, 1424 (1998).

110. W. W. Bewley, J. R. Lindle, C. S. Kim, M. Kim, C. L. Canedy, I. Vurgaftman, and J. R. Meyer, 'Lifetimes and Auger coefficients in type-II W interband cascade lasers', *Appl. Phys. Lett*. **93**, 041118 (2008).
111. I. Vurgaftman, M. Kim, C. S. Kim, W. W. Bewley, C. L. Canedy, J. R. Lindle, and J. R. Meyer, 'Auger recombination, internal loss, and other processes in interband cascade lasers', *Proc. SPIE*, **7211**, 721111 (2009).
112. B. A. Ikyo, I. P. Marko, A. R. Adams, S. J. Sweeney, C. L. Canedy, I. Vurgaftman, C. S. Kim, M. Kim, W. W. Bewley, and J. R. Meyer, 'Temperature dependence of 4.1 μm mid-infrared type II "W" interband cascade lasers', *Appl. Phys. Lett*. **99**, 021102 (2011).
113. W. W. Bewley, C. L. Felix, I. Vurgaftman, E. H. Aifer, J. R. Meyer, L. Goldberg, J. R. Lindle, D. H. Chow, and E. Selvig, 'Continuous-wave mid-infrared VCSELs', *IEEE Photo. Technol. Lett*. **10**, 660 (1998).

13

Terahertz (THz) quantum cascade lasers

S. BARBIERI, University of Paris Diderot
and CNRS, France and S. KUMAR, Lehigh
University, USA

DOI: 10.1533/9780857096401.3.514

Abstract: This chapter is dedicated to terahertz (THz) quantum cascade laser technology. After a brief introduction that contains a description of the current state of the art in terms of performance, the following important technological aspects are reviewed in more detail: waveguide and photonic structures, frequency and phase stabilisation, and active mode-locking.

Key words: semiconductor lasers, terahertz (THz), quantum cascade lasers, distributed-feedback lasers, photonic crystals, microwave modulation, active mode-locking, phase locking, frequency locking, optical sampling, frequency combs, frequency stabilisation.

13.1 Terahertz quantum cascade laser technology

This section introduces the terahertz (THz) frequency range of the electromagnetic spectrum, some common THz applications, and the existing technology that is being developed to address those applications. THz quantum-cascade lasers (QCLs) are then introduced as one of the most promising sources of THz radiation. State-of-the-art developments related to THz QCLs are described briefly in a variety of areas such as materials, performance characteristics, and developments targeted to make QCLs ready for specific applications.

13.1.1 State of the art

The terahertz (THz) region of the electromagnetic spectrum has remained underdeveloped, in large part due to lack of suitable techniques to generate coherent high-power radiation. Many molecules and solids have strong and distinct spectral signatures at THz frequencies, which makes THz technology important for both science and commercial applications related to spectroscopy and imaging.[1] Some potentially important applications include remote-sensing of earth's atmosphere and, in astronomy, understanding the formation of planets, stars, and galaxies.[2] This is because THz optical transitions are readily thermally excited due to their low-energies making them ideal for passive emission-spectroscopy. For imaging applications,[3] THz radiation is useful for security-related detection of weapons, drugs, and explosives since many materials such as paper, plastics, and ceramics, which are opaque to visible frequencies, are transmissive at longer wavelengths.

In comparison to microwaves, THz radiation provides a better spatial resolution, due to its shorter wavelength. When compared to imaging with high energy X-rays, THz imaging is non-invasive and can provide much better contrast in terms of identification of different materials, due to their largely different absorption and refraction indices across the THz spectrum. For similar reasons, THz imaging can find potential application in biology and medicine,[4] in areas as diverse as cancer research, label-free DNA sensing, and non-destructive evaluation of pharmaceutical products. All of the aforementioned applications would benefit from compact high-power (tens of milliwatts) coherent sources of radiation to enable imaging in real-time, and sensing with array detectors operating at room temperature. In comparison to narrow-band sources such as lasers, broadband sources of THz radiation are more widely available; however, such sources are inherently low power (average power is of the order of few microwatts). They are useful, nevertheless, because of room-temperature operation and for their ability to be detected coherently. Techniques such as generation of THz bandwidth time-domain pulses in high-resistivity semiconductors,[5] non-linear generation by electro-optical rectification in crystals such as ZnTe,[6] or non-linear generation by optical parametric conversion in materials such as $LiNbO_3$[7] or by difference-frequency generation in semiconductors,[8] have been used for various raster-scanned imaging and broadband spectroscopic applications.

There has been a spur of research activities in terms of technology development to advance the field of THz science,[9,10] of which the advent of a THz quantum cascade laser (QCL)[11] carries particular importance. THz QCLs are arguably the only solid-state THz sources that can deliver average optical power levels much greater than the milliwatts essential for imaging applications, and also continuous-wave (CW) operation for the frequency stability desired in high-resolution spectroscopy techniques. THz QCLs are semiconductor lasers in which radiation is due to electronic intersubband transitions in semiconductor superlattices that have been demonstrated in GaAs/AlGaAs,[11] InGaAs/InAlAs,[12] and InGaAs/GaAsSb[13] heterostructures. These devices now provide CW spectral coverage in the frequency range of 1.2 THz (and even < 1 THz with magnetic-field assisted operation) through THz with optical power output in the tens of milliwatts range.[14,15] In terms of optical power output, frequency linewidth, and frequency stability they are arguably on par with the much bigger and more expensive molecular gas lasers. Additionally, their emission frequency could be artificially adjusted by band structure engineering, which makes them attractive for a variety of applications. A wide variety of active-region designs have been published.[14] The initial demonstration of THz QCLs was done with the aid of a single-plasmon waveguiding scheme,[11] and threshold densities as low as 100 A/cm^2 were soon demonstrated in both pulsed and CW operation.[16] The subsequent development of double-plasmon metal-metal waveguides[17] has led to higher operating temperatures in both pulsed (200 K)[18] and CW (117 K)[19] operation.

Unique distributed-feedback (DFB) techniques have been recently demonstrated to achieve single-mode operation of THz QCLs with narrow beam patterns.[20–24] Techniques for continuous frequency tuneability in the range of >300 GHz[25] have been demonstrated. Owing to the ultrafast intersubband transitions, unique time-domain techniques have been employed for THz QCLs, such as time-resolved measurement of its stimulated emission.[26] THz QCLs have been frequency and phase-stabilised using the compact fibre technology[27] which is promising for applications in high-resolution sensing. Also, unique methods of generation and measurement of mode-locked THz QCL pulses have been realised.[28] With recent demonstrations of real-time imaging[29] and heterodyne spectroscopy[30] using THz QCLs, THz QCLs have come a long way to meeting some of important characteristics required from such narrow-band THz sources for targeted application in spectroscopy, imaging, and remote-sensing.

13.2 Waveguides and photonic structures

This section reviews different types of sub-wavelength waveguides that are commonly used for THz QCLs, namely metal–metal (MM) and semi-insulating single-plasmon (SISP) waveguides. The long-wavelength range associated with such schemes introduces unique emission properties in THz QCLs, and hence novel techniques have been devised to improve their spectral and modal characteristics for practical applications. Periodic photonic structures are discussed that improve the beam-profile for THz QCLs while obtaining robust single-frequency spectral behaviour.

13.2.1 Metal–metal versus semi-insulating single-plasmon waveguides

The following expressions can be written for a laser operating above threshold:

$$\begin{aligned}\Gamma g(\omega) &= \alpha_{\mathrm{w}} + \alpha_{\mathrm{m}} \\ &= \alpha_{\mathrm{w}} + (\alpha_{\mathrm{m,f}} + \alpha_{\mathrm{m,r}})\end{aligned} \qquad [13.1]$$

$$\frac{dP_{\mathrm{out}}}{dI} \propto \hbar\omega \frac{\alpha_{\mathrm{m,f}}}{\alpha_{\mathrm{m}} + \alpha_{\mathrm{m,f}} + \alpha_{\mathrm{m,r}}} \qquad [13.2]$$

$$\alpha_{\mathrm{m,f/r}} = \frac{1}{2L}\log_{\mathrm{e}}(R_{\mathrm{f/r}}) \qquad [13.3]$$

Equation [13.1] is the well known condition that the gain must be equal to the loss during laser operation. In this expression, Γ is the fraction of the mode that propagates in the active medium (also known as the mode confinement factor) and g is the material gain of the active medium, therefore, Γg becomes the modal gain. Also, α_{w} is the modal propagation loss in the waveguide cavity used for mode confinement, and α_{m} is the out-coupling (mirror) loss in the cavity. For a Fabry–Pérot ridge cavity of length L, with $R_{\mathrm{f/r}}$ being the reflectivity of mode from the front/rear facet respectively, $\alpha_{\mathrm{m,f/r}}$ is the mirror loss due to the corresponding facet. For the output power $\mathrm{P}_{\mathrm{out}}$ collected from the front facet and a current I flowing in the device, the slope efficiency dP_{out}/dI can be written as in Equation [13.2], where $\hbar\omega$ is the photon energy for the lasing mode.

Conventional dielectric waveguiding is impractical at THz frequencies due the long wavelengths involved. Waveguides for THz QCLs therefore utilise surface-plasmons propagating at a metal–semiconductor interface that allows mode confinement within sub-wavelength dimensions.

Two types of surface-plasmon waveguides have been demonstrated for THz QCLs: the semi-insulating surface-plasmon (SISP) waveguides[11] and the metal–metal (MM) waveguides.[17] Figure 13.1 shows the schematics, and typical finite-element electromagnetic mode calculations for both types of waveguides for a comparison. Note that the active region is assumed to be lossless in these calculations for an accurate comparison of the contribution due to the waveguide itself. A more comprehensive treatment of the electromagnetic modelling of such waveguides can be found in Reference 33.

The MM waveguides confine the mode in sub-wavelength dimensions in the vertical direction, by virtue of a *double-plasmon* mode that is bound to both the bottom and the top metal cladding. This leads to a large mismatch in the mode shapes of a mode that can propagate in free-space and the mode inside the waveguide. Consequently, the mirror reflectivity in MM waveguides becomes very high (R ~ 0.7–0.9[33]), as opposed to that expected for plane wave reflection at a normal air/GaAs boundary ($R_{\mathrm{norm}} = [(n_{\mathrm{GaAs}} - 1)/(n_{\mathrm{GaAs}} + 1)]^2 \sim 0.32$). In contrast, even though the mode in a SISP waveguide is also a double-plasmon mode, which is bound to the top metal and the thin n^+ GaAs layer at the bottom, it is not confined within sub-wavelength dimensions. Hence, the mirror reflectivity in SISP waveguides is approximately 0.32.[33]

As can be noticed from the calculated values in Fig. 13.1, MM waveguides have a smaller value of the waveguide losses α_w/Γ in comparison to the SISP waveguides. It may be noted that the semi-insulating GaAs substrate is likely to contribute additional losses for SISP waveguides that have not been included in Fig. 13.1. These losses can occur due to impurity absorption at THz frequencies caused by shallow donors and acceptors in the nominally semi-insulating substrate. Also, $\alpha_m/\Gamma \sim 0.5$–$2\ \text{cm}^{-1}$ per facet for a 1 mm long cavity in MM waveguides (calculated for $R \sim 0.9$–0.7), as compared

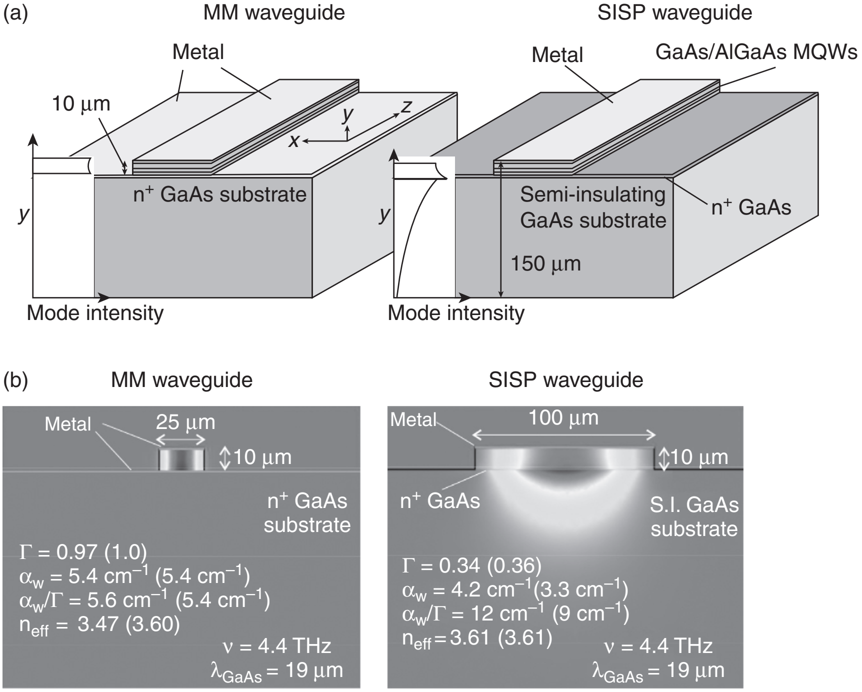
(a)
MM waveguide
SISP waveguide
Metal
10 μm
y
z
x
n+ GaAs substrate
y
Mode intensity
Metal
GaAs/AlGaAs MQWs
Semi-insulating GaAs substrate
n+ GaAs
y
150 μm
Mode intensity
(b)
MM waveguide
SISP waveguide
Metal
25 μm
10 μm
n+ GaAs substrate
Γ = 0.97 (1.0)
αw = 5.4 cm−1 (5.4 cm−1)
αw/Γ = 5.6 cm−1 (5.4 cm−1)
neff = 3.47 (3.60)
ν = 4.4 THz
λGaAs = 19 μm
Metal
100 μm
10 μm
n+ GaAs
S.I. GaAs substrate
Γ = 0.34 (0.36)
αw = 4.2 cm−1 (3.3 cm−1)
αw/Γ = 12 cm−1 (9 cm−1)
neff = 3.61 (3.61)
ν = 4.4 THz
λGaAs = 19 μm

13.1 (a) Schematics of the MM and the SISP waveguides, and (b) two-dimensional electromagnetic mode calculations for the fundamental lateral modes. The calculations are done within a Drude model at $\nu = 4.4$ THz (λ air ~ 68 μm, λ GaAs ~ 19 μm). For SISP waveguides, the n^+ GaAs layer is 0.4 μm thick and is doped to $3 \times 10^{18}\ \text{cm}^{-3}$. The total energy density across the cross-section of the waveguide for a mode propagating perpendicular to the plane of the figure is plotted. A Drude scattering time of $\tau = 50$ fs and a doping density of $5.9 \times 10^{22}\ \text{cm}^{-3}$ is used for metal (Au),[31] and a $\tau = 0.1$ ps is used for the n^+ GaAs layer.[17] The refractive index of GaAs is taken to be $n_{\text{GaAs}} = 3.6$. n_{eff} is the effective index of the propagating mode. The values in parentheses are the results for infinitely wide waveguides. For these calculations the active region is taken to be lossless, and so is the semi-insulating GaAs substrate for the SISP waveguides. These calculations are performed using a finite-element solver.[32]

to $\alpha_m/\Gamma \sim 15–30\ \mathrm{cm}^{-1}$ per facet for a 1 mm long cavity in SISP waveguides (calculated for $\Gamma \sim 0.4–0.2$). Hence, even for relatively long cavity lengths, the mirror losses in SISP waveguides are an order of magnitude greater than those in MM waveguides.

The aforementioned arguments indubitably suggest that the overall losses in SISP waveguides are higher compared to those in MM waveguides. Hence, QCLs realised in MM waveguides show much improved temperature performance. In contrast, the factor $\alpha_{m,f}/(\alpha_w+\alpha_{m,f}+\alpha_{m,r})\lesssim 0.1$ for MM waveguides as compared to the values of $\alpha_{m,f}/(\alpha_w+\alpha_{m,f}+\alpha_{m,r})>0.2–0.3$ that are possible for SISP waveguides. This suggests that the slope efficiency for MM QCLs is expected to be considerably smaller than that for SISP QCLs. This has indeed been observed experimentally. Where THz QCLs with SISP waveguides have shown optical power output as high as 250 mW,[34] the power output with MM waveguides remains in the range of 10–60 mW for the best reported results.[18,35,36]

Apart from their lower optical loss and the resulting higher-temperature operation, MM waveguides for THz QCLs offer several advantages owing to their ability to confine radiation in sub-wavelength scales even in the lateral dimensions. CW operation above liquid-nitrogen temperature has been demonstrated by improving the flip-chip wafer bonding process required for fabricating such structures and by making the ridge devices narrow for efficient heat removal through the substrate.[19] Ultra-low threshold microcavity lasers with sub-wavelength optical volumes have also been realised.[37–39] However, from a usability perspective the primary requirement has been improvement of their emission characteristics to obtain narrow output-beams with single-mode operation.

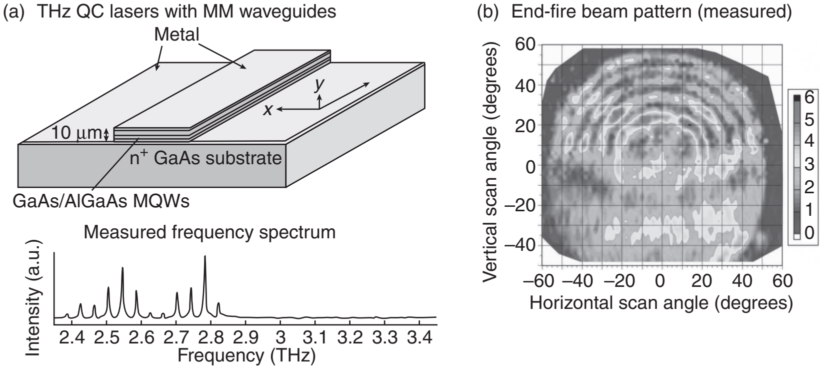

13.2 (a) Parallel-plate ridge cavity THz QCL, wherein multiple-mode lasing is generally observed; (a) typically measured single-bias optical spectrum from an edge-emitting MM. (b) Measured far-field beam pattern of a MM THz QC laser.[40] Optical emission is highly divergent with distorted ring-like wavefronts.

13.2.2 Poor emission characteristics of THz QC lasers with metal–metal microcavities

The best performing THz QC lasers utilise MM microcavities as shown in Fig. 13.2a,[41] for the reasons explained above. However, the emission properties of such ridge cavity lasers are very poor. First, such lasers easily excite several lateral and longitudinal order modes simultaneously, invariably leading to multi-mode lasing across the gain bandwidth, typically up to 0.5 THz around the designed frequency. Also, the lasing modes often switch unpredictably as a function of applied bias. An example of a multi-mode optical spectrum of such a laser is also shown in Fig. 13.2a.

For high-resolution sensing and spectroscopy applications, multi-mode lasing is undesirable and in some cases strictly unacceptable. Second, THz QC lasers have very poor beam patterns, an example of which is shown in Fig. 13.2b.[40] Such a beam pattern results due to the highly diffracted beam from a sub-wavelength aperture, which shows a ring-like beam pattern due to the microcavity laser acting like a radiating antenna at such long wavelengths. Such beam patterns make such a laser less attractive for coherent detection since the phase of the electromagnetic field shows a rapid variation spatially and also because the optical power is no longer concentrated in a small area, and hence only a small fraction of the output power could be utilised.

13.2.3 Single-mode THz QCLs with periodic photonic cavities

THz QC lasers with highest operating temperatures are typically realised in a Fabry–Pérot ridge cavity configuration as illustrated in Fig. 13.2a with peak optical power output in the range of 10–50 mW at 10 K for the best reported results.[18,36] However, as argued in Section 13.2.1, the emission characteristics (multimoded spectral behaviour, divergent beam patterns, and low output power) for such lasers are poor owing to the sub-wavelength dimensions of the cavities at THz frequencies. Two of those three problems have more-or-less been rectified by implementation of various DFB schemes in the past five years by several research groups. DFB in the form of one-dimensional gratings or two-dimensional photonic-crystal-like structures allow robust single-mode operation and show improved beam properties, thereby improving both the spectral and modal properties of the lasers simultaneously. However, the poor out-coupling from THz microcavity resonators still remains a considerable challenge, and hence the overall output power from single-mode THz QC lasers remains in the range of 10 mW at 10 K, which reduces to approximately 1 mW at 77 K for the best reported results.[20,42]

Figure 13.3 is an illustration for a semiconductor laser cavity with an embedded periodic grating, which we will use to describe some of the

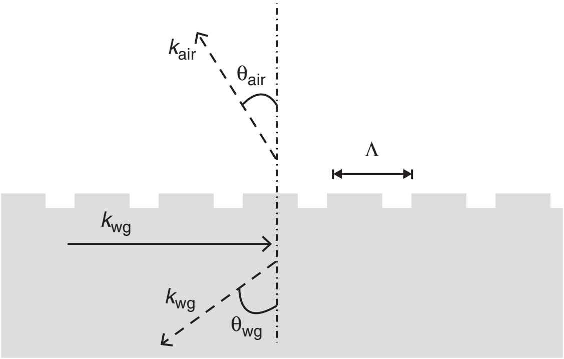

13.3 Schematics of a distributed Bragg grating implemented in a semiconductor gain medium to improve spectral and modal characteristics of laser cavities.

present DFB schemes (Sections 13.2.4 and 13.2.5). Any aspect of a cavity that periodically perturbs the propagating electromagnetic mode leads to Bragg diffraction of the wave both inside and outside the cavity. For a wave propagating from left to right with a wavevector k_{wg} ($k_{wg} = 2\pi n_r/\lambda_0$ for a plane wave, where n_r is the refractive index of the semiconductor and λ_0 is the free-space wavelength), a wave is diffracted inside the cavity for which we can write the Bragg condition:

$$k_{wg} = nk_\Lambda - k_{wg}\sin(\theta_{wg}) \qquad [13.4]$$

where $k_\Lambda = 2\pi/\Lambda$ is the grating wavevector, n is an integer ($n = 1, 2, 3, \ldots$) that specifies the diffraction order, and θ_{wg} is the angle of diffraction. Similarly, for a wave diffracted outside the cavity, we can write:

$$k_{wg} = nk_\Lambda - k_{air}\sin(\theta_{air}) \qquad [13.5]$$

where k_{air} is the free-space wavevector. Equations [13.4] and [13.5] will now be used to some of the subsequent discussions to describe the operation of single-mode THz QC lasers.

13.2.4 Surface-emitting second-order DFB THz QC lasers in metal–metal cavities

Figure 13.4 shows the schematic, operating principle and experimental results from the first single-mode THz QC laser in a MM microcavity that lased in CW operation with a single-lobed beam pattern.[20] This design is among the best performing single-mode THz QC lasers in terms of operating temperature (although, similar operating temperatures have also recently been realised but only in pulsed mode in Reference 43), and is one

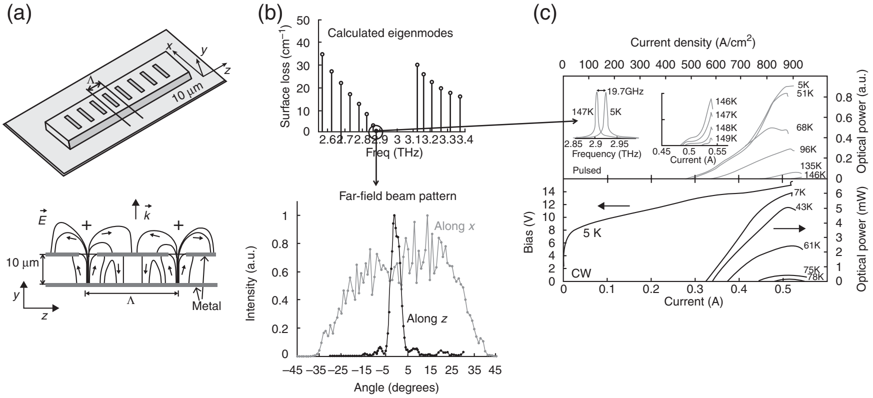

13.4 Surface-emitting single-mode THz QC lasers with second-order DFB. (a) Illustration of a MM THz microcavity with embedded second-order grating in the top metallic layer. The electric-field lines for the lowest loss resonant cavity mode are drawn from a side-view of the microcavity. (b) Calculated eigenmode spectrum of the grating microcavity, where the surface loss (units are cm^{-1}) is plotted for each resonant-mode. The lowest loss eigenmode (circled) is the one that eventually lases. Experimentally measured far-field beam pattern of the optical power emitted from the surface is also plotted for the lasing mode. (c) Light-current characteristics of the single-mode THz QC laser in both pulsed and CW operation. The lasing mode tunes with temperature due to a change in the refractive index of the semiconductor. The maximum operating temperature of 149 K for this laser is the highest reported for any single-mode THz QCL to date.

of the two reported results (the other one being Reference 42) of single-mode THz QC lasers with narrow beam output, which operate in CW mode at the temperature of liquid nitrogen (77 K).

The periodic grating in Fig. 13.4a provides DFB due to second-order Bragg diffraction, that is, $n = 2$ in Equation [13.4] for $\theta_{\text{wg}} = \pi/2$, which leads to $k_{\text{wg}} = k_{\Lambda}$. Hence, a mode which is exactly periodic with the grating is one that is excited due to its lowest loss. Note that the DFB structure could also be considered a one-dimensional photonic crystal in which the above mode is the one at the top of the lower band-edge of the eigenmode dispersion profile of the photonic crystal (as shown in Fig. 13.4b). The periodicity of the electric field along the grating could also be seen from the field diagram in Fig. 13.4a. As a result of this, emission from each successive grating aperture leads to constructive interference in the far-field on top of the surface (i.e., for = 0).

The surface-emitting DFB laser of Fig. 13.4 achieves robust single-mode operation as determined from the periodicity of the grating, as opposed to the unpredictable multi-mode lasing behaviour of the Fabry–Pérot cavity of Fig. 13.2. Also, it obtains a much improved beam pattern profile with a divergence of 5° in the longitudinal direction (even though the lateral emission is still broad due to the sub-wavelength width of the cavity). However, the design still does not solve the problem of efficient out-coupling. In fact, it is the E_z field that causes emission in the surface normal direction, which has nulls precisely at the grating apertures. Therefore, the surface loss of the lasing mode is close to zero (0.1 cm^{-1} for the lasing mode in Fig. 13.4b), which translates to negligible out-coupling of radiation, and hence very low output power.

13.2.5 Improved beam-profile in both dimensions for single-mode THz QC lasers

The surface-emitting DFB laser with second-order Bragg grating as shown in Fig. 13.4 obtained narrow beam pattern only in the longitudinal direction, whereas the emission is broad in the lateral direction, as is evident from Fig. 13.4b. This is an inherent characteristic of surface-emitting DFB lasers in rectangular ridge geometry,[20,44,45] especially at THz frequencies where the ridge width could be less than the wavelength. Although wider ridges could be made to circumvent this problem, higher current flow leads to higher heat dissipation, which prevents operation in CW mode.[44,45]

Several groups have pursued periodic photonic geometries of different types to obtain symmetric beam pattern in both dimensions, such as surface-emitting micro-disk,[22] and micro-ring[46] THz QC lasers. However, the best results in terms of the narrow beam patterns are obtained from two-dimensional photonic crystal[21] and one-dimensional third-order DFB[42] lasers, as shown in Fig. 13.5a and Fig. 13.5b respectively. The photonic-crystal structure in Fig. 13.5a is similar to the infrared photonic-crystal lasers that excited the delocalised band-edge resonant modes. The third-order DFB in Fig. 13.5b, on the other hand, works on a clever idea in that the third-order Bragg condition $(2/3)k_{\text{wg}} = k_{\Lambda}$, as obtained from Equation [13.4] for $n = 3$, makes it possible for the mode leaked outside the waveguide to combine coherently in the end-fire direction, since $2\Lambda = 3\lambda_{\text{wg}} \approx \lambda_0$ for GaAs that has $n_{\text{r}} \approx 3.6$. In other words, two grating periods, leading to same phase in the grating apertures for a third-order DFB, are approximately equivalent in length to the free-space wavelength λ_0. Hence, any mode leaked outside the cavity combines coherently in the longitudinal direction to give a tight-beam spot in the plane perpendicular to the ridge.

While the results shown in Fig. 13.5 have managed to improve the beam patterns for single-mode THz QC lasers in both dimensions, the best reported CW output power still remains in the range of 1 mW at 77 K for either of the schemes in Fig. 13.4 and Fig. 13.5b respectively. This is inherently a problem of the distributed-feedback scheme for MM cavities, in which case the lowest loss mode is the one that has in-plane field nulls in the metal apertures from where light is radiated, which leads to negligible out-coupling and hence very low output power. The present research focus is, therefore, primarily concentrated on improving the optical out-

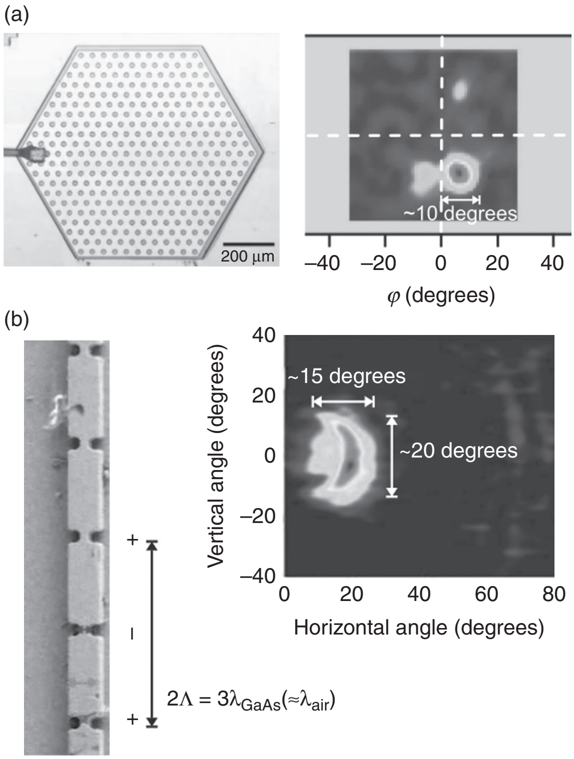

13.5 Single-mode THz QC lasers with narrow beam patterns in two dimensions. (a) A surface-emitting two-dimensional photonic-crystal THz QC laser using a trigonal lattice of etched holes in the top metallic cladding. An optical image of cavity and the measured beam pattern are shown (from Reference 21). (b) An edge-emitting THz QC laser with a third-order Bragg grating embedded in the semiconductor gain medium using laterally etched corrugations in the ridge. An electron image of the cavity and the measured beam pattern are shown (from Reference 42).

coupling from THz microcavities to increase the optical power output of THz QCLs.

Together with the output power and the beam quality, other crucial characteristics of a laser source are its frequency stability and spectral linewidth. In fact these are important parameters that will determine whether or not a given laser source is suitable to perform high-resolution spectroscopy, which, especially in the THz range, is particularly important for astronomical and atmospheric research. In the following chapter different techniques that allow active stabilisation of the frequency of THz QCLs will be discussed. Particular emphasis will be given to techniques that allow locking their frequency to the repetition rate of femtosecond (fs) mode-locked lasers. As we shall see, besides reaching extremely narrow linewidths, these techniques enable the coherent sampling of the THz wave amplitude emitted by the QCL using the optical pulses from the fs-laser. In the last part of the chapter we shall see how this coherent sampling has been used to demonstrate that THz QCLs can be operated in active mode-locking regime by modulating their drive current.

13.3 Stabilisation, microwave modulation and active mode-locking of terahertz quantum cascade lasers

This section reviews frequency, phase-locking and microwave modulation of THz QCLs. Future, general perspectives on THz QCL technology are discussed at the end.

13.3.1 Frequency and phase locking

Linewidth characteristics

QCLs are intrinsically narrow-linewidth sources, owing to a small linewidth enhancement factor (LEF) as a result of their symmetric, or almost symmetric, gain curve.[47–50] LEFs between ~0 and ~2 have been measured

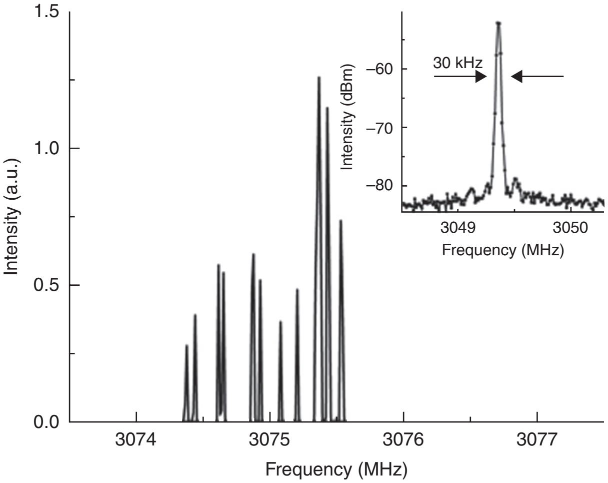

13.6 Difference-frequency spectrum between two Fabry–Pérot modes from two free-running, multi-mode QCLs operating at 3.4 THz. The trace was recorded in a single shot using a spectrum analyser RBW of 30 kHz, and a sweep rate of 8.3 MHz/s. The spectrum comprises several single lines resulting from a slow drift of ~1 MHz/s of the QCLs frequencies due to electrical and thermal instabilities. Inset: spectrum collected with the same parameters used for the main part of the figure showing a RBW linewidth of 30 kHz. Figure taken from Reference 53.

for QCLs operating in the mid-IR range using different techniques.[48–50] In the THz range, owing to the lower available power and the less sensitive detection, only one measurement has been reported so far, by R. P. Green *et al.*,[51] who obtained an LEF of ~0.5 by applying a self mixing technique to a 2.6 THz QCL. This is approximately a factor of 10 lower than typical interband diode lasers LEFs, and should lead to intrinsic linewidth limits in sub-kHz range. Although an accurate measurement of the intrinsic linewidth is still lacking for THz QCLs, a few heterodyne mixing experiments using Schottky diodes as non-linear detectors have revealed the free-running frequency stability of these sources.[52,53] A representative spectrum is reported in Fig. 13.6, showing the difference frequency between two Fabry–Pérot modes of two free-running, multi-mode QCLs operating at 3.4 THz. The trace was recorded in a single shot using a spectrum analyser with a resolution bandwidth (RBW) of 30 kHz, and a sweep rate of 8.3 MHz/s. The spectrum comprises several single lines resulting from a slow drift of ~1 MHz/s of the QCL frequencies due to electrical and thermal instabilities. Each line has a resolution limited linewidth of 30 kHz.[53] These well-behaved spectral characteristics render THz QCLs ideal sources for spectroscopic applications.[54] Besides, as we shall see in the following section, they allow efficient stabilisation of their emission frequency using frequency and phase-locking techniques. This enables the use of THz QCLs for high-resolution spectroscopy experiments or as stable local oscillators for high sensitivity heterodyne receivers.[55,56]

Frequency locking

In frequency locking the emission frequency of a laser is compared to the frequency of a more stable reference, that is, another laser or the absorption line of a gas, generating an error signal proportional to the difference between the two frequencies. By using an appropriate servo-circuit, this error signal is then used to correct the laser frequency and lock it to the reference.[57] The first demonstration of frequency locking of a THz QCL was reported by Betz *et al.* in 2005.[58] In this experiment a 3 THz QCL was stabilised on the line of a FIR gas laser corresponding to the 3105.9368 GHz methanol transition. The schematic of the experimental set-up is shown in Fig. 13.7a. The beams from the two lasers were mixed on a GaAs Schottky mixer, generating a beat-note at 48 GHz, that, in turn, beat with the second harmonic, at 49.2 GHz, of a 24.6 GHz YIG oscillator, producing an intermediate frequency (IF) output at 1.2 GHz. This signal was directed on a source-locking counter that fed back on the QCL to control its drive current. The loop bandwidth was 10 kHz, which was sufficient for frequency stabilisation. In Fig. 13.7b the spectrum of the stabilised beat-note with a linewidth of 65 kHz is displayed on a spectrum analyser with a spectral resolution of 100 kHz.

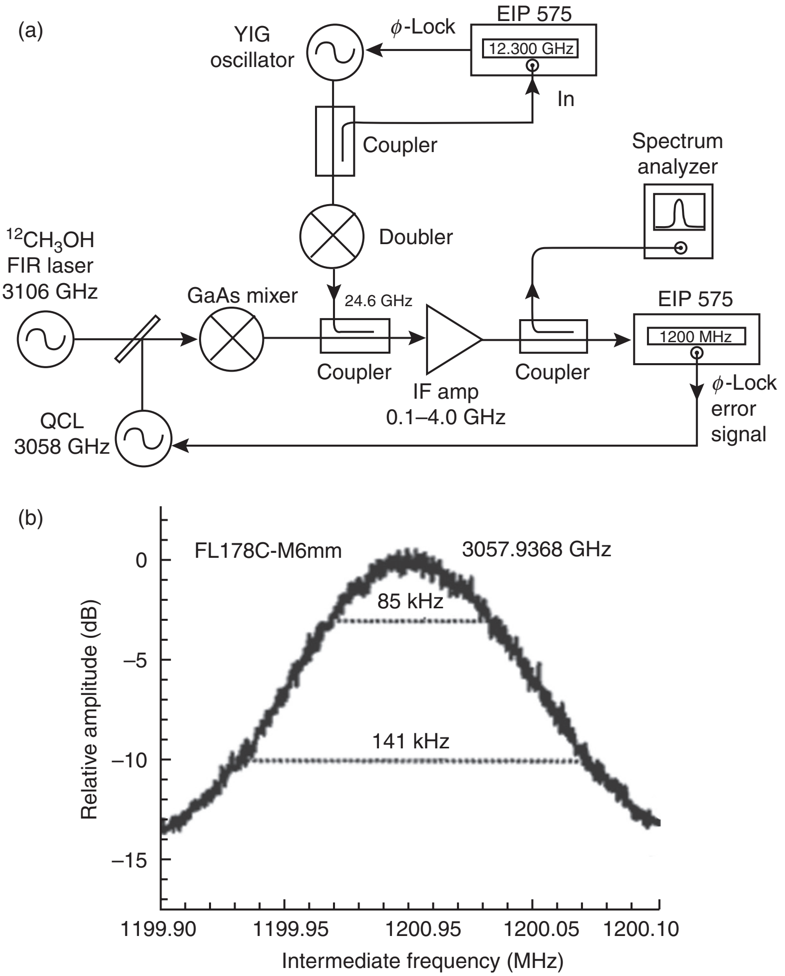
(a)
YIG oscillator
ϕ-Lock
EIP 575
12.300 GHz
In
Coupler
Spectrum analyzer
Doubler
12CH3OH FIR laser 3106 GHz
GaAs mixer
24.6 GHz
EIP 575
1200 MHz
Coupler
IF amp 0.1–4.0 GHz
Coupler
ϕ-Lock error signal
QCL 3058 GHz
(b)
FL178C-M6mm
3057.9368 GHz
85 kHz
141 kHz
Relative amplitude (dB)
0
–5
–10
–15
1199.90
1199.95
1200.95
1200.05
1200.10
Intermediate frequency (MHz)

13.7 (a) Schematic of the experimental set-up for the frequency locking of a 3THz QCL to a far-IR gas laser. See text for a detailed description. (b) Spectrum of the frequency-locked beat-note with a linewidth of 65 kHz as measured on a spectrum analyser with a spectral resolution of 100 kHz. Figures taken from Reference 58.

An alternative frequency locking technique has been recently exploited by Richter *et al.*, based on a molecular resonance serving as frequency reference for a 2.55 THz QCL.[59] This technique presents the advantage of not requiring a bulky THz gas laser. In the work by Richter *et al.* the frequency of the QCL was first fine-tuned by temperature and current in proximity to the 2.55025 THz absorption line of methanol gas maintained at a pressure of 1–2 hPa inside a sealed, 52 cm long absorption cell. The black line in Fig. 13.8a

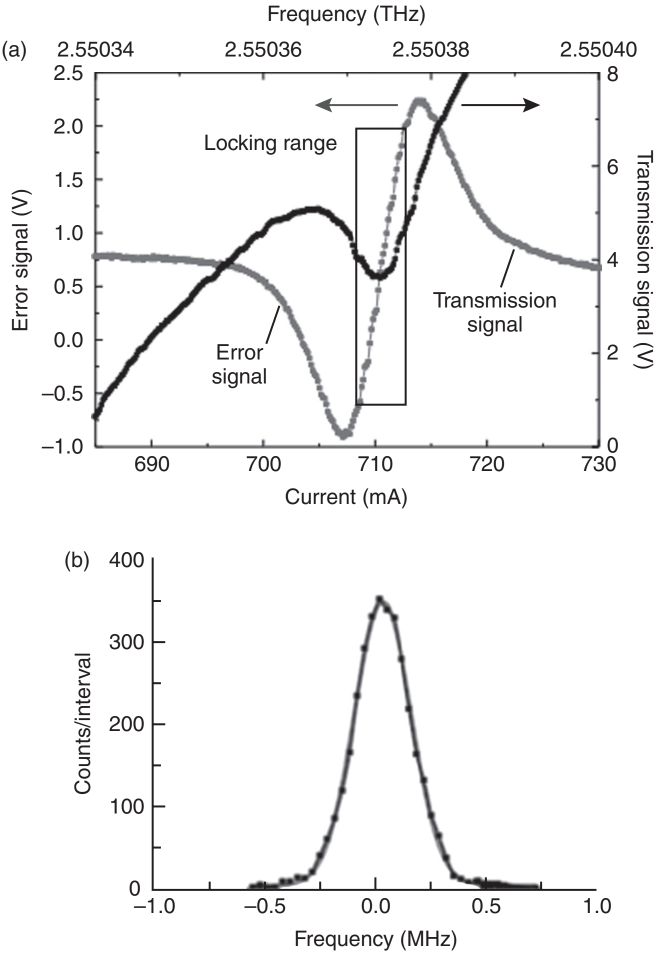

13.8 (a) Absorption line of methanol at 2.55 THz at a pressure of 1.7 hPa. The transmission signal (black line) is measured in direct detection; the error signal (gray line) is measured with a lock-in amplifier and the frequency of the QCL current modulation as reference (see text). The QCL is locked to the centre of the derivative-like error signal. The locking range is indicated by the rectangular box. (b) Number of counts in 34-kHz-wide intervals with the QCL in a frequency-locked state. The solid line is a Gaussian fit to the measurement. Figures taken from Reference 59.

shows the QCL power transmitted through the cell and detected with a liquid helium cooled Ge/Ga photoconductor. Here the QCL was driven in CW at a temperature of 46 K, with an emitted power of a few mW. Changing the drive current of the laser allowed scanning the methanol absorption line (the measured tuning coefficient was of a few MHz/mA), producing the deep at ~710 mA indicating the centre of the transition. The light gray curve shows instead the transmitted signal as a function of current obtained by adding a weak (<1 mA) current modulation to the QCL at a frequency of a few kHz. In this case the signal was recorded with a lock-in amplifier using the modulation frequency as a reference, therefore the light gray curve is proportional to the first derivative of the absorption line. Close to the centre of the absorption line the derivative is linear, and by compensating the *dc* offset caused by the positive slope of the absorption, an error signal with a zero-value at the line centre was generated. This was finally fed back into the QCL drive current using a PID control loop that locked the QCL frequency on the absorption minimum. Figure 13.8b shows the measured frequency-locked line over a time >10 s, obtained by dividing the frequency scale into 34-kHz-wide intervals, and by counting, using the error signal, the number of frequency values falling in each interval. The obtained linewidth was 300 kHz.

Phase locking

Contrary to frequency locking, in phase locking the phase of the laser source is locked to the phase of a reference source so that the integrated phase-noise outside the control bandwidth is << 1 rad^2. First attempts to phase-lock THz QCLs were carried out using multiplied electronic oscillators as reference sources, and hot-electron-bolometer (HEB) mixers as phase-detectors.[60,61] The latter provided the necessary sensitivity to detect the usually low power level from the multiplied source, typically in the pW range.[61] A schematic of the set-up used in Reference 60 is shown in Fig. 13.9a. The THz QCL and the multiplied oscillator were simultaneously focused on the HEB mixer, generating a beat-note in the 1–2 GHz range that oscillated at the difference frequency between the two sources. The beat-note was filtered, amplified and finally down-converted, using a radio-frequency (RF) mixer, into the ~100 MHz range. At this stage it could be phase-compared, through a second mixer, to the frequency of a stable RF oscillator, generating an error signal that was used to control the QCL current thanks to PID control electronics. Figure 13.9b shows the RF beat-note obtained by locking a 1.5 THz QCL emitting ~300 μW of power, to a multiplied YIG source oscillating at 1499.3 GHz.[60] A signal-to-noise (SNR) ratio of ~45 dB was obtained with a 100 Hz RBW of the spectrum analyser. With the 1.5 THz QCL phase-locked, the emitted power level was adjusted to the optimum operating point of the HEB, yielding a measured receiver noise temperature of 1740 K. This value was found to be comparable to the noise temperature obtained by pumping the same HEB with a multiplied oscillator.[60]

Phase-locking techniques such as those briefly described above are bound by the necessity of multiplying the original RF oscillator by a factor of 100–200. The use of such extreme multiplication orders has two main inconveniences: (i) it limits the spectral tuning at the end of the chain to

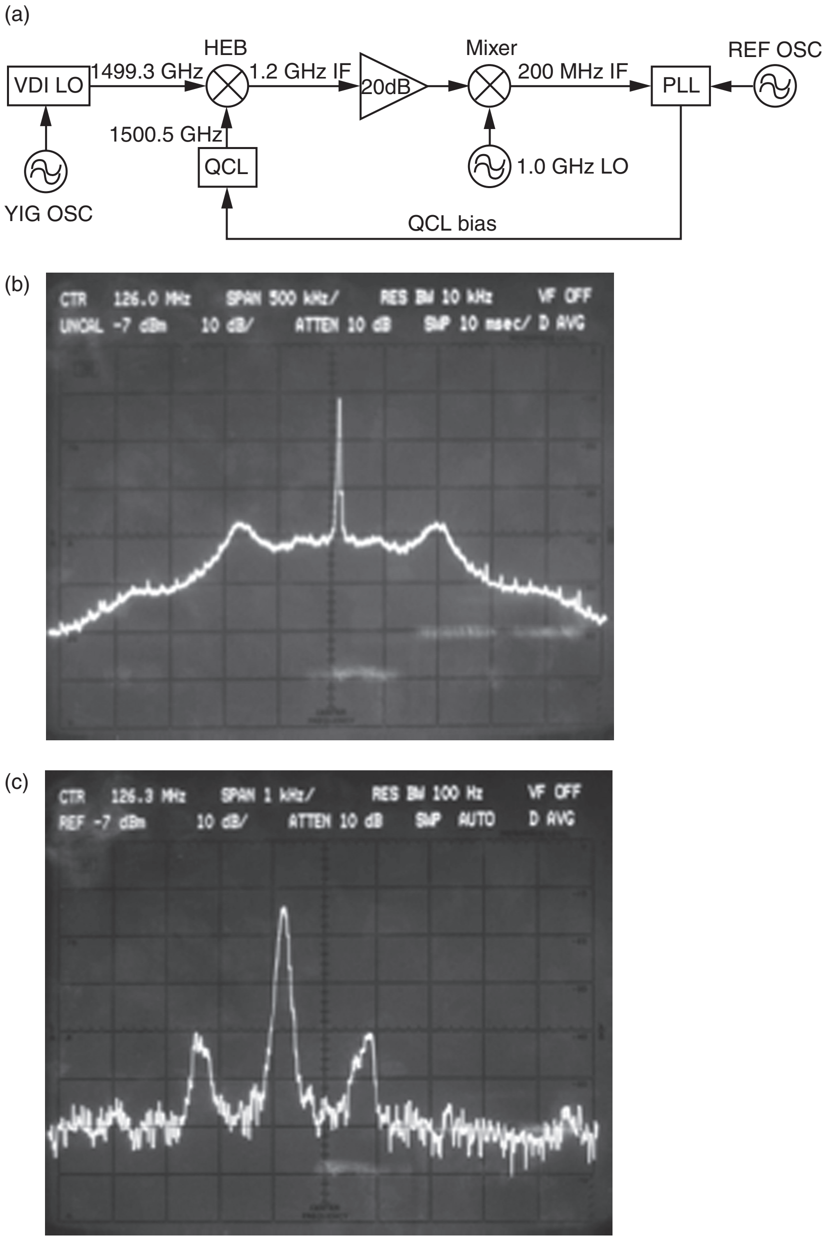

13.9 (a) Schematic of the experimental set-up used to phase-lock a QCL emitting at 1.5 THz to a solid-state multiplier chain (labelled VDI LO in the figure), driven by YIG oscillator. See the text for a detailed description. (b) RF beat-note spectrum of the phase-locked QCL obtained with the set-up of panel (a) and a RBW of 10kHz. (c) RF beat-note spectrum of the phase-locked QCL obtained with the set-up of panel (a) and a RBW of 10Hz. Figures taken from Reference 60.

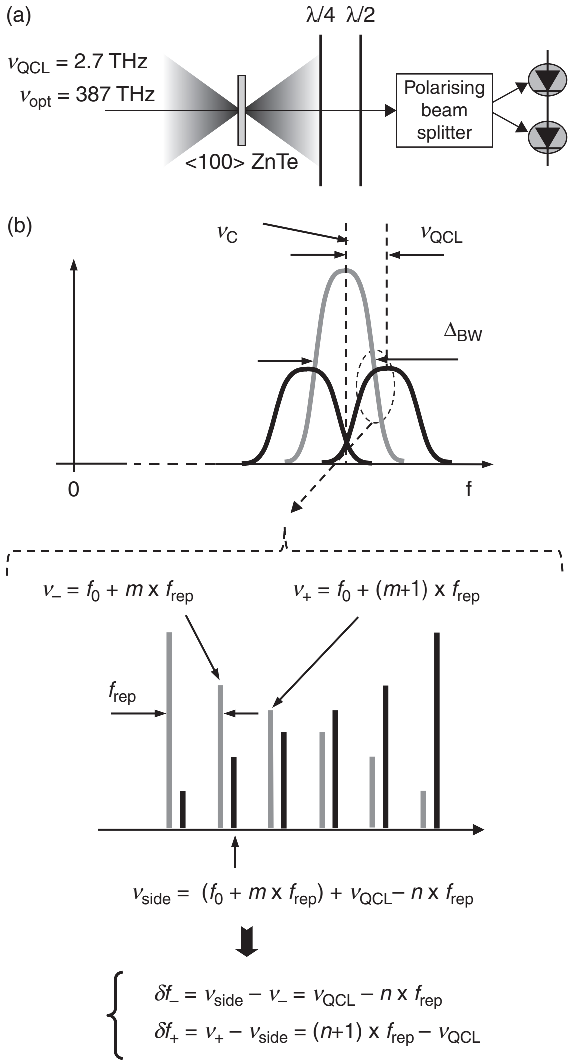
(a)
$\lambda/4$ $\lambda/2$
$\nu_{QCL} = 2.7$ THz
$\nu_{opt} = 387$ THz
<100> ZnTe
Polarising beam splitter
(b)
ν_C
ν_{QCL}
Δ_{BW}
0
f
$\nu_- = f_0 + m \times f_{rep}$
$\nu_+ = f_0 + (m+1) \times f_{rep}$
f_{rep}
$\nu_{side} = (f_0 + m \times f_{rep}) + \nu_{QCL} - n \times f_{rep}$
$\delta f_- = \nu_{side} - \nu_- = \nu_{QCL} - n \times f_{rep}$
$\delta f_+ = \nu_+ - \nu_{side} = (n+1) \times f_{rep} - \nu_{QCL}$

13.10 (a) Schematic of the electro-optical detection set-up. Shown from left to right are the ZnTe crystal, the $\lambda/4$ and $\lambda/2$ wave plates, the PBS and the two photodiodes. The QCL beam (shaded dark) was focused on the ZnTe crystal with an *f*/1, gold-coated parabolic mirror. The horizontal arrow represents the frequency-doubled fs-laser beam at $\lambda = 387$ THz ($\lambda = 775$ nm). (b) Top. Schematic of the spectral envelope of the amplitude-modulated optical beams at the output of the PBS. Dark and light gray curves represent the optical carrier and the sidebands, respectively, at +/− ν_{QCL}. Bottom. Enlargement of the left panel showing the individual comb teeth of the optical carrier and of the upper THz sideband. Here, ν_+ and ν_- are the optical carrier comb teeth that lie closest to the generic comb tooth from the upper sideband, labelled $\nu_{side,}$ and m and n are integer numbers. f_0 is the fs-laser frequency offset. δf_- is the low-frequency beat-note signal used for phase locking (see text). The figure is adapted from Reference 27.

~10% of the centre frequency, and (ii) it generates low power levels that restrict the choice of the mixer element to superconducting receivers. An alternative approach, based on the use of a mode-locked fibre laser, was demonstrated by Barbieri *et al.*[27] This technique replaces the multiplier chain with a mode-locked fibre laser as a reference source, and exploits a room-temperature-operated detector for beat-note detection. Moreover, as we shall see below, it is inherently broadband, that is, it allows the phase locking of any THz QCL, regardless of its emission frequency. The operating principle is schematically described in Fig. 13.10a, and is based on a ZnTe crystal electro-optic modulator. The THz QCL and the beam from a frequency-doubled 1550 nm fs-laser beam are focused onto a 2 mm thick (110) ZnTe electro-optic crystal. Both beams are linearly polarised along the [1,–1,0] axis. The THz electric field induces an a.c. birefringence, thus modulating the polarisation of the fs-laser beam. A quarter-wave plate placed after the crystal compensates the ZnTe static birefringence, so that the polarisation of the fs-laser remains linear in the absence of THz radiation. Next the fs-laser beam passes through a half-wave plate followed by a polarising beam splitter (PBS) rotated at 45deg with respect to the waveplate axis. This transforms the polarisation modulation driven by the THz a.c. field into an amplitude modulation of the two orthogonal polarisation components. The intensities of the two orthogonally polarised beams at the output of the PBS are finally detected with a balanced detection unit comprising two silicon photodiodes connected to a transimpedance amplifier, with a bandwidth of ~100 MHz.

The effect of the amplitude modulation on the fs-laser spectrum is shown in Fig. 13.10b. Two sidebands (black) centred at $+/-\nu_{\mathrm{QCL}}$, where ν_{QCL} is the frequency of the QCL, are generated on both sides of the carrier (light gray) at frequency ν_{C}. Both the carrier and the sidebands spectra are represented by a broadband curve of full width at half maximum Δ_{BW}. Therefore, if Δ_{BW} is larger than ν_{QCL}, the sidebands and carrier spectra will overlap, as shown schematically in the figure. A typical mode-locked fs-fibre laser generates ~100 fs long pulses at a repetition rate $f_{\mathrm{rep}} \sim 100$ MHz, therefore its spectrum is composed of an ensemble of narrow lines separated by ~100 MHz and spanning a spectral range of ~5 THz. The frequency of the nth line is given by $\nu_{\mathrm{n}} = \mathrm{n} \times \mathrm{f}_{\mathrm{rep}} + \mathrm{f}_0$, where n is an integer and f_0 is the fs-laser frequency offset. This means that the condition $\Delta_{\mathrm{BW}} > \nu_{\mathrm{QCL}}$ is satisfied for virtually any THz QCL demonstrated to date.[14] As a result, focusing of the modulated fs-laser beam on a silicon photodiode gives rise, on the photocurrent spectrum, to a number of beat notes oscillating at $\delta f_{-} = (\nu_{\mathrm{QCL}} - n \times f_{\mathrm{rep}})$ and $\delta f_{+} = (n + 1) \times f_{\mathrm{rep}} - \nu_{\mathrm{QCL}} = f_{\mathrm{rep}} - \delta f_{-}$ (see Fig. 13.10b), where n is an integer. For n such that $n \times f_{\mathrm{rep}}$ is the closest harmonic to ν_{QCL}, then $\delta f_{-}, \delta f^{+} < f_{\mathrm{rep}} \sim 100$ MHz, and a direct link from the THz to ~10 MHz range is obtained, allowing, without any further down-conversion stage, the phase-lock of ν_{QCL} to f_{rep}.[27] To

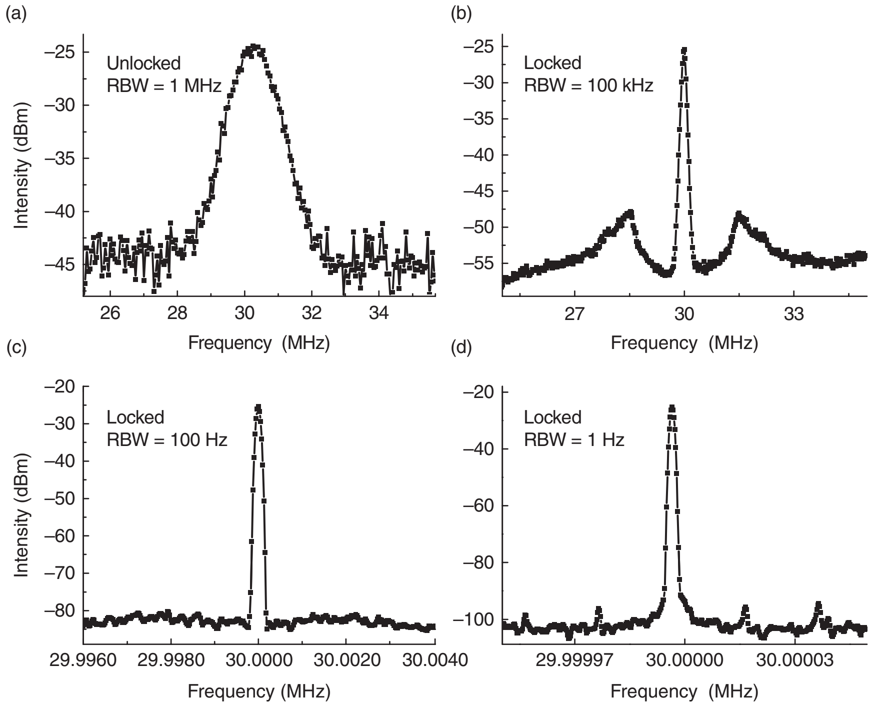

13.11 (a) Unlocked and (b–d) locked RF spectra of the beat-note signals with RBW decreasing from 1 MHz to 1 Hz, the spectral resolution limit of our spectrum analyser. Spectra were collected with 100 video bandwidth averages. The two sidebands of panel (b) indicate that the bandwidth of the phase-lock is ~1.5 MHz. The figure is adapted from Reference 27.

this end it is important to note that in this beat-note generation process the carrier frequency ν_C of the fs-laser (or the frequency offset f_o) is subtracted, hence δf_-, δf_+ depend *only* on ν_{QCL} and f_{rep}.[62] Figure 13.11 reports the result obtained using the detection technique of Fig. 13.10a to phase-lock a 2.7 THz QCL to the n^{th} harmonic of a fs-fibre. In Fig. 13.11a the spectrum of δf_- is shown without feedback control, that is, with the QCL in free-running mode: the linewidth is limited by the 1 MHz RBW of the spectrum analyser. The beat-note spectra when the feedback loop is closed are reported in Fig. 13.11b, 13.11c and 13.11d with RBWs from 100 kHz down to 1 Hz, the spectral resolution limit of the spectrum analyser. The sidebands of Fig. 13.11b indicate that the phase-lock bandwidth is 1.5 MHz, not limited by the electronic circuit. By numerically integrating the normalised beat-note spectrum from 1 Hz to 1.5 MHz from the centre frequency, it is found that >90% of the QCL power is effectively phase-locked.[27] In the next section it will be shown how this technique of phase-locking is equivalent to an optical sampling of the electric field emitted by the THz QCL using the pulses from an fs-laser.

13.3.2 Microwave modulation and active mode-locking of THz QCLs

Microwave modulation of THz QCLs

QCLs are unipolar semiconductor lasers based on electronic intersubband transitions in the conduction band of multi-layered heterostructures.[63] In contrast to interband diode lasers, where the lifetime of the electrons populating the upper laser state is determined by electron–hole recombination, the electron lifetime in QCLs is dominated by non-radiative phenomena, and in particular by optical-phonon scattering. This leads to fast relaxation times, on the picosecond (ps) timescale, which have an important impact on the dynamical properties of this family of devices.[64] From a 2-level system rate equation model, and neglecting the non-radiative lifetime of the lower state, the laser modulation response, proportional to the ratio between the variation of the output power and the modulated current amplitude, is given by the following expression:

$$\frac{SP}{SI} \propto \frac{1}{\left[\left(\omega^2 \frac{1}{\tau_s \tau_p}\right)^2 + \omega^2\left(\frac{1}{\tau_s} + \frac{1}{\tau_2}\right)^2\right]^{1/2}} \tag{13.6}$$

where ω is the modulation frequency, τ_2 is the upper-state non-radiative lifetime, and τ_p, τ_s are respectively the photon cavity lifetime and the stimulated lifetime. The latter is defined as $\tau_s = (\sigma S)^{-1}$, where σ is the optical cross-section, and S is the photon density. Equation [13.6] can be used to compare the normalised modulation response function of an interband diode laser with those of QCLs operating in the mid-IR and THz regions. The three curves are plotted in Fig. 13.12. They were computed using realistic values of τ_2, τ_p, and τ_s (Fig. 13.12). The change of non-radiative lifetime from ~ns to ~ps eliminates the relaxation oscillation resonance in QCLs. This results in a flat modulation response for both mid-IR and THz QCLs. The THz QCL has a wider modulation bandwidth ($f_{3\text{dB}}$ ~ 50 GHz) than the mid-IR QCL ($f_{3\text{dB}}$ ~ 25 GHz) because of (i) a slightly shorter τ_p due to higher total losses (see the caption of Fig. 13.12), and (ii) a *longer* upper-state lifetime of 5 ps, compared to 1 ps for the mid-IR laser.

The very large intrinsic modulation bandwidths shown in Fig. 13.12 can be exploited provided that the absorption length of the microwave modulation signal remains a significant fraction of the laser cavity length up to the modulation cut-off. In Fig. 13.13 the amplitude attenuation coefficient in dB/mm is reported as a function of the modulation frequency for an MM waveguide ridge.[66] This coefficient was derived by fitting the measured $(1 - |S_{11}|^2)$ curve using a transmission line model with distributed-parameters (see inset). As

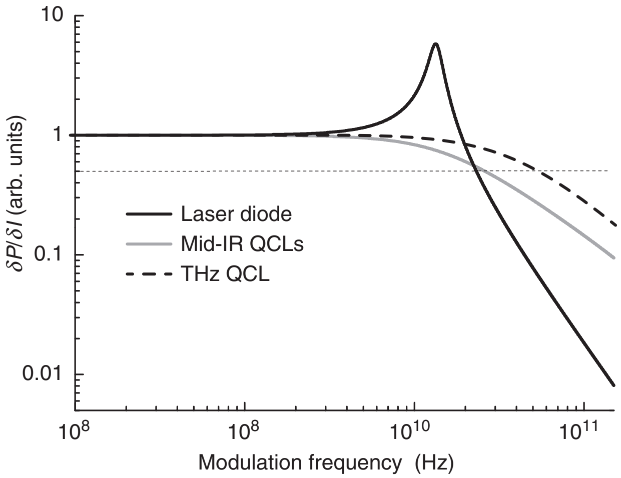

13.12 Normalised modulation response functions for a diode laser (black curve), a mid-IR QCL (grey curve), and a THz QCL (dashed curve), obtained from Equation [13.6]. The horizontal dashed line indicates the 3dB cut-off. For the diode laser and the mid-IR QCL we assumed an emitted power of 100 mW and 500 mW respectively. For the THz QCL we assumed an emitted power of 10 mW. We used a facet reflectivity of 0.3 for the diode laser and the mid-IR QCL, and of 0.9 for the THz QCL. The latter is the typical value for a MM waveguide QCL of width <50 mm and emission frequency below 3 THz see Section 13.2 and Reference 19. Cavity volumes of (5 × 0.25 × 200) μm^3, (8 × 4 × 1000) μm^3, and (50 × 12 × 3000) μm^3, and waveguide losses of 5 cm^{-1}, 5 cm^{-1}, and 20 cm^{-1}, were used for the diode laser, the mid-IR and the THz QCL respectively. Using a differential gain of 5×10^{-16} cm^2 for the diode laser,[65] and dipole matrix elements and spontaneous emission linewidths of 1.6 nm and 6 nm, and 10 meV and 1 meV, respectively for the mid-IR and THz QCLs, the above parameters give the following sets of values for τ_p, and τ_s: 2 ps, 70 ps (diode laser); 7 ps, 0.5 ps (mid-IR QCL); 5 ps, 0.5 ps (THz QCL). The values of the upper-state lifetimes are 3 ns (diode laser), 1 ps (mid-IR QCL), and 5 ps (THz QCL).

can be seen, the attenuation is below ~3.5 dB/mm up to 90 GHz, which, given the fact that typical ridge lengths are between ~1 mm and ~3 mm, allows access to the modulation bandwidths shown in Fig. 13.12. 35 GHz is so far the highest modulation frequency of a THz QCL experimentally demonstrated.[67] In the next section it will be shown how this excellent modulation potential can be used for RF-injection locking.

RF-injection locking of THz QCLs

The mechanism of RF-injection locking is schematically illustrated in Fig. 13.14.[67,68] By modulating the drive current of a laser at the RF frequency f_{RF}, sidebands (gray arrows) are generated on both sides of the laser Fabry–Pérot

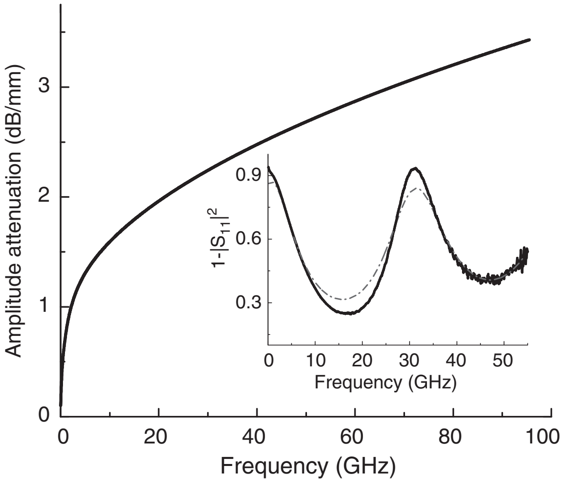

13.13 Microwave attenuation *vs* frequency for a 16 μm thick, 61 μm wide MM waveguide ridge. Inset, measured (black solid line) and simulated (gray dashed-dot line) ($1 - |S_{11}|^2$) curve plots in the 0.1–55 GHz range for a 1.06 mm long ridge, driven at a current density of 120 A cm^2 (see text) the figure is adapted from Reference 66.

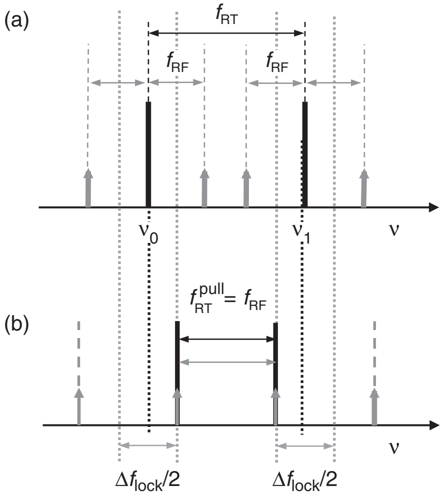

13.14 Schematic diagram describing the mechanism of RF-injection locking. The black lines represent two Fabry–Pérot mode frequencies n_0 and n_1, separated by the roundtrip frequency f_{RT}. The gray arrows represent the RF sidebands at +/– f_{RF} from the Fabry–Pérot mode frequencies. Note that the locking range in the optical (THz) domain (Δf_{lock}), indicated by the vertical dotted lines, is equal to half the locking range in the RF domain (see Reference 67). (a) f_{RF} is outside the locking range. (b) f_{RF} is inside the locking range and f_{RT} is injection locked. Note that inside the locking range, f_{RT} is pulled by f_{RF}, hence its value is changed to f_{RT}^{pull}.[67]

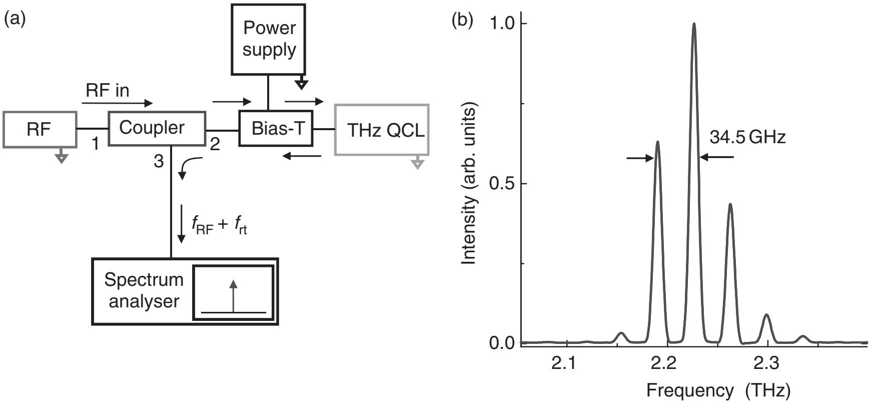

13.15 (a) Schematic of the measurement set-up for the RF-injection locking of MM waveguide THz QCLs (see text). (b) Representative THz emission spectrum of a 1.0 mm long and 70-μm-wide MM waveguide QCL. The FP modes are separated by approximately 34.5 GHz. The figure is adapted from Reference 67.

modes (black lines), separated by the roundtrip frequency f_{RT}. When f_{RF} is brought close enough to f_{RT}, the Fabry–Pérot modes are injection locked by the RF sidebands, meaning that their instantaneous phase is locked to that of the sidebands. For a given modulation depth (i.e., a given RF sideband intensity) a so-called *locking range* can be defined as the maximum separation between f_{RT} and f_{RF} below which f_{RT} gets injected by f_{RF}. The locking range is expected to scale proportionally to the square-root of the sideband intensity.[68]

The experimental demonstration of RF-injection locking of a 1 mm long, MM waveguide THz QCL emitting at 2.2 THz is shown in Fig. 13.15. The THz spectrum (see Fig. 13.15b) consists of six Fabry–Pérot modes, separated by a roundtrip frequency of ~34.5 GHz. The experimental set-up is shown in Fig. 13.15a: an RF-synthesiser is connected through a directional coupler to a bias-tee that allows amplitude modulation of the QCL, with the latter driven at constant current using a standard power supply. The RF + dc-bias signal is brought to the QCL via a 60 GHz, 50 Ω coplanar probe positioned at one end of the ridge, with the other end left open-ended. Close to ~34.5 GHz the power transmission coefficient is of 0.8 (see the inset of Fig. 13.13), therefore the RF signal from the synthesiser oscillating at f_{RF} is partially reflected and can be monitored using a spectrum analyser connected to port n.3 of the directional coupler. At the same time the spectrum analyser allows the roundtrip frequency of the QCL at f_{RT} to be monitored. This is thanks to the intrinsic non-linear voltage–current characteristic of the laser that rectifies the intracavity THz field. This generates a signal at the difference frequency between the Fabry–Pérot modes of the THz spectrum of Fig. 13.15b. The process of RF-injection is shown in Fig. 13.16a,b,c, and d. In Fig. 13.16a the RF-source is OFF and the peak associated to the

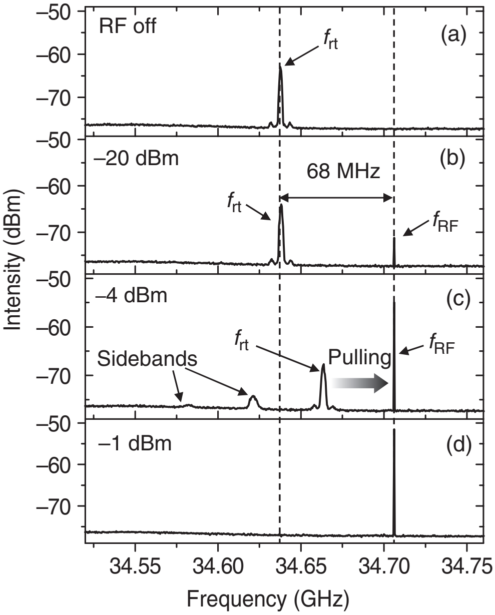

13.16 RF-injection locking of f_{RT} of a MM waveguide THz QCL (see Fig. 13.15 for the emission spectrum and the text for a detailed description). The spectra were collected using a RBW of 100 kHz, and a sweep time of 1 s on a 300 MHz span. The figure is adapted from Reference 67.

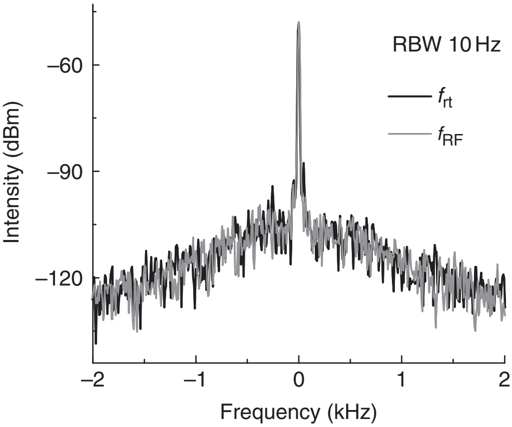

13.17 MM QCL. Spectra at 2 dBm RF power of the injection locked f_{RT} (black line), and of f_{RF} (gray line) measured with a RBW of 10 Hz, the spectral resolution limit of the spectrum analyser. Spectra were collected in RMS detection mode, with a 50 s sweep time.[67]

free-running beat-note is clearly visible at $f_{\mathrm{RT}} \sim 34.65$ GHz. In panels (b) to (d), the RF-source is switched ON at $f_{\mathrm{RF}} = f_{\mathrm{RT}} + 68$ MHz, with increasing power levels of −20, −4, and −1 dBm inside the device. At −4dBm f_{RT} is pulled towards f_{RF} and finally, at −1 dBm, it is injection locked. Locking ranges above 200 MHz were obtained with this device with −10 dBm of RF power.[67] The proof that f_{RT} is indeed injection locked by f_{RF} is reported in Fig. 13.17, showing that the two spectra, measured with a resolution bandwidth of 10 Hz, are perfectly superimposed.

Active mode-locking

When the roundtrip frequency of a diode laser is RF-injection locked to a synthesiser the phases of the longitudinal Fabry–Pérot modes are mutually locked to each other. In other words the laser is operating in a regime of active mode-locking, emitting a periodic train of pulses with a period equal to $1/f_{\mathrm{RT}}$. Pulse duration and shape are not known a priori, since they depend on each value of the mode phases. In the visible and near-IR spectral ranges the duration of mode-locked laser pulses is typically measured using second-order autocorrelation. Owing to the low peak powers this technique is not applicable to THz QCLs, therefore alternative probing methods need to be found. A successful technique is based on the asynchronous optical sampling (ASOPS) of the THz pulse train using an fs-laser beam.[28] ASOPS was developed during the 1980s in the context of pump-probe experiments, and is based on two fs-lasers having slightly different repetition rates. As a result the optical pulses from the probe laser periodically scan the transient phenomenon triggered by the pump laser, at a rate given by the difference between the repetition rates of the two lasers and without the need for a mechanical delay line.[69,70] In the THz range this technique is now routinely used for the sampling of the THz pulses obtained by focusing one fs-laser on a photomixer or a non-linear crystal.[71,72] In Reference 28 an ASOPS technique was used for the asynchronous sampling of an actively mode-locked QCL. The sampling method exploits the same detection set-up as shown schematically in Fig. 13.10a, where the QCL and a frequency-doubled mode-locked fs-fibre laser are simultaneously focused on a ZnTe electro-optical modulator. As explained in Section 3.1.3 the resulting photocurrent at the output of the balanced detection is proportional to the fs-laser pulse train modulated by the THz electric field, $E(t)$, emitted by the QCL:

$$I_p(t) \propto E(t) \sum_{n=-\infty}^{n=+\infty} \delta\left(t - \frac{n}{f_{\mathrm{rep}}^{fs}}\right), \tag{13.7}$$

where f_{rep}^{fs} is the repetition rate of the *fs*-laser. In this equation the *fs*-laser pulse train has been approximated by a series of δ-functions. This is a good

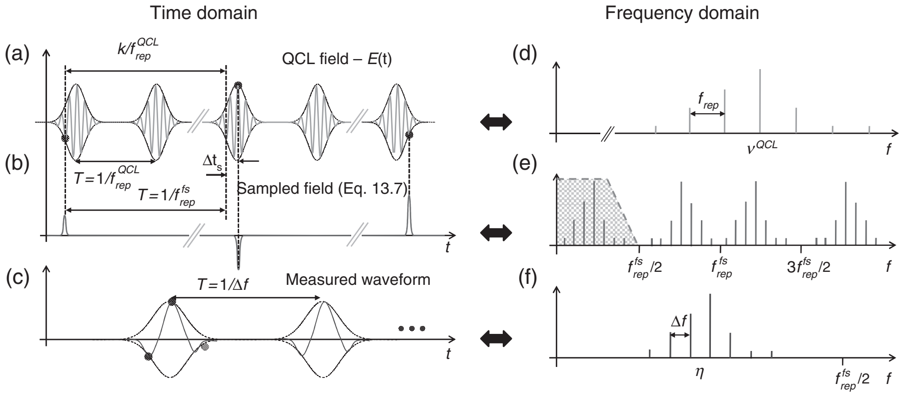

13.18 Schematic of the sampling process (see text for a detailed description). (Left) Time domain. (a) Electric-field amplitude of the pulse train emitted by the THz QCL. (b) Electric-field amplitude sampled by the fs-fibre laser. (c) Measured pulse train. Δt_s is the sampling step, given by $\Delta t_s = 1/f_{\text{rep}}^{fs} - k/f_{\text{rep}}^{\text{QCL}}$. (d–f) Frequency domain. Fourier transforms of the time traces (a–c). The shaded region in panel (e) represents the effect of low-pass filtering. The figure is adapted from Reference 28.

approximation, provided that the *fs*-laser pulse duration is shorter than the period of the THz wave. Since the pulse duration is of ~100 fs, this condition is satisfied for QCL frequencies smaller than ~5 THz, and the expression in Equation [13.7] can indeed be seen as a sampling of the THz field. Now, since the QCL repetition rate, $f_{\text{rep}}^{\text{QCL}}$,* is in the 10 GHz range while f_{rep}^{fs} is of the order of 100 MHz, the pulse train emitted by the mode-locked QCL is very heavily undersampled, therefore the sampling process does not reproduce the THz wave (the Nyquist sampling criterion is not satisfied). Actually, in complete analogy with Fig. 13.10b (see Fig. 13.18 and Reference 28 for a detailed derivation), it can be shown that the Fourier transform of Equation [13.2] is composed of down-converted replicas of the THz QCL spectrum, periodically repeated at integer multiples of f_{rep}^{fs}. Therefore, as shown in Fig. 13.18, a low-pass filter can be used to isolate to the lowest frequency replica of the THz spectrum. This is composed of the beat notes between the QCL Fabry–Pérot modes and their closest harmonics of f_{rep}^{fs}. In the time domain, the waveform related to this spectrum is composed of an envelope slowly varying at a repetition rate $\Delta f = f_{\text{rep}}^{\text{QCL}} - k \times f_{\text{rep}}^{fs}$, where k is an integer, and $k \times f_{\text{rep}}^{fs}$ is the harmonic of f_{rep}^{fs} closest to $f_{\text{rep}}^{\text{QCL}}$. The rapidly oscillating carrier frequency is instead given by $\eta = \nu^{\text{QCL}} - r \times f_{\text{rep}}^{fs}$, where ν^{QCL} is the frequency of one of the THz Fabry–Pérot modes, r is an integer, and $r \times f_{\text{rep}}^{fs}$ is the harmonic of

---

* Note that this is equivalent to f_{RT} used in the previous section.

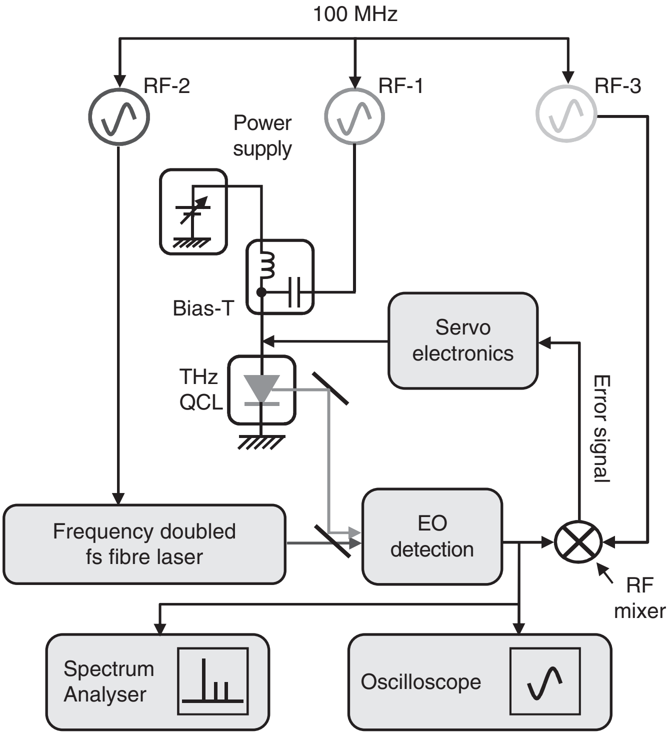
100 MHz
RF-2
RF-1
RF-3
Power supply
Bias-T
THz QCL
Servo electronics
Error signal
Frequency doubled fs fibre laser
EO detection
RF mixer
Spectrum Analyser
Oscilloscope

13.19 Experimental set-up for the asynchronous sampling of a THz QCL using a fs-fibre laser (see text).[28]

f_{rep}^{fs} closest to ν^{QCL}. Now, although the RF waveform is not an exact replica of the THz pulse train (the ratios $\nu^{\mathrm{QCL}}/f_{\mathrm{rep}}^{\mathrm{QCL}}$ and $n/\Delta f$ are not necessarily equal), nonetheless its coherence is identical to that of the original THz pulse train since the phases of the THz Fabry–Pérot modes are preserved in the down-conversion process. Despite the undersampling, the ASOPS technique allows therefore assessing the coherence properties of the THz waveform, that is, to verify whether or not the QCL is mode-locking (see below).

When using two fs-lasers, a key requirement of ASOPS is that the repetition rates of the two lasers must be phase-locked to each other, otherwise the intrinsic timing jitter between the two pulse trains cancels out the sampled trace.[72] Exploiting ASOPS to sample the pulses emitted by a mode-locked QCL imposes an additional requirement. Indeed in this case both the repetition rate *and* the THz carrier frequency of the QCL must be phase-locked to the repetition rate of the fs-laser used for the optical sampling. This is a consequence of the fact that in a mode-locked laser the frequencies of the Fabry–Pérot modes are not integer multiples of the repetition rate, hence stabilising the repetition rate does not automatically stabilises the carrier frequency.[73,†]

The ASOPS set-up used in Reference 28 is schematically reported in Fig. 13.19 and relies on three locked RF-synthesisers (RF-1, RF-2, and RF-3) synchronised on a common 10 MHz clock. Each synthesiser is used as a reference for a phase-lock loop controlling (i) $f_{\text{rep}}^{\text{QCL}}$, (ii), f_{rep}^{fs}, and (iii) one line of the QCL spectrum (defined as the carrier frequency). $f_{\text{rep}}^{\text{QCL}}$ is phase-locked to RF-1 by using the RF-injection locking technique described in Section 3.2.2. f_{rep}^{fs} is phase-locked to RF-2 by controlling the fs-laser cavity length through a piezoelectric transducer placed on one cavity mirror. Finally, the difference between one Fabry–Pérot mode of the QCL spectrum and its closest harmonic of f_{rep}^{fs} is phase-locked to RF-3 using the phase-locking technique described in Section 13.3.1.

In Fig. 13.20 the THz QCL spectrum collected with a Fourier Transform Infrared Spectrometer is shown together with the down-converted spectrum using the ASOPS set-up of Fig. 13.19, with all the loops closed. The RF beat notes are all extremely narrow (the linewidth is actually below 1 Hz, see Reference 28), showing that they are indeed all phase-locked to f_{rep}^{fs}. In other words the THz QCL is fully coherent with the fs-laser repetition rate. Three periods of the corresponding sampled RF waveform are shown in Fig. 13.21. As expected it shows a pulse train with a repetition rate $\Delta f = f_{\text{rep}}^{\text{QCL}} - k \times f_{\text{rep}}^{fs}$. In the experiment $f_{\text{rep}}^{\text{QCL}} = 1331589$ GHz, $k = 138$, and $f_{\text{rep}}^{fs} = 96513$ MHz, thus $\Delta f = 2.9$ MHz.

As explained above, the RF waveform of Fig. 13.21 contains all phases (the amplitudes are those of Fig. 13.20 of the original Fabry–Pérot modes. To retrieve the phases, one possibility is to Fourier transform the RF waveform.[74] Alternatively, one can make an ansatz on the values of the phases and, from the measured mode-amplitudes and frequencies of Fig. 13.20, reconstruct the sampled waveform and compare it to the measured one. This leads to the gray curve in Fig. 13.21, where it was assumed that the phases of the modes are equal, that is, that the phase dispersion is negligible. The agreement between the measured and computed waveform is good, showing that the QCL is indeed active mode-locking and emitting a train of transform limited pulses.

13.3.3 Perspectives

THz QCLs are the most powerful and compact semiconductor sources of coherent, narrow-linewidth radiation that are available today. While they

---

[†] Note that in THz time domain spectroscopy systems based on ASOPS, the frequencies of the THz comb generated by optical or electrical rectification of one fs-laser beam are exact multiples of the repetition rate.

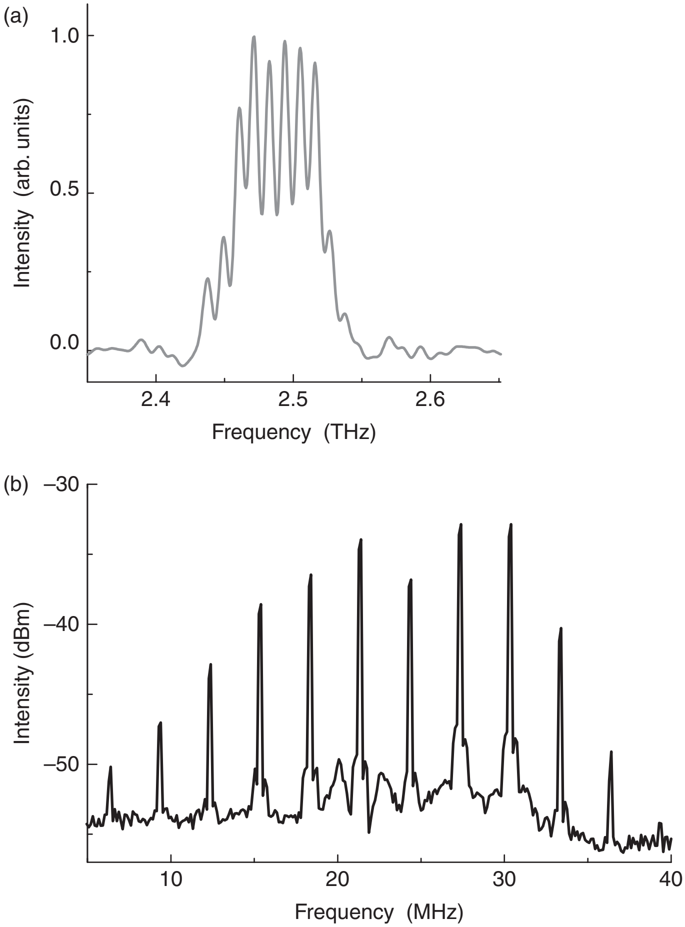

13.20 (a) THz QCL emission spectrum collected with a Fourier transform infrared spectrometer. The QCL is RF-injection locked with 10 dBm of RF power at $f_{\mathrm{RF1}} = f_{\mathrm{rep}}^{\mathrm{QCL}} = 13.3121794$ GHz. (b) Down-converted spectrum using the ASOPS set-up of Fig. 13.19, with all the loops closed. The spectrum was recorded with an RBW of 100 kHz, and a sweep time of 5.5 ms. The RF beat notes linewidths are all below 1 Hz (see Reference 28).

have inherent similarities with the conventional interband semiconductor lasers that operate at near-infrared frequencies, the much longer wavelength of operation for THz QCLs leads to unique challenges (i) in the design of waveguides for accurate tuning of their spectral and modal properties, and (ii) for the control of their frequency stability and of their linewidth characteristics. In a way, techniques for spectral, modal, and linewidth control that have been conventionally utilised for interband diode lasers had to be

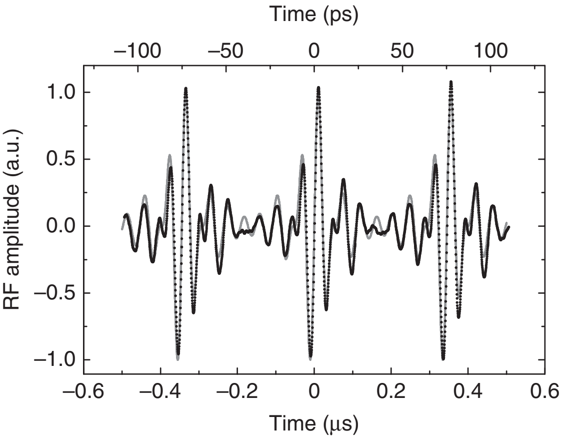

13.21 Three periods of the measured (dots) and calculated waveform (gray line), obtained assuming that all the modes of Fig. 13.15 have equal phases. The bottom axis shows the timescale measured on the oscilloscope. The top axis shows the original timescale obtained by rescaling the measured timescale by the factor $\Delta f / f_{\mathrm{rep}}^{\mathrm{QCL}}$. The sampling step is $\Delta ts = 2.3$ ps, corresponding to approximately six optical cycles at 2.5 THz.[28]

reinvented for THz QCLs owing to their longer wavelength and peculiar intersubband gain characteristics. The first part of this chapter has provided a detailed overview of both spectral and modal properties of THz QCLs, and on how these can be controlled through waveguide engineering. The second part was instead dedicated to an overview of the techniques used for their frequency and linewidth control and stability, as well as high speed modulation and active mode-locking operation.

The main conclusion from Section 13.2 is that parallel-plate MM cavities are ideal for mode confinement and waveguiding in THz QCLs, owing to their low optical loss and near unity mode concentration. However, such microcavities are of sub-wavelength dimensions when compared to the guided THz electromagnetic wave, which makes it easy to excite multiple lasing modes in the cavity. Additionally, it is difficult to increase the radiative loss in such cavities in order to increase the output power. At the same time the emitted radiation is highly divergent, producing a poor beam pattern. Significant progress has now been made in addressing all these challenges. In particular, incorporation of unconventional periodic photonic structures in the waveguides has led to THz QCLs operating in single-mode with emission in a narrow beam, which is typically a requirement for targeted application in high-resolution spectroscopy and sensing. The ongoing work is now directed towards realising QCLs with higher output power (in the hundred milliwatt range) for applications in video-rate THz imaging.

The main conclusion that can be drawn from Section 13.3 is that THz QCLs are ideal sources to be combined with fs-laser and microwave technologies. In fact, several characteristics of these devices are suitable for this merging: first of all, their (i) frequency of operation (see Fig. 13.10b) and also (ii) their narrow free-running linewidth, (iii) the fact that they are electrically pumped sources, (iv) their waveguide geometry and doping density, allowing for relatively low microwave attenuation, (v) their intrinsically high modulation bandwidths and their low parasitic capacitance.[66] As a consequence it is reasonable to expect that the results obtained today using microwave modulation and fs-lasers are the prologue to further developments, which will broaden the potentialities of THz QCLs for applications such as gas sensing, high-precision spectroscopy, metrology and imaging. For instance, the microwave modulation bandwidth can certainly be improved by introducing on-chip integrated impedance adaptations.[75] This will be beneficial for active mode-locking operation, since it will increase the amount of microwave power injected in the device, and possibly enable harmonic mode-locking. Among the most interesting potential applications of mode-locked THz QCLs is the generation of broad frequency combs for frequency metrology and spectroscopy of gases and solids. For these applications the actual spectral bandwidth of ~100 GHz (see Fig. 13.20a) should be broadened by at least a factor of 10. To this end, increasing the microwave modulation depth is certainly beneficial. At the same time, more fundamental work on the design of the active region in order to broaden the gain bandwidth must be undertaken.[76] Another route to explore for short pulse generation (i.e., broadband operation) is passive mode-locking through the use of an intersubband saturable absorber. To this end the ASOPS technique described in Section 3.2.3 would represent an extremely powerful pulse characterisation tool. Finally it is worth noting that the fs-laser based phase-locking technique described in Section 3.1.3, could potentially be used for electronic beam steering through the simultaneous phase-lock of several independent QCLs. In this case the fs-laser would be exploited as a common local oscillator, with its beam delivered to the various QCL sources via fibre-links. In this context, it is certainly worth investigating detection techniques/materials alternative to ZnTe-electro-optic sampling[77,78] that could improve the signal-to-noise and also allow detection directly at 1550 nm, rather than 800 nm.

13.4 References

1. D. L. Woolard, E. R. Brown, M. Pepper, and M. Kemp, 'Terahertz frequency sensing and imaging: a time of reckoning future applications?', *Proc. IEEE* **93**, 1722 (2005).
2. P. H. Siegel, 'Terahertz technology,' *IEEE Trans. Microwave Theory Tech.* **50**, 910–928 (2002).

3. W. L. Chan, J. Diebel, and D. M. Mittleman, 'Imaging with terahertz radiation', *Rep. Prog. Phys*. **70**, 1325–1379 (2007).
4. P. H. Siegel, 'Terahertz technology in biology and medicine', *IEEE Trans. Microwave Theory Tech*. **52**, 2438 (2004).
5. R. A. Cheville, M. R. Reiten, R. McGowan, and D. R. Grischkowsky, 'Applications of optically generated terahertz pulses to time domain ranging and scattering', in *Sensing with Terahertz Radiation*, D. Mittleman, ed. (Springer, Berlin, Germany, 2003), pp. 237–293.
6. Z. Jiang and X.-C. Zhang, 'Free-space electro-optic techniques', in *Sensing with Terahertz Radiation*, D. Mittleman, ed. (Springer, Berlin, Germany, 2003), pp. 155–192.
7. K. Kawase, M. Sato, T. Taniuchi, and H. Ito, 'Coherent tunable THz wave generation from LiNbO3 with monolithic grating coupler', *Appl. Phys. Lett*. **68**, 2483 (1996).
8. W. Shi, Y. J. Ding, N. Fernelius, and K. Vodopyanov, 'Efficient, tunable, and coherent 0.18 – 5.27 THz source based on GaSe crystal', *Optics Lett*. **27**, 1454 (2002).
9. B. Ferguson and X.-C. Zhang, 'Materials for terahertz science and technology', *Nat. Mater.* **1**, 26–33 (2006).
10. M. Tonouchi, 'Cutting-edge terahertz technology', *Nat. Photon.* **1**, 97–105 (2007).
11. R. Kohler, A. Tredicucci, F. Beltram, H. E. Beere, E. H. Linfield, A. G. Davies, D. A. Ritchie, R. C. Iotti, and F. Rossi, 'Terahertz semiconductor-heterostructure laser', *Nature* **417**, 156–159 (2002).
12. L. Ajili, G. Scalari, N. Hoyler, M. Giovannini, and J. Faist, 'InGaAsAlInAs/InP terahertz quantum cascade laser', *Appl. Phys. Lett*. **87**, 141107 (2005).
13. C. Deutsch, A. Benz, H. Detz, P. Klang, M. Nobile, A. M. Andrews, W. Schrenk, T. Kubis, P. Vogl, G. Strasser, and K. Unterrainer, 'Terahertz quantum cascade lasers based on type II InGaAs/GaAsSb/InP', *Appl. Phys. Lett*. **97**, 261110 (2010).
14. B. S. Williams, 'Terahertz quantum-cascade lasers', *Nat. Photon.* **1**, 517–525 (2007).
15. G. Scalari, C. Walther, M. Fischer, R. Terazzi, H. Beere, D. Ritchie, and J. Faist, 'THz and sub-THz quantum cascade lasers', *Laser Photon. Rev*. **3**, 45–66 (2009).
16. S. Barbieri, J. Alton, H. E. Beere, J. Fowler, E. H. Linfield, and D. A. Ritchie, '2.9 THz quantum cascade lasers operating up to 70 K in continuous wave', *Appl. Phys. Lett*. **85**, 1674 (2004).
17. B. S. Williams, S. Kumar, H. Callebaut, Q. Hu, and J. L. Reno, 'Terahertz quantum-cascade laser at $\lambda \approx 100$ μm using metal waveguide for mode confinement', *Appl. Phys. Lett*. **83**, 2124 (2003).
18. S. Fathololoumi, E. Dupont, C. W. I. Chan, Z. R. Wasilewski, S. R. Laframboise, D. Ban, Mátyás, C. Jirauschek, Q. Hu, and H. C. Liu, 'Terahertz quantum cascade lasers operating up to ~ 200 K with optimised oscillator strength and improved injection tunneling', *Opt. Exp.* **20**, 3866 (2012).
19. B. S. Williams, S. Kumar, Q. Hu, and J. L. Reno, 'Operation of terahertz quantum-cascade lasers at 164 K in pulsed mode and at 117 K in continuous-wave mode', *Opt. Exp.* **13**, 3331 (2005).
20. S. Kumar, B. S. Williams, Q. Qin, A. W. M. Lee, Q. Hu, and J. L. Reno, 'Surface-emitting dis- tributed feedback terahertz quantum-cascade lasers in metal-metal waveguides', *Opt. Express* **15**, 113 (2007).
21. Y. Chassagneux, R. Colombelli, W. Maineult, S. Barbieri, H. E. Beere, D. A. Ritchie, S. P. Khanna, E. H. Linfield, and A. G. Davies, 'Electrically pumped

photonic-crystal terahertz lasers controlled by boundary conditions', *Nature* **457**, 174 (2009).

22. L. Mahler, A. Tredicucci, F. Beltram, C. Walther, J. Faist, B. Witzigmann, H. E. Beere, and D. A. Ritchie, 'Vertically emitting microdisk lasers', *Nat. Photon.* **3**, 46 (2009).
23. M. I. Amanti, M. Fischer, G. Scalari, M. Beck, and J. Faist, 'Low-divergence single-mode terahertz quantum cascade laser', *Nat. Photon.* **3**, 586–590 (2009).
24. N. Yu, Q. J. Wang, M. A. Kats, J. A. Fan, S. P. Khanna, L. Li, A. G. Davies, E. H. Linfield, and F. Capasso, 'Designer spoof surface plasmon structures collimate terahertz laser beams', *Nat. Mater.* **9**, 730 (2010).
25. Q. Qin, J. L. Reno, and Q. Hu, 'MEMS-based tunable terahertz wire-laser over 330GHz', *Opt. Lett*. **36**, 692 (2011).
26. J. Kroll, J. Darmo, S. S. Dhillon, X. Marcadet, M. Calligaro, C. Sirtori, and K. Unterrainer, 'Phase-resolved measurements of stimulated emission in a laser', *Nature* **449**, 698 (2007).
27. S. Barbieri, P. Gellie, G. Santarelli, L. Ding, W. Maineult, C. Sirtori, R. Colombelli, H. Beere, and D. Ritchie, 'Phase-locking of a 2.7-thz quantum cascade laser to a mode-locked erbium-doped fibre laser', *Nat. Photon.* **4**, 636 (2010).
28. S. Barbieri, M. Ravaro, P. Gellie, G. Santarelli, C. Manquest, C. Sirtori, S. P. Khanna, E. H. Linfield, and A. G. Davies, 'Coherent sampling of active mode-locked terahertz quantum cascade lasers and frequency synthesis', *Nat. Photon.* **5**, 306 (2011).
29. A. Lee, Q. Qin, S. Kumar, B. S. Williams, Q. Hu, and J. L. Reno, 'Real-time terahertz imaging over a standoff distance (> 25 m)', *Appl. Phys. Lett*. **89**, 141125 (2006).
30. Y. Ren, J. N. Hovenier, R. Higgins, J. R. Gao, T. M. Klapwijk, S. C. Shi, B. Klein, T.-Y. Kao, Q. Hu, and J. L. Reno, 'High-resolution heterodyne spectroscopy using a tunable quantum cascade laser around 3.5 THz', *Appl. Phys. Lett*. **98**, 231109 (2011).
31. 'Optical properties of pure metals and binary alloys', in *Landolt-Bernstein*, vol. **III/15b** of New Series, K.-H. Hellwege and O. Madelung, eds. (Springer-Verlag, Berlin, Germany, 1985), chapter 4, pp. 210–222.
32. FEMLAB 3.1, a finite-element based partial differential equation software solver from COMSOL, Inc. (http://www.comsol.com).
33. S. Kohen, B. S. Williams, and Q. Hu, 'Electromagnetic modeling of terahertz quantum cascade laser waveguides and resonators', *J. Appl. Phys*. **97**, 053106 (2005).
34. B. S. Williams, S. Kumar, Q. Hu, and J. L. Reno, 'High-power terahertz quantum-cascade lasers', *Electron. Lett*. **42**, 89 (2006).
35. S. Kumar, Q. Hu, and J. L. Reno, '186 K operation of terahertz quantum-cascade lasers based on a diagonal design', *Appl. Phys. Lett*. **94**, 131105 (2009).
36. S. Kumar, C. W. I. Chan, Q. Hu, and J. L. Reno, 'A 1.8 THz quantum-cascade laser operating significantly above the temperature of ω/kB', *Nat. Phys.* **7**, 166 (2011).
37. Y. Chassagneux, J. Palomo, R. Colombelli, S. Dhillon, C. Sirtori, H. Beere, J. Alton, and D. Ritchie, 'Terahertz microcavity lasers with subwavelength mode volumes and thresholds in the milliampere range', *Appl. Phys. Lett*. **90**, 091113 (2007).

38. L. A. Dunbar, R. Houdŕ, G. Scalari, L. Sirigu, M. Giovannini, and J. Faist, 'Small optical volume terahertz emitting microdisk quantum cascade lasers', *Appl. Phys. Lett.* **90**, 141114 (2007).
39. C. Walther, G. Scalari, M. I. Amanti, M. Beck, and J. Faist, 'Microcavity laser oscillating in a circuit-based resonator', *Science* **327**, 1495 (2010).
40. A. J. L. Adam, I. Kasalynas, J. N. Hovenier, T. O. Klaassen, J. R. Gao, E. E. Orlova, B. S. Williams, S. Kumar, Q. Hu, and J. L. Reno, 'Beam patterns of terahertz quantum cascade lasers with subwavelength cavity dimensions', *Appl. Phys. Lett.* **88**, 151105 (2006).
41. S. Kumar, 'Recent progress in terahertz quantum cascade lasers', *IEEE J. Sel. Topics Quantum Electron.* **17**, 38 (2011).
42. M. I. Amanti, G. Scalari, F. Castellano, M. Beck, and J. Faist, 'Low divergence terahertz photonic-wire laser', *Opt. Express* **18**, 6390 (2010).
43. Y. Chassagneux, R. Colombelli, W. Maineult, S. Barbieri, S. P. Khanna, E. H. Linfield, and G. Davies, 'Graded photonic crystal terahertz quantum cascade lasers', *Appl. Phys. Lett.* **96**, 031104 (2010).
44. O. Demichel, L. Mahler, T. Losco, C. Mauro, R. Green, A. Tredicucci, J. Xu, F. Beltram, H. E. Beere, D. A. Ritchie, and V. Tamodinuas, 'Surface plasmon photonic structures in terahertz quantum cascade lasers', *Opt. Express* **14**, 5335 (2006).
45. J. A. Fan, M. A. Belkin, F. Capasso, S. Khanna, M. Lachab, A. G. Davies, and E. H. Linfield, 'Surface emitting terahertz quantum cascade laser with a double-metal waveguide', *Opt. Exp.* **14**, 11672 (2007).
46. E. Mujagic, C. Deutsch, H. Detz, P. Klang, M. Nobile, A. M. Andrews, W. Schrenk, K. Unterrainer, and G. Strasser, 'Vertically emitting terahertz quantum cascade ring lasers', *Appl. Phys. Lett.* **95**, 011120 (2009).
47. S. Bartalini, S. Borri, P. Cancio, A. Castrillo, I. Galli, G. Giusfredi, D. Mazzotti, L. Gianfrani, and P. De Natale, 'Observing the intrinsic linewidth of a quantum-cascade laser: beyond the Schawlow-Townes limit', *Phys. Rev. Lett.* **104**, 083904 (2010).
48. J. von Staden, T. Gensty, W. Elsäßer, G. Giuliani, and C. Mann, 'Measurements of the α-factor of a distributed-feedback quantum cascade laser by an optical feedback self-mixing technique', *Opt. Lett.* **31**, 2574 (2006).
49. T. Aellen, R. Maulini, R. Terazzi, N. Hoyler, M. Giovannini, J. Faist, S. Blaser, and L. Hvozdara, 'Direct measurement of the linewidth enhancement factor by optical heterodyning of an amplitude-modulated quantum cascade laser', *Appl. Phys. Lett.* **89**, 091121 (2006)
50. N. Kumazaki, Y. Takagi, M. Ishihara, K. Kasahara, A. Sugiyama, N. Akikusa, and T. Edamura, 'Detuning characteristics of the linewidth enhancement factor of a midinfrared quantum cascade laser', *Appl. Phys. Lett.* **92**, 121104 (2008).
51. R. P. Green, J. Xu, L. Mahler, A. Tredicucci, F. Beltram, G. Giuliani, H. E. Beere, and D. A. Ritchie, 'Linewidth enhancement factor of terahertz quantum cascade lasers', *Appl. Phys. Lett.* **92**, 071106 (2008).
52. A. Barkan, F. K. Tittel, D. M. Mittleman, R. Dengler, P. H. Siegel, G. Scalari, L. Ajili, F. Faist, H. E. Beere, E. H. Linfield, D. A. Ritchie, and A. G. Davies, 'Linewidth and tuning characteristics of terahertz quantum cascade lasers', *Opt. Lett.* **29**, 575 (2004).

53. S. Barbieri, J. Alton, H. E. Beere, E. H. Linfield, S. Withington, D. A. Ritchie, A. Lassaad, G. Scalari, and J. Faist, 'Difference frequency mixing of two far-infrared quantum cascade lasers using a point-contact Schottky diode', *Opt. Lett.* **29**, 1632 (2004).
54. H.-W. Hübers, S. G. Pavlov, H. Richter, A. D. Semenov, L. Mahler, A. Tredicucci, H. E. Beere, and D. A. Ritchie, 'High-resolution gas phase spectroscopy with a distributed feedback terahertz quantum cascade laser', *Appl. Phys. Lett.* **89**, 061115 (2006)
55. H. Richter, A. D. Semenov, S. G. Pavlov, L. Mahler, A. Tredicucci, H. E. Beere, D. A. Ritchie, K. S. Il'in, M. Siegel, and H.-W. Hübers, 'Terahertz heterodyne receiver with quantum cascade laser and hot electron bolometer mixer in a pulse tube cooler', *Appl. Phys. Lett.* **93**, 141108 (2008)
56. M. Hajenius, P. Khosropanah, J.N. Hovenier, J.R. Gao, T.M. Klapwijk, S. Barbieri, S. Dhillon, P. Filloux, C. Sirtori, D.A. Ritchie, and H.E. Beere, 'Surface plasmon quantum cascade lasers as terahertz local oscillators', *Opt. Lett.*, **33**, 312 (2008).
57. F. Riehle, *Frequency Standards. Basic and Applications* (Wiley-vch Verlag GmbH & Co. KGaA, Weinheim, 2004).
58. A. L. Betz, R. T. Boreiko, B. S. Williams, S. Kumar, Q. Hu, and J. L. Reno, 'Frequency and phase-lock control of a 3 THz quantum cascade laser', *Opt. Lett.*, **30**, 1837 (2005).
59. H. Richter, S. G. Pavlov, A. D. Semenov, L. Mahler, A. Tredicucci, H. E. Beere, D. A. Ritchie, and H.-W. Hübers, 'Submegahertz frequency stabilization of a terahertz quantum cascade laser to a molecular absorption line', *Appl. Phys. Lett.* **96**, 071112 (2010).
60. D. Rabanus, U. U. Graf, M. Philipp, O. Ricken, J. Stutzki, B. Vowinkel, M.C. Wiedner, C. Walther, M. Fischer, and J. Faist, 'Phase locking of a 1.5THz quantum cascade laser and use as a local oscillator in a heterodyne HEB receiver', *Opt. Expr.* **17**, 1159 (2009).
61. P. Khosropanah P. Khosropanah, A. Baryshev, W. Zhang, W. Jellema, J. N. Hovenier, J. R. Gao, T. M. Klapwijk, D. G. Paveliev, B. S. Williams, S. Kumar, Q. Hu, J. L. Reno, B. Klein, and J. L. Hesler, 'Phase Locking of a 2.7THz quantum cascade laser to a microwave reference', *Opt. Lett.* **34**, 2958 (2009).
62. A. Amy-Klein, A. Goncharov, M. Guinet, C. Daussy, O. Lopez, A. Shelkovnikov, and C. Chardonnet, 'Absolute frequency measurement of a SF6 two-photon line by use of a femtosecond optical comb and sum-frequency generation', *Opt. Lett.* **30**, 3320 (2005).
63. R. Paiella, *Intersubband Transitions in Quantum Structures* (McGraw Hill Nanoscience and Technology, 2006).
64. R. Paiella, R. Martini, F. Capasso, C. Gmachl, H. Y. Hwang, D. L. Sivco, J. N. Ballargeon, A. Y. Cho, E. A. Whyttaker, and H. C. Liu, 'High-frequency modulation without the relaxation oscillation resonance in quantum cascade lasers', *Appl. Phys. Lett.* **79**, 2526 (2001).
65. L. A. Coldren and S. W. Corzine, *Diode Lasers and Photonic Integrated Circuits* (Wiley series in microwave and optical engineering, New York, 1995).
66. W. Maineult, L. Ding, P. Gellie, P. Filloux, C. Sirtori, S. Barbieri, J–F. Lampin, T. Akalin, I. Sagnes, H. E. Beere, and D. A. Ritchie, 'Microwave modulation of terahertz quantum cascade lasers: a transmission-line approach', *Appl. Phys. Lett.* **96**, 021108 (2010).

67. P. Gellie, S. Barbieri, J-F. Lampin, P. Filloux, C. Manquest, C. Sirtori, I. Sagnes, S. P. Khanna, E. H. Linfield, A. G. Davies, H. Beere, and D. Ritchie, 'Injection–locking of terahertz quantum cascade lasers up to 35GHz using RF amplitude modulation', *Opt. Expr*. **18**, 20799 (2010).
68. A.E. Siegman, *Lasers* (University Science Books, Mill Valley, 1986).
69. P. A. Elzinga, F. E. Lytle, Y. Jian, G. B. King, and N. M. Laurendauet, 'Pump/probe method for fast analysis of visible spectral signatures utilizing asynchronous optical sampling', *Appl. Opt*. **26**, 4303 (1987).
70. S. Adachi, S. Takeyama, and Y. Tagaki, 'Dual wavelength optical sampling technique for ultrafast transient bleaching spectroscopy', *Opt. Commun*. **117**, 71 (1995).
71. T. Yasui, E. Saneyoshi, and T. Araki, 'Asynchronous optical sampling terahertz time-domain spectroscopy for ultrahigh spectral resolution and rapid data acquisition', *Appl. Phys. Lett*. **87**, 061101 (2005).
72. R. Gebs, G. Klatt, C. Janke, T. Dekorsy, and A. Bartels, 'High-speed asynchronous optical sampling with sub-50 fs time resolution', *Opt. Exp.* **18**, 5974 (2010).
73. D. J. Jones, S. A. Diddams, J. K. Ranka, A. Stentz, R. S. Windeler, J. L. Hall, and S. T. Cundiff, 'Carrier-envelope phase control of femtosecond mode-locked lasers and direct optical frequency synthesis', *Science* **288**, 635 (2000).
74. M. Ravaro, P. Gellie, G. Santarelli, C. Manquest, P. Filloux, C. Sirtori, J-F. Lampin, G. Ferrari, S. P. Khanna, E. H. Linfield, H.E. Beere, D.A. Ritchie, and S. Barbieri, 'Stabilization and mode-locking of terahertz quantum cascade lasers', submitted to *J. Sel. Top. Quantum. Eletron.* (April 2012).
75. P. D. Grant, R. Dudek, M. Buchanan, L. Wolfson, and H. C. Liu, 'An ultra fast quantum well infrared photodetector', *Infr. Phys. Technol*. **47**, 144 (2005).
76. G. Scalari, M. I. Amanti, C. Walther, R. Terazzi, M. Beck, and J. Faist, 'Broadband THz lasing from a photon-phonon quantum cascade structure', *Opt. Expr*. **18**, 8043 (2010).
77. Yokoyama, R. Nakamura, M. Nose, T. Araki, and T. Yasuil, 'Terahertz spectrum analyzer based on a terahertz frequency comb', *Opt. Expr*. **16**, 13052 (2008).
78. M. Ravaro, C. Manquest, C. Sirtori, S. Barbieri, G. Santarelli, K. Blary, J.-F. Lampin, S. P. Khanna, and E. H. Linfield, 'Phase-locking of a 2.5 THz quantum cascade laser to a frequency comb using a GaAs photomixer', *Opt. Lett*. **36**, 3969 (2011).

14

Whispering gallery mode lasers

A. MONAKHOV and N. SABLINA, Ioffe Institute, Russia

DOI: 10.1533/9780857096401.3.551

Abstract: This chapter is devoted to lasers operating on whispering gallery modes (WGM). The definition and specific features of these modes are discussed. Some examples of WGM lasers and their applications are presented.

Key words: semiconductor lasers, whispering gallery modes.

14.1 Introduction to whispering gallery modes (WGM)

Almost all reviews on WGM, and many papers on this subject, start with the story about St. Paul's Cathedral and Lord Rayleigh. We shall not break with that tradition. The whispering gallery effect has been well-known in acoustics for many years. There are also many writings describing similar acoustic effects. In China there is the so-called Echo Wall in the Temple of Heaven. It seems from this construction that the whispering gallery effect was being used deliberately in the fifteenth century. When two persons are standing near this round wall, each can clearly hear the other, even when whispering, but if one of them moves a few steps toward the center, the effect disappears. Systematic experimental study of this effect was carried out by a group of the British physicists, and in 1910 Rayleigh finally explained this effect theoretically (Rayleigh, 1910).

Acoustic waves are a good example of a WGM. Let us consider a cylindrical resonator. The wave propagation in the resonator is described by the Helmholtz equation:

$$\Delta F + \frac{\omega^2}{c^2} F = 0$$

$$F\big|_{\partial\Omega} = 0$$

For the sake of simplicity we put zero boundary conditions on the borders of the resonator. Because of the separation of variables in the cylindrical coordinate system the solution can be easily obtained:

$$F = F_0 J_m(æ r)\sin(m\phi + \psi_m)\cos(kz)e^{\pm i\omega t}, \qquad [14.1]$$

where ϕ is the polar angle, $k = \frac{\pi n}{\hbar}$, $n = 0,1,2\ldots$, $æ = \frac{\alpha_{mp}}{R}$, $\omega^2 = c^2(æ^2 + k^2)$, R is the radius of the resonator, h is the height and α_{mp} is the p^{th} root of the equation

$$J_m(\alpha_{\text{mp}}) = 0 \tag{14.2}$$

Solution [14.1] is the whole set of eigenmodes of a cylindrical resonator, and the question is which of them can be called WGM. Let us consider the case when the radius of a resonator R (but not the height h) is much larger than the wavelength λ. In this case, α_{mp} in Equation [14.2] should be large, because for $k = 0$ in Equation [14.1] $\omega = cæ$ and $æR = \alpha_{\text{mp}}$, so:

$$\alpha_{\text{mp}} = \frac{2\pi R}{\lambda} >> 1. \tag{14.3}$$

This inequality can be satisfied when $p >> 1$, but it is a common mode of a cylindrical resonator that fills the whole interior.

A more interesting mode corresponds to small p (say, $p = 1$), but with $m >> 1$. Then we find that the corresponding mode is located near the resonator's wall and this is the so-called WGM mode in a cylindrical resonator. It should be mentioned that in the same resonator there exist the usual modes with the close wavelengths corresponding to sufficiently large m and p and there is no strict border between WGM and non-WGM, so what one calls WGM is a matter of a definition. In Fig. 14.1 the Bessel function for $m = 600$ is shown. This function represents the radial WGM distribution.

The simplest way to define WGM, in a cylindrical resonator with the zero boundary condition on its walls, is to say that WGM is a mode corresponding to a large m and small $p \sim 1$ in Equation [14.2], but this definition

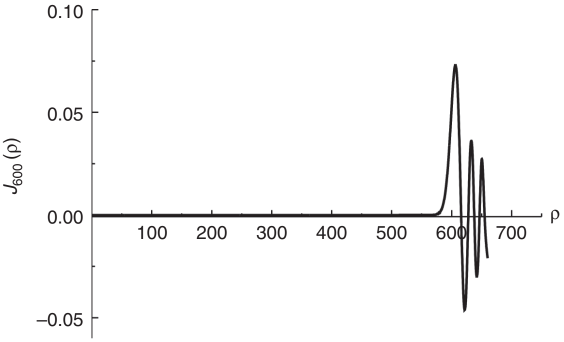

14.1 Bessel function for index $m = 600$.

can hardly be generalized for differently shaped resonators and different boundary conditions.

The ray optics approach allows one to make a more general definition of WGM. Indeed, Equation [14.3] shows that the necessary criterion for the applicability of the ray optics is fulfilled for WGM and all other modes with the close wavelengths. Let us try to find the difference between the ray picture for WGM and non-WGM. For the sake of simplicity we consider a two-dimensional system – a circle. In Fig. 14.2 two ray pictures are present.

It is intuitively clear that Fig. 14.2a is ‘more WGM’ than Fig. 14.2b. Let us clarify what this ‘more’ means.

It is known from the ray optics that a resonator mode is formed not by a single closed ray but by a set of rays of the same length. For a circular resonator this set of rays can be obtained just by the rotation of a closed ray – see Fig. 14.3.

One can see in this figure that along with the initial rays there appear two additional ‘phantom’ rays that are the ray-set envelopes (one is the border circle itself and another is a circle inside the resonator). These phantom rays are called caustic lines (caustic surfaces in the three-dimensional case). The caustic surface by definition is the envelope of a set of rays. Looking at Fig. 14.3 it can seen that the distance between the internal and the external

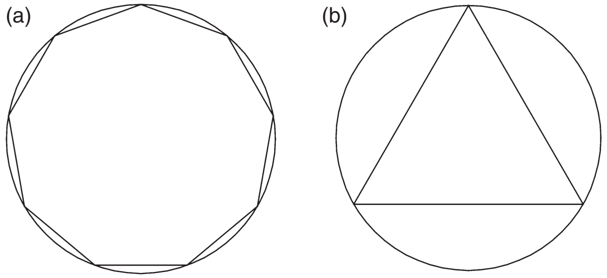

14.2 Basic ray pictures for two modes in a circle.

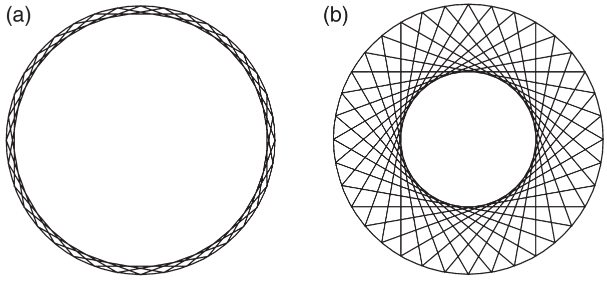

14.3 Family of rays forming WGM (a) and a common mode (b).

caustics are different for Fig. 14.3a and 14.3b. So, it is natural to say that WGM is a mode that arises from a system of closed rays, for which the external caustic coincides with the border of a resonator, the distance between the external and the internal caustics is of the order of the wavelength and the set of rays is stable.[1] Since there is no clear-cut distinction between WGM and other modes, the 'small enough distance between caustics' can vary from several wavelengths to several hundred wavelengths, at one's discretion. This last remark about the stability of a ray system has been made in order to avoid consideration of chaotic modes. These modes have different properties from stable modes. This definition is applicable to any arbitrary cavity shape and general boundary conditions.

The ray optics picture allows one to estimate the eigenfrequency (or eigenwavelength) of WGMs in a cylindrical resonator. The ray length should be equal to an integer number of the wavelengths $\lambda = m\lambda$ for a ray forming a resonator mode. When the circle length is much larger than λ and the number of reflections is very large, the length of a ray λ is very close to that of the circle $\lambda \approx 2\pi R$, so the estimation of the resonator mode wavelength is:

$$\lambda_m = \frac{2\pi Rn}{m}, \qquad [14.4]$$

where we include the refractive index n of the resonator interior for the sake of generality (λ is the wavelength in vacuum).

The same result for the eigenmode wavelength estimation can be obtained from Equation [14.1] using the asymptotic of the Bessel function root for a large index m (Korn and Korn, 2000):

$$J(\pi\alpha_{m1}) = 0 \Rightarrow \alpha_{m1} \approx \frac{m}{\pi} + 0.6\, m^{1/3}, \qquad [14.5]$$

which immediately leads to the equation $2\pi R \approx m\lambda_m$. So, for a cylindrical resonator, the WGM is indeed a mode with a large index m.

The second term in Equation [14.5] shows that the estimation of the eigenmode wavelength Formula [14.4] is not very accurate because the second term is greater than the intermodal distance. We will show below that Formula Equation [14.4] leads to a good estimation of the intermodal distance, but now we need to discuss the reason for this inaccuracy in the ray picture. The rays that form a WGM lie between two caustics and the distance between these caustics is small. It is known that near a caustic simple ray optics does not work and the intensity I of a wave goes to infinity. Rigorous analysis leads to $I \sim \lambda^{-1/3}$ (Landau and Lifshitz, 1983) – for this reason one can see caustics in the shadow of a glass of water. This means that the simple ray picture in Fig. 14.2a is not quite right for a small distance between caustics and condition [14.3] is a necessary but not sufficient criterion for a WGM. For a large distance between caustics, the ray length $\lambda < 2\pi R$, and again Equation [14.4] is an inaccurate approximation.

---

[1] Loosely speaking, the ray is stable if a slight perturbation results in a small shift of a ray. One can find the rigorous definition of ray-set stability in Babič and Buldyrev (1991, p. 98).

Modes in a cylinder are two-fold generated, due to the two directions (clockwise and anticlockwise) of wave propagation. Phases ψ_m in Equation [14.1] are arbitrary, and for this reason standing waves in a cylinder are unstable. Some standing waves in, say, a semidisk resonator also fit our definition of a WGM. In order to distinguish two-fold degenerated traveling waves and standing waves, the latter will be called quasi-WGM (QWGM).

High Q-factor is the main attractive feature of the WGM resonator. We will talk about it when discussing dielectric optical resonators, because resonators with zero boundary conditions do not dissipate energy. The high Q-factor allows making a laser having active media with very low optical gain. On the other hand, when the optical gain is high enough, this high Q-factor prevents light extraction from the resonator.

It is necessary to make some additional remarks about the definition of WGM used here, which in fact is borrowed from (Babič and Buldyrev, 1991). As well as the WGM in a convex cavity, there exist other remarkable modes. One such mode is the so-called bouncing-ball mode that traces out relatively simple and obviously closed rays, and in principle can travel through the central region of a cavity. The mode in a standard Fabry–Pérot resonator is the simplest possible bouncing-ball mode, as is the bow-tie mode.

Other remarkable modes are ‘chaotic’ modes, which arise from unstable rays that are periodic rays with the property that a slight perturbation results in a huge shift away from the original orbit. Chaotic modes arise from these unstable rays. Usually these modes are considered separately, but sometimes all these modes are called WGM.

In this paper we will consider WGM only, and not bouncing-ball or chaotic modes. The latter modes are, or may be, more interesting than WGM, but discussion of them is a matter for a separate paper. In Fig. 14.4. the bouncing-ball mode and chaotic modes are shown.

14.2 WGM in electrodynamics

Optical WGM in spherical dielectric resonators was revealed at the beginning of the 20th century (Mie, 1908; Debye, 1909) and up to the beginning of the ‘laser era’ it was considered an amusing optical toy. It was the necessity to have an optical resonator with high Q-factor in laser physics that again attracted attention to the WGM resonators. The first attempt we know to use a spherical WGM resonator for getting stimulated light emission was made in 1961 (Garrett *et al.*, 1961). In this section we will briefly discuss

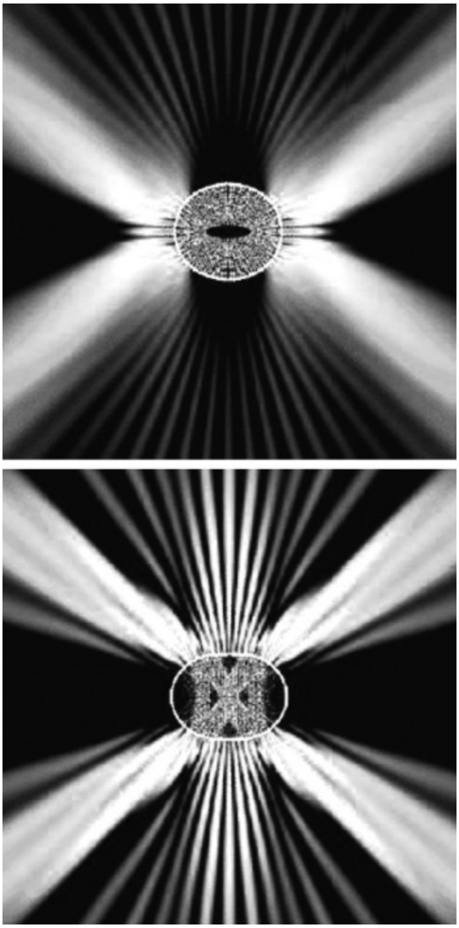

14.4 Chaotic mode (upper plot) and bouncing-ball bow-tie mode (lower plot). Directed light beams are seen. Image from Gmach *et al.* (1998).

the mathematical background of WGM phenomena in optics. This matter is discussed in more detail in many books and reviews (see e.g., Babič and Buldyrev, 1991; Oraevsky, 2002; Ilchenko and Matsko, 2006).

There are very few exactly solvable electrodynamics problems that allow one to illustrate the WGM problem. One of them is a cylindrical resonator with ideal metallic walls. The solution to this problem can be found in many electrodynamics courses. The main difference between acoustic and electromagnetic waves is that the former are longitudinal and the latter are transversal. For this reason in this system there exist two types of excitations, transversal electric (TE) and transversal magnetic (TM) modes. These terms originated from the theory of the infinite waveguides, where

TM means that the projection of the magnetic field on the direction of the wave propagation (the cylinder axis is z-axis in the further notation) is zero. Correspondingly $E_z = 0$ for TE mode.

It follows from the Maxwell equation with the zero boundary conditions on the resonator walls that all components of electric and magnetic fields can be expressed in terms of the single component H_z for TE mode and E_z for TM.

The whole set of TM modes in a cylindrical resonator with metallic walls is as follows:

$$\begin{aligned}
E_z &= \varepsilon_0 J_m(\text{æ}r)\sin(m\varphi+\psi_m)\cos(kz)e^{\pm i\omega t}\\
E_r &= \frac{k}{\text{æ}}\varepsilon_0 J_m'(\text{æ}r)\sin(m\varphi+\psi_m)\sin(kz)e^{\pm i\omega t}\\
E_\varphi &= -\frac{mk}{\text{æ}^2 r}\varepsilon_0 J_m(\text{æ}r)\cos(m\varphi+\psi_m)\sin(kz)e^{\pm i\omega t}\\
H_r &= -\frac{im\omega}{\text{æ}^2 cr}\varepsilon_0 J_m(\text{æ}r)\cos(m\varphi+\psi_m)\cos(kz)e^{\pm i\omega t}\\
H_\varphi &= \frac{i\omega}{\text{æ}c}\varepsilon_0 J_m'(\text{æ}r)\sin(m\varphi+\psi_m)\cos(kz)e^{\pm i\omega t}\\
H_z &= 0
\end{aligned}$$

Here $J_m'(x) = dJ_m(x)/dx$, J_m is the Bessel function of index m, $k = \pi\ell/h$; $\ell = 0, 1, 2 \ldots$, h is the cylinder height, $\text{æ} = \alpha_{\text{mp}}/R$, R is the radius of the cylinder and α_{mp} is the p^{th} root of the Bessel function of the index m: $J_m(\alpha_{\text{mp}}) = 0$. The angular frequency ω is expressed as $\omega^2 = c^2(\text{æ}^2 + k^2)$. The values ε_0 and ψ_m are the amplitude and phase that depend on the wave-excitation conditions.

For the TE mode $H_z = H_0 J_0(\text{æ}r)\sin(m\varphi+\psi_m)\sin(kz)e^{\pm i\omega t}$, all other components can be expressed in terms of H_z, and the difference between TE and TM is in the eigenfrequencies equation $J_m'(\alpha_{mn}) = 0$ for TE mode.

Let us consider a resonator with the height h much less than its radius. In this case the frequency distance between two eigenfrequencies with the same k and different æ is much larger than that for the same æ and different k. So, we can restrict ourselves to the cases where $k = 0$ for TM mode, or $k = \pi/h$ for TE mode. This geometry and values of k is usual for WGM, lasers except for so-called pillar lasers (Gayral *et al.*, 1998; Nowicki-Bringuier *et al.*, 2007; Reitzenstein *et al.*, 2008; Jaffrennou *et al.*, 2010; Jones *et al.*, 2010; Hill, 2011). The mode picture of such resonator looks like is as shown in Fig. 14.5.

Using the above-mentioned asymptotic formula for the roots of the Bessel function for large index m, one can find the approximate expression for the intermodal wavelength distance: $\Delta\lambda = \lambda^2/2\pi Rn$.

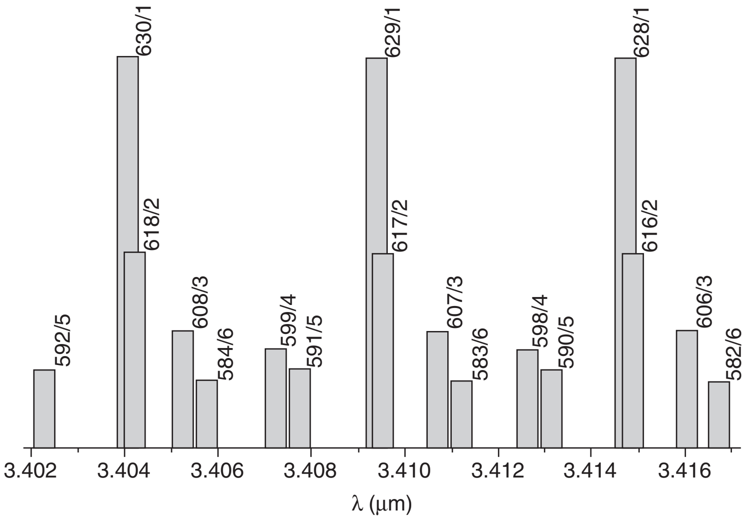

14.5 Wavelength positions of some WGMs for the metallic disk resonator 200 μm in diameter. The different bar heights correspond to the different root number *p*. XXX/X indicates Bessel function index/root number.

Here *n* is the refractive index inside the resonator. This formula seems to be almost the only expression in WGM theory that is useful in practice, and can be applied with minor modification not only to the cylindrical resonator but also for a general convex resonator. We will discuss this matter below, but now we will briefly discuss dielectric resonators.

In dielectric resonators one should apply Maxwell's boundary conditions instead of zero ones. These conditions are the continuity of the normal component of the $\mathbf{D}$ and tangent components of the $\boldsymbol{E}$, where $D_i = \varepsilon_{ik}E_k$ and ε_{ik} is the dielectric permittivity tensor. Even with the dielectric permittivity being a constant, the only well-studied exactly solvable problem is that of the eigenfrequencies in a dielectric sphere. This problem is minutely discussed in Oraevsky (2002) and here we represent only the solution of the problem.

Similar to the case of a metallic cylindrical resonator, in a dielectric sphere there exist two sets of eigenmodes. In the E-type set the H_r component of the magnetic field is equal to zero, while in the H-type set $E_r = 0$ in the spherical coordinate system. The components of fields for E-type mode have the following form in the spherical coordinate system (Oraevsky, 2002).

$$
\begin{aligned}
&E_r = m(m+1)P_m^n(\cos\theta)\frac{Z_\nu(kr)}{(kr)^{3/2}}e^{\pm in\varphi}\\
&E_\theta = \frac{d}{d\theta}(\cos\theta)P_m^n\frac{1}{kr}\frac{d}{d(kr)}\left((kr)^{1/2}Z_\nu(kr)\right)e^{\pm in\varphi}\\
&E_\varphi = \pm i\frac{n}{\sin\theta}P_m^n(\cos\theta)\frac{1}{kr}\frac{d}{d(kr)}\left((kr)^{1/2}Z_\nu(kr)\right)e^{\pm in\varphi}\\
&H_r = 0\\
&H_\theta = \frac{n}{\sin\theta}P_m^n(\cos\theta)\frac{Z_\nu(kr)}{(kr)^{1/2}}e^{\pm in\varphi}\\
&H_\varphi = \pm i\frac{d}{d\theta}P_m^n(\cos\theta)\frac{Z_\nu(kr)}{(kr)}e^{\pm in\varphi}
\end{aligned}
\qquad [14.6]
$$

Here P_m^n are the adjoint Legendre polynomials, $\nu = m + 1/2, k = \omega / c\sqrt{\varepsilon\mu}$, and it is different inside and outside of the sphere and Z_ν is equal to the Bessel function J_ν inside and the Hankel function of the first kind $H_\nu^{(1)}$ outside of the sphere.

The boundary conditions result in the equation for the eigenmodes of the dielectric sphere. For E-modes this equation is:

$$
\frac{\frac{d}{d(ka)}\left[(ka)^{1/2}J_\nu(ka)\right]}{(ka)^{1/2}J_\nu(ka)} = \sqrt{\frac{\varepsilon}{\mu}}\,\frac{\frac{d}{d(k_0a)}\left[(k_0a)^{1/2}H_\nu^{(1)}(k_0a)\right]}{(k_0a)^{1/2}H_\nu^{(1)}(k_0a)} \qquad [14.7]
$$

Here k is the value inside and k_0 is the value outside the sphere.

Asymptotic analysis of Equation [14.7] (see Oraevsky, 2002) shows that for large m the equation for the wavelength of eigenmodes for a dielectric sphere is $2\pi R\mathrm{n} / \lambda = m + \mathrm{O}(m)$ (here we neglect the difference between m and m + 1/2 for a large m), which is just Formula [14.4] for a metal cylindrical resonator. So, the approximate solution of both exactly solvable problems can be obtained using the simple physical assumption mentioned above: the eigenmodes wavelength can be obtained if one assumes that the closed optical path should contain an integer number of the wavelengths. This assumption has a strong mathematical support – it is indeed the first term in an asymptotic expansion over the large parameter – the ratio of the characteristic size of the resonator to the wavelength. The mathematically rigorous description of the application of the short-wavelength diffraction method to the studying of WGM one can find in Babič and Buldyrev (1991).

The diffraction methods allow us to calculate the eigenfunctions with much higher accuracy than that in Formula [14.4], but the calculations of the absolute value of the WGM frequency (wavelength) with high accuracy is useless in most cases. To illustrate this we will use the approximate Formula [14.4]. First of all let us illustrate the accuracy of Formula [14.4] itself. The high accuracy numerical calculations of the modes wavelengths for the metallic cylindrical resonator of $R = 350$ μm in radius and for the mode corresponding to the first root of the Bessel function with indices $m = 580$ and 581 gives $\lambda_{580} = 4.000875$ and $\lambda_{581} = 4.00197$ μm. The asymptotic Formula [14.4] gives $\lambda_{580}^{as} = 2\pi R / 580 = 4.11$ μm. So, the error in the absolute wavelength value is much greater than the intermodal distance. Now let us calculate the intermodal distance by the slightly modified Formula [14.4] (in our case $n = 1$):

$$\Delta\lambda = 2\pi R\left(\frac{1}{m} - \frac{1}{m+1}\right) \approx \frac{2\pi R}{m^2} = \frac{\lambda^2}{2\pi R}, \qquad [14.8]$$

using the 'experimentally measured' value $\lambda_{580} = 4.0$ μm as λ. The result is much more appropriate: $\Delta\lambda^{as} = 0.00670$ μm and the exact value is $\Delta\lambda = 0.00677$ μm. So, Formula [14.4] is a bad approximation for the absolute value of the wavelength of a resonator mode, but Formula [14.8] gives reasonable values for the intermodal distance.

Now let us consider the situation when the radius (or refractive index) is measured with some error $\delta R \approx 3$ μm (the measurement accuracy is less then 1%). According to Formula [14.4] the error in the absolute wavelength position is $\delta\lambda \approx 2\pi\delta R / m \approx 0.03$ μm that is greater than the intermodal distance. There is no doubt that the error calculation that uses the more accurate eigenfrequency estimation will get the same error. The similar error estimation for the intermodal distance gives $\delta(\Delta\lambda) \approx 2\pi\delta R / m^2 \approx 4 \times 10^{-5}$ μm for $m = 580$. This value is much less than the intermodal distance and there is no wonder that Formula [14.8] is the main piece of the WGM theory that is used in practice, because the accuracy of the real measurement of, say, resonator radius or refractive index is not enough.

The short-wave diffraction methods can be applied to cavities of different shape where the Maxwell equations can be solved only numerically, and obtaining the solution corresponding to the WGM is a challenging task. In order to get the main term in the short-wave expansion one should construct a set of closed rays that reflect from the walls of a resonator at angles greater than the total internal reflection angle (for a dielectric resonator) and obtain a curve on the surface of the resonator to which the set of rays transforms when the number of reflections goes to infinity. This curve appears to be some closed geodesic line on the resonator's surface and Formula [14.8] is still correct if one substitutes $2\pi R$ by the length of this curve. The correction to this term is not as universal as the first term and depends on the shape of the resonator under consideration. In this manner it can be shown that truncated-conical resonator in the first approximation has the same WGM as the cylindrical resonator with the diameter of cylinder equal to the larger base of the truncated cone (Alekseenko *et al.*, 2009).

The next problem we would like to discuss in this section is the eigenfrequency problem of the dielectric disk (cylindrical) resonator. Surprisingly, the exact solution of this problem has not yet been found, although it seems to be very similar to the problem of the metallic cylindrical resonator and seems be solved by the same methods. The difference between these two problems is in the boundary conditions. For a dielectric cylinder, the separation of variables method fails on the angles between the bases and the side face of a cylinder where the Maxwell's boundary conditions become dependent. Thus, to solve the eigenfrequency problem in a dielectric cylinder it is necessary to solve the prominent problem of the diffraction by a dielectric wedge. This problem is discussed in a good many mathematical papers (Rawlins, 1999; Salem *et al.*, 2006), but is not yet solved.

Nevertheless, the approximate solution of the problem discussed can be obtained by the method of separation of variables where one neglects the angle-diffraction effects. This solution of the problem is presented in some papers with no indication that it is an approximate one. Comparison of this solution with the results of numerical calculations shows a good agreement in the mode position. Moreover, inasmuch as the refractive index n of a common semiconductor material is large (for GaAs, InAs, etc., $n \approx 3$) approximate analytical and numerical calculations show that there is no big difference between the WGM positions in metallic and dielectric cylindrical resonators. In Fig. 14.6 the result of such a calculation is shown.

So, with experimental accuracy one can use Formula [14.8] for cylinder-like dielectric resonators.

The previous discussion may leave an impression that deep mathematical studies of WGM are practically useless. We would say that this impression is wrong. Indeed, the calculation of the mode spectra has little practical use but, for example, a mode stability aspect is practically important, and cannot be studied using the simple physical picture of the rays' propagation. One such result is the statement that in an elliptical resonator, or resonator of similar form that is prolonged in some direction and shrunk in the orthogonal one, hand in hand with the WGM there exists bouncing-ball mode, that is similar to a mode in a Fabry–Pérot resonator, and the matter of what mode will be an operating mode of the laser with such a resonator has many facets. Such a situation is shown in Fig. 14.7, where one can see the quasi-WGM in

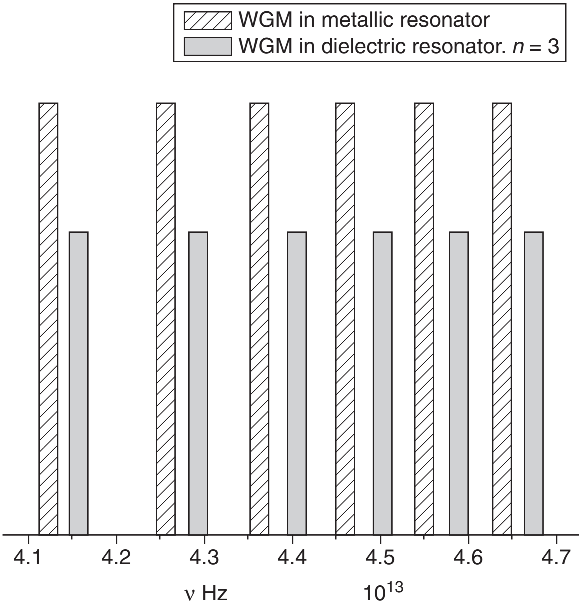

14.6 Comparison of the modes frequencies of the metallic and dielectric disk resonators. The refractive index of the interior of both resonators is equal to 3. The result of numerical simulation.

the left and bouncing-ball mode on the right. Both modes exist in the same resonator and have close frequencies.

Another question that can be answered by the mode stability consideration is the following one. Let us again consider the cylindrical resonator. In this resonator there exist many modes corresponding to the different roots of the same Bessel function (see Fig. 14.5). Why are only the first few roots experimentally observed? (Why do theorists consider only the first root?) The answer is that the greater the number of the oscillations inside the resonator, the more sensitive (less stable) is the mode to an external disturbance.

We have mentioned QWGM modes. By QWGM we meant the modes that are in some sense a mixture of WGM and bouncing-ball modes. The simplest example is modes of a sectoral cylindrical resonator (Monakhov *et al.*, 2009, p. 051102). For a metal resonator the problem is exactly solvable and the mathematical solution of the eigenmodes problem for such a resonator is very similar to that for a whole-disk resonator, but to guess the answer the simple physical consideration is enough. The closed optical path of a ray with very many reflections is equal to the doubled length of the arc line of the sector. So, the half-disk and the whole-disk resonator should have the same intermodal distance (the only theoretical value well-compatible with

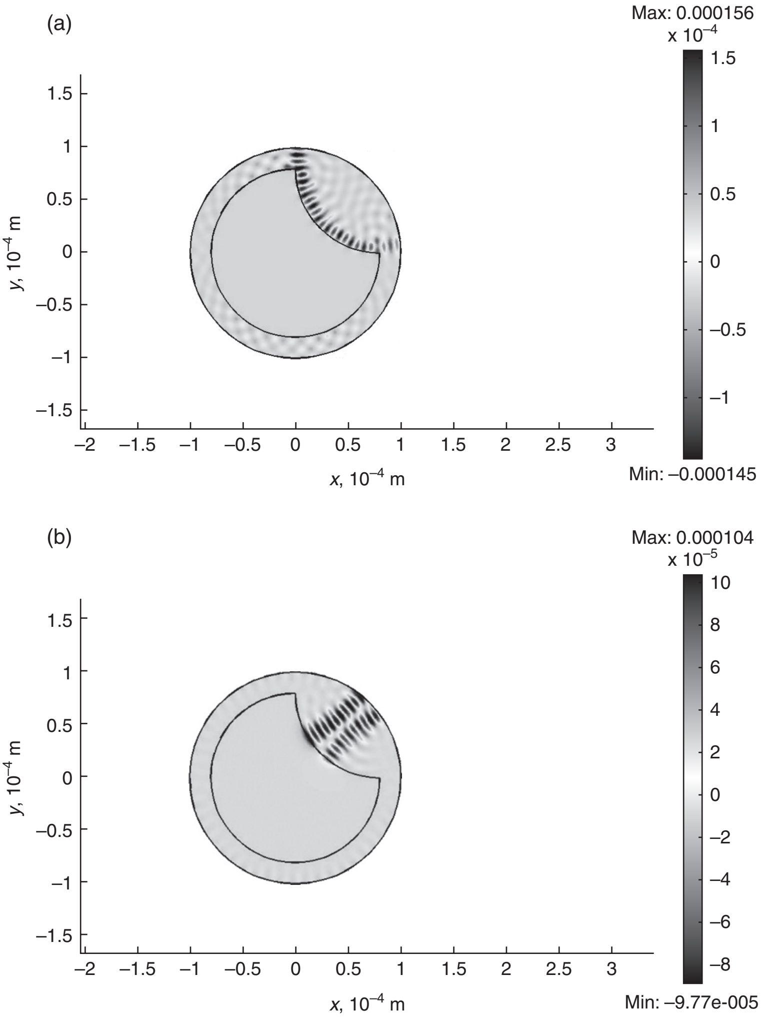

14.7 Quasi-WGM mode (a) and bouncing-ball mode (b) with close frequencies in the same resonator. Results of numerical simulation.

the experiment as mentioned above), the intermodal distance in a quarter-disk resonator is doubled compared with the whole-disk and so on. A more sophisticated example of QWGM is represented in Srinivasan and Painter (2007) where authors considered disk cavity with a quantum dot embedded in it. The picture of QWGM in this system is shown in Fig. 14.8.

The last, but not least, question that will be discussed in this section is the Q-factor of a dielectric WGM resonator. At a glance it seems to be infinite in the theory because there is no energy leakage for the total internal

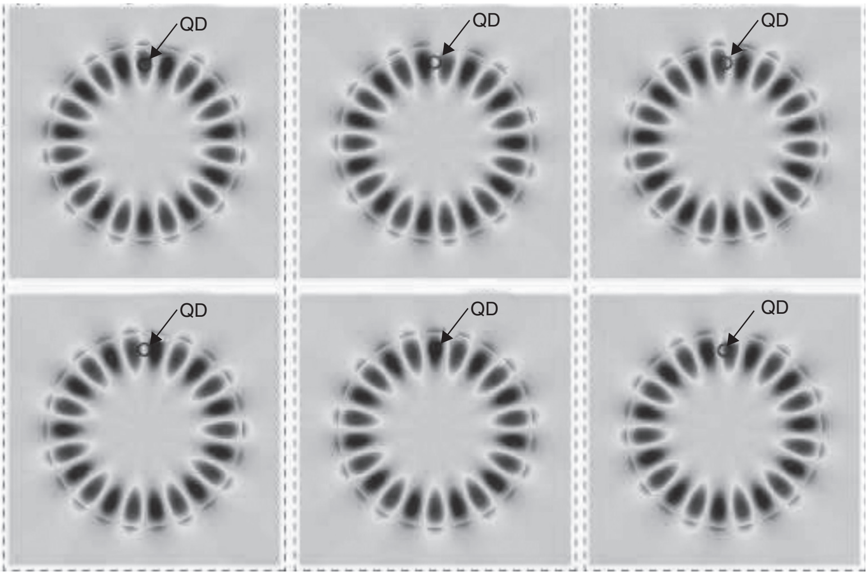

14.8 Different QWGM modes in a dielectric disk with a quantum dot in it. Image from Srinavasan and Painter (2007).

reflection. This is not the whole truth because, strictly speaking, the total internal reflection takes place only if the boundary surface is a plane. For a curved surface there is some energy leakage, but this leakage is very small and the Q-factor calculation of the quartz sphere of 100 μm in diameter for index $m = 2000$ gets the huge (and unreasonable) $Q = 10^{400}$ (Oraevsky, 2002). This means that the Q-factor is determined by the imperfection of a resonator (surface roughness, internal absorption etc.) and is not a matter of a 'pure science'. The experimentally achieved values of Q-factor for spherical resonators are up to 10^9 (Gorodetsky *et al.*, 1996). The cylindrical dielectric resonators commonly used in lasers have lower Q-factor. The best resonators have $Q \sim 10^6$ (Matsko *et al.*, 2005). One reason for the energy leakage from the disk resonator is the above-mentioned diffraction on a dielectric wedge that takes place on the angle. The amount of energy leakage that is due to this effect is still unknown, because of the absence of good theory. Another reason is that a cylindrical resonator has a worse surface than a spherical one.

The high Q-factor and sensitivity of WGM to the refractive index and the shape and size of a resonator have led to their exploitation for a wide variety of applications including tunable filters (Chu *et al.*, 1999), optical switches (Blom *et al.*, 1997), different sensors, and so on. A review of the application of WGM resonators is given in (Ilchenko and Matsko, 2006). Among these applications are WGM lasers, that will be discussed in the next section.

14.3 Semiconductor WGM lasers

For laser physics the most interesting feature of a WGM resonator is its high Q-factor. It is known that a laser is an optical amplifier with regenerative feedback. The self-excitation condition for such system is:

$$GR = 1,$$

where G is a net optical gain of a laser and R is a feedback regeneration coefficient, that is, a part of the output energy that returns to the input of the amplifier. So, to start lasing there should be either a high enough gain or high regeneration coefficient, and the higher the Q-factor the lower can be the optical gain of the active media.

On the other hand, lasing itself is not the main goal of a laser device. Usually, one needs to have high output optical power and for this purpose it is necessary to have, not high but optimal, Q-factor. Another problem for WGM resonators is the light extracting (output coupling) from the resonator. In common case without special arrangements, the light from a WGM resonator is undirected and the optical output power is rather low. For these reasons, WGM resonators are not used for visible and near-infrared (IR) semiconductor lasers-light sources because of the high optical gain in these devices, but they are very convenient for integrated optics..

There have been several papers discussing WGM lasers for the visible and near-IR wave range. In McCall *et al.* (1992) the microdisk mushroom-shaped WGM laser operated on $\lambda = 1.53$ μm at room temperature was demonstrated. This laser was 5 μm in diameter and was optically pumped. This device was proposed to be not a coherent light source but an element of photonic or optoelectronic circuit, and its advantages in this case are small size and low power consumption. Later the Levi *et al.* (1992) research group demonstrated the similar microdisk lasers with electrical pumping. In these papers, it was found that the undirected light from a disk WGM laser can hardly be practically used, and subsequently many papers were devoted to the light extraction problem.

One idea was to use a resonator prolonged in one direction instead of a circular one. The shape dependence of the emission from microdisk lasers was studied in Backes *et al.* (1997) where it was revealed that the maximum emission was achieved for the ellipsoid with the axis ratio equal to 2. Nevertheless, as it was pointed out above, it is possible that instead of WGM there can be the bouncing-ball mode along the small ellipsoid axis. To distinguish these two modes, either the directional diagram or intermodal distance should be studied, but this issue was not discussed in this paper. This problem was studied in Gmach *et al.* (1998). It was revealed that, indeed, the high-power directed emission from a circular deformed resonator takes place and the operating modes of such a laser are either bouncing-ball modes or chaotic ones. So, the lasers are not a WGM lasers in our sense. It does not mean that these deformed lasers are something defective; on the contrary, they are more promising light sources than WGM lasers, but such lasers are not the subject of this paper.

Thus, it was demonstrated that WGM lasers indeed operate and can be used in integrated optical devices. It was found that the Q-factor of a disk laser is higher than that of a stripe one, but the problem of the light extraction prevents their usage as a light source, although they can be used in signal processing

The mid-IR, far-IR and terahertz diapason is more promising for WGM lasers because of the high interval losses and low optical gain in the active media used in lasers for this range. The authors of this paper mainly dealt with the mid-IR WGM lasers and we will illustrate the properties of WGM lasers by the examples of mid-IR WGM lasers.

WGM resonators are useful for mid-IR since they have low optical losses that can potentially improve the performance of such devices that suffer from small gain and high internal loss. Therefore, the increase in Q-factor provided by a disc cavity opens a way for fabrication of a device that lases even when the optical gain in the active region is not high. Furthermore, since the wavelength in the range under study is $\lambda \approx 3\,\mu\text{m}$ (~1 μm within the cavity), the demands on surface quality are significantly lowered, and the treatment of the cavity surface can be reduced to the usual lithography and standard methods of post-grow processing. This allows fabrication of a laser matrix with high laser density.

The typical WGM laser discussed in Averkiev *et al.* (2000, p. 1087; 2009, p. 117) is shown in Fig. 14.9.

The laser structure comprised an InAs substrate with successfully grown $InAs_{0.65}Sb_{0.11}P_{0.24}$ emitter, InAs active layer and p-InAsSb emitter. The

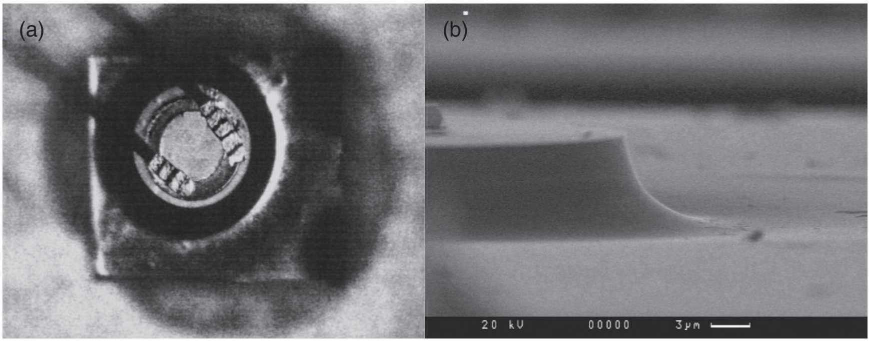

14.9 Micrographs of a disk WGM laser: (a) a side view and (b) a top view of the laser diode.

device under consideration is a round mesa with approximately 200 μm diameter base on the rectangular substrate 0.5 × 0.5 mm. The thickness of the substrate is about 300 μm, and the height of mesa is about 10 μm. The device has an upper ring contact and another contact on the bottom of the substrate. The fabricated lasers operate in continuous-running regime and have low threshold lasing currents of ~25 mA at a temperature of 77 K. Figure 14.10 shows a typical coherent emission spectrum for a laser with a cavity diameter of 200 μm. It can be seen that the emission spectrum has a multimode structure with equidistant peaks with a distance of approximately 40 Å between the modes, which is in good agreement with Equation [14.8]. Figure 14.10 clearly shows that there are two sets of modes that can probably be attributed to the different roots of the Bessel function (presumably the first and the second one), in the approximate Equation [14.2].

In the case under study, with a cavity diameter of 200 μm, wavelength of 3.04 μm in air, and refractive index $n \approx 3.5$, the Bessel function index m (see Equation [14.1]) is about 600, so this device indeed operates at high-index WGM. A significant disadvantage of WGM lasers shown in Fig. 14.9 is the near cone shape of the disk cavities in the vicinity of the active region, resulting in mode leakage toward the substrate that significantly decreases the Q-factor and, accordingly, increases the threshold current. The efficiency level of WGM lasers reported, for example in Sherstnev *et al.* (2000, 2005a, 2005b, 2006); Krier *et al.* (2003) was far from that required for practical application. For this reason, a convex disk-shaped cavity was created, in which a part of the active region would protrude beyond the emitter layers over the entire

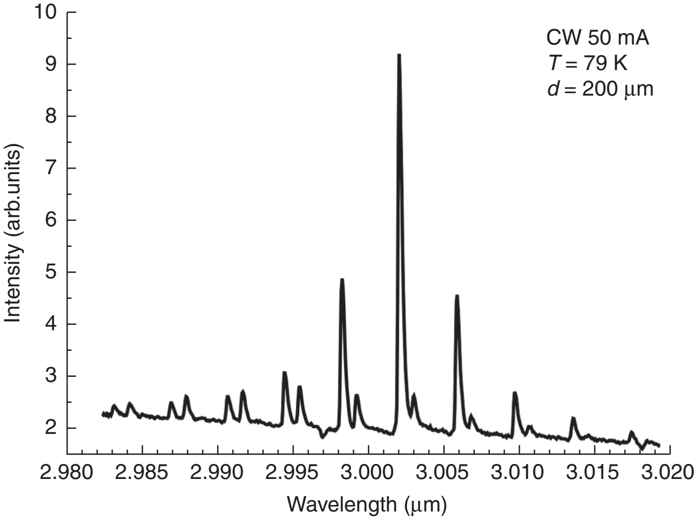

14.10 Lasing spectra of the device in Fig. 14.9.

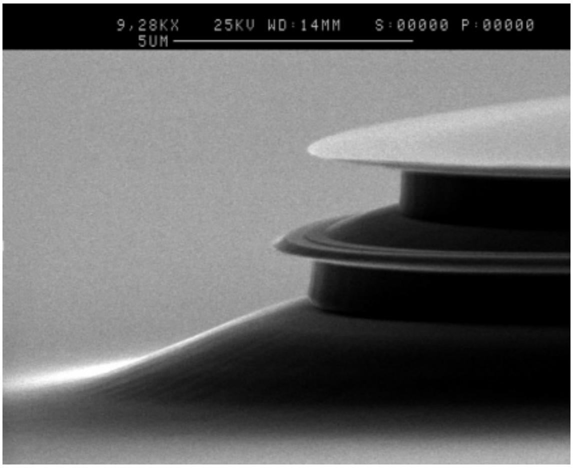

14.11 SEM image of the etched mesa.

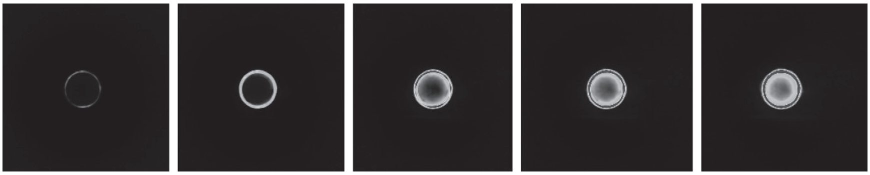

$I = 20$ mA $I = 50$ mA $I = 115$ mA $I = 150$ mA $I = 200$ mA

14.12 IR images of WGM lasers below (first and second pictures from the left) and above the threshold current. The threshold current is equal to 110 mA.

perimeter (Fig. 14.11). Such cavities provide conditions for the generation of a stable WGM in the protruding part of the active medium. Stabilization of the working mode in the vertical direction allows the laser structures to be created without internal layers responsible for the optical confinement.

These lasers operate at room temperature and have quite low threshold currents. The laser was grown on n-GaSb substrate. The active layer consisted of two stressed 13 nm thick $Ga_{0.85}In_{0.35}As_{0.11}Sb_{0.89}$ quantum wells separated by $Al_{0.25}Ga_{0.75}As_{0.02}Sb_{0.98}$ interlayers. The operating wavelength was about 2.3 μm.

The IR images of the operating WGM laser are shown in Fig. 14.12.

Before discussing Fig. 14.12, the current density distribution in the device should be considered. The current density distribution in such device is rather inhomogeneous. The distribution of the normal component of the current density $j_n = j_z$ on the interface of the active region calculated numerically is shown in Fig. 14.13. The same figure demonstrates the position of

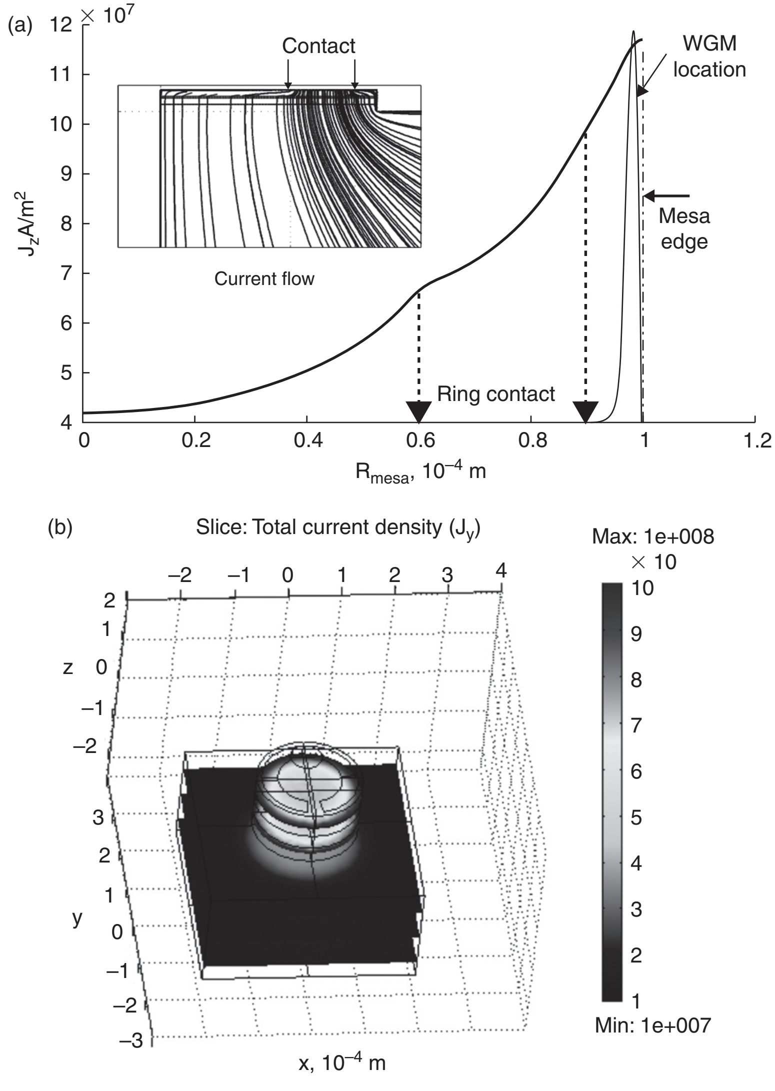

14.13 Current density distribution in the WGM laser device. The radial dependence of the normal current density (a), current lines (insert) and the total current density (b).

the WGM with respect to the mesa edge. The inset shows the scheme of current lines, which illustrates how such a distribution is attained. As can be seen in Fig. 14.13, the current density peaks exactly at the place where the WGM is localized.

The strong inhomogeneity of the current density can be qualitatively explained if one remembers that the current density distribution in a body

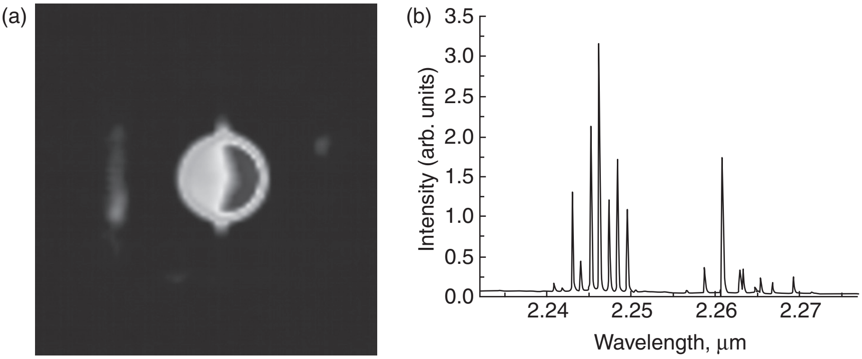

14.14 IR image of the WGM laser with the half-ring contact (a) and its spectrum (b).

minimizes the Joule heat of the body (Landau and Lifshitz, 1984). The main resistance of the sample under consideration is the resistance of the substrate, so it is necessary to minimize the current density in it. For this reason, the current crowding takes place near the walls of the mesa trying to spread in the substrate.

Returning to Fig. 14.12, one can see that this picture is very similar to the right picture in Fig. 14.13. It can also seen that there is no great difference between the pictures of the device in the spontaneous emission and laser regimes. In fact, the IR camera registered that the spontaneous emission and WGM can hardly be seen due to the high Q-factor of the resonator. This fact is demonstrated in Fig. 14.14, where the upper contact is a half of the ring, and the IR image clearly shows the emission under contact and almost nothing in the other part of the resonator. Nevertheless, the spectrum shows the typical WGM and intermodal distance coincides with Equation [14.8].

The last thing we would like to illustrate with IR lasers is the sensitivity of the lasing spectra to external perturbation. One such perturbation is the optical properties alteration with temperature. The Joule heating by the current should affect the mode spectral position. This effect was observed in Imenkov *et al.* (2009a, p. 857; 2009b, p. 1149). In these papers, the dependence of the laser emission spectra on the pump current of the half-disk QWGM laser was studied. It was revealed that there is a spectrum line shift with increase of current.

The output emission spectra of QWGM laser diodes were measured at room temperature in a pulsed regime. The pumping current pulses had a variable duration τ from 0.1 to 1.2 µs, with a repetition rate of 20 kHz, and amplitude of 200–600 mA. In Fig. 14.15 (a) the dependence of the mode position on pulse duration for different current amplitudes is shown. Figure 14.15(b) shows the same plots as Fig. 14.15(a), redrawn in the scale $I^2\tau$,

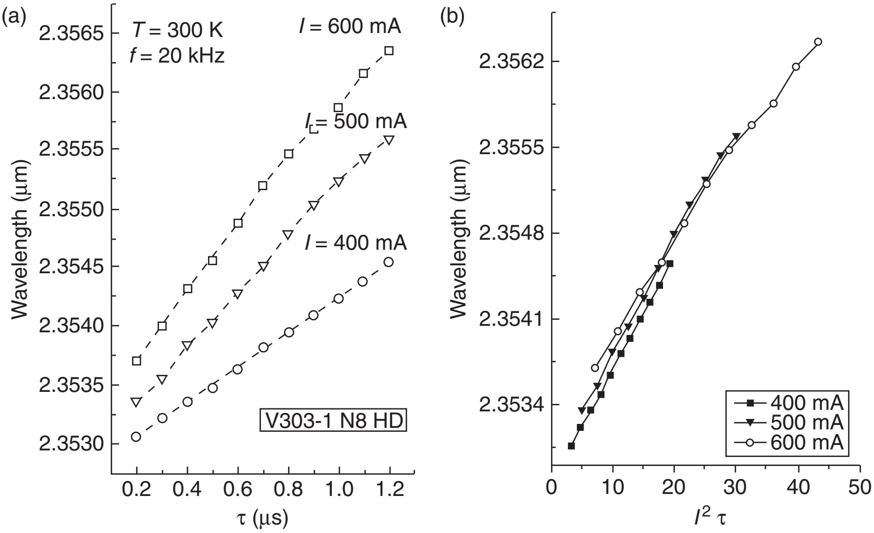

14.15 The mode position dependence on the pulse duration (a) and Joule heat (b).

proportional to the Joule heat. One can see that the tuning effect is mainly due to this heating, which slightly changes the refractive index.

As was mentioned above, WGM lasers were proposed as a base for integrated optical devices. Along with the high Q-factor there is another distinctive feature of WGM lasers – two-fold degeneration of each mode. The idea to utilize this property by switching between clockwise and anticlockwise mode in an optical switch is quite natural, but one needs first to arrange some coupling between the two lasers. The coupling between two disk resonators and corresponding effects were studied both theoretically and experimentally in Schmidt *et al.* (2009). In this paper it was shown that the strongest coupling takes place in two equal disks between the modes with the same index *m* rotating in the opposite directions. It was found (theoretically) that the two-fold degeneracy of a mode in a disk resonator is lifted for coupled disks. This effect was not observed experimentally, due to its small size.

The prototype of a real optical switching device was proposed in Hill *et al.* (2004). This device is shown in Fig. 14.16. Two micro-ring lasers are coupled via a waveguide. This system has two stable states. In the first state, clockwise light from laser A is injected via the waveguide into laser B. If sufficient light is injected into laser B, laser A captures or injection-locks laser B, forcing light to circulate only in the clockwise direction. The reverse situation with laser B injection-locking laser A is also a stable state of the system. Thus, one can have a system in two stable states and an external optical pulse switches it from one state to another.

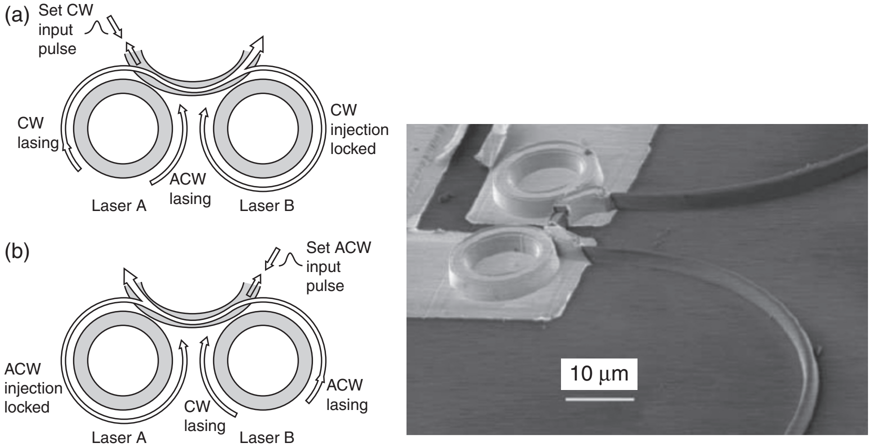

14.16 A memory element formed by two 16 μm diameter micro-ring lasers coupled via a waveguide on an InP/InGaAsP photonic integrated circuit (Hill *et al.*, 2004).

14.4 Light extraction from a WGM resonator

The main problem confronted in trying to use a WGM laser as a source of the coherent light is light extracting from a WGM resonator. In a common disk or spherical resonator, light emission is due to Rayleigh scattering on the defects, mode leakage into the substrate, and other uncontrolled effects, so the light propagates in all directions. This problem was considered in many papers and many possible solutions were proposed. The number of these attempts shows that the problem is not solved yet.

Usually one needs to have maximum output optical power from a laser. For this purpose, it is necessary that the internal energy losses in the active layer become equal to the energy losses through the output coupler (mirrors for a Fabry–Pérot resonator) in the maximum-pumping regime. This condition is equal to the well-known optimal-load condition in electrical engineering: the load resistance should be equal to the internal resistance of the generator. This condition is not fulfilled in a common stripe laser, where the transparency of the mirrors is a matter of the refractive index of the material and can hardly be changed. For a WGM laser the output coupler is artificial, so some tuning should be possible.

The easiest way to get the directed light beam from the WGM laser is just to cleave the resonator into two or more pieces. Such half-disk or quarter-disk laser is similar to the stripe laser, and the Q-factor of the resonator is determined by the mirror transparency. The possible advantages of such device are the small size and the doubling of the unidirectional optical power for a half-disk laser compared with a strip one. For a quarter-disk

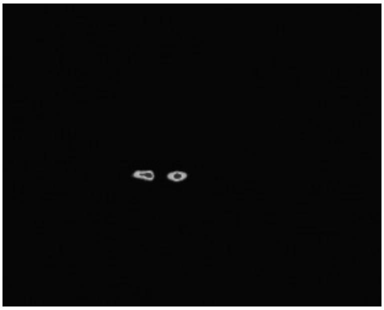

14.17 IR image of an operating half-disk QWGM laser.

laser, there are two perpendicular light beams that can be used for double-arm spectrometry. Of course, all the tales about high Q-factor and traveling waves in WGM lasers should be forgotten for these devices. Such a device was discussed in Monakhov *et al.* (2009). The IR image of the operating half-disk laser is shown in Fig. 14.17.

In order to have the Q-factor of the WGM resonator under control and simultaneously get the directed output light beam, some more sophisticated constructions were proposed. One of the first ideas was to deform the shape of the resonator. The ellipsoidal and stadium-shaped resonators (Gmach *et al.*, 1998), limaçon-shaped resonators (Yi *et al.*, 2009) and other 'warped' resonators were proposed. In some of these devices the directional beam was observed, but the devices where this effect took place appeared to operate in bouncing-ball mode in a confocal resonator (see Fig. 14.4). So, strictly speaking, instead of light extracting from WGM they operated on the other mode.

Another, but ideologically close, approach to the problem under consideration was proposed in Apalkov and Raikh (2004); Rubin and Deych (2010). Both these papers are theoretical studies of the influence of a single defect on light scattering in WGM resonators. The main result of these papers is that the proper-shaped defect in a proper position can provide a highly directive beam from the WGM resonator (cylindrical in the first and spherical in the second paper). To the best of our knowledge this effect has not yet been experimentally observed.

In our opinion, the most promising way to make use of the WGM laser as a light source is the coupling the WGM laser with the optical waveguide. The coupling of the WGM resonator with different shaped waveguides was studied in many papers, both theoretically and experimentally (von Klitzing *et al.*, 2001; Chiasera *et al.*, 2010; Murugan *et al.*, 2010). The optical trigger discussed above includes this coupling, but without optimization (Hill *et al.*, 2004). In the paper Nshii *et al.* (2010) a unidirectional quantum cascade ring

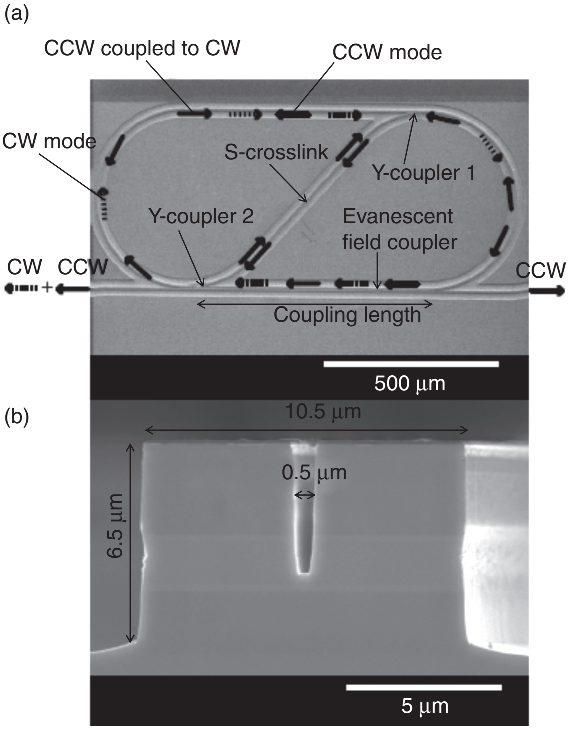
(a)
CCW coupled to CW
CCW mode
CW mode
S-crosslink
Y-coupler 1
Y-coupler 2
Evanescent field coupler
CW CCW
+
CCW
Coupling length
500 μm
(b)
10.5 μm
0.5 μm
6.5 μm
5 μm

14.18 WGM laser with suppressed counterclockwise (CCW) mode. From Nshii *et al.* (2010).

laser operating at a wavelength of around 3.4 μm at 200 K was reported. The distinctive feature of this device was the incorporation of the output coupler into the device and the suppression of the counterclockwise wave in the resonator. The design of the device is shown in Fig. 14.18.

A more sophisticated device based on the idea of the optimal coupling with internal waveguide was proposed in Andronov (2005). Here the effect of the mode leakage into the substrate was utilized. This device is shown in Fig. 14.19.

The WGM laser has been coupled with the vertical waveguide of the complex shape that provides the optimal impedance match between the WGM laser and the waveguide. The matrix of these devices can theoretically provide sufficient output optical power. The design has not yet been realized.

14.5 Conclusion

About 100 years have passed since the explanation of the whispering gallery phenomena by Rayleigh. This effect is not widely used in practice, yet

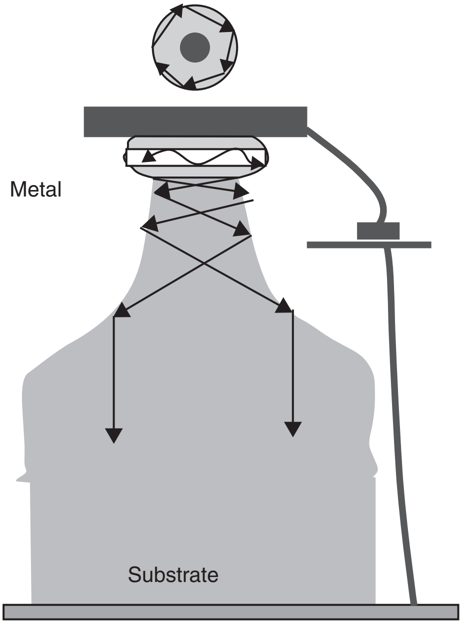

14.19 Vertically emitting WGM laser with the matched waveguide.

but it is a beautiful effect. It may be for that reason that the number of publications that mention WGM numbers thousands. The authors apologise to those who were not mentioned in this short review, but the review would have consisted only of the reference list. Apparently, all who have had a WGM laser in the hand remembers their surprise – it works! It works, despite the awry resonator and bad contacts. It works at currents at which other lasers will fail (Averkiev *et al.*, 2009, p. 717) and its work is perfectly described by equations that were developed a hundred years ago. It is even possible to check the theorem about the Bessel function roots interleaving. One clever man has said that the occupation of physics is a way to indulge your curiosity at the expense of the state. The WGM lasers is an ideal object for this purpose.

Probably WGM devices will find their application. Maybe it will be not light sources but some parts of the integrated optical circuits, or it could be something rather unexpected now. For example, the quantum computers are widely discussed now. Such a computer (that exists now only in theory) is based on so-called entangled states that are loosely speaking, the mixing of two quantum states with the same energy. The key words here are ‘quantum’ and ‘same’. As the candidates for such states the spin states of an electron or polarization states of a photon are considered now. The quantum superposition of these states is rather instable because of the spin relaxation of electron and photon absorption. The laser beam inside the ring laser seems to be a perfect candidate as a qubit component – it is two-fold degenerated in rotation direction, it is stable and it is a coherent quantum state. Maybe we missed something that prevents this usage of WGM, but who knows…

14.6 Acknowledgements

The authors are grateful to A. Baranov for constructive criticism of the draft of this chapter, V. Sherstnev for supplying some experimental data and N. S. Averkiev and Yu. P. Yakovlev for supporting the activity this chapter is based on.

14.7 References

Alekseenko, Ya. V., Monakhov, A.M. and Rozhanskii, I.V. 2009. Whispering gallery modes in a conical resonator. *Technical Physics*, **54**(11), 1633–1638.

Andronov, A. 2005. Vertically emitted leaking whispering gallery mode semiconductor lasers and laser systems. *Proceedings of 13 International symposium 'Nanostructures: Physics and Technology'*,98.

Apalkov, V.M. and Raikh, M.E. 2004. Directional emission from a microdisk resonator with a linear defect. *Physical Review B*, **70**(19), 195317 (6).

Averkiev, N.S., Astakhova, A.P., Grebenshchikova, E.A., Il'inskaya and N.D., Kalinina, K.V., Kizhaev, S.S., Kislyakova, A. Yu., Monakhov, A.M., Sherstnev, V.V. and Yakovlev, Yu. P. 2009. Continuous-wave disk WGM lasers (λ = 3.0 μm) based on InAs/InAsSbP heterostructures. *Semiconductors*, **43**(1), 117–120.

Babič, V.M. and Buldyrev, V.S. 1991. *Short-wavelength diffraction theory. Asymptotic methods*, Springer-Verlag, New York, ISBN 3–540–19189–5, 445 p.

Backes, A., Heberle, A.P., Cleaver, J.R.A. and Köhler, K. 1997. Shape dependence of emission from microdisk lasers. *Physica Status Solidi*.(b), **204**, 581–583.

Blom, F.C., van Dijk, D.R., Hoekstra, H.J.W.D., Driessen, A., Popma, T.J.A. 1997. Experimental study of integrated-optics microcavity resonators: towards all-optics switching device. *Applied Physical Letters*, **71**, 747–749.

Chiasera, A., Dumeiga, Y., Feron, P., Ferrari, M., Jestin, Y., Conti, G.N., Pelli S., Soria, S. and Regini, G.C. 2010. Spherical whispering-gallery-mode microresonators. *Laser and Photonic Reviews*, **4**(3), 457–482.

Chu, S.I., Pan, W., Sato, S., Kaneko, T., Little, B. and Kokubun, Y. 1999. Wavelength of a microring resonator filter by means of a UV sensitive polymer overlay. *IEEE Photonics Technology Letters*, **11**, 688–690.

Debye, P. 1909. Der Lichtdruck auf Kugeln von beliebigem. *Material Annalen der Physik*, **30**(11), 57–136.

Garrett, C.G.B., Kaiser, W. and Bond, W.L. 1961. Stimulated emission into optical whispering modes of spheres. *Physical Review*, **124**, 1807–1809.

Gayral, B., Gérard, J.M., Legrand, B., Costard, E. and Thierry-Mieg, V. 1998. Optical study of GaAs/AlAs pillar microcavities with elliptical cross section. *Applied Physics Letters*, **72**(12), 1421–1424.

Gmach, C., Capasso, F., Narimanov, E.E., Nöckel, I.U., Stone, A.D., Sivco, D.J., and Cho, A.Y. 1998. High-power directional emission from microlasers with chaotic resonators. *Science*, **280**, 1556–1564.

Gorodetsky, M.I., Savchenko, A.A., Ilchenko, V.S. 1996. Ultimate Q of optical microsphere resonators. *Optics Letters*, **21**(7), 453–455.

Hill, M.T. 2011. Nanolasers with a twist. *Nature photonics*, **5**, 130.

Hill, M.T., Dorren, J.S., de Vries, T., Leijtens, X.J.M., den Besten, J.H., Smalbrugge, B., Oei, Y.S., Binsma, H., Khoe, G.D. and Smit, M.K. 2004. A fast low-power optical memory based on coupled micro-ring lasers. *Nature*, **432**(11), 206.

Ilchenko, V.S. and Matsko, A.B. 2006. Optical resonators with whispering-gallery modes – part II: applications. *IEEE Journal of Selected Topics in Quantum Electronics*, **12**(1), 15–32.

Imenkov, A.N., Sherstnev, V.V., Sipovskaya, M.A., Astakhova, A.P., Grebenshchikova, E.A., Monakhov, A.M., Kalinina, K.V., Boissier, G., Teissier, R., Baranov, A.N. and Yakovlev, Yu.P. 2009a. Frequency-tuned semiconductor whispering-gallery-mode laser (λ = 2.35 μm) operating at room temperature. *Technical Physics Letters*, **35**(9), 857–860.

Imenkov, A.N., Sherstnev, V.V., Sipovskaya, M.A., Astakhova, A.P., Grebenshchikova, E.A., Monakhov, A.M., Kalinina, K.V., Boissier, G., Teissier, R., Baranov, A.N. and Yakovlev, Yu.P. 2009b. Visual observation of frequency tuning in whispering gallery mode diode laser at room temperature. *Technical Physics Letters*, **35**(12), 1149–1151.

Jaffrennou, P., Claudon, J., Bazin, M., Malik, N.S., Reitzenstein, S., Worschech, L., Kamp, M., Forchel, A. and Gérard, J.-M. 2010. Whispering gallery mode lasing in high quality GaAs/AlAs pillar microcavities. *Applied Physics Letters*, **96**(7), 071103.

Jones, B.D., Oxborrow, M., Astratov, V.N., Hopkinson, M., Tahraoui, A., Skolnick, M.S. and Fox, A.M. 2010. Splitting and lasing of whispering gallery modes in quantum dot micropillars. *Optics Express*. **18**(21), 22578–22592.

Korn, A. and Korn, M. 2000. *Mathematical Handbook for Scientists and Engineers*. McGraw –Hill Book Company, New York.

Krier, A., Sherstnev, V.V., Wright, D.A., Monakhov, A.M. and Hill, G. 2003. Mid-infrared ring laser. *Electronics Letters*, **39**, 916.

Landau, L.D. and Lifshitz, E.M. 1983. *Course of Theoretical Physics,. Vol. 2, The classical theory of fields*-4 edition – transl. from the Russian by Morton Hamermesh Uitgever, Oxford: Pergamon Press, 1983 **Pagina XI**, 402.

Levi, A.F.J., Slusher, R.E., McCall, S.L., Tanbun-Ek, T., Coblentz, D.L. and Pearton, S.J. 1992. Microdisclasers with submilliamp threshold current. *Electronics Letters*, **28**(11), 1010–1012.

Matsko, A.B., Savchenko, A.A., Strekalov, D., Ilchenko, V.S. and Maleki, S. 2005. IPN Report, August 15, 42–62.

Mie, G. 1908. Beiträge zur Optik trüber Medien, speziell kolloidaler Metallösungen. *Annalen der Physik*, **25**(3), 377–445.

McCall, S.L., Levi, A.F.J., Slusher, R.E., Pearton, S.J. and Logan, R.A. 1992. Whispering-gallery mode microdisk lasers. *Applied Physical Letters*, **60**(3), 289–291.

Monakhov, A.M., Sherstnev, V.V., Astakhova, A.P., Yakovlev, Yu.P., Boissier, G., Teissier, R. and Baranov, A.N. 2009. Experimental observation of whispering gallery modes in sector disk lasers. *Applied Physics Letters*, **94**(5), 051102.

Murugan, G.S., Panitchob, Y., Tull, E.J., Bartlett, P.N., Howak, D.W., Zervas, M.N. and Wilkinson, J.S. 2010. Tunable whispering gallery modes for spectroscopy and CQED experiments. *Journal of Applied Physics*, **107**, 053105.

Nowicki-Bringuier, Y.-R., Claudon, J., Böckler, C., Reitzenstein, S., Kamp, M., Morand, A., Forchel, A. and Gérard, J.M. 2007. High Q whispering gallery modes in GaAs/AlAs pillar microcavities. *Optics Express*, **15**(25), 17291–17304.

Nshii, C.C., Ironside, C.N., Sorel, M., Slight, T.J., Zhang, S.Y., Revin, D.G. and Cockburn, J.W. 2010. A unidirectional quantum cascade ring laser. *Applied Physical Letters*, **97**, 231107.

Oraevsky, A.N. 2002. Whispering gallery waves. *Quantum electronics*, **32**(5), 377–400.

Rawlins, A.D. 1999. Diffraction by, or diffusion into, a penetrable wedge. *Proceedings of the Royal Society A*, *London*, **455**, 2655–2686.

Rayleigh, L. 1910. The problem of the whispering gallery. *Philosophical Magazine*, **20**, 1001–1004.

Reitzenstein, S., Heindel, T., Kistner, C., Rahimi-Iman, A., Schneider, C., Höfling, S. and Forchel, A. 2008. Low threshold electrically pumped quantum dot-micropillar lasers. *Applied Physics Letters*, **93**(6), 061104.

Rubin, J.T. and Deych, L. 2010. *Ab initio* theory of defect scattering in spherical whispering-gallery-mode resonators. *Physical Review A*, **81**(5), 053827 (14).

Salem, M.A., Kamel, A.H. and Osipov, A.V. 2006. Electromagnetic fields in the presence of an infinite dielectric wedge. *Proceedings of the Royal Society A, London*, **462**, 2503–2522.

Schmidt, C., Chipouline, A., Käsebier, T., Kley, E.B., Tünnermann, A., Pertsch, T., Shuvayev, V. and Deych, L.I. 2009. Observation of optical coupling in microdisk resonators. *Physical Review A*, **80**(4), 043841 (1–9).

Sherstnev, V.V., Monakhov, A.M., Astakhova, A.P., Kislyakova, A. Yu., Yakovlev, Yu.P., Averkiev, N.S., Krier, A. and Hill, G. 2005. Semiconductor WGM-lasers for mid-infrared spectral range. *Semiconductors*, **39**(9), 1087–1122.

Sherstnev, V.V., Monakhov, A.M., Krier, A. and Hill, G. 2000. Superluminescence in InAsSb circular-ring-mode light-emitting diodes for CO gas detection. *Applied Physical Letters*, **77**, 3908–3911.

Sherstnev, V.V., Monakhov, A.M., Krier, A. and Wright, D.A. 2005. InAs whispering gallery mode lasers for the mid-infrared spectral range. *IEE Proceedings Optoelectronics*, **152**(1), 1–5.

Srinivasan, K. and Painter, O. 2007. Mode coupling and cavity-dot interaction in a fiber-coupled microdisk cavity. *Physical Review A*, **75**(2), 023814 (17p).

von Klitzing, W., Long, R., Ilchenko, V.S., Hare, J. and Lefevre-Seguin, V. 2001. Tunable whispering gallery modes for spectroscopy and CQED experiments. *New Journal of Physics*, **3**(1), 14–28.

Yi, C.H., Kim, M.W. and Kim, C.M. 2009. Lasing characteristics of a Limaçon-shaped microcavity laser. *Applied Physical Letters*, **95**, 141107.

15

Tunable mid-infrared laser absorption spectroscopy

F. K. TITTEL and R. LEWICKI, Rice University, USA

DOI: 10.1533/9780857096401.3.579

Abstract: This chapter discusses state-of-the-art, mid-infrared spectroscopic techniques used for the detection and monitoring of various specific molecular species, such as NH_3, NO and NO_2, based on laser absorption spectroscopy (LAS), cavity ring-down spectroscopy (CES), conventional and quartz-enhanced photoacoustic spectroscopy (CPAS and QEPAS) as well as Faraday rotation spectroscopy (FRS). A critical component for each technique is to use an optimum laser source and a detector matched to the detection technique with the option to apply wavelength, frequency and amplitude modulation to the laser source. A significant improvement to trace gas detection systems using spectroscopic techniques has been achieved with the development of high performance mid-infrared semiconductor lasers, in particular quantum cascade lasers (QCLs), since 1994. This has led to increased spectral resolution and high detection sensitivity of molecular trace gas species in the mid-infrared range. Spectroscopic sensors based on QCLs are capable of real time, ultra-sensitive detection of trace gas molecular species that vary in concentration from the per cent level down to parts per trillion (ppt). Such sensors can be used in a wide range of applications that include environmental monitoring, medical and biomedical diagnostics, public health issues, industrial process control and analysis as well as in national defense and security.

Key words: laser absorption spectroscopy, cavity-enhanced spectroscopy, photoacoustic and quartz-enhanced spectroscopy, Faraday rotation spectroscopy, quantum and interband cascade lasers, environmental monitoring, breath analysis.

15.1 Introduction

Laser-based spectroscopic techniques are useful for the quantitative detection and monitoring of molecular trace gas species in the mid-infrared spectral region. The spectroscopic instrumentation generates a measurable signal that depends on the absorption of the target medium. The choice of an optimum detection scheme depends on the requirements of the specific application and the characteristic features of the infrared laser source. Well established detection methods include several types of multipass gas absorption cells with the option to apply wavelength, frequency and amplitude modulation to the laser source. Intra and external cavity-enhanced spectroscopy are two methods to increase the magnitude of the absorption signal. Photoacoustic and photothermal, open path monitoring (with and without retro-reflector), such as light detection and ranging (LIDAR), differential optical absorption spectroscopy (DOAS) laser induced fluorescence (LIF), laser breakdown spectroscopy (LIBS) and fiberoptic or waveguide evanescent wave spectroscopy are other useful mid-infrared detection schemes. A key optical component for LAS has been the introduction and commercial availability of high performance semiconductor lasers, in particular quantum cascade lasers (QCLs) since 1994 (Faist *et al*., 1994) and interband cascade lasers since 1995–96 (Yang, 1995; Meyer *et al.*, 1996). The development of both QCLs and ICLs continues worldwide (Capasso, 2010; Vurgaftman *et al.*, 2010; Razeghi *et al.*, 2010; Bismuto *et al.*, 2011; Gupta *et al.*, 2010; Zeller, 2010). QCLs are convenient mid-infrared sources for ultra sensitive and highly selective trace gas monitoring as a result of recent advances in their design and technology. They can be fabricated to operate over a wide range of mid-infrared wavelengths from ~3 to ~24 μm. Continuous wave (CW) QCL devices capable of thermo-electrically cooled, room-temperature operation with several important practical features – including single mode emission with mode-hop free frequency tuning, high power (tens to hundreds of mWs), and intrinsic narrow emission line widths – are commercially available in the ~4–12 μm spectral region (Curl *et al.*, 2010; Capasso, 2010). These spectral characteristics permit the development of robust and fieldable trace gas sensors (Kosterev and Tittel, 2002; McManus *et al.*, 2010; Lee *et al.*, 2011; Lewicki *et al.*, 2011). For example, the Rice Laser Science group has explored the use of several methods for carrying out infrared laser absorption spectroscopy (LAS) with mid-infrared QCL and interband cascade laser (ICL) sources, which include multipass absorption spectroscopy (Weidmann *et al.*, 2005), cavity ring down spectroscopy (CRDS) (Kosterev *et al.*, 2001), integrated cavity output spectroscopy (ICOS) (Bakhirkin *et al.*, 2006; McCurdy *et al.*, 2007b), photoacoustic spectroscopy (PAS) and quartz-enhanced photoacoustic spectroscopy (QEPAS) (Kosterev *et al.*, 2005a; Lewicki *et al*, 2007b; Dong *et al*, 2010; Kosterev *et al*, 2010b), as well as Faraday rotation spectroscopy (Lewicki *et al.*, 2009; Zaugg *et al.*, 2011). These spectroscopic techniques permit the detection and quantification of molecular trace gases with demonstrated detection sensitivities ranging from parts per million by volume (ppmv) to parts per trillion by volume (pptv) levels depending on the specific gas species and the detection method employed.

15.2 Laser absorption spectroscopic techniques

In conventional absorption spectroscopy (CAS), using broadband incoherent radiation sources, such as thermal emitters, the wavelength resolution is determined by the resolving power of the spectral analyzer or spectrometer. LAS, on the other hand, uses coherent light sources, whose linewidths can be ultra-narrow and whose spectral densities can be made many orders of magnitude larger (~10^9W/(cm^{2}MHz)) than those of incoherent light sources. The key advantages of mid-infrared LAS include the following.

1. An absorption spectrum that can be acquired directly by scanning the laser source across a desired rotational-vibrational resolved feature of the target analyte.
2. High detection sensitivity with maximum accuracy and precision.
3. Improved spectral selectivity or resolution compared with CAS due to the narrow linewidths (i.e. for CW QCLs ~0.1–3 MHz with a high quality power supply or <10 kHz with frequency stabilization and for pulsed QCLs ~300 MHz).
4. Fast response time.
5. Good spatial resolution. This can involve remote sensing via LIDAR, a mobile laboratory, aircraft, or networks of ground- or marine-based sensors.
6. Detector noise that becomes negligible for sufficiently large laser intensities.
7. Non-intrusive methods, such as balanced detection or zero air subtraction, to suppress laser intensity fluctuations that can be readily applied to increase the signal-to-noise ratio (SNR) and hence improve the LAS detection sensitivity, i.e. the minimum detectable absorption limit.
8. Spatially coherent laser light that can be collimated, which allows the use of long pathlength absorption and cavity-enhanced spectroscopy (CES) cells.
9. The laser frequency can be locked to the center of a resolved molecular absorption line to determine the center wavelength or wavenumber of the line with ultra-high precision and accuracy.
10. Size, weight, electrical power, thermal management, gas and wavelength calibration, protection from harsh environment, autonomous operation and remote access for long periods of time.
11. Ease of instrument operation and data reduction.

15.2.1 Laser absorption spectroscopy

During the past 25 years, mid-infrared LAS techniques have become extremely sensitive, commercially available and effective spectroscopic tools from ~ 3 to 12 μm (it should be noted that Sb-based laser diodes, ICLs and QCLs spectral coverage from 2 to 24 μm has been demonstrated and reported in the literature (Belenky *et al.*, 2011; Christensen *et al.*, 2010; Curl *et al.*, 2010; Capasso, 2010) for the detection and quantification of numerous molecular trace gas species. As result of these LAS advances, molecular trace gases can now be measured in ultra small quantities in numerous laboratory and field applications. Furthermore, single atoms and different isotopes of the same atom can be detected for different chemical species. In the mid-infrared region, the optical sensor systems, which employ different spectroscopic techniques, can be employed to obtain detection sensitivities in the ppmv to pptv range, depending on the specific gas species and the detection method employed. These high sensitivities are obtained using various overtone combination and fundamental rotational-vibrational molecular absorption bands located between the 3 and 24 μm wavelengths of the mid-infrared region. The mid-infrared absorption spectra of several small molecules of potential interest for trace gas monitoring are shown in Fig. 15.1 within two mid-infrared atmospheric transmission windows.

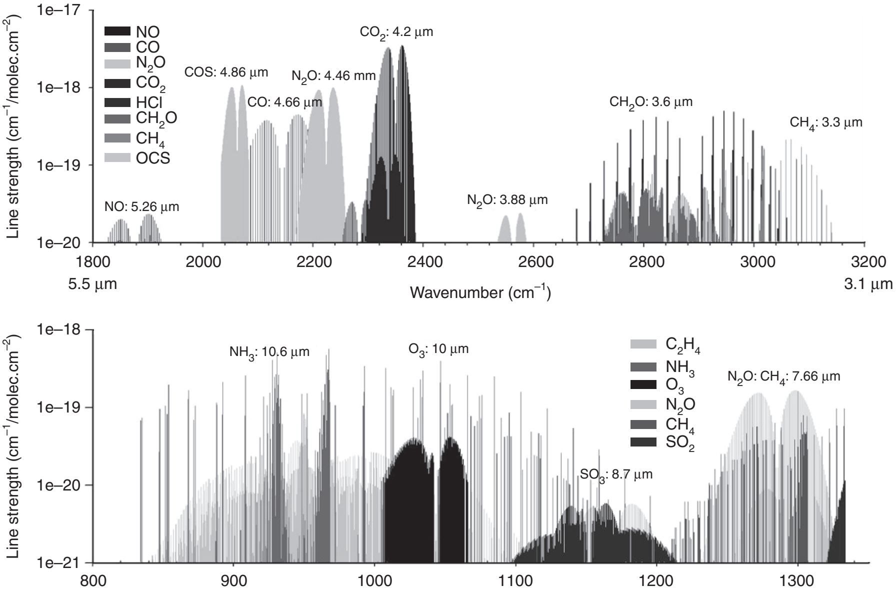

15.1 High-resolution transmission molecular absorption database (HITRAN) simulation of absorption spectra in two mid-infrared atmospheric transmission windows (Kosterev *et al.,* 2008).

The primary requirements for trace gas sensing are sensitivity and selectivity. For small molecules with resolved rotational structure, the selectivity is obtained by choosing an absorption line that is free of interference from other species that might be present in the analyzed sample. Moreover, selectivity is obtained by implementing a laser source that possesses a sufficiently narrow linewidth. For small molecules, reducing the sample pressure sharpens the absorption line without reducing the peak absorption, which significantly improves selectivity. This condition continues until the linewidth begins to approach the Doppler width (Kosterev *et al.*, 2008).

Fundamentals of LAS at a certain frequency υ (cm^{-1}) can be expressed by Beer–Lambert's law:

$$I(\upsilon) = I_o(\upsilon)e^{-\alpha(\upsilon)L} \qquad [15.1]$$

where $I(\upsilon), I_o(\upsilon)$ are the intensity of transmitted and incident laser light, $\alpha(\upsilon)$ is the absorption coefficient (cm^{-1}), and L is the effective optical path-length (cm). Therefore, to obtain the best absorption sensitivity one needs to choose a strong molecular absorption line, use a long effective optical path-length, and have a distinguishable absorption from baseline variations and laser power fluctuations. The first requirement is best met by choosing a target line associated with fundamental absorption bands, as these are stronger than overtone or combination bands. A sufficiently long path-length can be obtained by using multipass cells or cavity enhancement techniques. For sharp absorption lines, noise associated with laser power fluctuations can be reduced by averaging rapid scans over the line or by employing the wavelength modulation spectroscopy (WMS) technique in the kHz regime (Schilt *et al.*, 2003; Schilt and Thévenaz, 2006). In most applications, one detects the modulated absorption at twice the modulation frequency using a lock-in amplifier set to second harmonic (2f). The second harmonic signal is maximum at the absorption line center. The final requirement to distinguish absorption from baseline variations is the most challenging. Every long pass arrangement exhibits accidental etalons, which typically have widths comparable to that of an absorption line. In principle, these can be removed by evacuating the cell, replacing the sample with 'zero air' gas, which contains no trace gas species of interest, and then dividing the sample trace by this background trace. However, this approach assumes that these accidental etalons do not shift their pattern during the process of sample replacement, although this is often not the case (Curl *et al.*, 2010). Numerous research groups (Fried *et al.*, 1997, 1998; Fried and Richter, 2007; Zahniser *et al.*, 1995; Werle *et al.*, 2011) have investigated and reported on the merits of rapid background subtraction, in particular WMS and frequency modulation spectroscopy (FMS), to effectively remove optical noise.

For more complex, multi-atomic molecules, which do not have resolved rotational structure, the spectroscopic detection process is more demanding. The only way to detect absorption is through the process of pumping the sample out and replacing it with zero air, due to the absence of a nearby baseline for comparison. For weak absorption features, this imposes severe limits on the long-term power stability of the laser source, the absence of low frequency laser noise, and baseline stability. Furthermore, in the mid-infrared fingerprint region, where many gases absorb, there may be other gases contributing to a broad absorption that might significantly disrupt the selectivity of concentration measurements.

For open path systems, a serious risk for selective measurements might be encountered because (1) there is no way to replace the sample with zero air for providing a baseline trace, and (2) there is no way to reduce the linewidths (typically 0.1 cm^{-1} at atmospheric pressure), which in some cases might be too large to perform wavelength modulation spectroscopy at an optimum modulation depth. Obtaining a long pathlength by using a multipass cell suffers from neither of these problems. The only issue with this approach is that long path multipass cells are intrinsically bulky. Long optical pathlengths are obtained by employing multipass absorption cells where the optical beam is reflected back and forth between concave mirrors. Numerous implementations have been reported in the literature, but four fundamental designs (White, Herriott, astigmatic Herriott and Chernin) have been used to achieve optical pathlengths of ~100 m physical lengths for ~0.5 m distance between the mirrors (McManus *et al.*, 1995). Cavity ringdown spectroscopy (CRDS) has been demonstrated to give excellent sensitivity (Kosterev *et al.*, 2001; Tittel *et al.*, 2003; Rao and Karpf, 2010), but requires very high quality, low loss mirrors. Long path lengths in small volumes can be provided by off-axis integrated cavity output spectroscopy (ICOS) which has considerable promise for trace gas sensing (Bakhirkin *et al.*, 2004; Bakhirkin *et al.*, 2006; McCurdy *et al.*, 2007b). Other ultra-sensitive and highly selective spectroscopic techniques that are employed by research groups for trace gas detection are: balanced detection (Sonnenfroh *et al.*, 2001), laser induced breakdown spectroscopy (LIBS) (Gottfried *et al.*, 2009), noise immune cavity enhanced optical heterodyne molecular spectroscopy (NICE-OHMS) (Ye *et al.*, 1998; Foltynowicz *et al.*, 2008), conventional photoacoustic spectroscopy (CPAS) (Elia *et al.*, 2009; Lima *et al.*, 2006), quartz-enhanced photoacoustic spectroscopy (QEPAS) (Kosterev and Tittel 2004; Kosterev *et al.*, 2005b), and Faraday rotation spectroscopy (FRS) (Litfin *et al.*, 1980; Ganser *et al.*, 2003; Lewicki *et al.*, 2009). The latter three techniques, and CRDS and ICOS will be described in the following sections of this chapter.

15.2.2 Cavity enhanced spectroscopy: CRDS and ICOS

The conventional method to perform sensitive laser-based absorption spectroscopy measurements is to increase optical path-length by using an optical multipass gas cell. However, such an approach can be difficult to implement in certain field applications, requiring compact gas sensor configurations. For example, a typical commercial 100 m path-length multipass cell has a volume of 3.5 l (Curl *et al.*, 2010). An alternative way to obtain a long optical path is to make the light bounce along the same path between two ultralow-loss dielectric mirrors forming a high finesse optical resonator, called a ringdown cavity (RDC). Cavity ring-down spectroscopy is based on the principle of measuring the rate of decay of light intensity inside the RDC. The transmitted wave from an injected pulsed or CW laser into the CRD decays exponentially in time. The decay rate is proportional to the losses inside the RDC. For typical RDC mirrors having a reflectivity of 99.995%, and spaced ~20 cm, an effective optical pathlength of 8 km is obtained, which exceeds the best performance of multi-pass cell spectroscopy. The light leaking out of the RDC can be used to characterize the absorption of the intracavity medium. The optical loss is the difference between total cavity losses and empty cavity losses. Once the absorption spectrum of the sample has been measured, then the sample concentration can be determined using the absorption cross-section and the lineshape parameters. A good CRDS system can achieve a minimum detectable absorption limit of $\sim 4 \times 10^{-10}$. Detailed mathematical treatment of CRDS can be found in the literature (Busch and Busch 1999; Paldus and Kachanov 2005).

Several techniques exist to perform CRDS (O'Keefe and Deacon 1988; Ramponi *et al.*, 1988; Scherer *et al.*, 1997) or integrated cavity output spectroscopy (ICOS) and its variant, off-axis ICOS (OA-ICOS), a technique where one observes time integrated ring-down events (O'Keefe, 1998; O'Keefe *et al.*, 1999; Bakhirkin *et al.*, 2004; McCurdy *et al.*, 2007b). In these techniques the coupling efficiency of the laser radiation into the resonant cavity is extremely critical and determines the amount of light which can be collected by a photodetector placed after the absorption cell.

The CRDS technique is intrinsically background-free. When carried out with high power pulsed lasers, CRDS requires only high quality cavity mirrors, a reasonably fast detector and appropriate data acquisition electronics. This technique is harder to implement with QCLs, which have pulse powers of only a few times their CW output (Manne *et al.*, 2006). This power limitation can be overcome by locking the cavity to the laser to fill the cavity followed by rapid laser turn off. Alternatively, the cavity can be dithered while a CW laser is scanned slowly (Paldus *et al.*, 2000; Kosterev

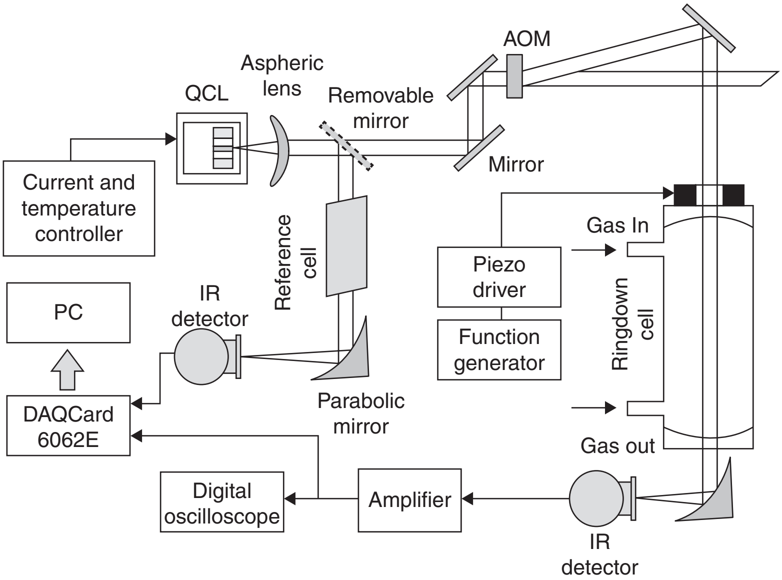
AOM
Aspheric lens
QCL
Removable mirror
Mirror
Current and temperature controller
Reference cell
Gas In
Piezo driver
Function generator
Ringdown cell
PC
IR detector
Parabolic mirror
DAQCard 6062E
Gas out
Digital oscilloscope
Amplifier
IR detector

15.2 A typical CRDS-based sensor platform using an acousto-optic modulator (AOM) as a high speed beam chopper.

et al., 2001; Sukhorukov *et al.*, 2006; Rao and Karpf, 2010). A typical CRDS-based sensor platform is shown schematically in Fig. 15.2.

For off-axis ICOS (OA-ICOS), in which the optical sensor system is aligned in such a way that a maximum number of longitudinal and transverse modes is excited within the cavity, the typical optical throughput of the cavity is on the order of $\leq T/2$ (where T is transmission of the cavity mirrors) (Paul *et al.*, 2001). This method is related to absorption spectroscopy using a multipass cell with the significant difference that in ICOS the beams are allowed to overlap on the mirrors after many cavity passes. The principal effect limiting sensitivity is output fluctuations (noise) caused by transmission noise due to the resonant mode structure. One approach for minimizing this noise is to arrange that the laser spots on the mirrors exhibit a circular pattern similar to those of the Herriot multipass cell. If many passes of the cavity take place before any of these spots overlap, interference effects are minimal because the path-length before overlap exceeds the coherence length of the laser. By introducing a small amount of astigmatism, the entire surface of the mirrors can be used (Paul *et al.*, 2001). Another approach for removing mode noise in OA-ICOS is to vibrate the mirrors (Bakhirkin *et al.*, 2006, Engel *et al.*, 2006). This causes many mode hops to take place within the time required to empty the cavity, effectively averaging out this noise. Thus the trade-off between multipass absorption and ICOS is that in multipass absorption, this mode noise is not present because the spots never overlap, but for similar mirror size and separation, the total path-length can be much greater in ICOS. Since there are no mirror holes in the ICOS cavity configuration to admit and allow the exit of the beam (laser radiation is transmitted through the cavity mirrors), ICOS requires more laser power, which is available with QCL excitation. A medical application of QCL-based OA-ICOS for the measurement of NO and CO_2 in exhaled breath was reported in McCurdy *et al.* (2007b). More recently, an OA-ICOS instrument for the measurement of isotope ratios in water in order to obtain information about the role of water in global climate change was reported (Sayres *et al.*, 2009). Furthermore, by combining OA-ICOS with multiple line integrated absorption spectroscopy an ultrahigh sensitivity of 28 ppt for NO_2 detection was achieved (Rao and Karpf, 2011).

15.2.3 Conventional and quartz-enhanced photoacoustic spectroscopy

CPAS is a well-established trace gas detection method based on the photoacoustic effect. In this method the acoustic wave is created as a result of molecular absorption of laser radiation which is either intensity or wavelength modulated. Such an acoustic wave, when it propagates within the photoacoustic (PA) cell, can be detected by a sensitive microphone (Miklos *et al.*, 2001; Rossi *et al.*, 2005). Instead of a single microphone device, an array of microphones is employed in some CPAS systems to achieve more sensitive results for trace gas detection (Hofstetter *et al.*, 2001b; Elia *et al.*, 2005). In contrast to other infrared absorption techniques, CPAS is an indirect technique in which the effect on the absorbing medium, rather than the direct light attenuation, is analyzed. Therefore, no photodetector is required in the CPAS technique. However, an infrared detector right after the photoacoustic (PA) cell is usually employed for the purpose of monitoring laser power and performing a line locking procedure.

In order to obtain an optimal acoustic signal for amplitude modulated CPAS measurements, the laser modulation frequency is typically selected to match the first longitudinal acoustic resonance of the PA cell, given by the equation $f = v/2L$, where v is the speed of sound and L is the length of cell. The resonance frequencies of PA cells are usually selected to be > 1 kHz in order to make the CPAS technique immune to the intrinsic $1/f$ type noise of the microphone and its pre-amplifier and to low frequency external acoustic noise (da Silva *et al.*, 2004; Pushkarsky *et al.*, 2006b; Lima *et al.*, 2006). However, the PAS design does not allow a reduction of the photoacoustic cell volume below ~10 cm^3.

The detected PA signal (S_{PA}) is described by the following equation:

$$S_{\text{PA}} = CP\alpha cM, \qquad [15.2]$$

where C is the PA cell constant (Pa/(Wcm^{-1})), P is optical power of the laser (W), α is the absorption coefficient of the targeted gas (cm^{-1}/(molecule cm^{-3})), c is concentration (molecule/cm^3), and M is the microphone response (V/Pa).

Ideally, CPAS is a background-free technique because only the absorption of modulated laser radiation generates an acoustic signal. However, background signals can originate from nonselective absorption of the gas cell windows (coherent noise) and external acoustic (incoherent) noise. Therefore, proper isolation of the photoacoustic cell from any mechanical vibrations will result in an improvement of the measured signal-to-noise ratio (SNR). Further CPAS signal enhancement can be achieved by employing a different PAS cell design, such as a resonance photoacoustic cell with two buffer tubes (Rey and Sigrist, 2008) or a ring differential resonance photoacoustic cell (Miklos *et al.*, 1999; Lee *et al.*, 2007). Schematic diagrams of both designs are depicted in Fig. 15.3.

In the two-buffer-tubes PA cell design (Fig. 15.3a), the $\lambda/4$ buffer volume in line with the longitudinal acoustic resonator acts as an acoustic notch filter at the frequency of the resonator, in order to effectively suppress system flow noise (Bijnen *et al.*, 1996). In a differential PA cell (Fig. 15.3b), two identical cylindrical channels are equipped with a microphone, which is placed in the middle of each channel, where the maximum pressure oscillations are observed. Because the CPAS signal is proportional to the absorption coefficient and the laser power, it is possible for both designs to achieve minimum detectable concentrations at the sub-ppb level by selecting the strongest absorption lines of the target gas and by using high power laser sources such as CW CO_2 and CO lasers, optical parametric oscillators, fiber amplifiers, or CW DFB-QCLs or EC-QCLs (Bernegger and Sigrist, 1990; Sigrist and Thoeny, 1993; Costopoulos *et al.*, 2002; Pushkarsky *et al.*, 2003, 2006; Webber *et al.*, 2003; Ng *et al.*, 2004; Mukherjee *et al.*, 2008).

A novel approach to the photoacoustic detection of trace gases, utilizing a quartz tuning fork as an acoustic transducer, was first reported in 2002 (Kosterev *et al.*, 2002, 2005b). The key innovation of this new method, named quartz enhanced photoacoustic spectroscopy (QEPAS), is to invert the common CPAS approach and accumulate the acoustic energy in a sharply resonant piezoelectric transducer with a very high quality factor (Q-factor) of >10 000, rather than in a broadband microphone and low *Q* (~200) resonant CPAS gas cell. A suitable candidate for such a transducer is a quartz tuning fork (QTF), which is commonly used as a frequency standard in digital clocks and watches. When the QTF is mechanically deformed, electrical charges are generated on its surface only when the

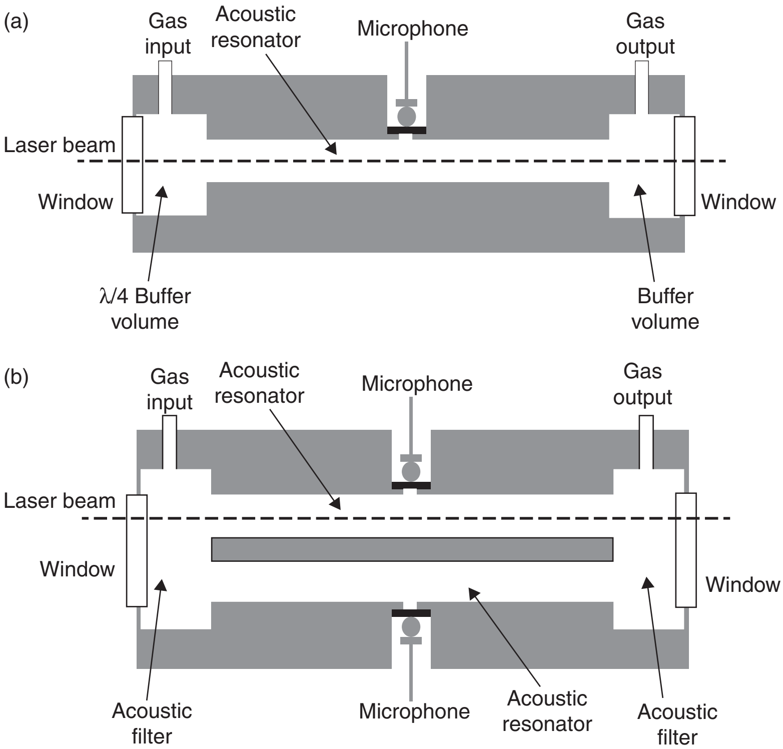
(a)
Gas input
Acoustic resonator
Microphone
Gas output
Laser beam
Window
Window
λ/4 Buffer volume
Buffer volume
(b)
Gas input
Acoustic resonator
Microphone
Gas output
Laser beam
Window
Window
Acoustic filter
Microphone
Acoustic resonator
Acoustic filter

15.3 (a) Block diagram of a two-buffer-tubes PA cell design and (b) a ring differential resonance PA cell design.

two prongs move in opposite directions (antisymmetric mode of vibration). Thin silver films deposited on the quartz surfaces collect these charges, which can then be measured as either a voltage or a current, depending on the electronic circuit used. In vacuum, QTFs typically resonate at 32 768 (2^{15}) Hz which results in a high immunity of QEPAS devices to environmental acoustic noise.

The photoacoustic signal measured by a QEPAS sensor is proportional to:

$$S_0 \sim \frac{\alpha \cdot P \cdot Q}{f_0}, \qquad [15.3]$$

where α is an absorption coefficient, P is optical power, Q is the quality factor of the resonator and f_0 is resonant frequency (Kosterev *et al.*, 2005a). The Q-factor is dependent upon pressure p and can be expressed as:

$$Q = \frac{Q_{\text{vac}}}{1 + Q_{\text{vac}} \cdot a \cdot p^b}, \qquad [15.4]$$

where Q_{vac} is the quality factor in vacuum and a and b are parameters dependent on a specific quartz TF design (Kosterev *et al.*, 2005b). The pressure corresponding to optimum sensitivity depends upon the vibrational to translational (V-T relaxation) energy conversion cross-section of the gas of interest. In addition, if the V-T relaxation rate is lower than the optical excitation modulation frequency, the amplitude of the optically induced acoustic signal is reduced. This effect is more significant for QEPAS due to the high modulation frequency of ~32.8 kHz. It is more likely to occur with small (2–3 atoms) molecules such as NO, CO, or CO_2, which do not have a dense ladder of energy levels to facilitate V-T relaxation. It was experimentally determined in Kosterev *et al.* (2005b) that the optimum pressure for fast-relaxing molecules with resolved optical transitions is <100 Torr, which also ensures Doppler-limited spectral resolution. For slow relaxing gases this optimum pressure is higher and may give a broader linewidth than desirable for the best selectivity.

In a typical QEPAS scheme the laser beam is focused between the QTF prongs as shown in Fig. 15.4a. In this case, the probed optical path is only as long as thickness of the QTF, or ~0.3 mm. Therefore, QEPAS is mostly sensitive to a sound source positioned in a 0.3 mm gap between the prongs. Sound waves from distant acoustic sources tend to move the QTF prongs in the same direction, which results in a zero net piezo-current and makes this element insensitive to such excitation. A configuration shown in Fig. 15.4a can be useful when the excitation radiation cannot be shaped into a near-Gaussian beam, like spatially multimode lasers. The simplest configuration with bare QTF was used in some experiments (Wysocki *et al.*, 2006) and theoretically analyzed in Petra *et al.* (2009). However, the sensitivity can be significantly improved using a configuration as shown in Fig. 15.4b, where a metal tube is added on each side of the QTF to confine the optically generated acoustic vibrations in the gas and increase the effective interaction length between the radiation-induced sound and the QTF (Lewicki *et al.*, 2007a). With respect to the QTF, these tubes can act as an additional acoustic microresonator. Recent experimental studies have revealed that the optimum length for each microresonator tube is somewhere between $\lambda_s/4$ and $\lambda_s/2$ of the propagating sound wavelength (λ_s) (Dong *et al.*, 2010). Thus, for optimal microresonator configuration, where each microresonator tube is 4.4 mm in length and 0.6 mm in inner diameter, an up-to-30 times improvement in SNR can be observed in comparison to the bare QTF configuration (Dong *et al.*, 2010). Most QEPAS-based sensors utilize a configuration illustrated in Fig. 15.4b. A typical QTF, used in most QEPAS measurements to date, is illustrated in Fig. 15.4c. Other QEPAS spectrophone configurations, such as off-beam QEPAS, are also possible (Liu *et al.*, 2009, 2010). Furthermore, two novel modifications of the QEPAS sensor architecture based on interferometric photoacoustic spectroscopy (Köhring *et al.*, 2011)

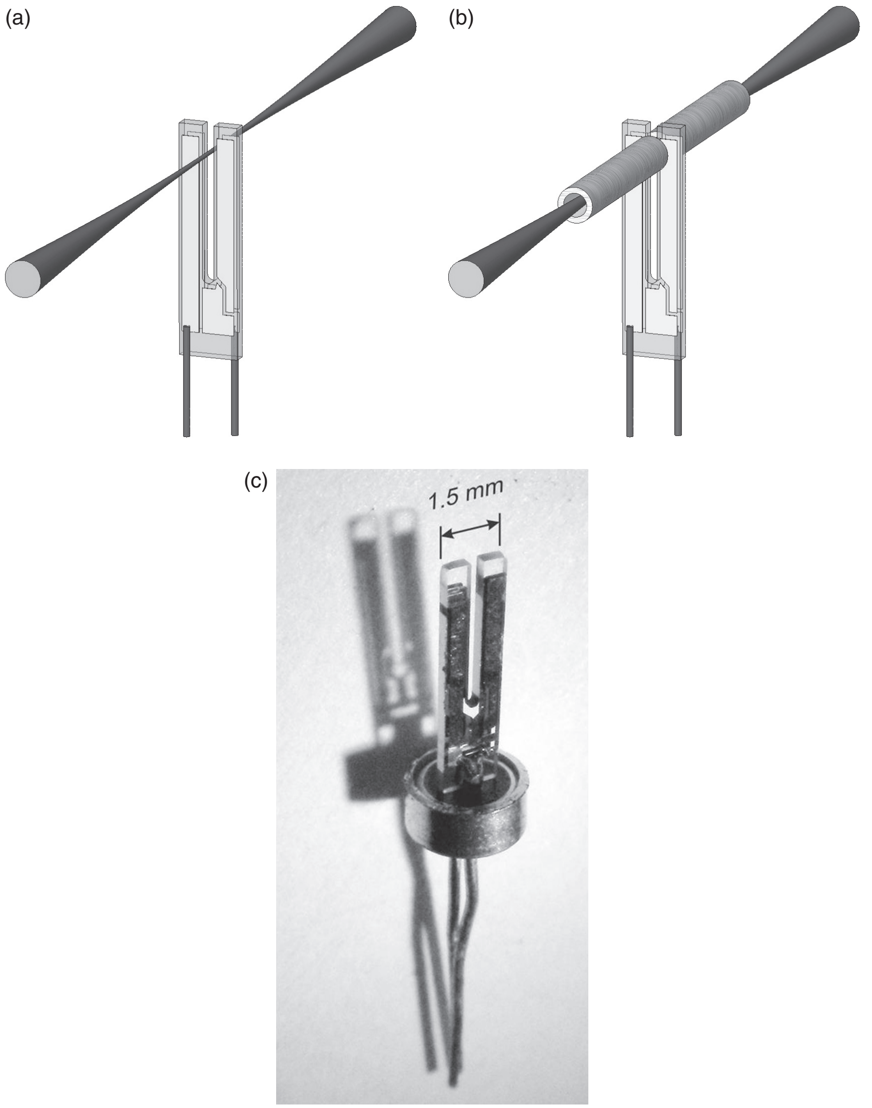

15.4 QTF-based spectrophones: (a) simplest spectrophone configuration and (b) an improved spectrophone configuration with an acoustic resonator formed by two pieces of rigid tubing (Kosterev *et al.*, 2010b); (c) a typical quartz tuning fork geometry used in QEPAS trace gas measurements.

and resonant optothermoacoustic detection (Kosterev and Doty, 2010) were reported recently.

Like conventional photoacoustic spectroscopy, QEPAS does not require optical detectors and also benefits from the high optical power of laser source. This feature is especially attractive for gas sensing in the 4–20 μm region, where the availability of high-performance optical detectors is limited, and cryogenic cooling is often required. In spectroscopic measurements based on the QEPAS technique, either the laser wavelength is modulated at $f_{\mathrm{m}} = f_0/2$, or its intensity is modulated at $f_m = f_0$ frequency (where f_0 is the QTF resonant frequency), depending on whether a wavelength modulation or amplitude modulation technique is used, respectively. In most QEPAS sensor designs, a $2f$ wavelength modulation (WM) spectroscopy has been used (Kosterev and Tittel 2004; Kosterer *et al.*, 2004b, 2005a, 2006; Horstjann *et al.*, 2004; Wysocki *et al.*, 2006; Lewicki *et al.*, 2007a; Spagnolo *et al.*, 2010). This technique provides complete suppression of any coherent acoustic background that might be created when stray modulated radiation is absorbed by nonselective absorbers, such as the gas cell elements and the QTF itself. In this case, the noise floor is usually determined by thermal noise of the QTF (Grober *et al.*, 2000). In the case of amplitude modulation (AM), the QEPAS sensitivity limit is no longer determined by the QTF thermal noise alone, but by laser power fluctuations and spurious interference features as well. Therefore, AM is often used for detecting large, complex molecules, when individual rovibrational transitions are not resolved and applying the WM technique is not possible (Wojcik *et al.*, 2006; Lewicki *et al.*, 2007b; Bauer *et al.*, 2009, 2010; Kosterev *et al.*, 2010a).

A direct, side-by side comparison of a QEPAS sensor using a QTF enhanced with a microresonator and a CPAS sensor based on a state-of-the-art differential resonance photoacoustic cell (Lee *et al.*, 2007) was demonstrated in Dong *et al.* (2010). Using the $2f$ WM technique, the sensitivities obtained for both QEPAS and CPAS were within the same detection range when both fast (10 ppmv C_2H_2 in N_2) and slow (pure CO_2) relaxing molecules were investigated. A small advantage of the CPAS technique over the QEPAS technique for the analysis of pure CO_2, results from a lower modulation frequency and therefore a longer response time ($\tau = Q/\pi f$) of the CPAS spectrophone. However, in most cases the QEPAS detection sensitivity for slow relaxing molecules can be improved by adding a molecular species such as H_2O (Lewicki *et al.*, 2007a; Spagnolo *et al.*, 2010) or SF_6 (Kosterev *et al.*, 2005a), which eliminates the V-T relaxation bottleneck.

15.2.4 Faraday rotation spectroscopy (FRS)

FRS has been used for many years as a very sensitive and selective technique for the spectroscopic investigation of paramagnetic molecules such as nitric oxide (Litfin *et al.*, 1980; Adams *et al.*, 1984; Ganser *et al.*, 2003; Fritsch *et al.*, 2008; Sabana *et al.*, 2009; Lewicki *et al.*, 2009; Kluczynski *et al.*, 2011), nitrogen dioxide (Dillenschneider and Curl, 1983; Smith *et al.*, 1995), oxygen (Brecha *et al.*, 1997; So *et al.*, 2011) and hydroxyl radicals (Pfeiffer *et al.*, 1981; Zhao *et al.*, 2011). This technique takes advantage of the dispersion effects of paramagnetic molecules immersed in a longitudinal magnetic field to reveal their unique property to rotate light polarization.

In the presence of a magnetic field, rovibrational transitions of molecules that possess a permanent magnetic dipole moment undergo Zeeman splitting. The magnetic field breaks the degeneracy of the molecular rotation states into $2J + 1$ sublevels labeled by the quantum number M_J. Moreover, in the vicinity of a Zeeman-split absorption line of the paramagnetic molecule, circularly polarized components have different wavelength dependent complex propagation constants. Each circularly polarized component interacts either with the $\Delta M_J = +1$ or $\Delta M_J = -1$ NO transition components. For linearly polarized light, which can be considered a superposition of right hand (RHCP) and left hand circularly polarized (LHCP) light, propagation for a distance L through a paramagnetic medium rotates its plane of polarization by an angle $\Theta = \Delta n L\pi / \lambda$, where $\Delta n = n_R - n_L$ is the difference between the refractive index for RHCP (n_R) and LHCP (n_L), respectively. The change in polarization state can be monitored by placing the gas cell between two nearly crossed Rochon polarizers (RP) and detecting the intensity modulation of the light emerging from the second polarizer, also called an analyzer. For small rotation angles, the polarization rotation and thus the detector signal is directly proportional to the concentration of paramagnetic species inside the cell. The polarization rotation angle can be detected very precisely using an applied modulated magnetic field and phase sensitive detection. Since the polarization rotation, and thus the variation, of the analyzer transmission exist only when the paramagnetic molecules are present in the gas cell, FRS is considered a zero optical background technique.

The basic FRS setup is shown in Fig. 15.5. For low gas concentrations and short optical paths, the magnetic circular dichroism associated with the

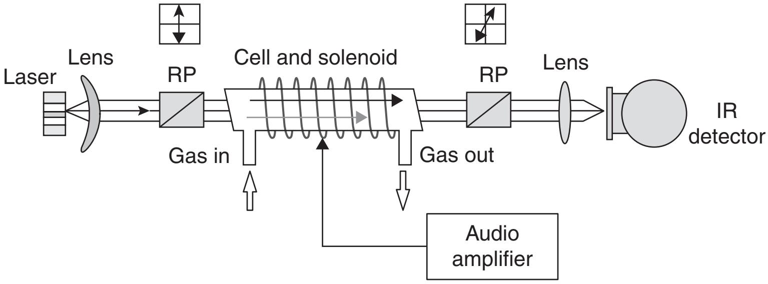

15.5 Schematic diagram of the 90° FRS scheme. Two RPs are nearly crossed at an angle determined to give the best S/N. Black and grey arrows indicate different light velocities observed for RHCP and LHCP light propagated within the gas cell.

difference between absorption coefficients for RHCP and LHCP light is negligible. In a good approximation, only the magnetic circular birefringence (MCB) signal resulting from the difference between two dispersion curves contributes to the final FRS signal recorded by a low-noise photodetector. This detection method was first reported in the 1980s with a color-center laser source to reduce source noise and improve the sensitivity of the FRS method (Litfin *et al.*, 1980).

For the FRS technique two methods have been used for polarization rotation measurements. The first measurement method, called the 90-degree method, uses two polarizers and a single photodetector to sense the transmitted light intensity (Litfin *et al.*, 1980). In the 90-degree method, laser noise suppression is achieved by nearly crossing the analyzer, thus reducing the amount of laser amplitude noise arriving at the detector. In a situation where the main noise source arises from laser amplitude fluctuations, improved sensitivity through FRS is achieved by reducing laser source noise by a factor larger than the simultaneous reduction of signal. Source noise from laser amplitude fluctuations is at a minimum when the polarizers are exactly crossed and initially increases quadratically upon uncrossing. The FRS signal is null at the exact crossing, but increases linearly upon uncrossing. Therefore, the SNR enhancement can be obtained because the signal is an approximately linear function of the displacement of the analyzer angle from minimum transmitted light, while the noise has a quadratic dependence on the angle. In addition, detector noise is unaffected by the polarizer crossing angle. Quantum or shot noise grows with uncrossing in the same way as the signal. The second measurement method, called a differential detection scheme (Adams *et al.*, 1984) orients the second Rochon polarizer at 45° to the first. This splits the original beam into two equally intense beams of perpendicular polarization; these beams are directed to two balanced detectors and the Faraday rotation is measured as a difference between the two signals. Which method is best depends on several factors: laser power, source noise in the laser, saturation of the absorption, and detector parameters (such as sensitivity, saturation, and linearity). Frequency modulation can be used with any of the FRS methods to approach quantum noise (QN) limited performance (Smith *et al.*, 1995).

The SNR enhancement for both methods is achieved in slightly different ways, but, fundamentally, both are based upon the efficient suppression of laser amplitude noise while maximizing the Faraday rotation signal. Moreover, in both methods, the spectral shape of the FRS signal is the sum of the differences between Zeeman shifted dispersion curves. Depending on the ratio of laser intensity fluctuations to detector noise at the modulation frequency, the SNR can be limited either by detector noise for quiet sources or by polarizer quality for noisier sources. There is an optimum analyzer angle for the 90-degree method, which depends upon detector noise or polarizer quality (Lewicki *et al.*, 2009).

15.3 Quantum-cascade lasers (QCLs) for trace gas detection

Distributed feedback QCLs (DFB-QCLs) and external cavity QCLs (EC-QCLs) are reviewed followed by broad gain medium designs.

15.3.1 Distributed feedback quantum-cascade lasers (DFB-QCLs)

In order to utilize QC laser sources for accurate spectroscopic measurements, narrow linewidth and single longitudinal mode operation of the QCLs are essential. The single longitudinal mode operation of QCL devices based on Fabry–Pérot cavities can be achieved either creating a distributed feedback (DFB) at a precisely selected wavelength (Faist *et al.*, 1997; Gmachl *et al.*, 1998; Hofstetter *et al.*, 1999; Hofstetter *et al.*, 2001a; Aellen *et al.*, 2003; Xu *et al.*, 2006) by introducing a periodic grating structure on the top of the QCL waveguide, or by using an external cavity (EC) configuration (Wysocki *et al.*, 2005; Maulini *et al.*, 2005; Wysocki *et al.*, 2008).

The single-mode wavelength λ_B of the DFB laser is determined by the Bragg reflection condition $\lambda_B = 2n_{\mathrm{eff}}d$, where n_{eff} is the effective refractive index of the waveguide and d is the period of the diffraction grating. Light satisfying this condition is strongly reflected off the grating and is selected for laser action. Wavelength tuning of the DFB lasers is mainly achieved by the temperature dependence of the refractive index and can be obtained by changing the temperature or by varying the injection current (Joule heating) of the laser. By increasing the temperature of the laser structure, the effective refractive index n_{eff} increases resulting in a higher emitted wavelength (lower emitted frequency). For state-of-the-art DFB-QCLs, typical current and temperature tuning coefficients are -0.01 cm^{-1}/mA and -0.16 cm^{-1}/K, respectively. This results in a total spectral range of 4 to 5 cm^{-1} and 15 to 20 cm^{-1} for maximum current and temperature tuning ranges, respectively. However, an increase of the QCL temperature during the tuning process can result in a decrease of the output optical power, which must be avoided for power dependent spectroscopic techniques such as CPAS or QEPAS. Therefore, DFB-QCLs are typically designed for operation at a single target frequency with a practical tuning range of few cm^{-1} (Yu *et al.*, 2005). Moreover, they are usually used in trace gas detection and quantification of small molecules with narrow, well resolved rotational-vibrational lines (Bakhirkin *et al.*, 2006; McCurdy *et al.*, 2007a; Grossel *et al.*, 2008).

The spectral tuning range of DFB-QCLs was recently extended by fabricating an array of 32 DFB lasers that were grown on a single chip and driven individually by a microelectronic controller (Lee *et al.*, 2007). The active region of each laser consists of 35 stages based on bound-to continuum design centered at 9 μm. The DFB-QCLs array operating in a pulsed mode offers a wide continuous spectral tuning range of 85 cm^{-1} from ~1064 cm^{-1} (9.4 μm) to 1149 cm^{-1} (8.7 μm) (Lee *et al.*, 2009a). The continuous spectral coverage of the DFB-QCLs array is achieved by small range temperature tuning to eliminate any spectral gaps. The lasers can be heated locally by changing dc current value delivered to the individual laser or heated by changing the temperature of the heatsink on which the laser array is mounted. The former process can reach the desired wavelength in milliseconds, while the latter process requires several seconds. The DFB QC lasers linewidth, estimated to be ~0.01 cm^{-1} in pulsed operation and ~0.001 cm^{-1} in CW operation, is significantly better than the resolution offered by a typical 'bench top' FTIR (~0.1 cm^{-1}). Furthermore, the same group fabricated an ultra-broadband DFB-QCLs array, consisting 24 DFB-QCLs which have a heterogeneous cascade structure based on two bound-to-continuum designs centered at 8.4 and 9.6 μm (Lee *et al.*, 2009b). This resulted in an overall frequency tuning range of 225 cm^{-1}, centered at 1150 cm^{-1} (~8.7 μm). The 24 single-mode DFB-QCLs array has proven its capability as a spectroscopic source for sensitive detection of different broadband absorbing molecular species including isopropanol, methanol, and acetone (Lee *et al.*, 2007).

Nowadays single frequency CW DFB-QCLs can provide >100 mW of optical power at room temperature (Yu *et al.*, 2005). Recently, a single-mode emission of more than 150 mW output power was demonstrated for CW RT (room temperature) 7.74 μm DFB-QCL devices fabricated with a buried grating geometry (Troccoli *et al.*, 2010). Approximately 100 mW of optical power was demonstrated for 3.8 W of electrical power consumption with a DFB device at a TEC accessible temperature of 263 K (Wittmann *et al.*, 2009). A state-of-the-art 2.4 W TEC CW operated DFB-QCL was recently demonstrated at 4.8 μm (Lu *et al.*, 2011). High power single mode operation and 10% peak wall plug efficiency from one facet at 298 K was obtained. This was achieved by a surface-plasmon coupling mechanism as well as a combination of high-reflection and antireflection dielectric coatings. Moreover, high power, CW, TE-cooled DFB-QCLs are also commercially available (e.g., www.3–5lab.fr, www.alpeslasers.ch, www.atoptics.com, www.hamamatsu.com, www.nanoplus.com, www.maxion.com).

15.3.2 External cavity quantum-cascade lasers (EC-QCLs)

Another approach to achieve single frequency operation is to integrate a Fabry–Pérot QCL with broadband gain medium (Faist *et al.*, 2001; Faist *et al.*, 2002) into an EC configuration (Maulini *et al.*, 2004; Maulini *et al.*, 2005; Wysocki *et al.*, 2005; Maulini *et al.*, 2006). The main advantage of using EC-QCL sources, as compared to DFB-QCLs and DFB-QCL array devices, is primarily due the fact that they have a much wider wavelength tuning range which is only limited by the effective bandwidth of the QCL gain medium. Hence, EC-QCL sources are better choices to perform simultaneous spectroscopic measurements of multiple chemicals species or broadband absorbing molecular species detection. The implementation of the near RT and wide gain profile pulsed Fabry–Pérot QCLs into external cavities resulted in a wide frequency tuning range of 432 cm^{-1} (Hugi, 2009; Hugi, 2010) and ~200 cm^{-1} in CW mode (Maulini, 2006; Pushkarsky, 2006a; 2006b; Wysocki, 2008; Wittmann, 2008; Hugi, 2009; Hugi, 2010).

An EC-QCL system consists of three main optical elements: a QCL gain chip, an aspherical lens to collimate laser light, and a diffraction grating which acts as a wavelength-selective filter. The two most commonly used configurations for grating-coupled EC systems which employ a QCL as a gain medium are the Littman-Metcalf (Phillips, 2007) and the Littrow configurations (Arnold, 1998). Each type of EC configuration has its special advantage, which makes it best suitable for a certain type of applications. General performance and wavelength tuning behavior of QC lasers in Littrow and Littman-Metcalf cavity configurations were studied in detail in Guipeng (2002), demonstrating similar wavelength tuning properties for both configurations. For trace gas detection, Littrow configured external cavity quantum-cascade laser (EC-QCL) systems (Lewicki *et al.*, 2007b; Wysocki *et al.*, 2008; Karpf and Rao 2009; Scherer *et al.*, 2009; Tsai and Wysocki 2010; Spagnolo *et al.*, 2010) are more often employed than Littman-Metcalf systems (Phillips *et al.*, 2007). In the Littrow configuration, the first-order diffraction beam is directly feedback to the laser, which results in obtaining an optimal condition for the QCL tuning range. Due to the double diffraction from the grating the Littman-Metcalf configuration offers narrower linewidth than the Littrow configuration at the expense of both optical power and spectral tuning range due to decreased grating feedback strength.

In a Littrow configured EC-QCL a coarse wavelength tuning is achieved by varying the angle of the diffraction grating. This will result in discrete tuning jumps between the internal Fabry–Pérot cavity modes of the laser chip or between EC modes. Both cavity modes are separated by $\nu \approx 1/2nL$, where L is the cavity length and n is the refractive index of the cavity medium. In order to achieve continuous, fine mode-hop free tuning, the cavity length and grating angle must track each other. The mode-hop free tuning ability and tuning range is significantly improved when an anti-reflection (AR) coating is implemented at the front facet of the Fabry–Pérot QCL. In this case, the effect of the optical cavity formed by the laser itself is eliminated and stronger feedback from the diffraction grating to the laser chip is achieved. Furthermore, a high reflection coating deposited on the back facet improves the optical gain within the QCL gain structure.

Several interesting schemes of fine wavelength tuning based on EC systems were demonstrated in the following publications (Maulini *et al.*, 2005; Wysocki *et al.*, 2005; Pushkarsky *et al.*, 2006a; 2008; Day, 2010). In the first scheme, a fine wavelength tuning was achieved by varying the grating angle and the laser current or the heatsink temperature at the same time (Maulini *et al.*, 2005). However, this configuration suffers from mode hopping due to the lack of control for the EC length when the laser was tuned. Thus, the laser jumped between modes separated by ν ~0.05 cm^{-1}, which was very hard to observe with 0.125 cm^{-1} maximum resolution of FTIR spectrometer. Wysocki *et al.* at Rice University demonstrated an EC-QCL architecture that employed a piezo-activated cavity mode tracking system that provided independent control of the EC and the QCL lengths as well as the diffraction grating angle for mode hop free operation (Wysocki *et al.*, 2005; 2008). The wavelength tuning is realized by simultaneous control of all three system features significant for the mode tracking: grating angle, EC length, and the laser current. Another approach enabling continuous mode hop free tuning of the EC-QCL system was achieved by simultaneously adjusting the grating angle and periodically varying the laser injection current to achieve a continuous shift of the Fabry–Pérot comb of the gain chip (Pushkarsky *et al.*, 2006b). In this method the laser current value is selected to have one of the Fabry–Pérot modes of the gain chip exactly coincide with the desired output frequency as the laser is tuned. To support single-mode operation at every selected grating angle, fine adjustments of the EC length was achieved by the grating mounted on the rotational stage operated by a piezoelectric linear translator. To minimize the effect of spectral mode hops across the modes of the EC, a very long EC length of 1 m was used, resulting in Fabry–Pérot mode spacing of 0.005 cm^{-1}.

An interesting scheme based on a miniature EC system wavelength tuning has been implemented by Daylight Solutions (www.daylightsolutions.com). The Daylight Solutions EC-QCL consists of a 25 mm long optical cavity length, miniature grating tuning mechanism, and integrated current and temperature controls. The laser chip facet facing the grating is AR coated, while the output facet is left uncoated. The radiation from both facets was collimated with a pair of AR coated aspheric lenses. Wavelength tuning of these systems is realized with a Littrow grating angle controlled by means of a stepper motor and an integrated absolute optical encoder with microprocessor-based closed loop controller (Pushkarsky *et al.*, 2008; Caffey *et al.*, 2010). The grating motion is mechanically constrained to follow a trajectory allowing for the simultaneous tuning of the diffraction grating angle and the laser cavity length, thereby constraining the EC mode to coincide with the wavelength selected by the grating. Another miniature EC-QCL from

Daylight Solutions using a microelectromechanical systems (MEMS)-based grating for fine adjustment of the laser wavelength within limited tuning range was recently demonstrated in Weida *et al.*, (2010). The MEMS-based EC-QCL system, inside a 2 cc volume high heat load (HHL) laser package will offer a precise mode hop free tuning within approximately ± 8 cm^{-1} from its center wavelength. This tuning range is sufficient to perform high-resolution gas-phase spectroscopy of molecules with narrow spectral features.

15.3.3 Quantum-cascade laser broad gain medium designs

Several schemes of broad gain QCL designs have been demonstrated by several groups. The first scheme employs at least two stacks of cooperative quantum-well active regions of dissimilar intersubband optical transitions, leading to a heterogeneous cascade over a very wide spectral range (Gmachl *et al.*, 2001). Each active region stage needs to be specially engineered to achieve an optimally flat gain spectrum over the emission range of interest. For two active regions designed to emit at 5 and 8 μm, a supercontinuum emission of the laser from 6 to 8 μm was achieved and demonstrated for the first time in Gmachl *et al.* (2002).

The second scheme is based on a single bound-to continuum active region design (Faist *et al.*, 2002) or heterogeneous quantum-cascade structure based on two bound-to-continuum designs (Maulini *et al.*, 2006; Wittmann *et al.*, 2008). In a bound-to continuum design the radiative transitions occur between a single upper state and closely spaced sublevels (quasi-miniband) of final lower states. Therefore, the oscillator strength that describes the strength of the transition is not concentrated in a single radiative transition but is extended over multiple transitions, giving rise to a broad gain spectrum of the QCL. The first implementation of a Fabry–Pérot QC laser based on the bound-to-continuum design coupled to an EC was demonstrated in 2004 exhibiting a broad tuning range of 150 cm^{-1} at 10 μm (Maulini *et al.*, 2004). The first heterogeneous cascade QCL based on two bound-to-continuum active region designs, exhibiting a gain spectrum width (FWHM) as large as 350 cm^{-1}, was demonstrated in 2008 (Wittmann *et al.*, 2008). Each active region of this heterogeneous laser structure was designed to emit radiation at 8.2 and 9.3 μm wavelengths. A coarse frequency tuning from 1013 cm^{-1} (9.87 μm) to 1305 cm^{-1} (7.66 μm) and from 1045 cm^{-1} (9.57 μm) to 1246 cm^{-1} (8.02 μm) was achieved in pulsed and CW operation, respectively for the laser implemented into a Littrow type EC-QCL configuration and operated at RT. The demonstrated spectral tuning range for the pulse operated EC-QCL is 292 cm^{-1} which is 25% of the laser center frequency.

The ultra-broad gain quantum-cascade laser was developed using five distinctive substacks (ST) based on bound-to continuum design to form the active region (Hugi *et al.*, 2009). In order to obtain a flat gain spectrum and achieve a gap free tuning over the whole spectral emission range, the gain of each substack of the active region, centered at 7.3, 8.5, 9.4, 10.4, and 11.5 μm wavelength was optimized. After coupling the laser in a Littrow EC setup a total wavelength coverage from 7.6 μm to 11.4 μm (1309–878 cm^{-1}), with a peak optical output power of 1W and an average output power of 15 mW at RT was demonstrated. The obtained frequency tuning of 432 cm^{-1} results in a record spectral tuning range of 39.5% at about the QCL center frequency. In addition, this design scheme is not limited to the specific wavelength and can be customized to access other mid-IR spectral regions. Recent advances in broadly tunable EC-QCL systems comprising different bound-to continuum active region designs are demonstrated in Hugi *et al.* (2010).

Recently, an interesting approach to the fabrication of homogeneous broad gain QCLs based on dual upper state design was demonstrated by researchers from Hamamatsu (Fujita *et al.*, 2010). In their design, the electrons are injected into the higher upper state 4 of active regions, via resonant tunneling from ground state, and then, they are quickly distributed in the two upper laser states by optical-phonon scattering or by electron-electron scattering. The broad and symmetric optical gain is achieved not only due to $E_{43} \sim 20$ meV in energy difference, between two 4-to-2 and 3-to-2 radiative transition levels, but also due to equal oscillator strengths of the transitions from both upper laser states to the lower common laser state. The dual upper state-based QCL devices exhibit a homogeneously wide electroluminescence spectra of >330 cm^{-1} and insensitivity to the temperature or voltage changes. In CW operation at 300 K, the optical output laser power was 152 mW.

Another example of broadband QCL gain medium is based on 'continuum-to-bound' active region design, where the two lower injector states are strongly coupled with the upper laser state (Yao *et al.*, 2010a). Ultra-strong coupling between the injector states and the upper laser state improves electron injection efficiency, reduces the transit time from injectors to the active region, and provides three laser transitions that are separated by an energy of ~20 meV. The radiative transitions from these three coupled states contribute to a large gain spectrum width of ~250 cm^{-1} full width at half maximum, which enables EC tuning of the lasers over 200 cm^{-1}. Recently, the same group demonstrated a 'continuum-to-continuum' quantum-cascade laser design (Yao *et al.*, 2010b), where optical transitions from four strongly coupled upper states to lower laser states contribute to the gain spectrum. In this design, a broad gain bandwidth of over 400 cm^{-1} has been demonstrated in the 4–5 μm wavelength region.

15.4 Specific examples of QCL-based sensor systems

Various applications of EC-QCL-FRS and DFB-QCL-QEPAS are described in the following subsections.

15.4.1 Faraday rotation spectroscopy for ultra-sensitive detection of nitric oxide and nitrogen dioxide

FRS is a well-recognized detection technique that is highly sensitive and selective to paramagnetic molecules only. Therefore, the FRS technique is well suited for atmospheric detection of prominent air pollutants (NO, NO_2) or for exhaled breath analysis (NO) (Mürtz and Hering, 1999). This is because interference from diamagnetic species, such as water and carbon dioxide, is effectively eliminated. Biogenic NO released from human sweat, has also been monitored with the FRS technique (Ganser *et al.*, 2004).

Access to the optimum spectral range for FRS measurements molecular transitions of the paramagnetic species of interest allow accurate quantitative measurements at or below the parts-per-billion by volume (ppbv) levels (Lewicki *et al.*, 2009; Kluczynski *et al.*, 2011; Zaugg *et al.*, 2011). For sensitive FRS detection of NO the best choice is the $Q_{3/2}(3/2)$ molecular transition at 1875.81 cm^{-1} (5.33 μm) (Ganser *et al.*, 2003). Tuning to this line was made possible by employing a widely tunable CW TE-cooled EC-QCL as a spectroscopic source (Wysocki *et al.*, 2008). The total EC-QCL frequency tuning range, between 1825 cm^{-1} (5.48 μm) and 1980 cm^{-1} (5.05 μm), allows most of the lines within the fundamental absorption band of NO at 5.2 μm to be targeted with a single laser source.

The experimental arrangement of the FRS platform shown in Fig. 15.6 was operated at three different laboratory locations. A widely tunable 5.3 μm EC-QCL with high-resolution MHF wavelength tuning capability was used as the spectroscopic source. In this experiment, the laser was operated in a CW mode at –20°C and provided a maximum output power of 2.9 mW at the wavelength coincident with the target NO line. MHF tuning of up to 2.5 cm^{-1} permitted high-resolution spectroscopy within the tuning range.

The collimated EC-QCL beam (4 mm in diameter) was split by a ZnSe wedge into two independent optical paths. In the main path the laser beam propagated through a 50 cm long optical gas cell located inside a 44 cm long solenoid. The gas cell was placed between two nearly crossed MgF_2 RPs (the extinction ratio for both polarizers is $\xi < 10^{-5}$). When a longitudinal magnetic field was applied, the linearly polarized QCL beam experienced a Faraday rotation of the plane of polarization as a result of the interaction with paramagnetic NO molecules. The Faraday rotated light, passing through a second polarizer, was detected by either a mid-infrared

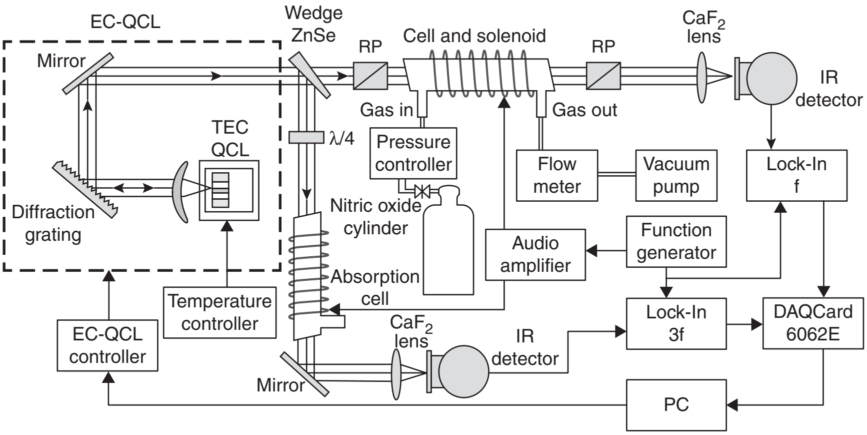
EC-QCL
Mirror
Wedge ZnSe
RP
Cell and solenoid
RP
CaF_2 lens
IR detector
Gas in
Gas out
TEC QCL
λ/4
Pressure controller
Flow meter
Vacuum pump
Lock-In f
Nitric oxide cylinder
Diffraction grating
Audio amplifier
Function generator
Absorption cell
Temperature controller
EC-QCL controller
CaF_2 lens
IR detector
Lock-In 3f
DAQCard 6062E
Mirror
PC

15.6 Schematic diagram of an EC-QCL-based FRS experimental setup. RP – Rochon polarizer, λ/4 – quarter wave plate, PC – personal computer (Lewicki *et al.*, 2009).

thermoelectrically cooled mercury-cadmium-telluride (MCT) photodetector or liquid-nitrogen cooled indium-antimonide (InSb) photodetector. The solenoid current was driven at f_m = 950 Hz with a commercial high power audio amplifier (QSC audio model: RMX850). To minimize the power requirements for driving the reactive load of the solenoid at ~1 kHz, a series resonant circuit was constructed matching the modulation frequency (f_m). The modulated Faraday rotation resulted in AC amplitude modulation of the transmitted light intensity, which was detected using a phase sensitive lock-in detection at the frequency f_m. For calibration of the FRS spectrometer, two cylinders containing a mixture of 10 ppmv and 96 ppbv of NO in N_2 were used. The system gas flow rate was set to ~300 ml/min.

The second optical branch of the sensor was used as the reference channel for frequency control of the EC-QCL. The initial linear polarization of the laser radiation was transformed into circular polarization by passing it through a quarter wave-plate (λ/4) (Alphalas, tunable quarter wave-plate). The beam was directed through a 20 cm absorption gas cell filled with a mixture of 5% NO by volume in air at 25 Torr. The reference absorption cell was placed inside a 10-cm long solenoid that produced an axial magnetic field. The second solenoid was a part of the series RLC circuit formed with the main solenoid, and was supplied from the same high power audio amplifier. In the presence of alternating magnetic field, a Zeeman modulation signal resulting from the interaction between circularly polarized light and NO molecules through magnetic circular dichroism was observed. The Zeeman signal was recorded by a thermoelectrically cooled MCT photodetector and demodulated by a second lock-in amplifier at the third harmonic of f_m. Zeeman detection at the third harmonic, although providing a lower SNR than the conventional 1st harmonic detection, is less sensitive to the electromagnetic interference induced in the system at the fundamental modulation frequency (e.g. electromagnetic interference induced in the signal interconnects and front-end electronics). The zero-crossing of the third harmonic signal is used to lock the EC-QCL frequency to the peak of the optimum $Q_{3/2}(3/2)$ molecular transition of NO at 1875.81 cm^{-1} (5.33 μm). This active wavelength locking technique significantly reduces frequency drift and improves the long-term system stability.

A series of experiments were performed to determine the optimum magnetic field strength, sample gas pressure, and the analyzer offset angle. The best result for the FRS signal amplitude was obtained experimentally at a pressure of 40 Torr and for a magnetic field of B = 110 Gauss$_{\text{rms}}$, measured inside the main magnetic coil. The best SNR for a lock-in time constant of 1 sec occurs an angle offset of ~7° from the crossed position when using a thermoelectrically cooled MCT photodetector (with area of 1 mm^2 and peak detectivity of $D^* > 2 \times 10^{10}\,\text{cm}\sqrt{\text{Hz}}/\text{W}$ at 5 μm). However, for better long-term stability of the system, it is preferable to work with smaller offset angles. For an experimental demonstration of the effect of improved photodetector performance on the system SNR, measurements using a 1 mm diameter liquid-nitrogen cooled InSb photodetector with a specified peak detectivity at 5 μm of $D^* > 1 \times 10^{11}\,\text{cm}\sqrt{\text{Hz}}/\text{W}$ were performed. For this case, the optimum analyzer offset was found to be 2–3° from its crossed position.

The high-resolution magnetic rotation spectra of nitric oxide acquired with two different photodetectors for a certified reference gas mixture of 96 ppbv of NO in nitrogen are depicted in Fig. 15.7. Both spectra were recorded under the same experimental conditions (p = 40 Torr, B = 110 Gauss$_{\text{rms}}$), and show only the two strongest $Q_{3/2}(3/2)$ and $Q_{3/2}(5/2)$ molecular transitions at 1875.81 cm^{-1} (5.33 μm) and 1875.72 cm^{-1}, respectively. For the MCT detector (Fig. 15.7a), a 1σ minimum detection limit (MDL) of 4.3 ppbv was obtained for NO concentrations with a 1 s lock-in time constant and analyzer offset angle of $\alpha = 7°$. A significantly improved detection limit was obtained with the LN$_2$ cooled InSb photodetector, resulting in a 1σ MDL of 380 ppt for the same 1 sec lock-in amplifier time constant and analyzer offset angle of 3° (Fig. 15.7b). Equivalent minimum detectible fractional absorptions of 6.7×10^{-7} and 5.9×10^{-8} were obtained for the MCT and InSb detector, respectively. All of these results were achieved with short active optical paths of 44 cm. Usually to obtain similar detection limits with standard laser absorption spectroscopic techniques, significantly longer optical path lengths, ranging from several to hundreds of meters, are required (Moeskops *et al.*, 2006; McManus *et al.*, 2006).

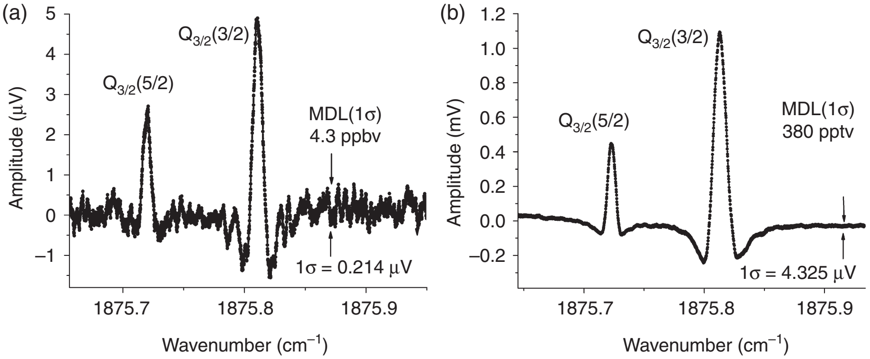

15.7 (a) Faraday rotation spectrum of $Q_{3/2}(3/2)$ and $Q_{3/2}(5/2)$ transitions of nitric oxide centered at 1875.8 cm^{-1} measured with a thermoelectrically cooled MCT photodetector and (b) with a liquid nitrogen cooled InSb photodetector (Lewicki *et al.*, 2009).

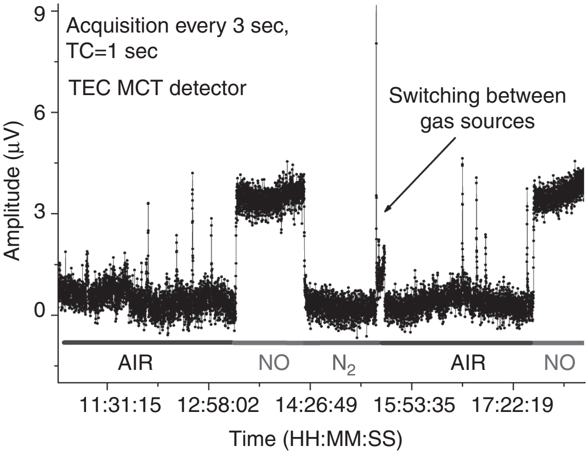

15.8 Long-term NO concentration measurements performed with active laser frequency locking to the NO absorption line at 1875.81 cm^{-1} (5.33 μm) with MCT photodetector. Acquisition every 3s, lock-in amplifier time constant (TC) set to 1 s.

In order to perform continuous and long-term autonomous operation of the FRS sensor platform on the selected molecular transition (1875.81 cm^{-1}) an active EC-QCL frequency locking technique was implemented. To prevent detuning of the laser from the resonance with the NO $Q_{3/2}(3/2)$ transition, a computer-based active feedback loop provides simultaneous control of the three independent laser parameters: the EC length, the diffraction grating angle and QCL injection current. The atmospheric data, measured alternately with a certified mixture of 96 ppbv NO in N_2 and pure N_2, are shown in Fig. 15.8 as an example for FRS system's capability for continuous unattended operation. During measurements of the air, a number of sharp peaks of NO concentration, primarily related to automobile activity, were detected. The data were acquired every 3 s with a lock-in time constant of 1 s by using the RT MCT detector (7° analyzer offset angle).

The MDL observed in the absorption line-locked mode of operation is about two times higher than the MDL determined from the spectral measurements in Fig. 15.7. This increase in the observed MDL value is related to the limited precision of a relatively slow computer-based active feedback control of the laser wavelength. A more important issue is an offset from the zero signal and a baseline drift which can be caused by electronic pick-up of the 950 Hz modulation current, into the detection system, the laser driver system, or both. For a system limited by photodetector noise a decrease of the analyzer offset is affecting the SNR. In addition, if the analyzer angle is too large the laser intensity variations will be incident on the detector and thus appear in the FRS signal. Therefore, it is necessary to select the conditions that provide optimum long-term stability and a sufficient MDL required for the particular application. Thus, better long-term performance is achieved by using smaller polarizer angle offsets.

The effective suppression of a slow system drift and extended long-term stability was achieved for an analyzer offset angle of 4°. For this condition, the Allan variance calculated for recorded over ~9 h time series of nitrogen shows exceptional stability of the system, which allows for averaging times of up to ~4000 s. Allan variance plots were first introduced by Werle (Werle *et al.*, 1993) for the assessment of LAS-based instrument performance. Moreover, the long-term drift problem can be also eliminated by: (1) identifying and eliminating ground loops and electromagnetic pickup, which cause the modulation of the laser by the magnet current, or (2) scanning the laser over the line and averaging series of acquired scans. The final signal, proportional to NO concentration, can be obtained by least squares fitting the amplitude parameter of the known lineshape (as shown in Fig. 15.7) to the observed average traces.

The FRS sensor was configured as a transportable platform with a automatic gas handling and periodic calibration system for a long-term field test of NO monitoring applications. An automated and autonomous EC-QCL Faraday rotation spectroscopic sensor system was deployed at an environmental test site in Beijing operated by the Institute of Atmospheric Physics (IAP), Chinese Academy of Sciences, for continuous atmospheric NO air-quality monitoring during the 2008 Olympic Games.

Furthermore sensitive detection of NO_2 at single ppb concentration levels was performed based on a double pass configured Faraday rotation spectrometer, which is a modified version of the NO FRS system illustrated in Fig. 15.6. NO_2 is also a major atmospheric pollutant and is mostly emitted by internal combustion engines (e.g., car, trucks, or jet engines) and thermal power plants. The NO_2 FRS sensor employs a widely tunable CW EC-QCL (Daylight Solutions, Model 21062-MHF-012) operating at a temperature of 18°C and providing a maximum optical power of 150 mW. The available EC-QCL frequency tuning range, between 1538.3 cm^{-1} and 1703.3 cm^{-1}, covers the entire fundamental ν_3 band of NO_2, centered at ~1600 cm^{-1}. The optimum $4_{41} \leftarrow 4_{40}$ Q-branch NO_2 transition at 1613.25 cm^{-1} was located within the available MHF frequency tuning range between 1600 cm^{-1} and 1650 cm^{-1}. To our best knowledge, this is the first time that NO_2 was detected at this transition with an EC-QCL-based FRS technique.

For the selected NO_2 absorption line at 1613.25 cm^{-1} the optimum pressure, with respect to the highest SNR for the FRS measurements, was selected to be 30 Torr. An optimum analyzer angle of 3° from the crossed position was found to be a trade-off between the TE-cooled MCT detector signal and laser noise level transmitted by the analyzer. The experimentally determined optimum magnetic field is ~200 Gauss (rms), which corresponds to a solenoid current of ~6 A (rms). The FRS spectrum of the Q-branch NO_2 transitions in the fundamental ν_3 band was recorded for single pass configuration of the sensor and plotted for comparison with a HITRAN simulated spectrum (Fig. 15.9a). As a reference, a calibration mixture of 2 ppmv NO_2 in N_2 at the pressure of 30 Torr was used. The analyzer angle is set to 2° from the totally crossed position. The laser frequency was mod-hop free tuned over ~0.8 cm^{-1} by applying a 1 mHz sine wave with an amplitude of 60.5 V to the piezo element. The spectrum was recorded with a lock-in amplifier time constant set to 1 s. The mismatch of the transition frequencies between the simulated and measured spectrum is caused by a slight non-linearity in the frequency tuning of the EC-QCL (Zaugg *et al.*, 2011).

The FRS signal of NO_2 at the preferable $4_{41} \leftarrow 4_{40}$ transition (1613.25 cm^{-1}) for double pass configuration was acquired over a narrow frequency spectral range of ~0.04 cm^{-1} and illustrated in Fig. 15.9b. For an optimum system pressure of 30 Torr and 2 ppmv of NO_2 concentration, a minimum sensitivity was found to be 1.1 ppbv (1σ) for a 1 s lock-in time constant. However, for laser frequency locked to the NO_2 transition at 1613.25 cm^{-1}, a slow drift and FRS signal fluctuations during the long-term measurements limit the minimum detection to ~2.5 ppbv. Similar to NO FRS measurements, the observed fluctuations are caused by electrical noise generated in the FRS system (ground loops and electromagnetic coupling between coil and detector), since the FRS system is insensitive to optical noise and no additional background signal is present. Further improvement in the SNR can be achieved by using better quality polarizers, more sensitive photodetectors, or by reducing the system noise. In addition, the improved detection limit of the FRS signal can be achieved by increasing the active path-length.

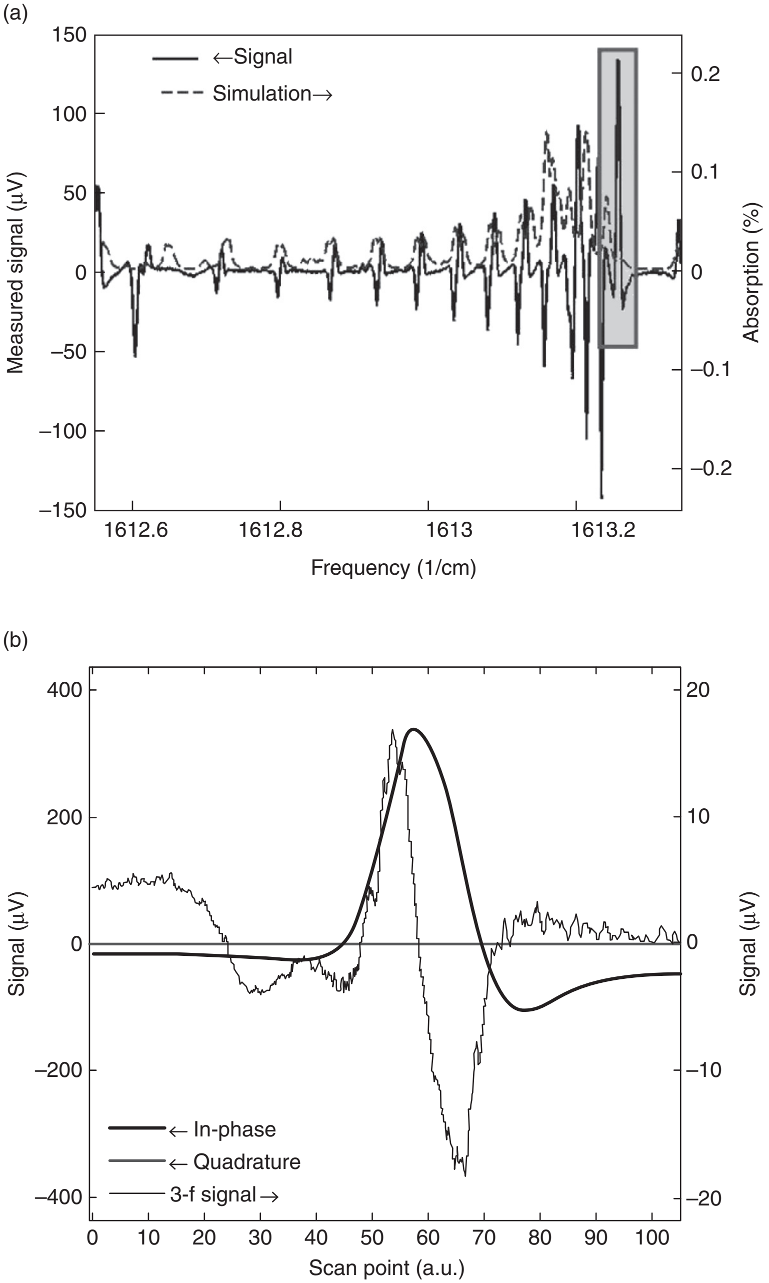

15.9 (a) NO_2 FRS signal within Q-branch of the fundamental ν_3 band for a single pass system configuration; (b) FRS signal of NO_2 at the optimum $4_{41} \leftarrow 4_{40}$ transition at 1613.25 cm^{-1} (6.2 μm) for double pass system configuration. 2 ppm NO_2 at 30 Torr.

15.4.2 Real time ammonia detection in exhaled human breath using a 10.4 μm DFB-QCL-QEPAS-based sensor

Exhaled breath is a mixture of more than four hundred molecules, some of which are present at parts-per-billion (ppb) or even parts per trillion (ppt) concentration levels (Dweik and Amann, 2008). Moreover, some of the exhaled molecules can provide a unique breath profile of the health condition and therefore can be used as biomarkers for the identification and monitoring of various types of human diseases or wellness states (Risby and Tittel, 2010). Currently, the standard analytical chemistry instrumentation used for human breath analysis is gas chromatography, based on various detection methods such as flame ionization detection (Kneepkens *et al.*, 1994; Phillips *et al.*, 1991), mass spectrometry (Cheng and Lee, 1999), ion mobility spectrometry (Westhoff *et al.*, 2009), or selected ion flow tube mass spectrometry (Smith and Španěl, 2005). However, sensitive, real time detection of molecular species in breath samples, was recently demonstrated with laser-based breath analyzers employing different spectroscopic techniques (McCurdy *et al.*, 2007b; Roller *et al.*, 2007; Mürtz and Hering, 2008; Shorter *et al.*, 2010; Thorpe *et al.*, 2008). In this section, a quantum-cascade laser-based optical breath sensor for ammonia detection will be described. By monitoring ammonia concentration levels in exhaled breath, a fast, non-invasive diagnostic method for treatment of patients with liver and kidney disorders is feasible.

The schematic diagram of the ammonia breath sensor architecture based on a QEPAS technique (Kosterev *et al.*, 2002; Kosterev and Tittel, 2004) is depicted in Fig. 15.10. The QEPAS system employs an ultra-small piezoelectric QTF enhanced with optimal microresonator tubes design, where the inner diameter and length of each tube are 0.6 mm and 4.4 mm, respectively (Dong *et al.*, 2010). The QEPAS-based trace gas sensor is capable of ultra-sensitive trace gas detection and is suitable for real time breath measurements, due to the fast gas exchange inside a compact (<4 cm^3) QEPAS gas cell, which acts as an absorption detection module (ADM) or spectrophone.

The NH_3 breath sensor employs a CW, RT, DFB-QCL in a HHL package from Hamamatsu (www.hamamatsu.com). The RT operated DFB-QCL uses only air cooling, produced by a small electronics fan and a heatsink attached to the back of the QCL. A 4 mm diameter ZnSe aspheric lens, with a working distance of 0.65 mm and clear aperture of 3.6 mm, was used to collimate the laser beam. The laser optical power, after being transmitted through the spectrophone was found to be 22 mW, which is ~90% of the initial power of the DFB-QCL operated at 17.5°C. The photoacoustic signal is detected by the QTF, amplified by a low-noise transimpedance preamplifier and delivered to a control electronics unit (CEU) for further data

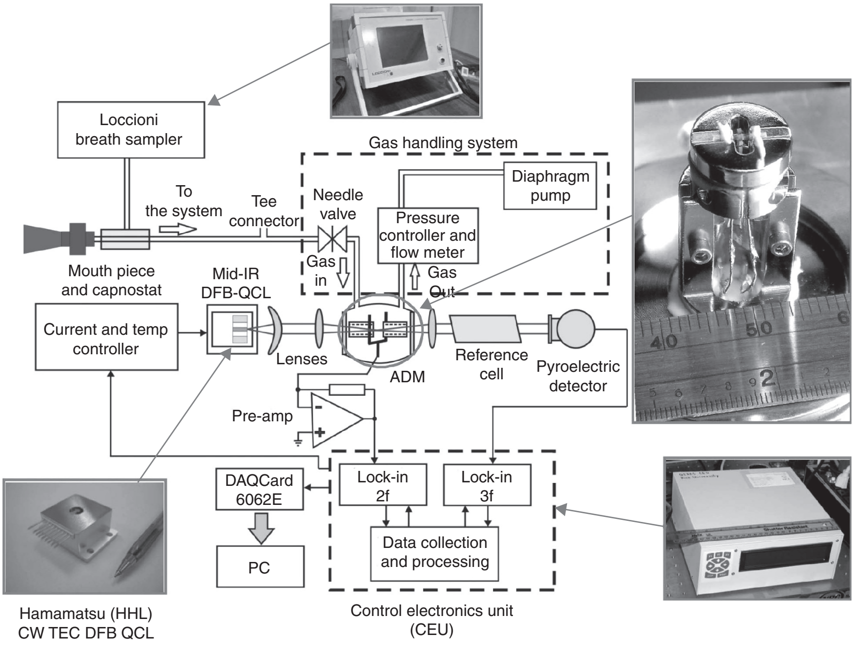
Loccioni breath sampler
Gas handling system
Diaphragm pump
To the system
Tee connector
Needle valve
Pressure controller and flow meter
Gas in
Gas Out
Mouth piece and capnostat
Mid-IR DFB-QCL
Current and temp controller
Lenses
ADM
Reference cell
Pyroelectric detector
Pre-amp
DAQCard 6062E
PC
Lock-in 2f
Lock-in 3f
Data collection and processing
Control electronics unit (CEU)
Hamamatsu (HHL) CW TEC DFB QCL

15.10 Block diagram of NH_3 breath sensor architecture.

processing. A 10 cm long reference cell, filled with 0.2 % of NH_3 in N_2 at 130 Torr, and a pyroelectric detector were installed after the ADM module to lock the laser frequency to the center of the selected NH_3 absorption line. In addition, the NH_3 sensor employs a commercially available breath sampler (Loccioni, Italy) in order to monitor and maintain the pressure of the exhaled breath within an acceptable range and to measure the associated breath CO_2 concentration level. After a subject breathes into a mouth piece, the collected breath gas sample simultaneously enters the Loccioni breath sampler and the optical breath sensor. The flow rate through the NH_3 sensor was fixed by means of a needle valve to 220 ml/min and the pressure value was set and controlled at 130 Torr. In addition, the ADM, needle valve, and the mouth piece together with the Loccioni breath sampler pipe line were heated to $\geq 38^{o}$C to avoid NH_3 adsorption on the various component surfaces of the sensor, as well as to prevent from condensation of the water vapor inside the NH_3 sensor.

The CW RT DFB-QCL was designed to emit radiation at a wavelength of 10.34 μm, within the v_2 fundamental absorption band of ammonia. Within the available DFB-QCL tuning range (Fig. 15.11a) two potential NH_3 absorption lines of the similar intensity, which are free from H_2O, CO_2 and methanol interferences, can be targeted at 967.35 cm^{-1} (10.34 μm) and 965.35 cm^{-1} (10.36 μm). For QEPAS-based NH_3 measurements, where the detected signal

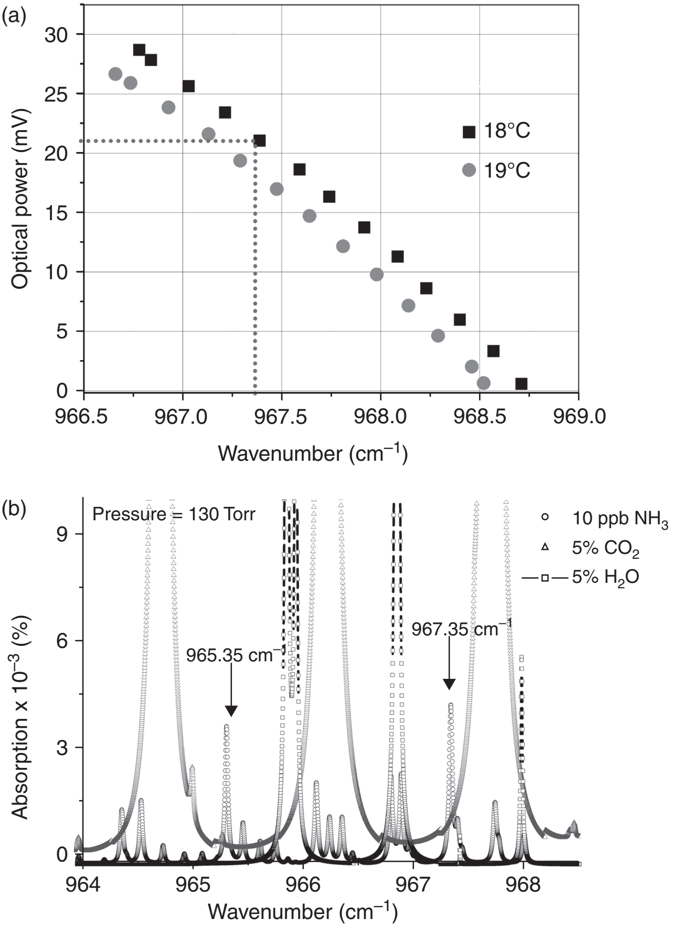

15.11 (a) Optical power and current tuning of the CW DFB-QCL operated at two different quasi-RTs. Laser power at targeted NH_3 line (967.35 cm^{-1}) is ~21mW. (b) HITRAN simulated spectra at 130 Torr indicating two potential NH_3 absorption lines of interest for exhaled breath measurements.

scales linearly with optical power, the absorption line located at 967.35 cm^{-1} was the optimum selection due to a higher laser power compared to the power at 965.35 cm^{-1}. The HITRAN simulated spectra at 130 Torr, indicating NH_3 absorption lines together with the CO_2 and H_2O absorption lines in the ~966 cm^{-1} (10.35 μm) spectral region, are illustrated in Fig. 15.11b. Experimental data showed that for a 2f WM QEPAS scan performed within the spectral range of interest no overlap between 967.35 cm^{-1} NH_3 and the adjacent CO_2 absorption line centered at 967.71 cm^{-1} is present (Lewicki *et al.*, 2011). For a 2f WM QEPAS measurement, a 1σ minimum detectable

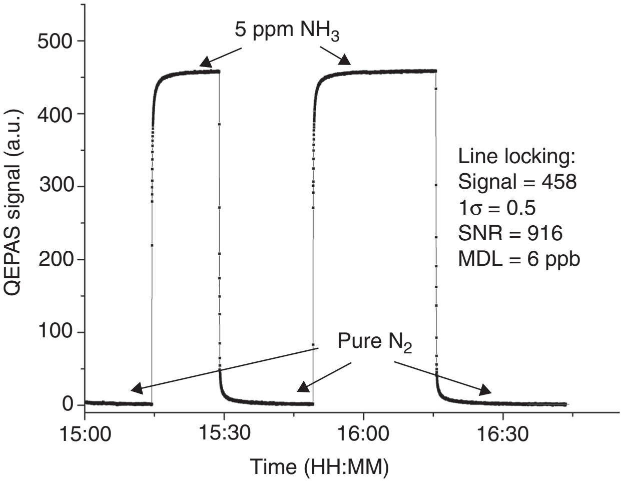

15.12 2f WM QEPAS signal when QCL was locked to the 967.35 cm^{-1} (10.34 μm) NH$_3$ line. P = 130 Torr.

concentration of ammonia was achieved at ~8 ppb when the laser frequency was current tuned over the 967.35 cm^{-1} NH$_3$ absorption line. After locking the laser frequency to the 967.35 cm^{-1} line, a 1σ minimum detectable NH$_3$ concentration was achieved of ~6 ppb with a 1 s time resolution (see Fig. 15.12). A similar detection limit of ~5.4 ppb (1σ) was obtained after diluting a calibrated mixture of 5 ppm NH$_3$ in N$_2$ to a level of ~160 ppb (Lewicki *et al.*, 2011). This confirms the linear response of the QEPAS-based NH$_3$ sensor platform.

The NH$_3$ sensor system for the real time monitoring of ammonia concentration levels in exhaled breath was designed to collect breath samples multiple times with ~3 min intervals between each sample. These intervals are needed to remove the remaining ammonia out of the system. Examples of single breath exhalation profiles for NH$_3$ concentration (ppb), CO$_2$ concentration (%), and airway pressure (mbar) are depicted in Fig. 15.13. No significant delay between airway pressure and breath ammonia profile is observed, which confirms that the NH$_3$ sensor has an extremely fast response (<3 s). In addition, after the breath sampling process is completed, a fast ammonia decay from the system is also observed.

The NH$_3$ sensor is currently installed at a medical breath research center in Hellertown, PA, and is being evaluated as an instrument for non-invasive verification of liver and kidney disorders based on human breath samples. Real time exhaled human ammonia breath data, acquired in the medical breath research center, will be compared with simultaneously clinically acquired ammonia blood data.

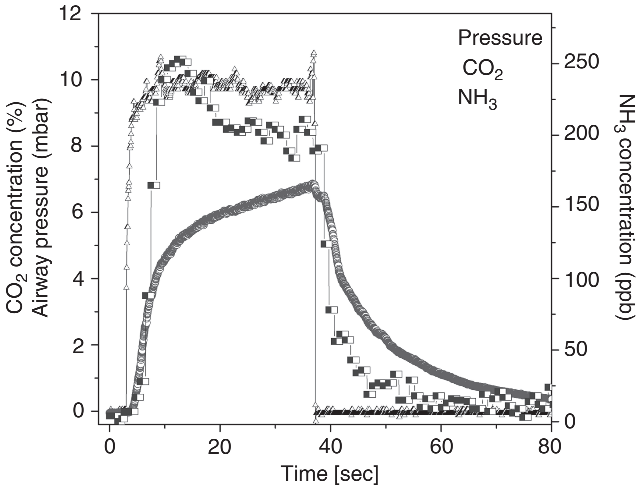

15.13 NH$_3$ concentration, CO$_2$ concentration, and airway pressure profiles of a single breath exhalation.

15.4.3 Ammonia sensor for environmental monitoring based on a 10.3 μm EC-QCL

Ammonia (NH$_3$) is normally present in the atmosphere at trace concentration levels, and like other nitrogen-containing trace gases, such as N$_2$O, NO, NO$_2$, and HNO$_2$ or HNO$_3$, plays a significant role in atmospheric chemistry. The largest emission of NH$_3$ to the atmosphere is caused by anthropogenic sources such as animal waste, poultry, mineral fertilizers, agricultural crops, or biomass burning. Other significant sources of ammonia emission are natural sources such as animals, oceans, vegetation, and the decomposition of plants (Dentener and Crutzen, 1994). Moreover, for highly developed urban areas, an additional increase of atmospheric ammonia may be observed as the result of industrial activities and motor vehicles (Kean *et al.*, 2000). From an environmental perspective, NH$_3$ is a precursor of particulate matter, due to its chemical reaction with sulfuric and nitric acids to produce different ammonium salts such as ammonium sulfate ((NH$_4$)$_2$SO$_4$), ammonium nitrate (NH$_4$NO$_3$), and ammonium bisulfate (NH$_4$HSO$_4$). Generally, for rural areas, a main source of ammonia is cattle and other livestock, whereas in most of urban areas, other sources are dominant, such as industrial and traffic emissions (Russell *et al.*, 2004). The atmospheric concentrations of NH$_3$ for urban areas may vary between 0.1 and 10 ppbv, depending on the proximity to the source (Seinfeld and Pandis, 1998).

Therefore, to improve our understanding of the dynamics of NH$_3$ in industrial and urban area such as the Greater Houston area, where atmospheric

NH_3 data are limited, an EC-QCL-based ammonia sensor platform was deployed on the roof of the 60 m high North Moody Tower. The Moody Tower location (University of Houston, TX) was a perfect sampling site due to its proximity to many potential NH_3 emission sources such as the Houston Ship Channel and several highways (I-610, US 59, I-45). In addition, atmospheric NH_3 data were compared with data acquired by other advanced gas sensing instruments that were also installed at the Moody Tower air-quality monitoring site. This is useful for the determination of the implications of NH_3 with respect to atmospheric chemistry and air quality in Houston.

Determination of environmental ammonia concentration levels was performed with a 10.4 μm EC-QCL-based sensor platform (Fig. 15.14a). A CW TEC EC-QCL system from Daylight Solutions (Model 21106-MHF), emitting a maximum optical power of 72 mW within total tuning range from 933 cm^{-1} to 1006 cm^{-1}, was implemented. As a detection technique, an amplitude modulated photoacoustic spectroscopy (AM-PAS) employing a ring differential resonant photoacoustic cell was used (Lee *et al.*, 2007). The differential cell with two cylindrical channels (each 6 mm diameter and 90 mm long) has an electret microphone placed in the middle, at a distance of 4 mm from the axis. A collimated laser beam (3 mm diameter) propagating through only one of the channels, was modulated by a mechanical chopper at 1.8 kHz in order to match the resonance frequency of the photoacoustic (PA) cell. To achieve NH_3 detection at single ppbv concentration levels, which is required for sensitive atmospheric measurements, the optical beam was passed through the cell three times (Fig. 15.14a). A pyroelectric detector placed after a 10-cm reference cell, which was filled with 0.2% of NH_3 at 30 Torr, is used for frequency locking EC-QCL wavelength to the selected optimum NH_3 absorption line as well as for monitoring the EC-QCL power.

The pressure inside the sensor system was kept at 220 Torr and the flow was maintained at 150 ml/min. In order to minimize the ammonia adsorption to surfaces and to prevent water vapor condensation in the sensor, the sensor enclosure was heated to +38°C. Moreover, a pump maintained a high flow of ~10 l/s between sampling port and the NH_3 sensor inlet in order to ensure laminar flow inside the tubing and to improve the NH_3 sensor response time to <2 min. The 965.35 cm^{-1} (see Fig. 15.11b) absorption line in the ν_2 fundamental absorption band of NH_3 was targeted for the monitoring of environmental NH_3 at trace gas concentration levels. Upon consideration of laser power, NH_3 absorption strength, and potential interferences from H_2O, CO_2, and methanol (CH_3OH) molecules, this frequency was the optimum selection for the AM-PAS technique.

For high-resolution NH_3 measurements with the AM-PAS technique, an EC-QCL MHF tuning range of 0.15 cm^{-1} was selected to cover only the NH_3 absorption line of interest. The NH_3 measurements for the detection of

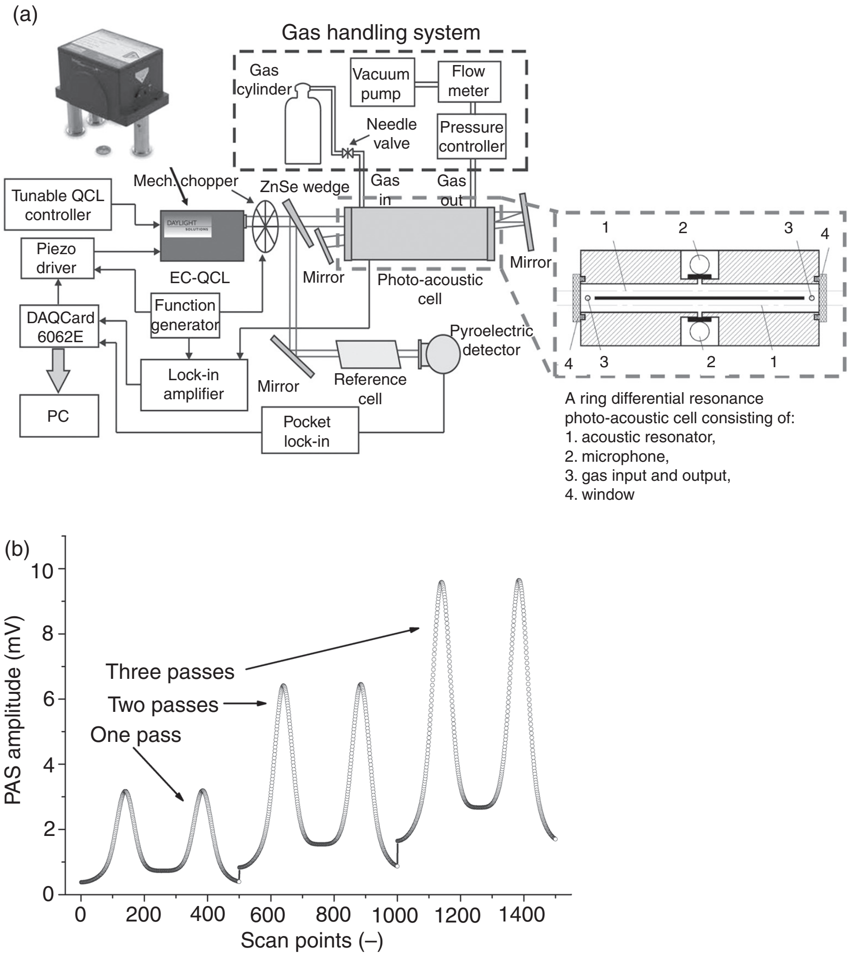
(a)
Gas handling system
Gas cylinder
Vacuum pump
Flow meter
Needle valve
Pressure controller
Mech. chopper
ZnSe wedge
Gas in
Gas out
Tunable QCL controller
Piezo driver
EC-QCL
Mirror
Photo-acoustic cell
Mirror
DAQCard 6062E
Function generator
Lock-in amplifier
Mirror
Reference cell
Pyroelectric detector
PC
Pocket lock-in
1
2
3
4
4
3
2
1
A ring differential resonance photo-acoustic cell consisting of:
1. acoustic resonator,
2. microphone,
3. gas input and output,
4. window
(b)
PAS amplitude (mV)
0
2
4
6
8
10
Three passes
Two passes
One pass
0
200
400
600
800
1000
1200
1400
Scan points (–)

15.14 (a) Mid-infrared AM-PAS-based sensor platform for atmospheric NH_3 detection; (b) AM-PAS signal for a reference mixture of 5 ppmv NH_3 in N_2 after one, two, and three QCL output beam passes through the photoacoustic cell. 5 ppmv of NH_3 in N_2 at 220 Torr; NH_3 line at 965.35 cm^{-1}; MDL ~2 ppbv.

ammonia concentration levels were performed using a scan mode, where the EC-QCL wavelength was scanned back and forth across the 965.35 cm^{-1} NH_3 line, with a frequency of $f = 0.2$ Hz. In this case a profile of the NH_3 absorption line was detected twice in order to improve the accuracy of the NH_3 concentration calculation procedure. The minimum detectable concentration of ammonia for the laboratory tested sensor, when the laser beam passes three times through the PA cell, was ~2 ppbv for a 5-second data acquisition time (Fig. 15.14b). By monitoring the peak position of the NH_3 absorption line profile recorded by the pyroelectric detector, any potential EC-QCL wavelength drift can be identified and used for laser frequency stabilization. Thus, any laser drift was eliminated by sending a PID correction signal to the EC-QCL piezo element which is responsible for wavelength tuning.

In order to calibrate the NH_3 sensor, a LabView-based, general least-square (LS) linear fitting algorithm was implemented to determine the best correlation between each acquired sample scan and the 5 ppmv NH_3 reference scan. For each scan the concentration levels (expressed in unit of parts-per-billion) of atmospheric ammonia were calculated based on a fit coefficient, which was found and returned by the LS linear fitting procedure. For the sample scan data that perfectly coincides with a reference scan data, the linear fit coefficient will be equal to unity, which implies that the measured ammonia concentration is identical with reference concentration. The benefit of using scan mode and the linear fitting procedure is its insensitivity to potential baseline drifts or background variations, which are typically observed for AM-based spectroscopic measurements. Therefore, by using a direct comparison of measured and reference scans, an exact evaluation of the gas concentration was achieved. An alternative to the AM detection scheme would be a background-free 2f WM scheme. However, the frequency range acceptable for the EC-QCL for current modulation is limited to frequencies between 10 kHz and 2 MHz. This frequency range is too high to perform WM-based spectroscopic measurements that employs a PA cell that possesses an internal resonance frequency of ~1.8 kHz.

The AM-PAS-based sensor platform was deployed at an environmental test site located on the roof of the Moody Tower building (University of Houston campus) to monitor atmospheric ammonia concentration levels between a two-week period in February 2010, a two-month period over the course of August to October 2010, and a two-week period during February 2011. To investigate the long-term stability of the ammonia sensor system, a set of data was acquired while pure nitrogen was flushed through the sensor PA cell and an Allan variance analysis was performed. The EC-QCL-based NH_3 sensor platform (see Fig. 15.14a), after its installation at the Moody Tower site, demonstrated an MDL for ammonia concentration at the ~ 3.4 ppbv level with a 5-second data acquisition time. After averaging the NH_3 concentration data for ~300 s, a sub-ppbv NH_3 concentration level of ~0.72 ppbv was achieved. For the purpose of environmental monitoring, where sensor time response is not a critical parameter, even longer averaging times can be utilized to allow a sub-ppb detection limit of NH_3.

A time series of atmospheric NH_3 concentration levels (after 300-seconds averaging time), measured during the 2010 summer/fall season, was demonstrated in Fig. 15.15. Within the two months of the NH_3 sensor deployment at Moody Tower, several unexpected events of high NH_3 concentrations levels were observed. The emission sources of several long lasting NH_3

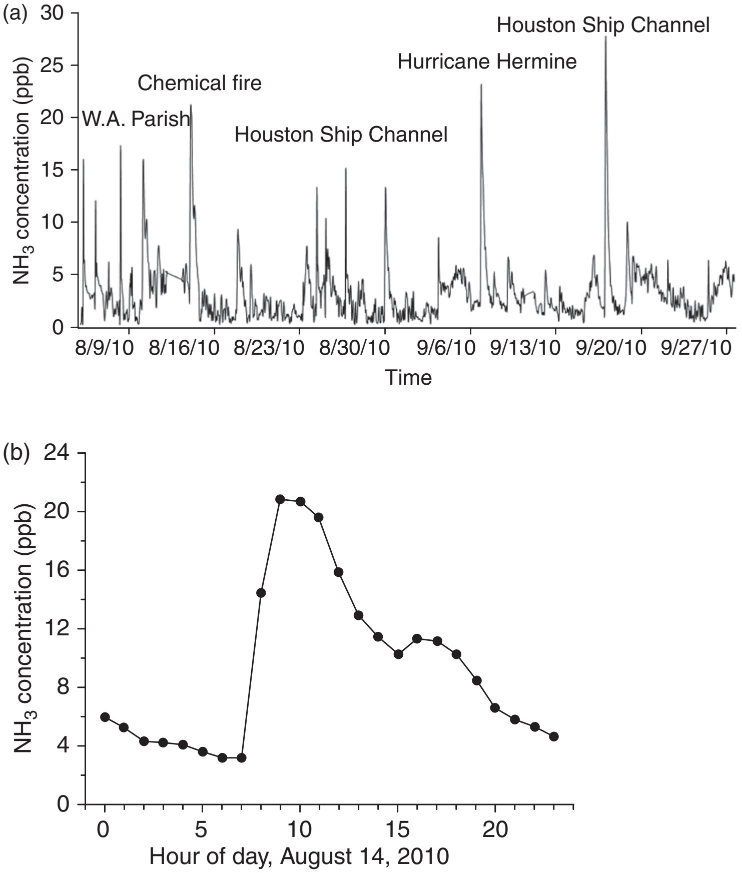

15.15 (a) A time series of NH_3 concentrations measured during summer/fall 2010. (b) Accidental ammonia release from a chemical fire resulting from a collision of 18-wheeler trucks on the Houston-Gulf Freeway (I-45) only 2 miles from the sampling site.

concentration peaks were determined by monitoring wind direction and employing backward trajectory analysis in order to check the air mass transport path. The emission sources that were identified as being responsible for increased NH_3 concentration levels in the Greater Houston urban area are: the Houston Ship Channel, W. A. Parish electric power plant, the ocean (Hurricane Hermine), and traffic activity including a traffic accident that caused a chemical fire on I-45 freeway.

The dominant NH_3 source for the Greater Houston area was found to be related to industrial and petrochemical activity around the Houston Ship Channel. This is not surprising, because hourly estimated NH_3 emission into the atmosphere from the Houston Ship Channel area is estimated to be ~120 kg (Mellqvist *et al.*, 2007). The NH_3 emission from the W. A. Parish power plant located 27 miles SE of Moody Tower also strongly contributed to the atmospheric NH_3 concentration level. This is because the selective catalytic reduction process in the power plant employs ammonia gas as a reactant to reduce NOx emissions by converting it into nitrogen gas and water. During this process NH_3 is released into the atmosphere when the temperature levels of the chemical reaction are not properly maintained or when too much ammonia is injected into the system. An unexpected increase of the NH_3 concentration (~21 ppb) on August 14, 2010 was observed (see Fig. 15.15b), when a major accident occurred during the same time period on the Houston-Gulf Freeway (I-45), two miles from the sampling site. The elevated concentration levels are due to NH_3 generation from a chemical fire resulting from a collision of two 18-wheeler trucks, one of which was carrying a fertilizer (trimethylammonium) and liquid pesticide (dimethylamine).

15.5 Conclusions and future trends

Spectroscopic techniques that include compact, reliable, real time, sensitive ($<10^{-4}$), and highly selective (<3 to 500 MHz) gas sensors based on LAS, CRDS, ICOS, CPAS and QEPAS, evanescent wave spectroscopy, laser-induced breakdown spectroscopy (LIBS), noise-immune cavity-enhanced optical heterodyne molecular spectroscopy (NICE-OHMS), cavity-enhanced optical frequency comb spectroscopy (CE-FCS) have become important as scientific and industrial techniques. LAS has benefited significantly from the development of infrared laser sources that can access the desired mid-infrared wavelengths, novel measurement techniques and improved data acquisition and reduction methods. The choice of a specific spectroscopic measurement method is determined by the application as well as the readily commercial availability of QCLs with powers of >100 mW and operating lifetimes comparable to near-infrared laser diodes (~10 years). Furthermore, improvements and innovations in LAS, CRDS, ICOS and QEPAS sensor platforms – in particular, more stable, mass produced optical/mechanical designs – as well as data acquisition and reduction techniques, will lead to mid-infrared QCL- and ICL-based instruments that can be operated by non-technical personnel and be manufactured at costs leading to sensor networks that permit both temporal and spatial trace gas monitoring.

Autonomously operated compact, reliable, real time, sensitive ($<10^{-4}$), and highly selective (<3 to 500 MHz) gas sensors based on various spectroscopic techniques using QCLs and ICLs have been demonstrated to be effective in numerous real world and fundamental science applications. These include such diverse fields as atmospheric chemistry and environmental monitoring (e.g., CO, CO_2, CH_4 and H_2CO are important carbon gases in global warming, ozone depletion studies, acid rain, photo smog formation), industrial emission measurements (e.g., quantification of smokestack emissions, fence line perimeter monitoring by the petrochemical industry, combustion incinerators, down hole gas monitoring, gas pipeline and industrial plant safety), urban (e.g., automobile, truck, aircraft, marine and electrical power generation) and rural emissions (e.g., horticultural greenhouses, fruit storage and rice agro-ecosystems). Furthermore sensors are used in chemical analysis and process control for manufacturing processes (e.g., petrochemical processing and exploration, alternative energy technologies and production, semiconductor wafer manufacture, pharmaceutical, metal processing, nuclear safeguards, food and beverage industries), applications in biomedical and the life sciences, such as non-invasive medical diagnostics that involves the detection and monitoring of numerous exhaled breath biomarkers (e.g., NO, CO, CO_2, NH_3, C_2H_6 and CH_3COCH_3). In addition, EC-QCL- and DFB-QCL-based spectroscopic methods and instruments for sensing of toxic gases and explosives relevant to law enforcement, national security and defense (Willer and Schade, 2009; Bauer *et al.*, 2010; Holthoff *et al.*, 2010), as well as spacecraft habitat air quality and safety (e.g., outgassing of H_2CO from industrial components, fire and post fire detection) and planetary atmospheric science (e.g., planetary gases such as H_2O, CH_4, CO, CO_2 and C_2H_2). With the development of efficient mid-infrared lasers (Curl *et al.*, 2010; Bewley *et al.*, 2010; Troccoli *et al.*, 2010; Razeghi *et al.*, 2010; Lyakh *et al.*, 2010) we envision a significantly improved performance coupled with a reduction in size and cost of thermoelectrically cooled QCL- and ICL-based trace gas monitors that will lead to the implementation of sensor networks (So *et al.*, 2009, 2010). Sensor networks based on LAS and QEPAS will enable large-area detection of trace gas fluxes, mapping and localization of emission sources, as well as the identification of unknown natural gas sinks.

15.6 References

Adams, H., Reinert, D., Kalkert, P. and Urban, W. (1984) ‘A differential detection scheme for Faraday rotation spectroscopy with a color center laser’, *Appl. Phys. B*, **34**, 179–185.

Aellen, T., Blaser, S., Beck, M., Hofstetter, D., Faist, J. and Gini, E. (2003) ‘Continuous-wave distributed-feedback quantum-cascade lasers on a Peltier cooler’, *Appl. Phys. Lett.*, **83**, 1929–1931.

Arnold, A. S., Wilson, J. S. and Boshier, M. G. (1998) ‘A simple extended-cavity diode laser’, *Rev. Sci. Instrum.*, **69**, 1236–1239.

Bakhirkin, Y. A., Kosterev, A. A., Curl, R. F., Tittel, F. K., Yarekha, D. A., Hvozdara, L., Giovannini, M. and Faist, J. (2006) ‘Sub-ppbv nitric oxide concentration measurements using cw thermoelectrically cooled quantum cascade laser-based integrated cavity output spectroscopy’, *Appl. Phys. B*, **82**, 149–154.

Bakhirkin, Y. A., Kosterev, A. A., Roller, C., Curl, R. F. and Tittel, F. K. (2004) 'Mid-infrared quantum cascade laser based off-axis integrated cavity output spectroscopy for biogenic nitric oxide detection', *Appl. Opt.*, **43**, 2257–2266.

Bauer, C., Willer, U., Lewicki, R., Pohlkötter, A., Kosterev, A., Kosynkin, D., Tittel, F. K. and Schade, W. (2009) 'A Mid-infrared QEPAS sensor device for TATP detection', *Journal of Physics: Conference Series*, **157**, 012002.

Bauer, C., Willer, U. and Schade, W. (2010) 'Use of quantum cascade lasers for detection of explosives: progress and challenges', *Opt. Eng.*, **49**, 111126.

Belenky, G., Shterengas, L., Kipshidze, G. and Hosoda, T. (2011) 'Type-I diode lasers for spectral region above 3 mm', *IEEE J. Sel. Topics in Quantum Electron.*, **17**, 1426–1434.

Bernegger, S. and Sigrist, M. W. (1990) 'CO-laser photoacoustic spectroscopy of gases and vapours for trace gas analysis', *Infrared Phys.*, **30**, 375–429.

Bewley, W., Canedy, C., Kim, C. S., Kim, M., Lindle, J. R., Abell, J., Vurgaftman, I. and Meyer, J. (2010) 'Ridge-width dependence of midinfrared interband cascade laser characteristics', *Opt. Eng.*, **49**, 111116.

Bijnen, F. G. C., Reuss, J. and Harren, F. J. M. (1996) 'Geometrical optimization of a longitudinal resonant photoacoustic cell for sensitive and fast trace gas detection', *Rev. Sci. Instrum.*, **67**, 2914–2923.

Bismuto, A., Beck, M. and Faist, J. (2011) 'High power Sb-free quantum cascade laser emitting at 3.3 mm above 350 K', *Appl. Physics Lett.*, **98**, 191104.

Brecha, R. J., Pedrotti, L. M. and Krause, D. (1997) 'Magnetic rotation spectroscopy of molecular oxygen with a diode laser', *J. Opt. Soc. Am. B*, **14**, 1921–1930.

Busch, W. K. and Busch, A. M. (1999) 'Introduction to cavity-ringdown spectroscopy'. In *Cavity-Ringdown Spectroscopy*, American Chemical Society, pp. 7–19.

Caffey, D., Day, T., Kim, C. S., Kim, M., Vurgaftman, I., Bewley, W. W., Lindle, J. R., Canedy, C. L., Abell, J. and Meyer, J. R. (2010) 'Performance characteristics of a continuous-wave compact widely tunable external cavity interband cascade lasers', *Opt. Express*, **18**, 15691–15696.

Capasso, F. (2010) 'High-performance midinfrared quantum cascade lasers', *Opt. Eng.*, **49**, 111102.

Cheng, W.-H. and Lee, W.-J. (1999) 'Technology development in breath microanalysis for clinical diagnosis', *J. Lab. Clin. Med.*, **133**, 218–228.

Christensen, L. E., Mansour, K. and Yang, R. Q. (2010) 'Thermoelectrically cooled interband cascade laser for field measurements', *Opt. Eng.*, **49**, 111119.

Costopoulos, D., Miklós, A. and Hess, P. (2002) 'Detection of N_2O by photoacoustic spectroscopy with a compact, pulsed optical parametric oscillator', *Appl. Phys. B: Lasers and Optics*, **75**, 385–389.

Curl, R. F., Capasso, F., Gmachl, C., Kosterev, A. A., McManus, B., Lewicki, R., Pusharsky, M., Wysocki, G. and Tittel, F. K. (2010) 'Quantum cascade lasers in chemical physics', *Chem. Phys. Lett.*, **487**, 1–18.

da Silva, M. G., Vargas, H., Miklós, A. and Hess, P. (2004) 'Photoacoustic detection of ozone using a quantum cascade laser', *Appl. Phys. B: Lasers and Optics*, **78**, 677–680.

Day, T. (2010) External cavity quantum cascade lasers: recent advances, applications, comparisons with alternative sources in the MIR. In *Laser Applications to Chemical, Security and Environmental Analysis*, San Diego, California, Optical Society of America, JTuA1.

Dentener, F. J. and Crutzen, P. J. (1994) ‘A three-dimensional model of the global ammonia cycle’, *J. Atmos. Chem.*, **19**, 331–369.

Dillenschneider, W. and Curl, R. F. (1983) ‘Color center laser spectroscopy of n1 + n2 + n3 of NO_2 using magnetic rotation’, *J. Mol. Spectrosc.*, **99**, 87–97.

Dong, L., Kosterev, A., Thomazy, D. and Tittel, F. (2010) ‘QEPAS spectrophones: design, optimization, and performance’, *Appl. Phys. B: Lasers and Optics*, **100**, 627–635.

Dweik, R. A. and Amann, A. (2008) ‘Exhaled breath analysis: the new frontier in medical testing’, *J. Breath Res.*, **2**, 030301.

Elia, A., Lugarà, P. M., Di Franco, C. and Spagnolo, V. (2009) ‘Photoacoustic techniques for trace gas sensing based on semiconductor laser sources’, *Sensors*, **9**, 9616–9628.

Elia, A., Lugarà, P. M. and Giancaspro, C. (2005) ‘Photoacoustic detection of nitric oxide by use of a quantum-cascade laser’, *Opt. Lett.*, **30**, 988–990.

Engel, G. S., Drisdell, W. S., Keutsch, F. N., Moyer, E. J. and Anderson, J. G. (2006) ‘Ultrasensitive near-infrared integrated cavity output spectroscopy technique for detection of CO at 1.57 μm: new sensitivity limits for absorption measurements in passive optical cavities’, *Appl. Opt.*, **45**, 9221–9229.

Faist, J., Beck, M., Aellen, T. and Gini, E. (2001) ‘Quantum-cascade lasers based on a bound-to-continuum transition’, *Appl. Phys. Lett.*, **78**, 147–149.

Faist, J., Capasso, F., Sivco, D. L., Hutchinson, A. L. and Cho, A. Y. (1994) ‘Quantum cascade laser’, *Science*, **264**, 553–556.

Faist, J., Gmachl, C., Capasso, F., Sitori, C., Sivco, D. L., Baillargeon, J. N., Hutchinson, A. L. and Cho, A. Y. (1997) ‘Distributed feedback quantum cascade lasers’, *Appl. Phys. Lett.*, **70**, 2670–2672.

Faist, J., Hofstetter, D., Beck, M., Aellen, T., Rochat, M. and Blaser, S. (2002) ‘Bound-to-continuum and two-phonon resonance quantum-cascade lasers for high duty cycle, high-temperature operation’, *IEEE J. Quantum Electron.*, **38**, 533–546.

Foltynowicz, A., Schmidt, F. M., Ma, W. and Axner, O. (2008) ‘Noise-immune cavity-enhanced optical heterodyne molecular spectroscopy: Current status and future potential’, *Appl. Phys. B: Lasers and Optics*, **92**, 313–326.

Fried, A., Henry, B., Wert, B., Sewell, S. and Drummond, J. R. (1998) ‘Laboratory, ground-based, and airborne tunable diode laser systems: performance characteristics and applications in atmospheric studies’, *App. Phys. B: Lasers and Optics*, **67**, 317–330.

Fried, A. and Richter, D. (2007) ‘Infrared absorption spectroscopy’. In *Analytical Techniques for Atmospheric Measurement*, Blackwell Publishing, pp. 72–146.

Fried, A., Sewell, S., Henry, B., Wert, B. P., Gilpin, T. and Drummond, J. R. (1997) ‘Tunable diode laser absorption spectrometer for ground-based measurements of formaldehyde’, *J. Geophys. Res*., **102**(D5), 6253–6266.

Fritsch, T., Horstjann, M., Halmer, D., Sabana, Hering, P. and Mürtz, M. (2008) ‘Magnetic Faraday modulation spectroscopy of the 1–0 band of ^{14}NO and ^{15}NO’, *Appl. Phys. B: Lasers and Optics,* **93**, 713–723.

Fujita, K., Edamura, T., Furuta, S. and Yamanishi, M. (2010) ‘High-performance, homogeneous broad-gain quantum cascade lasers based on dual-upper-state design’, *Appl. Phys. Lett.*, **96**, 241107.

Ganser, H., Horstjann, M., Suschek, C. V., Hering, P. and Mürtz, M. (2004) ‘Online monitoring of biogenic nitric oxide with a QC laser-based Faraday modulation technique’, *Appl. Phys. B: Lasers and Optics*, **78**, 513–517.

Ganser, H., Urban, W. and Brown, A. M. (2003) 'The sensitive detection of NO by Faraday modulation spectroscopy with a quantum cascade laser', *Molec. Phys.*, **101**, 545–550.

Gmachl, C., Capasso, F., Faist, J., Hutchinson, A. L., Tredicucci, A., Sivco, D. L., Baillargeon, J. N., Chu, S. N. G. and Cho, A. Y. (1998) 'Continuous-wave and high-power pulsed operation of index-coupled distributed feedback quantum cascade laser at l≈ 8.5 μm', *Appl. Phys. Lett.*, **72**, 1430–1432.

Gmachl, C., Sivco, D. L., Baillargeon, J. N., Hutchinson, A. L., Capasso, F. and Cho, A. Y. (2001) 'Quantum cascade lasers with a heterogeneous cascade: Two-wavelength operation', *Appl. Phys. Lett.*, **79**, 572–574.

Gmachl, C., Sivco, D. L., Colombelli, R., Capasso, F. and Cho, A. Y. (2002) 'Ultra-broadband semiconductor laser', *Nature*, **415**, 883–887.

Gottfried, J., De Lucia, F., Munson, C. and Miziolek, A. (2009) 'Laser-induced breakdown spectroscopy for detection of explosives residues: a review of recent advances, challenges, and future prospects', *Anal. Bioanal. Chem.*, **395**, 283–300.

Grober, R. D., Acimovic, J., Schuck, J., Hessman, D., Kindlemann, P. J., Hespanha, J., Morse, A. S., Karrai, K., Tiemann, I. and Manus, S. (2000) 'Fundamental limits to force detection using quartz tuning forks', *Rev. Sci. Instrum.*, **71**, 2776–2780.

Grossel, A., Zéninari, V., Parvitte, B., Joly, L., Courtois, D. and Durry, G. (2008) 'Quantum cascade laser spectroscopy of N_2O in the 7.9 μm region for the in situ monitoring of the atmosphere', *J. Quant. Spectrosc. Radiat. Transfer*, **109**, 1845–1855.

Guipeng, L., Chuan, P., Le, H. Q., Shin-Shem, P., Hao, L., Wen-Yen, H., Ishaug, B. and Jun, Z. (2002) 'Broadly wavelength-tunable external cavity, mid-infrared quantum cascade lasers', *IEEE J. Quantum Electron.*, **38**, 486–494.

Gupta, J. A., Ventrudo, B. F., Waldron, P. and Barrios, P. J. (2010) 'External cavity tunable type-I diode laser with continuous-wave singlemode operation at 3.24 μm', *Electron. Lett.*, **46**, 1218–1220.

Hofstetter, D., Beck, M., Aellen, T. and Faist, J. (2001a) 'High-temperature operation of distributed feedback quantum-cascade lasers at 5.3 μm', *Appl. Phys. Lett.*, **78**, 396.

Hofstetter, D., Beck, M., Faist, J., Nägele, M. and Sigrist, M. W. (2001b) 'Photoacoustic spectroscopy with quantum cascade distributed-feedback lasers', *Opt. Lett.*, **26**, 887–889.

Hofstetter, D., Faist, J., Beck, M., Muller, A. and Oesterle, U. (1999) 'Demonstration of high-performance 10.16 μm quantum cascade distributed feedback lasers fabricated without epitaxial regrowth', *Appl. Phys. Lett.*, **75**, 665–667.

Holthoff, E. L., Heaps, D. A. and Pellegrino, P. M. (2010) 'Development of a MEMS-scale photoacoustic chemical sensor using a quantum cascade laser', *Sensors J., IEEE*, **10**, 572–577.

Horstjann, M., Bakhirkin, Y. A., Kosterev, A. A., Curl, R. F., Tittel, F. K., Wong, C. M., Hill, C. J. and Yang, R. Q. (2004) 'Formaldehyde sensor using interband cascade laser based quartz-enhanced photoacoustic spectroscopy', *Appl. Phys. B*, **79**, 799–803.

Hugi, A., Maulini, R. and Faist, J. (2010) 'External cavity quantum cascade laser', *Semiconductor Sci. Technol.*, **25**, 083001.

Hugi, A., Terazzi, R., Bonetti, Y., Wittmann *et al.*, A., Fischer, M., Beck, M., Faist, J. and Gini, E. (2009) 'External cavity quantum cascade laser tunable from 7.6 to 11.4 μm', *Appl. Phys. Lett.*, **95**, 061103.

Karpf, A. and Rao, G. N. (2009) 'Absorption and wavelength modulation spectroscopy of NO_2 using a tunable, external cavity continuous wave quantum cascade laser', *Appl. Opt.*, **48**, 408–413.

Kean, A. J., Harley, R. A., Littlejohn, D. and Kendall, G. R. (2000) 'On-road measurement of ammonia and other motor vehicle exhaust emissions', *Environ. Sci. Technol.*, **34**, 3535–3539.

Kluczynski, P., Lundqvist, S., Westberg, J. and Axner, O. (2011) 'Faraday rotation spectrometer with sub-second response time for detection of nitric oxide using a cw DFB quantum cascade laser at 5.33 μm', *Appl. Phys. B: Lasers and Optics*, **103**, 451–459.

Kneepkens, F., Lepage, G. and Roy, C. C. (1994) 'The potential of the hydrocarbon breath test as a measure of lipid peroxidation', *Free Radical Biol. Med.*, **17**, 127–160.

Köhring, M., Pohlkötter, A., Willer, U., Angelmahr, M. and Schade, W. (2011) 'Tuning fork enhanced interferometric photoacoustic spectroscopy: a new method for trace gas analysis', *Appl. Phys. B: Lasers and Optics*, **102**, 133–139.

Kosterev, A. A., Bakhirkin, Y. A., Curl, R. F. and Tittel, F. K. (2002) 'Quartz-enhanced photoacoustic spectroscopy', *Opt. Lett.*, **27**, 1902–1904.

Kosterev, A. A., Bakhirkin, Y. A. and Tittel, F. K. (2005a) 'Ultrasensitive gas detection by quartz-enhanced photoacoustic spectroscopy in the fundamental molecular absorption bands region', *Appl. Phys. B*, **80**, 133–138.

Kosterev, A. A., Bakhirkin, Y. A., Tittel, F. K., Blaser, S., Bonetti, Y. and Hvozdara, L. (2004) 'Photoacoustic phase shift as a chemically selective spectroscopic parameter', *Appl. Phys. B*, **78**, 673–676.

Kosterev, A. A., Buerki, P., Dong, L., Reed, M., Day, T. and Tittel, F. (2010a) 'QEPAS detector for rapid spectral measurements', *Appl. Phys. B: Lasers and Optics*, **100**, 173–180.

Kosterev, A. A., Dong, L., Thomazy, D., Tittel, F. and Overby, S. (2010b) 'QEPAS for chemical analysis of multi-component gas mixtures', *Appl. Phys. B: Lasers and Optics*, **101**, 649–659.

Kosterev, A. A. and Doty, J. H. III (2010) 'Resonant optothermoacoustic detection: technique for measuring weak optical absorption by gases and micro-objects', *Opt. Lett.*, **35**, 3571–3573.

Kosterev, A. A., Malinovsky, A. L., Tittel, F. K., Gmachl, C., Capasso, F., Sivco, D. L., Baillargeon, J. N., Hutchinson, A. L. and Cho, A. Y. (2001) 'Cavity ringdown spectroscopic detection of nitric oxide with a continuous-wave quantum-cascade laser', *Appl. Opt.*, **40**, 5522–5529.

Kosterev, A. A., Mosely, T. S. and Tittel, F. K. (2006) 'Impact of humidity on quartz-enhanced photoacoustic spectroscopy based detection of HCN', *Appl. Phys. B: Lasers and Optics*, **85**, 295–300.

Kosterev, A. A. and Tittel, F. K. (2004) 'Ammonia detection by use of quartz-enhanced photoacoustic spectroscopy with a near-IR telecommunication diode laser', *Appl. Opt.*, **43**, 6213–6217.

Kosterev, A. A. and Tittel, F. K. (2002b) 'Chemical sensors based on quantum cascade lasers', *IEEE J. Quantum Electron.*, **38**, 582–591.

Kosterev, A. A., Tittel, F. K., Serebryakov, D. V., Malinovsky, A. L. and Morozov, I. V. (2005b) 'Applications of quartz tuning forks in spectroscopic gas sensing', *Rev. Sci. Instrum.*, **76**, 43105–43105.

Kosterev, A. A., Wysocki, G., Bakhirkin, Y., So, S., Lewicki, R., Fraser, M., Tittel, F. and Curl, R. F. (2008) 'Application of quantum cascade lasers to trace gas analysis', *Appl. Phys. B: Lasers and Optics*, **90**, 165–176.

Lee, B., Wood, E., Zahniser, M., McManus, J., Nelson, D., Herndon, S., Santoni, G., Wofsy, S. and Munger, J. (2011) 'Simultaneous measurements of atmospheric HONO and NO_2 via absorption spectroscopy using tunable mid-infrared continuous-wave quantum cascade lasers', *Appl. Phys. B: Lasers and Optics*, **102**, 417–423.

Lee, B. G., Belkin, M. A., Audet, R., MacArthur, J., Diehl, L., Pflugl, C. and Capasso, F. (2007) 'Widely tunable single-mode quantum cascade laser source for mid-infrared spectroscopy', *Appl. Phys. Lett.*, **91**, 231101.

Lee, B. G., Belkin, M. A., Pfugl, C., Diehl, L., Zhang, H. F. A., Audet, R. M., MacArthur, J., Bour, D. P., Corzine, S. W., Hofler, G. E. and Capasso, F. (2009a) 'DFB Quantum Cascade Laser Arrays', *IEEE J. Quantum Electron.*, **45**, 554–565.

Lee, B. G., Zhang, H. F. A., Pflugl, C., Diehl, L., Belkin, M. A., Fischer, M., Wittmann, A., Faist, J. and Capasso, F. (2009b) 'Broadband distributed-feedback quantum cascade laser array operating from 8.0 to 9.8 μm', *IEEE Photon. Technol. Lett.*, **21**, 914–916.

Lee, C.-M., Bychkov, K. V., Kapitanov, V. A., Karapuzikov, A. I., Ponomarev, Y. N., Sherstov, I. V. and Vasiliev, V. A. (2007) 'High-sensitivity laser photoacoustic leak detector', *Opt. Eng.*, **46**, 064302.

Lewicki, R., Doty, J. H., Curl, R. F., Tittel, F. K. and Wysocki, G. (2009) 'Ultrasensitive detection of nitric oxide at 5.33 μm by using external cavity quantum cascade laser-based Faraday rotation spectroscopy', *Proc. Natl Acad. Sci. USA*, **106**, 12587–12592.

Lewicki, R., Kosterev, A. A., Thomazy, D. M., Risby, T. H., Solga, S., Schwartz, T. B. and Tittel, F. K. (2011) 'Real time ammonia detection in exhaled human breath using a distributed feedback quantum cascade laser based sensor', *Proc. of SPIE 7945: 50K-2*.

Lewicki, R., Wysocki, G., Kosterev, A. A. and Tittel, F. K. (2007a) 'Carbon dioxide and ammonia detection using 2 μm diode laser based quartz-enhanced photoacoustic spectroscopy', *Appl. Phys. B: Lasers and Optics*, **87**, 157–162.

Lewicki, R., Wysocki, G., Kosterev, A. A. and Tittel, F. K. (2007b) 'QEPAS based detection of broadband absorbing molecules using a widely tunable, cw quantum cascade laser at 8.4 μm', *Opt. Express*, **15**, 7357–7366.

Lima, J. P., Vargas, H., Miklós, A., Angelmahr, M. and Hess, P. (2006) 'Photoacoustic detection of NO_2 and N_2O using quantum cascade lasers', *Appl. Phys. B: Lasers and Optics*, **85**, 279–284.

Litfin, G., Pollock, C. R., Curl, R. F. and Tittel, F. K. (1980) 'Sensitivity enhancement of laser absorption spectroscopy by magnetic rotation effect', *J. Chem. Phys.*, **72**, 6602–6605.

Liu, K., Guo, X. Y., Yi, H. M., Chen, W. D., Zhang, W. J. and Gao, X. M. (2009) 'Off-beam quartz-enhanced photoacoustic spectroscopy', *Opt. Lett.*, **34**, 1594–1596.

Liu, K., Yi, H., Kosterev, A. A., Chen, W., Dong, L., Wang, L., Tan, T., Zhang, W., Tittel, F. K. and Gao, X. (2010) 'Trace gas detection based on off-beam quartz enhanced photoacoustic spectroscopy: Optimization and performance evaluation', *Rev. Sci. Instrum.*, **81**, 103103.

Lu, Q. Y., Bai, Y., Bandyopadhyay, N., Slivken, S. and Razeghi, M. (2011) '2.4 W room temperature continuous wave operation of distributed feedback quantum cascade lasers', *Appl. Phys. Lett.*, **98**, 181106.

Lyakh, A., Maulini, R., Tsekoun, A. G. and Patel, C. K. N. (2010) 'Progress in high-performance quantum cascade lasers', *Opt. Eng.*, **49**, 111105.

Manne, J., Sukhorukov, O., Jager, W. and Tulip, J. (2006) 'Pulsed quantum cascade laser-based cavity ring-down spectroscopy for ammonia detection in breath', *Appl. Opt.*, **45**, 9230–9237.

Maulini, R., Beck, M., Faist, J. and Gini, E. (2004) 'Broadband tuning of external cavity bound-to-continuum quantum-cascade lasers', *Appl. Phys. Lett.*, **84**, 1659–1661.

Maulini, R., Mohan, A., Giovannini, M., Faist, J. and Gini, E. (2006) 'External cavity quantum-cascade laser tunable from 8.2 to 10.4 μm using a gain element with a heterogeneous cascade', *Appl. Phys. Lett.*, **88**, 201113.

Maulini, R., Yarekha, D. A., Bulliard, J. M., Giovannini, M. and Faist, J. (2005) 'Continuous-wave operation of a broadly tunable thermoelectrically cooled external cavity quantum-cascade laser', *Opt. Lett.*, **30**, 2584–2586.

McCurdy, M. R., Bakhirkin, Y., Wysocki, G., Lewicki, R. and Tittel, F. K. (2007a) 'Recent advances of laser-spectroscopy-based techniques for applications in breath analysis', *J. Breath Res.*, **1**, 014001.

McManus, J. B., Kebabian, P. L. and Zahniser, W. S. (1995) 'Astigmatic mirror multipass absorption cells for long-path-length spectroscopy', *Appl. Opt.*, **34**, 3336–3348.

McCurdy, M. R., Bakhirkin, Y., Wysocki, G. and Tittel, F. K. (2007b) 'Performance of an exhaled nitric oxide and carbon dioxide sensor using quantum cascade laser-based integrated cavity output spectroscopy', *J. Biomed. Opt.*, **12**.

McManus, J. B., Kebabian, P. L. and Zahniser, W. S. (1995) 'Astigmatic mirror multipass absorption cells for long-path-length spectroscopy', *Appl. Opt.*, **34**, 3336–3348.

McManus, J. B., Nelson, D. D., Herndon, S. C., Shorter, J. H., Zahniser, M. S., Blaser, S., Hvozdara, L., Muller, A., Giovannini, M. and Faist, J. (2006) 'Comparison of cw and pulsed operation with a TE-cooled quantum cascade infrared laser for detection of nitric oxide at 1900 cm^{-1}', *Appl. Phys. B: Lasers and Optics*, **85**, 235–241.

McManus, J. B., Zahniser, M. S., Nelson, J. D. D., Shorter, J. H., Herndon, S., Wood, E. and Wehr, R. (2010) 'Application of quantum cascade lasers to high-precision atmospheric trace gas measurements', *Opt. Eng.*, **49**, 111124–11.

Mellqvist, J., Samuelsson, J., Rivera, C., Lefer, B. and M., P. (2007) 'Measurements of industrial emissions of VOCs, NH_3, NO_2 and SO_2 in Texas using the Solar Occultation Flux method and mobile DOAS', in *American Geophysical Union, Fall Meeting* Aug 20, 2007.

Meyer, J. R., Vurgaftman, I., Yang, R. Q. and Ram-Mohan, L. R. (1996) 'Type-II and type-I interband cascade lasers', *Electron. Lett.*, **32**, 45–46.

Miklos, A., Hess, P. and Bozoki, Z. (2001) 'Application of acoustic resonators in photoacoustic trace gas analysis and metrology', *Rev. Sci. Instrum.*, **72**, 1937–1955.

Miklos, A., Hess, P., Mohacsi, A., Sneider, J., Kamm, S. and Schafer, S. (1999) 'Improved photoacoustic detector for monitoring polar molecules such as ammonia with a 1.53 μm DFB diode laser', *AIP Conference Proceedings*, **463**, 126–128.

Moeskops, B. W. M., Cristescu, S. M. and Harren, F. J. M. (2006) 'Sub-part-per-billion monitoring of nitric oxide by use of wavelength modulation spectroscopy in combination with a thermoelectrically cooled, continuous-wave quantum cascade laser', *Opt. Lett.*, **31**, 823–825.

Mukherjee, A., Prasanna, M., Lane, M., Go, R., Dunayevskiy, I., Tsekoun, A. and Patel, C. K. N. (2008) 'Optically multiplexed multi-gas detection using quantum cascade laser photoacoustic spectroscopy', *Appl. Opt.*, **47**, 4884–4887.

Mürtz, M. and Hering, P. (2008) 'Online monitoring of exhaled breath using mid-infrared laser spectroscopy' in *Mid-Infrared Coherent Sources and Applications*, Springer Netherlands, 535–555.

Mürtz, P., Menzel, L., Bloch, W., Hess, A., Michel, O. and Urban, W. (1999) 'LMR spectroscopy: a new sensitive method for on-line recording of nitric oxide in breath', *J. Appl. Physiol.*, **86**, 1075–1080.

Ng, J., Kung, A. H., Miklós, A. and Hess, P. (2004) 'Sensitive wavelength-modulated photoacoustic spectroscopy with a pulsedoptical parametric oscillator', *Opt. Lett.*, **29**, 1206–1208.

O'Keefe, A. (1998) 'Integrated cavity output analysis of ultra-weak absorption', *Chem. Phys. Lett.*, **293**, 331–336.

O'Keefe, A. and Deacon, D. A. G. (1988) 'Cavity ring-down optical spectrometer for absorption measurements using pulsed laser sources', *Rev. Sci. Instrum.*, **59**, 2544–2551.

O'Keefe, A., Scherer, J. J. and Paul, J. B. (1999) 'cw Integrated cavity output spectroscopy', *Chem. Phys. Lett.*, **307**, 343–349.

Paldus, B. A., Harb, C. C., Spence, T. G., Zare, R. N., Gmachl, C., Capasso, F., Sivco, D. L., Baillargeon, J. N., Hutchinson, A. L. and Cho, A. Y. (2000) 'Cavity ring-down spectroscopy using mid-infrared quantum-cascade lasers', *Opt. Lett.*, **25**, 666–668.

Paldus, B. A. and Kachanov, A. A. (2005) 'An historical overview of cavity-enhanced methods', *Can. J. Phys*., **83**, 975–999.

Paul, J. B., Lapson, L. and Anderson, J. G. (2001) 'Ultrasensitive absorption spectroscopy with a high-finesse optical cavity and off-axis alignment', *Appl. Opt.*, **40**, 4904–4910.

Petra, N., Zweck, J., Kosterev, A. A., Minkoff, S. E. and Thomazy, D. (2009) 'Theoretical analysis of a quartz-enhanced photoacoustic spectroscopy sensor', *Appl. Phys. B*, **94**, 673–680.

Pfeiffer, J., Kirsten, D., Kalkert, P. and Urban, W. (1981) 'Sensitive magnetic rotation spectroscopy of the OH free radical fundamental band with a colour centre laser', *Appl. Phys. B: Lasers and Optics*, **26**, 173–177.

Phillips, M. and Greenberg, J. (1991) 'Method for the collection and analysis of volatile compounds in the breath', *J. Chromatogr. B*, **564**, 242–249.

Phillips, M. C., Myers, T. L., Wojcik, M. D. and Cannon, B. D. (2007) 'External cavity quantum cascade laser for quartz tuning fork photoacoustic spectroscopy of broad absorption features', *Opt. Lett.*, **32**, 1177–1179.

Pushkarsky, M. B., Dunayevskiy, I. G., Prasanna, M., Tsekoun, A. G., Go, R. and Patel, C. K. N. (2006a) 'High-sensitivity detection of TNT', *Proc. Natl Acad. Sci. USA*, **103**, 19630–19634.

Pushkarsky, M. B., Tsekoun, A., Dunayevskiy, I. G., Go, R. and Patel, C. K. N. (2006b) 'Sub-parts-per-billion level detection of NO_2 using room-temperature quantum cascade lasers', *Proc. Natl Acad. Sci. USA*, **103**, 10846–10849.

Pushkarsky, M. B., Webber, M. E. and Patel, C. K. N. (2003) 'Ultra-sensitive ambient ammonia detection using CO_2-laser-based photoacoustic spectroscopy', *Appl. Phys. B*, **77**, 381–385.

Pushkarsky, M. B., Weida, M., Day T., Arnone, D., Pritchett, R., Caffey, D. and Crivello. S. (2008) 'High-power tunable external cavity quantum cascade laser in the 5–11 micron regime', *Anglais*, **6871**, 68711X.

Ramponi, A. J., Milanovich, F. P., Kan, T. and Deacon, D. (1988) 'High sensitivity atmospheric transmission measurements using a cavity ringdown technique', *Appl. Opt.*, **27**, 4606–4608.

Rao, G. N. and Karpf, A. (2011) 'Extremely sensitive detection of NO_2 employing off-axis integrated cavity output spectroscopy coupled with multiple line integrated absorption spectroscopy', *Appl. Opt.*, **50**, 1915–1924.

Rao, G. N. and Karpf, A. (2010) 'High sensitivity detection of NO_2 employing cavity ringdown spectroscopy and an external cavity continuously tunable quantum cascade laser', *Appl. Opt.*, **49**, 4906–4914.

Razeghi, M., Bai, Y., Slivken, S. and Darvish, S. R. (2010) 'High-performance InP-based midinfrared quantum cascade lasers at Northwestern University', *Opt. Eng.*, **49**, 111103.

Rey, J. M. and Sigrist, M. W. (2008) 'New differential mode excitation photoacoustic scheme for near-infrared water vapour sensing', *Sens. Actuators B*, **135**, 161–165.

Risby, T. and Tittel, F. K. (2010) 'Current status of mid-infrared quantum and interband cascade lasers for clinical breath analysis', *Opt. Eng.*, **49**, 000000–1.

Roller, C. B., Holland, B. P., McMillen, G., Step, D. L., Krehbiel, C. R., Namjou, K. and McCann, P. J. (2007) 'Measurement of exhaled nitric oxide in beef cattle using tunable diode laser absorption spectroscopy', *Appl. Opt.*, **46**, 1333–1342.

Rossi, A., Buffa, R., Scotoni, M., Bassi, D., Iannotta, S. and Boschetti, A. (2005) 'Optical enhancement of diode laser-photoacoustic trace gas detection by means of external Fabry-Perot cavity', *Appl. Phys. Lett.*, **87**, 041110.

Russell, M., Allen, D. T., Collins, D. R. and Fraser, M. P. (2004) 'Daily, seasonal, and spatial trends in PM2.5 mass and composition in Southeast Texas', *Aerosol Science and Technology*, **38**, 14–26.

Sabana, H., Fritsch, T., Boyomo Onana, M., Bouba, O., Hering, P. and Mürtz, M. (2009) 'Simultaneous detection of 14NO and 15NO using Faraday modulation spectroscopy', *Appl. Phys. B: Lasers and Optics*, **96**, 535–544.

Sayres, D. S., Moyer, E. J., Hanisco, T. F., Clair, J. M., Keutsch, F. N., O'Brien, A., Allen, N. T., Lapson, L., Demusz, J. N., Rivero, M., Martin, T., Greenberg, M., Tuozzolo, C., Engel, G. S., Kroll, J. H., Paul, J. B. and Anderson, J. G. (2009) 'A new cavity based absorption instrument for detection of water isotopologues in the upper troposphere and lower stratosphere', *Rev. Sci. Instrum.*, **80**, 44102–44102.

Scherer, D. R., Montoya, J., Hensley, J. M. and Allen, M. G. (2009) *Tunable External-Cavity Quantum Cascade Laser Sources for Gas Sensing and Spectroscopy,* translated by Optical Society of America, JTuD18.

Scherer, J. J., Paul, J. B., O'Keefe, A. and Saykally, R. J. (1997) 'Cavity ringdown laser absorption spectroscopy: History, development, and application to pulsed molecular beams', *Chem. Rev.*, **97**, 25–51.

Schilt, S. and Thévenaz, L. (2006) 'Wavelength modulation photoacoustic spectroscopy: Theoretical description and experimental results', *Infrared Phys. Techn.*, **48**, 154–162.

Schilt, S., Thévenaz, L. and Robert, P. (2003) ‘Wavelength modulation spectroscopy: combined frequency and intensity laser modulation’, *Appl. Opt.*, **42**, 6728–6738.

Seinfeld, J. and Pandis, S. (1998) *Atmospheric Chemistry and Physics: From Air Pollution to Climate Change*, Wiley, New York.

Shorter, J. H., Nelson, D. D., McManus, J. B., Zahniser, M. S. and Milton, D. K. (2010) ‘Multicomponent breath analysis with infrared absorption using room-temperature quantum cascade lasers’, *Sensors Journal, IEEE*, **10**, 76–84.

Sigrist, M. W. and Thoeny, A. (1993) *Atmospheric trace gas monitoring by CO_2 laser photoacoustic spectroscopy,* translated by Harold, I. S. and Ulrich, P., SPIE, 174–184.

Smith, D. and Španěl, P. (2005) ‘Selected ion flow tube mass spectrometry (SIFT-MS) for on-line trace gas analysis’, *Mass Spectrom. Rev.*, **24**, 661–700.

Smith, J. M., Bloch, J. C., Field, R. W. and Steinfeld, J. I. (1995) ‘Trace detection of NO_2 by frequency-modulation-enhanced magnetic rotation spectroscopy’, *J. Opt. Soc. Am. B*, **12**, 964–969.

So, S., Amiri Sani, A., Zhong, L. and Tittel, F. (2009) ‘Laser spectroscopic trace-gas sensor networks for atmospheric monitoring applications’, in *ESSA Workshop ‘09*, San Francisco, California, USA.

So, S., Jeng, E., Smith, C., Krueger D. and Wysocki, G. (2010) Next generation infrared sensor instrumentation: remote sensing and sensor networks using the openPHOTONS repository, translated by Marija, S. and Gonzalo, P., SPIE, 780818.

So, S., Jeng, E. and Wysocki, G. (2011) ‘VCSEL based Faraday rotation spectroscopy with a modulated and static magnetic field for trace molecular oxygen detection’, *Appl. Phys. B*, **102**, 279–291.

Sonnenfroh, D. M., Rawlins, W. T., Allen, M. G., Gmachl, C., Capasso, F., Hutchinson, A. L., Sivco, D. L., Baillargeon, J. N. and Cho, A. Y. (2001) ‘Application of balanced detection to absorption measurements of trace gases with room-temperature, quasi-cw quantum-cascade lasers’, *Appl. Opt.*, **40**, 812–820.

Spagnolo, V., Kosterev, A., Dong, L., Lewicki, R. and Tittel, F. (2010) ‘NO trace gas sensor based on quartz-enhanced photoacoustic spectroscopy and external cavity quantum cascade laser’, *Appl. Phys. B: Lasers and Optics*, **100**, 125–130.

Sukhorukov, O., Lytkine, A., Manne, J., Tulip, J. and Jager, W. (2006) *Cavity ring-down spectroscopy with a pulsed distributed feedback quantum cascade laser,* translated by Manijeh, R. and Gail, J. B., SPIE, 61270A.

Thorpe, M. J., Balslev-Clausen, D., Kirchner, M. S. and Ye, J. (2008) ‘Cavity-enhanced optical frequency combspectroscopy: application to human breathanalysis’, *Opt. Express*, **16**, 2387–2397.

Tittel, F. K., Kosterev, A. A., Bakhirkin, Y. A., Roller, C. B., Weidmann, D. and Curl, R. F. (2003) *Chemical sensors based on quantum cascade lasers*, translated by 893–894 Vol.2.

Troccoli, M., Wang, X. and Fan, J. (2010) ‘Quantum cascade lasers: high-power emission and single-mode operation in the long-wave infrared ($\lambda > 6$ μm)’, *Opt. Eng.*, **49**, 111106–9.

Tsai, T. and Wysocki, G. (2010) ‘External-cavity quantum cascade lasers with fast wavelength scanning’, *Appl. Phys. B: Lasers and Optics*, **100**, 243–251.

Vurgaftman, I., Kim, M., Kim, C. S., Bewley, W. W., Canedy, C. L., Lindle, J. R., Abell, J. and Meyer, J. R. (2010) *Challenges for mid-IR interband cascade lasers*, 1 ed., translated by Belyanin, A. A. and Smowton, P. M., San Francisco, California, USA: SPIE, 761619-10.

Webber, M. E., Pushkarsky, M. and Patel, C. K. N. (2003) 'Fiber-amplifier-enhanced photoacoustic spectroscopy with near-infrared tunable diode lasers', *Appl. Opt.*, **42**, 2119–2126.

Weida, M. J., Caffey, D., Rowlette, J. A., Arnone, D. F. and Day, T. (2010) 'Utilizing broad gain bandwidth in quantum cascade devices', *Opt. Eng.*, **49**, 111120–5.

Weidmann, D., Wysocki, G., Oppenheimer, C. and Tittel, F. K. (2005) 'Development of a compact quantum cascade laser spectrometer for field measurements of CO_2 isotopes', *Appl. Phys. B: Lasers and Optics*, **80**, 255–260.

Werle, P. (2011) 'Accuracy and precision of laser spectrometers for trace gas sensing in the presence of optical fringes and atmospheric turbulence', *Appl. Phys. B: Lasers and Opt.*, **102**, 313–329.

Werle, P., Mücke, R. and Slemr, F. (1993) 'The limits of signal averaging in atmospheric trace-gas monitoring by tunable diode-laser absorption spectroscopy (TDLAS)', *Appl. Phys. B: Lasers and Opt.*, **57**, 131–139.

Westhoff, M., Litterst, P., Freitag, L., Urfer, W., Bader, S. and Baumbach, J.-I. (2009) 'Ion mobility spectrometry for the detection of volatile organic compounds in exhaled breath of patients with lung cancer: results of a pilot study', *Thorax*, **64**, 744–748.

Willer, U. and Schade, W. (2009) 'Photonic sensor devices for explosive detection', *Anal. Bioanal. Chem.*, **395**, 275–282.

Wittmann, A., Bonetti, Y., Fischer, M., Faist, J., Blaser, S. and Gini, E. (2009) 'Distributed-Feedback Quantum-Cascade Lasers at 9 μm Operating in Continuous Wave Up to 423 K', *Photon. Technol. Lett., IEEE*, **21**, 814–816.

Wittmann, A., Hugi, A., Gini, E., Hoyler, N. and Faist, J. (2008) 'Heterogeneous high-performance quantum-cascade laser sources for broad-band tuning', *IEEE J. Quantum Electron.*, **44**, 1083–1088.

Wojcik, M. D., Phillips, M. C., Cannon, B. D. and Taubman, M. S. (2006) 'Gas-phase photoacoustic sensor at 8.41 μm using quartz tuning forks and amplitude-modulated quantum cascade lasers', *Appl. Phys. B*, **85**, 307–313.

Wysocki, G., Curl, R. F., Tittel, F. K., Maulini, R., Bulliard, J. M. and Faist, J. (2005) 'Widely tunable mode-hop free external cavity quantum cascade laser for high resolution spectroscopic applications', *Appl. Phys. B*, **81**, 769–777.

Wysocki, G., Kosterev, A. A. and Tittel, F. K. (2006) 'Influence of molecular relaxation dynamics on quartz-enhanced photoacoustic detection of CO2 at λ =2 μm', *Appl. Phys. B: Lasers and Optics*, **85**, 301–306.

Wysocki, G., Lewicki, R., Curl, R. F., Tittel, F. K., Diehl, L., Capasso, F., Troccoli, M., Hofler, G., Bour, D., Corzine, S., Maulini, R., Giovannini, M. and Faist, J. (2008) 'Widely tunable mode-hop free external cavity quantum cascade lasers for high resolution spectroscopy and chemical sensing', *Appl. Phys. B*, **92**, 305–311.

Xu, G., Li, A., Li, Y., Wei, L., Zhang, Y., Lin, C. and Li, H. (2006) 'Low threshold current density distributed feedback quantum cascade lasers with deep top gratings', *Appl. Phys. Lett.*, **89**, 161102.

Yang, R. Q. (1995) 'Infrared laser based on intersubband transitions in quantum wells', *Superlattices and Microstruct.*, **17**, 77–83.

Yao, Y., Charles, W. O., Tsai, T., Chen, J., Wysocki, G. and Gmachl, C. F. (2010a) 'Broadband quantum cascade laser gain medium based on a "continuum-to-bound" active region design', *Appl. Phys. Lett.*, **96**, 211106.

Yao, Y., Wang, X., Fan, J.-Y. and Gmachl, C. F. (2010b) 'High performance "continuum-to-continuum" quantum cascade lasers with a broad gain bandwidth of over 400 cm-1', *Appl. Phys. Lett.*, **97**, 081115.

Ye, J., Ma, L.-S. and Hall, J. L. (1998) 'Ultrasensitive detections in atomic and molecular physics: demonstration in molecular overtone spectroscopy', *J. Opt. Soc. Am. B*, **15**, 6–15.

Yu, J. S., Slivken, S., Darvish, S. R., Evans, A., Gokden, B. and Razeghi, M. (2005) 'High-power, room-temperature, and continuous-wave operation of distributed-feedback quantum-cascade lasers at lambda ~ 4.8 mm', *Appl. Phys. Lett.*, **87**, 041104.

Zahniser, M. S., Nelson, D. D., McManus, J. B., Kebabian, P. L. and Lloyd, D. (1995) 'Measurement of trace gas fluxes using tunable diode laser spectroscopy', *Phil. Trans.: Physical Sci. Eng*., **351**, 371–382.

Zaugg, C. A., Lewicki, R., Day, T., Curl, R. F. and Tittel, F. K. (2011) 'Faraday rotation spectroscopy of nitrogen dioxide based on a widely tunable external cavity quantum cascade laser', *Proc. of SPIE 7945:* 500–1.

Zeller, W., Naehle, L., Fuchs, P., Gerschuetz, F., Hildebrandt, L. and Koeth, J. (2010) 'DFB Lasers Between 760 nm and 16 μm for Sensing Applications', *Sensors*, **10**, 2492–2510.

Zhao, W., Wysocki, G., Chen, W., Fertein, E., Le Coq, D., Petitprez, D. and Zhang, W. (2011) 'Sensitive and selective detection of OH radicals using Faraday rotation spectroscopy at 2.8 μm', *Opt. Express*, **19**, 2493–2501.

Index

α–factor, 96
acoustic waves, 551
active mode-locking, 168, 539–42
  asynchronous sampling of THz QCL using a fs-fibre laser, 541
  sampling process, 540
  three periods of measured and calculated waveform, 544
  THz QCL emission and down-converted spectrum, 543
active Q-switching, 160–1
active region, 345–6
advanced hybrid silicon lasers, 408–25
  AWG laser with four channels, 424
  AWG transmission for randomly polarised light, 425
  bending loss simulation, 418
  DBR laser LI curve, 414
  grating strength, 411
  hybrid DBR laser, 413
  hybrid microring laser, 419
  hybrid microring lasers LI characteristic, 420
  LI curve for the clockwise lasing mode, 423
  odd and even supermodes, 416
  passive Si grating, Si hybrid grating and III-V hybrid grating, 409
  power coupling ratio of Si directional and hybrid directional coupler, 417
  racetrack resonator and the photodetectors layout, 418
  Si DFB laser experimental spectrum, 412
  threshold current as a function of device cavity length, 422
advanced self-assembled indium arsenide (InAs) QD lasers, 272–310
  Fabry-Pérot and distributed feedback (DFB) lasers, 282–92
  FB and DFB lasers for high temperature application, 292–9
  high density and highly uniform InAs, 274–82
    future direction for achieving novel optical devices, 280–1
    roadmap of properties in view of increasing optical gain, 276
    self-assembled quantum dots for optical devices, 274–6
  high density for increased optical gain, 277–8
    AFM images of 1x1 micrometer scale InAs QFs QDs on GaAs, 277
    TEM image of eight QD layers, 278
  highly uniform structure for sharpening the optical gain, 279–80
    normalised photoluminescence spectra measurement, 281
    photoluminescence characterisation of high-density QDs, 280
  QD Laser, Inc., 299–303
  silicon hybrid, 303–9
aluminium lasers, 221–61
amplified spontaneous emission (ASE), 422
amplitude modulated photoacoustic spectroscopy (AM-PAS), 613–14, 615
amplitude modulation (AM), 166, 592

Andronov-Hopf bifurcation, 177–8
anti-reflection (AR) facet coating, 255–6
antiguiding effect, 97
arrayed waveguide grating (AWG), 423–4
asynchronous optical sampling (ASOPS), 539–41
atomic force microscope (AFM), 277
Auger recombination, 34
auto-power-control (APC) mode, 297

β factor, 60–2
bandgap-tapering technique, 67
basic laser diode, 7–15
  carrier injection, 8–10
    band diagram illustrating electron loss at heterobarrier due to drift, 10
    schematic band diagram of electron loss, 9
  efficiency definitions, 14–15
  quantum confined structures formation, 7–8
    energy band diagrams of type I and II quantum wells, 8
  threshold and light-current curve, 12–14
    quantum well band diagram with quasi-Fermi level separation, 13
    schematic illustrating the identification of threshold current, 12
  waveguide and cavity, 10–12
    transverse optical field profile due waveguiding by index profile of SCH structure, 11
beam combining
  semiconductor laser, 121–45
    experiments on external cavity broad-area laser diode arrays, 125–38
    modelling of a single-mode semiconductor laser array in external cavity, 138–42
beam propagation method (BPM), 400
beam quality factor, 85–7
Bessel function, 552, 554, 558, 562
birefringence, 252–3
birefringent filter (BRF), 347
bit rate engineering
  high-power and high-bit-rate operation and harmonic ML, 194–6
    schematic of external cavity QD laser configuration and RF spectra, 195
Blu-Ray technology, 222
Bose-Einstein phonon distribution, 31–2
bouncing-ball mode, 555, 561–2
bound-to-continuum quantum-cascade lasers, 599
bow-tie mode, 555
Bragg Scattering, 56
brightness, 85–7
Brillouin zone, 67
buried oxide (BOX) layer, 403, 405–6, 408

catastrophic facet failure
  passivation techniques in high-power diode lasers, 90–1
    electroluminescence from the output facet of an AlGalnP broad-area lasers, 90
catastrophic optical mirror damage (COMD), 82, 88, 90–1
caustic lines, 553
cavity-dumped semiconductor disk lasers, 370–1
  performance and modelled characteristics, 371
  schematic diagram, 371
cavity enhanced spectroscopy, 585–7
cavity resonance
  spectral alignment, 325–7
    vs gain bandwidth, 325–6
cavity ring-down spectroscopy (CRDS), 584–7
chaotic modes, 555
chemical-mechanical polishing (CMP), 255
coefficient of thermal expansion (CTE), 111
compressive strain, 459–65

  - current dependence of the peak modal gain, 462
  - peak modal gain, 465
  - pulsed light-current characteristics of uncoated lasers, 461
  - subband dispersion, 463
- conductively cooled packages (CCP), 110
- continuum-to-bound quantum-cascade lasers, 600
- continuum-to-continuum quantum-cascade lasers, 600
- conventional photoacoustic spectroscopy (CPAS), 587–92
  - CRDS based sensor platform using AOM, 586
  - PA cell design, 589

- 90-degree method, 594
- delay-differential equation (DDE) model, 172–3
- density of states (DOS), 443, 445, 459, 462–4
- dielectric cavity, 62
- differential quantum efficiency, 83
- dimensional scaling, 26
- 2.5 μm diode lasers, 448–65
  - asymmetric waveguide and beam properties, 451–9
    - band alignment and transverse near field distribution, 454
    - cladding and core layer composition and width, 454
    - current dependence of the peak modal gain of laser, 457
    - CW power and power conversion of long AR/HR coated device, 459
    - fast axis far field distribution and threshold current density, 455
    - modal gain spectra, 456
    - near field distribution and far field patterns in slow and fast axis direction, 458
  - band diagram of laser heterostructure, 449
  - current dependence of the modal gain spectra, 451
  - CW power and power conversion of single emitter laser, 450
  - fast and slow axis far field distribution for long AR/HR coated single emitter lasers, 452
- 3 μm diode lasers, 465–77
  - band alignment for 3.1 μm emitting lasers, 468
  - current, internal optical loss and internal efficiency dependence, 470
  - CW RT operation, 470–7
    - light-current characteristics and current dependence, 472
    - positions of the band edges on absolute energy scale for GaInAsSb QW alloy, 477
  - pulsed light-current and threshold current density, 469
- 3.1 μm diode lasers
  - CW RT operation, 470–7
    - CW output power and spectral characteristics, 475
    - light-current characteristics and current dependence, 473
    - positions of the band edges on absolute energy scale for GaInAsSb QW alloy, 477
- 3.2 μm diode lasers
  - CW RT operation, 470–7
    - CW output power and spectral characteristics, 475
    - light-current, voltage-current characteristics and current dependence, 474
    - peak modal gain dependence on current of uncoated lasers, 475
- 3.3 μm diode lasers
  - CW RT operation, 470–7
    - peak modal gain dependence on current of uncoated lasers, 475
    - positions of the band edges on absolute energy scale for GaInAsSb QW alloy, 477
- 3.4 μm diode lasers
  - CW RT operation, 470–7
    - light-current characteristics and current dependence, 476

3.4 μm diode lasers (*cont.*)
        positions of the band edges on absolute energy scale for GaInAsSb QW alloy, 477
diode-pumped solid-state laser (DPSS), 303
discrete mode, 196
distributed Bragg reflector (DBR), 87, 345
    lasers, 408, 413, 426
    mirror, 342
distributed feedback (DFB), 87, 516
    IC lasers, 494–6
    lasers, 408, 413, 430, 447
distributed feedback quantum-cascade lasers (DFB-QCL), 595–6
    real time ammonia detection in exhaled human breath, 608–11
        NH_3 breath sensor architecture, 609
        NO_2 FRS signal, 607
        optical power and current tuning and NH_3 absorption line, 610
distributed optical feedback, 4
distributed time-domain model, 171
distributor Bragg reflector (DBR), 320, 321–2, 324–5, 327–8
    mirrors, 317, 319–2, 324–5, 327–8, 329–30
dot-in-a-well (DWELL), 8
double- plasmon mode, 517
double heterostructure (DH) GaSb-based lasers, 446

e-beam, 67–8
edge-emitting laser, 157
elastic strain, 40–1
    diagrams showing the densities of states of conduction, 41
electric fields, 228–31
electroabsorption modulator (EAM), 429–30
energy band diagram, 231–3
entangled states, 575
epitaxial lateral overgrowth (ELO) techniques, 227–8
epitaxy, 293
etch-stop layer (ESL), 250
etched grating, 410
ethernet passive optical network (EPON), 288–9
external-cavity diode laser (ECDL), 356
external cavity quantum-cascade lasers (EC-QCL), 596–9
    environmental monitoring ammonia sensor, 612–17
        mid-infrared AM-PAS-based sensor platform and signal, 614
        NH_3, CO_2 concentration and airway pressure profiles of single breath exhalation, 612
        NH_3 concentration measurement and accidental release, 616
external differential quantum efficiency, 15
external Talbot cavity, 122, 124, 129
extinction ratio (ER), 288

fabrication techniques, 254–6
    SEM image of facet area of commercial III-nitride ridge laser, 256
    wafer level fabrication steps for basic self-aligned III-nitride ridge laser, 255
Fabry-Perot cavities, 60
Fabry-Perot IC lasers, 495
Fabry-Perot lasers, 34
    broad-area, 92–3
Fabry-Perot optical cavity, 319–20
far-field pattern (FFP), 249
far-infrared WGM lasers, 566
Faraday rotation spectroscopy (FRS), 592–4
    QTF based spectrophones, 591
    ultra-sensitive detection of nitric oxide and nitrogen dioxide, 601–7
        EC-QCL based FRS experimental set-up, 602
        Faraday rotation spectrum and liquid nitrogen cooled InSb photodetector, 604
        long-term NO concentration measurements, 604
        schematic diagram, 602

fast-axis collimation (FAC) lens, 125
feedback path, 125, 131–2
femtosecond pulse generation, 202–3
Fermi-Dirac distribution, 32
Fermi's Golden Rule, 17, 28
finite-difference-time-domain (FDTD), 56
finite element method (FEM), 56
Fourier transformation (FT), 67
free-carrier absorption (FCA), 396
free-spectral range, 60
free-standing GaN substrates, 242–3
  schematic diagram and sawed cross-section of nonpolar substrate, 242
frequency locking, 526–9
  experimental set-up, 527
  QCL in a frequency-locked state, 528
full-width at half-maximum (FWHM), 69, 127, 450–1, 451–4

gain bandwidth
  spectral alignment, 325–7
    vs. cavity resonance, 325–7
gain clamping *see* gain saturation
gain-current relations, 34–42
  engineering and gain-current curve, 39–42
    elastic strain, 40–1
    p-doping, 41–2
    peak modal gain for thermal population at 300 k, 39
  parameterisation and optimisation, 37–8
  peak gain and radiative current, 34–6
    calculated spontaneous emission spectra, 35
    illustrative calculated peak modal gain vs radiative current density, 36
gain saturation, 63
gain-switching, 150–7
  basic features, 150–1
  theoretical foundations, 151–7
    schematics diagram of process, 153
gallium antimonide (GaSb)-based type-I quantum well diode lasers, 441–81
  diode lasers operating below 2.5 μm, 448–65
  diode lasers spectral range above 3 μm, 465–77
  metamorphic GaSb-based diode lasers, 477–81
  overview, 441–8
    band-edge positions for AlGaAsSb and GaInAsSb alloys, 442
    band gap positions of selected binary alloys, 442
    QW characteristics *vs.* 2D carrier concentration level, 444
gallium nitride lasers, 221–61
GaSb separate confinement layers, 498–500
  current-voltage-light characteristics for an IC laser, 499
  optical mode and refractive index, 498
Gaussian beam, 86
Ge-on-Si lasers, 398
Gen-III MBE system, 494
generalised New's model, 175
geometric power scaling, 96
green noise, 357
group III-nitride laser diodes, 221–62
  applications, 222–3
  bandgaps and lattice constants, 226–8
    energy gap vs in-plane lattice constant for wurtzite III-nitride material system, 227
  density of states, gain and transparency, 238–41
    polarised peak optical gain vs inclination angle, 240
  energy band diagram, 231–3
    ground-state wavefunctions, 232
  motivations for nonpolar and semipolar orientations, 233–4
  nonpolar and semipolar orientations, 224–6
    various crystal planes and associated values, 226
    various polar, nonpolar and semipolar orientations along with coordinate system, 225
  optical properties of nonpolar and semipolar, 234–41

group III-nitride laser diodes (*cont.*)
    density of states, gain and transparency, 238–41
    transition matrix element, band structure and polarised light emission, 234–8
  polarisation and internal electric fields, 228–31
    spontaneous polarisation, piezoelectric and elastic coefficients, 229
    total polarisation discontinuity along growth direction, 230
    unstrained, compressively, tensiley strained, nonpolar and semipolar films, 229
  properties, 223–34
    GaN crystal structure, 224
    values for lattice constraints, 224
  substrates, crystal growth, and material issues, 241–6
group velocity dispersion, 186

Hakki-Paoli method, 239–40, 456, 460
Haus model, 176–7
heat spreader, 346
heavy-hole (HH) state, 66
heterogeneous integration technology, 399, 400
high heat load (HHL), 599
high-index-contrast (HIC), 415, 417
high-reflection (HR) facet coating, 255–6
high-temperature-resistant semiconductor lasers
  design direction, 294–5
    enhancing maximum operation temperature, 295
  device characteristics, 295–8
    DFB lasers, 297–8
    FP lasers, 295–7
  device fabrication and characterisation, 293–4
    schematic structure of fabricated ridge FP laser, 294
  quantum-dot FP and DFB lasers applications, 292–9
    epitaxy and wafer characterisation, 293
    summary, 299
homogenous broad gain
    quantum-cascade laser, 600
hot-electron-bolometer (HEB), 529
hybrid mode-locking, 169
hybrid Si AWG lasers, 423–4
hybrid Si Fabry-Pérot (FP) lasers, 402, 407
hybrid Si platform, 399, 430
hybrid Si ring lasers, 422
hybrid silicon laser-based photonic integrated circuits, 425–30
  hybrid laser QWI process, 429
  hybrid Si SGDBR-EAM cross section, 430
  hybrid silicon integrated triplexer chip, 427
  laser array chip and four-channel DBR laser array, 427
  lasing spectra, threshold current and slope efficiency of lasers, 429
hybrid silicon lasers, 394–431
  fundamentals, 395–425
    basics, 398–408
    current flow and equivalent circuit, 404
    CW LI experimental results and theoretical predictions, 408
    energy band and major carrier transition processes, 395
    finite element hybrid laser structure dimension, 405
    fundamental TE mode profiles with different waveguide widths, 401
    III-V epitaxial layer structure, 400
    LI curves for hybrid Si FP laser, 403
    simplified fabrication process to form hybrid Si device platform, 399
    temperature 2D profile and electrical power dissipation, 406
  Si terabit transmitter, 431
hydride vapour phase epitaxy (HVPE), 242
Hydrogen Silsesquioxane (HSQ), 67

III-V DFB/DBR lasers, 410
III-V diode lasers, 401
III-V edge emitters, 405

III-V-on-Si directional coupler, 416
III-V ring resonator, 419
index-guiding, 159
indium, 244–5
indium lasers, 221–61
individually addressing array, 335
inductively coupled plasma reactive-ion etching (ICP-RIE), 68
integrated cavity output spectroscopy (ICOS), 585–7
interband cascade lasers (ICL), 107, 487–505
  early development and challenges, 492–7
    current-voltage-light characteristics, 495
    DFB laser wavelength tuning, 496
  future trends, 503–5
    maximum temperature *vs.* wavelength for mid IR Sb-based interband diode lasers, 504
  operating principle, 488–91
    energy band-edge diagram, 490
    forward bias, 488
    W-shape QW active regions, 491
  recent progress and new developments, 497–503
intermodal wavelength distance, 557–5, 560
internal differential quantum efficiency, 15
internal quantum efficiency, 83
intracavitary reflectors (ICR), 195
intracavity frequency control, 352–67
intracavity optics, 347–8

Jaynes-Cummings Hamiltonian, 60

Lang-Kobayashi model, 138–40
large mode-area lasers
  master-oscillator power amplifiers, 98
  slab-coupled optical waveguide lasers (SCOWL), 100–2
    schematic cross-section and example of modal index vs modal loss, 101
  surface-emitting distributed Bragg feedback lasers (SE-DFB)
    plan-view of curved grating and schematic of an electrically-injected SE-DFB, 103
  tapered unstable resonator lasers (TURL)
    integrated high-brightness laser examples, 99
large-signal harmonic modulation, 150
laser absorption spectroscopy, 581–4
  absorption spectra in two mid-infrared atmospheric transmission windows, 582
laser diode
  nonpolar and semipolar performance, 256–60
    CW light vs current for high-power blue MM single emitter LDs, 258
    lasing wavelength progression vs time, 259
    light vs current and WPE vs light for blue and green SM LDs, 258
    progress in peak WPE and output power vs time for blue and green LD, 259
    threshold current density vs lasing wavelength, 260
laser diode arrays
  external cavity broad-area, 125–38
    close V-shape external cavity for an individual broad-area laser diode, 133
    CW L-I characteristic of AR-coated broad-area laser diode array, 136
    effective external Talbot cavity, 128
    experimental results of far-field profile and numerical simulation, 128
    far-field profile and spectrum of phase-locked laser array, 130
    measurements for far-field profile and spectrum at injection current 32A, 137
    results of far-field profile and spectrum of phase-locked laser array at 60A, 138
    schematic design of V-shape external cavity, 126

laser diode arrays (*cont.*)
    schematic diagram of close V-shape external cavity, 132
    transition between incoherent and coherent addition, 130
    two-different symmetric far-field profiles, 135
    unfolded close V-shape external cavity, 134
    V-shape external cavity for individual broad-area laser diode, 127
laser stripe orientation, 253
lateral confinement, 327–9
  oxide-confined VCSEL aperture, 328
lateral waveguides, 249–50
left hand circularly polarised (LHCP) light, 593
light emitting diode (LED), 225, 493
light extraction
  WGM resonator, 572–4
    operating half-disk QWGM laser, 573
    vertically emitting WGM laser with the matched waveguide, 575
    WGM laser with suppressed counterclockwise (CCW) mode, 574
light-hole (LH) state, 66
lineshape functions, 18
linewidth enhancement factor (LEF), 525–6
  difference-frequency spectrum between two Fabry-Perot modes and multi-model QCL, 525
local area network (LAN), 282
longitudinal confinement, 319–23
  Al, C, and Si concentration as a function of depth into a VCSEL, 323
  calculated VCSEL reflectance spectrum, 323
  oxide-confined VCSEL, 321
  refractive index and optical density profile in the optical cavity, 322
Lorentzian, 17
low-pressure metal-organic chemical vapour deposition (LP-MOCVD), 92
magnetic circular birefringence (MCB), 594
master-oscillator power amplifiers (MOPA), 98
matrix addressing array, 335
maximum output power, 87–9
  appropriate power densities necessary to cause COMD in different QW materials, 89
Maxwell's equation, 17–18
metal-metal (MM) microcavities
  surface-emitting second-order DFB THz QCL, 521–3
  THz QCL emission characteristics, 519–20
    single-bias optical spectrum and parallel-plate ridge cavity, 519
metal-metal (MM) waveguides, 516–19
  dimensional electromagnetic mode calculations for the fundamental lateral mode, 518
metal-organic chemical vapour deposition (MOCVD), 57
metamorphic GaSb-based diode lasers, 477–81
  band edges position on absolute energy scale, 478
  CW power and power-conversion characteristics of AR/HR coated devices, 481
  virtual substrate, 480
micro channel cooled packages (MCCP), 110
microelectromechanical systems (MEMS), 599
microwave modulation, 534–5
  diode laser normalised modulation response, 535
  microwave attenuation *vs.* frequency for MM waveguide ridge, 536
mid infrared diode lasers, 443
mid-infrared WGM lasers, 566
minimum detection limit (MDL), 603
modal analysis, 172
modal gain spectra, 456
mode-locked integrated external cavity surface-emitting laser (MIXSEL), 193, 375–6

mode-locked semiconductor disk lasers, 372–6
  configurations, 374
  SESAM characteristics, 373
  ultrashort pulse generation, 374
  wavelength diversification, 375
mode-locking (ML), 166–81
  general principles and place of SLs among Ml laser sources, 166–8
  important tendencies in optimising the ML laser performance, 187–96
    achieving a high gain-to-absorber saturation energy ratio, 188–9
    bit rate engineering, 194–6
    increasing optical power and broadening the effective modal cross-section, 190–3
    stability and pulse duration by reducing saturable absorber recovery time, 189–90
  laser behaviour, 183–7
    gain and group velocity dispersion parameters, 185–6
    gain suppression and absorber compression coefficients, 186–7
    gain suppression and absorber linewidth enhancement factors, 187
    s-factor or absorber to gain saturation energy ratio, 184
    simulated dependence of pulse amplitude and duration on pumping current, 185
    typical simulated dependence of pulse duration on absorber recovery time, 186
  modelling progress, 170–81
    bifurcation analysis of steady-state solutions of DDE model, 178
    bifurcation diagram by direct numerical implementation of DDE model, 179
    stability boundaries of ML with respect to leading and trailing edge instabilities, 177
  novel principles, 196–206
    femtosecond pulse generation by mode-locked vertical cavity lasers, 202–3
    miniaturisation and integration and ring and microring resonator cavities, 205–6
    quantum dot materials, 197–202
    spontaneous mode-locking in single-section lasers, 203–5
  predictions, 181–7
    main parameters that affect ML laser behaviour, 183–7
    operating regime depending on operating point, 182–3
  techniques, 168–9
    mechanism of passive ML, 169
molecular beam epitaxy (MBE), 57, 275, 492, 499
multiple quantum well (MQW), 400–1

narrow asymmetric waveguide lasers, 158–9
near-infrared (NIR) camera, 69
near-infrared WGM lasers, 565
non-linear frequency conversion, 357–67
  crystal used for second order (parametric) non-linear frequency conversion, 360
  crystalline Raman laser, 366
  output power for InGaAs-based semiconductor disk laser, 361
  Raman gain crystal properties, 367
  Raman Stokes scattering via a virtual energy level, 365
  SDL cavity configurations, 363
  sum-frequency generation (SFG), SHG and DFG energy level, 359
  ultra-compact, frequency-doubled SDL, 362
non-radiative processes, 34
numerical simulation
  semiconductor laser array, 144
    parameter values for laser diode, 142
    time series of chaotic output intensity from array element 1 and total intensity, 143

numerical simulation (*cont.*)
    time series of chaotic output intensity from elements 45 and 49, 143
    time series of chaotic output intensity with external cavity feedback, 142

off-axis integrated cavity output spectroscopy (OA-ICOS), 585–6
operating regime
  depending on operating point, 182–3
    schematic diagrams in generic QW mode-locked laser operating at 40GHz, 183
optical cavity, 323–5
optical coherence tomography (OCT), 207
optical communication, 206
  Fabry-Pérot and distributed feedback (DFB) lasers, 282–92
    current trends in semiconductor lasers, 282–3
    quantum-dot DFB lasers, 288–92
    quantum-dot FP lasers, 283–8
optical gain, 286–7
  roadmap of quantum dot properties, 276–7
    formation methods shows how to improve to increase peak optical gain, 276
optical loss, 246–53, 250–2
optical network units (ONU), 289
optical power
  broadening the effective modal cross-section, 190–3
    schematic of tapered QD laser and achieved pulse, 192
optical spectrum analyser (OSA), 69
optical time-division multiplexing (OTDM), 204
optical waveguides
  birefringence, 252–3
    mode orientations for LDs with stripes oriented along projection of c and m-axis, 253
  lateral waveguides, 249–50
    layer structure and etch depth vs etch time for LD, 250
  optical loss, 246–53, 250–2
    laser stripe orientation, 253
    layer structure, transverse optical mode profile and index of refraction, 251
  transverse waveguides, 246–9
optically pumped semiconductor laser (OPSL), 108
optimisation, 37–9
optoelectronic integrated circuits (OEIC), 205
output beam, 347
output coupler, 346
oxide-confined vertical cavity surface emitting lasers, 328, 329

p-doping, 41–2
Padé approximation, 155
parameterisation, 37–9
  cavity length and multiple quantum wells, 37–8
    modal gain vs radiative current density for 1,2 and 3 identical quantum wells, 38
  gain-current parameters, 37
passivation techniques, 90–1
passive mode-locking, 168–9
passive Q-switching, 161
phase locking, 529–33
  electro-optical detection and spectral envelope of amplitude-modulated optical beams, 531
  experimental set-up, 530
  unlocked and locked RF spectra, 533
photoacoustic (PA) cell, 587–8
photolithography, 255
photoluminescence (PL), 66, 233, 276
photonic bandgap (PBG), 56, 159
photonic crystal disk lasers, 72–4
  images with different scaling factors and electric field density profile, 73
  schematic and SEM images, microdisk laser and photonic crystal nanobeam laser, 72
  SEM images and L-L curve and log-log plot and lineshape of lasing mode, 75

photonic crystal lasers, 56–76
  disk, 72–4
  first reported PhC laser, 58
  future trends, 74–6
  lasing threshold, 60–5
    purcell effect and β factor, 60–2
    rate equations, 63–5
  nanobeam, 65–71
    material system layout of semiconductor QW sample, 65
  schematic diagram and SEM micrograph of buried heterostructure PhCL, 59
photonic crystal nanobeam lasers
  cavity design, 66–7
    cavity mode, spatial fourier transform and second-order mode profile, 68
    layout, 67
  characterisation, 69–71
    laser emitted power, spectrum of emitted light, output of laser power and polarisation dependence, 70
    log-log plot of L-L curve, 71
    measurement setup, 69
  fabrication, 67–9
    scanning electron micrograph images, 69
  material system, 65–6
    energy band diagram, LH and HH band and PL emission spectrum, 66
photonic integrated circuits (PIC), 398
pico projector, 223, 303
Planck law, 16
plasmon waveguide IC lasers
  InAs substrates, 501–3
    lasing spectrum, 503
    optical modal and refractive index profiles, 502
Poisson's equation, 234
polarisation, 228–31
polarised light emission, 234–8
potential well confinement, 19–22
  envelope function in quantum wells, 19–21
    energy vs *k* curves for in-plane electron motion and hole confined states, 21
  quantum dots, 21–2
  solutions for Schrodinger's equation in conduction and valence band diagram, 20
power conversion efficiencies (PCE), 84
power scaling, 110–12
process laws, 34
pulsed current injection, 407
pulsed-pumped semiconductor disk lasers, 367–70
  average temperature evolution of active region, 368
  continuous-wave and quasi-continuous-wave pumping performance, 369
  gain-switched SDL, 370
  power transfer of continuous-wave diamond Raman laser, 368
pump beam, 346
Purcell effect, 60–2
pure dephasing, 18
pyramidal hillocks
  basal-plane stacking faults, 243–4
    Nomarski optical micrograph, schematic and panchromatic cathodoluminescence image, 244

Q-switching, 160–5
  foundations of theory, 161–4
    stability limits of Q-switched SL operation, 163
  main features, 160–1
    schematic diagram of monolithic two-section lasers, 162
  passive applications, 164–5
QD Laser, Inc., 299–303
  DFB lasers on GaAs substrates, 301
  mass production of quantum-dot FP lasers for optimal communication, 301
  MBE crystal growth, 299–301
    growth system and photoluminescence peak wavelength mapping, 300

QD Laser, Inc. (*cont.*)
  other products, 301–3
    1000-1120 nm DFB lasers for material processing and sensing, 303
    green, yellow and orange lasers, 303
    product images, 302
quantum approach, 16–17
  normalised homogenous broadening Lorentzian lineshape, 17
quantum cascade, 106–9
quantum cascade lasers (QCL), 487, 488, 489, 496, 505
  broad gain medium designs, 599–600
  sensor systems, 601–17
  trace gas detection, 595–600
quantum-confined Starck effect (QCSE), 232
quantum-dot distributed feedback (DFB) lasers, 282–92, 288–92, 297–8
  CW L-I curves of QD DFB laser from 25°C to 150°C, 298
  device structure, fabrication and gain characteristics of high-density QDs, 289–91
    AFM image of high-density QDs and gain characteristics at 25°C, 290
    schematic structure of DFB laser on GaAs structure, 290
  DFB lasers for 10G-EPON (ethernet passive optical network), 288–9
  lasing spectra of QD DFB laser with output power of 4mW at 100, 125 and 150°C, 298
  light current and modulation characteristics, 291–2
    10.3-Gb/s eye diagram, 292
    L-I characteristics and lasing spectra at 5 mW, 291
quantum-dot Fabry-Pérot lasers, 282–92, 283–8
  CW L-I curves of QD FP laser from 30 to 220°C, 296
  laser design for high-speed modulation, 283–5
  lasing spectrum, 285–6
  light current and modulation characteristics, 287–8
    high-mesa waveguide FP laser characteristics in continuous wave condition, 287
    room temperature eye diagrams at 20 and 25 Gbps modulations, 288
    small signal modulation characteristics, 288
  optical gain, 286–7
    net modal gain curves as current density function, 286
  preliminary ageing test result, 297
  temperature dependence on centre lasing wavelength for QD FP laser at 30-220°C, 296
quantum dot lasers
  advanced self-assembled indium arsenide (InAs), 272–310
    active regions and electron density of states, 273
    Fabry-Pérot and distributed feedback (DFB) lasers, 282–92
    FB and DFB lasers for high temperature application, 292–9
    QD Laser, Inc., 299–303
    silicon hybrid, 303–9
quantum dots, 21–2, 27–32, 44–6, 349–51
  materials, 197–202
    optical spectrum and RF spectrum of dual wavelength mode, 201
    optical spectrum and sub-picosecond pulse from two-section QD laser, 198
    pumped-probe measurements of QS SA, 200
  occupation of dot states, 30–2
    calculated modal gain spectra, 32
    determined by capture and emission of carriers from and to wetting layer, 30
    rate equation calculations of ground and first excited states, 31
  optical gain, 28–30
    homogeneously broadened transitions, 29
    localised states in an isolated quantum dot, 28

  temperature dependence of radiative current density, 45
quantum efficiency, 14–15
quantum threshold, 64–5
quantum well intermixing (QWI), 428
quantum well lasers type II, 106–9
quantum wells (QW), 22–7, 43–4, 342, 349, 351, 488, 489, 490
  gain equation implementation, 26–7
    spectra for transitions between a single pair of sub-bands, 27
  modal gain and local or material origin, 25–6
  optical transition at photon energy, 25
  thin gain region, 25–6
  true spontaneous emission spectrum measurements and exhibit dependence, 43
quartz-enhanced photoacoustic spectroscopy (QEPAS), 587–92
  CRDS based sensor platform using AOM, 586
  PA cell design, 589
  real time ammonia detection in exhaled human breath, 608–12
    2f WM QEPAS signal, 611
    NH_3 breath sensor architecture, 609
    NO_2 FRS signal, 607
    optical power and current tuning and NH_3 absorption line, 609
quartz tuning fork (QTF), 588–92
quasi-Fermi level, 27
quasi whispering gallery mode (QWGM), 555, 562–3

R3 lasers, 416–17
racetrack ring resonator (R3), 415
rapid thermal anneal (RTA), 428
rate equations, 46–8
  formulations, 46–7
  small signal modulation response, 48–9
    model calculations, 48
  steady state solutions, 47
ray optics, 553–4
recombination processes, 32–4
  non-radiative processes and process laws, 34
  spontaneous emission, 33
relative intensity noise (RIN), 356
resonant periodic gain (RPG), 103
resonator mode wavelength, 554
RF-injection locking, 535–9
  f_{RT} of a MM waveguide THz QCL, 538
  measurement set-up for MM waveguide THz QCL, 537
  mechanism, 536
  MM QCL, 538
RF-synthesisers, 542
right hand circularly polarised (RHCP) light, 593

saturable absorbers (SA), 159
saturation carrier density, 63
scanning electron microscope (SEM), 255–6
Schockley-Read-Hall (SRH), 107
Schrodinger's equation, 234
second harmonic generation (SHG), 223
  devices, 303
second-order Bragg grating, 523
self-assembled quantum dots
  optical devices, 274–6
    schematic illustration InAs QD formation on GaAs surface, 275
self-consistent profile (SCP), 170
self-(injection) seeding, 160
semi-insulating single-plasmon (SISP) waveguides, 516–19
  dimensional electromagnetic mode calculations for the fundamental lateral modes, 518
semiconductor disk lasers (SDL), 341–78
  further reading lest, 377
  future trends and applications, 376–8
  intracavity frequency control, 352–67
  principles of operation, 342–52
    design features and performance characteristics, 344–8
    fundamental spectral coverage, 353
    gain structure semiconductor bandgap profile and active region optical field, 343
    GaInP quantum wells and InP quantum dots, 350

semiconductor disk lasers (*cont.*)
    materials, 348–52
    normalised laser emission spectra of a PbSe/PbSrSe multiquantum-well, 353
    wavelength range for all semiconductor material systems, 343
  pulsed operation, 367–76
semiconductor lasers
  absorption and gain in low dimensional semiconductor structures, 22–32
    quantum dots, 27–32
    quantum wells, 22–7
    slab waveguide geometry for calculation of optical gain, 23
  array model, 140–2
  beam combining, 121–45
    experiments on external cavity broad-area laser diode arrays, 125–38
    modelling of a single-mode semiconductor laser array in external cavity, 138–42
  developments in gain-switched, 157–60
    gain switching structures with saturable absorbers (SA), 159
    narrow asymmetric waveguide lasers and related structures, 158–9
    single-heterostructure lasers, 157–8
    spectral properties and control, 159–60
  device characteristics, 83–9
    brightness and beam quality factor, 85–7
    maximum output power, 87–9
    spectral linewidth and stability, 87
    temperature, 84–5
  failure mechanisms, 89–91
    catastrophic facet failure and passivation techniques, 90–1
  general high-power quantum well design concepts, 81–3
    schematic of high-power FP laser, 82
  high-power, 81–112
    array concept for power scaling, 110–12
    future trends, 112
    single emitters, 92–109
  key physical concepts, 16–22
    confinement in a potential well, 19–22
    light and matter interaction, 16–18
  mode-locking (ML), 166–81
    general principles and place of SLs among Ml laser sources, 166–8
    techniques, 168–9
  operation principles, 4–6
    energy band diagram of conduction and valence band edges, 6
    generic diode laser chip, 5
  principles, 3–50
    basic laser diode, 7–15
    future trends, 49–50
    gain-current relations, 34–42
    historical background, 3–4
    rate equations, 46–8
    recombination processes, 32–4
    temperature dependence of threshold current, 42–6
  ultrafast pulse generation, 149–208
    gain-switching, 150–7
    important tendencies in optimising the ML laser performance, 187–96
    main predictions of mode-locked laser theory, 181–7
    mode-locked diode lasers applications, 206–7
    novel ML principles, 196–206
    Q-switching, 160–5
semiconductor saturable absorber mirror (SESAM), 372–5
semiconductor WGM lasers, 565–72
  current density distribution, 569
  device lasing spectra, 567
  disk WGM laser, 566
  etched mesa, 568
  half-ring contact and spectrum, 570
  memory element, 572
  mode position dependence on the pulse duration and Joule heat, 571
  WGM lasers below and above threshold current, 568

separate confinement heterostructure (SCH), 4, 400
Shockley-Read-Hall (SRH), 14, 34
Shockley-Read-Hall (SRH) recombination, 240
Si PIC lasers, 408, 425–6
side-mode suppression ratios (SMSR), 291
silicon hybrid quantum-dot lasers, 303–9
  III-V quantum-dot lasers on Si substrates by heteroepitaxial growth, 304–6
    cross-sectional schematic of In0.5Ga0.5As QD laser heterostructure, 305
    room temperature photoluminescence spectra and bright-field TEM image, 305
  III-V quantum-dot lasers on Si substrates by wafer bonding, 306–7
    cross-sectional TEM image of fabricated InAs/GaAs QD laser, 307
  III-V quantum-dot-photonic crystal nanocavity lasers on Si substrates, 308–9
silicon light emitters, 397–8
silicon photonics, 394, 430
silicon Raman lasers, 397
single emitters, 92–109
  broad-area Fabry-Pérot lasers, 92–3
  high-power distributed feedback and distributed Bragg reflector lasers, 93–6
    peak gain wavelength and spectral resolve gain, 94
    wavelength stabilisation through external VBG and internal DBR, 95
  large mode-area lasers, 96–103
    master-oscillator power amplifiers, 98
    slab-coupled optical waveguide lasers and other large-mode-volume lasers, 100–2
    surface-emitting distributed Bragg feedback lasers, 102–3
    tapered unstable resonator lasers, 98–100
  long-wavelength approaches, 106–9
    Auger recombination coefficient, 108
    room-temperature continuous wave semiconductor laser, 109
  vertical external-cavity surface-emitting laser, 103–6
    schematic of canonical OP-VECSEL cavity, 104
single-frequency lasers, 446
single-frequency operation, 353–7
  actively stabilised SDL, 355
  narrow-linewidth single-frequency SDL, 355
  schematic diagram, 35
single-heterostructure lasers, 157–8
single-mode terahertz (THz) quantum cascade lasers (QCL)
  beam profile, 523–5
    two dimension narrow beam patterns, 524
  periodic photonic cavities, 520–1
    distributed Bragg grating, 521
slab-coupled optical waveguide lasers (SCOWL), 100–2
spectrally selective laser cavity, 195
spontaneous emission, 33
Stranski-Krastanov growth mode, 275
stress relaxation, 245–6
stroboscopic technique, 165
substrate, 344–5
surface-emitting distributed Bragg feedback lasers (SE-DFB), 102–3
surface-emitting second-order DFB lasers, 521–3
  operating principles and experimental results, 521

T_0 parameter, 42–3
tapered unstable resonator lasers (TURL), 98–100
terahertz (THz) quantum cascade lasers (QCL), 514–45
  stabilisation, microwave modulation and active mode-locking, 525–45
    perspectives, 542–5

terahertz (THz) quantum (*cont.*)
  state of the art, 514–16
  waveguides and photonic structures, 516–25
    emission characteristics with metal-metal microcavities, 520
    metal-metal *vs.* semi-insulating single-plasmon waveguides, 516–19
    single-mode dimension beam profile, 523–5
    single-mode with periodic photonic cavities, 520–1
    surface-emitting second-order DFB in metal-metal microcavities, 521–3
thermal electric controller (TEC), 402
third-order Bragg grating, 523
time-domain lumped models, 170
transition matrix element
  band structure and polarised light emission, 234–8
    normalised matrix element, effective mass and quasi-Fermi levels separation, 238
    square of electron and hole wavefunction overlap vs inclination angle, 235
    valence band dispersion curves, 236
transmission electron microscope (TEM), 278
transversal electric (TE) modes, 556–7
transversal magnetic (TM) modes, 556–7
transverse optical modes, 332–4
  multi-mode VCSEL emission, 332
  single mode photonic crystal VCSEL, 333
transverse waveguides, 246–9
  cross-section of typical ACF ridge laser, 247
  index contrast between GaN and In0.04Ga0.96N and GaN and Al0.05Ga0.95N vs wavelength, 249
  typical design for c-plane LD, 248
  typical design for nonpolar ACF LD, 248
travelling-wave resonator, 415, 421
travelling-wave model, 171
tunable mid-infrared laser absorption spectroscopy, 579–618
  future trends, 617–18
  laser absorption spectroscopic techniques, 581–94
  quantum-cascade lasers (QCL) based sensor systems, 601–17
  quantum-cascade lasers (QCL) for trace gas detection, 595–600
tuneable single-frequency operation, 354
type-I quantum well (QW) lasers, 491, 500
type-II interband cascade (IC) lasers, 490, 492
type-II quantum well (QW) lasers, 490, 491, 499, 504

ultra-broad gain quantum-cascade laser, 600
ultrafast pulse generation
  semiconductor lasers, 149–208
    developments in gain-switched, 157–60
    gain-switching, 150–7
    important tendencies in optimising the ML laser performance, 187–96
    main predictions of mode-locked laser theory, 181–7
    mode-locked diode lasers applications, 206–7
    mode-locking (ML), 166–9
    novel ML principles, 196–206
    Q-switching, 160–5
unstable resonator, 99

variable stripe length (VSL) method, 239
Varian Gen-II MBE system, 493
Vegard's Law, 228
vertical cavity lasers, 46
vertical cavity surface emitting lasers (VCSEL), 57, 316–37, 399, 447, 505
  device structure, 319–29

  - optical performance, 329–35
    - hexagonal individually and square matrix VCSEL array, 335
    - light and voltage curves *vs.* injection current, 329, 330
    - light *vs.* injection current, 331
    - output and efficiency, 329–32
    - threshold current and differential slope efficiency, 331
    - two-dimensional arrays, 334–5
  - overview, 316–19
    - applications, 317–19
    - history, 317
- vertical external-cavity surface-emitting laser (VECSEL), 103–6
  - intracavity functionality enabling, 105–6
    - frequency-doubled, single longitudinal-mode and intracavitary birefringent filter, 106
  - power scaling, 104–5
    - schematic setup of two-chip VECSEL vs performance of single and two-chip, 105
- vertical external cavity surface-emitting lasers (VECSEL), 181
- virtual substrates, 479
- volume Bragg grating (VBG), 94

- W-active-region IC lasers, 493
- W-QW IC laser, 491
- wafer bonding, 306–7
- wall-plug efficiency (WPE), 223
- wavelength division multiplexing (WDM), 204, 426
- whispering gallery mode (WGM), 551–5
  - basic ray for two modes in a circle, 553
  - Bessel function for index $m = 600$, 552
  - chaotic and bouncing-ball bow-tie mode, 556
  - electrodynamics, 555–64
    - modes frequencies of metallic and dielectric disk resonators, 562
    - quasi-WGM and bouncing-ball mode with close frequencies, 563
    - QWGM modes in a dielectric disk with quantum dot, 564
    - wavelength positions, 558
  - family rays and common mode, 553
- whispering gallery mode (WGM) lasers, 551–76
  - light extraction from WGM resonator, 572–4
  - semiconductor, 565–72
  - whispering gallery mode (WGM) in electrodynamics, 555–64
- whispering gallery mode (WGM) resonator
  - light extraction, 572–4
    - operating half-disk QWGM laser, 573
    - vertically emitting WGM laser with the matched waveguide, 575
    - WGM laser with suppressed counterclockwise (CCW) mode, 574